Transactions of the ASME®

Journal of Applied Mechanics

Published Quarterly by The American Society of Mechanical Engineers

VOLUME 62 • NUMBER 1 • MARCH 1995

Transactions of the ASME, Journal of Applied Mechanics (ISSN 0021-8936) is published quarterly (Mar., June, Sept., Dec.) for $185.00 per year by The American Society of Mechanical Engineers, 345 East 47th Street, New York, NY 10017. Second class postage paid at New York, NY and additional mailing office. POSTMASTER: Send address changes to Transactions of the ASME, Journal of Applied Mechanics, c/o THE AMERICAN SOCIETY OF MECHANICAL ENGINEERS, 22 Law Drive, Box 2300, Fairfield, NJ 07007-2300.

CHANGES OF ADDRESS must be received at Society headquarters seven weeks before they are to be effective. Please send old label and new address.

PRICES: To members, $40.00, annually: to nonmembers, $185.00.
Add $30.00 for postage to countries outside the United States and Canada.

INDEXED by Applied Mechanics Reviews and Engineering Information, Inc. Canadian Goods & Services Tax Registration #126148048

TECHNICAL PAPERS

(Contents continued on Outside Back Cover)

BRIEF NOTES

BOOK REVIEWS

ANNOUNCEMENTS AND SPECIAL NOTES

ISSN 0021-8936 JOURNAL CODE JE ISSUE CODE 9501

Stress Transmission in Polycrystals With Frictionless Grain Boundaries

G. J. Rodin
Department of Aerospace Engineering
and Engineering Mechanics,
The University of Texas at Austin,
Austin, TX 78712
Assoc. Mem. ASME

A simple method of analysis of stress transmission in polycrystals with frictionless grain boundaries is presented. This method applies to a large class of two-dimensional and three-dimensional polycrystals which can be modeled as either periodic or disordered arrays of polyhedra. Calculations are performed for the periodic arrays of rhombic dodecahedra and truncated octahedra, and for arrays generated by the Voronoy tessellation of disordered point lattices. Results of these calculations show that normal stresses transmitted by frictionless grain boundaries are significantly different from applied stresses. In particular, it is predicted that, in disordered polycrystals subjected to uniaxial compression, 45 percent of grain boundaries are in tension and the maximum tensile stress is one half of the applied stress.

1 Introduction

In this paper, we are concerned with stress transmission in polycrystals with frictionless grain boundaries. This idealization of polycrystals is relevant to their behavior under conditions encountered during high-temperature service and fabrication. Under those conditions, it is common that grain boundary shear tractions are rapidly relaxed as a result of easy transport of matter along grain boundaries. The transport occurs either by grain boundary diffusion or flow of an intergranular liquid phase, or a combination of these two mechanisms. The objective of this paper is to evaluate the average normal stresses transmitted by individual grain boundaries or, following Nix et al. (1989), the facet stresses.

So far, the facet stresses have been determined for periodic arrays of regular squares, hexagons, cubes (Beere, 1982), and truncated octahedra (Anderson and Rice, 1985; Dib and Rodin, 1993). In this paper we develop an approach relevant to both periodic and disordered arrays. The present approach is motivated by the observation that the facet stresses in some periodic arrays can be determined directly from the equilibrium equations. In two dimensions this can be done for the periodic array of regular hexagonal homogeneous grains; a three-dimensional example is the periodic array of rhombic dodecahedra (the surface of the rhombic dodecahedron is formed by 12 rhombic faces). In contrast, in the periodic array of truncated octahedra (the surface of the truncated octahedron is formed by six square and eight hexagonal faces), the number of independent facet stresses exceeds the number of independent equations by one. In the present approach, such statical indeterminacy is resolved with a stress-based variational principle which generalizes the one proposed by Anderson and Rice (1985) for the periodic array of truncated octahedra. The variational principle proposed here applies to periodic and disordered arrays alike.

This paper is organized as follows. In the text section, we analyze three-dimensional periodic arrays with special emphasis on those which exhibit central symmetry. Specific examples include the periodic arrays of rhombic dodecahedra and truncated octahedra. Also, Section 2 should be regarded as background for Section 3 where we focus on disordered arrays. In Section 4, we summarize results for both two-dimensional and three-dimensional arrays and discuss certain implications of our analysis for micromechanical constitutive modeling.

Throughout the paper we interchange the geometrical terms, face, and polyhedron with the corresponding physical terms, grain boundary, and grain.

2 Three-Dimensional Periodic Arrays

2.1 Equilibrium Equations. In this section, we derive equilibrium equations for the representative polyhedral grain $\mathcal{P}$ of a general three-dimensional periodic array in terms of the resultants acting on the grain boundaries. Since it is supposed that the grain boundaries are frictionless, there are only three nonzero resultants per grain boundary. The total number of equilibrium equations for the grain is 12. Beside the six standard equations, there are six equations which relate the resultants to a prescribed macroscopic stress.

First let us consider a finite planar surface $\mathcal{S}$ subjected to normal tractions. For this surface we introduce a Cartesian

Contributed by the Applied Mechanics Division of THE AMERICAN SOCIETY OF MECHANICAL ENGINEERS for publication in the ASME JOURNAL OF APPLIED MECHANICS.

Discussion on this paper should be addressed to the Technical Editor, Professor Lewis T. Wheeler, Department of Mechanical Engineering, University of Houston, Houston, TX 77204-4792, and will be accepted until four months after final publication of the paper itself in the ASME JOURNAL OF APPLIED MECHANICS.

Manuscript received and accepted by the ASME Applied Mechanics Division, May 25, 1993. Associate Technical Editor: G. J. Dvorak.

coordinate system with the origin at the centroid of $\mathcal{S}$ and base vectors $\mathbf{e}_1$, $\mathbf{e}_2$, and $\mathbf{n}$. In this coordinate system, the vector $\mathbf{n}$ is normal to $\mathcal{S}$ and the position vector of a point $\mathbf{y} \in \mathcal{S}$ is $\mathbf{y} = y_1\mathbf{e}_1 + y_2\mathbf{e}_2$. In the absence of shear tractions, the traction field on $\mathcal{S}$ is of the form $\mathbf{t}(\mathbf{y}) = \sigma(\mathbf{y})\mathbf{n}$, and the nonzero resultants of $\sigma(\mathbf{y})$ are

$$N = \int_{\mathcal{S}} \sigma(\mathbf{y})dA, \quad M_1 = \int_{\mathcal{S}} y_2\sigma(\mathbf{y})dA,$$

$$\text{and } M_2 = -\int_{\mathcal{S}} y_1\sigma(\mathbf{y})dA. \quad (1)$$

Here N is the normal force, M_1 is the counterclockwise moment about the y_1-axis, and M_2 is the counterclockwise moment about the y_2-axis. The moments M_1 and M_2 are the only nonzero components of the torque vector,

$$\mathbf{T} \overset{\text{def}}{=} \int_{\mathcal{S}} \mathbf{y} \times \mathbf{t}(\mathbf{y})dA = M_1\mathbf{e}_1 + M_2\mathbf{e}_2, \quad (2)$$

and of the dipole tensor,

$$\mathbf{D} \overset{\text{def}}{=} \frac{1}{2}\int_{\mathcal{S}} [\mathbf{y} \otimes \mathbf{t}(\mathbf{y}) + \mathbf{t}(\mathbf{y}) \otimes \mathbf{y}]dA$$

$$= \frac{1}{2}[-M_2(\mathbf{e}_1 \otimes \mathbf{n} + \mathbf{n} \otimes \mathbf{e}_1) + M_1(\mathbf{e}_2 \otimes \mathbf{n} + \mathbf{n} \otimes \mathbf{e}_2)]. \quad (3)$$

The facet stress on $\mathcal{S}$ is defined as the average of $\sigma(\mathbf{y})$.

In a periodic array, the volume of the representative polyhedron is denoted by V and the centroid, which is also chosen as the origin for the position vectors, by O. For each face, $\mathcal{S}_\alpha$, $\alpha = 1, \ldots, p$, we denote the outward unit normal by $\mathbf{n}_\alpha$ and the centroid by O_α; the position vector of O_α is denoted by $\mathbf{l}_\alpha$. If the array is subjected to a uniform macroscopic stress $\bar{\boldsymbol{\sigma}}$, the equilibrium equations for $\mathcal{P}$, evaluated with respect to O, are

$$\sum_{\alpha=1}^{p} N_\alpha \mathbf{n}_\alpha = \mathbf{0}, \quad (4)$$

$$\sum_{\alpha=1}^{p} N_\alpha \mathbf{l}_\alpha \times \mathbf{n}_\alpha + \mathbf{T}_\alpha = \mathbf{0}, \quad (5)$$

and

$$\sum_{\alpha=1}^{p} \frac{1}{2} N_\alpha(\mathbf{l}_\alpha \otimes \mathbf{n}_\alpha + \mathbf{n}_\alpha \otimes \mathbf{l}_\alpha) + \mathbf{D}_\alpha = V\bar{\boldsymbol{\sigma}}. \quad (6)$$

Here N_α, $\mathbf{T}_\alpha$, and $\mathbf{D}_\alpha$ are defined for $\mathcal{S}_\alpha$ according to (1)–(3). Equation (6) is obtained by integrating a divergence-free stress field inside $\mathcal{P}$ (Hashin, 1983).

There are $3p$ unknowns in the 12 equilibrium equations, thus, in general, only periodic arrays formed by tetrahedra can be regarded as statically determinate. Those arrays, however, do not resemble real polycrystals, which have about 13 faces per grain and five edges per face (Underwood, 1970), so it is desirable to supplement (4)–(6) with additional equations for the resultants. Typically, such equations have to be derived from compatibility conditions and constitutive equations. Nevertheless, in some cases it is possible to invoke symmetry conditions such that additional equations can be derived without introducing the strain field.

2.2 Arrays With Central Symmetry. In this section, we demonstrate that, in the presence of central symmetry, (4)–(6) can be substituted by a system of six equations for $p/2$ unknowns. As a result, polyhedra with up to 12 faces can be treated as statically determinate.

Definition: The polyhedron $\mathcal{P}$ possesses central symmetry, or is symmetric about O, if and only if $\mathbf{x} \in \mathcal{P} \Rightarrow -\mathbf{x} \in \mathcal{P}$.

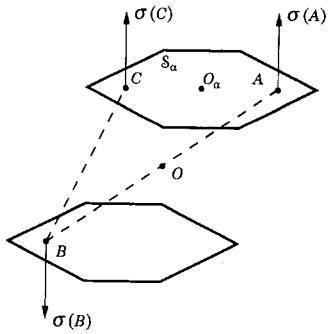

Fig. 1 Periodic arrays with central symmetry: The face $\mathcal{S}_\alpha$ and the face opposite to it. The points *A* and *B* are related by symmetry, and *B* and *C* by periodicity.

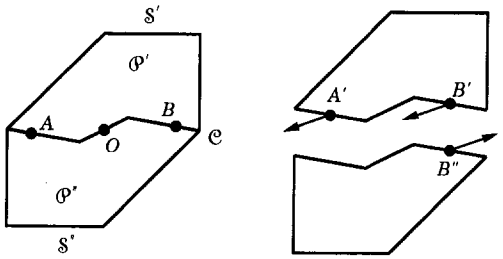

Fig. 2 Periodic arrays with central symmetry: the cut by the surface $\mathcal{C}$. The arrows designate the traction vectors.

Definition: A tensor field $\mathbf{F}(\mathbf{x})$ of rank r possesses central symmetry, or is symmetric about O, if and only if $\mathcal{P}$ is symmetric about O and $\mathbf{F}(\mathbf{x}) = (-1)^r\mathbf{F}(-\mathbf{x})$, $\forall \mathbf{x} \in \mathcal{P}$.

Dib and Rodin (1993) have shown that if $\mathcal{P}$ is symmetric about O and the material comprising $\mathcal{P}$ is homogenous then the fields induced by $\bar{\boldsymbol{\sigma}}$ are symmetric about O. In this section, we suppose that both restrictions on $\mathcal{P}$ have been satisfied.

In order to prove that the number of unknowns in (4)–(6) can be reduced to $p/2$, let us consider a face $\mathcal{S}_\alpha$ and the face opposite to it (Fig. 1). Periodicity and symmetry imply that these faces are equal and each is symmetric about its centroid. For an arbitrary point $A \in \mathcal{S}_\alpha$, we identify two related points: B and C. The former is symmetric to A about O, and the latter is related to B by periodicity. It is straightforward to show that A and C are symmetric about O_α, and that $\sigma(A) = \sigma(B) = \sigma(C)$. By considering the properties of A and C, we conclude that the normal stress distribution is even on $\mathcal{S}_\alpha$, thus according to (1)–(3)

$$\mathbf{T}_\alpha = \mathbf{D}_\alpha = \mathbf{0};$$

of course the torque and dipole vanish on the opposite face as well. Further, the normal forces on the two faces are equal, thus the number of unknowns in (4)–(6) can be reduced to $p/2$.

Now we prove that there are only six independent equilibrium equations for the $p/2$ normal forces. Further, (4) and (5) are satisfied trivially, so that the set of independent equations,

$$2\sum_{\alpha=1}^{p/2} N_\alpha \mathbf{l}_\alpha \otimes \mathbf{n}_\alpha = V\bar{\boldsymbol{\sigma}}, \quad (7)$$

is derived solely from (6); the sum in (7) includes only one face per pair of opposite faces.

Although it is obvious that (4) is satisfied trivially, the proof for (5) requires the following construction (Fig. 2):

Step 1: Identify $p/2$ faces such that none of them is the opposite of the other, and their union, $\mathcal{S}'$, is a simply connected surface. The surface $\mathcal{S}'$ can be chosen such that

the remaining faces, which form the surface $\mathcal{S}''$, satisfy the same requirements. The faces in the set $\mathcal{S}'$ are numbered from 1 to $p/2$, and the remaining faces from $p/2 + 1$ to p.

Step 2: Cut $\mathcal{P}$ by a surface $\mathcal{C}$ which is symmetric about O and intersects the surface of $\mathcal{P}$ along the boundary between $\mathcal{S}'$ and $\mathcal{S}''$. The body bounded by $\mathcal{S}'(\mathcal{S}'')$ and $\mathcal{C}$ is denoted by $\mathcal{P}'(\mathcal{P}'')$.

Step 3: Choose a point $A' \in \mathcal{P}'$ infinitesimally close to the surface $\mathcal{C}$, and identify $B'' \in \mathcal{P}''$ as the point symmetric to A' about O. A point inside $\mathcal{P}'$ which is infinitesimally close to B'' is denoted by B'.

Step 4: Invoke symmetry for the traction vectors at A' and B'' and continuity for the traction vectors at B'' and B', and show that $\mathbf{t}(A') = \mathbf{t}(B')$; thus

$$\int_{\mathcal{C}} \mathbf{x} \times \mathbf{t}(\mathbf{x}) dA \equiv \mathbf{0}$$

for any traction field symmetric about O. Since the tractions on $\mathcal{C}$ acting on $\mathcal{P}'$ are statically equivalent to the system of forces acting on $\mathcal{S}''$, we conclude that

$$\sum_{\alpha=p/2+1}^{p} N_\alpha \mathbf{l}_\alpha \times \mathbf{n}_\alpha \equiv \mathbf{0}.$$

Apparently the same identity holds for the forces acting on $\mathcal{S}'$,

$$\sum_{\alpha=1}^{p/2} N_\alpha \mathbf{l}_\alpha \times \mathbf{n}_\alpha \equiv \mathbf{0}.$$

Thus (5) is trivially satisfied for periodic arrays with central symmetry.

The equivalence between (6) and (7) is established once we observe that the tensors

$$\sum_{\alpha=1}^{p/2} N_\alpha \mathbf{l}_\alpha \otimes \mathbf{n}_\alpha \quad \text{and} \quad \sum_{\alpha=p/2+1}^{p} N_\alpha \mathbf{l}_\alpha \otimes \mathbf{n}_\alpha$$

are symmetric, thanks to the identities just proved, and equal to each other.

2.3 Array of Rhombic Dodecahedra. This array is chosen in order to demonstrate how statically determinate periodic arrays are analyzed. The rhombic dodecahedron can be defined as the Voronoy polyhedron of the face-centered cubic lattice. It is constructed in three steps. First, the lattice point at the centroid of a face is connected by straight line segments with 12 nearest neighbors. Second, each segment is bisected by a plane. Third, the rhombic dodecahedron is formed as a body bounded by these planes (Fig. 3). The rhombic dodecahedron possesses central symmetry and its surface consists of 12 identical rhombic faces equidistant from the centroid. If the period of the cubic lattice is $2a$, then A, is the area of each face, l, the distance between each face and the centroid of the polyhedron, and V are given by

$$A = \frac{\sqrt{2}}{2}a^2, \quad l = \frac{\sqrt{2}}{2}a, \quad \text{and } V = 2a^3.$$

Also each $\mathbf{l}_\alpha = l\mathbf{n}_\alpha$.

For the calculations in (7), we choose six faces with outward normals (Fig. 3)

$$\mathbf{n}_1 = \frac{\sqrt{2}}{2}(\mathbf{i}_2 + \mathbf{i}_3), \quad \mathbf{n}_2 = \frac{\sqrt{2}}{2}(\mathbf{i}_2 - \mathbf{i}_3),$$

$$\mathbf{n}_3 = \frac{\sqrt{2}}{2}(\mathbf{i}_1 + \mathbf{i}_3), \quad \mathbf{n}_4 = \frac{\sqrt{2}}{2}(\mathbf{i}_1 - \mathbf{i}_3),$$

$$\mathbf{n}_5 = \frac{\sqrt{2}}{2}(\mathbf{i}_1 + \mathbf{i}_2), \quad \mathbf{n}_6 = \frac{\sqrt{2}}{2}(\mathbf{i}_1 - \mathbf{i}_2).$$

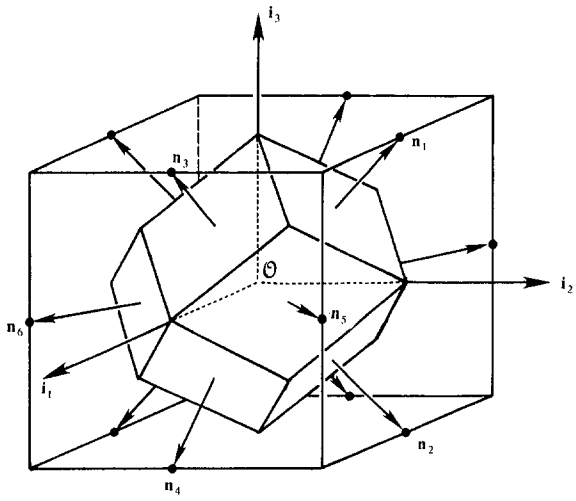

Fig. 3 The rhombic dodecahedron as the Voronoy polyhedron of the face-centered cubic lattice

Further, (7) can be expressed in terms of the facet stresses,

$$\frac{1}{2}\sum_{\alpha=1}^{6} \sigma_\alpha \mathbf{n}_\alpha \otimes \mathbf{n}_\alpha = \bar{\boldsymbol{\sigma}}, \tag{8}$$

with the solution[1]

$$\sigma_1 = -\bar{\sigma}_{11} + \bar{\sigma}_{22} + \bar{\sigma}_{33} + 2\bar{\sigma}_{23},$$

$$\sigma_2 = -\bar{\sigma}_{11} + \bar{\sigma}_{22} + \bar{\sigma}_{33} - 2\bar{\sigma}_{23},$$

$$\sigma_3 = +\bar{\sigma}_{11} - \bar{\sigma}_{22} + \bar{\sigma}_{33} + 2\bar{\sigma}_{13},$$

$$\sigma_4 = +\bar{\sigma}_{11} - \bar{\sigma}_{22} + \bar{\sigma}_{33} - 2\bar{\sigma}_{13},$$

$$\sigma_5 = +\bar{\sigma}_{11} + \bar{\sigma}_{22} - \bar{\sigma}_{33} + 2\bar{\sigma}_{12},$$

$$\sigma_6 = +\bar{\sigma}_{11} + \bar{\sigma}_{22} - \bar{\sigma}_{33} - 2\bar{\sigma}_{12}.$$

In order to elucidate the relationship between σ_α and $\bar{\boldsymbol{\sigma}}$, let us determine the facet stresses with the provision that one of them, say σ_1, is maximized as a result of a particular alignment of the macroscopic stress eigenvectors with respect to $\mathcal{P}$. If the principal macroscopic stresses are such that $\bar{\sigma}_1 \geq \bar{\sigma}_2 \geq \bar{\sigma}_3$, the macroscopic stress tensor which maximizes σ_1 is

$$\bar{\boldsymbol{\sigma}} = \bar{\sigma}_1 \mathbf{n}_1 \otimes \mathbf{n}_1 + \bar{\sigma}_2 \mathbf{n}_2 \otimes \mathbf{n}_2 + \bar{\sigma}_3 \mathbf{i}_1 \otimes \mathbf{i}_1.$$

The corresponding facet stresses are

$$\sigma_1 = 2\bar{\sigma}_1 - \bar{\sigma}_3, \quad \sigma_2 = 2\bar{\sigma}_2 - \bar{\sigma}_3,$$

$$\text{and } \sigma_3 = \sigma_4 = \sigma_5 = \sigma_6 = \bar{\sigma}_3.$$

2.4 Array of Truncated Octahedra. In this section, we consider the periodic array of truncated octahedra as an example of how the facet stresses are determined in statically indeterminate periodic arrays. Our analysis follows closely that of Anderson and Rice (1985) but, in contrast to their calculations, the macroscopic stress is not required to exhibit axial symmetry.

The truncated octahedron can be defined as the Voronoy polyhedron of the body-centered cubic lattice (Fig. 4). The truncated octahedron possesses central symmetry and its

[1]Obtained with *Mathematica*.

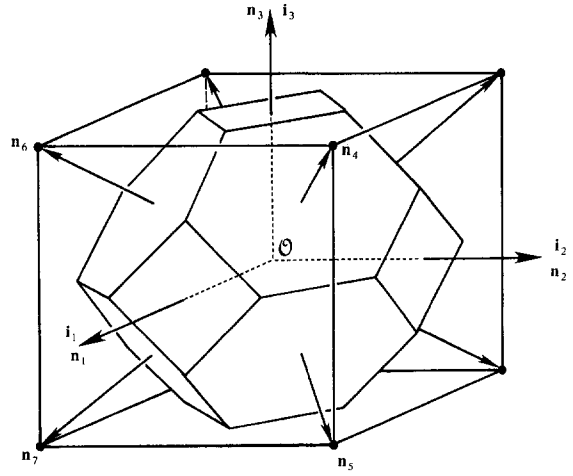

Fig. 4 The truncated octahedron as the Voronoy polyhedron of the body-centered cubic lattice

surface is formed by 14 faces: six identical squares and eight identical regular hexagons. Thus, for the truncated octahedron, the number of unknowns exceeds the number of equilibrium equations by one. If the cubic lattice period is $2a$, then

$$A^s = \frac{1}{2}a^2, \quad A^h = \frac{3\sqrt{3}}{4}a^2, \quad l^s = a, \quad l^h = \frac{\sqrt{3}}{2}a,$$

and $V = 4a^3$.

Here the superscripts s and h are assigned to square and hexagonal faces, respectively. Also each $\mathbf{l}_\alpha = l\mathbf{n}_\alpha$.

For the calculations we choose seven faces with outward normals (Fig. 4)

$$\mathbf{n}_1 = \mathbf{i}_1, \quad \mathbf{n}_2 = \mathbf{i}_2, \quad \mathbf{n}_3 = \mathbf{i}_3,$$

$$\mathbf{n}_4 = \frac{\sqrt{3}}{3}(\mathbf{i}_1 + \mathbf{i}_2 + \mathbf{i}_3), \quad \mathbf{n}_5 = \frac{\sqrt{3}}{3}(\mathbf{i}_1 + \mathbf{i}_2 - \mathbf{i}_3),$$

$$\mathbf{n}_6 = \frac{\sqrt{3}}{3}(\mathbf{i}_1 - \mathbf{i}_2 + \mathbf{i}_3), \quad \mathbf{n}_7 = \frac{\sqrt{3}}{3}(\mathbf{i}_1 - \mathbf{i}_2 - \mathbf{i}_3).$$

In terms of the facet stresses, (7) is rewritten in the form

$$\frac{1}{4}\sum_{\alpha=1}^{3}\sigma_\alpha \mathbf{n}_\alpha \otimes \mathbf{n}_\alpha + \frac{9}{16}\sum_{\alpha=4}^{7}\sigma_\alpha \mathbf{n}_\alpha \otimes \mathbf{n}_\alpha = \bar{\boldsymbol{\sigma}}. \qquad (9)$$

Following Anderson and Rice (1985), the statical indeterminacy is resolved by using the minimum complementary energy principle of linear elasticity. Accordingly, the stress field inside the truncated octahedron is approximated as

$$\boldsymbol{\sigma}(\mathbf{x}) = \sum_{\alpha=1}^{7}\sigma_\alpha \mathbf{n}_\alpha \otimes \mathbf{n}_\alpha I_\alpha(\mathbf{x}). \qquad (10)$$

Here I_α is the indicator function of the domain of the prism whose bases are $\mathcal{S}_\alpha$ and the face opposite to it. Anderson and Rice (1985) used one more coordinate function, uniformly distributed hydrostatic pressure; for our purposes, this function is neither necessary nor useful. Based on (10), the complementary energy Ψ of $\mathcal{P}$ is

$$\Psi(\sigma_\alpha) = \frac{a^3}{2E}\sum_{\alpha=1}^{3}\sigma_\alpha^2 + \frac{9a^3}{8E}\sum_{\alpha=4}^{7}\sigma_\alpha^2, \qquad (11)$$

where E is the elasticity modulus of the material comprising the grain. At this point, the facet stresses can be determined if $\Psi(\sigma_\alpha)$ is minimized with respect to σ_α subject to (9). The minimization procedure is carried out readily using a Lagrange multiplier for (9); the solution is

$$\sigma_1 = 4\bar{\sigma}_{11} - \mathrm{tr}\bar{\boldsymbol{\sigma}}, \quad \sigma_2 = 4\bar{\sigma}_{22} - \mathrm{tr}\bar{\boldsymbol{\sigma}}, \quad \sigma_3 = 4\bar{\sigma}_{33} - \mathrm{tr}\bar{\boldsymbol{\sigma}},$$

$$\sigma_4 = \frac{1}{3}\mathrm{tr}\bar{\boldsymbol{\sigma}} + \frac{4}{3}(+\bar{\sigma}_{12} + \bar{\sigma}_{13} + \bar{\sigma}_{23}),$$

$$\sigma_5 = \frac{1}{3}\mathrm{tr}\bar{\boldsymbol{\sigma}} + \frac{4}{3}(+\bar{\sigma}_{12} - \bar{\sigma}_{13} - \bar{\sigma}_{23}),$$

$$\sigma_6 = \frac{1}{3}\mathrm{tr}\bar{\boldsymbol{\sigma}} + \frac{4}{3}(-\bar{\sigma}_{12} + \bar{\sigma}_{13} - \bar{\sigma}_{23}),$$

$$\sigma_7 = \frac{1}{3}\mathrm{tr}\bar{\boldsymbol{\sigma}} + \frac{4}{3}(-\bar{\sigma}_{12} - \bar{\sigma}_{13} + \bar{\sigma}_{23}).$$

For prescribed principal macroscopic stresses, the facet stress σ_1 is maximized if the normal $\mathbf{n}_1$ coincides with the eigenvector of the maximum principal macroscopic stress. In particular, if the macroscopic stress is uniaxial tension T normal to the square $\mathcal{S}_1$, we obtain

$$\sigma_1 = 3T, \quad \sigma_2 = \sigma_3 = -T, \quad \sigma_4 = \sigma_5 = \sigma_6 = \sigma_7 = \frac{1}{3}T.$$

Analogously, the facet stress σ_4 is maximized if the normal $\mathbf{n}_4$ coincides with the eigenvector of the maximum principal macroscopic stress. If the macroscopic stress is uniaxial tension T normal to the hexagon S_4, we obtain

$$\sigma_1 = \sigma_2 = \sigma_3 = \frac{1}{3}T, \quad \sigma_4 = \frac{5}{3}T, \quad \sigma_5 = \sigma_6 = \sigma_7 = -\frac{1}{9}T.$$

In each case, the maximum facet stress coincides with the one predicted by Anderson and Rice (1985). A remarkable feature of these estimates is that they are less than eight percent different from those predicted from detailed finite element computations (Dib and Rodin, 1993): 3 versus 2.77 for the maximum σ_1, and $5/3 \approx 1.67$ versus 1.72 for the maximum σ_4. Also, let us emphasize that, according to Dib and Rodin (1993), the variational approach of Anderson and Rice (1985) is insufficiently accurate as far as the displacement and strain fields are concerned.

3 Three-Dimensional Disordered Arrays

3.1 Background. In Section 3, we consider disordered arrays of polyhedra which satisfy the following restrictions:

- Each array is comprised of a large number of grains.
- Dimensions of the polyhedra comprising the array are not correlated with any particular orientation.
- Each array is the Voronoy tessellation of a point lattice.

Although all three restrictions are introduced in order to simplify calculations, the first two can be viewed as a loose definition of a disordered polycrystalline representative material element (Hashin, 1983). The third restriction is somewhat artificial but it can be easily justified since the Voronoy tessellation is a well-accepted geometrical construction for polyhedral grains.

In disordered arrays, we do not consider individual grains; instead governing equations are formulated for the entire array. Accordingly, all predictions must be interpreted as appropriate averages.

3.2 Equilibrium Equations. Equilibrium equations for a disordered array can be derived directly from (4)–(6). This task is simplified if the vectors $\mathbf{l}_\alpha$ in (4)–(6) are redefined as follows. First, for each grain, the origin O is shifted from the

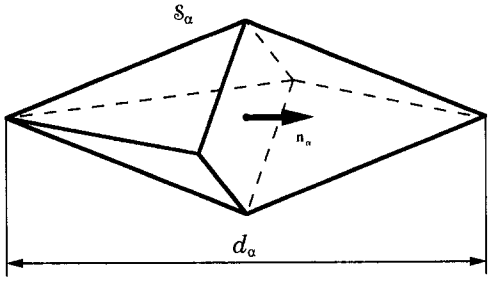

Fig. 5 Two pyramids formed by the face S_α and the two adjacent lattice points

centroid to the lattice point. Second, the point O_α is chosen such that the vector $\mathbf{l}_\alpha = \vec{OO}_\alpha$ is normal to $\mathcal{S}_\alpha$. With these changes, the first term in (5) as well as the skew-symmetric part of $\mathbf{l}_\alpha \otimes \mathbf{n}_\alpha$ vanish. Upon application of Newton's third law to the tractions on each grain boundary, we conclude that the sums arising from (4) and (5) are identically equal to zero, and the sum arising from (6) can be written as

$$\sum_{\alpha=1}^{q} N_\alpha d_\alpha \mathbf{n}_\alpha \otimes \mathbf{n}_\alpha = V\bar{\boldsymbol{\sigma}}. \tag{12}$$

Here the sum is over all grain boundaries in the array, d_α is the distance between the two lattice points associated with the grain boundary $\mathcal{S}_\alpha$ (Fig. 5), V is the volume of the array, and $\mathbf{n}_\alpha$ is a unit normal to $\mathcal{S}_\alpha$ whose sign does not have to be specified. Equation (12) can be also expressed in terms of the facet stresses,

$$3\sum_{\alpha=1}^{q} \sigma_\alpha V_\alpha \mathbf{n}_\alpha \otimes \mathbf{n}_\alpha = V\bar{\boldsymbol{\sigma}}, \tag{13}$$

where V_α is the volume of the two pyramids which share the base $\mathcal{S}_\alpha$ (Fig. 5).

3.3 Determination of the Facet Stresses. Apparently the six equations in (13) are insufficient to determine the many facet stresses in the array, therefore, following the analysis for the periodic array of truncated octahedra, a variational formulation is introduced. For the disordered array, instead of choosing a statically admissible stress field, we construct an ad hoc expression for the complementary energy as a function of the facet stresses. To this end it is expedient to emphasize two properties of the complementary energy $\Psi(\sigma_\alpha)$ in (11). First, as far as the determination of the facet stresses is concerned, $\Psi(\sigma_\alpha)$ can be multiplied by any positive constant, i.e., it is sufficient to establish how the complementary energy is partitioned with respect to the facet stresses. Second, it is apparent that $\Psi(\sigma_\alpha)$, as determined for the truncated octahedron, is partitioned such that the weight of each σ_α^2 is proportional to the volume of the pyramid with apex at O and base $\mathcal{S}_\alpha$. If the same partition is adopted for the disordered array, the weight of each σ_α^2 becomes proportional to the volume of the two pyramids shown in Fig. 5, so that the complementary energy can be chosen as

$$\Psi(\sigma_\alpha) = \frac{1}{2}\sum_{\alpha=1}^{q} \sigma_\alpha^2 V_\alpha. \tag{14}$$

In order to minimize $\Psi(\sigma_\alpha)$ with respect to σ_α subject to (13), we introduce a second rank symmetric tensor $\boldsymbol{\lambda}$ as the Lagrange multiplier for (13). Accordingly, the augmented energy is

$$\tilde{\Psi}(\sigma_\alpha) = \frac{1}{2}\sum_{\alpha=1}^{q} \sigma_\alpha^2 V_\alpha - \boldsymbol{\lambda} \cdot \left(3\sum_{\alpha=1}^{q} \sigma_\alpha V_\alpha \mathbf{n}_\alpha \otimes \mathbf{n}_\alpha - V\bar{\boldsymbol{\sigma}}\right).$$

After obvious manipulations we obtain

$$\sigma_\alpha = 3\boldsymbol{\lambda} \cdot (\mathbf{n}_\alpha \otimes \mathbf{n}_\alpha) \tag{15}$$

and

$$9\boldsymbol{\lambda} \cdot \left(\sum_{\alpha=1}^{q} V_\alpha \mathbf{n}_\alpha \otimes \mathbf{n}_\alpha \otimes \mathbf{n}_\alpha \otimes \mathbf{n}_\alpha\right) = V\bar{\boldsymbol{\sigma}}. \tag{16}$$

Since the array is disordered and q is large, the sum in (16) is evaluated as

$$\sum_{\alpha=1}^{q} V_\alpha \mathbf{n}_\alpha \otimes \mathbf{n}_\alpha \otimes \mathbf{n}_\alpha \otimes \mathbf{n}_\alpha = V\langle \mathbf{n} \otimes \mathbf{n} \otimes \mathbf{n} \otimes \mathbf{n} \rangle$$

$$= \frac{1}{15} V(\boldsymbol{\delta} \otimes \boldsymbol{\delta} - 2\mathbf{I}).$$

Here the corner brackets denote the averaging operation over the surface of a unit sphere, $\boldsymbol{\delta}$ and $\mathbf{I}$ are the second and fourth rank symmetric identity tensors, respectively. Now it is easy to solve for $\boldsymbol{\lambda}$ and obtain the expression for the facet stresses,

$$\sigma_\alpha = \frac{5}{2}\bar{\boldsymbol{\sigma}} \cdot (\mathbf{n}_\alpha \otimes \mathbf{n}_\alpha) - \frac{1}{2}\mathrm{tr}\bar{\boldsymbol{\sigma}}. \tag{17}$$

The maximum facet stress is

$$\max\{\sigma_\alpha\} = \frac{5}{2}\bar{\sigma}_1 - \frac{1}{2}\mathrm{tr}\bar{\boldsymbol{\sigma}} = 2\bar{\sigma}_1 - \frac{1}{2}(\bar{\sigma}_2 + \bar{\sigma}_3). \tag{18}$$

Expression (18) for the maximum facet stress is close to the one suggested by Nix et al. (1989) who, based on the analysis of Anderson and Rice (1985), used 2.24 and 0.62 instead of 2 and 1/2, respectively. If the expression suggested by Nix et al. (1989) were based on the more accurate analysis of Dib and Rodin (1993a), the numerical coefficients would be 2.08 and 0.54, respectively. Also, in (18), the maximum facet stress is a linear combination of $\bar{\sigma}_1$ and $\mathrm{tr}\bar{\boldsymbol{\sigma}}$. This supports the functional form of Nix et al. (1989) rather than that of Dib and Rodin (1993b), who chose the maximum facet stress as a linear combination of $\bar{\sigma}_1$ and the Mises macroscopic stress. Although it may be appropriate to modify the expressions for the maximum facet stress used by Nix et al. (1989) and Dib and Rodin (1993b), we do not believe that these changes would significantly affect the conclusions of those papers.

4 Discussion

In the preceding sections, we developed an approach which lends itself to simple calculations of the facet stresses in a large class of arrays with frictionless grain boundaries. While the arrays considered there are exclusively in three-dimensions, it is clear that two-dimensional arrays can be analyzed as well[2]. In particular, it can be shown that in two-dimensional disordered arrays

$$\sigma_\alpha = 2\bar{\boldsymbol{\sigma}} \cdot (\mathbf{n}_\alpha \otimes \mathbf{n}_\alpha) - \frac{1}{2}(\bar{\sigma}_1 + \bar{\sigma}_2)$$

and

$$\max\{\sigma_\alpha\} = \frac{3}{2}\bar{\sigma}_1 - \frac{1}{2}\bar{\sigma}_2.$$

Here $\bar{\sigma}_1$ and $\bar{\sigma}_2$ are in-plane principal macroscopic stresses. Note that the estimate for the maximum facet stress coincides with the one for the periodic regular hexagonal array (Beere, 1982).

Based on (17), let us examine how the macroscopic stress

[2]Two-dimensional arrays are relevant to micromechanical modeling of the so-called S2 columnar ice.

is transmitted in polycrystals with frictionless grain boundaries. In doing this, we restrict our attention to axisymmetric macroscopic stress tensors,

$$\bar{\boldsymbol{\sigma}} = T_A \mathbf{e} \otimes \mathbf{e} + T_L(\boldsymbol{\delta} - \mathbf{e} \otimes \mathbf{e}),$$

such that the axial principal stress, $T_A > 0$, is fixed and the two lateral principal stresses, T_L, vary from minus infinity to plus infinity. If the fraction of grain boundaries in compression is denoted by c and $\eta = T_L/T_A$, the facet stress distribution in (17) yields the following expression:

$$c(\eta) = \begin{cases} \sqrt{\dfrac{3\eta - 1}{5\eta - 5}} & \text{if } \eta < 1/3 \\ 0 & \text{if } 1/3 \le \eta \le 2 \\ 1 - \sqrt{\dfrac{3\eta - 1}{5\eta - 5}} & \text{if } \eta > 2. \end{cases} \tag{19}$$

In the limit as $\eta \to -\infty$, which is in effect biaxial compression, $c \approx 0.77$; if $\eta \to \infty$, $c \approx 0.23$. Under uniaxial tension ($\eta = 0$), the fraction of grain boundaries in compression is almost 45 percent! In this case the overall equilibrium is maintained because grain boundaries in tension transmit higher facet stresses than those in compression. For example, the maximum tensile facet stress is $2T_A$ while the maximum compressive facet stress is only $T_A/2$. The presence of compressive stresses under macroscopic tension and tensile stresses under macroscopic compression has not received much attention in the mechanics community so far. This phenomenon, however, is critical to the understanding of high-temperature fracture of ceramics, particularly because the majority of creep tests on ceramics are conducted under bending so that both macroscopic tension and compression are involved (Chuang and Wiederhorn, 1988).

In our analysis of disordered arrays, the maximum facet stress is calculated as the average over the facet stresses transmitted by the many grain boundaries aligned normal to the direction of the maximum principal macroscopic stress. This averaging procedure is relevant to micromechanical modeling of materials whose failure is associated with gradual accumulation of intergranular cracks (Dib and Rodin, 1993b). The other extreme, relevant to materials which fail shortly after the first intergranular crack is formed, requires the determination of the maximum facet stress transmitted by a single grain boundary. In this case, it is necessary to specify explicitly the polycrystalline geometry and perform large-scale finite element computations. Results of such an analysis in two-dimensions are forthcoming (van der Giessen and Tvergaard, 1994).

In conclusion, let us observe that the present approach can be extended to cellular solids with truss-like microstructure and polycrystals with traction-free grain boundaries. The connection with cellular solids becomes obvious if one models their geometry using the Delaunay tessellation of random point lattices. Accordingly, such a truss is constructed by assigning a member between the lattice points of any two adjacent polyhedra of the Voronoy tessellation. In this case, the sums in (13) and (14) must be interpreted as follows: α runs over the members, V_α is the volume of the member α, and the complementary energy of the truss is obtained by dividing the sum in (14) in E. If the energy is minimized, one finds that the overall elastic constants of the cellular solids are

$$\bar{E} = \frac{1}{6}\phi E \quad \text{and} \quad \bar{\nu} = \frac{1}{4}, \tag{20}$$

where ϕ is the volume fraction of the members. This result, well-known in mechanics of cellular solids, is due to Gent and Thomas (1959). In (20), the overall constants are derived by minimizing an exact expression for the complementary energy subject to relaxed equilibrium conditions (13). Implications of this approximation are unclear, and the validity of (20) is still debated in the literature (Christensen, 1986; Gibson and Ashby, 1988). The present approach is applicable to polycrystals with traction-free grain boundaries simply because the sums over grain boundaries do not have to include all grain boundaries but only those with nonzero facet stresses. Furthermore, such an exclusion of grain boundaries can simplify the calculations. For example, if in the periodic array of truncated octahedra one pair of faces is traction-free, then the array becomes statically determinate. Also it is possible to consider arrays with voids at the vertices. For example, if in the periodic array of rhombic dodecahedra there is a spherical void at each vertex, such that the volume fraction of the grains is ϕ, then the facet stresses derived in Section 2.3 should be multiplied by $\phi^{-2/3}$.

Acknowledgment

This work was supported by the ALCOA Foundation, NSF grant MSM-9114856, and ONR grant N00014-92J1332, Program Director Yapa D. S. Rajapakse. I am indebted to Altha B. Rodin (The University of Texas at Austin) for editorial assistance and to Vitaly R. Skvortsov (St. Petersburg University of Ocean Technology, Russia) for pointing at minor algebraic mistakes.

References

Anderson, P. E., and Rice, J. R., 1985, "Constrained Creep Cavitation of Grain Boundary Facets," *Acta Metallurgica et Materialia*, Vol. 33, pp. 409–422.

Beere, W., 1982, "Stress Redistribution due to Grain Boundary Sliding during Creep," *Metal Science*, Vol. 16, pp. 223–227.

Christensen, R. M., 1987, "Mechanics of Low Density Materials," *Journal of the Mechanics and Physics of Solids*, Vol. 34, pp. 563–578.

Chuang, T.-J., and Wiederhorn, S. M., 1988, "Damage-Enhanced Creep in a Siliconized Silicon Carbide: Mechanics of Deformation," *Journal of the American Ceramic Society*, Vol. 71, pp. 595–601.

Dib, M. W., and Rodin, G. J., 1993a, "Three-Dimensional Analysis of Creeping Polycrystals Using Periodic Arrays of Truncated Octahedra," *Journal of the Mechanics and Physics of Solids*, Vol. 41, pp. 725–747.

Dib, M. W., and Rodin, G. J., 1993b, "Continuum Damage Mechanics of Constrained Intergranular Cavitation," *Acta Metallurgica et Materialia*, Vol. 41, pp. 1567–1575.

Gent, A. N., and Thomas, A. G., 1959, "The Deformation of Foamed Elastic Materials," *Journal of Applied Polymer Science*, Vol. 1, pp. 107–113.

Gibson, L. J., and Ashby, M. F., 1988, *CELLULAR SOLIDS Structure & Properties*, Pergamon Press, Oxford, U.K.

Hashin, Z., 1983, "Analysis of Composite Materials," ASME JOURNAL OF APPLIED MECHANICS, Vol. 50, pp. 481–505.

Nix, W. D., Earthman, J. C., Eggeler, G., and Ilschner, B., 1989, "The Principal Facet Stress as a Parameter for Predicting Creep Rupture under Multiaxial Stresses," *Acta Metallurgica et Materialia*, Vol. 37, pp. 1067–1077.

van der Giessen, E., and Tvergaard, V., 1994, "Effect of Random Variations in Microstructure on the Development of Final Creep Failure in Polycrystalline Aggregates," *Modelling Simulations in Materials Science and Engineering*, Vol. 2, pp. 721–738.

Underwood, E. E., 1970, *Quantitative Stereology*, Addison-Wesley, Reading, MA.

Two-Phase Potentials for the Treatment of an Elastic Inclusion in Plane Thermoelasticity

M. A. Kattis
Mem. ASME

S. A. Meguid
Mem. ASME

Engineering Mechanics and Design Laboratory,
Department of Mechanical Engineering,
University of Toronto,
5 King's Road,
Toronto, ON M5S 1A4, Canada

A solution to the uncoupled two-dimensional steady-state heat conduction and thermoelastic problems of an elastic curvilinear inclusion embedded in an elastic matrix, with different thermomechanical properties, is provided. The proposed analysis describes the heat conduction problem in terms of one holomorphic complex potential and the thermoelastic problem in terms of two holomorphic potentials; known hereafter as two-phase potentials. The general results of the developed analysis are applied to specific examples and explicit forms of the solution are obtained. It is shown that a uniform heat flow at infinity induces a linear stress distribution within the elliptic inclusion.

Introduction

A model, which is often adopted in the analysis of the thermomechanical behavior of heterogeneous materials, is that of the infinite elastic matrix containing an elastic inclusion with different thermomechanical properties. Although the elastic inclusion problem under mechanical loadings have been examined extensively, only a limited number of studies have been made of the corresponding problem under thermal loading. The thermoelastic problem is receiving considerable attention as a result of the widespread use of high-temperature composites in engineering applications.

The elastic elliptic inclusion for a uniform temperature change has been studied earlier by Mindlin and Cooper (1950). They showed that such a temperature change introduces a uniform stress field within the inclusion. The interface penny-shaped crack in two bonded isotropic bodies under a uniform heat flow at infinity has been treated by Bregman and Kassir (1975). The same problem has been examined in combination with a particular thermal boundary condition on the crack faces (Martin-Moran et al., 1983; Barber and Comninou, 1983). The corresponding two-dimensional interfacial problem has also been discussed and solutions have been provided for certain special cases (Brown and Erdogan, 1968; Kuo, 1990). Rigid inclusions with an interfacial crack in infinite elastic planes have also been considered (Kattis and Duka, 1990, 1991; Hasebe et al., 1991; Prysov, 1972; Kattis, 1991a,b). Elastic line inclusion in an infinite elastic plane was further examined by Sekine (1977), and Grilitskii et al. (1983).

The analysis is based upon the conformal mapping technique of the complex variable theory of elasticity with the matrix region of the physical plane (z-plane) being mapped to the external region of the unit circle of another plane (ζ-plane). Extending analytically the mapping function definition in the internal of the unit circle and using the mapped plane as a parametric plane, general representations of the complex potentials are constructed so that the required thermal and mechanical interface continuity of the relevant quantities are satisfied. In these representations, the complex potentials of the thermoelastic problem are expressed in terms of two holomorphic functions, while those of the heat conduction problem are expressed in terms of a single holomorphic function. These functions constitute the two-phase potentials of the current two-phase system. The proposed relationships provide, as special cases, the well-known results of the continuation method for the case of a curvilinear rigid inclusion or a hole in an infinite plane matrix.

The two-phase potentials can be sought in series forms adapted to the singular requirements of the problems. The series coefficients are calculated so that the single-valuedness condition of the temperature and displacements are ensured and the thermal and mechanical singular conditions are satisfied. Such a technique is completely illustrated in the case of an elastic circular inclusion where the thermal singular conditions correspond to a uniform heat flow at infinity and to a point heat source at a point of the matrix. The latter case, along with the concentrated force results, provide the necessary tools to treat some interesting and more complicated thermoelastic problems. Also, two-phase potential solutions are given for an elliptical elastic inclusion and for a hypotrochoidal rigid inclusion with an insulated boundary disturbing a uniform heat flow of the matrix.

Contributed by the Applied Mechanics Division of THE AMERICAN SOCIETY OF MECHANICAL ENGINEERS for publication in the ASME JOURNAL OF APPLIED MECHANICS.

Discussion on this paper should be addressed to the Technical Editor, Professor Lewis T. Wheeler, Department of Mechanical Engineering, University of Houston, Houston, TX 77204-4792, and will be accepted until four months after final publication of the paper itself in the ASME JOURNAL OF APPLIED MECHANICS.

Manuscript received by the ASME Applied Mechanics Division, July 7, 1992; final revision, Sept. 20, 1993. Associate Technical Editor: X. Markenscoff.

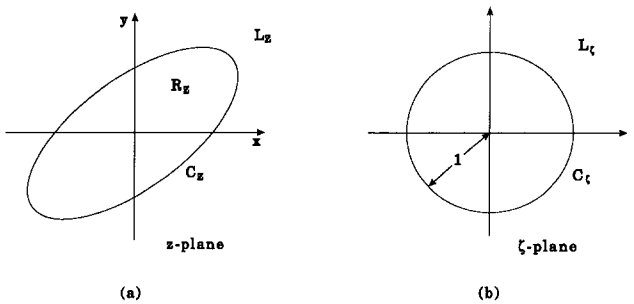

Fig. 1 *(a)* **A curvilinear elastic inclusion in an elastic plane matrix and** *(b)* **the corresponding mapped ζ-plane**

Statement of the Problem and Governing Equations

Consider an infinite elastic matrix containing a curvilinear elastic inclusion with different thermomechanical properties. The two materials are assumed to be perfectly bonded along the interface C_z at a reference temperature $\mathfrak{I}_0$ and in such a way that the connected system remains unstressed. The elastic matrix occupies the open region L_z and the inclusion of the region R_z of the z-plane. The z-plane refers to a Cartesian orthogonal system (x, y) whose origin lies inside R_z. The region L_z is conformally mapped by $z = m(\zeta)$ into the exterior L_ζ of the unit circumference C_ζ, $|\zeta| = 1$, of the ζ-plane with the interface C_z corresponding to the circumference C_ζ (Fig. 1).

A temperature change $T = \mathfrak{I} - \mathfrak{I}_0$, with $\mathfrak{I}$ being the absolute temperature, in the system causes a thermal stress distribution as a result of the different thermomechanical properties of the two phases, each one of which has been assumed to be thermally and mechanically homogeneous and isotropic. According to Muskhelishvili (1953), the Cartesian components of the stresses σ_x, σ_y, σ_{xy} and the Cartesian components of the displacements u, v can be written in terms of the two complex potentials W and $\mathfrak{W}$ in the form

$$\sigma_x + \sigma_y = W(z) + \overline{W(z)}, \tag{1}$$

$$2(\sigma_y - i\sigma_{xy}) = W(z) + \overline{W(z)} + z\overline{W'(z)} + \mathfrak{W}(z), \tag{2}$$

$$4\mu(u + iv) = \kappa \grave{W}(z) - z\overline{W(z)} - \grave{\mathfrak{W}}(z) + \beta_t \grave{\Psi}(z), \tag{3}$$

where $\Psi(z)$ is an analytic function which accounts for the presence of the temperature field in the thermoelastic problem and must be determined a priori by solving the corresponding heat conduction problem. In (3), $\kappa = 3 - 4\nu$ and $\beta_t = 4\mu a_t(1 + \nu)$ for plane strain, $\kappa = (3 - \nu)/(1 + \nu)$ and $\beta_t = 4\mu a_t$ for plane stress, with μ and ν being the shear modulus and Poisson's ratio, respectively, and a_t is the coefficient of linear thermal expansion. Left and right prime functions denote indefinite integration and differentiation with respect to the appropriate variable.

The Cartesian components of the heat flow q_x, q_y and the temperature change T of the heat conduction problem of the uncoupled thermoelastic problem can be expressed in terms of a single complex potential F such that

$$-\frac{q_x}{k_t} = F'(z) + \overline{F'(z)}, \tag{4}$$

$$i\frac{q_y}{k_t} = F'(z) - \overline{F'(z)}, \tag{5}$$

$$T = F(z) + \overline{F(z)}, \tag{6}$$

where k_t is the thermal conductivity. Once the heat conduction problem is solved, the temperature function Ψ is determined

$$\Psi(z) = 2F(z). \tag{7}$$

In the following, the traction and heat flow continuity along the interface will be used in their equivalent integrated forms. These forms can be expressed by the resultant force R and the total heat flow $\mathfrak{Q}$ on an arc by

$$2iR(z, \bar{z}) = \grave{W}(z) + z\overline{W(z)} + \grave{\mathfrak{W}}(z), \tag{8}$$

$$-\frac{i}{k_t}\mathfrak{Q}(z, \bar{z}) = F(z) - \overline{F(z)}. \tag{9}$$

If the complex potentials of the heat conduction and the thermoelastic problems are known, the field variables of both problems are completely defined by means of Eqs. (1)–(6). These variables must satisfy the imposed boundary conditions and ensure the required interfacial continuity. Since the interfacial continuity constitutes a defined internal condition of the multiphase system, a question arises regarding the least number of independent functions necessary to completely describe the state variables of the system. Such a question will be discussed with respect to the current problem.

It is further assumed that there is a perfect thermal contact between the two phases and the system is free from external surface or body forces. Furthermore, the subscripts 1 and 2 are used to denote quantities associated with the matrix and inclusion, respectively.

Two-Phase Potentials

1 The Heat Conduction Problem. The temperature and heat flow continuity across the interface can be expressed in terms of the following complex potentials:

$$F_1(t) + \overline{F_1(t)} = F_2(t) + \overline{F_2(t)}, \tag{10}$$

$$F_1(t) - \overline{F_1(t)} = k\left[F_2(t) - \overline{F_2(t)}\right], \tag{11}$$

where t denotes a point on the interface C_z and $k = k_2/k_1$. Expressions (10) and (11) can be reduced to a single equivalent equation in which the complex potential of one phase is expressed in terms of the other. In the ζ-plane, this equation takes the form

$$F_1(m(\sigma)) = \frac{1 + k}{2}F_2(m(\sigma)) + \frac{1 - k}{2}\overline{F_2}\left(\overline{m}\left(\frac{1}{\sigma}\right)\right), \tag{12}$$

where σ is a point on C_ζ. Based on (12), the general representation of the thermal potentials of the two phases can be constructed so that the thermal continuity is ensured. However, functional quantities associated with the inclusion should not be defined in terms of the variable ζ, as is suggested by (12), since the region R_z is not represented by means of conformal mapping in the ζ-plane. Hence, functions referring to the inclusion will be expressed in terms of the variable z of the physical region, while those of the matrix will be expressed in terms of the variable ζ of the ζ-plane. Thus, a general form of the thermal potentials of the two phases can be defined as

$$F_1(m(\zeta)) = F_0(m(\zeta)) + \frac{1 - k}{1 + k}\overline{F_0}\left(\overline{m}\left(\frac{1}{\zeta}\right)\right), \quad \zeta \text{ in } L_\zeta, \tag{13}$$

$$F_2(z) = \frac{2}{1 + k}F_0(z), \quad z \text{ in } R_z, \tag{14}$$

where F_0 is a holomorphic function. This function is defined in the region R_z of the physical plane and in the entire ζ-plane, except, maybe, in a number of points where it exhibits a singular behavior. F_0 depends on the thermal

loading and the geometrical shape of the interface, and its determination defines the temperature fields of both phases completely. This function will be denoted as the two-phase potential of the system.

A series technique can be applied to determine the two-phase potential F_0. Assuming a form of F_0, that is consistent with the singular conditions of the problem, its complete determination will depend upon the known behavior of the thermal potentials at the singular points.

2 The Thermoelastic Problem. The traction and displacement continuity along the interface imply that

$$\Gamma\left[\kappa_1 \grave{W}_1(t) - t\overline{W_1(t)} - \grave{\overline{\mathfrak{W}}}_1(t) + \beta_{1t}\grave{\Psi}_1(t)\right] = \kappa_2 \grave{W}_2(t) - t\overline{W_2(t)} - \overline{\mathfrak{W}_2(t)} + \beta_{2t}\grave{\Psi}_2(t), \quad (15)$$

$$\grave{W}_1(t) + t\overline{W_1(t)} + \grave{\overline{\mathfrak{W}}}_1(t) = \grave{W}_2(t) + t\overline{W_2(t)} + \grave{\overline{\mathfrak{W}}}_2(t) \quad (16)$$

where $\Gamma = \mu_2/\mu_1$. Equations (15) and (16) can equivalently be replaced by the following set of equations:

$$\grave{W}_1(m(\sigma)) = \frac{1-\beta}{1+\alpha}\grave{W}_2(m(\sigma)) + \frac{\alpha-\beta}{1+\alpha} \times \left\{ m(\sigma)\overline{W_2}\left(\overline{m}\left(\frac{1}{\sigma}\right)\right) + \grave{\overline{\mathfrak{W}}}_2\left(\overline{m}\left(\frac{1}{\sigma}\right)\right)\right\} + \frac{\gamma}{1+\alpha}\grave{\Psi}_0(m(\sigma)), \quad (17)$$

$$\grave{\mathfrak{W}}_1(m(\sigma)) = \frac{1+\beta}{1+\alpha}\grave{\mathfrak{W}}_2(m(\sigma)) + \frac{\alpha+\beta}{1+\alpha}\grave{\overline{W}}_2\left(\overline{m}\left(\frac{1}{\sigma}\right)\right) + \frac{2\beta}{1+\alpha}\overline{m}\left(\frac{1}{\sigma}\right)W_2(m(\sigma)) - \frac{\alpha-\beta}{1+\alpha}\frac{\overline{m}(1/\sigma)}{m'(\sigma)}\frac{d}{d\sigma}\left[m(\sigma)\overline{W_2}\left(\overline{m}\left(\frac{1}{\sigma}\right)\right) + \grave{\overline{\mathfrak{W}}}_2\left(\overline{m}\left(\frac{1}{\sigma}\right)\right)\right] - \frac{\gamma}{1+\alpha}\left[\grave{\overline{\Psi}}_0\left(\overline{m}\left(\frac{1}{\sigma}\right)\right) + \overline{m}\left(\frac{1}{\sigma}\right)\Psi_0(m(\sigma))\right], \quad (18)$$

where σ represents a point on the circumference C_ζ, and

$$\Psi_0(z) = a_{2t}\Psi_2(z) - a_{1t}\Psi_1(z). \quad (19)$$

for plane stress conditions. In Eqs. (17) and (18), α and β are the Dundurs parameters (Dundurs, 1970)

$$\alpha = \frac{\Gamma(1+\kappa_1) - (1+\kappa_2)}{\Gamma(1+\kappa_1) + (1+\kappa_2)}, \quad \beta = \frac{\Gamma(\kappa_1-1) - (\kappa_2-1)}{\Gamma(1+\kappa_1) + (1+\kappa_2)}$$

and

$$\gamma = \frac{8\mu_1\mu_2}{\mu_1(1+\kappa_2) + \mu_2(1+\kappa_1)}.$$

Based on Eqs. (17) and (18), the general representation of the thermoelastic potentials can be constructed so that the required continuity along the interface is satisfied. This leads to the following expressions:

$$\grave{W}_1(m(\zeta)) = \grave{W}_0(m(\zeta)) - \Omega m(\zeta)\overline{W_0}\left(\overline{m}\left(\frac{1}{\zeta}\right)\right) + \Pi\grave{\overline{\mathfrak{W}}}_0\left(\overline{m}\left(\frac{1}{\zeta}\right)\right) + \frac{4\mu_1}{1+\kappa_1}\grave{\Psi}_0(m(\zeta)), \quad \zeta \text{ in } L_\zeta, \quad (20)$$

$$\grave{\mathfrak{W}}_1(m(\zeta)) = \grave{\mathfrak{W}}_0(m(\zeta)) + \Lambda\grave{\overline{W}}_0\left(\overline{m}\left(\frac{1}{\zeta}\right)\right) + (\Lambda+\Omega)\overline{m}\left(\frac{1}{\zeta}\right)W_0(m(\zeta)) + \frac{\overline{m}(1/\zeta)}{m'(\zeta)}\frac{d}{d\zeta}\left[\Omega m(\zeta)\overline{W_0}\left(\overline{m}\left(\frac{1}{\zeta}\right)\right) - \Pi\grave{\overline{\mathfrak{W}}}_0\left(\overline{m}\left(\frac{1}{\zeta}\right)\right)\right] - \frac{4\mu_1}{1+\kappa_1}\left[\grave{\overline{\Psi}}_0\left(\overline{m}\left(\frac{1}{\zeta}\right)\right) + \overline{m}\left(\frac{1}{\zeta}\right)\Psi_0(m(\zeta))\right], \quad \zeta \text{ in } L_\zeta, \quad (21)$$

for the matrix, and

$$\grave{W}_2(z) = (1+\Lambda)W_0(z), \quad z \text{ in } L_z, \quad (22)$$

$$\grave{W}_2(z) = (1+\Pi)\grave{\mathfrak{W}}_0(z), \quad z \text{ in } L_z, \quad (23)$$

for the inclusion, where Λ, Π, and Ω are auxiliary two-phase parameters given by (Gao, 1990)

$$\Lambda = \frac{\alpha+\beta}{1-\beta}, \quad \Pi = \frac{\alpha-\beta}{1+\beta}, \quad \Omega = -\frac{\alpha-\beta}{1-\beta}.$$

In Eqs. (20)–(23), W_0 and $\mathfrak{W}_0$ are two holomorphic functions, which represent the two-phase potentials of the system. These functions are defined in the region L_z and in the entire ζ-plane, except at a certain number of points where they exhibit a singular behavior. These points can be determined by means of (20)–(23) taking into account the singular behavior of functions Ψ_0 and $m(\zeta)$. If the temperature terms of (20) and (21) are absent, the expressions reduce to the general representations proposed by Sendeckyj (1970).

When the temperature state and the geometry of the system are defined, the two-phase potentials W_0 and $\mathfrak{W}_0$ are determined such that the stress field vanishes at infinity. This means that the complex potentials of the matrix W_1 and $\mathfrak{W}_1$ should converge to zero at infinity. A series technique can be used for the determination of W_0 and $\mathfrak{W}_0$ as in the case of F_0.

3 Special Cases. For the extreme case of a rigid inclusion with an insulated boundary ($\mu_2 \to \infty$, $\Psi_2 = 0$) the complex potentials of the matrix take the form

$$F_1(\zeta) = F_0(\zeta) + \overline{F_0}\left(\frac{1}{\zeta}\right), \quad \zeta \text{ in } L_\zeta, \quad (24)$$

$$\grave{W}_1(\zeta) = \grave{W}_0(\zeta) + \frac{1}{\kappa_1}\grave{\overline{\mathfrak{W}}}_0\left(\frac{1}{\zeta}\right) - \frac{4\mu_1 a_{1t}}{1+\kappa_1}\grave{\Psi}_1(\zeta), \quad \zeta \text{ in } L_\zeta, \quad (25)$$

$$\grave{\mathfrak{W}}_1(\zeta) = \grave{\mathfrak{W}}_0(m\zeta) + \kappa_1\grave{\overline{W}}_0\left(\frac{1}{\zeta}\right) - \frac{\overline{m}(1/\zeta)}{m'(\zeta)}\frac{d}{d\zeta}\left[\grave{W}_0(\zeta) + \frac{1}{\kappa_1}\grave{\overline{\mathfrak{W}}}_0\left(\frac{1}{\zeta}\right)\right] + \frac{4\mu_1 a_{1t}}{1+\kappa_1}\left[\Psi_1(\zeta)\overline{m}\left(\frac{1}{\zeta}\right) + \grave{\overline{\Psi}}_1\left(\frac{1}{\zeta}\right)\right], \quad \zeta \text{ in } L_\zeta, \quad (26)$$

where in the above expressions $\grave{F}_1(m(\zeta))$ was written as $\grave{F}_1(\zeta)$ and $\grave{W}_1(m(\zeta))$ as $\grave{W}_1(\zeta)$, etc. Introducing now a new holomorphic function W such that

$$\int W(\zeta)d\zeta = \grave{W}_0(\zeta) + \frac{1}{\kappa_1}\grave{\overline{\mathfrak{W}}}\left(\frac{1}{\zeta}\right) \quad (27)$$

and substituting (27) in (25) and (26), after differentiation expressions (25) and (26) become

$$m'(\zeta)W_1(\zeta) = W(\zeta) - \frac{4\mu_1\alpha_{1t}}{1+\kappa_1}\Psi_1(\zeta), \quad \zeta \text{ in } L_\zeta, \quad (28)$$

$$m'(\zeta)\mathfrak{W}(\zeta) = -\frac{\kappa_1}{\zeta_2}\overline{W}\left(\frac{1}{\zeta}\right) - \frac{d}{d\zeta}\left[\frac{\overline{m}(1/\zeta)}{m'(\zeta)}W(\zeta)\right]$$
$$+\frac{4\mu_1 a_{1t}}{1+\kappa_1}\left[\frac{d}{d\zeta}\left(\overline{m}\left(\frac{1}{\zeta}\right)\Psi_1(\zeta)\right) - \frac{1}{\zeta^2}\overline{\Psi}_1\left(\frac{1}{\zeta}\right)\overline{m}'\left(\frac{1}{\zeta}\right)\right]. \quad (29)$$

The thermoelastic potentials of the matrix for a rigid inclusion are now expressed by (28) and (29) in terms of a single potential W. Equations (24), (28), and (29) can represent the complex potentials for a curvilinear hole with an insulated boundary, if the plus sign of the right-hand side of (24) is substituted by minus and κ_1 of (29) by -1. In this last case, if $W(\zeta)$ is replaced by $m'(\zeta)W(\zeta)$ and $\Psi_1 = 0$ in (28) and (29), the well-known result of the continuation method is obtained (Milne-Thomson, 1968, p. 144).

For a circular inclusion, the complex potentials of the matrix can be written in terms of the variable z of the region L_z of the physical plane (Eqs. (A1)–(A3) in the Appendix). In this case, Eqs. (A1) and (14) constitute the well-known relationships of the extended circle theorem of Smith (1975).

Applications

The previously developed analysis will now be applied to some particular cases of perfectly bonded inclusions. Specifically, the circular and elliptic elastic inclusions, and the rigid hypotrochoidal inclusion with an insulated boundary, are considered subjected to a uniform heat flow at infinity.

1 Circular Elastic Inclusion. Consider now that an elastic circular inclusion occupies the region $|z| \le R$ of the physical plane and that the matrix is subjected to a temperature change

$$T = \frac{q_0}{k_{1t}}y + T_c \quad (30)$$

at infinity, where q_0 represent a uniform heat flow along the y-axis and T_c is a uniform temperature change. Expression (30) provides the following expansion of $F_1(z)$ at infinity:

$$F_1(z) = \frac{q_0 i}{k_{1t}}z + \frac{1}{2}T_c + \mathcal{O}\left(\frac{1}{z}\right), \quad z = \infty \quad (31)$$

which imposes a pole of the first order on F_0 at infinity. Assuming that F_0 has a linear form, its unknown coefficients are calculated by comparing (31) and (46) at infinity. It is found that

$$F_0(z) = \frac{q_0 i}{2k_{1t}}z + \frac{1+k}{4}T_c. \quad (32)$$

The temperature terms of (20) and (21) impose a pole of the first order at infinity on W_0 and $\mathfrak{W}_0$. Assuming that W_0 and $\mathfrak{W}_0$ have a linear form, the unknown coefficients are determined from the condition of convergence of the complex potentials W_1 and $\mathfrak{W}_1$ at infinity. It is obtained that

$$W_0(z) = \frac{4\mu_1 a_{1t}}{1+\kappa}\left[\frac{q_0 i}{k_{1t}}\left(1 - \frac{2a}{1+k}\right)z + \frac{1-a}{1-\Omega}T_c\right], \quad (33)$$

$$\mathfrak{W}_0(z) = 0, \quad (34)$$

where $a = a_{2t}/a_{1t}$. The stress and displacement fields obtained with respect to a polar coordinate system (r, ϕ) are given by Eqs. (A4)–(A19) in the Appendix for each of the terms of Eq. (30). For the case of a rigid inclusion or a hole with an insulated boundary ($\Lambda = 1/\Pi = \kappa_1$ or -1 and $a_{2t} = 0$, $k_{2t} = 0$), Eqs. (A10)–(A19) are reduced to the known results of Lee and Choi (1989) and Florence and Goodier (1960).

If the matrix is subjected to a heat source of strength Q at the point z_0 ($|z_0| > R$), the following expansion of the complex potential F_1 at $z = z_0$ is valid:

$$F_1(z) = -\frac{Q}{4\pi k_{1t}}\log(z - z_0) + \mathcal{O}\left(|z - z_0|^0\right), \quad z = z_0. \quad (35)$$

The two-phase potentials satisfying the holomorphy condition in R_z can be assumed in the form

$$F_0(z) = (A_0 + A_1 z)\log(z - z_0) + a_0 + a_1 z + \ldots, \quad (36)$$

$$W_0(z) = (B_0 + B_1 z)\log(z - z_0) + b_0 + b_1 z + \ldots, \quad (37)$$

$$\mathfrak{W}_0(z) = (C_0 + C_1 z)\log(z - z_0) + c_0 + c_1 z + \ldots. \quad (38)$$

The complex constants $A_0, A_1, a_0, \ldots, B_0, B_1, b_0, \ldots$ and $C_0, C_1, c_0, \ldots$ are calculated so that the convergence condition of the complex potentials at infinity are ensured and the single-valuedness condition of the temperature and displacements are satisfied. It is found that

$$F_0(z) = -\frac{Q}{4\pi k_{1t}}\log(z - z_0), \quad (39)$$

$$W_0(z) = \frac{2\mu_1 a_{1t} Q}{(1+\kappa_1)k_{1t}\pi}$$
$$\times\left[\left(\frac{2a}{1+k} - 1\right)(z - z_0) + \frac{R^2}{\overline{z}_0}\frac{1-k}{1+k}\right]\log(z - z_0)$$
$$-\frac{2\mu_1 a_{1t} Q}{(1+\kappa_1)k_{1t}\pi}\left[\left(\frac{2a}{1+k} - 1\right) + \frac{\Omega}{1-\Omega}\frac{R^2}{|z_0|^2}\frac{1-k}{1+k}\right]z, \quad (40)$$

and

$$\mathfrak{W}_0(z) = 0. \quad (41)$$

2 Elliptic Elastic Inclusion. The mapping function for an elliptic inclusion with semi-major and semi-minor axes α_1 and α_2, respectively, is given by

$$z = m(z) = R\left(\zeta + \frac{m}{\zeta}\right)(R > 0, 0 \le m \le 1) \quad (42)$$

where

$$\alpha_1 = R(1+m), \quad \alpha_2 = R(1-m). \quad (43)$$

For a temperature change of the form provided by Eq. (30) at infinity, the two-phase potentials are calculated using the procedure described above, viz,

$$F_0(z) = \frac{q_0 i k_m}{2k_{1t}}z + \frac{1+k}{4}T_c, \quad (44)$$

$$W_0(z) = \frac{4\mu_1 a_{1t}}{(1+\kappa_1)}\left[-\frac{q_0 i k_m \mathfrak{A}}{k_{1t}\mathfrak{C}}z + (1-a)\frac{T_c}{\mathfrak{D}}\right], \quad (45)$$

$$\mathfrak{W}_0(z) = \frac{4\mu_1 a_{1t}}{(1+\kappa_1)}\left[\frac{q_0 i k_m \mathfrak{B}}{k_{1t}\mathfrak{C}}z - m(1-a)(1+\Pi)\frac{T_c}{\mathfrak{D}}\right], \quad (46)$$

where $\mathfrak{A}$, $\mathfrak{B}$, $\mathfrak{C}$, $\mathfrak{D}$, and k_m are given by (A26)–(A30) in the Appendix. Equations (45) and (46) provide a linear stress distribution within the inclusion, as given by (A20)–(A25) in the Appendix for the two terms of (30). This conclusion is consistent with that of Mindlin and Cooper (1950) for the case of uniform temperature change. When $T_c = 0$, the complex potential W_1 of the matrix takes the form

$$m'(\zeta)W_1(\zeta) = \frac{4\mu_1 a_{1t} q_0 i R^2 k_m}{k_{1t}(1+\kappa_1)}\left[\frac{1-m^2}{\zeta} - \frac{(1+\Pi)m^2\delta(1/m) + (1-\Pi\Lambda)m^2\mathfrak{A}/\mathfrak{C}}{\zeta^3}\right]. \quad (47)$$

Putting $\mu_2 = \infty$ ($\Lambda = 1/\Pi = \kappa_1$, $\Omega = -1$) and $a = 0$ in (40), the equation obtained coincides with the complex potential of a rigid inclusion with an insulated boundary (Kattis, 1991a).

3 Hypotrochoidal Rigid Inclusion With an Insulated Boundary. The mapping function for a hypotrochoidal inclusion inscribed in a circle of radius R is

$$z = m(\zeta) = R\left(\zeta + \frac{m}{\rho\zeta^\rho}\right) \quad (\rho \geq 2 \quad 0 \leq m \leq 1). \quad (48)$$

For a temperature change given in the form $-\mathrm{Re}(\bar{q}_\infty z)/k_{1t}$ at infinity, with q_∞ being a uniform heat flow, the thermal potential F_0 is calculated as

$$F_0(\zeta) = -\frac{\bar{q}_\infty R}{2k_{1t}}\zeta. \quad (49)$$

Equations (28) and (29) show that W should have a pole of the first order at infinity and a pole of $\rho + 2$ order at zero, since W_1 and $\mathfrak{W}_1$ should converge to zero at infinity. Thus, assuming that W has the form

$$W(\zeta) = A_1\zeta + A_0 + \frac{A_{-1}}{\zeta} + \ldots + \frac{A_{-(\rho+2)}}{\zeta^{\rho+2}} \quad (50)$$

the constants A_1, A_0, ... $A_{-(\rho+2)}$ are calculated from the condition of convergence of the complex potentials W_1 and $\mathfrak{W}_1$ at infinity. It is obtained that

$$W(\zeta) = -\frac{4\mu_1 a_{1t} q_\infty R^2}{k_{1t}\kappa_1(1+\kappa_1)} \times\left[\kappa_1 e^{-2i\gamma}\zeta + \frac{m(2\rho-1)}{\rho\zeta^\rho}e^{-2i\gamma} + \frac{m}{\zeta^{\rho+2}}\right], \quad (51)$$

where γ is the angle between the direction of the heat flow and the x-axis. Substituting (50) in (28), it can be deduced that

$$m'(\zeta)W_1(\zeta) = \frac{4\mu_1 a_{1t} q_\infty R^2}{\kappa_1 k_{1t}} \times\left[\frac{\kappa_1}{1+\kappa_1}\frac{1}{\zeta} - \left(1 + \frac{\rho-1}{\rho(1+\kappa_1)}\right)\frac{me^{-2i\gamma}}{\zeta^\rho} - \frac{m}{\zeta^{\rho+2}}\right] \quad (52)$$

which coincides with the result obtained by the continuation method (Kattis, 1991a).

Concluding Remarks

The general representation of the complex potentials of both heat conduction and thermoelastic problems of a curvilinear elastic inclusion embedded in a plane elastic matrix was established. The proposed complex potentials of the two phases were expressed in terms of two holomorphic functions for the thermoelastic problem and one holomorphic function for the heat conduction problem. A number of specific examples were considered to demonstrate the general character of the resulting expressions. It was shown that a uniform heat flow at infinity induces a linear stress distribution within an elastic elliptical inclusion.

References

Barber, J. R., and Comninou, M., 1983, "The Penny-Shaped Interface Crack With Heat Flow, Part 2: Imperfect Contact," ASME JOURNAL OF APPLIED MECHANICS, Vol. 50, pp. 770–776.

Bregman, A. M., and Kassir, M. K., 1974, "Thermal Fracture of Bonded Dissimilar Media Containing a Penny-Shaped Crack," ASME JOURNAL OF APPLIED MECHANICS, Vol. 10, pp. 87–98.

Brown, E. J., and Erdogan, F., 1968, "Thermal Stresses in Bonded Materials Containing Cuts on the Interface," *Int. J. Engngn Sci.*, Vol. 6, pp. 517–529.

Dundurs, J., 1970, "Some Properties of Elastic Stresses in a Composite," *Proc. 6th Annual Meeting Soc. Engngn Sci.*, Vol. 5, pp. 203–216.

Florence, A. L., and Goodier, J. N., 1960, "Thermal Stresses Due to Disturbance of Uniform Heat Flow by an Insulated Ovaloid Hole," ASME JOURNAL OF APPLIED MECHANICS, Vol. 82, pp. 635–639.

Gao, H., 1991, "A Boundary Perturbation Analysis for Elastic Inclusions and Interfaces," *Int. J. Solids Structures*, Vol. 28, pp. 703–725.

Grilitskii, D. V., Dragan, M. S., and Opanasovich, V. K., 1980, "The Temperature Field and the Thermoelastic State in a Plate Containing a Thin-Walled Elastic Inclusion," *PMM USSR*, Vol. 44, pp. 236–240.

Hasebe, N., Irikuro, H., and Nakamura, T., 1991, "A Solution of the Mixed Boundary Value Problem for an Infinite Plate with a Hole Under Uniform Heat Flux," ASME JOURNAL OF APPLIED MECHANICS, Vol. 58, pp. 996–1000.

Kattis, M. A., and Duka, E. D., 1990, "Thermal Stresses in an Infinite Plate Containing a Partly Unbonded Inclusion," *Proceedings of the Conference on Computer Aided Assessment and Control of Localized Damage*, Portsmouth, U.K., Vol. 3, pp. 73–83.

Kattis, M. A., and Duka, E. D., 1991, "Thermal Stresses in an Elastic Plane Matrix Containing a Circular Inclusion with an Interface Crack," *Ceramics Today—Tomorrow's Ceramics*, Elsevier, Amsterdam, pp. F37–F45.

Kattis, M. A., 1991a, "Thermoelastic Plane Problems With Curvilinear Boundaries," *Acta Mechanica*, Vol. 87, pp. 93–103.

Kattis, M. A., 1991b, "Thermal Stress Intensity Factors for a Partially Bonded Rigid Fiber Inclusion," *Engineering Fracture Mechanics*, Vol. 40, pp. 159–165.

Kuo, A., 1990, "Interface Crack Between Two Dissimilar Half-Spaces Subjected to a Uniform Heat Flow at Infinity-Open Crack," ASME JOURNAL OF APPLIED MECHANICS, Vol. 57, pp. 359–364.

Lee, K. Y., and Choi, H. S., 1989, "Determination of Thermal Stress Intensity Factors for Rigid Cusp Crack Under Uniform Heat Flow," *Engineering Fracture Mechanics*, Vol. 32, pp. 183–193.

Martin-Moran, G. J., Barber, J. R., and Comninou, M., 1983, "The Penny-Shaped Interface Crack With Heat Flow, Part 1: Perfect Contact," ASME JOURNAL OF APPLIED MECHANICS, Vol. 50, pp. 29–36.

Mindlin, R. D., and Cooper, H. L., 1950, "Thermoelastic Stress Around a Cylindrical Inclusion of Elliptic Cross-Section," ASME JOURNAL OF APPLIED MECHANICS, Vol. 17, pp. 265–268.

Milne-Thomson, L. M., 1968, *Plane Elastic Systems*, Springer-Verlag, Berlin.

Muskhelishvili, N. I., 1953, *Some Basic Problems of the Mathematical Theory of Elasticity*, P. Noordhoff Co., Groningen, The Netherlands.

Prysov, I. A., 1972, *Certain Problems of Thermoelasticity*, Byelorussian University Press, Minsk (in Russian).

Sekine, H., 1977, "Thermal Stress Problem for a Ribbon-Like Inclusion," *Letters Appl. Engngn Sci.*, Vol. 5, pp. 51–61.

Sendeckyj, G. P., 1970, "Elastic Inclusion Problems in Plane Elastostatics," *Int. J. Solids Structures*, Vol. 6, pp. 1535–1543.

Smith, E., 1968, "The Interaction Between Dislocations and Inhomogeneities—I," *Int. J. Engngn Sci.*, Vol. 6, pp. 129–143.

APPENDIX

Complex Potentials of the Matrix for the Circular Inclusion Problem

$$F_1(z) = F_0(z) + \frac{1-k}{1+k}\bar{F}_0\left(\frac{R^2}{z}\right) \quad (A1)$$

$$\grave{W}_1(z) = \grave{W}_0(z) - \Omega z\overline{W}_0\left(\frac{R^2}{z}\right) + \Pi\grave{\overline{\mathfrak{W}}}_0\left(\frac{R^2}{z}\right) + \frac{4\mu_1}{1+\kappa_1}\grave{\Psi}_0(z) \quad (A2)$$

$$\grave{\mathfrak{W}}_1(z) = \grave{\mathfrak{W}}_0(z) + \Lambda\grave{\overline{W}}_0\left(\frac{R^2}{z}\right) + (\Lambda+\Omega)\frac{R^2}{z}W_0(z) + \frac{R^2}{z}\frac{d}{dz}\left[\Omega z\overline{W}_0\left(\frac{R^2}{z}\right) - \Pi\grave{\overline{\mathfrak{W}}}_0\left(\frac{R^2}{z}\right)\right] - \frac{4\mu_1}{1+\kappa_1}\left[\grave{\overline{\Psi}}_0\left(\frac{R^2}{z}\right) + \frac{R^2}{z}\Psi_0(z)\right] \quad (A3)$$

Thermal Stresses and Displacements for an Elastic Circular Inclusion

For a uniform temperature change T_c:

$$\sigma_{1r} = -\sigma_{1\phi} = \frac{4\mu_1(a_{1t} - a_{2t})(1 + \Lambda)T_c}{(1 + \kappa_1)(1 - \Omega)} \frac{R^2}{r^2} \quad \text{(A4)}$$

$$\sigma_{2r} = \sigma_{2\phi} = \frac{4\mu_1(a_{1t} - a_{2t})(1 + \Lambda)T_c}{(1 + \kappa_1)(1 - \Omega)} \quad \text{(A5)}$$

$$\sigma_{1r\phi} = \sigma_{2r\phi} = 0 \quad \text{(A6)}$$

$$u_{1r} = \frac{2(a_{2t} - a_{1t})(1 + \Lambda)T_c}{(1 + \kappa_1)(1 - \Omega)} \frac{R^2}{r} + a_{1t}T_c r \quad \text{(A7)}$$

$$u_{2r} = \frac{2(a_{2t} - a_{1t})(1 + \Lambda)T_c}{(1 + \kappa_1)(1 - \Omega)} r + a_{1t}T_c r \quad \text{(A8)}$$

$$u_{1\phi} = u_{2\phi} = 0. \quad \text{(A9)}$$

For a temperature change $-q_0 y/k_{1t}$ at infinity,

$$\sigma_{1r} = \frac{4\mu_1 a_{1t} q_0 R}{(1 + \kappa_1)k_{1t}} \left[\frac{1 + \Lambda}{2} \left(\frac{2a}{1 + k} - 1 \right) \frac{R^3}{r^3} + \frac{1 - k}{1 + k} \left(1 - \frac{R^2}{r^2} \right) \frac{R}{r} \right] \sin \phi \quad \text{(A10)}$$

$$\sigma_{1\phi} = -\frac{4\mu_1 a_{1t} q_0 R}{(1 + \kappa_1)k_{1t}} \left[\frac{1 + \Lambda}{2} \left(\frac{2a}{1 + k} - 1 \right) \frac{R^3}{r^3} - \frac{1 - k}{1 + k} \left(1 + \frac{R^2}{r^2} \right) \frac{R}{r} \right] \sin \phi \quad \text{(A11)}$$

$$\sigma_{1r\phi} = -\frac{4\mu_1 a_{1t} q_0 R}{(1 + \kappa_1)k_{1t}} \left[\frac{1 + \Lambda}{2} \left(\frac{2a}{1 + k} - 1 \right) \frac{R^3}{r^3} + \frac{1 - k}{1 + k} \left(1 - \frac{R^2}{r^2} \right) \frac{R}{r} \right] \cos \phi \quad \text{(A12)}$$

$$\sigma_{2r} = \frac{2\mu_1 a_{1t} q_0 (1 + \Lambda)}{(1 + \kappa_1)k_{1t}} \left(\frac{2a}{1 + k} - 1 \right) r \sin \phi \quad \text{(A13)}$$

$$\sigma_{2\phi} = \frac{6\mu_1 a_{1t} q_0 (1 + \Lambda)}{(1 + \kappa_1)k_{1t}} \left(\frac{2a}{1 + k} - 1 \right) r \sin \phi \quad \text{(A14)}$$

$$\sigma_{2r\phi} = -\frac{2\mu_1 a_{1t} q_0 (1 + \Lambda)}{(1 + \kappa_1)k_{1t}} \left(\frac{2a}{1 + k} - 1 \right) r \cos \phi \quad \text{(A15)}$$

$$u_{1r} = -\frac{2a_{1t} q_0 R^2}{(1 + \kappa_1)k_{1t}} \left\{ \frac{1 + \kappa_1}{4} \left[\frac{r^2}{R^2} + \frac{1 + \Lambda}{1 + \kappa_1} \times \left(\frac{2a}{1 + k} - 1 \right) \frac{R^2}{r^2} \right] + \frac{1 - k}{2(1 + k)} \left(1 - \frac{R^2}{r^2} \right) + \frac{1 - k}{1 + k} \log \frac{r}{R} + \frac{1}{2} \left(\frac{2a}{1 + k} - 1 \right) \epsilon \right\} \sin \phi \quad \text{(A16)}$$

$$u_{1\phi} = \frac{2a_{1t} q_0 R^2}{(1 + \kappa_1)k_{1t}} \left\{ \frac{1 + \kappa_1}{4} \left[\frac{r^2}{R^2} + \frac{1 + \Lambda}{1 + \kappa_1} \times \left(\frac{2a}{1 + k} - 1 \right) \frac{R^2}{r^2} \right] + \frac{1 - k}{2(1 + k)} \left(1 - \frac{R^2}{r^2} \right) - \frac{1 - k}{1 + k} \log \frac{r}{R} - \frac{1}{2} \left(\frac{2a}{1 + k} - 1 \right) \epsilon \right\} \cos \phi \quad \text{(A17)}$$

$$u_{2r} = -\frac{2a_{1t} q_0 r^2}{(1 + \kappa_1)k_{1t}} \left\{ \frac{1 + \kappa_1}{4} \left[1 + \frac{1 + \Lambda}{1 + \kappa_1} \left(\frac{2a}{1 + k} - 1 \right) \right] + \frac{1}{2} \left(\frac{2a}{1 + k} - 1 \right) \epsilon \right\} \sin \phi \quad \text{(A18)}$$

$$u_{2\phi} = \frac{2a_{1t} q_0 r^2}{(1 + \kappa_1)k_{1t}} \left\{ \frac{1 + \kappa_1}{4} \left[1 + \frac{1 + \Lambda}{1 + \kappa_1} \left(\frac{2a}{1 + k} - 1 \right) \right] - \frac{1}{2} \left(\frac{2a}{1 + k} - 1 \right) \epsilon \right\} \cos \phi \quad \text{(A19)}$$

where

$$\epsilon = 1 + \Lambda + (1 + \kappa_1)\Omega.$$

Thermal Stresses Within an Elastic Elliptic Inclusion

For a uniform temperature change T_c,

$$\sigma_{2x} = \frac{2\mu_1(a_{1t} - a_{2t})T_c}{(1 + \kappa_1)\,\mathfrak{D}} \left[2(1 + \Lambda) + m(1 + \Pi)^2 \right], \quad \text{(A20)}$$

$$\sigma_{2y} = \frac{2\mu_2(a_{1t} - a_{2t})T_c}{(1 + \kappa_1)\,\mathfrak{D}} \left[2(1 + \Lambda) - m(1 + \Pi)^2 \right], \quad \text{(A21)}$$

$$\sigma_{2xy} = 0. \quad \text{(A22)}$$

For a temperature change $-q_0 y/k_{1t}$ at infinity,

$$\sigma_{2x} = \frac{2\mu_1 q_0 a_{1t} k_m}{(1 + \kappa_1)k_{1t}\mathfrak{C}} \left[3(1 + \Lambda)\mathfrak{A} + (1 + \Pi)\mathfrak{B} \right] y \quad \text{(A23)}$$

$$\sigma_{2y} = \frac{2\mu_1 q_0 a_{1t} k_m}{(1 + \kappa_1)k_{1t}\mathfrak{C}} \left[(1 + \Lambda)\mathfrak{A} - (1 + \Pi)\mathfrak{B} \right] y \quad \text{(A24)}$$

$$\sigma_{2xy} = -\frac{2\mu_1 q_0 a_{1t} k_m}{(1 + \kappa_1)k_{1t}\mathfrak{C}} \left[3(1 + \Lambda)\mathfrak{A} - (1 + \Pi)\mathfrak{B} \right] x. \quad \text{(A25)}$$

In (65)–(70), $|x| \le \alpha_1$, $|y| \le \alpha_2$, and

$$\mathfrak{A} = \delta(m) + m^4 \Pi \delta\left(\frac{1}{m} \right) \quad \text{(A26)}$$

$$\mathfrak{B} = \left[2m(1 + \Lambda + \Omega) - m^2\Lambda \right] \delta(m) - (1 + 2\Omega m)m^2 \delta\left(\frac{1}{m} \right) \quad \text{(A27)}$$

$$\mathfrak{C} = 1 - 2\Omega m(m^2 - 1) - m^4 \Pi\Lambda \quad \text{(A28)}$$

$$\mathfrak{D} = 1 - \Omega + m^2(\Omega - \Pi\Lambda) \quad \text{(A29)}$$

$$k_m = \frac{1 + k}{1 + k - m(1 - k)} \quad \text{(A30)}$$

$$\delta(m) = \frac{2a}{1 + k} - 1 + m\frac{1 + k}{1 - k}. \quad \text{(A31)}$$

M. Ganapathi
Scientist,
Institute of Armament Technology,
Pune 411 025, India

T. K. Varadan
Professor,
Department of Aerospace Engineering,
Indian Institute of Technology,
Madras 600 036, India

Dynamic Buckling of Laminated Anisotropic Spherical Caps

The dynamic axisymmetric behavior of clamped laminated composite spherical caps subjected to suddenly applied loads is investigated using an eight-noded quadrilateral doubly curved shear flexible shell element based on the field-consistency approach. Geometric nonlinearity is considered using von Karman's strain-displacement relations. The solution is obtained using the Wilson-θ numerical integration scheme. The pressure corresponding to a sudden jump in the maximum average deflection in the time history of the shell structure is taken as dynamic buckling pressure. A detailed parametric study is carried out to bring out the effects of shell geometries and material properties, number of layers, lamination schemes, and type of loading on a dynamic buckling load.

1 Introduction

In general, a structure designed for static loading condition may fail in a dynamic situation for the same loads. Hence, the study of the dynamic response of structures is important in assessing the structural failure and has constituted a major field of research in structural mechanics. Specifically, such studies in spherical shell structures have wide applications in the area of aerospace and mechanical engineering.

The study of axisymmetric dynamic snap-through buckling of pressure-loaded isotropic shallow spherical shells has received considerable attention over the past few decades. Important contributions are cited here. The analysis of axisymmetric dynamic instability of isotropic shallow spherical shells has been carried out by Budiansky and Roth (1962), Simitses (1967), Haung (1969), Stephens and Fulton (1969), Ball and Burt (1973), Stricklin and Martinez (1969), and Saigal et al. (1987) . Budiansky and Roth (1962) employed the Galerkin method and the Ritz-Galerkin procedure was adopted by Simitses (1967). A finite difference scheme was incorporated in the method of solution by Haung (1969), Ball and Burt (1973), Stephens and Fulton (1969), and Kao and Perrone (1978) while the more powerful finite element method was employed by Stricklin and Martinez (1969) and Saigal et al. (1987). Experimental results have been reported by Lock et al. (1968).

Composite materials are playing an increasing role nowadays in aerospace and other engineering applications where high strength-to-weight ratios are desired. Hence, there is a strong need for predicting the structural behavior of components constructed of such materials. However, due to the complexity of the analysis due to the inherent directional properties of the materials, the study of dynamic buckling behavior of composite spherical shells has been rather limited (Alwar and Shekhar Reddy, 1979; Dumir et al., 1984; Chao and Lin, 1990). The above references in the field of composites considered the dynamic buckling of single-layered orthotropic shallow spherical shells. Alwar and Shekhar Reddy (1979) solved the problem by making use of the Chebyshev series. Collocation method was utilized by Dumir et al. (1984). In all these investigations, analysis has been carried out using the classical shell theory based on the Love-Kirchhoff hypotheses.

Due to the low transverse shear moduli of modern advanced composite materials relative to their in-plane tensile moduli, transverse shear deformation effects may be significant, even in thin composite structures compared to homogeneous isotropic materials. Hence, it is more appropriate to analyze the dynamic response of composite structures by including shear deformation and rotary inertia. To the authors' knowledge, there seems to be no work available in the literature on the dynamic snap-through buckling of single-layered and laminated anisotropic shallow spherical shells. An attempt is made here to study the axisymmetric dynamic buckling behavior of laminated orthotropic/anisotropic shallow spherical shells using a shear-flexible theory and the finite element method.

Here, an eight-noded shear flexible quadrilateral doubly curved shell element, based on the field-consistency principle (Somashekar and Prathap, 1987; Prathap et al., 1988), is extended for the first time to analyze the dynamic buckling of laminated anisotropic shallow spherical shells under externally applied pressure loads. Field consistency is a systematic approach to eliminate spurious constraints causing shear and membrane locking when the shear-flexible theory is applied to thin shells. The formulation described here is general and

Contributed by the Applied Mechanics Division of THE AMERICAN SOCIETY OF MECHANICAL ENGINEERS for publication in the ASME JOURNAL OF APPLIED MECHANICS.

Discussion on this paper should be addressed to the Technical Editor, Professor Lewis T. Wheeler, Department of Mechanical Engineering, University of Houston, Houston, TX 77204-4792, and will be accepted until four months after final publication of the paper itself in the ASME JOURNAL OF APPLIED MECHANICS.

Manuscript received by the ASME Applied Mechanics Division, Mar. 4, 1992; final revision, June 22, 1993. Associate Technical Editor: A. K. Noor.

can be applied to various geometries and loadings, and can take care of asymmetric deformations also. Geometric nonlinearity is considered using von Karman's strain-displacement relations. In addition, the formulation includes in-plane and rotary inertia effects. The nonlinear governing equations are solved using the Wilson-θ numerical integration technique coupled with the modified Newton-Raphson iteration scheme. The pressure corresponding to a sudden jump in the maximum average deflection in the time history of the shell structure is taken as dynamic buckling pressure (Budiansky and Roth, 1962; Simitses, 1989). Numerical results are presented for isotropic, orthotropic, and laminated anisotropic shallow spherical shells and are compared with results wherever available. Different loading conditions such as a step pressure load of finite and infinite durations, and a right angle triangular pulse of various time durations are considered. A detailed investigation is carried out to bring out the influence of the number of layers, ply-angle, and geometric parameters on the dynamic buckling load.

2 Formulation

A doubly curved laminated composite shell is considered with the coordinates x, y along the in-plane directions and z along the radial/thickness direction. Using Mindlin formulation, the displacements u, v, w at a point (x, y, z) from the median surface are expressed as functions of midplane displacements u_0, v_0, and w, and independent rotations θ_x and θ_y of the normal in the xz and yz-planes, respectively, as

$$\begin{aligned} u(x,y,z,t) &= u_0(x,y,t) + z\,\theta_x(x,y,t) \\ v(x,y,z,t) &= v_0(x,y,t) + z\,\theta_y(x,y,t) \\ w(x,y,z,t) &= w(x,y,t). \end{aligned} \tag{1}$$

von Karman's assumptions for moderately large deformation analysis allow Green's strains to be written in terms of midplane deformation of Eq. (1) for a shell as

$$\{\epsilon\} = \{\epsilon^L\} + \{\epsilon^{NL}\} \tag{2}$$

where

$$\{\epsilon^L\} = \begin{Bmatrix} \epsilon_p^0 \\ 0 \end{Bmatrix} + \begin{Bmatrix} z\epsilon_b \\ \epsilon_s \end{Bmatrix} \text{ and } \{\epsilon^{NL}\} = \begin{Bmatrix} \epsilon_p^{NL} \\ 0 \end{Bmatrix}. \tag{3a}$$

The midplane strains $\{\epsilon_p^0\}$, bending strain $\{\epsilon_b\}$, and shear strains $\{\epsilon_s\}$ in Eq. (3a) are written by

$$\{\epsilon_p^0\} = \begin{Bmatrix} u_{0,x} + (w/R_x) \\ v_{0,y} + (w/R_y) \\ u_{0,y} + v_{0,x} + (2w/R_{xy}) \end{Bmatrix} \tag{3b}$$

$$\{\epsilon_b\} = -\begin{Bmatrix} \theta_{x,x} \\ \theta_{y,y} \\ \theta_{x,y} + \theta_{y,x} - (u_{0,y}/R_x) - (v_{0,x}/R_y) \end{Bmatrix} \tag{3c}$$

$$\{\epsilon_s\} = \begin{Bmatrix} \theta_x - w_{,x} + (u_0/R_x) + (v_0/R_{xy}) \\ \theta_y - w_{,y} + (v_0/R_y) + (u_0/R_{xy}) \end{Bmatrix} \tag{3d}$$

where R_x, R_y, and R_{xy} are the usual radii of curvature.

The nonlinear components of in-plane strains are

$$\{\epsilon_p^{NL}\} = \begin{Bmatrix} (1/2)\,w_{,x}^2 \\ (1/2)\,w_{,y}^2 \\ w_{,x}\,w_{,y} \end{Bmatrix}. \tag{3e}$$

If $\{N\}$ represents the membrane stress resultants (N_{xx}, N_{yy}, N_{xy}) and $\{M\}$ the bending stress resultants (M_{xx}, M_{yy}, M_{xy}), one can relate these to membrane strains $\{\epsilon_p\}$ (i.e., $\{\epsilon_p^0\} + \{\epsilon_p^{NL}\}$) and bending strains $\{\epsilon_b\}$ through the constitutive relations as

$$\{N\} = [A_{ij}]\{\epsilon_p\} + [B_{ij}]\{\epsilon_b\} \text{ and}$$

$$\{M\} = [B_{ij}]\{\epsilon_p\} + [D_{ij}]\{\epsilon_b\} \tag{4}$$

where $[A_{ij}]$, $[D_{ij}]$ and $[B_{ij}]$ $(i, j = 1, 2, 3)$ are extensional, bending and bending-extensional coupling stiffness coefficients of the composite laminate. Similarly, the transverse shear force $\{Q\}$ representing the quantities $\{Q_{xz}, Q_{yz}\}$ are related to the transverse shear strains$\{\epsilon_s\}$ through the constitutive relations as

$$\{Q\} = [E_{ij}]\{\epsilon_s\} \tag{5}$$

where $[E_{ij}]$ $(i, j = 4, 5)$ are the transverse shear stiffness coefficients of the laminate.

For a composite laminate of thickness h, consisting of N layers with stacking angles $\phi_i (i = 1, N)$ and layers thickness h_i $(i = 1, N)$, the necessary expressions to compute the stiffness coefficients, available in the literature (Jones, 1975) are used here. The potential energy functional U is given by

$$\begin{aligned} U(\delta) = \frac{1}{2}\int_A \Big[&\{\epsilon_p\}^T[A_{ij}]\{\epsilon_p\} + \{\epsilon_p\}^T[B_{ij}]\{\epsilon_b\} \\ &+ \{\epsilon_b\}^T[B_{ij}]\{\epsilon_p\} + \{\epsilon_b\}^T[D_{ij}]\{\epsilon_b\} + \{\epsilon_s\}^T[E_{ij}]\{\epsilon_s\}\Big] dA \\ &- \int_A q\,w\,dA \end{aligned} \tag{6}$$

where δ and q are the vectors of degrees-of-freedom and applied loads, respectively.

Following the procedure given in the work of Rajasekaran et al. (1973), the potential energy functional is rewritten as

$$\begin{aligned} U(\delta) = \{\delta\}^T\big[(1/2)[K_L] + (1/6)[N_1] + (1/12)[N_2]\big]\{\delta\} \\ + \{\delta\}^T\big[(1/2)[N_3]\{\delta\} + \{\delta\}^T\{F\}\big] \end{aligned} \tag{7}$$

where $[K_L]$ is a linear stiffness matrix, and $[N_1]$, $[N_2]$ are nonlinear stiffness matrices. $[N_3]$ and $\{F\}$ are the shear stiffness matrix and load vector, respectively.

The kinetic energy of the shell is given by

$$T(\delta) = (1/2)\int_A \Big[p\big(\dot{u}_o^2 + \dot{v}_o^2 + \dot{w}^2\big) + I\big(\dot{\theta}_x^2 + \theta_y^2\big)\Big] dA \tag{8}$$

where $p = \int_0^h \rho\, dz$, $I = \int_0^h z^2\, \rho\, dz$ and ρ is mass density.

Substituting Eqs. (7) and (8) in Lagrange's equation of motion, one obtains the governing equations for the forced flexural vibration of the shell as

$$\begin{aligned} [M]\{\ddot{\delta}\} + \big[[K_L] + (1/2)[N_1] + (1/3)[N_2] \\ + [N_3]\big]\{\delta\} = \{F\} \end{aligned} \tag{9}$$

where $[M]$ is the mass matrix.

Equations (9) is solved using the implicit method, as mentioned by Subbaraj and Dokainish (1989). In this method, equilibrium conditions are considered at the same time step for which solution is sought. If the solution is known at time t and one wishes to obtain the displacements, etc., at time $t + \Delta t$, then equilibrium equations at time $t + \Delta t$ are given as

$$[M]\{\ddot{\delta}\}_{t+\Delta t} + [[N(\delta)]\{\delta\}]_{t+\Delta t} = \{F\}_{t+\Delta t} \tag{10}$$

where $\{\delta\}_{t+\Delta t}$ and $\{\ddot{\delta}\}_{t+\Delta t}$ are the vectors of nodal displacements and accelerations at time $t + \Delta t$, respectively. $[[N(\delta)]\{\delta\}]_{t+\Delta t}$ is the internal force vector at time $t + \Delta t$ and is given as

$$\begin{aligned} [[N(\delta)]\{\delta\}]_{t+\Delta t} = \big\{\big[[K_L] + (1/2)[N_1] + (1/3)[N_2] \\ + [N_3]\big]\{\delta\}\big\}_{t+\Delta t}. \end{aligned} \tag{11}$$

In developing equations for the implicit integration, the

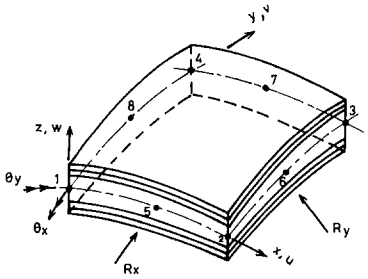

Fig. 1 Geometry of a laminated curved shell element

internal force vector $[[N(\delta)]\{\delta\}]$ at time $t + \Delta t$ are written in terms of internal forces at time t using tangent stiffness approach as

$$[[N(\delta)]\{\delta\}]_{t+\Delta t} = [[N(\delta)]\{\delta\}]_t + [K_T(\delta)]_t\{\Delta\delta\} \quad (12)$$

where $[K_T(\delta)] = [[K_L] + [N_1] + [N_2] + [N_3]]$ is the tangential stiffness matrix and $\{\Delta\delta\} = \{\delta\}_{t+\Delta t} - \{\delta\}_t$.

Substituting Eq. (12) into Eq. (10), one obtains the governing equations at $t + \Delta t$ as

$$[M]\{\ddot{\delta}\}_{t+\Delta t} + [K_T(\delta)]_t\{\Delta\delta\} = \{F\}_{t+\Delta t} - [[N(\delta)]\{\delta\}]_t. \quad (13)$$

To improve the solution accuracy and to avoid the numerical instabilities, it is necessary to employ iteration within each time-step, thus maintaining equilibrium.

The nonlinear equations obtained by the above procedure are solved by the Wilson-θ numerical integration method. Equilibrium is achieved for each time-step through the modified Newton-Raphson iteration scheme until the convergence criteria given by Bergan and Clough (1972) are satisfied within the specific tolerance limit of less than one percent.

3 Dynamic Buckling Criteria

Criteria for static buckling of axisymmetric shallow spherical shell are well defined, whereas it is not so far the dynamic case. The dynamic buckling criterion suggested by Budiansky and Roth (1962) is generally accepted because the results obtained by various investigators by different numerical methods using this criterion are in reasonable agreement with each other. This criterion is based on the plot of the peak nondimensional average displacement in the time history of the structure with respect to the amplitude of the load. The average displacement Δ is defined as the ratio of volume generated by the shell deformation and the constant volume under the spherical cap.

The load corresponding to a sudden jump in peak average displacement is taken as dynamic snap-through load. This buckling load is checked with another criterion where, instead of maximum average deflection, maximum deflection occurring at the apex is used.

4 Element Description

The laminated shell element used here is a C^0 continuous shear flexible element and has five nodal degrees-of-freedom, u_0, v_0, w, θ_x, and θ_y at eight nodes in a QUAD-8 element, as shown in Fig. 1.

If the interpolation functions for QUAD-8 are used directly to interpolate the five field variables u_0 to θ_y in deriving the shear strains and membrane strains, the element will lock and show oscillations in the shear and membrane stresses. Field consistency requires that the transverse shear strains and membrane strains must be interpolated in a consistent manner. Thus u_0, v_0, θ_x, and θ_y terms in the expressions for $\{\epsilon_s\}$ given in Eq. (3*d*) have to be consistent with field functions $w_{,x}$ and $w_{,y}$ as shown in the works of Somashekar and Prathap (1987) and Prathap et al. (1988). Similarly, the w term in the expressions of $\{\epsilon_p^0\}$ given in Eqs. (3*b*) has to be consistent with the field functions $(u_{0,x}, v_{0,y})$ and $(u_{0,y}, v_{0,x})$. This is achieved by using field-redistributed substitute shape functions to interpolate those specific terms which must be consistent as described by Prathap et al. (1988) and Somashekar and Prathap (1987).

5 Results and Discussion

An eight-noded quadrilateral isoparametric field-consistent doubly curved shell element is employed. Since the element is derived from the field-consistency approach, exact integration is used to evaluate all the strain energy terms. The shear correction factor which is required in a first-order theory to account for the variation of transverse shear stresses through the thickness, is taken as 5/6. The initial conditions for obtaining the nonlinear dynamic response are assumed as zero values for the displacements, velocities, and accelerations. The value of θ in Wilson-θ method is assumed as 1.4 which corresponds to an unconditionally stable scheme in linear analysis.

Since no estimate on the time-step for the nonlinear analysis is available in the literature, the critical time-step of a conditionally stable finite difference schemes (Leech, 1965; Tsui and tong, 1971) is used as a guide and a convergence study is conducted to select a time-step which yields a stable and accurate solution. The critical steps given in Leech (1965) and Tsui and Tong (1971) for thin and moderately thick plates, respectively, with suitable modifications for the case of orthotropy are taken as

$$\Delta t \le 0.25\left(\frac{\rho h}{D_{11}}\right)^{1/2}\Delta x$$

$$\Delta t \le \left[\left\{\rho\left(1 - \nu_{12}^2\right)/E_1\right\}/\left\{2 + (1 - \nu_{12})(\pi^2/12)\right.\right.$$
$$\left.\left.\times\left(1 + 1.5(\Delta x/h)^2\right)\right\}\right]^{1/2}\Delta x \quad (14)$$

where Δx, E_1 are the minimum distance between the elment node points and Young's modulus along the longitudinal direction of the fiber. ν_{12} is the major Poisson's ratio and D_{11} is defined as $E_1 h^3/12\,(1 - \nu_{12}\,\nu_{21})$.

Due to coupling effects in composite plates/shells, one has to be careful in assuming biaxial symmetry even when the geometry and loading are symmetric about the axes. Hence, the results of quarter plate/shell idealization have been verified here with full plate/shell idealization initially before proceeding to detailed numerical studies.

Laminated cross-ply and angle-ply spherical shells clamped all along the edges are considered for the numerical analysis. The details of the boundary conditions are the following:

$u_0 = v_0 = w = \theta_x = \theta_y = 0$ along the clamped boundary.

Cross-ply:

$v_0 = \theta_y = 0$ on $y = 0$, and $u_0 = \theta_x = 0$ on $x = 0$ (line of symmetry).

Angle-ply:

$u_0 = \theta_y = 0$ on $y = 0$ and $v_0 = \theta_x = 0$, on $x = 0$ (line of symmetry). (15)

The material properties are assumed as the

Orthotropic case:

(*a*) $E_1/E_2 = 2$, $G_{12}/E_2 = G_{13}/E_2 = 0.5$, $G_{23}/E_2 = 0.2$, $\nu_{12} = 0.3$,

(*b*) $E_1/E_2 = 20$, $G_{12}/E_2 = G_{13}/E_2 = 0.5$, $G_{23}/E_2 = 0.2$, $\nu_{12} = 0.3$,

and

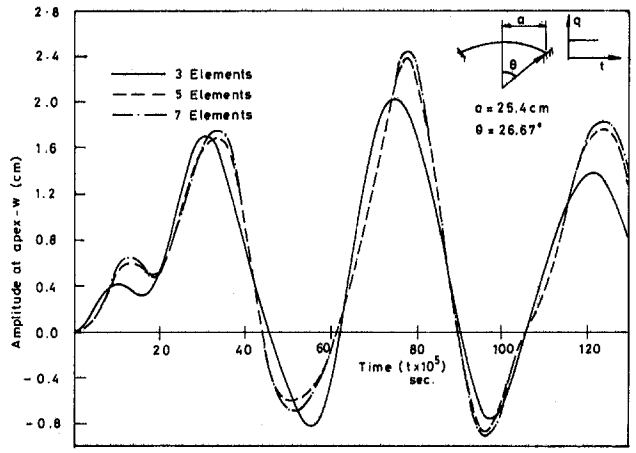

Fig. 2 Dynamic response of a spherical shell

Table 1 Dynamic buckling pressure (P) for various values of isotropic spherical cap parameter (λ)

λ		4	5	6	7.5	10
Present		0.455	0.46	0.605	0.45	0.495
Huang et al.	(1969)	0.450	0.49	---	0.50	0.420
Stephens et al.	(1969)	---	0.45	0.620	0.44	0.370
Stricklin et al.	(1969)	0.440	0.48	0.650	0.50	0.430
Ball et al.	(1973)	---	0.48	0.610	0.54	0.500
Kao et al.	(1980)	---	0.46	---	0.44	0.490
Alwar et al.	(1979)	0.440	0.48	0.580	---	0.530

Laminated case:

$$E_1/E_2 = 20,\ G_{12}/E_2 = G_{13}/E_2 = 0.5,$$
$$G_{23}/E_2 = 0.2,\ \nu_{12} = 0.3, \quad (16)$$

where E_1 and E_2 are Young's moduli along the directions parallel and perpendicular, respectively, to the fibers. G_{ij} are the relevant shear moduli.

All the computations are carried out using the Cyber 180/840A processor with double precision arithmetic.

To determine the number of elements required for the evaluation of response history, dynamic analysis is carried out by varying the number of elements for the following geometry and loading:

$$R = 56.57\,\text{cm},\ a = 25.4\ cm,\ h = 1.04\ cm,\ E = 0.739 \times 10^6\ \text{kgf/cm}^2,\ \nu = 0.3,\ q = 7.042\,\text{kgf/cm}^2 \quad (17)$$

where a, q are the base radius of the spherical cap and the externally applied pressure load. Results are shown in Fig. 2 and on this basis, the five-element idealization is chosen for further analysis.

Results of nondimensional dynamic pressure, P_{cr}, are presented for isotropic, orthotropic, cross-ply, and angle-ply laminates for different values of the geometric parameter λ. P_{cr} and λ are given by

$$P_{cr} = \left(\frac{1}{8}\right)\left[3(1-\nu_{12}\nu_{21})\right]^{1/2}\left(\frac{h}{H}\right)^2 \frac{q a^4}{\bar{E} h^4}$$

$$\lambda = 2\left[3(1-\nu_{12}\nu_{21})\right]^{1/4}\left(\frac{H}{h}\right)^{1/2}. \quad (17)$$

Here H is the central shell rise. $\bar{E}$ is the reference stiffness of the material under consideration. It is Young's modulus for an isotropic material and $[(3/8)E_1 + (5/8)E_2]$ for orthotropic materials, as given by Tsai and Pagano (1968). For a chosen shell parameter and lamination scheme, the dynamic buckling study is carried out for step loading/right triangular pulse with different time durations. The length of response calculation time $\tau\left(=\sqrt{\frac{E_1}{\rho R^2}}\,t\right)$ carried out in computer runs is varied between 40 to 60 with the criterion that in the neighborhood of the buckling load, τ is large enough to allow deflection-time curves to fully develop. The time-step selected, based on the convergence study, is $\delta\tau = 0.1$. It is mentioned in the experimental works of Lock et al. (1968) that axisymmetric buckling occurs shortly after the application of load. The value selected for τ and $\delta\tau$ is of the same order as that of Ball and Burt (1973), Kao and Perrone (1978), and Chao and Lin (1990).

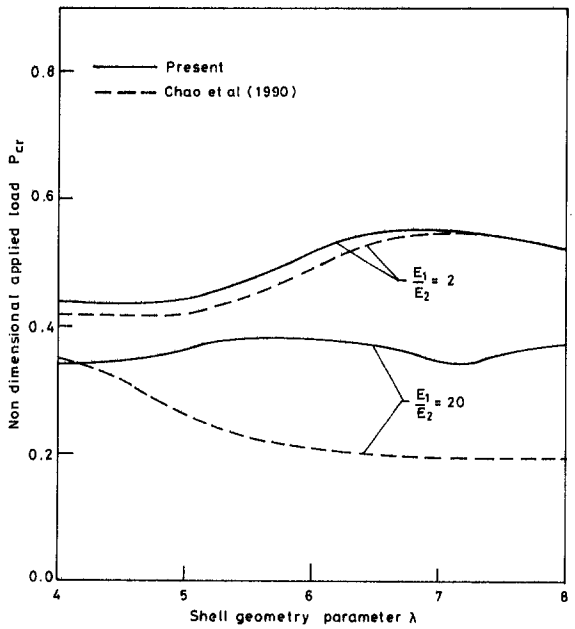

Fig. 3 Nondimensional applied load versus shell geometry parameter for an orthotropic spherical cap

The formulation developed here is validated in Table 1 for isotropic material for different values of shell parameters by comparing with the available results (Huang, 1969; Stephens and Fulton, 1969; Stricklin and Martinez, 1969; Ball and Burt 1973; Kao and Perrone, 1978).

In Fig. 3, for two different orthotropic material properties, the variations of dynamic buckling load with geometric parameter are plotted for a single layered shallow spherical shell subjected to uniform pressure of infinite duration and these are compared with the results based on classical shell theory (Chao and Lin, 1990). The figure shows that the present shear flexible theory predicts a higher buckling pressure compared to the classical theory. This behavior of a spherical shell is in contrast with that of a flat plate or cylindrical shell panel and has been reported earlier in connection with studies on bending (Alwar and Narasimhan, 1990, 1991), vibrations (Tene and Sheinman, 1978), and static buckling (Chao et al., 1988). It can further be noted from Fig. 3 that the discrepancy between the classical and shear deformation theories increases as the degree of orthotropy increases. That is, for the low shear stiffnesses (G_{12}/E_1), the behavior of the spherical cap approaches membrane response. Consequently, this leads to decrease in the lateral deflection w and in turn increases the load-carrying capacity.

The dynamic response at different load levels for $\lambda = 6$ is

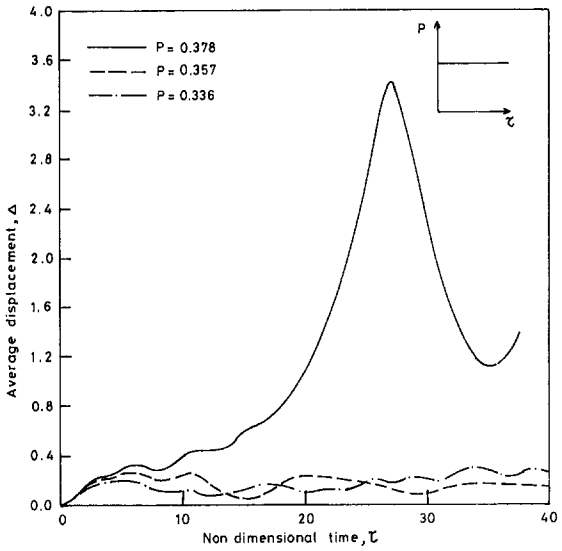

Fig. 4 Average displacement versus nondimensional time for an orthotropic spherical cap ($\lambda = 6$, $E_1/E_2 = 20$)

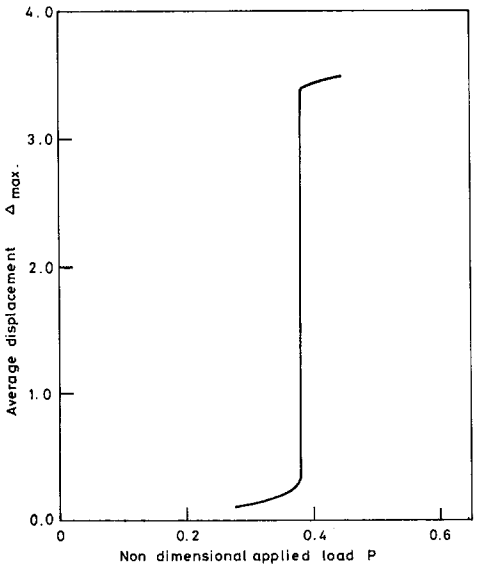

Fig. 5 Average maximum displacement versus a nondimensional applied load for orthotropic spherical cap ($\lambda = 6$, $E_1/E_2 = 20$)

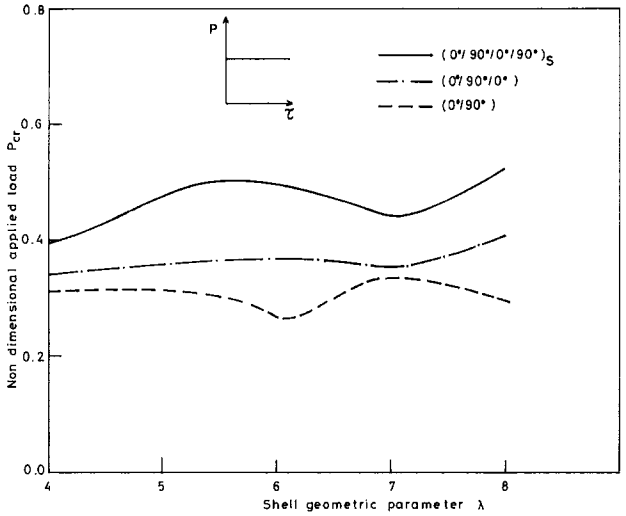

Fig. 6 Nondimensional applied load versus shell geometry parameter for cross-ply spherical caps

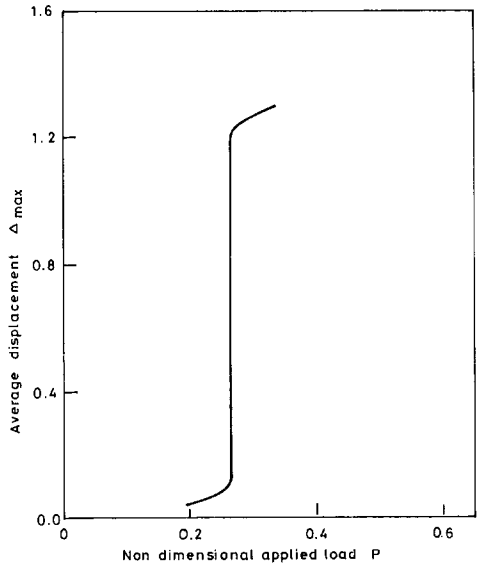

Fig. 7 Average maximum displacement versus nondimensional applied load for two-layered spherical cap (0 deg / 90 deg, $\lambda = 6$)

shown in Fig. 4. From these results, the plot between the average displacement and applied pressure load is drawn in Fig. 5 for $\lambda = 6$. It can be seen that there is a sudden jump in the value of average displacement when the external pressure reaches the value $P = 0.378$ and hence this value corresponds to the dynamic buckling load, P_{cr}.

A parametric study of a laminated anisotropic shallow spherical cap is now carried out for the following combination of ply-angles and number of layers:

Cross-ply: (0 deg/90 deg), (0 deg/90 deg/0 deg), (0 deg/90 deg/0 deg/90 deg)$_s$

Angle-ply: (45 deg/ − 45 deg), (45 deg/ − 45 deg/45 deg), (45 deg/ − 45 deg/45 deg/ − 45 deg)$_s$.For (0 deg/90 deg) and (45 deg/ − 45 deg) laminates $B_{ij} \neq 0$ and the existence of B_{ij} is equivalent to having an imperfection. For the other laminates considered above, $B_{ij} = 0$.

The critical nondimensional buckling pressure is shown in Fig. 6 for the cross-ply laminates for different values λ. For $\lambda = 6$, the dynamic snap-through behavior can be observed to occur at $P_{cr} = 0.265$ from the plot of the variation of maximum average displacement with the applied load as given in Fig. 7. Similar results for angle-ply laminates are plotted in Fig. 8. For $\lambda < 4.5$, snap buckling does not occur for a three and eight-layered shell. For cross-ply and angle-ply laminates, it is noticed from Figs. 6 and 8 that the dynamic buckling pressure increases with the increase in the number of layers. However, this increase is considerable for the cross-ply shell compared to the angle-ply shell. It can be noted that the coupling rigidities, B_{ij}, in general reduce the stiffness of the laminated shells and these coupling effects get weakened when the number of layers are increased.

The influence of the different pulses on dynamic buckling characteristics is brought out in Fig. 9 for the three-layered (cross-ply and angle-ply) shell with $\lambda = 6$. It can be seen that the buckling load decreases as pulse duration increases. It can be noticed that the dynamic buckling load increases rapidly as τ decreases, and is in fact infinitely large for an ideal impulse ($\tau_0 = 0$). As τ_0 increases, the buckling load approaches asymptotically the value corresponding to a pulse of infinite duration. Further, the triangular pulse shown in the subset of Fig. 9 results always in a higher buckling load compared to the rectangular pulses, as can be expected.

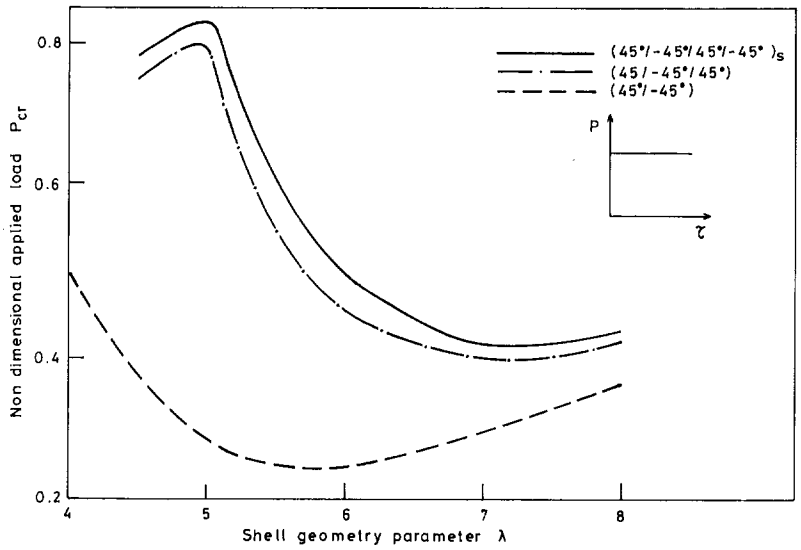

Fig. 8 Nondimensional applied load versus a shell geometry parameter for angle-ply spherical caps

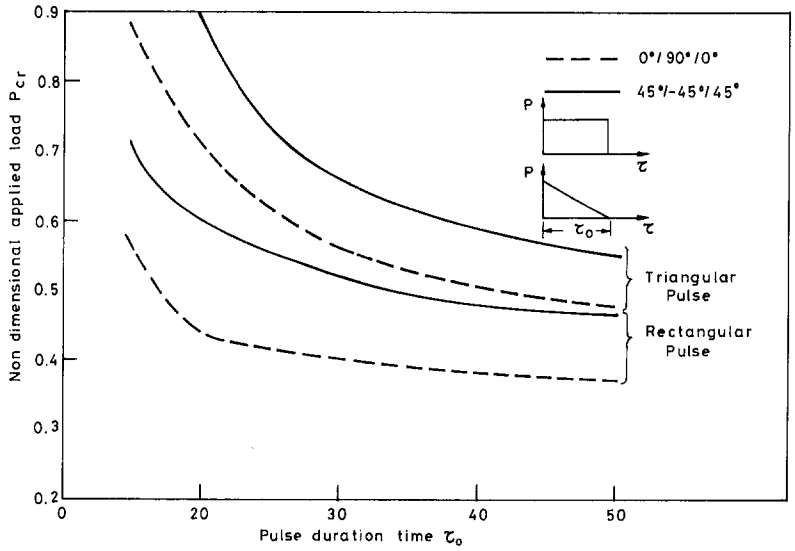

Fig. 9 Nondimensional applied load versus pulse duration time for three-layered spherical caps ($\lambda = 6$)

6 Conclusions

Dynamic buckling analysis of clamped spherical caps, made up of isotropic, orthotropic, and laminated anisotropic materials, subjected to externally applied loading, has been investigated here. An eight-noded quadrilateral doubly curved shear flexible shell element based on the field-consistency principle has been used for the first time for this purpose. Numerical results obtained here for an isotropic material are found to be fairly in agreement with previous findings. Detailed parametric studies reveal the following observations:

(i) As the degree of orthotropy increases, there is a significant difference in the value of the buckling load as predicted by the classical and shear deformation theories.

(ii) Different coupling effects that arise in anisotropic laminates reduce the buckling load. This reduction is more pronounced for a two-layered shell.

(iii) Increase in number of layers, either cross-ply or angle-ply, results in the increase of buckling load.

(iv) In all the cases considered here, dynamic snap-through buckling does not occur for λ less than 4, when subjected to a pulse of infinite duration.

(v) With the increase in the number of layers from three to eight, there is a considerable increase in the critical dynamic pressure. This effect is more for the cross-ply laminate compared to the angle-ply laminate.

(vi) The dynamic critical peak load for a triangular pulse considered here is more than that for a rectangular pulse.

References

Alwar, R. S., and Sekhar Reddy, B., 1979, "Dynamic Buckling of Isotropic and Orthotropic Shallow Spherical Caps with Circular Hole," *International Journal of Mechanical Science*, Vol. 21, pp. 681–688.

Alwar, R. S., and Narasimhan, M. C., 1990, "Application of Chebyshev Polynomials to the Analysis of Laminated Axisymmetric Spherical Shells," *Composite Structures*, Vol. 15, pp. 215–237.

Alwar, R. S., and Narasimhan, M. C. 1991, "Analysis of Laminated Orthotropic Spherical Shells," *Computers and Structures*, Vol. 41, pp. 611–620.

Ball, R. E., and Burt, J. A., 1973, "Dynamic Buckling of Shallow Spherical Shells," ASME JOURNAL OF APPLIED MECHANICS, Vol. 40, pp. 411–416.

Bergan, P. G., and Clough, R. W., 1972, "Convergence Criteria for Iterative Process," *American Institute of Aeronautics and Astronautics Journal*, Vol. 10, pp. 1107–1108.

Budiansky, B., and Roth, R. S., 1962, "Axisymmetric Dynamic Buckling of Clamped Shallow Spherical Shells," NASA TND-1510, pp. 597-609.

Chao, C. C., Tung, T. P., and Chern, Y. C., 1988, "Buckling of Thick Orthotropic Spherical Shells," *Composite Structures*, Vol. 9, pp. 113–137.

Chao, C. C., and Lin, I. S., 1990, "Static and Dynamic Snap-Through of Orthotropic Spherical Caps," *Composite Structures*, Vol. 14, pp. 281–301.

Dumir, P. C., Gandhi, M. L., and Nath, Y., 1984, "Axisymmetric Static and Dynamic Buckling of Orthotropic Shallow Spherical Caps with Flexible Supports," *Acta Mechanica*, Vol. 52., pp. 93–106.

Huang, N. C., 1969, "Axisymmetric Dynamic Snap-Through of Elastic Clamped Shallow Shell," *American Institute of Aeronautics and Astronautics Journal*, Vol. 7, pp. 215–220.

Jones, R. M., 1975, *Mechanics of Composite Materials*, McGraw-Hill, New York.

Kao, R., and Perrone, N., 1978, "Dynamic Buckling of Axisymmetric Spherical Caps with Initial Imperfection," *Computers and Structures*, Vol. 9, pp. 463–473.

Leech, J. N., 1965, "Stability of Finite Difference Equations for the Transient Response of a Flat Plate," *American Institute of Aeronautics and Astronautics Journal*, Vol. 3, pp. 1772–1773.

Lock, M. H., Okubo, S., and Whitter, J. S., 1968, "Experiments on the Snapping of a Shallow Dome under a Step Pressure Load," *American Institute of Aeronautics and Astronautics Journal*, Vol. 6, pp. 1320–1326.

Prathap, G., Naganarayana, B. P., and Somashekar, B. R., 1988, "Field Consistency Analyses of the Isoparametric Eight-Noded Plate Bending Elements," *Computers and Structures*, Vol. 29, pp. 857–874.

Rajasekaran, S., and Murray, D. W., 1973, "Incremental Finite Element Matrices," *ASCE Journal of Structural Division*, Vol. 99, pp. 2423–2438.

Saigal, S., Yang, T. Y., and Kapania, R. K., 1987, "Dynamic Buckling of Imperfection-Sensitive Shell Structures," *Journal of Aircraft*, Vol. 24, pp. 718–724.

Simitses, G. J., 1967, "Axisymmetric Dynamic Snap-Through Buckling of Shallow Spherical Caps," *American Institute of Aeronautics and Astronautics Journal*, Vol. 5, pp. 1019–1021.

Simitses, G. J., 1989, *Dynamic Stability of Suddenly Loaded Structures*, Springer-Verlag, New York.

Somashekar, B. R., and Prathap, G., 1987, "A Field Consistent 4-Noded Laminated Anisotropic Plates/Shells Element," *Computers and Structures*, Vol. 25, pp. 345–353.

Stephens, W. B., and Fulton, R. E., 1969, "Axisymmetric Static and Dynamic Buckling of Spherical Caps Due to Centrally Distributed Pressures," *American Institute of Aeronautics and Astronautics Journal*, Vol. 7, pp. 2120–2126.

Stricklin, J. A., and Martinez, J. E., 1969, "Dynamic Buckling of Clamped Spherical Cap Under Step Pressure Loadings," *American Institute of Aeronautics and Astronautics Journal*, Vol. 7, pp. 1212–1213.

Subbaraj, K., and Dokainish, M. A., 1989, "A Survey of Direct Time Integration Methods in Computational Structural Dynamics-II, Implicit Methods," *Computers and Structures*, Vol. 32, pp. 1387–1401.

Tsui, T. Y., and Tong, P., 1971, "Stability of Transient Solution of Moderately Thick Plate by Finite Difference Method," *American Institute of Aeronautics and Astronautics Journal*, Vol. 9, pp. 2062–2063.

Tsai, S. W., and Pagano, N. J., 1968, "Invariant Properties of Composite Materials," *Composite Materials Workshop*, S. W. Tsai, J. C. Halpin, and N. J. Pagano, eds., Technomic Publishing Co., Stanford, CT, pp. 233–253.

Tene, Y., and Sheinmann, I., 1978, "Dynamics of Shells of Revolution under Axisymmetric Load Involving Shear Deformation," *Computers and Structures*, Vol. 8, pp. 563–568.

Finite Element Analysis of Repeated Indentation of an Elastic-Plastic Layered Medium by a Rigid Sphere, Part I: Surface Results

E. R. Kral
Graduate Research Assistant,
Assoc. Mem. ASME.

K. Komvopoulos
Associate Professor,
Mem. ASME.

D. B. Bogy
Professor,
Fellow ASME.

Department of Mechanical Engineering,
University of California,
Berkeley, CA 94720

A comprehensive elastic-plastic finite element analysis is presented for the axisymmetric problem of a frictionless rigid sphere indenting a half-space with a harder and stiffer layer. The indenter is modeled by contact elements, thereby avoiding a priori assumptions for the pressure profile. Two layer thicknesses are examined, with layer elastic modulus and yield stress both two and four times greater than those of the substrate. Perfectly plastic and isotropic strain-hardening behavior of the layer and substrate media are investigated. At least three complete load-unload cycles are applied to a peak load of 300 times the load necessary to initiate yielding in a half-space of the substrate material. The effect of hardening properties on the loaded and residual stresses is presented and the consequences for crack initiation at the surface are discussed. Results for the contact pressure and surface stresses and deformations are presented, and the influence of residual displacements and load cycles on the contact pressure and the loaded and residual surface stresses is investigated.

1 Introduction

Improvements in the fatigue and tribological properties of contacting surfaces are commonly achieved through the application of hard and tough layers exhibiting low friction coefficients. Applications of wear-resistant layers range from cutting tools coated with 1 to 10-μm thick ceramic layers to thin-film magnetic rigid disks coated with only 20 to 30 nm of sputtered carbon. In addition, softer surface layers are often applied for reasons of performance, as in electrical contact applications where gold is often used as a surface layer to improve electrical conductivity and decrease noise. In recent years, analyses of both elastic and elastic-plastic indentations of layered media have been presented by several investigators. The formulation for the elastic indentation of a single layer on a half-space under axisymmetric surface loading has been given by Burmister (1945). Chen (1971) extended this work to axisymmetric and nonaxisymmetric surface loadings applied to single- and double-layered elastic media. Gupta and Walowit (1974) used a Green's function approach to develop a plane-strain elastic theory for arbitrary surface loadings applied to a single layer on a half-space. More recently, King and O'Sullivan (1987) presented plane-strain elastic solutions for a rigid cylinder sliding over a layered medium, and O'Sullivan and King (1988) extended this analysis to study the three-dimensional elastic problem of a sphere sliding on a single-layered half-space. Komvopoulos (1988) used the finite element technique to analyze the plane-strain problem of an elastic half-space with a harder elastic layer indented by a rigid cylinder and found that the maximum contact pressure increased considerably with the layer thickness and only marginally with friction at the contact interface.

The elastic-plastic indentation of a layered medium having a substrate stiffer than the layer has been analyzed by Kennedy and Ling (1974) using the finite element method. It was found that plastic deformation had a large effect on the contact pressure, and that the surface displacements, particularly the pile-up of material at the contact edge, depended significantly on the mechanical properties of the layer and substrate and the frictional characteristics at the layer/substrate interface. Bhattacharya and Nix (1988) used the finite element method to study the axisymmetric indentation of an elastic-perfectly plastic layered medium by a rigid cone. Load versus indentation depth curves and hardness calculations were given for both relatively hard and soft layers and were used to derive relationships for the effective hardness in terms of the layer thickness, the elastic and plastic properties of the layer and substrate, and the indentation depth. Laursen and Simo (1992) performed a similar study and presented results for load versus indentation

Contributed by the Applied Mechanics Division of THE AMERICAN SOCIETY OF MECHANICAL ENGINEERS for publication in the ASME JOURNAL OF APPLIED MECHANICS.

Discussion on this paper should be addressed to the Technical Editor, Professor Lewis T. Wheeler, Department of Mechanical Engineering, University of Houston, Houston, TX 77204-4792, and will be accepted until four months after final publication of the paper itself in the ASME JOURNAL OF APPLIED MECHANICS.

Manuscript received by the ASME Applied Mechanics Division, Dec. 21, 1992; final revision, May 30, 1993. Associate Technical Editor: L. M. Keer.

depth, surface displacement profiles, and hardness values for laminated aluminum/silicon media exhibiting linear isotropic strain hardening.

Komvopoulos (1989) used the finite element method to investigate the plane-strain problem of a rigid cylinder indenting an elastic-plastic layered medium with a layer harder and stiffer than the substrate. Significant flattening of the contact pressure profile was found, especially with increasing plastic deformation, and the maximum pressure was found to move outward toward the contact edge. Tian and Saka (1991) investigated the plane-strain elastic-plastic indentation of a multilayered half-space consisting of a gold top layer, a nickel interlayer, and a copper substrate, all exhibiting linear isotropic strain hardening. Elastic indentations produced contact pressures bounded by parabolic and elliptical distributions, while elastic-plastic indentations produced relatively uniform pressure distributions with a slightly higher pressure near the contact edge for sufficiently deep indentations or a sufficiently thin interlayer. Recently, Montmitonnet et al. (1993) performed a finite element analysis of elastic-plastic indentation of a steel substrate and a thin chromium layer by a ruby sphere. Results were given for stresses on the surface and the axis of symmetry of the layered medium. High tensile stresses were observed under both loaded and residual conditions, with the highest stresses occurring at the surface of the medium. Kral et al. (1993) studied the repeated indentation of a half-space by a rigid sphere, performing up to four complete load and unload cycles on half-spaces possessing different elastic and plastic properties. It was found that the surface stresses depended primarily on the strain-hardening parameters and only secondarily on the elastic properties, and that reyielding occurred upon unloading in a small surface region near the edge of the contact at maximum load.

Although the aforementioned studies have yielded valuable insight into contact mechanics of layered media, detailed information about the significance of the layer thickness, elastic-plastic properties of the layer and substrate materials, and loading cycles on the surface stresses and deformations of repeatedly indented layered media is relatively sparse. The objective of the present investigation, therefore, is to provide a comprehensive finite element analysis of the surface stress and deformation fields resulting from the repeated frictionless indentation of an elastic-plastic layered medium by a rigid sphere. The sphere was modeled by contact elements, and loads up to 300 times the initial yield load of a half-space of the substrate material were applied. To examine the effects of the layer thickness and the elastic and plastic properties on the contact pressure and surface stresses and deformations, two layer thicknesses and layers two and four times stiffer and harder than the substrate were considered. The significance of the plastic flow behavior was studied by assuming elastic-perfectly plastic and isotropic strain-hardening behavior for both the layer and substrate media. Results revealing the effects of the layer thickness and material properties of the layer and substrate on the contact pressure distribution, surface displacements, and the surface stress field will be presented for repeated elastic-plastic indentations. In addition, the significance of material properties on the residual displacements and surface stresses will be examined in light of the finite element solutions. In a subsequent paper (Kral et al., 1995), the effect of layer thickness and material properties on the subsurface stresses and plastic deformation will be examined.

2 Modeling Procedures

2.1 Finite Element Mesh. To investigate the deformation arising in microhardness indentation testing and to enhance the convergence, a smooth, rigid spherical indenter of radius, R, equal to 1500 nm was modeled. Since the indentation depths and contact radii considered were relatively small, the solutions are also representative of an elastic-plastic layered medium indented by a blunt indenter. The analysis was performed with the multipurpose finite element code ABAQUS. The sphere was modeled by a total of 44 three-node rigid-surface contact (interface) elements. Two nodes of each contact element corresponded to surface nodes of the layered medium from $r/R = 0.0$ to $r/R = 0.04$, which was sufficient for modeling the anticipated contact radius. The third node was a common master node assigned to the indenter, which was constrained against rotation and radial displacement. Indentation was modeled by incrementally applying normal loads to the master node. The penetration of the indenter into the layered medium and the relative displacement at the interface were determined by the contact elements. This information was used in surface constitutive models (contact and surface friction) in the program to determine the surface traction. The traction was then decomposed into normal and tangential components based on the outward normal vector of the rigid surface. In view of the marginal effect of friction in normal contact (Komvopoulos, 1988), only frictionless indentations were considered. Hard contact was modeled, in which normal traction was applied only when the clearance between the surface nodes of the layered medium and the indenter surface reached zero.

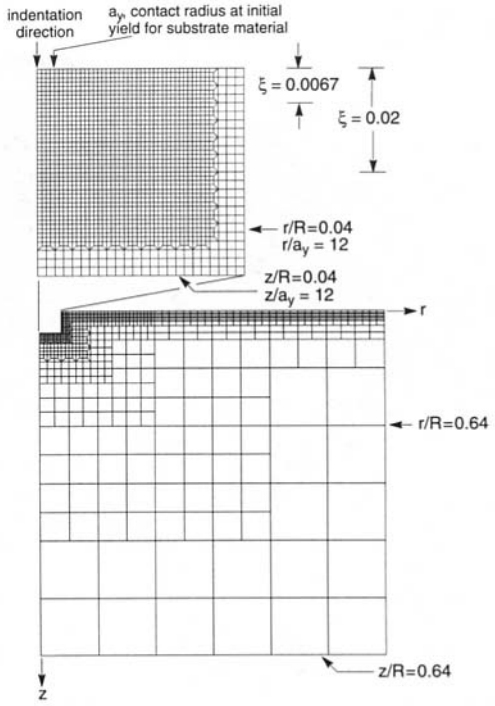

Fig. 1 Finite element discretization of the layered medium

The finite element mesh, shown in Fig. 1, consisted of 2721 four-node quadrilateral axisymmetric elements comprising 2848 nodes. A linear 2×2 integration scheme was used. The r- and z-dimensions of the mesh were set equal to 960 nm, i.e., $r/R = z/R = 0.64$. The vertical boundaries of the mesh at $r/R = 0.0$ and 0.64 were constrained against displacement in the r-direction, and the bottom boundary, $z/R = 0.64$, against displacement in the z-direction. The mesh is appropriate for modeling up to six layers of 5-nm thickness each. The region of the mesh bounded by $r/R = 0.033$ are $z/R = 0.033$ was refined, as shown in the inset of Fig. 1, to account for the high stress gradients at the edge of the contact region. Mesh refinement was accomplished by using trapezoidal elements near the contact region and by imposing linear constraints farther away. The smallest elements were 1.25 nm square. Favorable comparisons between finite element and analytical

results for elastic indentations, in conjunction with results for repeated elastic-plastic indentations of a homogeneous half-space based on the present mesh configuration, have been presented in a previous publication (Kral et al., 1993).

2.2 Material Properties and Plasticity Models. According to the von Mises yield criterion adopted in this study, the yield condition is

$$f = J_2 - k^2 = 0,$$

where k is a material constant and J_2 is the second invariant of the deviatoric stress tensor, given by

$$J_2 = \frac{1}{2} S_{ij} S_{ij}, \text{ where } S_{ij} = \sigma_{ij} - \frac{1}{3} \delta_{ij} \sigma_{kk}.$$

In terms of the uniaxial yield stress, the yield criterion reduces to

$$\sigma_M = \left[\frac{3}{2} S_{ij} S_{ij} \right]^{1/2} = \sigma^o, \tag{1}$$

where σ_M is the von Mises equivalent stress and σ^o is the yield stress. The material model used for plastic deformation was based on the flow rule

$$d\epsilon_{ij}^p = d\lambda S_{ij},$$

where $d\epsilon_{ij}^p$ are the components of plastic strain increment and $d\lambda$ is a function of the flow stress and the plastic strain rate. The usual assumption of negligible plastic volume change was maintained. To account for boundary nonlinearities arising from the use of contact elements, an updated Lagrangian formulation was used.

Since isotropic strain hardening was assumed for both the layer and substrate materials, the existence of the multiplicative decomposition of the deformation gradient into elastic and plastic parts that is used in the finite element code is ensured (Kral et al., 1993). Strain hardening was represented by the following relationship:

$$\frac{\sigma^o}{\sigma_y} = \frac{K}{\sigma_y} \epsilon_{eq}^n, \tag{2}$$

where σ_y is the initial yield stress of the substrate material, K is the strength coefficient, n is the strain-hardening exponent, and ϵ_{eq} is the equivalent plastic strain, defined as

$$\epsilon_{eq} = \int_S \left[\frac{2}{3} d\epsilon_{ij}^p \, d\epsilon_{ij}^p \right]^{1/2}, \tag{3}$$

where S is the strain path. The hardening relation and flow rule apply only to yielding material for which $\sigma_M = \sigma^o$. When $\sigma_M < \sigma^o$, the usual elastic constitutive equations apply.

Elastic moduli, stresses, and pressures were normalized by the initial yield stress of the substrate, σ_y. Loads and distances were normalized respectively by the load, P_y, and the contact radius, a_y, corresponding to the initial yield condition of a homogeneous substrate with an elastic modulus equal to $684.6\sigma_y$. Results are presented in terms of the parameter β, which is the ratio of both the layer-to-substrate normalized elastic moduli and the layer-to-substrate initial yield stresses. The values of β assumed in the analysis were equal to 2 and 4, representing a layer two and four times, respectively, stiffer and harder than the substrate. The layer thickness is represented by the nondimensional parameter ξ, which is the ratio of the layer thickness to the sphere radius. Two different layer thicknesses, 10 nm (ξ = 0.0067) and 30 nm (ξ = 0.02), were modeled, as shown in Fig. 1. The elastic and plastic material properties of the layer and the substrate are listed in Table 1. The values of K were calculated from the hardening equation at the initial yield stress, i.e., σ/σ_y = 1.0 for the substrate material, σ/σ_y = 2.0 for the layer with β = 2, and σ/σ_y = 4.0 for the layer with β = 4. The same strain-hardening exponent was used in both the layer and substrate media.

Table 1 Elastic and plastic material properties

	E/σ_y	ν	β	K/σ_y	n
Substrate	684.6	0.3	1	1.00 7.09 26.17	0.0 0.3 0.5
Layer 1	1369.2	0.3	2	2.00 14.18 52.33	0.0 0.3 0.5
Layer 2	2738.4	0.3	4	4.00 28.36 104.66	0.0 0.3 0.5

2.3 Nondimensional Indentation Parameter. To obtain generalized solutions for the contact pressure and stresses as a function of the layer and substrate properties, a dimensionless strain parameter which depends on the indentation depth or contact radius was used. This strain parameter, Λ, is defined as

$$\Lambda = \left(\frac{E/\sigma_y}{1-\nu^2} \right)_{\text{eff}} \frac{a}{R(\sigma_o^R/\sigma_y)_{\text{eff}}}, \tag{4}$$

where E and ν are the elastic modulus and Poisson's ratio, respectively, R is the sphere radius, a is the contact radius, and σ_y is the initial tensile yield stress of the substrate. A similar strain parameter was used in the previous study (Kral et al., 1993), in which σ_o^R was a representative flow stress corresponding to a representative strain $\epsilon_R = 0.2a/R$, as suggested by Johnson (1985) for indentations of a homogeneous half-space. For indentation of a layered half-space, however, this parameter must be expressed in terms of the effective stiffness and effective representative flow stress to account for the properties of both the layer and the substrate, the indentation depth or contact radius, and the layer thickness. These effective values are indicated in Eq. (4) above.

Relations for the elastic compliance of a layered medium as a function of the projected area of contact underneath the indenter have been derived by King (1987) for flat-ended punches of various cross-sections. Based on this analysis, simplified for a rigid indenter, the effective stiffness in Eq. (4) may be defined as

$$\left(\frac{E/\sigma_y}{1-\nu^2} \right)_{\text{eff}} = \left[\frac{1-\nu_l^2}{E_l/\sigma_y} (1 - e^{-\alpha t/a\sqrt{\pi}}) + \frac{1-\nu_s^2}{E_s/\sigma_y} e^{-\alpha t/a\sqrt{\pi}} \right]^{-1}, \tag{5}$$

where the subscripts s and l refer to substrate and layer properties, respectively, t is the layer thickness, and α is a numerical factor for the indentation of a circular flat-ended rigid punch calculated by a sixth-order polynomial fit to selected data points obtained from the analysis by King (1987).

The expression for the effective representative flow stress of the layered medium was obtained from finite element results given by Bhattacharya and Nix (1988) for the elastic-plastic indentation of a layered half-space by a rigid cone. They obtained relations for the effective hardness of the layered structure as a function of the indentation depth, layer thickness, and material properties of the layer and the substrate. The expression given by Bhattacharya and Nix (1988) for the effective hardness of a layer on a softer substrate was modified by replacing the layer-to-substrate hardness ratio by the appropriate tensile yield stress ratio and the indentation depth with the contact radius. The latter change was motivated by the expectation that for similar sizes of the plastic zone under a sharp conical or a spherical indenter, much greater indentation depths will be observed for the cone than for the sphere, whereas the contact radii will be similar. This assumption was qualitatively verified by comparing the plastic zone size underneath a conical indenter presented by Bhattacharya and Nix (1991) with that underneath a spherical indenter given in the previous work (Kral et al., 1993). Bhattacharya and Nix (1991)

have shown that for indentations of bulk silicon and aluminum the plastic zone depth is typically about 1.5 and 3.0 times the contact radius, respectively. Results from Kral et al. (1993) indicate that for the range of materials investigated, the depth of the plastic zone is typically about twice the contact radius. However, given the same contact radius, the indentation depth for the cone is approximately 24 nm, whereas that for the sphere is only 1.15 nm. Thus, the size of the plastic zone, and the extent of plastic deformation, is best correlated between spherical and conical indenters on the basis of the contact radius rather than the indentation depth.

Using the above modifications, the expression relating the effective hardness to indentation parameters for a hard layer on a softer substrate given by Bhattacharya and Nix (1988) becomes

$$\left(\frac{\sigma_o^R}{\sigma_y}\right)_{\text{eff}} = \frac{\sigma_s}{\sigma_y}\left\{1+\left(\frac{\sigma_l}{\sigma_s}-1\right)\exp\left[-\left(\frac{a}{t}\right)\Big/\left(\frac{E_l}{E_s}\right)^{1/2}\right]\right\}, \quad (6)$$

where the subscripts and variables are the same as those defined previously. The representative flow stresses for the layer and the substrate, σ_l and σ_s, respectively, are calculated from Eq. (2) using the representative strain $\epsilon_R = 0.2a/R$, i.e.,

$$\sigma_l = K_l \quad \epsilon_R^n,$$

and

$$\sigma_s = K_s \quad \epsilon_R^n.$$

Equations (5) and (6) yield expressions corresponding to the substrate material for contact radii much larger than the layer thickness and expressions corresponding to the layer material for contact radii much smaller than the layer thickness.

To verify the validity of Eqs. (4)–(6), results for the indentation of a half-space with substrate material properties (Kral et al., 1993) were compared with results for the indentation of the thinner, more compliant, and softer layer ($\xi = 0.0067$, $\beta = 2$). In this case, the layer thickness is less than 20 percent of the final contact radius and the layer is relatively compliant and soft. Thus, it is expected that the plastic deformation in the substrate will be similar to that in the half-space with substrate properties for equivalent Λ values. Comparable Λ values occurred at $P/P_y = 300$ for the layered half-space ($\Lambda = 27.04$) and $P/P_y = 275$ for the homogeneous half-space ($\Lambda = 27.68$). For these load conditions, the maximum equivalent plastic strain was 0.021 for both cases, and the depth of the plastic zone was approximately $23a_y$ for the half-space and $23.6a_y$ for the layered medium. Thus, the degree of plastic deformation is very similar in the two cases having similar Λ parameters.

2.4 Modeling of Repeated Indentations. For each set of material properties, interaction between the indenter and the layered medium was simulated by incrementally increasing the indentation load in 20 steps to a maximum of 300 times the initial yield load of a half-space made of substrate material, P_y. The layered medium was then unloaded incrementally back to zero following the same path. The convergence tolerance for establishing nodal force equilibrium was equal to $10^{-9}\,\sigma_y$. The load in each step was applied linearly in 10 increments, and a maximum of 15 iterations was allowed in each increment to reach equilibrium within the specified tolerance. Repeated indentations were simulated by applying identical load-unload cycles.

Software was developed to analyze the results and generate plots of user-defined variables. For preprocessing, several FORTRAN subroutines were written to convert the finite element mesh data generated with the MENTAT preprocessor to input data files in the ABAQUS format. CAEDS was used to read ABAQUS results and generate contour plots of the data. The finite element calculations and post-processing were performed on an IBM RS6000 Model 540 workstation. The typical CPU time for an elastic-plastic indentation from zero load to maximum load was about 9.5 hours.

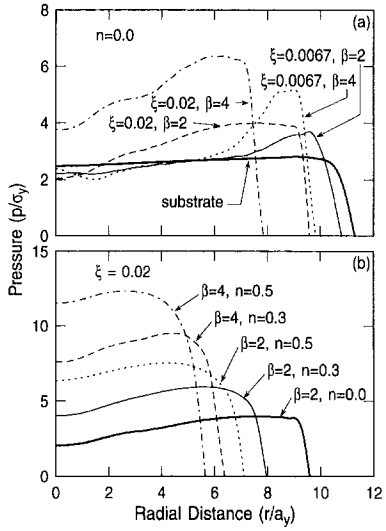

Fig. 2 Contact pressure distribution at the peak load $P/P_y = 300$ of the first load half-cycle

3 Results and Discussion

Finite element results demonstrating the significance of the thickness and elastic-plastic properties of the layer, the indentation load, and the number of load cycles on the resulting surface stress and deformation fields are presented in the following sections. The incremental increase of the load to its maximum value and the subsequent incremental unloading to zero load will be termed a "load cycle." Either the loading or unloading portion of this entire cycle will be known hereafter as a "half-cycle." In the subsequent discussion, it will be understood that either "stiffer" or "harder" refers to the layer with the larger elastic modulus and yield strength (or hardness) ratio (i.e., $\beta = 4$), while "softer" or "more compliant" refers to the layer with the smaller elastic modulus and yield strength ratio (i.e., $\beta = 2$).

3.1 Contact Pressure Distribution. Figure 2 shows the variation of the contact pressure at the peak load $P/P_y = 300$ of the first load half-cycle in terms of the layer thickness and elastic-plastic material properties. The contact pressure corresponding to a homogeneous elastic-perfectly plastic half-space having the substrate material properties is also shown in Fig. 2(*a*) for comparison. While the homogeneous half-space develops an approximately uniform contact pressure over the entire contact radius, Fig. 2(*a*) shows that the presence of a hard and stiff layer intensifies the pressure distribution significantly, producing a higher pressure peak near the contact edge and a correspondingly smaller contact radius. Similar results have been reported for indentation of half-spaces coated with harder and softer surface layers (Komvopoulos, 1989; Montmitonnet et al., 1993; Kennedy and Ling, 1974). Although the pressure peak increases with both layer thickness and stiffness, the localization of a high maximum pressure to a small region near the contact edge is particularly pronounced with relatively thin layers. The final contact radius decreases by increasing either the thickness or the stiffness of the layer. Figure 2(*b*) shows that increasing the layer and substrate strain-hardening exponent also increases the maximum contact pressure and decreases the final contact radius. Although the pressure peak again occurs near the contact edge, the pressure profiles shown in Fig. 2(*b*) are relatively more uniform than those shown in Fig. 2(*a*) for the same layer thickness.

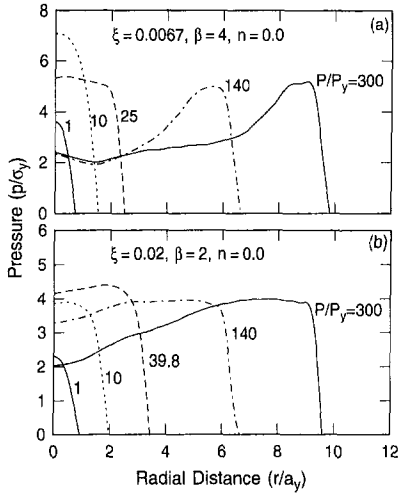

Fig. 3 Variation of contact pressure with indentation load during the first load half-cycle

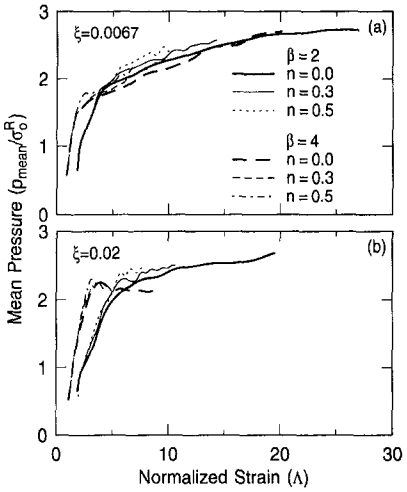

Fig. 4 Variation of mean contact pressure with normalized strain during the first load half-cycle

Figure 3 demonstrates the development of the contact pressure during the first load half-cycle for two nonhardening cases. Figure 3(*a*) shows the contact pressure as a function of load for the thinner and harder layer ($\xi = 0.0067$, $\beta = 4$), while Fig. 3(*b*) shows similar results for the thicker and softer layer ($\xi = 0.02$, $\beta = 2$). In both cases, the contact pressure profile lies between elliptical and parabolic distributions at a load $P/P_y = 1$, i.e., the load at which yielding commences in a homogeneous half-space with substrate properties ($\beta = 1$). Elastic contact pressures bounded by elliptical and parabolic distributions were also observed by Tian and Saka (1991) for the indentation of a two-layer half-space. For loads $P/P_y \geq 10$ (Fig. 3(*a*)) or $P/P_y \geq 39.8$ (Fig. 3(*b*)), the maximum pressure decreases and the contact radius increases significantly. Comparison of Figs. 3(*a*) and 3(*b*) indicates that higher pressures are generated with the relatively thinner and stiffer layer, suggesting a lower yield limit. In all the nonhardening cases, the central pressure begins to decrease and the maximum pressure begins to move toward the contact edge when both the layer and the substrate yield along the axis of symmetry. The development of a maximum pressure at the contact edge becomes more pronounced at heavy loads, when plasticity effects become dominant. Thus, the decrease in the maximum pressure at the center of contact followed by an outward movement of the maximum pressure toward the contact edge may be attributed to plastification of the underlying material. As a consequence, the increasing load is accommodated by the expansion of the contact area and the increased pressure near the outer elastic-plastic boundary. In general, there seems to be no relationship between the maximum central pressure and yielding at the interface for the hardening cases. This may be due to the material underneath the indenter continuing to support the increasing load through strain hardening, as well as the expansion of the contact area and the increased pressure near the contact edge that also occurs in the nonhardening cases.

Figure 4 shows the mean pressure normalized by the effective representative flow stress, given by Eq. (6), as a function of the strain parameter Λ for all material cases. Figures 4(*a*) and 4(*b*) show results for the thinner and thicker layers, respectively. In all cases examined, the maximum value of Λ is less than 30, which corresponds to the threshold value for fully plastic deformation of a homogeneous half-space indented by a spherical indenter (Johnson, 1985); hence, all indentations are in the elastic-plastic regime. The cases exhibiting the most advanced plastic deformation, as indicated by the largest Λ values, approach a maximum mean pressure of about $2.8\ \sigma_o^R$. This is in good agreement with the value of $2.85\ \sigma_o^R$ given by the slip-line solution for a rigid circular punch on a homogeneous rigid-plastic medium (Johnson, 1985), and also with the empirical value of $2.8\ \sigma_o^R$ given by Tabor (1970) for fully plastic indentation of an elastic-plastic half-space by a sphere. Thus, the normalized mean pressure for indented layered media approaching fully plastic deformation correlates well with that for indented half-spaces in the fully plastic region.

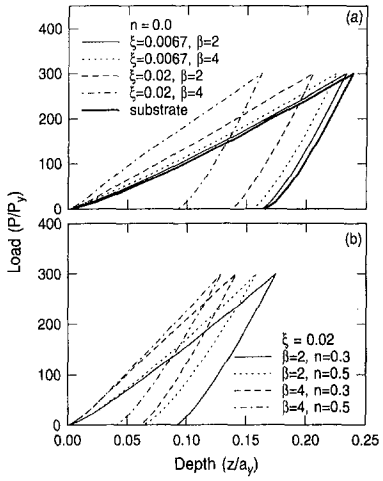

Fig. 5 Variation of indentation load with depth during the first load cycle

3.2 Load Versus Indentation Depth. The significance of the layer thickness and material properties on the relationship between the sphere load and indentation depth can be interpreted in light of the results shown in Fig. 5. Results for nonhardening layered media and a half-space with substrate properties are shown in Fig. 5(*a*), while Fig. 5(*b*) demonstrates the effect of strain hardening of both the layer and substrate on the load versus indentation depth response for the thicker layer. According to Fig. 5(*a*), both the maximum and residual indentation depths for the thinner layers decrease slightly with increasing elastic modulus and hardness of the layer. Comparison with the results for the homogeneous half-space shows that the effect of the thinner layer on the maximum and residual depths is small. However, the thicker layer produces a pronounced effect on the maximum and residual indentation depths, especially with increasing layer stiffness (and hard-

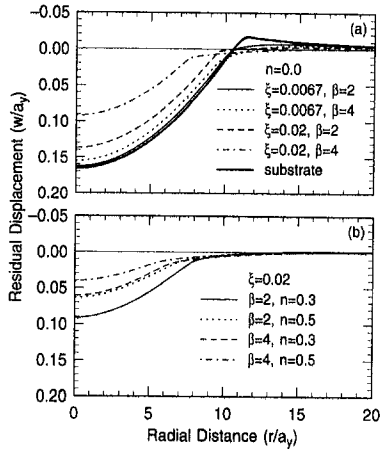

Fig. 6 Residual surface displacements after the first unload half-cycle

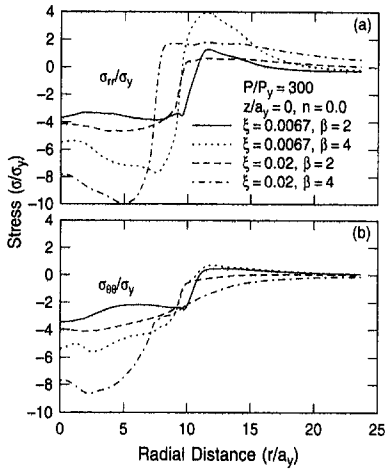

Fig. 7 Effect of layer thickness, stiffness, and hardness on the surface stresses for the first load half-cycle

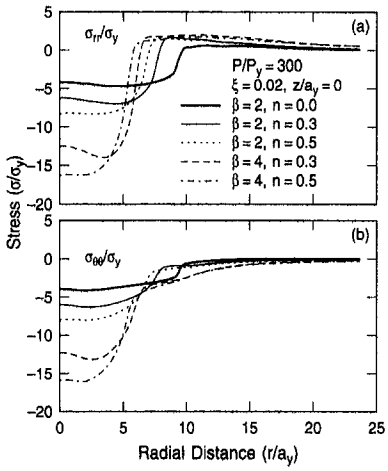

Fig. 8 Effect of layer stiffness and hardness and strain hardening of the layer and substrate on the surface stresses for the first load half-cycle

ness); compared with the homogeneous half-space, the maximum and residual indentation depths for $\beta = 2$ and 4 are smaller by approximately 25 and 50 percent, respectively. Figure 5(*b*) shows that while the maximum indentation depth for the case having $\beta = 2$ and $n = 0.3$ is slightly lower than that of the nonhardening case shown in Fig. 5(*a*), the corresponding residual displacement is significantly smaller. Figure 5(*b*) demonstrates that increasing the strain-hardening exponent and/or the layer elastic modulus and hardness leads to smaller indentation depths. For the stiffer and harder layer, the reduction in indentation depth due to strain hardening is slightly less pronounced than the more compliant and softer layer. As anticipated, increasing the thickness, stiffness, and hardness of the layer and the strain-hardening exponent of both the layer and substrate materials leads to greater deviations from the load versus indentation depth relationship of the homogeneous medium. Subsequent load cycles essentially retrace the unloading portion of the load versus indentation depth curves shown in Fig. 5 with very little deviation.

All the unloading curves shown in Fig. 5 reveal an initially linear response, which is characteristic of elastic-plastic indentations. This behavior is due to the elastic recovery of the material and the small changes in the contact width and pressure profile occurring during the initial stages of unloading. While the different slopes of the loading curves reveal a significant effect of the layer thickness and material properties, the similar slopes of the linear portions of the unloading curves indicate that the linear elastic behavior during unloading is not significantly affected by the presence of the layer. Thus, the linear portion of the unloading curve is primarily influenced by the relaxation of the substrate material.

3.3 Residual Displacements. Figure 6 shows the effect of the layer thickness and material properties on the residual vertical displacement of the surface, w/a_y, after the first load cycle. Results for the indentation of both layered media and a half-space of the substrate material are shown in Fig. 6(*a*) for comparison. The substrate material shows a pronounced region of pileup at the maximum contact radius that is absent in the layered cases. The layer causes a gradual rise of displaced material above the original flat surface outside the maximum contact radius. The amount of material rising above the original surface and the depth of the residual indentation decrease with increasing layer thickness and/or stiffness and hardness. The pronounced pile-up of displaced material at the contact edge in the case of homogeneous media is associated with yielding of a surface region at this location during the unload half-cycle (Kral et al., 1993). It has been found that this particular reyielding behavior does not occur with layered media (Kral et al., 1995).

Strain hardening of both the layer and the substrate also decreases the depth of the residual indentation, as shown for the thicker layer in Fig. 6(*b*). This is expected, since the maximum indentation depth also decreases with hardening, as evident in Fig. 5(*b*). Comparison of Figs. 6(*a*) and 6(*b*) reveals that strain hardening virtually eliminates the rise of displaced material beyond the maximum contact radius.

3.4 Surface Stresses. Stress distributions for the surface nodes at the maximum load of the first load half-cycle are shown in Figs. 7 and 8. The effect of thickness, stiffness, and hardness of the layer on the radial and hoop stresses, σ_{rr} and $\sigma_{\theta\theta}$, is shown in Figs. 7(*a*) and 7(*b*), respectively. For all cases shown in Fig. 7(*a*), the radial stress is compressive inside the contact region and becomes tensile at the free surface after passing through zero approximately at the contact edge. The tensile radial stress increases with layer stiffness and hardness but decreases with layer thickness. Figure 7(*b*) indicates that the surface hoop stress is also compressive inside the contact region. However, the thinner layers exhibit a tensile hoop stress at the contact edge, while the hoop stress in the thicker layers remains compressive. The appearance of a tensile hoop stress at the contact edge may be attributed to the development of a band of tensile hoop stress surrounding and constraining the plastic zone (Kral et al., 1995). The tensile hoop stress for the thinner layer increases slightly with layer stiffness and hard-

ness, indicating that radial cracking may occur in the case of a harder and stiffer surface layer under relatively heavy loads. However, the significantly larger tensile radial stress makes the formation of ring cracks more likely in thinner layers with randomly oriented microdefects. These results may be compared with those obtained for indentation of a half-space of the substrate material (Kral et al., 1993), in which the nonhardening material exhibited an entirely compressive radial stress at the surface, while the hoop stress reached a tensile peak at the contact edge. Thus, surface radial crack formation is dominant in homogeneous media due to the tensile hoop stress. Indeed, from the radial stress results shown in Fig. 7(*a*), it follows that as the layer stiffness and hardness decrease, approaching the properties of the substrate, the tensile radial stress peak also decreases. For the hoop stress in the thicker layer shown in Fig. 7(*b*), the stress at the contact edge increases significantly as the layer stiffness and hardness decrease, revealing a trend toward the tensile hoop stress at the contact edge encountered in the indentation of a homogeneous half-space. The thinner layer already exhibits a tensile hoop stress which decreases slightly with decreasing layer stiffness. However, since this decrease is very small for a 50 percent reduction in stiffness and hardness, it is considered that the hoop stress will asymptotically approach a tensile value as the layer stiffness is further reduced. In addition, the results for surface radial stresses are consistent with those of Montmitonnet et al. (1993), who also observed a tensile radial stress beyond the contact edge. However, for a ξ ratio equal to 0.0069, their results showed compressive hoop stresses throughout the surface. This may be attributed to the smaller applied load (P/P_y = 32) used in that study. At the lower load, the tensile hoop stress surrounding the plastic zone (Kral et al., 1995) may not have reached the surface.

The effect of strain hardening on the surface stresses during the first load half-cycle is shown in Fig. 8 for the thicker layer. Results for the nonhardening layer with $\beta = 2$ are also included for comparison. As shown in Fig. 8(*a*), strain hardening intensifies the compressive radial stress in the central region of the contact and increases the tensile radial stress just outside the contact edge, compared with the stress in the nonhardening medium; however, the difference between the maximum tensile radial stresses among the hardening cases is very small. As shown in Fig. 8(*b*), the hoop stress remains entirely compressive, becoming slightly more compressive at the contact edge with increasing strain hardening. This influence of strain hardening on the surface stresses is consistent with results for the indentation of a homogeneous half-space, where the compressive radial stress at the contact edge increased with hardening, becoming tensile for pronounced strain hardening, while the tensile hoop stress decreased with hardening, becoming entirely compressive for severe strain hardening (Kral et al., 1993). Thus, for a homogeneous half-space, the tendency for cracking at the contact edge changes from radial cracks to ring cracks as the maximum principal stress on the surface changes from the hoop to the radial direction as a consequence of the increasing strain hardening. In contrast, for a layered half-space, strain hardening in the layer and the substrate promotes only the formation of ring cracks at the contact edge, since the maximum principal stress at the surface remains in the radial direction and increases with strain hardening.

3.5 Residual Surface Stresses. Figure 9 shows the effect of the thickness and material properties of the layer on the residual surface stresses for the nonhardening cases after the first unload half-cycle. Both the residual and hoop stresses exhibit maximum tensile values near the maximum contact radius which increase with layer stiffness and hardness and decrease with layer thickness. Comparison of the results shown in Figs. 7 and 9 demonstrates that the maximum residual tensile radial stress is less than that under maximum load, while the

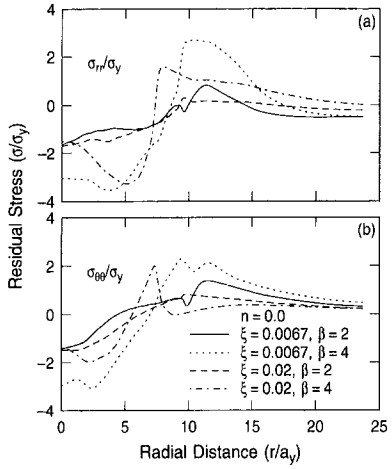

Fig. 9 Effect of layer thickness, stiffness, and hardness on the residual surface stresses after the first unload half-cycle

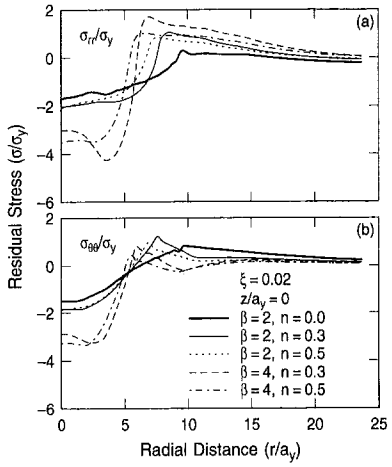

Fig. 10 Effect of layer stiffness and hardness and strain hardening of the layer and substrate on the residual surface stresses after the first unload half-cycle

maximum residual tensile hoop stress is greater than the corresponding stress under maximum load. Thus, the greatest tendency to initiate ring cracks occurs during the load half-cycle, while initiation of radial cracks is favored at the end of the unload half-cycle.

The effect of strain hardening of the layer and substrate media on the residual surface stresses is shown in Fig. 10 for the thicker layer. All hardening cases exhibit compressive residual radial and hoop stresses within the contact region and tensile stresses outside the contact region that reach a maximum at roughly the maximum contact radius of the previous load half-cycle. The maximum stress actually decreases as the hardening exponent increases from 0.3 to 0.5. The maximum residual surface stresses after the first unload half cycle for all the material cases analyzed are listed in Table 2. The peak residual radial stress is always greatest when $n = 0.3$. For the more compliant layers, both $\xi = 0.0067$ and 0.02, the maximum residual radial stress for $n = 0.5$ is less than that for $n = 0.3$, but greater than that for $n = 0.0$. For the stiffer layers, the maximum residual radial stress for $n = 0.5$ is less than that for both $n = 0.0$ and 0.3. The maximum residual hoop stress for the stiffer layers exhibits a monotonic decrease with increasing hardening exponent, while for the more compliant layers it exhibits a maximum for $n = 0.3$. Thus the initiation of surface cracks, both ring and radial, will be more likely for

Table 2 Maximum residual surface stress at the end of the first unload half-cycle

stress	$\xi = 0.0067$					
	$\beta = 2$			$\beta = 4$		
	n = 0.0	n = 0.3	n = 0.5	n = 0.0	n = 0.3	n = 0.5
max σ_{rr}/σ_y	0.8561	1.4827	1.2715	2.7756	3.2391	2.6779
max $\sigma_{\theta\theta}/\sigma_y$	1.3972	1.5606	1.1423	2.3626	2.0604	1.4843
stress	$\xi = 0.02$					
	$\beta = 2$			$\beta = 4$		
	n = 0.0	n = 0.3	n = 0.5	n = 0.0	n = 0.3	n = 0.5
max σ_{rr}/σ_y	0.3475	1.0682	0.8473	1.5983	1.7224	1.0228
max $\sigma_{\theta\theta}/\sigma_y$	0.8556	1.3035	1.0405	2.1913	0.9132	0.4638

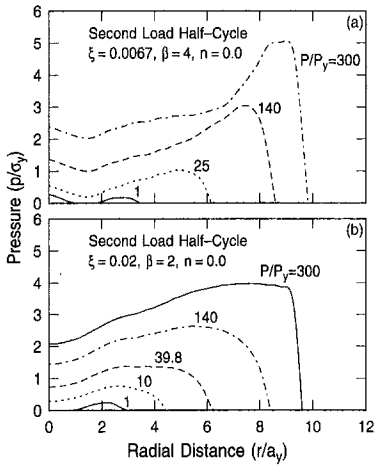

Fig. 11 Variation of contact pressure with indentation load during the second load half-cycle

most of the hardening cases with $n = 0.3$ than for the nonhardening cases, but may be higher or lower for $n = 0.5$. As in the nonhardening cases, the maximum residual radial stress is less than that under the maximum load, while the maximum residual hoop stress is greater (see Fig. 8). The layered case may be contrasted with indentations performed on a half-space of the substrate material, in which the residual radial and hoop stresses were tensile throughout the contact region, with the radial stress becoming compressive and the tensile hoop stress asymptotically approaching zero beyond the contact edge. However, in almost all cases, the maximum residual tensile radial and hoop stresses are higher in the layered cases than in the homogeneous cases, the only exception being the radial stress for the case having $\xi = 0.02$, $\beta = 2$, and $n = 0.0$.

3.6 Effect of Repeated Indentation on the Contact Pressure Distribution. Subsequent load cycles produced only negligible changes in the final (fully loaded) contact pressure profiles compared with those shown in Fig. 2. However, the evolution of the pressure distribution to the fully loaded profile shows substantial differences between the first and subsequent load half-cycles. The development of the contact pressure during the second load half-cycle for two nonhardening material cases is shown in Fig. 11. Figure 11(*a*) shows the contact pressure for the stiffer and harder thin layer. This case exhibits multiple contact regions in the beginning of the reloading half-cycle, indicating that the residual surface profile has a radius of curvature slightly smaller than the indenting sphere. Figure 11(*b*) shows the variation of the contact pressure for the more compliant and softer thick layer during the second load half-cycle. This case exhibits a noncentral contact in the first reloading step, rather than the multiple contact shown in Fig. 11(*a*). The cases shown here are the only ones exhibiting either multiple or noncentral contact upon reloading. Both cases shown in Fig. 11 exhibit a progression of broader, less intense, and almost self-similar pressure distributions up to the final distribution at a load $P/P_y = 300$. The high peak pressures on the axis of symmetry that were evident in the first load half-cycle (Fig. 3) have disappeared. This trend is characteristic of all the reloading cases. Thus, the second and subsequent reloading half-cycles are mainly characterized by the growth of a broader but less intense pressure profile up to the final pressure distribution. Such behavior, also found with the reloading pressures during the indentation of a homogeneous half-space (Kral et al., 1993), stems from the increased conformity between the plastically deformed layered medium and the spherical indenter due to the residual displacement of the surface occurring after the first load cycle.

The surface stresses in the subsequent load and unload half-cycles show relatively small differences from the results already presented. The variation of stress with load cycle is most pronounced for the nonhardening material cases, while the hardening cases exhibit virtually no difference in the surface stresses for subsequent load and unload half-cycles. Even for the nonhardening cases, the loaded and residual surface stresses are virtually identical to those shown in Figs. 7 and 9 for all subsequent load cycles. Results for the subsurface stresses, accumulation of plastic strain, and shakedown under repeated loading are presented in the companion paper (Kral et al., 1994).

4 Conclusions

The surface deformation characteristics resulting from repeated elastic-plastic indentation of a half-space covered with a harder and stiffer layer were investigated with the finite element method. Indentations were performed up to loads of 300 times the load necessary to initiate yielding in a homogeneous half-space consisting of the substrate material. The contact pressure exhibited a higher pressure peak at the contact edge, rather than a relatively uniform contact pressure characteristic of the indentation of a homogeneous half-space approaching full plasticity. The high pressure at the contact edge was promoted by thinner, stiffer, and harder layers. Broader and less intense pressure distributions arose in subsequent load cycles due to the increased conformity between the sphere and the layer surface. Some material cases exhibited multiple contact regions at the beginning of subsequent load half-cycles due to the residual displacement of the deformed surface.

A nondimensional strain parameter corresponding to that used in the half-space indentations (Kral et al., 1993) was introduced, and expressions for the effective modulus and representative flow stress of a layered medium were obtained.

The mean pressure normalized by the effective representative flow stress was shown to asymptotically approach a maximum value of 2.8 for indentations approaching fully plastic deformation, which is consistent with half-space indentations. This confirmed that the newly introduced indentation parameter is suitable for comparing results from indentation experiments.

A significant tensile radial stress occurred at the surface near the contact edge under the maximum load. This surface tensile stress increased for thinner, stiffer, and harder layers and with strain hardening of the layer and substrate. For the thinner layers, a tensile hoop stress also arose at the surface near the contact edge which decreased with increasing strain hardening. The tensile radial and hoop stresses are critical to the susceptibility of the layer surface to ring and radial cracking, respectively.

Tensile residual radial and hoop stresses also occurred at the surface after the first unload half-cycle. The maximum residual radial stress was less than that at the end of the first load half-cycle, while the maximum residual hoop stress was greater. Thus, a greater tendency for the formation of surface ring cracks existed during loading and for surface radial cracks during unloading. The surface stresses showed only very slight changes with subsequent load cycles for the nonhardening materials and virtually no change for the hardening materials.

Acknowledgments

This work was partially supported by the Surface Engineering and Tribology Program of the National Science Foundation under Grant No. MSS-8996309 and the Computer Mechanics Laboratory at the University of California at Berkeley.

References

Bhattacharya, A. K., and Nix, W. D., 1988, "Analysis of Elastic and Plastic Deformation Associated with Indentation Testing of Thin Films on Substrates," *Int. J. Solids Structures*, Vol. 24, No. 12, pp. 1287–1298.

Bhattacharya, A. K., and Nix, W. D., 1991, "Finite Element Analysis of Cone Indentation," *Int. J. Solids Structures*, Vol. 27, No. 8, pp. 1047–1058.

Burmister, D. M., 1945, "The General Theory of Stresses and Displacements in Layered Systems," *J. Appl. Phys.*, Vol. 16, pp. 89–94.

Chen, W. T., 1971, "Computation of Stresses and Displacements in a Layered Elastic Medium," *Int. J. Engng. Sci.*, Vol. 9, pp. 775–800.

Gupta, P. K., and Walowit, J. A., 1974, "Contact Stresses Between an Elastic Cylinder and a Layered Elastic Solid," ASME *Journal of Lubrication Technology*, Vol. 96, pp. 250–257.

Johnson, K. L., 1985, *Contact Mechanics*, Cambridge University Press, Cambridge, U.K., pp. 159–184.

Kennedy, F. E., and Ling, F. F., 1974, "Elasto-Plastic Indentation of a Layered Medium," ASME *Journal of Engineering Materials and Technology*, Vol. 96, pp. 97–103.

King, R. B., 1987, "Elastic Analysis of Some Punch Problems for a Layered Medium," *Int. J. Solids Structures*, Vol. 23, No. 12, pp. 1657–1664.

King, R. B., and O'Sullivan, T. C., 1987, "Sliding Contact Stresses in a Two-Dimensional Layered Elastic Half-Space," *Int. J. Solids Structures*, Vol. 23, No. 5, pp. 581–597.

Komvopoulos, K., 1988, "Finite Element Analysis of a Layered Elastic Solid in Normal Contact With a Rigid Surface," ASME *Journal of Tribology*, Vol. 110, pp. 477–485.

Komvopoulos, K., 1989, "Elastic-Plastic Finite Element Analysis of Indented Layered Media," ASME *Journal of Tribology*, Vol. 111, pp. 430–439.

Kral, E. R., Komvopoulos, K., and Bogy, D. B., 1993, "Elastic-Plastic Finite Element Analysis of Repeated Indentation of a Half-Space by a Rigid Sphere," ASME JOURNAL OF APPLIED MECHANICS, Vol. 60, pp. 829–841.

Kral, E. R., Komvopoulos, K., and Bogy, D. B., 1995, "Finite Element Analysis of Repeated Indentation of an Elastic-Plastic Layered Medium by a Rigid Sphere, Part II: Subsurface Results," ASME JOURNAL OF APPLIED MECHANICS, Vol. 62, pp. 29–42.

Laursen, T. A., and Simo, J. C., 1992, "A Study of the Mechanics of Microindentation Using Finite Elements," *J. Mater. Res.*, Vol. 7, No. 3, pp. 618–626.

Montmitonnet, P., Edlinger, M. L., and Felder, E., 1993, "Finite Element Analysis of Elastoplastic Indentation: Part II—Application to Hard Coatings," ASME *Journal of Tribology*, Vol. 115, pp. 15–19.

O'Sullivan, T. C., and King, R. B., 1988, "Sliding Contact Stress Field Due to a Spherical Indenter on a Layered Elastic Half-Space," ASME *Journal of Tribology*, Vol. 110, pp. 235–240.

Tabor, D., 1970, "The Hardness of Solids," *Rev. Phys. Tech.*, Vol. 1, No. 3, pp. 145–179.

Tian, H., and Saka, N., 1991, "Finite Element Analysis of an Elastic-Plastic Two-Layer Half-Space: Normal Contact," *Wear*, Vol. 148, pp. 47–68.

Finite Element Analysis of Repeated Indentation of an Elastic-Plastic Layered Medium by a Rigid Sphere, Part II: Subsurface Results

E. R. Kral
Graduate Research Assistant,
Assoc. Mem. ASME.

K. Komvopoulos
Associate Professor,
Mem. ASME.

D. B. Bogy
Professor,
Fellow ASME.

Department of Mechanical Engineering,
University of California,
Berkeley, CA 94720

Finite element solutions are presented for the subsurface stress and deformation fields in a layered elastic-plastic half-space subjected to repeated frictionless indentation by a rigid sphere. A perfectly adhering layer is modeled using two different thicknesses and elastic modulus and yield stress two and four times greater than those of the substrate. The significance of strain hardening during plastic deformation is investigated by assuming elastic-perfectly plastic and isotropically strain-hardening constitutive laws for both the layer and substrate materials. At least three load-unload cycles are applied to a peak load of 300 times the load necessary to initiate yielding in a homogeneous half-space with substrate properties. The effects of the layer thickness and material properties of the layer and substrate on the loaded and residual stresses are interpreted, and the consequences for subsurface crack initiation are discussed. The maximum principal and interfacial shear stresses are given as a function of a nondimensional strain parameter. The effect of subsequent load cycles on the loaded, residual, and maximum tensile and interfacial shear stresses and the protection provided by the harder and stiffer layer are analyzed. Reyielding during unloading and the possibility of elastic shakedown are discussed, and the accumulation of plastic strain in the yielding regions is tracked through subsequent load cycles.

1 Introduction

Fundamental understanding of the stresses and deformations involved in contact of layered media is of paramount importance in engineering practice. Both analytical and numerical contact mechanics analyses of layered elastic media have been presented by several investigators. Burmister (1945a, b) presented an axisymmetric formulation for specified surface loads applied to an elastic single-layered medium with both frictionless and perfectly adhering layer interface conditions and for an elastic double-layered medium with perfectly adhering interfaces. Chen (1971) extended Burmister's work to nonaxisymmetric surface loadings applied to single- and double-layered elastic media. The plane-strain contact problem of an elastic layered medium subjected to normal and tangential surface tractions has been studied by Gupta et al. (1973) and King and O'Sullivan (1987), and results for the three-dimensional elastic problem of a sphere sliding on a single-layered half-space have been presented by O'Sullivan and King (1988). Kennedy and Ling (1974) investigated the elastic-plastic indentation of a half-space with a softer and more compliant layer, considering both frictionless and perfectly adhering layer interface conditions. The mechanical properties of the layer and substrate and the interfacial friction characteristics were found to have a significant effect on the stresses and deformations in the layered medium. Tangena and Hurkx (1985) investigated the axisymmetric indentation by a rigid sphere on a nickel half-space covered with a gold layer and reported that the von Mises equivalent stress in the gold layer increased with the layer thickness. Komvopoulos et al. (1987, 1988) presented finite element results for the plane-strain problem of an elastic half-space with a harder elastic layer indented by a rigid cylinder and qualitatively addressed the issues of subsurface plastic deformation and fracture. Montmitonnet et al. (1993) used the finite element method to analyze the indentation of an elastic-plastic layered medium by an elastic indenter and discussed the effect of the layer thickness on the stress field and the significance of tensile stresses to fracture and delamination of the layer.

Contributed by the Applied Mechanics Division of THE AMERICAN SOCIETY OF MECHANICAL ENGINEERS for publication in the ASME JOURNAL OF APPLIED MECHANICS.

Discussion on this paper should be addressed to the Technical Editor, Professor Lewis T. Wheeler, Department of Mechanical Engineering, University of Houston, Houston, TX 77204-4792, and will be accepted until four months after final publication of the paper itself in the ASME JOURNAL OF APPLIED MECHANICS.

Manuscript received by the ASME Applied Mechanics Division, Dec. 21, 1992; final revision, May 30, 1993. Associate Technical Editor: L. M. Keer.

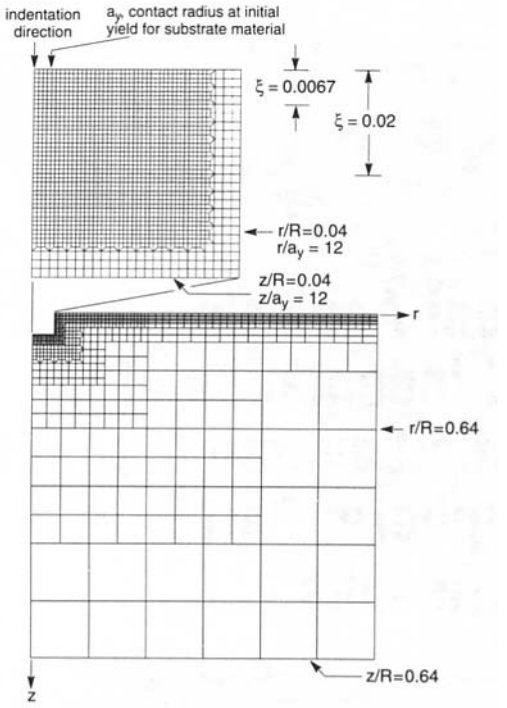

Fig. 1 Finite element discretization of the layered medium

The plane-strain problem of a rigid cylinder indenting an elastic-plastic layered medium with a layer harder and stiffer than the substrate was investigated by Komvopoulos (1989). In this study, plastic flow initiated at the layer/substrate interface, and the plastic zone remained restricted to the bottom of the hard layer and the substrate. In addition, it was found that the thinnest layer promoted yielding at a pressure lower than that of a homogeneous half-space of the substrate material. Tian and Saka (1991) investigated the plane-strain elastic-plastic indentation of a two-layer half-space and reported a significant effect of the interlayer thickness on both the location of initial yielding and the stresses at the interlayer/substrate interface. Kral et al. (1993) studied the repeated elastic-plastic indentation of a half-space possessing different elastic properties and strain-hardening characteristics by a rigid spherical indenter. It was demonstrated that the surface and subsurface stresses depended strongly on strain hardening and relatively less on elastic properties, and that reyielding occurred upon unloading in a small surface region near the edge of the contact at maximum load. Moreover, elastic-perfectly plastic materials continued to accumulate plastic strain during subsequent load cycles, eventually approaching a steady-state elastic cycle.

Although previous studies have provided valuable insight into contact mechanics aspects of layered media, the significance of several important parameters, such as the layer thickness and hardness, strain-hardening behavior, and number of loading repetitions, on the stress and deformation fields of layered media in the elastic-plastic regime has not been fully investigated. Of particular interest, for example, is the effect of material properties and load cycles on the steady-state deformation cycle. The aim of this investigation, therefore, is to provide a complete finite element analysis of the subsurface stress and deformation fields arising in an elastic-plastic layered half-space due to repeated indentation by a rigid sphere. Indentation loads are applied incrementally to 300 times the initial yield load of the substrate material, and the contact is assumed to be frictionless. Two layer thicknesses and layer elastic moduli and yield stresses two and four times greater than those of the substrate material are investigated. In addition, the effect of plastic deformation is considered by assuming elastic-perfectly plastic or isotropically strain-hardening constitutive relationships for both the layer and substrate media. Results demonstrating the effects of the layer thickness and material properties of the layer and the substrate on the evolution of the plastic zone and the spatial variation of the stresses and strains will be presented for repeated elastic-plastic indentations. In addition, the significance of material properties on the residual stresses and the tendency for reyielding will be interpreted, and the effect of repeated load cycles on the resulting stress and plastic deformation fields will be shown. The finite element solutions in this publication pertain to the subsurface region, while results for the surface stresses and deformations in the layered medium under the same loading conditions have been presented elsewhere (Kral et al., 1995).

2 Finite Element Modeling Procedures

2.1 Contact Model. A smooth, frictionless, and rigid spherical indenter of radius, R, equal to 1500 nm was modeled by a total of 44 three-node interface (contact) elements. This eliminated the need to assume a pressure profile a priori. In view of the relatively small indentation depths and resulting contact radii, the finite element solutions are also representative of elastic-plastic indentations by a blunt indenter. The finite element mesh of the layered half-space, shown in Fig. 1, consisted of 2721 four-node quadrilateral axisymmetric elements comprising 2848 nodes and using a linear 2×2 integration scheme. The r- and z-dimensions of the mesh were set equal to 960 nm, sufficiently isolating the boundaries from the contact region. The vertical boundaries of the mesh were constrained against displacement in the r-direction, and the bottom boundary against displacement in the z-direction. The region of the mesh bounded by $r/R = 0.033$ and $z/R = 0.033$ was refined, as shown in the inset of Fig. 1, to account for the high stress gradients at the edge of the contact region. The finite element simulations were performed with the general purpose finite element package ABAQUS. Further details about the finite element discretization, favorable comparisons between finite element and analytical solutions for elastic indentations, and results for repeated elastic-plastic indentations of homogeneous and layered half-spaces based on the present mesh configuration can be found in other publications (Kral et al., 1993, 1995).

2.2 Material Properties and Plasticity Models. The yield condition adopted in this study was based on the von Mises yield criterion,

$$f = J_2 - k^2 = 0,$$

where k is a material constant and J_2 is the second invariant of the deviatoric stress tensor, given by

$$J_2 = \frac{1}{2} S_{ij} S_{ij}, \quad \text{where} \quad S_{ij} = \sigma_{ij} - \frac{1}{3} \delta_{ij} \sigma_{kk}.$$

The yield criterion may be expressed in terms of the uniaxial yield stress, σ^o, as

$$\sigma_M = \left[\frac{3}{2} S_{ij} S_{ij} \right]^{1/2} = \sigma^o, \tag{1}$$

where σ_M is the von Mises equivalent stress. An incremental plasticity formulation based on the associated flow rule was used for material exceeding the yield limit. The usual assumption of negligible plastic volume change was maintained. To account for boundary nonlinearities arising from the use of contact elements, an updated Lagrangian formulation was used.

Both the layer and substrate media were modeled as isotropic strain-hardening materials according to the relationship

$$\frac{\sigma^o}{\sigma_y} = \frac{K}{\sigma_y}\epsilon_{eq}^n, \tag{2}$$

where σ_y is the initial yield stress of the substrate material, K is the strength coefficient, n is the strain-hardening exponent, and ϵ_{eq} is the equivalent plastic strain, defined as

$$\epsilon_{eq} = \int_S \left[\frac{2}{3} d\epsilon_{ij}^p d\epsilon_{ij}^p\right]^{1/2}, \tag{3}$$

where S is the strain path. The same strain-hardening exponent was used in both the layer and the substrate. The hardening relation and flow rule apply only to yielding material for which $\sigma_M = \sigma^o$. When $\sigma_M < \sigma^o$, the usual elastic constitutive equations apply.

Results are presented in terms of the parameter β, which is the ratio of both the layer-to-substrate elastic moduli and the layer-to-substrate initial yield stresses. The values of β assumed in the analysis were equal to 2 and 4, representing a layer two and four times, respectively, stiffer and harder than the substrate. The normalized layer thickness, ξ, is defined as the ratio of the layer thickness to the sphere radius. Two different layer thicknesses, 10 nm ($\xi = 0.0067$) and 30 nm ($\xi = 0.02$), were modeled, as shown in Fig. 1. The strain-hardening exponent, n, was varied from zero to 0.5.

2.3 Nondimensional Indentation Parameter. A dimensionless strain parameter for indentations of layered media, Λ, was introduced in the previous study (Kral et al., 1995). This indentation (strain) parameter was defined as

$$\Lambda = \left(\frac{E/\sigma_y}{1-\nu^2}\right)_{\text{eff}} \frac{\alpha}{R(\sigma_o^R/\sigma_y)_{\text{eff}}}, \tag{4}$$

where E and ν are the elastic modulus and Poisson's ratio, respectively, R is the sphere radius, a is the contact radius, σ_y is the initial tensile yield stress of the substrate, and σ_o^R is a representative flow stress corresponding to a representative strain $\epsilon_R = 0.2a/R$. The effective elastic compliance was given as

$$\left(\frac{E/\sigma_y}{1-\nu^2}\right)_{\text{eff}} = \left[\frac{1-\nu_l^2}{E_l/\sigma_y}(1-e^{-\alpha t/\alpha\sqrt{\pi}}) + \frac{1-\nu_s^2}{E_s/\sigma_y}e^{-\alpha t/\alpha\sqrt{\pi}}\right]^{-1}, \tag{5}$$

where the subscripts s and l refer to substrate and layer properties, respectively, t is the layer thickness, and α is a numerical factor for the indentation of a circular flat-ended punch that can be determined numerically.

The expression for the effective representative flow stress of the layered medium was given as

$$\left(\frac{\sigma_o^R}{\sigma_y}\right)_{\text{eff}} = \frac{\sigma_s}{\sigma_y}\left\{1 + \left(\frac{\sigma_l}{\sigma_s} - 1\right)\exp\left[-\left(\frac{a}{t}\right)\Big/\left(\frac{E_l}{E_s}\right)^{1/2}\right]\right\}, \tag{6}$$

where the subscripts and variables are the same as those defined previously. The representative flow stresses for the layer and the substrate, σ_l and σ_s, respectively, are calculated from Eq. (2) using the representative strain $\epsilon_R = 0.2a/R$, i.e.,

$$\sigma_l = K_l\epsilon_R^n,$$

and

$$\sigma_s = K_s\epsilon_R^n.$$

2.4 Simulation of Repeated Indentations. Indentation was simulated by incrementally increasing the indentation load in 20 steps to a maximum of 300 times the initial yield load of the homogeneous substrate material, P_y. The layered medium was then unloaded incrementally back to zero following the same path. The convergence tolerance for establishing nodal force equilibrium was equal to $10^{-9}\sigma_y$. The load in each step was applied linearly in 10 increments, and a maximum of 15 iterations was allowed in each increment to reach equilibrium within the specified tolerance. Repeated indentations were simulated by applying identical load-unload cycles. Special software was developed to analyze the results and generate plots of user-defined variables. The finite element calculations and post-processing were performed on an IBM RS6000 Model 540 workstation. The typical CPU time for an elastic-plastic indentation from zero load to maximum load was about 9.5 hours.

3 Results and Discussion

Finite element solutions illustrating the effects of the thickness and elastic-plastic properties of the layer, the indentation load, and the number of load cycles on the subsurface stress and deformation fields are presented in the following sections. Results for the contact pressure and surface stresses as a function of the layer thickness and material properties have been presented elsewhere (Kral et al., 1995). The incremental increase of the load to its maximum value and the subsequent incremental unloading to a zero load will be termed a "load cycle." Either the loading or unloading portion of this entire cycle will be known hereafter as a "half-cycle." In the subsequent discussion, it will be understood that either "stiffer" or "harder" refers to the layer with the larger elastic modulus and yield strength (or hardness) ratio (i.e., $\beta = 4$), while "softer" or "more compliant" refers to the smaller elastic modulus and yield strength ratio (i.e, $\beta = 2$).

3.1 Subsurface Stresses. Figure 2 shows the evolution of the von Mises equivalent stress for the thicker and more compliant layer ($\xi = 0.02$, $\beta = 2$) with no strain hardening. The results are qualitatively typical of all the nonhardening cases. The von Mises stress exhibits a discontinuity at the layer interface since the radial and hoop stresses are discontinuous due to the different layer and substrate material properties. The normal and shear stresses, however, are required to be continuous across the interface. Consequently, subsequent figures showing the radial and hoop stresses along the interface will be presented for both the layer and the substrate. Contour number 5 represents yielding in the layer ($\sigma_M/\sigma_y = 2$), while contour number 2 represents yielding in the substrate ($\sigma_M/\sigma_y = 1$). Figure 2(a) shows that yielding commences in the layer at a depth of about one-half the contact radius. At a load $P/P_y = 6.4$, the plastic zone is surrounded by elastic material. As the load increases, the plastic zone in the layer enlarges, eventually reaching both the surface and the interface, as shown in Fig. 2(b) for a load $P/P_y = 39.8$. At this load, substrate yielding is also encountered. In all cases, substrate yielding first occurs at the interface on the axis of symmetry. As the load is further increased to $P/P_y = 100.6$ (Fig. 2(c)), the yielding region in the substrate continues to expand downward and along the interface, assuming an approximately elliptical shape. The yielding region in the layer forms a nose reaching to the surface and moving outward with the contact edge. At the maximum load $P/P_y = 300$, Fig. 2(d) shows that the size of the elliptical yielding region in the substrate has increased significantly, while the yielding region in the layer has retained the high stress yielding nose from the surface to the layer interface, leaving behind a wake of relaxed (but plasti-

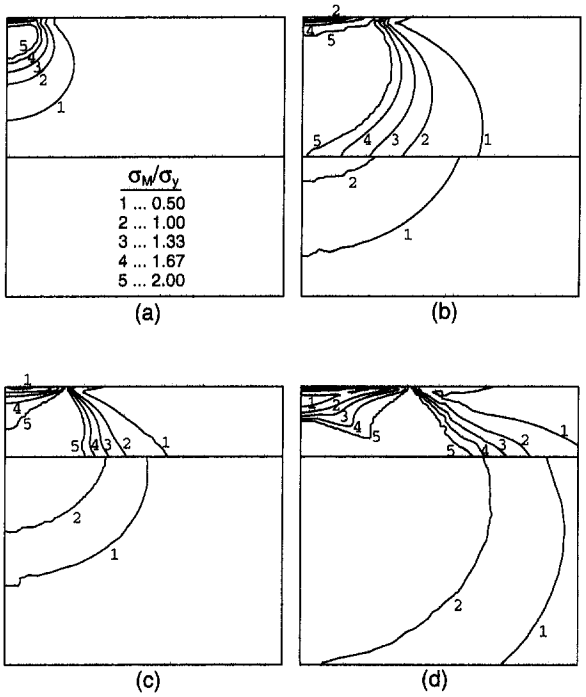

Fig. 2 Contours of von Mises equivalent stress during the first load half-cycle for $\xi = 0.02$, $\beta = 2$, $n = 0.0$, and load P/P_y equal to: (a) 6.4, (b) 39.8, (c) 100.6, and (d) 300. ((a) and (b) show the region $0 \le r/a_y \le 12$, $0 \le z/a_y \le 12$, while (c) and (d) show the region $0 \le r/a_y \le 24$, $0 \le z/a_y \le 24$)

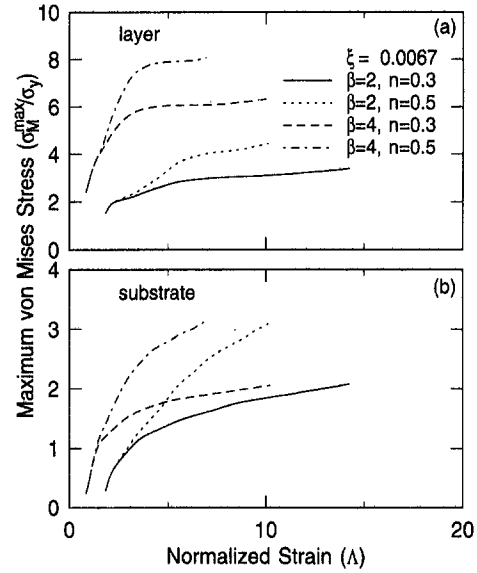

Fig. 3 Maximum von Mises stress versus normalized strain for $\xi = 0.0067$ during the first load half-cycle: (a) layer and (b) substrate

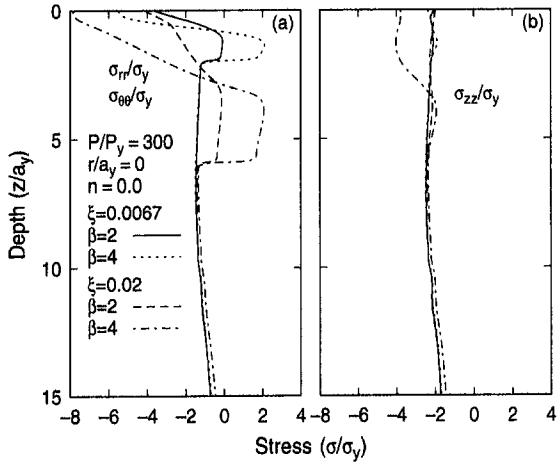

Fig. 4 Effect of layer thickness, stiffness, and hardness on the stresses along the axis of symmetry at the maximum load of the first load half-cycle: (a) radial (hoop) and (b) normal stress

cally deformed) material in the upper half of the layer below the center of contact.

The other nonhardening cases demonstrated characteristics similar to those shown in Fig. 2(d) for $P/P_y = 300$, with a high stress yielding nose in the layer at the contact edge encompassing the entire thickness of the layer, and only approximately half of the layer closest to the interface undergoing yielding near the axis of symmetry. The substrates covered by thinner layers exhibited slightly larger plastic zones than that shown in Fig. 2(d), indicating that the thicker layers slightly inhibit the development of plasticity in the substrate. For the thicker layers, the substrate plastic zone was smaller for $\beta = 4$ than for $\beta = 2$, suggesting an enhancement of the resistance of the substrate to plastic deformation in the presence of the stiffer and harder layer. For the thinner layers, however, the substrate plastic zone for the more compliant layer was nearly identical to that of the stiffer layer, indicating that the effect of the layer stiffness and hardness on the extent of plasticity in the substrate was secondary in this case.

Comparison of the von Mises stress contours for the hardening cases, not shown here for the sake of brevity, revealed results qualitatively similar to those shown in Fig. 2(d). The width of the plastic zone in the layer decreased only slightly with increasing strain hardening, and the effect of strain hardening on the size of the plastic zone in the substrate was marginal for a given layer stiffness. The maximum von Mises stress in the substrate occurred at the interface on the axis of symmetry and increased significantly with hardening. This result differs from the indentation of a homogeneous hardening half-space, where the maximum von Mises equivalent stress was found to move toward the surface near the contact edge (Kral et al., 1993). The maximum von Mises stress in the layer increased significantly with strain hardening and the layer stiffness and hardness.

The maximum von Mises equivalent stress versus the normalized strain Λ is shown in Fig. 3 for the thinner layer, which exhibits the larger range of Λ values. The maximum von Mises stress in the layer, shown in Fig. 3(a), exhibits a significant initial increase but shows only a marginal variation for $\Lambda > 4$ when $\beta = 4$ and for $\Lambda > 7$ when $\beta = 2$. Figure 3(b) shows that as the normalized strain increases, the slope of the maximum von Mises stress in the substrate approaches a value dependent only on the strain-hardening exponent. This is most apparent for $n = 0.3$. A similar trend was observed for the thicker layers; however, the smaller range of Λ values for these cases makes this trend less obvious. For indentation of a homogeneous half-space, the maximum von Mises stress has been shown to be a function of only the strain-hardening exponent when the indentation approaches the fully plastic regime, i.e., $\Lambda = 30$ (Kral et al., 1993). Thus, for a given layer and sufficiently advanced plastic deformation, the maximum von Mises stress in the substrate exhibits a behavior similar to that of a half-space with substrate material properties.

Figures 4 and 5 show the effect of the layer thickness and material properties on the stresses along the axis of symmetry at the peak load $P/P_y = 300$ of the first load half-cycle. The radial (hoop) stress for the nonhardening cases, shown in Fig. 4(a), exhibits a region where it is relatively uniform with

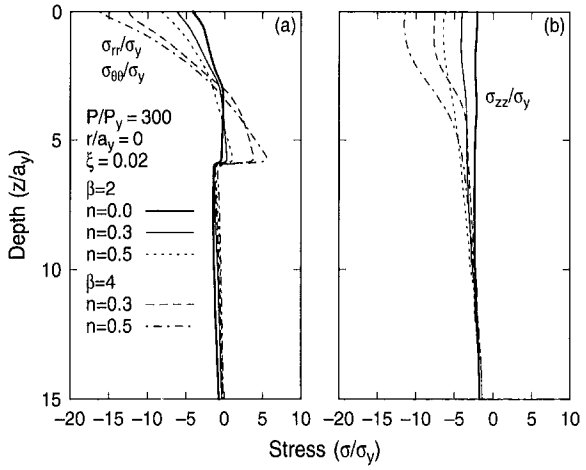

Fig. 5 Effect of layer stiffness and strain-hardening exponent on the stresses along the axis of symmetry at the maximum load of the first load half-cycle: (*a*) radial (hoop) and (*b*) normal stress

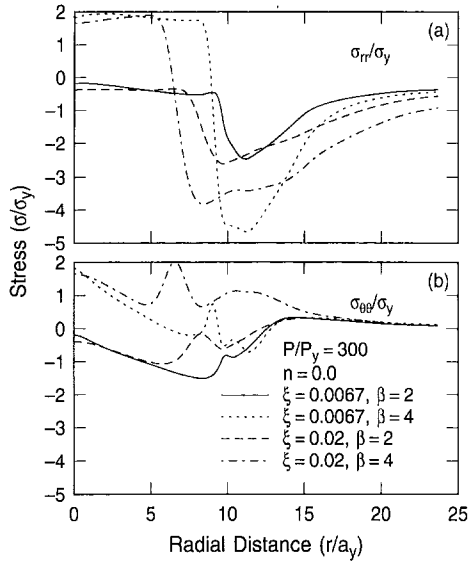

Fig. 6 Effect of layer thickness, stiffness, and hardness on the stresses at the layer interface ($z/a_y = 2^-$ for $\xi = 0.0067$ and $z/a_y = 6^-$ for $\xi = 0.02$) at the maximum load of the first load half-cycle: (*a*) radial and (*b*) hoop stress

depth. This region corresponds to the yielding region in the layer, as shown in Fig. 2(*d*) for $\xi = 0.02$ and $\beta = 2$. This uniform radial (hoop) stress occurs in the perfectly plastic material since the radial, hoop, and normal stresses are the principal stresses along the axis of symmetry and the normal stress, shown in Fig. 4(*b*), is also relatively uniform. Due to the higher tensile radial stress, the stiffer and harder layers will be more vulnerable to the initiation of median cracks. The radial stress in the substrate is essentially the same for all material combinations. The normal stress along the axis of symmetry is remarkably similar for all cases, except for the thicker and harder layer, where the compressive normal stress near the surface is almost twice that of the other cases. This is consistent with the contact pressure for $\xi = 0.02$ and $\beta = 4$, which does not exhibit a uniform distribution near the axis of symmetry at the maximum load (Kral et al., 1995). Since the thicker, stiffer, and harder layer possesses a higher resistance to plastic deformation, a larger load is required to achieve the relatively uniform contact pressure near the axis of symmetry shown by other material cases. At greater depths, i.e., $z/a_y \approx 22$, the radial (hoop) stress on the axis of symmetry becomes slightly positive, as in the case of indentation of a homogeneous half-space (Kral et al., 1993).

Figure 5 shows the effect of strain hardening in the layer and substrate on the radial (hoop) and normal stresses along the axis of symmetry for the thicker layer. The nonhardening curve for $\beta = 2$ is also shown for comparison. In the hardening cases shown in Fig. 5(*a*), the radial (hoop) stress in the layer is no longer uniform, but increases toward the interface with a slope depending upon the layer stiffness and hardness and the strain-hardening exponent. This indicates that material hardening occurs near the interface, which is consistent with the location of the maximum von Mises equivalent stress at the layer interface on the axis of symmetry, as mentioned for the hardening cases in the discussion pertaining to Fig. 2. The significantly higher tensile radial (hoop) stress at the layer interface indicates that hardening promotes the susceptibility for initiation of median cracks at the interface. The radial stress in the substrate is essentially the same for all the hardening material combinations. The normal stress is again everywhere compressive, with the peak compressive stress at the surface intensifying with increasing layer stiffness and strain hardening, consistent with the results for the contact pressure profiles (Kral et al., 1995).

Stress distributions at the layer interface for the nonhardening materials at the peak load of the first load half-cycle are shown in Fig. 6. The stresses were obtained at the interface nodes by extrapolating from the integration point data in the layer. Figure 6(*a*) shows that the variation of the radial stress is similar for all the material combinations, with the largest stress occurring from the axis of symmetry to a distance approximately equal to the contact radius, followed by a rapid decrease to a maximum compressive stress and an asymptotic approach to zero as the radial distance increases. The maximum compressive radial stress occurs approximately below the contact edge. The radial stress in the region from the axis of symmetry to the contact radius depends strongly on the layer stiffness. While a high tensile radial stress arises in the stiffer and harder layers, the more compliant and softer layers are subjected to a purely compressive radial stress. The effect of layer thickness on the peak radial stress in this region is marginal. Similar behavior is observed for the hoop stress, as shown in Fig. 6(*b*), which is also tensile within the contact radius for stiffer and harder layers. In addition, the hoop stress develops a local peak just before the contact edge. As shown in Figs. 4 and 6, the radial and hoop stresses in the layer may reach tensile values within the contact radius, depending on the layer properties, thus increasing the susceptibility to subsurface circumferential and radial cracking in the layer.

The tensile stresses at the layer interface may be attributed to the elastic modulus difference between the layer and the substrate. The compliant substrate material has less resistance to radial and circumferential expansion than the stiffer layer. Thus, at the interface, the more compliant substrate promotes radial and circumferential deformation of the stiffer layer, producing tensile stresses for a sufficiently large difference in stiffness, as shown in Fig. 6. The same effect may be seen in the results presented in Figs. 4(*a*) and 5(*a*), where the radial (hoop) stress increases from compressive at the surface to tensile or only slightly compressive at the interface as a consequence of the more compliant substrate. These results contrast with those for the indentation of a homogeneous half-space, in which the radial (hoop) stress on the axis of symmetry remains entirely compressive to a depth $z/a_y \approx 22$ (Kral et al., 1993).

Figure 7 shows the effect of the layer thickness and stiffness on the substrate interfacial stresses. These results are reported at the same nodes as those shown in Fig. 6, but are extrapolated from the substrate integration points. The radial

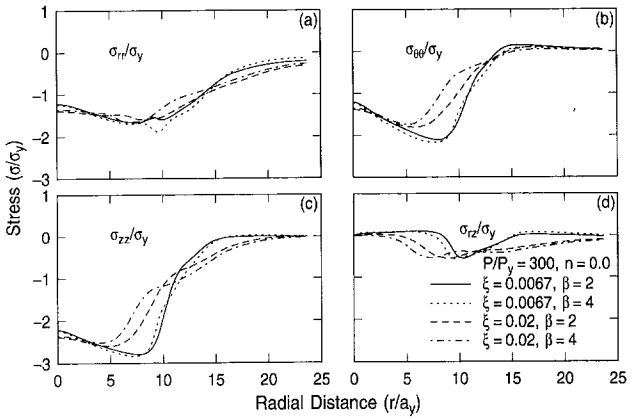

Fig. 7 Effect of layer thickness, stiffness, and hardness on the stresses at the substrate interface ($z/a_y = 2^+$ for $\xi = 0.0067$ and $z/a_y = 6^+$ for $\xi = 0.02$) at the maximum load of the first load half-cycle: (*a*) radial, (*b*) hoop, (c) normal, and (*d*) shear stress

stress, shown in Fig. 7(*a*), is compressive throughout and shows little sensitivity to the layer thickness and material properties. The hoop stress, shown in Fig. 7(*b*), exhibits a slightly larger compressive maximum for the thinner layers, but varies only marginally with the layer stiffness and hardness for a given thickness. The hoop stress becomes slightly tensile beginning at $r/a_y \approx 15$, which corresponds to the boundary of the substrate plastic zone, as demonstrated by the contours of von Mises equivalent stress. The tensile hoop stresses shown in Fig. 7(*b*), in conjunction with the tensile hoop stresses on the axis of symmetry at $z/a_y \approx 22$ (refer to the discussion of Fig. 4), indicate the presence of a band of tensile hoop stress in the substrate constraining the plastic zone, similar to that arising in the indentation of a half-space consisting of the substrate material (Kral et al., 1993). Contours of hoop stress, not shown here, confirmed this prediction. Figures 7(*c*) and 7(*d*) show small variations in the normal and shear stresses with layer thickness and only marginal variations with layer material properties for a given thickness.

The effect of the elastic and plastic material properties on the interfacial stresses in the thicker layer is shown in Fig. 8. Also shown for comparison are the results for $\beta = 2$ and $n = 0.0$ presented in Fig. 6. Figure 8(*a*) shows that increasing the layer stiffness and the strain-hardening exponent promotes the development of a tensile radial stress within the contact radius. For the stiffer layer exhibiting nonhardening behavior, a tensile radial stress at the layer interface within the contact radius was also obtained (Fig. 6(*a*)). A similar situation exists in the thinner layers, not shown here, with respect to the effect of hardening; however, only the stiffer layer exhibits tensile radial stresses, while the maximum radial stress in the more compliant layer does not differ appreciably from that of the nonhardening case (Fig. 6(*a*)). The interfacial hoop stress in the thicker layer, shown in Fig. 8(*b*), exhibits a similar strain-hardening effect. A tensile hoop stress exists at the interface from the axis of symmetry to beyond the contact radius. The maximum tensile stress increases with the layer stiffness and hardness and the strain hardening of the layer and substrate. Similarly, for the thinner layers, tensile hoop stresses occur in the same region only for the stiffer layer, while for the more compliant layer the hoop stress is purely compressive for all the hardening cases. Thus, strain hardening increases both the tensile radial and tensile hoop stresses at the layer interface, thereby increasing the susceptibility to interfacial cracking for thicker and stiffer layers. The effect of strain hardening on the interfacial stresses in the layer becomes less pronounced as the thickness, stiffness, and hardness of the layer decrease.

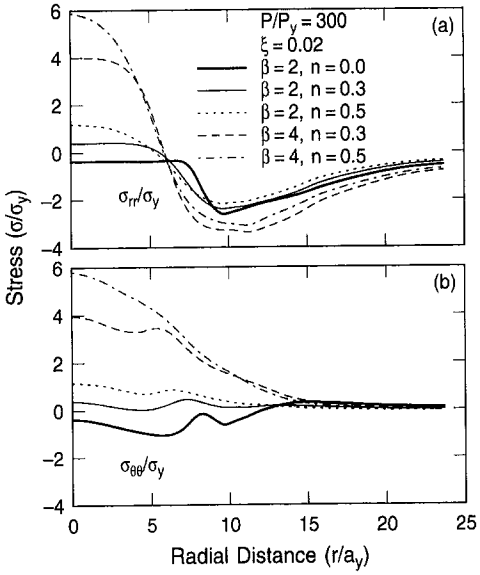

Fig. 8 Effect of layer stiffness and strain-hardening exponent on the stresses at the layer interface ($z/a_y = 6^-$) at the maximum load of the first load half-cycle: (*a*) radial and (*b*) hoop stress

The interfacial substrate stresses for the hardening cases, not presented here for the sake of brevity, are similar to those shown in Fig. 7. The radial stresses are compressive and vary insignificantly with the layer properties. The hoop stresses are also primarily compressive but become slightly tensile at $r/a_y \approx 15$ for $n = 0.3$. The hoop stress remains entirely compressive for $n = 0.5$, indicating that the band of tensile hoop stress which constrains the substrate plastic zone in the nonhardening case does not reach the interface for this case. This is again quite similar to the effect of hardening on the hoop stress arising in the indentation of a homogeneous half-space examined in the previous work, and is due to the material supporting greater stresses by strain hardening rather than entirely through the development of a constraining band of tensile hoop stress surrounding the plastic zone.

The variation of the maximum shear stress at the layer/substrate interface as a function of the nondimensional strain parameter Λ is shown in Fig. 9 for different material cases. Figure 9(*a*) shows the effect of the layer thickness and stiffness on the maximum interfacial shear stress for $n = 0.0$. For values of Λ less than approximately 10, the maximum shear stress depends strongly on the layer thickness and material properties, increasing with layer stiffness (and hardness) and decreasing with layer thickness. However, as the indentation approaches a fully plastic state, the maximum interfacial shear stress approaches a constant value of approximately $0.58\sigma_y$, which is equal to the shear yield stress of the substrate. Figure 9(*b*) shows the maximum interfacial shear stress as a function of strain hardening and stiffness of the thinner layers, which exhibit the greater range of Λ values. Results for the nonhardening layered medium with $\beta = 2$ are also shown for comparison. Similarly to the substrate maximum von Mises stress, shown in Fig. 3(*b*), the maximum interfacial shear stress depends only on the strain-hardening exponent as the indentation approaches the fully plastic state. Thus, according to the results shown in Figs. 9(*a*) and 9(*b*), thinner and harder layers require a greater interfacial strength during the initial stages of indentation, but as plastic deformation increases, the interfacial shear strength is controlled solely by the strain-hardening characteristics of the layer and the substrate for a given layer thickness. Similar trends are observed for the thicker layer,

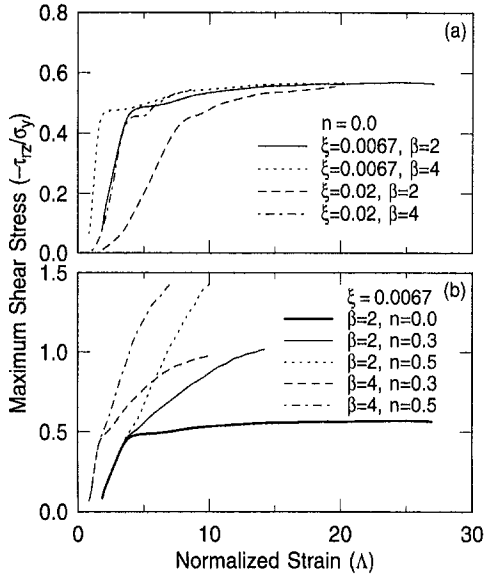

Fig. 9 Maximum shear stress at the substrate interface versus normalized strain during the first load half-cycle

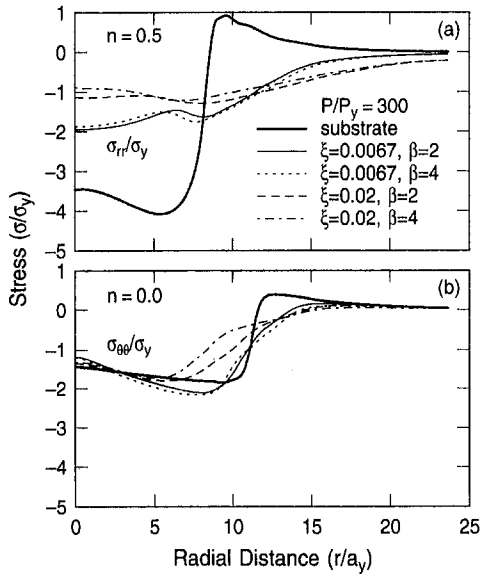

Fig. 10 Stresses at the substrate interface ($z/a_y = 2^+$ for $\xi = 0.0067$ and $z/a_y = 6^+$ for $\xi = 0.02$) for layered media and surface stresses ($z/a_y = 0$) for a homogeneous half-space at the maximum load of the first load half-cycle: (*a*) radial stress for hardening materials with $n = 0.5$ and (*b*) hoop stress for nonhardening materials

but in view of the smaller range of Λ values the trends are less obvious.

In the previous study of indentation of a homogeneous half-space (Kral et al., 1993), tensile surface stresses occurred at the contact edge under maximum load. These arose in the radial direction for the hardening materials and in the hoop direction for the nonhardening materials. The interface stresses in the substrate and the surface stresses for a half-space with substrate properties obtained in the previous work are presented in Fig. 10. Figure 10(*a*) shows radial stress distributions for the material cases with $n = 0.5$, which exhibited the highest tensile radial stress in the homogeneous half-space indentations. As shown in Fig. 10(*a*), in the presence of a hard layer, the substrate is subjected to only compressive radial stresses. Thus, the layer protects the substrate from the high tensile stresses at the contact edge produced from direct indentation, thereby enhancing the substrate's resistance to crack initiation and subsequent wear. In the previous study of indented homogeneous half-spaces, a compressive hoop stress at the surface was observed for hardening materials. The nonhardening homogeneous half-space exhibited entirely compressive radial stresses at the surface, but was subjected to a tensile hoop stress at the contact edge. Figure 10(*b*) shows that the intervening hard layer significantly reduces the peak tensile stress occurring in the nonhardening homogeneous half-space, generating in the substrate a much smaller tensile hoop stress at a larger radius. Therefore, the hard layer protects the substrate from potential damage at the contact edge under direct indentation due to either the tensile radial stress encountered in hardening materials or the tensile hoop stress arising in perfectly plastic materials.

Table 1 Approximate indentation loads for initial yield*

Medium	P/P_y			
	ξ=0.0067		ξ=0.02	
	β=2	β=4	β=2	β=4
Layer	2.6	10.0	2.6	6.4
Substrate	6.4	6.4	39.8	39.8

*For strain hardening exponents in the range of zero to 0.5.

3.2 Evolution of Plasticity. The loads at which yielding is first observed in both the layer and the substrate are given in Table 1 for all the material cases investigated. In all cases, except for $\xi = 0.0067$ and $\beta = 4$, yielding occurs first in the layer. Hence, the inception of yielding in the layer is favored, except for sufficiently thin, stiff, and hard layers. In the presence of the layers, the load for the inception of yielding in the substrate is at least six times greater than the load at the onset of yielding in a homogeneous half-space with substrate properties, i.e., $P/P_y = 1.0$. The yield loads of the substrates covered by the thicker layers are significantly greater than those with the thinner layers.

Figure 11 shows the evolution of the equivalent plastic strain for the thicker and relatively softer layer. Figure 11(*a*) demonstrates that the inception of yielding occurs in the layer, as indicated in Table 1, on the axis of symmetry. As the load increases, the size of the plastic zone in the layer increases and an elastic core forms at the center of the contact area, as was also the case with the indentation of the homogeneous half-space. At a load $P/P_y = 39.8$, yielding begins in the substrate at the interface near the axis of symmetry (Fig. 11(*b*)). At a heavier load, $P/P_y = 100.6$, the elastic core at the surface disappears, and the maximum equivalent plastic strain in the layer moves away from the axis of symmetry and toward the contact edge near the surface (Fig. 11(*c*)). At the maximum load $P/P_y = 300$, the layer exhibits a maximum plastic strain near the surface and close to the contact edge, while the substrate maximum occurs at the interface at a distance from the axis of symmetry of about two-thirds of the contact radius. This is similar to the behavior of the homogeneous half-space, where the constraint of the rigid indenter and the outlying elastic material caused the maximum plastic strain to move away from the axis of symmetry and toward the surface (Kral et al., 1993).

Contours of equivalent plastic strain for the other nonhardening cases at the maximum load $P/P_y = 300$ of the first load half-cycle demonstrated similar characteristics. The plastic strain in the layer reached a maximum just below the contact edge, while the substrate maximum occurred at the interface and moved outward with the contact edge. In all cases, the maximum equivalent plastic strain occurred in the substrate and decreased with both layer thickness and hard-

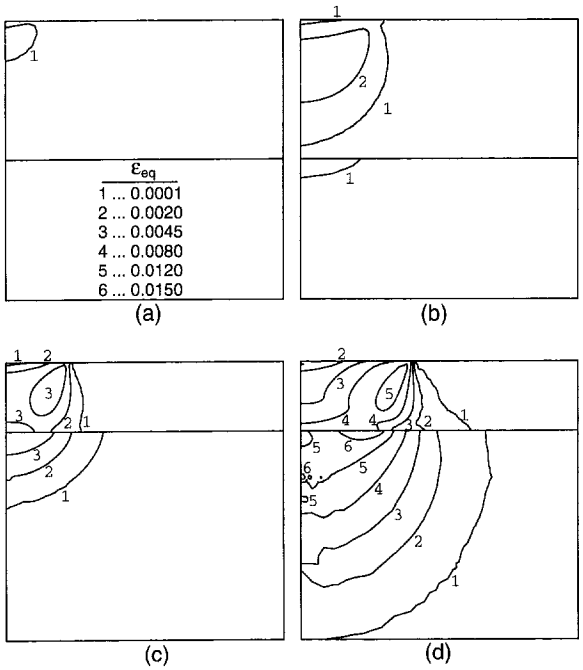

Fig. 11 Evolution of equivalent plastic strain during the first load half-cycle for $\xi = 0.02$, $\beta = 2$, $n = 0.0$, and load P/P_y equal to: (*a*) 6.4, (*b*) 39.8, (*c*) 100.6, and (*d*) 300. ((*a*) and (*b*) show the region $0 \le r/a_y \le 12$, $0 \le z/a_y \le 12$, while (c) and (*d*) show the region $0 \le r/a_y \le 24$, $0 \le z/a_y \le 24$).

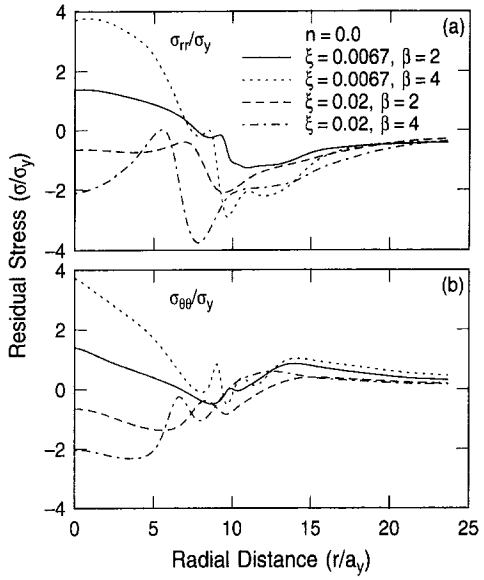

Fig. 12 Residual stresses at the layer interface ($z/a_y = 2^-$ for $\xi = 0.0067$ and $z/a_y = 6^-$ for $\xi = 0.02$) after the first unload half-cycle as a function of layer thickness, stiffness, and hardness: (*a*) radial and (*b*) hoop stress

ness. The size of the plastic zone in the layer decreased with increasing layer stiffness and hardness, the difference being more pronounced for the thicker layer. However, the size of the plastic zone in the substrate decreased only slightly with layer thickness and was only marginally affected by the layer material properties. Strain hardening in the thicker layer and the substrate caused the maximum plastic strain in the layer to remain at the interface, although a local maximum still occurred in the layer near the contact edge, similar to that shown in Fig. 11(*d*) for the nonhardening medium. Since the hardening material can support a greater load by increasing the resistance to plastic deformation, in addition to expansion of the plastic zone, the full development of the maximum plastic strain near the contact edge will not occur until reaching a load heavier than that of the nonhardening cases. Similarly, the hardening cases did not exhibit the excursion of the maximum plastic strain in the substrate away from the axis of symmetry that was apparent in the nonhardening cases, as shown in Fig. 11 for example. The maximum plastic strain decreased with increasing hardening, again because strain hardening allows the material to support a greater stress for the same plastic strain. The sizes of the plastic zones in the layer and substrate for the hardening cases were slightly smaller than the companion nonhardening cases with the same material properties, for the same reason discussed above.

3.3 Residual Stresses and Reyielding. Figure 12 shows the residual radial and hoop stresses at the layer interface for the nonhardening cases as a function of the layer thickness and stiffness. The residual radial stress, shown in Fig. 12(*a*), is compressive for the thicker layer, but for the thinner layer it reaches high tensile values near the axis of symmetry, with the maximum increasing significantly with layer stiffness. The minimum radial stress again occurs at about the maximum contact radius. A similar trend is shown in Fig. 12(*b*) for the residual hoop stress, with the stress for the thicker layer being compressive near the axis of symmetry but reaching high tensile values for the thinner layer. All the layers exhibit a tensile residual hoop stress for $r/a_y \ge 12$. The tensile maximum in that region decreases with increasing layer thickness and/or decreasing layer stiffness and hardness. The residual stress distributions at the layer interface shown in Fig. 12 should be compared with those occurring at the end of the first load half-cycle (Fig. 6). The thinner layers exhibit greater tensile radial stresses after the first unload half-cycle; conversely, the thicker and harder layer exhibits a greater tensile radial stress at the interface during the load half-cycle, while the thicker and softer layer experiences entirely compressive loaded and residual radial stress distributions. A similar situation exists with the hoop stress. From the axis of symmetry to a radial distance $r/a_y \approx 12$, the thinner layers are subjected to a greater tensile hoop stress after the unload half-cycle, while a greater tensile hoop stress occurs in the thicker and harder layer during the load half-cycle. The thicker and softer layer maintains a compressive hoop stress in this region during the entire load cycle. All cases exhibit a tensile residual hoop stress for $r/a_y > 15$ which is higher or comparable to the loading stress in the same region. Thus, large tensile residual stresses may occur in the nonhardening layers, especially as the layer thickness decreases. In particular, the thinner layers exhibit tensile residual radial and hoop stresses near the axis of symmetry and for $r/a_y > 15$ which are significantly higher than those occurring under load, thereby increasing the tendency to initiate cracks during unloading.

Figure 13 shows the interface stresses in the thicker layer as a function of the layer stiffness and hardness and the strain-hardening properties of the layer and substrate. The results presented in Fig. 12 for the softer nonhardening layer are also shown for comparison. A tensile residual radial stress may develop inside the contact region, depending on the layer stiffness and the strain-hardening properties of the medium, as shown in Fig. 13(*a*). The tendency to generate a tensile residual radial stress increases with both the layer stiffness and strain-hardening exponent. A comparison with the results shown in Fig. 8(*a*) indicates that the tensile residual radial stresses are smaller than the tensile stresses at the end of the first load half-cycle. Thus, the greatest susceptibility to circumferential cracks at the interface of the thicker layers occurs during the load half-cycle. Results for the

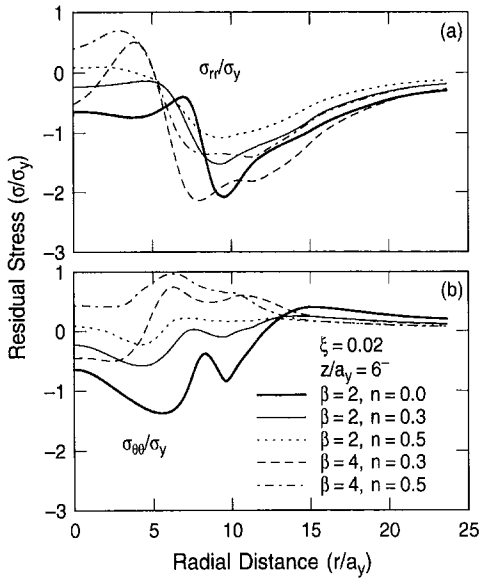

Fig. 13 Residual stresses at the layer interface after the first unload half-cycle as a function of layer stiffness and strain-hardening exponent: (*a*) radial and (*b*) hoop stress

thinner layers, not presented here for the sake of brevity, also indicated an increase in the tensile residual radial stress at the axis of symmetry with hardening, although there was little difference in the tensile maximum stress between $n = 0.3$ and 0.5. As in the thinner nonhardening layers discussed above, the maximum residual interfacial radial stress within the contact radius in the thinner hardening layers is greater than the corresponding radial stress under the maximum load.

For the stiffer layers with greater strain-hardening exponents, Fig. 13(b) shows that the residual hoop stress at the layer interface is also tensile in the region $r/a_y < 12$, similar to the thinner layers shown in Fig. 12(b). Again, comparison with the results shown in Fig. 8(b) indicates that the tensile residual stresses in this region are significantly less than those at the end of the first load half-cycle. All materials exhibit a tensile residual hoop stress in the region $r/a_y \geq 13$ which decreases with increasing strain hardening. These stresses are comparable to those shown in Fig. 8(b) for the end of the load half-cycle. Thus, the greatest tendency to initiate radial cracks at the interface of the thicker layers again exists during the load half-cycle. For the thinner layers, the residual stress at the interface from the axis of symmetry to the contact radius is greater than the stress in the loaded condition, which is similar to the nonhardening layered medium. Thus for the thinner layers, the tendency for interfacial layer cracking is greatest after the completion of the entire load cycle.

Figure 14 shows the residual stresses at the substrate interface for the nonhardening layers. Figures 14(a) and 14(b) illustrate that the residual radial stress is compressive in the entire region, while the residual hoop stress is compressive until roughly the contact radius, where it becomes tensile. The tensile hoop stress decreases with increasing layer thickness and stiffness. The residual normal stress, shown in Fig. 14(c), is tensile on the axis of symmetry and at other interfacial points for all the material cases shown, indicating the possibility of interface delamination. The maximum tensile normal stress occurs on the axis of symmetry and increases with layer thickness and stiffness. The tensile residual normal stress decreases with decreasing layer thickness since the layer interface is closer to the stress-free surface boundary. The residual shear stress at the interface,

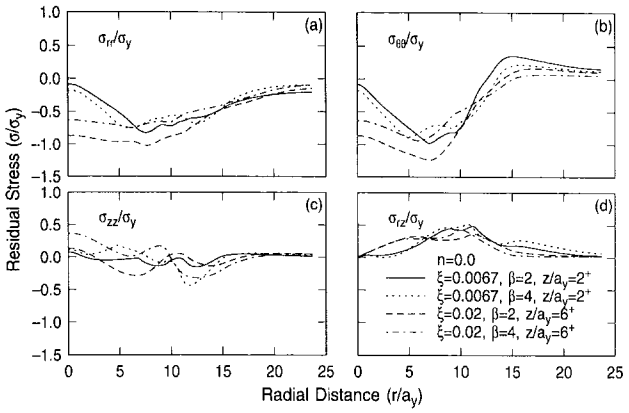

Fig. 14 Residual stresses at the substrate interface after the first unload half-cycle as a function of layer thickness, stiffness, and hardness: (*a*) radial, (*b*) hoop, (*c*) normal, and (*d*) shear stress

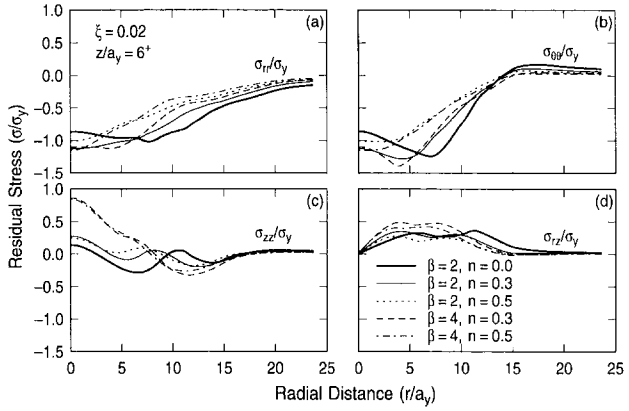

Fig. 15 Residual stresses at the substrate interface after the first unload half-cycle as a function of layer stiffness and strain-hardening exponent: (*a*) radial, (*b*) hoop, (*c*) normal, and (*d*) shear stress

shown in Fig. 14(d), is only marginally influenced by the layer thickness and stiffness.

Figure 15 shows the variation of the residual stresses at the substrate interface for the thicker layer as a function of strain hardening and layer material properties. Results for $\beta = 2$ and $n = 0.0$ are also shown for comparison. The residual radial stress, shown in Fig. 15(a), is again compressive over the region shown for all material cases, while the hoop stress, shown in Fig. 15(b), becomes slightly tensile for $r/a_y > 14$, with the maximum tensile stress decreasing with increasing strain hardening and layer stiffness. Figure 15(c) shows that tensile normal stresses exist for all the material cases, with the peak tensile stress on the axis of symmetry increasing primarily with the layer stiffness. The peak tensile normal stress also increases with hardening of the layer and the substrate, but the increase is significant only when the strain-hardening exponent increases from zero to 0.3. There is no appreciable difference in the results corresponding to $n = 0.3$ and 0.5. Thus, the layer may be subject to delamination upon removal of the load, with the greatest tendency to delaminate occurring on the axis of symmetry and increasing predominantly with the layer stiffness and hardness and secondarily with the amount of strain hardening. Figure 15(d) shows that the residual shear stress also increases slightly with the layer stiffness. However, comparison with the shear stresses at the maximum load showed insignificant differences in maximum magnitude. Consequently, layer debonding due to high interfacial shear stress may occur during either loading or unloading.

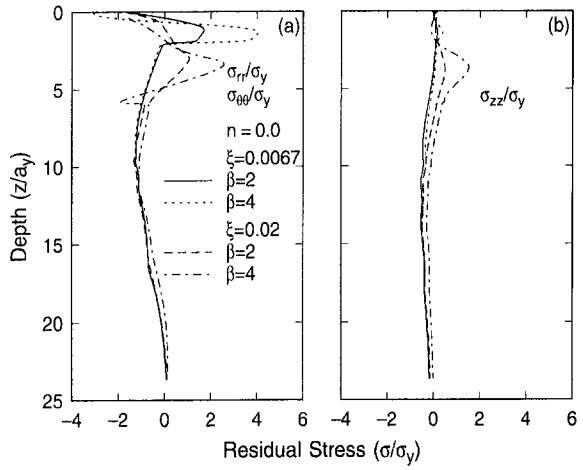

Fig. 16 Effect of layer thickness, stiffness, and hardness on the residual stresses along the axis of symmetry: (*a*) radial (hoop) and (*b*) normal stress

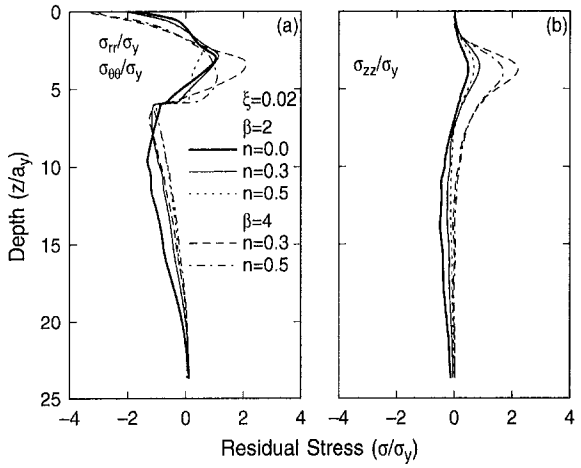

Fig. 17 Effect of layer stiffness and strain-hardening exponent on the residual stresses along the axis of symmetry: (*a*) radial (hoop) and (*b*) normal stress

The results for the residual radial and hoop stresses at the substrate interface, shown in Figs. 14 and 15, differ from those for the indentation of a homogeneous half-space, in which the residual radial and hoop surface stresses were tensile throughout the contact region. It was previously shown in Fig. 10 that the layer protected the substrate from tensile stresses occurring under direct contact during the load half-cycle. Thus, the layer protects the substrate from high tensile stresses arising due to direct contact with the homogeneous half-space during both the load and unload half-cycles.

The distribution of the residual stresses along the axis of symmetry for the nonhardening layered media is shown in Fig. 16. Figure 16(*a*) shows that all the material cases exhibit a tensile radial (hoop) stress in the layer at depths $z/a_y \leq 2$ for $\xi = 0.0067$ and $z/a_y \leq 5$ for $\xi = 0.02$. The tensile radial stress in the layer increases with layer stiffness and hardness and decreases with layer thickness. Figure 16(*b*) shows that the residual normal stress along the axis of symmetry also exhibits tensile values for all the layers, with the maximum tensile stress increasing with layer thickness and stiffness. For the thinner layers, $\xi = 0.0067$, the maximum tensile residual normal stress occurs at the layer/substrate interface ($z/a_y = 2$), while for the thicker layers, $\xi = 0.02$, the maximum occurs in the layer prior to the interface ($z/a_y = 6$) at a depth $z/a_y \approx 4$. The residual normal stress is always tensile at the layer interface, as was mentioned in the discussion of the interface stresses shown in Fig. 14, and thus may lead to delamination of the layer.

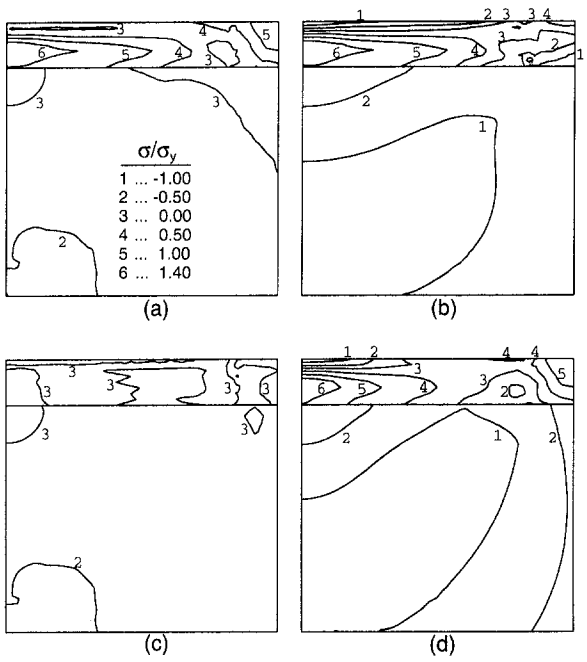

Fig. 18 Contours of residual stresses for $\xi = 0.0067$, $\beta = 2$, and $n = 0.0$ after the first load cycle in the region $0 \leq r/a_y \leq 12$, $0 \leq z/a_y \leq 12$: (*a*) σ_1/σ_y, (*b*) σ_{rr}/σ_y, (*c*) σ_{zz}/σ_y, and (*d*) $\sigma_{\theta\theta}/\sigma_y$

Figure 17 shows the effect of strain hardening on the residual stresses along the axis of symmetry for the thicker layer. The results for $\beta = 2$ and $n = 0.0$ are also shown for comparison. The peak tensile radial (hoop) stress in the layer changes insignificantly as the strain-hardening exponent increases from zero to 0.3. However, as the strain-hardening exponent increases to 0.5, the peak tensile radial stress in the layer decreases. The radial (hoop) stress is compressive in the substrate, with the compressive maximum decreasing with strain hardening. Beyond $z/a_y \approx 23$, there is no discernible difference between the residual stresses for the various material properties. Results for the thinner layer, not shown here, are somewhat different in that the peak tensile stress in the layer increases slightly as the hardening exponent increases from zero to 0.3, but then changes little between $n = 0.3$ and 0.5. The residual normal stresses, shown in Fig. 17(*b*), exhibit a tensile maximum in the layer above the interface which increases between $n = 0.0$ and 0.3 and decreases between $n = 0.3$ and 0.5. However, at the layer interface ($z/a_y = 6$) there is practically no difference between the tensile normal stresses for $n = 0.3$ and 0.5, although both are higher than the corresponding value for the nonhardening case. Thus, the tendency for delamination of the thicker layer due to a tensile residual normal stress at the layer interface ($z/a_y = 6$) increases as strain hardening is introduced, but does not change appreciably when the strain-hardening exponent is in the range of 0.3 to 0.5. Results for the thinner layer, not presented here, demonstrated insignificant variations in the residual normal stress with strain hardening. All cases revealed slightly tensile values at the layer interface, but the stresses were considerably less than those for the thicker layer with the same material properties.

Figure 18 shows contours of residual stresses for the thinner layer, $\xi = 0.0067$, with properties $\beta = 2$ and $n = 0.0$. The contours of maximum principal stress, σ_1, shown in Fig. 18(*a*), demonstrate several regions of tensile residual stress. The highest tensile stress occurs in the layer from the interface up to approximately half the layer thickness. Comparison with the contours shown in Fig. 18(*b*) indicates that this

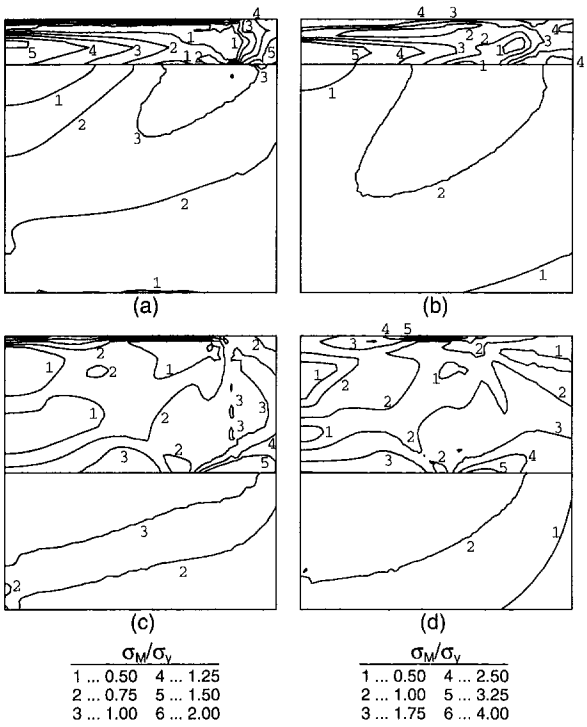

Fig. 19 Contours of residual von Mises equivalent stress after the first load cycle for $n = 0.0$ in the region $0 \le r/a_y \le 12$, $0 \le z/a_y \le 12$: (a) $\xi = 0.0067$, $\beta = 2$, (b) $\xi = 0.0067$, $\beta = 4$, (c) $\xi = 0.02$, $\beta = 2$, and (d) $\xi = 0.02$, $\beta = 4$

maximum tensile principal stress is in the radial direction. This region of tensile stress produces the tensile residual stresses at the layer interface observed in Fig. 12(*a*). For the thicker nonhardening layers, this region of high tensile radial stress exists in roughly the middle of the layer, so that the tensile stress does not reach the interface. Thus, the stresses at the layer interface for the thicker nonhardening layers are compressive in the region $r/a_y \le 12$, as shown in Fig. 12. Strain hardening produces a thicker region of tensile residual radial and hoop stress in the layer, causing the tensile residual stress to reach the interface, thus producing the tensile residual stresses at the interface shown in Fig. 13. Finally, a region of relatively high residual principal stress exists at the surface just beyond the final contact radius. Comparison of the contours shown in Figs. 18(*a*) and 18(*d*) indicates that this principal stress is in the hoop direction, as was also indicated previously by Kral et al. (1995). The contours of normal stress, shown in Fig. 18(*c*), exhibit slight discontinuities across the interface, which are due to the necessarily incomplete averaging of the integration point data to the interface nodes, and very small residual normal stress values in the layered medium.

In contrast to the homogeneous medium, which exhibited limited yielding during the unload half-cycle in only a small surface region at the contact edge (Kral et al., 1993), Fig. 19 shows that the nonhardening layered media contain large regions of reyielding material in the substrate at the layer/substrate interface. Shown in the figure are contours of residual von Mises equivalent stress revealing the yielding regions after the indentation load is completely removed. The substrate yielding regions are given by the contours with $\sigma_M/\sigma_y = 1.0$, i.e., contour number 3 in Figs. 19(*a*) and 19(*c*) ($\beta = 2$) and contour number 2 in Figs. 19(*b*) and 19(*d*) ($\beta = 4$). The thinner layers exhibit reyielding in the substrate at the interface just inside the maximum contact radius and approaching the axis of symmetry (Figs. 19(*a*) and 19(*b*)). The thicker layers exhibit yielding along the entire interface from the axis of symmetry to just inside the maximum contact radius in a roughly semi-elliptical region (Figs. 19(*c*) and 19(*d*)). In both cases, the yielding region for the stiffer layer is larger than that for the more compliant layer of the same thickness.

Although there were no yielding regions in the layer when the contact load was completely removed, the nonhardening material cases did exhibit yielding regions in the layer during the unload half-cycle. For the thicker layers ($\xi = 0.02$) and the thinner and softer layer ($\xi = 0.0067$, $\beta = 2$), layer yielding during unloading involved only a few isolated integration points, primarily near the surface. The thinner and harder layer ($\xi = 0.0067$, $\beta = 4$) exhibited yielding during the unload half-cycle in a relatively large region, given roughly by the area enclosed by contour number 4 in Fig. 19(*b*). Points within this region continued to yield between loads $P/P_y = 300$ and 25, with the size of the yielding region gradually decreasing as the load was reduced. There was no further yielding in this region when the load was reduced below $P/P_y = 25$.

For the hardening layered media, reyielding during the unload half-cycle was much more restricted. Only the hardening case with $\xi = 0.02$, $\beta = 4$, and $n = 0.3$ exhibited reyielding in the substrate. This is the most likely hardening case to reyield, given the tendency of substrate reyielding to be slightly promoted by the thicker layers and substantially enhanced by the stiffer layers, as shown in Fig. 19 for the nonhardening layered media. However, this reyielding region was much smaller than those for the nonhardening cases, forming a semi-ellipse extending from the axis of symmetry to a distance of only $r/a_y = 4$ and from the interface ($z/a_y = 6$) to a depth of only $z/a_y = 7$. This region still yields at $P/P_y = 0$. In addition, several of the hardening cases exhibited limited regions of reyielding in the layer near the surface, which became elastic prior to complete unloading. Only the cases with $\xi = 0.0067$, $\beta = 4$, and $n = 0.3$ and 0.5 showed yielding in a sizable region, given approximately by the area enclosed by contour number 5 in Fig. 19(*b*), and in both cases the unloading became elastic after reaching a load $P/P_y = 15.5$. No other significant reyielding occurred in the hardening cases. Thus, the large regions of increasing plastic strain that existed in the nonhardening materials are significantly reduced or eliminated because of strain hardening.

3.4 Subsequent Load Cycles. The stresses at the layer interface and along the axis of symmetry show relatively little change during the subsequent load and unload half-cycles from the results already presented for the first half-cycles. The variation of stress with load cycle is most pronounced for the nonhardening material cases, while the hardening cases exhibit virtually no variation in the stresses at the layer interface or the axis of symmetry. A similar situation existed for the surface stresses (Kral et al., 1995). As a typical case, Fig. 20 shows the stresses at the layer interface as a function of the load half-cycle. The general characteristics of the stress distributions remain the same, except for a slight decrease in the radial and hoop stresses near the axis of symmetry with repeated loading. Virtually no difference exists beyond $r/a_y = 10$. These variations are typical of all the nonhardening materials. Therefore, the stress distributions remain fairly similar to those presented previously, with only relatively minor variations arising in subsequent load cycles.

Figure 21 shows the dependence of the maximum tensile principal stress in both the layer and the substrate on the load cycle. Results for the maximum stress in the layer and the substrate are shown for the nonhardening cases in Figs. 21(*a*) and 21(*c*) and for the hardening cases in Figs. 21(*b*) and 21(*d*), respectively. The maximum tensile principal stress during the first load half-cycle (load cycle = 0.5) is shown for consistency with the stress results presented previously. The

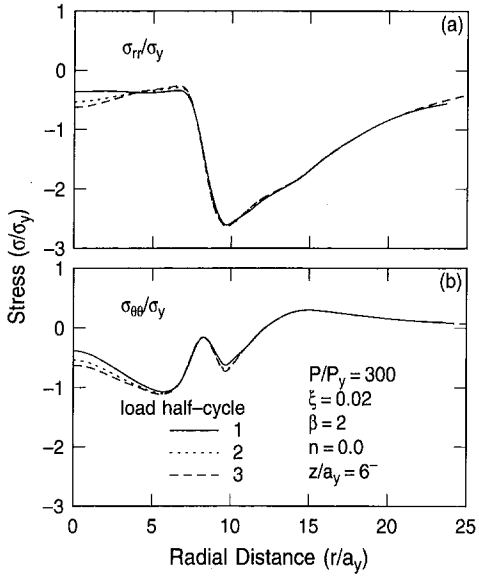

Fig. 20 Stresses at the layer interface as a function of load half-cycle: (*a*) radial and (*b*) hoop stress

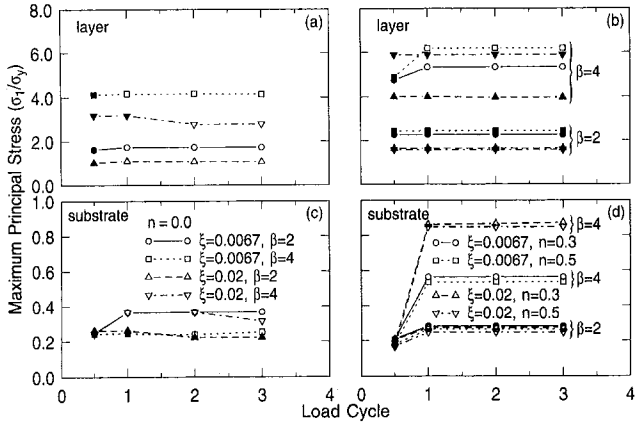

Fig. 21 Maximum principal stress during the first load half-cycle and complete load-unload cycles for nonhardening, (*a*) and (*c*), and hardening, (*b*) and (*d*), material cases. Filled symbols indicate maximum during the load half-cycle, and open symbols indicate maximum during the unload half-cycle.

values at load cycles equal to 1, 2, and 3 are the maximum tensile principal stresses over the entire load cycle. Filled symbols indicate that the maximum occurred during the loading portion of the cycle, while open symbols indicate that the maximum occurred during the unloading portion of the cycle or in the completely unloaded (residual) state. If the maximum during the first load cycle occurs during loading, that point is simply repeated at 0.5 and 1. In most cases, the maximum tensile principal stress occurs during the first load cycle, and subsequent cycles produce a maximum principal stress equal to or slightly less than that of the first cycle. In those cases where the maximum stress increases in subsequent cycles, the increase is only a few percent; therefore, to a good approximation, the highest principal stress is achieved during the first load cycle. For the nonhardening cases, Fig. 21(*a*) shows that the maximum principal stress in the layer increases with layer stiffness and hardness and decreases with layer thickness. For the more compliant layers, the maximum tensile stress occurs in the unloaded condition for all three cycles. This is also the case for the stiffer layers, with the exception of the maximum stress during the first load cycle for the case with $\xi = 0.02$ and $\beta = 4$. Figure 21(*b*) shows that although strain hardening slightly increases the maximum tensile stress in the more compliant layers, significantly higher maximum tensile stresses arise in the stiffer layers. In the more compliant hardening layers, the maximum principal stress decreases with increasing layer thickness but is relatively insensitive to the strain-hardening exponent, and all maxima occur during the load half-cycles. The tensile stress in the stiffer hardening layers increases significantly with hardening and, again, decreases with increasing layer thickness. In the thicker layers, the maxima always occur during the load half-cycles, while the thinner layers always exhibit a maximum during the unload half-cycles. Thus, strain hardening increases the maximum tensile stress in the layer, while generally the maximum tensile stress is decreased by increasing the layer thickness and/or decreasing the layer stiffness and hardness.

According to Fig. 21(*c*), the maximum tensile principal stress in the nonhardening substrates is significantly less than that in the layer, with maxima between $0.25\sigma_y$ and $0.4\sigma_y$. The maxima occur predominantly during the unload half-cycles and their location is always at or near the axis of symmetry near the maximum depth of the plastic zone. This maximum is due to the tensile hoop stress surrounding the plastic zone, as was previously discussed. For the hardening cases, shown in Fig. 21(*d*), the peak of the maximum tensile principal stress is always reached during unloading. For substrates with the more compliant layers ($\beta = 2$), the maximum tensile stress is relatively independent of the layer thickness and the strain-hardening exponent of the media. The maximum tensile stress is significantly higher in the substrates with the stiffer and harder layers ($\beta = 4$); additionally, the maximum tensile stress in these substrates increases significantly with the layer thickness and decreases only slightly with strain hardening.

During subsequent load cycles, the maximum von Mises equivalent stress oscillates between the same maximum and minimum values established in the first load cycle, with the maximum over a cycle always occurring during loading. The only exception is the case with $\xi = 0.02$, $\beta = 4$, and $n = 0.3$, which is the only hardening case to exhibit reyielding of the substrate during unloading and appreciable accumulation of plastic strain during the subsequent cycles. In this case, the maximum von Mises stress in the substrate increases slightly with each half-cycle. During subsequent load cycles, the maximum interfacial shear stress for all cases oscillates between the negative maximum established during the first load half-cycle and a positive maximum at the end of the unload half-cycle. The maximum residual shear stress lies between approximately $0.4\sigma_y$ and $0.6\sigma_y$ for most cases, but is always less than the interfacial shear stress during the load half-cycle. The thinner layers exhibit higher maximum interfacial shear stresses than the thicker layers.

The size and shape of the established plastic zones do not change during subsequent load and unload half-cycles. All the material cases continue to yield and to accumulate plastic strain during repeated indentation, although most of the hardening cases exhibit almost insignificant increases in plastic strain, i.e., of the order of 10^{-6} or less. Continued yielding is identified by those integration points exhibiting an increase in equivalent plastic strain during the half-cycle. The average increase in equivalent plastic strain, $\overline{\Delta\epsilon_{eq}}$, is given by the average computed over all these points. Figure 22 shows $\overline{\Delta\epsilon_{eq}}$ as a function of the number of load and unload half-cycles for the various material cases considered. Points labeled 0.0 indicate no increase in plastic strain during the particular half-cycle. Results for the thinner layers are shown in Figs. 22(*a*) and 22(*c*) and for the thicker layers in Figs. 22(*b*) and 22(*d*). Between the first and second load half-

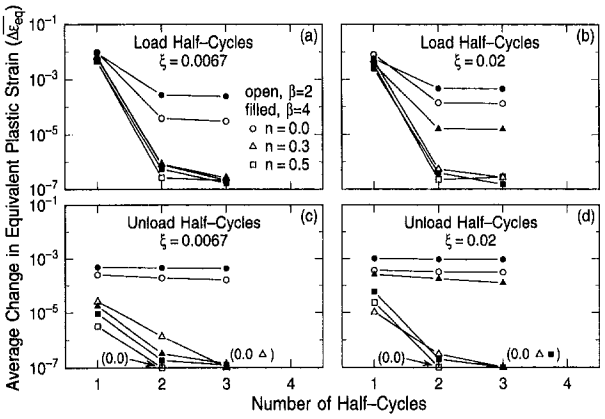

Fig. 22 Average change in equivalent plastic strain in each half-cycle as a function of layer thickness and material properties: (a) and (b) load half-cycles, (c) and (d) unload half-cycles

cycles, the nonhardening cases exhibit at least an order of magnitude decrease in the accumulation of plastic strain. The accumulation of plastic strain remains relatively constant between the second and third load half-cycles. The case having $\xi = 0.02$, $\beta = 4$, and $n = 0.3$ exhibits a decrease in the accumulation of plastic strain of about two orders of magnitude between the first and second load half-cycles, followed by a constant accumulation in the third load half-cycle. This is the only hardening case exhibiting reyielding in the substrate during the unload half-cycles. The remainder of the hardening cases exhibit a decrease of about four orders of magnitude between the first and subsequent load half-cycles, decreasing to negligible average increases of the order of 10^{-7}. The accumulation of plastic strain during the unload half-cycles, shown in Figs. 22(c) and 22(d), shows similar trends. The nonhardening cases and the case with $\xi = 0.02$, $\beta = 4$, and $n = 0.3$ exhibit only a small decrease in $\overline{\Delta \epsilon_{eq}}$ over the unload half-cycles. The remainder of the hardening cases show a substantial decrease in the accumulation of plastic strain with subsequent unload half-cycles, with all cases reaching average increases in equivalent plastic strain of the order of 10^{-6} or less during subsequent cycles. Accumulations of the order of 10^{-6} or less may be attributed to numerical error, and these cases may be considered to have reached a steady-state elastic cycle. In addition, the accumulation of plastic strain in these cases occurs over relatively few integration points, and the stress distributions are indistinguishable from those established during the first load cycle. Several cases do reach complete shakedown for the unload half-cycles, i.e., they show no further increase in plastic strain during the unload half-cycles. The accumulation of plastic strain during subsequent load cycles appears to be most sensitive to the reyielding of the substrate during the unload half-cycle. All the nonhardening cases exhibit substrate yielding during unloading and appreciable continued yielding during subsequent cycles. Only the hardening case with $\xi = 0.02$, $\beta = 4$, and $n = 0.3$ exhibits significant continued yielding; this is the only hardening case in which yielding of the substrate occurs during unloading. Even though hardening in this study is isotropic, reyielding of the substrate for this case requires a sufficient adjustment in the equilibrium stresses of the subsequent loaded state to produce continued plastic deformation. This follows a consistent trend with the nonhardening cases, since the thicker and harder layers exhibit more plastic strain accumulation during unloading and also more accumulation of plastic strain during the subsequent load half-cycle. Thus, the thicker and harder layer with the least strain hardening would be expected to follow the same pattern, which is indeed the case. As pointed out by Moyar in the discussion of Merwin and Johnson (1963), a material with isotropic hardening would be expected to eventually shake down to an elastic steady-state cycle, although this may take several cycles.

Though the stress state in an elastic-plastic layered medium under repeated indentation loading is complex, some predictions can be made regarding shakedown. According to the statical, or lower bound, theorem (Johnson, 1985), if any self-equilibrating residual stress field can be found which, in combination with the elastic stresses resulting from the repeated load, never exceeds the yield limit, then the material will shake down to an elastic steady-state. Conversely, if no such residual stress field exists, then the material will not achieve a steady-state elastic cycle under repeated loading. For the thicker layers, $\xi = 0.02$, yielding occurs in the substrate on the axis of symmetry during both the load and unload half-cycles, as shown in Figs. 19(c) and 19(d). Along the axis of symmetry there is no shear stress and the radial and hoop stresses are equal. Thus, the maximum shear stress can be directly obtained from the difference of the radial (hoop) and normal stresses. Due to symmetry, the maximum shear stress and maximum von Mises equivalent stress on the axis of symmetry are the same, i.e., the Tresca and von Mises yield conditions are identical. Results from Fig. 7 for the radial and normal stresses at the substrate interface indicate that the normalized maximum shear stress on the axis of symmetry is $(\sigma_{zz} - \sigma_{rr})/2\sigma_y = -0.5$, the negative shear yield stress. Results from Fig. 14 indicate that the normalized maximum residual shear stress at the substrate interface on the axis of symmetry is $(\sigma_{zz} - \sigma_{rr})/2\sigma_y = 0.5$, the positive shear yield stress. Thus, the maximum shear stress alternates between the negative and positive shear yield stresses, passing through the center of the yield locus. Consequently, it is not possible to add a residual stress distribution to prevent the material from yielding. Although these are elastic-plastic stresses, it is expected that the elastic stresses due to the repeated load will be at least of this magnitude, since the stress state moves from a yield point through the elastic state to another yield point diametrically opposite on the yield locus. Indeed, the stress state must move only along the diameter of the yield locus due to the symmetries involved. Thus, according to the lower bound theorem, the material will not shake down to an elastic steady-state.

The situation for the thinner layers, $\xi = 0.0067$, is more difficult to analyze because the yielding region during both the load and unload half-cycles, shown in Figs. 19(a) and 19(b), includes all four stress components, and thus the stress state at these material points may be anywhere inside or on the yield locus. In order to assess the likelihood of shakedown, the stress state for each integration point inside the unload yielding region, shown in Figs. 19(a) and 19(b), was transformed to the deviatoric principal stresses (stresses on the π-plane) and was compared with the deviatoric principal stresses at the end of the previous load half-cycle. The distance between the two points on the yield locus was then calculated. This distance was considerably smaller than the diameter of the yield locus for all integration points. Thus, shakedown to an elastic steady-state cannot in principle be ruled out, since it may be possible to add a residual stress that will shift the stress path entirely inside the yield locus. Three additional complete load cycles, for a total of six, were performed for the case $\xi = 0.0067$, $\beta = 2$, and $n = 0.0$ in order to track the average change in equivalent plastic strain. For both the load and unload half-cycles, the average change in plastic strain decreased slightly with each cycle, but at a decreasing rate, indicating that the system may eventually approach a plastically deforming steady-state cycle.

The foregoing theorem and discussions regarding shakedown apply to only elastic-perfectly plastic materials. The materials exhibiting strain hardening must always shake down

to an elastic cycle by virtue of the isotropic strain hardening, though this may take several cycles to occur, as was stated above. Three additional complete load cycles were also performed for the case $\xi = 0.02$, $\beta = 4$, and $n = 0.3$, also for a total of six cycles. For both the load and unload half-cycles, a steadily decreasing accumulation of equivalent plastic strain was observed.

4 Conclusions

The deformation characteristics resulting from repeated elastic-plastic indentation of a half-space covered with a harder and stiffer layer were investigated with the finite element method. Indentations were performed up to loads of 300 times the load necessary to initiate yielding in a homogeneous half-space consisting of the substrate material.

Large tensile radial and hoop stresses occur in the layer at the layer/substrate interface under the maximum load. These tensile stresses increase with the layer stiffness and hardness and also with the strain-hardening exponent of both the layer and the substrate. Such tensile stresses may promote the initiation of subsurface circumferential and radial cracks at the layer interface and eventually lead to debonding of the layer upon subsequent loading. For a given layer thickness, the interfacial shear stress and the maximum von Mises equivalent stress in the substrate are functions of only the strain-hardening exponent when the indentation approaches fully plastic deformation, which is consistent with indentation results for homogeneous half-spaces.

Thinner and harder layers promote large tensile residual stresses at the layer interface. A tensile residual normal stress also occurs at the layer interface after the first load cycle. This stress increases with the layer thickness, stiffness, and hardness, and could lead to eventual delamination of the layer.

The stresses at the substrate interface remain predominantly compressive for both load and unload half-cycles, except for small tensile hoop stresses slightly beyond the contact edge and on the axis of symmetry just below the plastically deformed region. The tensile hoop stress arises as a band surrounding the plastic zone in the substrate and prevents the expansion of the plastic zone for the nonhardening materials, similar to the indentation of a homogeneous half-space. Since the substrate stresses remain predominantly compressive, the substrate is not subjected to the relatively large tensile radial and hoop stresses arising in the indentation of a homogeneous half-space with substrate properties.

Yielding in the nonhardening materials occurs during the first unload half-cycle in large substrate regions and, in some cases, in the layer. Only the substrate regions continue to yield in the residual (completely unloaded) state. Strain hardening in the layer and the substrate virtually eliminates yielding during the unload half-cycle for most cases, except for a few isolated integration points. In some hardening cases, yielding continues to occur in small regions in the layer, and one hardening case exhibits a small yielding region in the substrate.

To a good approximation, the maximum tensile stresses in both the layer and the substrate are established during the first load cycle, indicating that the greatest propensity for crack initiation is during the first cycle. The stresses at the layer/substrate interface (both in the layer and the substrate) and on the axis of symmetry show only slight changes with subsequent load cycles for the nonhardening materials and virtually no change for the hardening materials.

Subsequent load cycles produce continued yielding within the established plastic zones. In general, the increase in average equivalent plastic strain decreases with subsequent load cycles, much more so in the hardening cases than the nonhardening cases. With only one exception, all hardening cases exhibit a decrease in the average equivalent plastic strain accumulation to less than 3×10^{-7} during each of the last load and unload half-cycles, which is considered to be indicative of a steady-state elastic cycle. For the elastic-perfectly plastic material cases, the media having the thicker layers will not shake down to an elastic steady-state cycle. Shakedown to an elastic cycle, however, cannot be ruled out for the thinner layers. The cases with strain hardening will eventually shake down to an elastic steady-state by virtue of the isotropic strain-hardening behavior.

Acknowledgments

This work was partially supported by the Surface Engineering and Tribology Program of the National Science Foundation under Grant No. MSS-8996309 and the Computer Mechanics Laboratory at the University of California at Berkeley. We are grateful to Professor K. L. Johnson for his invaluable help regarding the application of shakedown theorems to this problem.

References

Burmister, D. M., 1945a, "The General Theory of Stresses and Displacements in Layered Systems," *J. Appl. Phys.*, Vol. 16, pp. 89–94.

Burmister, D. M., 1945b, "The General Theory of Stresses and Displacements in Layered Systems," *J. Appl. Phys.*, Vol. 16, pp. 126–127; 296–302.

Chen, W. T., 1971, "Computation of Stresses and Displacements in a Layered Elastic Medium," *Int. J. Engng. Sci.*, Vol. 9, pp. 775–800.

Gupta, P. K., Walowit, J. A., and Finkin, E. F., 1973, "Stress Distributions in Plane Strain Layered Elastic Solids Subjected to Arbitrary Boundary Loading," ASME *Journal of Lubrication Technology*, Vol. 95, pp. 427–433.

Johnson, K. L., 1985, *Contact Mechanics*, Cambridge University Press, Cambridge, U.K., pp. 286–292.

Kennedy, F. E., and Ling, F. F., 1974, "Elasto-Plastic Indentation of a Layered Medium," ASME *Journal of Engineering Materials and Technology*, Vol. 96, pp. 97–103.

King, R. B., and O'Sullivan, T. C., 1987, "Sliding Contact Stresses in a Two-Dimensional Layered Elastic Half-Space," *Int. J. Solids Structures*, Vol. 23, No. 5, pp. 581–597.

Komvopoulos, K., Saka, N., and Suh, N. P., 1987, "The Role of Hard Layers in Lubricated and Dry Sliding," ASME *Journal of Tribology*, Vol. 109, pp. 223–231.

Komvopoulos, K., 1988, "Finite Element Analysis of a Layered Elastic Solid in Normal Contact With a Rigid Surface," ASME *Journal of Tribology*, Vol. 110, pp. 477–485.

Komvopoulos, K., 1989, "Elastic-Plastic Finite Element Analysis of Indented Layered Media," ASME *Journal of Tribology*, Vol. 111, pp. 430–439.

Kral, E. R., Komvopoulos, K., and Bogy, D. B., 1993, "Elastic-Plastic Finite Element Analysis of Repeated Indentation of a Half-Space by a Rigid Sphere," ASME JOURNAL OF APPLIED MECHANICS, Vol. 60, pp. 829–841.

Kral, E. R., Komvopoulos, K., and Bogy, D. B., 1995, "Finite Element Analysis of Repeated Indentation of an Elastic-Plastic Layered Medium by a Rigid Sphere, Part I: Surface Results," ASME JOURNAL OF APPLIED MECHANICS, Vol. 62, pp. 20–28.

Merwin, J. E., and Johnson, K. L., 1963, "An Analysis of Plastic Deformation in Rolling Contact," *Proc. Instn. Mech. Engrs.*, Vol. 177, No. 25, pp. 676–690.

Montmitonnet, P., Edlinger, M. L., and Felder, E., 1993, "Finite Element Analysis of Elastoplastic Indentation: Part II—Application to Hard Coatings," ASME *Journal of Tribology*, Vol. 115, pp. 15–19.

O'Sullivan, T. C., and King, R. B., 1988, "Sliding Contact Stress Field Due to a Spherical Indenter on a Layered Elastic Half-Space," ASME *Journal of Tribology*, Vol. 110, pp. 235–240.

Tangena, A. G., and Hurkx, G. A. M., 1985, "Calculations of Mechanical Stresses in Electrical Contact Situations," *IEEE Trans. on Components, Hybrids, and Manuf. Tech.*, Vol. CHMT-8, No. 1, pp.13–20.

Tian, H., and Saka, N., 1991, "Finite Element Analysis of an Elastic-Plastic Two-Layer Half-Space: Normal Contact," *Wear*, Vol. 148, pp. 47–68.

Bifurcation of Equilibrium in Thick Orthotropic Cylindrical Shells Under Axial Compression

G. A. Kardomateas
Assoc. Professor,
School of Aerospace Engineering,
Georgia Institute of Technology,
Atlanta, GA 30332-0150
Mem. ASME.

The bifurcation of equilibrium of an orthotropic thick cylindrical shell under axial compression is studied by an appropriate formulation based on the three-dimensional theory of elasticity. The results from this elasticity solution are compared with the critical loads predicted by the orthotropic Donnell and Timoshenko nonshallow shell formulations. As an example, the cases of an orthotropic material with stiffness constants typical of glass/epoxy and the reinforcing direction along the periphery or along the cylinder axis are considered. The bifurcation points from the Timoshenko formulation are always found to be closer to the elasticity predictions than the ones from the Donnell formulation. For both the orthotropic material cases and the isotropic one, the Timoshenko bifurcation point is lower than the elasticity one, which means that the Timoshenko formulation is conservative. The opposite is true for the Donnell shell theory, i.e., it predicts a critical load higher than the elasticity solution and therefore it is nonconservative. The degree of conservatism of the Timoshenko theory generally increases for thicker shells. Likewise, the Donnell theory becomes in general more nonconservative with thicker construction.

Introduction

The buckling strength of composite structural members is an important design parameter because of the large strength-to-weight ratio and the lack of extensive plastic yielding in these materials. Fiber-reinforced composite materials can be used in the form of laminated shells in several important structural applications. Although thin plate construction has been the thrust of the initial applications, much attention is now being paid to configurations classified as moderately thick shell structures. Such designs can be used, for example, in the marine industry, as well as for components in the aircraft and automobile industries. Moreover, composite laminates have been considered in space vehicles in the form of circular cylindrical shells as a primary load-carrying structure.

Stability equations for cylindrical shells have been available in the literature mainly for isotropic material (e.g., Flügge, 1960; Danielson and Simmonds, 1969) and a number of analyses have been performed for the buckling strength, based on the application of the cylindrical shell theories (e.g., Simitses, Shaw, and Sheinman, 1985). The relatively simple equations suggested by Donnell (1933) have formed the basis for stability analyses in the literature more than any other set of cylindrical shell equations. Besides the original first set of Donnell equations, a second, more accurate set of cylindrical shell equations that are not subject to some of the shallowness limitation of the first set is also well quoted in the literature (Brush and Almroth, 1975). The latter one will be used in the comparison studies in this paper. Furthermore, in presenting a shell theory formulation for isotropic shells, Timoshenko and Gere (1961) included an additional term in the circumferential displacement part of the second equation (these equations are briefly described in Appendix II). Both the isotropic "nonshallow" Donnell and Timoshenko and Gere formulations can be readily extended for the case of orthotropic material.

In view of possible structural applications of anisotropic shells with sizable thickness, it is desirable to conduct a comprehensive study of the performance of both the readily available Donnell and Timoshenko orthotropic shell theories with respect to the shell thickness. An accurate solution for the stability characteristics of moderately thick shells is also needed in order to enable a future comparison of the accuracy of the predictions from various improved shell theories (e.g., Whitney and Sun, 1974; Librescu, 1975; Reddy and Liu, 1985; see also Noor and Burton, 1990 for a review of shear deformation theories).

Elasticity solutions for the buckling of cylindrical shells have been recently presented by Kardomateas (1993a) for the case of uniform external pressure and orthotropic material; a simplified problem definition was used in this study ("ring"

Contributed by the Applied Mechanics Division of THE AMERICAN SOCIETY OF MECHANICAL ENGINEERS for publication in the ASME JOURNAL OF APPLIED MECHANICS.

Discussion on this paper should be addressed to the Technical Editor, Professor Lewis T. Wheeler, Department of Mechanical Engineering, University of Houston, Houston, TX 77204-4792, and will be accepted until four months after final publication of the paper itself in the ASME JOURNAL OF APPLIED MECHANICS.

Manuscript received by the ASME Applied Mechanics Division, Nov. 13, 1992; final revision, June 30, 1993. Associate Technical Editor: F. Y. M. Wan.

assumption), in that the prebuckling stress and displacement field was axisymmetric, and the buckling modes were assumed two-dimensional, i.e., no z component of the displacement field, and no z-dependence of the r and θ displacement components. It was shown that the critical load for external pressure loading, predicted by shell theory can be highly nonconservative for moderately thick construction. A more thorough investigation of the thickness effects was conducted by Kardomateas (1993b) for the case of a transversely isotropic thick cylindrical shell under axial compression. In that work, a full dependence on r, θ, and z of the buckling modes was assumed. The reason for restricting the material to transversely isotropic was the desire to produce closed-form analytical solutions.

Regarding numerical treatments of this problem, Bradford and Dong (1978) performed an analysis of laminated orthotropic cylinders using semianalytical finite elements, with the modeling occurring in the thickness direction. Although the main focus was on natural vibrations, the case of elastic buckling was also discussed. Results for the isotropic and transversely isotropic case, based on that finite element model, were computed by Dong (1994) and compared with these in Kardomateas (1993b), with good agreement.

In the present work, a generally cylindrically orthotropic material under axial compression is considered. Again, the nonlinear three-dimensional theory of elasticity is appropriately formulated, and reduced to a standard eigenvalue problem for ordinary linear differential equations in terms of a single variable (the radial distance r), with the applied axial load P the parameter. The formulation employs the exact elasticity solution by Lekhnitskii (1963) for the prebuckling state. A full dependence on r, θ, and z of the buckling modes is assumed. The work by Kartomateas (1993b) included a comprehensive study of the performance of the Donnell (1933), the Flügge (1960), and the Danielson and Simmonds (1969) theories for isotropic material. These theories were all found to be nonconservative in predicting bifurcation points, the Donnell theory being the most nonconservative. In addition to considering general orthotropy for the material constitutive behavior, the present work extends the latter work by investigating the performance of another classical formulation, i.e., the Timoshenko and Gere (1961) shell theory. In this paper specific results will be presented for the critical load and the buckling modes; these will be compared with both the orthotropic "nonshallow" Donnell and Timoshenko shell formulations. As an example, the cases of an orthotropic material with stiffness constants typical of glass/epoxy and the reinforcing direction along the periphery or along the cylinder axis will be considered.

Formulation

Let us consider the equations of equilibrium in terms of the second Piola-Kirchhoff stress tensor $\mathbf{\Sigma}$ in the form

$$\mathrm{div}(\mathbf{\Sigma}.\mathbf{F}^{\mathrm{T}}) = 0, \tag{1a}$$

where $\mathbf{F}$ is the deformation gradient defined by

$$\mathbf{F} = \mathbf{I} + \mathrm{grad}V, \tag{1b}$$

where V is the displacement vector and $\mathbf{I}$ is the identity tensor.

Notice that the strain tensor is defined by

$$\mathbf{E} = \frac{1}{2}(\mathbf{F}^{\mathrm{T}}.\mathbf{F} - \mathbf{I}). \tag{1c}$$

More specifically, in terms of the linear strains,

$$e_{rr} = \frac{\partial u}{\partial r}, \quad e_{\theta\theta} = \frac{1}{r}\frac{\partial v}{\partial \theta} + \frac{u}{r}, \quad e_{zz} = \frac{\partial w}{\partial z}, \tag{2a}$$

$$e_{r\theta} = \frac{1}{r}\frac{\partial u}{\partial \theta} + \frac{\partial v}{\partial r} - \frac{v}{r}, \quad e_{rz} = \frac{\partial u}{\partial z} + \frac{\partial w}{\partial r},$$

$$e_{\theta z} = \frac{\partial v}{\partial z} + \frac{1}{r}\frac{\partial w}{\partial \theta}, \tag{2b}$$

and the linear rotations,

$$2\omega_r = \frac{1}{r}\frac{\partial w}{\partial \theta} - \frac{\partial v}{\partial z}, \quad 2\omega_\theta = \frac{\partial u}{\partial z} - \frac{\partial w}{\partial r},$$

$$2\omega_z = \frac{\partial v}{\partial r} + \frac{v}{r} - \frac{1}{r}\frac{\partial u}{\partial \theta}, \tag{2c}$$

the deformation gradient $\mathbf{F}$ is

$$\mathbf{F} = \begin{bmatrix} 1 + e_{rr} & \frac{1}{2}e_{r\theta} - \omega_z & \frac{1}{2}e_{rz} + \omega_\theta \\ \frac{1}{2}e_{r\theta} + \omega_z & 1 + e_{\theta\theta} & \frac{1}{2}e_{\theta z} - \omega_r \\ \frac{1}{2}e_{rz} - \omega_\theta & \frac{1}{2}e_{\theta z} + \omega_r & 1 + e_{zz} \end{bmatrix}. \tag{3}$$

At the critical load there are two possible infinitely close positions of equilibrium. Denote by u_0, v_0, w_0 the r, θ, and z components of the displacement corresponding to the primary position. A perturbed position is denoted by

$$u = u_0 + \alpha u_1; \quad v = v_0 + \alpha v_1; \quad w = w_0 + \alpha w_1, \tag{4}$$

where α is an infinitesimally small quantity. Here, $\alpha u_1(r, \theta, z)$, $\alpha v_1(r, \theta, z)$, $\alpha w_1(r, \theta, z)$ are the displacements to which the points of the body must be subjected to shift them from the initial position of equilibrium to the new equilibrium position. The functions $u_1(r, \theta, z)$, $v_1(r, \theta, z)$, $w_1(r, \theta, z)$ are assumed finite and α is an infinitesimally small quantity independent of r, θ, z.

Following Kardomateas (1993a), we obtain the following buckling equations:

$$\frac{\partial}{\partial r}\left(\sigma'_{rr} - \tau^0_{r\theta}\omega'_z + \tau^0_{rz}\omega'_\theta\right) + \frac{1}{r}\frac{\partial}{\partial \theta}\left(\tau'_{r\theta} - \sigma^0_{\theta\theta}\omega'_z + \tau^0_{\theta z}\omega'_\theta\right) + \frac{\partial}{\partial z}\left(\tau'_{rz} - \tau^0_{\theta z}\omega'_z + \sigma^0_{zz}\omega'_\theta\right) + \frac{1}{r}\left(\sigma'_{rr} - \sigma'_{\theta\theta} + \tau^0_{rz}\omega'_\theta + \tau^0_{\theta z}\omega'_r - 2\tau^0_{r\theta}\omega'_z\right) = 0, \tag{5a}$$

$$\frac{\partial}{\partial r}\left(\tau'_{r\theta} + \sigma^0_{rr}\omega'_z - \tau^0_{rz}\omega'_r\right) + \frac{1}{r}\frac{\partial}{\partial \theta}\left(\sigma'_{\theta\theta} + \tau^0_{r\theta}\omega'_z - \tau^0_{\theta z}\omega'_r\right) + \frac{\partial}{\partial z}\left(\tau'_{\theta z} + \tau^0_{rz}\omega'_z - \sigma^0_{zz}\omega'_r\right) + \frac{1}{r}\left(2\tau'_{r\theta} + \sigma^0_{rr}\omega'_z - \sigma^0_{\theta\theta}\omega'_z + \tau^0_{\theta z}\omega'_\theta - \tau^0_{rz}\omega'_r\right) = 0, \tag{5b}$$

$$\frac{\partial}{\partial r}\left(\tau'_{rz} - \sigma^0_{rr}\omega'_\theta + \tau^0_{r\theta}\omega'_r\right) + \frac{1}{r}\frac{\partial}{\partial \theta}\left(\tau'_{\theta z} - \tau^0_{r\theta}\omega'_\theta + \sigma^0_{\theta\theta}\omega'_r\right) + \frac{\partial}{\partial z}\left(\sigma'_{zz} - \tau^0_{rz}\omega'_\theta + \tau^0_{\theta z}\omega'_r\right) + \frac{1}{r}\left(\tau'_{rz} - \sigma^0_{rr}\omega'_\theta + \tau^0_{r\theta}\omega'_r\right) = 0 \tag{5c}$$

In the previous equations, σ^0_{ij} and ω^0_j are the values of σ_{ij} and ω_j at the initial equilibrium position, i.e., for $u = u_0$, $v = v_0$ and $w = w_0$, and σ'_{ij} and ω'_j are the values at the perturbed position, i.e., for $u = u_1$, $v = v_1$ and $w = w_1$.

The boundary conditions associated with (1*a*) can be expressed as

$$(\mathbf{F}.\boldsymbol{\Sigma}^{\mathrm{T}}).\hat{N} = t(V), \tag{6}$$

where t is the traction vector on the surface which has outward unit normal $\hat{N} = (\hat{l}, \hat{m}, \hat{n})$ before any deformation. The traction vector t depends on the displacement field $V = (u, v, w)$. Again, following Kardomateas (1993a), we obtain for the lateral and end surfaces:

$$\left(\sigma'_{rr} - \tau^0_{r\theta}\omega'_z + \tau^0_{rz}\omega'_\theta\right)\hat{l} + \left(\tau'_{r\theta} - \sigma^0_{\theta\theta}\omega'_z + \tau^0_{\theta z}\omega'_\theta\right)\hat{m} + \left(\tau'_{rz} - \tau^0_{\theta z}\omega'_z + \sigma^0_{zz}\omega'_\theta\right)\hat{n} = 0, \tag{7a}$$

$$\left(\tau'_{r\theta} + \sigma^0_{rr}\omega'_z - \tau^0_{rz}\omega'_r\right)\hat{l} + \left(\sigma'_{\theta\theta} + \tau^0_{r\theta}\omega'_z - \tau^0_{\theta z}\omega'_r\right)\hat{m} + \left(\tau'_{\theta z} + \tau^0_{rz}\omega'_z - \sigma^0_{zz}\omega'_r\right)\hat{n} = 0, \tag{7b}$$

$$\left(\tau'_{rz} + \tau^0_{r\theta}\omega'_r - \sigma^0_{rr}\omega'_\theta\right)\hat{l} + \left(\tau'_{\theta z} + \sigma^0_{\theta\theta}\omega'_r - \tau^0_{r\theta}\omega'_\theta\right)\hat{m} + \left(\sigma'_{zz} + \tau^0_{\theta z}\omega'_r - \tau^0_{rz}\omega'_\theta\right)\hat{n} = 0. \tag{7c}$$

Pre-buckling State. The problem under consideration is that of an orthotropic cylindrical shell compressed by an axial force applied at one end. The stress-strain relations for the orthotropic body are

$$\begin{bmatrix} \sigma_{rr} \\ \sigma_{\theta\theta} \\ \sigma_{zz} \\ \tau_{\theta z} \\ \tau_{rz} \\ \tau_{r\theta} \end{bmatrix} = \begin{bmatrix} c_{11} & c_{12} & c_{13} & 0 & 0 & 0 \\ c_{12} & c_{22} & c_{23} & 0 & 0 & 0 \\ c_{13} & c_{23} & c_{33} & 0 & 0 & 0 \\ 0 & 0 & 0 & c_{44} & 0 & 0 \\ 0 & 0 & 0 & 0 & c_{55} & 0 \\ 0 & 0 & 0 & 0 & 0 & c_{66} \end{bmatrix} \begin{bmatrix} \epsilon_{rr} \\ \epsilon_{\theta\theta} \\ \epsilon_{zz} \\ \gamma_{\theta z} \\ \gamma_{rz} \\ \gamma_{r\theta} \end{bmatrix}, \tag{8}$$

where c_{ij} are the stiffness constants (we have used the notation $1 \equiv r$, $2 \equiv \theta$, $3 \equiv z$).

Let R_1 be the internal and R_2 the external radius (Fig. 1). Lekhnitskii (1963) gave the stress field for an applied compressive load of absolute value P, in terms of the quantities:

$$k = \sqrt{\frac{a_{11}a_{33} - a_{13}^2}{a_{22}a_{33} - a_{23}^2}}, \tag{9a}$$

$$\tilde{h} = \frac{(a_{23} - a_{13})a_{33}}{(a_{11} - a_{22})a_{33} + (a_{23}^2 - a_{13}^2)}. \tag{9b}$$

$$\tilde{T} = \pi\left(R_2^2 - R_1^2\right) - \frac{2\pi\tilde{h}}{a_{33}} \times \left[\frac{R_2^2 - R_1^2}{2}(a_{13} + a_{23}) - \frac{\left(R_2^{k+1} - R_1^{k+1}\right)^2}{R_2^{2k} - R_1^{2k}}\frac{a_{13} + ka_{23}}{k+1} - \frac{\left(R_2^{k-1} - R_1^{k-1}\right)^2 (R_1R_2)^2}{R_2^{2k} - R_1^{2k}}\frac{a_{13} - ka_{23}}{k-1}\right]. \tag{9c}$$

Notice that the formula quoted in Lekhnitskii (1963) for $\tilde{T}$ has a slight error in the last term.

The stress field for orthotropy is as follows:

$$\sigma^0_{rr} = P\left(C_0 + C_1 r^{k-1} + C_2 r^{-k-1}\right), \tag{10a}$$

$$\sigma^0_{\theta\theta} = P\left(C_0 + C_1 k r^{k-1} - C_2 k r^{-k-1}\right), \tag{10b}$$

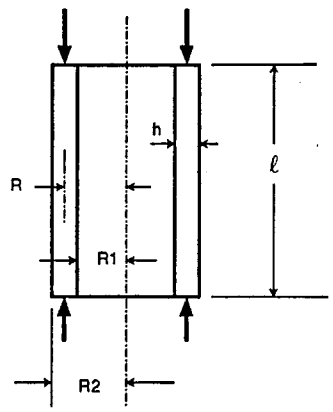

Fig. 1 Cylindrical shell under axial compression

$$\sigma^0_{zz} = -\frac{P}{\tilde{T}} - P\left(C_0\frac{a_{13} + a_{23}}{a_{33}} + C_1\frac{a_{13} + ka_{23}}{a_{33}}r^{k-1} + C_2\frac{a_{13} - ka_{23}}{a_{33}}r^{-k-1}\right), \tag{10c}$$

$$\tau^0_{r\theta} = \tau^0_{rz} = \tau^0_{\theta z} = 0, \tag{10d}$$

where

$$C_0 = -\frac{\tilde{h}}{\tilde{T}}; \quad C_1 = \frac{R_2^{k+1} - R_1^{k+1}}{R_2^{2k} - R_1^{2k}}\frac{\tilde{h}}{\tilde{T}}, \tag{10e}$$

$$C_2 = \frac{R_2^{k-1} - R_1^{k-1}}{R_2^{2k} - R_1^{2k}}(R_1R_2)^{k+1}\frac{\tilde{h}}{\tilde{T}}. \tag{10f}$$

Notice that for general orthotropy, both σ^0_{rr} and $\sigma^0_{\theta\theta}$ are nonzero. For an isotropic or transversely isotropic body, these two stress components are zero.

In the previous equations, a_{ij} are the compliance constants, i.e.,

$$\begin{bmatrix} \epsilon_{rr} \\ \epsilon_{\theta\theta} \\ \epsilon_{zz} \\ \gamma_{\theta z} \\ \gamma_{rz} \\ \gamma_{r\theta} \end{bmatrix} = \begin{bmatrix} a_{11} & a_{12} & a_{13} & 0 & 0 & 0 \\ a_{12} & a_{22} & a_{23} & 0 & 0 & 0 \\ a_{13} & a_{23} & a_{33} & 0 & 0 & 0 \\ 0 & 0 & 0 & a_{44} & 0 & 0 \\ 0 & 0 & 0 & 0 & a_{55} & 0 \\ 0 & 0 & 0 & 0 & 0 & a_{66} \end{bmatrix} \begin{bmatrix} \sigma_{rr} \\ \sigma_{\theta\theta} \\ \sigma_{zz} \\ \tau_{\theta z} \\ \tau_{rz} \\ \tau_{r\theta} \end{bmatrix}. \tag{11}$$

The prebuckling solution just described is an exact elasticity solution based on the assumption that the stresses do not vary along the shell axis. Hence, this solution does not take into account the end effects. Recent work by Kollár (1994) has focused on including an axial variation. However, any end effects, being of local nature, would not affect the (global) buckling behavior.

Perturbed State. Using the constitutive relations (8) for the stresses σ'_{ij} in terms of the strains e'_{ij}, the strain-displacement relations (2) for the strains e'_{ij} and the rotations ω'_j in terms of the displacements u_1, v_1, w_1, and taking into account (10), the buckling Eq. (5*a*) for the problem at hand is written in terms of the displacements at the perturbed state as follows:

$$c_{11}\left(u_{1,rr}+\frac{u_{1,r}}{r}\right)-c_{22}\frac{u_1}{r^2}+\left(c_{66}+\frac{\sigma_{\theta\theta}^0}{2}\right)\frac{u_{1,\theta\theta}}{r^2}$$
$$+\left(c_{55}+\frac{\sigma_{zz}^0}{2}\right)u_{1,zz}+\left(c_{12}+c_{66}-\frac{\sigma_{\theta\theta}^0}{2}\right)\frac{v_{1,r\theta}}{r}$$
$$-\left(c_{22}+c_{66}+\frac{\sigma_{\theta\theta}^0}{2}\right)\frac{v_{1,\theta}}{r^2}+\left(c_{13}+c_{55}-\frac{\sigma_{zz}^0}{2}\right)w_{1,rz}$$
$$+(c_{13}-c_{23})\frac{w_{1,z}}{r}=0. \quad (12a)$$

The second buckling Eq. (5b) gives

$$\left(c_{66}+\frac{\sigma_{rr}^0}{2}\right)\left(v_{1,rr}+\frac{v_{1,r}}{r}-\frac{v_1}{r^2}\right)+\left(\frac{\sigma_{rr}^0-\sigma_{\theta\theta}^0}{2}\right)\left(\frac{v_{1,r}}{r}+\frac{v_1}{r^2}\right)$$
$$+c_{22}\frac{v_{1,\theta\theta}}{r^2}+\left(c_{44}+\frac{\sigma_{zz}^0}{2}\right)v_{1,zz}+\left(c_{66}+c_{12}-\frac{\sigma_{rr}^0}{2}\right)\frac{u_{1,r\theta}}{r}$$
$$+\left(c_{66}+c_{22}+\frac{\sigma_{\theta\theta}^0}{2}\right)\frac{u_{1,\theta}}{r^2}+\left(c_{23}+c_{44}-\frac{\sigma_{zz}^0}{2}\right)\frac{w_{1,\theta z}}{r}$$
$$+\frac{1}{2}\frac{d\sigma_{rr}^0}{dr}\left(v_{1,r}+\frac{v_1}{r}-\frac{u_{1,\theta}}{r}\right)=0. \quad (12b)$$

In a similar fashion, the third buckling Eq. (5c) gives

$$\left(c_{55}+\frac{\sigma_{rr}^0}{2}\right)\left(w_{1,rr}+\frac{w_{1,r}}{r}\right)+\left(c_{44}+\frac{\sigma_{\theta\theta}^0}{2}\right)\frac{w_{1,\theta\theta}}{r^2}$$
$$+c_{33}w_{1,zz}+\left(c_{13}+c_{55}-\frac{\sigma_{rr}^0}{2}\right)u_{1,rz}+\left(c_{23}+c_{55}-\frac{\sigma_{rr}^0}{2}\right)\frac{u_{1,z}}{r}$$
$$+\left(c_{23}+c_{44}-\frac{\sigma_{\theta\theta}^0}{2}\right)\frac{v_{1,\theta z}}{r}+\frac{1}{2}\frac{d\sigma_{rr}^0}{dr}(w_{1,r}-u_{1,z})=0, \quad (12c)$$

In the perturbed position, we seek equilibrium modes in the form

$$u_1(r,\theta,z)=U(r)\cos n\theta\sin\lambda z;$$
$$v_1(r,\theta,z)=V(r)\sin n\theta\sin\lambda z,$$
$$w_1(r,\theta,z)=W(r)\cos n\theta\cos\lambda z, \quad (13)$$

where the functions $U(r)$, $V(r)$, $W(r)$ are uniquely determined for a particular choice of n and λ.

Notice that these modes correspond to the condition of "simply supported" ends since u_1 varies as $\sin\lambda z$ and

$$u_1=\frac{d^2u_1}{dz^2}=0 \quad \text{at} \quad z=0,\ \ell.$$

Denote now $U^{(i)}(r)$, $V^{(i)}(r)$ and $W^{(i)}(r)$ the ith derivative of $U(r)$, $V(r)$, and $W(r)$, respectively, with the additional notation $U^{(0)}(r)=U(r)$, $V^{(0)}(r)=V(r)$ and $W^{(0)}(r)=W(r)$.

Substituting in (12a), we obtain the following linear homogeneous ordinary differential equation:

$$U(r)''c_{11}+U(r)'\frac{c_{11}}{r}$$
$$+U(r)\left[(b_{00}+b_{01}P)r^{-2}+b_{02}Pr^{k-3}+\right.$$
$$\left.+b_{03}Pr^{-k-3}+(b_{04}+b_{05}P)+b_{06}Pr^{k-1}+b_{07}Pr^{-k-1}\right]$$
$$+\sum_{i=0}^{1}V^{(i)}(r)\left[(d_{i0}+d_{i1}P)r^{i-2}\right.$$
$$\left.+d_{i2}Pr^{k-3+i}+d_{i3}Pr^{-k-3+i}\right]$$
$$+\sum_{i=0}^{1}W^{(i)}(r)\left[(f_{i0}+f_{i1}P)r^{i-1}\right.$$
$$\left.+f_{i2}Pr^{k-2+i}+f_{i3}Pr^{-k-2+i}\right]=0$$
$$R_1\le r\le R_2. \quad (14a)$$

The second differential Eq. (12b) gives

$$V(r)\left[(g_{04}+g_{05}P)+g_{06}Pr^{k-1}+g_{07}Pr^{-k-1}\right]$$
$$+\sum_{i=0}^{2}V^{(i)}(r)\left[(g_{i0}+g_{i1}P)r^{i-2}+g_{i2}Pr^{k-3+i}+g_{i3}Pr^{-k-3+i}\right]$$
$$+\sum_{i=0}^{1}U^{(i)}(r)\left[(h_{i0}+h_{i1}P)r^{i-2}\right.$$
$$\left.+h_{i2}Pr^{k-3+i}+h_{i3}Pr^{-k-3+i}\right]$$
$$+W(r)\left[(t_{00}+t_{01}P)r^{-1}+t_{02}Pr^{k-2}+t_{03}Pr^{-k-2}\right]=0$$
$$R_1\le r\le R_2. \quad (14b)$$

In a similar fashion, (12c) gives

$$W(r)q_{04}+\sum_{i=0}^{2}W^{(i)}(r)\left[(q_{i0}+q_{i1}P)r^{i-2}\right.$$
$$\left.+q_{i2}Pr^{k-3+i}+q_{i3}Pr^{-k-3+i}\right]$$
$$+\sum_{i=0}^{1}U^{(i)}(r)\left[(s_{i0}+s_{i1}P)r^{i-1}+s_{i2}Pr^{k-2+i}+s_{i3}Pr^{-k-2+i}\right]$$
$$+V(r)\left[(\beta_{00}+\beta_{01}P)r^{-1}+\beta_{02}Pr^{k-2}+\beta_{03}Pr^{-k-2}\right]=0$$
$$R_1\le r\le R_2. \quad (14c)$$

All the previous three Eqs. (14) are linear, homogeneous, ordinary differential equations of the second order for $U(r)$, $V(r)$ and $W(r)$. In these equations, the constants b_{ij}, d_{ij}, f_{ij}, g_{ij}, h_{ij}, t_{ij}, q_{ij}, s_{ij}, and β_{ij} are given in Appendix I and depend on the material stiffness coefficients c_{ij} and k as well as the buckling mode constants n and λ.

Now we proceed to the boundary conditions on the lateral surfaces $r=R_j$, $j=1,2$. These will complete the formulation of the eigenvalue problem for the critical load.

From (7), we obtain for $\hat{l}=\pm1$, $\hat{m}=\hat{n}=0$:

$$\sigma_{rr}'=0;\quad \tau_{r\theta}'+\sigma_{rr}^0\omega_z'=0;\quad \tau_{rz}'-\sigma_{rr}^0\omega_\theta'=0,$$
$$\text{at} \quad r=R_1,R_2. \quad (15)$$

Substituting in (8), (2), (13), and (10), the boundary condition $\sigma_{rr}'=0$ at $r=R_j$, $j=1,2$ gives

$$U'(R_j)c_{11}+\left[U(R_j)+nV(R_j)\right]\frac{c_{12}}{R_j}-c_{13}\lambda W(R_j)=0,$$
$$j=1,2 \quad (16a)$$

The boundary condition $\tau_{r\theta}'+\sigma_{rr}^0\omega_z'=0$ at $r=R_j$, $j=1,2$ gives

$$V'(R_j)\left[\left(c_{66}+\frac{C_0}{2}P\right)+\frac{C_1}{2}PR_j^{k-1}+\frac{C_2}{2}PR_j^{-k-1}\right]$$
$$+\left[V(R_j)+nU(R_j)\right]\left[\left(-c_{66}+\frac{C_0}{2}P\right)R_j^{-1}\right.$$
$$\left.+\frac{C_1}{2}PR_j^{k-2}+\frac{C_2}{2}PR_j^{-k-2}\right],\quad j=1,2. \quad (16b)$$

In a similar fashion, the condition $\tau'_{rz} - \sigma^0_{rr}\omega'_\theta = 0$ at $r = R_j$, $j = 1,2$, gives

$$\lambda U(R_j)\left[\left(c_{55} - \frac{C_0}{2}P\right) - \frac{C_1}{2}PR_j^{k-1} - \frac{C_2}{2}PR_j^{-k-1}\right] + W'(R_j)\left[\left(c_{55} = \frac{C_0}{2}P\right) + \frac{C_1}{2}PR_j^{k-1} + \frac{C_2}{2}PR_j^{-k-1}\right], \quad j = 1,2. \quad (16c)$$

Equations (14) and (16) constitute an eigenvalue problem for differential equations, with the applied compressive load P the parameter, which can be solved by standard numerical methods (two-point boundary value problem).

Before discussing the numerical procedure used for solving this eigenvalue problem, one final point will be addressed. To completely satisfy all the elasticity requirements, we should discuss the boundary conditions at the ends. From (7), the boundary conditions on the ends are

$$\tau'_{rz} + \sigma^0_{zz}\omega'_\theta = 0; \quad \tau'_{\theta z} - \sigma^0_{zz}\omega'_r = 0; \quad \sigma'_{zz} = 0, \quad \text{at} \quad z = 0,\ \ell. \quad (17)$$

Since σ'_{zz} varies as $\sin \lambda z$, the condition $\sigma'_{zz} = 0$ on both the lower end $z = 0$, and the upper end $z = \ell$, is satisfied if

$$\lambda = \frac{m\pi}{\ell}. \quad (18)$$

In a cartesian coordinate system (x, y, z), the first two of the conditions in (17) can be written as follows:

$$\tau'_{xz} + \sigma^0_{zz}\omega'_y = 0; \quad \tau'_{yz} - \sigma^0_{zz}\omega'_x = 0. \quad (19)$$

It will be proved now that these remaining two conditions are satisfied on the average.

The lateral surface boundary conditions in the cartesian coordinate system (analogous to (7)), with $\hat{N}$ the normal to the circular contour are

$$\left(\sigma'_{xx} - \tau^0_{xy}\omega'_z\right)\cos(\hat{N}, x) + \left(\tau'_{xy} - \sigma^0_{yy}\omega'_z\right)\cos(\hat{N}, y) = 0, \quad (20a)$$

$$\left(\tau'_{xy} + \sigma^0_{xx}\omega'_z\right)\cos(\hat{N}, x) + \left(\sigma'_{yy} + \tau^0_{xy}\omega'_z\right)\cos(\hat{N}, y) = 0. \quad (20b)$$

Using the equilibrium equation in cartesian coordinates (analogous to (5)), gives

$$\frac{\partial}{\partial z}\int\int_A \left(\tau'_{xz} + \sigma^0_{zz}\omega'_y\right)dA = -\int\int_A \left[\frac{\partial}{\partial x}\left(\sigma'_{xx} - \tau^0_{xy}\omega'_z\right) + \frac{\partial}{\partial y}\left(\tau'_{xy} - \sigma^0_{yy}\omega'_z\right)\right]dA. \quad (21a)$$

Using now the divergence theorem for transformation of an area integral into a contour integral, and the condition (20a) on the contour, gives the previous integral as

$$+\int_\gamma \left[\left(\sigma'_{xx} - \tau^0_{xy}\omega'_z\right)\cos(\hat{N}, x) + \left(\tau'_{xy} - \sigma^0_{yy}\omega'_z\right)\cos(\hat{N}, y)\right]ds = 0,$$

where A denotes the area of the annular cross-section and γ the corresponding contour.

Therefore

$$\int\int_A \left(\tau'_{xz} + \sigma^0_{zz}\omega'_y\right)dA = \text{const}. \quad (21b)$$

Since based on the buckling modes (13) and (18), τ'_{rz}, ω'_θ, $\tau'_{\theta z}$, and ω'_r and hence τ'_{xz}, ω'_y, τ'_{yz}, and ω'_x, all have a $\cos(m\pi z/\ell)$ variation, they become zero at $z = \ell/(2m)$. Therefore, it is concluded that the constant in (21b) is zero. Similar arguments hold for τ'_{yz}.

Moreover, it can also be proved that the system of resultant stresses (19) would produce no torsional moment. Indeed,

$$\frac{\partial}{\partial z}\int\int_A \left[x\left(\tau'_{yz} - \sigma^0_{zz}\omega'_x\right) - y\left(\tau'_{xz} + \sigma^0_{zz}\omega'_y\right)\right]dA = -\int\int_A \left\{x\left[\frac{\partial\left(\tau'_{xy} + \sigma^0_{xx}\omega'_z\right)}{\partial x} + \frac{\partial\left(\sigma'_{yy} + \tau^0_{xy}\omega'_z\right)}{\partial y}\right] - y\left[\frac{\partial\left(\sigma'_{xx} - \tau^0_{xy}\omega'_z\right)}{\partial x} + \frac{\partial\left(\tau'_{xy} - \sigma^0_{yy}\omega'_z\right)}{\partial y}\right]\right\}dA.$$

Again, using the divergence theorem, and taking into account (20), the previous integral becomes

$$-\int_\gamma \left\{x\left[\left(\tau'_{xy} + \sigma^0_{xx}\omega'_z\right)\cos(\hat{N}, x) + \left(\sigma'_{yy} + \tau^0_{xy}\omega'_z\right)\cos(\hat{N}, y)\right] - y\left[\left(\sigma'_{xx} - \tau^0_{xy}\omega'_z\right)\cos(\hat{N}, x) + \left(\tau'_{xy} - \sigma^0_{yy}\omega'_z\right)\cos(\hat{N}, y)\right]\right\}ds = 0, \quad (22a)$$

hence

$$\int\int_A \left[x\left(\tau'_{yz} - \sigma^0_{zz}\omega'_x\right) - y\left(\tau'_{xz} + \sigma^0_{zz}\omega'_y\right)\right]dA = \text{const}, \quad (22b)$$

and this constant is again zero since $\tau'_{xz} = \tau'_{yz} = \omega'_x = \omega'_y = 0$ at $z = \ell/(2m)$.

As has already been stated, Eqs. (14) and (16) constitute an eigenvalue problem for ordinary second-order linear differential equations in the r variable, with the applied compressive load P the parameter. This is essentially a standard two-point boundary value problem. The relaxation method was used (Press et al., 1989) which is essentially based on replacing the system of ordinary differential equations by a set of finite difference equations on a grid of points that spans the entire thickness of the shell. For this purpose, an equally spaced mesh of 241 points was employed and the procedure turned out to be highly efficient with rapid convergence. As an initial guess for the iteration process, the shell theory solution was used. An investigation of the convergence showed that essentially the same results were produced with even three times as many mesh points. Finding the critical load involves a minimization step in the sense that the eigenvalue is obtained for different combinations of n, m, and the critical load is the minimum. These results are discussed in the following.

Discussion of Results. Results for the critical compressive load, normalized as

$$\hat{P} = \frac{P}{\pi\left(R_2^2 - R_1^2\right)}\frac{R_2}{E_3 h},$$

were produced for a typical glass/epoxy material with moduli in GN/m^2 and Poisson's ratios listed below, where 1 is the radial (r), 2 is the circumferential (θ), and 3 the axial (z) direction: $E_1 = 14.0$, $E_2 = 57.0$, $E_3 = 14.0$, $G_{12} = 5.7$, $G_{23} = 5.7$, $G_{31} = 5.0$, $\nu_{12} = 0.068$, $\nu_{23} = 0.277$, $\nu_{31} = 0.400$. It has been assumed that the reinforcing direction is along the periphery.

In the shell theory solutions, the radial displacement is constant through the thickness and the axial and circumferential ones have a linear variation, i.e., they are in the form

Table 1 Comparison with shell theories

Orthotropic with circumferential reinforcement, $\ell/R_2 = 5$

Critical Loads, $\tilde{P} = \dfrac{P}{\pi(R_2^2 - R_1^2)} \dfrac{R_2}{E_3 h}$

Moduli in GN/m^2: $E_2 = 57$, $E_1 = E_3 = 14$, $G_{31} = 5.0$, $G_{12} = G_{23} = 5.7$
Poisson's ratios: $\nu_{12} = 0.068$, $\nu_{23} = 0.277$, $\nu_{31} = 0.400$

R_2/R_1	Elasticity (n,m)	Donnell Shell† (n,m) (% Increase)	Timoshenko Shell† (n,m) (% Increase)
1.05	0.6764 (2,1)	0.7904 (4,9) (16.9%)	0.6735 (2,1) (-0.4%)
1.10	0.6641 (2,2)	0.7883 (3,6) (18.7%)	0.6461 (2,2) (-2.7%)
1.15	0.6284 (2,2)	0.7716 (2,3) (22.8%)	0.6218 (2,3) (-1.1%)
1.20	0.6134 (2,3)	0.7505 (2,3) (22.4%)	0.5559 (1,1) (-9.4%)
1.25	0.5186 (1,1)	0.7560 (2,4) (45.8%)	0.4549 (1,1) (-12.3%)
1.30	0.4429 (1,1)	0.7771 (1,1) (75.5%)	0.3876 (1,1) (-12.5%)

† See Appendix II

Table 2 Comparison with shell theories

Isotropic, $E = 14$ GN/m^2, $\nu = 0.3$, $\ell/R_2 = 5$

Critical Loads, $\tilde{P} = \dfrac{P}{\pi(R_2^2 - R_1^2)} \dfrac{R_2}{E_3 h}$

R_2/R_1	Elasticity (n,m)	Donnell† (n,m) % Increase	Timoshenko† (n,m) % Increase	Flügge‡ (n,m) % Increase	Danielson‡ & Simmonds (n,m) % Increase
1.05	0.4426 (2,1)	0.5474 (2,1) 23.7%	0.4348 (2,1) -1.8%	0.4525 (2,1) 2.2%	0.4559 (2,1) 3.0%
1.10	0.3910 (2,1)	0.4871 (2,1) 24.6%	0.3865 (2,1) -1.2%	0.4019 (2,1) 2.8%	0.4088 (2,1) 4.6%
1.15	0.4547 (2,1)	0.5488 (2,2) 20.7%	0.4373 (2,2) -3.8%	0.4710 (2,1) 3.6%	0.4814 (2,1) 5.9%
1.20	0.4371 (2,2)	0.5272 (2,2) 20.6%	0.4184 (2,2) -4.3%	0.4620 (2,2) 5.7%	0.4705 (2,2) 7.6%
1.25	0.4426 (2,2)	0.5403 (2,2) 22.0%	0.4269 (2,2) -3.5%	0.4728 (2,2) 6.8%	0.4837 (2,2) 9.3%
1.30	0.4487 (1,1)	0.5709 (2,2) 27.2%	0.3895 (1,1) -13.2%	0.4915 (1,1) 9.5%	0.4987 (1,1) 11.1%

† See Appendix II
‡ From equations (24).

$$u_1(r, \theta, z) = U_0 \cos n\theta \sin \lambda z,$$

$$v_1(r, \theta, z) = \left[V_0 + \frac{r - R}{R}(V_0 + nU_0)\right] \sin n\theta \sin \lambda z. \quad (23a)$$

$$w_1(r, \theta, z) = \left[W_0 - (r - R)\lambda U_0\right] \cos n\theta \cos \lambda z \quad (23b)$$

where U_0, V_0, W_0 are constants (these displacement field variations would satisfy the classical assumptions of $e_{rr} = e_{r\theta} = e_{rz} = 0$).

A distinct eigenvalue corresponds to each pair of the positive integers m and n. The pair corresponding to the smallest eigenvalue can be determined by trial. It should be noted that for isotropic material, some additional shallowness assumptions lead to the well known direct and simple formula: $P_{cr} = E\pi h^2/\sqrt{3(1 - \nu^2)}$; the performance of this formula with moderate thickness in isotropic shells was discussed in Kardomateas (1993b).

As noted in the Introduction, there are two sets of the Donnell equations that are most widely used for shell theory solutions. The original first set has been referred as the "shallow" shell formulation, whereas, a second, more accurate set of cylindrical shell equations that are not subject to some of the shallowness limitations of the first set has been referred as the "nonshallow" formulation. The latter has been also called the "nonsimplified" Donnel theory in Kardomateas (1993b). The other benchmark shell theory used in this paper is the one described in Timoshenko and Gere (1961). In this theory, an additional term in the circumferential displacement part of the second equation is included. This additional term is the $RN^0_{zv,zz} = -P^0 v_{,zz}/2\pi$ where P^0 is the absolute value of the compressive load at the critical point. In the comparison studies we have used an extension of the original, isotropic Donnell and Timoshenko formulations for the case of orthotropic material. The linear algebraic equations for the eigenvalues of both the Donnell and Timoshenko theories are given in Appendix II.

Concerning the present elasticity formulation, the critical load is obtained by finding the solution P for a range of n and m, and keeping the minimum value. Table 1 shows the critical load and the corresponding n, m, as predicted by the present three-dimensional elasticity formulation, and the critical load and the corresponding n, m, as predicted by both the "nonshallow" Donnell and Timoshenko shell equations. A length ratio $\ell/R_2 = 5$ has been assumed. A range of outside versus inside radius, R_2/R_1 from somewhat thin, 1.05, to thick, 1.30, is examined.

Tables 1 and 2 give the predictions of the Donnell and Timoshenko shell theories for the orthotropic and isotropic material, respectively, in comparison with the elasticity one. It is clearly seen that

(1) the bifurcation points from the Timoshenko formulation are always closer to the elasticity predictions than the ones from the Donnell formulation.

(2) For both the orthotropic material cases and the isotropic one, the Timoshenko bifurcation point for the Donnell shell theory, is always higher than the elasticity solution, which means that the Donnell formulation is nonconservative. Moreover, the Donnell theory becomes in general more nonconservative with thicker construction.

(3) On the contrary, the Timoshenko bifurcation point is *lower* than the elasticity one in all cases considered, i.e., the Timoshenko formulation is actually conservative in predicting stability loss. The degree of conservatism of the Timoshenko theory generally increases for thicker shells.

Furthermore, the bifurcation load for the isotropic case (Table 2) is smaller than the corresponding one for the circumferentially reinforced orthotropic case (Table 1), the difference becoming increasingly smaller for thicker construction. This conclusion is true for either the elasticity or the shell theory results (with one exception: for $R_2/R_1 = 1.30$ the Timoshenko prediction is larger for the isotropic case by 1.3 percent). More specifically, based on the elasticity solution, for $R_2/R_1 = 1.10$, the orthotropic case shows a 70 percent higher bifurcation load than the isotropic material, whereas for $R_2/R_1 = 1.25$, the orthotropic material shows only a 17 percent higher bifurcation load than the isotropic case. Therefore, the effect of the circumferential reinforcement in raising the critical load relative to the isotropic case is diminished with thicker construction.

For isotropic materials, two other shell theories, namely the Flügge (1960) and the Danielson and Simmonds (1969) can easily produce results for the critical loads in shells and should, therefore, be compared with the present elasticity

solution. The expression for the eigenvalues derived from the Flügge (1960) equations, P_F^0 and the more simplified but just as accurate one by Danielson and Simmonds (1969), P_{DS}^0 are

$$P_{\{F,DS\}}^0 = E\frac{Q_{F,DS}}{\tilde{m}^2\left[\left(\tilde{m}^2+n^2\right)^2+n^2\right]}, \qquad (24a)$$

where the numerator for the Flügge theory is

$$Q_F = \frac{\pi h^3}{6R(1-\nu^2)}\left\{\left(\tilde{m}^2+n^2\right)^4 - 2\left[\nu\tilde{m}^2 + 3\tilde{m}^4n^2 + (4-\nu)\tilde{m}^2n^4 + n^6\right] + 2(2-\nu)\tilde{m}^2n^2 + n^4\right\} + \tilde{m}^4, \qquad (24b)$$

and for the Danielson and Simmonds equations,

$$Q_{DS} = \frac{\pi h^3}{6R(1-\nu^2)}\left(\tilde{m}^2+n^2\right)^2\left(\tilde{m}^2+n^2-1\right)^2 + \tilde{m}^4, \qquad (24c)$$

where R is the mean radius and h the shell thickness Again, a distinct eigenvalue corresponds to each pair of the positive integers m and n, the critical load being for the pair that renders the lowest eigenvalue.

A comparison of the data in Table 2 shows that the values of n, m at the critical point for the elasticity, as well as the

Table 3 Comparison with shell theories

Orthotropic with axial reinforcement, $\ell/R_2 = 5$

Critical Loads, $\tilde{P} = \dfrac{P}{\pi(R_2^2 - R_1^2)}\dfrac{R_2}{E_2h}$

Moduli in GN/m^2: $E_3 = 57$, $E_2 = E_1 = 14$, $G_{31} = G_{23} = 5.7$, $G_{12} = 5.0$
Poisson's ratios: $\nu_{12} = 0.400$, $\nu_{23} = 0.068$, $\nu_{31} = 0.277$

R_2/R_1	Elasticity (n,m)	Donnell Shell† (n,m) % Increase	Timoshenko Shell† (n,m) % Increase
1.05	0.7666 (4,4)	0.7913 (4,4) (3.2%)	0.7517 (4,4) (-1.9%)
1.10	0.6794 (2,1)	0.7879 (3,3) (16.0%)	0.6473 (2,1) (-4.7%)
1.15	0.6575 (2,1)	0.7877 (2,1) (19.8%)	0.6287 (2,1) (-4.4%)
1.20	0.6686 (2,2)	0.7547 (2,2) (12.9%)	0.6157 (2,2) (-7.9%)
1.25	0.6646 (2,2)	0.7563 (2,2) (13.8%)	0.6140 (2,2) (-7.6%)
1.30	0.6801 (2,2)	0.7823 (2,2) (15.0%)	0.6319 (2,2) (-7.1%)

† See Appendix II

Table 4 Results for thin shells

Critical Loads, $\tilde{P} = \dfrac{P}{\pi(R_2^2 - R_1^2)}\dfrac{R_2}{E_3h}$

1. Orthotropic with circumferential reinforcement

R_2/R_1	Elasticity (n,m)	Donnell Shell† (n,m) (% Increase)	Timoshenko Shell† (n,m) (% Increase)
1.04	0.6872 (2,1)	0.8049 (4,8) (17.1%)	0.6811 (2,1) (-0.9%)
1.02	0.7822 (6,13)	0.7957 (6,13) (1.7%)	0.7786 (6,13) (-0.5%)
1.01	0.7904 (9,20)	0.7971 (9,20) (0.9%)	0.7895 (9,20) (-0.1%)

2. Isotropic

R_2/R_1	Elasticity (n,m)	Donnell† (n,m) % Increase	Timoshenko† (n,m) % Increase	Flügge‡ (n,m) % Increase	Danielson‡ & Simmonds (n,m) % Increase
1.04	0.5034 (2,1)	0.5723 (3,2) 13.7%	0.4940 (2,1) -1.8%	0.5143 (2,1) 2.2%	0.5170 (2,1) 2.7%
1.02	0.4999 (3,1)	0.5548 (3,1) 11.0%	0.4983 (3,1) -0.3%	0.5033 (3,1) 0.7%	0.5052 (3,1) 1.1%
1.01	0.5517 (3,1)	0.5977 (7,5) 8.3%	0.5493 (3,1) -0.4%	0.5549 (3,1) 0.6%	0.5559 (3,1) 0.8%

† See Appendix II
‡ From equations (24).

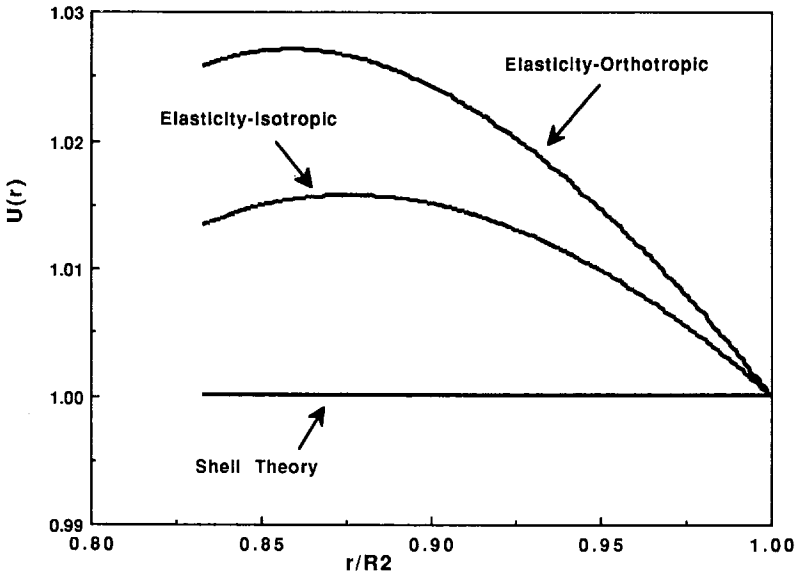

Fig. 2(a) "Eigenfunction" $U(r)$ versus normalized radial distance r/R_2, for the orthotropic with circumferential reinforcing direction case and the isotropic one (shell theory would have a constant value throughout, $U(r) = 1$ for both cases)

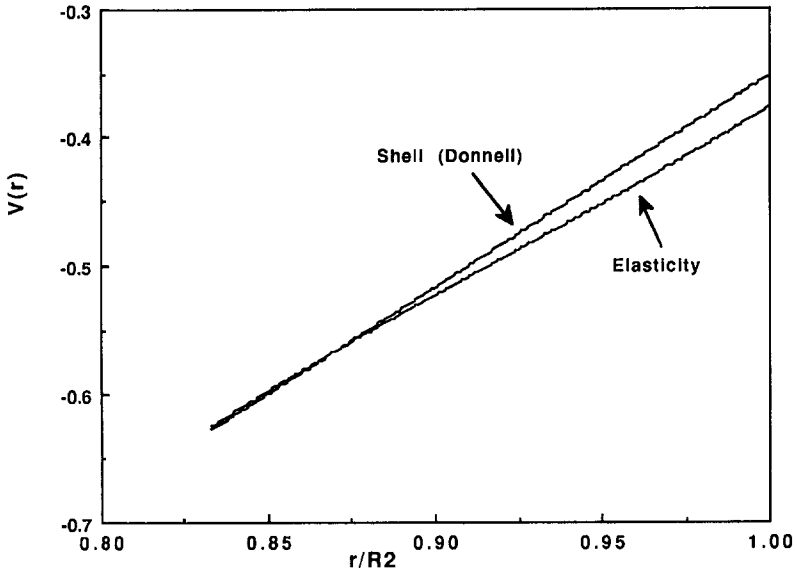

Fig. 2(*b*) "Eigenfunction" $V(r)$ versus normalized radial distance r/R_2 from the elasticity solution and the Donnell shell theory, which would show linear variation. The results are for the orthotropic with circumferential reinforcing direction case.

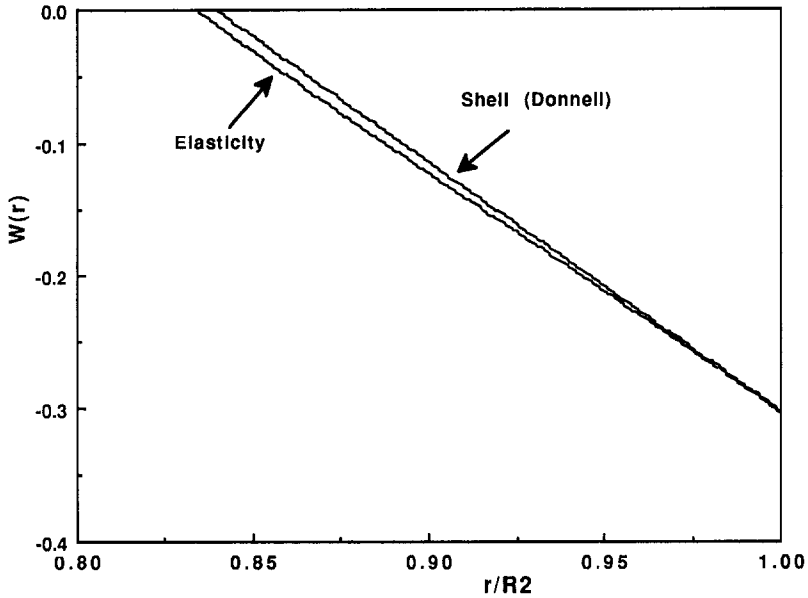

Fig. 2(*c*) "Eigenfunction" $W(r)$ versus normalized radial distance r/R_2, from the elasticity solution and the Donnell shell theory (the latter has a linear variation). The results are for the orthotropic with circumferential reinforcing direction case.

Flügge and the Danielson and Simmonds theories show perfect agreement, and that both Flügge, and the Danielson and Simmonds theories are nonconservative, the degree of nonconservatism increasing with thicker shells. We may now rank these theories for isotropic materials by concluding that the best estimates are provided by the Timoshenko theory, followed by the Flügge and the Danielson and Simmonds theories and finally the Donnell theory. Of these, only the Timoshenko theory is conservative.

Table 3 presents the results for the bifurcation load in the case of the same orthotropic material (typical of glass/epoxy), which is now positioned so that the reinforcement is axial. To be able to perform direct comparisons, the load has now been normalized with E_2, which is the same as E_3 in the other two cases (Tables 1, 2). It can be seen that the bifurcation load now is in general higher than both the isotropic and the orthotropic with circumferential reinforcement cases. Again, based on the elasticity solution, for $R_2/R_1 = 1.10$, the axially reinforced case shows a 74 percent higher bifurcation load than the isotropic material, whereas for $R_2/R_1 = 1.25$, the axially reinforced material shows a 49 percent higher bifurcation load than the isotropic case. Therefore, the effect of the axial reinforcement in raising the critical load relative to the isotropic case is much less sensitive to the thickness than with circumferential reinforcement. Another interesting observation is that in all cases, n, m at the critical load for the elasticity theory are always less or equal to the corresponding values of the Donnell shell theory.

It should also be mentioned that the elasticity results of Table 2 for isotropic material that were produced through the present formulation, confirm the results from the closed-form analytical isotropic solution of Kardomateas (1993b). Moreover, this work complements the latter by including a comparison with the Timoshenko and Gere shell theory,

which is actually found to be the only shell theory that results in conservative estimates of the critical load.

Although the focus of this work is the study of moderately thick shells, one would expect buckling to be even more important for very thin shell construction. Therefore, Table 4 shows the bifurcation load from the three-dimensional elasticity analysis for thin shells in order of decreasing thickness (thickness over mean radius, h/R, up to 1/100), in comparison with these shell theories. The results are for the mildly orthotropic glass/epoxy material, as well as the isotropic case. In all cases, it is seen that the Timoshenko theory renders conservative estimates for the critical load, and it is again much more closer to the elasticity prediction than the Donnell theory. Moreover, the values of (n, m) at the critical point for both the elasticity and the Timoshenko theory agree perfectly for the thin shells of Table 4, unlike the Donnell theory. For the isotropic material, the Flügge and Danielson and Simmonds theories have also been examined and are shown to provide much better (although nonconservative) estimates than the Donnell theory, with perfect agreement with the elasticity results on the values of (n, m) at the critical point.

Finally, to obtain more insight into the displacement field, Figs. 2(a,b,c) show the variation of $U(r)$, $V(r)$, and $W(r)$, which define the eigenfunctions, for $R_2/R_1 = 1.2$, as derived from the present elasticity solution, and in comparison with the Donnell shell theory assumptions of constant $U(r)$, and linear $V(r)$ and $W(r)$. These values have been normalized by assigning a unit value for U at the outside boundary $r = R_2$. These plots illustrate graphically the deviation of U from constant and the deviation of V and W from linearity. Although the Donnell shell theory eigenfunction has been plotted for $V(r)$ and $W(r)$, the Timoshenko theory line would nearly coincide with the latter.

Acknowledgment

The financial support of the Office of Naval Research, Mechanics Division, Grant N00014-91-J-1892, and the interest and encouragement of the Grant Monitor, Dr. Y. Rajapakse, are both gratefully acknowledged.

References

Bradford, L. G., and Dong, S. B., 1978, "Natural Vibrations of Orthotropic Cylinders Under Initial Stress," *Journal of Sound and Vibration*, Vol. 60, No. 2, pp. 157–175.

Brush, D. O., and Almroth, B. O., 1975, *Buckling of Bars, Plates, and Shells*, McGraw-Hill, New York.

Danielson, D. A., and Simmonds, J. G., 1969, "Accurate Buckling Equations for Arbitrary and Cylindrical Elastic Shells," *Int. J. Eng. Sci.*, Vol. 7, pp. 459–468.

Dong, S. B., 1994, discussion of the two papers by Kardomateas (1993a,b), ASME JOURNAL OF APPLIED MECHANICS, Vol. 61, p. 225.

Donnell, L. H., 1933, "Stability of Thin-Walled Tubes Under Torsion," NACA Rep. 479.

Flügge, W., 1960, *Stresses in Shells*, Springer, Berlin, pp. 426–432.

Kardomateas, G. A., 1993a, "Buckling of Thick Orthotropic Cylindrical Shells Under External Pressure," ASME JOURNAL OF APPLIED MECHANICS, Vol. 60, pp. 195–202.

Kardomateas, G. A., 1993b, "Stability Loss in Thick Transversely Isotropic Cylindrical Shells Under Axial Compression," ASME JOURNAL OF APPLIED MECHANICS, Vol. 60, pp. 506–513.

Kollár, L. P., 1994, "Three Dimensional Analysis of Composite Cylinders Under Axially Varying Hygrothermal and Mechanical Loads," *Computers and Structures*, Vol. 17, No. 50-4, pp. 525–540.

Lekhnitskii, S. G., 1963, *Theory of Elasticity of an Anisotropic Elastic Body*, Holden Day, San Francisco; also Mir Publishers, Moscow, 1981.

Librescu, L., 1975, *Elastostatics and Kinetics of Anisotropic and Heterogeneous Shell-Type Structures*, Nordhoff International, Leyden.

Noor, A. K., and Burton, W. S., 1990, "Assessment of Computational Models for Multilayered Composite Shells," ASME *Appl. Mech. Rev.*, Vol. 43, No. 4, pp. 67–97.

Press, W. H., Flannery, B. P., Teukolsky, S. A., and Vetterling, W. T., 1989, *Numerical Recipes*, Cambridge University Press, Cambridge, U.K.

Reddy, J. N., and Liu, C. F., 1985, "A Higher-Order Shear Deformation Theory of Laminated Elastic Shells," *Int. J. Eng. Sci.*, Vol. 23, No. 3, pp. 319–330.

Simitses, G. J., Shaw, D., and Sheinman, I., 1985, "Stability of Cylindrical Shells by Various Nonlinear Shell Theories," *ZAMM, Z. Angew. Math. u. Mech.*, Vol. 65, No. 3, pp. 159–166.

Timoshenko, S. P., and Gere, J. M., 1961, *Theory of Elastic Stability*, McGraw-Hill, New York.

Whitney, J. M., and Sun, C. T., 1974, "A Refined Theory for Laminated Anisotropic Cylindrical Shells," ASME JOURNAL OF APPLIED MECHANICS, Vol. 41, No. 2, pp. 471–476.

APPENDIX I

For convenience define

$$D_0 = -\frac{1}{\hat{T}} - C_0\frac{a_{13} + a_{23}}{a_{33}}, \tag{A1}$$

$$D_1 = -C_1\frac{a_{13} + ka_{23}}{a_{33}}; \quad D_2 = -C_2\frac{a_{13} - ka_{23}}{a_{33}}. \tag{A2}$$

The coefficients of the first differential Eq. (14a) are

$$b_{00} = -(c_{22} + c_{66}n^2); \quad b_{01} = -n^2C_0/2.0;$$
$$b_{02} = -C_1kn^2/2; \quad b_{03} = C_2kn^2/2;$$
$$b_{04} = -c_{55}\lambda^2; \quad b_{05} = -D_0\lambda^2/2;$$
$$b_{06} = -D_1\lambda^2/2; \quad b_{07} = -D_2\lambda^2/2, \tag{A3}$$

$$d_{10} = n(c_{12} + c_{66}); \quad d_{11} = -nC_0/2; \quad d_{12} = -nkC_1/2;$$
$$d_{13} = nkC_2/2; \quad d_{00} = -n(c_{22} + c_{66}); \quad d_{01} = -nC_0/2;$$
$$d_{02} = -nkC_1/2; \quad d_{03} = nkC_2/2, \tag{A4}$$

$$f_{10} = -\lambda(c_{13} + c_{55}); \quad f_{11} = \lambda D_0/2; \quad f_{12} = \lambda D_1/2;$$
$$f_{13} = \lambda D_2/2; \quad f_{00} = \lambda(c_{23} - c_{13}); \quad f_{01} = f_{02} = f_{03} = 0. \tag{A5}$$

The coefficients of the second differential Eq. (14b) are given as follows:

$$g_{20} = c_{66}; \quad g_{21} = C_0/2; \quad g_{22} = C_1/2; \quad g_{23} = C_2/2$$
$$g_{10} = c_{66}; \quad g_{11} = C_0/2; \quad g_{12} = C_1/2; \quad g_{13} = C_2/2$$
$$g_{00} = -(c_{22}n^2 + c_{66}); \quad g_{01} = -C_0/2; \quad g_{02} = -C_1/2;$$
$$g_{03} = -C_2/2; \quad g_{04} = -c_{44}\lambda^2; \quad g_{05} = -D_0\lambda^2/2;$$
$$g_{06} = -D_1\lambda^2/2; \quad g_{07} = -D_2\lambda^2/2, \tag{A6}$$

$$h_{10} = -(c_{66} + c_{12})n; \quad h_{11} = nC_0/2; \quad h_{12} = nC_1/2;$$
$$h_{13} = nC_2/2; \quad h_{00} = -(c_{22} + c_{66})n; \quad h_{01} = -nC_0/2;$$
$$h_{02} = -nC_1/2; \quad h_{03} = -nC_2/2, \tag{A7}$$

$$t_{00} = (c_{23} + c_{44})n\lambda; \quad t_{01} = -n\lambda D_0/2;$$
$$t_{02} = -n\lambda D_1/2; \quad t_{03} = -n\lambda D_2/2. \tag{A8}$$

Finally, the coefficients of the third differential Eq. (14c) are

$$q_{20} = c_{55}; \quad q_{21} = C_0/2; \quad q_{22} = C_1/2; \quad q_{23} = C_2/2$$
$$q_{10} = c_{55}; \quad q_{11} = C_0/2; \quad q_{12} = kC_1/2; \quad q_{13} = -kC_2/2$$
$$q_{00} = -c_{44}n^2; \quad q_{01} = -C_0n^2/2; \quad q_{02} = -kn^2C_1/2;$$
$$q_{03} = kn^2C_2/2; \quad q_{04} = -c_{33}\lambda^2, \tag{A9}$$

$$s_{10} = (c_{55} + c_{13})\lambda; \quad s_{11} = -\lambda C_0/2; \quad s_{12} = -\lambda C_1/2;$$
$$s_{13} = -\lambda C_2/2; \quad s_{00} = (c_{23} + c_{55})\lambda; \quad s_{01} = -\lambda C_0/2;$$
$$s_{02} = -k\lambda C_1/2; \quad s_{03} = k\lambda C_2/2, \tag{A10}$$

$$\beta_{00} = (c_{23} + c_{44})n\lambda; \quad \beta_{01} = -n\lambda C_0/2;$$
$$\beta_{02} = -kn\lambda C_1/2; \quad \beta_{03} = kn\lambda C_2/2. \qquad \text{(A11)}$$

APPENDIX II

Eigenvalues From Nonshallow Donnell and Timoshenko Shell Theories

In the shell theory formulation, the displacements are in the form

$$u_1 = U_0 \cos n\theta \sin \lambda z, \quad v_1 = V_0 \sin n\theta \sin \lambda z,$$
$$w_1 = W_0 \cos n\theta \cos \lambda z,$$

where U_0, V_0, W_0 are constants.

The equations for the nonshallow (or nonsimplified) Donnell shell theory for $N_\theta^0 = N_{z\theta}^0 = 0$, $N_z^0 = -P^0/(2\pi R)$ are (Brush and Almroth, 1975)

$$RN_{z,z} + N_{z\theta,\theta} = 0$$
$$RN_{z\theta,z} + N_{\theta,\theta} + \frac{M_{\theta,\theta}}{R} + M_{z\theta,z} = 0$$
$$N_\theta - RN_z^0 u_{,zz} - RM_{z,zz} - \frac{M_{\theta,\theta\theta}}{R} - 2M_{z\theta,z\theta} = 0.$$

The Timoshenko shell theory has the additional term $RN_z^0 v_{,zz}$ in the second equation. We have denoted by R the mean shell radius and by P^0 the absolute value of the compressive load.

In terms of the "equivalent property" constants

$$C_{22} = E_2 h/(1 - \nu_{23}\nu_{32}); \quad C_{33} = E_3 h/(1 - \nu_{23}\nu_{32})$$
$$C_{23} = \frac{E_3 \nu_{23} h}{1 - \nu_{23}\nu_{32}}; \quad C_{44} = G_{23} h, \quad D_{ij} = C_{ij}\frac{h^2}{12},$$

the coefficient terms in the homogeneous equations system that gives the eigenvalues are

$$\alpha_{11} = C_{23}\lambda; \quad \alpha_{12} = (C_{23} + C_{44})n\lambda;$$
$$\alpha_{13} = -\left(C_{33}R\lambda^2 + C_{44}n^2/R\right),$$
$$\alpha_{21} = -\left(\frac{C_{22}}{R} + \frac{D_{22}n^2}{R^3} + \frac{D_{23}\lambda^2}{R} + 2\frac{D_{44}\lambda^2}{R}\right)n,$$
$$\alpha_{22} = -\left(\frac{C_{22}n^2}{R} + C_{44}R\lambda^2 + \frac{D_{22}n^2}{R^3} + 2\frac{D_{44}\lambda^2}{R}\right),$$
$$\alpha_{23} = (C_{23} + C_{44})n\lambda,$$
$$\alpha_{31} = \frac{C_{22}}{R} + \frac{D_{22}n^4}{R^3} + 2\frac{D_{23}\lambda^2 n^2}{R} + D_{33}\lambda^4 R + 4\frac{D_{44}\lambda^2 n^2}{R},$$
$$\alpha_{32} = \left(\frac{C_{22}}{R} + \frac{D_{22}n^2}{R^3} + \frac{D_{23}\lambda^2}{R} + 4\frac{D_{44}\lambda^2}{R}\right)n,$$
$$\alpha_{33} = -C_{23}\lambda.$$

Notice that in the above formulas we have used the curvature expression $\kappa_{z\theta} = (v_{,z} - u_{,z\theta})/R$ for both theories.

Then the linear homogeneous equations system that gives the eigenvalues for the Timoshenko shell formulation is

$$\alpha_{11}U_0 + \alpha_{12}V_0 + \alpha_{13}W_0 = 0, \qquad \text{(B1)}$$
$$\alpha_{21}U_0 + \left(\alpha_{22} + \frac{\lambda^2}{2\pi}P^0\right)V_0 + \alpha_{23}W_0 = 0, \qquad \text{(B2)}$$
$$\left(\alpha_{31} - \frac{\lambda^2}{2\pi}P^0\right)U_0 + \alpha_{32}V_0 + \alpha_{33}W_0 = 0. \qquad \text{(B3)}$$

For the Donnell shell formulation, the additional term in the coefficient of V_0 in (B2) is omitted, i.e., the coefficient of V_0 is only α_{22}. The eigenvalues are naturally found by equating to zero the determinant of the coefficients of U_0, V_0, and W_0.

Yutaka Arimitsu
Associate Professor,
Department of Mechanical Engineering,
Ehime University,
3 Bunkyocho, Matsuyama,
790 Japan

Kazumi Nishioka
Professor,
Department of Mechanical Engineering,
The University of Tokushima,
2-1 Minamijosanjima,
Tokushima, 770 Japan

Toyomitsu Senda
Department of Mechanical Engineering,
Ehime University,
3 Bunkyocho, Matsuyama,
790 Japan

A Study of Saint-Venant's Principle for Composite Materials by Means of Internal Stress Fields

It is well known that end effects in a composite material do not always decay as they do in a homogeneous and isotropic material, but there is no unified explanation for this difference. We note that the stress field in a composite material can be resolved into two kinds: one is the stress distribution in an isotropic and homogeneous reference system where Saint-Venant's principle is satisfied and the other is the internal stress field induced by the incompatibility. Considering that the incompatibility is proportional to the difference between the elastic compliances of the components or to the deviation from isotropy, we propose, based on an argument concerning the dislocations associated with the incompatibility, a reason why end effects may survive to a long distance in a composite material.

1 Introduction

Saint-Venant's principle (de Saint-Venant, 1855) for an isotropic and homogeneous material is well understood. However, it has been pointed out by Horgan (1972 a, b), Choi and Horgan (1977, 1978), and Horgan (1982) that end effects for an anisotropic or inhomogeneous material survive to a long distance from the end. This becomes important in the design or testing of structural composite materials, though it is often neglected tacitly in the analysis through the employment of simplified boundary conditions.

For a comprehensive survey on Saint-Venant's principle, we refer to the review articles by Horgan and Knowles (1983) and Horgan (1989). The early work of Zanaboni (1937) and Goodier (1937) formulated the principle using strain energy, and von Mises (1945) and Sternberg (1954) gave another formulation (see Fung (1965) for a survey). Motivated by the results of Horgan (1972 a, b), Choi and Horgan (1977) investigated Saint-Venant's principle for *plane anisotropic elasticity* and semianalytically evaluated the decay of self-equilibrated eigenfunctions. A similar analysis for sandwich strips was carried out by Choi and Horgan (1978). In these papers, the *slow decay* of end effects due to anisotropy and inhomogeneity was established. Saint-Venant's principle for composite materials has been discussed by Horgan (1982) for plane problems for anisotropic and laminated materials and for cylindrical rods, and by Dong and Goetschel (1982) and Okumura et al. (1985) for laminated materials. See Horgan (1989) for a discussion of how the foregoing results for anisotropic and composite materials play fundamental roles in the mechanics of composite materials.

In the previous papers, the authors proposed the method of superposing the stress field of a reference isotropic system and the associated internal stress field in obtaining the stress field for an inhomogeneous elastic body (Nishioka et al., 1987) or for an anisotropic one (Arimitsu et al., 1994). In this paper, we apply the method to a study of Saint-Venant's principle for a composite material. Accepting Saint-Venant's principle for a homogeneous and isotropic material, we propose an interpretation for the reason why end effects in a composite material decay slowly.

2 Saint-Venant's Principle for Homogeneous and Isotropic Materials

We first illustrate Saint-Venant's principle for plane deformations of a homogeneous and isotropic material by using a finite element method (FEM). The dimensions of the specimen are 100 mm × 10 mm in size and the domain (50 mm × 10 mm) is divided into 5364 elements with 2707 nodal points (triangular isoparametric element). Since the stress profile given in this paper is normalized by the maximum of σ_{11}, where x_1 is taken as shown in Fig. 1, the stress profile in plane stress becomes identical with that in plane strain. The effect of a self-equilibrating load acting on the end of a strip decreases to about one percent at a distance equal to the width of a strip as shown in Fig. 1. From Fig. 1(*a*) and (*b*), we see that this tendency is almost independent of the distribution of the self-equilibrating load. A similar demonstration using eigenfunction expansions was provided by Choi and

Contributed by the Applied Mechanics Division of THE AMERICAN SOCIETY OF MECHANICAL ENGINEERS for publication in the ASME JOURNAL OF APPLIED MECHANICS.

Discussion on this paper should be addressed to the Technical Editor, Professor Lewis T. Wheeler, Department of Mechanical Engineering, University of Houston, Houston, TX 77204-4792, and will be accepted until four months after final publication of the paper itself in the ASME JOURNAL OF APPLIED MECHANICS.

Manuscript received by the ASME Applied Mechanics Division, Dec. 11, 1992; final revision, Aug. 16, 1993. Associate Technical Editor: G. J. Dvorak.

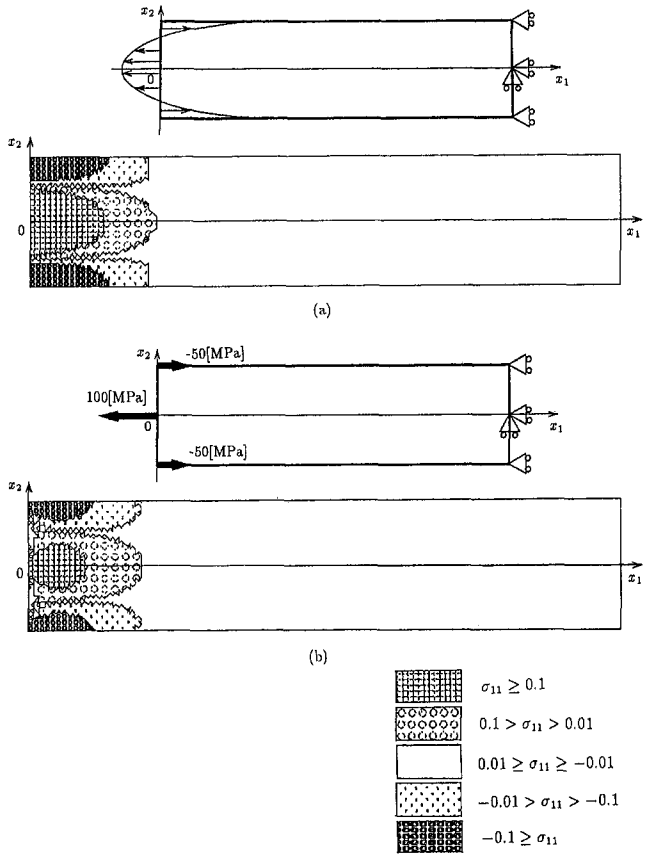

Fig. 1 Stress profile σ_{11} under self-equilibrating load; (a) $P_1(x_2) = -3x_2^2 + 25$ [MPa], (b) $P_1(\pm 5) = -50$ [MPa], $P_1(0) = 100$ [MPa], $P_1 = 0$ [MPa] on $x_2 \neq \pm 5$, $x_2 \neq 0$

Horgan (1977) (see Figs. 2, 3 in that reference). Other finite element studies are cited in Horgan (1989).

For an analytical approach to Saint-Venant's principle, Timoshenko and Goodier (1970) introduced the following Airy stress function:

$$\phi = C\exp\left(\frac{-\gamma x_1}{c}\right)\left(\kappa \cos\frac{\gamma x_2}{c} + \frac{\gamma x_2}{c}\sin\frac{\gamma x_2}{c}\right), \quad (1)$$

where C, γ, and κ denote arbitrary constants, $2c$ the width of a strip. This stress function must satisfy the following boundary conditions:

$$\sigma_{22} = 0, \quad \sigma_{12} = 0 \quad \text{on } x_2 = \pm c. \quad (2)$$

Boundary condition at the ends perpendicular to the x_1-axis is assumed to be an even function of x_2, and the arbitrary constants γ and κ are complex numbers. The value of γ with the smallest positive real part (the lowest decay rate) is

$$\gamma = 2.1061 + 1.1254i. \quad (3)$$

The decay rate from the end of a strip is determined by the real part of γ, and it agrees with the numerical results in that end effects decrease to about one percent at the distance equal to $2c$ from the edge. Since any self-equilibrating load can be expressed with the series of eigenfunctions (1) (see the discussion of pp. 231–232 of Horgan and Knowles (1983)), we see that the decay rate is independent of the distribution of the self-equilibrating load and agrees with the numerical results shown in Fig. 1(*a*) and (*b*). Consequently, when we discuss the decay rate from the end of a strip, we can employ the stress function expressed in Eq. (1) or the exponential factor $\exp(-2.1061x_1/c)$ to represent end effects in the homogeneous and isotropic body. This will be referred to later as the reference system.

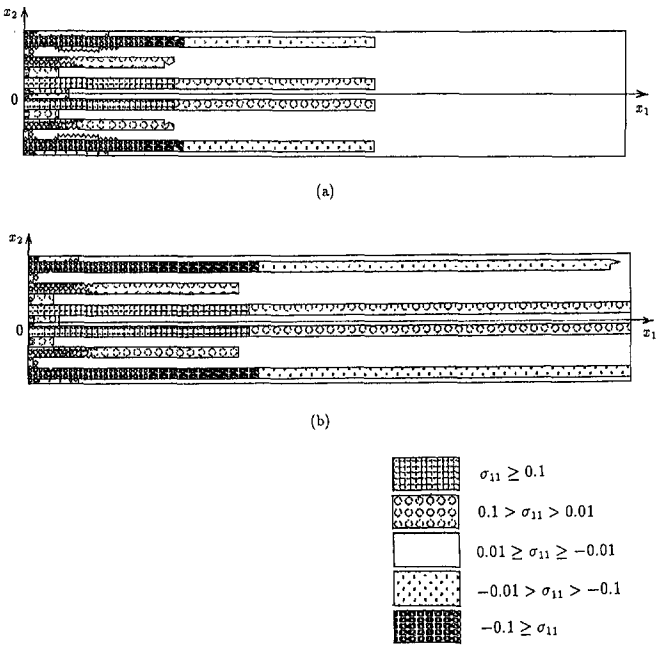

Fig. 2 Stress profile of σ_{11} in longitudinally fiber-reinforced composite; (a) GFRP (epoxy: $E_m = 2.93$ [GPa], $\nu = 0.3$, glass fiber: $E_f = 73.5$ [GPa]), (b) CFRP (epoxy: $E_m = 2.93$ [GPa], $\nu = 0.3$, carbon fiber: $E_f = 196$ [GPa])

3 Saint-Venant's Principle for Composite Materials

Directionally fiber-reinforced composite materials can be considered either microscopically inhomogeneous elastic bodies consisting of isotropic components or macroscopically homogeneous anisotropic elastic bodies. The fibers may further be anisotropic and the following considerations can be extended to such a case. Let us consider those two viewpoints separately in the following with the same idea of employing a reference isotropic system and the associated internal stress field induced by the incompatibility.

3.1 Inhomogeneity. Using a FEM similar to that used in Fig. 1, we show numerical results for the hypothetical glass/epoxy (Fig. 2(*a*)) and carbon/epoxy (Fig. 2(*b*)) inhomogeneous materials containing six longitudinal fibers (volume fraction: 50 percent). We assume continuity of displacements at interfaces between fiber and matrix. In Fig. 2, E and ν denote Young's modulus and Poisson's ratio, respectively. The subscripts m and f distinguish the matrix and the fiber. In the numerical calculation, we employ $P_1(x_2) = -3x_2^2 + 25$ [MPa] (corresponding to Fig. 1(*a*)) as a self-equilibrating load in order to compare the result with that by Okumura et al. (1982). We notice that the end effects are transmitted along the fibers and that this tendency becomes more pronounced as the difference between the elastic constants of the component materials increases. A similar result was found by Choi and Horgan (1978) for a sandwich strip.

To interpret the above results, let us consider a bimaterial consisting of isotropic component materials as shown in Fig. 3, and introduce the internal stress field as follows (Nishioka et al., 1987):

1 Introduce two homogeneous and isotropic reference systems represented in Fig. 3, and let them be subjected to the same boundary condition as the real system. In these reference systems, end effects decay in accordance with Saint-Venant's principle.

2 Cutting along the hypothetical boundaries of the reference systems with the reference deformations unchanged, two of the segments corresponding to the real system are connected at the boundary. In general, neither the continuity

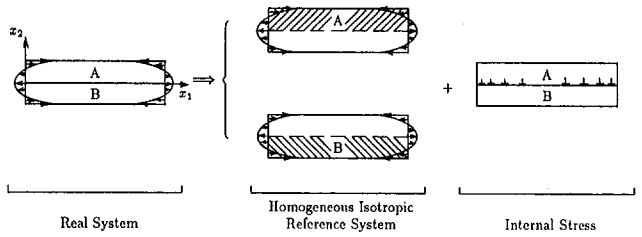

Fig. 3 Reference system and the internal stress for an inhomogeneous body

of displacement nor the action-reaction relation for the stress vector is satisfied at the boundary.

3 We must distribute a body force to nullify the traction incompatibility and a surface dislocation to cancel the incompatibility of displacement. The internal stress field is then induced due to the body force and the surface dislocation distributed along the boundary. However, it is difficult to actually get the internal stress field analytically in an inhomogenous body.

Since the stress distribution for isotropic two-dimensional problems under a given traction boundary condition is independent of the elastic constants, the traction incompatibility in this case does not arise and only the displacement incompatibility arises along the interphase boundary. The relation between the strain field ε_{kl}^A for the reference system A shown in Fig. 3 and the stress field σ_{ij} is written by

$$\varepsilon_{kl}^A = S_{klij}^A \sigma_{ij}, \tag{4}$$

where S_{klij}^A denotes the elastic compliance (tensor notation by Nye (1967)) for the reference system A and the Einstein summation convention is employed. We get also the relation for the reference system B, which is similar to Eq. (4).

Applying Eq. (4) to the isotropic reference system, the displacement component u_i^A for the reference system A satisfies the following relations:

$$u_{1,1}^A = S_{11}^A \phi_{,22} + S_{12}^A \phi_{,11}, \tag{5}$$

$$u_{2,2}^A = S_{12}^A \phi_{,22} + S_{11}^A \phi_{,11}, \tag{6}$$

$$\left(u_{1,2}^A + u_{2,1}^A\right) = -2\left(S_{11}^A - S_{12}^A\right)\phi_{,12}, \tag{7}$$

where ϕ and the symbol $,i$ denote the stress function and the operator $\partial/\partial x_i$ and we have rewritten the elastic compliance for isotropic body into that with the matrix notation, S_{11}^A, etc.

Upon integrating Eqs. (5) and (6), u_i^A becomes as follows:

$$u_1^A = S_{11}^A \int \phi_{,22} dx_1 + S_{12}^A \phi_{,1} + f_1^A(x_2), \tag{8}$$

$$u_2^A = S_{12}^A \phi_{,2} + S_{11}^A \int \phi_{,11} dx_2 + f_2^A(x_1) \tag{9}$$

where $f_1^A(x_2)$ and $f_2^A(x_1)$ are arbitrary functions. Upon substituting Eqs. (8) and (9) into Eq. (7), we get the following relation:

$$S_{11}^A\left[\int \phi_{,222} dx_1 + \int \phi_{,111} dx_2 + 2\phi_{,12}\right] + f_1^A(x_2)_{,2} + f_2^A(x_1)_{,1} = 0. \tag{10}$$

Taking account of $\nabla^2\nabla^2\phi = 0$ and Eq. (10), the arbitrary functions $f_1^A(x_2)$ and $f_2^A(x_1)$ should be linear functions which represent the rigid translation and rotation of the reference system A.

Subtracting the displacement for the reference system B from Eqs. (8) and (9), we can get the incompatibility of

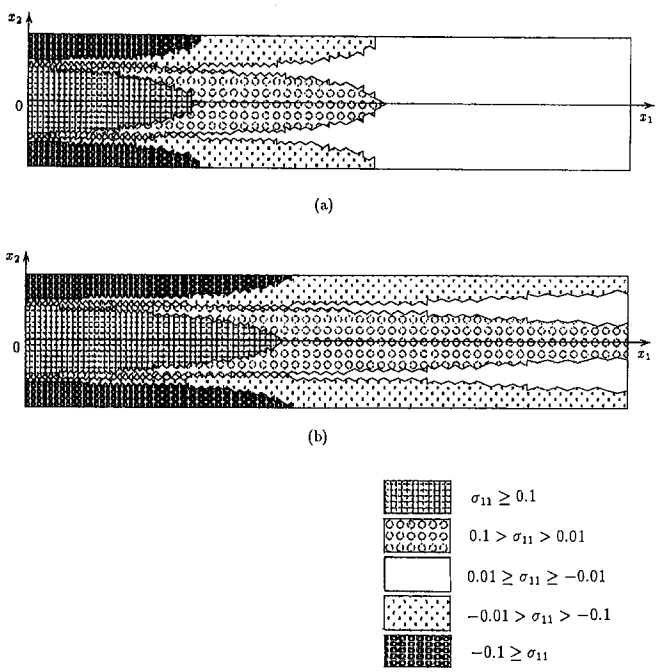

Fig. 4 Stress profile of σ_{11} in longitudinally fiber-reinforced composite; (a) GFRP, (b) CFRP

displacement $\delta u_i(x_1)$ on $x_2 = a$ (interphase boundary) as follows:

$$\delta u_1 \mid_{x_2=a} = \left(S_{11}^A - S_{11}^B\right)\int \phi_{,22} dx_1 \mid_{x_2=a} + \left(S_{12}^A - S_{12}^B\right)\int \phi_{,11} dx_1 \mid_{x_2=a}, \tag{11}$$

$$\delta u_2 \mid_{x_2=a} = \left(S_{12}^A - S_{12}^B\right)\int \phi_{,22} dx_1 \mid_{x_2=a} + \left(S_{11}^A - S_{11}^B\right)\int \phi_{,11} dx_2 \mid_{x_2=a}. \tag{12}$$

When we fix the datum point in connecting the reference deformation, we can set the rigid translation and rotation to be equal to zero (Nishioka et al., 1987).

Since the surface dislocation density α_{ij} to cancel the displacement incompatibility on the $x_i x_k$-plane is defined by the following:

$$\alpha_{ij} = \delta u_{j,k}, \tag{13}$$

we obtain

$$\alpha_{31} \mid_{x_2=a} = \left(S_{11}^A - S_{11}^B\right)\phi_{,22} \mid_{x_2=a} + \left(S_{12}^A - S_{12}^B\right)\phi_{,11} \mid_{x_2=a}, \tag{14}$$

$$\alpha_{32} \mid_{x_2=a} = \left(S_{12}^A - S_{12}^B\right)\phi_{,12} \mid_{x_2=a} + \left(S_{11}^A - S_{11}^B\right)\int \phi_{,111} dx_2 \mid_{x_2=a}, \tag{15}$$

where we employ the dislocation density and the direction of the Burgers vector defined by Mura (1982). The direction of dislocation line, the x_3-axis, is perpendicular to the x_1x_2-plane. From Eqs. (14) and (15) where we can choose ϕ expressed in Eq. (1), we see that the dislocation density is proportional to the difference of elastic compliances of the components. From the considerations to be given in Section 4, end effects decay more slowly as the difference between the elastic compliances of the component materials increases, though it is difficult to evaluate analytically the internal stress field from the density of surface dislocations.

3.2 Anisotropy. We show numerical results for GFRP and CFRP which are considered macroscopically as homogeneous and anisotropic bodies (Fig. 4). The examples shown in

Fig. 4(*a*) and (*b*) correspond to those shown in Fig. 2(*a*) and (*b*), respectively, and we employ the macroscopic elastic constants obtained by the following rule of mixtures (volume fraction of glass or carbon fiber V_f: 50 percent):

$$E_L = E_f V_f + E_m(1 - V_f), \tag{16}$$

$$\frac{1}{E_T} = \frac{V_f}{E_f} + \frac{1 - V_f}{E_m}, \tag{17}$$

$$\nu_{LT} = \nu_f V_f + \nu_m(1 - V_f), \tag{18}$$

and the reciprocal relation:

$$\frac{\nu_{LT}}{E_L} = \frac{\nu_{TL}}{E_T}, \tag{19}$$

where subscripts L denotes the longitudinal direction, T the transverse one, LT the transverse direction in longitudinal tension, and TL the longitudinal direction in transverse tension.

We notice that the end effects are transmitted further into the inner domain, and that this tendency becomes more pronounced as the degree of anisotropy increases. Hoff (1945) showed an example of a framed structure where the stress decays slowly, and this may also be interpreted as a homogeneous anisotropic structure reinforced by diagonal beams.

We can formally express the relation between the stress and the strain in an anisotropic body as follows (Arimitsu et al., 1994):

$$\begin{aligned}\varepsilon_{kl} &= (S^*_{klij} + S^{**}_{klij})(\sigma^*_{ij} + \sigma^{**}_{ij}) \\ &= S^*_{klij}\sigma^*_{ij} + S^{**}_{klij}\sigma^*_{ij} + S^*_{klij}\sigma^{**}_{ij} + S^{**}_{klij}\sigma^{**}_{ij} \\ &\equiv \varepsilon^*_{kl} + \varepsilon'_{kl} + \varepsilon''_{kl} + \varepsilon'''_{kl},\end{aligned} \tag{20}$$

where S^*_{klij} denotes the isotropic elastic compliance, S^{**}_{klij} the deviating elastic compliance, σ^*_{ij} the isotropic stress solution, and σ^{**}_{ij} the difference between the stress in the real system and σ^*_{ij}. If the stress field σ^*_{ij} is known and we arbitrarily choose a certain value for S^*_{klij}, ε^*_{kl} and ε'_{kl} can be determined uniquely.

From the following compatibility condition,

$$\epsilon_{kpq}\epsilon_{lmn}\varepsilon_{qn,pm} \equiv -\eta_{kl} = 0, \tag{21}$$

$$\epsilon_{kpq}\epsilon_{lmn}\varepsilon^*_{qn,pm} \equiv -\eta^*_{kl} = 0, \tag{22}$$

$$\epsilon_{kpq}\epsilon_{lmn}\varepsilon'_{qn,pm} \equiv -\eta'_{kl}, \tag{23}$$

$$\epsilon_{kpq}\epsilon_{lmn}\varepsilon''_{qn,pm} \equiv -\eta''_{kl}, \tag{24}$$

$$\epsilon_{kpq}\epsilon_{lmn}\varepsilon'''_{qn,pm} \equiv -\eta'''_{kl}, \tag{25}$$

where ϵ_{kpq} denotes the permutation tensor, get the relation between incompatibilities η'_{kl}, η''_{kl}, and η'''_{kl} as follows:

$$\eta'_{kl} = -(\eta''_{kl} + \eta'''_{kl}) \quad (k, l = 1, 2, 3). \tag{26}$$

Eliminating ε'_{qn} in Eq. (23) with the three-dimensional stress function tensor ϕ^*_{kl}, which corresponds to σ^*_{ij}, (defined by Kröner (1958)), the incompatibility which induces the internal stress field is expressed as follows:

$$\eta'_{kl} = \epsilon_{kij}\epsilon_{lmn}S^{**}_{jnrs}\epsilon_{rvw}\epsilon_{stu}\phi^*_{wu,vtim}, \tag{27}$$

where we must pay attention to the definition and the sign of the ordinary Airy's stress function ϕ and ϕ^*_{33} in the stress function tensor (Arimitsu et al., 1994). For two-dimensional problems, we can also choose the function expressed in Eq. (1) as ϕ^*_{33}.

In general, the relation between the incompatibility and the dislocation density α_{kl} is given by

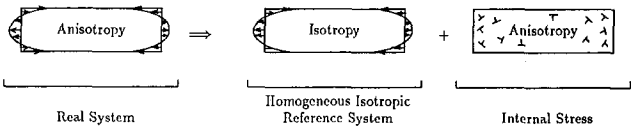

Fig. 5 Reference system and the internal stress for an anisotropic body

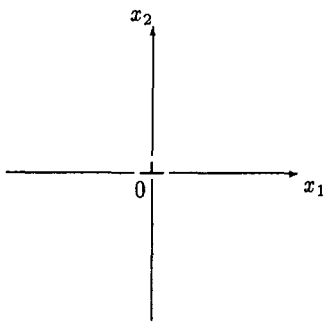

Fig. 6 Discrete dislocation in a infinite body

$$\eta'_{kl}(\mathbf{x}) = \frac{-1}{2}\left[\epsilon_{kpq}\alpha_{lq}(\mathbf{x})_{,p} + \epsilon_{lpq}\alpha_{kq}(\mathbf{x})_{,p}\right] \quad (k, l, p, q = 1, 2, 3). \tag{28}$$

Let us express the stress field in a homogeneous and anisotropic material with the following procedure, which is schematically summarized in Fig. 5.

1 Distributing hypothetically the isotropic stress solution σ^*_{ij} in an anisotropic body, the total strain $\varepsilon^*_{kl} + \varepsilon'_{kl}$ arises. The compatibility condition is not satisfied at this stage, i.e., the incompatibility η'_{kl} expressed by Eq. (23) appears. Note that Saint-Venant's principle holds for σ^*_{ij} in spite of the fact that it is in the anisotropic body.

2 Distributing the resultant incompatibility $\eta''_{kl} + \eta'''_{kl}$ from Eqs. (24) and (25) to cancel η'_{kl} in the anisotropic body, the internal stress is induced by the incompatibility $\eta''_{kl} + \eta'''_{kl}$. Though we cannot analytically get this internal stress field in the anisotropic body, we can see that the dislocation density is proportional to the deviating elastic compliance S^{**}_{klij} from Eqs. (27) and (28) and that end effects decay more slowly as the degree of anisotropy of a material increases according to the consideration given in Section 4.

3 Superposing σ^*_{ij} and the internal stress field, which is denoted as σ^{**}_{ij}, we get the stress field in the real anisotropic system. The superposition of an isotropic system and an anisotropic system shown in Fig. 5 is not intended for the strain but just for the stress. We see that end effects may decay slowly due to the stress field induced by incompatibility.

4 Estimation of Internal Stress

Though the magnitude of dislocation density is proportional to the difference of the elastic compliance of component materials or to the deviation from isotropy, we see from Eqs. (14) and (15) that the damping behavior of dislocation density from the end, which may be represented by the attenuation constant γ included in the stress function, is independent of the elastic constants. Hence, it seems that Saint-Venant's principle would hold in composite materials as in an isotropic and homogeneous body. However, when we estimate the internal stress field induced by the incompatibility dislocation, we must take account of the following four factors (for simplicity we consider, in this section, discrete dislocations in a homogeneous and isotropic body).

1 Stress field of a single dislocation. The stress fields of a single dislocation in an infinite body as shown in Fig. 6 are given by

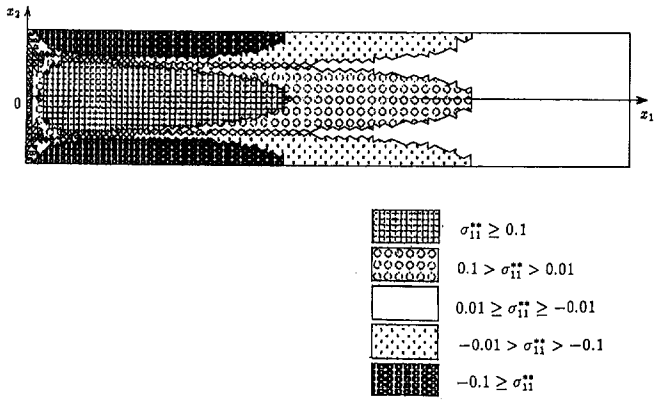

Fig. 7 Internal stress field σ_{11}^{**} in longitudinally glass fiber-reinforced plastics

$$\sigma_{11} = -\frac{\mu b}{2\pi(1-\nu)} \frac{x_2\left(3x_1^2 + x_2^2\right)}{\left(x_1^2 + x_2^2\right)^2}, \tag{29}$$

$$\sigma_{22} = \frac{\mu b}{2\pi(1-\nu)} \frac{x_2\left(x_1^2 - x_2^2\right)}{\left(x_1^2 + x_2^2\right)^2}, \tag{30}$$

where b and μ denote the Burgers vector and the shear modulus, respectively. Since the stress field σ_{11} of a dislocation decays with x_1^{-2} for any direction of the Burgers vector, the range of the internal stress field σ_{11}^{**} is longer than that induced by the external force which decays with $\exp(-x_1)$. This factor causes the slow decay of end effects in a composite material.

2 Effect of free surface. However high the incompatibility dislocation density becomes near the end, the internal stress component must satisfy the free boundary condition at the end surface (Nishioka et al., 1987; Arimitsu et al., 1994). Figure 7 shows the internal stress field which is obtained by subtracting the stress field of the isotropic system shown in Fig. 1(a) from that of the anisotropic one shown in Fig. 4(a). We see that the internal stress thus obtained decreases near the end of a strip in spite of the high dislocation density. This implies that the end effects decay slowly, because the internal stress near the end of a strip is smaller than that of the inner domain and end effects are represented by the stress normalized by the value near the end.

3 Stress field induced by dislocation dipole. The stress fields of dislocation dipoles shown in Fig. 8(a) and (b) are obtained by the suitable combination of Eqs. (29) and (30), and we notice that the stress field σ_{11} of a dislocation dipole shown in Fig. 8(a) is intensified but σ_{11} shown in Fig. 8(b) is mutually canceled along the x_1-axis. The dislocation dipoles shown in Fig. 8(a) and (b) correspond to the longitudinal fiber reinforced model and the transverse one, respectively. This factor corresponds to the numerical result that end effects of a transversely fiber reinforced composite material decay at the same rate as those of a homogeneous material (see Fig. 9).

4 Magnitude of Burgers vector. As given by Eqs. (29) and (30), the stress field induced by a dislocation is proportional to the Burgers vector b, which corresponds to the dislocation density in the continuous distribution of dislocations employed in the previous section. Since the transverse strain ε_{22} of the reference system is smaller than the longitudinal one ε_{11} by Poisson's ratio under the x_1-axial loading, the surface dislocation density induced by the incompatibility of displacement due to the transverse strain is also smaller than that due to the longitudinal one by the same ratio. The difference between the stress profile shown in Fig. 4(a) and that shown in Fig. 9 is caused also by this factor, i.e., the magnitude of

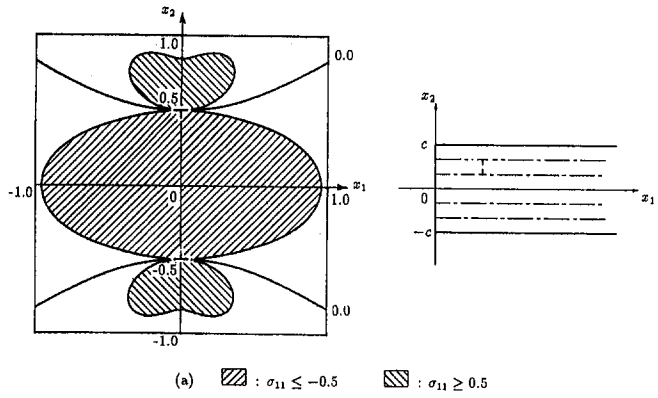

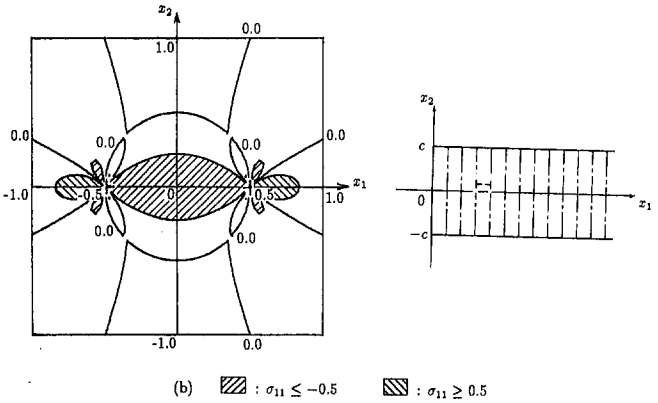

Fig. 8 Stress profile σ_{11} of a dislocation dipole. ($\mu = 1.0$, $\nu = 0.3$, $b = 1.0$); (a) longitudinally fiber-reinforced model, (b) transversely fiber-reinforced model

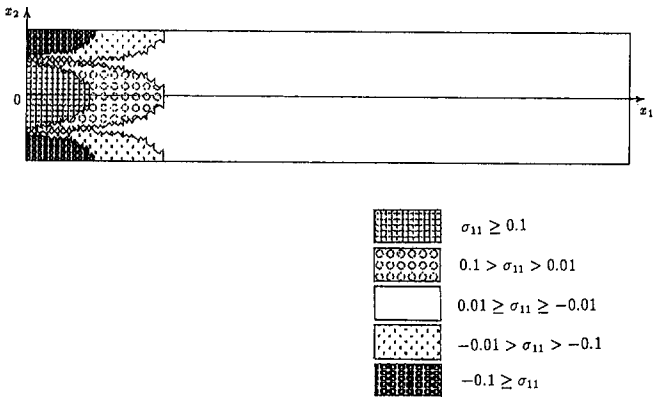

Fig. 9 Stress profile of σ_{11} in transversely fiber-reinforced composite (volume fraction of the transverse glass fiber: 50 percent)

the Burgers vector of a dislocation dipole shown in Fig. 8(a) is larger than that shown in Fig. 8(b) because the incompatibility in Fig. 8(b) is smaller than that in Fig. 8(a) by Poisson's ratio.

5 Discussion and Conclusions

Decomposing the stress field in a composite material into the stress field in the homogeneous and isotropic reference system where Saint-Venant's principle holds and the internal stress field induced by dislocations distributed continuously, we propose that the slow decay of end effects peculiar to composite materials is due to the stress field associated with the incompatibility dislocation. The dislocation density is proportional to the difference in the elastic compliances of

component materials for an inhomogeneous material and to the deviating elastic compliance (defined in Eq. (20)) for an anisotropic material. Consequently, we establish a unified and systematic interpretation of the reason why end effects in a composite material decay slowly, irrespective of whether we consider it inhomogeneous or anisotropic. The distinction between those two views can be considered as a matter of the pattern size in a composite relative to the size of a specimen.

It is expected that the present method, through dislocation theory, can be qualitatively extended to end effects for a composite material under plastic deformation, where Okumura et al. (1985) have carried out a numerical study.

In formulating Saint-Venant's principal for a homogeneous and isotropic body, the *strain* plays an important role in spite of the fact that the emphasis is on the *stress* as in the strain energy formulation by Zanaboni (1937) or in the astatic equilibrium formulation by von Mises (1945). This also suggests that the incompatibility (a quantity in the "strain" space) plays an important role in studying Saint-Venant's principle for composite materials.

References

Arimitsu, Y., Nishioka, K., and Senda, T., 1994, "Analysis of Anisotropic Elasticity by Means of Internal Stress in Reference Isotropic Elastic Body," *Z. Angew. Math. Mech.*, Vol. 74, pp. 465–473.

Choi. I., and Horgan, C. O., 1977, "Saint-Venant's Principle and End Effects in Anisotropic Elasticity," ASME JOURNAL OF APPLIED MECHANICS, Vol. 44, pp. 424–430.

Choi, I., and Horgan, C. O., 1978, "Saint-Venant End Effects for Plane Deformation of Sandwich Strips," *Int. J. of Solid Structures*, Vol. 14, pp. 187–195

Dong, S. B., and Goetschel, D. B., 1982, "Edge Effect in Laminated Composite Plates," ASME JOURNAL OF APPLIED MECHANICS, Vol. 49, pp. 129–135.

Fung, Y. C., 1965, *Foundations of Solid Mechanics*, Prentice-Hall, Englewood Cliffs, NJ.

Goodier, J. N., 1937, "A General Proof of Saint-Venant's Principle," *Phil. Mag. Ser.* 7, Vol. 23, pp. 607–609.

Hoff, N. J., 1945, "The Applicability of Saint-Venant's Principle to Airplane Structures," *J. Aeronautical Sci.*, Vol. 12, pp. 455–460.

Horgan, C. O., 1972a, "On Saint-Venant's Principle in Plane Anisotropic Elasticity," *J. of Elasticity*, Vol. 2, pp. 169–180.

Horgan, C. O., 1972b, "Some Remarks on Saint-Venant's Principle for Transversely Isotropic Composites," *J. of Elasticity*, Vol. 2, pp. 335–339.

Horgan, C. O., 1982, "Saint-Venant End Effects in Composites," *J. Compos. Mater.*, Vol. 16, pp. 411–422.

Horgan, C. O., 1989, "Recent Developments Concerning Saint-Venant's Principle: An Update," *Applied Mechanics Reviews*, Vol. 42, pp. 295–303.

Horgan, C. O., and Knowles, J. K. 1983, "Recent Developments Concerning Saint-Venant's Principle," *Advances in Applied Mechanics*, Vol. 23, Academic Press, San Diego, CA, pp. 179–269.

Kröner, E., 1958, *Kontinuumstheorie der Versetzungen und Eigenspannungen*, Springer-Verlag, Berlin.

Mura, T., 1982, *Micromechanics of Defects in Solids*, Martinus Nijhoff, The Hague, The Netherlands.

Nishioka, K., Takai, T., Arimitsu, Y., and Ohashi, T., 1987, "A Method of Analyzing Elastic Constraints due to Grain or Interphase Boundaries," *Mechanics of Materials*, Vol. 6, pp. 139–145.

Nye, J. F., 1967, *Physical Properties of Crystals*, Oxford University Press, London.

Okumura, H., Watanabe K., and Yamada, Y., 1985, "Finite-Element Analyses of Saint-Venant End Effects for Composite Materials," ASTM Spec. Tech. Publ., pp. 225–235.

de Saint-Venant, B., 1855, *Mémoire sur la Torsion des Prismes*, Mém. des Savants étrangers, Paris.

Sternberg, E., 1954, "On Saint-Venant's Principle," *Quart. Appl. Math.*, Vol. 11, pp. 393–402.

Timoshenko, S. P., and Goodier, J. N., 1970, *Theory of Elasticity*, 3rd ed., McGraw-Hill, New York.

von Mises, R., 1945, "On Saint-Venant's Principle," *Bull. Amer. Math. Soc.*, Vol. 51, pp. 555–562.

Zanaboni, O., 1937, "Dimostrazione General del Principio del de Saint-Venant," *Atti. Accad. Lincei*, Roma, Vol. 25, pp. 117–121.

Natural Frequencies of a Penny-Shaped Crack With Spring Boundary Condition

A. S. Eriksson[1]
Division of Mechanics,
Chalmers University of Technology,
S-412 96 Goteborg, Sweden

Natural frequencies of a penny-shaped crack are calculated for the three-dimensional elastic problem. The crack is imbedded in a homogeneous medium and on the crack surface the spring boundary conditions are assumed. Only the symmetric problem is considered and the complex frequencies are given as the SEM (singularity expansion method) poles of the symmetric part of the transition (T) matrix. The T matrix is calculated with a direct integral equation method leading to integral equations relating normal stress and displacement on the crack surface. The location of the poles in the complex frequency plane are compared with the scattering cross-section versus frequency and with Rayleigh surface waves.

1 Introduction

In this paper we study the natural frequencies of a penny-shaped crack with spring boundary condition in an elastic medium. These frequencies, given as the poles of the transition matrix (the T matrix) in the complex frequency plane, are the elastic counterparts of the singularity expansion method poles in the electromagnetic literature. The singularity expansion method was originally developed for electromagnetic scattering and radiation (Baum, 1976), and stems from the observation that the transient scattered field can be modeled in terms of the natural frequencies of the scattering body, i.e., as a Prony series of damped sinusoids

$$f(t) = \sum_{n=1}^{N} A_n e^{s_n t} \tag{1}$$

where s_n is complex and the real part Re s_n is negative (note that this paper uses the convention $e^{-i\omega t}$ for the time factor). The Laplace transform of Eq. (1)

$$F(s) = \sum_{n=1}^{N} \frac{A_n}{s - s_n} \tag{2}$$

is a series of poles s_n in the complex frequency plane with residues A_n.

An important feature is that these poles, called the singularity expansion method poles, are characteristic for each scatterer This indicates that, e.g., in ultrasonic NDT, scattering objects may be characterized if these frequencies can be extracted from the scattering echo response. Überall et al. (1983) give a survey of some electromagnetic and acoustic problems where the singularity expansion method poles are calculated. They discuss the possibility of extracting singularity expansion method poles from scattering data to predict the properties and the shape of an unknown scatterer. In this context they introduce the concept of "Acoustic and Radar Spectroscopy." Recently, Björkberg (1991) studied a problem in electromagnetics similar to the elastodynamic problem studied here. He calculated the natural frequencies and the corresponding eigencurrents of a perfectly conducting elliptic disk. Bollig and Langenberg (1983) extended the singularity expansion method to elastodynamic scattering, but, to the author's knowledge, not much work has been done in three-dimensional elastic problems. Bollig and Langenberg (1983) derived singularity patterns for various acoustic, electromagnetic, and elastic scatterers in different host media. In particular, they gave the singularity pattern for spherical, prolate spheroidal and oblate spheroidal cavities in elastic media. In this paper we establish some relations between poles of the T matrix, resonance peaks of the scattering cross-sections, and Rayleigh surface waves on the crack surface.

2 The T Matrix and its Poles

To investigate the natural resonance frequencies and singularity expansion method poles of the penny-shaped crack with spring boundary conditions we use the procedure of Boström and Eriksson (1993). They compute the T matrix for the crack by suitably modifying the integral equation method of Krenk and Schmidt (1982) and use this to consider two cracks. Here we employ the same method and therefore review some of the pertinent details from Boström and Eriksson (1993).

[1]Present address: ABB Tekniska Röntgencentralen AB, P. O. Box 121, S-183 22 Täby, Sweden.

Contributed by the Applied Mechanics Division of THE AMERICAN SOCIETY OF MECHANICAL ENGINEERS for publication in the JOURNAL OF APPLIED MECHANICS.

Discussion on this paper should be addressed to the Technical Editor, Professor Lewis T. Wheeler, Department of Mechanical Engineering, University of Houston, Houston, TX 77204-4792, and will be accepted until four months after final publication of the paper itself in the ASME JOURNAL OF APPLIED MECHANICS.

Manuscript received by the ASME Applied Mechanics Division, Jan. 25, 1993; final revision, Aug. 30, 1993. Associate Technical Editor: S. K. Datta.

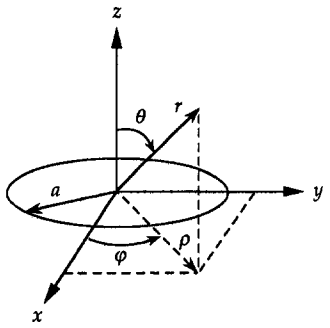

Fig. 1 Geometry of the crack. Cylindrical (ρ, φ, z) and spherical (r, θ, φ) coordinates.

Briefly, in the T matrix method (Varadan and Varadan, 1980), the total displacement field is divided into an incoming field and a scattered field

$$\mathbf{u} = \mathbf{u}^{in} + \mathbf{u}^{s}. \tag{3}$$

Both the incoming and the scattered field are expanded in a complete set of spherical vector wave functions Ψ_n

$$\mathbf{u}^{in} = \sum_n a_n \mathrm{Re}\Psi_n, \quad \mathbf{u}^{s} = \sum_n f_n \Psi_n. \tag{4}$$

Re means "the regular part," so that the incoming wave is not singular at the origin inside the scatterer and n is a multiple index. The linear relation between the two sets of expansion coefficients is given by the T matrix as

$$f_n = \sum_{n'} T_{nn'} a_{n'}. \tag{5}$$

This T matrix contains all necessary information about crack geometry and boundary conditions, and it is the (SEM) poles of this frequency-dependent matrix, i.e., the natural frequencies of the penny-shaped crack, that we want to calculate. However, it is not necessary to fully calculate the T matrix to get the natural frequencies as the singularity expansion method poles can be extracted from a determinantal condition when the integral equation is solved.

The penny-shaped crack, see Fig. 1, is imbedded in a homogeneous, isotropic, linearly elastic medium with density ρ and Lamé parameters λ and μ. A time factor $e^{-i\omega t}$, where ω is the angular frequency, is suppressed in all formulas. The transverse wave number is $k_s^2 = \rho\omega^2/\mu$ and the longitudinal wave number is $k_p^2 = \rho\omega^2/(\lambda + 2\mu)$. The total displacement field is governed by the elastodynamic equation of motion

$$k_p^{-2}\nabla\nabla\cdot\mathbf{u} - k_s^{-2}\nabla\times(\nabla\times\mathbf{u}) + \mathbf{u} = \mathbf{0}. \tag{6}$$

On the crack surface, defined by $z = 0$ and $x^2 + y^2 < a^2$ in cartesian coordinates (see Fig. 1), the so-called spring boundary conditions are assumed:

$$\mathbf{u}_+ - \mathbf{u}_- = \frac{1}{\mu k_s}\left(\frac{1}{\alpha}\hat{z}\hat{z}\cdot\mathbf{t}_+ \frac{1}{\beta}\hat{z}\times(\hat{z}\times\mathbf{t}_+)\right) \tag{7a}$$

$$\mathbf{t}_+ = \mathbf{t}_-. \tag{7b}$$

A subscript $+(-)$ indicates the limit taken from positive (negative) z-coordinates. $\hat{z}$ is the unit normal on the crack surface. α and β are dimensionless and in general complex and frequency dependent. By choosing α and β properly it is possible to model, e.g., an open, a partly closed (Boström and Wickham, 1991), and a fluid-filled crack (Persson and Olsson, 1991). Equation (7*b*) states that the traction $\mathbf{t}$ is continuous over the crack surface and Eq. (7*a*) relates the discontinuity of the displacement $\mathbf{u}$ to the traction.

Following Krenk and Schmidt (1982) the scattered field in the upper half-space is expanded in series of Fourier-Hankel transforms with cylindrical vector wave functions. Since the geometry is symmetric with respect to the crack plane ($z = 0$), the problem is divided into a symmetric and an antisymmetric part. The expansions of the scattered field leads in the symmetric case to integral equations relating normal stress and displacement on the crack surface and in the antisymmetric case to integral equations relating tangential stress and displacement on the crack surface. The stress components are due to the incoming displacement field, which is assumed to be known. So the remaining unknowns are the displacement components on the crack surface, or rather the crack-opening displacement, i.e., the discontinuity of the displacement field over the crack surface.

From here on we only consider the symmetric part of the problem, but the antisymmetric problem could be solved in the same way. The normal crack-opening displacement component Δu_z^s in the integral equation is expanded in partial waves as

$$\Delta u_z^s = \sum_{m=0}^{\infty} \Delta u_z^{s,m} \begin{Bmatrix} \cos m\varphi \\ \sin m\varphi \end{Bmatrix} \tag{8}$$

with $\cos m\varphi$ ($\sin m\varphi$) when the function is even (odd) with respect to φ. Each partial wave crack-opening displacement, $\Delta u_z^{s,m}$, must fulfill the correct edge condition, i.e., $\Delta u_z^{s,m}$ must turn to zero at the crack edge as the square root of the distance to the crack edge. Thus we expand each partial wave in the crack-opening displacement in series of associated Legendre functions P_l^m in the radial direction ρ

$$\Delta u_z^{s,m} = \sum_{j=0}^{\infty} a_j^m p_j^m(\rho) \quad m = 0, 1, \ldots \tag{9}$$

where

$$p_j^m(\rho) = (-1)^j P_{m+2j+1}^m\left(\sqrt{1-\rho^2/a^2}\right)/P_{m+2j+1}^{m+1}(0). \tag{10}$$

This expansion is inserted into the integral equation and then the equation is projected on the same polynomial $p_j^m(\rho)$. This leads to the following system of equations:

$$S_j^m = \sum_{j'=0}^{\infty} Q_{jj'}^m a_{j'}^m \tag{11}$$

where

$$S_j^m = \frac{1}{\mu k_s}\int_0^a \sigma_{zz}^{in,m}\frac{\rho}{a^2}p_j^m(\rho)\,d\rho \tag{12}$$

and

$$Q_{jj'}^m = \int_0^{\infty}\left(\alpha - \frac{iR(q)}{2k_s^3 h_p}\right) j_{m+2j'+1}(aq) j_{m+2j+1}(aq)\frac{dq}{q} \tag{13}$$

where

$$R(q) = \left(2q^2 - k_s^2\right)^2 + 4h_s h_p q^2. \tag{14}$$

a_j^m are the unknown expansion coefficients for the crack-opening displacement in Eq. (9). $j_m(aq)$ is a spherical Bessel function of order m. q is the integration variable in the Fourier-Hankel transform. The wave numbers along the z-axis are

$$h_s = \left(k_s^2 - q^2\right)^{1/2}, \quad \mathrm{Im}\,h_s \geq 0$$

$$h_p = \left(k_p^2 - q^2\right)^{1/2}, \quad \mathrm{Im}\,h_p \geq 0$$

for real k_s, k_p.

We need not go further in the calculations of the T matrix but now the natural frequencies sought for may be characterized as the frequencies at which a scattered field, or rather a surface field $\Delta u_z^{s,m}$, with the expansion coefficients a_j^m, may

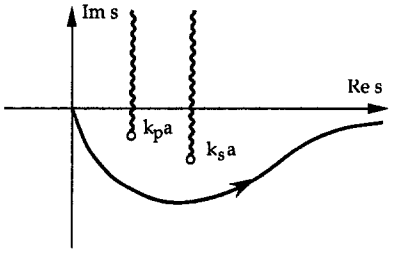

Fig. 2 The cuts (~~~) and the integration contour of Equation (21) in the complex s-plane.

exist without any incoming field. If the incoming field $\mathbf{u}^{in}$ is zero so is the stress $\sigma_{zz}^{in,m}$ in Eq. (12). Thus we have

$$0 = \sum_{j'=0}^{\infty} Q_{jj'}^{m} a_{j'}^{m} \tag{15}$$

and the natural frequencies are given by the condition

$$\det\left[Q_{jj'}^{m}\right] = 0 \tag{16}$$

regarded as an equation in $k_s a = \omega a/c_s$ (where the shear wave speed $c_s^2 s = \mu/\rho$).

3 Numerical Considerations

Introducing the dimensionless variable $s = aq$ in Eq. (13) results in

$$Q_{jj'}^{m} = \int_0^{\infty} \left(\alpha - \frac{iR(s)}{2(k_s a)^3 h_p a} \right) j_{m+2j'+1}(s) j_{m+2j+1}(s) \frac{ds}{s} \tag{17}$$

where

$$R(s) = \left(2s^2 - (k_s a)^2\right)^2 + 4 h_s a h_p a s^2 \tag{18}$$

and

$$h_s a = \sqrt{(k_s a)^2 - s^2}, \quad h_p a = \sqrt{(k_p a)^2 - s^2}. \tag{19}$$

The integral is naturally divided into two separate parts where the first one may be calculated analytically (Gradshteyn and Ryzhik, 1980):

$$^{I}Q_{jj'}^{m} = \int_0^{\infty} \alpha j_{m+2j'+1}(s) j_{m+2j+1}(s) \frac{ds}{s} = \frac{\alpha(-1)^{j+j'+1}}{\left(8(j-j')^2 - 2\right)(m+j'+j+2)(m+j'+j+1)}. \tag{20}$$

The second part of the integral is to be calculated numerically but to improve the convergence we first subtract off the leading term for large s from $R(s)/(h_p a s)$ in the integrand. Thus, the remaining integrand turns to zero as $1/s^4$ instead of $1/s^2$ when $s \to \infty$. The remaining integral becomes

$$^{II}Q_{jj'}^{m} = -\frac{i}{2(k_s a)^3} \int_0^{\infty} \left[\frac{R(s)}{h_p a s} - 2i\left((k_s a)^2 - (k_p a)^2\right) \right] \times j_{m+2j'+1}(s) j_{m+2j+1}(s) ds. \tag{21}$$

This integral has branch points located at the complex values $s = \pm k_s a$ and $s = \pm k_p a$. When the frequency ω has negative imaginary part (as is the case for the singularity expansion method poles) $^{II}Q_{jj'}^{m}$ must be continued analytically and forces us to introduce new cuts and a new integration contour. The new cuts and contour are shown in Fig. 2. The branches of $h_s a$ and $h_p a$ are chosen so that for $s = 0$ $\mathrm{Im} h_s a < 0$ and $\mathrm{Im} h_p a < 0$. Then they vary continuously along the integration contour. In this way the matrix elements are uniquely determined.

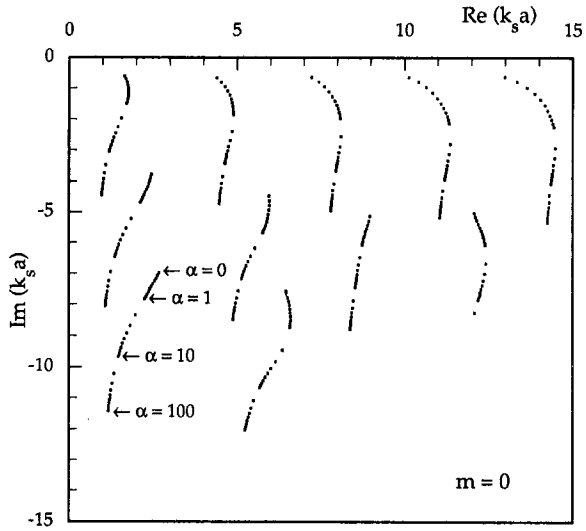

Fig. 3 The trajectories of the natural frequencies for $m = 0$ for the penny-shaped crack. The boundary condition constant α is varied from 0 to 100.

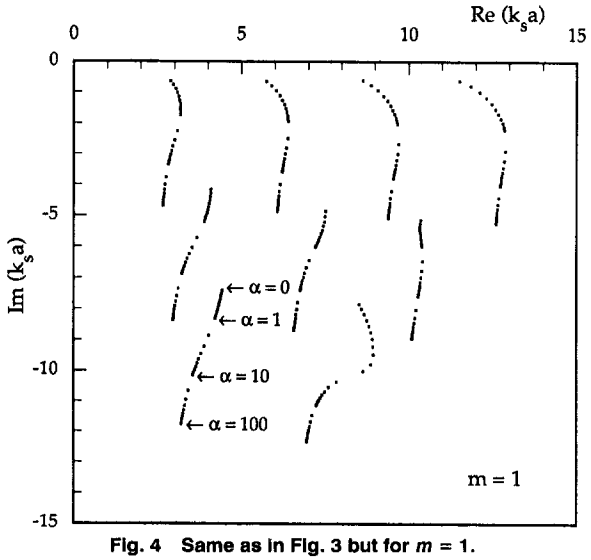

Fig. 4 Same as in Fig. 3 but for $m = 1$.

To compensate for the subtraction of the leading term in the integral above, Eq. (21), we must add the following integral which is calculated analytically (Gradshteyn and Ryzhik, 1980):

$$^{III}Q_{jj'}^{m} = \frac{(k_s a)^2 - (k_p a)^2}{(k_s a)^3} \int_0^{\infty} j_{m+2j'+1}(s) j_{m+2j+1}(s) ds = \frac{(k_s a)^2 - (k_p a)^2}{(k_s a)^3} \cdot \frac{\pi \delta_{jj'}}{8j + 4m + 6} \tag{22}$$

where $\delta_{jj'}$ is a Kronecker delta. Thereby the matrix $Q_{jj'}^{m}$ is fully calculated by adding the contributions from Eqs. (20), (21), and (22) and we may calculate the zeroes of Eq. (16).

The zeroes of this complex function, $\det[Q_{jj'}^{m}]$, are calculated simply by the secant method and by guessing the initial values. Once a first root is found this guessing is easy since the roots obey a typical layer structure (cf. Figs. 3 and 4).

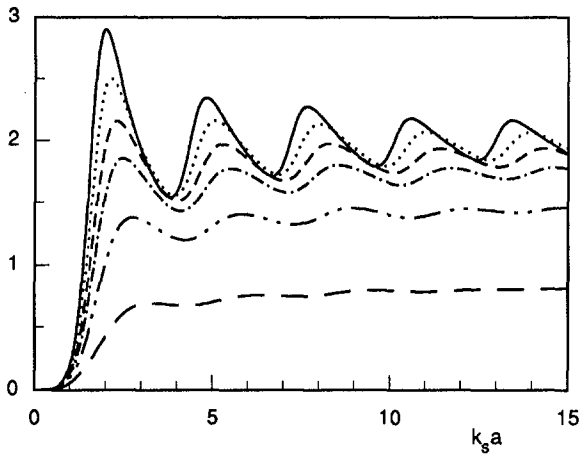

Fig. 5 The scattering cross-sections as a function of frequency $k_s a$ for an incident plane P-wave with an angle $\theta_0 = 0$ to the z-axis. From top to bottom α is 0, 0.1, 0.2, 0.3, 0.5, and 1.0.

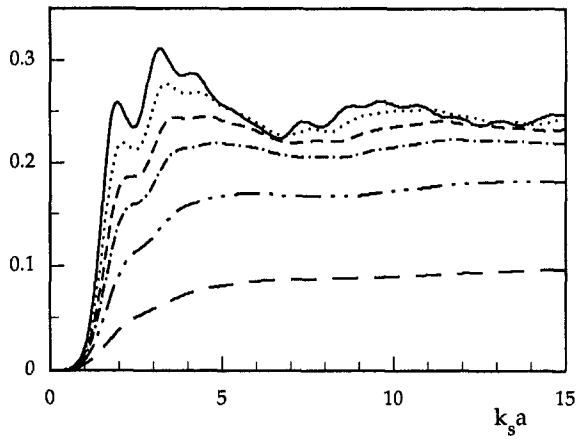

Fig. 6 Same as Fig. 5, but for an incident plane P-wave with an angle $\theta_0 = 90$ deg to the z-axis

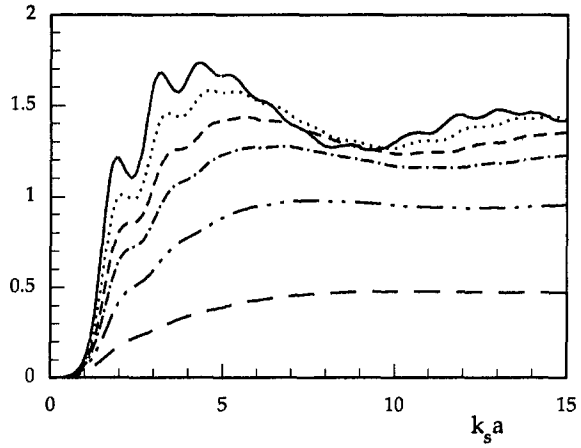

Fig. 7 Same as Fig. 5, but for an incident plane SV-wave with an angle $\theta_0 = 45$ deg to the z-axis

The integrals in Eq. (21) were truncated at $s = 400$ and calculated with an 800-point Gaussian quadrature. The roots, equal to the singularity expansion method poles, were calculated for $m = 0$ and $m = 1$. For $m = 0$ and $\alpha = 0$, the upper left pole in Fig. 3 was calculated with four significant figures when the Q-matrix was truncated at $j_{max} = j'_{max} = 3$ (4×4 matrix). Truncation at $j_{max} = j'_{max} = 20$ gives at least three significant figures for all the calculated poles ($m = 0$, 1 and $0 < \alpha < 100$).

4 Discussion

Some of the natural frequencies ω of the above considered symmetric problem, given as the normalized frequencies $k_s a = a\omega/c_s$, are calculated for $m = 0$ and $m = 1$ and are plotted in Figs. 3 and 4, respectively. Each pole is calculated for values of the boundary condition constant α ranging from 0 to 100 except for pole number 4 in layer II (see below) with $m = 0$, which is calculated from 0 to 20. The poles are indicated by dots in steps of 0.1 for $0 < \alpha < 1$, in steps of 1 for $1 < \alpha < 10$ and in steps of 10 for $10 < \alpha < 100$. The Poisson ratio is fixed to 0.25.

For a given value of α the poles follow the typical layer pattern that has been observed earlier (Überall et al., 1983; Björkberg, 1991; Bollig and Langenberg, 1983). We label each layer by layer I, layer II, etc., starting from the top. Within each layer the poles are numbered 1, 2, 3, . . . from left to right. If we follow the trajectory of a pole for increasing α we see that for every increase of α with a factor 10, the absolute value of the imaginary part of the root increases with roughly equal amounts ($\alpha = 1000$ has been calculated but is not shown). In the limit $\alpha \to \infty$, all poles will have disappeared at infinity. This is natural as the limit $\alpha \to \infty$ corresponds to no crack at all.

A way to gain further insight into the significance of the natural frequencies is to compare their location with some scattering data. Therefore, Figs. 5–7 show the total scattering cross-section as a function of the normalized frequency $k_s a$ for those incident plane waves that excite only the symmetric crack-opening displacement. The scattering cross-section is defined as the total crack scattered energy divided by the energy flux in the incoming plane wave and the crack area πa^2. Figures 5 and 6 show results for an incoming plane P-wave making an angle $\theta_0 = 0$ deg and 90 deg, respectively, to the z-axis. In Fig. 7 we have an incoming plane SV-wave with $\theta_0 = 45$ deg.

We begin with studying the case of an incoming P-wave with $\theta_0 = 0$ deg and note that since this case is rotationally symmetric around the z-axis only $m = 0$ contributes to the solution. This explains why the peaks in Fig. 5 are sparse compared to the cases shown in Fig. 6 and 7 where all m values are included in the solution. Every two neighboring peaks in Fig. 5 are separated by approximately 2.8–2.9. For the poles in layer I in Fig. 3 we see that, for $\alpha = 0$, the real parts are also separated by approximately 2.8–2.9. But it should be noted that the peaks and the real parts of the poles do not correspond exactly, each peak being located about 0.4–0.5 higher than the real part of the closest pole. Thus we have established a clear relation between the poles (i.e., the natural frequencies of the crack) and the scattered energy.

For increasing α, starting from zero, the peaks of the cross-sections decrease in value but they also appear at higher values of $k_s a$. This behavior is more apparent for the peaks at higher $k_s a$. Also the poles in layer I starts with a migration to higher real parts but at $\alpha = 0.7$–2.0 the real part starts to decrease. For $\alpha = 0.5$ the peaks in Fig. 5 are separated by approximately 3.0–3.2, and the same is true for the real part of the poles in layer I, Fig. 3. With a priori information about the crack, scattering data such as Fig. 5 can thus give more information. If it is known that if the crack is open, the distances between the resonance peaks will give the crack radius. On the other hand, if the crack radius is known, we can estimate the value of α, i.e., how much the crack is closed. It should be further investigated if this increase in the separation of the resonance peaks offers a possibility to predict the properties of the crack or if it obscures a correct size estimation of the crack.

Another physical explanation to the distance between the real parts of the poles is offered. As shown by Bollig and Langenberg (1983), the resonances of an object are related to different kinds of surface waves or creeping waves repeatedly circumnavigating it and radiating back to the observer. In this case it is a Rayleigh surface wave with the wave speed c_R that travels over the crack width $2a$ on the time $t_R = 2a/c_R$ that gives rise to a diffracted field each time it reaches the crack edge. With a Poisson ratio of 0.25 we have the relation $c_R = 0.919\ c_S$ and the frequency at which the Rayleigh wave hits the crack edge may thus be written as $k_s a = a\omega/c_s \approx 2.887$, where $\omega = 2\pi/t_R$, which is indeed very close to the observed distances between both the poles and the resonance peaks. In Boström and Eriksson (1993) and in Peterson (1989) the P back-scattered far-field amplitude by a penny-shaped crack is viewed in the time domain. There it is clearly seen that for the late-time response (i.e., after the direct diffracted echos have passed) clear echos appear at times distanced by $t_R = 2a/c_R$. Thus the natural frequencies are clearly related to the Rayleigh wave.

Since the peaks of the scattering cross-section so clearly can be related to the poles in layer I, it is reasonable to assume that the poles in the lower layers correspond to resonance frequencies with very little influence on the scattered field. This reasoning is supported if we study the poles for higher α. For $\alpha = 1.0$, the roots in layer I has moved down into the complex plane from imaginary values of -0.6 to values from -1.5 to -2.2. The corresponding cross-section in Fig. 5 hardly shows any resonance effects at all.

Finally, we comment on the two cases of incident P-wave with $\theta_0 = 90$ deg and incident SV-wave with $\theta_0 = 45$ deg, shown in Figs. 6 and 7, respectively. Here all values of m contribute to the solution and we have to consider poles for other m values than the $m = 0$ and 1 shown in Figs. 3 and 4. For $m = 2$ and 3 the poles are located as for $m = 0$ and 1, respectively, with the exception that the first pole in layer I is missing and the remaining poles have a real part just a tenth lower than the poles for $m = 0$ and 1. For $m = 4$ and 5 the two first poles in layer I are missing, and so on. This means that for higher frequencies the poles come closer and closer and the influence from a single pole on the scattering cross-section is difficult to recover in Figs. 6 and 7. Only the first two peaks at approximately $k_s a = 1.9$ and 3.2 with $\alpha = 0$ can easily be connected with particular poles, namely pole number 1 in layer I for $m = 0$ and 1. For $\alpha = 0.1$ it is difficult to discern more than the first two peaks but as in Fig. 5 they appear at slightly higher values of $k_s a$ than they do for $\alpha = 0$.

5 Concluding Remarks

Natural frequencies for a penny-shaped crack with spring boundary conditions are calculated. The frequencies are given as the singularity expansion method poles of the T matrix of the crack by imposing the condition that the crack-opening displacement can exist without any incoming displacement field. The location of the poles in the complex frequency plane are compared with scattering data (scattering cross-section versus normalized frequency) and some correlations between poles and scattering data for various values on boundary condition constants are pointed out. Also its relation to Rayleigh surface waves is discussed. In general, only the influence from the lowest resonance frequencies can be traced in the cross-sections. It should be further investigated if the results can be used in the work of characterizing properties of cracks. Future work could include the extraction of singularities from time records (cf. Bollig and Langenberg, 1983) which allows the late-time response to be written as a superposition of damped exponentials (cf. Eq. (1)–(2)). Also, eigenvectors of the eigenvalue problem, Eq. (15), that gives the crack-opening displacement contribution related to each pole, and effects due to an elliptic crack (cf. Björkberg, 1991) could be studied.

Acknowledgment

The author is grateful to Prof. A. Boström for valuable discussions and for carefully reading the manuscript.

References

Baum, C. E., 1976, "The Singularity Expansion Method," *Transient Electromagnetic Fields*, L. E. Felsen, ed., Springer-Verlag, New York, pp. 129–179.

Björkberg, J., 1991, "Natural Frequencies and Eigencurrents of the Elliptic Disc," *Radio Science*, Vol. 26, pp.149–160.

Bollig, G., and Langenberg, K. J., 1983, "The Singularity Expansion Method as Applied to the Elastodynamic Scattering Problem," *Wave Motion*, Vol. 5, pp. 331–354.

Boström, A., and Eriksson, A. S., 1993, "Scattering by Two Penny-shaped Cracks with Spring Boundary Conditions," *Proceedings of the Royal Society of London*, Vol. A443, pp. 183–201.

Boström, A., and Wickham, G., 1991, "On the Boundary Conditions for Ultrasonic Transmission by Partially Closed Cracks," *Journal of Nondestructive Evaluation*, Vol. 10, pp. 139–149.

Gradshteyn, I. S., and Ryzhik, I. M., 1980, *Tables of Integrals, Series and Products*, Academic Press, New York.

Krenk, S., and Schmidt, H., 1982, "Elastic Wave Scattering by a Circular Crack," *Philosophical Transactions of the Royal Society, London*, Vol. A308, pp. 167–198.

Persson, G., and Olsson, P., 1991, "2-D Elastodynamic Scattering from a Semi-infinite Cracklike Flaw with Interfacial Forces," *Wave Motion*, Vol. 13, pp. 21–41.

Peterson, L., 1989, "Elastic Wave Scattering by Two Penny-shaped Cracks," *Elastic Wave Propagation*, M. F. McCarthy and M. A. Hayes, eds., North-Holland, Amsterdam, pp. 437–442.

Überall, H., Moser, P. J., Murphy, J. D., Nagl, A., Igiri, G., Subrahmanyam, J. V., Gaunaurd, G. C., Brill, D., Delsanto, P. P., Alemar, J. D., and Rosario, E., 1983, "Electromagnetic and Acoustic Resonance Scattering Theory," *Wave Motion*, Vol. 5, pp. 307–329.

Varadan, V. K., and Varadan, V. V., eds., 1980, *Acoustic, Electromagnetic and Elastic Wave Scattering—Focus on the T Matrix Approach*, Pergamon, New York.

Load Buckling of a Layer Bonded to a Half-Space With an Interface Crack

Wen-Xue Wang
Assoc. Professor.

Yoshihiro Takao
Professor.

Research Institute for
Applied Mechanics,
Kyushu University,
Kasuga, Fukuoka 816, Japan

An analytical solution is presented for local buckling of a model of delaminated composites, that is, a layer bonded to a half-space with an interface crack. The layered system is subjected to compressive load parallel to the free surface. Basic stability equations derived from the mathematical theory of elasticity are employed to study this local buckling behavior. They are different from the conventional buckling equations used in most previous studies and based on the classical structural mechanics of beams and plates. A system of homogeneous Cauchy-type singular integral equations of the second kind is formulated by means of the Fourier integral transform and is solved numerically by utilizing Gauss-Chebyshev integral formulae. Numerical results for the buckling load and shape are presented for various delamination geometries and material properties of both the layer and half-space.

1 Introduction

Embedded delaminations are a kind of damage being frequently observed in composite laminates due to either manufacturing processes or low-velocity lateral impact. Such damage may significantly reduce the load-carrying capacity of composite structures under compressive loads even though it has little influence on their tensile strength. Once an embedded delamination is sufficiently large, local buckling of sublaminates may occur at relative small compressive loads. Finally, the delamination may grow under post-buckling stage, thereby leading to the loss of global stability of the structure. Thus a better understanding of the strength reduction due to the presence of embedded delaminations is quite important to the design of composite structures.

Many investigations have been performed to clarify the influence of delaminations on the compressive strength of composite laminates (for example, Chai, Babcock, and Knauss, 1981; Whitcomb, 1981; Bottega and Maewal, 1983; Yin, Sallam, and Simitses, 1984; Rothschilds, Gillespie, and Carlsson, 1988; Peck and Springer, 1991; Kutlu and Chang, 1992). Most of them have employed the classical structural mechanics theory of beams and plates to estimate the buckling loads. Such approximate analyses greatly simplify the problem and have given a good insight into the phenomenon of the delamination buckling. However, because of the limitations of the classical structural theory, boundary conditions at the edges of the delamination and effects of different material properties of the sublaminate and the substrative laminate cannot be described accurately. Hence, an exact analysis based on the precise mathematical theory of elasticity seems to be necessary.

Dorris and Nemat-Nasser (1980) and Keer, Nemat-Nasser, and Oranratnachai (1982) have utilized exact equilibrium equations for the Janmann rate of the Kirchhoff stress to estimate the buckling loads of a layer on a half-space and a half-space (or a layer) containing an array of equally spaced co-planar cracks, respectively. Recently, Madenci and Westmann (1991) and Wang et al. (1991) have solved local buckling problems of a layer containing a circular crack and a half-space containing a through-the-width crack by the use of the stability equation derived from the mathematical theory of elasticity, respectively. These exact analyses with accurate boundary conditions could evaluate buckling loads for various size of delaminations.

Furthermore, the influence of different material properties of the sublaminate and substrative laminate on the buckling loads is also important because the delaminated layer usually has different material properties from those of the substrative laminate in practical composite structures. All the existing exact analyses are limited to the case in which the delaminated layer and substrative layer or half-space have the same material properties, to date.

In the present paper, a layer bonded to a half-space with an embedded through-the-width interface crack is investigated. It is assumed that the material properties of the layer are different from those of the half-space, and their effects on the local delamination buckling behavior of composite

Contributed by the Applied Mechanics Division of THE AMERICAN SOCIETY OF MECHANICAL ENGINEERS for publication in the ASME JOURNAL OF APPLIED MECHANICS.

Discussion on this paper should be addressed to the Technical Editor, Professor Lewis T. Wheeler, Department of Mechanical Engineering, University of Houston, Houston, TX 77204-4792, and will be accepted until four months after final publication of the paper itself in the ASME JOURNAL OF APPLIED MECHANICS.

Manuscript received by the ASME Applied Mechanics Division, Feb. 26, 1993; final revision, Aug. 20, 1993. Associate Technical Editor: A. K. Noor.

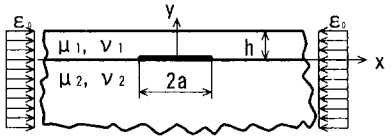

Fig. 1 A calculation model of delamination buckling

laminates are obtained based on the exact boundary and equilibrium equations of elasticity.

2 Formulation

A plane-strain problem described in Fig. 1 is considered. A layer of thickness h is perfectly bonded to a half-space, except for a through-the-width interface crack of length $2a$. The layered system is subjected to a uniform compressive strain, ϵ_0, parallel to the free surface. The μ_1 and μ_2 denote shear moduli, and ν_1 and ν_2 denote Poisson's ratios. The subscripts, $i = 1, 2$, denote the layer and half-space. It is obvious that the layered system undergoes uniform deformation until the compressive load reaches a critical value, which is usually called as a buckling load. When the compressive load increases and reaches its critical value, an adjacent equilibrium state, called as the buckled state, becomes possible. Then, the local delaminated layer deflects into a nonflat configuration and in addition to the initial uniform deformation state, incremental stresses, σ_{ij}, strains, ϵ_{ij}, and displacements along the x and y coordinate, u, and v, are induced. These increments are assumed to be infinitesimal quantities. Furthermore, we suppose an isotropic and linear relationship similar to Hook's law between the incremental stresses and strains. That is, the layer and the half-space are not necessary to be linear elastic materials.

Based on the mathematical theory of elasticity related to elastic stability (Washizu, 1968; Flugge, 1972), equilibrium equations for buckling may be expressed in terms of displacement increments and the compressive load, P_i, as

$$2(1-\nu_i)\frac{\partial^2 u_i}{\partial x^2} + (1-2\nu_i)\frac{\partial^2 u_i}{\partial y^2} + \frac{\partial^2 v_i}{\partial x \partial y} - \frac{P_i(1-2\nu_i)}{\mu_i}\frac{\partial^2 u_i}{\partial x^2} = 0,$$

$$2(1-\nu_i)\frac{\partial^2 v_i}{\partial y^2} + (1-2\nu_i)\frac{\partial^2 v_i}{\partial x^2} + \frac{\partial^2 u_i}{\partial x \partial y} - \frac{P_i(1-2\nu_i)}{\mu_i}\frac{\partial^2 v_i}{\partial x^2} = 0, \quad (i = 1, 2), \quad (1)$$

where, here is no body force and

$$P_1 = \frac{2\mu_1}{1-\nu_1}\epsilon_0,$$

$$P_2 = \frac{\mu_2}{\mu_1}\frac{1-\nu_1}{1-\nu_2}P_1. \quad (2)$$

Equation (1) is reduced to the conventional equilibrium equations before buckling if the load P_i are equal to zero. Here it should be pointed out that the material constants μ_i and ν_i would be the functions of the compressive load P_i and the μ_i would be the tangent shear modulus (Timoshenko and Gere, 1961) if the layer and half-space are not linear elastic materials.

The solution of the above differential Eq. (1) can be written (Wang et al., 1991) as

$$u_i = -\frac{\partial^2 \varphi_i}{\partial x \partial y},$$

$$v_i = \left[2(1-\nu_i) - \frac{P_i}{\mu_i}(1-2\nu_i)\right]\frac{\partial^2 \varphi_i}{\partial x^2} + (1-2\nu_i)\frac{\partial^2 \varphi_i}{\partial y^2}, \quad (3)$$

by introducing displacement functions, φ_i, $i = 1, 2$, and expressing them as

$$\varphi_1(x,y) = \frac{2}{\pi}\int_0^\infty \left(A_1 e^{t\alpha_{11}y} + B_1 e^{t\alpha_{12}y} + C_1 e^{-t\alpha_{11}y} + D_1 e^{-t\alpha_{12}y}\right)\cos(tx)\,dt,$$

$$\varphi_2(x,y) = \frac{2}{\pi}\int_0^\infty \left(A_2 e^{t\alpha_{21}y} + B_2 e^{t\alpha_{22}y}\right)\cos(tx)\,dt, \quad (4)$$

where α_{ij}, $i, j = 1, 2$, are four characteristic roots and are functions of both the compressive load P_i and material constants as follows:

$$\alpha_{i1} = \sqrt{1 - \frac{P_i(1-2\nu_i)}{2\mu_i(1-\nu_i)}},$$

$$\alpha_{i2} = \sqrt{1 - \frac{P_i}{\mu_i}}. \quad (5)$$

It can be easily demonstrated that the displacement increments expressed by Eq. (3) together with Eqs. (4) and (5) satisfy the conditions at infinity, that is $\sigma_{ij} = 0$, too.

Substituting from Eq. (4) into Eq. (3) and using the relations between the strain and displacement increments and the isotropic one between the stress and strain increments lead to the displacement and stress increments corresponding to the layer ($i = 1$) and the half-space ($i = 2$) as follows:

$$u_i = \frac{2}{\pi}\int_0^\infty t^2\left(A_i\alpha_{i1}e^{t\alpha_{i1}y} + B_i\alpha_{i2}e^{t\alpha_{i2}y} - C_i\alpha_{i1}e^{-t\alpha_{i1}y} - D_i\alpha_{i2}e^{-t\alpha_{i2}y}\right)\sin(tx)\,dt,$$

$$v_i = -\frac{2}{\pi}\int_0^\infty t^2\left(A_i\alpha_{i1}^2 e^{t\alpha_{i1}y} + B_i e^{t\alpha_{i2}y} + C_i\alpha_{i1}^2 e^{-t\alpha_{i1}y} + D_i e^{-t\alpha_{i2}y}\right)\cos(tx)\,dt, \quad (6)$$

and

$$\sigma_{ix} = \frac{2}{\pi}\int_0^\infty t^3\left(A_i\alpha_{ia}t^{t\alpha_{i1}y} + B_i\alpha_{ib}e^{t\alpha_{i2}y} - C_i\alpha_{ia}e^{-t\alpha_{i1}y} - D_i\alpha_{ib}e^{-t\alpha_{i2}y}\right)\cos(tx)\,dt,$$

$$\sigma_{iy} = \frac{2}{\pi}\int_0^\infty t^3\left(A_i\alpha_{ic}e^{t\alpha_{i1}y} + B_i\alpha_{id}e^{t\alpha_{i2}y} - C_i\alpha_{ic}e^{-t\alpha_{i1}y} - D_i\alpha_{id}e^{-t\alpha_{i2}y}\right)\cos(tx)\,dt,$$

$$\sigma_{ixy} = \frac{2}{\pi}\mu_i\int_0^\infty t^3\left[2A_i\alpha_{i1}^2 e^{t\alpha_{i1}y} + B_i(1+\alpha_{i2}^2)e^{t\alpha_{i2}y} + 2C_i\alpha_{i1}^2 e^{-t\alpha_{i1}y} + D_i(1+\alpha_{i2}^2)e^{-t\alpha_{i2}y}\right]\sin(tx)\,dt, \quad (7)$$

where

$$C_2 = 0, \quad D_2 = 0, \tag{8}$$

$$\alpha_{ia} = \frac{2\mu_i}{1-2\nu_i}\left[(1-\nu_i)\alpha_{i1} - \nu_i\alpha_{i1}^3\right],$$

$$\alpha_{ib} = 2\mu_i\alpha_{i2},$$

$$\alpha_{ic} = \frac{2\mu_i}{1-2\nu_i}\left[\alpha_{i1} - (1-\nu_i)\alpha_{i1}^3\right],$$

$$\alpha_{id} = -\alpha_{ib}, \tag{9}$$

and the remaining six unknown functions, A_1, B_1, C_1, D_1, A_2, B_2, with respect to t are determined by following continuity and boundary conditions:

$$\begin{aligned}
&\sigma_{1y}(x,h) = 0, && \sigma_{1xy}(x,h) = 0, && |x| < \infty,\\
&\sigma_{1y}(x,0) = \sigma_{2y}(x,0), && \sigma_{1xy}(x,0) = \sigma_{2xy}(x,0), && |x| < \infty,\\
&\sigma_{1y}(x,0) = \sigma_{2y}(x,0) = 0, && \sigma_{1xy}(x,0) = \sigma_{2xy}(x,0) = 0, && |x| < a,\\
&u_1(x,0) = u_2(x,0), && v_1(x,0) = v_2(x,0), && |x| > a.
\end{aligned} \tag{10}$$

Substituting from Eqs. (6) and (7) into Eq. (10) yields

$$A_1\alpha_{1c}e^{t\alpha_{11}h} + B_1\alpha_{1d}e^{t\alpha_{12}h} - C_1\alpha_{1c}e^{-t\alpha_{11}h} - D_1\alpha_{1d}e^{-t\alpha_{12}h} = 0,$$

$$2A_1\alpha_{11}^2e^{t\alpha_{11}h} + B_1(1+\alpha_{12}^2)e^{t\alpha_{12}h} + 2C_1\alpha_{11}^2e^{-t\alpha_{11}h} + D_1(1+\alpha_{12}^2)e^{-t\alpha_{12}h} = 0,$$

$$A_1\alpha_{1c} + B_1\alpha_{1d} - C_1\alpha_{1c} - D_1\alpha_{1d} = A_2\alpha_{2c} + B_2\alpha_{2d},$$

$$\mu_1\left[2A_1\alpha_{11}^2 + B_1(1+\alpha_{12}^2) + 2C_1\alpha_{11}^2 + D_1(1+\alpha_{12}^2)\right] = \mu_2\left[2A_2\alpha_{21}^2 + B_2(1+\alpha_{22}^2)\right],$$

$$\frac{2}{\pi}\int_0^\infty t^2\left[A_1\alpha_{11} - A_2\alpha_{21} + B_1\alpha_{12} - B_2\alpha_{22} - C_1\alpha_{11} - D_1\alpha_{12}\right]\sin(tx)dt = 0,$$

$$\frac{2}{\pi}\int_0^\infty t^2\left[A_1\alpha_{11}^2 - A_2\alpha_{21}^2 + B_1 - B_2 + C_1\alpha_{11}^2 + D_1\right]\cos(tx)dt = 0,$$

$$\frac{2}{\pi}\int_0^\infty t^3(A_2\alpha_{2c} + B_2\alpha_{2d})\cos(tx)dt = 0,$$

$$\frac{2}{\pi}\int_0^\infty t^3\left[2A_2\alpha_{21}^2 + B_2(1+\alpha_{22}^2)\right]\sin(tx)dt = 0. \tag{11}$$

From the above equations, we could obtain the six unknown functions. Here we will alternatively use the following two new unknown functions (Erdogan and Gupta, 1971):

$$f_u(x) = \frac{d}{dx}\left[u_1(x,0) - u_2(x,0)\right],$$

$$f_v(x) = \frac{d}{dx}\left[v_1(x,0) - v_2(x,0)\right]. \tag{12}$$

Referring to Fig. 1, it can be seen that

$$f_u(x) = 0, \quad f_v(x) = 0, \quad |x| > \alpha. \tag{13}$$

Inserting Eq. (6) into Eq. (12) and using Eq. (13) and the Fourier transform lead to

$$t^2\left[A_1\alpha_{11} - A_2\alpha_{21} + B_1\alpha_{12} - B_2\alpha_{22} - C_1\alpha_{11} - D_1\alpha_{12}\right] = F_u(t),$$

$$t^2\left[A_1\alpha_{11}^2 - A_2\alpha_{21}^2 + B_1 - B_2 + C_1\alpha_{11}^2 + D_1\right] = F_v(t), \tag{14}$$

where

$$F_u(t) = \frac{1}{t}\int_0^a f_u(\xi)\cos(t\xi)d\xi,$$

$$F_v(t) = \frac{1}{t}\int_0^a f_v(\xi)\sin(t\xi)d\xi, \tag{15}$$

From the first four equations of Eq. (11) and Eq. (14), we can express the six unknown functions in terms of $f_u(x)$ and $f_v(x)$ as follows:

$$\begin{aligned}
A_1 &= C_1R_{11}(t) + D_1R_{12}(t),\\
B_1 &= C_1R_{21}(t) + D_1R_{22}(t),\\
A_2 &= C_1R_{31}(t) + D_1R_{32}(t),\\
B_2 &= C_1R_{41}(t) + D_1R_{42}(t),\\
C_1 &= \frac{1}{t^2\Delta}\left[F_u(t)R_{62}(t) - F_v(t)R_{52}(t)\right],\\
D_1 &= \frac{1}{t^2\Delta}\left[F_v(t)R_{51}(t) - F_u(t)R_{61}(t)\right],
\end{aligned} \tag{16}$$

where,

$$\Delta = R_{51}(t)R_{62}(t) - R_{61}(t)R_{52}(t), \tag{17}$$

and R_{ij}, $(i = 1, \ldots, 6;\ j = 1, 2)$, are known functions of material constants, compressive loads and parameter t, and the details are presented in the Appendix.

Using the remaining four equations of Eq. (11) and Eqs. (14) and (15) and A_2 and B_2 in Eq. (16), and performing some routine manipulations, we can obtain a system of homogeneous Cauchy-type singular integral equations of the second kind as follows:

$$\beta_1 f_u(x) + \frac{1}{\pi}\int_{-a}^{a}\frac{f_v(\xi)}{\xi - x}d\xi + \frac{1}{\pi}\int_{-a}^{a}\left[f_u(\xi)K_{11}(\xi,x) + f_v(\xi)K_{12}(\xi,x)\right]d\xi = 0,$$

$$-\beta_2 f_v(x) + \frac{1}{\pi}\int_{-a}^{a}\frac{f_u(\xi)}{\xi - x}d\xi + \frac{1}{\pi}\int_{-a}^{a}\left[f_u(\xi)K_{21}(\xi,x) + f_v(\xi)K_{22}(\xi,x)\right]d\xi = 0,$$

$$\int_{-a}^{a} f_u(\xi)d\xi = 0, \qquad |x| < a, \tag{18}$$

where β_1 and β_2 are two known functions of material constants and compressive loads, and the kernels, K_{ij}, are also known functions and can be found in the Appendix.

It is pointed out that the third integral equation of the above Eq. (18) is derived from the fifth equation of Eq. (11) together with the first one of Eq. (14), and that the sixth equation of Eq. (11) is satisfied by the second equation of Eq. (14), and furthermore that the first two integral equations of Eq. (18) are derived from the last two equations of Eq. (11), which represent the boundary conditions along the interface crack. Generally, β_1 does not have the same value as β_2, which is quite different from the case of usual unbuckled interface crack problems with equal constants. Moreover, if the layer has the same material properties as the half-space, β_1 and β_2 are equal to zero and the kernels, K_{ij}, can be written explicitly (Wang et al., 1991).

Now, the problem described in Fig. 1 is reduced to a system of integral equations of Eq. (18). The buckling load P_{cr}, that is, the critical value of compressive stress P_1, can be determined from the condition that the integral equations have a nontrival solution. However, because of the complexity of the above integral equations, a numerical analysis is necessary to solve these equations. In the next section, the Gauss-Chebyshev integral formula will be employed to reduce the integral equations to a system of homogeneous linear algebraic equations, and then the buckling load P_{cr} and the buckling shape will be calculated.

3 Numerical Analysis

First, by changing variables as follows:

$$\xi = as, \quad x = at, \tag{19}$$

the integral equations of Eq. (18) can be rewritten as

$$\beta_1 f_u^*(t) + \frac{1}{\pi}\int_{-1}^{1} \frac{f_v^*(s)}{s-t}ds + \frac{1}{\pi}\int_{-1}^{1}\left[f_u^*(s)K_{11}^*(s,t) + f_v^*(s)K_{12}^*(s,t)\right]ds = 0,$$

$$-\beta_2 f_v^*(t) + \frac{1}{\pi}\int_{-1}^{1} \frac{f_u^*(s)}{s-t}ds + \frac{1}{\pi}\int_{-1}^{1}\left[f_u^*(s)K_{21}^*(s,t) + f_v^*(s)K_{22}^*(s,t)\right]ds = 0,$$

$$\int_{-1}^{1} f_u^*(s)ds = 0, \quad |t| < 1, \tag{20}$$

where the superscript, *, denotes the quantity after transformation. And from Eqs. (18), (19), and (20) it is clear that

$$f_u^*(s) = f_u(as), \quad f_v^*(s) = f_v(as)$$
$$K_{ij}^*(s,t) = aK_{ij}(as, at). \tag{21}$$

Next, based on the Muskhelishvili's theory (1958) related to Cauchy-type singular integrals, the general solution of the above equations can be assumed in the form of complex function as follows:

$$f_u^*(s) + if_v^*(s) = \frac{g_1^*(s) + ig_2^*(s)}{(1-s^2)^{1/2+i\gamma}}, \tag{22}$$

$$\gamma = \frac{1}{2\pi}\ln\left(\frac{1+\sqrt{\beta_1\beta_2}}{1-\sqrt{\beta_1\beta_2}}\right). \tag{23}$$

Separating the real and imaginary parts leads to (Wang, Takao and Suhara, 1988)

$$f_u^*(s) = \frac{1}{(1-s^2)^{1/2}}\left[g_1^*(s)\cos\theta - g_2^*(s)\sin\theta\right],$$

$$f_v^*(s) = \frac{1}{(1-s^2)^{1/2}}\left[g_1^*(s)\sin\theta + g_2^*(s)\cos\theta\right], \tag{24}$$

where θ is

$$\theta = -\gamma\ln(1-s^2). \tag{25}$$

Finally, substituting from Eq. (24) into integral equations of Eq. (20) and employing the Gauss-Chebyshev integral formula,

$$\frac{1}{\pi}\int_{-1}^{1}\frac{\psi(s)}{\sqrt{1-s^2}}\frac{ds}{(s-t)} = \sum_{i=1}^{n}\frac{1}{n}\psi(s_i)\frac{1}{s_i - t_k},$$

$$s_i = \cos\left(\pi\frac{2i-1}{2n}\right), \quad (i = 1, 2, \ldots, n),$$

$$t_k = \cos\left(\pi\frac{k}{n}\right), \quad (k = 1, 2, \ldots, n-1), \tag{26}$$

and the following approximation,

$$f_i^*(t_k) = \frac{1}{2}\left[f_i^*(s_k) + f_i^*(s_{k+1})\right], \quad (i = u, v) \tag{27}$$

for $f_u^*(t)$ and $f_v^*(t)$ in Eq. (20), we can reduce Eq. (20) into a system of $2m$ homogeneous algebraic equations with $2m$ discrete unknowns, $g_1^*(s_i)$ and $g_2^*(s_i)$, $(i = 1, 2, \ldots, m)$. It is noted that on account of the symmetry of $f_u^*(t)$, $f_v^*(t)$ and K_{ij}^* only half of the discrete equations or half of the discrete points will be treated, that is,

Table 1 Effect of the number, m, of algebraic equations on the calculated buckling load P_{cr}; $h/a = 0.1$, $\mu_2/\mu_1 = 10$, $\nu_1 = 0.3$, and $\nu_2 = 0.2$.

m	20	22	24	26	28	30
Pcr/μ_1	0.02279	0.02263	0.02252	0.02239	0.02228	0.02226

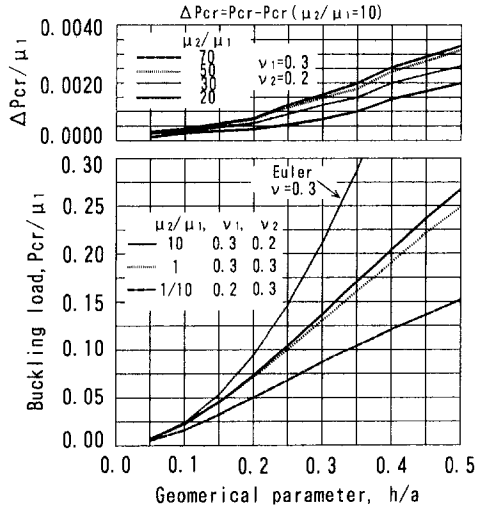

Fig. 2 Small change of buckling load ΔP_{cr} with geometrical parameter, h/a, for $\mu_1 < \mu_2$

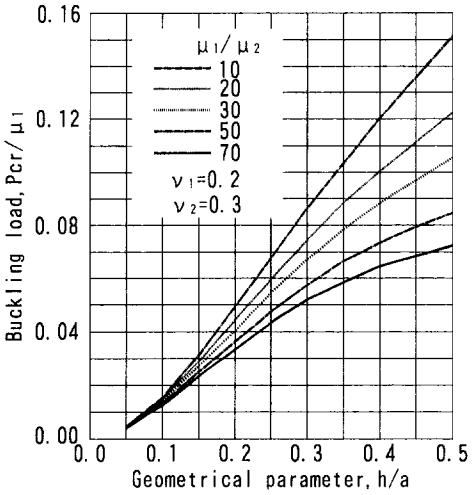

Fig. 3 Variation of buckling load P_{cr} with geometrical parameter, h/a, for $\mu_1 > \mu_2$

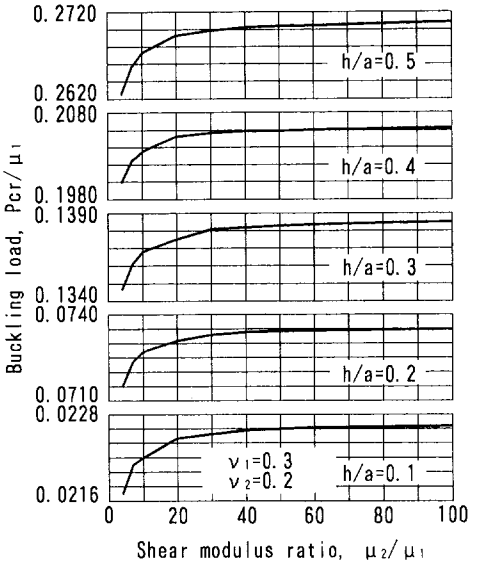

Fig. 4 Variation of buckling load with shear modulus ratio, for $\mu_1 < \mu_2$

$$s_i = \cos\left(\pi\frac{2i-1}{4m}\right), \quad (i = 1, 2, \ldots, m),$$

$$t_k = \cos\left(\pi\frac{k}{2m}\right), \quad (k = 1, 2, \ldots, m-1). \qquad (28)$$

The details of the algebraic equations are not shown in this paper.

We can obtain the buckling load P_{cr} from the condition that the determinant of the matrix formed by the coefficients of the homogeneous algebraic equations must be zero. The nontrivial solution of $g_1^*(s_i)$ and $g_2^*(s_i)$ can be reached, although they contain an arbitrary constant. Furthermore, when substituting Eq. (24) into the following equation

$$\delta v(x,0) = v_1(x,0) - v_2(x,0) = -a\int_t^1 f_v^*(s)ds, \quad (29)$$

which is derived from the second equation of Eq. (12), we can calculate the deflection difference. This can be regarded as the buckling shape at the buckling load P_{cr}, because the deflection of the half-space is negligible compared to the one of the buckled layer.

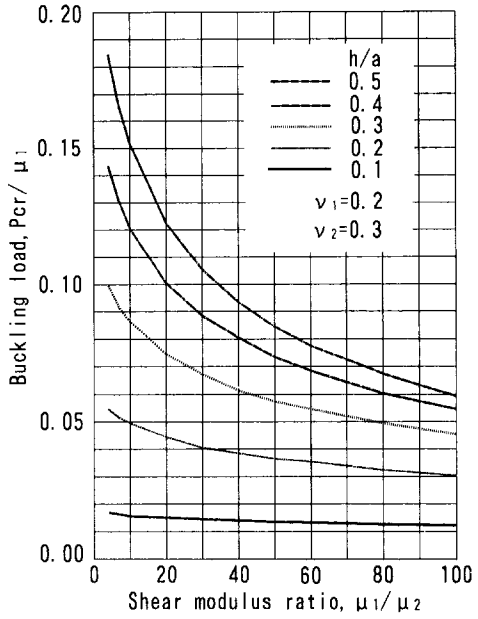

Fig. 5 Variation of buckling load with shear modulus ratio, for $\mu_1 > \mu_2$

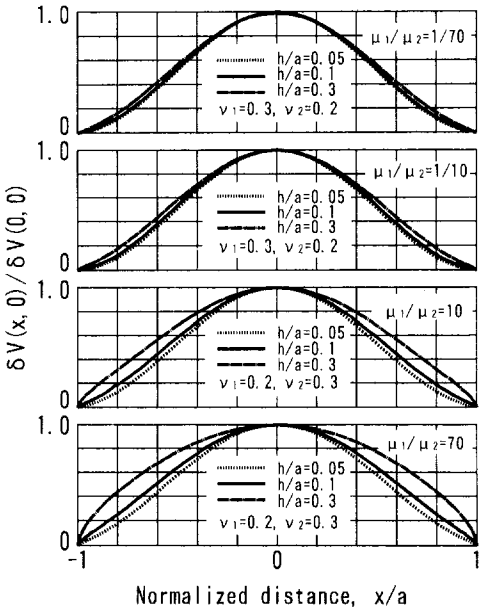

Fig. 6 Buckling shapes for various h/a and μ_1/μ_2

4 Results and Discussions

Numerical results for the buckling load and shape of the delaminated layer are presented in Table 1 and Figs. 2 to 6. Here the layer and substrative half-space are assumed to be linear elastic materials. The influence of the stiffness ratio of a delaminated layer to a substrative half-space, μ_1/μ_2, on the buckling loads are specially emphasized, which cannot be considered in the previous literature.

Table 1 exhibits the effect of the number of discrete algebraic equations on the calculated buckling load, P_{cr}, where m, as given in Eq. (28), denotes the number of algebraic equations. The geometrical parameter is taken as $h/a = 0.1$ and the material constants are taken as $\mu_2/\mu_1 = 10$, $\nu_1 = 0.3$, and $\nu_2 = 0.2$. It is seen that a good convergence is achieved with m increasing and a reasonable result is obtained with $m = 30$, which is employed in the following calculation.

Buckling loads are shown as a function of geometrical parameter, h/a, in Figs. 2 and 3 for various shear modulus ratios. The Euler's solution (Timoshenko and Gere, 1961) with clamped ends is also presented in Fig. 2 for a comparison and is close to the present results of $\mu_1 < \mu_2$ for small h/a, which means large delaminations. It is obvious that the dimensionless buckling load, P_{cr}/μ_1, increases with increasing h/a in both figures. However, the influence of shear modulus ratios on the buckling load seems to be quite different. In Fig. 2, where the curve of $\mu_2/\mu_1 = 10$ is again presented, an increasing μ_2 ($\mu_2 > \mu_1$) has little influence on the buckling load, while a decreasing μ_2($\mu_2 < \mu_1$) greatly reduces the load-bearing capacity of the delaminated layer in Fig. 3. These phenomena deserve the careful consideration in the design of composite structures. It is pointed out that most of conventional metals, plastics, and composites have their buckling loads below ten percent of their shear moduli, only few hypoelastic materials, such as rubber system materials, might have their buckling loads beyond ten percent of their shear moduli. More detail information about the influence of shear modulus ratios can be found in Figs. 4 and 5. Figure 4 shows that the buckling loads are almost constant for $\mu_2/\mu_1 > 40$ and any h/a. The buckling loads in Fig. 5 decrease rapidly with increasing μ_1/μ_2 for $\mu_1 > \mu_2$ and relatively large h/a.

Figure 6 describes the dimensionless deflection difference between the crack surfaces, $\delta v(x, 0) = v_1(x, 0) - v_2(x, 0)$, which could be the buckling deflection of the delaminated layer. These curves are close to the buckling shape with clamped ends for small μ_1/μ_2 or h/a.

References

Bottega, W. J., and Maewal, A., 1983, "Delamination Buckling and Growth in Laminates," ASME JOURNAL OF APPLIED MECHANICS, Vol. 50, pp. 184–189.

Chai, H., Babcock, C. D., and Knauss, W. G., 1981, "One-Dimensional Modeling of Failure in Laminated Plates by Delamination Buckling," *Int. J. Solids Structures*, Vol. 17, pp. 1069–1083.

Dorris, J. F., and Nemat-Nasser, S., 1980, "Instability of a Layer on a Half Space," ASME JOURNAL OF APPLIED MECHANICS, Vol. 47, pp. 304–312.

Erdogan, F., and Gupta, G. D., 1971, "Layered Composites with an Interface Flaw," *Int. J. Solids and Structures*, Vol. 7, pp. 1089–1107.

Flugge, W., 1972, *Tensor Analysis and Continuum Mechanics*, Springer-Verlag, New York.

Keer, L. M., Nemat-Nasser, S., and Oranratnachai, A., 1982, "Surface Instability and Splitting in Compressed Brittle Elastic Solids Containing Crack Arrays," ASME JOURNAL OF APPLIED MECHANICS, Vol. 49, pp. 761–767.

Kutlu, Z., and Chang, F. K., 1992, "Modeling Compression Failure of Laminated Composites Containing Multiple Through-the-Width Delaminations," *Journal of Composite Materials*, Vol. 26, pp. 350–387.

Madenci, E., and Westmann, R. A., 1991, "Local Delamination Buckling in Layered Systems," ASME JOURNAL OF APPLIED MECHANICS, Vol. 47, pp. 157–166.

Muskhelishvili, N. I., 1958, *Singular Integral Equations*, (revised translation from Russian; edited by J. R. M. Radok), P. Noordhoff, Holland.

Peck, S. O., and Springer, G. S., 1991, "The Behavior of Delaminations in Composite Plates—Analytical and Experimental Results," *Journal of Composite Materials*, Vol. 25, pp. 907–929.

Rothschilds, R. J., Gillespie, Jr., J. W., and Carlsson, L. A., 1988, "Instability-Related Delamination Growth in Thermoset and Thermoplastic Composites," ASTM STP 972, pp. 161–179.

Timoshenko, S. P., and Gere, J. M., 1961, *Theory of Elastic Stability*, McGraw-Hill, New York.

Wang, W. X., Shen, W., Takao, Y., Shen, Z., and Chen, P., 1991, "An Analysis of Compressive Stability of Elastic Solids Containing a Crack Parallel to the Surface," *Eng. Fract. Mech.*, Vol. 40, pp. 1023–1033.

Wang, W. X., Takao, Y., and Suhara, T., 1988, "Interaction Between Cracks Perpendicular to and on the Interface in Composite Materials," *JSME International Journal, I*, Vol. 31, pp. 201–208.

Washizu, K., 1968, *Variational Methods in Elasticity and Plasticity*, Pergamon Press, London.

Whitcomb, J. D., 1981, "Finite Element Analysis of Instability Related Delamination Growth," *Journal of Composite Materials*, Vol. 15, pp. 403–426.

APPENDIX

In Eqs. (16) and (17), the functions R_{ij}, ($i = 1, \ldots, 6$; $j = 1, 2$), are related to the material constants, compressive loads, and parameter t as follows:

$$R_{11}(t) = \frac{1}{\Delta t}\left[\alpha_{1c}(1+\alpha_{12}^2) + 2\alpha_{1d}\alpha_{11}^2\right]e^{-2t\alpha_{11}h},$$

$$R_{12}(t) = \frac{2}{\Delta_1}\alpha_{1d}(1+\alpha_{12}^2)e^{-t(\alpha_{11}+\alpha_{12})h},$$

$$R_{21}(t) = -\frac{4}{\Delta_1}\alpha_{1c}\alpha_{11}^2 e^{-t(\alpha_{11}+\alpha_{12})h},$$

$$R_{22}(t) = -\frac{1}{\Delta_1}\left[\alpha_{1c}(1+\alpha_{12}^2) + 2\alpha_{1d}\alpha_{11}^2\right]e^{-2t\alpha_{12}h},$$

$$R_{31}(t) = \frac{1}{\Delta_2}\left[a_{11}R_{11}(t) + a_{12}R_{21}(t) + a_{13}\right],$$

$$R_{32}(t) = \frac{1}{\Delta_2}\left[a_{21}R_{12}(t) + a_{22}R_{22}(t) + a_{23}\right],$$

$$R_{41}(t) = \frac{1}{\Delta_2}\left[a_{31}R_{11}(t) + a_{32}R_{21}(t) + a_{33}\right],$$

$$R_{42}(t) = \frac{1}{\Delta_2}\left[a_{41}R_{12}(t) + a_{42}R_{22}(t) + a_{43}\right],$$

$$R_{51}(t) = \left[\alpha_{11}R_{11}(t) + \alpha_{12}R_{21}(t) - \alpha_{21}R_{31}(t) - \alpha_{22}R_{41}(t) - \alpha_{11}\right],$$

$$R_{52}(t) = \left[\alpha_{11}R_{12}(t) + \alpha_{12}R_{22}(t) - \alpha_{21}R_{32}(t) - \alpha_{22}R_{42}(t) - \alpha_{12}\right],$$

$$R_{61}(t) = \left[\alpha_{11}^2R_{11}(t) + R_{21}(t) - \alpha_{21}^2R_{31}(t) - R_{41}(t) + \alpha_{11}^2\right],$$

$$R_{62}(t) = \left[\alpha_{11}^2R_{12}(t) + R_{22}(t) - \alpha_{21}^2R_{32}(t) - R_{42}(t) + 1\right], \quad \text{(A1)}$$

where

$$\Delta_i = \alpha_{ic}(1+\alpha_{i2}^2) - 2\alpha_{id}\alpha_{i1}^2, \quad (i = 1, 2), \quad \text{(A2)}$$

$$a_{11} = \alpha_{1c}(1+\alpha_{22}^2) - 2\alpha_{2d}\alpha_{11}^2\frac{\mu_1}{\mu_2},$$

$$a_{12} = \alpha_{1d}(1+\alpha_{22}^2) - \alpha_{2d}(1+\alpha_{12}^2)\frac{\mu_1}{\mu_2},$$

$$a_{13} = -\left[\alpha_{1c}(1+\alpha_{22}^2) + 2\alpha_{2d}\alpha_{11}^2\frac{\mu_1}{\mu_2}\right],$$

$$a_{21} = a_{11},$$

$$a_{22} = a_{12},$$

$$a_{23} = -\left[\alpha_{1d}(1+\alpha_{22}^2) + \alpha_{2d}(1+\alpha_{12}^2)\frac{\mu_1}{\mu_2}\right],$$

$$a_{31} = 2\alpha_{2c}\alpha_{11}^2\frac{\mu_1}{\mu_2} - 2\alpha_{1c}\alpha_{21}^2,$$

$$a_{32} = \alpha_{2c}(1+\alpha_{12}^2)\frac{\mu_1}{\mu_2} - 2\alpha_{1d}\alpha_{21}^2,$$

$$a_{33} = 2\alpha_{2c}\alpha_{11}^2\frac{\mu_1}{\mu_2} + 2\alpha_{1c}\alpha_{21}^2,$$

$$a_{41} = a_{31},$$
$$a_{42} = a_{32},$$
$$a_{43} = \alpha_{2c}\left(1 + \alpha_{12}^2\right)\frac{\mu_1}{\mu_2} + 2\alpha_{1d}\alpha_{21}^2. \tag{A3}$$

In Eq. (18), the functions of β_1 and β_2 and the kernels, K_{ij}, are expressed as follows:

$$\beta_1 = \frac{Q_{11}^{\infty}}{Q_{12}^{\infty}}, \quad \beta_2 = \frac{Q_{22}^{\infty}}{Q_{21}^{\infty}}, \tag{A4}$$

$$K_{11}(\xi, x) = \frac{1}{Q_{12}^{\infty}}\int_0^{\infty}\left[Q_{11}(t) - Q_{11}^{\infty}\right]\cos(t\xi)\cos(tx)dt,$$
$$K_{12}(\xi, x) = \frac{1}{Q_{12}^{\infty}}\int_0^{\infty}\left[Q_{12}(t) - Q_{12}^{\infty}\right]\sin(t\xi)\cos(tx)dt,$$
$$K_{21}(\xi, x) = -\frac{1}{Q_{21}^{\infty}}\int_0^{\infty}\left[Q_{21}(t) - Q_{21}^{\infty}\right]\cos(t\xi)\sin(tx)dt,$$
$$K_{22}(\xi, x) = -\frac{1}{Q_{21}^{\infty}}\int_0^{\infty}\left[Q_{22}(t) - Q_{22}^{\infty}\right]\sin(t\xi)\sin(tx)dt, \tag{A5}$$

where

$$Q_{i1}(t) = \frac{1}{\Delta}\left[N_{i1}(t)R_{62}(t) - N_{i2}(t)R_{61}(t)\right],$$
$$Q_{i2}(t) = \frac{1}{\Delta}\left[N_{i2}(t)R_{51}(t) - N_{i1}(t)R_{52}(t)\right], \quad (i = 1, 2), \tag{A6}$$

$$Q_{ij}^{\infty} = \lim_{t\to\infty} Q_{ij}(t), \quad (i, j = 1, 2), \tag{A7}$$

and

$$N_{11}(t) = \alpha_{1c}R_{11}(t) + \alpha_{1d}R_{21}(t) - \alpha_{1c},$$
$$N_{12}(t) = \alpha_{1c}R_{12}(t) + \alpha_{1d}R_{22}(t) - \alpha_{1d},$$
$$N_{21}(t) = 2\alpha_{11}^2R_{11}(t) + \left(1 + \alpha_{12}^2\right)R_{21}(t) + 2\alpha_{11}^2,$$
$$N_{22}(t) = 2\alpha_{11}^2R_{12}(t) + \left(1 + \alpha_{12}^2\right)R_{22}(t) + \left(1 + \alpha_{12}^2\right). \tag{A8}$$

Stiffness Evaluation for Solids Containing Dilute Distributions of Inclusions and Microcracks

Y. Huang
Department of Aerospace and Mechanical Engineering, University of Arizona, Tucson, AZ 85721

K. X. Hu
Corporate Manufacturing Research Center, Motorola Inc., Schaumberg, IL 60196

A. Chandra
Department of Aerospace and Mechanical Engineering, University of Arizona, Tucson, AZ 85721
Mem. ASME.

Materials, such as ceramics, intermetallics, and rocks, contain varying amounts of inhomogeneities, and the matrix material is vulnerable to microcracking in the neighborhood around these inhomogeneities. In an attempt to model the micromechanical aspects of this type of material, a solid containing dilute inclusions surrounded by cracks is investigated in this paper. The dilute-inclusion assumption neglects any interactions among different inclusion-crack clusters, but local inclusion-crack and crack-crack interactions are taken into account fully. It is shown that additional strain due to microcracking in a solid containing inclusions can be represented by an integral of crack opening displacements weighted by a nonuniform stress field induced by inclusions alone (in the absence of microcracking). An effective numerical approach is then developed to evaluate the effective moduli and additional macroscopic strain due to microcracking in composites. It is found that an increase in the number of hard inclusions may not always lead to expected strengthening of the materials, if the matrix material is vulnerable to microcracking around inclusions and a relatively large microcracking zone develops. The limited calculations show that a quasi-static crack-growing process can lead to an actively growing crack being arrested or to a stationary crack starting to grow. This suggests that self-similar crack growth may not be enough to describe the behavior of microcracked composites.

Introduction

Cracks closely surrounding inhomogeneities exist in polycrystalline and multiphase materials when residual stress of sufficient magnitude develops in these materials. The residual stress can be due to a number of sources, such as thermal mismatch between phases of multiphase materials, thermal anisotropy in the single crystals of polycrystalline materials, or crystallographic transformation of particles in a ceramic matrix (Marshall et al., 1985; Rühle et al., 1986; Tvergaard and Hutchinson, 1988). In the neighborhood of a material interface, matrix cracking can create a well-developed fracture zone (e.g., Luh and Evans, 1987). One such situation, a two-dimensional solid containing inclusions, with cracks surrounding each inclusion, is illustrated in Fig. 1. The inclusions are assumed to be spaced apart from each other so that the inclusion alone is dilute. The cracks are assumed to be closely situated around the inclusion such that the inclusion-crack and crack-crack interactions are important. Based on these assumptions, we neglect the interaction between different inclusion sets, i.e., we accurately account for the interactions among cracks and the inclusion within each cluster (Fig. 1), while the interaction between clusters is neglected. The geometry shown in Fig. 1 represents a variety of practical situations, such as foreign grains in metamorphic rocks, second-phase particles in metals, or intermetallics and zirconia-containing ceramics. In the continuum modeling of the constitutive behavior of materials undergoing microcracking, the

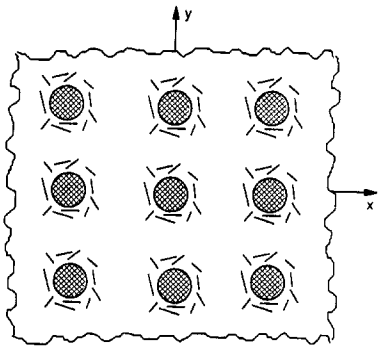

Fig. 1 A schematic diagram of a solid containing a dilute distribution of inclusions, with cracks surrounding the inclusions

Contributed by the Applied Mechanics Division of THE AMERICAN SOCIETY OF MECHANICAL ENGINEERS for publication in the ASME JOURNAL OF APPLIED MECHANICS.

Discussion on this paper should be addressed to the Technical Editor, Professor Lewis T. Wheeler, Department of Mechanical Engineering, University of Houston, Houston, TX 77204-4792, and will be accepted until four months after final publication of the paper itself in the ASME JOURNAL OF APPLIED MECHANICS.

Manuscript received by the ASME Applied Mechanics Division, Oct. 28, 1992; final revision, Feb. 15, 1994. Associate Technical Editor: G. J. Dvorak.

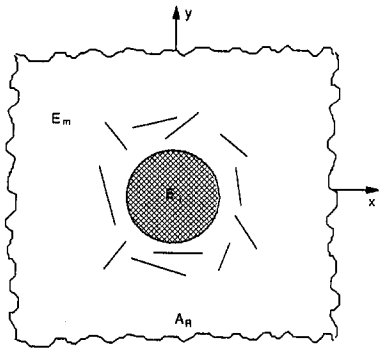

Fig. 2 A schematic diagram of the fundamental problem—an infinite solid containing a single inclusion surrounded by matrix cracks

primary quantities of interest are the effective moduli of these microcracked materials and additional strains that show up at the macroscopic level due to microcracking. For general stress, Σ_{kl}, imposed on the composite, the corresponding total macroscopic strain contribution, E_{ij}, due to a volume fraction, ρ, of particles is simply (e.g., Hutchinson, 1987)

$$E_{ij} = E_{ij}^0 + \rho \Delta E_{ij}, \tag{1}$$

where E_{ij}^0 is the macroscopic strain corresponding to Σ_{kl} imposed on the uncracked composite, i.e., a matrix containing dilute distributions of inclusions only (no cracks); and ΔE_{ij} represents the additional strain, or strain increase, per *unit volume* of particle due to the existence of interacting cracks around an inclusion for the same applied stress Σ_{kl}; ΔE_{ij} is to be obtained by solving the fundamental problem shown in Fig. 2; i.e., for an infinite body containing a cluster (a single inclusion, of *unit volume*, surrounded by cracks),

$$\Delta E_{ij} = \frac{1}{2}\int_{A_R} \left\{ \left(u_i - u_i^0\right) n_j + \left(u_j - u_j^0\right) n_i \right\} dA, \tag{2}$$

where A_R and n_i denote the outer boundary and normal of the matrix, respectively; u_i denotes the displacement along A_R due to applied stress Σ_{kl} in the presence of a particle and cracks; and u_i^0 denotes the displacement along A_R due to the same applied stress Σ_{kl} in the absence of cracks but in the presence of a particle. In general, the microcracked composites behave anisotropically due to the distribution pattern of the microcrack.

It should be noted that, due to the interaction between the inclusion and the cracks, no direct expression, such as that presented by Hill (1965) and Kachanov (1987), exists for ΔE_{ij}. In the following presentation, we derive a formula for the evaluation of additional macroscopic strain due to cracks for a solid containing inclusions and cracks. While the formula for evaluation of additional strain due to cracks is valid for the three-dimensional case, numerical results are presented only for a two-dimensional solid containing a dilute distribution of inclusions surrounded by cracks.

Numerical Evaluation of Additional Macroscopic Strains, ΔE_{ij}

While the formal definition of ΔE_{ij} in Eq. (2) involves a surface integral over the outer surface, A_R, in Fig. 2, it is more feasible for numerical purposes to evaluate ΔE_{ij} over the microcrack surfaces. This reformulation requires that we consider two separate elasticity problems of a particle inside an infinite matrix, where both particle and matrix are assumed to possess elastic isotropy.

Auxiliary Problem. The geometry of this auxiliary problem is that given in Fig. 2, except that the cracks are absent. Loading is applied via auxiliary uniform remote stresses, $\mathfrak{S}_{kl}^{\infty}$. The resultant field quantities of stresses, strains, and displacements everywhere are denoted as $\mathfrak{S}_{ij}$, $\mathfrak{E}_{ij}$, and $\mathfrak{U}_i$. They are readily available in closed form as given by Muskhelishvili (1953). While this problem has no direct bearing on the definition of ΔE_{ij}, the solution to this problem will allow backing-out values of ΔE_{ij} and facilitate evaluation of the effective moduli in a manner that will become apparent later.

Main Problem. Let the resultant field quantities of stresses, strains, and displacements everywhere in the solid with the inclusion and cracks (Fig. 2) due to remote loading Σ_{kl} (generally different from $\mathfrak{S}_{kl}^{\infty}$) be denoted as σ_{ij}, ϵ_{ij}, and u_i; determination of these quantities will be addressed later. The corresponding quantities in the absence of cracks due to the same remote loading Σ_{kl} are denoted as σ_{ij}^0, ϵ_{ij}^0, and u_i^0 and may be evaluated in a fashion similar to that used for the auxiliary problem.

Reformulation of ΔE_{ij} begins with premultiplication of Eq. (2) with stresses $\mathfrak{S}_{ij}^{\infty}$ of the auxiliary problem such that

$$\mathfrak{S}_{ij}^{\infty}\Delta E_{ij} = \frac{1}{2}\int_{A_R} \mathfrak{S}_{ij}\left\{ \left(u_i - u_i^0\right) n_j + \left(u_j - u_j^0\right) n_i \right\} dA. \tag{3}$$

Keeping in mind that the stresses $\mathfrak{S}_{ij}$ are symmetric and in equilibrium, and making use of the following notation,

$$\delta_i^k = u_i^{k+} - u_i^{k-}$$

$$= \text{opening of the } k\text{th crack due to remote stress } \Sigma_{kl}$$

$$A_c^{k+},\ A_c^{k-} = \text{top and bottom surfaces of the } k\text{th crack}, \tag{4}$$

it follows directly from successive applications of both the reciprocity and divergence theorems that

$$\mathfrak{S}_{ij}^{\infty}\Delta E_{ij} = \int_V \mathfrak{S}_{ij}\left(\epsilon_{ij} - \epsilon_{ij}^0\right) dV + \sum_k \int_{A_c^{k+}} \mathfrak{S}_{ij}\delta_i^k n_j dA, \tag{5}$$

where the unit normal vector, n_j, in the crack face integral points into the matrix.

A straightforward application of the reciprocity theorem for the volume integral similarly gives

$$\int_V \mathfrak{S}_{ij}\left(\epsilon_{ij} - \epsilon_{ij}^0\right) dV = \int_V \mathfrak{E}_{ij}\left(\sigma_{ij} - \sigma_{ij}^0\right) dV. \tag{6}$$

The volume integral in Eq. (5) can thus be transformed, using the divergence theorem, into two surface integrals of the form

$$\int_V \mathfrak{S}_{ij}\left(\epsilon_{ij} - \epsilon_{ij}^0\right) dV = \int_{A_R} \left(\sigma_{ij} - \sigma_{ij}^0\right) \mathfrak{U}_i n_j dA$$

$$- \sum_k \int_{A_c^{k\ell}} \left(\sigma_{ij} - \sigma_{ij}^0\right) \mathfrak{U}_i n_j dA. \tag{7}$$

By keeping in mind the fact that

$$\text{on } A_R, \quad \sigma_{ij} = \sigma_{ij}^0 \tag{8}$$

$$\text{on } A_c^{k\pm}, \quad \sigma_{ij} n_j = 0, \quad \left(\sigma_{ij}^0\right)^+ = \left(\sigma_{ij}^0\right)^-, \quad \mathfrak{U}_i^+ = \mathfrak{U}_i^-, \tag{9}$$

the integral over the volume V in Eq. (7) is identically zero. Finally, Eq. (3) takes the form

$$\mathfrak{S}_{ij}^{\infty}\Delta E_{ij} = \sum_k \int_{A_c^{k+}} \mathfrak{S}_{ij}\delta_i^k n_j dA. \tag{10}$$

It should be emphasized that Eq. (10) also holds for a solid containing nondilute inclusions, since the derivation of Eq. (10) does not impose any restrictions on the distribution of inclusions. Recently, Fares (1993) presented an approach for the decomposition of the overall concentration factor into

contributions from the crack opening and those from material inhomogeneities. Alternatively, Eq. (10) may be obtained by specializing Fares' finite deformation formulation to the case of small strain. For nondilute inclusions, the solution of $\mathcal{S}_{ij}$, which is often a difficult and challenging task, would be required. The reason for solving the auxiliary problem is now clear: by evaluating Eq. (10) using the solutions to the auxiliary problem corresponding to auxiliary loading

$$\mathcal{S}_{11}^{\infty} = \mathcal{S}_{22}^{\infty} = 1, \tag{11}$$

the integral expression in Eq. (10) reduces to the two-dimensional additional macroscopic dilatational strain, $\Delta E_{11} + \Delta E_{22}$ due to applied stress Σ_{kl}. By evaluating Eq. (10) using the solutions to the auxiliary problem where the only nonzero component of the auxiliary uniform remote stresses is $\mathcal{S}_{22}^{\infty} = 1$, the integral expression in Eq. (10) reduces to the additional macroscopic uniaxial strain, ΔE_{22}, due to the same applied stress Σ_{kl}. Therefore, the aim of the auxiliary problem is only to obtain the corresponding component of the additional macroscopic strain, and the auxiliary loading $\mathcal{S}_{kl}^{\infty}$ and remote stress Σ_{kl} imposed on the composite are completely independent.

It is important to note that Eq. (10) is equivalent to that of Hill (1965) and Kachanov (1987) when the inclusion and matrix share the same material properties such that $\mathcal{S}_{ij} = \mathcal{S}_{ij}^{\infty}$. For inhomogeneous inclusions, $\mathcal{S}_{ij}$ is not the same as $\mathcal{S}_{ij}^{\infty}$ in the auxiliary problem. In general, there is no simple analytical expression of $\mathcal{S}_{ij}$ for nondilute inclusions in a solid. However, in the case of dilute distributions of inclusions, the solution of $\mathcal{S}_{ij}$ for various remote loadings can be found in Muskhelishvili (1953) for a single inclusion embedded in a solid. In what follows, we will focus on the case of a dilute distribution of inclusions.

Evaluation of the Crack-Opening Displacements

For a solid containing a single inclusion surrounded by cracks, solutions due to remote loading Σ_{kl} have been obtained based on a method described by Hu et al. (1993a), who give the details of the numerical procedure and investigate various composite toughening mechanisms. As applied in the present context, this method involves formulating the singular integral equations governing the traction-free conditions on the microcrack faces, where the kernel of the singular integral equations is associated with the stress field due to a unit dislocation outside a circular inclusion embedded in an infinite matrix given by Dundurs and Mura (1964) and Erdogan et al. (1974). Hence, interactions among cracks and the inclusion are accounted for accurately. The unknown functions that arise naturally in this formulation are dislocation densities of each crack defined as

$$b_t^i = \frac{d\delta_t^i}{dt^{(i)}} \tag{12a}$$

$$b_s^i = \frac{d\delta_s^i}{dt^{(i)}}, \tag{12b}$$

where $(t^{(i)}, s^{(i)})$ is a local Cartesian coordinate defined such that $t^{(i)}$ is aligned along the ith crack, and occupancy of the ith crack is $-a^{(i)} < t^{(i)} < a^{(i)}$ [$a^{(i)}$ is the half-length of the ith crack]; $s^{(i)}$ is normal to the ith crack; δ_t^i and δ_s^i are the openings of the ith crack in the $t^{(i)}$ and $s^{(i)}$ directions; and b_t^i and b_s^i are the corresponding dislocation densities of the ith crack and are obtained by solving the singular integral equations governing the traction-free conditions on the crack surface. Then, the stresses and strains in the fractured solid can be evaluated through the integration of dislocation densities with the Green's function. Stress intensity factors at all crack tips can be evaluated according to an extrapolation scheme derived by Krenk (1975). The required quantities of primary interest, as shown in Eq. (10), are the crack-opening displacements, δ_x^k and δ_y^k, which are obtainable through the direct integration, over each crack, of the dislocation densities in Eqs. (12*a*) and (12*b*). The macroscopic strain increase can then be evaluated according to Eq. (10). Such an approach can provide very accurate effective properties. We have obtained the crack opening volume for a collinear crack system with a relative error of less than four percent, compared to the closed-form solutions (Erdogan, 1962), using 30 Gauss points on each crack, with the separation of crack tips equal to five percent of the crack length.

Effective Moduli of a Solid Containing a Dilute Distribution of Inclusions Surrounded by Cracks

For a solid containing dilute inclusions surrounded by cracks, the strain E_{ij} is related to the stress Σ_{kl} imposed on the solid by

$$E_{ij} = S_{ijkl}\Sigma_{kl}, \tag{13}$$

where S_{ijkl} is the effective compliance of the solid to be determined. On the other hand, as in Eq. (1), the strain can be evaluated in terms of the strain E_{ij}^0 in the uncracked solid containing dilute inclusions subject to Σ_{kl} and the additional strain, ΔE_{ij}, due to microcracks surrounding the inclusions for the same remote stress Σ_{kl}.

Comparing Eqs. (1) and (13), we have

$$S_{ijkl}\Sigma_{kl} = E_{ij}^0 + \rho\Delta E_{ij}. \tag{14}$$

Equation (14) provides a way of evaluating effective properties of the solid containing dilute inclusions surrounded by cracks. For example, let the solid be subject to plane-strain tension, Σ_{22}, and note that the left-hand side of Eq. (14) becomes $\Sigma_{22}/\bar{E}_2$, where $\bar{E}_2$ is the plane-strain Young's modulus in the x_2 direction. Equation (14) gives

$$\frac{1}{\bar{E}_2} = \frac{1}{\bar{E}_0} + \rho\frac{\Delta E_{22}}{\Sigma_{22}}, \tag{15}$$

where $\bar{E}_0$ is the plane-strain Young's modulus of the solid containing dilute inclusions with no cracks and ΔE_{22} is the additional strain due to microcracking subject to plane-strain tension Σ_{22}. The additional strain, ΔE_{22}, can be obtained from Eq. (10) by taking the auxiliary loading as $\mathcal{S}_{22}^{\infty} = 1$, others = 0. The evaluation of $\bar{E}_0$ is given in the Appendix.

Numerical Results and Discussion

The additional strain and effective elastic moduli of microcracked composites are presented in this section through two examples. Figure 3(*a*) shows an array of radial cracks surrounding an inclusion. The cracks are of equal length and are spaced apart from each other at an angle of 45 deg. A remote biaxial loading ($\sigma_x = \sigma_y = \sigma_0$) is applied to the system in order to obtain the two-dimensional additional macroscopic dilatational strain, $\Delta E_{11} + \Delta E_{22}$. The Poisson's ratios of the inclusions and matrix are taken as 0.3. We consider a particular case where the crack length equals the inclusion diameter, $R = a$. The ratios of inclusion-to-matrix modulus are taken as $E_i/E_m = 0.25$, 1.0, and 4.0. Shown in Fig. 3(*b*) is the variation of two-dimensional dilatational strain increase ($\Delta E_{11} + \Delta E_{22}$), with spacing $d/R - 2$ between the centers of the inclusion and crack, where the normalization factor, σ_0/E_m, is on the order of the remote strain. Recall that $\Delta E_{11} + \Delta E_{22}$ is the additional strain per unit volume (area for the two-dimensional case) that is attributed to the cracks.

For a fixed ratio of the inclusion diameter over crack length ($R/a = 1$) and the present inclusion-crack distribution

pattern, the spacing d characterizes how the inclusion and cracks are clustered together. For large spacing, i.e., inclusion and cracks are far apart, the interactions among the inclusion and cracks are weak and all three curves are asymptotes to the same limit. This asymptotic additional dilatational strain tends to approach the stable, noninteracting solution as spacing d increases. It must be pointed out that this limiting value, though not depending on the inclusion/matrix modulus ratio, E_i/E_m, when the inclusion and cracks are far apart, does depend approximately linearly on the number of cracks surrounding the inclusion (8 in this pattern). The contribution to $\Delta E_{11} + \Delta E_{22}$ from each crack in general is $2(1 - \nu_m^2)(\sigma_0 a^2/E_m R^2)$, accounting for the total stable value of $16(1 - \nu_m^2)$ (which is not fully reached at $d/R = 6$).

As the inclusion and cracks are clustered together, the inclusion-crack and crack-crack interactions become strong. In general, the additional strain, $\Delta E_{11} + \Delta E_{22}$, decreases, except for the case of a soft inclusion ($E_i/E_m = 0.25$) and a small spacing ($d/R < 3$). The decrease in $\Delta E_{11} + \Delta E_{22}$ for homogeneous inclusions, i.e., $E_i/E_m = 1$, indicates that the crack-crack interaction tends to resist the average crack opening and reduces $\Delta E_{11} + \Delta E_{22}$.

The large deviations in $\Delta E_{11} + \Delta E_{22}$ among three curves at small spacings (small ratios of d/R) reflect the inclusion-crack interaction. For hard inclusions (e.g., $E_i/E_m = 4$), the additional strain decreases even more than for homogeneous inclusions, implying that the inclusion-crack interaction enhances the resistance to average crack openings for hard inclusions. For the case of soft inclusions ($E_i/E_m = 0.25$), the inclusion-crack interaction tends to weaken this resistance by producing more additional strain. This is consistent with an extreme limit—a void ($E_i/E_m = 0$) interacting with cracks (Hu et al., 1993b). For a soft inclusion in the configuration considered here, the competition between the crack-crack interaction attempting to enhance the resistance to average crack openings and the inclusion-crack interaction attempting to weaken the resistance yields a minimum value for normalized additional strain at $d/R = 2.9$.

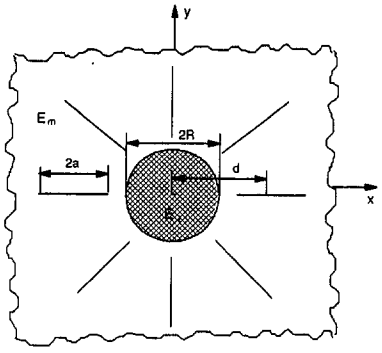

Fig. 3(*a*) Schematic diagram

Figure 4(*a*) shows an inclusion surrounded by eight equal-length parallel cracks. The crack spacings are chosen such that the horizontal and vertical crack spacings are the same and are fixed at $d_1/R = d_2/R = 2.1$. The Poisson's ratios of the inclusion and matrix are chosen as $\nu_i = \nu_m = 0.3$.

The modulus reduction for a solid containing dilute inclusions with the same inclusion-crack pattern (Fig. 4(*a*)) is considered next. The elastic modulus in the direction normal to the cracks, $\bar{E}_2$ (Eq. (15)), is related to the additional strain ΔE_{22}, which in turn is determined by Eq. (10) with auxiliary loading $S_{22}^{\infty} = 1$, others = 0. The variation of modulus $\bar{E}_2$ versus the normalized crack length, a/R, is shown in Figs. 4(*b*) and 4(*c*) for soft ($E_i/E_m = 0.25$) and hard ($E_i/E_m = 4$) inclusions, respectively. For soft inclusions, the effective moduli normalized against the plane-strain modulus of the matrix, $\bar{E}_m[= E_m/(1 - \nu_m^2)]$, $\bar{E}_2/\bar{E}_m$, are 0.99, 0.97, and 0.94 at $a/R = 0$ for $\rho = 0.01$, 0.02, and 0.04, respectively. These are the moduli of the solid with dilute inclusions (no microcracks). As crack length increases, the moduli decrease rapidly. For example, the normalized modulus assumes the value of 0.48 at $a/R = 1$ for $\rho = 0.04$. The modulus ratios are larger than 1 at small crack length in Fig. 4(*c*) due to the strengthening effect of hard inclusions. However, as crack length increases, the weakening by the cracks overwhelms the strengthening effect such that $\bar{E}_2/E_m$ can be smaller than 1. An increase in the number of hard inclusions may not always lead to expected strengthening of the materials, if the matrix material is vulnerable to microcracking around inclusions and a well-developed microcracking zone exists. It is noted that

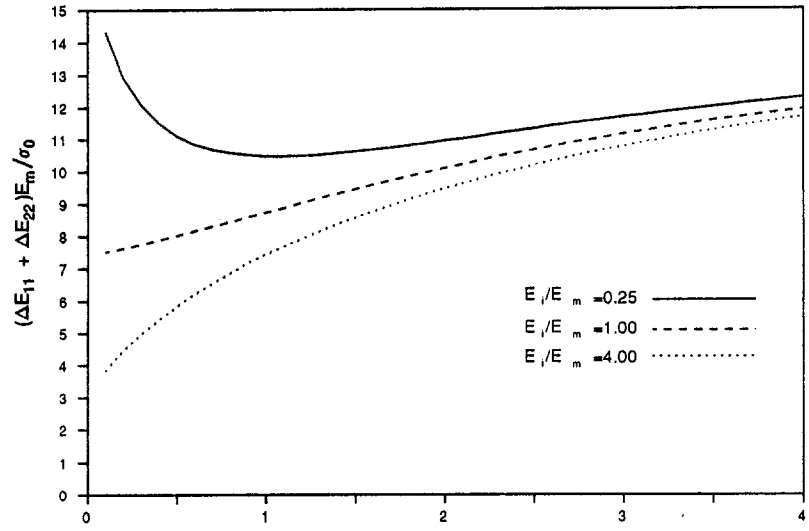

Fig. 3(*b*) Variation of the normalized two-dimensional dilatational strain increase, $(\Delta E_{11} + \Delta E_{22})E_m/\sigma_0$, with distance between the centers of the inclusion and the crack

Fig. 3 An inclusion surrounded by an array of radial cracks

the case with the highest inclusion volume fraction ($\rho = 0.04$) produces the largest decrease in effective moduli.

In order to look into the local crack-tip behavior under quasi-static crack growth, consider a solid with the same geometry as shown in Fig. 4(a) subject to a uniaxial remote loading, σ_0. The stress intensity factors normalized against the stress intensity factor for a single crack in a homogeneous matrix, $\sigma_0\sqrt{\pi a}$ ("a" is half the crack length), at three crack tips, A, B, and C, are shown in Figs. 4(d) and 4(e) for the soft ($E_i/E_m = 0.25$) and hard ($E_i/E_m = 4.0$) inclusions, respectively. For the soft inclusion, the stress intensity factor at tip A is greatly shielded due to the crack-inclusion interaction when the crack length is so small that crack-crack interaction is limited. Also note that the stress intensity factor at tip A does not change much as the crack length increases due to competition between inclusion-crack and crack-crack interactions when a/R is less than 0.9. The normalized stress intensity factors in increasing order of their magnitudes are tips C, B, and A. When cracks are quasi-statistically growing to a value of a/R greater than 0.9, the order of magnitude of the stress intensity factors changes to A, B, and C. This observation suggests that a quasi-static crack-growing process may change the interactions among the inclusion and cracks. As a result, a growing crack tip may become inactive or may be relayed to some previously inactive crack tips. An accurate description of the sequence of

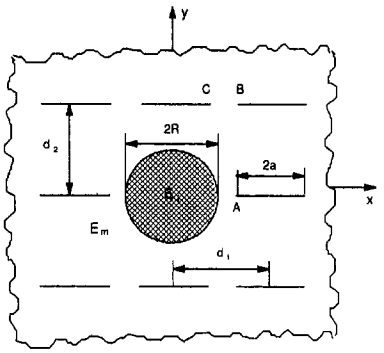

Fig. 4(a) Schematic diagram

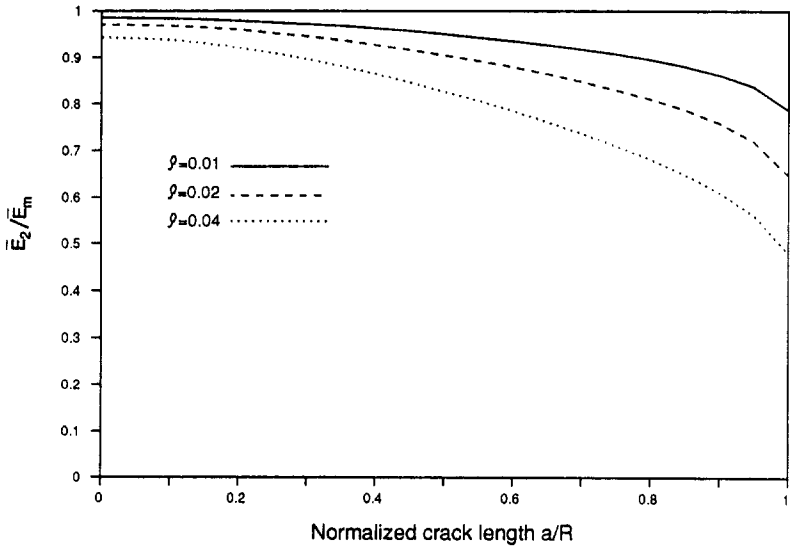

Fig. 4(b) Variation of in-plane modulus in the direction perpendicular to the cracks with crack length—soft inclusion: $E_i/E_m = 0.25$

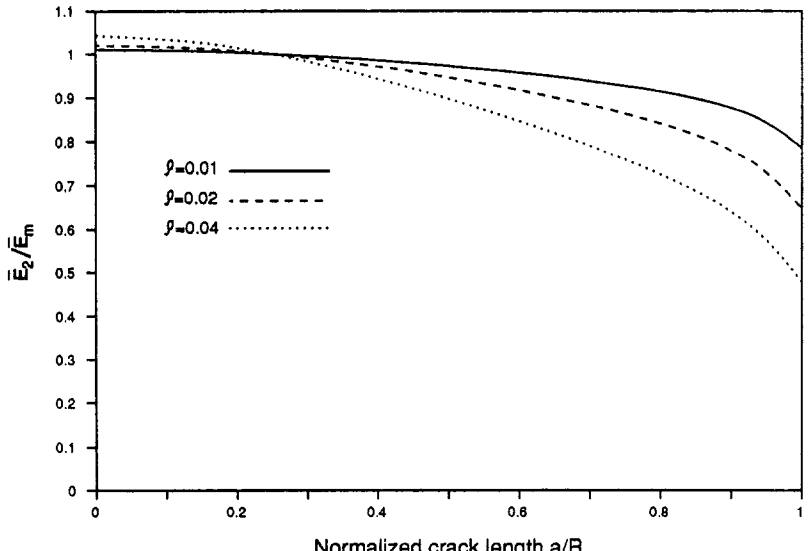

Fig. 4(c) Variation of in-plane modulus in the direction perpendicular to the cracks with crack length—hard inclusion:: $E_i/E_m = 4.0$

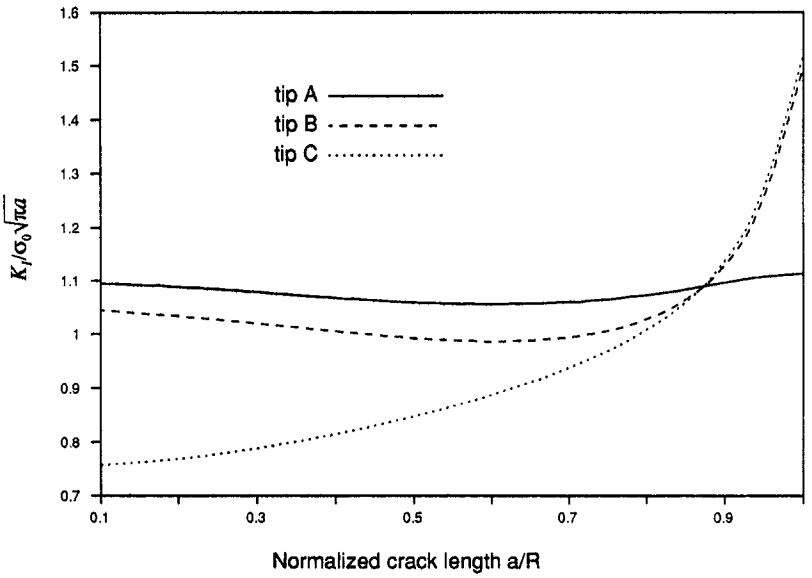

Fig. 4(*d*) Variation of the stress intensity factors with crack length—soft inclusion: $E_i/E_m = 0.25$.

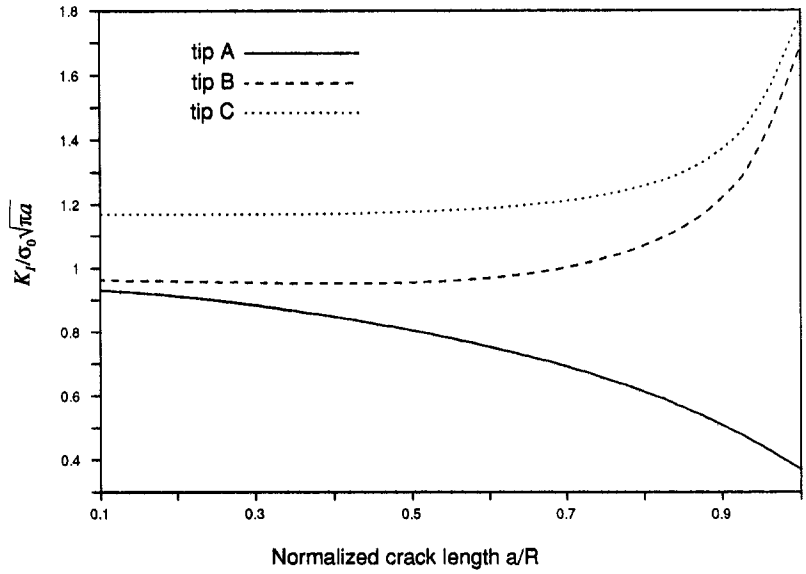

Fig. 4(e) Variation of the stress intensity factors with crack length—hard inclusion: $E_i/E_m = 4.00$.

Fig. 4 An inclusion surrounded by eight parallel cracks

crack-tip action requires a complete local analysis. Self-similar crack growth can be maintained only to where such interactions are very weak. Figure 4(*e*) does not show a switch in magnitude of the stress intensity factors for the hard inclusion. Note that stress amplification at tips B and C exists for both the soft and hard inclusions due to crack-crack interaction as cracks are growing. Stress intensity factor at crack tip A for the hard inclusion, Fig. 4(*e*), decreases as the crack grows closer to the inclusion. This indicates that the interaction between the hard inclusion and the matrix crack perpendicular to the inclusion-matrix interface produces stress shielding (particulate toughening). Nonetheless, the interactions between the hard inclusion and the crack do not always provide crack-tip stress shielding. For example, the stress intensity factor at tip C, Fig. 4(*e*), is mainly due to an interaction between the hard inclusion and the crack because the crack length is very small. The normalized value of the stress intensity factor at tip C is greater than 1.0, suggesting a crack-tip stress amplification. Finally, it is noted from Figs. 4(*c*) and 4(*e*) that effective moduli decrease steadily as the crack length increases, although local stress intensity factors vary in a much more complicated way. This is somewhat similar to the calculations done by Montagut and Kachanov (1988).

Acknowledgments

The authors gratefully acknowledge the financial support provided under Grant No. DMC 8657345 from the U.S. National Science Foundation.

References

Dundurs, J., and Mura, T., 1964, "Interaction Between an Edge Dislocation and a Circular Inclusion," *J. Mech. Phys. Solids*, Vol. 12, pp. 177–189.

Erdogan, F., 1962, "On the Stress Distribution on Plates with Collinear Cuts Under Arbitrary Loads," *Proceedings, 4th U.S. National Congress of Applied Mechanics*, ASME, New York, pp. 547–553.

Erdogan, F., Gupta, G. D., and Ratwani, M., 1974, "Interaction Between a Circular Inclusion and an Arbitrarily Oriented Crack," ASME JOURNAL OF APPLIED MECHANICS, Vol. 41, pp. 1007–1013.

Fares, N., 1993, "Effective Mechanical Properties of Composites at Finite Deformations," ASME JOURNAL OF APPLIED MECHANICS, Vol. 60, pp. 8–14.

Hill, R., 1965, "A Self-Consistent Mechanics of Composite Materials," *J. Mech. Phys. Solids*, Vol. 13, pp. 213–222.

Hu, K. X., Chandra, A., and Huang, Y., 1993a, "Fundamental Solutions for Dilute Inclusions Embedded in Microcracked Solids," *Mechanics of Materials*, Vol. 16, pp. 281–294.

Hu, K. X., Chandra, A., and Huang, Y., 1993b, "Multiple Void-Crack Interaction," *Int. J. Solids Struc.*, Vol. 30, pp. 1473–1489.

Hutchinson, J. W., 1987, "Micro-Mechanics of Damage in Deformation and Fracture," Dept. of Solid Mechanics, Technical University of Denmark, Lyngby, Denmark.

Kachanov, M., 1987, "Elastic Solids With Many Cracks: A Simple Method of Analysis," *Int. J. Solids Structures*, Vol. 23, pp. 23–43.

Krenk, S., 1975, "On the Use of the Interpolation Polynomial for Solutions of Singular Integral Equations," *Quart. Appl. Math.*, Vol. 32, pp. 479–484.

Luh, E. Y., and Evans, A. G., 1987, "High Temperature Mechanical Properties of a Ceramic Matrix Composite," *J. Am. Ceram. Soc.*, Vol. 70, pp. 466–469.

Marshall, D. B., Cox, B. N., and Evans, A. G., 1985, "The Mechanics of Matrix Cracking in Brittle-Matrix Fiber Composites," *Acta Metall.*, Vol. 33, pp. 2013–2021.

Montagut, E., and Kachanov, M., 1988, "On Modeling a Microcracked Zone by 'Weakened' Elastic Materials and on Statistical Aspects of Crack-Microcrack Interactions," *Int. J. Fracture*, Vol. 37, pp. R55–R62.

Muskhelishvili, N. I., 1953, *Some Basic Problems of the Mathematical Theory of Elasticity*, Noorhoff, Ltd., Groningen, The Netherlands.

Rohle, M., Claussen, N., and Heur, A. H., 1986, "Transformation and Microcrack Toughening as Complementary Processes in ZrO_2-Toughened Al_2O_3," *J. Am. Ceram. Soc.*, Vol. 69, pp. 195–197.

Tvergaard, V., and Hutchinson, J., 1988, "Microcracking in Ceramics Induced by Thermal Expansion or Elastic Anisotropy," *J. Am. Ceram. Soc.*, Vol. 71, pp. 157–166.

APPENDIX

The effective moduli of a solid containing dilute inclusions are given by

$$\frac{2(1+\bar{\nu}_0)}{\bar{E}_0} = \frac{2(1+\nu_m)}{E_m} + \rho\left[1 - \frac{E_i(1+\nu_m)}{E_m(1+\nu_i)}\right]\frac{\bar{\gamma}}{\tau^0} \quad \text{(A1)}$$

and

$$\frac{2(1-\bar{\nu}_0)}{\bar{E}_0} = \frac{2(1+\nu_m)(1-2\nu_m)}{E_m} + \rho\left[1 - \frac{E_i(1+\nu_m)(1-2\nu_m)}{E_m(1+\nu_i)(1-2\nu_i)}\right]\frac{\bar{\epsilon}_{kk}}{\sigma_0} \quad \text{(A2)}$$

where $\bar{E}_0$ and $\bar{\nu}_0$ are the plane-strain modulus and Poisson's ratio, respectively, and $\bar{\gamma}$ and $\bar{\epsilon}_{kk}$ are the average shear strain and two-dimensional dilatational strain corresponding to remote shear stress, τ_0, and biaxial tensile stress, σ_0, imposed on the composite. For the dilute inclusions, $\bar{\gamma}$ and $\bar{\epsilon}_{kk}$ are evaluated by corresponding strains in an inclusion embedded in an infinite matrix subject to remote shear stress, τ_0, and remote biaxial tension, σ_0, respectively. The expressions of $\bar{\gamma}$ and $\bar{\epsilon}_{kk}$ (Muskhelishvili, 1953) are

$$\frac{\bar{\gamma}}{\tau^0} = \frac{2(1+\nu_m)}{E_m}\frac{1}{1 - \left[\frac{3-4\nu_m}{4(1-\nu_m)}\left(1 - \frac{E_i(1+\nu_m)}{E_m(1+\nu_i)}\right)\right]} \quad \text{(A3)}$$

$$\frac{\bar{\epsilon}_{kk}}{\sigma^0} = \frac{4(1-\nu_m^2)}{E_m}\frac{1}{1 + \frac{E_i(1+\nu_m)}{E_m(1+\nu_i)(1-2\nu_i)}}. \quad \text{(A4)}$$

Equations (A1)–(A4) provide analytical solutions to $\bar{E}_0$ and $\bar{\nu}_0$.

Analysis of a Crack Embedded in a Linear Elastic Half-Plane Solid

J. C. Sung
Assoc. Professor.

J. Y. Liou
Graduate Student.

Department of Civil Engineering,
National Cheng Kung University,
Tainan, Taiwan, 70101, R.O.C.

A crack embedded in a half-plane solid traction-free on the infinite straight boundary is analyzed. The response of the material is linear elastic. A system of singular integral equations for the unknown dislocation densities defined on the crack faces is derived. These equations are then specialized to the problem of a crack located arbitrarily in an orthotropic material which are found to depend on two material parameters only. For a crack oriented either perpendicular or parallel to the infinite straight boundary, the kernel functions appearing in the singular integral equations are obtained in real form which are valid for arbitrary alignment of the orthotropic material. Furthermore, these kernel functions are found to be valid even for degenerate materials and can directly lead to those kernel functions for isotropic materials. Numerical results have been carried out for horizontal or vertical crack problems to elucidate the effect of material parameters on the stress intensity factors. The effect of the alignment of the material on the stress intensity factors is also presented for degenerate materials.

1 Introduction

The analysis of a straight crack with finite length inside a linear elastic half-plane solid or other half-plane related solid is of considerable importance in the field of fracture mechanics. This type of problems has been investigated by many researchers for isotropic materials. (Gupta and Erdogan, 1974; Erdogan and Arin, 1975; Erdogan et al., 1973; Zang and Gudmundson, 1989; Bueckner, 1970, 1971; Bowie, 1973; Isida, 1966; Higashida and Kamada, 1982; among others.) A variety of techniques have been used in investigating these kind of problems. A detailed description of these methods can be found in Sih (1973). As in anisotropic materials few of these types of problems were treated. Heng et al. (1986) uses the boundary collocation method to analyze the stress field in the vicinity of the crack tip in edge-cracked anisotropic plates. Wen (1989) applies the displacement discontinuity method to deal with the problems similar by and large to the one investigated by Heng et al. (1986). Miller (1989) treated the dissimilar anisotropic materials where the problem of a crack of arbitrary size and orientation near bimaterial interfaces is considered. All these authors use basically the Lekhnitskii formulation (1963). For the problem of an infinite long strip, Erdogan and his co-workers (Delale and Erdogan, 1977; Delale et al., 1979; Kaya and Erdogan, 1980; Cinar and Erdogan, 1983) have made many contributions in the study of internal and edge cracks in an orthotropic material.

In this paper, the problem of a crack embedded arbitrarily in a half-plane solid with pressure or shear loading on the crack faces is studied. The boundary condition on the infinite straight boundary of the half-plane is traction-free (or called free surface). The geometry of the problem is shown in Fig. 1. The response of the material is generally anisotropic in the sense that in-plane and antiplane deformation in the formulation are coupled. With the Eshelby (1953)-Stroh (1958) formulation and the basic solution to the half-plane solid due to point dislocations the problem can be formulated by a system of singular integral equations for the unknown dislocation densities defined on the crack faces. These equations are then specialized to the problem of a crack located arbitrarily in an orthotropic material. With four material parameters introduced by Krenk (1979) for an orthotropic material, these equations can be rewritten in a form that depends on two material parameters, κ and δ, only. For a crack lying either in parallel with or perpendicular to the free boundary (i.e., horizontal crack or vertical crack), the kernel functions appearing in the singular integral equations have been given explicitly in real form which are valid for arbitrary alignment of the orthotropic material. From the explicit form of these kernel functions we are able to show that they are regular even for the degenerate material, i.e., when the material parameter $\kappa = 1$. Furthermore, these kernel functions can be reduced directly to those for isotropic materials, i.e., when material parameters κ and δ are both equal to one. The

Contributed by the Applied Mechanics Division of THE AMERICAN SOCIETY OF MECHANICAL ENGINEERS for publication in the ASME JOURNAL OF APPLIED MECHANICS.

Discussion on this paper should be addressed to the Technical Editor, Professor Lewis T. Wheeler, Department of Mechanical Engineering, University of Houston, Houston, TX 77204-4792, and will be accepted until four months after final publication of the paper itself in the ASME JOURNAL OF APPLIED MECHANICS.

Manuscript received by the ASME Applied Mechanics Division, Nov. 9, 1992; final revision, Feb. 24, 1994. Associate Technical Editor: C. F. Shih.

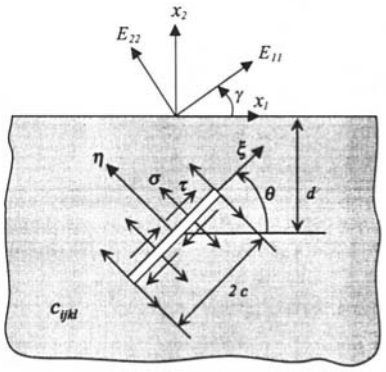

Fig. 1 Geometry of the problem

dependence of the stress intensity factors on the two material parameters κ and δ on the geometry of the crack is studied numerically. The effect of the alignment of the material on the stress intensity factors is also presented for degenerate materials. All these studies are for horizontal or vertical crack problems.

2 Basic Equations

In the following, a two-dimensional elastic deformation where the displacement field, $\mathbf{u}$ with components u_k ($k = 1, 2, 3$) being the function of x_1 and x_2 only (i.e., $\mathbf{u} = \mathbf{u}(x_1, x_2)$) are considered. Cartesian coordinate systems x_1, x_2, and x_3 are used for the description of all field quantities and, for the convenience sake, we adopt the convention that all Latin indices range from 1 to 3 and Greek indices take on the values 1 and 2. Repeated indices imply summation and a comma stands for differentiation. Boldfaced symbols stand for either column vectors or matrices, depending on whether lower case or upper case is used. As usual, the stress field σ_{ij} of the elastic solids has to satisfy the equilibrium equations (with body forces absent)

$$\sigma_{i\beta,\beta} = 0 \tag{1}$$

and the stresses are related to the displacements field u_k by the generalized Hooke's law:

$$\sigma_{ij} = c_{ijkl} u_{k,l} \tag{2}$$

where c_{ijkl} are the elastic moduli. Substituting Eq. (2) to (1) we obtain

$$c_{i\alpha k\beta} u_{k,\alpha\beta} = 0. \tag{3}$$

The form of the general solution to Eq. (3) can be assumed to be

$$\mathbf{u} = \mathbf{a} f(z), \quad z = x_1 + p x_2 \tag{4}$$

where p and $\mathbf{a}$ are complex constants to be determined and $f(z)$ is an arbitrary function of z. Substituting Eq. (4) into (3) we will end up with the eigenvalue problem

$$\{c_{i1k1} + p(c_{i1k2} + c_{i2k1}) + p^2 c_{i2k2}\} a_k = 0 \tag{5}$$

from which the eigenvalue p and eigenvector $\mathbf{a}$ can be determined. It can be shown that these eigenvalues, denoted by $p_n (n = 1,2, \ldots,6)$, appear in three pairs of complex conjugate roots provided that c_{ijkl} is positive definite. Therefore, without loss of generality, we can let

$$\mathrm{Im}\{p_n\} > 0, \quad p_{n+3} = \overline{p_n}, \quad n = 1, 2, 3 \tag{6}$$

where Im{ } denotes the imaginary part and the overbar denotes the complex conjugate. Let $\mathbf{a}_n$ be the eigenvector corresponding to the eigenvalue $p_n (n = 1, 2, 3)$ then, from Eq. (5), we observe that

$$\mathbf{a}_{n+3} = \overline{\mathbf{a}_n}, \quad n = 1, 2, 3 \tag{7}$$

since material constants are all real values. Introducing two matrices $\mathbf{P}$ and $\mathbf{A}$ by

$$\mathbf{P} = diag\langle p_1, p_2, p_3 \rangle \tag{8}$$

$$\mathbf{A} = [\mathbf{a}_1, \mathbf{a}_2, \mathbf{a}_3] \tag{9}$$

and defining the matrix $\mathbf{B}$ as

$$\mathbf{B} = \mathbf{R}^T\mathbf{A} + \mathbf{T}\mathbf{A}\mathbf{P}, \tag{10}$$

where the components of matrices $\mathbf{R}$ and $\mathbf{T}$ are defined by $R_{ik} = c_{i1k2}$ and $T_{ik} = c_{i2k2}$, respectively, the general representation for the displacements and stresses can be written as

$$\mathbf{u} = 2\mathrm{Re}\{\mathbf{A}\mathbf{f}(\mathbf{z})\} \tag{11}$$

$$\mathbf{t}_1 = (\sigma_{11}, \sigma_{12}, \sigma_{13})^T = -2\mathrm{Re}\{\mathbf{B}\mathbf{P}\mathbf{f}'(\mathbf{z})\} \tag{12}$$

$$\mathbf{t}_2 = (\sigma_{21}\sigma_{22}, \sigma_{23})^T = 2\mathrm{Re}\{\mathbf{B}\mathbf{f}'(\mathbf{z})\} \tag{13}$$

where

$$\mathbf{f}(\mathbf{z}) = (f_1(z_1), f_2(z_2), f_3(z_3))^T \tag{14}$$

$$\mathbf{f}'(\mathbf{z}) = \frac{d\mathbf{f}(\mathbf{z})}{d\mathbf{z}} = \left(\frac{df_1(z_1)}{dz_1}, \frac{df_2(z_2)}{dz_2}, \frac{df_3(z_3)}{dz_3}\right)^T \tag{15}$$

and Re{ } denotes the real part. Define the stress vector function $\boldsymbol{\phi}$ by

$$\boldsymbol{\phi} = 2\mathrm{Re}\{\mathbf{B}\mathbf{f}(\mathbf{z})\} \tag{16}$$

then it can be shown that the surface traction at a point s on a curved boundary is given by

$$\mathbf{t}_n = \frac{\partial \boldsymbol{\phi}}{\partial s} \tag{17}$$

where s is the arc length measured along curved boundary in the direction such that, when one faces the direction of increasing s, the material is located on the right-hand side. The matrices $\mathbf{A}$ and $\mathbf{B}$ defined by Eq. (9) and (10) satisfy the following orthogonality relations (Stroh, 1958; Ting, 1986):

$$\begin{bmatrix} \mathbf{A} & \overline{\mathbf{A}} \\ \mathbf{B} & \overline{\mathbf{B}} \end{bmatrix} \begin{bmatrix} \mathbf{B} & \overline{\mathbf{B}} \\ \mathbf{A} & \overline{\mathbf{A}} \end{bmatrix}^T = \begin{bmatrix} \mathbf{I} & \mathbf{0} \\ \mathbf{0} & \mathbf{I} \end{bmatrix} \tag{18}$$

where $\mathbf{I}$ is a 3×3 unit matrix. It follows from Eq. (18) that the matrix $\mathbf{L}$ defined as (Ting, 1986)

$$\mathbf{L} = -2i\mathbf{B}\mathbf{B}^T \tag{19}$$

where $i^2 = -1$, is real, symmetric, and positive definite (Chadwick and Smith, 1977).

3 Singular Integral Equations

Consider the problem of a straight crack with length $2c$ embedded in a two-dimensional anisotropic elastic half-plane solid (see Fig. 1). The orientation of the crack in the formulation can be arbitrary. The depth of the center of the crack from the infinite straight boundary of the half-plane is denoted by d. Uniform pressure and shear are applied on both faces of the crack while the straight boundary of the half-plane is assumed to be traction-free. The mathematical statement of this problem can be stated more precisely as follows:

$$\mathbf{t}_\eta^\pm = \pm\boldsymbol{\Omega}(\theta)^T[\tau, \sigma, 0]^T \qquad |\xi| < c, \ \eta = 0^\pm \tag{20}$$

$$\mathbf{t}_2 = \mathbf{0} \qquad -\infty < x_1 < \infty, \ x_2 = 0 \tag{21}$$

$$\left.\begin{matrix} \mathbf{t}_1 \to \mathbf{0}, \\ \mathbf{t}_2 \to \mathbf{0} \end{matrix}\right\} \text{ as } x_2 < 0, \ |x_1^2 + x_2^2| \to \infty \tag{22}$$

where (ξ, η, x_3) is the local coordinates with the origin centered at the middle point of the crack and the direction of ξ

is parallel to the crack faces; see Fig. 1. The traction applied on the lower crack face is denoted by $[-\tau, -\sigma, 0]^T$ where the components are expressed in terms of the local coordinates (ξ, η, x_3). The 3×3 matrix $\mathbf{\Omega}(\theta)$ whose components are the cosine of the angle between the local coordinates and the global coordinates is given by

$$\mathbf{\Omega}(\theta) = \begin{bmatrix} \cos(\theta) & \sin(\theta) & 0 \\ -\sin(\theta) & \cos(\theta) & 0 \\ 0 & 0 & 1 \end{bmatrix}. \quad (23)$$

Note that θ defined here is positive when measured from the positive direction of the x_1-axis to the positive direction of the ξ-axis, as shown in Fig. 1.

It is well known that the problem stated above can be simulated by a continuous distribution of the dislocations on the crack faces. The fundamental step of this approach is to determine the basic solution to the half-plane uncracked solid subjected to point dislocations situated at point $z_k^D = x_1^D + p_k x_2^D$, $(k = 1, 2, 3)$, where superscript D is used here and in what follows to emphasize the term that is related to the action of dislocations. The strength of the dislocations is denoted by $\mathbf{b} = [b_1, b_2, b_3]^T$. This basic solution has been investigated recently by Ting (1992) and Suo (1990). For the purpose of reference, we give the explicit expression for the stress function as

$$\boldsymbol{\phi}^D = 2\mathrm{Re}\{\mathbf{B}\mathbf{f}(\mathbf{z})\} \quad (24)$$

where

$$2\pi i\mathbf{f}'(\mathbf{z}) = \mathrm{diag} < \left(z_1 - z_1^D\right)^{-1}, \left(z_2 - z_2^D\right)^{-1}, \left(z_3 - z_3^D\right)^{-1} > \mathbf{B}^T\mathbf{b} + \sum_{k=1}^{3} \mathrm{diag} < \left(z_1 - \overline{z_k^D}\right)^{-1}, \left(z_2 - \overline{z_k^D}\right)^{-1}, \left(z_3 - \overline{z_k^D}\right)^{-1} > \mathbf{M}\mathbf{I}_k\overline{\mathbf{B}^T}\mathbf{b} \quad (25)$$

and $\mathbf{I}_1 = \mathrm{diag} < 1, 0, 0 >$, $\mathbf{I}_2 = \mathrm{diag} < 0, 1, 0 >$, $\mathbf{I}_3 = \mathrm{diag} < 0, 0, 1 >$, $\mathbf{M} = \mathbf{B}^{-1}\overline{\mathbf{B}}$. Note that in the derivation of the stress function in Eq. (24), the boundary conditions of Eqs. (22) and (21) are satisfied. To satisfy the condition in (20), point dislocations $\mathbf{b}$ are replaced by $\mathbf{b}(t)dt$ with densities $\mathbf{b}(t)$ distributed on the crack face where t is a parameter defined on the crack face. Enforcing the satisfaction of the applied traction conditions on the crack faces, a singular integral equations for the dislocation densities are obtained:

$$\frac{-\mathbf{L}}{2\pi}\int_{-c}^{c} \frac{\mathbf{b}(t)}{t - \xi}dt + \int_{-c}^{c} \mathbf{K}(\xi, t)\mathbf{b}(t)dt = \mathbf{t}_\eta^-(\xi), \quad |\xi| < c \quad (26)$$

where the matrix $\mathbf{L}$ has been defined in Eq. (19). The kernel function appearing in the second integral is given by

$$\mathbf{K}(\xi, t) = \frac{1}{\pi}\mathrm{Im}\left\{ \sum_{k=1}^{3} \mathbf{B}\mathrm{diag} < z_1^*\left(z_1 - \overline{z_k^D}\right)^{-1}, z_2^*\left(z_2 - \overline{z_k^D}\right)^{-1}, z_3^*\left(z_3 - \overline{z_k^D}\right)^{-1} > \mathbf{M}\mathbf{I}_k\overline{\mathbf{B}^T} \right\} \quad (27)$$

where

$$z_k^* = \cos\theta + p_k \sin\theta \quad (28a)$$

$$z_k = \xi z_k^* - dp_k, \quad z_k^D = tz_k^* - dp_k, \quad -c \le \xi, t \le c. \quad (28b)$$

For single displacements around a closed contour surrounding the whole crack, the following auxiliary conditions have to be satisfied:

$$\int_{-c}^{c} \mathbf{b}(t)dt = \mathbf{0}. \quad (29)$$

The coupled singular integral equations for the dislocation densities in Eq. (26) combined with Eq. (29) can be solved numerically (Gerasoulis, 1982). Once the dislocation density functions have been found, one can then compute the stress intensity factors at the crack tips with the formula which will be introduced in the following. Since the solutions of the coupled singular integral equations for the dislocation densities $\mathbf{b}(t)$ have a square root singular at both crack tips, it is more efficient for the numerical calculations by letting

$$\mathbf{b}(t) = (c^2 - t^2)^{-1/2}\boldsymbol{\alpha}(t) \quad (30)$$

where $\boldsymbol{\alpha}(t)$ is a regular vector function defined in the interval $|t| \le c$. The formula for the stress intensity factors at the tips, e.g., at the right tip ($\xi = c$), can be derived by first considering the traction on the crack line (i.e., the positive ξ-axis) and considering the traction very near the crack tip ($\xi \to c$) which is given by, from Eq. (26),

$$\boldsymbol{\sigma}_\eta(\xi) = [\sigma_{\eta\xi}, \sigma_{\eta\eta}, \sigma_{\eta 3}]^T = \mathbf{\Omega}(\theta)\mathbf{t}_\eta(\xi) \approx \frac{1}{\sqrt{8c}}\mathbf{\Omega}(\theta)\mathbf{L}\frac{\boldsymbol{\alpha}(c)}{\sqrt{\xi - c}} \quad (31)$$

where, in obtaining the above result, the definition of Eq. (30) has been used. With the following definition

$$\mathbf{k} = [K_{II}, K_I, K_{III}]^T = \lim_{\xi \to c^+} \sqrt{2\pi(\xi - c)}\,\boldsymbol{\sigma}_\eta(\xi) \quad (32)$$

combined with the result of equation (31), one then leads to the expression for the stress intensity factor at a right tip as

$$\mathbf{k} = \sqrt{\frac{\pi}{4c}}\,\mathbf{\Omega}(\theta)\mathbf{L}\boldsymbol{\alpha}(c). \quad (33)$$

Thus once $\boldsymbol{\alpha}(t)$ has been obtained by solving numerically the coupled singular integral equations, the stress intensity factors can be evaluated directly on the basis of Eq. (33). Note that when discussing the isotropic material the matrix $\mathbf{L}$ appearing in Eq. (33) reduces to

$$\mathbf{L} = \mathrm{diag} < \frac{E_i}{2(1 - \nu_i^2)}, \frac{E_i}{2(1 - \nu_i^2)}, \frac{E_i}{2(1 + \nu_i)} > \quad (34)$$

where E_i is the Young's modulus and ν_i is the Poission's ratio.

4 Horizontal or Vertical Crack in an Orthotropic Material

The singular integral Eqs. (26) derived in previous section are for general anisotropic materials. In this section we will focus on the discussions of orthotropic materials. Assuming that the coordinate axes coincide with the material axes, then the explicit expressions for $\mathbf{B}$ and $\mathbf{L}$, obtained by Dongye and Ting (1989), are

$$\mathbf{B} = \begin{bmatrix} -k_1 p_1 C_{66}\left(C_{12} - p_1^2 C_{22}\right) & -k_2 p_2 C_{66}\left(C_{12} - p_2^2 C_{22}\right) & 0 \\ k_1 C_{66}\left(C_{12} - p_1^2 C_{22}\right) & k_2 C_{66}\left(C_{12} - p_2^2 C_{22}\right) & 0 \\ 0 & 0 & k_3 p_3 C_{44} \end{bmatrix} \quad (35)$$

$$\mathbf{L} = \text{diag}\left\langle L_{11}, \left(\frac{C_{22}}{C_{11}}\right)^{1/2} L_{11}, (C_{44}C_{55})^{1/2}\right\rangle \tag{36}$$

where

$$L_{11} = \left[(C_{11}C_{22})^{1/2} + C_{12}\right] \times \left[\frac{C_{66}\left((C_{11}C_{22})^{1/2} - C_{12}\right)}{C_{22}\left(2C_{66} + C_{12} + (C_{11}C_{22})^{1/2}\right)}\right]^{1/2}. \tag{37}$$

$C_{\alpha\beta}(\alpha,\beta = 1, 2, \ldots, 6)$ is a contracted notation for c_{ijkl}, and k_1, k_2, k_3 are complex constants which can be determined by the normalization condition (18). The assumption that x_3-axis coincides with the material alignments will decouple the antiplane behavior from the in-plane response and henceforth we will ignore the antiplane problem in what follows. For an in-plane problem there are four constants involved in the constitutive equations, i.e., C_{11}, C_{22}, C_{12}, and C_{66}, which are related to the engineering material constants by

$$C_{11} = \frac{E_{11}(1 - \nu_{23}\nu_{32})}{1 - \nu_{12}\nu_{21} - \nu_{23}\nu_{32} - \nu_{31}\nu_{13} - 2\nu_{21}\nu_{32}\nu_{13}} \tag{38a}$$

$$C_{22} = \frac{E_{22}(1 - \nu_{31}\nu_{13})}{1 - \nu_{12}\nu_{21} - \nu_{23}\nu_{32} - \nu_{31}\nu_{13} - 2\nu_{21}\nu_{32}\nu_{13}} \tag{38b}$$

$$C_{12} = \frac{E_{11}(\nu_{21} + \nu_{23}\nu_{31})}{1 - \nu_{12}\nu_{21} - \nu_{23}\nu_{32} - \nu_{31}\nu_{13} - 2\nu_{21}\nu_{32}\nu_{13}} \tag{38c}$$

$$C_{66} = G_{12} \tag{38d}$$

for the plane-strain case. As has been discussed by Krenk (1979), the study of stress boundary value problems of plane elasticity can be greatly facilitated by introducing four effective parameters, E, ν, δ, and κ, which are defined by

$$E = \sqrt{\frac{E_{11}E_{22}}{(1 - \nu_{13}\nu_{31})(1 - \nu_{23}\nu_{32})}} \tag{39a}$$

$$\nu = \sqrt{\frac{(\nu_{12} + \nu_{13}\nu_{32})(\nu_{21} + \nu_{23}\nu_{31})}{(1 - \nu_{13}\nu_{31})(1 - \nu_{23}\nu_{32})}} \tag{39b}$$

$$\delta = \left(\frac{E_{11}(1 - \nu_{23}\nu_{32})}{E_{22}(1 - \nu_{13}\nu_{31})}\right)^{1/4} \tag{39c}$$

$$\kappa = \sqrt{\frac{E_{11}E_{22}}{(1 - \nu_{13}\nu_{31})(1 - \nu_{23}\nu_{32})}}\left(\frac{1}{2G_{12}} - \frac{\nu_{12} + \nu_{13}\nu_{32}}{E_{11}}\right) \tag{39d}$$

where E is the plane-strain effective stiffness, ν is the effective Poisson ratio, δ is the stiffness ratio, and κ is the shear parameter. The positive definiteness of the strain energy density requires that $\delta > 0, E > 0, |\nu| < 1$ and $\kappa > -1$. Note that for isotropic material, $\delta = \kappa = 1$ and E, ν are reduced to $E_i/(1 - \nu_i^2)$ and $\nu_i/(1 - \nu_i)$, respectively, for the plane-strain case where E_i is the Young's modulus and ν_i is the Poisson ratio for isotropic material. Comparing (38) and (39) one obtains

$$C_{11} = \frac{\delta^2 E}{1 - \nu^2}, C_{22} = \frac{E}{\delta^2(1 - \nu^2)}, \quad C_{12} = \frac{\nu E}{1 - \nu^2}, C_{66} = \frac{E}{2(\kappa + \nu)}. \tag{40}$$

When substituting Eq. (40) to Eqs. (35) and (36) with some manipulations one obtains

$$\mathbf{B} = \left(\frac{E}{4(\kappa^2 - 1)^{1/2}}\right)^{1/2} \times \begin{bmatrix} (\delta\rho_+)^{1/2}e^{i5\pi/4} & (\delta\rho_-)^{1/2}e^{-i\pi/4} \\ (\delta\rho_+)^{-1/2}e^{-i\pi/4} & (\delta\rho_-)^{1/2}e^{i\pi/4} \end{bmatrix}. \tag{41a}$$

$p_1 = i\delta\rho_+$, $p_2 = i\delta\rho_-$, $\rho_+ = (\kappa + (\kappa^2 - 1)^{1/2})^{1/2}$, $\rho_- = (\kappa - (\kappa^2 - 1)^{1/2})^{1/2}$ for $\kappa > 1$, and

$$\mathbf{B} = \left(\frac{E}{4(1 - \kappa^2)^{1/2}}\right)^{1/2} \times \begin{bmatrix} \delta^{1/2}e^{i(\pi/4 - \varphi/2)} & \delta^{1/2}e^{i(5\pi/4 + \varphi/2)} \\ \delta^{-1/2}e^{i(\pi/4 + \varphi/2)} & \delta^{-1/2}e^{i(\pi/4 - \varphi/2)} \end{bmatrix} \tag{41b}$$

$$p_1 = \delta e^{i(\pi - \varphi)}, \quad p_2 = \delta e^{i\varphi}, \quad \varphi = \tan^{-1}\left[\left(\frac{1 + \kappa}{1 - \kappa}\right)^{1/2}\right]$$

for $|\kappa| < 1$, and

$$\mathbf{L} = \frac{E}{(2\kappa + 2)^{1/2}}\begin{bmatrix} \delta & 0 \\ 0 & \delta^{-1} \end{bmatrix}. \tag{42}$$

Here and in what follows, the size of the matrices and vectors are 2×2 and 2×1, respectively, since only the plane problem is considered. It is easily seen that when $\kappa = 1$, one encounters the degenerate materials since the eigenvalues p_1 and p_2 are the same and in this case the matrix $\mathbf{B}$, unlike matrix $\mathbf{L}$, will be singular. One can expect that the parameter κ will play an important role in the study of degenerate materials. Note also that matrices $\mathbf{B}$ and $\mathbf{L}$ are independent of ν. Substituting results of (41) and (42) into Eq. (26), recalling that matrix $\mathbf{M}$ is related to $\mathbf{B}$ by $\mathbf{M} = \mathbf{B}^{-1}\bar{\mathbf{B}}$ and noting also that one should replace p_k, $\mathbf{B}$ and $\mathbf{L}$ by $(\sin(\gamma) + p_k\cos(\gamma))/(\cos(\gamma) - p_k\sin(\gamma))$, $\mathbf{\Omega}(\gamma)^T\mathbf{B}$ and $\mathbf{\Omega}(\gamma)^T\mathbf{L}\mathbf{\Omega}(\gamma)$, respectively, when the principal material axes have an angle γ relative to the reference coordinates x_1 and x_2 (see Fig. 1) (Ting, 1982), one leads to the singular integral equations for orthotropic materials:

$$\frac{-1}{2\pi}\left\{\int_{-c}^{c}\frac{\hat{\mathbf{b}}(t)}{t - \xi}dt + \int_{-c}^{c}\mathbf{\Omega}(\gamma)^T\begin{bmatrix} F_{11} & \delta F_{12} \\ \delta^{-1}F_{21} & F_{22} \end{bmatrix} \times \mathbf{\Omega}(\gamma)\hat{\mathbf{b}}(t)dt\right\} = -\mathbf{\Omega}(\theta)^T\begin{Bmatrix}\tau \\ \sigma\end{Bmatrix}, \quad |\xi| < c \tag{43a}$$

where

$$\hat{\mathbf{b}}(t) = \mathbf{\Omega}(\gamma)^T\mathbf{L}\mathbf{\Omega}(\gamma)\mathbf{b}(t), \tag{43b}$$

$$\mathbf{\Omega}(\gamma) = \begin{bmatrix} \cos(\gamma) & \sin(\gamma) \\ -\sin(\gamma) & \cos(\gamma) \end{bmatrix} \tag{43c}$$

and

$$F_{11} = \frac{1}{2(\kappa - 1)}\left\{(2\kappa + 2)^{1/2}\text{Re}[\rho_+D_{11} + \rho_-D_{22}] - 2\text{Re}[D_{12} + D_{21}]\right\}$$

$$F_{22} = \frac{1}{2(\kappa - 1)}\left\{(2\kappa + 2)^{1/2}\text{Re}[\rho_-D_{11} + \rho_+D_{22}] - 2\text{Re}[D_{12} + D_{21}]\right\}$$

$$F_{21} = \frac{-1}{2(\kappa-1)}\{(2\kappa+2)^{1/2}\mathrm{Im}[D_{11}+D_{22}] - 2\mathrm{Im}[\rho_- D_{12} + \rho_+ D_{21}]\}$$

$$F_{12} = \frac{1}{2(\kappa-1)}\{(2\kappa+2)^{1/2}\mathrm{Im}[D_{11}+D_{22}] - 2\mathrm{Im}[\rho_+ D_{12} + \rho_- D_{21}]\} \quad (44a)$$

for $\kappa > 1$, and

$$F_{11} = \frac{1}{2(\kappa-1)}\{(2\kappa+2)^{1/2}\mathrm{Im}[e^{+i\varphi}D_{21} - e^{-i\varphi}D_{12}] - (2\kappa+2)\mathrm{Re}[D_{11}+D_{22}]\}$$

$$F_{22} = \frac{1}{2(\kappa-1)}\{(2\kappa+2)^{1/2}\mathrm{Im}[e^{+i\varphi}D_{12} - e^{-i\varphi}D_{21}] - (2\kappa+2)\mathrm{Re}[D_{11}+D_{22}]\}$$

$$F_{21} = \frac{-1}{2(\kappa-1)}\{(2\kappa+2)^{1/2}\mathrm{Im}[D_{12}+D_{21}] + (2\kappa+2)\mathrm{Re}[e^{i\varphi}D_{11} - e^{-i\varphi}D_{22}]\}$$

$$F_{12} = \frac{1}{2(\kappa-1)}\{(2\kappa+2)^{1/2}\mathrm{Im}[D_{12}+D_{21}] + (2\kappa+2)\mathrm{Re}[e^{i\varphi}D_{22} - e^{-i\varphi}D_{11}]\} \quad (44b)$$

for $|\kappa| < 1$. In Eq. (44)

$$D_{jk} = \frac{\cos(\theta) + p_j^*\sin(\theta)}{(\xi - t)\cos(\theta) + p_j*(\xi\sin(\theta) - d) - \overline{p_k^*}(t\sin(\theta) - d)}, \quad -c \le \xi, t \le c,$$

$$p_k^* = \frac{\sin(\gamma) + p_k\cos(\gamma)}{\cos(\gamma) - p_k\sin(\gamma)}, \quad k,j = 1,2. \quad (45)$$

Since the kernel functions in Eq. (44) depend on two material parameters, κ and δ, only so that only these two material parameters have to be considered in the solutions of the singular integral equations in (43*a*). Note that the kernel functions in Eq. (44) are for cracks oriented arbitrarily and are for materials with arbitrary material angle γ. We can not tell from the present form that they are valid for degenerate cases or not since the factor $(\kappa - 1)$ appears in the denominator. However, we will see that this factor will be cancelled out for problems when crack is located either parallel or perpendicular to the free surface. In these two special cases, the kernel functions have been worked out in real form and the general expressions are shown in the Appendix. Note that these expressions are valid for the material principal axes having an arbitrary angle γ relative to the reference axes. From the explicit forms of the kernel functions shown in the Appendix, we can conclude that the kernel functions are do regular even for degenerate materials since the factor $\kappa - 1$ do not appear in the denominator.

When material principal axes coincide with the reference axes, i.e., $\gamma = 0$ deg or 90 deg, the problems for orthotropic materials will have some interesting features which are discussed below. For example, when $\gamma = 0$ deg, the kernel functions for a horizontal crack problem become

$$F_{11} = \frac{(\xi - t)}{d_1 d_2}\{(\xi - t)^4 + 2(\kappa - 3)h^2(\xi - t)^2 + 8(\kappa + 3)h^4\}$$

$$F_{22} = \frac{(\xi - t)}{d_1 d_2}\{(\xi - t)^4 + 2(5\kappa + 1)h^2(\xi - t)^2 + 8(2\kappa^2 + 5\kappa + 5)h^4\}$$

$$F_{21} = -F_{12} = \frac{4(\kappa+1)h^3}{d_1 d_2}\{3(\xi - t)^2 - 4h^2\} \quad (46)$$

where $h = d\delta/\Delta$,($\Delta = 1$ for $\gamma = 0$ deg),

$$d_1 = (\xi - t)^4 + 8\kappa h^2(\xi - t)^2 + 16h^4,$$

$$d_2 = (\xi - t)^2 + 2(\kappa + 1)h^2. \quad (47)$$

Note that these kernel functions are functions of κ, h, ξ, and t, and they are reduced to those for an isotropic material ($\kappa = 1$, $\delta = 1$) (Erdogan et al. (1973) note a sign error for F_{12} in the results given by Erdogan et al. (1973)). Substituting Eq. (46) into (43) and normalizing the integration from $|t| < c$ to $|t|$ 1 one obtains

$$\frac{-1}{2\pi}\left\{\int_{-1}^{1}\frac{\mathbf{b}^*(t)}{t-\xi}dt + \int_{-1}^{1}\begin{bmatrix} F_{11}^* & F_{12}^* \\ F_{21}^* & F_{22}^* \end{bmatrix}\mathbf{b}^*(t)dt\right\} = -\begin{bmatrix} 1 & 0 \\ 0 & \delta \end{bmatrix}\begin{Bmatrix} \tau \\ \sigma \end{Bmatrix}, \quad |\xi| < 1 \quad (48)$$

where

$$\mathbf{b}^*(t) = \begin{bmatrix} 1 & 0 \\ 0 & \delta \end{bmatrix}\mathbf{L}\mathbf{b}(t) \quad (49)$$

and matrix $\mathbf{L}$ has been defined by Eq. (42). Functions $F_{\alpha\beta}^*$ are obtained from (46) by replacing h by h/c and are related to the material parameter and geometry effect though κ and $h/c = d\delta/c$, respectively, only. Therefore, the solutions of $\mathbf{b}^*$ will depend only on these two parameters too, and will in general have the following form:

$$\mathbf{b}^* = -\begin{bmatrix} f_{11}^* & f_{12}^* \\ f_{21}^* & f_{22}^* \end{bmatrix}\begin{bmatrix} 1 & 0 \\ 0 & \delta \end{bmatrix}\begin{Bmatrix} \tau \\ \sigma \end{Bmatrix} \quad (50)$$

where $f_{\alpha\beta}^* = f_{\alpha\beta}^*(t, \kappa, d\delta/c)$. Once $\mathbf{b}^*(t)$ has been determined numerically or analytically if possible, the stress intensity factors then can be computed by the formula (32) which is

$$\begin{Bmatrix} K_{II} \\ K_I \end{Bmatrix} = \sqrt{\pi c}\begin{bmatrix} f_{11} & \delta f_{12} \\ \delta^{-1} f_{21} & f_{22} \end{bmatrix}\begin{Bmatrix} \tau \\ \sigma \end{Bmatrix} \quad (51)$$

where functions $f_{\alpha\beta}$ are defined by

$$f_{\alpha\beta}\left(\kappa,\frac{d\delta}{c}\right)=\frac{-1}{2\pi}\lim_{\xi\to 1^+}\sqrt{2(\xi-1)}\times\int_{-1}^{1}f^*_{\alpha\beta}\left(t,\kappa,\frac{d\delta}{c}\right)\frac{dt}{\xi-t}. \quad (52)$$

One should note that if the material principal axis is rotated from 0 deg to 90 deg, one can just replace δ in Eq. (51) by δ^{-1} to obtain the stress intensity factors for $\gamma = 90$ deg.

As to the problem for a crack normal to the traction-free boundary, the kernel functions F_{12} and F_{21} (from Appendix ((A3)) are identically zero, and $F_{11} = F_{22}$ (denoted by F hereafter) become, for $\gamma = 0$ deg,

$$F(\xi,t,\kappa,d)=\frac{(\xi-d)^2+2(\kappa+1)(\xi-d)(t-d)-(t-d)^2}{(\xi+t-2d)\left[(\xi-d)^2+2\kappa(\xi-d)(t-d)+(t-d)^2\right]} \quad (53)$$

which depends on material parameter κ only. By letting $\kappa = 1$ in the above equation one leads to the kernel function for isotropic material (Kaya, 1984). Substituting these special kernel functions $F_{\alpha\beta}$ to Eq. (43) one can obtain

$$\frac{-1}{2\pi}\left\{\int_{-1}^{1}\frac{\mathbf{b}^*(t)}{t-\xi}dt+\int_{-1}^{1}F^*\left(\xi,t,\kappa,\frac{d}{c}\right)\mathbf{b}^*(t)dt\right\}=\begin{bmatrix}0&1\\-1&0\end{bmatrix}\begin{Bmatrix}\tau\\\sigma\end{Bmatrix},\ |\xi|<1 \quad (54)$$

where

$$\mathbf{b}^*(t)=\mathbf{L}\mathbf{b}(t). \quad (55)$$

Function F^* in Eq. (54) is obtained from (53) by replacing d by d/c. One can easily see that these equations are decoupled and they share the same kernel function F^*. This implies that only one loading case, either pressure or shear, acting on the crack faces has to be considered for vertical crack problem. The solutions of the dislocation densities $\mathbf{b}^*(t)$ will depend on material parameter κ and will have the following form:

$$\mathbf{b}^*(t)=g^*\begin{bmatrix}0&1\\-1&0\end{bmatrix}\begin{Bmatrix}\tau\\\sigma\end{Bmatrix} \quad (56)$$

where $g^* = g^*(t, \kappa, d/c)$. The stress intensity factors (at the upper crack tip) is then

$$\begin{Bmatrix}K_{II}\\K_I\end{Bmatrix}=\sqrt{\pi c}\,g\left(\kappa,\frac{d}{c}\right)\begin{Bmatrix}\tau\\\sigma\end{Bmatrix} \quad (57)$$

where

$$g\left(\kappa,\frac{d}{c}\right)=\frac{-1}{2\pi}\lim_{\xi\to 1^+}\sqrt{2(\xi-1)}\int_{-1}^{1}g^*\left(t,\kappa,\frac{d}{c}\right)\frac{dt}{\xi-t}. \quad (58)$$

One can easily show that the formula leading to Eqs. (53), (54), and (57) are the same for $\gamma = 90$ deg, which implies that for vertical crack problem the stress intensity factors for both K_I and K_{II} are invariant with respect to a 90-deg rotation of the principal axes of the material. This fact has also been noted by Delale and Erdogan (1977) in the studies of cracks in an infinite long orthotropic strip.

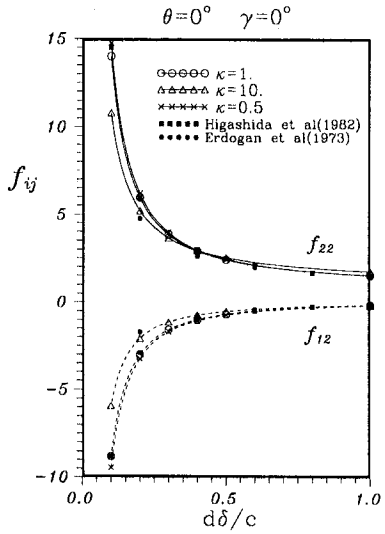

Fig. 2 Functions f_{12} and f_{22} defined in Eq. (51) versus $d\delta/c$ for various values of κ

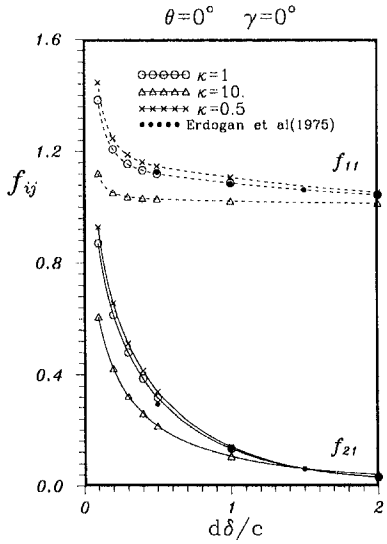

Fig. 3 Functions f_{11} and f_{21} defined in Eq. (51) versus $d\delta/c$ for various values of κ

5 Numerical Results for Horizontal or Vertical Crack Problems

(A) Material Alignment With $\gamma = 0$ deg or $\gamma = 90$ deg. As has been discussed in the previous section that for material alignment along the reference axes the dependence of the stress intensity factors on the material parameters and on the geometry effect are related to certain functions, which are given by Eqs. (51) or (57). These functions have been computed numerically and results are shown in Figs. 2 to 4. Figures 2 and 3 are the functions $f_{\alpha\beta}$ for a horizontal crack problem plotted versus $d\delta/c$ for several values of material parameter κ. It is seen that our results for $\kappa = 1$ are in good agreement with those results obtained by Higashida and Kamada (1982) or Erdogan et al. (1975). Their results are for isotropic material ($\delta = 1$, $\kappa = 1$). It is also observed that functions f_{12} and f_{21} approach zero while functions f_{11} and f_{22} become unity as $d\delta/c$ becomes large, an expected results for an infinite medium. Plotted in Fig. 4 is the function g versus d/c for vertical crack problem and only the result for the upper crack tip is presented in the present analysis.

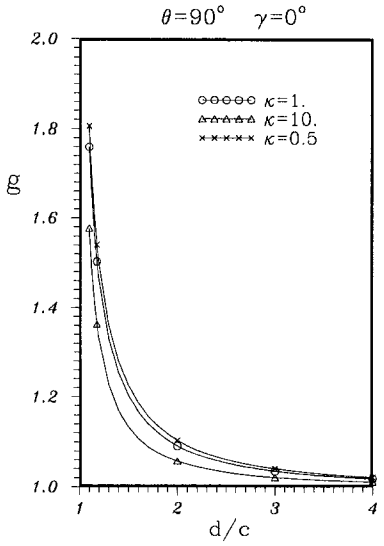

Fig. 4 Function g defined in Eq. (57) versus d/c for various values of κ

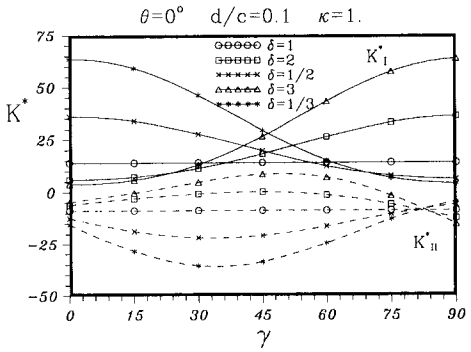

Fig. 5 Normalized stress intensity factors versus material angle γ for horizontal crack subjected to uniform pressure ($\kappa = 1$)

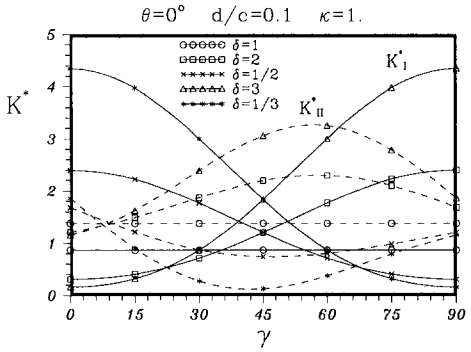

Fig. 6 Normalized stress intensity factors versus material angle γ for horizontal crack subjected to uniform shear ($\kappa = 1$)

(B) Dependence of the Stress Intensity Factors on γ for Degenerate Materials. In many cases the material alignment will have an angle with respect to the reference axes and in this case the features of the above subsection (A) would not preserve. Therefore, we will present in this subsection the effect of the material angle γ on the stress intensity factors, In the following, we will restrict our discussions to the degenerate materials, i.e., $\kappa = 1$, while crack orientation is still kept horizontally or vertically. Figures 5 and 6 are the results of a horizontal crack ($d/c = 0.1$) subjected to uniform pressure and uniform shear, respectively, while Fig. 7 and Fig. 8 are the results for a vertical crack ($d/c = 1.1$). From

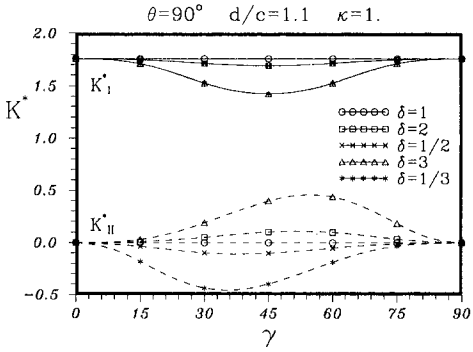

Fig. 7 Normalized stress intensity factors versus material angle γ for vertical crack subjected to uniform pressure ($\kappa = 1$)

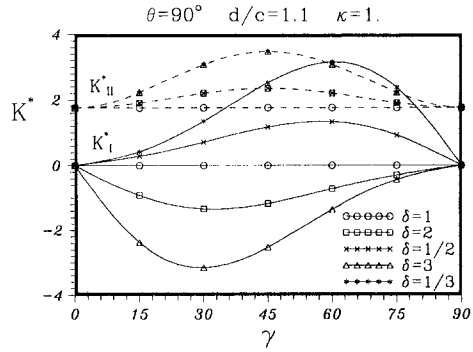

Fig. 8 Normalized stress intensity factors versus material angle γ for vertical crack subjected to uniform shear ($\kappa = 1$)

the numerical studies, we found that only the values of γ between 0 deg to 90 deg have to be investigated, since there is a common feature that

$$K^*_{I,II}\left(\delta,\gamma+\frac{\pi}{2}\right)=K^*_{I,II}(\delta^{-1},\gamma) \tag{59}$$

holds. In all presentations, K^* is the normalized stress intensity factor defined by $K^*=K/(\sigma^*\sqrt{\pi c})$ where $\sigma^*=\sigma$ or $\sigma^*=\tau$. For horizontal crack problems (Figs. 5 and 6) the extremes of K^*_I occur when $\gamma=0$ deg and 90 deg for both shear and pressure loading while the places of extremes for K^*_{II} are different for different values of δ. It is also observed from Fig. 6 that, under uniform shear loading.

$$K^*_I(\delta,\gamma)=K^*_I\left(\delta^{-1},\frac{\pi}{2}-\gamma\right) \tag{60}$$

for a Mode I stress intensity factor. For vertical crack problems, more features can be observed from the numerical results shown in Figs. 7 and 8. For example, from Fig. 7,

$$K^*_I(\delta,\gamma)=K^*_I\left(\delta,\frac{\pi}{2}-\gamma\right),\quad\text{(symmetrical property)}$$

$$K^*_I(\delta,\gamma)=K^*_I(\delta^{-1},\gamma),$$

$$K^*_{II}(\delta,\gamma)=-K^*_{II}\left(\delta^{-1},\frac{\pi}{2}-\gamma\right), \tag{61}$$

under uniform normal pressure loading. The above properties are still preserved for uniform shear loading if one interchanges the subindex I by II in Eq. (61).

Acknowledgment

The authors wish to thank the reviewers for bringing some

important literature to our attention and for their valuable criticism.

References

Bowie, O. L., 1973, "Solutions of Plane Crack Problems By Mapping Technique," *Methods of Analysis and Solutions of Crack Problems*, G. C. Sih, ed., Noordhoff International Publishing, Leyden.

Bueckner, H. F., 1970, "A Novel Principle for Computation of Stress Intensity Factors," *Zeistchrift fr angewandte Mathematik und Mechanik*, Vol. 50, pp. 529–545.

Bueckner, H. F., 1971, "Weight Functions for the Notched Bar," *Zeistchrft fr angewandte Mathematik und Mechanik*, Vol. 51, pp. 97–109.

Chadwick, P., and Smith, G. D., 1977, "Foundations of the Theory of Surface Waves in Anisotropic Elastic Materials," *Advances in Applied Mechanics*, Vol. 17, pp. 303–376.

Cinar, A., and Erdogan, F., 1983, "The Crack and Wedging Problem for an Orthotropic Strip," *International Journal of Fracture*, Vol. 23, pp. 83–102.

Delale, F., and Erdogan, F., 1977, "The Problem of Internal and Edge Cracks in an Orthotropic Strip," ASME JOURNAL OF APPLIED MECHANICS, Vol. 44, pp. 237–242.

Delale, F., Bakirtas, I., and Erodgan, F., 1979, "The Problem of an Inclined Crack in an Orthotropic Strip," ASME JOURNAL OF APPLIED MECHANICS, Vol. 46, pp. 90–96.

Dongye, C., and Ting, T. C. T., 1989, "Explicit Expressions of Barnett-Lothe Tensors and Their Associated Tensors for Orthotropic Materials," *Quarterly of Applied Mathematics*, Vol. 47, pp. 723–734.

Erdogan, F., Gupta, G. D., and Cook, T. S., 1973, "Numerical Solution of Singular Integral Equations," *Methods of Analysis and Solutions of Crack Problems*, G. C. Sih, ed., Noordhoff International publishers, Leyden, pp. 368–425.

Erdogan, F., and Arin, K., 1975, "A Half Plane and a Strip With an Arbitrarily Located Crack," *International Journal of Fracture*, Vol. 11, pp. 191–204.

Eshelby, J. D., Read, W. T., and Shockley, W., 1953, "Anisotropic Elasticity With Applications to Dislocations Theory," *Acta Metallurgica*, Vol. 1, pp. 251–259.

Gerasoulis, A., 1982, "The Use of Piecewise Quadratic Polynomials for the Solutions of Singular Integral Equations of Cauchy Type," *Computational Mathematics with Applications*, Vol. 8, pp. 15–22.

Gupta, G. D., and Erdogan, F., 1974, "The Problem of Edge Cracks in an Infinite Strip," ASME JOURNAL OF APPLIED MECHANICS, Vol. 41, pp. 1001–1006.

Heng, Z., McCammond, D., and Tabarrok, B., 1986, "Stress Determination in Edge-Cracked Anisotropic Plates by an Extension of Boundary-Collocation Method," *Computer Methods in Applied Mechanics and Engineering*, Vol. 54, pp. 187–195.

Heng, Z., McCammond, D., and Tabarrok, B., 1986, "Stress Determination in Edge-Cracked Anisotropic Plates by an Extension of Boundary-Collocation Method," *Computer Methods in Applied Mechanics and Engineering*, Vol. 54, pp. 187–195.

Higashida, Y., and Kamada, K., 1982, "Stress Fields Around a Crack Lying Parallel to a Free Surface," *International Journal of Fracture*, Vol. 19, pp. 39–52.

Isida, M., 1966, "Stress-Intensity Factors for the Tension of an Eccentrically Cracked Strip," ASME JOURNAL OF APPLIED MECHANICS, Vol. 33, pp. 674–675.

Kaya, A. C., and Erdogan, F., 1980, "Stress Intensity Factors and COD in an Orthotropic Strip," *International Journal of Fracture*, Vol. 16, pp. 171–190.

Kaya, A. C., 1984, "Applications of Integral Equations with Strong Singularities in Fracture Mechanics," Ph.D. Dissertation, Department of Applied Mechanics, Lehigh University.

Krenk, S., 1979, "On the Elastic Constants of Plane Orthotropic Elasticity," *Journal of Composite Materials*, Vol. 13, pp. 108–116.

Lekhnitskii, S. G., 1963, *Theory of Elasticity of an Anisotropic Body*, Holden Day, San Francisco.

Miller, G. R., 1989, "Analysis of Crack Near Interfaces Between Dissimilar Anisotropic Materials," *International Journal of Engineering Science*, Vol. 27, pp. 667–678.

Sih, G. C., 1973, *Methods of Analysis and Solutions of Crack Problems*, Noordhoff International Publishers, Leyden.

Stroh, A. N., 1958, "Dislocations and Cracks in Anisotropic Elasticity," *Philos. Mag.*, Vol. 7, pp. 625–646.

Suo, Z., 1990, "Singularities, Interfaces and Cracks in Dissimilar Anisotropic Media," *Proceedings of the Royal Society of London*, Vol. A427, pp. 331–358.

Ting, T. C. T., 1982, "Effects of Change of Reference Coordinates In the Stress Analyses of Anisotropic Elastic Materials," *International Journal of Solids and Structures*, Vol. 18, pp. 139–152.

Ting, T. C. T., 1986, "Explicit Solution and Invariance of The Singularities at an Interface Crack in Anisotropic Composites," *International Journal of Solids and Structures*, Vol. 22, pp. 965–983.

Ting, T. C. T., 1992, "Image Singularities of Green's Functions for Anisotropic Elastic Half-Spaces and Bimaterials," *The Quarterly Journal of Mechanics and Applied Mathematics*, Vol. 22, pp. 119–139.

Wen, P., 1989, "The Solution of a Displacement Discontinuity for an Anisotropic Half-Plane and Its Applications to Fracture Mechanics," *Engineering Fracture Mechanics*, Vol. 34, pp. 1145–1154.

Zang, W., and Gudmundson, P., 1989, "An Integral Equation Method for Piece-Wise Smooth Cracks in an Elastic Half-Plane," *Engineering Fracture Mechanics*, Vol. 32, pp. 889–897.

APPENDIX

The kernel functions appearing in Eq. (43) have been worked out in real form for the special cases when a crack is either parallel or perpendicular to the free surface. The material alignment can have an angle γ with respect to the reference axis. For a horizontal crack, the kernel functions are given by

$$F_{11} = \frac{\xi - t}{d_1 d_2}\Bigg\{(\xi - t)^6 + 4\Bigg[\kappa - 1 - 2(\kappa + 1) \times \frac{\delta^2 \sin^2(\gamma)}{\Delta^2}\left[(2\kappa - 3)\cos^2(\gamma) - \delta^2 \sin^2(\gamma)\right]\Bigg] h^2(\xi - t)^4 + 4\Bigg[\kappa^2 + 3 + 8(\kappa + 1)\frac{\delta^2 \sin^2(\gamma)}{\Delta^2}\left[2(\kappa - 1)\cos^2(\gamma) - (\kappa + 1)(\cos^2(\gamma) + \delta^2 \sin^2(\gamma))\Gamma_1\right]\Bigg] h^4(\xi - t)^2 + 16(\kappa + 1)\Bigg[\kappa + 3 + \frac{2\delta^2 \sin^2(\gamma)}{\Delta^2}\left[(\kappa + 1)^2(\delta^2 \sin^2(\gamma) - \cos^2(\gamma)) + 8\cos^2(\gamma)\right]\Bigg] h^6\Bigg\}$$

$$F_{22} = \frac{\xi - t}{d_1 d_2}\Bigg\{(\xi - t)^6 + 4\Bigg[3\kappa + 1 - \frac{2\delta^2 \sin^2(\gamma)}{\Delta^2}\left[(4\kappa^2 + \kappa - 3)\cos^2(\gamma) + (\kappa + 1)\delta^2 \sin^2(\gamma)\right]\Bigg] h^2(\xi - t)^4 + 4\Bigg[9\kappa^2 + 16\kappa + 11 + \frac{8\delta^2 \sin^2(\gamma)}{\Delta^2} \times \left[(\kappa + 1)^2\left[(2\kappa - 1)\cos^2(\gamma) + \delta^2 \sin^2(\gamma)\right] \times \Gamma_1 - 2(\kappa^2 - 1)(2\kappa + 1)\cos^2(\gamma)\right]\Bigg] h^4(\xi - t)^2 + 16(\kappa + 1)\Bigg[2\kappa^2 + 5\kappa + 5 - \frac{2\delta^2 \sin^2(\gamma)}{\Delta^2}\left[(\kappa + 1)^2 \times \delta^2 \sin^2(\gamma) + (2\kappa^3 + 5\kappa^2 + 4\kappa - 7)\cos^2(\gamma)\right]\Bigg] h^6\Bigg\}$$

$$F_{21} = 4(\kappa + 1)\frac{\cos^2(\gamma) + \delta^2 \sin^2(\gamma)}{\Delta} \times \left\{\frac{d_3}{d_1 d_2}h^3 + \frac{2\delta \sin(\gamma)\cos(\gamma)}{\Delta}\frac{(\xi - t)}{d_2}h^2\right\}$$

$$F_{12} = 4(\kappa+1)\frac{\cos^2(\gamma)+\delta^2\sin^2(\gamma)}{\Delta} \times\left\{\frac{-d_3}{d_1 d_2}h^3 + \frac{2\delta\sin(\gamma)\cos(\gamma)}{\Delta}\frac{(\xi-t)}{d_2}h^2\right\} \quad \text{(A1)}$$

where

$$d_1 = (\xi-t)^4 + 8\Gamma_2 h^2(\xi-t)^2 + 16h^4,$$

$$d_2 = (\xi-t)^4 - 4(\kappa+1)\Gamma_1 h^2(\xi-t)^2 + 4(\kappa+1)^2 h^4,$$

$$d_3 = 3(\xi-t)^4 + 2(1-\kappa+4\Gamma_2)h^2(\xi-t)^2 - 8(\kappa+1)h^4,$$

$$\Gamma_1 = 4(\kappa-1)\frac{\delta^2\sin^2(\gamma)\cos^2(\gamma)}{\Delta^2} - 1,$$

$$\Gamma_2 = \kappa - 2(\kappa^2-1)\frac{\delta^2\sin^2(\gamma)\cos^2(\gamma)}{\Delta^2},$$

$$h = d\delta/\Delta, \qquad \Delta^2 = \cos^4(\gamma) + 2\kappa\delta^2\sin^2\sin^2(\gamma)\cos^2(\gamma) + \delta^4\sin^4(\gamma). \quad \text{(A2)}$$

It is noted that these kernel functions are regular even when $\kappa = 1$. For the vertical crack problem, the kernel functions are given by

$$F_{11} = \frac{1}{d_1 d_2\Delta(\kappa-1)}\{-2\Delta d_1[\Delta\xi_d^3 - 3R_2 R\xi_d^2 t_d + (2R_2^2+2R^2-\Delta)\xi_d t_d^2 - R_2 R t_d^3] + (\kappa+1)d_2[(\Delta\xi_d - (R_1 R + 2(\kappa-1)R_5 R_6)t_d) \times(\Delta\xi_d^2 - 2R_1 R\xi_d t_d + (2R^2-\Delta)t_d^2) + 4R_5((\kappa-1)(R_5 R_1 - R_6 R) + 2R_5 R_1)t_d^2(R_1\xi_d - R t_d)]\}$$

$$F_{22} = \frac{1}{d_1 d_2\Delta(\kappa-1)}\{-2\Delta d_1[\Delta\xi_d^3 - 3R_2 R\xi_d^2 t_d + (2R_2^2+2R^2-\Delta)\xi_d t_d^2 - R_2 R t_d^3] + (\kappa+1)d_2[(\Delta\xi_d - (R_1 R - 2(\kappa-1)R_5 R_6)t_d) \times(\Delta\xi_d^2 - 2R_1 R\xi_d t_d + (2R^2-\Delta)t_d^2) + 4R_5((\kappa-1)(R_5 R_1 + R_6 R) + 2R_5 R_1)t_d^2(R_1\xi_d - R t_d)]\}$$

$$F_{21} = \frac{2(\kappa+1)R_5 t_d}{d_1 d_2(\kappa-1)}\{d_2[R_1\xi_d^2 - 2R\xi_d t_d + R_1 t_d^2] + d_1[(R_3-2R_2)\xi_d^2 + 2R\xi_d t_d - R_3 t_d^2]\}$$

$$F_{12} = \frac{-2(\kappa+1)R_5 t_d}{d_1 d_2(\kappa-1)}\{d_2[R_1\xi_d^2 - 2R\xi_d t_d + R_1 t_d^2] + d_1[(R_4-2R_2)\xi_d^2 + 2R\xi_d t_d - R_4 t_d^2]\} \quad \text{(A3)}$$

where $\xi_d = (\xi - \mathrm{d})$, $t_d = (t-d)$ and

$$d_1 = \Delta(\xi_d^2 - t_d^2)^2 + 4\xi_d t_d(R_1 t_d - R\xi_d)(R_1\xi_d - R t_d),$$

$$d_2 = \Delta(\xi_d^2 - t_d^2)^2 + 4\xi_d t_d(R_2 t_d - R\xi_d)(R_2\xi_d - R t_d),$$

$$\Delta = \left[(1-\delta^2)^2\sin^2(\gamma)\cos^2(\gamma) + \delta^2\right]^2 + 2(\kappa-1)\delta^2\sin^2(\gamma)\cos^2(\gamma)\left[1+\delta^4 - 2(1-\delta^2)^2 \times\sin^2(\gamma)\cos^2(\gamma) + 2(\kappa-1)\delta^2\sin^2(\gamma)\cos^2(\gamma)\right],$$

$$R = \left[(1-\delta^2)^2\sin^2(\gamma)\cos^2(\gamma) - \delta^2\right] + (\kappa-1)\left[-2\delta^2\sin^2(\gamma)\cos^2(\gamma)\right]$$

$$R_1 = \left[(1-\delta^2)^2\sin^2(\gamma)\cos^2(\gamma) + \delta^2\right] + (\kappa-1)\left[-2\delta^2\sin^2(\gamma)\cos^2(\gamma)\right],$$

$$R_2 = \left[(1-\delta^2)^2\sin^2(\gamma)\cos^2(\gamma) + \delta^2\right] + (\kappa-1)\left[-2\delta^2\sin^2(\gamma)\cos^2(\gamma) + \delta^2\right],$$

$$R_3 = \left[(1-\delta^2)^2\sin^2(\gamma)\cos^2(\gamma) + \delta^2\right] + (\kappa-1)\left[2\delta^2\sin^4(\gamma)\right],$$

$$R_4 = \left[(1-\delta^2)^2\sin^2(\gamma)\cos^2(\gamma) + \delta^2\right] + (\kappa-1)\left[2\delta^2\cos^4(\gamma)\right],$$

$$R_5 = (1-\delta^2)\delta\sin(\gamma)\cos(\gamma),$$

$$R^6 = (1+\delta^2)\delta\sin(\gamma)\cos(\gamma). \quad \text{(A4)}$$

Although these kernel functions in (A3) contain the factor $(\kappa-1)$ in the denominator, one can find that this factor can be cancelled out if one completes the calculation in the brackets. This completes the statements that these kernel functions are regular when $\kappa = 1$.

Mechanics of the Segmentation of an Embedded Fiber, Part I: Experimental Investigations

A. ten Busschen
Laboratory of Engineering Mechanics,
and Marine Technology,
Delft University of Technology,
Delft, The Netherlands

A. P. S. Selvadurai
Department of Civil Engineering
and Applied Mechanics,
Faculty of Engineering,
McGill University,
Montreal, QC H3A 2K6, Canada
Mem. ASME

Micromechanical modeling is an important aspect in the study of fiber-reinforced composites. In such studies, an important class of structural parameters is formed by the interaction between the matrix and the embedded fibers. These interactive processes can be investigated by an appeal to a test which involves the segmentation of an embedded fiber. This test is referred to as a "fragmentation test." During a fragmentation test, two distinct fracture phenomena are observed. These phenomena are directly related to the integrity of bond between the embedded fiber and the matrix. The first phenomenon involves situations where the interface bond is weaker than the matrix material. In this case the fiber fragment ends will slip and in this region shear stresses are transmitted by friction and/or interlocking mechanical actions. In contrast, when the interface bond has stronger properties than the matrix material, cracking will occur in the matrix region. Here, a crack initiated in the fiber will propagate into the matrix region typically forming conoidal cracks, or combinations of conoidal and flat cracks. This paper describes the background of the fragmentation test and the associated experimental research. Attention is focused on the experimental evaluation of matrix fracture topographies encountered in the fragmentation test.

Introduction

Composite materials offer new possibilities for the design of engineering structures. A majority of modern advanced composite materials is formed by fiber-reinforced plastics which can combine low specific weights with high strength. A critical engineering property of such composites is the transverse strength, i.e., the strength normal to the aligned fibers. The wide variations in the transverse strength property places a severe restriction on the wider applications of fiber-reinforced plastics (see, e.g., Hull, 1981; Pagano, 1989; Friedrich, 1989; Kedward et al., 1989; Pantano and Chen, 1990; ten Busschen, 1991). By gaining insight into the mechanisms that are responsible for the magnitude of transverse strength, it is possible to identify techniques and properties which could lead to improvements in the transverse strength characteristics. Micromechanical modeling provides a basis for the prediction of macroscopic mechanical properties of a composite, based on the so-called structural parameters. Thus, relationships can be obtained between the properties at the microscale (structural parameters) and macroscopic composite behavior (effective behavior). This is an effective basis for the identification of the parameters which contribute to low transverse strengths in composites (ten Busschen, 1991).

The structural parameters needed for micromechanical modeling can be divided into three groups; the first group consists of the properties of the constituents of the composite (i.e., matrix, fibers); the second group is formed by the properties of the interaction between the constituents (i.e., interfaces, delaminations); the third group is formed by the morphology of the reinforcement (i.e., fiber content, fiber distribution, and arrangement). In the second group of structural parameters, the interaction between the constituents, or more specifically the mechanical contact between the fiber and the matrix is known to affect the mechanical properties of the composite, and especially the transverse strength (Moran et al., 1991). A variety of tests can be developed to characterize the mechanical response of the contact between a fiber and the surrounding matrix; these include, for example, the single fiber pull-out test and fragmentation test involving a single filament composite specimen.

The composites research program at the Laboratory of Engineering Mechanics at Delft University of Technology has initiated a series of experimental investigations geared to the evaluation of the mechanical characteristics of a fiber-matrix interface by appeal to the fragmentation test (van den Berg, 1990). The fragmentation test uses a specimen that consists of a single fiber filament which is embedded in a polymer matrix specimen (Fig. 1). Upon application of a

Contributed by the Applied Mechanics Division of THE AMERICAN SOCIETY OF MECHANICAL ENGINEERS for publication in the ASME JOURNAL OF APPLIED MECHANICS.

Discussion on this paper should be addressed to the Technical Editor, Processor Lewis T. Wheeler, Department of Mechanical Engineering, University of Houston, Houston, TX 77204-4792, and will be accepted until four months after final publication of the paper itself in the ASME JOURNAL OF APPLIED MECHANICS.

Manuscript received by the ASME Applied Mechanics Division, Dec. 2, 1992; final revision, Oct. 8, 1993. Associate Technical Editor: G. J. Dvorak.

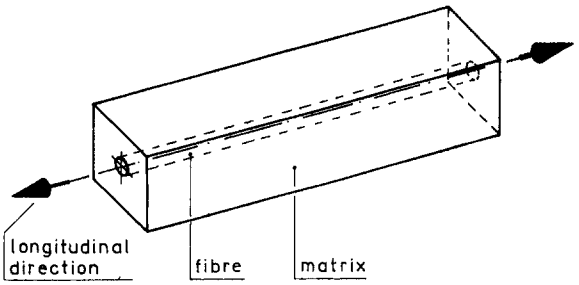

Fig. 1 Configuration of test specimen with embedded fiber

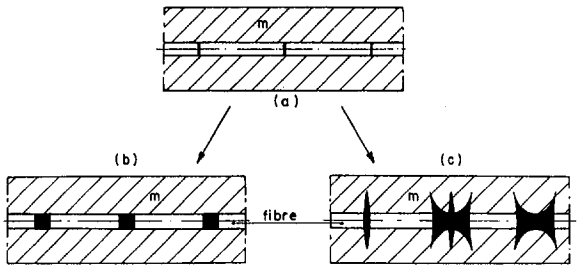

Fig. 2 Observed damage phenomena during fragmentation tests (*a*) cracked fiber, (*b*) formation of voids (weak interface), (*c*) matrix crack formation (strong interface)

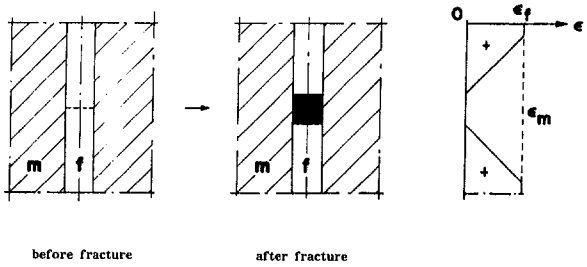

Fig. 3 Formation of a void at a cracked fiber

longitudinal strain to the specimen, the intact fiber will also be subjected to an identical strain. When the longitudinal strain reaches a certain magnitude, the fiber will experience fracture at several locations (Fig. 2(*a*)). If the strain is increased further, two distinct phenomena can be observed. These phenomena are directly related to the adhesive properties of the fiber-matrix interface. When the strength or fracture properties of the mechanical contact are weaker than those of the matrix, the fiber fragment ends will move relative to the specimen (slip), forming an increasing void with increasing strain (Fig. 2(*b*)). In contrast, when the interface strength and fracture properties are stronger than those of the matrix material, the fiber crack will extend into the matrix region (Fig. 2(*c*)). The occurrence of both phenomena at prolonged fragmentation was reported by Selvadurai et al. (1991). The occurrence of either slip at the interface or cracks in the matrix is directly influenced by the integrity of the interface. Consequently, identical fiber-matrix systems will display radically different post fiber-fracture processes depending upon the coupling agents that are utilized to enhance the interface fracture and failure characteristics.

This paper forms the first part of a study which investigates the mechanics of a fragmentation test. It discusses the experimental investigations which were carried out at the Laboratory of Engineering Mechanics at Delft University of Technology. The mechanical background of the fragmentation test and the test procedure are described. Special attention is given to the techniques used in the measurement of strains in the specimen and the characterization of fine matrix microcracks which occur at the cracked fiber locations. An image analysis technique forms the basis for such experimental evaluations. The experimental results are presented and the characteristic features of "Bat Cracks" are quantified. A companion paper will focus on the computational modeling of the process of matrix crack extension at cracked fiber locations.

Mechanics of the Fragmentation Test

Fiber Reinforcement. Most reinforcing fibers employed in advanced composite materials are composed of brittle elastic materials. Typical examples of such materials include carbon fibers, graphite fibers, boron fibers, silicon carbide fibers and E-Glass. In this article attention is focused on the class of fiber-reinforced composites composed of E-Glass fibers. These brittle materials generally have an extremely high intrinsic strength (theoretical strength); however, in practice, the actual strength of such materials is strongly influenced by the geometrical imperfections. This can be attributed to processes such as notch, surface flaw, or internal flaw sensitivity which can drastically reduce the measured strength (see, for example, the classical study by Griffith, (1921). For this reason, fibers for composite reinforcement are manufactured as thin as possible; this reduces the probability of occurrence of strength-reducing flaws. From these observations it becomes evident that the effective strength of a reinforcing fiber is dependent on the fiber length; i.e., it increases with decreasing length (see, e.g., Merle and Xie, 1991). Although long fibers used in composites do contain many flaws, it is assumed there are no disadvantageous effects in the generation of longitudinal strength in a composite due to the load transfer mechanisms that occur within the matrix phase.

The Fragmentation Test. The fragmentation test consists of the straining of a matrix specimen which contains a co-axial single fiber (or single filament). The dimensions of the single fiber, relative to the dimension of the matrix region are such that, effectively, the fiber is embedded in a matrix region of infinite extent (i.e., $d/t = 0.015$; where $d = 15\mu$m; $t = 1$ mm and t is the thickness of the specimen). The fragmentation test specimen is subjected to uniform strain over its entire cross-section. When the strain reaches a certain value, the fiber will fracture at its weakest locations. If the strength and fracture characteristics of the fiber-matrix interface are lower than those of the matrix material, interface slipping and/or interface locking can occur at a detached interface. This phenomenon can be explained by the unloading of cracked fiber ends after fracture. In this instance the fiber strain will be zero at the cracked ends and by gradual load transfer processes the longitudinal strains in the fiber will reach the same magnitude as the matrix strain. Over the distance where gradual load transfer takes place the incompatibility of strains between the matrix and the fiber usually results in the formation of a void (Fig. 3).

In Fig. 3, the fiber strain is assumed to be linear in the longitudinal direction over this slipped section. It is often assumed that the shear stresses in the interface region where slipping takes place has constant value (see, e.g., Piggot, 1980). This constant shear stress is regarded as a strength property of the interface (i), indicated by τ_i. To account for the difference in fiber strain and the matrix strain, the matrix exhibits shear deformation besides slip at the fiber-matrix interface. Such mechanisms can be described by shear-lag theory (Cox, 1952) and by more advanced load transfer models (McCartney, 1989). However, the effects of shear deformation of the matrix material is negligible when compared to the effect of slipping of the interface (van den Berg, 1990).

Critical Fiber Length. With the assumption that the shear stress is constant in the parts of the fiber-matrix interface where slip occurs (slip theory), attention can be focused on a fiber fragment between two fractures with slip regions (S) at the ends (Fig. 4). By means of the shear stresses at the fragment ends, the fiber can be loaded in the middle part (M) until the fiber strength is reached again forming a new fracture in the fiber, etc. A critical situation occurs when the middle part disappears (slip over the entire fragment). In this case the largest possible loading of the fiber occurs, which gives the maximum fiber stress in the middle of the fiber fragment, indicated by $\sigma_{f,\max}$:

$$\sigma_{f,\max} = \frac{2l\tau_i}{d_f}. \tag{1}$$

In this connection, the critical fiber length is defined as the length at which the maximum fiber stress in (1) equals the fiber strength indicated by $\langle \sigma_f \rangle$ (belonging to a particular fiber length) i.e.,

$$l_{cr} = \frac{d_f \langle \sigma_f \rangle}{2\tau_i}. \tag{2}$$

This critical fiber length is the shortest fiber fragment that can fracture under the given assumptions. In the case of fiber slip, the fragmentation test is terminated when further straining of the specimen does not cause new fractures in the fiber fragments; in this case all the fragments will not be longer than the critical length (assuming the validity of the slip theory). When the fiber diameter and fiber strength (at critical length) are known the average fragment length indicated by l can be used to determine the slip length of the interface, e.g.,

$$\tau_i = \frac{d_f \langle \sigma_f \rangle}{3l}. \tag{3}$$

The above result is based on the fact that fiber fragments with critical length have equal probability either to fracture or not to fracture. In this case of fracture the resulting separate parts have to be accounted for in the calculations. With this simple model, the mean fragment length can be expressed in terms of the critical length: i.e.,

$$l = \frac{2}{3} l_{cr} \tag{4}$$

The result (4) which was also reported by Merle and Xie (1991) can also be derived by employing a more sophisticated simulation where the fragment lengths are not required to assume the critical length or half of the critical length.

Formation of Cracks. If the strength and fracture toughness of the interface are higher than those of the matrix material, the ends of the cracked fiber will remain adhered to the matrix thus forcing the crack to extend into the matrix. The explanation and evaluation of the mechanical aspects of this crack growth will be given in the ensuing sections.

Let us first consider the case of the classical penny-shaped crack which is located in an elastic matrix of infinite extent and subjected to a uniform stress field at infinity (σ_∞) (see, e.g., Fig. 5). The Mode I stress intensity factor at the crack tip can be obtained from the classical result given by Sneddon (1946) (see also Kassir and Sih, 1975), i.e.,

$$K_I^0 = \frac{2\sigma_\infty \sqrt{c}}{\pi} \tag{5}$$

where c is the radius of the penny-shaped crack. For a polyester matrix it is possible to determine the extent of cracking necessary prior to reaching the strength of the matrix material σ_{mt}. The limiting case occurs when the remote stress σ_∞ reaches the material strength at the same instance when the stress intensity factor reaches its critical value K_{Ic}, i.e.,

$$K_{Ic} = \frac{2\sigma_{mt}\sqrt{c}}{\pi}. \tag{6}$$

Thus for crack extension prior to reaching the material strength, the minimum crack radius required is given by

$$c_{\min} = \left(\frac{\pi K_{Ic}}{2\sigma_{mt}} \right)^2 \tag{7}$$

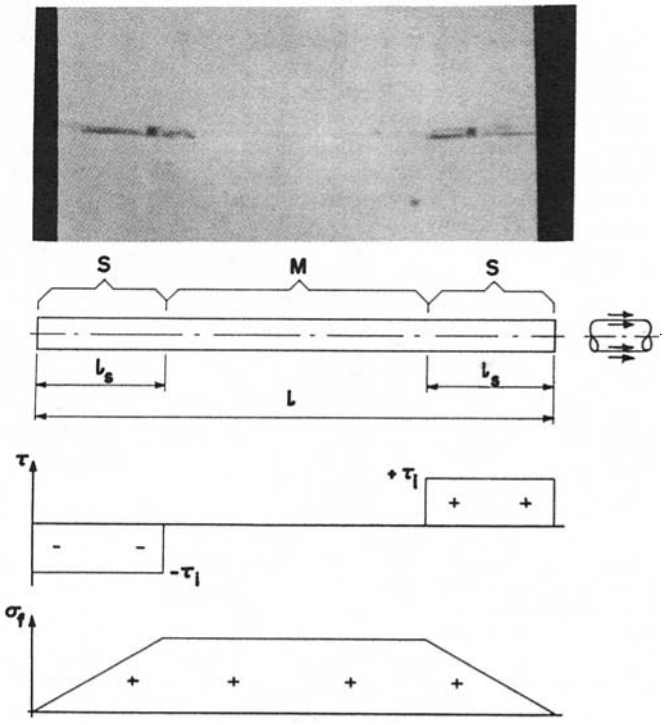

Fig. 4 Fiber fragment with slipping end; observed phenomena and modeling

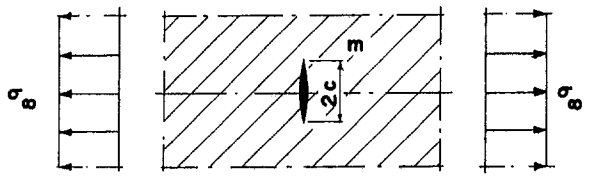

Fig. 5 Penny-shaped crack in an elastic medium of infinite extent

Table 1 Minimum crack radii for a polyester matrix

Curing state	K_{Ic} (MPa $\sqrt{m}$) Rebelo et al. (1986)	σ_{mt} (MPa) Berg (1990)	$c_{\min}$ (μm) From Eq.(7)
seven days after solidification	1.0	53	846
after post-cure treatment	0.6	87	117

The Table 1 gives results for c_{min} for polyester matrices at various stages of the hardening phase. From Table 1 it can be concluded that pre-existing penny-shaped cracks have to be several times the size of the fiber diameter (15 μm) to permit crack propagation. It should be noted that polyester shows the lowest critical Mode I stress intensity factor and the highest material strength after a full post-cure treatment. This hardening state, therefore, yields the lower bound for the minimum crack radius.

Let us now focus attention on the case of the *fiber matrix crack* in which a penny-shaped crack extends through a cracked fiber into the matrix region (Fig. 6). This problem was investigated by Selvadurai (1991) by using a boundary element modeling of the fracture mechanics problem. More recently Selvadurai et al. (1995) have also developed a complete analytical solution for the integral equations governing the mixed boundary value problem. In the case of the fiber-matrix crack, the Mode I stress intensity factor is significantly higher than that for the penny-shaped crack. For typical fiber-matrix cracks (Fig. 6), the stress intensity factors are given as a function of the modulus mismatch between the fiber and the matrix (Fig. 7). From these results it may be concluded that in situations where the interface strength and fracture toughness are sufficient enough to prevent slip processes, the fiber crack will propagate into the matrix. With stiffer fibers (i.e., $E_f/E_m > 1$) the stress intensity factor at the matrix-fiber crack tip is sufficiently amplified to cause crack propagation prior to reaching the matrix strength. Although a penny-shaped crack is intuitively thought to be the most likely crack propagation mode subsequent to fiber fracture, other crack topographies are possible depending upon local inhomogeneities and the degree of localized damage that can be induced in the matrix region at the location

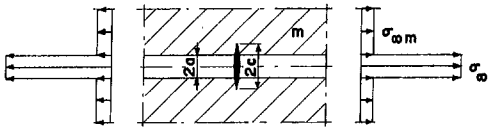

Fig. 6 The matrix-fiber crack in an elastic medium of infinite extent

of a cracked fiber (Selvadurai et al., 1991). Figure 8 illustrates four crack topographies that were observed in the fragmentation tests involving an E-Glass Fiber embedded in a polyester matrix. Other researchers have also observed similar crack patterns in materials with stiff inclusions. For example, penny-shaped cracks and conoidal cracks were observed in Boron fiber-Epoxy systems (Chamis, 1974) and glass bead-polystyrene composite systems (Dekkers, 1985). Similar crack patterns in fragmentation tests with carbon fiber-epoxy systems were reported by Sancaktar (1991). The main categories of crack patterns observed in actual fragmentation tests are shown in Fig. 9. These fracture patterns are characterized by the fiber crack separation distance $2u_0$, the diameter of penny-shaped cracks $2c$, the crack termination diameter of purely conoidal crack ($2c$), the crack termination diameters for combined cracks involving penny-shaped ($2c_2$) and conoidal cracks ($2c_1$) and the inclination of the conoidal crack to the axis of the fiber (θ_0). In general

$$\left\{\frac{u_0}{a}, \frac{c}{a}, \frac{c_1}{a}, \frac{c_2}{a}\right\} = f\left\{\frac{E_f}{E_m}, \nu_f, \nu_m, K_{Ic}, K_{IIc}, \epsilon_\infty\right\} \quad (8)$$

where $\epsilon_\infty \simeq \sigma_\infty/E_m$.

In connection with the crack inclination θ_0, the following observations can be made. First, in the experiments, this angle can have different values; in any calculation (Selvadurai and ten Busschen, 1995) this parameter needs to be assigned a specific value in order to examine the progress of matrix crack extension at a cracked fiber location. Secondly, consider the local geometry in the vicinity of a cracked fiber location. Referring to Fig. 10, two possible scenarios exist. In the first case strong interface bond will propagate the elemental or starter matrix cracks (e.g., penny-shaped and conical) into the matrix region. With weaker interface bond, delaminations can occur along the interface ($\theta_0 = 0$ deg). As can be observed in Fig. 10, the locations A correspond to points which are located at bi-material interface regions. Consequently, oscillatory stress singularities will be observed at the locations A. The stress singularities K_I and K_{II} at such crack extremities will exhibit an oscillatory character (see, e.g., Williams, 1959; England, 1965; Sih and Chen, 1980;

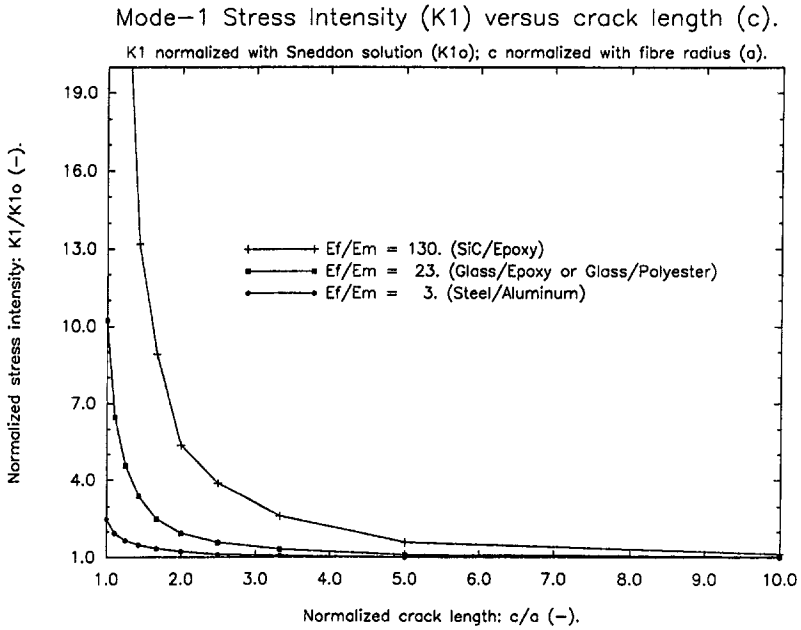

Fig. 7 The stress intensity factor for the penny-shaped matrix-fiber crack: influence of fiber-matrix mismatch, K_1 = stress intensity factor for the penny-shaped matrix fiber crack, K_0 = stress intensity factor for the penny-shaped crack in a matrix region

Atkinson, 1979). In the case of the matrix crack (locations B in Fig. 10) the stress intensity factors will either be purely K_I or K_I and K_{II}, depending upon the crack type. When the stress intensity factors at the fiber-matrix interface at the location A are lower than the associated critical values and when the stress intensity factors at the matrix location B reach their critical values, the crack will propagate into the matrix.

Experimental Procedure

Materials. The fibers used in the experiments were supplied by PPG Industries Fiber Glass bv. The commercially available fibers contain a sizing; however, the fibers used in the current series of tests were especially prepared by PPG Industries Fiber Glass bv and contained only a coupling agent (Gamma-glycid-oxypropyl-trimethoxy-silaan, A-187). For the matrix material, an isophtalic-based unsaturated Polyester was used; Synolite 593-A-2 (see, e.g., DSM Resins, 1991). The choice for these materials is based on prior experience with these materials which enables the use of results derived from other experimental investigations to supplement the required material characteristics (ten Busschen, 1991).

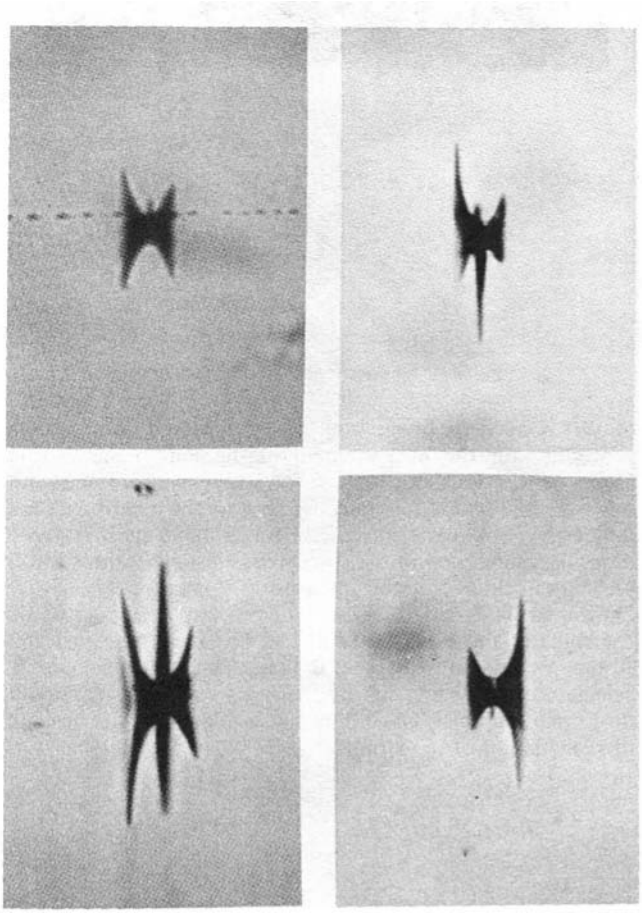

Fig. 8 Photographs of observed cracks during a fragmentation test

Manufacture of Specimens. In order to cast single filaments in the polyester matrix a special mould is constructed. The co-axial alignment of the fiber of filament within the test specimen is an important requirement of the specimen fabrication process. In order to maintain the filaments straight, they are subjected to a nominal tension by the application of static weights (Fig. 11). The application of the tension is also necessary to prevent the filaments from touching the sides of the mould. Due to the exothermic reaction during solidification, the thicker regions of the cast (these locations are indicated by a star (*) in the mould illustrated in Fig. 11) will first start to become a solid. Thus the middle part that is still liquid (located at the removable part) will be insulated during solidification between blocks of matrix material that have already solidified. Unfortunately, polyester exhibits volume shrinkage during solidification, which results in "lake formation" at the surfaces of this captured midsection. The remedy to alleviate this problem was to install a removable part in the mould that can follow the shrinkage of the middle part of the cast (see Fig. 11). During solidification, the bolts of the removable parts are released so that these parts can follow the shrinkage. After completion of solidification, the cast is released from the mould and sawed into specimens, using a

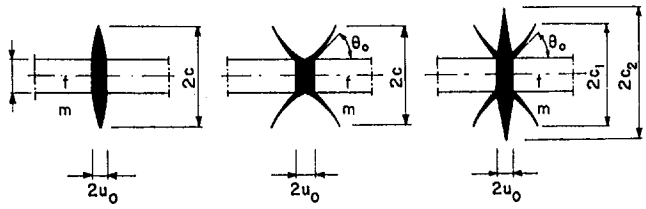

Penny-shaped crack Conical crack Combined crack

Fig. 9 Main crack extension geometries

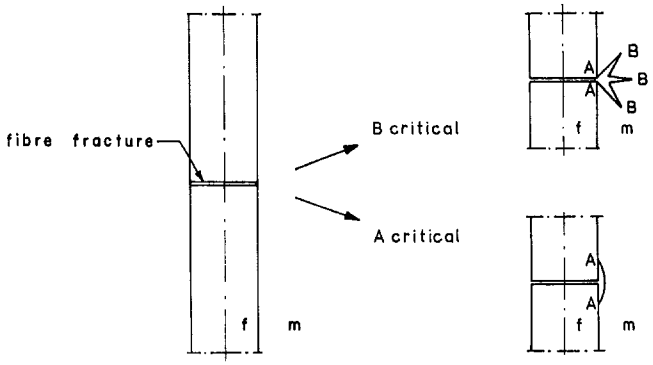

a) Crack encountering the interface. b) Crack propagation into the matrix or along the interface

Fig. 10 Matrix and interface crack configurations at a cracked fiber location

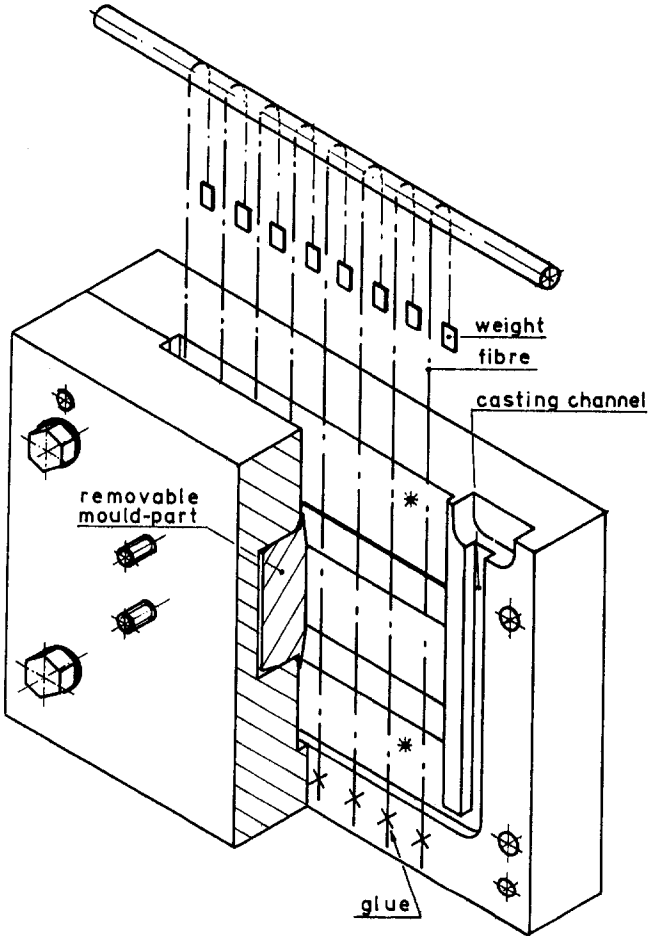

Fig. 11 Fiber filament assembly in casting location

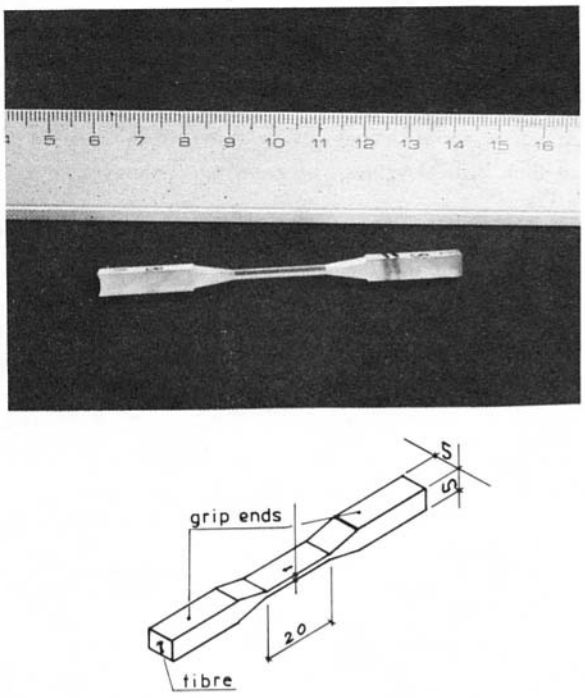

Fig. 12 The fragmentation test specimen

diamond saw. The shape and dimensions of the final specimen are shown in Fig. 12. The precise dimensions of the middle section of the specimen are carefully measured for each specimen in order to accurately define the matrix stress in this region during testing. The test is carried out seven days after solidification (the specimens are kept at 23°C at 50 percent relative humidity).

Testing. The specimens are tested in a servo-controlled tensile testing machine, which applies a constant displacement rate at the free grip end. The rate corresponds to

$$\dot{u}_{\text{grip}} = 0.40 \text{ mm/min}.$$

Initially the specimen exhibits linear elastic response and the strain rate in the midsection ($d\epsilon^o_{zz}/dt$) can be approximated by the result

$$\frac{d\epsilon^o_{zz}}{dt} = \dot{\epsilon}^o_{zz} \simeq \frac{\dot{u}_{\text{grip}}}{20} = 0.02 \text{ (min)}^{-1} = 2 \text{ percent (min)}^{-1} \tag{9}$$

(It should be noted that the components of the overall strain of the specimen (ϵ^o_{ij}) are macroscopic or homogenized components, as opposed to the components of the strains in the specimen (ϵ_{ij}), which are microscopic components. The z-axis is defined to be the fiber direction and the y-z plane is defined to be the plane in which the strains are measured).

At relatively high stress levels, (stresses approaching the tensile strength σ_T of the polyester = 87 MPa), the polyester behavior exhibits a nonlinear response. Furthermore, a more accurate approximation of the strain in the middle section (than those that can be derived from the strain rate defined by (9)) is needed. Image analysis is identified as a suitable procedure for the measurement of the longitudinal strain. Other conventional techniques for strain measurement cannot be adopted for this purpose due to the relatively small dimensions of the test specimen. In the image analysis procedure, the midsection of the specimen is installed with sprayed or marker dots of paint measuring approximately 20μm. During straining of the specimen, the displacements of the centroids of these marker dots are observed. The principal strains associated with the in-plane deformations can be calculated by utilizing the displacements of the centroids of three marker dots. The following relationships are used in the calculation of the strains:

$$\begin{aligned}
\Delta y_{021} &= y_{02} - y_{01} \quad ; \quad \Delta u_{y21} = u_{y2} - u_{y1} \\
\Delta z_{021} &= z_{02} - z_{01} \quad ; \quad \Delta u_{z21} = u_{z2} - u_{z1} \\
\Delta y_{031} &= y_{03} - y_{01} \quad ; \quad \Delta u_{y31} = u_{y3} - u_{y1} \\
\Delta z_{031} &= z_{03} - z_{01} \quad ; \quad \Delta u_{z31} = u_{z3} - u_{z1}
\end{aligned} \tag{10}$$

in which y_{0i} and z_{0i} are coordinates of point i in the undeformed state. Provided the macroscopic strain field is homogeneous and the displacement gradients are small, the displacement field for the kth load step can be obtained from the relationships

$$\begin{bmatrix} \Delta u_{y21} \\ \Delta u_{z21} \\ \Delta u_{y31} \\ \Delta u_{z31} \end{bmatrix}_k = \begin{bmatrix} \Delta y_{021} & \Delta z_{021} & 0 & 0 \\ 0 & 0 & \Delta y_{021} & \Delta z_{021} \\ \Delta y_{031} & \Delta z_{031} & 0 & 0 \\ 0 & 0 & \Delta y_{031} & \Delta z_{031} \end{bmatrix} \times \begin{bmatrix} \partial u_y/\partial y \\ \partial u_y/\partial z \\ \partial u_z/\partial y \\ \partial u_z/\partial z \end{bmatrix}_k . \tag{11}$$

This result can be written in the compact form

$$[\Delta \mathbf{u}]_k = [\Delta \mathbf{r}_0] \left[\frac{\partial \mathbf{u}}{\partial \mathbf{r}}\right]_k . \tag{12}$$

The vector of displacement gradients $[\partial \mathbf{u}/\partial \mathbf{r}]_k$ can be determined from the initial relative positions of the centroids, $[\Delta \mathbf{r}_0]$, and the relative displacements of the centroids $[\Delta \mathbf{u}]_k$ by inversion of the result (12), i.e.,

$$\left[\frac{\partial \mathbf{u}}{\partial \mathbf{r}}\right]_k = [\Delta \mathbf{r}_0]^{-1} [\Delta \mathbf{u}]_k. \tag{13}$$

The strain in the specimen along the direction of loading (ϵ^o_{zz}) and perpendicular to this direction (ϵ^o_{yy}) can be calculated from the results

$$\epsilon^o_{zz} = \frac{\partial u_z}{\partial z}; \quad \epsilon^o_{yy} = \frac{\partial u_y}{\partial y} \tag{14}$$

During an experiment, the camera is accurately positioned with its horizon parallel to the axis of the specimen. The maximum misalignment in this configuration is found to be 0.01 radians, so that the difference between the strains that can be calculated in (14) and the principal strains in the $y - z$ plane of the specimen will be negligible. Using the Image Analysis System, the strain field in a stressed specimen could be determined to within an accuracy of $2\,\mu$m/mm (= 0.2 percent strain). It is also noted that the initial elastic properties of the matrix material can be estimated by using the results for the applied load and the resulting strain. This procedure was carried out by optimizing five sampling points that were determined when the specimen strain was between 0.5 percent and 1.0 to be representative of the range of strain for initial elastic behavior of the matrix material. The results associated with this procedure is shown in Table 2. The results indicate a large variation in the value of E_m which can be attributed to the incomplete curing of the polyester matrix. The representative value of $E_m \simeq 1500$ MPa is consistent with results derived from other investigations (Busschen, 1991). Testing is terminated after the fragmentation process is saturated (i.e., no new fragments are observed during further straining). After a test, the cracks are investigated with the Image Analysis System, using the TCL-Programme (Toussaint, 1991) for processing the images. The complete procedure for analyzing the images of the matrix cracks is described in the ensuing section.

Experimental Results

Data Evaluation. After a fragmentation test, each specimen contains about 50 cracks. A large proportion of these cracks can be classified according to the three main crack geometries illustrated in Fig. 8. Other cracks can have helicoidal shapes (see, e.g., Fig. 13). These cracks, however, will not be taken into consideration in the data reduction process. The cracks to be evaluated will be subjected to the ensuing procedure for purposes of comparison with numerical simulations. The image of the crack is first recorded using a microscope (Type Panphot 407650, Ernst Leitz GmbH) with a magnification of either 165x, 225x, or 450x (depending on the dimensions of the cracks, the measurements will be scaled to the fiber radius) and a digital camera (type CCD video camera 91750155 Sanyo). With the digital camera a picture is recorded, containing 256×256 pixels in which each pixel has grey-value that may range from 0 (black) to 255 (white). The 386, 25 MHz computer (with math coprocessor) in which these images are recorded also contains the TCL-Programme (Toussaint, 1991). After the image of the crack is stored, the contrast is stretched; i.e., the range of grey-values of the actual image (which usually does not cover the range from 0 to 255) is stretched from 0 (black) to 255 (white). The effect of this stretching process is illustrated in Fig. 14.

After this procedure a threshold value of grey-values is chosen. Pixels with a grey value below this value are considered to be a part of the crack and are made black; other pixels are considered to be outside of the crack and are made white. Thus a binary image is obtained. The choice for a threshold value is made by taking the largest value that is possible provided that (i) discrepancies that do not belong to the crack (shadows, etc.) are not connected to the upper or

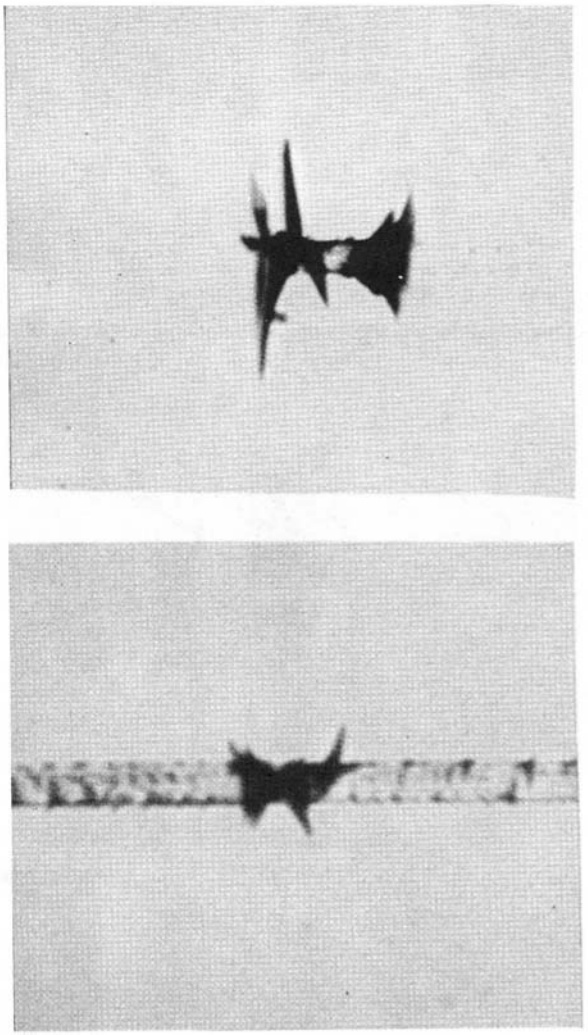

Fig. 13 Helicoidal matrix cracks

Table 2 Measured data for test specimen

Specimen	Maximum strain $\epsilon^o_{zz,\max}$ (%)	Initial stiffness E_m (MPa)	Initial Poisson's Ratio ν_m (-)
1	4.3	1550	0.35
2	7.7	2060	0.33
3	8.6	2190	0.35
4	8.8	1080	0.40
5	10.8	1390	0.26

lower part of the crack and (ii) the disturbances themselves do not have an area larger than the crack area. In Fig. 15, this is illustrated with three threshold values, employed on the same crack. With the high threshold value, disturbances around the crack are assigned to the crack region; the middle value shows disturbances that are unconnected to the crack; the low value shows a crack that has smaller dimensions than in the case of the midvalue.

The binary image that is obtained after the threshold procedure of contour of the image is determined with the TCL Programme (Fig. 16). Of this contour only the upper part and the lower part are needed to determine parameters necessary for comparison with numerical simulations. From the contour lines, the skeletal lines or crack outlines are determined (Fig. 17(*a*)). The end points of the skeleton lines are used for the *y*-coordinate of the position of a box region employed to remove tips of conical cracks (Fig. 17(*b*)). This procedure is adopted to remove from the crack tip the following: the side contour of the entire crack and the strongly curved part of the tips of the conical cracks. Also, the tip of the penny-shaped crack is used to determine the location of *y*-axis; in the conical case, the point with the lowest absolute value of *y* in the upper or lower contours is used for this purpose. Thus the upper and lower contours of the crack under consideration are determined (Fig. 18).

The upper and lower contours are rastered in order to define discrete points in pixel coordinates. The fiber location is indicated manually by specifying four separate points corresponding to fiber edges around the crack. If only three fiber edges are visible, the fiber radius and the middle of the fiber are determined by an iterative procedure. In this case the crack image under consideration is classified as *accurate*. If this is not possible (due to the fact that two or more of the fiber edges are not visible), the edges are indicated as accurately as permissible and the crack image under consideration is classified as *approximate*. The results of these two

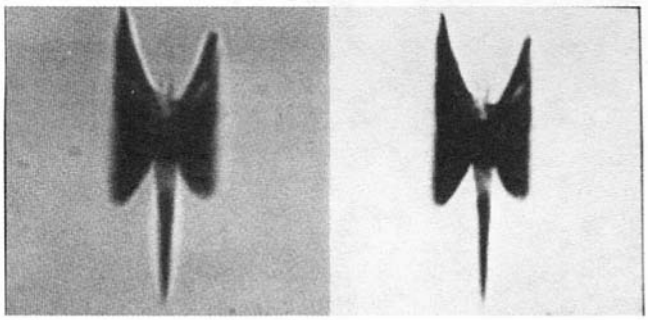

Fig. 14 Effect of stretching of grey-values on definition of crack outline

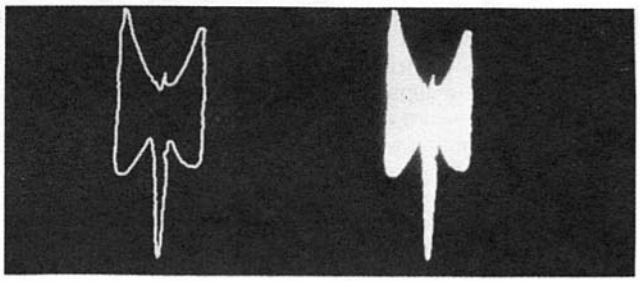

Fig. 16 Contour of the binary image of matrix crack

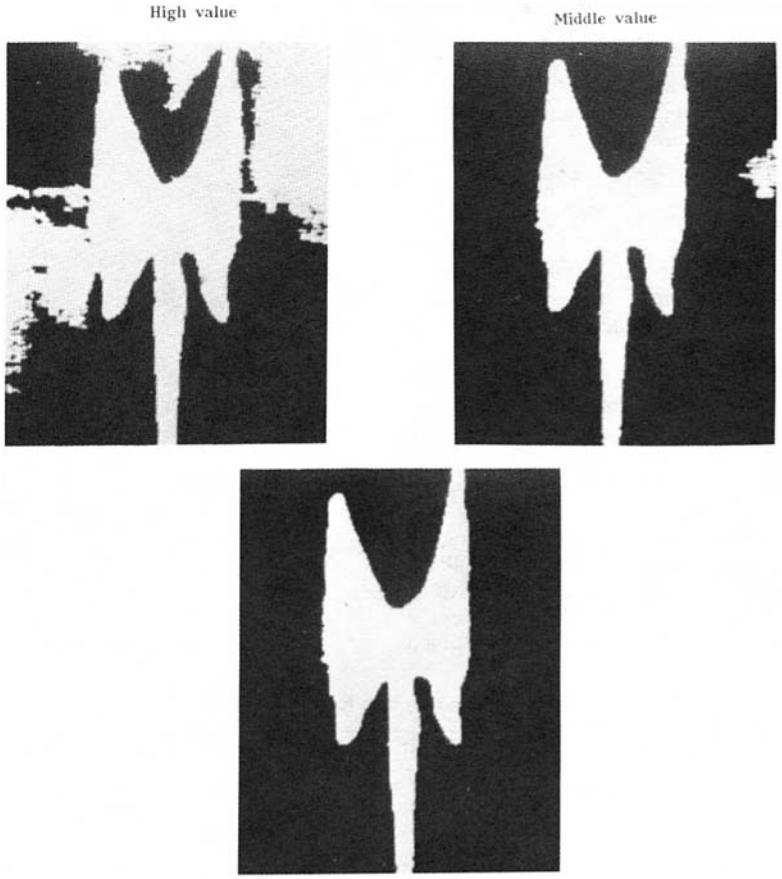

Fig. 15 Results for different threshold values

classes of crack images will be treated separately. The fiber edges that are indicated (either *accurate* or *approximate*) will determine the location of the z-axis (the direction of the z-axis is taken as the same as the horizontal of the image of the camera). Furthermore, the fiber radius (required for nondimensional plots) is also confirmed by this procedure. All the contour halves of the cracks are made dimensionless with respect to the fiber radius (a). For each class of contour halves, the results are superimposed. Examples of such grouped results are shown in Fig. 19. For each class of contour halves and for each specimen, an average contour is determined by means of a path searching technique procedure available in the TCL software. Also, an optimum path is determined by considering all contour halves.

The contour halves determined via the above procedure are used to determine the values of c/a, c_1/a, c_2/a, and θ_0. The crack images do not possess the degree of refinement which enable the determination of u_0/a. The crack topographies generally obstruct the visibility of the cracked fiber.

Fracture Geometries

In this section, the results determined from five specimens are presented. These specimens have different levels of strain at which the fragmentation test is terminated. Furthermore, for every specimen, the initial elastic properties of the matrix are calculated for purposes of comparison. The results are listed in Table 2.

For each specimen the cracks (including the irregular helicoidal type) are numbered. The cracks are subdivided into (i) the group of cracks that cannot be classified according to the three main types of fracture topographies (penny-shaped, conoidal and combination of conoidal, and penny-shaped); (ii) the group of cracks that can be classified with an accurate fiber location determination. The results of this classification is shown in Table 3. The dimensions and orientation of the cracks specified geometries are determined with the image analysis procedure. These results are summarized

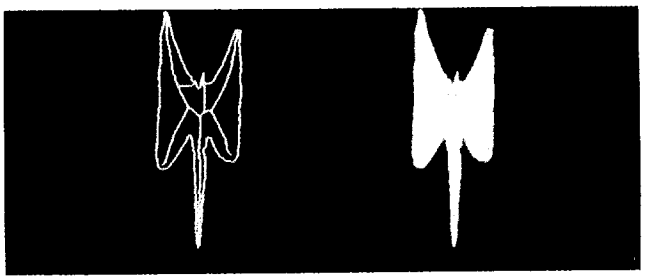

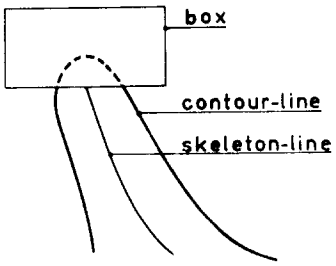

b) Position of removal-box.

Fig. 17 Use of skeletel lines for the isolation of parts of contour

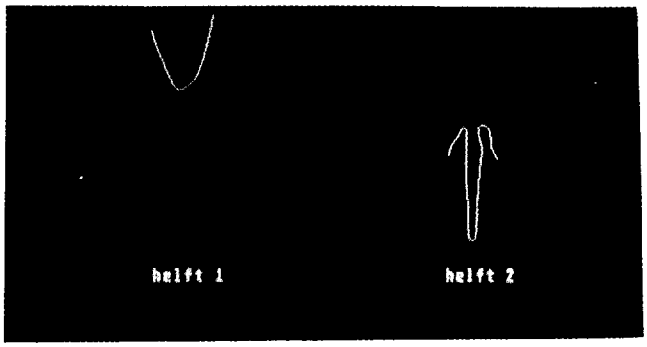

Upper contour. Lower contour.

Fig. 18 Extracted upper and lower contours of matrix crack

Accurate, conical
(3 contour-halves, sp. 4)

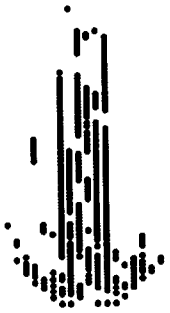

Accurate, combined
(8 contour-halves, sp. 3)

Approximate, conical
(18 contour-halves, sp. 4)

Approximate, combined
(11 contour-halves, sp. 3)

Fig. 19 Cumulative image of contour halves (specimens 3 and 4)

Table 3 Distribution of cracks in the tested specimens

Specimen	Number of Cracks			
	Total	Helicoidal (1)	Approximate (2)	Accurate (3)
1	33	21	13	5
2	52	43	5	4
3	46	36	6	4
4	41	16	22	3
5	56	25	26	5

Table 4 Results of crack measurements

Specimen	Number of Crack-Halves	(c/a)	$(c1/a)$	$(c2/a)$	φ_0
Conical (approximate)					
1	12	2.91	-	-	*
2	0	*	-	-	*
3	1	2.05	-	-	57°
4	18	3.19	-	-	45°
5	6	3.18	-	-	45°
Conical (accurate)					
1	6	2.53	-	-	51°
2	3	2.37	-	-	51°
3	0	*	-	-	*
4	3	2.63	-	-	57°
5	1	2.96	-	-	57°
Combined (approximate)					
1	14	-	2.42	3.36	56°
2	10	-	2.78	6.12	63°
3	11	-	1.98	5.63	45°
4	22	-	1.60	4.32	51°
5	46	-	2.44	7.20	56°
Combined (accurate)					
1	4	-	1.69	2.84	56°
2	5	-	1.31	6.53	*
3	8	-	*	*	*
4	3	-	*	*	*
5	9	-	2.17	4.79	56°

(- indicates that the parameter is not applicable; * indicates that no reliable measurement was possible)

in Table 4. In these studies only one isolated penny-shaped crack was observed. Consequently, this category of cracks is not considered further. The results in Table 4 are those for contour-halves, (i.e., one observed crack is divided into two halves and thus yields two contour halves (after image processing).

Conclusions

The engineering properties of a fiber-reinforced composite are strongly influenced by the micromechanical processes that take place within the fibers, the matrix, and at the fiber-matrix interface. The fragmentation tests involving the axial loading of a matrix specimen, containing a single coaxial embedded fiber filament is a possible test for examining the micromechanical processes at the scale of a fiber. In fragmentation tests two phenomena are observed after fiber fracture. When the interface has strength and fracture toughness characteristics that are lower than those of the matrix, fiber ends will experience slip. With the advent of coupling agents, the bond at the fiber-matrix interface can be enhanced with the result that matrix cracking occurs at a cracked fiber location. In this sense the cracked fiber locations act as nuclei for matrix cracking. Fragmentation tests with embedded single-fiber filaments require advanced experimental procedures involving accurate preparation of specimens, their precise uniaxial loading and the development of computer-aided techniques for the evaluation of matrix crack topographies, particularly at cracked fiber locations. This research has developed efficient experimental schemes and computer-aided data evaluation techniques for the study of matrix crack evolution at cracked fiber locations. The experimental studies indicate that at the micromechanical level, stable matrix crack extension can take place at cracked fiber locations. In particular, three major matrix crack propagation patterns are observed. With the aid of the computer-aided image analysis technique, these patterns can be quantified for several levels of longitudinal straining of the fragmentation specimen. The quantification of specific geometrical features of the matrix crack configurations can also be achieved. These include the inclination of the matrix crack at the fiber-matrix interface, the radii of single conoidal cracks and multiple cracks involving conoidal and penny-shaped cracks. The data on crack topographies have been evaluated with a view to examining the efficiency of elementary computational models of crack extension in brittle elastic solids.

The primary motivation for the development and examination of fragmentation tests involving embedded fiber filaments stem from the need to understand micro-mechanical level matrix cracking at cracked fiber locations in fiber-reinforced composites. The methodologies, however, have applications to the study of crack extension at rock anchor re-

gions, anchor bolts in concrete and cracking at the extremities of multiphase composites reinforced with elongated inclusions. The experimental methodologies involving the specimen fabrication and testing are directly applicable to the latter topic. The evaluation of the extent of crack extension can be achieved by ultrasonic and acoustic emission techniques, which can adequately describe the formation of discrete cracks and the precursor microcracks.

Acknowledgments

The authors wish to express their thanks to PPG Industries Fiber Glass bv (Hoogezand, The Netherlands) for supplying specially prepared fibers for the experimentation. The following people from the Laboratory of Engineering Mechanics at Delft University of Technology are thanked for carrying out the experiments: Mr. J. C. Sterk, Miss C. M. van Daalen, and Mr. C. A. J. Toussaint.

References

Atkinson, C., 1979, "Stress Singularities in Fracture Mechanics," ASME *Applied Mechanics Review*, Vol. 32, pp. 123–155.

Berg, R. M., van den, 1990, "Fragmentation Tests with Glass/Polyester and Glass/Epoxy," (in Dutch), Report No. LTM-918 Laboratory of Engineering Mechanics, University of Technology, Delft, The Netherlands.

Busschen, A., ten, 1991, "Micromechanical Modelling of Uni-Directional Glass Fiber Reinforced Polyester: Effect of Matrix Shinkage," *Proc. Euromech Colloquium 269*, A. Vautrin, ed., St. Etienne, France, pp. 1–8.

Chamis, C. C., 1974, "Mechanics of Load Transfer at the Interface," *Interfaces in Polymer Matrix Composites*, Vol. 6, L. J. Broutman and R. H. Crock, eds., Academic Press, New York, pp. 31–77.

Cox, H. L., 1952, "The Elasticity and Strength of Paper and Other Fibrous Materials," *British Jour. Appl. Phys.*, Vol. 3, pp. 72–79.

Dekkers, M. E. J., 1985, "The Deformation Behaviour of Glass Bead Filled Glassy Polymers," Ph.D. Thesis, Tech. Univ. Eindhoven, The Netherlands.

DSM Resins, 1991, *Brochure Synolite*, The Netherlands.

England, A. H., 1965, "A Crack Between Dissimilar Media," ASME JOURNAL OF APPLIED MECHANICS, Vol. 32, pp. 400–404.

Friedrich, K., ed., 1989, *Application of Fracture Mechanics to Composite Materials*, *Composite Materials Series*, Vol. 6, R. B. Pipes, ed., Elsevier, Amsterdam, The Netherlands.

Griffith, A. A., 1921, "The Phenomena of Rupture and Flow in Solids," *Phil. Trans. Roy. Soc. London*, Vol. A221, pp. 163–179.

Hull, D., 1981, *An Introduction to Composite Materials*, Cambridge University Press, Cambridge, U.K.

Kassir, M. K., and Sih, G. C., 1975, *Three Dimensional Crack Problems*, Mechanics of Fracture Series, Vol. 2, G. C. Sih, ed., Noordhoff, Leyden, The Netherlands.

Kedward, K. T., Wilson, R. S., and McLean, S. K., 1989, "Flexure of Simply Curved Composite Shapes," *Composites*, Vol. 20, pp. 527–536.

McCartney, L. N., 1989, "New Theoretical Model of Stress Transfer Between Fibre and Matrix in a Uniaxially Fibre-Reinforced Composite," *Proc. Roy. Soc.*, Vol. A425, pp. 215–244.

Merle, G., and Xie, M., 1991, "Measurement of the Adhesion of Polyester Block Amine to E-Glass by Single Filament Fragmentation," *Composites Science and Technology*, Vol. 40, pp. 19–30.

Moran, B., Gosz, M., and Achenbach, J. D., 1991, "Effect of a Viscoelastic Interfacial Zone on the Mechanical Behaviour and Failure of Fibre-Reinforced Composites," *Proc. IUTAM Symposium: Inelastic Deformation of Composite Materials*, G. J. Dvorak, ed., Springer-Verlag, Berlin, pp. 35–49.

Pagano, N. J., ed., 1989, *Interlaminar Response of Composite Materials*, Composite Materials Series, Vol. 3, R. B. Pipes, ed., Elsevier Scientific Publ., Amsterdam.

Pantano, C. G., and Chen, E. J. H., eds., 1990, *Interfaces in Composites, Proceedings of the MRS Symposium, Boston*, Materials Research Society Symposium Proceedings, Vol. 170, Pittsburgh, PA.

Piggott, M. R., 1980, *Load Bearing Fibre Composites*, Pergamon Press, New York.

Rebelo, C. A. C. C., Ferreira, A. J. M., Marques, A. T., and de Castro, P. M. S. T., 1986, "The Influence of Processing Conditions on Mechanical and Fracture Properties of GRP Plates," *Mechanical Behavior of Composites and Laminates*, W. A. Green and M. Micunovic, eds., Proc. Euromech. Colloquium 214, Kupari, Yugoslavia, Elsevier, Amsterdam, The Netherlands, pp. 54–63.

Sancaktar, E., 1991, "Nonlinear Viscoelastic Behaviour of the Fibre-Matrix Interface, Theory and Experiment," *Proc. Euromech Colloquium* 269, A. Vautrin, ed., St. Etienne, France.

Selvadurai, A. P. S., 1991, "Cracks at the Extremities of Cylindrical Fiber Inclusions," *Proc. IUTAM Symposium on Inelastic Deformation of Composites Materials*, G. J. Dvorak, ed., Springer-Verlag, Berlin, pp. 147–171.

Selvadurai, A. P. S., and Busschen, A. ten, 1995, "Mechanics of a Fragmentation Test Involving an Embedded Fiber, Part II: Computational Modeling and Comparisons," ASME JOURNAL OF APPLIED MECHANICS, Vol. 62, pp. 98–107.

Selvadurai, A. P. S., Busschen, A., ten, and Ernst, L. J., 1991, "Batman-Cracks: Observations and Numerical Simulations," *Proc. 13 Can. Congr. Appl. Mech. CANCAM '91*, Winnipeg, Canada, pp. 382–383.

Selvadurai, A. P. S., Singh, B. M., and Au, M. C., 1992, "The Matrix-Fiber Crack in an Elastic Solid," unpublished,

Sih, G. C., and Chen, E. P., 1981, *Cracks in Composite Materials*, *Mechanics of Fracture*, Vol. 6, Martinus Nijhoff, The Hague.

Sneddon, I. N., 1946, "The Stress Distribution in the Neighbourhood of a Crack in an Elastic Solid," *Proc. Roy. Soc., London*, Vol. A187, pp. 229–260.

Toussaint, C. A. J., 1991, "Manual for the Image Analysis Programme TCL," (in Dutch) Report No. LTM 953, Laboratory for Engineering Mechanics, University of Technology, Delft, The Netherlands.

Williams, M. L., 1959, "The Stresses Around a Fault or Crack in Dissimilar Media," *Bulletin Seismological Soc. of America*, Vol. 49, pp. 199–204.

Mechanics of the Segmentation of an Embedded Fiber, Part II: Computational Modeling and Comparisons

A. P. S. Selvadurai
Department of Civil Engineering and Applied Mechanics, Faculty of Engineering, McGill University, Montreal, QC H3A 2K6, Canada
Mem. ASME

A. ten Busschen
Laboratory of Engineering Mechanics, Faculty of Mechanical Engineering and Marine Technology, Delft University of Technology, Delft, The Netherlands

A fragmentation test has been developed for the study of the influence of the adhesive characteristics of the interface between reinforcing fibers and the matrix on the development of matrix cracking at a cracked single fiber location. The present paper examines the numerical modeling of the crack extension process within the matrix region. The numerical modeling focuses on the application of boundary element techniques to the study of an axisymmetric fiber-matrix model and quasi-static crack extension criteria are employed to determine the path of crack extension. The result for the crack extension patterns obtained from the numerical models are compared with the results derived from the experiments. It is shown that elastic fracture mechanics simulations of quasi-static crack extension can successfully model the observed experimental phenomena.

Introduction

The integrity of bond between a fiber and the surrounding matrix is of fundamental importance to the successful development and adaptation of fiber-reinforced composite materials. The interface bond characteristics are important from the point of view of both longitudinal and transverse resistance to fracture and failure of fiber-reinforced composites. Debonding, delamination, and cracking at a fiber-matrix interface can be initiated by a variety of factors including stress concentrations at sharp edges, inhomogeneities, thermal mismatch between the matrix, and the reinforcement and other environmentally induced loading effects. The evaluation of the influence of such defects on fracture propagation, stiffness degradation, etc., can significantly enhance both performance evaluation and material selection for fiber-reinforced composites (Sih and Tamuzs, 1979; Selvadurai, 1981; Hashin and Herakovich, 1983; Kelly and Rabotnov, 1983; and Dvorak, 1991).

The companion paper (Busschen and Selvadurai, 1995) focussed on the experimental evaluation of the influence of interface strength characteristics on the development of matrix cracking at a cracked fiber location. The stress transfer between the fiber and the matrix and vice versa, is achieved by means of a bonding mechanism (i.e., chemical bonding and mechanical interlock) or by means of a slip mechanism (friction between matrix and crack). These two mechanisms can be characterized experimentally for a specific fiber-matrix combination. A well-known test used for this purpose is a "pull-out" test (Piggott, 1980), which consists of a single fiber which is embedded in a matrix. This method of fiber-matrix interface characterization is, however, both time-consuming and highly sensitive to the test procedure. This research program advocates the development and use of the fragmentation test which provides information about the role of the interface strength characteristics on the subsequent development of matrix fracture. The testing of a composite specimen, in which a single fiber is embedded within a larger matrix region, permits not only ease of testing but also a clearer study of extended matrix fracture generation at a cracked fiber location. The companion paper has characterized the morphology of matrix crack patterns which can exist in a fragmentation test particularly in the presence of strong interface bonding, i.e., the interface strength and fracture toughness characteristics are expected to be much larger than the corresponding properties for the matrix region.

The primary objective of this paper is to examine whether the fracture morphologies observed in the fragmentation tests can be predicted by appeal to current developments in fracture mechanics. It must be observed that fracture morphology is one of the main observations of the fragmentation test. Due to the relatively small area of the fiber cross-section its influence on the overall load-displacement behavior of the

Contributed by the Applied Mechanics Division of THE AMERICAN SOCIETY OF MECHANICAL ENGINEERS for publication in the ASME JOURNAL OF APPLIED MECHANICS.

Discussion on this paper should be addressed to the Technical Editor, Professor Lewis T. Wheeler, Department of Mechanical Engineering, University of Houston, Houston, TX 77204-4792, and will be accepted until four months after final publication of the paper itself in the ASME JOURNAL OF APPLIED MECHANICS.

Manuscript received by the ASME Applied Mechanics Division, Dec. 2, 1992; final revision, Oct. 8, 1993. Associate Technical Editor: G. J. Dvorak.

fragmentation specimen is not significant. Attention is therefore focussed on a numerical modeling scheme which will examine the quasi-static crack extension within the matrix in the presence of strong adhesion.

The numerical modeling of fracture can be approached by adopting either finite element techniques or boundary element techniques. Accounts of these developments together with extensive references to developments in these areas are given by Zienkiewicz (1977), Brebbia et al. (1984), Brebbia and Aliabadi (1991), and Atluri (1991). In this paper, the boundary element technique is used to study the evolution of quasi-static crack extension into the matrix region at a cracked fiber location.

The Boundary Element Method

The formulation of the boundary element method for elastostatic problems is given by Banerjee and Butterfield (1981) and Brebbia et al. (1984). In this section a brief exposition of the basic features of the method are summarized for completeness. Further details of the application of boundary element techniques to the computational modeling of problems in fracture mechanics are given by Cruse and Wilson (1977), Blandford et al. (1981), Smith and Mason (1982), and Selvadurai and Au (1986, 1988, 1989, 1991).

We specifically consider the problem of a cylindrical elastic fiber which is embedded in bonded contact with an elastic matrix region of infinite extent. We assume that the fiber develops a plane crack normal to its axis due to the application of a uniform axial strain to the entire composite region. As indicated previously (Busschen and Selvadurai, 1995), the further application of uniform straining will induce either matrix cracking or fiber-matrix interface delamination. In the numerical modeling we primarily focus attention on the matrix cracking problem which persists in the presence of strong interface adhesion. The three main modes of matrix cracking include the following: (i) the development of a penny-shaped crack, (ii) the development of a conoidal crack, or (iii) the development of a combined conoidal crack-penny-shaped crack, at the cracked fiber location. As observed in the experiments, three-dimensional helicoidal cracks can occur in the fragmentation tests; these, however, do not abound. The boundary element technique in conjunction with crack extension criteria are used to establish the computational predictions for crack extension. Admittedly, the fracture propagation in a brittle material such as the matrix of a fiber-reinforced structural element is usually a dynamic phenomenon. In the fragmentation test, however, it is observed that the growth of the fracture in the matrix region can be effectively controlled to minimize dynamic aspects of crack extension. For this reason, the boundary element modeling is restricted only to the static problem.

We assume that both the uniform straining of the fragmentation test specimen and the resulting extension of matrix cracking exhibit a state of symmetry about the axis of the embedded fiber (Fig. 1). Both the fiber and matrix regions are assumed to be isotropic elastic materials which satisfy the stress-strain relationship

$$\sigma_{ij}^{(\alpha)} = \lambda_\alpha \delta_{ij} u_{k,k}^{(\alpha)} + G_\alpha \left\{ u_{i,j}^{(\alpha)} + u_{j,i}^{(\alpha)} \right\} \tag{1}$$

and the Navier equations

$$G_\alpha \nabla^2 u_i^{(\alpha)} + (\lambda_\alpha + G_\alpha) u_{k,ki}^{(\alpha)} = 0 \tag{2}$$

where G_α and λ_α are Lame's constants; the subscript or superscript "α" refers to the matrix (m) and fiber (f) regions; u_i and σ_{ij} are, respectively, the displacement components and stress tensor referred to the rectangular Cartesian coordinate system x, y, z; $i, j = x, y, z$; $\lambda_\alpha = 2G_\alpha \nu_\alpha/(1 - 2\nu_\alpha)$; ν_α are Poisson's ratios; $G_\alpha = E_\alpha/2(1 + \nu_\alpha)$; ∇^2 is Laplace's operator referred to the rectangular Cartesian coordinate system; and δ_{ij} is Kronecker's delta function. Here, and in what follows, the Greek indices and subscripts will refer to quantities pertaining to the matrix and fiber regions.

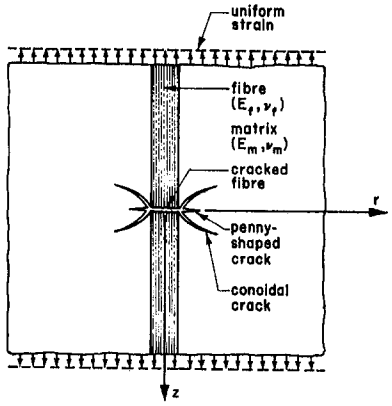

Fig. 1 The axisymmetric model of the fragmentation tests for an embedded fiber

The boundary integral equation for the axisymmetric problem pertaining to the fiber-matrix composite region can be written in the form (see, e.g., Kermanidis, 1975; Cruse and Wilson, 1977)

$$c_{\ell k} u_k^{(\alpha)} + \int_{\Gamma_\alpha} \left\{ P_{\ell k}^{*(\alpha)} u_k^{(\alpha)} - u_{\ell k}^{*(\alpha)} P_k^{(\alpha)} \right\} \frac{r}{r_i} d\Gamma = 0 \tag{3}$$

where Γ_α is the boundary of the region α; $u_k^{(\alpha)}$ and $P_k^{(\alpha)}$ are, respectively, the displacements and tractions on the boundary Γ_α and $u_{ik}^{*(\alpha)}$ and $P_{ik}^{*(\alpha)}$ are fundamental solutions. Also in (3), c_{ij} is a constant ($= 0$, if the point is outside the body; $= \delta_{ij}$ if the point is inside the body; $= \delta_{ij}/2$ if the point is located at a smooth boundary, and is a function of discontinuity at a corner and of Poisson's ratio (Banerjee and Butterfield, 1981)).

For axial symmetry

$$u_{rr}^{*(\alpha)} = C_1 \left\{ \frac{4(1 - \nu_\alpha)(\rho^2 + \bar{z}^2) - \rho^2}{2r\bar{R}} \right\} K(\bar{m}) - \left\{ \frac{(7 - 8\nu_\alpha)}{4r} \bar{R} - \frac{(e^4 - \bar{z}^4)}{4r\bar{R}^3 m_1} \right\} E(\bar{m}) \tag{4}$$

$$u_{rz}^{*(\alpha)} = C_1 \bar{z} \left[\frac{(e^2 + \bar{z}^2)}{2\bar{R}^3 m_1} E(\bar{m}) - \frac{1}{2\bar{R}} K(\bar{m}) \right] \tag{5}$$

$$u_{zr}^{*(\alpha)} = C_1 r_i \bar{z} \left[\frac{(e^2 - \bar{z}^2)}{2r\bar{R}^3 m_1} E(\bar{m}) + \frac{1}{2r\bar{R}} K(\bar{m}) \right] \tag{6}$$

$$u_{zz}^{*(\alpha)} = C_1 r_i \left[\frac{(3 - 4\nu_\alpha)}{\bar{R}} K(\bar{m}) + \frac{\bar{z}^2}{\bar{R}^3 m_1} E(\bar{m}) \right] \tag{7}$$

where

$$\bar{z} = (z - z_i); \quad \bar{r} = (r + r_i); \quad \rho^2 = (r^2 + r_i^2)$$

$$e^2 = (r^2 - r_i^2); \quad \bar{R}^2 = \bar{r}^2 + \bar{z}^2; \quad C_1 = \frac{1}{4\pi G_\alpha (1 - \nu_\alpha)}$$

$$\bar{m} = \frac{2rr_i}{\bar{R}^2}; \quad m_1 = 1 - \bar{m} \tag{8}$$

and $K(\bar{m})$ and $E(\bar{m})$ represent, respectively, the complete elliptic integrals of the first and second kind. The corre-

sponding terms for the traction fundamental solution $P_{lk}^{*(\alpha)}$ can be obtained by the manipulation of the results (4) to (7).

Upon discretization of the boundaries Γ_α into boundary elements, the integral Eq. (3) can be represented in the form of a boundary element matrix equation as follows:

$$\left[\mathbf{H}^{(\alpha)}\ \mathbf{H}_I^{(\alpha)}\right]\begin{bmatrix}\mathbf{u}^{(\alpha)}\\ \mathbf{u}_I^{(\alpha)}\end{bmatrix} = \left[\mathbf{M}^{(\alpha)}\ \mathbf{M}_I^{(\alpha)}\right]\left[\mathbf{P}^{(\alpha)}\ \mathbf{P}_I^{(\alpha)}\right] \quad (9)$$

where **H**'s and **M**'s are the influence coefficient matrices derived from the integration of the fundamental solutions $P_{lk}^{*(\alpha)}$ and $u_{lk}^{*(\alpha)}$, respectively. In the instance where there is complete bonding between the fiber-matrix interface we have

$$\mathbf{u}_I^{(f)} = \mathbf{u}_I^{(m)} = \mathbf{u}_I$$
$$\mathbf{P}_I^{(f)} = -\mathbf{P}_I^{(m)} = \mathbf{P}_I. \quad (10)$$

Using the above result, the complete matrix equation governing the fiber composite-crack interaction problem can be expressed in the form

$$\begin{bmatrix}\mathbf{H}^{(f)} & \mathbf{H}_I^{(f)} & 0\\ 0 & \mathbf{H}_I^{(m)} & \mathbf{H}^{(m)}\end{bmatrix}\begin{bmatrix}\mathbf{u}^{(f)}\\ \mathbf{u}_I\\ \mathbf{u}^{(m)}\end{bmatrix} = \begin{bmatrix}\mathbf{M}^{(f)} & \mathbf{M}_I^{(f)} & 0\\ 0 & \mathbf{M}_I^{(m)} & \mathbf{M}^{(m)}\end{bmatrix}\begin{bmatrix}\mathbf{P}^{(f)}\\ \mathbf{P}_I\\ \mathbf{P}^{(m)}\end{bmatrix}. \quad (11)$$

Modeling of Crack-Tip Behavior

In the boundary element discretizations discussed in the previous section, quadratic elements will be employed to model the boundaries of the matrix and fiber regions. That is, the variation of the displacements and tractions within an element can be described by

$$\left.\begin{matrix}u_i^{(\alpha)}\\ P_i^{(\alpha)}\end{matrix}\right\} = a_0 + a_1\zeta + a_2\zeta^2 \quad (12)$$

where ζ is the local coordinate of the element and a_r ($r = 0$, 1, 2) are constants of interpolation. However, in the context of linear elastic fracture mechanics, the stress field at the crack tip should contribute to a $1/\sqrt{r}$-type singularity. In the finite element technique, the quarter-point element of the type proposed by Henshell and Shaw (1975) and Barsoum (1976) can be used to model the required $\sqrt{r}$-type variation of the displacements. That is, if the same type of element is implemented in a boundary element method where b_i ($i = 0$, 1, 2) are constants

$$\left.\begin{matrix}u_i^{(\alpha)}\\ P_i^{(\alpha)}\end{matrix}\right\} = b_0 + b_1\sqrt{r} + b_2 r. \quad (13)$$

Since the $P_i^{(\alpha)}$ in (13) does not produce a $1/\sqrt{r}$-type singularity, Cruse and Wilson (1977) developed the so-called "singular traction quarter-point boundary element," where the traction variations in (13) are multiplied by a nondimensional $\sqrt{\ell/r}$ where ℓ is the length of the crack-tip element. The variations of tractions can be expressed in the form

$$P_i = \frac{c_0}{\sqrt{r}} + c_1 + c_2\sqrt{r} \quad (14)$$

where c_i ($i = 0$, 1, 2) are constants. The performance of both types of quarter-point elements have been studied by Blandford et al. (1981), Smith and Mason (1982), and Selvadurai and Au (1989) and their accuracy established by comparison with known exact solutions.

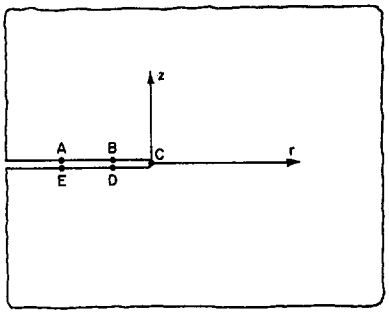

Fig. 2 Detail at the crack tip. Node arrangement for the computation of the stress intensity factor.

In the crack-fiber interaction problem examined in this paper the axial straining induces a state of axial symmetry in the fiber-matrix composite region. Consequently, only the Mode I and Mode II stress intensity factors are present at the tips of the crack region. The flaw opening-mode stress intensity factor can be evaluated by applying the displacement correlation method which utilizes the nodal displacements at four locations A, B, E, D, and the crack tip (Fig. 2) i.e.,

$$K_I^{(\alpha)} = \frac{G_\alpha}{(k_\alpha + 1)}\sqrt{\frac{2\pi}{\ell_0}}\left\{4[u_z(B) - u_z(D)] + u_z(E) - u_z(A)\right\} \quad (15)$$

where $k_\alpha = (3 - 4\nu_\alpha)$ and ℓ_0 is the length of the crack-tip element. Similarly the flaw shearing mode stress intensity factor can be written in the form

$$K_{II}^{(\alpha)} = \frac{G_\alpha}{(k_\alpha + 1)}\sqrt{\frac{2\pi}{\ell_0}}\left\{4[u_r(B) - u_r(D)] + u_r(E) - u_r(A)\right\}. \quad (16)$$

Crack Extension Criteria

The boundary element technique described in the previous section can be applied to examine the mechanics of matrix crack extension at the cracked fiber location. In order to develop the computational model it is necessary to establish a crack extension criterion applicable to the brittle matrix region. The subject of fracture extension in brittle elastic solids has been studied very extensively over the past two decades. Such studies have been motivated by the interest in the examination of crack extension in both metallic materials such as steel and nonmetallic materials such as concrete, rock, ceramic materials, polymeric materials at low temperatures, and ice. Extensive accounts of these developments can be found in the literature on fracture mechanics (see, e.g., Liebowitz, 1968; Kassir and Sih, 1975; Atkinson, 1979; Cherepanov, 1979; Lawn and Wilshaw, 1980; Broek, 1982; Kanninen and Popelar, 1985; Shaw and Swartz, 1987; Sih, 1991). In studies related to crack extension in brittle elastic solids, it is necessary to postulate two criteria. The crack extension criterion establishes the stress conditions necessary for the onset of crack extension. The second relates to the criterion which establishes the orientation of crack growth.

(a) Criteria for Onset of Crack Extension. The onset of crack extension in brittle elastic solids can be described by a variety of criteria. Such criteria are invariably developed on the basis of experimental investigations on fracture toughness testing of materials such as concrete mortar, rock, and brittle ceramics. A simple form of a criterion for the onset of crack extension can be expressed in terms of the fracture toughness

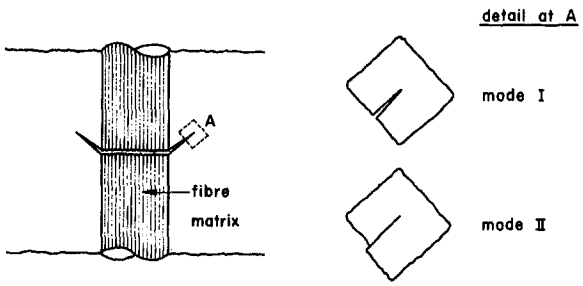

Fig. 3 Fracture modes at tip of matrix crack

of the material in the crack-opening mode. Accordingly, crack extension can be initiated when

$$K_I = K_{Ic} \tag{17}$$

where K_{Ic} is the critical value of the stress intensity factor in the crack-opening mode.

The result (17) can be generalized to include the influence of mode II or flaw shearing effects. The simplest form of a generalization due to Hellan (1985) takes the form

$$a_1\left(\frac{K_I}{K_{Ic}}\right)^2 + a_2\left(\frac{K_I}{K_{Ic}}\right) + a_3\left(\frac{K_{II}}{K_{IIc}}\right)^2 + a_4\left(\frac{K_{II}}{K_{IIc}}\right) = a_1 + a_2 \tag{18}$$

where K_{IIc} is the critical value of the stress intensity factor in the flaw shearing mode and a_i ($i = 1, 2, 3, 4$) are experimentally derived constants.

The studies by Sih (1974) indicate that a generalized theory for the onset of crack extension can be posed in relation to the local strain energy density at the crack tip. The theory does not require the calculation of energy release rate and thus possesses the inherent advantage of being able to accommodate crack extension processes in which all modes of crack extension (in this case the Modes I and II) contribute to the local strain energy density function. The strain energy density function S at the crack boundary (Fig. 3) can be written as

$$S = \alpha_{11}K_I^2 + 2\alpha_{12}K_IK_{II} + \alpha_{22}K_{II}^2 \tag{19}$$

where

$$\alpha_{11} = \frac{1}{16G_m}(1 + \cos\theta)(\Omega - \cos\theta)$$

$$\alpha_{12} = \frac{1}{16G_m}\sin\theta[2\cos\theta(\Omega - 1)]$$

$$\alpha_{22} = \frac{1}{16G_m}[(\Omega + 1)(1 - \cos\theta) + (1 + \cos\theta)(3\cos\theta - 1)] \tag{20}$$

and

$$\Omega = \begin{cases} (3 - 4\nu_m) & \text{plane strain} \\ \dfrac{(3 - \nu_m)}{(1 + \nu_m)} & \text{plane stress} \end{cases} \tag{21}$$

depending upon whether the local stress field conforms either to a state of plane strain or plane stress. It can be shown that the stationary value of $S_{\min}$ can be used as an intrinsic material parameter the value of which at the onset of crack extension S_{cr} is independent of the crack geometry and loading.

(b) Orientation of Crack Growth. If we consider the conical elemental matrix crack with an arbitrary orientation to the cracked fiber location (Fig. 3), it is evident that at the crack-tip location both the stress intensity factors K_I and K_{II} are present. Consequently, a generalized crack extension criterion should incorporate the influence of both stress intensity factors. In this study the orientation of crack growth is examined by employing the criteria postulated by Erdogan and Sih (1963).

The maximum stress criterion assumes that the crack will start to extend in the plane which is normal to the maximum circumferential stress $\sigma_{\theta\theta}$ (i.e., stress state referred to the local polar coordinate system located at the crack tip) in accordance with the condition

$$K_I \sin\theta + K_{II}(3\cos\theta - 1) = 0 \tag{22}$$

for determining the initial angle of crack growth θ.

The criterion defined by (22) has been used quite extensively for the study of quasi-static crack extension paths in brittle elastic materials such as concrete, epoxy, ceramics, and rock. This is by no means the only available criterion which has been proposed for crack extension in mixed mode. References to such developments are given by Sih and Theocaris (1979) and Sih (1991).

Matrix Crack Development at the Cracked Fiber

First, the methodologies outlined in the previous sections are utilized to examine the crack extension into the matrix region at the cracked fiber location. In view of the application to the fragmentation test described by Busschen and Selvadurai (1995), attention is restricted to a typical E-glass fiber-polyester matrix system with the following basic properties.

E-Glass Fiber.

Diameter of fiber = 1.5×10^{-5} m = 15 μm
Elastic modulus of fiber = 70,000 MPa
Poisson's ratio of fiber = 0.20
Uniaxial tensile strength of fiber = 2500 MPa

Polyester Matrix.

Elastic modulus of matrix (E_m) = 1500 MPa
Poisson's ratio (ν_m) = 0.35
Uniaxial tensile strength (σ_T) = 87 MPa
Uniaxial compressive strength (σ_c) = 140 MPa
Critical stress intensity factor at seven days (K_{Ic}) = 1.0 MPa$\sqrt{m}$
Critical stress intensity factor post cure (K_{Ic}) = 0.6 MPa$\sqrt{m}$

The cross-sectional dimensions of the fragmentation test specimen in its midsection are 1 mm × 5 mm. When comparing the cross-sectional dimensions of the specimen with the diameter of the embedded fiber it is evident that the traction-free outer boundary of the specimen is located remote from the fiber (aspect ratio of 1/50). Consequently, in the numerical modeling attention is focussed on the problem of an elastic fiber which is embedded in an elastic matrix of infinite extent.

The primary objective of the exercise in numerical modeling is to use the concepts in crack extension discussed previously to predict the matrix crack patterns which originate at cracked fiber locations. It is assumed that at a cracked fiber location matrix cracking can originate in a variety of configurations. The origination of matrix cracking can be modeled as incremental starter cracks with basic conical or penny-shaped configurations which can occur either individually or simultaneously. The incremental penny-shaped starter cracks can

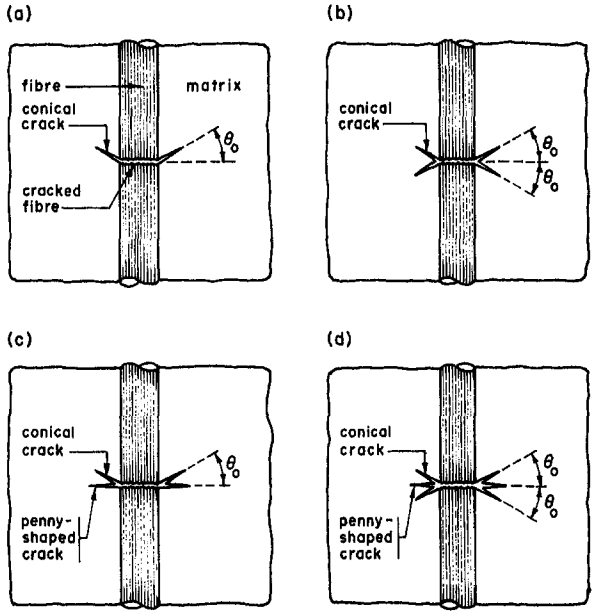

Fig. 4 Elemental matrix crack configurations at cracked fiber locations; (*a*) elemental conical crack, (*b*) elemental conical cracks which are symmetrically located about the plane of the cracked fiber, (c) a combination of an elemental penny-shaped crack and a single elemental conical crack, (*d*) a combination of an elemental penny-shaped crack and symmetrically placed elemental conical cracks, ($\theta_0 = \pi/2 - \varphi_0$)

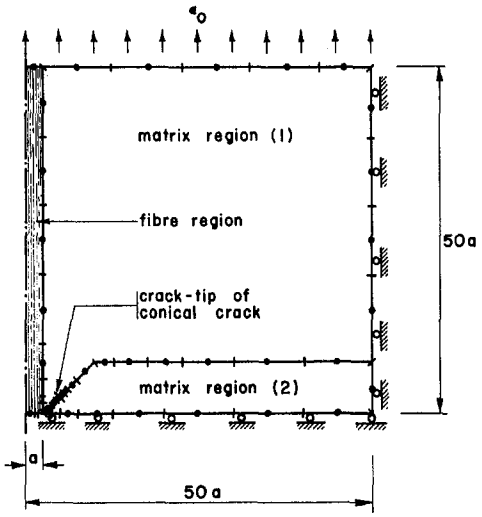

Fig. 5 Boundary element discretization used in the numerical modeling of the fragmentation test

occur in the plane of the cracked fiber and the incremental conical starter cracks are at an arbitrary orientation to the axis of the cracked fiber. Altogether four types of initial starter crack configurations can be examined. These include the following:

1 an elemental conical crack which is oriented at an arbitrary inclination to the fiber axis (Fig. 4(*a*)).
2 elemental conical cracks which are symmetrically located about the plane of the cracked fiber and oriented at an arbitrary inclination to the fiber axis (Fig. 4(*b*)).
3 a combination of an elemental penny-shaped crack and a single elemental conical crack which is oriented at an arbitrary inclination to the fiber axis (Fig. 4(*c*)).
4 a combination of an elemental penny-shaped cracked and symmetrically placed elemental conical cracks which are oriented at an arbitrary inclination to the fiber axis (Fig. 4(*d*)).

Admittedly, the scope of the numerical modeling can be extended to cover other conical elemental matrix crack configurations which are located nonsymmetrically with respect to the plane of the cracked fiber. The composite region containing the cracked fiber and the elemental cracks (Fig. 4) is subjected to a uniform far-field axial strain. A typical boundary element mesh discretization used in the numerical modeling of the fragmentation test is shown in Fig. 5. The extension of the crack and the path extension of the crack can be determined by considering the criteria for the onset of crack extension and the criteria for the orientation of incremental quasi-static crack growth.

In order to perform the numerical computations for the onset of crack extension by using the result (18) it is necessary to establish the critical values of the stress intensity factors governing both Mode I (K_{Ic}) and Mode II (K_{IIc}) fracture processes in the Polyester matrix. An examination of the literature on fracture toughness testing for the Polyester matrix material indicates that most such experimental evaluations of fracture toughness primarily focus on the determination of K_{Ic}. Further, for the Polyester matrix material, K_{IIc}, is expected to be much larger than the K_{Ic}. For this reason the criterion for the onset of crack extension is defined by the simpler criterion (17). This criterion has been very successfully adopted for the examination of fracture initiation in brittle solids such as concrete, rock, and ceramics.

With this *onset of crack extension criterion*, attention is focused on the specification of the orientation of crack growth. Preliminary investigations conducted by the authors on typical elemental starter crack configurations indicate that both criteria (22) and (24) give approximately the same results for the orientation of crack growth. The result of these studies cannot in any way be generalized. It is, however, convenient to adopt the simplified orientation of crack growth criterion defined by (22). With these simplified representations in mind, i.e., result (17) for the onset of crack extension and result (22) for the orientation of crack growth, the boundary element modeling procedure can be used to establish the quasi-static crack extension paths associated with the various starter crack configurations.

In the computations, the inclination of the conical starter crack to the axis of the fiber (θ_0) is set equal to 45 deg, 50 deg, 55 deg, and 60 deg. By assigning this range of conical starter crack orientations it is possible to assess their influence on the mode of crack extension. The lengths of the starter crack can be a variable; however, for the purposes of the numerical computations, the length of the starter crack (either conical or penny-shaped) is set equal to 0.01 a where a is the radius of the fiber.

We first consider the results developed for the case of an elemental conical crack which is located at an arbitrary orientation to the axis of the fiber. Figure 6 shows the crack extension pattern within the matrix region for starter crack orientation $\theta_0 \in$ (45 deg, 60 deg). The extent of matrix crack extension shown in Fig. 6 takes into consideration various levels of axial strain $\epsilon_0 \in (0.01, 0.12)$. In Fig. 7 we present the results for the strain-level-dependent crack extension patterns derived for the situation where conical starter cracks are symmetrically situated at the cracked fiber location. As is evident, either the symmetry or asymmetry in the orientation of the conical starter cracks appears to have a significant influence on the path of crack extension within the matrix.

We next consider the situation where both a penny-shaped starter crack and a nonsymmetric conical starter crack are present at the cracked fiber location. In this arrangement quasi-static crack extension can take place at either crack-tip

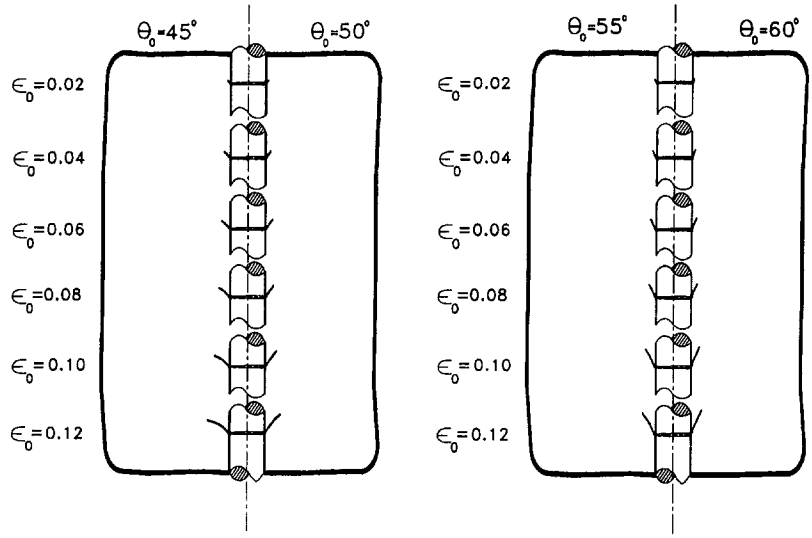

Fig. 6 Matrix crack extension at a cracked fiber location: elemental conical crack oriented at an arbitrary inclination to the fiber

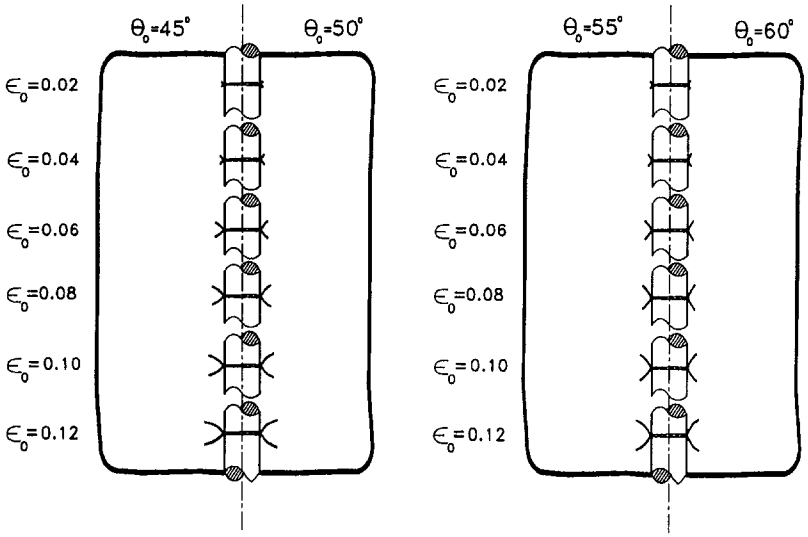

Fig. 7 Matrix crack extension at a cracked fiber location: elemental conical cracks symmetrically placed about the plane of crack fiber

location. In the numerical computations, the criteria for crack extension is checked at both crack-tip locations and the crack extension is allowed to take place at the appropriate location which satisfies the crack extension criterion. Figure 8 illustrates the crack extension patterns derived for initial conical crack orientations in the range $\theta_0 \in$ (45 deg, 60 deg). Figure 8 also illustrates the extent of crack extension either at the tip of the conical crack or at the penny-shaped crack consistent with the level of axial strain in the composite region. The results of additional computations indicate that for θ_0 within the range (0, 45 deg), the conical starter cracks essentially remain dormant and the crack extension mainly occurs at the location of the penny-shaped crack. For $\theta_0 = 60$ deg and 70 deg, crack extension can occur at both crack-tip locations. When $\theta_0 = 75$ deg, the conical crack extension mode dominates initially, and the tip of crack extension must be remote from the fiber to initiate the extension of the penny-shaped crack. Figure 9 illustrates the matrix crack extension characteristics for the situation where the penny-shaped crack at the cracked fiber location interacts with conical starter cracks which are symmetrically inclined to the axis of the fiber. Here again, computations carried out indicate that the conical starter crack does not extend at values of $\theta_0 < 30$ deg. With increasing θ_0 (e.g., $\theta_0 = 45$ deg), the conical starter crack will extend but such crack extensions will take place only as the penny-shaped crack extends to regions remote from the cracked fiber locations. For the larger values of θ_0, crack extension takes place mainly within the conical crack tip. The results are presented for various values of the applied strain ϵ_0. It is also evident that the extent of crack extension can be influenced by the symmetry or asymmetry in the orientation of the conical starter cracks.

The numerical modeling technique is now used to provide a comparison for the experimental results derived from the actual fragmentation tests. From the experimental results presented in the companion paper (Busschen and Selvadurai (1995), Table 2) it is evident that all fragmentation test specimens display a variable matrix modulus E_m. The development of numerical results for all fragmentation test specimens 1 to 5 will involve an inordinate amount of computation. For this reason, attention is focused on the two fragmentation test specimens which give the largest group of conical and combined cracks. From Table 4 of Busschen and Selvadurai (1995) it is evident that test specimens 1 and 5 can be used as typical experimental data sets for purposes of comparison. It is also noted that in these specimens the

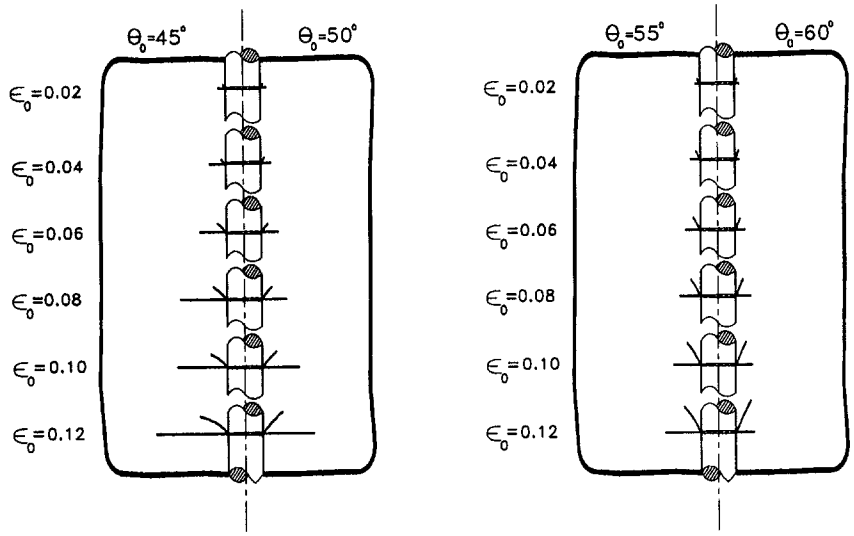

Fig. 8 Matrix crack extension at a cracked fiber location: a combination of an elemental penny-shaped crack and an elemental conical crack

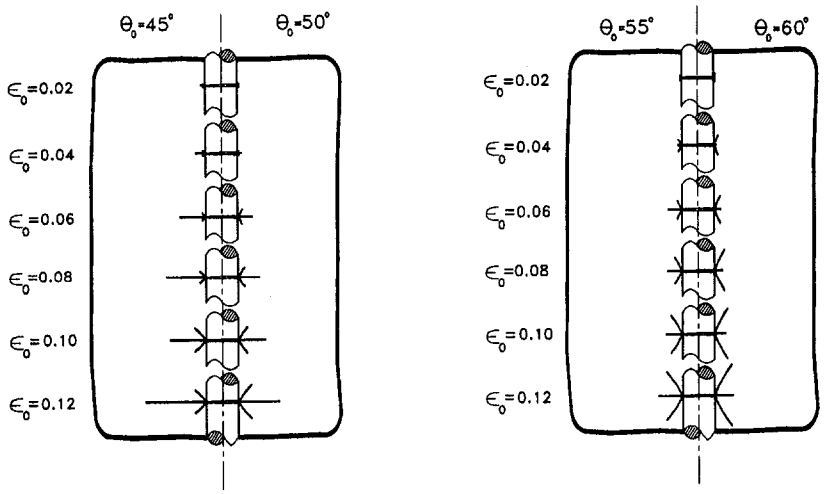

Fig. 9 Matrix crack extension at a cracked fiber location: a combination of an elemental penny-shaped crack and symmetrically placed elemental conical cracks

orientations of the initial starter crack have been accurately determined. The elastic properties of the polyester matrix used in these specimens are given in Table 2 of the companion article. The boundary element method and the fracture mechanics computations are used to compute the crack extension paths for both symmetrically placed single conical cracks and symmetrically placed single conical cracks interacting with a penny-shaped crack. Figure 10 presents the results of the comparison derived for the cases of the symmetrically placed conical cracks with $\theta_0 = 39$ deg and $\theta_0 = 45$ deg. The result for $\theta_0 = 45$ deg is provided only for purposes of comparison. The experimental results derived via the image analysis technique are classified as the *accurate mean contour*. The extended path of the cracks are derived for a strain level of $\epsilon_0 = 0.043$. Figure 11 presents the comparison between the computations for $\theta_0 = 39$ deg and $\theta_0 = 45$ deg and analogous results derived via the experimental data set which is classified as the *approximate mean contour*. It is clearly evident that the general trends indicated in the computations compare well with experimental data. We now focus on the comparison of results derived for the situation where the symmetrically placed conical crack interacts with a penny-shaped crack during the simultaneous crack extension process. In this case the initial inclination of the conical crack is assumed to be $\theta_0 = 34$ deg and the applied maximum strain $\epsilon_0 = 0.108$. Figure 12 illustrates the limits of crack extension derived via the computational scheme and the set of experimental data identified as the *accurate mean contour*. The result for $\theta_0 = 45$ deg is again presented for purposes of comparison. Analogous comparisons of computational results and the data identified with the approximate mean contour are presented in Fig. 13. In these representations the experimental results for the penny-shaped crack record either accurate or approximate contours. As is evident, these contour bounds for the penny-shaped crack indicate trends consistent with experimental data. A further comparison can be made by examining the values of c (radius of purely conical crack), c_1 (radius of the conical crack part of combined crack), and c_2 (radius of the penny-shaped crack) obtained at the limit of the axial strain $\epsilon_0 = 0.108$. The comparisons are given in Table 1. Further comparisons can be also made by using the results for the computational modeling given in Table 1 with the experimental results for specimens 2, 3, and 4 given in Table 4 of Busschen and Selvadurai (1995).

Conclusions

The integrity of bond between a reinforcing fiber and the surrounding matrix is an important property of a fiber-reinforced composite material. As the bond strength is enhanced

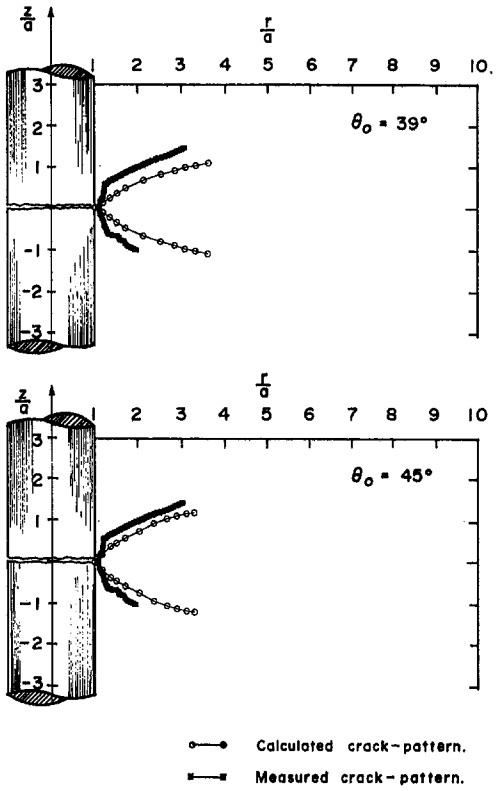

Fig. 10 Matrix crack extension due to the growth of conoidal cracks: a comparison of experimental results and computational estimates (accurate experimental data)

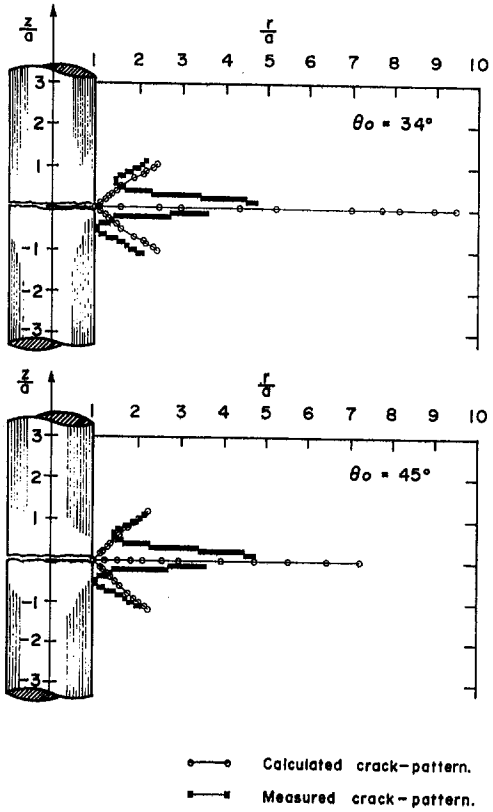

Fig. 12 Matrix crack extension due to the simultaneous growth of conoidal and penny-shaped cracks: a comparison of experimental results and computational estimates (accurate experimental data)

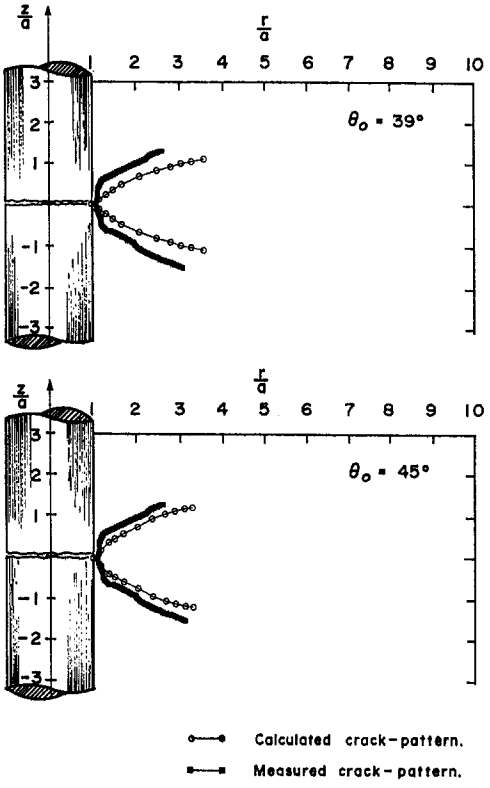

Fig. 11 Matrix crack extension due to the growth of conoidal cracks: a comparison of experimental results and computational estimates (approximate experimental data)

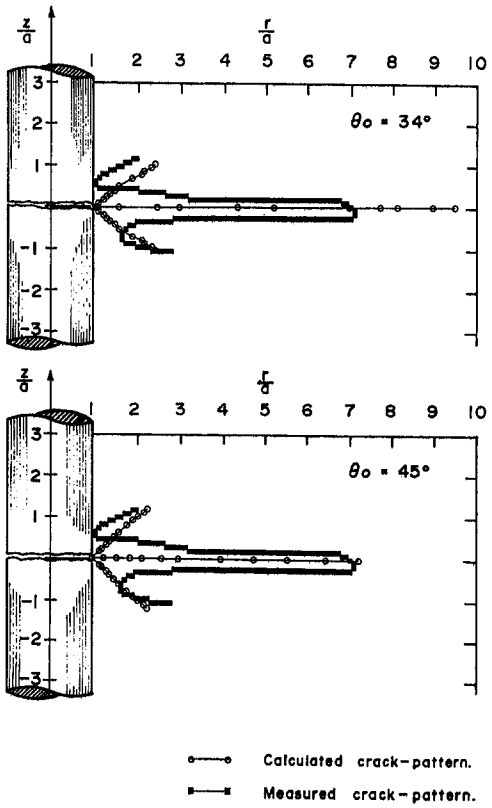

Fig. 13 Matrix crack extension due to the simultaneous growth of conoidal and penny-shaped cracks: a comparison of experimental results and computational estimates (approximate experimental data)

Table 1 Comparison of computational estimates and experimental data

	Specimen 1			Specimen 5		
	c/a	c_1/a	c_2/a	c/a	c_1/a	c_2/a
Theory	3.65	2.38	9.01	3.65	2.38	9.01
$(\text{Experiment})_{\text{Accurate}}$	2.53	1.69	2.84*	2.96	2.17	4.79
$(\text{Experiment})_{\text{Approximate}}$	2.91	2.42	3.36*	3.18	2.44	7.20

[* In these cases the boundary of the penny-shaped crack is not completely defined.]

by the use of coupling agents the role of matrix fracture has an important influence in determining the transverse strength of unidirectional fiber-reinforced composites. The fragmentation test is an effective method for the observation of fracture processes in the matrix in the presence of strong interface adhesion. This test is considered to be a more realistic analogue, in contrast to the testing of the matrix alone, for the investigation of matrix fracture in the vicinity of a fiber fracture. The objective of this phase of the research program is to provide a suitable computational procedure which can adequately model the developing matrix cracking in the fragmentation test. The modeling of fracture processes in predominantly brittle elastic materials such as brittle matrices in composites, ceramics, concrete, rock, etc., is a difficult exercise in computational mechanics. The crack extension is invariably a dynamic process. In the fragmentation test, however, the stable growth of matrix cracking can be exercised by suitable controlled straining of the active section of the fragmentation test specimen. Consequently, the mechanics of crack extension can be examined by appeal to quasi-static computational modeling. In such an exercise, the growth of matrix cracking at a cracked fiber location is assumed to occur by the extension of a nucleated or starter crack, which extends to the matrix region. In general, these starter cracks could have arbitrary three-dimensional configurations; for the purposes of the analyses it is assumed that the nucleated cracks can be composed of either individual or combined arrangements of conical and penny-shaped cracks. An alternative to the nucleated crack concept is to postulate a criterion, which could initiate cracking into the matrix region commencing at the boundary of a cracked fiber. Such an analysis is a complex exercise in fracture mechanics involving crack initiation at a bimaterial corner region. In addition to the assumption of a nucleated starter crack, it is necessary to specify criteria for the onset of crack extension and for the orientation of crack growth. In this study two relatively simple forms of these criteria are adopted for the computational modeling of crack extension.

The methodologies discussed here are implemented in a boundary element model which examines the quasi-static growth of a variety of configurations of starter cracks with conical and/or penny-shaped forms.

It is shown that the *boundary element based* computational scheme can be successfully employed to examine the matrix crack growth with conoidal and penny-shaped topographies. The boundary element scheme is particularly efficient for the study of crack extension in brittle solids since the incremental growth of the crack can be accommodated very conveniently. This is in contrast to other numerical schemes such as finite element schemes where constant remeshing at the crack-tip location is necessary to accommodate crack growth processes without specified orientations for the growth direction.

Finally, the computational procedure is employed to predict the growth of matrix cracking at a cracked fiber location. The correlations are established for conical cracks which have been measured accurately in the experimental research program. In order to establish the correlation it is necessary to specify the orientation of the conical crack, with respect to the fiber axis, as determined in the experiments. The specification of the orientation of the conical starter crack can certainly be regarded as a limitation of the modeling exercise. It is foreseeable certain additional criteria may need to be invoked to determine precisely the orientation of such conical matrix cracks which can initiate at the inception (dynamic fracture) of an embedded fiber. Similar uncertainties are encountered in the consideration of fracture initiation due to indentation where the elasticity mismatch between the indentor and the contacting surface and the local geometry at the contact boundary (in this case the local geometry at the fractured fiber boundary) will influence the orientation of the starter crack. It is, however, observed that when the initial conical crack orientations are specified, the crack growth paths observed in the experiments are predicted, reasonably accurately, with the computational model.

Studies in fracture mechanics of the brittle matrix phase of composite materials have important considerations in establishing the transverse strength of unidirectional fiber reinforced materials. With the availability of a computational modeling procedure it is possible to contemplate on the prediction of crack propagation within the matrix of a fiber-reinforced material in which the transverse tensile matrix fracture is governed by matrix crack extension within the random network of reinforcing fibers. The research also identifies certain fundamental issues pertaining to matrix crack initiation at cracked fiber boundaries which merit further study.

References

Atkinson, C., 1979, "Stress Singularities and Fracture Mechanics," ASME *Applied Mechanics Reviews*, Vol. 32, pp. 123–135.

Atluri, S. N., ed., 1991, *Computational Methods in Mechanics of Fracture, Vol. 2, Computational Methods in Mechanics*, J. D. Achenbach, ed., North-Holland, The Netherlands.

Banerjee, P. K., and Butterfield, R., 1981, *Boundary Element Methods for Engineering Science*, McGraw-Hill, New York.

Barsoum, R. S., 1976, "On the Use of Isoparametric Finite Elements in Linear Fracture Mechanics," *Int. J. Num. Meth. Engng.*, Vol. 10, pp. 25–37.

Blandford, G. E., Ingraffea, A. R., and Liggett, J. A., 1981, "Two-Dimensional Stress Intensity Factor Computations Using the Boundary Element Method," *Int. J. Num. Meth. Engng.*, Vol. 17, pp. 387–404.

Brebbia, C. A., Telles, J. C. F., and Wrobel, L. C., 1984, *Boundary Element Techniques*, Springer-Verlag, Berlin.

Brebbia, C. A., and Aliabadi, M. H., 1991, *Numerical Fracture Mechanics*, Computational Mechanics Publications, U.K.

Broek, D., 1982, *Elementary Engineering Fracture Mechanics*, Martinus Nijhoff Publ., The Hague.

Busschen, A., ten, and Selvadurai, A. P. S., 1995, "Mechanics of the Segmentation of an Embedded Fiber, Part I: Experimental Investigations," ASME JOURNAL OF APPLIED MECHANICS, Vol. 62, pp. 87–97.

Cruse, T., and Wilson, R. B., 1977, "Boundary Integral Equation Method for Elastic Fracture Mechanics," AFSOR-TR-78-0355, 10–11.

Cherepanov, G. P., 1979, *Mechanics of Brittle Fracture*, McGraw-Hill, New York.

Dvorak, G. J., ed., 1991, "Inelastic Deformations of Composite Materials," *Proc. IUTAM Symposium*, Springer-Verlag, Berlin.

Erdogan, F., and Sih, G. C., 1963, "On the Crack Extension of Plates Under Plane Loading and Transverse Shear," ASME *Journal of Basic Engineering*, Vol. 85, pp. 519–527.

Hashin, Z., and Herakovich, C. T., eds., 1983, "Mechanics of Composite Materials: Recent Advances," *Proceedings of the IUTAM Symposium on Mechanics of Composite Materials*, Pergamon Press, New York.

Hellan, K., 1985, *Introduction to Fracture Mechanics*, McGraw-Hill, New York.

Henshell, R. D., and Shaw, K. G., 1975, "Crack Tip Finite Elements are Unnecessary," *Int. J. Num. Math. Eng.*, Vol. 9, pp. 495–507.

Kanninen, M. F., and Popelar, C. H., 1985, *Advanced Fracture Mechanics*, Oxford University Press, Oxford, U.K.

Kassir, M. K., and Sih, G. C., 1975, *Three-Dimensional Crack Problems, Vol. 2, Mechanics of Fracture*, G. C. Sih, ed., Nordhoff Int. Publ., Leyden, The Netherlands.

Kelly, A., and Rabotnov, Yu, N., eds., 1983, *Handbook of Composites*, Vol. 1–4, North-Holland, Amsterdam, The Netherlands.

Kermanidis, Th., 1975, "Numerical Solution for Axially Symmetrical Elasticity Problems," *Int. J. Solids Struct.*, Vol. 11, pp. 495–500.

Lawn, B. R., and Wilshaw, T. R., 1975, *Fracture of Brittle Solids*, Cambridge University Press, Cambridge, U.K.

Liebowitz, H., ed., 1968, *Fracture*, Vol. I–IV, Pergamon Press, Oxford.

Piggott, M. R., 1980, *Load Bearing Fibre Composites*, Pergamon Press, New York.

Selvadurai, A. P. S., ed., 1981, *Mechanics of Structured Media, Proceedings of the Int. Symp. on the Mechanical Behaviour of Structured Media* (Studies in Applied Mechanics, Vols. 5A and 5B), Elsevier, Amsterdam, The Netherlands.

Selvadurai, A. P. S., and Au, M. C., 1988, "Cracks with Frictional Surfaces: A Boundary Element Approach," *Proceedings of the 9th Boundary Element Conference*, C. A. Brebbia, ed., Springer-Verlag, Berlin, pp. 211–230.

Selvadurai, A. P. S., and Au, M. C., 1989, "Crack Behaviour Associated with Contact Problems with Non-linear Interface Constraints," *Boundary Element Techniques: Applications in Engineering*, C. A. Brebbia and N. Zamani, eds., Proceedings of the Boundary Element Technology Conference, Windsor, Ontario, Computational Mechanics Publ., pp. 1–17.

Selvadurai, A. P. S., 1991, "Cracks at the Extremities of Cylindrical Fibre Inclusion," *Proc. IUTAM Symp. Inelastic Deformation of Composite Materials*, G. J. Dvorak, ed., Springer-Verlag, Berlin, pp. 147–171.

Shah, S. P., and Swartz, S. E., eds., 1987, *Fracture of Concrete and Rock, SEM-RILEM International Conference*, Springer-Verlag, Berlin.

Sih, G. C., 1973, "Some Basic Problems in Fracture Mechanics and New Concepts," *Journal of Engineering Fracture Mechanics*, Vol. 5, pp. 365–377.

Sih, G. C., 1974, "Strain Energy Density Factor Applied to Mixed Mode Crack Problems," *International Journal of Fracture*, Vol. 10, pp. 305–321.

Sih, G. C., 1975, "Application of the Strain Energy Density Theory to Fundamental Fracture Problems," *Recent Advances in Engineering Science*, Vol. 6, T. S. Chang, ed., Scientific Publ., Boston, pp. 221–234.

Sih, G. C., 1991, *Mechanics of Fracture Initiation and Propagation*, Kluwer Academic Publisher, Dordrecht, The Netherlands.

Sih, G. C., and Tamusz, V. P., eds., 1979, *Fracture of Composite Materials, Proceedings of the 1st USA-USSR Symposium*, Sijthoff and Noordhoff, The Netherlands.

Sih, G. C., and Theocaris, P. S., eds., 1981, *Mixed Mode Crack Propagation*, Proc. 1st U.S.-Greece Symposium, Athens, Greece, Sijthoff and Noordhoff, Alpen aan den Rijn, The Netherlands.

Smith, R. N. L., and Mason, J. C., 1982, "A Boundary Element Method for Curved Crack Problems in Two Dimensions," *Boundary Element Methods in Engineering*, C. A. Brebbia, ed., Springer-Verlag, Berlin, pp. 472–484.

Zienkiewicz, O. C., 1977, *The Finite Element Method*, McGraw-Hill, New York.

Quanxin Guo

Jian-Juei Wang
Mem. ASME.

TerraTek, Inc.,
420 Wakara Way,
Salt Lake City, UT 84108

R. J. Clifton
Division of Engineering,
Brown University,
Providence, RI 02912
Mem. ASME.

L. J. Mertaugh
Naval Air Warfare Center Division,
Rotary Wing, RW82H
Patuxent River, MD 20670

Elastic Analyses of Planar Cracks of Arbitrary Shape

A numerical method is presented for planar cracks of arbitrary shape. The fundamental solution for a dislocation segment is obtained from the point force solution and used to derive three coupled surface integral equations in which the crack-face tractions are expressed in terms of the gradients of the relative crack-surface displacements. Because the singularity of the kernel in the integral equations is one order less for fundamental solutions based on dislocation segments than for those based on dislocation loops or the body force method, no special numerical techniques are required. Most of the integrations over elements are evaluated analytically. The integral equations are solved numerically by covering the crack surface with triangular elements, and taking the relative displacements to vary linearly over the elements. The mesh is generated by optimizing the local aspect ratio, which is related to the difference in the principal stretches of the mapping of a square reference mesh onto the fracture surface. This mesh generator allows cracks of a wide variety of shapes to be analyzed with good accuracy. Comparison with known solutions indicate that accurate numerical solutions are obtained with a relatively coarse mesh.

Introduction

In fracture mechanics applications, three-dimensional elasticity solutions are often called for by the geometry of the body, the loading, and the cracks, but not considered because of the much greater difficulty involved. In critical applications, three-dimensional analysis is essential for obtaining reliable solutions. Analytical solutions have been obtained for some three-dimensional cracks, for instance, circular and elliptical cracks in an infinite, isotropic body, by Kassir and Sih (1975, 1966), Shah and Kobayashi (1971), Sneddon and Lowengrub (1969), Westmann (1965), Keer (1964), and Segedin (1950). Analytical solutions for irregularly shaped three-dimensional cracks are not available and numerical methods have been developed for finding the stress distribution and relative crack-surface displacements for these cases by a number of researchers. For example, Bui (1977), following Kossecka (1971), obtained a singular integral equation by the use of single layer and double layer potentials for a three-dimensional crack. Bui (1977) obtained numerical solutions for a square crack under uniform pressure.

Murakami and Nemat-Nasser (1983), Murakami (1985), Lee and Keer (1986), and Lee, Farris, and Keer (1987), among many others, used a body-force method developed by Murakami and Nemat-Nasser (1983) from Mura's eigenstrain approach (see, for example, Mura, 1987) to reduce the problem of a planar crack to singular integral equations over the crack surface in terms of the relative crack-face displacements. Special numerical techniques are required to solve the integral equations because the kernels are singular. A numerical procedure has been given by Murakami and Nemat-Nasser (1983). Solving the singular integral equations numerically gives the relative crack-surface displacements and stress intensity factors for the three modes of crack opening.

Weaver (1977) presented a different method for solving three-dimensional cracks. In his method, the governing singular integral equations are expressed in terms of the gradients of the relative crack-surface displacements. Because the singularity of these integral equations is one order less than for the integral equations expressed in terms of the relative crack-face displacements, no special numerical techniques are required in obtaining numerical solution of the integral equations. He gave a numerical procedure only for rectangular cracks in an infinite body. Clifton and Abou-Sayed (1981) used equivalent integral equations in a variational approach for solving three-dimensional problems for cracks of arbitrary shape in the simulation of hydraulic fracturing.

In this paper, fundamental solutions for a dislocation segment are derived from the point force solution and the reciprocal theorem (Kurashige and Clifton, 1992). Three coupled integral equations over the crack surface are obtained from these fundamental solutions. The variational numerical method introduced by Clifton and Abou-Sayed (1981) for solving a pure opening-mode three-dimensional crack is extended to a mixed-mode three-dimensional crack.

Contributed by the Applied Mechanics Division of THE AMERICAN SOCIETY OF MECHANICAL ENGINEERS for publication in the ASME JOURNAL OF APPLIED MECHANICS.

Discussion on this paper should be addressed to the Technical Editor, Professor Lewis T. Wheeler, Department of Mechanical Engineering, University of Houston, Houston, TX 77204-4792, and will be accepted until four months after final publication of the paper itself in the ASME JOURNAL OF APPLIED MECHANICS.

Manuscript received by the ASME Applied Mechanics Division, Jan. 19, 1993; final revision, Aug. 23, 1993. Associate Technical Editor: X. Markenscoff.

Numerical solutions provide the three relative displacement components over the crack and the three stress intensity factors along the crack front. An adaptive mesh generator developed by Clifton and Wang (1991) is implemented in the present code for analyzing cracks of a wide variety of shapes with good accuracy. Comparisons of the numerical results with known solutions for cases of a penny-shaped crack, an elliptical crack, and a rectangular crack show that accurate numerical solutions are obtained even for a relatively coarse mesh.

Method of Analysis

Consider a planar crack of arbitrary shape in an isotropic, linearly elastic space. The Cartesian coordinate (x, y, z) or $x_i (i = 1, 2, 3)$ is oriented such that the crack lies on the x-y plane. The tractions $\sigma_{zx}(x, y)$, $\sigma_{zy}(x, y)$, $\sigma_{zz}(x, y)$ or $\sigma_{3k}(x, y)(k = 1, 2, 3)$ are prescribed on the crack surface $z = 0$.

Suppose that the stress tensor $\boldsymbol{\sigma}(\mathbf{x}', \mathbf{x})$ at point $\mathbf{x}'$ due to a point load $\mathbf{P}\delta(\mathbf{x}' - \mathbf{x})$ at the point $\mathbf{x}$ is known. Then, by means of the reciprocal theorem, the displacement $\mathbf{u}(\mathbf{x})$ at the point $\mathbf{x}$ due to a dislocation loop that bounds a surface A can be expressed as (see, e.g., Kurashige and Clifton, 1992)

$$\mathbf{P} \cdot \mathbf{u}(\mathbf{x}) = -\iint_A \{\boldsymbol{\sigma}(\mathbf{x}'; \mathbf{x})\mathbf{b}(\mathbf{x}')\} \cdot \mathbf{n}(\mathbf{x}')dS', \quad (1)$$

where $\mathbf{b} = \mathbf{u}_+ - \mathbf{u}_-$ is the jump in displacement across the surface; $\mathbf{n} = \mathbf{n}_+ = -\mathbf{n}_-$ is the unit normal to the lower surface of A; subscripts "+" and "−" denote evaluation on the lower and upper surface of A; and the dot "·" denotes dot product of two vectors. From Eq. (1)

$$u_m(\mathbf{x}) = -\iint_A \sigma_{(m)ij}(\mathbf{x}'; \mathbf{x})b_i(\mathbf{x}')n_j(\mathbf{x}')dS', \quad (2)$$

where $\sigma_{(m)ij}(\mathbf{x}'; \mathbf{x})$ is the stress σ_{ij} at $\mathbf{x}'$ due to a unit force in the x_m-direction at $\mathbf{x}$ and the summation convention on repeated indexes is used here and throughout the paper.

Differentiating Eq. (2) with respect to x_s and then applying Stokes' theorem one obtains (Kurashige and Clifton, 1992; Mura, 1987)

$$\frac{\partial u_m(\mathbf{x})}{\partial x_s} = \epsilon_{jsn}\oint b_i \sigma_{(m)ij}(\mathbf{x}'; \mathbf{x})dx'_n, \quad (3)$$

where the permutation symbols ϵ_{ijk} are zero, except $\epsilon_{123} = \epsilon_{312} = \epsilon_{231} = 1$, $\epsilon_{132} = \epsilon_{321} = \epsilon_{213} = -1$. The stress gradient caused by dislocations with Burgers vector b_i and line segment dx'_n can be obtained from Eq. (3) and Hooke's law as

$$d\sigma_{pq}(\mathbf{x}) = L_{pqms}\epsilon_{jsn}b_i\sigma_{(m)ij}(\mathbf{x}; \mathbf{x}')dx'_n, \quad (4)$$

where, for isotropic materials, the elastic moduli L_{pqms} are given as

$$L_{pqms} = G\left[\delta_{pm}\delta_{qs} + \delta_{ps}\delta_{qm} + \left(\frac{2}{1-2\nu}\right)\delta_{pq}\delta_{ms}\right], \quad (5)$$

where G and ν are shear modulus and Poisson's ratio, respectively, and δ_{ij} is the Kronecker delta.

For a dislocation segment with components dx in the x-direction and dy in the y-direction, the products of Burgers vector $\mathbf{b}$ and the dislocation segment can be expressed in terms of the relative crack-surface displacements $w_i(x, y) = u_i(x, y, z = 0^+) - u_i(x, y, z = 0^-)$ as

$$b_i dx = -\frac{\partial w_i}{\partial y}dxdy, \quad (6)$$

$$b_i dy = \frac{\partial w_i}{\partial x}dxdy. \quad (7)$$

Substituting Eqs. (6) and (7) into Eq. (4) allows the line integral to be replaced by an area integral. The result is the following surface integral equation that relates the traction on the crack surface to the derivatives of the relative displacements over the crack surface as

$$\sigma_{3q}(x, y) = L_{3qms}\iint_A \sigma_{(m)ij}(x', y'; x, y) \times \left\{-\epsilon_{js1}\frac{\partial w_i}{\partial y'} + \epsilon_{js2}\frac{\partial w_i}{\partial x'}\right\}dx'dy' \quad (8)$$

where A is the area of the fracture surface. The stresses $\sigma_{(m)ij}(\mathbf{x}'; \mathbf{x})$ for a unit concentrated force at point $\mathbf{x}$ in the x_m-direction in Eq. (8) are available for a full space (Kelvin, 1882)

$$\sigma_{(m)ij}(\mathbf{x}'; \mathbf{x}) = \frac{1}{8\pi(1-\nu)}\left\{-(1-2\nu) \times \frac{\delta_{im}(x'_j - x_j) + \delta_{jm}(x'_i - x_i) - \delta_{ij}(x'_m - x_m)}{|\mathbf{x}' - \mathbf{x}|^3} - 3\frac{(x'_m - x_m)(x'_i - x_i)(x'_j - x_j)}{|\mathbf{x}' - \mathbf{x}|^5}\right\}. \quad (9)$$

Substituting Eq. (9) into Eq. (8) gives three singular integral equations, one for each component of the tractions $\sigma_{3k}(x, y)$ $(k = 1, 2, 3)$ on the crack surface, in terms of the derivative of the relative crack-surface displacements $w_n (n = 1, 2, 3)$:

$$\sigma_{3k}(x, y) = \sigma_0\iint S_{3k}^{n\beta}\frac{\partial w_n}{\partial x'_\beta}dx'dy', \quad (10)$$

where

$$\sigma_0 = \frac{G}{4\pi(1-\nu)}, \quad (11)$$

and the nonzero terms of $S_{3k}^{n\beta}$ are

$$S_{33}^{3\beta} = (x'_\beta - x_\beta)/R^3, \quad (12)$$

$$S_{3\gamma}^{\alpha\beta} = 3(x'_\alpha + x_\alpha)(x'_\beta - x_\beta)(x'_\gamma - x_\gamma)/(2R^5) + (1-2\nu)\left(\delta_{\alpha\beta}(x'_\gamma - x_\gamma) - \delta_{\alpha\gamma}(x'_\beta - x_\beta)\right)/(2R^3), \quad (13)$$

for $\alpha, \beta, \gamma = 1, 2$, and

$$R^2 = (x' - x)^2 + (y' - y)^2. \quad (14)$$

Using different approaches, Eq. (10) was obtained by Kossecka (1971), Bui (1977), Weaver (1977), and Sladek and Sladek (1986) for a Mode I planar crack under dynamic loading.

Integrating Eq. (10) by parts would result in integral equations in terms of the relative displacements $w_i(x, y)$. However, it is advantageous to have the governing integral Eq. (10) in terms of the gradient of $w_i(x, y)$ because the singularity of the kernel of Eq. (10) is one order less than that of the kernel of the integral equations in terms of crack opening, e.g., Murakami and Nemat-Nasser (1983), Lee, Farris and Keer (1987), among many others. As will be shown in the next section, no special numerical techniques are required to evaluate matrix elements for the integral Eq. (10).

Numerical Implementation

The integral equations can be solved numerically using a variational approach similar to the one introduced by Clifton and Abou-Sayed (1981) for a pure opening crack. From the principle of the minimum of the total potential energy, the relative crack displacements $w_i(x, y)$ that vanish along the

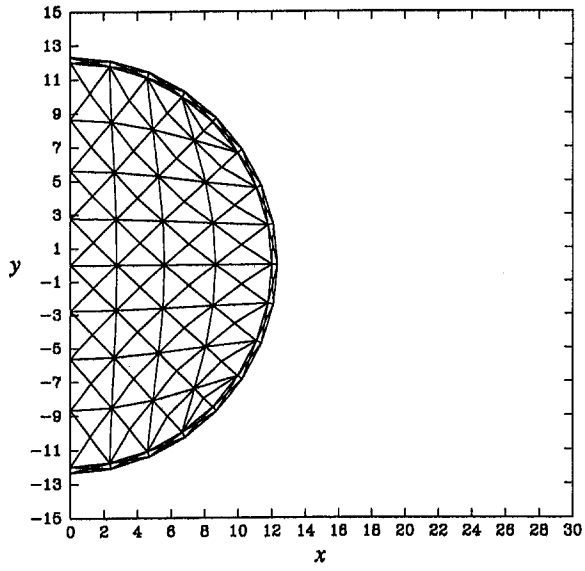

Fig. 1 One half of the meshed region for a penny-shaped crack. The mesh is an 8 × 8 mesh.

crack front and satisfy Eq. (10) are the functions that minimize the total potential energy $U + V$, where

$$U = \frac{\sigma_0}{2}\iint_A w_k(x, y)\iint_A S_{3k}^{n\beta}(x', y'; x, y)\frac{\partial w_n}{\partial x'_\beta}dx'dy'dxdy, \tag{15}$$

$$V = -\iint_A w_k(x, y)\sigma_{3k}(x, y)dxdy. \tag{16}$$

The crack surface "A" is divided into a meshed region "A_0", which is subdivided into triangles, and a crack-tip region "∂A". Figure 1 shows one half of the meshed region for a penny-shaped crack. The narrow crack-tip region "∂A" outside the meshed region is not shown in Fig. 1. Over each triangle, the three relative crack-surface displacements $w_j(x, y)$ and three tractions $\sigma_{3k}(x, y)$ are expressed in terms of the local trial functions $f_i(x, y)(i = 1, 2, 3)$ and nodal values w_j^i and $\sigma_{3k}^i(i = 1, 2, \ldots, N)$, according to

$$w_j(x, y) = \sum_{i=1}^{i=N} w_j^i f_i(x, y), \tag{17}$$

$$\sigma_{3k}(x, y) = \sum_{i=1}^{i=N} \sigma_{3k}^i f_i(x, y), \tag{18}$$

where N is the total number of nodes and the trial function $f_i(x, y)$ has (i) the value of unity at the ith node, (ii) varies linearly over adjacent triangles, and (iii) vanishes along the opposite side of these triangles and outside the adjacent triangles. In the near-tip region "∂A", the relative displacements $w_j(x, y)$ vary as the square root of the distance from the crack tip. That is, the relative displacements in the region "∂A" are expressed as

$$w_j(x, y) = w_j(s)\left(\frac{\eta}{\epsilon}\right)^{1/2} \tag{19}$$

where ϵ is the width of the crack-tip region "∂A" and η is the distance from the crack tip to point (x, y). The function $w_j(s)$ is taken to vary linearly over the straight line segments which represent the inner boundary of "∂A". Since ϵ is very small and the tractions $\sigma_{3k}(x, y)$ do not vary much across this narrow region, we assume that the traction is constant over each near-tip element.

A numerical method for finding an approximate solution $w_i(x, y)$ is based on minimizing the total potential energy, $U + V$, for a restricted class of functions $w_i(x, y)$ that are determined by a finite number of nodal values of the three relative displacements over the crack as indicated in Eqs. (17) and (19). Minimizing the total potential energy one obtains, from Eq. (15)–(19), a system of algebraic equations for the nodal relative displacements w_k^i. These equations can be written in the partitioned form

$$\frac{\sigma_0}{2}\begin{bmatrix}\mathbf{K}_{33} & \mathbf{K}_{32} & \mathbf{K}_{31}\\ \mathbf{K}_{23} & \mathbf{K}_{22} & \mathbf{K}_{21}\\ \mathbf{K}_{13} & \mathbf{K}_{12} & \mathbf{K}_{11}\end{bmatrix}\begin{bmatrix}\mathbf{w}_3\\ \mathbf{w}_2\\ \mathbf{w}_1\end{bmatrix} = \begin{bmatrix}\mathbf{p}_3\\ \mathbf{p}_2\\ \mathbf{p}_1\end{bmatrix}, \tag{20}$$

where $\mathbf{w}_k(k = 1, 2, 3)$ is an N-dimensional column vector of nodal displacement components w_k^i and $\mathbf{p}_k$ is an N-dimensional column vector of nodal forces

$$(p_k)_i = \iint \sigma_{3k}(x, y)f_i(x, y)dxdy. \tag{21}$$

The stiffness matrix $\mathbf{K}_{ij}$, comprised of submatrices

$$(K_{kn})_{ij} = \iint dxdy\iint\left(S_{3k}^{n\beta}f_j\frac{\partial f_i}{\partial x'_\beta} + S_{3n}^{k\beta}f_i\frac{\partial f_j}{\partial x'_\beta}\right)dx'dy', \tag{22}$$

is a full, symmetric matrix. The submatrices (22) satisfy the symmetry relation $(K_{kn})_{ij} = (K_{nk})_{ji}$.

To construct the stiffness matrix, we need to consider two cases: (1) *overlapping elements*, where (x, y) and (x', y') belong to the same element A_p, and (2) *nonoverlapping elements*, where (x, y) and (x', y') belong to different elements A_p and A_q, respectively. For each case, we also need to differentiate between elements which are in the near-tip region ∂A or in the interior region A_0 because different trial functions are used in the two regions.

Procedures for evaluating the integrals are the same for all indices k, n. The method is illustrated below by considering the first term in Eq. (22) and the case of $k = n = 1$, i.e.,

$$(\Delta K_{11})_{ij} = \iint_{A_p} f_i dxdy\iint_{A_q}\frac{\partial f_j}{\partial x'_\beta}S_{31}^{1\beta}dx'dy', \tag{23}$$

where

$$S_{31}^{11} = \frac{3(x' - x)^3}{2R^5},$$

$$S_{31}^{12} = \frac{1}{2}\left(\frac{3(x' - x)^2(y' - y)}{R^5} + \frac{(1 - 2\nu)(y' - y)}{R^3}\right). \tag{24}$$

Nonoverlapping. If neither element A_p nor A_q belongs to the near-crack-tip region, then the trial functions are linear functions and we have

$$(\Delta K_{11})_{ij} = \sum_{\alpha=1}^{\alpha=3}\frac{A_p}{3}f_i(x_\alpha, y_\alpha)\frac{\partial f_j}{\partial x'_\beta}$$

$$\times\iint_{A_q} S_{31}^{1\beta}(x', y'; x_\alpha, y_\alpha)dx'dy' = -\sum_{\alpha=1}^{\alpha=3}\frac{A_p}{3}f_i(x_\alpha, y_\alpha)$$

$$\times\left\{\frac{\partial f_j}{\partial x'}\frac{n_x}{2}\oint_{S_q}\left(\frac{3}{R} - \frac{(y_\alpha - y')^2}{R^3}\right)ds'\right.$$

$$\left. + \frac{\partial f_j}{\partial y'}\frac{n_y}{2}\oint_{S_q}\left(\frac{(x_\alpha - x')^2}{R^3} + \frac{(1 - 2\nu)}{R}\right)ds'\right\}. \tag{25}$$

Here three-point Gaussian integration is used for the integration over the element A_p with area A_p and quadrature

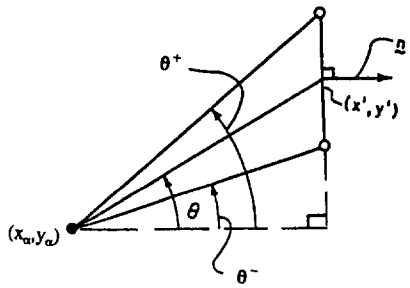

Fig. 2 Geometry for integration along a side of a triangle

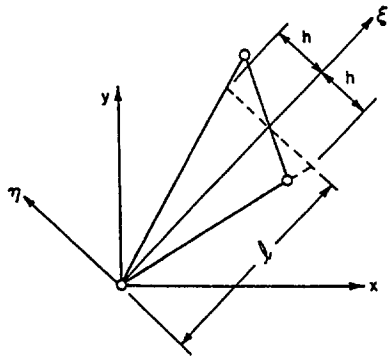

Fig. 3 Local coordinates of an isosceles triangle approximation of a triangular element

points (x_α, y_α) $(\alpha = 1, 2, 3)$. The vector $\mathbf{n} = (n_x, n_y)$ is the unit exterior normal of the perimeter s_q of the element A_q.

All the integrals in Eq. (25) can be evaluated analytically through the following two integrals. For each side of a triangular element A_q, say the side 2, we have (Fig. 2)

$$\int \frac{1}{R} ds' = \frac{1}{2}\left(\ln \frac{1+\sin\theta}{1-\sin\theta}\right)_{\theta^-}^{\theta^+},$$

$$\int \frac{(y_\alpha - y')^2}{R^3} ds' = \left\{ n_x^2 \frac{1}{2} \ln\left(\frac{1+\sin\theta}{1-\sin\theta}\right) - 2n_x n_y \cos\theta - \left(n_x^2 - n_y^2\right)\sin\theta \right\}_{\theta^-}^{\theta^+}. \quad (26)$$

For the case where a quadrature point lies along the extension of the side of the triangle, we have, instead of Eq. (26),

$$\int \frac{1}{R} ds' = \ln\left(\frac{r^+}{r^-}\right),$$

$$\int \frac{(y_\alpha - y')^2}{R^3} ds' = n_x^2 \ln\left(\frac{r^+}{r^-}\right), \quad (27)$$

where r^- and r^+ $(r^- < r^+)$ are the distances from the quadrature point to the two ends of the side of the triangle.

Overlapping. For an overlapping element, it is more convenient to use the local coordinates (ξ, η) (see Fig. 3) in constructing the stiffness matrix. Since $f_i(x, y)$ is a linear function, we have

$$f_i(\xi, \eta) = f_i(0, 0) + f_{i,1}\xi + f_{i,2}\eta. \quad (28)$$

Subscripts ",1" and ",2" denote differentiation with respect to ξ and η, respectively. From Eqs. (23) and (28) one has

$$(\Delta K_{11})_{ij} = \iint_{A_p} f_j \left(f_{i,1} \iint_{A_p} S_{31}^{1\xi} d\xi' d\eta' + f_{i,2} \iint_{A_p} S_{31}^{1\eta} d\xi' d\eta' \right)$$
$$= -l^3 \left(f_{i,1} f_{j,1} Z_{2111} + f_{i,1} f_{j,2} Z_{3111} + f_{i,2} f_{j,1} Z_{2211} + f_{i,2} f_{j,2} Z_{3211} \right), \quad (29)$$

where

$$\{Z_{21kn}, Z_{31kn}\} = \iint_{A_p}\iint_{A_p} \{s, t\} S_{3k}^{n\xi} ds dt ds' dt',$$

$$\{Z_{22kn}, Z_{32k_n}\} = \iint_{A_p}\iint_{A_p} \{s, t\} S_{3k}^{n\eta} ds dt ds' dt', \quad (30)$$

and $s = \xi/l$, $t = \eta/l$ are the normalized local coordinates; l is the height of the triangular element. Z_{21kn}, Z_{31kn}, Z_{22kn}, and Z_{32kn} $(k, n = 1, 2, 3)$ are evaluated numerically and stored in arrays for stiffness matrix calculations. For an *isosceles* triangle, it can be shown that Z_{21kn}, Z_{31kn}, Z_{22kn}, and Z_{32kn} $(k, n = 1, 2, 3)$ can be expressed in terms of the following four integrals:

$$\alpha_{\xi\xi} = \iint_{A_p} s ds dt \iint_{A_p} \frac{s - s'}{R^3} ds' dt' \quad (31)$$

$$\alpha_{\eta\eta} = \iint_{A_p} t ds dt \iint_{A_p} \frac{t - t'}{R^3} ds' dt' \quad (32)$$

$$\beta_{\xi\xi} = \iint_{A_p} s ds dt \iint_{A_p} \frac{3(s - s')^2}{R^5} ds' dt' = 2\alpha_{\xi\xi} - \frac{\zeta^2}{3\sqrt{1+\zeta^2}} + 2\zeta^2 \int_0^1 y dy \int_0^1 \left\{ \frac{y - x}{\sqrt{(1-y)^2 + \zeta^2 (y-x)^2}} + \frac{x + y}{\sqrt{(1-y)^2 + \zeta^2 (x+y)^2}} - \frac{x + y}{\sqrt{(y-x)^2 + \zeta^2 (x+y)^2}} \right\} dx \quad (33)$$

$$\beta_{\eta\eta} = \iint_{A_p} t ds dt \iint_{A_p} \frac{3(t - t')^2}{R^5} ds' dt' = 2\alpha_{\eta\eta} - \frac{\zeta^2}{3\sqrt{1+\zeta^2}} + 2\zeta^2 \int_0^1 y dy \int_0^1 \left\{ \frac{y - x}{\sqrt{(y-x)^2 + \zeta^2 (y+x)^2}} + \frac{1 - x}{\sqrt{(1-x)^2 + \zeta^2 (x-y)^2}} - \frac{1 - x}{\sqrt{(1-x)^2 + \zeta^2 (x+y)^2}} \right\} dx \quad (34)$$

where $\zeta = h/l$. Integrals (31) and (32) have been evaluated by Clifton and Abou-Sayed (1981) in closed form, but the final expressions are cumbersome. Integrals (33) and (34), which may be expressed in closed form, are evaluated numerically and stored in tabular form as functions of ζ. Numerical evaluations of integrals (33) and (34) are validated with asymptotic expansions of Eqs. (33) and (34) for large ζ. For large ζ, we have $\beta_{\xi\xi} \approx \alpha_{\xi\xi}$ and $\beta_{\eta\eta} \approx 3\alpha_{\eta\eta} - 2\zeta/3$. In our numerical implementation, the approximation of replacing the actual triangle by an isosceles triangle (see Fig. 3) is used to save computational time. This appears to be a reasonable approximation from all the case we have studied.

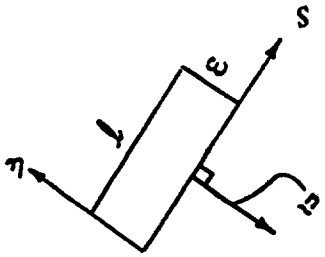

Fig. 4 A crack-tip element

Near-Crack-Tip. For a near-crack-tip element, instead of a linear trial function, we have

$$f_i(x, y) = \phi_i(s)\left(\frac{\eta}{\epsilon}\right)^{1/2}, \tag{35}$$

where $\phi_i(s)$ can be a constant or a linear function of "s" over the length of the element with width ϵ and length l (see Fig. 4). The same method used above for cases of overlapping and nonoverlapping elements can also be used here for the evaluation of the integral (23). The only difference is the trial function.

If the element A_p is in the near-crack-tip region ∂A, but A_q is not, then from Eqs. (23) and (35) we have

$$(\Delta K_{11})_{ij} = \frac{\partial f_j}{\partial x'_\beta}\frac{2\epsilon}{3}\int_0^l \phi_j(s)ds \iint_{A_q} S_{31}^{1\beta}(x', y'; s, \eta = 4\epsilon/9)dx'dy'. \tag{36}$$

The integrals over element A_q have been evaluated as given in Eq. (26) or Eq. (27).

If the element A_q is in the near-crack-tip region ∂A, but A_p is not, then we have

$$(\Delta K_{11})_{ij} = \iint_{A_p} f_i dxdy \int_0^l \left\{S_{31}^{1\eta}\phi_j(s') + \frac{2\epsilon}{3}S_{31}^{1\xi}\phi_j'(s')\right\}ds'. \tag{37}$$

The integration over A_p is handled by three-point Gaussian quadrature in the same way as in Eq. (25) and the line integral can be evaluated analytically.

If both A_p and A_q are in the near-crack-tip region, trial functions of Eq. (35) should be used for both f_i and f_j in Eq. (23) and the contribution from the overlapping near-crack-tip element is

$$(\Delta K_{11})_{ij} = \iint_{\epsilon\times l}\phi_j(s)\sqrt{\frac{\eta}{\epsilon}}\,dsd\eta \iint_{\epsilon\times l}\left\{\phi_i(s')\frac{1}{2\sqrt{\epsilon\eta'}}S_{31}^{1\eta} + \phi_i'(s')\sqrt{\frac{\eta'}{\epsilon}}\,S_{31}^{1\xi}\right\}ds'd\eta'. \tag{38}$$

If $\phi_i(s) = \phi_j(s) = 1/2$ (, $j = 1, 2, 3$) are taken, then one can obtain from Eq. (38)

$$2(\Delta K_{11})_{ij} = -n_y^2(2 - \nu)(l - \epsilon/3) - \left(n_x^2 - n_y^2\right)(l - \epsilon/6). \tag{39}$$

Mesh Generation

In the numerical simulation of a planar crack of arbitrary shape, a robust and optimal mesh generator is critically important due to the variety of crack shapes and the need to remesh at each step if the crack is allowed to grow. A good mesh must optimize the local aspect ratio, which is related to the difference in the principal stretches of the mapping of a square reference mesh onto the crack surface. The mesh generator used for this study (Clifton and Wang, 1991) maps a reference mesh of $M \times N$ squares onto a crack surface. A narrow annular region is added outside the $M \times N$ mesh to capture the large crack-opening gradient near the crack front; however, in the following the whole mesh is referred to as an $M \times N$ mesh. For example, the mesh shown in Fig. 1 for a circular crack (only one half of the mesh is shown because of symmetry with respect to the y-axis) is called an 8×8 mesh. Location of the nodes on the boundary is determined by considering a weight average of the boundary curvature and the sector area bounded by adjacent nodes. The nodal coordinates within the fracture are obtained by optimizing the local aspect ratio. This mapping provides triangles which are nearly isosceles as used in evaluating the integrals $\alpha_{\xi\xi}$, $\alpha_{\xi\xi}$, $\beta_{\theta\theta}$, and $\beta_{\eta\eta}$ over overlapping elements.

Numerical Results

The above analysis has been implemented in a computer code in which the symmetry of the stiffness matrix is used to minimize storage requirements, and computational time—both in evaluation of its elements and in its numerical inversion by means of the Cholesky scheme. Numerical results provide the three relative displacement components (w_1, w_2, w_3) over the crack and the three stress intensity components (K_I, K_{II}, K_{III}) along the crack front. The stress intensity factors at point (x, y) on the crack front are defined as

$$K_I = \lim_{r\to 0^+}\left\{(2\pi r)^{1/2}\sigma_{zz}|_{z,\theta=0}\right\},$$
$$K_{II} = \lim_{r\to 0^+}\left\{(2\pi r)^{1/2}\sigma_{nz}|_{z,\theta=0}\right\},$$
$$K_{III} = \lim_{r\to 0^+}\left\{(2\pi r)^{1/2}\sigma_{tz}|_{z,\theta=0}\right\}, \tag{40}$$

where the polar coordinate (r, θ) on the plane $z = 0$ is centered at the point (x, y) with $\theta = 0$ corresponding to the normal direction $\mathbf{n}$ of the crack front, and $\mathbf{t}$ is the tangent to the crack front contour. Using the relations between stress intensity factors and the crack displacements near the crack-tip (see for example, Eq. (3.1-16), (3.1-39), and (3.1-42) in Kanninen and Popelar (1985)), one can extract the stress intensity factors along the crack front from the crack surface displacements by means of

$$K_I = \sigma_0\pi w_3\sqrt{2\pi/\epsilon},$$
$$K_{II} = \sigma_0\pi(w_1n_x + w_2n_y)\sqrt{2\pi/\epsilon},$$
$$K_{III} = (1 - \nu)\sigma_0\pi(-w_1n_y + w_2n_x)\sqrt{2\pi/\epsilon}, \tag{41}$$

where w_i ($i = 1, 2, 3$) are the relative crack-surface displacements evaluated at points a small distance "ϵ" from the crack front, again (n_x, n_y) is the unit outward normal to the crack front.

To validate the code by comparison with a closed-form solution, numerical results have been obtained for a penny-shaped crack of radius "a" in an infinite body. The exact solution for uniform pressure or uniform shear in the y-direction has been given by Segedin (1950), Westmann (1965), Kassir and Sih (1975) and others. The mesh used in the calculations is shown in Fig. 1 for one half of the crack. For the case of constant applied pressure p, the crack openings with different meshes (4×4 mesh or 40 nodes; 8×8 mesh or 110 nodes and 12×12 mesh or 212 nodes) are shown in Fig. 5, where $w_{\max}$ is the exact solution of the displacement at the center of the crack, and R is the distance from the center of the crack. From Fig. 5 one can see that greater accuracy is obtained for a finer mesh. Accuracy of the results using 110 nodes is within five percent, which is regarded as

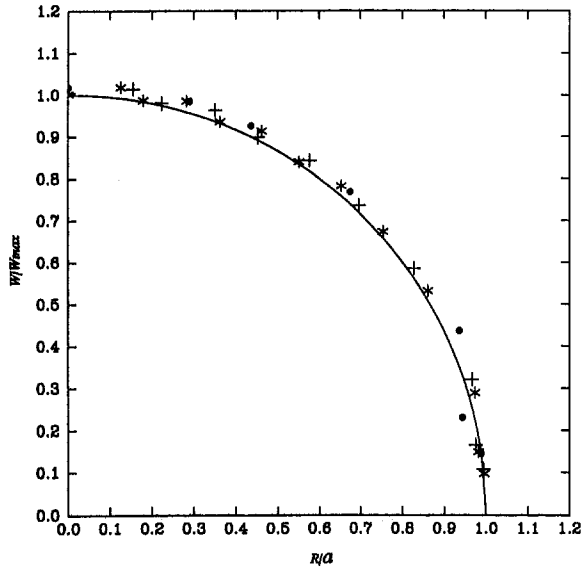

Fig. 5 Comparison of calculated and analytical crack-opening displacement for a penny-shaped crack under uniform pressure and different meshes (•—40 nodes, +—110 nodes and ∗—212 nodes). The curve is the theoretical result.

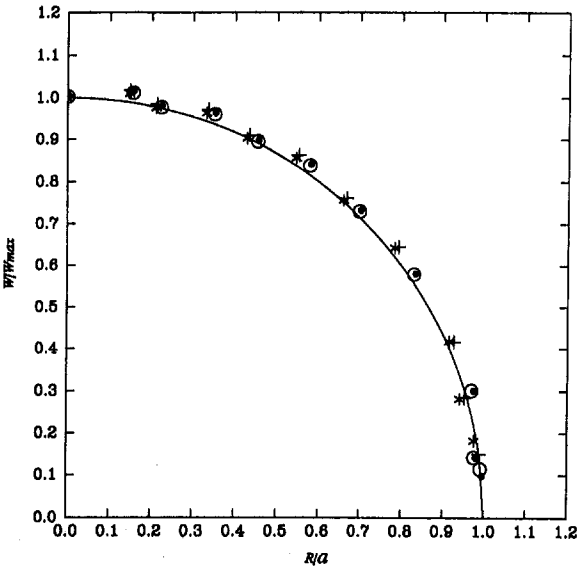

Fig. 6 Dependence of numerical results on the limiting aspect ratio of the annular region (Δ) and the width of the near-tip region (ϵ) for a penny-shaped crack (•—Δ = 1:9, ϵ = 0.004a; +—Δ = 1:3, ϵ = 0.012a; ○—Δ = 1:9, ϵ = 0.009a; ∗—1:3, ϵ = 0.024a)

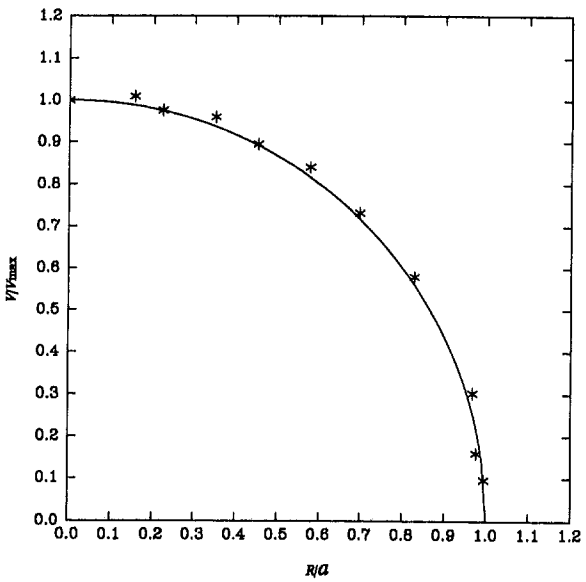

Fig. 7 Comparison of calculated (mesh of Fig. 1) and analytical displacement for a penny-shaped crack under uniform shear. v is the relative displacement in the applied shear direction. The line is the theoretical result.

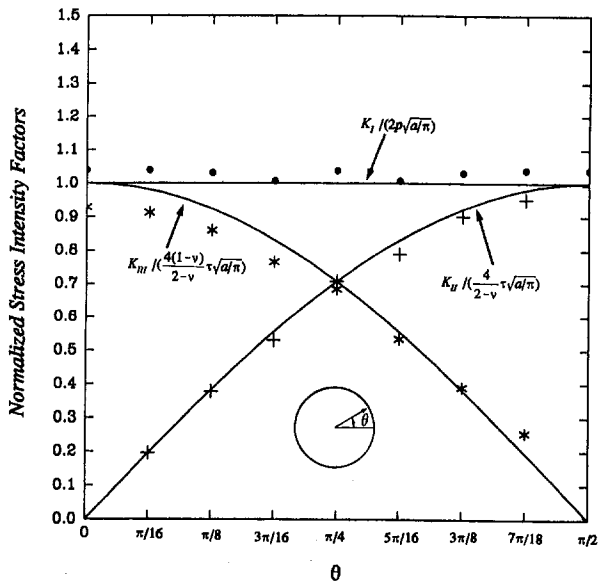

Fig. 8 Comparison of calculated (mesh of Fig. 1) and analytical stress intensity factors (K_I for uniform pressure p; K_{II} and K_{III} for uniform shear τ) along the crack front for a penny-shaped crack. The curves represent the analytical results.

acceptable. Although the accuracy can be improved by finer meshes, the required additional computational time may hinder our application for crack growth problems. The width of the discretized annular region adjacent to the crack front (Fig. 1) is controlled by the specified limiting aspect ratio of the elements of the annular region. Varying the limiting aspect ratio from 1:3 to 1:9 and varying the width "ϵ" of near-tip region from 0.4 percent to 2.4 percent of the radius causes little change in the computed crack opening (Fig. 6).

Comparison of the normalized numerical and analytical displacements for a penny-shaped crack subject to a uniform shear τ in the y-direction is shown in Fig. 7; $v_{\max}$ is the exact solution for the relative displacement at the crack center. The displacements in the direction perpendicular to the applied shear are either equal to zero or very nearly so, and therefore are not shown here. The normalized numerical and theoretical stress intensity factors for the case of uniform pressure (K_I), and for the case of uniform shear (K_{II} and K_{III}) are shown in Fig. 8. For a penny-shaped crack under linear pressure, $p(x, y) = p_0 + p_1(y/a)$, Fig. 9 shows the normalized stress intensity factors along the crack front for the case $p_1/p_0 = 0.2$.

Numerical results are also presented for an elliptic crack. Figure 10 shows the calculated stress intensity factors calculated from a 10×10 mesh in the first quadrant for the case when the major axis, b is twice the minor axis, a, together with the analytical solution of Irwin (1962) and Kassir and Sih (1966). Figure 10 shows that the maximum error is about eight percent and appears near the point $x = b$ due to the large radius of curvature there and the isosceles triangle approximation used in the evaluation of the stiffness matrix.

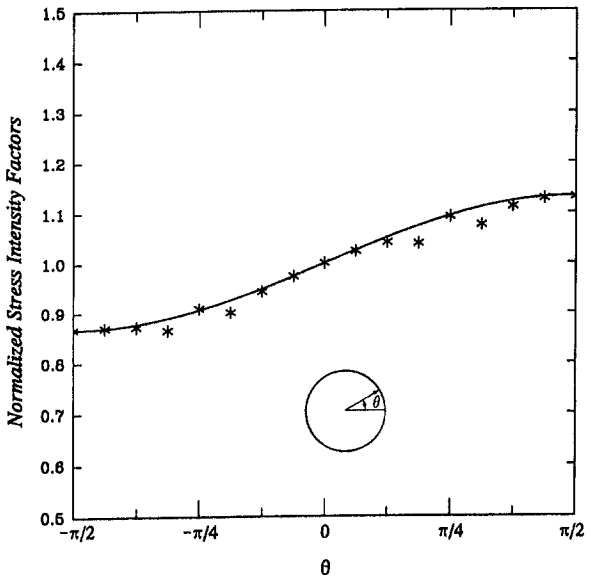

Fig. 9 Normalized stress intensity factor for a penny-shaped crack under linear pressure $p(x, y) = p_0 + p_1(y/a)$, $p_1/p_0 = 0.2$. The numerical results are normalized by the result at $y = 0$, which is one percent larger than the theoretical value of $2p_0(a/\pi)^{1/2}$.

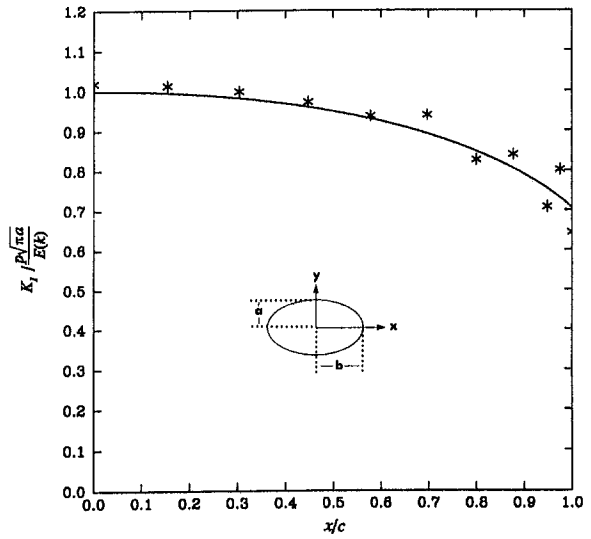

Fig. 10 Stress intensity factors along an elliptical crack front in the first quadrant. The curve is the analytical results. $E(k)$ is the complete elliptic integral of the second kind and $k^2 = (b^2 - a^2)/b^2$, where $2a$ and $2b$ are the minor and major dimensions of the elliptic crack.

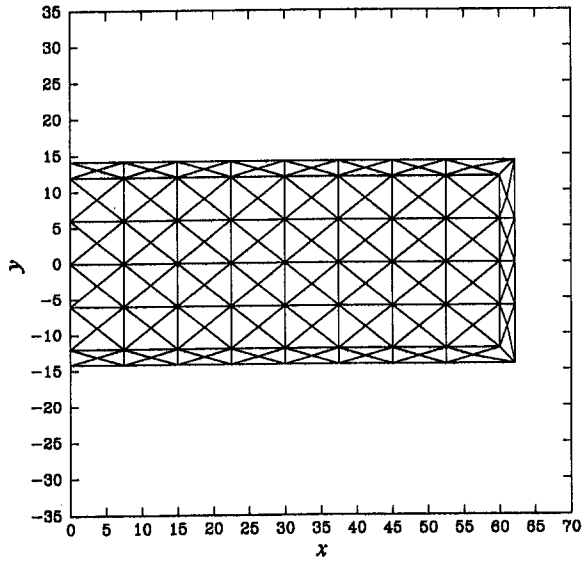

Fig. 11 One half of the meshed region for a rectangular crack. The length is 4.4 times of the width.

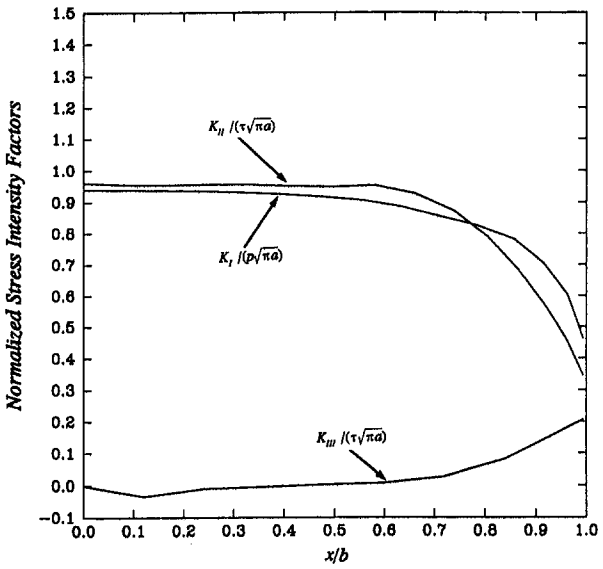

Fig. 12 Normalized stress intensity factors (mesh of Fig. 11) along the longer side of the rectangular crack in Fig. 11—K_I for uniform pressure (p); K_{II}, K_{III} for uniform shear (τ) in the y direction

Figure 11 shows the mesh for one half of a rectangular crack of width "$2a$" and length "$2b$", where b is 4.4 times a. Figure 12 depicts the stress intensity factors calculated from the 16×4 mesh shown in Fig. 11 along the crack front $y = a$ for the rectangular crack in an infinite body under uniform surface tractions. K_I is the opening stress intensity factor for the case of a uniform pressure p, while K_{II} and K_{III} are the shear stress intensity factors for the case of a uniform shear in the y-direction. The values of the stress intensity factors near the center of a long crack are approximately equal to the corresponding values for plane strain. The stress intensity factors defined by Eq. (40) should be zero at the corners because for polygonal cracks, the stress singularity at such points of abrupt change of slope is less severe than the square-root singularity. Since no special measures are taken in the numerical procedure at the corners (Weaver, 1977), the numerical results at the corners of the rectangular crack are not accurate. The stress intensity factors K_I and K_{III} at the center of the short side of the rectangular crack is $0.77p/(\pi a)^{1/2}$ and $0.66p/(\pi a)^{1/2}$, while the results obtained by Weaver (1977) are $0.80p/(\pi a)^{1/2}$ and $0.67p/(\pi a)^{1/2}$, respectively.

Concluding Remarks

Three coupled integral equations over the crack surface are derived in terms of the gradients of the relative crack displacements. A variational numerical procedure is developed by minimizing the total potential energy. No special numerical techniques are required in evaluating the elements of the symmetric stiffness matrix; most integrals are evaluated analytically. Comparisons with exact solutions for several cases of three-dimensional cracks in an infinite medium indicate that accurate numerical solutions are obtained even for a relatively coarse mesh.

The present formulation has been extended to planar surface cracks in a half-space (Guo, Wang and Clifton, 1995). Xu and Ortiz (1993) recently considered nonplanar cracks in an unbounded elastic space.

Acknowledgment

This work was carried out in the course of a project sponsored by the Naval Air Warfare Center through the Small Business Innovation Research (SBIR) program under Contract No. N00421-91-C-0119.

References

Bui, H. D., 1977, "An Integral Equations Method for Solving the Problem of a Plane Crack of Arbitrary Shape," *Journal of the Mechanics and Physics of Solids*, Vol. 25, pp. 29–39.

Clifton, R. J., and Abou-Sayed, A. S., 1981, "A Variational Approach to the Prediction of the Three-Dimensional Geometry of Hydraulic Fractures," SPE/DOE Paper No. 9879, *Proceedings of Low Permeability Symposium*, Denver, CO, pp. 457–463.

Clifton, R. J., and Wang, J. J., 1991, "Adaptive Optimal Mesh Generator for Hydraulic Fracturing Modeling," *Rock Mechanics as a Multidisciplinary Science*, pp. 607–616.

Guo, Q., Wang, J. J., and Clifton, R. J., 1995, "Three-Dimensional Analysis of Surface Cracks in an Elastic Half-Space," submitted to ASME JOURNAL OF APPLIED MECHANICS.

Irwin, G. R., 1962, "Crack-Extension Force for a Part-through Crack in a Plate," ASME JOURNAL OF APPLIED MECHANICS, Vol. 29, pp. 651–654.

Kanninen, M. F., and Popelar, C. H., 1985, *Advanced Fracture Mechanics*, Cambridge University Press, pp. 142–145.

Kassir, M. K., and Sih, G. C., 1966, "Three-Dimensional Stress Distribution Around an Elliptical Crack Under Arbitrary Loadings," ASME JOURNAL OF APPLIED MECHANICS, Vol. 33, pp. 601–611.

Kassir, M. K., and Sih, G. C., 1975, *Three-Dimensional Crack Problems*, Noordhoff International Publishing.

Keer, L. M., 1963, "A Class of Nonsymmetrical Punch and Crack Problems," *Quarterly Journal of Mechanics and Applied Mathematics*, Vol. 27, pp. 423–436.

Lord Kelvin, 1882, "Note on the Integration of the Equations of Equilibrium on an Elastic Solid," *Mathematical and Physical Papers*, Vol. 1, Cambridge University Press, Cambridge, U.K., pp. 97–98.

Kossecka, E., 1971, "Defects as Surface Distributions of Double Forces," *Archives of Mechanics*, Vol. 23, pp. 481–494.

Kurashige, M., and Clifton, R. J., 1992, "Integral Equations for the Problem of a 3D Crack in an Infinite, Fluid-filled, Poroelastic Solid," *SPE Production Engineering*, Feb., 1992, pp. 34–38.

Lee, J. C., Farris, T. N., and Keer, L. M., 1987, "Stress Intensity Factors for Cracks of Arbitrary Shape Near an Interfacial Boundary," *Engineering Fracture Mechanics*, Vol. 27, pp. 27–41.

Lee, J. C., and Keer, L. M., 1986, "Study of a Three-Dimensional Crack Terminating at an Interface," ASME JOURNAL OF APPLIED MECHANICS, Vol. 53, pp. 311–316.

Mura, T., 1987, *Micromechanics of Defects in Solids*, Martinus Nijhoff Publishers, Amsterdam, The Netherlands.

Murakami, Y., 1985, "Analysis of Stress Intensity Factors of Modes I, II and III for Inclined Surface Cracks of Arbitrary Shape," *Engineering Fracture Mechanics*, Vol. 22, pp. 101–114.

Murakami, Y., and Nemat-Nasser, S., 1983, "Growth and Stability of Interacting Surface Flaws of Arbitrary Shape," *Engineering Fracture Mechanics*, Vol. 17, pp. 193–210.

Segedin, C. M., 1950, "Note on a Penny-Shaped Crack Under Shear," *Proceedings of the Cambridge Philosophical Society*, Vol. 47, pp. 396–400.

Shah, R. C., and Kobayashi, A. S., 1971, "Stress Intensity Factor for an Elliptical Crack Under Arbitrary Normal Loading," *Engineering Fracture Mechanics*, Vol. 3, pp. 71–96.

Sladek, J., and Sladek, V., 1986, "Dynamic Stress Intensity Factors Studied by Boundary Integrodifferential Equations," *International Journal for Numerical Methods in Engineering*, Vol. 23, pp. 919–928.

Sneddon, I. N., and Lowengrub, M., 1969, *Crack Problems in the Classical Theory of Elasticity*, John Wiley and Sons, New York.

Weaver, J., 1977, "Three-dimensional Crack Analysis," *International Journal of Solids and Structures*, Vol. 13, pp. 321–330.

Westmann, R. A., 1965, "Asymmetric Mixed Boundary Value Problems of the Elastic Half-Space," ASME JOURNAL OF APPLIED MECHANICS, Vol. 32, pp. 411–417.

Xu, G., and Ortiz, M., 1993, "A Variational Boundary Integral Method for the Analyses of 3D Cracks of Arbitrary Geometry Modeled as Continuous Distributions of Dislocation Loops," *International Journal for Numerical Methods in Engineering*, Vol. 36, pp. 3675–3701.

An Axisymmetric Crack in Bonded Materials With a Nonhomogeneous Interfacial Zone Under Torsion

M. Ozturk

F. Erdogan
Fellow ASME.

Department of Mechanical Engineering and Mechanics, Lehigh University, Bethlehem, PA 18015-3006

In this study the mode III axisymmetric crack problem for two dissimilar homogeneous materials bonded through a thin layer of nonhomogeneous interfacial region is considered. The shear modulus of the interfacial layer is assumed to be $\mu_2(z) = \mu_1 \exp(\alpha z)$. *It is also assumed that* $\mu_3 = \mu_1 \exp(\alpha h)$, *h being the thickness of the layer and* μ_1 *and* μ_3 *the shear moduli of the adherents. The main results of the study are the stress intensity factors, the strain energy release rates and, to a limited extent, the crack-opening displacements obtained as functions of the two primary variables h/a and* μ_3/μ_1 *under various loading conditions, where a is the radius of the crack. Some results are also presented for a penny-shaped crack in an unbounded nonhomogeneous medium.*

Introduction

In studying the fracture mechanics of bonded materials the structure and thickness of the interfacial zones seem to play an important role in determining the crack growth resistance parameters as well as the crack driving force. Very often, however, the interfacial zone is simply neglected and the medium is assumed to be piecewise homogeneous. Such a simplified model is generally adequate if the purpose is to evaluate, for example, the strain energy release rate (see, for example, Hutchinson, 1990). One could also model the interfacial zone as a thin layer of homogeneous continuum with thermomechanical properties different than that of the adherents (Erdogan and Gupta, 1971a, 1971b; Arin and Erdogan, 1971). A further simplification of this model is obtained by neglecting the thickness variation of stresses in the layer and by assuming that its tensile and shear deformations are uncoupled (Erdogan, 1972; Erdogan and Joseph, 1990; Gecit and Erdogan, 1978). On the other hand, recent studies indicate that in many cases the interfacial zone consists of a very thin layer with steeply varying composition profile and, hence, highly nonhomogeneous physical properties. This nonhomogeneous region may correspond to the chemical reaction or diffusion zone, or it may develop as a result of certain processing techniques such as ion plating, sputtering or plasma spray coating (Batakis and Vogan, 1985; Houck, 1987; Brennan, 1991; Shiau et al., 1988). The nonhomogeneous interfacial zone may also result from intentional grading of the material composition for the purpose of reducing the concentration of residual and thermal stresses and increasing the bonding strength (Kurihara et al., 1990; Kawasaki and Watanabe, 1990; Hirano et al., 1988; Hirano and Yamada, 1988; Chigasaki et al., 1990).

Fatigue and fracture analysis and characterization of bonded materials require the solution of certain standard crack problem. With the exception of torsion problem considered by Kassir (1972) and the axisymmetric mixed-mode problem studied by Ozturk and Erdogan (1993) in an unbounded medium, the existing solutions of the crack problems in nonhomogeneous materials have been obtained under the assumption of plane strain or antiplane shear loading (Gerasoulis and Srivastav, 1980; Delale and Erdogan, 1983, 1988a; Erdogan et al., 1991a, 1991b). In this paper we consider the axisymmetric crack problem for two dissimilar homogeneous materials bonded through a nonhomogeneous interfacial zone and subjected to "torsion" (Fig. 1). Some results for the simpler problem of infinite nonhomogeneous medium containing a penny-shaped crack under various mode III loading conditions are also given. It is assumed that the shear modulus μ_2 of the interfacial zone is a function z only and is approximated by $\mu_2 = \mu_1 \exp(\alpha z)$. The crack problems in nonhomogeneous materials do not appear to be analytically tractable for arbitrary variation of the elastic parameters λ and μ. Usually one tries to generate the forms of nonhomogeneities for which the problem becomes tractable. The actual material property distribution is then

Contributed by the Applied Mechanics Division of THE AMERICAN SOCIETY OF MECHANICAL ENGINEERS for publication in the ASME JOURNAL OF APPLIED MECHANICS.

Discussion on this paper should be addressed to the Technical Editor, Professor Lewis T. Wheeler, Department of Mechanical Engineering, University of Houston, Houston, TX 77204-4792, and will be accepted until four months after final publication of the paper itself in the ASME JOURNAL OF APPLIED MECHANICS.

Manuscript received by the ASME Applied Mechanics Division, Sept. 9, 1992; final revision, Oct. 28, 1993. Associate Technical Editor: C. F. Shih.

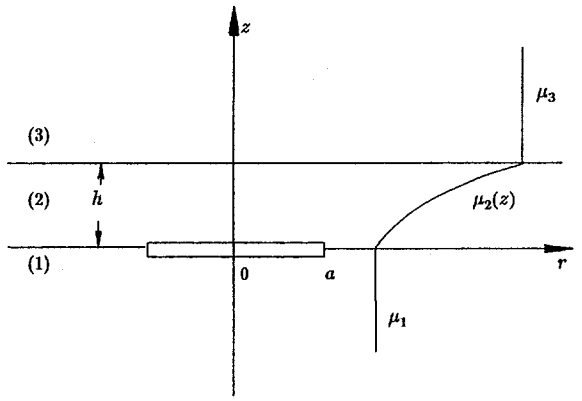

Fig. 1 The geometry of two dissimilar homogeneous materials bonded through a nonhomogeneous interfacial layer

approximated by one of these forms (Erdogan and Ozturk, 1992).

Formulation of the Nonhomogeneous Interfacial Zone Problem

Consider the axisymmetric crack problem for two dissimilar homogeneous half-spaces bonded through a nonhomogeneous interfacial zone described in Fig. 1. It is assumed that the radius of the crack and the thickness of the layer are small compared to the bulk dimensions of the medium, the geometry of the medium and the applied loads are axisymmetric, all applied loads act in the circumferential direction, and through a proper superposition the problem has been reduced to a perturbation problem in which the crack surface tractions are the only external loads. Thus, the displacement component $u_\theta = v$ and the stress components $\sigma_{\theta r}$ and $\sigma_{\theta z}$ are the only nonvanishing field quantities and the medium may be assumed to be unbounded.

By substituting from the constitutive relations

$$\sigma_{\theta z} = 2\mu\epsilon_{\theta z} = \mu\frac{\partial v}{\partial z}, \quad \sigma_{\theta r} = 2\mu\epsilon_{\theta r} = \mu\left[\frac{\partial v}{\partial r} - \frac{v}{r}\right], \quad (1)$$

into the equilibrium equation

$$\frac{\partial\sigma_{\theta r}}{\partial r} + \frac{\partial\sigma_{\theta z}}{\partial z} + \frac{2}{r}\sigma_{\theta r} = 0, \quad (2)$$

and assuming

$$\mu_1 = \text{constant}, \quad \mu_3 = \text{constant}, \quad \mu_2 = \mu_2(z) = \mu_1 e^{\alpha z}, \quad (3)$$

we find

$$\frac{\partial^2 v_i}{\partial r^2} + \frac{1}{r}\frac{\partial v_i}{\partial r} - \frac{v_i}{r^2} + \frac{\partial^2 v_i}{\partial z^2} = 0, \quad i = 1, 3, \quad (4)$$

$$\frac{\partial^2 v_2}{\partial r^2} + \frac{1}{r}\frac{\partial v_2}{\partial r} - \frac{v_2}{r^2} + \frac{\partial^2 v_2}{\partial z^2} + \alpha\frac{\partial v_2}{\partial z} = 0, \quad (5)$$

where subscripts $i = 1, 2, 3$ refer to the materials shown in Fig. 1 and the nonhomogeneity parameter α is given by

$$\alpha = \frac{1}{h}\ln(\mu_3/\mu_1). \quad (6)$$

Equations (4) and (5) are subject to

$$\sigma_{2\theta z}(r, h) = \sigma_{3\theta z}(r, h), \quad 0 \le r < \infty, \quad (7)$$

$$v_2(r, h) = v_3(r, h), \quad 0 \le r < \infty, \quad (8)$$

$$\sigma_{1\theta z}(r, 0) = \sigma_{2\theta z}(r, 0), \quad 0 < r < \infty, \quad (9)$$

$$\sigma_{1\theta z}(r, 0) = p(r), \quad 0 \le r < a,$$

$$v_2(r, +0) - v_1(r, -0) = 0, \quad r > a \quad (10a,b)$$

and the regularity conditions at $z = \mp\infty$. Thus, the displacements v_i, $(i = 1, 2, 3)$ may be expressed as

$$v_i(r, z) = \int_0^\infty F_i(z, \rho)J_1(r\rho)\rho d\rho, \quad i = 1, 2, 3 \quad (11)$$

where J_1 is the Bessel function of the first kind. From (4), (5), and (11) it follows that

$$\left[\frac{d^2}{dz^2} - \rho^2\right]F_i(z, \rho) = 0, \quad i = 1, 3,$$

$$\left[\frac{d^2}{dz^2} + \alpha\frac{d}{dz} - \rho^2\right]F_2(z, \rho) = 0. \quad (12a\text{–}c)$$

By making use of the regularity conditions at $|z| = \infty$, solutions of the differential Eqs. (12) may be expressed as

$$F_1(z, \rho) = A_1 e^{\rho z}, \quad z < 0, \quad (13)$$

$$F_2(z, \rho) = A_2 e^{m_1 z} + A_3 e^{m_2 z}, \quad 0 < z < h, \quad (14)$$

$$F_3(z, \rho) = A_4 e^{-\rho z}, \quad z > h \quad (15)$$

where

$$m_1 = -\frac{\alpha}{2} - \lambda, \quad m_2 = -\frac{\alpha}{2} + \lambda, \quad \lambda = \sqrt{\rho^2 + \alpha^2/4}. \quad (16)$$

By substituting from (13)–(15) and (11) into (1), the nonvanishing stress components are found to be

$$\sigma_{1\theta z}(r, z) = \mu_1\int_0^\infty A_1(\rho)\rho^2 e^{\rho z}J_1(r\rho)d\rho, \quad (17)$$

$$\sigma_{2\theta z}(r, z) = \mu_2(z)\int_0^\infty \sum_1^2 A_{k+1}(\rho)m_k e^{m_k z}J_1(r\rho)\rho d\rho, \quad (18)$$

$$\sigma_{3\theta z}(r, z) = -\mu_3\int_0^\infty A_4(\rho)\rho^2 e^{-\rho z}J_1(r\rho)d\rho, \quad (19)$$

$$\sigma_{1\theta r}(r, z) = \mu_1\int_0^\infty A_1(\rho)e^{\rho z}\rho\left[\rho J_0(r\rho) - \frac{2J_1(r\rho)}{r}\right]d\rho, \quad (20)$$

$$\sigma_{2\theta r}(r, z) = \mu_2(z)\int_0^\infty \sum_1^2 A_{k+1}(\rho)e^{m_k z}\rho \times\left[\rho J_0(r\rho) - \frac{2J_1(r\rho)}{r}\right]d\rho, \quad (21)$$

$$\sigma_{3\theta r}(r, z) = \mu_3\int_0^\infty A_4(\rho)e^{-\rho z}\rho\left[\rho J_0(r\rho) - \frac{2J_1(r\rho)}{r}\right]d\rho. \quad (22)$$

The unknown functions $A_1, \ldots, A_4$ are determined from the boundary and the continuity conditions (7)–(10). Substituting from the general solution given by (11) and (13)–(19) into the homogeneous conditions (7)–(9) we find

$$A_2 = \frac{1}{m_1 - m_2 E}(\rho A_1), \quad (23)$$

$$A_3 = -\frac{E}{m_1 - m_2 E}(\rho A_1) \quad (24)$$

$$A_4 = -\frac{m_1 e^{(m_1+\rho)h} - m_2 E e^{(m_2+\rho)h}}{\rho(m_1 - m_2 E)}(\rho A_1), \quad (25)$$

where

$$E = \frac{m_1 + \rho}{m_2 + \rho} e^{-2\lambda h}. \tag{26}$$

The remaining unknown A_1 may then be determined from the mixed boundary conditions (10).

Derivation of the Integral Equation

To reduce the mixed boundary conditions (10) to an integral equation we first define the following new unknown function

$$g(r) = \frac{1}{r}\frac{\partial}{\partial r}[rv_2(r, +0) - rv_1(r, -0)]. \tag{27}$$

From (10), (17), and (27) it can then be shown that

$$g(r) = \int_0^\infty \rho^2 A_1(\rho) H(\rho) J_0(r\rho) d\rho, \tag{28}$$

$$\sigma_{1\theta z}(r, 0) = \mu_1 \int_0^\infty \rho^2 A_1(\rho) J_1(r\rho) d\rho \tag{29}$$

where

$$H(\rho) = -\frac{2(\lambda + \rho \tanh(\lambda h))}{\lambda + \left(\rho + \frac{\alpha}{2}\right)\tanh(\lambda h)}. \tag{30}$$

From (28) and (10*b*) by observing that

$$A_1(\rho) = \frac{1}{\rho H(\rho)} \int_0^a g(s) J_0(s\rho) s ds, \tag{31}$$

and by using (29), Eq. (10*a*) may be expressed as

$$\int_0^a k(s, r) s g(s) ds = \frac{p(r)}{\mu_1}, \quad 0 < r < a \tag{32}$$

where

$$k(s, r) = \int_0^\infty \frac{\rho}{H(\rho)} J_0(s\rho) J_1(r\rho) d\rho. \tag{33}$$

To examine the singular behavior of the kernel $k(s, r)$ we first note that for $\rho \to \infty$, $\rho/H(\rho)$ has the following asymptotic form:

$$\frac{\rho}{H(\rho)} = -\frac{\rho}{2} + \frac{\alpha}{4} + \frac{\alpha^3}{64}\rho^{-2} + O(\rho^{-4}). \tag{34}$$

Equation (32) may then be expressed as

$$\int_0^a [-R_0(s, r) + R_1(s, r)] g(s) s ds = \frac{2p(r)}{\mu_1}, \quad 0 < r < a, \tag{35}$$

$$R_0(s, r) = \int_0^\infty J_0(s\rho) J_1(r\rho) \rho d\rho$$

$$= -\frac{2}{\pi}\begin{cases} \frac{1}{s^2 - r^2} E\left(\frac{s}{r}\right), & s < r \\ \frac{s}{r}\frac{1}{s^2 - r^2} E\left(\frac{r}{s}\right) - \frac{1}{rs} K\left(\frac{r}{s}\right), & s > r \end{cases} \tag{36}$$

$$R_1(s, r) = \int_0^\infty \left(\frac{2}{H(\rho)} + 1\right) \rho J_0(s\rho) J_1(r\rho) d\rho, \tag{37}$$

and K and E are complete elliptic integrals of first and second kind, respectively.

Further, by examining the singular behavior of R_0 we find

$$-sR_0(s, r) = \frac{1}{\pi}\left[\frac{1}{s - r} - \frac{1}{s + r} + \frac{1}{2r}\ln|s - r| + M_1(s, r)\right], \tag{38}$$

$$M_1(s, r) = \frac{M_2(s, r) - 1}{s - r} - \frac{M_2(s, r) - 1}{s + r} - \frac{1}{2r}\ln|s - r|, \tag{39}$$

$$M_2(s, r) = \begin{cases} \frac{s}{r} E\left(\frac{s}{r}\right), & s < r \\ \frac{s^2}{r^2} E\left(\frac{r}{s}\right) - \frac{s^2 - r^2}{r^2} K\left(\frac{r}{s}\right), & s > r. \end{cases} \tag{40}$$

The logarithmic singularity in (38) follows from

$$K(\lambda) \to \ln\left(4/\sqrt{1 - \lambda^2}\right) \quad \text{for} \quad \lambda \to 1$$

which leads to

$$\frac{M_2(s, r) - 1}{s - r} \to -\frac{1}{2r}\ln|s - r| \quad \text{for} \quad s \to r. \tag{42}$$

Similarly, the convergence of R_1 may be improved considerably by evaluating its leading term for $\rho \to \infty$ in closed form. Thus, from (34) and (37) it can be shown that

$$R_1(s, r) = \int_0^\infty \left[\frac{2\rho}{H(\rho)} + \rho + \frac{\alpha}{2}\right] J_0(s\rho) J_1(r\rho) d\rho$$

$$- \frac{\alpha}{2}\int_0^\infty J_0(s\rho) J_1(r\rho) d\rho \tag{43}$$

$$\int_0^\infty J_0(s\rho) J_1(r\rho) d\rho = \begin{cases} \frac{1}{r}, & s < r \\ 0, & s > r. \end{cases} \tag{44}$$

Collecting now the square integrable kernels, from (35) and (38) we obtain

$$\frac{1}{\pi}\int_0^a \left[\frac{1}{s - r} - \frac{1}{s + r} + k_1(s, r)\right] g(s) ds$$

$$= \frac{2}{\mu_1} p(r), \quad 0 < r < a, \tag{45}$$

where the kernel k_1 is a known function (see (35), (38), and (43)).

Physically since $(rv_2^+ - rv_1^-)$ is zero at $r = 0$ and $r > a$, from (27) it follows that the unknown function g must satisfy the following condition:

$$\int_0^a rg(r) dr = 0. \tag{46}$$

Also, since $(s + r) \to 0$ as s and r approach the end point $r = 0$ simultaneously, (45) has a generalized Cauchy kernel in the sense that the kernels $1/(s + r)$ as well as $1/(s - r)$ contribute to the singular nature of $g(s)$ at $s = 0$ (Erdogan, 1978). Therefore, expressing $g(s)$ by

$$g(s) = \frac{h(s)}{s^\beta (a - s)^\gamma}, \quad 0 < s < a, \tag{47}$$

and using a function theoretic method, from (45) and (47) the characteristic equations giving γ and β may be obtained as

$$\cot \pi\gamma = 0, \quad \cos \pi\beta = 1. \tag{48a,b}$$

In (47), $h(s)$ is bounded in $0 \le s \le a$ and nonzero at $s = 0$ and $s = a$. The admissible root of (48a) is $\gamma = \frac{1}{2}$. Since in the "torsion" problem under consideration we must have $v_2(0, z) = 0$, $z \ge 0$, $v_1(0, z) = 0$, $z \le 0$, from (48b) it follows that $\beta = 0$, giving

$$g(s) = \frac{h(s)}{\sqrt{a - s}}, \quad 0 < s < a,$$

$$v_2(r, +0) - v_1(r, -0) \simeq \frac{h(0)}{2\sqrt{a}} r, \quad r \ll a. \tag{49a,b}$$

The Infinite Nonhomogeneous Medium

Consider now the infinite nonhomogeneous medium which has a shear modulus $\mu(z) = \mu_0 \exp(\alpha z)$, contains a penny-shaped crack of radius a at $z = 0$, and is subjected to the external load

$$\sigma_{\theta z}(r, 0) = p(r), \quad 0 \le r < a. \tag{50}$$

From (11), (12c), (14), and (16) it may be seen that

$$v(r, z) = \begin{cases} \int_0^\infty A(\rho) e^{m_1 z} J_1(r\rho) \rho d\rho, & z > 0, \\ \int_0^\infty B(\rho) e^{m_2 z} J_1(r\rho) \rho d\rho, & z < 0. \end{cases} \tag{51}$$

Now, by using the condition

$$\sigma_{\theta z}(r, +0) = \sigma_{\theta z}(r, -0) \tag{52}$$

we find

$$A(\rho) = \frac{m_2^2}{\rho^2} B(\rho). \tag{53}$$

Also, by defining the unknown function

$$g(r) = \frac{1}{r} \frac{\partial}{\partial r} [rv(r, +0) - rv(r, -0)], \tag{54}$$

and by using the following mixed boundary conditions

$$\sigma_{\theta z}(r, 0) = p(r), \quad 0 \le r < a,$$
$$v(r, +0) - v(r, -0) = 0, \quad r > a, \tag{55}$$

we obtain

$$\int_0^a k(s, r) g(s) s ds = \frac{p(r)}{\mu_0}, \quad 0 < r < a, \tag{56}$$

$$k(s, r) = -\int_0^\infty \frac{\rho^2}{2\lambda} J_0(s\rho) J_1(r\rho) d\rho \tag{57}$$

where λ is given by (16).

By observing that for large values of ρ

$$\frac{\rho^2}{2\lambda} = \frac{\rho}{2} + \frac{\alpha^2}{8} \rho^{-1} + O(\rho^{-3}), \tag{58}$$

from (56)–(58) we find

$$\int_0^a [-R_0(s, r) - R_2(s, r)] s g(s) ds = \frac{2p(r)}{\mu_0}, \quad 0 < r < a, \tag{59}$$

where

$$R_2(s, r) = \int_0^\infty \left[\frac{\rho^2}{\lambda} - \rho - \frac{\alpha^2}{4\rho} \right] J_0(s\rho) J_1(r\rho) d\rho + \frac{\alpha^2}{4} \int_0^\infty \frac{J_0(s\rho) J_1(r\rho)}{\rho} d\rho, \tag{60}$$

$$\int_0^\infty \frac{J_0(s\rho) J_1(r\rho)}{\rho} d\rho = \frac{2}{\pi} \begin{cases} E\left(\frac{s}{r}\right), & s < r \\ \frac{s}{r} E\left(\frac{r}{s}\right) - \frac{s^2 - r^2}{rs} K\left(\frac{r}{s}\right), & s > r, \end{cases} \tag{61}$$

and $R_0(s, r)$ is given by (36) or (38)–(40).

It is seen that the dominant parts of the integral Eqs. (45) and (59) are identical. Therefore, the solution of (59) too would have the form given by (49). Also, it is clear that in this problem too the unknown function g must satisfy the single-valuedness condition (46).

The Solution

Equations (45) and (59) may be solved after normalizing the interval by defining $y = (2s/a) - 1$ and by observing that the orthogonal polynomials associated with the weight function $w(y) = 1/(1 - y)^{1/2}$ of the integral equations are the Jacobi polynomials $P_n^{(-1/2, 0)}(y)$. Thus, expressing

$$g(s) = \phi(y) \simeq \frac{1}{\sqrt{1 - y}} \sum_0^N A_n P_n^{(-1/2, 0)}(y), \tag{62}$$

the integral equations may be regularized by using the properties of Jacobi polynomials and the unknown coefficients A_n may be determined by collocation (Mahajan, 1992). In this study, however, the somewhat more direct method described by Ozturk and Erdogan (1993) is used to solve (45) and (59). The unknown function is defined by

$$\frac{\mu_1}{2} g(as') = \frac{1}{\sqrt{s'(1 - s')}} \sum_0^\infty B_j T_j(2s' - 1), \quad s' = s/a \tag{63}$$

where $T_j(x)$ is the Chebyshev polynomial of the first kind.

From (63), (49), and (46) it follows that

$$\sum_0^\infty (-1)^j B_j = 0, \quad B_0 + \frac{1}{2} B_1 = 0. \tag{64}$$

The remaining unknowns are then determined by truncating the series and by using a simple collocation technique. The following relations are used to remove the singularities of the

integral equations and to calculate the stress intensity factor:

$$\frac{1}{2\pi}\int_0^1 \frac{T_j(2s'-1)}{(s'-r')\sqrt{s'(1-s')}}ds' = \begin{cases} U_{j-1}(2r'-1), & 0<r'<1, \quad r'=r/a, \\ -\dfrac{\left(x-\sqrt{x^2-1}\right)^j}{\sqrt{x^2-1}}, & x=2r'-1>1, \end{cases} \tag{65}$$

$$\frac{1}{\pi}\int_0^1 \ln|s'-r'|\frac{T_j(2s'-1)}{\sqrt{s'(1-s')}}ds' = \begin{cases} -2\ln 2, & j=0, \\ -\dfrac{1}{j}T_j(2r'-1), & j\geq 1. \end{cases} \tag{66}$$

After determining the constants B_j, by observing that in (45) the left-hand side of the integral equation represents $\sigma_{1\theta z}(r,0)$ outside as well as within the cut $(0,a)$, the mode III stress intensity factor may be defined and evaluated as follows:

$$k_3 = \lim_{r\to a}\sqrt{2(r-a)}\,\sigma_{1\theta z}(r,0) = -\sqrt{2a}\sum_0^\infty B_n. \tag{67}$$

Also, from (27) and (63) the crack-opening displacement may be determined as

$$r[v_2(r,+0)-v_1(r,-0)] = -\int_r^a sg(s)ds = -\frac{2a^2}{\mu_1}\left\{B_1\left(\frac{1}{4}\sin 2\phi+\frac{1}{8}\sin 4\phi\right) + \sum_2^\infty B_n\left[\frac{1}{2n}\sin 2n\phi+\frac{1}{4n+4}\sin(2n+2)\phi + \frac{1}{4n-4}\sin(2n-2)\phi\right]\right\} \tag{68}$$

where

$$\cos^2\phi = \frac{r}{a}, \quad 0\leq r<a. \tag{69}$$

It should be observed that $v_2(r,+0)-v_1(r,-0)$ vanishes for $r\to 0$. This may be seen from (27), (46), and (63) as follows:

$$\lim_{r\to 0}[v_2(r,+0)-v_1(r,-0)] = -\lim_{r\to 0}\frac{1}{r}\int_r^a sg(s)ds = -\lim_{r\to 0}\frac{d}{dr}\int_r^a sg(s)ds = \lim_{r\to 0} rg(r) = 0. \tag{70}$$

After determining the crack-opening displacement and the corresponding stress component $\sigma_{1\theta z}(r,0)$, $r>a$, the strain energy release rate may be obtained from

$$\mathcal{G}da = \int_a^{a+da}\frac{1}{2}\sigma_{1\theta z}(r,0)[v_2(r-da,+0)-v_1(r-da,-0)]dr. \tag{71}$$

Thus, using the asymptotic relations

$$\sigma_{1\theta z}\simeq\frac{k_3(a)}{\sqrt{2(r-a)}},$$

$$v_2(r,+0)-v_1(r,-0) = \frac{k_3}{\bar{\mu}}\sqrt{2(a-r)}, \tag{72}$$

we find

$$\mathcal{G} = \frac{\pi}{4}\frac{k_3^2}{\bar{\mu}}. \tag{73}$$

In (72), $\bar{\mu}$ is the stiffness coefficient that relates the displacement derivative to the stress in the dominant part of the singular integral equation, which usually has the form

$$\frac{1}{\pi}\int_0^a\left(\frac{1}{s-r}+K(r,s)\right)g(s)ds = p(r)/\bar{\mu}, \quad 0<r<a. \tag{74}$$

From (45) it may be seen that in the problem under consideration $\bar{\mu}=\mu_1/2$ giving

$$\mathcal{G} = \frac{\pi}{2}\frac{k_3^2}{\mu_1}. \tag{75}$$

Note that Eqs. (67), (68), and (73) are equally valid for the special case of nonhomogeneous infinite medium described in the previous section.

The Limiting Cases

Referring to Fig. 1 and (6), for $h\to 0$ or $\alpha\to\infty$ the problem would reduce to that of two bonded homogeneous materials with shear moduli μ_1 and μ_3 containing an axisymmetric interface crack. In this case from (16), (30), and (33)

Table 1 The stress intensity factors in an infinite nonhomogeneous medium containing a penny-shaped crack; $\mu(z)=\mu_0\exp(\alpha z)$. (See Eq. (81) for loading conditions.)

αa	$\frac{k_3}{p_0\sqrt{a}}$	$\frac{k_3}{p_1\sqrt{a}}$	$\frac{k_3}{p_2\sqrt{a}}$
0.0	0.5	0.4244	0.3750
0.1	0.5000	0.4244	0.3750
0.2	0.5002	0.4245	0.3751
0.4	0.5008	0.4249	0.3754
0.6	0.5018	0.4256	0.3759
0.8	0.5032	0.4266	0.3766
1.0	0.5049	0.4277	0.3775
1.5	0.5105	0.4316	0.3803
2.0	0.5177	0.4365	0.3839
2.5	0.5262	0.4424	0.3883
3.0	0.5356	0.4489	0.3931
3.5	0.5457	0.4558	0.3982
4.0	0.5564	0.4632	0.4037

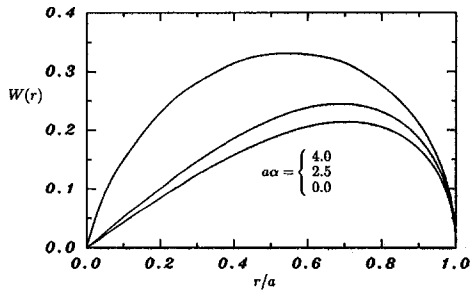

Fig. 2 The normalized crack-opening displacement, in an infinite nonhomogeneous medium; $W(r)=(v(r,+0)-v(r,-0))/v_1$, $v_1=ap_1/\mu_0$, $\sigma_{\theta z}=-p_1 r/a$

for $\alpha \to \infty$ or $h \to 0$ it can be shown that

$$\lambda h = \frac{\alpha h}{2}\left[1 + \left(\frac{2\rho}{\alpha}\right)^2\right]^{1/2} = \frac{1}{2}\left[1 + \left(\frac{2\rho}{\alpha}\right)^2\right]^{1/2} \ln\left(\frac{\mu_3}{\mu_1}\right),$$

$$\tanh(\lambda h) \simeq \tanh\left[\frac{1}{2}\ln\left(\frac{\mu_3}{\mu_1}\right)\right] = \frac{\mu_3 - \mu_1}{\mu_3 + \mu_1},$$

$$H(\rho) \to -\frac{\mu_3 + \mu_1}{\mu_3},$$

$$k(s,r) \to -\frac{\mu_3}{\mu_1 + \mu_3}\int_0^\infty \rho J_0(s\rho) J_1(r\rho) d\rho$$

$$= -\frac{\mu_3}{\mu_1 + \mu_3} R_0(s,r), \quad (76a\text{–}d)$$

and the integral Eq. (35) becomes

$$\int_0^a R_0(s,r) g(s) s ds = -\frac{p(r)}{\mu^*}, \quad \mu^* = \frac{\mu_1 \mu_3}{\mu_1 + \mu_3}, \quad 0 < r < a \tag{77}$$

where R_0 is given by (36). Equation (77) is the integral equation for two dissimilar bonded half-spaces.

In the other limiting case of $h \to \infty$ or $\alpha \to 0$ it may easily be shown that $H(\rho) \to -2$ and (32) become

$$\int_0^a R_0(s,r) g(s) s ds = -\frac{p(r)}{\mu_1/2}, \quad 0 < r < a, \tag{78}$$

which is the integral equation for a homogeneous medium containing a penny-shaped crack. From (74), (77), and (78) it is seen that (77) and (78) are identical except for the stiffness $\bar{\mu}$ which is μ^* in (77) and $\mu_1/2$ in (78). Thus, for crack surface tractions $-p_0$, $-p_1(r/a)$ and $p_2(r/a)^2$, the stress intensity factors and strain energy release rates for these two problems may be evaluated as follows:

$$k_3 = \left(\frac{1}{2}p_0\sqrt{a}, \quad \frac{4}{3\pi}p_1\sqrt{a}, \quad \frac{3}{8}p_2\sqrt{a}\right), \tag{79}$$

$$\mathcal{G} = \frac{\pi}{4\bar{\mu}}k_3^2 = \left(\frac{\pi}{16\bar{\mu}}p_0^2 a, \quad \frac{4}{9\pi\bar{\mu}}p_1^2 a, \quad \frac{9\pi}{256\bar{\mu}}p_2^2 a\right), \tag{80}$$

where $\bar{\mu} = \mu^* = \mu_1\mu_3/(\mu_1 + \mu_3)$ for $h = 0$ (or $\alpha = \infty$) and $\bar{\mu} = \mu_1/2$ for $h = \infty$ (or $\alpha = 0$).

Table 2 Stress intensity factors and strain energy release rates in bonded dissimilar materials with a nonhomogeneous interfacial zone (Fig. 1); $\mathcal{G}_l = \pi p_l^2 a / (2\mu_1)$, $l = 0, 1, 2$, $\mu_3 < \mu_1$, p_0, p_1, p_2 are given by (81)

$\mu_3/\mu_1 = 1/22$						
h/a	$\frac{k_3}{p_0\sqrt{a}}$	$\frac{k_3}{p_1\sqrt{a}}$	$\frac{k_3}{p_2\sqrt{a}}$	$\frac{\mathcal{G}}{\mathcal{G}_0}$	$\frac{\mathcal{G}}{\mathcal{G}_1}$	$\frac{\mathcal{G}}{\mathcal{G}_2}$
0.0	1.6956	1.4392	1.2717	2.875	2.0713	1.6172
0.1	1.019	0.808	0.673	1.039	0.653	0.453
0.2	0.835	0.672	0.465	0.697	0.451	0.319
0.4	0.698	0.566	0.484	0.488	0.320	0.234
0.6	0.636	0.522	0.449	0.404	0.273	0.202
0.8	0.603	0.498	0.432	0.363	0.248	0.186
1.0	0.582	0.483	0.420	0.339	0.233	0.177
1.5	0.554	0.463	0.405	0.307	0.214	0.164
2.0	0.539	0.453	0.397	0.291	0.205	0.158
2.5	0.532	0.447	0.393	0.283	0.199	0.154
3.0	0.526	0.443	0.389	0.277	0.196	0.152
∞	0.5	0.4244	0.3750	0.25	0.1801	0.1406

$\mu_3/\mu_1 = 1/3$						
h/a	$\frac{k_3}{p_0\sqrt{a}}$	$\frac{k_3}{p_1\sqrt{a}}$	$\frac{k_3}{p_2\sqrt{a}}$	$\frac{\mathcal{G}}{\mathcal{G}_0}$	$\frac{\mathcal{G}}{\mathcal{G}_1}$	$\frac{\mathcal{G}}{\mathcal{G}_2}$
0.0	0.7071	0.6002	0.5303	0.5	0.3602	0.2813
0.1	0.640	0.531	0.459	0.409	0.282	0.211
0.2	0.601	0.499	0.434	0.361	0.249	0.188
0.4	0.563	0.470	0.410	0.317	0.221	0.168
0.6	0.545	0.457	0.399	0.297	0.208	0.159
0.8	0.534	0.449	0.394	0.285	0.202	0.155
1.0	0.527	0.444	0.390	0.278	0.197	0.152
1.5	0.518	0.437	0.385	0.268	0.191	0.148
2.0	0.514	0.434	0.383	0.264	0.188	0.146
2.5	0.511	0.432	0.381	0.261	0.187	0.145
3.0	0.509	0.431	0.380	0.259	0.186	0.144
∞	0.5	0.4244	0.3750	0.25	0.1801	0.1406

The Results and Discussion

The main results of this study are the stress intensity factors calculated for crack surface tractions

$$\sigma_{1\theta z}(r,0) = \sigma_{2\theta z}(r,0) = \left(-p_0, -p_1(r/a), -p_2(r/a)^2\right), \quad 0 < r < a. \quad (81)$$

The variables in the problem are αa for the infinite nonhomogeneous medium and h/a and μ_3/μ_1 for the two dissimilar materials bonded through a nonhomogeneous interfacial zone (Fig. 1). In the latter case αa, h/a and μ_3/μ_1, are related by (6). For reference the stress intensity factors and strain energy release rates in a homogeneous medium, having shear modulus μ_1 and subjected to the external loads (81), are given by (79) and (80) (with $\overline{\mu} = \mu_1/2$).

Table 1 shows the stress intensity factors for a penny-shaped crack of radius a in an infinite nonhomogeneous medium with a shear modulus $\mu(z) = \mu_0 \exp(\alpha z)$. The results given for $\alpha a = 0$, i.e., for the corresponding homogeneous medium, are obtained from (79). It may be seen that for all loading conditions the stress intensity factor increases slightly and monotonically with the increasing value of the nonhomogeneity parameter αa. One would then expect the crack-opening displacement (COD) too would increase the increasing αa. This may indeed be seen from Fig. 2 where for the external load $-p_1(r/a)$ the dimensionless COD defined by

$$W(r) = \frac{1}{v_1}(v(r,+0) - v(r,-0)), \quad v_1 = ap_1/\mu_1 \quad (82)$$

is shown for various values of αa.

The results for the dissimilar homogeneous materials bonded through a nonhomogeneous interfacial zone (Fig. 1) are given in Tables 2–4 and Figs. 3–5. For the loading conditions (81) the tables show the normalized stress intensity factors and the strain energy release rates as functions of h/a and μ_3/μ_1 (Fig. 1). In Tables 2 and 3 the results given for $h/a = \infty$ correspond to an infinite homogeneous medium having the shear modulus μ_1 and are obtained from (79) and (80) (with $\overline{\mu} = \mu_1/2$). For $\mu_3 < \mu_1$, since the overall stiffness of the half-space $z > 0$ increases with increasing h/a, as expected, k_3 and $\mathcal{G}$ are seen to decrease monotonically as h/a increases (Table 2). The opposite effect is expected for $\mu_3 > \mu_1$ and is observed in Table 3. For $h/a \to 0$, the problem shown in Fig. 1 reduces to that of two bonded dissimilar materials the solution of which is given by (79) and (80) with $\overline{\mu} = \mu^* = \mu_1\mu_3/(\mu_1 + \mu_3)$. The strain energy release rates, $\mathcal{G}/\mathcal{G}_i$, $i = 0, 1, 2$, shown in Tables 2 and 3 for $h/a = 0$ are obtained from (80) and are seen to be continuous smooth limits of the values obtained from (71) and (75) for $(h/a) > 0$.

Table 3 Stress intensity factors and strain energy release rates in bonded dissimilar materials with a nonhomogeneous interfacial zone (Fig. 1); $\mathcal{G}_i = \pi p_i^2 a / (2\mu_1)$, $i = 0, 1, 2$, $\mu_3 > \mu_1$

$\mu_3/\mu_1 = 22$						
h/a	$\frac{k_3}{p_0\sqrt{a}}$	$\frac{k_3}{p_1\sqrt{a}}$	$\frac{k_3}{p_2\sqrt{a}}$	$\frac{\mathcal{G}}{\mathcal{G}_0}$	$\frac{\mathcal{G}}{\mathcal{G}_1}$	$\frac{\mathcal{G}}{\mathcal{G}_2}$
0.0	0.3615	0.3068	0.2711	0.1307	0.0942	0.0735
0.1	0.369	0.319	0.286	0.136	0.102	0.082
0.2	0.384	0.335	0.301	0.148	0.112	0.091
0.4	0.407	0.355	0.319	0.166	0.126	0.102
0.6	0.423	0.368	0.329	0.179	0.135	0.109
0.8	0.435	0.375	0.337	0.189	0.141	0.114
1.0	0.445	0.383	0.343	0.197	0.146	0.118
1.5	0.458	0.394	0.351	0.210	0.155	0.123
2.0	0.467	0.401	0.356	0.218	0.160	0.127
2.5	0.473	0.405	0.359	0.224	0.164	0.129
3.0	0.477	0.408	0.362	0.228	0.166	0.131
∞	0.5	0.4244	0.3750	0.25	0.1801	0.1406

$\mu_3/\mu_1 = 3$						
h/a	$\frac{k_3}{p_0\sqrt{a}}$	$\frac{k_3}{p_1\sqrt{a}}$	$\frac{k_3}{p_2\sqrt{a}}$	$\frac{\mathcal{G}}{\mathcal{G}_0}$	$\frac{\mathcal{G}}{\mathcal{G}_1}$	$\frac{\mathcal{G}}{\mathcal{G}_2}$
0.0	0.4082	0.3465	0.3062	0.1667	0.1201	0.0938
0.1	0.422	0.364	0.325	0.178	0.133	0.106
0.2	0.436	0.376	0.336	0.189	0.142	0.113
0.4	0.453	0.389	0.348	0.206	0.152	0.121
0.6	0.464	0.398	0.354	0.215	0.158	0.125
0.8	0.471	0.403	0.358	0.222	0.163	0.128
1.0	0.476	0.407	0.361	0.227	0.166	0.131
1.5	0.484	0.412	0.366	0.234	0.170	0.134
2.0	0.487	0.415	0.368	0.238	0.172	0.135
2.5	0.489	0.417	0.369	0.240	0.174	0.136
3.0	0.492	0.418	0.370	0.242	0.175	0.137
∞	0.5	0.4244	0.3750	0.25	0.1801	0.1406

Table 4 The variation of stress intensity factors and strain energy release rates with μ_3/μ_1 for various loading conditions and thickness ratios h/a; $\mathcal{G}_l = \pi p_l^2 a/(2\mu_1)$, $l = 0, 1, 2$.

$h/a = 0.1$						
μ_3/μ_1	$\frac{k_3}{p_0\sqrt{a}}$	$\frac{k_3}{p_1\sqrt{a}}$	$\frac{k_3}{p_2\sqrt{a}}$	$\frac{\mathcal{G}}{\mathcal{G}_0}$	$\frac{\mathcal{G}}{\mathcal{G}_1}$	$\frac{\mathcal{G}}{\mathcal{G}_2}$
0.1	0.860	0.694	0.589	0.740	0.481	0.347
0.2	0.723	0.595	0.509	0.522	0.354	0.259
0.4	0.611	0.509	0.443	0.373	0.259	0.196
0.6	0.556	0.467	0.409	0.309	0.218	0.168
0.8	0.523	0.442	0.389	0.273	0.195	0.152
1.0	0.5	0.4244	0.3750	0.25	0.1801	0.1406
1.5	0.465	0.396	0.353	0.216	0.157	0.125
2.0	0.445	0.382	0.340	0.198	0.146	0.116
2.5	0.433	0.371	0.331	0.187	0.138	0.109
3.0	0.423	0.364	0.325	0.179	0.132	0.106

$h/a = 0.5$						
μ_3/μ_1	$\frac{k_3}{p_0\sqrt{a}}$	$\frac{k_3}{p_1\sqrt{a}}$	$\frac{k_3}{p_2\sqrt{a}}$	$\frac{\mathcal{G}}{\mathcal{G}_0}$	$\frac{\mathcal{G}}{\mathcal{G}_1}$	$\frac{\mathcal{G}}{\mathcal{G}_2}$
0.1	0.618	0.509	0.440	0.382	0.259	0.193
0.2	0.580	0.482	0.419	0.336	0.232	0.176
0.4	0.543	0.455	0.399	0.295	0.207	0.159
0.6	0.523	0.441	0.388	0.274	0.194	0.151
0.8	0.510	0.432	0.381	0.260	0.187	0.145
1.0	0.5	0.4244	0.3750	0.25	0.1801	0.1406
1.5	0.484	0.412	0.366	0.234	0.170	0.134
2.0	0.473	0.405	0.359	0.224	0.164	0.129
2.5	0.465	0.399	0.355	0.217	0.159	0.126
3.0	0.459	0.395	0.352	0.211	0.156	0.124

$h/a = 2.0$						
μ_3/μ_1	$\frac{k_3}{p_0\sqrt{a}}$	$\frac{k_3}{p_1\sqrt{a}}$	$\frac{k_3}{p_2\sqrt{a}}$	$\frac{\mathcal{G}}{\mathcal{G}_0}$	$\frac{\mathcal{G}}{\mathcal{G}_1}$	$\frac{\mathcal{G}}{\mathcal{G}_2}$
0.1	0.529	0.445	0.391	0.278	0.198	0.153
0.2	0.520	0.439	0.386	0.270	0.193	0.149
0.4	0.511	0.432	0.381	0.261	0.187	0.145
0.6	0.506	0.429	0.378	0.256	0.184	0.143
0.8	0.503	0.426	0.376	0.252	0.182	0.142
1.0	0.5	0.4244	0.3750	0.25	0.1801	0.1406
1.5	0.495	0.421	0.372	0.245	0.177	0.139
2.0	0.492	0.419	0.371	0.242	0.175	0.137
2.5	0.489	0.417	0.369	0.239	0.174	0.136
3.0	0.487	0.415	0.368	0.238	0.173	0.135

This is the expected results. However, there seems to be somewhat of a paradox regarding the limit of k_3 as h/a approaches zero. The values of k_3 for $h/a = 0$ are given by (79) and clearly do not agree with the trends seen in the tables.[1] In this case the physical quantity which is expected to and does remain continuous in limit is the strain energy release rate $\mathcal{G}$. For $h > 0$, $\mathcal{G}$ is related to k_3 through (75). Thus, observing that $\bar{\mu} = \mu^* = \mu_1\mu_3/(\mu_1 + \mu_3)$, for example, for the external loading p_0, from (75) and (80) we find

$$\lim_{h\to 0} \mathcal{G}(h) = \frac{\pi(\mu_1 + \mu_3)}{16\mu_1\mu_3} p_0^2 a = \frac{\pi}{2\mu_1} \lim_{h\to 0} k_3^2(h) \quad (83)$$

giving

[1] As observed by the reviewer, this discrepancy may further be clarified by invoking the path independence of the J integral.

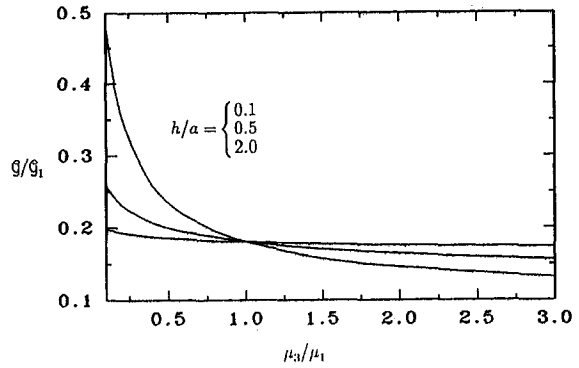

Fig. 3 Strain energy release rate as a function of the stiffness ratio, for $\sigma_{1\theta z} = -p_1 r/a$, $\mathcal{G}_1 = \pi p_1^2 a/(2\mu_1)$

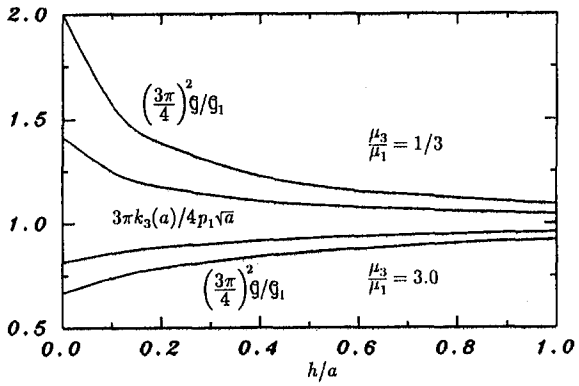

Fig. 4 Stress intensity factor and strain energy release rate as a function of the thickness to ratio h/a, $\mathcal{G}_1 = \pi p_1^2 a/(2\mu_1)$, $\sigma_{1\theta z}(r, 0) = -p_1 r/a$

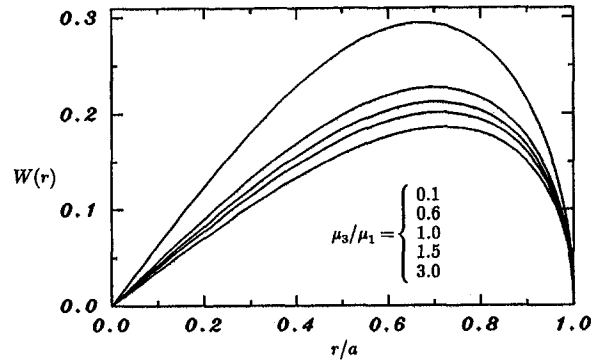

Fig. 5 The normalized crack-opening displacement, $W(r) = (v_2(r, +0) - v_1(r, -0))/v_1$, $v_1 = ap_1/\mu_1$ for the external load $\sigma_{1\theta z} = -p_1 r/a$, $h/a = 0.5$

$$\lim_{h \to 0} k_3(h) = \frac{1}{2}\sqrt{\frac{\mu_1 + \mu_3}{2\mu_3}}\, p_0\sqrt{a}\,. \tag{84}$$

Similarly, for the external loads $-p_1(r/a)$ and $-p_2(r/a)^2$ we obtain

$$\lim_{h \to 0} k_3(h) = \frac{4}{3\pi}\sqrt{\frac{\mu_1 + \mu_3}{2\mu_3}}\, p_1\sqrt{a}\,, \tag{85}$$

$$\lim_{h \to 0} k_3(h) = \frac{3}{8}\sqrt{\frac{\mu_1 + \mu_3}{2\mu_3}}\, p_2\sqrt{a}\,. \tag{86}$$

Thus, it may easily be observed that the limits of k_3 given in Tables 2 and 3 and Fig. 4 for $h \to 0$ correspond to the values calculated from (84)–(86).

One may note that for $\mu_3 \to \infty$ and $h \to 0$ the problem becomes one of an elastic medium bonded to a rigid half-space containing a penny-shaped interface crack. In this case the strain energy release rate would be one half of that of the corresponding homogeneous infinite medium given by (80) with $\bar{\mu} = \mu_1/2$ or by the last lines in Tables 2 and 3. The $\mathcal{G}$ values given in Table 3 clearly show this trend.

Table 4 gives the variation of stress intensity factors and the strain energy release rates with the stiffness ratio μ_3/μ_1 for some fixed values of h/a. The table shows the expected trends, namely that k_3 and $\mathcal{G}$ are monotonically decreasing functions of μ_3/μ_1. The dependence of $\mathcal{G}$ on μ_3/μ_1 is also shown in Fig. 3. It is seen that $\mathcal{G}$ becomes much more sensitive to the variations in μ_3/μ_1 for smaller values of h/a and this dependence becomes much more significant as μ_3/μ_1 decreases.

Figure 4 shows the thickness dependence of $\mathcal{G}$ and k_3 normalized with respect to the homogeneous medium results given by (79) and (80) (with $\bar{\mu} = \mu_1/2$). It may again be seen that the variation in k_3 and $\mathcal{G}$ becomes increasingly significant for $\mu_3 < \mu_1$ and as h/a tends to zero. Some sample results for the normalized crack-opening displacement (Fig. 1) defined by

$$W(r) = \frac{1}{v_1}\left[v_2(r, +0) - v_1(r, -0)\right], \quad v_1 = ap_1/\mu_1 \tag{89}$$

are given in Fig. 5. The external load in the examples considered in Figs. 4 and 5 is "pure torsion." The results given in Tables 2–4 and Figs. 3 and 4 generally indicate that extreme care may be needed in using any stress-based theory and in interpreting the experimental results with the energy based theories in studying the interfacial fracture of bonded materials, particularly if $h/a \neq 0$. The stress intensity factor k_3 (calculated as a function of h/a) has validity only in the "near-field" $0 < r < r_1$, $r \ll h$, $r_1 \ll a$. k_3 calculated by assuming $h/a = 0$ may have a region of approximate validity $r_2 < r < r_3$, only for $(h, r_2, r_3) \ll a$ and $r_2 \gg h$. $\mathcal{G}$, on the other hand, is a far more physically meaningful quantity but could be highly dependent on the properties and the thickness of the interfacial zone.

The results given in the Tables may be used to obtain the solution for arbitrary external loads provided the crack surface tractions in the corresponding perturbation problem can be approximated by a second degree polynomial.

Acknowledgments

This research was supported by the National Science Foundation under the Grant MSS-9114439.

References

Arin, K., and Erdogan, F., 1971, "Penny-Shaped Crack in an Elastic Layer Bonded to Dissimilar Half Spaces," *Int. J. Engng. Sci.*, Vol. 9, pp. 213–232.

Batakis, A. P., and Vogan, J. M., 1985, "Rocket Thrust Chamber Thermal Barrier Coating," NASA CR-1750222.

Brennan, J. J., 1991, "Interfacial Studies of Refractory Glass-Ceramic Matrix/Advanced SiC Fiber Reinforced Composites," Annual Report, ONR Contract N00014-87-C-0699, UTRC, Apr.

Chigasaki, M., Kojima, Y., and Nakashima, S., and Fukaya, Y., 1990, "Partially Stabilized ZrO_2 and Cu FGM Prepared by Dynamic Ion Mixing Process," *FGM '90*, Proc. of the First Int. Symp. on Functionally Gradient Materials, M. Yamanouchi, M. Koizumi, T. Hirai, and I. Shiota, eds., Sendai, Japan, 1990, pp. 269–272.

Delale, F., and Erdogan, F., 1983, "The Crack Problem for a Nonhomogeneous Plane," ASME JOURNAL OF APPLIED MECHANICS, Vol. 50, pp. 609–614.

Delale, F., and Erdogan, F., 1988a, "Interface Crack in a Nonhomogeneous Medium," *Int. J. Engng. Sci.*, Vol. 26, pp. 559–568.

Delale, F., and Erdogan, F., 1988b, "On the Mechanical Modeling of the Interfacial Region in Bonded Materials," ASME JOURNAL OF APPLIED MECHANICS, Vol. 55, pp. 317–324.

Erdogan, F., and Gupta, G. D., 1971a, "Layered Composites with an Interface Flaw," *Int. J. Solids Structures*, Vol.7, pp. 1089–1107.

Erdogan, F., and Gupta, G. D., 1971, "The Stress Analysis of Multi-Layered Composites with a Flaw," *Intl. J. Solids Structures*, Vol. 7, pp. 39–61.

Erdogan, F., 1972, "Fracture Problems in Composite Materials," *J. Engng. Fracture Mechanics*, Vol. 4, pp. 811–840.

Erdogan, F., 1978, "Mixed Boundary Value Problems in Mechanics," *Mechanics Today*, S. Nemat-Nasser, ed., Vol. 4, pp. 1–86.

Erdogan, F., and Joseph, P. F., 1990, "Mechanical Modeling of Multilayered Films on an Elastic Substrate—Part I: Analysis; Part II: Results and Discussion," ASME *Journal of Electronic Packaging*, Vol. 112, pp. 309–326.

Erdogan, F., Kaya, A. C., and Joseph, P. F., 1991a, "The Mode III Crack Problem in Bonded Materials with a Nonhomogeneous Interfacial Zone," ASME JOURNAL OF APPLIED MECHANICS, Vol. 58, pp. 419–427.

Erdogan, F., Kaya, A. C., and Joseph, P. F., 1991b, "The Crack Problem in Bonded Nonhomogeneous Materials," ASME JOURNAL OF APPLIED MECHANICS, Vol. 58, pp. 410–418.

Erdogan, F., and Ozturk, M., 1992, "Diffusion Problems in Bonded Nonhomogeneous Materials with an Interface Cut," *Int. J. Engng. Sci.*, Vol. 30, pp. 1570–1523.

Gecit, M. R., and Erdogan, F., 1978, "The Effect of Adhesive Layers on the Fracture of Laminated Structures," ASME *J. Engng. Mat. and Technology*, Vol. 100, pp. 3–9.

Gerasoulis, A., and Srivastav, R. P., 1980, "A Griffith Crack Problem for a Nonhomogeneous Medium," *Int. J. Engng. Sci.*, Vol. 18, pp. 239–247.

Hirano, T., Yamada, T., Teraki, J., Niino, M., and Kumakawa, A., 1988, "A Study on a Functionally Gradient Material Design System for a Thrust Chamber," *Proc. 16th Int. Symposium On Space Technology and Science*, Sapporo, Japan.

Hirano, T., and Yamada, T., 1988, "Multi-Paradigm Expert System Architecture Based Upon the Inverse Design Concept," Int. Workshop On Artificial Intelligence for Industrial Applications, Hitachi, Japan.

Houck, D. L., ed., 1987, *Thermal Spray: Advances in Coating Technology*, Proc. of the National Thermal Spray Conference, Orlando, FL, ASM International.

Hutchinson, J. W., Mear, M. E., and Rice, J. R., 1990, "Crack Paralleling an Interface Between Dissimilar Materials," ASME JOURNAL OF APPLIED MECHANICS, Vol. 54, pp. 821–832.

Kassir, M. K., 1972, "A Note on the Twisting Deformation of a Nonhomogeneous Shaft Containing a Circular Crack," *Int. J. Fracture Mech.*, Vol. 8, pp. 325–334.

Kawasaki, A., and Watanabe, R., 1990, "Fabrication of Sintered Functionally Gradient Material by Powder Spray Forming Process," *FGM '90*, pp. 197–202.

Kurihara, K., Sasaki, K., and Kawarada, M., 1990, "Adhesion Improvement of Diamond Films," *FGM '90*, pp. 65–69.

Mahajan, R., 1992, "Crack Problems for an Elastic Film Bonded to an Orthotropic Substrate," Ph.D. Dissertation, Lehigh University, Bethlehem, PA.

Ozturk, M., and Erdogan, F., 1993, "The Axisymmetric Crack Problem in a Nonhomogeneous Medium," ASME JOURNAL OF APPLIED MECHANICS, Vol. 60, pp. 406–413.

Shiau, F. Y., Zuo, Y., Zeng, X. Y., Lin, J. C., and Chang, Y. A., 1988, "Interfacial Reactions Between Co and GaAs," *Adhesion in Solids*, Material Research Society Symposium, Proc. Vol. 119, D. M. Mattox, J. E. E. Baglin, R. J. Gottshall, and C. D. Batich, eds., pp. 171–176, MRS, Pittsburgh, PA.

Particle Orientation and Velocity Equations of Clay in a Plane-Strain Condition

M. Djavid
Harza Environmental Services, Inc.
Sears Tower,
233 S. Wacker Drive,
Chicago, IL 60606-6392

The directional property of soils, particularly clays, are directly related to the particle orientations. The platy clay particles do possess the tendency to reorient themselves in the most stable condition against applied stress. One may conceive of developing a soil model directly relating particle orientation and applied stress. In this study an angle θ, which is the preferred (therefore stable) orientation of clay particles, is introduced. Using this concept and slip-line theory, the velocity equations of clay in a plane-strain condition are developed. In this approach any change in clay particle orientation is essentially dependent on principal stresses magnitudes as well as their directions. Therefore, the effect of rotation of principal stresses can be included and quantified.

Background

Studies of the structure of clays have shown that platy clay particles tend to become oriented perpendicular to the direction of applied stress in drained conditions such as in consolidation tests. During isotropic consolidation a random structure is produced; however, in an anisotropic consolidation an oriented structure with respect to the higher or lower stress directions is observed. Since in general the natural state of in-situ stress is not isotropic, this variation in particle orientation is expected which in turn affects the directional properties of clay deposits. Kirkpatrick and Rennie (1973), after shooting a large number of micrographs from the slurry samples consolidated under isotropic and anisotropic (K_0) conditions, reported that "Electron micrographs of laboratory consolidated kaolinite samples have shown that the clay microstructure is controlled by the consolidation stress régime. Kaolinite samples consolidated under isotropic pressure conditions are shown to have an isotropic structure with the particles oriented randomly with respect to each other. Samples consolidated anisotropically, especially under K_0 conditions, are found to have a severely oriented structure with particles faces aligned at right angles to the direction of major consolidation pressure." They also found that clay is more compressible in directions parallel to the aligned plate structure than at right angles to it.

Mitchell (1956) concluded that six out of seven undisturbed marine clays and one lacustrine clay had some degree of parallel orientation particles. Rosenqvist (1959) studied lightly consolidated Norwegian marine clays using electron microscopy. He found that all of the clays conformed nearly exactly to the salt-flocculated clays hypothesized by Lambe (1953); characterized by edge-to-face and random particle orientation. Martin (1962) compared the peak amplitudes of diffracted x-rays from different planes of kaolinite clay and concluded that the clay was approximately "ideally random" for isotropic consolidation pressure up to 98.1 KPa and was approximately "ideally oriented" for one-dimensional consolidation pressure up to 19.33 MPa. Any orientation due to flucculations or other chemical agents is negated after isotropic consolidation up to 98.1 KPa.

Hvorslev (1960) showed that specimens trimmed from Vienna and Little Belt clays had different undrained strengths in different directions. Broms and Casbarian (1965) conducted three series of consolidated undrained triaxial tests on hollow cylindrical specimens of a remolded kaolinite clay. In test series I the effects of principal stress direction and in series II the effects of intermediate principal stress were investigated on the friction angle and induced pore water pressure, while in series III the combined effect was investigated. The investigators attributed the effect of the rotation of the principal stress direction to the reorientation of the individual clay particles. The tendency of the individual clay particles to align themselves parallel with the final failure plane will increase with increasing rotation of the principal stress axes. It was concluded that the maximum deviator stress and the frictional angle ϕ' will decrease with increasing rotation of the principal stress axes. The excess pore water pressure due to rotation of principal stress directions is also explained by the following statement. "Due to the alignment of the individual clay particles and the resulting decrease of particle interlocking, it is also expected that the pore water pressure at failure at a given void ratio will increase with increasing rotation of the principal stress axes." From a study of the isotropically consolidated specimens in

Contributed by the Applied Mechanics Division of THE AMERICAN SOCIETY OF MECHANICAL ENGINEERS for publication in the ASME JOURNAL OF APPLIED MECHANICS.

Discussion on this paper should be addressed to the Technical Editor, Professor Lewis T. Wheeler, Department of Mechanical Engineering, University of Houston, Houston, TX 77204-4792, and will be accepted until four months after final publication of the paper itself in the ASME JOURNAL OF APPLIED MECHANICS.

Manuscript received by the ASME Applied Mechanics Division, June 2, 1993; final revision, Oct. 14, 1993. Associate Technical Editor: R. M. Bowen.

series I and III (total of 36 tests), two more interesting conclusions may be made.

(i) The minimum strength belongs to the direction of 45 degrees.

(ii) The strengths of other directions are symmetric with respect to the 45-deg direction which clearly indicates that in isotropic consolidation, preferred orientation is about 45 deg.

Duncan and Seed (1966) performed an extensive series of undrained tests on the specimens of kaolinite trimmed from a block in different orientations. The specimens were trimmed from a block of kaolinite consolidated under vertical pressure of about 900 KPa and lateral pressure of about 550 KPa. They clearly exhibited that anisotropically consolidated clays are anisotropic with respect to the undrained strength. In a diagram in which the variation of strength with respect to angle of orientation is plotted, the lowest strength corresponds to the one with an angle of orientation of about 32 deg with respect to the horizontal.

Morgenstern and Tchalenko (1967) performed a drained direct shear test on kaolinite samples which have been trimmed at various angle of orientation. For that specific kaolinite, samples with various orientations were found to have little difference in drained strengths. Based on polarized microscope observation, they concluded that perfect particle alignment is necessary in a kinematically admissible direction to obtain the residual angle of shearing resistance. Additionally, the irreversible deformations must be accommodated by the rigid-body movements of the clay particles. Morgenstern and Tchalenko (1967) in yet another study observed that the optical determination of preferred orientation in clays is extremely useful in interpreting the changes in the fabric of kaolinite samples prepared in different techniques. It is also shown that after consolidation pressure of 10 KPa, the preferred direction would not depend on the method of preparation but on the history of loading. *The degree of preferred orientation can be determined by measuring the birefringence*[1] *ratio for a thin section of clay.*

Barden (1972) presented some examples of clay structure and its influence on engineering behavior. He concluded that the structure of clay is strongly related to the stress system operating during the initial consolidation. Anisotropic structure leads to anisotropic deformation behavior, but in the case of kaolinite led to less anisotropic shear strength behavior. By using a polarized microscope the presence of oriented shear zones in the samples of K_0-consolidated kaolinite under undrained shear in the plane-strain condition at about 6.5 percent strain were observed.

Lo and Morin (1972) performed an experimental study on two sensitive clays. The results of CID and CIU tests (Consolidated Isotropically and sheared in Drained or Undrained condition) indicate that the strength of specimens trimmed in different directions are strongly anisotropic and the ratio of minimum strength to strength of vertical samples varies from 0.54 to 0.70. They also concluded that in the drained tests, the time to failure has an important effect on the peak strength[2].

Saxena et al. (1978) conducted an experimental investigation on Hackensack Valley varved clay. The samples were taken from depths of 10 to 20 meters and were trimmed in different orientations of 0 deg, 45 deg, 60 deg, 75 deg, 90 deg with vertical direction. The specimens were sheared in undrained conditions under different confining pressure. The results of tests on specimens from a depth of 17 meters (and laboratory confining pressure of 108 KPa) indicated that the minimum strength belonged to the specimen with an angle of orientation of 60 deg. This minimum strength was 31 percent of the vertical specimen's strength. However, horizontal specimen exhibited a strength equivalent to 78 percent of that in the vertical direction. They reported the results of yet another extensive study, (MIT, Ladd and Wissa, 1970), on varved clay specimens from the Connecticut Valley and Welland, Ontario with similar results; that is, the horizontal specimens had an average strength of 88 percent, and 60-deg oriented samples yielding strengths of only 33 percent of the vertical specimens, respectively. Djavid (1991) conducted a series of triaxial static and dynamic tests on kaolinite. Blocks of kaolinite were prepared by consolidation of slurry under K_0 ($\sigma_v/\sigma_h \simeq 2$) condition. Specimens were trimmed from blocks in different orientations of 0 deg, 30 deg, 60 deg, and 90 deg with a vertical direction. It is shown that 60 deg specimens had the minimum strength and maximum axial deformation in undrained static and dynamic loading. Regarding the consolidation regime, the particles are mainly oriented in the direction of 60 deg with vertical.

From these studies, it may be concluded that there is a tendency for particles to become oriented parallel to the plane on which the effective principal stresses act. That is at any given time, the particles orientation is in the direction of maximum effective stress obliquity (Fig. 1). Since the effective stress ratio is not generally equal to one, the soil sample would possess anisotropy and, i.e., the major principal stress direction should be an axis of radial symmetry of the anisotropy.

Basic Assumptions for Preferred Angle of Orientation

In view of the above-related experimental works, the following can be concluded. The clay particles under effective stress conditions distribute themselves in a manner which tend to align their largest dimensions in the direction of maximum effective stress obliquity. Let us introduce now an angle θ, which is the angle of preferred orientation of platy clay particles at each side of the algebraically greater principal stress with respect to the plane of action of the major principal stress as shown in Fig. 1. This angle has three important characters:

(i) Angle θ is effectively stress-dependent.

(ii) Due to isotropic consolidation $\theta = 45$ deg, that is; clay particles are oriented "ideally random."

(iii) Due to increasing $\bar{\sigma}_1$ (or $\bar{\sigma}_3$), θ begins to decrease (or increase) in a manner that all times $\tan(\theta) = \bar{\sigma}_3/\bar{\sigma}_1$ ($\bar{\sigma}_1$ and $\bar{\sigma}_3$ are effective major and minor principal stresses). This is confirmed by the experimental study reported by Duncan and Seed (1966), Djavid (1991), and other previous studies described in the preceding section.

Accordingly, one may introduce the existence of two different characteristic fields called α lines and β lines, which coincide with θ lines. The angle between two characteristic fields is bisected by the direction of an algebraically greater principal stress. In undrained shearing condition, α lines and β lines coincide with slip lines. Furthermore, the velocity of particles in the field are proposed as *any change in velocity of two successive points on the α line that is in the direction of the β line and vice versa.*

Velocity Equations

The development of the velocity equations (based on the slip line theory) presented in this study parallels the development presented by Spencer (1964) wherein a theory of the kinematics of ideal soils under plane-strain conditions was developed. Following Spencer (1964), Mehrabadi and Cowin (1978) extended the same concept for dilatant granular materials using angle of dilatancy. Nemat-Nasser (1981) in yet

[1]This method is described in the Appendix.

[2]One may conclude that in a drained test the particles have enough time to reorient themselves in a more stable condition.

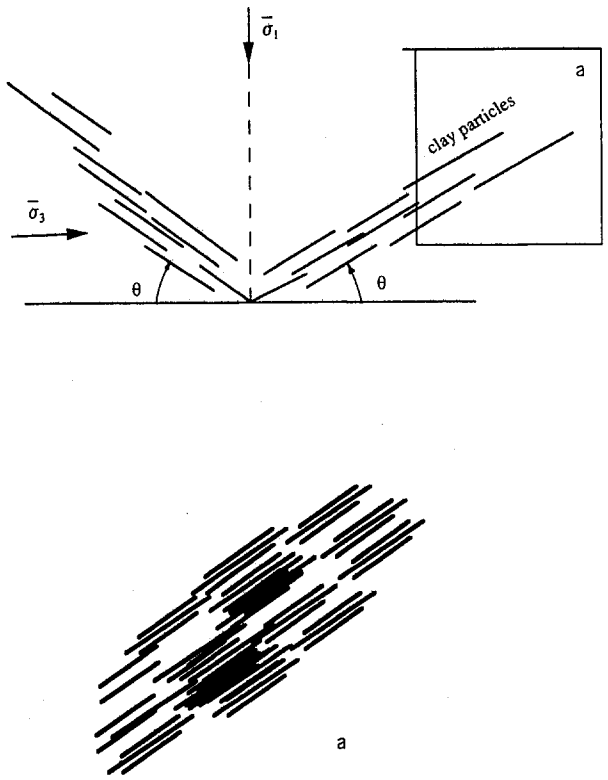

Fig. 1 Schematic representation of clay particles and particle orientation due to effective stress

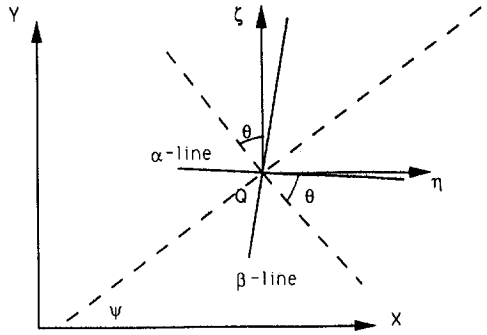

Fig. 2 Schematic of slip lines

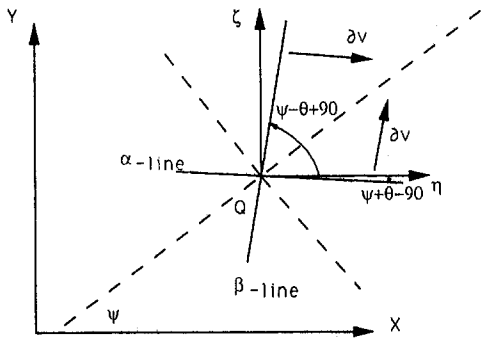

Fig. 3 Slip lines and velocity equations

another different approach obtained similar relations for the dilatancy case as well as a densification case of granular materials. Jahedi et al. (1990) also developed the Spencer's theory for granular materials by using the idea of angle of contact normals. In the present investigation, a similar approach is followed for clay materials with the exception of defining the characteristic lines as the preferred orientation of clay particles based on various experimental investigations. A set of characteristic lines are passing through a typical point Q shown in Fig. 2 and each characteristic line makes an angle of θ with a major principal stress plane (characteristic lines are assumed to be slip lines if no compression or dilation occurs). At the point Q, a local rectangular cartesian coordinate system (ζ, η) may be introduced which is in motion relative to the reference x,y-system, Fig. 3. Then the following velocity equations for clayey materials were developed similar to those for granular material described in Mehrabadi et al. (1978) and Jahedi et al. (1990) (compression is taken positive).

$$(D_{11} + D_{33}) = -2\dot{\theta} \cot (2\theta)$$

$$(D_{11} - D_{33})\sigma_{13} - 2D_{13}(\sigma_{11} - \sigma_{33}) = \frac{(\sigma_{11} - \sigma_{33})\sigma'_{13} - \sigma_{13}(\sigma'_{11} - \sigma'_{33})}{\sqrt{(\sigma_{11} - \sigma_{33})^2 + 4\sigma_{13}^2}} \cos (2\theta) \quad (1)$$

where

$$D_{11} = \frac{\partial v_x}{\partial x}, \quad D_{33} = \frac{\partial v_y}{\partial y}, \quad (2)$$

and v_{ij}, σ_{ij}, and σ'_{ij} are components of velocity (versus x, y), stress, and Jauman stress rate, respectively.

Equations (1) in indicial notation can be written as

$$D_{ii} = -2\dot{\theta} \cot (2\theta)$$

$$D_{ik}\sigma_{kj} - \sigma_{ik}D_{kj} = (\sigma_{ik}\sigma'_{kj} - \sigma'_{ik}\sigma_{kj}) \frac{\cos (2\theta)}{\sqrt{(\sigma_{11} - \sigma_{33})^2 + 4\sigma_{13}^2}}. \quad (3)$$

The only material parameter in Eqs. (1) and (3) is the angle of preferred orientation of particles θ which is required to be known at the initial stage and measured at the required course of load application. The degree of preferred orientation can be determined by measuring the birefringence ratio for a thin section of clay which has been successfully conducted by Morgenstern and Tchalenko (1967). Also one may suggest that the initial value of single θ and the deviation thereof may be related to the initial void ratio and change of void ratio during load application, respectively. Conceptually, this theory based on angle θ (preferred angle of particle orientations) presents a powerful tool for incorporating the change in material behavior due to change in stress path. According to the velocity equations (Eqs. (1)) if the angle $\theta = 45$ deg, the first part of Eq. (1) represents the incompressibility condition $(D_{11} + D_{33} = 0)$ similar to the Spencer's Equations (1964). However, from the second part, the coaxiality of stress and strain rate may be obtained. On the other hand, due to rotation of major principal stress direction clay particles will tend to reorient themselves resulting in the change of θ and consequently volume change of the soil (in drained condition) and induced pore water pressure in the undrained condition.

A complete stress-deformation theory for clay materials can be defined by the system of equations consisting of Eqs. (1), the continuity equation, the stress equations of motion (the equilibrium equations), and yield stress criterion. This system of equations contains six unknowns as v_x, v_y, σ_{11}, σ_{33}, σ_{13}, and pore water pressure (u). According to the test results in previous studies mentioned in the preceding sec-

tion (particularly Duncan and Seed (1966), Broms et al. (1965), Hvorslev (1960), and Djavid (1991)), the stress criterion may be defined as

$$\tan(\theta) = \frac{\bar{\sigma}_{33}}{\bar{\sigma}_{11}}. \tag{4}$$

On the other hand, continuity equation is simplified (Djavid, 1991) in the following form for estimation of pore water pressure in an undrained condition:

$$\epsilon_v = b_u \cdot \log\left(\frac{\frac{\sigma_{ii}}{3}}{\frac{\sigma_{ii}}{3} - u}\right) + C_p \cdot u \cdot n + C_s \cdot u \cdot (1 - n) \tag{5}$$

where the left side of Eq. (5) is the volumetric strain, b_u is the slope of the curve of an unloading path in a consolidation test, σ_{ii} is the mean total stress, n is porosity, and C_p and C_s are coefficients of compressibility of pore fluid and soil particles, respectively. This relation is obtained by comparison of soil behavior in a drained and undrained condition under identical stress paths.

The first equation of Eqs. (1) can be rewritten as

$$\dot{\epsilon}_v = D_{11} + D_{33} = -2\dot{\theta}\cot(2\theta). \tag{6}$$

By integrating this equation (time rate of change of volumetric strain) with respect to time and the assumption of small deformations, one may write

$$\epsilon_v = -Ln[\text{cosec}(2\theta)]. \tag{7}$$

Thus, by replacing volumetric strain from Eq. (7) in Eq. (5), the latter equation may be written as

$$-Ln[\text{cosec}(2\theta)] = 0.43 b_u \cdot Ln\left(\frac{\frac{\sigma_{ii}}{3}}{\frac{\sigma_{ij}}{3} - u}\right) + C_p \cdot u \cdot n + C_s \cdot u \cdot (1 - n) \tag{8}$$

which relates the induced pore water pressure (u) to preferred orientation of clay particles (θ) in a closed-form solution.

Summary and Conclusions

Directional property of soils, particularly clays, is directly related to the particle orientation. Also any change in applied stress results in reorientation of particles towards the most stable condition. Accordingly, for clay behavior in a drained and plane-strain condition, a constitutive equation has been developed and modified for an undrained condition. The model is defined as a function of particle orientation called average angle of orientation or preferred angle of orientation. Preferred angle of orientation of clay particles is effectively stress-dependent and its change is proportional to the $\bar{\sigma}_{33}/\bar{\sigma}_{11}$ ratio. Conceptually this theory based on angle θ (preferred angle of particle orientations) presents a powerful tool for incorporating the change in material behavior due to a change in the stress path.

The only material parameter in this model is the angle of preferred orientation which is required to be known at the initial stage (degree of anisotropy) and measured in the course of a load application for model calibration. The measurement of angle θ has been possible and successfully determined even in 1967 by measuring the birefringence ratio of a thin section of clay at the various course of load application (Morgenstern and Tchalenko, 1967).

The author is working to establish a relation between angle θ and void ratio by defining θ_{initial}, θ_{critical}, and $\theta_{\text{instantaneous}}$ and relating them to corresponding well-known terms for void ratio terms as e_{initial}, e_{critical}, $e_{\text{instantaneous}}$.

References

Barden, L., 1972, "Examples of Clay Structure and its Influence on Engineering Behavior," *Stress Strain Behavior of Soils*, R. H. G. Parry, ed., pp. 195–205.

Broms, B. B., and Casbarian, A. O., 1965, "Effect of Rotation of the Principal Stress Axes and the Intermediate Principal Stress on Shear Strength," *Proceedings of the Sixth International Conference on Soil Mechanics and Foundation Engineering*, Montreal, Canada, Vol. 1, pp. 179–183.

Djavid, M., 1991, "Behavior of Clay under Large Strain With Wave Loading," Ph.D. Thesis, Illinois Institute of Technology, Chicago, IL.

Duncan, J. M., and Seed, B. H., 1966, "Anisotropy and Stress Reorientation in Clay," *Journal of Soil Mechanics and Foundation Division*, Proceeding of ASCE, Vol. 92, No. SM5, pp. 21–49.

Hvorslev, M. J., 1960, "Physical Components of the Shear Strength of Saturated Clays," *Proceedings of the ASCE Research Conference on the Shear Strength of Cohesive Soils*, Boulder, CO, pp. 169–273.

Jahedi, J., Mohammadi, J., and Nair, S., 1990, "A Fabric Related Constitutive Model for Granular Materials," ASME JOURNAL OF APPLIED MECHANICS, Vol. 57, pp. 507–512.

Kirkpatric, W. M., and Rennie, I. A., 1972, "Directional Properties of Consolidated Kaolin," *Geotechnique*, pp. 166–169.

Ladd, C. C., and Wissa, A. E. Z., 1970, "Geology and Engineering Properties of Connecticut Valley Varved Clays with Special Reference to Embankment Construction," Department of Civil Engineering, MIT Res. Rep. R70-56, Soils Publ. 264.

Lambe, T. W., 1953, "The Structure of Inorganic Soils," *Proceedings of the ASCE*, Vol. 79, No. 315.

Lo, K. Y., and Morin, J. P., 1972, "Structure Anisotropy and Time Effect of Two Sensitive Clays," *Canadian Journal of Geotechnical Engineering*, Vol. 9, No. 261, pp. 261–277.

Martin, T. R., 1962, "Research on the Physical Properties of Marine Soils," 1961–1962 Research Report, R62-42, Soil Engineering Division, Publication No. 127 MIT, Cambridge, MA.

Mehrabadi, M. M., and Cowin, S. C., 1978, "Initial Planar Deformation of Dilatant Granular Materials," *Journal of the Mechanics and Physics of Solids*, Vol. 26, pp. 269–284.

Mitchel, J. K., 1956, "The Fabric of Natural Clays and Its Relation to Engineering Properties," *Proceedings of Highway Research Board*, Washington, D.C., Vol. 35, pp. 693–713.

Morgenstern, N. R., and Tchalenko, J. S., 1967, "Microscopic Structure in Kaolin Subjected to Direct Shear," *Geotechnique*, pp. 309–328.

Nemat-Nasser, S., 1980, "On Behavior of Granular Materials in Simple Shear," *Soils and Foundations*, Japanese Society of Soil Mechanics and Foundation Engineering, Vol. 20, No. 3, pp. 52–72.

Rosenqvist, T. I., 1959, "Physico-Chemical Properties of Soils: Soil-Water System," *Journal of Soil Mechanics and Foundations Division, ASCE*, Vol. 85, No. SM2, Paper 2000, pp. 31–53.

Saxena, S. K., Hedberg, J., and Ladd, C. C., 1978, "Geotechnical Properties of Hackensack Valley Varved Clays of New Jersey," *Geotechnical Testing Journal*, ASTM 1, pp. 148–161.

Spencer, A. J. M., 1964, "A Theory of the Kinematics of Ideal Soils under Plane Strain Conditions," *Journal of the Mechanics and Physics of Solids*, Vol. 12, 1964, pp. 337–351.

APPENDIX

Birefringence

Morgenstern and Tchalenko (1967) reported "A single kaolin crystal is birefringent, and when viewed under crossed nicols in a polarizing microscope with its basal plane parallel to the viewing direction, it behaves like a uniaxial negative crystal. That is, as the crystal is rotated with respect to the direction of the vibration of the wave front emerging from the polarizer it may be seen to transmit zero light intensity when one of the optical axes is parallel to this direction and a maximum light intensity when an optical axis is at 45 deg to it. Since the optical axes are orthogonal and coincide for all practical purposes with the crystallographic axes, this means

that when the trace of the basal plane of the crystal is parallel or orthogonal to the polarizing direction, the crystal is in an extinction position, and when it is at 45 deg to this direction maximum illumination is observed. As a single crystal is rotated through 360 deg there are four extinction positions and four positions of maximum illumination. It is also known that a single kaolin crystal displays positive elongation and hence any ambiguity regarding the inclination of the trace of the basal plane may be resolved by viewing with a suitable retardation plate."

They have also shown that the birefringence of an aggregate of clay particles depends solely upon the intrinsic birefringence of the constituent particles and their spatial configuration. When a random structure is viewed in a thin section under crossed nicols, no variation in transmitted light intensity is observed as the section is rotated. If the aggregate has a preferred orientation, the minimum and maximum light intensities will depend upon the degree of orientation. These intensities may be measured and interpreted to give a quantitative measure of the preferred orientation of the aggregate.

Milos Novak

Dr. MILOS NOVAK, Professor of Civil Engineering at the University of Western Ontario in London, Ontario, Canada, died on April 28, 1994, in the seventieth year of his life.

He was a frequent contributor to our Journal, our frequent reviewer, and a valuable member of several committees.

He received his civil engineering degree in 1949 from the Czech Technical University in Prague (CVUT). In 1957, he earned a Ph.D. in mechanics from the Czechoslovak Academy of Sciences (CSAV) in Prague. Then, he conducted research in the Institute of Theoretical and Applied Mechanics of CSAV, reaching the position of Principal Scientist. In 1967, during a period of relaxation of the communist dictatorship, Novak was allowed to take a one-year leave at the University of Western Ontario, where he worked in the Boundary Layer Wind Tunnel Laboratory. In 1968, after Russian tanks crushed the Prague Spring, he accepted an offer of a permanent faculty position. He proceeded to earn the reputation of a truly outstanding teacher and researcher.

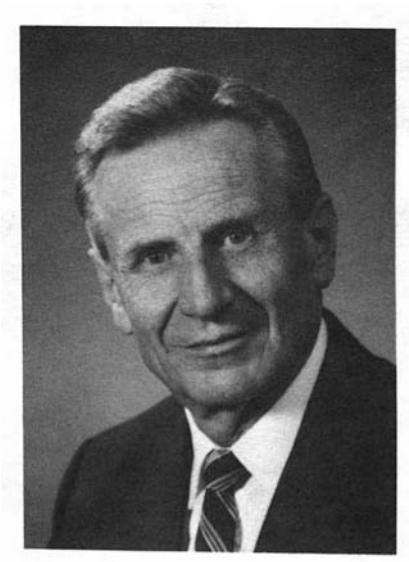

Considered one of the foremost world experts in dynamics of civil engineering structures and foundations, Novak published over 160 refereed papers. He was a member of the editorial boards of Journal of Soil Dynamics and Earthquake Engineering and of International Journal of Software and Engineering Workstations. He was active as a member of the American Society of Civil Engineers and of the Society of Professional Engineers of Ontario. He made important contributions to earthquake engineering, particularly to dynamic structure-soil interaction, to wind engineering, where he investigated the galloping instability, and to wave action on structures. He developed powerful computer programs for suspension bridges, transmission lines, guyed masts, tall chimneys, nuclear power plants and offshore oil rigs. He taught 18 short specialized courses at leading universities and research laboratories in Canada, the United States, Japan, China, India, Australia, New Zealand, and other countries. He consulted on nuclear power plants in Germany, Switzerland, Brazil, Finland and Yugoslavia; on large offshore towers in Texas, Venezuela, China and Canada; and on foundations for turbine generators, compressors and paper mill machines. He served as consultant to the United Nations on projects in India and Yugoslavia, as well as on the Chinese University Development Project. Recently he went to Armenia as a U.N. expert to advise on earthquake-resistant structural design. In 1986, Japan Society of Building Research held a 'Novak Symposium' on Dynamics of Embedded Foundations and Piles. The Czech Technical University, Novak's alma mater, awarded him an honorary doctorate in 1993. He also received the Medal for Research and Development from the Association of Professional Engineers of Ontario, the Medal of Merit from the Czech Society for Mechanics, and a Gold Medal from the Czechoslovak Academy of Sciences, and at his university was inducted to the Gzowski Society Honor Roll. In August of 1994, the Canadian Geotechnical Society had chosen him as the first recipient of the G. Geoffrey Meyerhoff Award. Dr. Novak's last paper in the *Journal of Applied Mechanics*, coauthored with F. Guan, and entitled "Transient Response of an Elastic Homogeneous Half-Space to Suddenly Applied Rectangular Loading" appeared in Vol. 61, pp. 256–263, June 1994.

Our engineering mechanics community lost a great scholar, researcher, and engineer.

Z. P. Bazant, Northwestern University,
and G. J. Dvorak, Rensselaer Polytechnic Institute,
Fellows, ASME.

Milos Novak

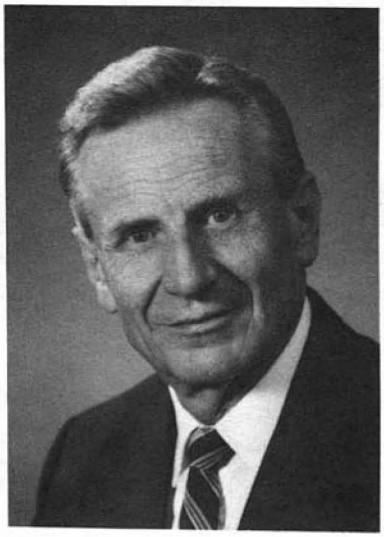

Dr. MILOS NOVAK, Professor of Civil Engineering at the University of Western Ontario in London, Ontario, Canada, died on April 28, 1994, in the seventieth year of his life.

He was a frequent contributor to our Journal, our frequent reviewer, and a valuable member of several committees.

He received his civil engineering degree in 1949 from the Czech Technical University in Prague (CVUT). In 1957, he earned a Ph.D. in mechanics from the Czechoslovak Academy of Sciences (CSAV) in Prague. Then, he conducted research in the Institute of Theoretical and Applied Mechanics of CSAV, reaching the position of Principal Scientist. In 1967, during a period of relaxation of the communist dictatorship, Novak was allowed to take a one-year leave at the University of Western Ontario, where he worked in the Boundary Layer Wind Tunnel Laboratory. In 1968, after Russian tanks crushed the Prague Spring, he accepted an offer of a permanent faculty position. He proceeded to earn the reputation of a truly outstanding teacher and researcher.

Considered one of the foremost world experts in dynamics of civil engineering structures and foundations, Novak published over 160 refereed papers. He was a member of the editorial boards of Journal of Soil Dynamics and Earthquake Engineering and of International Journal of Software and Engineering Workstations. He was active as a member of the American Society of Civil Engineers and of the Society of Professional Engineers of Ontario. He made important contributions to earthquake engineering, particularly to dynamic structure-soil interaction, to wind engineering, where he investigated the galloping instability, and to wave action on structures. He developed powerful computer programs for suspension bridges, transmission lines, guyed masts, tall chimneys, nuclear power plants and offshore oil rigs. He taught 18 short specialized courses at leading universities and research laboratories in Canada, the United States, Japan, China, India, Australia, New Zealand, and other countries. He consulted on nuclear power plants in Germany, Switzerland, Brazil, Finland and Yugoslavia; on large offshore towers in Texas, Venezuela, China and Canada; and on foundations for turbine generators, compressors and paper mill machines. He served as consultant to the United Nations on projects in India and Yugoslavia, as well as on the Chinese University Development Project. Recently he went to Armenia as a U.N. expert to advise on earthquake-resistant structural design. In 1986, Japan Society of Building Research held a 'Novak Symposium' on Dynamics of Embedded Foundations and Piles. The Czech Technical University, Novak's alma mater, awarded him an honorary doctorate in 1993. He also received the Medal for Research and Development from the Association of Professional Engineers of Ontario, the Medal of Merit from the Czech Society for Mechanics, and a Gold Medal from the Czechoslovak Academy of Sciences, and at his university was inducted to the Gzowski Society Honor Roll. In August of 1994, the Canadian Geotechnical Society had chosen him as the first recipient of the G. Geoffrey Meyerhoff Award. Dr. Novak's last paper in the *Journal of Applied Mechanics*, coauthored with F. Guan, and entitled "Transient Response of an Elastic Homogeneous Half-Space to Suddenly Applied Rectangular Loading" appeared in Vol. 61, pp. 256–263, June 1994.

Our engineering mechanics community lost a great scholar, researcher, and engineer.

Z. P. Bazant, Northwestern University,
and G. J. Dvorak, Rensselaer Polytechnic Institute,
Fellows, ASME.

Comparison of Experimental and Simulated Grain Flows

T. G. Drake[1]
Center for Coastal Studies,
Scripps Institution of Oceanography,
La Jolla, CA 92093-0209

O. R. Walton
Earth Sciences Division,
Lawrence Livermore National Laboratory,
Livermore, CA 94550

Fully three-dimensional computer simulations of identical spheres flowing in an inclined glass-walled channel only slightly wider than a particle diameter successfully reproduce profiles of mean velocity, bulk density, and particle rotations as well as profiles of fluctuating quantities measured from high-speed motion pictures of physical experiments. All simulation parameters are measured experimentally. Both full simulations of the geometry of the physical experiments and simulations using periodic boundary conditions in the downchute direction are used to gather micromechanical information. For these collision-dominated flows, quantitative predictions of the simulations are relatively insensitive to details of the particle-interaction model and particularly the particle stiffness, but are relatively sensitive to extraneous fluid drag forces and the chute geometry.

Introduction

Particle-scale observations of flowing granular materials are exceedingly difficult to make, and the paucity of such observations poses a serious obstacle to understanding and predicting the mechanics of industrial and geophysical grain flows. Computer simulations have been used to great advantage in testing kinetic theories for granular flow, but those theories, limited to collision-dominated flows (e.g., Lun et al., 1984), address only a small subset of the rich variety of granular flow phenomena. Particle-scale comparison of simulations with physical experiments is required to confidently extend simulation-based techniques for general study of granular flows. This paper compares particle-scale information derived from a set of physical experiments with the results of a fully three-dimensional computer simulation model for collision-dominated granular flows of spherical particles. The comparison thus serves as a necessary first step toward extending calculations to friction-dominated flows. Below we briefly describe the physical experiments and the calculational scheme for simulating them. We pay particular attention to the particle-contact models used in the simulations and the role of such extraneous forces as fluid drag. Comparison of results for two physical experiments with simulated flows reveals several features of interest. Additional simulations demonstrate the sensitivity of the calculations to parameter variation within a selected small subset of the parameter space.

Description of Physical Experiments

Flows of 6-mm diameter spheres were generated in a glass-walled chute 3.7 m long, 0.5 m deep, and just 6.7 mm wide, confining the motion of the particles to essentially two dimensions, except for their spins (Fig. 1). The chute could be inclined at any angle; and within it the bed could be moved independently to fine tune the inclination. The cellulose acetate spheres used in the experiments were smooth, white, highly spherical, and uniform in both size and density. Each was randomly imprinted with about 15 small black dots to enable the measurement of particle spins. Over the range of experimental conditions the coefficient of restitution $\epsilon = 0.84 \pm 0.01$. The Appendix lists the material properties of the experimental spheres.

The fixed bed, which was intended to simulate naturally occurring beds of geophysical interest, consisted of immovable 6-mm spheres identical to those in the flows glued to the top

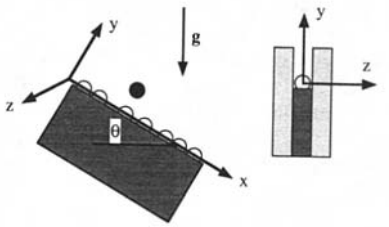

Fig. 1 Schematic view of the experimental glass-walled chute. The fixed bed consists of 6-mm diameter cellulose acetate spheres like those in the flows glued on a rigid aluminum bar centered between the glass sidewalls. Gaps between bed particles are uniformly distributed on the interval 0 to 5 mm so that moving particles could not touch the bar. Coordinate system for measurements in the glass-walled chute inclined at an angle θ to the horizontal; g is the gravitational acceleration. The bed-normal y-coordinate originates at the centerline of the fixed bed spheres, the x-coordinate extends downstream parallel to the bed, and the z-coordinate is perpendicular to the glass sidewall such that a particle rolling downhill has rotation $\omega_z < 0$.

[1]Present address: Department of Marine, Earth and Atmospheric Sciences, North Carolina State University, Raleigh, NC 27695-8208.

Contributed by the Applied Mechanics Division of THE AMERICAN SOCIETY OF MECHANICAL ENGINEERS for publication in the ASME JOURNAL OF APPLIED MECHANICS.

Discussion on this paper should be addressed to the Technical Editor, Professor Lewis T. Wheeler, Department of Mechanical Engineering, University of Houston, Houston, TX 77204-4792, and will be accepted until four months after final publication of the paper itself in the ASME JOURNAL OF APPLIED MECHANICS.

Manuscript received by the ASME Applied Mechanics Division, Oct. 19, 1992; final revision, July 6, 1993. Associate Technical Editor: R. M. Bowen.

of a stiff aluminum bar with randomly spaced gaps between them uniformly distributed over the range 0–5 mm, so that the moving particles could not touch the bar.

Flows were generated by placing about 15,000 to 30,000 spheres in a wide, V-shaped hopper above and to one side of the upstream end of the chute. They fed onto a slightly inclined, smooth tray, where they organized into a single layer that spilled over the edge of the tray and fell vertically between the glass walls to the chute bed. The flux of particles was controlled by blocking portions of the layer on the tray.

The flows were photographed about 0.7 m upstream of the chute outlet using a high-speed 16-mm camera operating at a nominal rate of 1440 frames per second, or 60 times the normal projection speed. The particles were frontally illuminated against a black background. The films were analyzed frame by frame to determine positions of the centers of the spheres and dots in machine-readable form by projecting the film image onto a digitizing tablet. Further details of data-gathering and analysis can be found in Drake (1988).

Detailed profiles of mean and fluctuating quantities were obtained from films of two nominally steady, uniform flows having fluxes of about 1280 and 2230 particles^{-1}. The flows exemplify the disperse and dense end-member cases treated by kinetic theories of grain flow (e.g., Lun et al., 1984). For both flows the chute inclination was 42.75 deg, which provides relatively long-duration flows which are nearly steady and uniform and have an optimal combination of moderate bulk density and high total flux. The mean-free path corresponding to such moderate bulk densities allows measurement of intercollision velocities, while a high total flux increases the number of measurements and thereby decreases statistical uncertainty. A complete description of the physical experiments and discussion of the issues surrounding experimental acquisition of particle-scale information can be found in Drake (1991).

Description of Computer Simulations

Particle-dynamics computer simulations (e.g., Cundall and Strack 1979; Walton and Braun, 1986a,b) explicitly solve the equations of motion for an assemblage of particles under the influence of body and interparticle forces. Because fluid drag affects fast-moving particles in the glass-walled chute (Drake, 1991), we also incorporated a simple fluid-drag model in the simulations.

Particle-Interaction Models. The particle-interaction model used in the calculations is based on a model for identical, homogeneous spheres described in detail in Walton and Braun (1986a, b) and Walton (1993a, b). The normal force F_n between contacting particles is given by $F_n = K_1\alpha$ for loading, and $F_n = K_2(\alpha - \alpha_0)$ for unloading, where α is the overlap of particles after initial contact, α_0 is the value of α where the unloading curve goes to zero, and K_1 and K_2 are constants. No negative values are allowed for F_n. For binary collisions, the coefficient of normal restitution is $\epsilon = (K_1/K_2)^{1/2}$.

The tangential friction force model is based on approximations (Walton and Braun, 1986a; Walton, 1993a) to theoretical models for friction between Hertzian elastic spheres developed by Mindlin and Deresiewicz (1953). The full Walton model incorporates a computationally intense calculation for the effective tangential stiffness, K_t, and also requires one additional variable to be stored in memory for each contact pair. In the present simulation the new tangential force calculated at each explicit time step is $F_t = F_{to} + K_t\Delta s$, where Δs is the new tangential displacement, F_{to} is the total tangential force from the previous time step, and $K_t = K_o(1 - F_{to}/\mu F_n)^\gamma$, where μ is the coefficient of friction (no distinction is made here between static and sliding friction coefficients), K_o is the initial value of the tangential stiffness, and $\gamma = 1/3$ for Hertzian spheres.

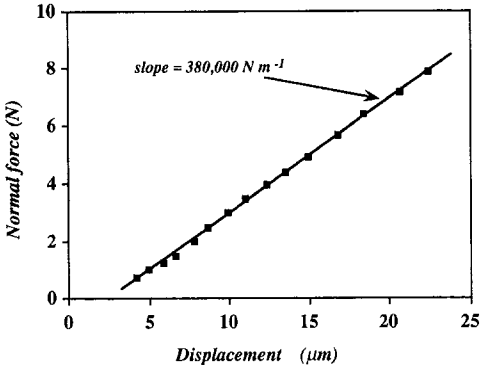

Fig. 2 Force-displacement curve for 6-mm diameter cellulose acetate spheres. Particle stiffness is the slope of the least-squares line through data points having normal force greater than 0.5N (from Mullier et al., 1991).

Experimental measurements of the particle properties entering into the simulations were made by Mullier et al. (1991). For normal loads of interest (typically a few N and ranging up to about 10N) the spheres exhibit a nearly linear force-displacement relation, although for normal loads less than about 0.5N (corresponding to displacements of a few microns), the force-displacement curve deviates from the simple linear relation due to the complex interaction of asperities on the sphere surfaces. A linear fit through their data for normal loads greater than 0.5N gives a normal stiffness of 380,000 Nm^{-1} (Fig. 2). For the collision-dominated flows studied here, the calculations were insensitive to the value of the normal stiffness, and we used a value of 38,000 Nm^{-1} for computational efficiency. However, in dense, compact flows or quasi-static calculations in which particles may be in nearly continuous contact (e.g., Drake, 1990), changes in the normal stiffness directly affect wave speeds and other quantities of interest; and thus caution must be exercised in decreasing the normal stiffness for computational efficiency. Using these parameters, the interaction model yields a (fixed) time step of 1.31×10^{-5} s, using 40 time steps per collision, and virtual overlaps of particles did not exceed one percent of the particle radius during collisions. The experimentally measured ratio of the initial tangential to normal stiffnesses is about 0.1 for normal loads greater than about 1.5N (Mullier et al., 1991, p. 69). Mindlin's theory for the tangential force gives $\gamma = 1/3$ for Hertzian spheres; we used $\gamma = 1$ after comparisons with micro-displacement versus tangential force measurements (Mullier et al., 1991) showed better agreement than the $\gamma = 1/3$ model. Finally, the measured interparticle coefficient of sliding friction is 0.41 and the particle-glass coefficient is 0.24, again restricting attention to normal loads greater than 0.5N.

Extraneous Forces. Such extraneous forces as fluid drag may unavoidably arise in physical experiments, though they are rarely incorporated into grain flow theories. Experiments to determine the effects of fluid drag within the chute yielded a drag coefficient of 3.4 ± 2.2 for single particles tracing long trajectories in relatively still air (Drake, 1991). The drag coefficient for 6-mm-diameter spheres in an unbounded fluid at comparable particle Reynolds numbers is about 0.6. A rough rule-of-thumb for collision-dominated flows in the glass-walled chute is that the velocity of the entrained air is about half the mean particle velocity at any given level in the flow. Flows having high bulk densities entrain air more effectively, reducing the relative velocity between particle and air, and are thus relatively unaffected by fluid drag. Although the restrictive geometry of the glass-walled chute greatly enhances drag effects, results from the chute experiments imply that such effects may be important in other collision-dominated flows of small particles in air or more viscous fluids. In the simulation, fluid

drag effects are incorporated by assuming that the fluid within the chute is still, and that the drag force is proportional to the square of the magnitude of the velocity. The simulation assumes that particle rotations are unaffected by fluid drag.

Simulation Chute. Major features of the physical experiments are incorporated into the simulation in the following way: the simulation chute consists of two parallel, vertical planar boundaries having the frictional properties of glass; a 5-m long bed of fixed spheres inclined at 42.75 deg centered between the planar boundaries and having the same geometric roughness as the fixed bed; a 5-m long horizontal bed of fixed spheres connected to the downchute end of the inclined bed and a short vertical "backstop". The length of the simulation chute is thus considerably longer than the physical one to allow greater spatial evolution of the simulated flows than was practical in the laboratory.

The V-shaped hopper and inclined tray used to feed particles into the chute was simulated by adding groups of 100 particles (the width of the inclined tray was 60 cm, or 100 particle diameters) into the simulation at a constant interval corresponding to the two fluxes measured from the films in the physical experiments (0.0448 s for the 2230 particles s^{-1} flow and 0.0781 s for the 1280 particles s^{-1} flow). The particles, each having a small random velocity normal to the chute sidewalls, were introduced along a horizontal line positioned at the same elevation as the lip of the inclined tray in the physical experiments, and allowed to freely accelerate downward until reaching the fixed bed.

The simulations employ different versions of vectorized Fortran code for Cray YMP and IBM 3090 platforms. Typical computation times for flows of about 10,000 particles were on the order of one CPU hour per second of real time, the actual time varying by up to a factor of ten, depending on material properties of the particles (computation time proportional to the square root of the particle stiffness), and bulk density of the flow (computation time roughly proportional to the number of pairs of contacting particles). Comparison simulations using identical input on the two platforms produced statistically identical results.

Comparison of Physical Experiments and Computer Simulations

Computing the velocities and rotations of individual particles and the density of the flow from the location of particle centers and dot positions on film frames from the physical experiments is conceptually straightforward, although it entails numerous practical difficulties. A Cartesian coordinate system (Fig. 1) is set up with origin located on the line of centers of the fixed bed spheres and axes oriented upward normal to the bed and downchute parallel to it. The usable field of view in each film was about 8.35 cm in the bed-parallel (x) direction and 11.1 cm in the bed-normal (y) direction; the center of the field was about 70 cm upstream of the chute outlet. The flow is divided into bed-parallel layers or bins two particle diameters thick, and the desired quantities are calculated for each bin. All of a particular particle property (e.g., its mass) is applied to the bin containing the particle center. The area of the bin nearest the bed used to calculate the bulk density excludes that area unavailable to the centers of flow particles. The excluded area is computed assuming the bed-sphere centers are uniformly spaced a distance equal to the mean of the true spacing distribution.

We employed full simulations of the glass-walled chute to study the spatial and temporal evolution of both disperse and dense flows. A second set of calculations using periodic boundary conditions in the downchute direction was used to study the flow response to variations in selected parameters.

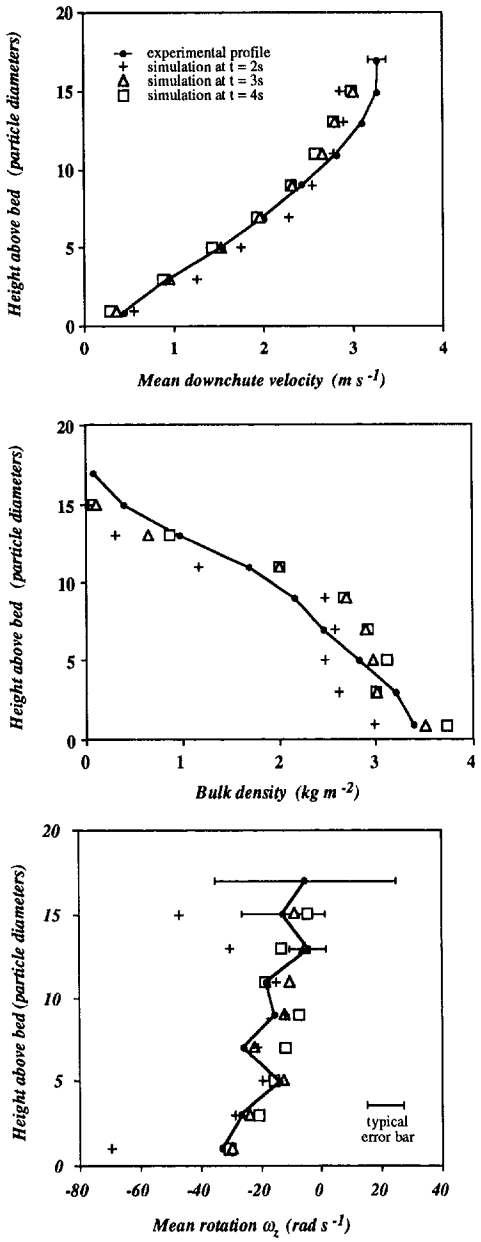

Fig. 3 Time evolution of mean downchute velocity (top), bulk density (middle) and mean in-plane rotation ω_z (bottom) profiles for full simulation of 2230 particles s^{-1} flow at chute location corresponding to filming area for physical experiments. Chute inclination is 42.75 deg, and simulation drag coefficient set at 3.4, the mean value measured in ancillary experiments. Data for t = 5s and t = 6s (not shown) overlies data for t = 4s, indicating nearly steady, uniform flow for $t \geq$ 5s. Error bars for near-bed rotation data points omitted for clarity; typical error bar is shown.

Full Simulations. Particle-scale comparison of full simulations with the physical experiments is a synergistic, iterative process to establish the dominant physics of the flows that must be captured in the computer models. For example, quasi-two-dimensional simulations in which the centers of flow spheres were confined to lie in a vertical plane (thus preventing any sidewall interactions) accelerated down the length of the chute, unless fluid drag forces were increased well beyond the measured values obtained from the chute experiments. Likewise, simulations faithfully reproducing the chute geometry (including frictional sidewalls) while neglecting fluid drag forces also produced accelerating flows. We directly simulated both the disperse and dense flows using the mean value of the fluid drag coefficient as determined from ancillary physical exper-

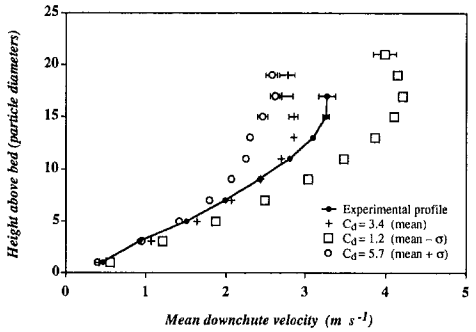

Fig. 4 Effect of drag coefficient on mean downchute velocity profiles from simulations of 2230 particles s^{-1} flow at chute location corresponding to filming area for physical experiments, using periodic boundaries spaced 20-particle diameters apart in the downchute direction. Initial conditions for each simulation from full simulation at t = 2s (drag coefficient in the full simulation set at the mean value determined from ancillary experiments). Error bars underestimate true errors in velocity in highest bins due to repeatedly sampling the same particles passing through the periodic control volume without collisions.

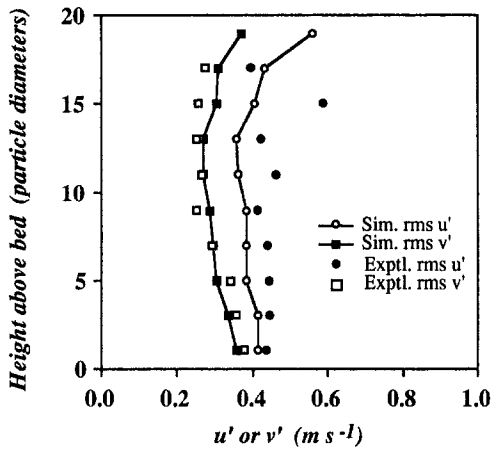

Fig. 5 Root-mean-square fluctuating downchute (u') and bed-normal (v') velocities from physical experiments and simulations using periodic boundaries spaced 20 particle diameters apart in the downchute direction. Initial conditions for each simulation from full simulation at t = 2s, with drag coefficient set at the mean value determined from ancillary experiments. Downchute component is consistently larger than the bed-normal component because particles transported without collisions across the mean-flow velocity gradient in u acquire greater u' than v'.

iments. Figure 3 depicts the time evolution of profiles of the mean downchute velocity, bulk density, and mean in-plane rotations from the simulation and the corresponding profiles from the physical flows for the dense flow (2230 particles s^{-1}); the corresponding mean profiles for the disperse flow are in similar agreement.

The simulated flows are somewhat slower and more compact than the physical flows. We ascribe the differences to the simple fluid-drag model used in the simulation. In particular, the simulation does not properly account for air entrained by the flows, which reduces the relative velocity of the particles with respect to the fluid and thus the fluid drag forces. A more realistic simulation might determine the fluid velocity profile produced by the flowing particles and iterate to find the coupled fluid-particle motion (e.g., Anderson and Haff, 1988). In the next section, we describe a suite of simulations using periodic boundaries in the downchute direction that permit an economical approach to determining the sensitivity of the simulations to variations in such parameters as the fluid drag.

Simulations Using Periodic Boundaries. The number of particles used in simulations of normally steady, uniform flows can be reduced to a computationally tractable number by the artifice of *periodic boundaries*. In the case of nominally steady, uniform, inclined-plane flow, computations include only particles within a small control volume; when a particle passes through the downchute boundary of the control volume, it is reintroduced at the upstream end with identical position and velocity. From the full simulations we extracted positions, velocities, and rotations of flow particles from a 20-particle diameter length of the chute centered on the filming area from the physical experiments. Using these initial conditions, we restarted the simulations with periodic boundaries separated by 20 particle diameters (hereafter designated 20σ). In separate periodic boundary simulations we both doubled and halved the velocities of all particles to see the flow response to perturbations; in each case the flow properties reconverged to those obtained from the full simulations. Furthermore, convergence to nominally steady, uniform flow occurred in 2–4 seconds, which is similar to that observed in the physical experiments.

Using the same 20σ initial conditions, we set the fluid drag coefficient one standard deviation above and below the experimentally measured value; the resulting simulated profiles bracket the corresponding ones from the physical experiments. Figure 4 depicts drag effects on the mean downchute velocity profile for three simulations of the dense flow. Simulations in which the chute width was decreased from the experimental value exhibited higher mean velocities, particularly within a few particle diameters of the bed, but the increase in total flux was small. Increasing the chute width decreased the total flux. Simulations of disperse flows were generally more sensitive to variations in fluid drag and chute geometry than simulations of the dense flows.

We used periodic boundary simulations to generate statistics of fluctuating quantities for comparison with the physical experiments. Although the distributions of the fluctuations form the foundation for micromechanical theories of grain flow, they are among the most difficult quantities to obtain experimentally because the sample size is typically small, and thus the concomitant uncertainty in the desired fluctuating quantities is large. Also, in flows having large gradients in mean quantities, partitioning the flow into bins can produce erroneous estimates of fluctuating components (Drake, 1991). We typically sampled the simulated flows at 0.1s intervals, a period long enough to ensure statistical independence of samples at heights less than about 25 particle diameters above the bed. Higher in the flows, however, the collision rate can be comparable to the sampling rate, and thus particles on long collisionless trajectories may pass through the periodic volume many times, producing spurious estimates of fluctuating quantities. Because of these considerations, we concentrated our simulation efforts on the 2230 particle s^{-1} flow because the statistical uncertainties in experimentally measured fluctuating quantities for the disperse, 1280 particles s^{-1} flow preclude meaningful comparison with the fluctuating quantities obtained from the simulations.

Fluctuating quantities from the simulated flows exhibit many of the distinctive features measured in the physical experiments. For example, the downchute (u') and bed-normal (v') fluctuation velocities are distinctly anisotropic (Fig. 5). The anisotropy is particularly prominent in low-bulk density, high-shear regions of the flow (Richman, 1989) and arises because particles transported parallel to the mean-flow velocity gradient in u acquire greater u' relative to v' merely by virtue of collisionless travel.

Conclusion

Comparison of physical experiments with results of computer simulations of collision-dominated granular flows reveals several important points and caveats for future work. The glass-walled chute flows considered here provide an extremely

stringent test of the simulations, and emphasize the sensitivity of the flows to details of the chute geometry and entrance conditions, and in particular, the nature of such extraneous forces as fluid drag. A useful rule of thumb for collision-dominated flows in the glass-walled chute is that the velocity of the entrained air is about half the mean-particle velocity at any given level in the flow. Flows having high bulk densities entrain air more effectively, reducing the relative velocity between particle and air, and are thus relatively unaffected by fluid drag. Although the restrictive geometry of the glass-walled chute greatly enhances drag effects, our results imply that such effects may be important in many applications involving collision-dominated flows of small particles in air or more viscous fluids.

Computationally efficient, robust particle-interaction models incorporating only measurable parameters successfully describe the statistics of the motion of individual particles in the glass-walled chute flows. For collision-dominated flows the normal stiffness can be decreased considerably (thus increasing the fixed calculational time step) provided that the concomitant increase in particle overlap is acceptable within the context of the simulation. In dense flows or quasi-static calculations in which particles may be in nearly continuous contact, changes in the stiffness directly affect wave speeds and other quantities of interest; and thus caution must be exercised in decreasing the stiffness for computational efficiency.

Acknowledgments

T. G. Drake acknowledges the valuable assistance of D. N. Shirley, Cray Research, and the support of the Institute of Geophysics and Planetary Physics at Lawrence Livermore National Laboratory; the Office of Academic Computing, University of California, Los Angeles; the San Diego Supercomputer Center; and the Office of Naval Research, grant N00014-90-J-1451. Partial support for this work was obtained from the U.S. Department of Energy Office of Fossil Energy, Advanced Research and Technology Development, administered through the Pittsburgh Energy Technology Center, Pittsburgh, PA. Work performed under the auspices of the U.S. Department of Energy by the Lawrence Livermore National Laboratory under Contract W-7405-Eng-48.

References

Anderson, R. S., and Haff, P. K., 1988, "Simulation of Eolian Saltation," *Science*, Vol. 241, pp. 820–823.

Cundall, P. A., and Strack, O. D. L., 1979, "A Discrete Numerical Model for Granular Assemblies," *Geotechnique*, Vol. 29, pp. 47–65.

Drake, T. G., 1988, "Experimental Flows of Granular Material," Ph.D. dissertation, University of California, Los Angeles, CA.

Drake, T. G., 1990, "Structural Features in Granular Flows," *Journal of Geophysical Research*, Vol. 95, pp. 8681–8696.

Drake, T. G., 1991, "Granular Flow: Physical Experiments and Their Implications for Microstructural Theories," *Journal of Fluid Mechanics*, Vol. 225, pp. 121–152.

Johnson, K. L., 1985, *Contact Mechanics*, Cambridge University Press, Cambridge, U.K.

Lun, C. K. K., Savage, S. B., Jeffery, D. J., and Chepurniy, N., 1984, "Kinetic Theory for Granular Flow: Inelastic Particles in Couette Flow and Slightly Inelastic Particles in a General Flow Field," *Journal of Fluid Mechanics*, Vol. 140, pp. 223–256.

Mindlin, R. D., and Deresiewicz, H., 1953, "Elastic Spheres Under Varying Oblique Forces," ASME Journal of Applied Mechanics, Vol. 21, pp. 237–244.

Mullier, M., Tüzün, U., and Walton, O. R., 1991, "A Single-Particle Friction Cell for Measuring Contact Frictional Properties of Granular Materials," *Powder Technology*, Vol. 65, pp. 61–74.

Richman, M. W., 1989, "The Source of Second Moment in Dilute Granular Flows of Highly Inelastic Spheres," *Journal of Rheology*, Vol. 33, pp. 1293–1306.

Soga, N., and Anderson, O. L., 1967, "Elastic Properties of Tektites Measured by Resonant Sphere Technique," *Journal of Geophysical Research*, Vol. 72, pp. 1733–1739.

Walton, O. R., 1993a, "Numerical Simulation of Inclined Chute Flows of Monodisperse, Inelastic, Frictional Spheres," *Mechanics of Materials*, Vol. 16, pp. 239–247.

Walton, O. R., 1993b, "Numerical Simulation of Inelastic, Frictional Particle-Particle Interactions," *Particulate Two-Phase Flow*, M. C. Roco, ed., Butterworth-Heineman, Boston, pp. 884–911.

Walton, O. R., and Braun, R. L., 1986a, "Viscosity, Granular-Temperature & Stress Calculations for Shearing Assemblies of Inelastic, Frictional Disks," *Journal of Rheology*, Vol. 30, pp. 949–980.

Walton, O. R., and Braun, R. L., 1986b, "Stress Calculations for Assemblies of Inelastic Spheres in Uniform Shear," *Acta Mechanica*, Vol. 63, pp. 45–60.

APPENDIX

Material properties of cellulose acetate spheres

Diameter σ	5.99 ± 0.03 mm	Micrometer measurement
Mass m	0.1481 ± 0.002 g	Direct measurement
Density ρ	1.319 g cm^{-2}	Calculated from σ and m
Poisson's ratio ν	0.28	Free-oscillation method (estimate)[1]
Young's modulus E	3.2×10^{10} dynes cm^{-2}	Free-oscillation method (estimate)[1]
Shear modulus G	1.3×10^{10} dynes cm^{-2}	Calculated from E and ν
Strength Y	3.3×10^{8} dynes cm^{-2}	Eastman Bulletin MB-34C
Hardness H	9.3×10^{8} dynes cm^{-2}	Calculated from $1.1Y = 0.39\ H^2$
Friction coefficient μ	0.41 ± 0.02	Slow slider measurement[3] (particle/particle)
Friction coefficient μ_g	0.24 ± 0.07	Kinematic sliding measurement (particle/glass)

[1]Free-oscillation method (e.g., Soga and Anderson, 1967) has not been reliably tested for plastics
[2]Johnson (1985)
[3]Tüzün (personal communication, 1987)

H. A. Wienecke

J. R. Brockenbrough
Mem. ASME

A. D. Romanko

Alcoa Laboratories,
Alcoa Center, PA 15069

A Three-Dimensional Unit Cell Model With Application Toward Particulate Composites

A formulation of a fully three-dimensional unit cell model is presented for uniform general deformation at a point in a composite material. The unit cell model is constructed as a finite element discretization of the unit cube. General displacement periodicity boundary conditions are prescribed such that the cell may be considered as a representative volume element of material. As a particular application of the model, the problem of determining the least anisotropic periodic model of a particulate composite is considered, and comparisons are made with bounds for elastic two-phase composites possessing cubic symmetry.

1 Introduction

This paper is concerned with the development of a three-dimensional unit cell model for multiphase materials that can represent arbitrary particulate microgeometries. An assumption of periodicity is made such that the entire solid may be considered as a replication of the unit cell. Conceptually the development of the model is similar to the periodic hexagonal array (PHA) model of Teply and Dvorak (1988) for deformations of a continuous fiber composite. In their model, the unit cell geometry is an equilateral triangle whose vertices coincide with adjacent fiber centers such that each unit cell contains one-sixth of three fibers. General periodicity boundary conditions are prescribed so that during deformation, the cell will continually tile space. For continuous fiber composites, the PHA model has the advantage that it is the only periodic arrangement of fibers that yields an elastically transversely isotropic response. Thus, in this sense the PHA represents an ideal microgeometry. Although the PHA model of Teply and Dvorak (1988) was restricted to periodic arrangements of fibers, arbitrary spatial arrangement of fibers which correspond to actual microgeometries are of interest. With this in mind, Brockenbrough et al. (1991) formulated a square unit cell model and studied the response of an aluminum-boron continuous fiber composite containing random arrangements of boron fibers. At a fixed volume fraction of fibers, it was found that under transverse loading, the spatial arrangement of fibers can have a large effect on the overall material response. Also it was found that a hexagonal array of circular fibers behaves more like a random array of fibers than any other periodic model. Recently extensions of this work that incorporate actual microstructural geometry within a two-dimensional unit cell model have been reported by Sautter et al. (1992) and Brockenbrough et al. (1992).

The three-dimensional unit cell geometry of a truncated octahedron has been used by Dib and Rodin (1991) in studies of creep of polycrystals due to grain boundary sliding. While this unit cell could be adopted for the study of multiphase materials, a simpler unit cell geometry is the unit cube. Unit cell models based on a unit cube have been used by Hom and McMeeking (1991), and Nemat-Nassar et al. (1982). These formulations were restricted to simple loading states and simple cubic arrangements of the second phase. Although the unit cube is a particularly bad representation of a grain for polycrystal models, it is well suited to the study of multiphase materials. It can represent both random microgeometries and those based on cubic symmetry. The arrangements based on cubic symmetry have a distinguished position in that they are the least anisotropic periodic arrangements. It is the development of the unit cube as a unit cell for arbitrary microgeometries under general deformations that forms the subject of this paper.

2 Unit Cell Formulation

Here we formulate the unit cell boundary conditions for finite periodic deformation within a full Lagrangian framework. Let X_1, X_2, and X_3 be rectangular Cartesian coordinates such that the undeformed unit cell occupies the unit cube $[0, 1] \times [0, 1] \times [0, 1]$ at time $t = 0$. Let $\mathbf{u}(\mathbf{X}, t)$ be the displacement of the material point initially at $\mathbf{X}$. To consider the unit cell as a representative volume element of material, boundary conditions need to be applied that enforce general periodic deformation. For two-dimensional deformation, general periodic boundary conditions have been given by Nagpal, McClintock, Berg, and Subudhi (1972). Conditions for general periodic deformation of a two-dimensional hexagonal

Contributed by the Applied Mechanics Division of THE AMERICAN SOCIETY OF MECHANICAL ENGINEERS for publication in the ASME JOURNAL OF APPLIED MECHANICS.

Discussion on this paper should be addressed to the Technical Editor, Professor Lewis T. Wheeler, Department of Mechanical Engineering, University of Houston, Houston, TX 77204-4792, and will be accepted until four months after final publication of the paper itself in the ASME JOURNAL OF APPLIED MECHANICS.

Manuscript received by the ASME Applied Mechanics Division, Mar. 10, 1993; final revision, Jan. 11, 1994. Associate Technical Editor: G. J. Dvorak.

array have been derived by Teply and Dvorjak (1988) and used to construct a finite element unit cell of a continuous fiber composite. For the three-dimensional deformation of the cube, periodicity can be expressed as constraints between displacements on opposing faces of the cube. Material points initially on the positive X_1 face are constrained according to

$$\mathbf{u}(1, X_2, X_3, t) = \mathbf{u}(0, X_2, X_3, t) + \mathbf{u}(1, 0, 0, t) - \mathbf{u}(0, 0, 0, t). \quad (1)$$

While material points initially on the positive X_2 face are constrained according to

$$\mathbf{u}(X_1, 1, X_3, t) = \mathbf{u}(X_1, 0, X_3, t) + \mathbf{u}(0, 1, 0, t) - \mathbf{u}(0, 0, 0, t), \quad (2)$$

and material points initially on the positive X_3 face are constrained according to

$$\mathbf{u}(X_1, X_2, 1, t) = \mathbf{u}(X_1, X_2, 0, t) + \mathbf{u}(0, 0, 1, t) - \mathbf{u}(0, 0, 0, t), \quad (3)$$

material points initially on more than one face are not over constrained because Eqs. (1)–(3) are redundant for those points. The boundary conditions of Eqs. (1)–(3) are equivalent to the condition that the deforming unit cell remain space-tiling. The vertices of the unit cell remain vertices of a parallelepiped and opposing faces of the unit cell remain surfaces that are translations of each other. Note that the faces need not remain flat. Rigid-body motions are eliminated by requiring

$$\mathbf{u}(\mathbf{0}, t) = \mathbf{0},$$

and

$$u_2(1, 0, 0, t) = u_3(1, 0, 0, t) = u_3(0, 1, 0, t) = 0. \quad (4)$$

and $v(t)$ is its current volume. Quantities of interest in the current configuration are the averages of the Cauchy stress, $\bar{\sigma}$ and its work conjugate strain measure, the rate of deformation, $\bar{\mathbf{D}}$. Let $\mathbf{x} = \mathbf{X} + \mathbf{u}(\mathbf{X}, t)$ be the position of the material point initially at $\mathbf{X}$ and let $\mathbf{v}(\mathbf{x}, t)$ be velocity in the unit cell. The boundary of $V(t)$ is a surface $A(t)$ with outward unit normal $\mathbf{n}(\mathbf{x}, t)$. The volume integral defining $\bar{\mathbf{D}}$ can be transformed to a surface integral as

$$\bar{\mathbf{D}} = \frac{1}{v}\int_V \mathrm{sym}\left(\frac{\partial \mathbf{v}}{\partial \mathbf{x}}\right) = \frac{1}{v}\int_A \mathrm{sym}(\mathbf{v} \otimes \mathbf{n}) \quad (6)$$

where $\otimes$ denotes the tensor product, and sym($\mathbf{T}$) is the symmetric part of any second-order tensor $\mathbf{T}$. The area A is composed of six surfaces $A_{\pm i}$ which are the images under $\mathbf{x}(\mathbf{X}, t)$ of the $\pm X_i$ faces of the undeformed unit cell. Let $\dot{\mathbf{u}} = \partial \mathbf{u}/\partial t = \mathbf{v}(\mathbf{x}(\mathbf{X}, t), t)$. Also let $\mathbf{a} = \mathbf{u}(1, 0, 0, t)$, $\mathbf{b} = \mathbf{u}(0, 1, 0, t)$, $\mathbf{c} = \mathbf{u}(0, 0, 1, t)$, $\dot{\mathbf{a}} = \dot{\mathbf{u}}(1, 0, 0, t)$, $\dot{\mathbf{b}} = \dot{\mathbf{u}}(0, 1, 0, t)$, and $\dot{\mathbf{c}} = \dot{\mathbf{u}}(0, 0, 1, t)$ denote the displacements and velocities of the free vertex points. If the integral over A is broken up into integrals over the $A_{\pm i}$ and boundary conditions of Eqs. (1)–(4) are employed, then Eq. (6) reduces to

$$\bar{\mathbf{D}} = \frac{1}{v}\mathrm{sym}\left(\dot{\mathbf{a}} \otimes \int_{A_{+1}} \mathbf{n} + \dot{\mathbf{b}} \otimes \int_{A_{+2}} \mathbf{n} + \dot{\mathbf{c}} \otimes \int_{A_{+3}} \mathbf{n}\right). \quad (7)$$

The periodicity conditions imply that $v(t)$ is equal to the volume of the parallelepiped defined by the vertices of the unit cell. The integrals in Eq. (7) are evaluated by using the periodicity conditions and the statement that the integral of the unit normal over a simple closed surface is zero. The result is the integral of $\mathbf{n}$ over A_{+i} is equal to the area of the parallelogram defined by the vertices of A_{+i} times a unit normal to that parallelogram. Thus the six degrees-of-freedom of the unit cell vertices determine the overall rate of deformation as

$$\bar{\mathbf{D}} = \begin{bmatrix} \dfrac{\dot{a}_1}{a_1+1} & \dfrac{(a_1+1)\dot{b}_1 - b_1\dot{a}_1}{2(a_1+1)(b_2+1)} & \dfrac{(b_1c_2 - c_1b_2 - c_1)\dot{a}_1 - (a_1c_2 + c_2)\dot{b}_1 + (a_1b_2 + a_1 + b_2 + 1)\dot{c}_1}{2(a_1+1)(b_2+1)(c_3+1)} \\ & \dfrac{\dot{b}_2}{b_2+1} & \dfrac{(b_2+1)\dot{c}_2 - c_2\dot{b}_2}{2(b_2+1)(c_3+1)} \\ \mathrm{SYM} & & \dfrac{\dot{c}_3}{c_3+1} \end{bmatrix}. \quad (8)$$

For purposes of calculating the overall response of the material at a point that is represented by the unit cell, the volumetric averages over the unit cell are of interest. These averages will be denoted by an overbar. Thus for any function f,

$$\bar{f} = \frac{1}{v}\int_V f dV, \quad (5)$$

where $V(t)$ is the current region occupied by the unit cell and

Conversely, the overall rate of deformation determines the six degrees-of-freedom of the unit cell vertices. This is shown by rewriting Eq. (8) as

$$\begin{bmatrix} \dot{a}_1 \\ \dot{b}_2 \\ \dot{c}_3 \\ \dot{b}_1 \\ \dot{c}_2 \\ \dot{c}_1 \end{bmatrix} = \begin{bmatrix} \bar{D}_{11} & 0 & 0 & 0 & 0 & 0 \\ 0 & \bar{D}_{22} & 0 & 0 & 0 & 0 \\ 0 & 0 & \bar{D}_{33} & 0 & 0 & 0 \\ 0 & 2\bar{D}_{12} & 0 & \dot{D}_{11} & 0 & 0 \\ 0 & 0 & 2\bar{D}_{23} & 0 & \bar{D}_{22} & 0 \\ 0 & 0 & 2\bar{D}_{13} & 0 & 2\bar{D}_{12} & \bar{D}_{11} \end{bmatrix} \begin{bmatrix} a_1 \\ b_2 \\ c_3 \\ b_1 \\ c_2 \\ c_1 \end{bmatrix} + \begin{bmatrix} \bar{D}_{11} \\ \bar{D}_{22} \\ \bar{D}_{33} \\ 2\bar{D}_{12} \\ 2\bar{D}_{23} \\ 2\bar{D}_{13} \end{bmatrix}. \quad (9)$$

Equations (8), (9) are valid for finite strains under the special case of the periodicity conditions, Eqs. (1)–(4).

Under uniform far-field rate of deformation, the average Cauchy stress $\bar{\sigma}$ in the unit cell is computed by using the relation that the average of the deformation power is equal

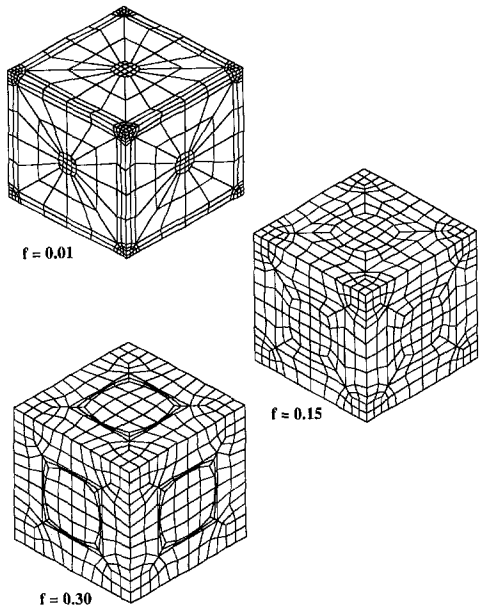

Fig. 1 BCC mesh, refinement level 1

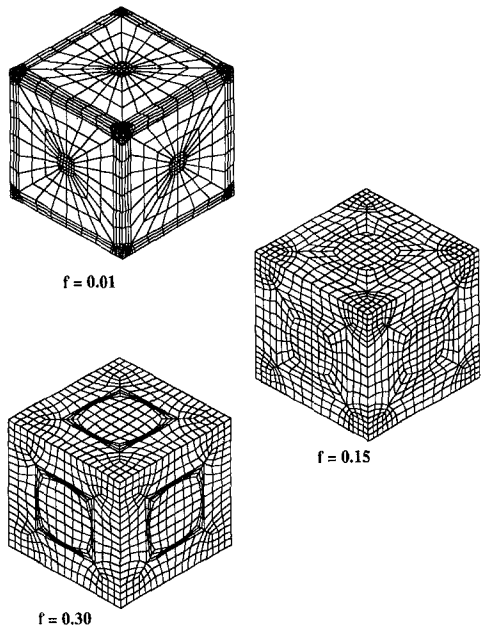

Fig. 2 BCC mesh, refinement level 2

to the power computed from the stress and deformation averages, that is

$$\overline{\sigma \cdot \mathbf{D}} = \bar{\sigma} \cdot \bar{\mathbf{D}}. \tag{10}$$

The deformation power in the unit cell equals the power delivered to the unit cell by the forces conjugate to the degrees-of-freedom of the vertices. Let f_{a1} be the force conjugate to a_1 etc. Then

$$\bar{\sigma} \cdot \bar{\mathbf{D}} = \frac{f_{a1}\dot{a}_1 + f_{b1}\dot{b}_1 + f_{b2}\dot{b}_2 + f_{c1}\dot{c}_1 + f_{c2}\dot{c}_2 + f_{c3}\dot{c}_3}{(a_1 + 1)(b_2 + 1)(c_3 + 1)}. \tag{11}$$

In particular, Eq. (11) holds when all but one of the free vertex velocities are zero. Thus (11) provides six equations that determine the six components of overall stress,

spheres in microgeometries that possess cubic symmetry. Thus the undeformed microstructure is modeled as spheres in each array of cubic symmetry: simple cubic (SC), face-centered cubic (FCC), and body-centered cubic (BCC). In each model, the undeformed unit cell is the smallest cube that has a particle center at each vertex. Convergence of the solution to the overall elastic response was shown by successive mesh refinement. Figure 1 shows refinement level 1 of the BCC mesh at three volume fractions, f, and $f = 1$ percent, $f = 15$ percent, and $f = 30$ percent. Figure 2 shows refinement level 2 of the same mesh. At refinement level 1, the SC, BCC, and FCC meshes contain 448, 1280, and 2048 elements, respectively. Refinement level 2 increases these numbers by a factor of $(3/2)^3$. The meshes are automatically

$$\bar{\sigma} = \begin{bmatrix} \dfrac{(a_1+1)f_{a1} + b_1 f_{b1} + c_1 f_{c1}}{(a_1+1)(b_2+1)(c_3+1)} & \dfrac{(b_2+1)f_{b1} + c_2 f_{c1}}{(a_1+1)(b_2+1)(c_3+1)} & \dfrac{f_{c1}}{(a_1+1)(b_2+1)} \\ \dfrac{(b_2+1)f_{b1} + c_2 f_{c1}}{(a_1+1)(b_2+1)(c_3+1)} & \dfrac{(b_2+1)f_{b2} + c_2 f_{c2}}{(a_1+1)(b_2+1)(c_3+1)} & \dfrac{f_{c2}}{(a_1+1)(b_2+1)} \\ \dfrac{f_{c1}}{(a_1+1)(b_2+1)} & \dfrac{f_{c2}}{(a_1+1)(b_2+1)} & \dfrac{f_{c3}}{(a_1+1)(b_2+1)} \end{bmatrix}. \tag{12}$$

3 Numerical Implementation

A numerical implementation of the above unit cell formulation was considered within the context of a finite element discretization of the unit cube. The boundary conditions of Eqs. (1)–(4) are set up with constraints on pairs of nodes which are initially located in similar positions on opposite faces. A given overall deformation history is modeled by integrating Eq. (9) to determine the appropriate vertex node displacement history. Overall stress history is then given by Eq. (12).

To implement the unit cell model for a specific problem and to make contact with other results, consider the problem of determining the overall elastic response of a particulate composite where the particles can be idealized as equisized

constructed at any volume fraction between 1 percent and 30 percent by a command file procedure written in PATRAN (1990). Each mesh is composed of single integration eight-noded bricks, and the finite element code ABAQUS is used for analysis. ABAQUS limits the singular deformation modes of these elements with an artificial stiffness equal to 0.005 times the elastic shear modulus. Spurious modes are thus rendered negligible in elastic analysis and in small strain elastoplastic analysis. The periodicity conditions of Eqs. (1)–(3) are enforced by using linear multipoint constraints between degrees-of-freedom of nodal points on opposing faces of the cube. The implementation of these constraints within ABAQUS requires identical meshes on opposing cube faces. In fact the meshes used possess cubic symmetry. ABAQUS uses a wavefront scheme to solve equations and a

Table 1(*a*) Elastic constants for cubic arrays of rigid spheres

	$\bar{\kappa}/\kappa$			$\bar{\mu}/\mu$			$\bar{\mu}^*/\mu$		
f	SC	FCC	BCC	SC	FCC	BCC	SC	FCC	BCC
0.10	1.184	1.181	1.188	1.219	1.244	1.270	1.298	1.226	1.257
0.20	1.409	1.412	1.405	1.457	1.594	1.565	1.737	1.525	1.489
0.30	1.702	1.687	1.696	1.750	1.975	2.020	2.416	1.824	1.823

Table 1(*b*) Elastic constants for cubic arrays of voids

	$\bar{\kappa}/\kappa$			$\bar{\mu}/\mu$			$\bar{\mu}^*/\mu$		
f	SC	FCC	BCC	SC	FCC	BCC	SC	FCC	BCC
0.10	0.778	0.776	0.774	0.814	0.830	0.840	0.847	0.821	0.834
0.20	0.605	0.611	0.604	0.642	0.695	0.684	0.724	0.675	0.660
0.30	0.468	0.464	0.469	0.494	0.553	0.552	0.616	0.519	0.521

Table 2 Anisotropy measure for cubic arrays of rigid spheres and voids

	a* - Voids			a* - Rigid Spheres		
f	SC	FCC	BCC	SC	FCC	BCC
0.10	0.023	0.007	0.005	0.037	0.009	0.007
0.20	0.072	0.019	0.023	0.109	0.027	0.031
0.30	0.139	0.040	0.037	0.212	0.050	0.064

measure of the CPU time required for solution is the square of the average wavefront. For the level 1 BCC mesh shown in Fig. 1, the implementation of the periodicity conditions causes the wavefront to increase by a factor of 1.42 over the motion of the cube without the periodicity constraints. Thus the implementation of general periodicity conditions doubles the necessary solution time.

Since each model possesses cubic symmetry, the overall elastic response is governed by the three elastic constants $\bar{C}_{1111}$, $\bar{C}_{1122}$, and $\bar{C}_{1212}$. These constants computed with a level 1 mesh differ by less than one percent from the same constants computed with a level 2 mesh. The discrepancy is less than one percent regardless of constituent materials and regardless of volume fraction up to thirty percent. Solutions for the elastic constants with the level 1 mesh will be used to make contact with other results. For purposes of comparison, the bulk modulus and the two shear moduli are employed.

$$\bar{\kappa} = \frac{1}{3}\bar{C}_{1111} + \frac{2}{3}\bar{C}_{1122}$$

$$\bar{\mu} = \bar{C}_{1212}$$

$$\bar{\mu}^* = \frac{1}{2}\bar{C}_{1111} - \frac{1}{2}\bar{C}_{1122}. \tag{13}$$

4 Results and Comparisons

Table 1 contains the elastic constants computed with the unit cell model for the limiting states of rigid inclusions and voids at volume fractions of $f = 10$ percent, $f = 20$ percent, and $f = 30$ percent. The matrix Poisson's ratio is fixed at $\nu = 0.3$. Elastic constants in the table are normalized with respect to the elastic constants of the matrix. Rigid inclusions were modeled as isotropic elastic material with 1000 times greater moduli than the matrix. Correspondingly, voids were modeled as isotropic elastic material with 1000 times smaller moduli than the matrix. These moduli ratios for voids and rigid spheres were found to provide converged results for overall moduli. The bulk moduli of all three cubic arrays are similar for all the cubic arrangements. The FCC and BCC array possess similar shear moduli for both rigid particles and voids. The SC array has a softer response in the first shear modulus, $\bar{\mu}$, and a stiffer response in the second shear modulus, $\bar{\mu}^*$.

Table 3(*a*) Comparison of elastic constants for BCC rigid spheres

	$\bar{\kappa}/\kappa$			$\bar{\mu}/\mu$			$\bar{\mu}^*/\mu$		
f	UC	R	A-lb	UC	R	A-lb	UC	R	A-lb
0.10	1.188	1.180	1.179	1.270	1.240	1.166	1.257	1.224	1.166
0.20	1.405	1.404	1.403	1.565	1.552	1.374	1.489	1.489	1.374
0.30	1.696	1.693	1.691	2.020	1.963	1.641	1.823	1.821	1.641

Table 3(*b*) Comparison of elastic constants for BCC voids

	$\bar{\kappa}/\kappa$			$\bar{\mu}/\mu$			$\bar{\mu}^*/\mu$		
f	UC	R	A-ub	UC	R	A-ub	UC	R	A-ub
0.10	0.774	0.774	0.774	0.840	0.829	0.854	0.834	0.819	0.825
0.20	0.604	0.604	0.604	0.684	0.686	0.722	0.660	0.662	0.677
0.30	0.469	0.471	0.471	0.552	0.564	0.603	0.521	0.527	0.550

To determine the periodic arrangement with the least anisotropy, an anisotropy measure is introduced as, a^*,

$$a^* = \max \left| \frac{\bar{C}_{1111}(\alpha,\beta,\gamma) - \bar{C}_{1122}(\alpha,\beta,\gamma) - 2\bar{C}_{1212}(\alpha,\beta,\gamma)}{\bar{C}_{1111}(\alpha,\beta,\gamma)} \right| \tag{14}$$

where the maximum is over all rotations of the lattice. This parameter is a generalization of one introduced by Nemat-Nasser, Iwakuma, and Hejazi (1982) in the study of the anisotropy associated with SC arrays of inhomogeneities. Table 2 lists the anisotropy measure for each cubic array. The anisotropy associated with rigid spheres is greater than that for voids for all cases. For rigid spheres it is seen that the anisotropies associated with the FCC and BCC arrays are nearly equal while the SC anisotropy is about 3–4 times greater. The situation is similar for voids. Since the FCC and BCC arrays possess about the same degree of anisotropy, the BCC array is preferred as the simpler model.

Table 3 compares the elastic behavior predicted by the unit cell model (UC) for the BCC array to recent calculations of Rodin (1993), (R), and bounds derived for two phase materials possessing cubic symmetry by Avellaneda (1987), (A-b). Rodin's results were obtained by an Eshelby-type equivalent inclusion method which accounts for particle interactions. Always the calculated moduli lie within the Avellaneda upper bounds (A-ub) and the Avellaneda lower bounds (A-lb). For rigid spheres and voids, the calculated results for the bulk modulus are nearly equal to the revelant bound. For the shear moduli there is close agreement between the unit cell calculations and those of Rodin.

Acknowledgment

The authors are grateful to G. J. Rodin of the University of Texas at Austin and J. T. Teply of Alcoa Laboratories for helpful discussions throughout the course of this work.

References

ABAQUS, 1991, 4.9 User's Manual, Hibbitt, Karlsson and Sorensen, Providence, RI.

Avellaneda, M., 1987, "Optimal Bounds and Microgeometries for Elastic Two-Phase Composites," *SIAM Journal of Applied Mathematics*, Vol. 47, pp. 1216–1228.

Brockenbrough, J. R., Suresh, S., and Wienecke, H. A., 1991, "Deformation of Metal-Matrix Composites with Continuous Fibers: Geometrical Effects of Fiber Distribution and Shape," *Shape Metallurgica Materialia*, Vol. 39, No. 5, pp. 735–752.

Brockenbrough, J. R., Hunt, W. H. Jr., and Richmond, O., 1992, "A Reinforced Material Model Using Actual Microstructural Geometry," *Scripta Metallurgica Et Materialia*, Vol. 27, No. 4, pp. 385–390.

Dib, M. W., and Rodin, G. J., 1993, "Three Dimensional Analysis of Creeping Polycrystals Using Periodic Arrays of Truncated Octahedron," *J. Mech. Phys. Solids*, Vol. 41, No. 4, pp. 725–748.

Hom, C. L., and McMeeking, R. M., 1991, "Plastic Flow in Ductile Materials Containing a Cubic Array of Rigid Spheres," *International Journal of Plasticity*, Vol. 8, pp. 239–267.

Nagpal, V., McClintock, F. A., Berg, C. A., and Subudhi, M., 1972, *Foundations of Plasticity*, A. Sawczuk, ed., Noordhoff, pp. 365–387.

Nemat-Nasser, S., Iwakuma, T., and Hejazi, M., 1982, "On Composites with Periodic Structure," *Mechanics of Materials*, Vol. 1, pp. 239–267.

PATRAN, 1990, 2.4 Users Manual, PDA Engineering, Costa Mesa, CA.

Rodin, G. J., 1993, "The Overall Elastic Response of Materials Containing Spherical Inhomogeneities," *International Journal of Solids and Structures*, Vol. 8, No. 14, pp. 1849–1863.

Sautter, M., Dietrich, Ch., Poech, M. H., Schmauder, S., and Fischmeister, H. F., 1992, "Finite Element Modeling of a Transverse-Loaded Fibre Composite," *Computational Material Science*, Vol. 26, pp. 12–22.

Teply, J. L., and Dvorak, G. J., 1988, "Bounds on Overall Instantaneous Properties of Elastic-Plastic Composites," *J. Mech. Phys. Solids*, Vol. 36, pp. 29–58.

C. W. Cai
Professor,
Department of Mechanics,
Zhongshan University,
Guangzhou, P.R. of China

Y. K. Cheung
Professor.

H. C. Chan
Reader.

Department of Civil and
Structural Engineering,
University of Hong Kong,
Pokfulam Road,
Hong Kong

Mode Localization Phenomena in Nearly Periodic Systems

The normal mode localization in nearly periodic systems with one-degree-of-freedom subsystems and a single subsystem departing from the regularity in one, two, and three dimensions has been studied. The closed-frequency equations may be derived by using the U-transformation technique. It is shown that in one- and two-dimensional problems any amount of simple disorder (for stiffness or mass), however small, is sufficient to localize one mode and in three-dimensional systems, a finite threshold of disorder is needed in order to localize one mode. These conclusions are in agreement with those predicted by Hodges.

1 Introduction

Recently, periodic systems have been shown to be sensitive to certain types of periodicity-breaking disorder, resulting in a phenomenon known as normal mode localization. This phenomenon was first predicted by Anderson (1958) in the field of solid-state physics. It was shown that the electron eigenstates in a disordered solid may become localized.

The localized vibrations in periodic structures with some degree of disorder have been investigated by several authors. Hodges (1982) showed that in one dimension, all modes are localized for arbitrarily small extended disorder. Bendiksen (1987) investigated theoretically and numerically the localized modes of vibration in large space structures. A perturbation method (Pierre and Dowell, 1987), (Pierre, Tang, and Dowell, 1987) was developed to obtain the localized modes of the disordered system. Keane and Price (1989) considered a single defect in an otherwise periodic system. The results showed that all the modes extend throughout the structure except for the one where the natural frequency lies in the stop band. The ensemble-averaging procedure was used to study the dynamics of structurally irregular mechanical systems (Hodges and Woodhouse, 1989a) providing some analytical results, while the complementary results from a numerical study were provided (Hodges and Woodhouse, 1989b). However, the methods presented in the aforementioned literatures are limited to one-dimensional problems. In two-dimensional problems, the localization behavior is believed to be similar to that in one dimension insofar as the arbitrarily weak and extended disorder localizes all modes, whereas in three dimensions, it is thought that a finite threshold of disorder is needed in order to localize all modes (Hodges, 1982).

In the present paper, the nearly periodic systems with one-degree-of-freedom subsystems and a single subsystem departing from the regularity are considered. The closed-frequency equations for the nearly periodic systems in one and two dimensions, may be derived by using the U- and double U-transformation methods which have been applied to the static and dynamic analysis of structures with periodicity in one and two directions (Cai et al., 1988; Cheung et al., 1989; Cheung et al., 1988; Chan et al., 1989; and Cai et al., 1990). Incidentally, a modal transformation which is identical to the U-transformation has been used to analyze the response of an infinite periodic chain (Goodman, 1972). In order to analyze the mode localization in three-dimensional periodic systems with a single defect, the U-transformation method has been extended to the triple U-transformation method. In three dimensions, the closed-frequency equation may also be derived by the triple U-transformation method. It is shown that in order to localize one mode, the threshold of disorder is actually in existence.

Contributed by the Applied Mechanics Division of THE AMERICAN SOCIETY OF MECHANICAL ENGINEERS for publication in the ASME JOURNAL OF APPLIED MECHANICS.

Discussion on this paper should be addressed to the Technical Editor, Professor Lewis T. Wheeler, Department of Mechanical Engineering, University of Houston, Houston, TX 77204-4792, and will be accepted until four months after final publication of the paper itself in the ASME JOURNAL OF APPLIED MECHANICS.

Manuscript received by the ASME Applied Mechanics Division, Sept. 17, 1992; final revision, Aug. 27, 1993. Associate Technical Editor: D. J. Inman.

2 One-Dimensional System

The essential behavior of mode localization in nearly periodic structures is best demonstrated using a simple model. A general model is illustrated in Fig. 1(*a*), where each substructure is modeled with one degree-of-freedom and only one substructure is departing from the regularity in both stiffness and mass. In order to apply the U-transformation to uncouple the governing equation, an equivalent system with cyclic

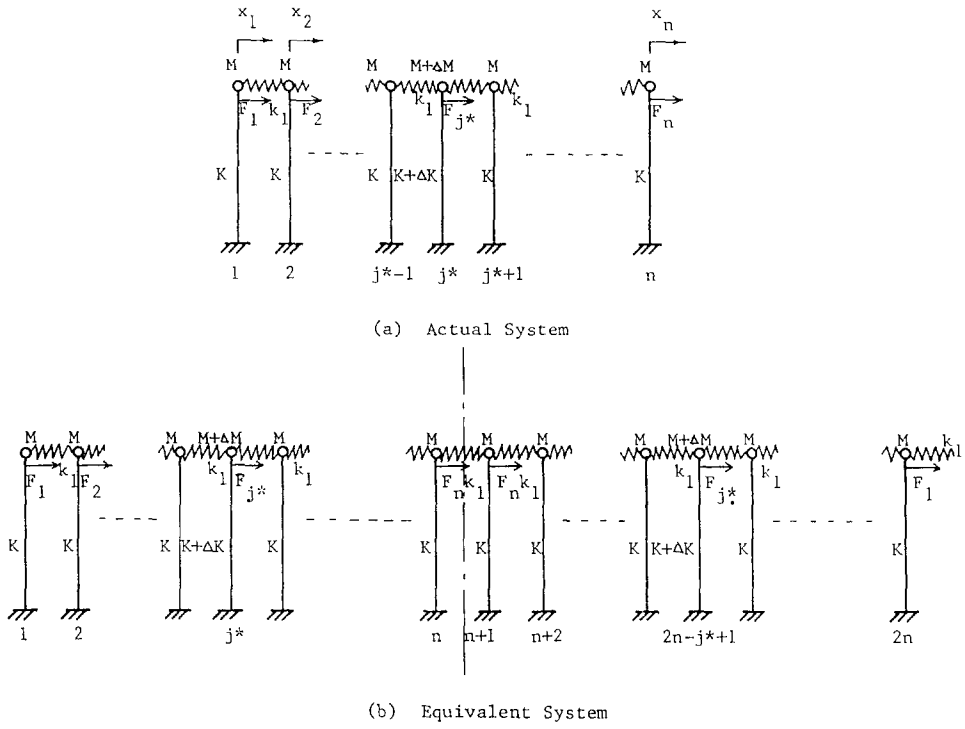

Fig. 1 One-dimensional system

periodicity must be created. In a similar manner to that described (Cheung et al., 1989), the actual system with linear periodicity and n substructures can be replaced by an equivalent system with cyclic periodicity and $2n$ substructures, where the structure is symmetrical but loads are antisymmetrical about the center line as shown in Fig. 1(b) where the first and last ($2n$th) masses are imaginarily jointed by a spring with stiffness k_1 which is not subjected to any load for antisymmetric vibration modes. Therefore, the antisymmetrical modes of the equivalent system are identical to the modes of the actual system. The dynamic equations for all substructures of the equivalent system may be expressed as

$$M\ddot{x}_j + (K + 2k_1)x_j - k_1(x_{j+1} + x_{j-1}) = F_j \qquad j \neq j^*, \quad 2n - j^* + 1 \quad (1)$$

$$(M + \Delta M)\ddot{x}_j + (K + \Delta K + 2k_1)x_j - k_1(x_{j+1} + x_{j-1}) = F_j \qquad j = j^* \quad \text{or} \quad 2n - j^* + 1 \quad (2)$$

where M, K denote the mass and stiffness of ordered subsystem; ΔM, ΔK denote the magnitude of disorder for mass and stiffness, and k_1 denotes the coupling stiffness. j^* denotes the ordinal number of the disordered subsystem; x_j, F_j denote the displacement and load of the jth subsystem. They must satisfy the antisymmetry condition, i.e.,

$$x_j = x_{2n-j+1}$$
$$F_j = F_{2n-j+1} \quad j = 1, 2, \ldots, n \quad (3)$$

where n denotes the total number of subsystems for the actual system.

The equations of natural vibration for the equivalent system may be written in the same form as

$$\left(K + 2k_1 - M\omega^2\right)x_j - k_1(x_{j+1} + x_{j-1}) = F_j \qquad j = 1, 2, \ldots, 2n \quad (4)$$

where ω denotes the natural frequency and

$$F_j = \begin{cases} (\Delta M\omega^2 - \Delta K)x_{j^*} & j = j^*, \quad 2n - j^* + 1 \\ 0 & j \neq j^*, \quad 2n - j^* + 1. \end{cases} \quad (5)$$

One can now apply the U-transformation (Cai et al., 1988) to Eqs. (4) and (5). The U and inverse U-transformation may be defined as

$$x_j = \frac{1}{\sqrt{2n}} \sum_{r=1}^{2n} e^{i(j-1)r\psi} q_r \quad (6)$$

and

$$q_r = \frac{1}{\sqrt{2n}} \sum_{j=1}^{2n} e^{-i(j-1)r\psi} x_j \quad (7)$$

where q_r ($r = 1, 2, \ldots, 2n$) is the image of x_j ($j = 1, 2, \ldots, 2n$) by U-transformation and $\psi = \pi/n$, $i = \sqrt{-1}$.

Equation (4) may be expressed in terms of q_r ($r = 1, 2, \ldots, 2n$) as

$$\left(K + 2k_1 - M\omega^2\right)q_r - 2k_1 \cos r\psi q_r = f_r \quad r = 1, 2 \ldots, 2n \quad (8)$$

in which

$$f_r = \frac{1}{\sqrt{2n}} \sum_{j=1}^{2n} e^{-i(j-1)r\psi} F_j. \quad (9)$$

Substituting Eq. (5) into Eq. (9) yields

$$f_r = \frac{F_j^*}{\sqrt{2n}} \left(e^{ij^* r\psi} + e^{-i(j^*-1)r\psi}\right). \quad (10)$$

The q_r in Eq. (8) may be formally expressed as

$$q_r = f_r / \left(K + 2k_1 - M\omega^2 - 2k_1 \cos r\psi\right). \quad (11)$$

Substituting Eqs. (11) and (10) into Eq. (6) yields

$$x_j = \frac{F_j^*}{2n} \sum_{r=1}^{2n} \frac{\cos(j + j^* - 1)r\psi + \cos(j - j^*)r\psi}{K + 2k_1 - M\omega^2 - 2k_1 \cos r\psi}. \quad (12)$$

It is obvious that the displacements of the equivalent system satisfy the antisymmetry condition (3). Since the system with infinite number of subsystems (i.e., $n \to \infty$) is to be considered, therefore, with no loss of generality, it is assumed that the disordered subsystem is situated in the middle of the actual system with n number of subsystems; i.e., let $n = 2j^* - 1$. For this case, Eq. (12) becomes

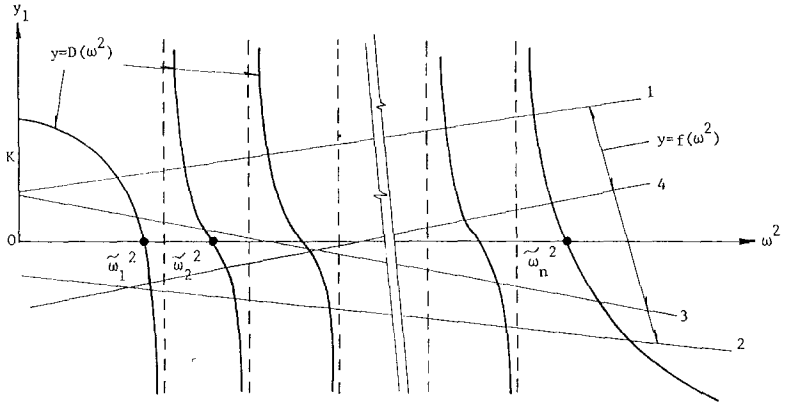

Fig. 2 $D(\omega^2)$ and $f(\omega^2)$

$$x_j = \frac{F_j^*}{n} \sum_{r=2,4\ldots}^{2n} \frac{\cos(j-j^*)r\psi}{K + 2k_1 - M\omega^2 - 2k_1 \cos r\psi} \equiv F_j^* \beta_j \tag{13}$$

where

$$\beta_j = \frac{1}{n} \sum_{r=1}^{n} \frac{\cos(j-j^*)2r\psi}{K + 2k_1 - M\omega^2 - 2k_1 \cos 2r\psi}. \tag{14}$$

Now the frequency equation may be obtained by substituting Eq. (5) and $j = j^*$ into Eq. (13)

$$\Delta M\omega^2 - \Delta K = \frac{1}{\beta_j^*} \tag{15}$$

where

$$\beta_j^* = \frac{1}{n} \sum_{r=1}^{n} 1/\left(K + 2k_1 - M\omega^2 - 2k_1 \cos 2r\psi\right). \tag{16}$$

For the ordered system, i.e., $\Delta M = \Delta K = 0$, the frequency equation may be simplified to

$$K + 2k_1 - M\omega^2 - 2k_1 \cos 2r\psi = 0 \quad r = 1, 2, \ldots, n. \tag{17}$$

The frequencies may be expressed as

$$\tilde{\omega}_{r+1}^2 = \left(K + 2k_1 - 2k_1 \cos\frac{2\pi r}{n}\right)/M \qquad r = 0, 1, 2, \ldots, n-1 \tag{18}$$

where $\tilde{\omega}_r$ $(r = 1, 2, \ldots, j^*)$ denotes the rth frequency for ordered system. Noting that $\tilde{\omega}_{n-r} = \tilde{\omega}_r$, the number of different frequencies is j^*. The lower and upper limits of the pass band are obtained as

$$\omega_L^2 = K/M, \quad \omega_U^2 = (K + 4k_1)/M \tag{19}$$

where ω_L and ω_U denote the lower and upper limits, respectively.

Substituting Eq. (18) into Eq. (16), yields

$$\beta_j^* = \frac{1}{n} \sum_{r=1}^{n} 1/M\left(\tilde{\omega}_r^2 - \omega^2\right) \tag{20}$$

and then the frequency Eq. (15) may be rewritten as

$$f(\omega^2) = D(\omega^2) \tag{21}$$

where

$$f(\omega^2) = \Delta M\omega^2 - \Delta K, \quad D(\omega^2) = nM/\sum_{r=1}^{n} \frac{1}{\tilde{\omega}_r^2 - \omega^2}. \tag{22}$$

The functions f and D of ω^2 may be qualitatively expressed as the curves shown in Fig. 2. The transverse coordinates of the intersections represent the roots for ω^2 of the frequency Eq. (21) and Eq. (22). The function $D(\omega^2)$, shown in Fig. 2, is made up of J^* number of continuous and monotonic drop curves. By observation from Fig. 2 it may be concluded that if $f(\tilde{\omega}_i^2) > 0$, $\omega_i < \tilde{\omega}_i$, and if $f(\tilde{\omega}_i^2) < 0$, $\omega_i > \tilde{\omega}_i$, where ω_i denotes the ith frequency for the disordered system. If and only if ω lies in the stop band, i.e., $\omega^2 < K/M$ or $\omega^2 > (K + 4k_1)/M$, the mode with frequency ω is localized. Four different cases may be obtained from Fig. 2.

1 $f(\tilde{\omega}_L^2) > 0$ and $f(\tilde{\omega}_U^2) \geq 0$, there is one localized mode with ω less than ω_L.

2 $f(\tilde{\omega}_L^2) \leq 0$ and $f(\tilde{\omega}_U^2) < 0$, there is one localized mode with ω greater than ω_U,

3 $f(\tilde{\omega}_L^2) > 0$ and $f(\tilde{\omega}_U^2) < 0$, there are two localized modes with ω less than ω_L and greater than ω_U, respectively.

4 $f(\tilde{\omega}_L^2) \leq 0$ and $f(\tilde{\omega}_U^2) \geq 0$, there is no localized mode.

Noting the definition of $f(\omega^2)$ given in Eq. (22), the above four cases are equivalent to four regions for the disordered parameters as shown in Fig. 3 where the nondimensional parameters ϵ_m, ϵ_k, and ϵ_1 are defined as

$$\epsilon_m = \frac{\Delta M}{M}, \quad \epsilon_k = \frac{\Delta K}{K}, \quad \epsilon_1 = \frac{k_1}{K}. \tag{23}$$

The region 4 may be expressed, in terms of the parameters ϵ_m, ϵ_k, and ϵ_1, as

$$0 \leq \epsilon_k - \epsilon_m \leq 4\epsilon_1\epsilon_m. \tag{24}$$

When the parameters satisfy the above equation, the small level of disorder is not enough to localize one mode. Systems having a strong coupling but with weak disorder fall into this category. However, for the simple case of disorder, i.e., $\epsilon_k \neq 0$, $\epsilon_m = 0$ or $\epsilon_m \neq 0$, $\epsilon_k = 0$, any magnitude of disorder can cause localization of one mode. It is interesting that if

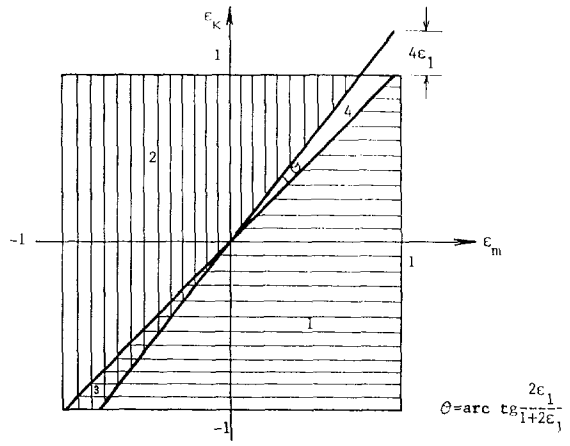

Fig. 3 Four regions for disordered parameters ϵ_m and ϵ_k

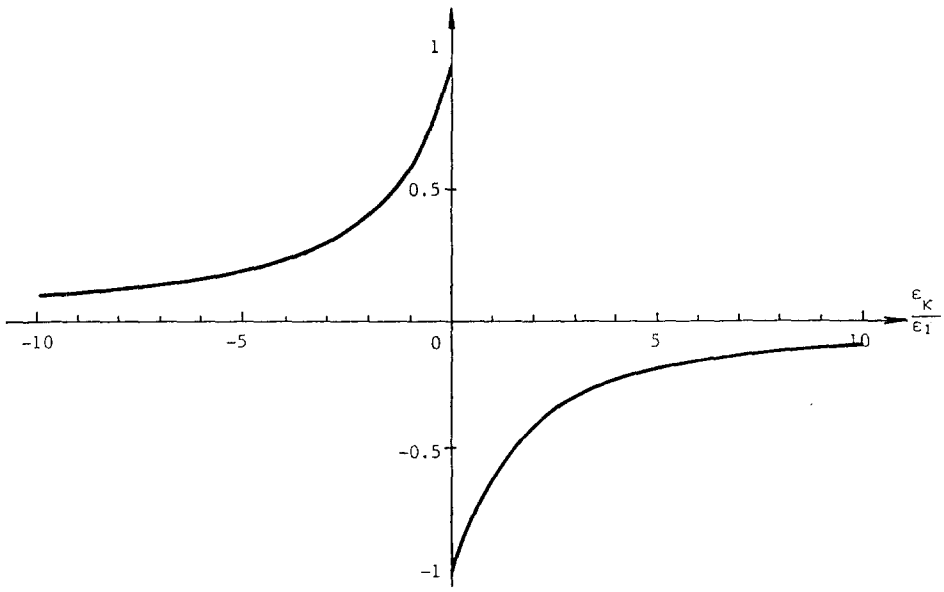

Fig. 4 Attenuation constant ξ versus disorder to coupling (ϵ_k/ϵ_l) ratio

$\epsilon_m < 0$ and $\epsilon_k = \epsilon_m$, i.e., the frequencies of all subsystems are the same, the localized mode still occurs, because the behavior of the disordered subsystem in high-frequency vibration is different from that of the ordered subsystem.

In order to find the solution for ω^2 of Eqs. (15) and (16) consider the limiting case when n is approaching infinity. By letting $n \to \infty$, the limit of the series summation in the right-hand side of Eq. (14) becomes the definite integral (Cheung, Chan and Cai, 1989), i.e.,

$$\lim_{n\to\infty} \beta_j = \frac{1}{\pi}\int_0^{\pi} \frac{\cos(j-j^*)\theta\, d\theta}{K + 2k_1 - M\omega^2 - 2k_1\cos\theta} \tag{25}$$

If the ω lies in the stop bend, the definite integral is in existence and can be expressed by an elementary function. For example,

$$\beta_j^* = \begin{cases} 1/\left(2k_1\sqrt{\eta^2-1}\right) & \text{when } \eta > 1 \\ -1/\left(2k_1\sqrt{\eta^2-1}\right) & \text{when } \eta < -1 \end{cases} \tag{26}$$

$$\beta_{j-1}^* = \beta_{j+1}^* = \begin{cases} \dfrac{1}{2k_1}\left(-1 + \dfrac{\eta}{\sqrt{\eta^2-1}}\right) & \text{when } \eta > 1 \\ \dfrac{1}{2k_1}\left(-1 - \dfrac{\eta}{\sqrt{\eta^2-1}}\right) & \text{when } \eta < -1 \end{cases} \tag{27}$$

where η denotes a frequency parameter defined as

$$\eta = \left(K + 2k_1 - M\omega^2\right)/2k_1, \tag{28}$$

if $\omega < \omega_L$, $\eta > 1$; and if $\omega > \omega_U$, $\eta < -1$.

Substituting Eq. (26) into Eq. (15) and eliminating ω^2 by Eq. (28) yields the frequency equation in terms of the elementary functions

$$-\epsilon_m\eta + \left(\frac{1}{2\epsilon_1} + 1\right)\epsilon_m - \frac{\epsilon_k}{2\epsilon_1} = \operatorname{sgn}(\eta)\sqrt{\eta^2-1} \quad \text{for } |\eta| > 1 \tag{29}$$

where the symbol sgn denotes the sign function.

The frequency parameter corresponding to the localized mode, i.e., $|\eta| > 1$, may be obtained from Eq. (29) as

$$\eta = \left(-\epsilon_m\alpha + \operatorname{sgn}(\eta)\sqrt{\alpha^2 + 4\left(1-\epsilon_m^2\right)}\right)/2\left(1-\epsilon_m^2\right) \tag{30}$$

where $\operatorname{sgn}(\eta)$ can be determined by using Fig. 3 and

$$\alpha = (\epsilon_m - \epsilon_k + 2\epsilon_m\epsilon_1)/\epsilon_1. \tag{31}$$

The attenuation rate ξ of localized modes is defined as

$$\xi = \frac{x_{j^*+1}}{x_{j^*}} = \frac{\beta_{j^*+1}}{\beta_{j^*}}. \tag{32}$$

Substituting Eqs. (26) and (27) into the above equation results in

$$\xi = \eta - \operatorname{sgn}(\eta)\sqrt{\eta^2-1} \quad \text{for } |\eta| > 1. \tag{33}$$

It is obvious that ξ and η are of the same sign. Equation (33) may be rewritten by using Eq. (29) as

$$\xi = (1+\epsilon_m)\eta - \left(\frac{1}{2\epsilon_1} + 1\right)\epsilon_m + \frac{\epsilon_k}{2\epsilon_1} \quad \text{for } |\eta| > 1 \tag{34}$$

where η has been defined by Eq. (30).

Let us consider a simple case, i.e., $\epsilon_k \neq 0$ and $\epsilon_m = 0$. For this case, Fig. 3 shows that if $\epsilon_k < 0$, one localized mode with $\eta > 1$ (i.e., $\omega < \omega_L$) occurs and if $\epsilon_k > 0$, one localized mode with $\eta < -1$ (i.e., $\omega > \omega_U$) occurs. Substituting $\epsilon_m = 0$ into Eqs. (30) and (31) yields

$$\eta = -\frac{\operatorname{sgn}(\epsilon_k)}{2}\sqrt{\left(\frac{\epsilon_k}{\epsilon_1}\right)^2 + 4} \tag{35}$$

and then substituting Eq. (35) and $\epsilon_m = 0$ into Eq. (34), yields

$$\xi = \frac{1}{2}\left[\frac{\epsilon_k}{\epsilon_1} - \operatorname{sgn}(\epsilon_k)\sqrt{\left(\frac{\epsilon_k}{\epsilon_1}\right)^2 + 4}\right]. \tag{36}$$

The attenuation rate ξ is the odd function of the ϵ_k/ϵ_1 ratio as shown in Fig. 4. Similarly, the attenuation rate may be obtained for other cases.

3 Two-Dimensional System

The system to be considered is made up of both a rectangular cable network with $m \times n$ uniform mesh and $m \times n$ number of mass-spring systems distributed uniformly as shown

in Fig. 5 where each lumped mass is attached to a node of network. The nodes at the four boundary edges are fixed. The pretensioned cables will act as the coupling springs but their masses will be neglected.

In a similar manner to that given by (Cheung et al., 1988, and Chan et al., 1989), the equivalent system with cyclic periodicity in the x and y directions may be obtained as shown in Fig. 6. The equivalent system is an extended system whose length and width are twice the actual size. Moreover, we regard the extended system as one having cyclic periodicity in the x and y directions. The loading pattern is antisymmetric with respect to two symmetric planes of the equivalent system so that the deformation is also antisymmetric. The fixed end conditions for the actual system will be satisfied automatically.

Consider now the harmonic vibration of the equivalent system. The dynamic equation for all subsystems may be expressed as

$$\begin{aligned}(K + 2k_1 + 2k_2 - M\omega^2)W_{(j,p)} - k_1(W_{(j+1,p)} + W_{(j-1,p)}) \\ -k_2(W_{(j,p+1)} + W_{(j,p-1)}) = F_{(j,p)} \\ j = 1, 2, \ldots, 2m \quad p = 1, 2, \ldots, 2n\end{aligned} \tag{37}$$

where K, M denote the stiffness and mass of the mass-spring system; $W_{(j,p)}$ and $F_{(j,p)}$ denote the amplitudes of the displacement and loading for the lumped mass of subsystem (j, p); and

$$k_1 = \frac{T_1}{a} \quad k_2 = \frac{T_2}{b} \tag{38}$$

in which T_1, T_2 denote the pretensions of the cables in the x and y directions, and a, b denote the spacing of y and x cables.

In order to uncouple the simultaneous Eq. (37), the double U-transformation (Cheung et al., 1988; and Chan et al., 1989) is applied. Let

$$W_{(j,p)} = \frac{1}{\sqrt{2m}} \frac{1}{\sqrt{2n}} \sum_{r=1}^{2m} \sum_{s=1}^{2n} e^{i(j-1)r\psi_1} e^{i(p-1)s\psi_2} q_{(r,s)} \tag{39a}$$

or

$$q_{(r,s)} = \frac{1}{\sqrt{2m}} \frac{1}{\sqrt{2n}} \sum_{j=1}^{2m} \sum_{p=1}^{2n} e^{-i(j-1)r\psi_1} e^{-i(p-1)s\psi_2} W_{(j,p)} \tag{39b}$$

in which $\psi_1 = \pi/m$, $\psi_2 = \pi/n$.

Applying the double U-transformation (39) to Eq. (37) yields

$$\begin{aligned}(K + 2k_1 + 2k_2 - M\omega^2 - 2k_1 \cos r\psi_1 \\ -2k_2 \cos s\psi_2) q_{(r,s)} = f_{(r,s)}\end{aligned} \tag{40}$$

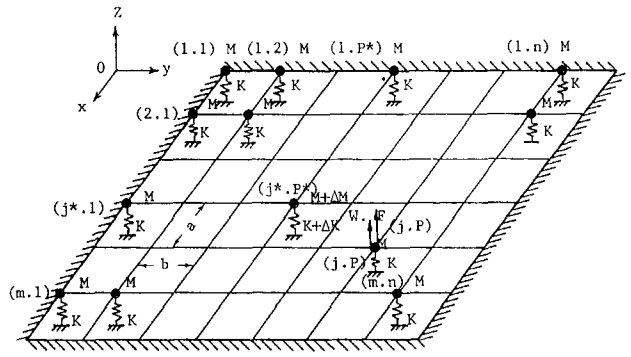

Fig. 5 Two-dimensional system—actual system

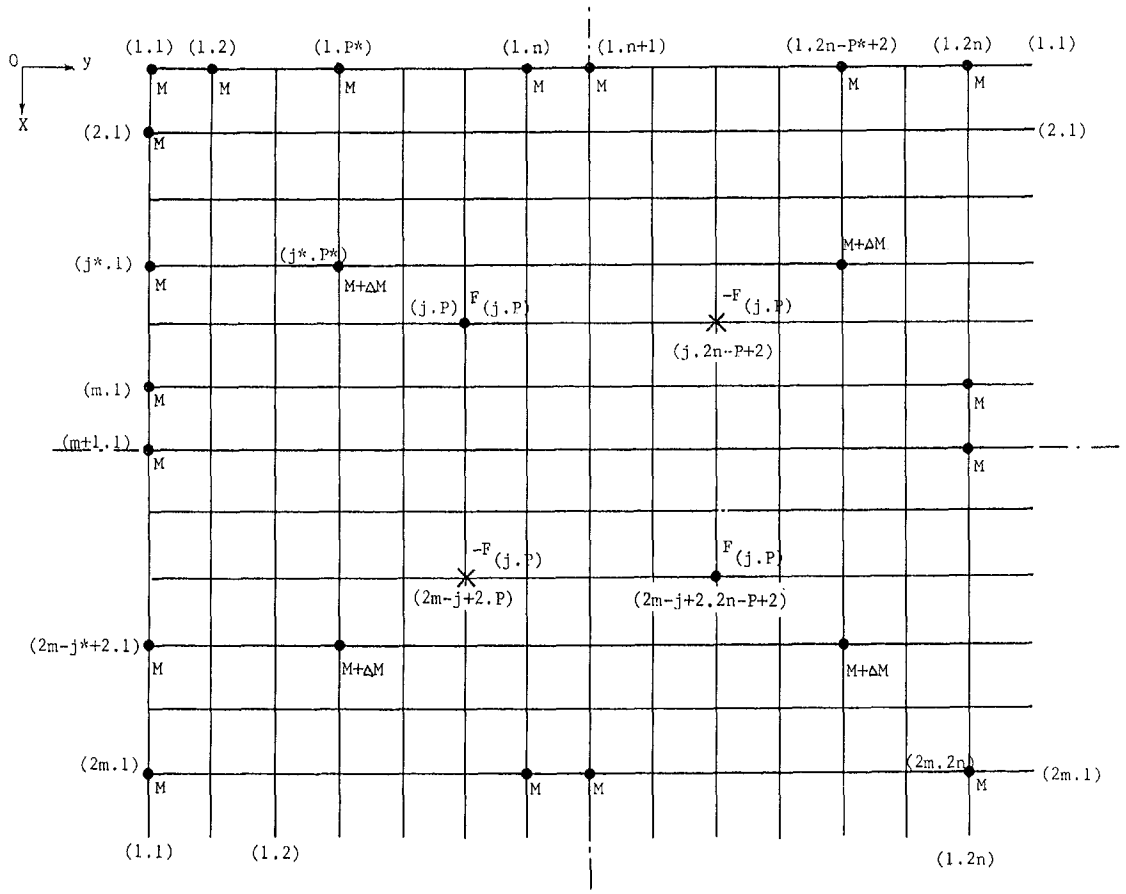

Fig. 6 Two-dimensional system—equivalent system

where

$$f_{(r,s)} = \frac{1}{\sqrt{2m}} \frac{1}{\sqrt{2n}} \sum_{j=1}^{2m} \sum_{p=1}^{2n} e^{-i(j-1)r\psi_1} e^{-i(p-1)s\psi_2} F_{(j,p)} \quad (41)$$

and then

$$q_{(r,s)} = f_{(r,s)} / \left(K + 2k_1 + 2k_2 - M\omega^2 - 2k_1 \cos r\psi_1 - 2k_2 \cos s\psi_2 \right). \quad (42)$$

The frequency equation for an ordered system may be obtained from Eq. (40)

$$K + 2k_1 + 2k_2 - M\omega^2 - 2k_1 \cos r\psi_1 - 2k_2 \cos s\psi_2 = 0 \qquad r = 1, 2, \ldots, 2m, \quad s = 1, 2, \ldots, 2n. \quad (43)$$

The lower and upper limits of the pass band may be expressed as

$$\omega_L^2 = K/M, \quad \omega_U^2 = (K + 4k_1 + 4k_2)/M. \quad (44)$$

Now let us consider the disordered system where only one subsystem is departing from the regularity. With no loss of generality, let (j^*, p^*) denote the ordinal number of the disordered subsystem whose stiffness and mass are of $K + \Delta K$ and $M + \Delta M$. For this case, the "loads" satisfying the antisymmetry condition may be given as follows:

$$F_{(j^*, p^*)} = F_{(2m - j^* + 2, 2n - p^* + 2)} = F$$

$$F_{(j^*, 2n - p^* + 2)} = F_{(2m - j^* + 2, p^*)} = -F$$

$$F \equiv (\Delta M\omega^2 - \Delta K) W_{(j^*, p^*)} \quad (45)$$

with other loads being equal to zero.

Substituting Eq. (45) into Eq. (41) yields

$$f_{(r,s)} = \frac{-4F}{\sqrt{2m}\sqrt{2n}} \sin(j^* - 1)r\psi_1 \sin(p^* - 1)s\psi_2. \quad (46)$$

Substituting Eqs. (42) and (46) into Eq. (39a) results in

$$W_{(j,p)} = \frac{4F}{mn} \sum_{r=1}^{m} \sum_{s=1}^{n} \frac{\sin(j-1)r\psi_1 \sin(j^* - 1)r\psi_1 \sin(p-1)s\psi_2 \sin(p^* - 1)s\psi_2}{K + 2k_1 + 2k_2 - M\omega^2 - 2k_1 \cos r\psi_1 - 2k_2 \cos s\psi_2}. \quad (47)$$

It is obvious that the displacements shown in Eq. (47) satisfy the boundary condition, i.e.,

$$W_{(j,1)} = 0, \quad W_{(j,n+1)} = 0 \quad (j = 1, 2, \ldots, m+1);$$
$$W_{(1,p)} = 0, \quad W_{(m+1,p)} = 0 \quad (p = 1, 2, \ldots, n+1).$$

By letting m and n approach infinity, the above equation becomes

$$W_{(j,p)} = \frac{4F}{\pi^2} \int_0^\pi \int_0^\pi \frac{\sin(j-1)\theta_1 \sin(j^* - 1)\theta_1 \sin(p-1)\theta_2 \sin(p^* - 1)\theta_2}{K + 2k_1 + 2k_2 - M\omega^2 - 2k_1 \cos\theta_1 - 2k_2 \cos\theta_2} d\theta_1 d\theta_2. \quad (48)$$

If and only if the ω in Eq. (48) lies in the stop band, i.e., $\omega < \omega_L$ or $\omega > \omega_U$, the definite integral shown in the right-hand side of Eq. (48) is in existence.

Let (j_1, p_1) denote the new ordinal number when the disordered subsystem acts as the origin, i.e., $j = j^* + j_1$, $p = p^* + p_1$, Eq. (48) may be rewritten as

$$W_{(j^* + j_1, p^* + p_1)} = \frac{F}{\pi^2} \int_0^\pi \int_0^\pi \frac{[\cos j_1\theta_1 - \cos(2j^* + j_1 - 2)\theta_1][\cos p_1\theta_2 - \cos(2p^* + p_1 - 2)\theta_2]}{K + 2k_1 + 2k_2 - M\omega^2 - 2k_1\cos\theta_1 - 2k_2\cos\theta_2} d\theta_1 d\theta_2. \quad (49)$$

In general, the disordered subsystem is located at an infinite distance from the boundary (at infinity). Letting j^* and p^* approach infinity and applying the well-known Reiman Lemma to Eq. (49) yields

$$\lim_{\substack{j^* \to \infty \\ p^* \to \infty}} W_{(j^* + j_1, p^* + p_1)} = F\beta_{(j_1, p_1)} \quad (50)$$

where

$$\beta_{(j_1, p_1)} = \frac{1}{\pi^2} \int_0^\pi \int_0^\pi \times \frac{\cos j_1\theta_1 \cos p_1\theta_2 d\theta_1 d\theta_2}{K + 2k_1 + 2k_2 - M\omega^2 - 2k_1 \cos\theta_1 - 2k_2 \cos\theta_2}. \quad (51)$$

Substituting Eq. (45) and $j_1 = p_1 = 0$ into Eq. (50), the frequency equation for the disordered system may be obtained as

$$\Delta M\omega^2 - \Delta K = \frac{1}{\beta_{(0,0)}} \quad (52)$$

where

$$\beta_{(0,0)} = \frac{1}{\pi^2} \int_0^\pi \int_0^\pi \left[K + 2k_1 + 2k_2 - M\omega^2 - 2k_1\cos\theta_1 - 2k_2\cos\theta_2 \right]^{-1} d\theta_1 d\theta_2. \quad (53)$$

The Eqs. (52) and (51) are similar to Eqs. (15) and (25). Therefore, their roots may be obtained by graphical method. The relationship of the disorder, coupling parameters, and localized modes may also be expressed by Fig. 3 in which the coupling parameter ϵ_1 must be defined as $(k_1 + k_2)/K$ instead of k_1/K. The conclusion is the same as in the case of the one-dimensional problem: i.e., arbitrarily small levels of disorder (ϵ_k or ϵ_m) can cause localization of one mode.

The attenuation rates in the x and y directions are of different values which may be expressed as

$$\xi_1 = \frac{\beta_{(1,0)}}{\beta_{(0,0)}} \quad \text{and} \quad \xi_2 = \frac{\beta_{(0,1)}}{\beta_{(0,0)}}. \quad (54)$$

4 Three-Dimensional System

The system considered consists of l number of two-dimensional systems as described in the previous section in which the corresponding nodes of any two adjacent networks are coupled with spring k_3 and the nodes in the top and bottom layers are free in the z direction as shown in Fig. 7. At the outset, let us consider the extended system whose length, width, and height are twice that of the actual ones as shown in Fig. 8. Moreover, we regard the extended system as one having cyclic periodicity in the x, y, and z directions. The corresponding nodes of both the top and bottom layers must be imagined to have been jointed by an additional spring with stiffness k_3. In order to satisfy automatically the boundary conditions of the actual system, the loading pattern must be antisymmetric with respect to three symmetric planes of the equivalent system as shown in Fig. 8.

In a similar manner as in analyzing the two-dimensional

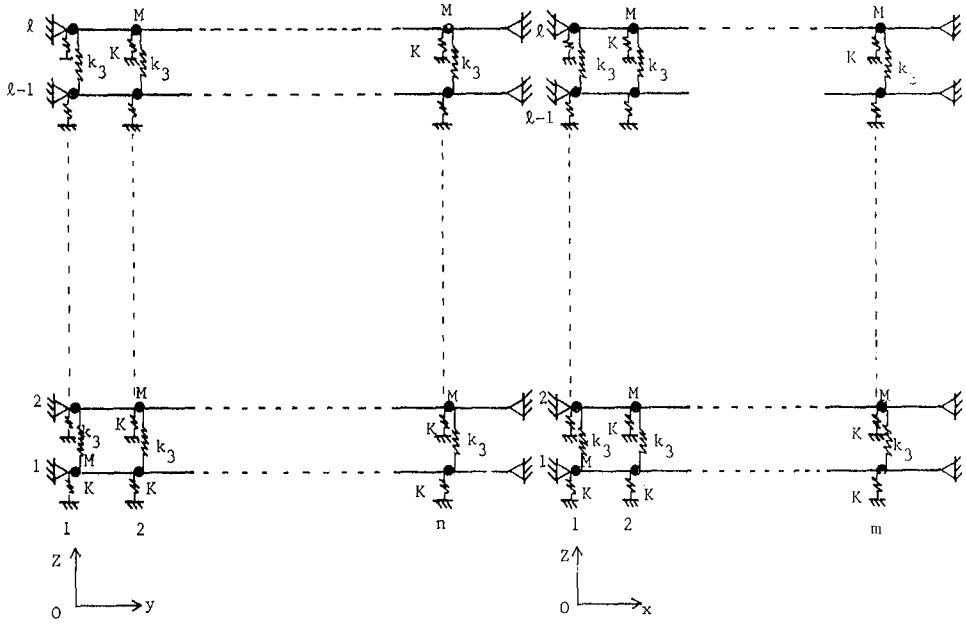

Fig. 7 Three-dimensional system—actual system

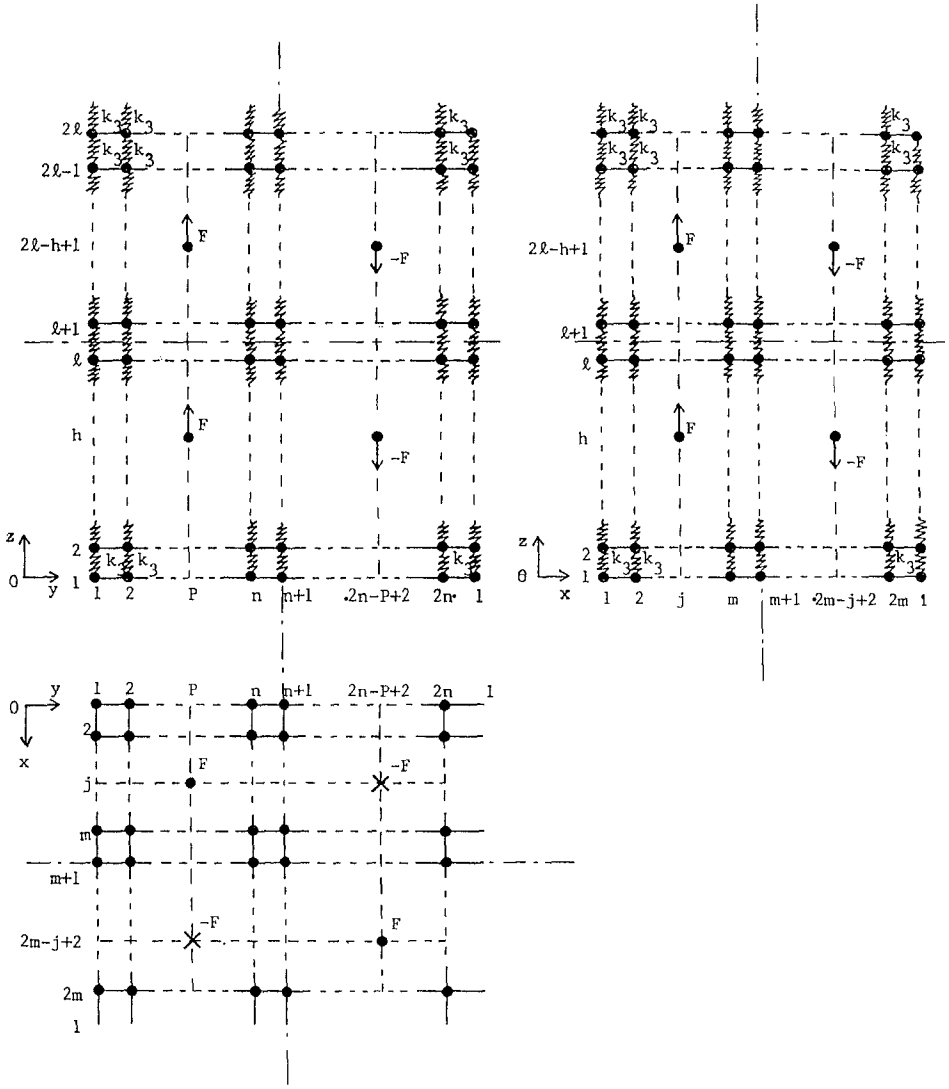

Fig. 8 Three-dimensional system—equivalent system

system, the governing equation for harmonic vibration of the equivalent system may be given as

$$(K + 2k_1 + 2k_2 + 2k_3 - M\omega^2)W_{(j,p,h)} - k_1(W_{(j+1,p,h)} + W_{(j-1,p,h)}) - k_2(W_{(j,p+1,h)} + W_{(j,p-1,h)}) - k_3(W_{(j,p,h+1)} + W_{(j,p,h-1)}) = F_{(j,p,h)}$$

$$j = 1, 2, \ldots, 2m, \quad p = 1, 2, \ldots, 2n, \quad h = 1,2, \ldots, 2l \quad (55)$$

where the subscripts j, p, h in the round brackets denote the ordinal numbers of the subsystem along the x, y, and z directions, respectively, and the other notations have been defined previously.

In order to uncouple the simultaneous Eqs. (55), the triple U-transformation has to be developed from the U-transformation. Let

$$W_{(j,p,h)} = \frac{1}{\sqrt{2m}\sqrt{2n}\sqrt{2l}} \sum_{r=1}^{2m}\sum_{s=1}^{2n}\sum_{t=1}^{2l} \times e^{i(j-1)r\psi_1}e^{i(p-1)s\psi_2}e^{i(h-1)t\psi_3}q_{(r,s,t)} \quad (56a)$$

or

$$q_{(r,s,t)} = \frac{1}{\sqrt{2m}\sqrt{2n}\sqrt{2l}} \sum_{j=1}^{2m}\sum_{p=1}^{2n}\sum_{h=1}^{2l} \times e^{-i(j-1)r\psi_1}e^{-i(p-1)s\psi_2}e^{-i(h-1)t\psi_3}W_{(j,p,h)} \quad (56b)$$

where $\psi_1 = \pi/m$, $\psi_2 = \pi/n$ and $\psi_3 = \pi/l$.

Applying the triple U-transformation (56) to Eq. (55) results in

$$[K + 2k_1 + 2k_2 + 2k_3 - M\omega^2 - 2k_1\cos r\psi_1 - 2k_2\cos s\psi_2 - 2k_3\cos t\psi_3]q_{(r,s,t)} = f_{(r,s,t)} \quad (57)$$

where

$$f_{(r,s,t)} = \frac{1}{\sqrt{2m}\sqrt{2n}\sqrt{2l}} \sum_{j=1}^{2m}\sum_{p=1}^{2n}\sum_{h=1}^{2l} \times e^{-i(j-1)r\psi_1}e^{-i(p-1)s\psi_2}e^{-i(h-1)t\psi_3}F_{(j,p,h)} \quad (58)$$

and then

$$q_{(r,s,t)} = f_{(r,s,t)}/[K + 2k_1 + 2k_2 + 2k_3 - M\omega^2 - 2k_1\cos r\psi_1 - 2k_2\cos s\psi_2 - 2k_3\cos t\psi_3]. \quad (59)$$

The frequency equation for an ordered system may be obtained from Eq. (57):

$$K + 2k_1 + 2k_2 + 2k_3 - M\omega^2 - 2k_1\cos r\psi_1 - 2k_2\cos s\psi_2 - 2k_3\cos t\psi_3 = 0. \quad (60)$$

The lower and upper limits of the pass band are

$$\omega_L^2 = K/M, \quad \omega_U^2 = [K + 4(k_1 + k_2 + k_3)]/M. \quad (61)$$

Now, let us consider the disordered system with only one subsystem departing from the regularity. Let (j^*, p^*, h^*) denote the ordinal number of the disordered subsystem with stiffness $K + \Delta K$ and mass $M + \Delta M$. For such a case, the loads with antisymmetry may be given as

$$F_{(j^*,p^*,h^*)} = F_{(2m-j^*+2,2n-p^*+2,h^*)} = F_{(j^*,p^*,2l-h^*+1)} = F_{(2m-j^*+2,2n-p^*+2,2l-h^*+1)} = F$$

$$F_{(2m-j^*+2,p^*,h^*)} = F_{(j^*,2n-p^*+2,h^*)} = F_{(2m-j^*+2,p^*,2l-h^*+1)} = F_{(j^*,2n-p^*+2,2l-h^*+1)} = -F$$

$$F = (\Delta M\omega^2 - \Delta K)W_{(j^*,p^*,h^*)} \quad (62)$$

with the other loads being equal to zero.

Substituting Eq. (62) into Eq. (58) yields

$$f_{(r,s,t)} = -\frac{4F}{\sqrt{2m}\sqrt{2n}\sqrt{2l}}\sin(j^* - 1)r\psi_1 \times \sin(p^* - 1)s\psi_2(e^{-i(h^*-1)t\psi_3} + e^{ih^*t\psi_3}). \quad (63)$$

Substituting Eqs. (59) and (63) into Eq. (56a) results in

$$W_{(j,p,h)} = \frac{2F}{m\bullet n\bullet l}\sum_{r=1}^{m}\sum_{s=1}^{n}\sum_{t=1}^{2l} \times \frac{\sin(j-1)r\psi_1 \sin(j^*-1)r\psi_1 \sin(p-1)s\psi_2 \sin(p^*-1)s\psi_2(\cos(h-h^*)t\psi_3 + \cos(h+h^*-1)t\psi_3)}{K + 2k_1 + 2k_2 + 2k_3 - M\omega^2 - 2k_1\cos r\psi_1 - 2k_2\cos s\psi_2 - 2k_3\cos t\psi_3}. \quad (64)$$

It can be verified that the displacements shown in (64) satisfy the antisymmetric condition (62) and the boundary condition of the actual system. By letting m, n, and l approach infinity, the right-hand side of Eq. (64) becomes a triple definite integral, i.e.,

$$W_{(j,p,h)} = \frac{4F}{\pi^3}\int_0^\pi\int_0^\pi\int_0^\pi \times \frac{\sin(j-1)\theta_1 \sin(j^*-1)\theta_1 \sin(p-1)\theta_2 \sin(p^*-1)\theta_2(\cos(h-h^*)\theta_3 + \cos(h+h^*-1)\theta_3)}{K + 2k_1 + 2k_2 + 2k_3 - M\omega^2 - 2k_1\cos\theta_1 - 2k_2\cos\theta_2 - 2k_3\cos\theta_3} d\theta_1 d\theta_2 d\theta_3. \quad (65)$$

Letting $j = j^* + j_1$, $p = p^* + p_1$, $h = h^* + h_1$ and then j^*, p^*, $h^* \to \infty$, Eq. (65) becomes

$$W_{(j^*+j_1,p^*+p_1,h^*+h_1)} = F\beta_{(j_1,p_1,h_1)} \quad (66)$$

where

$$\beta_{(j_1,p_1,h_1)} = \frac{1}{\pi^3}\int_0^\pi\int_0^\pi\int_0^\pi \frac{\cos j_1\theta_1 \cos p_1\theta_2 \cos h_1\theta_3}{K + 2k_1 + 2k_2 + 2k_3 - M\omega^2 - 2k_1\cos\theta_1 - 2k_2\cos\theta_2 - 2k_3\cos\theta_3} d\theta_1 d\theta_2 d\theta_3. \quad (67)$$

Substituting Eqs. (62), (67), and $j_1 = p_1 = h_1 = 0$ into Eq. (66), the frequency equation for a disordered system may be given as

$$\Delta M\omega^2 - \Delta K = \frac{1}{\beta_{(0,0,0)}} \quad (\omega < \omega_L, \text{ and } \omega > \omega_U) \quad (68)$$

in which

$$\beta_{(0,0,0)} = \frac{1}{\pi^3}\int_0^\pi\int_0^\pi\int_0^\pi [K + 2k_1 + 2k_2 + 2k_3 - M\omega^2 - 2k_1\cos\theta_1 - 2k_2\cos\theta_2 - 2k_3\cos\theta_3]^{-1} d\theta_1 d\theta_2 d\theta_3. \quad (69)$$

It is of interest to note that the frequency equations in one, two, and three dimensions are of the same form; however, they have an essential distinction, i.e., when ω in the stop band approach ω_L and ω_U, the dynamic flexibility $\beta_{(0,0,0)}$ in a three-dimensional system approaches a finite value as a limit but $\beta_{(0,0)}$ and β_{j^*} approach infinity.

$\beta_{(0,0,0)}$ for both cases of $\omega = \omega_L - 0$ and $\omega = \omega_U + 0$ are

of the same magnitude with opposite sign. Considering the specific case of $k_1 = k_2 = k_3$,

$$\beta_{(0,0,0)|\omega=\omega_L-0} = -\beta_{(0,0,0)|\omega=\omega_U+0}$$
$$= \frac{1}{2k_1}\frac{1}{\pi^3}\int_0^\pi\int_0^\pi\int_0^\pi (3 - \cos\theta_1 - \cos\theta_2 - \cos\theta_3)^{-1} d\theta_1 d\theta_2 d\theta_3 \approx \frac{0.504^*}{2k_1}. \quad (70)$$

(*This value is obtained by numerical integration.)

It indicates that in three dimensions, when the ordered system is subjected to a harmonic force with frequency ω_L or ω_U, the amplitude of the forced mass approaches a finite value as a limit. Let

$$D(\omega^2) \equiv \frac{1}{\beta_{(0,0,0)}} \quad \text{when } \omega \geq \omega_U, \quad \omega \leq \omega_L \quad (71)$$

where D denotes the dynamic stiffness of the ordered system.

It may be proved that if

$$\Delta M\omega_L^2 - \Delta K < D(\omega_L^2) \quad \text{and} \quad \Delta M\omega_U^2 - \Delta K > D(\omega_U^2), \quad (72)$$

the frequency Eq. (68) does not have any solution in the stop band, i.e., it is impossible for any localized mode to occur.

Substituting Eq. (61) into Eq. (72) yields

$$\epsilon_m - \epsilon_k < D(\omega_L^2)/K \quad \text{and} \quad \epsilon_m[1 + 4(\epsilon_1 + \epsilon_2 + \epsilon_3)] - \epsilon_k > D(\omega_U^2)/K \quad (73)$$

where $\epsilon_j = k_j/K$ $(j = 1, 2, 3)$, $\epsilon_m = \Delta M/M$, $\epsilon_k = \Delta K/K$, and

$$D(\omega_L^2)/K = -D(\omega_U^2)/K$$
$$= 2\pi^3 / \int_0^\pi\int_0^\pi\int_0^\pi [\epsilon_1(1 - \cos\theta_1) + \epsilon_2(1 - \cos\theta_2) + \epsilon_3(1 - \cos\theta_3)]^{-1} d\theta_1 d\theta_2 d\theta_3. \quad (74)$$

For the special case of $k_1 = k_2 = k_3$, Eq. (73) becomes

$$\epsilon_m - \epsilon_k < \epsilon_1/0.252$$

and

$$(1 + 12\epsilon_1)\epsilon_m - \epsilon_k > -\epsilon_1/0.252. \quad (75)$$

If $\epsilon_m = 0$, Eq. (75) is equivalent to

$$|\epsilon_k| < \epsilon_1/0.252 = 3.97\epsilon_1. \quad (76)$$

It is shown that a finite threshold of disorder is needed for a given magnitude of coupling in order to cause localization of one mode. For the present case, the ratio of the disorder (ϵ_k) to coupling (ϵ_1) must be greater than 3.97 in order to localize one mode.

If $\epsilon_k = 0$, Eq. (75) becomes

$$-\frac{3.97\epsilon_1}{1 + 12\epsilon_1} < \epsilon_m < 3.97\epsilon_1, \quad (77)$$

then the same conclusion may also apply.

5 Conclusion

In one, two, and three dimensions, the nearly periodic systems with one-degree-of-freedom subsystems and a single disordered subsystem have been analyzed by using the U-transformation method. The conditions to cause localization of one mode are discussed in detail. The following conclusions have been arrived at:

(*a*) In one- and two-dimensional systems, any amount of disorder (ϵ_k or ϵ_m) can localize one mode. Even for the special case of $\epsilon_k = \epsilon_m < 0$, i.e., the frequencies for all subsystems are the same, one mode can be localized.

(*b*) In a three-dimensional system, a finite threshold of disorder is needed in order to localize one mode. When all of the parameters are given, the threshold may be calculated accurately. As an example, for the case of $k_1 = k_2 = k_3$ and $\epsilon_m = 0$, the threshold of disorder ϵ_k is approximately equal to four times the coupling ϵ_1.

Acknowledgment

The financial support of the Lee Hysan Foundation Grant is gratefully acknowledged.

References

Anderson, P. W., 1958, "Absence of Diffusion in Certain Random Lattices," *Physical Review*, Vol. 109, pp. 1492–1505.

Bendiksen, O. O., 1987, "Mode Localization Phenomena in Large Space Structures," *AIAA Journal*, Vol. 25, No. 9, pp. 1241–1248.

Cai, C. W., Cheung, Y. K., and Chan, H. C., 1988, "Dynamic Response of Infinite Continuous Beams Subjected to a Moving Force—An Exact Method," *Journal of Sound and Vibration*, Vol. 123, No. 3, pp. 461–472.

Cai, C. W., Cheung, Y. K., and Chan, H. C., 1990, "Uncoupling of Dynamic Equations for Periodic Structures," *Journal of Sound and Vibration*, Vol. 139, No. 2, pp. 253–263.

Chan, H. C., Cai, C. W., and Cheung, Y. K., 1989, "Moments and Deflections of Simply Supported Rectangular Grids—An Exact Method," *International Journal of Space Structures*, Vol. 4, No. 3, pp. 163–173.

Cheung, Y. K., Chan, H. C., and Cai, C. W., 1988, "Natural Vibration Analysis of Rectangular Networks," *International Journal of Space and Structures*, Vol. 3, No. 3, pp. 139–152.

Cheung, Y. K., Chan, H. C., and Cai, C. W., 1989, "Exact Method for Static Analysis of Periodic Structures," *ASCE Journal of Engineering Mechanics*, Vol. 115, No. 2, pp. 415–434.

Goodman, F. O., 1972, "Propagation of a Disturbance on a One Dimensional Lattice Solved by Response Functions," *American Journal of Physics*, Vol. 40, pp. 92–100.

Hodges, C. H., 1982, "Confinement of Vibration by Structural Irregularity," *Journal of Sound and Vibration*, Vol. 82, No. 3, pp. 411–424.

Hodges, C. H., and Woodhouse, J., 1989a, "Confinement of Vibration by One Dimensional Disorder, I: Theory of Ensemble Averaging," *Journal of Sound and Vibration*, Vol. 130, No. 2, pp. 237–251.

Hodges, C. H., and Woodhouse, J., 1989b, "Confinement of Vibration by One Dimensional Disorder, II: A Numerical Experiment on Different Ensemble Averages," *Journal of Sound and Vibration*, Vol. 130, No. 2, pp. 253–268.

Keane, A. J., and Price, W. G., 1989, "On the Vibrations of Mono-Coupled Periodic and Near-Periodic Structures," *Journal of Sound and Vibration*, Vol. 128, No. 3, pp. 423–450.

Pierre, C., and Dowell, E. H., 1987, "Localization of Vibrations by Structural Irregularity," *Journal of Sound and Vibration*, Vol. 114, No. 3, pp. 549–564.

Pierre, C., Tang, D. M., and Dowell, E. H., 1987, "Localized Vibrations of Disordered Multispan Beams: Theory and Experiment," *AIAA Journal*, Vol. 25, No. 9, pp. 1249–1257.

Scattering of Longitudinal Elastic Waves From an Anisotropic Spherical Shell

J. Mittleman[1]

R. Roberts

R. B. Thompson
Mem. ASME.

Center for Nondestructive Evaluation
and Department of Aerospace Engineering
and Engineering Mechanics,
Iowa State University,
Ames, IA 50011

An exact solution for scattering of ultrasound from a spherically orthotropic shell is presented. The shell is assumed to be embedded in an isotropic elastic medium, and the core surrounded by the shell is also assumed to be isotropic. The shell itself is assumed to be "spherically orthotropic," with five independent elastic constants (the spherical analog of a transversely isotropic material in Cartesian coordinates). Field equations for this material are presented, and these equations are shown to be separable. Working with the displacement vector, we find that the radius dependent part of the solution satisfies coupled second-order ordinary differential equations. This system of equations is solved using the method of Frobenius, and results in four independent series determined by material properties to within a multiplicative constant. Use of boundary conditions expressed in terms of stresses and displacements at the inner and outer shell radii completes the solution. Numerical results for a range of shell elastic constants show that this solution matches known analytic results in the special case of isotropy and matches previously developed finite difference results for anisotropic elastic constants. The effect of shell anisotropy on far-field scattering amplitude is explored for an incident plane longitudinal wave.

Introduction

Motivation for this study arises from the profound effect that grain boundary composition has on the engineering properties of commonly used structural materials. Adverse microstructural conditions may be the result of improper processing, or may develop during the service life of the material, as by radiation embrittlement (Perks et al., 1989). Detection and characterization of anomalous grain boundary conditions by nondestructive means is of great practical importance in many major industries such as shipping, aviation, and power generation.

Previous studies of the effects of thin interface layers on discrete scatterers have generally been approximate, replacing a complete description of the field in the interface layer by suitable relationships between traction and displacement fields inside and outside the layer. This aspect of the "inclusion problem" was recently reviewed by Martin (1992), with attention given to several models of an imperfect matrix/inclusion interface. Notable among them are the Baik-Thompson model (Baik and Thompson, 1984), which includes a generalized spring constant and a generalized inertial term to relate the jump in traction (displacement) to the average displacement (traction) across the interface layer. For plane interfaces, at least, the Baik-Thompson parameters are derived from the global effect of the interface under quasi-static conditions. Rohklin and Wang (1991) present a variation on this approach with linear relationships between the jump in traction or displacement to the interior traction and displacement fields. These approximate descriptions of the interface layer are well suited to boundary integral equation methods, and therefore to obstacles of arbitrary form.

The spring model for compliant interface layers offers computational simplicity, and has been pursued by numerous researchers (viz., Kitahara et al., 1990). At the expense of complexity, but with considerable improvements in accuracy, $O(h)$ models (where h is layer thickness) described by Olsson et al. (1990) have been used. Boström et al. (1992a) compare exact $O(h)$ and spring model results for spherical scatterers, and show that spring model results are often contrary to exact and $O(h)$ results. Boström et al. (1992b) extend this work to prolate and oblate spheroids, with similar conclusions. Despite the shortcomings noted for spring and more generalized linear models, they do offer a means of incorporating fairly arbitrary interface layer anisotropy for which an exact solution may not be available.

In this paper we present theoretical studies of ultrasonic

[1]Present address: Code 2510, NSWC/DD, Coastal Systems Station, 6703 W. Highway 98, Panama City, FL 32407-7001.

Contributed by the Applied Mechanics Division of THE AMERICAN SOCIETY OF MECHANICAL ENGINEERS for publication in the ASME JOURNAL OF APPLIED MECHANICS.

Discussion on this paper should be addressed to the Technical Editor, Professor Lewis T. Wheeler, Department of Mechanical Engineering, University of Houston, Houston, TX 77204-4792, and will be accepted until four months after final publication of the paper itself in the ASME JOURNAL OF APPLIED MECHANICS.

Manuscript received by the ASME Applied Mechanics Division, Dec. 5, 1992; final revision, July 1, 1993. Associate Technical Editor: S. K. Datta.

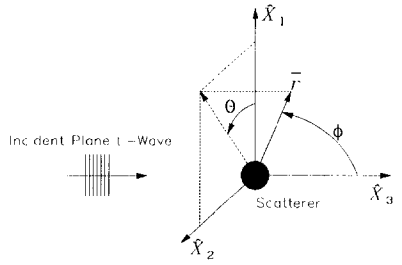

Fig. 1 Coordinate system

scattering from one form of interface layer anisotropy that does allow an exact solution in the case of spherical scatterers. The anisotropic interface layer described is thought of as a greatly simplified grain boundary model. The grain boundary is viewed as a distinct shell, although the exact relationship between grain boundary constituents and equivalent anisotropic elastic constants has yet to be developed. The interior, or core of the grain, and the surrounding host material are modeled as isotropic elastic solids using the notion of an effective isotropic medium (Stanke and Kino, 1984). Properties of the shell are thought of as being isotropic in any tangential direction, but different in the radial direction; we have called this condition "spherical orthotropy."

The presumption of isotropy for the host and core is an approximation, since even single metallic crystals are generally somewhat anisotropic (Musgrave, 1959; Bhatia, 1967). This approximation is better for aluminum than for steel, for example, but is quite reasonable in any case when the shell is taken to be grossly anisotropic. We use "effective" properties for the host material (derived by averaging single crystal properties over all rotations); these are isotropic in a polycrystalline material without texture (Hirsekorn, 1982). Modeling the grain boundary as a spherical shell is also an approximation, but a convenient one in developing exact, separable equations. Finally, we recognize that the solution for a single scatterer is but the first step in dealing with a material composed entirely or in part of such microstructural elements (Lax, 1951; Lax, 1952; Twersky, 1962; Rose, 1992).

Exact equations for this grain boundary model were recently developed and solved numerically by the authors (Mittleman et al., 1992). This work rests on the same differential equations but presents an exact solution in the form of a pair of power series which may be calculated by coupled recursion equations.

Analytic Solution for Isotropic Media

Ying and Truell (1956) solved the problem of a plane longitudinal wave scattered from a spherical, isotropic elastic scatterer in an infinite isotropic elastic medium. Our choice of variables and the general geometry of the problem, which is symmetric about the $\hat{x}_3$-axis, is shown in Fig. 1.

Ying and Truell exploit the symmetry of the problem through the following decomposition of the displacement vector:

$$\bar{u} = -\bar{\nabla}\Psi + \bar{\nabla} \times (\bar{\nabla} \times \bar{r}\Pi). \quad (1)$$

This leads to two Helmholtz equations for the potentials, Ψ and Π, which are associated with longitudinal and transverse components of the fields in either isotropic medium. Time-harmonic solutions[2] in spherical coordinates are expressed in spherical harmonics as

$$\Psi = \sum_{m=0}^{\infty} L_m f_m(kr) P_m(\cos\phi)$$

$$\text{and} \quad \Pi = \sum_{m=0}^{\infty} T_m f_m(\kappa r) P_m(\cos\phi) \quad (2)$$

where

- m is the separation constant (an integer);
- P_m is the mth order Legendre polynomial;
- f_m is an mth order spherical Bessel function inside the scatterer, and an mth order spherical Hankel function of the second kind outside the scatterer.

k and κ are wave numbers for longitudinal and shear waves.

A crucial point to be observed is that the angular dependence contained in the Legendre polynomials is entirely independent of material properties. This means that stresses and displacements can be matched at the boundary between the two media by matching only those parts of the separable solution which depend on radial position.

The complex coefficients L_m and T_m, which give longitudinal and transverse wave component amplitudes, may be different in the outer (host) material and the inner (core) material, resulting in four sets of independent coefficients that completely define the solution. Their values are found for each order, m, independently, from the four equations (Eqs. (20) and (22) in Ying and Truell (1956)) that match displacements and stresses (u_r^m, u_ϕ^m, σ_{rr}^m, and $\sigma_{r\phi}^m$) at the boundaries between the two media.

This method of solution can be applied to a spherical inclusion surrounded by concentric isotropic shells by expressing the radially dependent part of the field in each of the shells as a superposition of spherical Hankel functions of the first and second kind (corresponding to inward and outward traveling waves). This results in four unknown complex coefficients in each shell, two in the host and two in the core; the four equations available at each interface are sufficient to solve the problem analytically. We refer to this as the "extended" Ying and Truell solution and use it to validate the present anisotropic solution when shell constants are isotropic.

We also note that for a spherically orthotropic material, the angular dependences found for the isotropic case are still valid. This statement can be verified by simply following the assumption that u_r^m depends on $P_m(\cos\phi)$ and u_ϕ^m on $\partial P_m(\cos\phi)/\partial\phi$ through the field equations presented below, but a more physical argument provides motivation for doing this. If we look at a composite plate, composed of alternating layers of two dissimilar isotropic materials, effective elastic constants can be calculated by requiring that strains perpendicular to the thickness direction, and stresses in the thickness direction be constant through the thickness of the plate. Then stresses and strains, averaged across the plate thickness, are related by elastic constants that are derived from the two sets of Lamé constants in the isotropic layers, and the fraction of total thickness occupied by each material. These five independent quantities combine to form a matrix of effective elastic constants that displays transverse isotropy, the planar analog of our spherically orthotropic material (Postma, 1955). If the homogeneous, spherically orthotropic shell is thought of as a limiting case of a shell composed of very thin isotropic layers, then we would expect results from the extended Ying and Truell solution to apply; specifically, the same angular dependence should hold in both cases.

Exact Differential Equations for Anisotropic Media

In this section we derive exact differential field equations for waves in a medium with spherically orthotropic proper-

[2] In this paper we follow the convention used by Ying and Truell, assuming an $e^{i\omega t}$ time dependence, as opposed to the commonly used alternative, $e^{-i\omega t}$.

ties, when the problem is symmetric about the $\hat{x}_3$-axis. Like Ying and Truell, we have solved the scattering problem for an incident plane L-wave traveling in the $\hat{x}_3$-direction[3].

Spherically orthotropic materials are characterized by invariance of under rotation around any axis through an origin taken at the center of the sphere, and have five independent elastic constants. When writing the constitutive relationship

$$\left(\sigma_{ij} = C_{ijkl}\epsilon_{kl}\right), \tag{3}$$

the nonzero elastic constants are C_{rrrr}, $C_{rr\phi\phi} = C_{rr\theta\theta}$, $C_{\phi\phi\phi\phi} = C_{\theta\theta\theta\theta}$, $C_{\phi\theta\phi\theta}$, $C_{r\phi r\phi} = C_{r\theta r\theta}$, and $C_{\phi\phi\theta\theta}$. We introduce condensed notation and one relationship among constants:

$$C_{11} = C_{rrrr} \quad C_{12} = C_{rr\phi\phi} \quad C_{22} = C_{\phi\phi\phi\phi}$$
$$C_{44} = C_{\phi\theta\phi\theta} \quad C_{66} = C_{r\phi r\phi} \quad \text{and} \quad C_{23} = C_{22} - 2C_{44}.$$

The strain/displacement relationship

$$\bar{\bar{\epsilon}} = \frac{1}{2}\left(\bar{\nabla}\bar{u} + \bar{u}\bar{\nabla}\right) \tag{4}$$

also simplifies by virtue of the material's symmetry and symmetry of the incident wave around the $\hat{x}_3$-axis. In particular, we find that derivatives with respect to θ and the theta-direction displacement, u_θ, are zero.

The final equation needed is Newton's second law,

$$\bar{\nabla} \cdot \bar{\bar{\sigma}} = \rho\ddot{\bar{u}}. \tag{5}$$

In working through these equations it is convenient to define two operators (Mittleman et al., 1992; Ying and Truell, 1956):

$$\Phi(f(\phi)) = \left(\frac{1}{\sin\phi}\right)\frac{\partial}{\partial\phi}(f \cdot \sin\phi)$$

$$\text{and} \quad \Omega(f(\phi)) = \Phi(\partial f/\partial\phi).$$

Combining Eqs. (3)–(5) results in two coupled differential equations in the two variables u_r and u_ϕ:

$$\left(\bar{\nabla} \cdot \bar{\bar{\sigma}} + \rho\omega^2\bar{u}\right) \cdot \hat{e}_r = 0$$
$$= C_{11}u_{r,rr} + C_{11}\frac{2}{r}u_{r,r} + \rho\omega^2 u_r + (C_{12} - C_{22} - C_{23})\frac{2}{r^2}u_r$$
$$+ C_{66}\frac{1}{r^2}\Omega u_r + (C_{12} + C_{66})\frac{1}{r}(\Phi u_\phi)_{,r}$$
$$+ (C_{12} - C_{22} - C_{23} - C_{66})\frac{1}{r^2}\Phi u_\phi \tag{6a}$$

$$\left(\bar{\nabla} \cdot \bar{\bar{\sigma}} + \rho\omega^2\bar{u}\right) \cdot \hat{e}_\phi = 0$$
$$= \left\{(C_{12} + C_{66})\frac{1}{r}u_{r,r} + (C_{22} + C_{23} + 2C_{66})\frac{1}{r^2}u_r\right\}_{,\phi}$$
$$+ C_{66}u_{\phi,rr} + C_{66}\frac{2}{r}u_{\phi,r} + \rho\omega^2 u_\phi$$
$$+ (C_{22} - C_{23} - 2C_{66})\frac{1}{r^2}u_\phi + C_{22}\frac{1}{r^2}(\Phi u_\phi)_{,\phi} \tag{6b}$$

where $f_{,x} = \partial f/\partial x$ and $\hat{e}_x$ denotes a unit vector in the x direction.

Guided by the relationship between layered isotropic and transversely isotropic materials discussed above, we assume that, for each spherical harmonic, displacements can be expressed as the product of an angular function (the Legendre polynomial or its derivative) and an unknown function of radius:

$$u_r^m = P_m(\cos\phi)F_m(r) \quad \text{and} \quad u_\phi^m = (P_m(\cos\phi))_{,\phi}G_m(r). \tag{7a}$$

Substituting these forms into Eq. (3) gives expressions for stress, which will be used later in matching stresses at the interfaces:

$$\sigma_{rr}^m = P_m(\cos\phi)\left\{C_{11}F_m'(r) + C_{12}\left(\frac{2}{r}F_m(r) - \frac{1}{r}m(m+1)G_m(r)\right)\right\} \tag{7b}$$

$$\sigma_{r\phi}^m = (P_m(\cos\phi))_{,\phi}\left\{C_{66}\left(\frac{1}{r}F_m(r) + G_m'(r) - \frac{1}{r}G_m(r)\right)\right\} \tag{7c}$$

where primed quantities are differentiated with respect to r. Substituting Eq. (7) into Eq. (6) and using the recursion relationship for Legendre polynomials $\Omega P_m = -m(m+1)P_m$ gives the following two equations in which the radial and angular dependencies are separated:

$$0 = P_m(\cos\phi)\left\{C_{11}F_m'' + \frac{2}{r}C_{11}F_m' + \left(\rho\omega^2 + \frac{2}{r^2}(C_{12} - C_{22} - C_{23}) - \frac{1}{r^2}m(m+1)C_{66}\right)F_m - \frac{1}{r}m(m+1)(C_{12} + C_{66})G_m' + \frac{1}{r^2}m(m+1)(C_{22} + C_{23} + C_{66} - C_{12})G_m\right\} \tag{8a}$$

$$0 = \frac{\partial P_m(\cos\phi)}{\partial\phi}\left\{C_{66}G_m'' + \frac{2}{r}C_{66}G_m' + \left(\rho\omega^2 + \frac{1}{r^2}((1 - m(m+1))C_{22} - C_{23} - 2C_{66})\right)G_m + \frac{1}{r}(C_{12} + C_{66})F_m' + \frac{1}{r^2}(C_{22} + C_{23} + 2C_{66})F_m\right\}. \tag{8b}$$

These anisotropic field equations can be specialized to the isotropic case by setting $C_{11} = C_{22} = (\lambda + 2\mu)$, $C_{12} = C_{23} = \lambda$, and $C_{66} = (C_{11} - C_{12})/2 = \mu$.

Solutions in the Isotropic Host and Core

Substituting Eq. (2) into Eq. (1) gives the general form for the radially dependent parts of Eq. (7*a*) for the isotropic case:

$$F_m^I = L_m(f_m(kr))_{,r} - T_m(m(m+1))\frac{1}{r}f_m(\kappa r)$$

$$G_m^I = L_m\frac{1}{r}f_m(kr) - T_m\left(\frac{1}{r}f_m(\kappa r) + (f_m(\kappa r))_{,r}\right)$$

where L_m and T_m are constants associated with the amplitudes of longitudinal and transverse wave solutions in the isotropic media, denoted by the superscript I.

The functions $f_m(kr)$ and $f_m(\kappa r)$ are spherical Bessel functions in the core and spherical Hankel functions in the host.

[3]Details of this derivation are found in Mittleman et al. (1992).

Solutions in the Anisotropic Shell

To concentrate our efforts on generating a solution in the anisotropic shell, the "r"-dependent parts of the anisotropic field, Eqs. (8a) and (8b) will be written as

$$0 = r^2F'' + A_{11}rF' + A_{10}F + K_1^2r^2F + B_{11}rG' + B_{10}G \quad (9a)$$

$$0 = A_{21}rF' + A_{20}F + K_2^2r^2G + r^2G'' + B_{21}rG' + B_{20}G, \quad (9b)$$

where values of the coefficients can be read directly from Eqs. (8a) and (8b) after multiplication by r^2/C_{11}.

According to the method of Frobenius (Hildebrand, 1962) normally used for obtaining series solutions to second-order linear differential equations, we may assume solutions of the form

$$F = \sum_{i=0}^{\infty} f_i r^{i+p} \quad \text{and} \quad G = \sum_{i=0}^{\infty} g_i r^{i+p}$$

and differentiate term by term. The resulting series, substituted into Eqs. (9a) and (9b), give rise to a pair of algebraic equations for each power of "r" in order to satisfy the equations at all radii. The lowest power, obtained with $i = 0$, gives

$$0 = f_0 r^p(\, p(p-1) + A_{11}p + A_{10}) + g_0 r^p(B_{11}p + B_{10}) \quad (10a)$$

$$0 = f_0 r^p(A_{21}p + A_{20}) + g_0 r^p(\, p(p-1) + B_{21}p + B_{20}) \quad (10b)$$

which may be written in matrix form, for $r \neq 0$, noting that $A_{11} = B_{21} = 2$:

$$\begin{pmatrix} (p^2 + p + A_{10}) & (B_{11}p + B_{10}) \\ (A_{21} + A_{20}) & (p^2 + p + B_{20}) \end{pmatrix} \begin{pmatrix} f_0 \\ g_0 \end{pmatrix} = \begin{pmatrix} 0 \\ 0 \end{pmatrix}.$$

For nontrivial solutions we deduce the indicial equation by setting the determinant of the left-hand side matrix to zero:

$$0 = p^4 + 2p^3 + p^2(A_{10} + B_{20} - A_{21}B_{11} + 1)$$
$$+ p(A_{10} + B_{20} - A_{21}B_{10} - A_{20}B_{11}) + (A_{10}B_{20} - A_{20}B_{10}).$$

The four roots to this equation,

$$p = \frac{-1 \pm \sqrt{1 + 2\left((A_{21}B_{11} - A_{10} - B_{20}) \pm \sqrt{(A_{21}B_{11} - A_{10} - B_{20})^2 - 4(A_{10}B_{20} - A_{20}B_{10})}\right)}}{2},$$

are related in pairs, such that if p_i is one of the roots, then $-(p_i + 1)$ is another. For isotropic elastic constants the roots are $m + 1$, $-(m + 2)$, $m - 1$, and $-m$; these values lead to power series representations of the spherical Bessel and Hankel functions that appear in the Ying and Truell solution.

Associated with each root are values of f_0 and g_0 which may be determined (to within a multiplicative constant) by considering either Eq. (10a) or (10b). Once these are determined, other terms in the series are calculated by the iterative procedure described next.

For each order, m, of the indicial equation, we define

$$M(x) = \begin{pmatrix} (x^2 + x + A_{10}) & (B_{11}x + B_{10}) \\ (A_{21}x + A_{20}) & (x^2 + x + B_{20}) \end{pmatrix}$$

and $$K = \begin{pmatrix} K_1^2 & 0 \\ 0 & K_2^2 \end{pmatrix}.$$

The field equations may now be written:

$$\sum_{i=0}^{\infty} r^{i+p}\left(M(i+p) + Kr^2\right)\begin{pmatrix} f_i \\ g_i \end{pmatrix}_p = (0).$$

Requiring that this hold for all values of radius means that each power of "r" may be treated separately; indeed, the indicial equation corresponds to $i = 0$. For $i = 1$ we must satisfy

$$r^{p+1}M(p+1)\begin{pmatrix} f_1 \\ g_1 \end{pmatrix}_p = (0)$$

which will only have a nontrivial solution for $\mathrm{Det}(M(p+1)) = 0$. However, having already fixed values of p by solving the indicial equation, we know that this determinant will be nonzero, unless two of the roots differ by exact unity. In general this will not be the case, and we must choose f_1 and g_1 equal to zero[4]. This implies that the series will be either even or odd, as initiated by r^p.

For $i \geq 2$ and $r \neq 0$, values of $f_i r^i$ and $g_i r^i$ are calculated iteratively:

$$\begin{pmatrix} f_i r^i \\ g_i r^i \end{pmatrix}_p = -M^{-1}(i+p)Kr^2\begin{pmatrix} f_{i-2}r^{i-2} \\ g_{i-2}r^{i-2} \end{pmatrix}_p. \quad (11a)$$

In the special case of isotropic elastic constants we have already noted that the four roots of the indicial equation are $m + 1$, $-(m + 2)$, $m - 1$, and $-m$. Attempts to invert the matrix M for $i = 2$ and $p = m - 1$ or $p = -(m + 2)$ will fail since $\mathrm{Det}(M(m+1))$ and $\mathrm{Det}(M(-m))$ are zero (their arguments, $i + p$, also being roots of the indicial equation). Nonetheless, for $p_1 = (m - 1)$ or $p_1 = -(m + 2)$, one may show that

$$\begin{pmatrix} f_2 \\ g_2 \end{pmatrix}_{p_1} = \lim_{x \to p_1 + 2}\left(-M^{-1}(x)K\begin{pmatrix} f_0 \\ g_0 \end{pmatrix}_{p_1}\right) \quad (11b)$$

exists even though $M^{-1}(p_1 + 2)$ is indeterminate (explicit expressions are given in Appendix A). It should also be pointed out that for the roots $p_2 = (m + 1)$ and $p_2 = -(m)$,

[4] When roots do differ by unity (for example, in an isotropic material, when $m = 0$ the roots are 1, 0, -1, and -2, or when $m = 1$ two of the roots are 0 and -1) we will have $\mathrm{Det}(M(p_1)) = 0$ and $\mathrm{Det}(M(p_2 + 1)) = 0$ where both p_1 and p_2 are roots of the indicial equation and $p_2 + 1 = p_1$. In these cases, the series corresponding to the root p_2 will contain both even and odd powers of r. However, those initiated by the term r^{p_2+1} will be the same as the series generated by the root p_1. Hence, without loss of generality, we can set f_1 and g_1 to zero.

$$M(p_2)\begin{pmatrix} f_0 \\ g_0 \end{pmatrix}_{p2} = (0)$$

while for the roots $p_1 = (m-1)$ and $p_1 = -(m+2)$,

$$M(p_1+2)\begin{pmatrix} f_2 \\ g_2 \end{pmatrix}_{p1} = -K\begin{pmatrix} f_0 \\ g_0 \end{pmatrix}_{p1}.$$

Therefore, when $p_2 = p_1 + 2$, the values calculated by Eq. (11*b*) for $\begin{pmatrix} f_2 \\ g_2 \end{pmatrix}_{p1}$ may contain an additive multiple of $\begin{pmatrix} f_0 \\ g_0 \end{pmatrix}_{p2}$ and the series corresponding to the root p_1 may contain a multiple of the series corresponding to the root p_2. When boundary conditions are matched, however, the coefficients of each series will account for this uncertainty.

We are therefore led to a complete solution for displacements in the anisotropic shell formed by a linear combination of the four series

$$\begin{pmatrix} F_m^S \\ G_m^S \end{pmatrix} = \sum_{k=1}^{4} C_{mk} r^{p_{mk}} \sum_{i=0}^{\infty} \begin{pmatrix} f_i \\ g_i \end{pmatrix}_{p_{mk}} r^i, \qquad (12)$$

where the superscript "S" (denoting the shell) and subscripts have been fully restored ("m" denotes the order of the equation and "k" indicates which root of the indicial equation is involved in each series). This solution may now be differentiated term by term, as needed, to calculate stresses according to Eq. (7). For each value of m, the eight available boundary condition equations (matching two stresses and two displacements at each shell surface) are used to solve for the four coefficients in Eq. (12) and the four coefficients associated with the L-waves and T-waves in the isotropic host and core.

Far-Field Scattering Amplitude

Far-field longitudinal wave scattering amplitude and scattering cross-section may be calculated from the field equations in the isotropic host material, according to formulae presented by Ying and Truell:

$$SA(\phi) = -\sum_{m=0}^{\infty} P_m(\cos\phi)(L_m)e^{i\frac{\pi}{2}m}$$

$$\gamma = 4\pi \sum_{m=0}^{\infty} \frac{1}{2m+1}\left\{(L_m)^*(L_m) + m(m+1)\left(\frac{k_1}{\kappa_1}\right)(T_m)^*(T_m)\right\}$$

where $SA(\phi)$ is the longitudinal wave far-field scattering amplitude, γ is the total scattering cross-section, and the coefficients L_m and T_m describe L-wave and T-wave components of the scattered field in the isotropic host.

Numerical Validation

Numerical results for calculations based on the exact anisotropic solution (shown as "Series" in Table 1) for scattering from an anisotropic shell were verified by comparison with existing results for isotropic and anisotropic shells over a wide range of thicknesses and values of ka_1. In the limiting case where shell thickness approaches zero, comparison was made to the Ying and Truell solution, and in the case of a shell of finite thickness, but with isotropic properties, results were compared to those calculated by the extended Ying and Truell method, shown as "Y-T shell" in Table 1. (This latter method was itself validated by comparison to analytical results given by Datta et al., 1988). For anisotropic shells results were compared to earlier work based on a finite difference solution to the anisotropic field equations (Mittleman et al., 1992), as will be reported below. Because the finite difference solution is essentially a Taylor series solution, which is distinct from a Frobenius series solution, these two calculations are quite independent.

In Table 1, scattering cross-sections calculated in four

Table 1 Scattering cross-sections (mm²) calculated by the exact and finite difference methods for isotropic shells

$ka = 0.01$

Thickness (mm)	0.00	0.001	0.01	0.1
Ying & Truell	.73073E-08			
Y-T shell	.73070E-08	.72341E-08	.65933E-08	.22573E-08
Finite Diff.	.73072E-08	.72334E-08	.65922E-08	.22262E-08
Series	.73072E-08	.72332E-08	.65922E-08	.22075E-08

$ka = 0.1$

Thickness (mm)	0.00	0.001	0.01	0.1
Ying & Truell	.72480E-04			
Y-T shell	.72480E-04	.71749E-04	.65409E-04	.21988E-04
Finite Diff.	.72480E-04	.71749E-04	.65409E-04	.22173E-04
Series	.72480E-04	.71749E-04	.65409E-04	.21988E-04

$ka = 1.0$

Thickness (mm)	0.00	0.001	0.01	0.1
Ying & Truell	.25443E+00			
Y-T shell	.25443E+00	.25279E+00	.23837E+00	.12102E+00
Finite Diff.	.25443E+00	.25279E+00	.23837E+00	.12156E+00
Series	.25443E+00	.25279E+00	.23837E+00	.12102E+00

$ka = 10.0$

Thickness (mm)	0.00	0.001	0.01	0.1
Ying & Truell	.11237E+02			
Y-T shell	.11237E+02	.11199E+02	.10845E+02	.76792E+01
Finite Diff.	.11237E+02	.11199E+02	.10845E+02	.76674E+01
Series	.11237E+02	.11199E+02	.10845E+02	.76792E+01

MATERIAL PROPERTIES			
	Density (gm/cm³)	L-wave velocity (km/sec)	T-wave velocity (km/sec)
Host	7.00	6.00	3.00
Shell	8.00	6.50	3.20
Core	6.00	5.00	2.50
Outer radius for all shells: 1 mm			

Table 2 Comparison and maximum scattering amplitudes calculated by the finite difference method and the exact series solution for spherically orthotropic shells

Constituent Material Properties

Density (host & core)	2.706 gm/cm³
L-wave velocity (host & core)	6.39 km/sec
T-wave velocity (host & core)	3.141 km/sec
Outer shell radius, a_1	1.00 mm
Inner shell radius	0.99 mm
ka_1	10.0
Density (inclusion)	3.181 gm/cm³
L-wave velocity (inclusion)	12.21 km/sec
T-wave velocity (inclusion)	7.69 km/sec

Shell Properties

	Volume Fraction Inclusion			
	1.00	.90	.66	.10
Density (gm/cm³)	3.181	3.1335	3.195	2.7535
C_{11} (GPa)	474.2365	356.7819	223.7704	119.6705
C_{22} (GPa)	474.2365	436.8362	348.9590	146.5221
C_{66} (GPa)	188.1119	117.2317	61.5611	29.2029
C_{12} (GPa)	98.0126	84.8010	69.8394	58.1300
C_{23} (GPa)	98.0126	92.8953	82.4973	60.8449

Maximum Scattering Amplitudes (mm)

	Volume Fraction Inclusion			
	1.00	.90	.66	.10
Finite Difference Method	1.4860	1.3645	1.0518	.17935
Exact Series Solution	1.4865	1.3653	1.0527	.17954

different ways (i.e., Ying and Truell, "Y-T Shell", Finite Difference, and "Series") are compared for shells with isotropic properties. Thickness is given as a fraction of outer shell radius, and ka_1 is based on the incident longitudinal wave number and the outer shell radius.

In Table 2, the exact series solution is compared to the finite difference method for anisotropic shells. The elastic constants used for these calculations were taken to be the same as those of a transversely isotropic material having varying volume fractions of silicon carbide in aluminum and having the infinitesimally thin isotropic layered structure discussed in connection with the separation of variables. The excellent agreement between the finite difference and exact methods of solution is a result consistently obtained for thin shells such as this one, for which $k\Delta a = 0.1$; however, as shell thickness becomes comparable to wavelength, the finite difference solution outlined by Mittleman et al. (1992) deteriorates.

Results for Anisotropic Shells

The effect of shell anisotropy on scattering was studied by calculating the scattering amplitude for a variety of shells embedded in aluminum and surrounding an aluminum core. In a previous paper (Mittleman et al., 1992), elastic constants were arbitrarily varied to test the validity of finite difference calculations, and it was found that both the magnitude of scattering and the angular distribution of energy were sensitive to variations in $C_{\phi\phi\phi\phi}$. In this study, elastic constants are varied according to theories for transversely isotropic composite materials consisting of a mixture of aluminum and a second material representing precipitates which decorate the

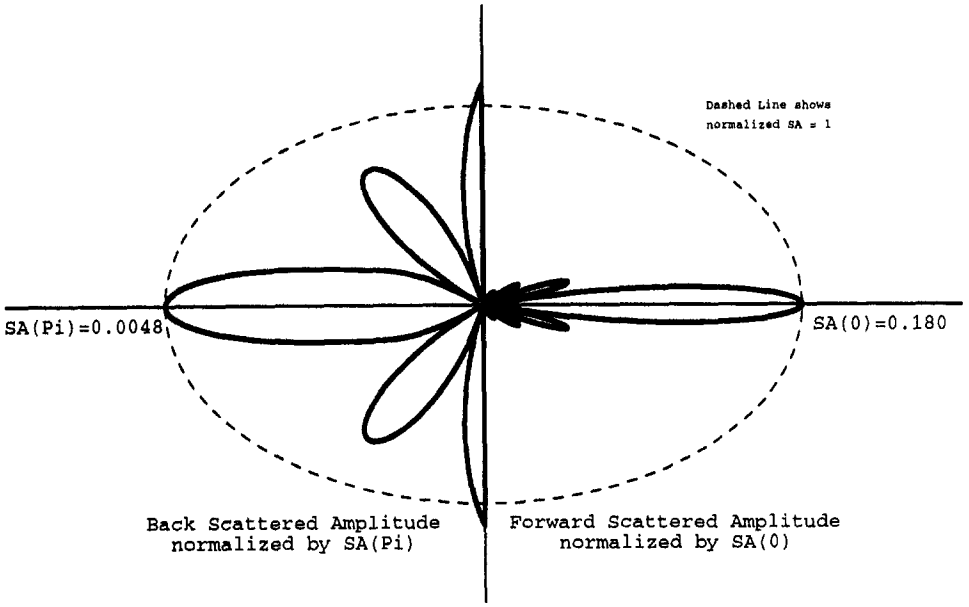

Fig. 2 Scattering amplitude for 10 percent SiC / 90 percent Al shell in aluminum. Maximum scattering amplitude = 0.18 mm.

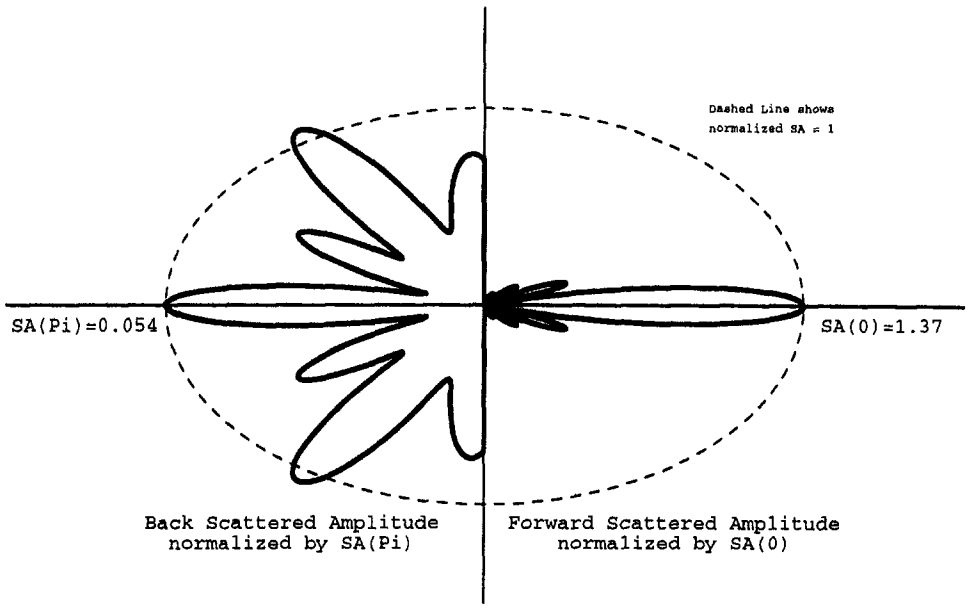

Fig. 3 Scattering amplitude for 90 percent SiC / 10 percent Al shell in aluminum. Maximum scattering amplitude = 1.37 mm.

grain boundaries. For these second phase precipitates, silicon carbide was chosen as a material having a density similar to that of aluminum, but very different wave speeds, while iron was chosen as a material having similar wave speeds but a different density.

Results shown in Table 2 are excerpted from a more complete set of calculations where scattering cross-section and maximum scattering amplitude were computed for shells composed of varying volume fractions of silicon carbide precipitated in aluminum. Figures 2 and 3 show polar plots of scattering amplitude for the shells presented in Table 2 that contain 10 percent and 90 percent SiC, respectively. To emphasize the angular distribution of scattered energy, the right half of each of these figures is normalized by the maximum forward scattering amplitude, while the left half is normalized by the maximum back scattering amplitude. While there is little variation in the forward scattered fields' angular distribution (this being the shadow-forming scattering), there is considerable variation in the distribution of back-scattered energy. Similar calculations for iron precipitated in aluminum showed similar results for the angular distribution of energy in the forward scattered lobe, but variations in the backscattered lobes were far less pronounced than was the case for second phase SiC.

Transverse isotropy in plates (or spherical orthotropy in shells) may be generated by the layered structure previously discussed; we call this the "plate model." In fiber-reinforced composite materials, however, transverse isotropy can also be produced in a number of other ways, one of which is to arrange the long axis of all fibers perpendicular to the thickness direction of the material (contrary to normal practice in laying up thin composite materials); we call this the "fiber model," and analytic results for elastic constants are available (Christensen, 1979). Principal elastic constants (C_{11}, C_{22}, and C_{66}) are shown in Fig. 4(a), for a shell composed of silicon carbide dispersed in aluminum. Note that the roles of C_{11} and C_{22} are reversed when the plate model is compared to the fiber model. The off-diagonal elastic constants (not shown) are quite similar for both models. Figure 4(b) compares anisotropy, $C_{11} - C_{12} - 2C_{66}$, for the plate and fiber models, under these same conditions, and shows a substantial difference, primarily due to the reversal roles of C_{11} and C_{22}

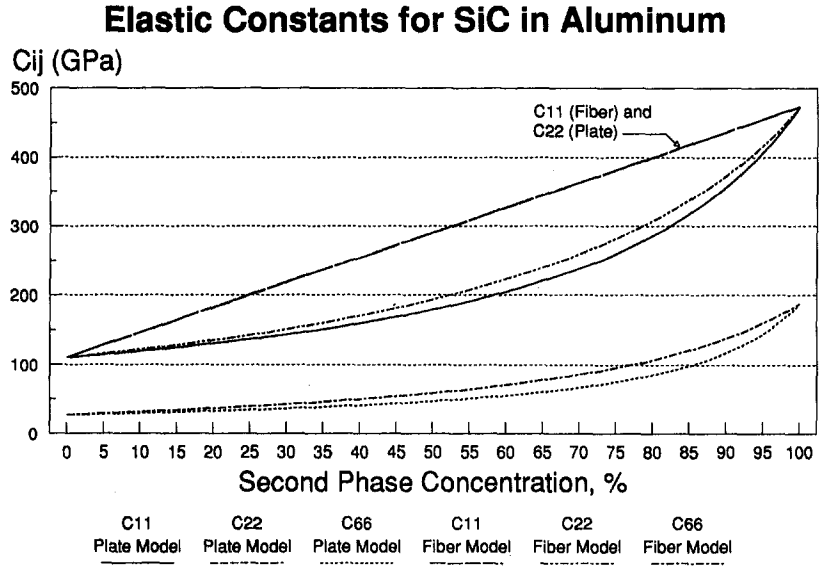

Fig. 4(a) Elastic constants for silicon carbide in aluminum

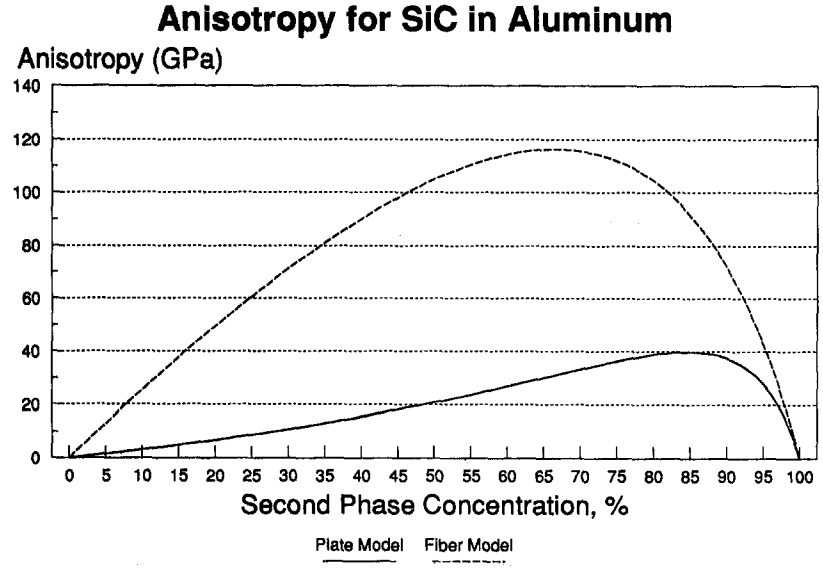

Fig. 4(b) Anisotropy for SIC in aluminum

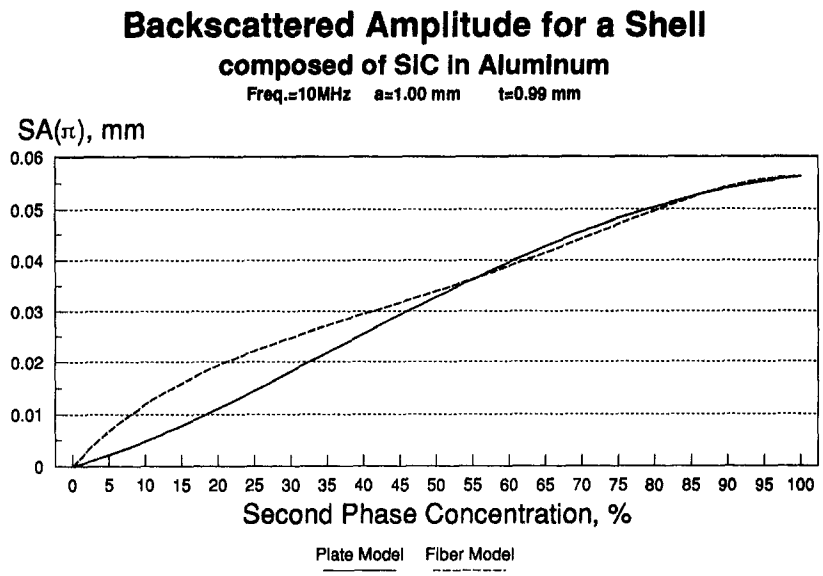

Fig. 5 Backscattered amplitude for a shell composed of SIC in aluminum

noted above. We now look at scattering amplitude in the backscattered direction, as a function of second phase concentration, for the two spherically orthotropic morphologies, as shown in Fig. 5. For each, we find a nearly linear dependence of scattering amplitude on concentration, with enough similarity in their magnitudes to suggest that for practical purposes, using either model for predictive calculations would be adequate. Numerical results for iron in aluminum showed a similarly linear dependence of backscattered amplitude on second phase concentration for both the plate and fiber models.

Conclusions

Exact differential equations for elastic wave scattering from spherical shells with transversely orthotropic properties (five independent elastic constants) have been derived. These equations, which are written in terms of displacement, are separable. As with scattering from an isotropic sphere, the angular equations are satisfied by Legendre polynomials which are independent of material properties. Unlike the isotropic case, the radial equations are not satisfied by spherical Bessel functions, but exact series solutions were obtained by the method of Frobenius. We found that the iterative procedure for calculating series' coefficients requires special treatment when elastic constants are isotropic and present the appropriate expressions.

Scattering amplitude and cross-section results were validated by comparison with exact solutions in the case of vanishing shell thickness and in the case of isotropic elastic constants. Agreement was excellent over a wide range of shell thicknesses and values of ka. Calculations were also performed for a variety of anisotropic cases and excellent agreement with a previously validated finite difference solution was found.

Numerical results for shells composed of SiC or Fe in aluminum showed a reasonably linear dependence of scattering amplitude (in the backscattered direction) on concentration. This dependence was found to be insensitive to the shell morphology assumed. Absolute amplitude measurements may therefore be useful in characterizing grain boundaries decorated by second-phase precipitates.

Acknowledgments

Portions of this work were funded as part of the Coastal Systems Station's FY91 IR/IED program. Significant contributions from David Budreck, Jim Rose, and Salahuddin Ahmed at the Center for Nondestructive Evaluation are gratefully acknowledged.

References

Baik, J.-M., and Thompson, R. B., 1984, "Ultrasonic Scattering from Imperfect Interfaces: A Quasi-Static Model," *Journal Nondestructive Evaluation*, Vol. 4, pp. 177–196.

Bhatia, A. B., 1967, *Ultrasonic Absorption*, Oxford University Press, London, pp. 278–289.

Boström, A., Bövik, P., and Olsson, P., 1992a, "A Comparison of Exact First Order and Spring Boundary Conditions for Scattering by Thin Layers," *Journal of Nondestructive Evaluation*, Vol. 11, pp. 175–184.

Boström, A., Olsson, P., and Datta, S. K., 1992b, "Effective Plane Wave Propagation Through a Medium with Spheroidal Inclusions Surrounded by Thin Interface Layers," *Mechanics of Materials*, Vol. 14, pp. 59–66.

Christensen, R. M., 1979, *Mechanics of Composite Materials*, John Wiley and Sons, New York, pp. 73–84.

Datta, S. K., Olsson, P., and Boström, A., 1988, "Elastodynamic Scattering from Inclusions with Thin Interface Layers," *Wave Propagation in Structural Composites—AMD Vol. 90*, A. K. Mal and T. C. T. Ting, eds., ASME, New York, pp. 109–116.

Hildebrand, F. B., 1962, *Advanced Calculus for Engineers*, Prentice-Hall, Inc., Englewood Cliffs, NJ, pp. 129–142.

Hirsekorn, S., 1982, "The Scattering of Ultrasonic Waves by Polycrystals," *Journal of the Acoustical Society of America*, Vol. 72, pp. 1021–1031.

Kitahara, M., Nakagawa, K., and Achenbach, J. D., 1990, "Scattering Characteristics of a Partially Debonded Compliant Inclusion-Matrix Interphase," *Review of Progress in Quantitative NDE*, Vol. 9A, D. O. Thompson and D. E. Chimenti, eds., Plenum Press, New York, pp. 69–76.

Lax, M., 1951, "Multiple Scattering of Waves," *Reviews of Modern Physics*, Vol. 23, pp. 287–310.

Lax, M., 1952, "Multiple Scattering of Waves, II. The Effective Field in Dense Systems," *Physical Review*, Vol. 85, pp. 621–629.

Martin, P. A., 1992, "Boundary Integral Equations for the Scattering of Elastic Waves by Elastic Inclusions with Thin Interface Layers," *Journal of Nondestructive Evaluation*, Vol. 11, pp. 167–174.

Mittleman, J., Thompson, R. B., and Roberts, R., 1992, "Ultrasonic Scattering from Anisotropic Shells," *Review of Progress in Quantitative NDE*, Vol. 11A, D. O. Thompson and D. E. Chimenti, eds., Plenum Press, New York, pp. 89–96.

Musgrave, M. J. P., 1959, "The Propagation of Elastic Waves in Crystals and other Anisotropic Media," *Reports on Progress in Physics*, Vol. 22, pp. 74–96.

Olsson, P., Datta, S. K., and Boström, A., 1990, "Elastodynamic Scattering from Inclusions Surrounded by Thin Interface Layers," ASME JOURNAL OF APPLIED MECHANICS, Vol. 57, pp. 672–676.

Perks, J. M., English, C. A., and Jenkins, M. L., 1989, "Radiation-Induced Segregation of Phosphorus in Nickel and Fe-Cr-Ni Alloys," *Effects of Radiation of Materials: 14th International Symposium*, Vol. I, ASTM STP 1046, N. H. Pacan, R. E. Stoller, and A. S. Kumar, eds., American Society for Testing and Materials, Philadelphia, pp. 379–395.

Postma, G. W., 1955, "Wave Propagation in a Stratified Medium," *Geophysics*, Vol. 20, pp. 780–806.

Rokhlin, S. I., and Wang, Y. J., 1991, "Analysis of Boundary Conditions for Elastic Wave Interaction with an Interface Between Two Solids," *Journal of the Acoustical Society of America*, Vol. 89, pp. 503–515.

Rose, J. H., 1992, "Ultrasonic Backscatter from Microstructure," *Review of Quantitative Nondestructive Evaluation*, Vol. 11B, D. O. Thompson and D. E. Chimenti, eds., Plenum Press, New York, pp. 1677–1684.

Stanke, F. E., and Kino, G. S., 1984, "A Unified Theory for Elastic Wave Propagation in Polycrystalline Materials," *Journal of the Acoustical Society of America*, Vol. 75, pp. 665–681.

Twersky, V., 1962, "Multiple Scattering by Arbitrary Configurations in Three Dimensions," *Journal of Mathematical Physics*, Vol. 3, pp. 83–91.

Ying, C. F., and Truell, R., 1956, "Scattering of a Plane Longitudinal Wave by a Spherical Obstacle in an Isotropically Elastic Solid," *Journal of Applied Physics*, Vol. 27, pp. 1086–1097.

APPENDIX A

Values of Coefficients

Equation (11*b*):

$$\begin{pmatrix} f_2 \\ g_2 \end{pmatrix}_{p_1} = \lim_{x \to p_1 + 2} \left(-M^{-1}(x) K \begin{pmatrix} f_0 \\ g_0 \end{pmatrix}_{p_1} \right) \qquad (11b)$$

* * * * *

$$\begin{pmatrix} f_0 \\ g_0 \end{pmatrix}_{(m-1)} = \begin{pmatrix} m \\ 1 \end{pmatrix}$$

$$\begin{pmatrix} f_2 \\ g_2 \end{pmatrix}_{(m-1)} = \frac{-K_1^2}{2(1+2m)(3+2m)} \times \begin{pmatrix} m((2+m) + \nu(1+m)) \\ m + \nu(3+m) \end{pmatrix}$$

$$\begin{pmatrix} f_0 \\ g_0 \end{pmatrix}_{-(m+2)} = \begin{pmatrix} -(1+m) \\ 1 \end{pmatrix}$$

$$\begin{pmatrix} f_2 \\ g_2 \end{pmatrix}_{-(m+2)} = \frac{-K_1^2}{2(1+2m)(1-2m)} \times \begin{pmatrix} (1+m)((1-m) - \nu m) \\ (1+m) - \nu(2-m) \end{pmatrix}$$

where $\nu = \dfrac{c_{11}}{c_{66}} = \dfrac{K_2^2}{K_1^2}$.

K. M. Liew
Director and Senior Lecturer,
Mem. ASME.

K. C. Hung
Teaching Assistant.

M. K. Lim
Dean and Associate Professor.

Dynamics and Vibration Centre,
School of Mechanical and
Production Engineering,
Nanyang Technological University,
Nanyang Avenue,
Singapore 2263

Free Vibration Studies on Stress-Free Three-Dimensional Elastic Solids

A comprehensive investigation on free vibration of three-dimensional elastic solids of rectangular planform is reported. The continuum is considered to be free from normal and in-plane stresses on the facets. Functions representing the spatial displacement fields of the continuum in a complete Cartesian coordinate system are expressed in terms of sets of orthogonal polynomial functions in the x, y, and z directions. The energy functional derived based on the three-dimensional elasticity theory is minimized to arrive at the governing eigenvalue equation. In this paper, the vibration of stress-free elastic solids in the forms of short columns, thick plates, and solid cubes are studied. Frequency parameters and the first known three-dimensional deformed mode shapes have been generated for these stress-free elastic solids.

1 Introduction

Despite the practical needs for three-dimensional elastic solutions to engineering problems, literature on this topic are very scarce. One of the earlier attempts to study the vibration motion of elastic solids using a three-dimensional analytical approach can be traced back to the work of Mindlin and Fox (1960). An important analytical study on the infinitely long bar of rectangular cross-section with traction-free faces by means of general elasticity equations has been performed.

A decade later, Fromme and Leissa (1970) have contributed a well-cited work on the free vibration of completely free rectangular parallelepipeds. The *associated-periodicity* extension of the Fourier analysis was used to obtain an approximate solution to the three-dimensional elasticity problem. By degenerating the three-dimensional characteristics equations into a two-dimensional one, Fromme and Leissa (1970) presented many interesting frequency results for planar vibration (plane-strain) of stress-free continuums. After another decade, an excellent study on the free vibration analysis of rectangular parallelepiped was reported by Hutchinson and Zillmer (1983) who extended the series solution scheme (Hutchinson, 1981) to a stress-free elastic solid. But no detailed study on the in-plane and transverse mode shapes has been reported.

This paper is a complement to the above works by providing a more general and comprehensive study on the free vibration characteristics of three-dimensional elastic solids. In the present study, the energy functional of the continuum is derived based on the three-dimensional elasticity theory. The solution spaces to this problem are approximated by sets of beam characteristic orthogonal polynomials. The Ritz procedure is subsequently applied to derive the governing eigenvalue equation. By solving this eigenvalue problem, sets of natural frequencies and mode shapes for a three-dimensional elastic solid column, plate, and cube are obtained. These results, where possible, are compared with the various existing solutions from the approximate theories and three-dimensional analytical methods. The three-dimensional mode shapes for these elastic solids presented herein are first known in the open literature.

2 Theoretical Formulation

2.1 Three-Dimensional Elasticity Formulation. Consider a homogeneous elastic solid, as shown in Fig. 1, bounded by the edges $-a/2 \le x \le a/2$, $-b/2 \le y \le b/2$, and $-c/2 \le z \le c/2$. The origin of the coordinate system is assumed to be located at the geometric center of the continuum. The surfaces of the elastic solid are assumed to be stress free, i.e., $\sigma_x = \sigma_y = \sigma_z = \tau_{xy} = \tau_{xz} = \tau_{yz} = 0$.

For small-amplitude vibratory motion, the strain energy of the continuum can be expressed as

$$\mathbb{U} = \frac{1}{2}\int_v \left[\Delta\left\{(1-\nu)\mathbb{U}_1 + 2\nu\mathbb{U}_2 + \frac{(1-2\nu)}{2}\mathbb{U}_3\right\}\right] dv \quad (1)$$

where

$$\mathbb{U}_1 = \epsilon_x^2 + \epsilon_y^2 + \epsilon_z^2 \quad (2)$$

$$\mathbb{U}_2 = \epsilon_x\epsilon_y + \epsilon_x\epsilon_z + \epsilon_y\epsilon_z \quad (3)$$

$$\mathbb{U}_3 = \gamma_{xy}^2 + \gamma_{xz}^2 + \gamma_{yz}^2 \quad (4)$$

Contributed by the Applied Mechanics Division of THE AMERICAN SOCIETY OF MECHANICAL ENGINEERS for publication in the ASME JOURNAL OF APPLIED MECHANICS.

Discussion on this paper should be addressed to the Technical Editor, Professor Lewis T. Wheeler, Department of Mechanical Engineering, University of Houston, Houston, TX 77204-4792, and will be accepted until four months after final publication of the paper itself in the ASME JOURNAL OF APPLIED MECHANICS.

Manuscript received by the ASME Applied Mechanics Division, Feb. 4, 1993; final revision, Dec. 7, 1993. Associate Technical Editor: X. Markenscoff.

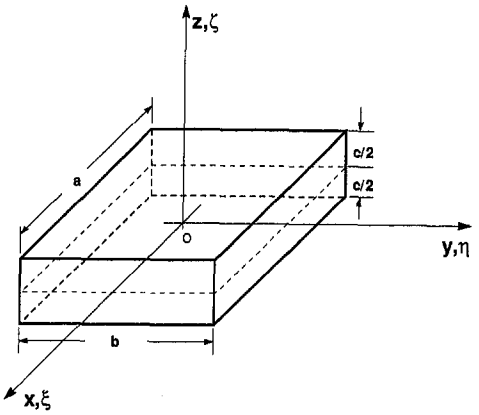

Fig. 1 Reference coordinates and dimensions of an elastic solid continuum

and

$$\Delta = E/[(1+\nu)(1-2\nu)] \tag{5}$$

in which E is the modulus of elasticity and ν the Poisson ratio.

The kinetic energy for free vibration is expressed as

$$\mathbb{T} = \frac{\rho}{2}\int_v \left[\left(\frac{\partial u}{\partial t}\right)^2 + \left(\frac{\partial v}{\partial t}\right)^2 + \left(\frac{\partial w}{\partial t}\right)^2\right] dv \tag{6}$$

where ρ is the mass density per unit volume of the continuum.

The displacement components u, v, and w for a linear, small-strain, simple harmonic motion assumed the following forms:

$$u = u(x,y,z,t) = U(x,y,z)e^{i\omega t}, \tag{7}$$

$$v = v(x,y,z,t) = V(x,y,z)e^{i\omega t}, \tag{8}$$

$$w = w(x,y,z,t) = W(x,y,z)e^{i\omega t}, \tag{9}$$

in which t is time and ω denotes the angular frequency of vibration.

2.2 Method of Solution. For simplicity and generality, the coordinates are normalized with respect to the elastic solid dimensions as $\xi = x/a$; $\eta = y/b$, and $\zeta = z/c$. In the present analysis, the displacement functions $U(\xi,\eta,\zeta)$, $V(\xi,\eta,\zeta)$, and $W(\xi,\eta,\zeta)$ are approximated by separable orthogonal polynomial functions in ξ, η, and ζ, respectively,

$$U(\xi,\eta,\zeta) = \sum_{i}^{I}\sum_{j}^{J}\sum_{k}^{K} C_{uijk}\phi_{ui}(\xi)\psi_{uj}(\eta)\chi_{uk}(\zeta) \tag{10}$$

$$V(\xi,\eta,\zeta) = \sum_{l}^{L}\sum_{m}^{M}\sum_{n}^{N} C_{vlmn}\phi_{vl}(\xi)\psi_{vm}(\eta)\chi_{vn}(\zeta) \tag{11}$$

$$W(\xi,\eta,\zeta) = \sum_{p}^{P}\sum_{q}^{Q}\sum_{r}^{R} C_{wpqr}\phi_{wp}(\xi)\psi_{wq}(\eta)\chi_{wr}(\zeta) \tag{12}$$

where C_{uijk}, C_{vlmn}, and C_{wpqr} are the undetermined coefficients and ϕ, ψ, and χ are the corresponding polynomial functions generated using the Gram-Schmidt process (Liew et al., 1993a). This is illustrated for $\phi(\xi)$ as follows:

$$\phi_{k+1}(\xi) = \{g(\xi) - \Theta_k\}\phi_k(\xi) - \Xi_k\phi_{k-1}(\xi); \quad k = 1,2,3,\ldots. \tag{13}$$

The polynomial $\phi_0(\xi)$ is defined as zero and the constants Θ_k and Ξ_k are chosen so as to satisfy the orthogonality $\int_{-0.5}^{0.5}\phi_i(\xi)\,\phi_j(\xi)\,d\xi = \delta_{ij}$. From the recurrence relation in Eq. (13), we derived the constants $\Theta_k = {}_1\Delta_k/{}_2\Delta_k$ and $\Xi_k = {}_2\Delta_k/{}_3\Delta_{k-1}$, in which

Table 1 Basic functions for u, v, and w components at different symmetry classes

Symmetry Class	U		V		W	
	$\phi_{u1}(\xi)$	$\psi_{u1}(\eta)$	$\phi_{v1}(\xi)$	$\psi_{v1}(\eta)$	$\phi_{w1}(\xi)$	$\psi_{w1}(\eta)$
SS	f_o	f_e	f_e	f_o	f_e	f_e
SA	f_o	f_o	f_e	f_e	f_e	f_o
AS	f_e	f_e	f_o	f_o	f_o	f_e
AA	f_e	f_o	f_o	f_e	f_o	f_o

$f_o(\xi;\eta) = (\xi;\eta)$; $f_e(\xi;\eta) = 1$; $\chi_{u1}(\zeta) = \chi_{v1}(\zeta) = \chi_{w1}(\zeta) = 1$
Generating function $g(\xi;\eta;\zeta) = (\xi^2;\eta^2;\zeta)$

$$ {}_1\Delta_k = \int_{-0.5}^{0.5} g(\xi)\phi_k^2(\xi)d\xi \tag{14}$$

$$ {}_2\Delta_k = \int_{-0.5}^{0.5} \phi_k^2(\xi)d\xi \tag{15}$$

$$ {}_3\Delta_{k-1} = \int_{-0.5}^{0.5} \phi_{k-1}^2(\xi)d\xi \tag{16}$$

The generating function, $g(\xi)$, in Eq. (13) is chosen for the higher terms to satisfy the essential geometric boundary conditions at the facets. A detailed proof on the orthogonality of these polynomials is given in the Appendix. Following the same procedure, functions in $\psi(\eta)$ and $\chi(\zeta)$ can be generated.

In this analysis, the deflection mode shapes are divided into four symmetry classes with respect to the xz and yz-planes. The basic function in the z-direction, $\chi(\zeta)$, is chosen to be unity [$\chi(\zeta) = 1$]. This choice satisfies the essential geometric requirements of stress-free surfaces at $z = -c/2$ and $c/2$. In the x and y-directions, depending on the symmetry classes of vibration, the basic functions in these directions take on different forms. Table 1 summarizes the respective basic functions chosen for each symmetry class.

Let the energy functional of the elastic solid be

$$\mathbb{F} = \mathbb{U}_{max} - \mathbb{T}_{max} \tag{17}$$

in which $\mathbb{U}_{max}$ and $\mathbb{T}_{max}$ are the maximum strain and kinetic energies, respectively.

Substituting the spatial displacement functions given in Eqs. (10–12) into the energy functional and minimizing according to the Ritz procedure,

$$\partial\mathbb{F}/\partial C_{uijk} = 0,\ \partial\mathbb{F}/\partial C_{vlmn} = 0 \text{ and } \partial\mathbb{F}/\partial C_{wpqr} = 0, \tag{18}$$

leads to the governing eigenvalue equation

$$(\mathbf{K} - \lambda^2\mathbf{M})\{\mathbf{C}\} = \{0\} \tag{19}$$

where $\mathbf{K}$ and $\mathbf{M}$ are the stiffness and mass matrices. The explicit expressions of $\mathbf{K}$ and $\mathbf{M}$ can be found in the work of Liew et al. (1993). The frequency parameters, $\lambda = \omega a(\rho/E)^{1/2}$, are obtained by solving the characteristic eigenvalue problem defined by Eq. (19).

3 Results and Discussion

3.1 Convergence Studies. Nondimensional frequency parameters, $\lambda = \omega a(\rho/E)^{1/2}$, for an elastic solid of rectangular platform with stress-free boundaries were computed. It is well known that eigenvalue problems formulated using the Ritz procedure have the desired embedding property in which the stiffness and mass matrices of a smaller size problem (corresponding to fewer terms in the admissible functions) are embedded in the larger matrices formed by using higher terms in the admissible functions. This property ensures a monotonic converging pattern that leads to an upper bound solutions. The rate of convergences of the present Ritz formulation is demonstrated in Table 2 for a

cubic elastic solid. In this analysis, vibration mode shapes are categorized into the doubly symmetry mode (SS), symmetry-antisymmetry mode (SA), antisymmetry-symmetry mode (AS) and doubly antisymmetry mode (AA) about the xz and yz-planes. It it observed that reasonable convergence up to four decimal places can be achieved with $5 \times 5 \times 9$ terms in the displacement functions. Hence, in the subsequent calculation, the results are computed from displacement functions of $5 \times 5 \times 9$ terms.

3.2 Comparison Studies. Table 3 compares the present three-dimensional solutions with that of the approximate theories for elastic columns of different lengths. The Timoshenko beam predictions (Huang, 1961) which consider both the shear deformation and rotary inertia effects are in excellent agreement with the present three-dimensional elasticity solutions. However, the two-dimensional elasticity solution by the method of *associated periodicity* (Fromme and Leissa, 1970) gives slightly higher frequency estimates than the Timoshenko beam theory (Huang, 1961) and the present three-dimensional results.

In Table 4, the vibration frequencies for thick plates computed from the classical plate theory (CPT), the Mindlin plate theory (also known as the first-order shear deformable plate theory (FSDT)) and the three-dimensional elasticity solutions are presented. It is observed that at thickness ratio $c/b = 0.1$, the frequency parameters predicted from the Mindlin plate formulation (Liew et al., 1993b) agrees very well with the present three-dimensional elasticity solutions. The classical plate theory (Leissa, 1973), however, gives much higher values than those of the Mindlin theory and the present three-dimensional elasticity solutions. This is expected since the classical plate theory ignores the shear deformation and rotary inertia effects which are significant for moderately thick plate analysis. The Mindlin's plate formulation, on the other hand, has implicitly accounted for these thickness effects which are inherent in the present three-dimensional elasticity formulation.

Table 2 Convergence of frequency parameters $\lambda = \omega a(\rho/E)^{1/2}$ for a stress-free elastic cubic solid ($a/b = 1.0$, $c/b = 1.0$, and $\nu = 0.3$)

Mode	Number of terms, $i \times j \times k$				
	3×3×4	4×4×6	4×4×8	5×5×8	5×5×9
SS-1	2.3926	2.3852	2.3852	2.3852	2.3852
SS-2	2.7554	2.7554	2.7554	2.7554	2.7554
SS-3	2.7587	2.7554	2.7554	2.7554	2.7554
SA-1†	2.4286	2.3856	2.3852	2.3852	2.3852
SA-2†	2.4421	2.4259	2.4257	2.4257	2.4257
SA-3†	2.9651	2.8375	2.8360	2.8359	2.8359
AA-1	1.7733	1.7713	1.7713	1.7712	1.7712
AA-2	1.7762	1.7714	1.7713	1.7712	1.7712
AA-3	2.4265	2.4257	2.4257	2.4257	2.4257

† For a stress free continuum with a/b=1.0, the SA and AS modes have identical frequencies.

Referring to Table 4, at a higher thickness ratio $c/b = 0.2$, the eigenvalues predicted in the Mindlin theory are in close agreement with the three-dimensional solutions. Except that, at this thickness ratio, the refined theory fails to identify certain modes. For SA mode of vibration, the three-dimensional solution gives an intermediate mode ($\lambda = 2.5889$) which cannot be found in the Mindlin solution. The other missing mode occurred at the second AA mode of vibration ($c/b = 0.2$). This observation agrees with the comment given by Srinivas et al. (1970) who stated that *if one is seeking only the flexural, thickness-twist and thickness-shear frequencies, Mindlin's approximation and simple theory are fully justified. However, it the full spectrum of modes need to be established, the exact three-dimensional analysis is necessary.*

To facilitate a comparison with the work of Hutchinson and Zillmer (1983), the frequency parameters from different sources were plotted in Fig. 2 for thickness ratios varying in the ranges from 0.0 to 0.5. The comparison has shown that the present predictions and that of Hutchinson and Zillmer (1983) are found to be in excellent agreement.

3.3 Three-Dimensional Model Shapes. The deflection mode shapes of elastic solids at each symmetry classes are depicted in three-dimensional contour plots that are arranged in terms of displacement components, u, v, and w, respectively. The corresponding three-dimensional deformed mode shapes are also included.

It should be noted that for a stress-free continuum, the first six modes are the rigid-body modes corresponding to the translation in and rotation about the x, y and z-directions. All these rigid-body modes are not shown in the present mode shape diagrams.

(a) Short Columns. The displacement contour plots and three-dimensional deformed mode shapes of an elastic solid column with $a/b = 1.0$ and $c/b = 3.0$ are presented in Fig. 3. The first SS mode can be clearly identified as the longitudinal extension and compression motion of the elastic solid column. The first SA modes (also the second and third AS modes), on the other hand, exhibit transverse bending motions. Axial torsional motions are observed in the first, second, and third AA modes of vibration. Apart from these, the other modes of vibration are more complex and involved the combinations of elongation, bending, and torsional motions.

Table 3 Comparison of fundamental frequency parameter $\lambda_1 = \omega_1 a(\rho/E)^{1/2}$ for an elastic solid column with stress-free boundaries ($a/b = 1.0$ and $\nu = 0.3$)

c/b	Huang (1961)	Fromme & Leissa (1970)	Present 3-D Solutions
3	0.547	0.567	0.5487
4	0.339	0.350	0.3393
5	0.229	0.237	0.2291
6	0.164	0.171	0.1644
8	0.096	0.099	0.0958

Table 4 Comparison of frequency parameters $\lambda = \omega a(\rho/E)^{1/2}$ for a moderately thick plate with stress-free boundaries ($a/b = 1.0$ and $\nu = 0.3$)

c/b	Source	Symmetry class and mode number								
		SS-1	SS-2	SS-3	SA-1	SA-2	SA-3	AA-1	AA-2	AA-3
0.1	CPT[a]	0.5988	0.7393	-	1.0599	1.8619	-	0.4082	-	-
	FSDT[b]	0.5733	0.7058	1.6860	0.9660	1.6750	-	0.3849	1.8348	2.0479
	Present	0.5736	0.7065	1.6902	0.9673	1.6793	2.5904	0.3851	1.8389	2.0542
0.2	CPT[a]	1.1977	1.4787	-	2.1197	-	-	0.8164	-	-
	FSDT[b]	1.0531	1.2827	2.7299	1.6688	-	2.7376	0.7082	-	2.9182
	Present	1.0551	1.2862	2.7423	1.6733	2.5889	2.7560	0.7087	2.4325	2.9326

[a]Classical plate theory (Leissa, 1973)
[b]First order shear deformable theory (Liew, Xiang and Kitipornchai, 1993b)

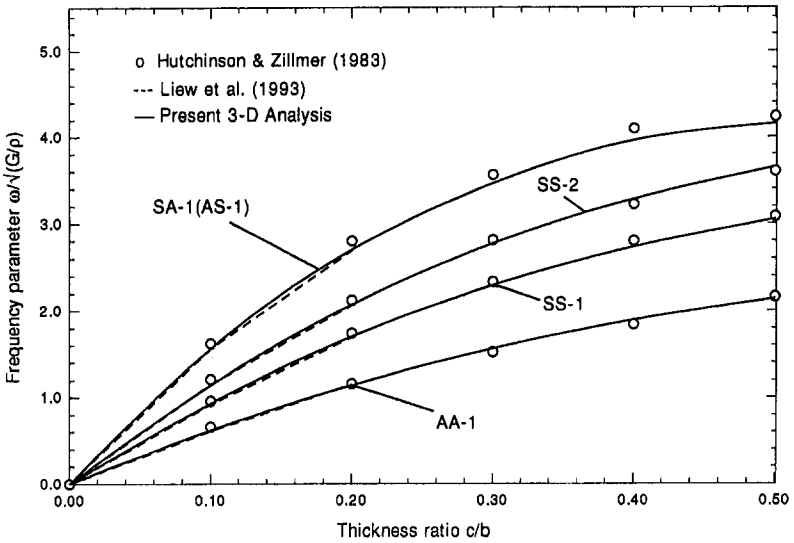

Fig. 2 Comparison of frequency parameters for an elastic solid plate

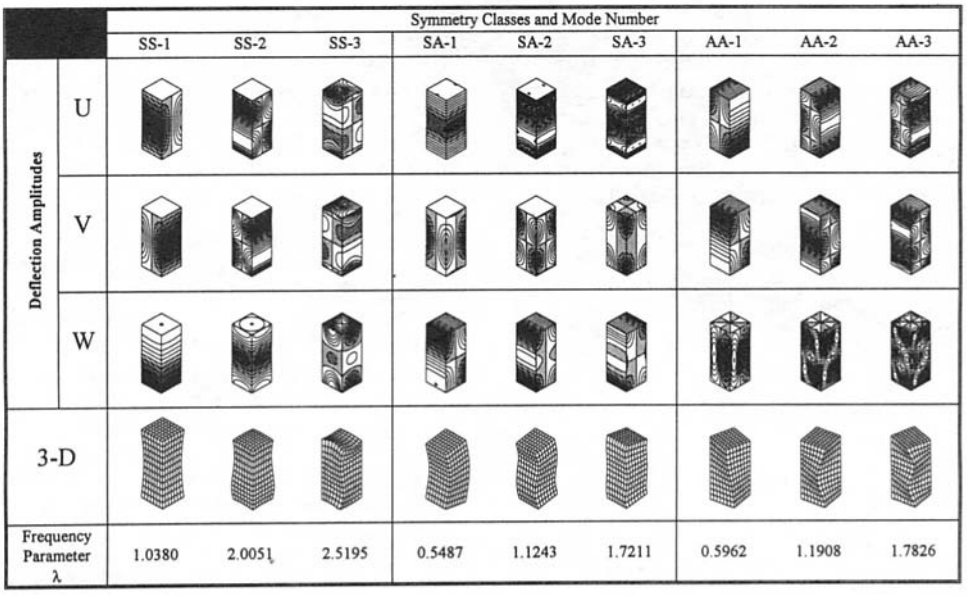

Fig. 3 Displacement contour plots of an elastic solid column ($a/b = 1.0$, $c/b = 3.0$ and $\nu = 0.3$)

(b) Thick Plates. The deflection mode shapes of the thick elastic plate with aspect ratio $a/b = 1.0$ and thickness ratio $c/b = 0.5$ are presented in Fig. 4. Flexural motion is found in the SS-1 and SS-2 modes. Pure in-plane vibratory motion occurs in the third SS mode. The first SA mode, is also predominantly an in-plane motion with negligible out-of-plane (w-component) deformation. The second and third SA modes exhibit flexural motions with distinct nodal lines appearing in the w-component. Warping motions with maximum deflection occurring at the corners are found in the first and third AA modes. The second AA mode is undergoing an in-plane shearing motion. The planar torsional motion about the z-direction is observed in the third AA mode of vibration.

(c) Solid Cubes. The contour plots of a solid cube are depicted in Fig. 5. It is interesting to observe that the first SS mode and SA mode (also the AS mode) have an identical frequency value. The modes of vibration are also found to be identical with displacement pattern interchangeable in the u, v, and w components. The second and third SS modes show a very similar deformed pattern. In addition, the frequencies of the SS-2 and SS-3 modes for a cubic solid are identical to the SS-3 modes for the plate in Fig. 4. These modes are the lowest of a series of modes which were obtained by Lamé as the exact solutions of the three-dimensional equation of elasticity and, therefore, are called Lamé modes (Lamé, 1866).

The frequencies for Lamé's equivoluminal modes are given by Mindlin (1955) as $\omega = (n\pi/a) \times (2G/\rho)^{1/2}$ where a is the width of the plate, $G = E/[2(1 + \nu)]$ is the shear modulus; n = odd for symmetric modes, and n = even for antisymmetric modes, and the frequencies are independent of the dimension, c. In terms of the present frequency parameter, $\lambda_n = (n\pi)/(1 + \nu)^{1/2}$, which gives $\lambda_1 = 2.75536$ for $n = 1$ and $\nu = 0.3$.

The second SA mode is identified to be the planar-shear mode in the xz-plane (y = constant). Fromme and Leissa (1970) presented a frequency value of 77,700 Hz as compared to the upper bound value of 80,300 Hz reported by Ekstein and Schiffman (1956), whereas the present three-dimensional elasticity method gives 77,060 Hz (calculated for 1-in. cubic steel with $E = 30 \times 10^6$ psi, $\nu = 1/3$ and $\rho = 0.735 \times 10^{-3}$,

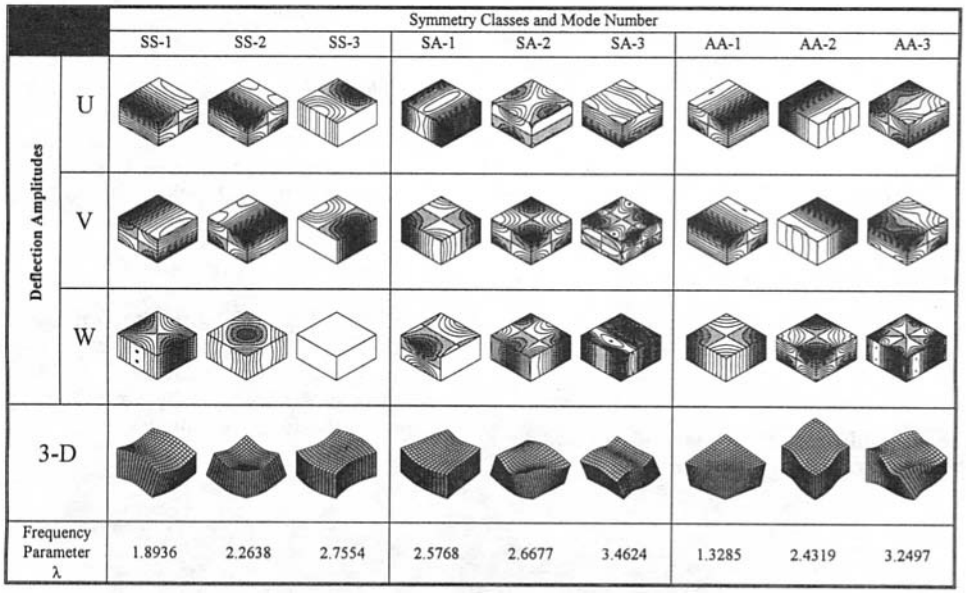

Fig. 4 Displacement contour plots of an elastic thick plate ($a/b = 1.0$, $c/b = 0.5$ and $\nu = 0.3$)

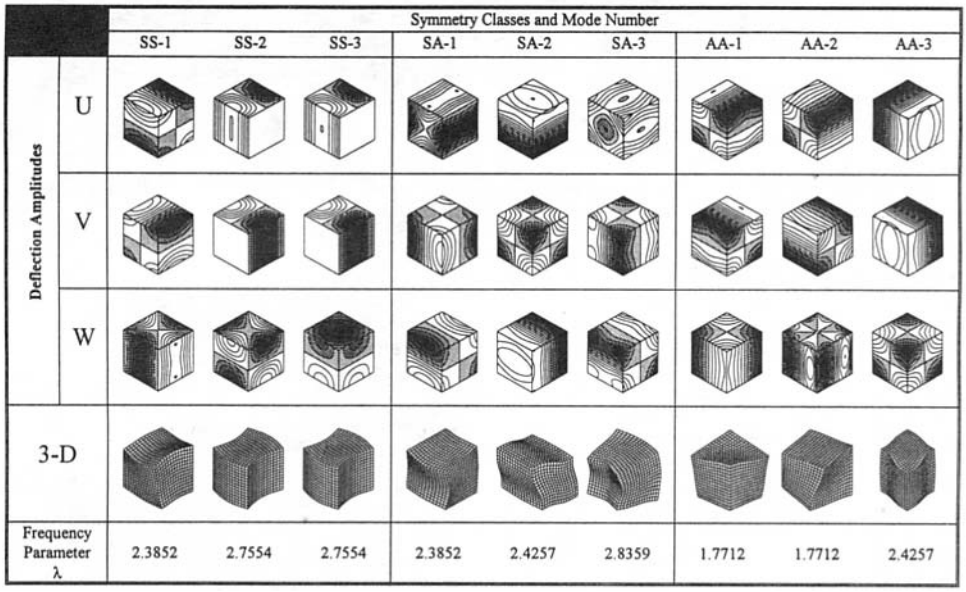

Fig. 5 Displacement contour plots of a cubic elastic solid ($a/b = 1.0$, $c/b = 1.0$ and $\nu = 0.3$)

lb sec^2/in.^{4}). This planar-shear motion is also found in the third AA mode of vibration. The third SA mode has been named the *podium mode* in the work of Kidger and Smith (1992). The first and second AA modes have the same frequency value, however, the deformed mode shapes are different. The first AA mode resembles the *bow-tie mode* presented by Kidger and Smith (1992) using an eight-node brick element. The second AA mode, on the other hand, shows coupling between the in-plane stretching motion in the x and y-directions and the axial torsional motion about the z-direction.

4 Conclusions

A comprehensive study of the free vibrations of three-dimensional elastic solids with stress-free boundaries was presented. The governing eigenvalue equation for the continuum was derived from the three-dimensional elasticity theory and Ritz minimization procedure. The spatial displacement components in the x, y and z directions were expressed in terms of sets of orthogonally generated polynomial functions. Vibration frequencies and first known mode shapes for the elastic solids in the forms of short column, thick plate, and solid cube were obtained by solving the resulting eigenvalue equation.

Convergence and comparison studies have been carried out to validate the applicability and accuracy of the present three-dimensional formulation. Frequency parameters and mode shapes for elastic solids of different volumetric sizes have been computed and their characteristics have been discussed in detail. Comparisons with the established approximation theories for the beams and plates have shown close agreement for limited ranges. For a plate with higher side to thickness ratios, it is believed that the present method provides more accurate results. Displacement mode shapes in three-dimensional were plotted to enhance our understanding on the vibratory motions of an elastic solid. A wider spectrum of mode shapes has been obtained by means of the

three-dimensional elasticity formulation. This finding is believed to be very useful for researchers who are developing the simpler and more economical refined theories, and also to engineers who need a better description on the vibratory motion of the structures that does not fall into the categories of slender beams and thin plates.

The present three-dimensional formulation based on the Ritz method will be extended to analyze the vibrations of composite laminates. By performing appropriate coordinate transformations, the method can also be employed to predict the frequency response of a wide range of elastic solids of practical shapes and sizes.

Acknowledgments

The authors are grateful to Prof. X. Markenscoff and the reviewers for their very constructive comments and suggestions.

References

Ekstein, H., and Schiffman, T., 1956, "Free Vibration of Isotropic Cubes and Nearly Cubic Parallelepipeds," *Journal of Applied Physics*, Vol. 27, pp. 405–412.

Fromme, J. A., and Leissa, A. W., 1970, "Free Vibration of the Rectangular Parallelepiped," *Journal of the Acoustical Society of America*, Vol. 48, No. 1, pp. 290–298.

Huang, T. C., 1961, "The Effect of Rotatory Inertia of Shear Deformation on the Frequency and Normal Mode Equations of Uniform Beams with Simple End Conditions," ASME JOURNAL OF APPLIED MECHANICS, Vol. 28, pp. 579–584.

Hutchinson, J. R., 1981, "Transverse Vibrations of Beams, Exact Versus Approximate Solutions," ASME JOURNAL OF APPLIED MECHANICS, Vol. 48, pp. 923–928.

Hutchinson, J. R., and Zillmer, S. D., 1983, "Vibration of a Free Rectangular Parallelepiped," ASME JOURNAL OF APPLIED MECHANICS, Vol. 50, pp. 123–130.

Kidger, D. J., and Smith, I. M., 1992, "Eigenvalues of Element Stiffness Matrices. Part II: Three-Dimensional Solid Elements," *Engineering Computations*, Vol. 9, pp. 317–328.

Lamé, G., 1866, *Lecons sur la théorie mathématique de L'éasticité des corps solides*, Gauthier-Villars, Paris, France, 2nd ed., pp. 170.

Leissa, A. W., 1973, "The Free Vibration of Rectangular Plates," *Journal of Sound and Vibration*, Vol. 31, pp. 257–293.

Liew, K. M., Hung, K. C., and Lim, M. K., 1993a, "A Continuum Three-Dimensional Vibration Analysis of Thick Rectangular Plates," *International Journal of Solids and Structures*, Vol. 30, pp. 3357–3379.

Liew, K. M., Xiang, Y., and Kitiporchai, S., 1993b, "Transverse Vibration of Thick Rectangular Plates—I: Comprehensive Sets of Boundary Conditions," *Computers and Structures*, Vol. 49, pp. 1–29.

Mindlin, R. D., 1955, "An Introduction to the Mathematical Theory of Vibrations of Elastic Plates," U.S. Army Signal Corps. Engineering Laboratories, Fort Monmouth, NJ, p. 215.

Srinivas, S., Rao, C. V., Joga, and Rao, A. K., 1970, "An Exact Analysis for Vibration of Simple-Supported Homogeneous and Laminated Thick Rectangular Plates," *Journal of Sound and Vibration*, Vol. 12, pp. 187–199.

APPENDIX

Given here is the proof for the orthogonality of the polynomials constructed from the recursive relation in Eq. (13). For simplicity, the functions $g(\xi)$ and $\phi_i(\xi)$ are replaced by g and ϕ_i. The integration limit is taken from -0.5 to 0.5.

The orthogonality between any three consecutive members can be deduced directly from Eqs. (13)–(16), i.e.,

$$\int \phi_k \phi_{k+2} d\xi = 0;\ k = 1, 2, 3, \ldots. \tag{A1}$$

Mathematical induction is used to prove the general orthogonality between n consecutive members, where $n \geq 3$. The procedures are outlined as follows.

First, we assumed that the orthogonality relation is valid for any $n (n \geq 3)$ consecutive members; i.e.,

$$\int \phi_r \phi_s d\xi = 0, r \geq k - n + 1, s \leq k \text{ and } \forall r \neq s. \tag{A2}$$

Next, we proceed to prove that when $n (n \geq 3)$ consecutive members are orthogonal, $(n + 1)$ consecutive members are also orthogonal to each other. In other words, we are to prove

$$\int \phi_{k-n+1} \phi_{k+1} d\xi = 0, \forall n \geq 3. \tag{A3}$$

Combining Eq. (A2) with the orthogonality relation between three consecutive members in Eq. (A1), we shall prove that the orthogonality relation is valid for any arbitrary consecutive members.

Consider the following integral:

$$\begin{aligned}\int \phi_{k-n+1} \phi_{k+1} d\xi &= \int \phi_{k-n+1} \{(g - \Theta_k)\phi_k - \Xi_k \phi_{k-1}\} d\xi \\ &= \int g \phi_{k-n+1} \phi_k d\xi - \Theta_k \int \phi_{k-n+1} \phi_k d\xi \\ &\quad - \Xi_k \int \phi_k -_{n+1} \phi_{k-1} d\xi. \end{aligned} \tag{A4}$$

Based on the assumption of Eq. (A2), we have

$$\int \phi_{k-n+1} \phi_k d\xi = \int \phi_{k-n+1} \phi_{k-1} d\xi = 0 \tag{A5}$$

and Eq. (A4) becomes

$$\int \phi_{k-n+1} \phi_{k+1} d\xi = \int g \phi_{k-n+1} \phi_k d\xi. \tag{A6}$$

From the recurrence relation of Eq. (13),

$$\phi_{k-n+2} = (g - \Theta_{k-n+1})\phi_{k-n+1} - \Xi_{k-n+1} \phi_{k-n} \tag{A7}$$

with re-arranging, we have

$$g \phi_{k-n+1} = \phi_{k-n+2} + \Theta_{k-n+1} + \Theta_{k-n+1} + \Xi_{k-n+1} \phi_{k-n}. \tag{A8}$$

Introducing Eq. (A8) into Eq. (A6) gives

$$\begin{aligned}\int \phi_{k-n+1} \phi_{k+1} d\xi &= \int \phi_{k-n+2} \phi_k d\xi + \Theta_{k-n+1} \int \phi_{k-n+1} d\xi \\ &\quad + \Xi_{k-n+1} \int \phi_{k-n} \phi_k d\xi. \end{aligned} \tag{A9}$$

From Eq. (A2) again we have

$$\int \phi_{k-n+1} \phi_k d\xi = \int \phi_{k-n+2} \phi_k d\xi = 0 \tag{A10}$$

and Eq. (A9) becomes

$$\int \phi_{k-n+1} \phi_{k+1} d\xi = \Xi_{k-n+1} \int \phi_{k-n} \phi_k d\xi. \tag{A11}$$

Expanding Eq. (A11) further in a recursive manner gives

$$\int \phi_{k-n+1} \phi_{k+1} d\xi = \Xi_{k-n+1} \Xi_{k-n} \Xi_{k-n-1} \cdots \Xi \phi_1 \phi_{n+1} d\xi. \tag{A12}$$

The right-hand integral, $\int \phi_1 \phi_{n+1} d\xi$, of Eq. (A12) can be rewritten as

$$\begin{aligned}\int \phi_1 \phi_{n+1} d\xi &= \int \phi_1 \{(g - \Theta_n)\phi_n - \Xi_n \phi_{n-1}\} d\xi \\ &= \int g \phi_1 \phi_n d\xi - \Theta_n \int \phi_1 \phi_n d\xi - \Xi_n \int \phi_1 \phi_{n-1} d\xi. \end{aligned} \tag{A13}$$

Using the assumption of Eq. (A2) with k taken as n, we have

$$\int \phi_r \phi_s d\xi = 0;\ r \geq 1,\ s \leq n \text{ and } \forall r \neq s \tag{A14}$$

and so

$$\int \phi_1 \phi_n d\xi = \int \phi_1 \phi_{n-1} d\xi = 0. \quad \text{(A15)}$$

Hence, Eq. (A13) becomes

$$\begin{aligned} \int \phi_1 \phi_{n+1} d\xi &= \int g \phi_1 \phi_n d\xi \\ &= \int (\phi_2 + \Theta_1 \phi_1) \phi_n d\xi \\ &= \int \phi_2 \phi_n d\xi + \Theta_1 \int \phi_1 \phi_n d\xi. \end{aligned} \quad \text{(A16)}$$

From Eq. (A14) we have

$$\int \phi_2 \phi_n d\xi = 0, \quad \text{(A17)}$$

which proves $\int \phi_1 \phi_{n+1} d\xi = 0$. Substituting this integral into Eq. (A12) yields

$$\int \phi_{n-n+1} \phi_{k+1} \phi_{k+1} d\xi = 0. \quad \text{(A18)}$$

Equation (A18) implies that if $n (n \geq 3)$ consecutive members are orthogonal, then $(n + 1)$ consecutive members are also orthogonal to each other. Since the orthogonality relation holds for $n = 3$, this together with Eq. (A18) verifies the overall orthogonality of the polynomials generated from the recurrence relation of Eq. (13).

A Study of Embedded Piezoelectric Layers in Composite Cylinders

J. A. Mitchell
Graduate Research Assistant.

J. N. Reddy
Oscar S. Wyatt Chair,
Fellow ASME.

Department of Mechanical Engineering,
Texas A & M University,
College Station, TX 77843-3123

A power series solution is presented for the static equilibrium equations of an axisymmetric composite cylinder under loadings due to surface mounted or embedded piezoelectric laminae. Both uniform and nonuniform distributions of the piezoelectric effect are studied and results are verified using a finite element model based on axisymmetric two-dimensional elasticity theory equations. A cylindrical truss element actuator is developed which may be used for damping vibrations of truss-type structures. Finally, the effects of a piezoelectric patch have been investigated. The axial forces generated at the fixed ends of a cylinder are found to be proportional to the length of the patch.

1 Introduction

One of the most recent advancements in the field of piezoelectricity is the discovery of the piezoelectric effect in a polymer based material called polyvinylidene fluoride (PVDF) (Kawai, 1979). Compared to other materials, PVDF is flexible, rugged, available in thin sheets and easily manufactured in large quantities and at a low cost (Sessler, 1981). For these reasons, PVDF is currently being studied for use as distributed sensors/actuators in flexible structures. However, before piezoelectric materials can be successfully used for control, the mechanical interaction between them and the structure being controlled must be well understood.

In this paper, two analytical tools are used to study the effects of embedded PVDF laminae in an axisymmetric composite cylinder. A power series solution is presented for the static equilibrium equations and verified using the finite element method. These tools are used to develop a cylindrical truss element actuator to damp vibrations of truss-type structures. Fanson and Garba (1988) have proposed damping for truss-type structures based on the same concept but different actuator design. Another application is an investigation of the effects of a piezoelectric patch. This topic has been investigated by Crawley and Luis (1987). In the case of surface bonded actuators, they presented an elasticity solution based on the assumption of pure one-dimensional shear in the bonding layer which is used to attach the piezoelectric material to the substructure, and pure extensional strains in the piezoelectric layer and substructure. The solution presented here differs in several respects. First, there are no assumptions on stresses and strains except that the governing equations and constitutive model is linear, and the solution may be used to model both bonding and piezoelectric layers including shear deformations. In addition, the piezoelectric effect is induced in a lamina over a finite area, by varying the polarization profile of the particular piezoelectric layer. Crawley and Luis (1987) modeled a piezoelectric layer of finite length bonded to a substructure with the piezoelectric effect uniformly distributed over the patch of piezoelectric.

Finally, it is necessary to comment on the scope of the current study concerning electromechanical coupling. In the present study, as in other published works in smart structures, Crawely and Luis (1987), C. K. Kee (1990), and Tzou and Gadre (1989), the constitutive relation itself represents the only source of coupling between mechanical and electrical effects. This is justified by the intended applications and by the fact that the electric fields induced in thin piezoelectric layers are essentially constant through the thickness direction when a voltage is applied across the piezoelectric lamina. These type of analyses can be properly classified as strain-induced because applied voltages simply induce strains in the piezoelectric layers analogous to that found in thermoelastic studies where temperature gradients induce strain fields. Two studies by Adelman, Stavsky, and Segal (1975) and Adelman and Stavsky (1975) on laminated composite cylinders have included the coupling both through the constitutive relation and the charge equations of electrostatics. In these cases, the intended applications were bandpass filters and high-energy ultrasonic devices using composite piezoelectric disks and long cylinders. Additional references on piezoelectric composite cylinders can be found in Karlash (1990) and Sun and Chen (1974).

Contributed by the Applied Mechanics Division of THE AMERICAN SOCIETY OF MECHANICAL ENGINEERS for publications in the ASME JOURNAL OF APPLIED MECHANICS.

Discussion on this paper should be addressed to the Technical Editor, Professor Lewis T. Wheeler, Department of Mechanical Engineering, University of Houston, Houston, TX 77204-4792, and will be accepted until four months after final publication of the paper itself in the ASME JOURNAL OF APPLIED MECHANICS.

Manuscript received by the ASME Applied Mechanics Division, Jan. 28, 1993; final revision, July 29, 1993. Associate Technical Editor: L. T. Wheeler.

2 Constitutive Relations

In the applications of piezoelectric materials for control of flexible structures, mechanical as well as electrical loadings exist on the material. The constitutive relations of the mechanical and electrical effects are superposed (assuming linearity). The combined relation is written as

$$\sigma = c^E \epsilon - (dc^E)^T E \tag{1}$$

where c^E represents the elastic stiffness matrix with the superscript indicating that the electric field E is held constant. The other variables, ϵ, σ, and d denote, respectively, strains, stresses, and the components of the piezoelectric tensor in matrix notation. The superscript T indicates matrix transpose. For PVDF, d in material coordinates is given as

$$[d] = \begin{bmatrix} 0 & 0 & 0 & 0 & d_{15} & 0 \\ 0 & 0 & 0 & d_{24} & 0 & 0 \\ d_{31} & d_{32} & d_{33} & 0 & 0 & 0 \end{bmatrix}. \tag{2}$$

PVDF is a thin film, and it is polarized and prepared for application of an electric field in the thickness direction only. Assuming that the material axes coincide with the coordinates of the problem being studied, the term $(dc^E)^T E$ can be written as

$$(dc^E)^T E = \begin{bmatrix} 0 & 0 & H_z \\ 0 & 0 & H_\theta \\ 0 & 0 & H_r \\ 0 & C_{44}d_{24} & 0 \\ d_{15}C_{55} & 0 & 0 \\ 0 & 0 & 0 \end{bmatrix} \begin{Bmatrix} 0 \\ 0 \\ E_r \end{Bmatrix} \tag{3}$$

where

$$\begin{aligned} H_z &= d_{31}C_{11} + d_{32}C_{12} + d_{33}C_{13} \\ H_\theta &= d_{31}C_{12} + d_{32}C_{22} + d_{33}C_{23} \\ H_r &= d_{31}C_{13} + d_{32}C_{23} + d_{33}C_{33}. \end{aligned} \tag{4}$$

3 Equilibrium Equations

PVDF, being available in thin sheets, is particularly suitable for introduction into laminated type structures as an embedded actuator. The cylinder analyzed in this study is axisymmetric and built up with composite cross-ply type material layers and PVDF layers.

For an axisymmetric cylinder, the static equilibrium equations (Timoshenko and Goodier, 1951) are

$$\frac{\partial \sigma_r}{\partial r} + \frac{\partial \sigma_{rz}}{\partial z} + \frac{\sigma_r - \sigma_\theta}{r} = 0 \tag{5}$$

$$\frac{\partial \sigma_{rz}}{\partial r} + \frac{\partial \sigma_z}{\partial z} + \frac{\sigma_{rz}}{r} = 0. \tag{6}$$

The cylindrical coordinate system for these equations is oriented with the z coordinate along the axis of the cylinder and the r and θ coordinates in the radial and hoop directions of the cylinder, respectively. The constitutive relation for an axisymmetric cylinder can be expressed as

$$\begin{Bmatrix} \sigma_z \\ \sigma_\theta \\ \sigma_r \\ \sigma_{rz} \end{Bmatrix} = \begin{bmatrix} c_{11} & c_{12} & c_{13} & 0 \\ c_{12} & c_{22} & c_{23} & 0 \\ c_{13} & c_{23} & c_{33} & 0 \\ 0 & 0 & 0 & c_{55} \end{bmatrix} \begin{Bmatrix} \epsilon_z \\ \epsilon_\theta \\ \epsilon_r \\ \epsilon_{rz} \end{Bmatrix} - \begin{Bmatrix} H_z \\ H_\theta \\ H_r \\ 0 \end{Bmatrix} E_r \tag{7}$$

where E_r is the electric field applied in the radial direction, (u, w) are the radial and axial displacements, and

$$\epsilon_z = \frac{\partial w}{\partial z}, \quad \epsilon_\theta = \frac{u}{r}, \quad \epsilon_r = \frac{\partial u}{\partial r}, \quad \epsilon_{rz} = \frac{\partial u}{\partial z} + \frac{\partial w}{\partial r}. \tag{8}$$

Due to the axisymmetry assumption and the fact that this is a specially orthotropic cylinder, the shearing strains and stresses, $\epsilon_{r\theta}$, $\epsilon_{z\theta}$, $\sigma_{r\theta}$, and $\sigma_{z\theta}$, are zero. The coordinate axes are oriented along the material axes of the cylinder and therefore the piezoelectric effect does not induce shearing strains.

Substituting the constitutive relations (7) into Eqs. (5) and (6), the equilibrium equations can be expressed in terms of the displacements (u, w) as

$$r^2\frac{\partial^2 u}{\partial r^2} + r\frac{\partial u}{\partial r} - \frac{c_{22}}{c_{33}}u + \frac{c_{55}}{c_{33}}r^2\frac{\partial^2 u}{\partial z^2} + \left(\frac{c_{13} + c_{55}}{c_{33}}\right)r^2\frac{\partial^2 w}{\partial r \partial z} + \left(\frac{c_{13} - c_{12}}{c_{33}}\right)r\frac{\partial w}{\partial z} = \left(\frac{H_r - H_\theta}{c_{33}}\right)rE_r \tag{9}$$

$$r\frac{\partial^2 w}{\partial r^2} + \frac{\partial w}{\partial r} + \frac{c_{11}}{c_{55}}r\frac{\partial^2 w}{\partial z^2} + \left(\frac{c_{13} + c_{55}}{c_{55}}\right)r\frac{\partial^2 u}{\partial z \partial r} + \left(\frac{c_{12} + c_{55}}{c_{55}}\right)\frac{\partial u}{\partial z} = \frac{H_z}{c_{55}}r\frac{\partial E_r}{\partial z}. \tag{10}$$

For these equations, it is assumed that the electric field does not vary in the thickness direction r, but may vary in the axial direction z. This variation in the electric field is created in the polarization process of PVDF (Sessler, 1981). The magnitude of the electric field is given as $E_r = V/t$, where V is applied voltage and t is the thickness of the PVDF lamina.

4 Composite Cylinder and Boundary Conditions

The cylinder analyzed here is assumed to be hollow and composed of n material layers. The solution for this problem is found by solving the equilibrium Eqs. (9) and (10) for each material layer and coupling the solution of each layer to adjacent layers through continuity of displacements and balance of stresses at common boundaries. In the present study it is assumed that each layer is perfectly bonded to adjacent layers.

There are two different boundary conditions for this problem, namely, interlaminar and end conditions. For the kth interface, the interlaminar boundary conditions are

$$u^k|_{r=r_k} = u^{k+1}|_{r=r_k}, \quad w^k|_{r=r_k} = w^{k+1}|_{r=r_k} \tag{11a}$$

$$\sigma_r^k|_{r=r_k} = \sigma_r^{k+1}|_{r=r_k}, \quad \sigma_{rz}^k|_{r=r_k} = \sigma_{rz}^{k+1}|_{r=r_k} \tag{11b}$$

for $k = 1, 2, \ldots, n-1$ where the superscript k refers to the particular layers and r_k is the radial position of the interface. In addition to this, inner and outer surface tractions are assumed to be homogeneous:

$$\sigma_r^n|_{r=r_n} = 0, \quad \sigma_{rz}^n|_{r=r_n} = 0, \quad \sigma_r^1|_{r=r_0} = 0, \quad \sigma_{rz}^1|_{r=r_0} = 0. \tag{12}$$

The ends of the cylinder are assumed to be free of shear stress and fixed or have uniform displacement in the z-direction. It is also assumed that the cylinder and loadings are symmetric about the $r - \theta$ plane at $z = 0$. These boundary conditions are expressed mathematically as

$$w^k|_{z=0} = 0, \quad \left.\frac{\partial u^k}{\partial z}\right|_{z=0} = 0, \quad \sigma_{rz}^k|_{z=l/2} = 0, \quad w^k|_{z=l/2} = w_0 \tag{13}$$

where w_0 is the applied uniform displacement at the end.

5 Power Series Solution

Solutions are assumed for u and w in the following form:

$$u(r, z) = \sum_{i=1}^{N} g_i(r) \cos \lambda_i z, \quad w(r, z) = \sum_{i=1}^{N} f_i(r) \sin \lambda_i z. \tag{14}$$

These equations satisfy homogeneous boundary conditions in Eq. (16), if $\lambda_i = 2i\pi/l$. The solution corresponding to the uniform displacement of the end can be superimposed with the solution for the homogeneous boundary conditions. Substituting Eq. (14) into Eqs. (9) and (10), and assuming that E_r can be written as

$$E_r = \frac{A_0}{2} + \sum_{i=1}^{N} A_i \cos(\lambda_i z), \tag{15}$$

then the dependence on r and z may be separated out by matching Fourier coefficients of the right-hand side with the left-hand side of Eqs. (9) and (10). By doing so, two coupled, second-order ordinary differential equations in r are obtained, corresponding to the ith term in the Fourier series. These equations are

$$r^2 g'' + rg' - \left[p_1 r^2 + p_2\right] g + p_3 r^2 f' + p_4 rf = H_1 r \tag{16a}$$

$$rf'' + f' - p_5 rf - p_6 rg' - p_7 g = H_2 r \tag{16b}$$

$$p_1 = \frac{c_{55}}{c_{33}}\lambda_i^2 \quad p_3 = \left(\frac{c_{13} + c_{55}}{c_{33}}\right)\lambda_i \quad p_5 = \frac{c_{11}}{c_{55}}\lambda_i^2$$

$$p_2 = \frac{c_{22}}{c_{33}} \quad p_4 = \left(\frac{c_{13} - c_{12}}{c_{33}}\right)\lambda_i \quad p_6 = \left(\frac{c_{13} + c_{55}}{c_{55}}\right)\lambda_i$$

$$p_7 = \left(\frac{c_{12} + c_{55}}{c_{55}}\right)\lambda_i \quad H_1 = \left(\frac{H_r - H_\theta}{c_{33}}\right)A_i$$

$$H_2 = \frac{-H_z \lambda_i A_i}{c_{55}} \tag{16c}$$

where a solution to these equations can be found using methods of power series (Boyce and Diprima, 1986) for both the homogeneous and nonhomogeneous parts of the solution.

The solution for a given problem is found by solving Eqs. (16) for each layer and then coupling layers through common boundaries. Therefore, it is convenient to look for solutions for each layer in the form of power series, expanding about one of its boundaries. The solutions for the homogeneous equations are taken as

$$f(r) = \sum_{n=0}^{\infty} a_n (r - r_0)^n, \quad g(r) = \sum_{n=0}^{\infty} b_n (r - r_0)^n \tag{17}$$

where r_0 is the inner radius of a particular layer. Before substituting Eqs. (17) into (16), a change of variables is necessary. Let $R = r - r_0$ then

$$\left(\frac{df}{dr} = \frac{df}{dR} \text{ and } \frac{d^2 f}{dr} = \frac{d^2 f}{dR^2}\right)$$

we have

$$\left[R^2 + 2r_0 R + r_0^2\right] g'' + \left[R + r_0\right] g' - \left[p_1\left(R^2 + 2r_0 R + r_0^2\right) + p_2\right] g + p_3\left[R^2 + 2r_0 R + r_0^2\right] f' + p_4\left[R + r_0\right] f = H_1 R + H_1 r_0 \tag{18a}$$

$$(R + r_0) f'' + f' - p_5 (R + r_0) f - p_6 (R + r_0) g' - p_7 g = H_2 R + H_2 r_0. \tag{18b}$$

Substituting Eq. (17) into Eq. (18) we obtain the solutions. Because of the complicated algebra only the procedure and final results are presented here.

The procedure involves finding values for a_n and b_n by setting coefficients of powers R_n to zero in Eq. (18) (after substituting Eq. (17) into Eq. (18)). However, because of the coupled nature of these equations it is necessary to alternate between the equations satisfying a_n and b_n successively. Because these are second-order equations there are four arbitrary constants a_0, a_1, b_0, and b_1. These are nonzero unknowns, and the remaining coefficients a_n and b_n for $n \geq 2$ are expressed in terms of these. For example, substituting Eq. (17) into Eq. (18a), and considering zeroth powers of R, we obtain

$$b_2 = \frac{\left(p_2 + p_1 r_0^2\right) b_0 - r_0 b_1 - p_4 r_0 a_0 - p_3 r_0^2 a_1}{2r_0^2}. \tag{19}$$

Therefore, b_2 is explicitly expressed as a function of the arbitrary constants b_0, b_1, a_0, and a_1. Similarly, for the first power of R, we have

$$b_3 = \frac{-6r_0 b_2 - \left(1 - p_2 - p_1 r_0^2\right) b_1 + 2p_1 r_0 b_0}{6r_0^2} + \frac{-2p_3 r_0^2 a_2 - \left(2p_3 r_0 + p_4 r_0\right) a_1 - p_4 a_0}{6r_0^2}. \tag{20}$$

It is only necessary to do this by hand to compute b_2, b_3, a_2, and a_3, after which a general recursion relation can be found. These results and some further manipulations are given in the Appendix along with solutions to the nonhomogeneous Eqs. (18).

So far, solutions for $f(r)$ and $g(r)$ have been found for each λ_i, $i = 1, 2, \ldots, N$. Substituting the form of these solutions (see the Appendix) into Eq. (14), one obtains

$$u(r, z) = \sum_{i=1}^{N} \left\{d_{0i} g_{0i}(r) + d_{1i} g_{1i}(r) + d_{2i} g_{2i}(r) + d_{3i} g_{3i}(r) + g_{4i}(r)\right\} \cos \lambda_i z \tag{21a}$$

$$w(r, z) = \sum_{i=1}^{N} \left\{d_{0i} f_{0i}(r) + d_{1i} f_{1i}(r) + d_{2i} f_{2i}(r) + d_{3i} f_{3i}(r) + f_{4i}(r)\right\} \sin \lambda_i z. \tag{21b}$$

Now is it necessary to consider the constant term in the Fourier cosine series for E_r given in Eq. (15). This represents the case where $\lambda_i = 0$, and thus, because of the form the solution takes, the second equilibrium equation given in Eq. (10) is automatically satisfied. However, to include the displacement condition for the end, it is necessary to look for solutions in the following form:

$$u = u^*(r), \quad w = w^*(z). \tag{22}$$

Using Eq. (22), the equilibrium Eqs. (9) and (10), which include the constant term from the Fourier cosine series expansion for E_r, are given by

$$r^2\frac{d^2u^*}{dr^2} + r\frac{du^*}{dr} - \frac{c_{22}}{c_{33}}u^* + \left(\frac{c_{13}-c_{12}}{c_{33}}\right)r\frac{dw^*}{dz} = \left(\frac{H_r - H_\theta}{c_{33}}\right)r\frac{A_0}{2} \quad (23a)$$

$$\frac{d^2w^*}{dz^2} = 0. \quad (23b)$$

The fact that the final solutions are a superposition of the homogeneous and particular solutions, the nonharmonic components of displacements for isotropic and orthotropic cylinders, respectively, are given by

$$u^*(r) = \frac{c_1}{r} + c_2 r + Ar\log r, \quad w^*(z) = c_3 z \quad (24a)$$

$$u^*(r) = c_1 r^\beta + c_2 r^{-\beta} + Br, \quad w^*(z) = c_3 z \quad (24b)$$

$$c_3 = \frac{2w_0}{l} \quad A = \frac{q_1}{2} \quad \beta^2 = \frac{C_{22}}{c_{33}} \quad B = \frac{q_1 + q_2 c_3}{1-\beta^2}$$

$$q_1 = \left(\frac{H_r - H_\theta}{c_{33}}\right)\frac{A_0}{2} \quad q_2 = \frac{c_{12}-c_{13}}{c_{33}} \quad (24c)$$

and c_1 and c_2 are arbitrary constants chosen to satisfy boundary conditions. This completes the derivation of the power series solution. However, for implementation, further manipulations are required to set up a system of algebraic equations which can be solved for the unknown arbitrary constants that satisfy boundary conditions. Boundary conditions for harmonic and nonharmonic terms are satisfied separately.

First, the algebraic equations that must be solved for the ith mode are derived. Applying the first boundary condition in Eq. (11a) for the kth interface yields

$$g_{0i}^k(r_k)d_{0i}^k + g_{1i}^k(r_k)d_{1i}^k + g_{2i}^k(r_k)d_{2i}^k + g_{3i}^k(r_k)d_{3i}^k - d_{2i}^{k+1} = -g_{4i}^k(r_k) \quad (25)$$

where superscripts indicate the particular lamina. It should be noted that, since all power series for each layer were expanded about the inner surface of the particular layer, all terms on the right-hand side of Eq. (11a) are zero except one. Similar situations arise for the remaining three boundary conditions in Eqs. (11), and the results are as follows:

$$f_{0i}^k(r_k)d_{0i}^k + f_{1i}^k(r_k)d_{1i}^k + f_{2i}^k(r_k)d_{2i}^k + f_{3i}^k(r_k)d_{3i}^k - d_{0i}^{k+1} = -f_{4i}^k(r_k) \quad (26)$$

$$\sum_{j=0}^{3}\left[c_{13}^k\lambda_i f_{ji}^k + \frac{c_{23}^k}{r_k}g_{ji}^k(r) + c_{33}^k\left.\frac{dg_{ji}^k}{dr}\right|_{r=r_k}\right]d_{ji}^k - c_{13}^{k+1}\lambda_i d_{0i}^{k+1} - \frac{c_{23}^{k+1}}{r_k}d_{2i}^{k+1} - c_{33}^{k+1}d_{3i}^{k+1} = H_r^k A_i^k - H_r^{k+1}a_t^{k+1} - c_{13}^k\lambda_i f_{4i}^k(r_k) - c_{23}^k\frac{g_{4i}^k}{r_k}(r_k) - c_{33}^k\left.\frac{dg_{4i}^k}{dr}\right|_{r=r_k} \quad (27)$$

$$c_{55}^k\sum_{j=0}^{3}\left[\left.\frac{df_{ji}^k}{dr}\right|_{r=r_k} - \lambda_i g_{ji}^k(r_k)\right]d_{ji}^k - c_{55}^{k+1}d_{1i}^{k+1} + c_{55}^{k+1}\lambda_i d_{2i}^{k+1} = c_{55}^k\left[\lambda_i g_{4i}^k(r_k) - \left.\frac{df_{4i}^k}{dr}\right|_{r=r_k}\right]. \quad (28)$$

Finally, the inner and outer surface boundary conditions given in (12) are derived in the same way and are as follows:

$$\sum_{j=0}^{3}\left[c_{13}^n\lambda_i f_{ji}^n(r_n) + \frac{c_{23}^n}{r_n}g_{ji}^n(r_n) + c_{33}^n\left.\frac{dg_{ji}^n}{dr}\right|_{r=r_n}\right]d_{ji}^n = H_r^n A_i^n - c_{13}^n\lambda_i f_{4i}^n(r_n) - c_{23}^n\frac{g_{4i}^n(r_n)}{r_n} - c_{33}^n\left.\frac{dg_{4i}^n}{dr}\right|_{r=r_n} \quad (29)$$

$$\sum_{j=0}^{3}\left[\left.\frac{df_{ji}^n}{dr}\right|_{r=r_n} - \lambda_i g_{ji}^n(r_n)\right]d_{ji}^n = \lambda_i g_{4i}^n(r_n) - \left.\frac{df_{4i}^n}{dr}\right|_{r=r_n} \quad (30)$$

$$c_{13}^1\lambda_i d_{0i}^1 + \frac{c_{23}^1}{r_0}d_{2i}^1 + c_{33}^1 d_{3i}^1 = H_r^1 A_i^1 \quad (31)$$

$$d_{1i}^1 - \lambda_i d_{2i}^1 = 0. \quad (32)$$

This completes the application of the boundary conditions for the harmonic components of the solution. Equations (25)–(32) yield $4n$ equations in $4n$ unknowns d_{0i}^k, d_{1i}^k, d_{2i}^k, d_{3i}^k for the ith mode and $k = 1, 2, \ldots, n$.

Similar derivations are required for the nonharmonic components $u^*(r)$ and $w^*(z)$. Due to the form of these solutions, all shear and axial displacement boundary conditions are automatically satisfied. These solutions yield no shear stresses or strains and all layers have the same axial displacement. Therefore, the boundary conditions in (11)–(13) are reduced, leaving $2n$ equations in $2n$ unknowns: c_1^k and c_2^k for $k = 1, 2, \ldots, n$.

6 Results

The power series solution developed in Section 5 is used to analyze the mechanical interaction between actuating laminae and surrounding structure. Two numerical examples are presented as possible applications of embedded actuating laminae, the second of which illustrates the effects of spatial discontinuities in actuating strains.

Cylindrical Truss Element Actuator. In this subsection a cylindrical bar with embedded PVDF layers is proposed for use as an active member to control the vibrations of a truss. Such a member would be placed in the load paths of the truss and thus serve both as an actuator to bring transient deformations to zero as well as a load-carrying member. This concept is given by Fanson and Garba (1988) based upon a different actuator design.

The actuator design consists of adding piezoelectric laminae to a composite cylinder such that axial forces may be generated at the ends based upon the piezoelectric effect. It should generate the largest possible loads while not excessively sacrificing axial stiffness. Therefore, the piezoelectric effect is uniformly distributed along the length of the cylinder in PVDF layers. This is equivalent to having a uniform polarization profile. On the other hand, axial stiffness depends upon ply orientations of the composite laminae. Therefore, various ply orientations are studied to determine their effects on axial stiffness and on the forces transmitted to the boundaries.

The radial dimensions for the cylinder used in this study are similar to that proposed by NASA for the truss structure of the space station (Derstine, Pindera, and Bowles, 1988). It has an inside diameter of 50 mm and a thickness of 1.5 mm. Additional PVDF layers bring the total thickness to 2.1 mm.

Table 1 Cylindrical truss element actuator results

Id	Case	Stiffness K(N/m)	Electric Stiffness P(N/V)
I	0°/*0°/0°/*0°/0°	6.55 x 10^7	-1.89 x 10^{-2}
II	0/*0°/90°/*0°/0°	5.38 x 10^7	-2.07 x 10^{-2}
III	90°/*0°/90°/*0°/90°	.587 x 10^7	-2.11 x 10^{-2}
IV	90°/*0°/90°/*0°/0°	3.05 x 10^7	-2.13 x 10^{-2}
V	90°/*0°/0°/*0°/0°	4.25 x 10^7	-2.13 x 10^{-2}
VI	*0°/0°/0°/0°/*0°	6.55 x 10^7	-1.89 x 10^{-2}
VII	*0°/0°/90°/0°*0°	5.38 x 10^7	-2.07 x 10^{-2}
VIII	*0°/90°/90°/90°/*0°	.586 x 10^7	-2.13 x 10^{-2}
IX	*0°/90°/90°/0°/*0°	3.02 x 10^7	-2.12 x 10^{-2}
X	*0°/90°/0°/0°/*0°	4.22 x 10^7	-2.10 x 10^{-2}

*indicates PVDF lamina

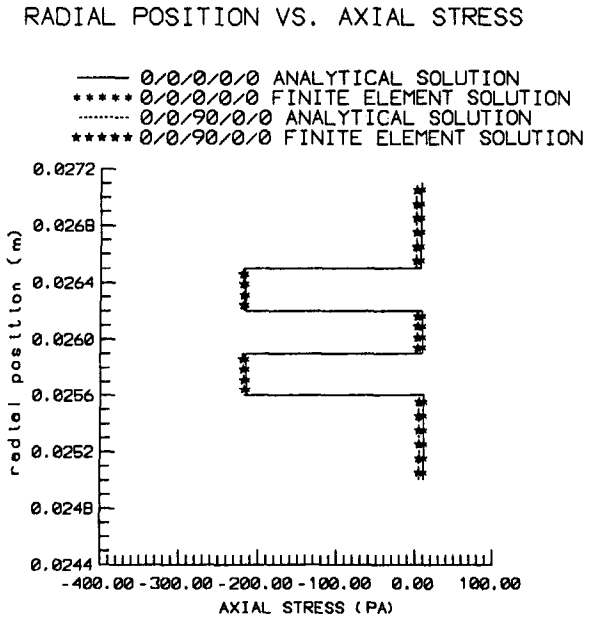

Fig. 1 Radial position versus axial stress

The passive portion of the cylinder is comprised of the composite material T300/5208, and is made up of three layers. Two PVDF layers are added giving a total of five layers for the cylinder. In all cases, the PVDF layers were 3×10^{-4} m thick and 1.0 volt was applied, giving an electric field of 3.33×10^3 volts/m. Properties assumed for T300/5208 and PVDF are: T300/5208 (orthotropic) $E_1 = 132 \times 10^9$ Pa, $E_2 = E_3 = 10.8 \times 10^9$ Pa, $G_{12} = G_{13} = 5.65 \times 10^9$ Pa, $G_{23} = 3.38 \times 10^9$ Pa, $\nu_{12} = \nu_{13} = .24$, $\nu_{23} = .49$, PVDF (assumed to be isotropic) $E_1 = 2.5 \times 10^9$ Pa, $\nu = .392$, $d_{31} = 21.4 \times 10^{-12}$ coulombs/Newton, $d_{32} = 2.3 \times 10^{-12}$ coulombs/Newton, and $d_{33} = -31.5 \times 10^{-12}$ coulombs/Newton. The length of the cylinder used here was 0.5 m.

Results are presented in Table 1 and Fig. 1 for various ply orientations and positions. P represents the axial force generated by PVDF layers and K represents the axial stiffness of the cylinder. Results indicate that by introducing a passive 90-deg lamina, approximately an eight percent increase in P can be achieved. However, this increase is at the expense of axial stiffness. Additional 90-deg layers yield smaller increases in P, and the effect of placing the PVDF layers on the outside is negligible.

The mechanism by which axial forces are transmitted to the boundary is indicated in Fig. 1. When the electric field is applied to PVDF layers in a positive sense, the material

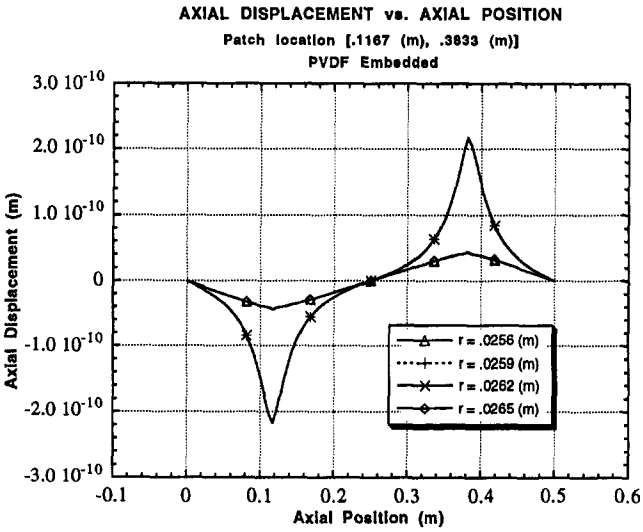

Fig. 2 Axial displacement versus axial position

expands axially. However, this expansion is constrained and therefore compressive forces are generated and transmitted to the boundary via PVDF layers themselves. It is also possible to generate tensile forces by applying the electric field in the opposite direction or the negative sense. This is physically realized by simply changing the polarity on the applied voltage. In an application (Mitchell, 1992), the forces generated by the actuator can be used to control transient vibrations of truss-type structures due to some perturbation of the system from its static equilibrium position. The relation between the applied voltage and force generated developed above can be used to judiciously select a voltage signal sent to active members, such that transient vibrations may be dampened quickly. This type of control mechanism is attractive because it becomes an integral part of the structure, controlling member deformations directly.

Polarization Patch. In this subsection, a polarization profile is taken in the form of a patch and modeled mathematically using Heaviside step function $h(z)$ as

$$E_r(z) = h(z - z_0) - h(z - z_1). \tag{33}$$

Equation (10) requires a derivative for E_r with respect to z. This is given by

$$\frac{\partial E_r}{\partial z} = \delta(z - z_0) - \delta(z - z_1) \tag{34}$$

where $\delta(z)$ is the Dirac delta function. The cylinder analyzed here is the same as that in Case II of the cylindrical truss element actuator section. The patch is centered at $z = .25$ m and has values for z_0 and z_1 as .1167 m and .3833 m, respectively.

As might be expected, the number of terms taken in the power series is critical to obtaining good results and the rate of convergence depends upon λ_i. For the results presented here, the first 100 nonzero Fourier coefficients for $E_r(z)$ were used. Due to the patch location in this problem, all odd modes were filtered out and it was necessary to use up to 130 terms in each associated power series based upon a stopping criteria requiring that the absolute value of additional terms be less than 1.0×10^{-45}.

Results indicate that the influence of the patch on displacements diminishes with points taken farther and farther away. This is easily seen in Figs. 2 and 3. Since the patch has been placed at the center along the length of the cylinder, its

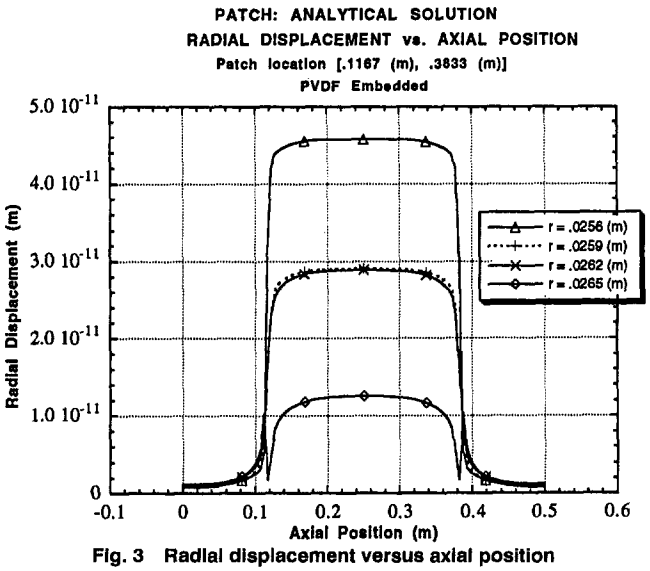

Fig. 3 Radial displacement versus axial position

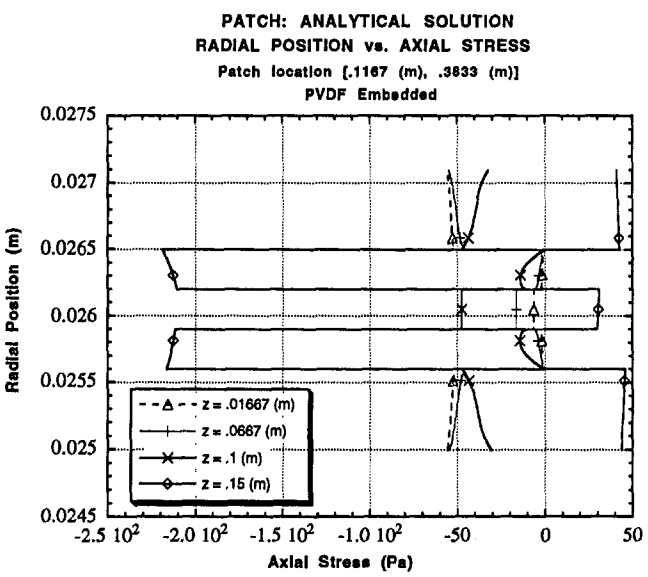

Fig. 4 Radial position versus axial stress

effects result in some antisymmetric and symmetric phenomena. For instance, the patch expands axially under the electric field and therefore points to the left of centerline ($z = .25$ m) move left or have a negative displacement and points to the right of centerline move to the right. This is indicated in Fig. 2. The radial displacement is primarily due to hoop expansion and is an example of a symmetric result with respect to z and is given in Fig. 3.

The stress distributions calculated for this case contrast with those in Case II of the cylindrical truss element actuator section in several ways. Since there are sharp discontinuities in the polarization profile for the patch, shear stress are introduced. Whereas in Case II, the polarization profile was uniform and therefore no shear stresses were induced. Due to this difference, the mechanism by which axial forces are transmitted to the boundaries is different for each.

In Case II of the cylindrical truss element actuator, the mechanism by which forces were generated at the ends was very simple. All compressive forces were transmitted to the boundaries via the PVDF layers themselves. This contrasts sharply with the present case. Compressive forces in PVDF layers are quickly transferred to adjacent passive laminae at the edges of the patch, and have zero axial stresses at the ends. Forces are then transmitted to the boundaries via passive laminae, and the net axial force transmitted is proportional to the length of the patch. A simple hand calculation using Figs. 4 and 5 and the appropriate cross-sectional areas bears this out.

To understand the mechanism by which axial forces are transferred from PVDF laminae to passive laminae, consider the following equilibrium equation for an outer laminae whose outer surface is stress-free:

$$\frac{\partial \sigma_z}{\partial z} dr = \sigma_{rz}. \tag{35}$$

Therefore, the rate of change of axial stress with respect to z depends upon shear stress. For example, using Figs. 5 and 6, and considering a value of $r_0 = .0265$ m in the figures, the axial stress variation with z follows according to the above equation except at the edges of the patch. At these points, Gibbs' phenomenon affects the numerical values of axial stress calculated and a jag in the curve is present. However, because of the apparent insensitivity of interlaminar shear stresses to Gibbs' phenomenon, the actual trace of the axial stress as the edge of the patch is crossed may be visualized and can be seen in results obtained by the finite element

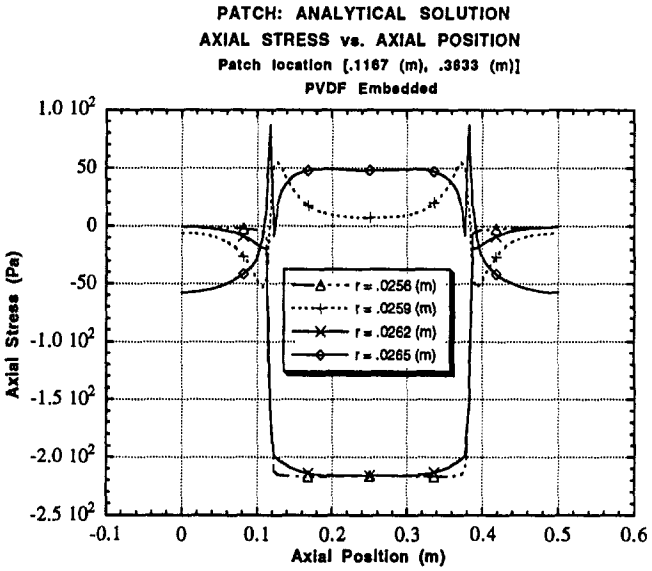

Fig. 5 Axial stress versus axial position

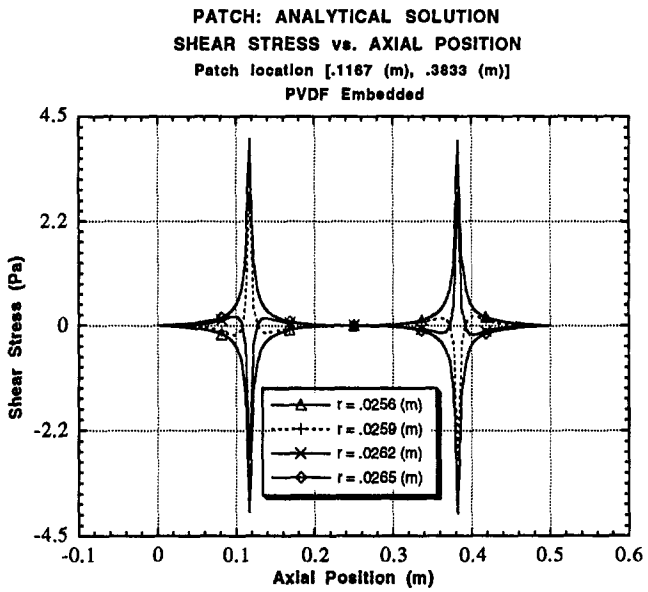

Fig. 6 Shear stress versus axial position

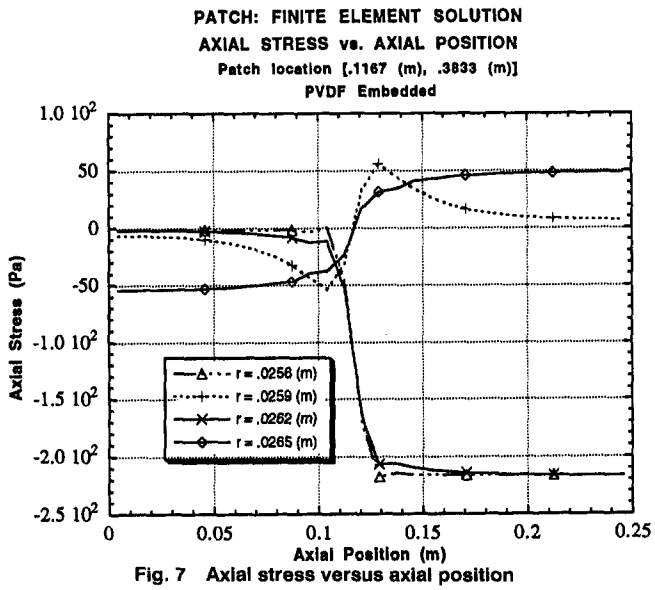

Fig. 7 Axial stress versus axial position

method (see Fig. 7). The finite element solution did not suffer from this problem and the axial stresses follow according to the above equation including the points at the edges of the patch. At all other values of r given in Fig. 5, Gibbs' phenomenon does not appear and both the analytical and FE results match identically.

The distribution of shear stress is connected to another interesting result. As might be expected, the maximum shear levels occur at the edge of the patch; however, their location does not occur at interlaminar positions through the thickness. This suggests that the axial expansion near the edge of the patch is not the main cause by which shear stresses are introduced. Although not given here, antisymmetric, parabolic shear stress distributions were found through the thickness (Mitchell, 1992). These results suggest bending at the edge of the patch.

7 Conclusions

A static analysis is presented for an axisymmetric composite cylinder under loadings due to embedded piezoelectric laminae using a power-series-type solution to the governing PDE's. Using this solution, two applications were given. A cylindrical truss element actuator was developed and various cases were studied to determine optimal ply orientations. This actuator was shown to transmit axial forces to the boundaries via PVDF layers themselves. The second application was a study of the effects of a polarization patch. The mechanism by which axial forces are transmitted to the boundaries was investigated and shown to be different from that for the cylindrical truss element actuator. In the case of the polarization patch, forces are transmitted to the boundaries via passive laminae and are proportional to the length of patch. This was investigated and shown to be attributable to the nonuniformity of the piezoelectric effect. From this nonuniformity, it follows that shear stresses must be introduced. For cases such as this, the analytical solution indicates that displacements through the thickness of piezoelectric layers are of quadratic and higher orders.

Acknowledgments

The first author wishes to thank the Department of Engineering Science and Mechanics at Virginia Polytechnic Institute and State University for the financial support during the course of the present study. The authors acknowledge the technical discussions and advice of Dr. Scott Hendricks (VPI & SU).

References

Adelman, N. T., Stavsky, Y., and Segal, E., 1975, "Axisymmetric Vibrations of Polarized Piezoelectric Ceramic Cylinders," *Journal of Sound and Vibration*, Vol. 38, No. 2, pp. 245–254.

Adelman, N. T., and Stavsky, Y., 1975, "Vibrations of Radially Polarized Composite Piezoelectric Cylinders and Disks," *Journal of Sound and Vibration*, Vol. 43, No. 1, pp. 37–44.

Babister, A. W., 1967, *Transcendental Functions Satisfying Nonhomogeneous Linear Differential Equations*, The Macmillan Company, New York, pp. 16–17.

Boyce, W. E., and Diprima, R. C., 1986, *Elementary Differential Equations and Boundary Value Problems*, 4th ed., John Wiley and Sons, New York.

Crawley, E. F., and Luis, J. de, 1987, "Use of Piezoelectric Actuators as Elements of Intelligent Structures," *AIAA Journal*, Vol. 25, No. 10, pp. 1373–1385.

Derstine, M. S., Pindera, M.-J., and Bowles, D. E., 1988, "Combined Mechanical Loading of Composite Tubes," *Center for Composite Materials and Structures*, CCMS-88-11, Virginia Tech.

Fanson, J. L., and Garba, J. A., 1988, "Experimental Studies of Active Members in Control of Large Space Structures," AIAA Paper No. 88-2207.

Karlash, V. L., 1990, "Electroelastic Oscillations of a Compound Hollow Piezoceramic Cylinder with Radial Polarization," *Soviet Applied Mechanics*, Vol. 26, No. 5, pp. 440–443.

Kawai, H., 1979, "The Piezoelectricity in Poly(Vinylidene Fluoride)," *Japanese Journal of Applied Physics*, Vol. 8, pp. 975–976.

Mitchell, J. A., 1992, "The Effects of Embedded Piezoelectric Layers in Composite Cylinders and Applications," Master's Thesis, Virginia Tech.

Sessler, G. M., 1981, "Piezoelectricity in Polyvinylidenefluoride," *Journal of the Acoustical Society of America*, Vol. 70, No. 6, pp. 1596–1608.

Sun, C. T., and Chen, N. C., 1974, "Piezoelectric Waves on a Layered Cylinder," *Journal of Applied Physics*, Vol. 45, No. 10, pp. 4288–4294.

Timoshenko, S. P., and Goodier, J. N., 1951, *Theory of Elasticity*, 2nd ed., McGraw-Hill, New York.

Tzou, H. S., and Gadre, M., 1989, "Theoretical Analysis of Multi-Layered Thin Shell Coupled with Piezoelectric Shell Actuators for Distributed Vibration Control," *Journal of Sound and Vibration*, Vol. 132, No. 3, pp. 433–450.

APPENDIX

$$a_2 = \frac{-a_1 + p_5 r_0 a_0 + p_6 r_0 b_1 + p_7 b_0}{2r_0} \tag{A1}$$

$$a_3 = \frac{-4a_2 + p_5 r_0 a_1 + p_5 a_0 + 2p_6 r_0 b_2 + (p_6 + p_7) b_1}{6r_0} \tag{A2}$$

$$b_{n+2} = \frac{-\left[r_0(n+1)(2n+1)\right]b_{n+1} - \left[n^2 - p_2 - p_1 r_0^2\right]b_n}{r_0^2(n+2)(n+1)} + \frac{2p_1 r_0 b_{n-1} + p_1 b_{n-2} - p_3 r_0^2 (n+1) a_{n+1}}{r_0^2(n+2)(n+1)} + \frac{-\left[2p_3 r_0 n + p_4 r_0\right]a_n - \left[p_3(n-1) + p_4\right]a_{n-1}}{r_0^2(n+2)(n+1)} \tag{A3}$$

$$a_{n+2} = \frac{-(n+1)(n+1)a_{n+1} + p_5 r_0 a_n + p_5 a_{n-1}}{r_0(n+2)(n+1)} + \frac{(np_6 + p_7)b_n + p_6 r_0 (n+1) b_{n+1}}{r_0(n+2)(n+1)} \tag{A4}$$

Equations (A3) and (A4) are valid for $n \geq 2$. This completes the development of the solution to the homogeneous Eqs. (16). However, a method for finding a_0, a_1, b_0, and b_1 is needed because these are embedded in the recursion relations (A3) and (A4). To circumvent this problem the solu-

tions are taken in the following form:

$$f(r) = d_0 f_0(r) + d_1 f_1(r) + d_2 f_2(r) + d_3 f_3(r) \quad \text{(A5)}$$

$$g(r) = d_0 g_0(r) + d_1 g_1(r) + d_2 g_2(r) + d_3 g_3(r) \quad \text{(A6)}$$

where the arbitrary constants a_0, a_1, b_0, and b_1 have been replaced by d_0, d_1, d_2, and d_3. Each function f_0, f_1, f_2, f_3, g_0, g_1, g_2, and g_3 has recursion relations based upon Eqs. (A3) and (A4) but in a special way. For example, by taking $a_1 = b_0 = b_1 = 0$ and using the recursion relations for $f(r)$ and $g(r)$, $f_0(r)$ and $g_0(r)$ are found as

$$f_0(r) = d_0\left[1 + \sum_{n=2}^{\infty} a_n R^n\right], \quad g_0(r) = d_0 \sum_{n=2}^{\infty} b_n R^n. \quad \text{(A7)}$$

This approach isolates a_0 in such a way that it may be calculated by a straightforward application of boundary conditions. Similarly, the remaining functions $f_1(r)$, $f_2(r)$, $f_3(r)$, $g_1(r)$, $g_2(r)$, and $g_3(r)$ are found (Mitchell, 1992).

The solution to the nonhomogeneous Eqs. (18) is found in the same way as that for the homogeneous equations. However, the form of the power series is taken as (Babister, 1967)

$$f_4(r) = R^2 \sum_{n=0}^{\infty} a_n R^n, \quad g_4(r) = R^2 \sum_{n=0}^{\infty} b_n R^n. \quad \text{(A8)}$$

Substituting Eq. (A8) into Eq. (18) and setting coefficients for each power of R to zero, recursive relations for the particular solutions are obtained. The first four terms for each function are calculated in the same way as described before. These terms are given by

$$b_0 = \frac{H_1}{2r_0}, \quad a_0 = \frac{H_2}{2} \quad \text{(A9)}$$

$$b_1 = \frac{H_1 - 6r_0 b_0 - 2p_3 r_0^2 a_0}{6r_0^2} \quad \text{(A10)}$$

$$a_1 = \frac{H_2 - 4a_0 + 2p_6 r_0 b_0}{6r_0} \quad \text{(A11)}$$

$$b_2 = \frac{-15r_0 b_1 - (4 - p_1 r_0^2 - p_2) b_0}{12r_0^2} + \frac{-3p_3 r_0^2 a_1 - (4p_3 r_0 + p_4 r_0) a_0}{12r_0^2} \quad \text{(A12)}$$

$$a_2 = \frac{-9a_1 + p_5 r_0 a_0 + 3p_6 r_0 b_1 + (2p_6 + p_7) b_0}{12r_0} \quad \text{(A13)}$$

$$b_3 = \frac{-28r_0 b_2 - (9 - p_1 r_0^2 - p_2) b_1 + 2p_1 r_0 b_0}{20r_0^2} + \frac{-4p_3 r_0^2 a_2 - (6p_3 r_0 + p_4 r_0) a_1 - (2p_3 + p_4) a_0}{20r_0^2} \quad \text{(A14)}$$

$$a_3 = \frac{-16a_2 + p_5 r_0 a_1 + p_5 a_0}{20r_0} + \frac{(3p_6 + p_7) b_1 + 4p_6 r_0 b_2}{20r_0}. \quad \text{(A15)}$$

The general recursive relations for a_n and b_n, for $n \geq 4$, are given by

$$b_n = \frac{p_1 b_{n-4} + 2p_1 r_0 b_{n-3} - [n^2 - p_1 r_0^2 - p_2] b_{n-2}}{r_0^2 (n+2)(n+1)} + \frac{-r_0 (2n+1)(n+1) b_{n-1} - [p_3 (n-1) + p_4] a_{n-3}}{r_0^2 (n+2)(n+1)} + \frac{-[2p_3 r_0 n + p_4 r_0] a_{n-2} - p_3 r_0^2 (n+1) a_{n-1}}{r_0^2 (n+2)(n+1)} \quad \text{(A16)}$$

$$a_n = \frac{-(n+1)^2 a_{n-1} + p_5 r_0 a_{n-2} + p_5 a_{n-3}}{(n+2)(n+1) r_0} + \frac{(np_6 + p_7) b_{n-2} + p_6 r_0 (n+1) b_{n-1}}{(n+2)(n+1) r_0}. \quad \text{(A17)}$$

SH-Wave Interaction in a Harmonically Inhomogeneous Elastic Plate

M. A. Hawwa
Vibration Acoustics Labs.,
Mechanical Engineering Department,
Virginia Polytechnic Institute
and State University,
Blacksburg, VA 24061

The study focuses on the propagation of SH waves in an elastic plate whose material properties are sinusoidally varying in the direction of propagation. In light of the weak variation of the materials properties, the perturbation method of multiple scales is utilized to analyze the modal interaction which occurs upon the satisfaction of certain resonant conditions. The derived coupled-mode equations together with relevant boundary conditions at the ends of the inhomogeneous section form a two-point boundary value problem, which is solved numerically. The power reflection coefficient is then calculated to present the reflection characteristics of the plate.

1 Introduction

Efforts to study elastic wave propagation in periodically inhomogeneous media have been spent in two directions: (1) modeling the propagation of waves in composites consisting of periodic arrays of homogeneous layers in which material properties are piecewise continuous and (2) investigation of waves traveling in structures with continuously varying material properties. While the mathematical treatment in (1) leads to equations of motion with constant coefficients satisfying certain continuity and periodicity conditions, the analytical formulation in (2) ends with a governing differential equation having periodic coefficients.

The present work belongs to the second direction. Relevant literature to this includes the work by Nayfeh and Nemat-Nasser (1972) who discussed the wave propagation in an unbounded medium whose properties vary as harmonic functions of the coordinate variable in the direction of propagation. They found that the material cannot maintain time-harmonic waves in certain special cases; these waves are not stable. Also the paper by Watanabe (1984) who considered the oblique propagation of plane SH waves in an inhomogeneous solid, with infinite extent, whose properties vary harmonically with a space variable, and discussed the effect of the angle of propagation on the instability phenomenon.

The instability phenomenon is due to the fact that periodic structures behave like pass-band filters, which allow waves to propagate only in certain frequency bands (Brillouin, 1953). This unique behavior of periodic systems motivates utilizing structures with periodic inhomogeneity as mechanical wave filters in order to control the oscillation levels.

In this article, we study guided SH waves in an elastic plate, with material properties varying harmonically along the plate in the direction of propagation. Assuming weak harmonic variations, approximate analytical solutions in the form of first-order asymptotic expansions are obtained. However, the existence of resonant conditions, and consequently, unstable regions, invalidates the expansions near these conditions. The method of multiple scales (Nayfeh, 1981) is therefore employed to seek uniform expansions valid near resonance. The presence of boundary condition at the plate-free outerfaces necessitates imposing certain solvability conditions on the first-order problem. This leads to the derivation of the coupled-mode equations governing the modulation of amplitudes. These equations are solved numerically in order to investigate the filtration characteristics of the inhomogeneous plate.

2 Problem Formulation

Consider the isotropically elastic plate shown in Fig. 1. The section extending from $\hat{x} = 0$ to $\hat{x} = L$ is assumed to have material inhomogeneities which are described as $\rho(\hat{x}) = \rho_0(1 + \epsilon \cos \alpha\hat{x})$, and $\mu(\hat{x}) = \mu_0(1 + \delta\epsilon \cos \beta\hat{x})$, where the subscript "0" indicates an average value; ρ is the material density; μ is the shear modulus of rigidity; α and β are, respectively, the wave numbers of the material density and rigidity; ϵ is a small dimensionless parameter much smaller than unity and equal to the ratio of the deviation from the average value of density; and δ is a constant allowing for different deviation in the rigidity.

The governing equation of horizontally polarized motion in terms of the displacement component in the y-direction

Contributed by the Applied Mechanics Division of THE AMERICAN SOCIETY OF MECHANICAL ENGINEERS for publication in the ASME JOURNAL OF APPLIED MECHANICS.

Discussion on this paper should be addressed to the Technical Editor, Professor Lewis T. Wheeler, Department of Mechanical Engineering, University of Houston, Houston, TX 77204-4792, and will be accepted until four months after final publication of the paper itself in the ASME JOURNAL OF APPLIED MECHANICS.

Manuscript received by the ASME Applied Mechanics Division, Jan. 28, 1993; final revision, Aug. 16, 1993. Associate Technical Editor: A. K. Noor.

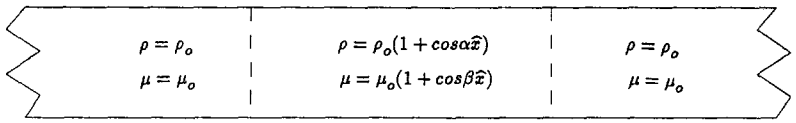

Fig. 1 The plate waveguide

$(\hat{v})$ is given by

$$\frac{\partial}{\partial \hat{x}}\left[\mu(\hat{x})\frac{\partial \hat{v}}{\partial \hat{x}}\right] + \frac{\partial}{\partial \hat{z}}\left[\mu(\hat{x})\frac{\partial \hat{v}}{\partial \hat{z}}\right] - \rho(\hat{x})\frac{\partial^2 \hat{v}}{\partial \hat{t}^2} = 0 \quad (1)$$

where $\hat{t}$ is the time coordinate.

We consider propagation of monochromatic harmonic waves so that $\hat{v} = \hat{V}(\hat{x}, \hat{z}) \exp(-i\hat{\omega}\hat{t})$, where ω is the frequency of oscillation. Moreover, we introduce dimensionless quantities (without the carets) by using the plate thickness $\hat{h}$ and $\hat{\omega}^{-1}$ as the characteristic length and time, respectively. The following dimensionless governing equation is obtained:

$$(1 + \epsilon \cos \beta x)\left[\frac{\partial^2 V}{\partial x^2} + \frac{\partial^2 V}{\partial z^2}\right] - (\epsilon\beta \sin \beta x)\frac{\partial V}{\partial x} + \left[k^2(1 + \epsilon \cos \alpha x)\right]V = 0 \quad (2)$$

where $k = \hat{\omega}\hat{h}(\rho_0/\mu_0)^{1/2}$ represents the wave numbers of bulk waves in a material with average properties.

Using a power series expansion, Eq. (2) can be written in the following approximate Hill-type form:

$$\frac{\partial^2 V}{\partial x^2} + \frac{\partial^2 V}{\partial z^2} + k^2 V = \epsilon\left\{(\beta \sin \beta x)\frac{\partial V}{\partial x} - \left[k^2(\cos \alpha x - \cos \beta x)\right]V\right\}. \quad (3)$$

The boundary conditions are the vanishing of the stress vector at the outerfaces of the plate. Thus

$$\frac{\partial V}{\partial z}(x, 0) = 0, \frac{\partial V}{\partial z}(x, 1) = 0. \quad (4)$$

A solution of the system (3) and (4) in the form of a first-order straightforward asymptotic expansion is found to break down when a material wave number (α, β) is twice that of the propagating mode (k_j); i.e.,

$$2k_j \approx \mp\alpha, \mp\beta. \quad (5)$$

The above conditions are known in the literature as Bragg conditions (Elachi, 1976), at which steady-state harmonic waves are unstable (resonance occurs). Physically, a Bragg condition implies that two contradirectional modes interact strongly with each other by exchanging energy, resulting in a high level of attenuation. Such an interaction can be analyzed using the method of multiple scales (Nayfeh, 1981), which leads to uniformly valid asymptotic expansions around resonance.

3 The Method of Multiple Scales

We seek a first-order perturbation expansion for V in powers of ϵ in the form

$$V(x, z) = V_0(X_0, X_1, \ldots, z) + \epsilon V_1(X_0, X_1, \ldots, z) + \ldots \quad (6)$$

where $X_0 = x$ is a short length scale of the order of the wavelength in the plate and $X_1 = \epsilon x$ is a long length scale which characterizes the spatial amplitude and phase modulations due to the material inhomogeneity.

Using the chain rule, we can write the derivatives with respect to x in terms of X_0 and X_1 as

$$\frac{\partial}{\partial x} = \frac{\partial}{\partial X_0} + \epsilon\frac{\partial}{\partial X_1} + \ldots \quad (7)$$

$$\frac{\partial^2}{\partial x^2} = \frac{\partial^2}{\partial X_0^2} + 2\epsilon\frac{\partial^2}{\partial X_0 \partial X_1} + \ldots. \quad (8)$$

Substituting (6)–(8) into (3) and (4), and equating the coefficients of ϵ^0 and ϵ^1 on both sides, we obtain

$O(1)$

$$\frac{\partial^2 V_0}{\partial z^2} + \frac{\partial^2 V_0}{\partial X_0^2} + k^2 V_0 = 0 \quad (9)$$

$$\frac{\partial V_0}{\partial z} = 0, \text{ at } z = 0, \quad \frac{\partial V_0}{\partial z} = 0, \text{ at } z = 1 \quad (10)$$

$O(\epsilon)$

$$\frac{\partial^2 V_1}{\partial z^2} + \frac{\partial^2 V_1}{\partial X_0^2} + k^2 V_1 = -2\frac{\partial^2 V_0}{\partial X_0 \partial X1} + (\beta \sin \beta X_0)\frac{\partial V_0}{\partial X_0} - \left[k^2(\cos \alpha X_0 - \cos \beta X_0)\right]V_0 \quad (11)$$

$$\frac{\partial V_1}{\partial z} = 0, \text{ at } z = 0, \quad \frac{\partial V_1}{\partial z} = 0, \text{ at } z = 1. \quad (12)$$

3.1 The Zeroth-Order Problem. Equation (9) admits solutions in the form of a linear combination of four propagating modes with wave numbers k_p and k_q; that is

$$V_0 = \sum_{j=p,q}\left[A_j^+(X_1)e^{ik_jX_0} + A_j^-(X_1)e^{-ik_jX_0}\right](\cos j\pi z) \quad (13)$$

where the superscript "+" ("−") indicates an incident (reflected) mode, and $A_j^{\mp}(X_1)$ are unknown functions at this level of approximation. They are determined by imposing the appropriate solvability condition at the next level of approximation.

Substitution of (13) into the boundary conditions (10) leads to the following well-known dispersion relation of guided SH modes:

$$k^2 - k_j^2 = (j\pi)^2. \quad (14)$$

3.2 The First-Order Problem. Since the homogeneous part of the first-order problem has a nontrivial solution, then the inhomogeneous first-order problem has a solution if, and only if, a solvability (consistency) condition is satisfied. To determine this condition, let us seek a particular solution for V_1 in the form

$$V_1 = \sum_{j=p,q}\left[\Phi_j^+(z)e^{ik_jX_0} + \Phi_j^-(z)e^{-ik_jX_0}\right]. \quad (15)$$

To describe quantitatively the nearness of k_j to resonance, we introduce the detuning parameters σ_1 and σ_2, such that

$$2k_p = \alpha + \epsilon\sigma_1 \quad (16)$$

$$2k_q = \beta + \epsilon\sigma_2. \quad (17)$$

Substituting (15) together with (13) into the governing Eq. (11), imposing the resonant conditions (16) and (17), and equating the coefficients of $\exp(\mp ik_j X_0)$ on both sides, we obtain

$$\left(\frac{d^2}{dz^2} + (p\pi)^2\right)\Phi_p^{\mp} = \left[\pm 2ik_p \frac{dA_p^{\mp}}{dX_1} - \frac{1}{2}k^2 A_p^{\pm} e^{\pm i\sigma_1 X_1}\right]\cos p\pi z \quad (18)$$

$$\left(\frac{d^2}{dz^2} + (q\pi)^2\right)\Phi_q^{\mp} = \left[\pm 2ik_p \frac{dA_q^{\mp}}{dX_1} - \frac{1}{2}\left(k^2 - \beta k_q\right)A_q^{\pm} e^{\pm i\sigma_2 X_1}\right]\cos q\pi z. \quad (19)$$

Substituting the solutions (13) and (15) into the boundary conditions (12), we get

$$\Phi_j^{\mp\prime}(0) = 0, \quad \Phi_j^{\mp\prime}(1) = 0 \quad (20)$$

where primes indicate derivatives with respect to the arguments.

To this end, we multiply (18) and (19) by $\cos(p\pi z)$ and $\cos(q\pi z)$, respectively, integrate the result by parts from $z = 0$ to $z = 1$, and invoke the boundary conditions (20). This leads to the following coupled-mode equations:

$$\frac{dA_p^+}{dX_1} = \frac{ik^2}{4k_p} A_p^- e^{-i\sigma_1 X_1} \quad (21)$$

$$\frac{dA_p^-}{dX_1} = \frac{-ik^2}{4k_p} A_p^+ e^{i\sigma_1 X_1} \quad (22)$$

$$\frac{dA_q^+}{dX_1} = \frac{-i}{4k_q}\left(k^2 - k_q\beta\right)A_q^- e^{-i\sigma_2 X_1} \quad (23)$$

$$\frac{dA_q^-}{dX_1} = \frac{i}{4k_q}\left(k^2 - k_q\beta\right)A_q^+ e^{i\sigma_2 X_1}. \quad (24)$$

In the case when $\alpha = \beta = \kappa$, two propagating modes only can interact. Hence, the above coupled-mode equations reduce to

$$\frac{dA_p^+}{dX_1} = \frac{i\kappa}{4} A_p^- e^{-i\sigma X_1} \quad (25)$$

$$\frac{dA_p^-}{dX_1} = \frac{-i\kappa}{4} A_p^+ e^{i\sigma X_1}. \quad (26)$$

4 Numerical Examples

For the purpose of illustration, a plate with $\rho_0 = 10^3$ kg/m^3, $\mu_0 = 10^{10}$ N/m^2, and $\hat{h} = 10^{-3}$ m is selected.

When α is different from β, the resonant frequency is taken at $\omega = 3.25$ MHz. Consequently, the wave numbers of the material properties are $\alpha = 11.284$ and $\beta = 2.980$.

The modal interaction in the plate is governed by the coupled-mode Eqs. (21)–(24). Without any loss of generality, the following end-point conditions are provided on both ends of the inhomogeneous section:

$$A_p^+ = A_q^+ = 1 \text{ at } X_1 = 0 \quad (27)$$

$$A_p^- = A_q^- = 0, \text{ at } X_1 = 30. \quad (28)$$

Note that the conditions in (27) represent the excitation amplitudes of the incident modes, while the condition in (28) express the fact that the reflected modes vanish at the end of the inhomogeneous section.

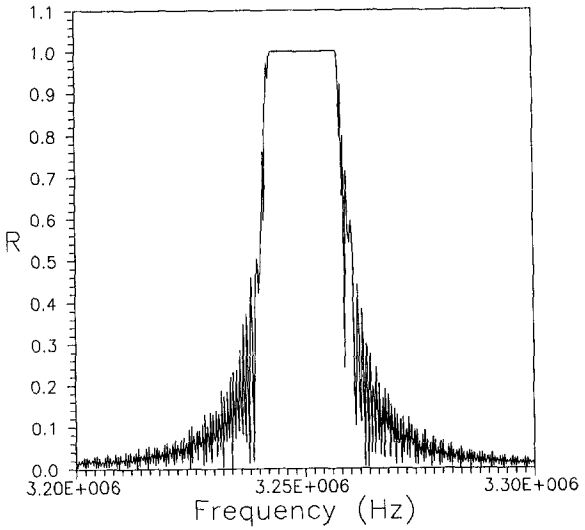

Fig. 2 Power reflection coefficient R for a four-mode waveguide, $\epsilon = 0.01$

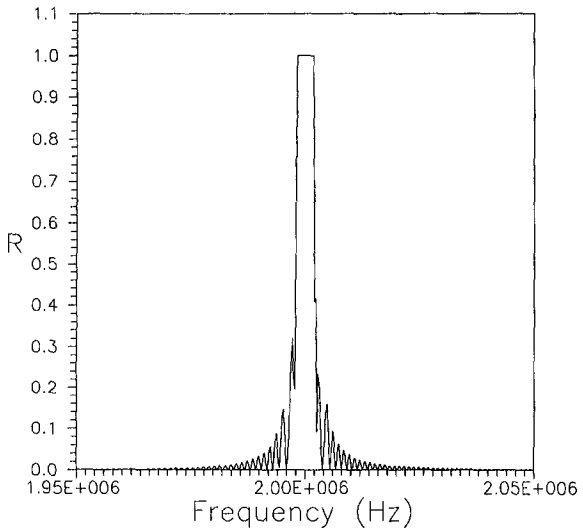

Fig. 3 Power reflection coefficient R for a two-mode waveguide, $\epsilon = 0.01$

The problem defined by (21)–(24) together with (27) and (28) constitutes a standard two-point boundary value problem, which is solved numerically by an efficient code based on the fundamental matrix method (Asfar and Hussein, 1989). The missing end-point conditions are obtained, and consequently, the power reflection coefficient can be calculated from

$$R = \frac{\sum_j k_j\left[A_j^-(X_1 = 0)\right]^2}{\sum_j k_j\left[A_j^+(X_1 = 0)\right]^2}. \quad (29)$$

The power reflection coefficient versus frequency for this case is depicted in Fig. 2. The figure shows a typical filter response with total reflection at the midband centered at the resonant frequency, and side ripples whose level decreases as one moves away from the resonant frequency. It is worth noting that the resonant frequency coincides with the center of the stop-band, which explains the high level of attenuation around resonance.

When $\alpha = \beta$, the resonant frequency is taken at $\omega = 2$ MHz corresponding to the wave number $k_p = 2.433$. The coupled-mode Eqs. (25) and (26) are solved numerically with relevant end-point conditions. The frequency response for this case is shown in Fig. 3. A narrow mid-band response is observed with negligible side ripples.

Comparison of Figs. 2 and 3 indicates that a material with two periodicities gives a stronger stop-band attenuation around resonance than a material with only one periodicity. This reflects the fact that a larger number of interactions occur in the first case than the latter.

5 Conclusion

The interaction of SH elastic modes in a plate whose material properties are sinusoidally varying in the direction of propagation has been investigated. The reflection characteristics have been presented for two cases. When four modes interact under certain resonant conditions, a wide midband response was obtained. A narrow midband response has been observed when only two modes interact.

References

Asfar, O. R., and Hussein, A. M., 1989, "Numerical Solution of Linear Two-Point Boundary-Value Problems Via the Fundamental Matrix Method," *International Journal of Numerical Methods in Engineering*, Vol. 28, pp. 1205–1216.

Brillouin, L., 1953, *Wave Propagation in Periodic Structures*, Dover Publications, New York.

Elachi, C., 1976, "Waves in Active and Passive Periodic Structures: A Review," *Proceedings of the IEEE*, Vol. 64, pp. 1666–1698.

Nayfeh, A. H., 1981, *Introduction to Perturbation Techniques*, John Wiley and Sons, New York.

Nayfeh, A. H., and Nemat-Nasser, S., 1972, "Elastic Waves in Inhomogeneous Elastic Media," ASME JOURNAL OF APPLIED MECHANICS, Vol. 39, pp. 696–702.

Watanabe, K., 1984, "Plane SH-Waves in Harmonically Inhomogeneous Elastic Media," *Wave Motion*, Vol. 6, pp. 477–488.

Y. Shindo
Department of Materials Processing,
Faculty of Engineering,
Tohoku University,
Aramaki-Aza-Aoba, Aoba-ku,
Sendai 980, Japan

H. Nozaki
Department of Mechanical Engineering,
Tokyo National College of Technology,
Kunugida-Machi 1220-2,
Hachioji 193, Japan

S. K. Datta
Department of Mechanical Engineering,
Campus Box 427,
University of Colorado,
Boulder, CO 80309-0427
Fellow ASME.

Effect of Interface Layers on Elastic Wave Propagation in a Metal Matrix Composite Reinforced by Particles

This study considers the scattering of compressional and shear waves in SiC-particle-reinforced Al composite with interfacial layers. We assume same-size inclusions and same-thickness layers with nonhomogeneous elastic properties. The effective complex wave numbers follow from the coherent wave equations which depend only upon the scattering amplitude of the single scattering problem. Numerical values of scattering cross-sections, and phase velocities and attenuations of coherent plane waves are obtained for a moderately wide range of frequencies, and the results are graphed to display the effects of concentration of scatterers and interface properties.

Introduction

Ultrasonic waves have proved to be useful for the nondestructive characterization of composite materials (Kinra et al., 1980; Sayers, 1985; Mal and Bose, 1974; Ledbetter and Datta, 1986; Datta and Ledbetter, 1986a). In composites, particularly metal-matrix composites reinforced by fibers or particles, it is often the case that there is an interface layer surrounding the particles or fibers induced by processing conditions (Olsson et al., 1990). It may be noted from several recent studies (Hashin, 1990; Chen et al., 1990; Datta and Ledbetter, 1986b) that interfaces have significant influence on mechanical behavior of fiber or particle-reinforced composites. Thus there is considerable interest in characterizing properties of interfaces nondestructively by ultrasonic techniques and understanding the effect of interface characteristics on wave propagation. The scattering of the ultrasonic waves in the composites results in a frequency-dependent velocity and attenuation of the wave (Varadan et al., 1985; Norris, 1986).

The purpose of this paper is to analyze the effect of interface layers on the wave propagation of time harmonic plane compressional and shear waves in a particle reinforced metal-matrix composite. For a composite medium with imperfect interfaces between the matrix and the second phase, the actual details of the calculation are complicated. In the earlier study, Datta et al. (1988) considered the influences of thin interface layers with nonhomogeneous elastic properties on the wave propagation in a particle-reinforced composite. In this study, it is assumed that the tractions are continuous across the layer, whereas the displacements satisfy jump conditions that are linear in the thickness of the layer. It may be noted that the approximate boundary conditions used in this study are based on the assumption that inertial and curvature effects are negligible.

In the present paper, it is assumed that the interface layer is of any desired finite thickness and nonhomogeneous material properties. The composite medium contains a random distribution of spherical inclusions of same size with interface layers of same thickness. The scattering of plane elastic waves by a spherical inclusion with an interface is analyzed and the results of the single scattering problem are applied to the composite medium. Even if the interface layer has variable material properties, solutions to the problem can be obtained by subdividing the layer into several thick-walled spherical shells with varying, but uniform within each shell, properties. Thus the inertial and curvature effects are considered in this study. Numerical results for SiC-particle-reinforced Al composite are obtained as a function of concentration of scatterers and frequency, and the effect of interface properties on scattering cross-sections, and phase velocities and attenuations of coherent plane waves is discussed in detail. The method of solution is such that numerical results can be obtained at any desired finite frequency.

Statement of the Problem and Single Scattering Field

We consider a random distribution of identical spherical inclusions of radius a_0 in an infinite matrix. Let λ, μ, ρ, ν

Contributed by the Applied Mechanics Division of THE AMERICAN SOCIETY OF MECHANICAL ENGINEERS for publication in the ASME JOURNAL OF APPLIED MECHANICS.

Discussion on this paper should be addressed to the Technical Editor, Professor Lewis T. Wheeler, Department of Mechanical Engineering, University of Houston, Houston, TX 77204-4792, and will be accepted until four months after final publication of the paper itself in the ASME JOURNAL OF APPLIED MECHANICS.

Manuscript received by the ASME Applied Mechanics Division, Apr. 20, 1993; final revision, July 29, 1993. Associate Technical Editor: L. T. Wheeler.

be the Lamé constants, the mass density, the Poisson's ratio of the matrix, and λ_0, μ_0, ρ_0, ν_0 those of the inclusions. We assume that thick layers of uniform thickness h with variable material properties are present at the interfaces separating the matrix from each sphere.

In order to study the scattering of plane waves in a metal-matrix composite with interface layers, we first consider the scattered field due to a single spherical inclusion with an interface layer. Also, let the inclusion be separated from the matrix by n layers. The geometry is depicted in Fig. 1 where (x, y, z) is the Cartesian coordinate system with origin at the center of the sphere and (r, θ, ϕ) is the corresponding spherical polar coordinate system. The layer is subdivided into several thin shells and the material properties within each shell of inner radius a_{m-1}, outer radius $a_m (m = 1 \sim n)$, and uniform thickness $h_m = a_m - a_{m-1}$ are λ_m, μ_m, ρ_m, ν_m.

Let the components of the displacement vector $\mathbf{u}$ in the r, θ and ϕ directions be labeled by u_r, u_θ, and u_ϕ. The displacement equation of motion is

$$(\lambda + 2\mu)\nabla\nabla \cdot \mathbf{u} - \mu\nabla \times \nabla \times \mathbf{u} = \rho\frac{\partial^2 \mathbf{u}}{\partial t^2} \tag{1}$$

where $\nabla = \mathbf{e}_r \partial/\partial r + \mathbf{e}_\theta (1/r)\partial/\partial\theta + \mathbf{e}_\phi (1/r \sin\theta)\partial/\partial\phi$ is the gradient operator and $\mathbf{e}_r$, $\mathbf{e}_\theta$, $\mathbf{e}_\phi$ are the unit vectors along the r, θ, ϕ directions.

We consider a plane longitudinal (P) wave propagating in the positive z-direction or a plane shear (S) wave polarized in the x-direction and propagating in the positive z-direction. Thus,

$$\mathbf{u}^i = w_0 \exp\left[i(k_p z - \omega t)\right]\mathbf{e}_z + u_0 \exp\left[i(k_s z - \omega t)\right]\mathbf{e}_x \tag{2}$$

where a superscript i stands for the incident component, ω is the circular frequency of the wave, t is the time, $\mathbf{e}_x$, $\mathbf{e}_z$ are unit vectors in the x, z-directions, and w_0, u_0 are the amplitudes of the incident P and S waves. k_p, k_s are the wave numbers of the P and S waves in the matrix

$$k_p = \frac{\omega}{c_p}, \quad k_s = \frac{\omega}{c_s}, \tag{3}$$

c_p, c_s are the longitudinal and shear wave speeds in the matrix

$$c_p = \sqrt{\frac{\lambda + 2\mu}{\rho}}, \quad c_s = \sqrt{\frac{\mu}{\rho}}. \tag{4}$$

In what follows, the time factor $\exp(-i\omega t)$ will be omitted from all the field quantities.

The boundary conditions for the scattered field are

$$\left.\begin{array}{lll} u_p^n = u_p^s + u_p^i & \sigma_{rp}^n = \sigma_{rp}^s + \sigma_{rp}^i & (r = a_n, p = r, \theta, \phi) \\ u_p^m = u_p^{m+1} & \sigma_{rp}^m = \sigma_{rp}^{m+1} & (r = a_m, m = 1 \sim n-1, p = r, \theta, \phi) \\ u_p^t = u_p^1 & \sigma_{rp}^t = \sigma_{rp}^1 & (r = a_0, p = r, \theta, \phi) \end{array}\right\} \tag{5}$$

where σ_{rr}, $\sigma_{r\theta}$, $\sigma_{r\phi}$ are the stress components, superscripts s, t and m, $m+1 (m = 1 \sim n-1)$ denote the scattered component within a matrix, the transmitted component within a spherical inclusion and the field quantities within each layer, and subscript p stands for the r, θ, ϕ directions.

The displacement fields in the matrix, the mth layer and the spherical inclusion may be expressed in the forms (Stratton, 1941)

$$\mathbf{u}^s = \sum_{l=0}^{\infty}\sum_{k=-1}^{1}\left[A_{kl}\mathbf{L}_{kl}^{(3)} + B_{kl}\mathbf{M}_{kl}^{(3)} + C_{kl}\mathbf{N}_{kl}^{(3)}\right] \tag{6}$$

$$\mathbf{u}^m = \sum_{l=0}^{\infty}\sum_{k=-1}^{1}\left[A_{kl}^m\mathbf{L}_{kl}^{(3)m} + B_{kl}^m\mathbf{M}_{kl}^{(3)m} + C_{kl}^m\mathbf{N}_{kl}^{(3)m} + D_{kl}^m\mathbf{L}_{kl}^{(1)m} + E_{kl}^m\mathbf{M}_{kl}^{(1)m} + F_{kl}^m\mathbf{N}_{kl}^{(1)m}\right] (m = 1 \sim n) \tag{7}$$

$$\mathbf{u}^t = \sum_{l=0}^{\infty}\sum_{k=-1}^{1}\left[A_{kl}^0\mathbf{L}_{kl}^{(1)0} + B_{kl}^0\mathbf{M}_{kl}^{(1)0} + C_{kl}^0\mathbf{N}_{kl}^{(1)0}\right] \tag{8}$$

where A_{kl}, B_{kl}, C_{kl}, A_{kl}^m, B_{kl}^m, C_{kl}^m, D_{kl}^m, E_{kl}^m, F_{kl}^m, A_{kl}^0, B_{kl}^0, and C_{kl}^0 are the unknowns to be solved. Spherical vector wave functions $\mathbf{L}_{kl}^{(3)}$, $\mathbf{M}_{kl}^{(3)}$, $\mathbf{N}_{kl}^{(3)}$, $\mathbf{L}_{kl}^{(i)m}$, $\mathbf{M}_{kl}^{(i)m}$, $\mathbf{N}_{kl}^{(i)m}$ $(i = 1, 3, m = 1 \sim n)$, $\mathbf{L}_{kl}^{(1)0}$, $\mathbf{M}_{kl}^{(1)0}$, $\mathbf{N}_{kl}^{(1)0}$ are given in Appendix A. The wave numbers k_p^m, k_s^m $(m = 1 \sim n)$ in the mth layer and k_p^0, k_s^0 $(m = 0)$ in the spherical inclusion are given by

$$\left.\begin{array}{ll} k_p^m = \dfrac{\omega}{c_p^m}, & k_s^m = \dfrac{\omega}{c_s^m} \ (m = 1 \sim n) \\ k_p^0 = \dfrac{\omega}{c_p^0}, & k_s^0 = \dfrac{\omega}{c_s^0} \ (m = 0) \end{array}\right\} \tag{9}$$

where the longitudinal and shear wave speeds c_p^m, c_s^m in the mth layer and c_p^0, c_s^0 in the spherical inclusion are

$$\left.\begin{array}{ll} c_p^m = \sqrt{\dfrac{\lambda_m + 2\mu_m}{\rho_m}}, & c_s^m = \sqrt{\dfrac{\mu_m}{\rho_m}} \ (m = 1 \sim n) \\ c_p^0 = \sqrt{\dfrac{\lambda_0 + 2\mu_0}{\rho_0}}, & c_s^0 = \sqrt{\dfrac{\mu_0}{\rho_0}} \ (m = 0) \end{array}\right\}. \tag{10}$$

From boundary conditions (5), the relationships among A_{kl}, C_{kl}, A_{kl}^m, C_{kl}^m, D_{kl}^m, F_{kl}^m, A_{kl}^0, and C_{kl}^0 are found to be (Datta et al., 1988)

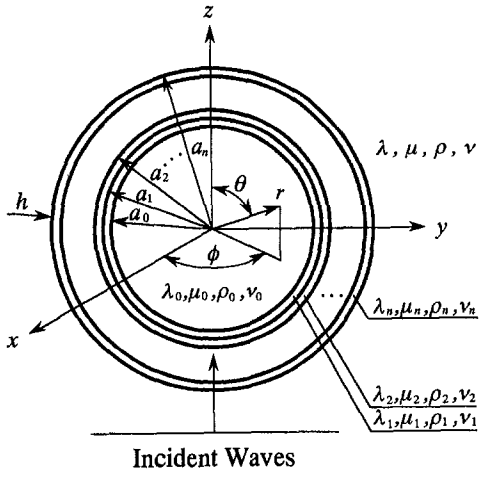

Fig. 1 A spherical inclusion with interface layers and incident waves

$$\mathbf{M}_l^n(a_n)\begin{Bmatrix} A_{kl}^n \\ C_{kl}^n \end{Bmatrix} + \mathbf{N}_l^n(a_n)\begin{Bmatrix} D_{kl}^n \\ F_{kl}^n \end{Bmatrix} = \mathbf{M}_l\begin{Bmatrix} A_{kl} \\ C_{kl} \end{Bmatrix} + \mathbf{N}_l^i\begin{Bmatrix} \Phi_{kl}w_0 \\ X_{kl}u_0 \end{Bmatrix}$$

$$\mu_n\mathbf{K}_l^n(a_n)\begin{Bmatrix} A_{kl}^n \\ C_{kl}^n \end{Bmatrix} + \mu_n\mathbf{L}_l^n(a_n)\begin{Bmatrix} D_{kl}^n \\ F_{kl}^n \end{Bmatrix} = \mu\mathbf{K}_l\begin{Bmatrix} A_{kl} \\ C_{kl} \end{Bmatrix} + \mu\mathbf{L}_l^i\begin{Bmatrix} \Phi_{kl}w_0 \\ X_{kl}u_0 \end{Bmatrix} \quad (11)$$

$$\mathbf{M}_l^m(a_m)\begin{Bmatrix} A_{kl}^m \\ C_{kl}^m \end{Bmatrix} + \mathbf{N}_l^m(a_m)\begin{Bmatrix} D_{kl}^m \\ F_{kl}^m \end{Bmatrix} = \mathbf{M}_l^{m+1}(a_m)\begin{Bmatrix} A_{kl}^m \\ C_{kl}^{m+1} \end{Bmatrix} + \mathbf{N}_l^{m+1}(a_m)\begin{Bmatrix} D_{kl}^{m+1} \\ F_{kl}^{m+1} \end{Bmatrix}$$

$$\mu_m\mathbf{K}_l^m(a_m)\begin{Bmatrix} A_{kl}^m \\ C_{kl}^m \end{Bmatrix} + \mu_m\mathbf{L}_l^m(a_m)\begin{Bmatrix} D_{kl}^m \\ F_{kl}^m \end{Bmatrix} = \mu_{m+1}\mathbf{K}_l^{m+1}(a_m)\begin{Bmatrix} A_{kl}^{m+1} \\ C_{kl}^{m+1} \end{Bmatrix} + \mu_{m+1}\mathbf{L}_l^{m+1}(a_m)\begin{Bmatrix} D_{kl}^{m+1} \\ F_{kl}^{m+1} \end{Bmatrix} \quad (m = 1 \sim n-1) \quad (12)$$

$$\mathbf{N}_l^0\begin{Bmatrix} A_{kl}^0 \\ C_{kl}^0 \end{Bmatrix} = \mathbf{M}_l^1(a_0)\begin{Bmatrix} A_{kl}^1 \\ C_{kl}^1 \end{Bmatrix} + \mathbf{N}_l^1(a_0)\begin{Bmatrix} D_{kl}^1 \\ F_{kl}^1 \end{Bmatrix}$$

$$\mu_0\mathbf{L}_l^0\begin{Bmatrix} A_{kl}^0 \\ C_{kl}^0 \end{Bmatrix} = \mu_1\mathbf{K}_l^1(a_0)\begin{Bmatrix} A_{kl}^1 \\ C_{kl}^1 \end{Bmatrix} + \mu_1\mathbf{L}_l^1(a_0)\begin{Bmatrix} D_{kl}^1 \\ F_{kl}^1 \end{Bmatrix}. \quad (13)$$

Also, the relationships among B_{kl}, B_{kl}^m, E_{kl}^m, and B_{kl}^0 are

$$B_{kl}^n h_l^{(1)}(k_s^n a_n) + E_{kl}^n j_l(k_s^n a_n) = B_{kl} h_l^{(1)}(k_s a_n) + j_l(k_s a_n) Y_{kl} u_0$$

$$\mu_n B_{kl}^n\{(l-1)h_l^{(1)}(k_s^n a_n) - k_s^n a_n h_{l+1}^{(1)}(k_s^n a_n)\} + \mu_n E_{kl}^n\{(l-1)j_l(k_s^n a_n) - k_s^n a_n j_{l+1}(k_s^n a_n)\} = \mu B_{kl}\{(l-1)h_l^{(1)}(k_s a_n) - k_s a_n h_{l+1}^{(1)}(k_s a_n)\} + \mu\{(l-1)j_l(k_s a_n) - k_s a_n j_{l+1}(k_s a_n)\} Y_{kl} u_0 \quad (14)$$

$$= \mu_{m+1} B_{kl}^{m+1}\{(l-1)h_l^{(1)}(k_s^{m+1} a_m) - k_s^{m+1} a_m h_{l+1}^{(1)}(k_s^{m+1} a_m)\} + \mu_{m+1} E_{kl}^{m+1}\{(l-1)j_l(k_s^{m+1} a_m) - k_s^{m+1} a_m j_{l+1}(k_s^{m+1} a_m)\} \quad (m = 1 \sim n-1) \quad (15)$$

$$B_{kl}^0 j_l(k_s^0 a_0) = B_{kl}^1 h_l^{(1)}(k^1{}_s a_0) + E_{kl}^1 j_l(k_s^1 a_0)$$

$$\mu_0 B_{kl}^0\{(l-1)j_l(k_s^0 a_0) - k_s^0 a_0 j_{l+1}(k_s^0 a_0)\} = \mu_1 B_{kl}^1\{(l-1)h_l^{(1)}(k_s^1 a_0) - k_s^1 a_0 h_{l+1}^{(1)}(k_s^1 a_0)\} + \mu_1 E_{kl}^1\{(l-1)j_l(k_s^1 a_0) - k_s^1 a_0 j_{l+1}(k_s^1 a_0)\}. \quad (16)$$

In Eqs. (11) and (14), Φ_{kl}, X_{kl}, and Y_{kl} are

$$\left.\begin{aligned} \Phi_{kl} &= \frac{i^{l-1}}{k_p}(2l+1)\delta_{k0} \\ X_{kl} &= \frac{i^{l-1}}{2k_s}\frac{2l+1}{l(l+1)}\{\delta_{k1} - l(l+1)\delta_{k,-1}\} \\ Y_{kl} &= \frac{i^{l-1}}{2}\frac{2l+1}{l(l+1)}\{\delta_{k1} + l(l+1)\delta_{k,-1}\} \end{aligned}\right\} \quad (17)$$

where δ_{k0}, δ_{k1}, $\delta_{k,-1}$ are the Kronecker delta. Solving these equations iteratively, we obtain equations for the determination of A_{kl}, B_{kl}, C_{kl} as

$$\begin{Bmatrix} A_{kl} \\ C_{kl} \end{Bmatrix} = -\mathbf{Q}_l^{-1}\mathbf{P}_l\begin{Bmatrix} \Phi_{kl}w_0 \\ X_{kl}u_0 \end{Bmatrix} \quad (18)$$

$$B_{kl} = -\frac{F_l}{G_l}Y_{kl}u_0. \quad (19)$$

The matrices $\mathbf{P}_l$, $\mathbf{Q}_l$ in Eqs. (18) are

$$\left.\begin{aligned} \mathbf{P}_l &= \mathbf{N}_l^i - \frac{\mu}{\mu_n}\mathbf{R}_l^n(\mathbf{S}_l^n)^{-1}\mathbf{L}_l^i \\ \mathbf{Q}_l &= \mathbf{M}_l - \frac{\mu}{\mu_n}\mathbf{R}_l^n(\mathbf{S}_l^n)^{-1}\mathbf{K}_l \end{aligned}\right\}. \quad (20)$$

The recurrence formulae for $\mathbf{R}_l^n$, $\mathbf{S}_l^n$ are given by

$$\left.\begin{aligned} \mathbf{R}_l^m &= \mathbf{N}_l^m(a_m) - \mathbf{M}_l^m(a_m)\left[\mathbf{M}_l^m(a_{m-1}) - \frac{\mu_m}{\mu_{m-1}}\mathbf{R}_l^{m-1}(\mathbf{S}_l^{m-1})^{-1}\mathbf{K}_l^m(a_{m-1})\right]^{-1} \times\left[\mathbf{N}_l^m(a_{m-1}) - \frac{\mu_m}{\mu_{m-1}}\mathbf{R}_l^{m-1}(\mathbf{S}_l^{m-1})^{-1}\mathbf{L}_l^m(a_{m-1})\right] \\ \mathbf{S}_l^m &= \mathbf{L}_l^m(a_m) - \mathbf{K}_l^m(a_m)\left[\mathbf{M}_l^m(a_{m-1}) - \frac{\mu_m}{\mu_{m-1}}\mathbf{R}_l^{m-1}(\mathbf{S}_l^{m-1})^{-1}\mathbf{K}_l^m(a_{m-1})\right]^{-1} \times\left[\mathbf{N}_l^m(a_{m-1}) - \frac{\mu_m}{\mu_{m-1}}\mathbf{R}_l^{m-1}(\mathbf{S}_l^{m-1})^{-1}\mathbf{L}_l^m(a_{m-1})\right] \end{aligned}\right\} \quad (m = 1\text{–}n) \quad (21)$$

$$B_{kl}^m h_l^{(1)}(k_s^m a_m) + E_{kl}^m j_l(k_s^m a_m) = B_{kl}^{m+1} h_l^{(1)}(k_s^{m+1} a_m) + E_{kl}^{m-1} j_l(k_s^{m+1} a_m)$$

$$\mu_m B_{kl}^m\{(l-1)h_l^{(1)}(k_s^m a_m) - k_s^m a_m h_{l+1}^{(1)}(k_s^m a_m)\} + \mu_m E_{kl}^m\{(l-1)j_l(k_s^m a_m) - k_s^m a_m j_{l+1}(k_s^m a_m)\}$$

$$\mathbf{R}_l^0 = \mathbf{N}_l^0, \quad \mathbf{S}_l^0 = \mathbf{L}_l^0. \quad (22)$$

In Eqs. (20)–(22), $\mathbf{L}_l^i$, $\mathbf{N}_l^i$, $\mathbf{K}_l$, $\mathbf{M}_l$, $\mathbf{K}_l^m(a_m)$, $\mathbf{L}_l^m(a_m)$, $\mathbf{M}_l^m(a_m)$, $\mathbf{N}_l^m(a_m)$ $(m = 1 \sim n)$, $\mathbf{L}_l^0$, $\mathbf{N}_l^0$ are given in Appendix B and F_l, G_l are

$$F_l = j_l(k_s a_n) - \frac{\mu}{\mu_n}\frac{T_l^n}{U_l^n}\{(l-1)j_l(k_s a_n) - k_s a_n j_{l+1}(k_s a_n)\}$$
$$G_l = h_l^{(1)}(k_s a_n) - \frac{\mu}{\mu_n}\frac{T_l^n}{U_l^n}\{(l-1)h_l^{(1)}(k_s a_n) - k_s a_n h_{l+1}^{(1)}(k_s a_n)\} \Bigg\}. \quad (23)$$

The recurrence formulae for T_l^n, U_l^n are given by

$$T_l^m = j_l(k_s^m a_m) - \frac{j_l(k_s^m a_{m-1}) - (\mu_m/\mu_{m-1})(T_l^{m-1}/U_l^{m-1})J_l^m(a_{m-1})}{h_l^{(1)}(k_s^m a_{m-1}) - (\mu_m/\mu_{m-1})(T_l^{m-1}/U_l^{m-1})H_l^m(a_{m-1})} h_l^{(1)}(k_s^m a_m)$$
$$U_l^m = J_l^m(a_m) - \frac{j_l(k_s^m a_{m-1}) - (\mu_m/\mu_{m-1})(T_l^{m-1}/U_l^{m-1})J_l^m(a_{m-1})}{h_l^{(1)}(k_s^m a_{m-1}) - (\mu_m/\mu_{m-1})(T_l^{m-1}/U_l^{m-1})H_l^m(a_{m-1})} H_l^m(a_m) \quad (m = 1 \sim n) \Bigg\} \quad (24)$$

$$T_l^0 = j_l(k_s^0 a_0), \quad U_l^0 = J_l^0(a_0) \quad (25)$$

where $j_l(\ )$ and $h_l^{(1)}(\ )$ are the lth order spherical Bessel and Hankel functions of the first kind, and $J_l^m(a_m)$ and $H_l^m(a_m)$ are

$$J_l^m(a_m) = (l-1)j_l(k_s^m a_m) - k_s^m a_m j_{l+1}(k_s^m a_m) \quad (m = 0 \sim n)$$
$$H_l^m(a_m) = (l-1)h_l^{(1)}(k_s^m a_m) - k_s^m a_m h_{l+1}^{(1)}(k_s^m a_m) \quad (m = 1 \sim n) \Bigg\} \quad (26)$$

The scattered field at a large distance from the sphere follows from Eq. (6) letting r tend to ∞. This yields

$$u_r^s \sim \frac{1}{r}e^{ik_p r}g(\theta, \phi)$$
$$u_\theta^s \sim \frac{1}{r}e^{ik_s r}h_1(\theta, \phi)$$
$$u_\phi^s \sim \frac{1}{r}e^{ik_s r}h_2(\theta, \phi) \Bigg\}. \quad (27)$$

The function $g(\theta, \phi)$ is termed the far-field scattering amplitude for the scattering P waves, and the functions $h_1(\theta, \phi)$ and $h_2(\theta, \phi)$ the far-field scattering amplitudes in the θ and ϕ directions, respectively, for the scattered S waves. The definitions of these functions are given in Appendix C. The scattering cross-sections for incident P and S waves are then (Barratt and Collins, 1965)

$$\Sigma_p = \frac{4\pi}{k_p}\mathrm{Im}[g(0, \phi)] = \frac{4\pi}{k_p}\mathrm{Im}\left[\sum_{l=0}^{\infty}(-i)^l A_{0l}\right] \quad (28)$$

$$\Sigma_s = \frac{4\pi}{k_s}\mathrm{Im}[\cos\phi h_1(0, \phi) - \sin\phi h_2(0, \phi)] = \frac{4\pi}{k_s}\mathrm{Im}\left[\sum_{l=1}^{\infty}\frac{(-i)^l}{2}\{l(l+1)C_{1l} - C_{-1l} + \frac{l(l+1)}{k_s}B_{1l} + \frac{1}{k_s}B_{-1l}\}\right]. \quad (29)$$

In the above equations, Σ_p and Σ_s do not depend on ϕ.

Scattering of Elastic Waves by Randomly Distributed Inclusions

We consider a random distribution of identical spherical inclusions with interfacial layers. Once the scattered field due to a single inclusion is known, the phase velocities and attenuations of the coherent waves through the composite can be easily calculated. At low concentrations of inclusions we can use the following dispersion relations (Foldy, 1945):

$$\left(\frac{K_p}{k_p}\right)^2 = 1 + \frac{3c}{k_p^2 a_0^3}g(0, \phi) \quad (30)$$

$$\left(\frac{K_s}{k_s}\right)^2 = 1 + \frac{3c}{k_s^2 a_0^3}\{\cos\phi h_1(0, \phi) - \sin\phi h_2(0, \phi)\} \quad (31)$$

where c is the volume concentration of randomly distributed inclusions in the matrix and K_p, K_s are the wave numbers of the effective P and S waves. In the above equations, K_p and K_s do not depend on ϕ.

Numerical Results and Discussions

To examine the effect of interface properties on the phase velocities and attenuations of coherent plane waves through the composite medium, the far-field scattering amplitudes have been computed numerically. The considered composite was an SiC-Al composite. The constituent properties are given in Table 1. Three special cases of interface material are considered. The elastic properties of Cases I, II, III are given by

Case I.

$$\lambda_I(r) = \frac{\lambda + \lambda_0}{2}, \quad \mu_I(r) = \frac{\mu + \mu_0}{2} \quad (a_0 \le r \le a_0 + h)$$
$$\rho_I(r) = \frac{\rho + \rho_0}{2} \quad (32)$$

Table 1 Material properties of SiC and Al

SiC	ρ_0(kg/m^3)	μ_0(GPa)	$\lambda_0 + 2\mu_0$(GPa)	ν_0
	3181	188.1	474.2	0.17
Al	ρ(kg/m^3)	μ(GPa)	$\lambda + 2\mu$(GPa)	ν
	2706	26.5	110.5	0.34

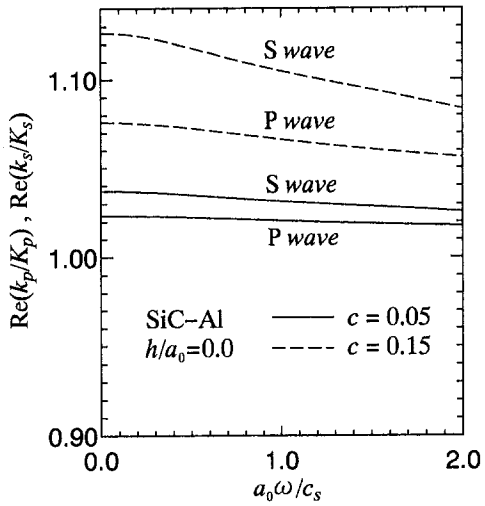

Fig. 2 Effect of concentration c on phase velocities versus frequency for effective P and S waves

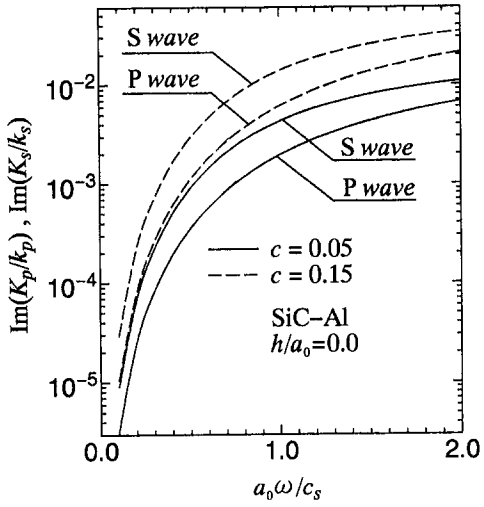

Fig. 3 Effect of concentration c on attenuations versus frequency for effective P and S waves

Case II.

$$\lambda_{II}(r) = (\lambda - \lambda_0)\left(\frac{r - a_0}{h}\right) + \lambda_0$$

$$\mu_{II}(r) = (\mu - \mu_0)\left(\frac{r - a_0}{h}\right) + \mu_0 \quad (a_0 \le r \le a_0 + h)$$

$$\rho_{II}(r) = (\rho - \rho_0)\left(\frac{r - a_0}{h}\right) + \rho_0 \qquad (33)$$

Case III.

$$\lambda_{III}(r) = 4(\lambda - \lambda_0)\left\{\frac{r - (a_0 + h/2)}{h}\right\}^3 + \frac{\lambda + \lambda_0}{2}$$

$$\mu_{III}(r) = 4(\mu - \mu_0)\left\{\frac{r - (a_0 + h/2)}{h}\right\}^3 + \frac{\mu + \mu_0}{2} \times (a_0 \le r \le a_0 + h)$$

$$\rho_{III}(r) = 4(\rho - \rho_0)\left\{\frac{r - (a_0 + h/2)}{h}\right\}^3 + \frac{\rho + \rho_0}{2} \qquad (34)$$

Case III approximates actual interfacial layers best, next does Case II and the third, Case I. The material properties of the layers given above are calculated at the midpoint of each layer assuming variations of Cases I, II, III from the boundary of the inclusion to the matrix medium. It is found that the truncation after $l = 8$ in Eqs. (28), (29) gives practically adequate results at any desired frequency for $0 < a_0\omega/c_s < 2.0$.

Figure 2 shows the variations of the phase velocities $\mathrm{Re}(k_p/K_p)$, $\mathrm{Re}(k_s/K_s)$ of the effective P and S waves with the frequency $a_0\omega/c_s$ for $h/a_0 = 0.0$. The solid curves refer to the case $c = 0.05$ and the dashed curves refer to $c = 0.15$. The quantities $\mathrm{Re}(k_p/K_p)$, $\mathrm{Re}(k_s/K_s)$ decay at a slower rate as the frequency increases. The P and S wave curves for $c = 0.15$ possess higher amplitudes than those for $c = 0.05$. Figure 3 shows the variations of the attenuations $\mathrm{Im}(K_p/k_p)$, $\mathrm{Im}\,(K_s/k_s)$ of the effective P and S waves with the frequency $a_0\omega/c_s$ for $h/a_0 = 0.0$ and $c = 0.05$, 0.15. The attenuations also increase in magnitude with the increasing volume concentration c. Datta et al. (1988) previously considered the influence of thin interfacial layers on elastic wave propagation in a particle-reinforced composites. The present results are, in the limit as $h/a_0 \to 0$, in agreement with the results in Datta et al. (1988).

Figure 4 shows the variation of the scattering cross-section

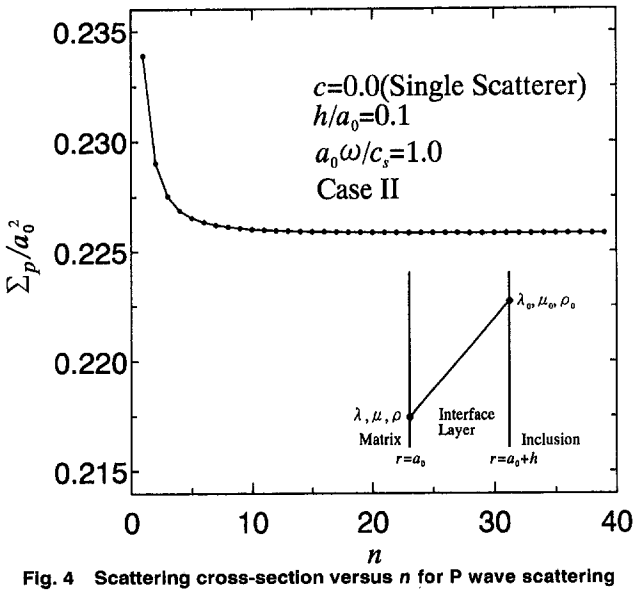

Fig. 4 Scattering cross-section versus n for P wave scattering

Σ_p/a_0^2 of the P wave with the number of layers n for Case II and $c = 0.0$ (single scatterer), $h/a_0 = 0.1$, $a_0\omega/c_s = 1.0$. Case II refers to the case of the interface material through which the elastic properties vary linearly from those of the inclusions to those of the matrix. It is found that the truncation after $n = 30$ gives practically adequate results for Cases II and III. The effect of the interface layer on Σ_p/a_0^2 at $a_0\omega/c_s = 1.0$ for $c = 0.0$ (single scatterer) is shown in Fig. 5. The figure shows that the cross section Σ_p/a_0^2 increases with the h/a_0 ratio, and depends on the constituents and the nature of the interface layer. In Fig. 6, the scattering cross-sections Σ_p/a_0^2, Σ_s/a_0^2 of the P and S waves are plotted as functions of the frequency $a_0\omega/c_s$ for $c = 0.0$ (single scatterer). The dashed curves refer to the case $h/a_0 = 0.0$ and the solid curves refer to $h/a_0 = 0.1$. The interface material for Case III is considered. The scattering cross-sections for Case I are obtained by Paskaramoorthy et al. (1988) using a finite element and eigenfunction expansion method. Case I refers to the case in which the interface material possesses constant properties. The present results for Case I are in good agreement with these previously published results.

Figure 7 shows the variations of the phase velocities $\mathrm{Re}(k_p/K_p)$, $\mathrm{Re}(k_s/K_s)$ of the effective P and S waves with the frequency $a_0\omega/c_s$ for Case III and $c = 0.1$, $h/a_0 = 0.0$,

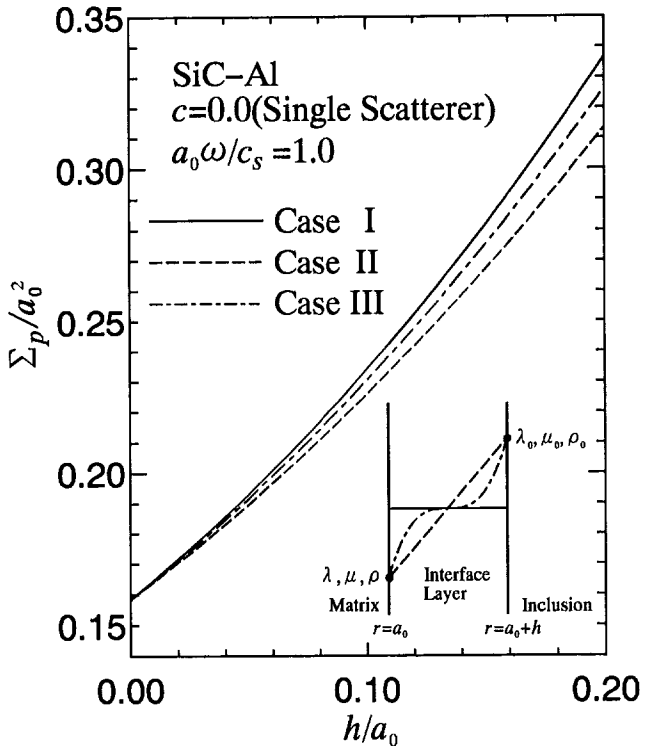

Fig. 5 Scattering cross-section versus h/a_0 for P wave scattering

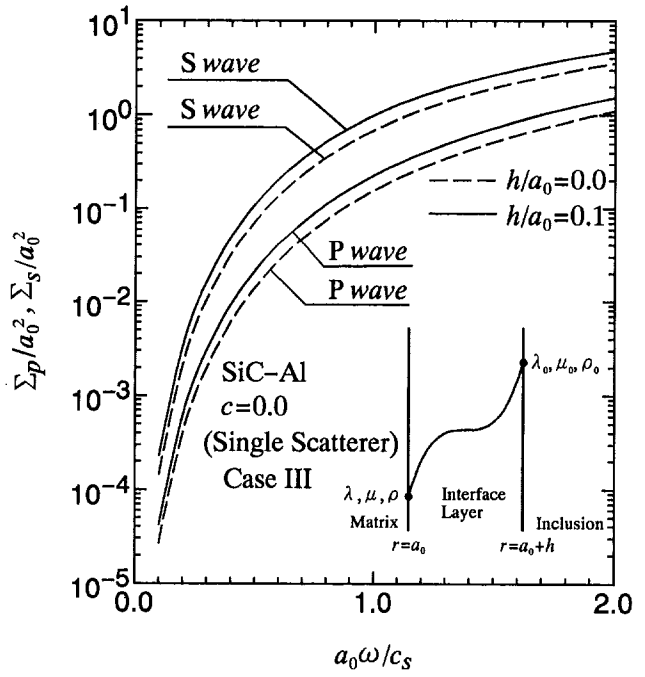

Fig. 6 Effect of interface on scattering cross-sections versus frequency for P and S waves scattering

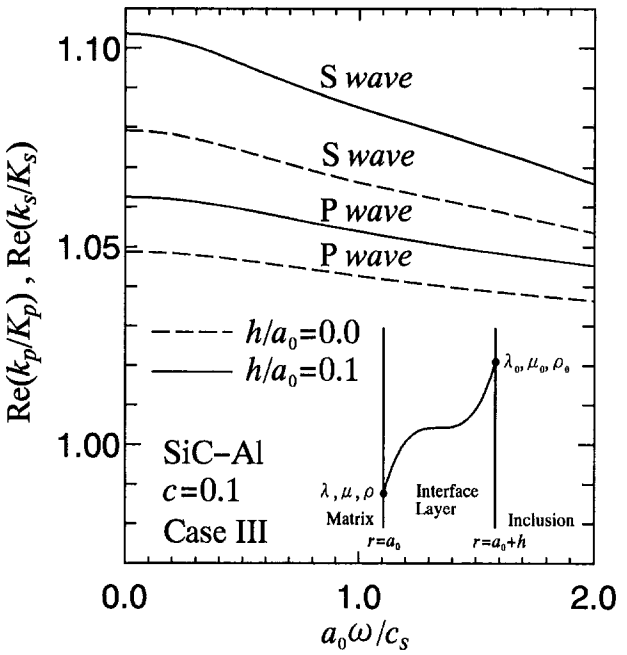

Fig. 7 Effect of interface on phase velocities versus frequency for effective P and S waves

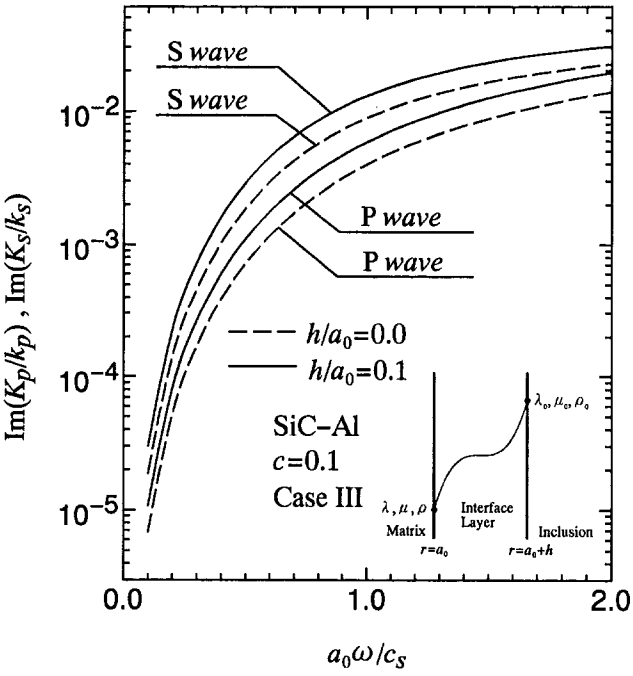

Fig. 8 Effect of interface on attenuations versus frequency for effective P and S waves

0.1. The phase velocities decrease with the frequency and the interface effect increases the phase velocities. Figure 8 shows the variations of the attenuations $\mathrm{Im}(K_p/k_p)$, $\mathrm{Im}(K_s/k_s)$ of the effective P and S waves with the frequency $a_0\omega/c_s$ for Case III and $c = 0.1$, $h/a_0 = 0.0$, 0.1. The attenuations increase with the frequency and the interface effect on the attenuations is pronounced. The existence of the interface layers produces bigger values of the attenuations.

In conclusion, scattering of compressional and shear waves by a spherical inclusion with a thick nonhomogeneous interface layer was analyzed and the results of the single scattering problem were applied to coherent plane waves in a metal matrix composite with interface layers. The interface effect can increase scattering cross-sections, phase velocities and attenuations, and depends on the frequency and the material properties of the interface layers. The numerical results were obtained for any given finite frequencies, and layers with nonhomogeneous elastic properties of any desired finite thickness. We show that it is possible to control the phase velocities and attenuations quantitatively by appropriately modifying the interface properties through process control. Also, effective Lamé constants λ_{eff} and μ_{eff} can be easily obtained from the phase velocities $\mathrm{Re}(k_p/K_p)$, $\mathrm{Re}(k_s/K_s)$ of the effective P and S waves as follows:

$$\lambda_{\text{eff}} + 2\mu_{\text{eff}} = (\lambda + 2\mu)\left[1 + c\left\{\left(\frac{\rho_0}{\rho} - 1\right) + H\left(\frac{\bar{\rho}}{\rho} - 1\right)\right\}\right]\left\{\text{Re}\left(\frac{k_p}{K_p}\right)\right\}^2$$

$$\mu_{\text{eff}} = \mu\left[1 + c\left\{\left(\frac{\rho_0}{\rho} - 1\right) + H\left(\frac{\bar{\rho}}{\rho} - 1\right)\right\}\right]\left\{\text{Re}\left(\frac{k_s}{K_s}\right)\right\}^2. \quad (35)$$

In the above equations, $\bar{\rho}$ and H are

$$\bar{\rho} = \frac{3}{Ha_0^3}\int_{a_0}^{a_0+h}\rho_C(r)r^2dr \quad (C = \text{I, II, III})$$

$$H = \left(\frac{h}{a_0}\right)^3 + 3\left(\frac{h}{a_0}\right)^2 + 3\left(\frac{h}{a_0}\right). \quad (36)$$

We hope to analyze the effects of interface delamination and multiple scattering by a distribution of inclusions on macroscopic materials properties of composites further in the future.

References

Barratt, P. J., and Collins, W. D., 1965, "The Scattering Cross-Section of an Obstacle in an Elastic Solid for Plane Harmonic Waves," *Proceedings of the Cambridge Philosophical Society*, Vol. 61, No. 4, pp. 969–981.

Chen, T., Dvorak, G. H., and Benveniste, Y., 1990, "Stress Fields in Composites Reinforced by Coated Cylindrically Orthotropic Fibers," *Mechanics of Materials*, Vol. 9, pp. 17–32.

Datta, S. K., and Ledbetter, H. M., 1986a, "Ultrasonic Characterization of Material Properties of Composite Materials," *Proceedings of the Tenth U.S. National Congress of Applied Mechanics*, J. P. Lamb, ed., pp. 377–387.

Datta, S. K., and Ledbetter, H. M., 1986b, "Effect of Interface Properties on Wave Propagation in a Medium with Inclusions," *Mechanics of Material Interfaces*, A. P. S. Selvadurai, and G. Z. Voyiadjis, eds., Elsevier, Amsterdam, pp. 131–141.

Datta, S. K., Ledbetter, H. M., Shindo, Y., and Shah, A. H., 1988, "Phase Velocity and Attenuation of Plane Elastic Waves in a Particle-Reinforced Composite Medium," *Wave Motion*, Vol. 10, pp. 171–182.

Foldy, L. L., 1945, "The Multiple Scattering of Waves," *Physical Review*, Vol. 67, No. 3, 4, pp.107–119.

Hashin, Z., 1990, "Thermoelastic Properties of Fiber Composites with Imperfect Inter Phase," *Mechanics of Materials*, Vol. 8, pp. 333–348.

Kinra, V. K., Petraitis, M. S., and Datta, S. K., 1980, "Ultrasonic Wave Propagation in a Random Particulate Composite," *International Journal of Solids and Structures*, Vol. 16, No. 4, pp. 301–312.

Ledbetter, H. M., and Datta, S. K., 1986, "Effective Wave Speeds in an SiC-Particle-Reinforced Al Composite," *Journal of the Acoustical Society of America*, Vol. 79, No. 2, pp. 239–248.

Mal, A. K., and Bose, S. K. 1974, "Dynamic Elastic Moduli of a Suspension of Imperfectly Bonded Spheres," *Proceedings of the Cambridge Philosophical Society*, Vol. 76, No. 3, pp. 587–600.

Norris, A. N., 1986, "Scattering of Elastic Waves by Spherical Inclusions with Applications to Low Frequency Wave Propagation in Composites," *International Journal of Engineering Science*, Vol. 24, No. 8, pp. 1271–1282.

Olsson, P., Datta, S. K., and Boström, A., 1990, "Elastodynamic Scattering from Inclusions Surrounded by Thin Interface Layers," ASME JOURNAL OF APPLIED MECHANICS, Vol. 57, pp. 672–676.

Paskaramoorthy, R., Datta, S. K., and Shah, A. H., 1988, "Effect of Interface Layers on Scattering of Elastic Waves," ASME JOURNAL OF APPLIED MECHANICS, Vol. 55, No. 4, pp. 871–878.

Sayers, C. M., 1985, "Scattering of Ultrasound by Minority Phases in Polycrystalline Metals," *Wave Motion*, Vol. 7, No. 1, pp. 95–104.

Stratton, J. A., 1941, *Electromagnetic Theory*, McGraw-Hill, p. 414.

Varadan, V. K., Ma, Y., and Varadan, V. V., 1985, "A Multiple Scattering Theory for Elastic Wave Propagation in Discrete Random Media," *Journal of the Acoustical Society of America*, Vol. 77, No. 2, pp. 375–385.

APPENDIX A

Spherical vector wave functions $\mathbf{L}_{kl}^{(3)}$, $\mathbf{M}_{kl}^{(3)}$, $\mathbf{N}_{kl}^{(3)}$ in Eq. (6) are

$$\left.\begin{aligned}
\mathbf{L}_{kl}^{(3)} &= \left[\frac{\partial}{\partial r}h_l^{(1)}(k_pr)P_l^k(\cos\theta)\mathbf{e}_r + h_l^{(1)}(k_pr)\frac{1}{r}\frac{\partial}{\partial\theta}P_l^k(\cos\theta)\mathbf{e}_\theta + \frac{ik}{r\sin\theta}h_l^{(1)}(k_pr)P_l^k(\cos\theta)\mathbf{e}_\phi\right]e^{ik\phi}\\
\mathbf{M}_{kl}^{(3)} &= \left[\frac{ik}{\sin\theta}h_l^{(1)}(k_sr)P_l^k(\cos\theta)\mathbf{e}_\theta - h_l^{(1)}(k_sr)\frac{\partial}{\partial\theta}P_l^k(\cos\theta)\mathbf{e}_\phi\right]e^{ik\phi}\\
\mathbf{N}_{kl}^{(3)} &= \left[\frac{l(l+1)}{r}h_l^{(1)}(k_sr)P_l^k(\cos\theta)\mathbf{e}_r + \frac{1}{r}\frac{\partial}{\partial r}\{rh_l^{(1)}(k_sr)\}\frac{\partial}{\partial\theta}P_l^k(\cos\theta)\mathbf{e}_\theta + \frac{ik}{r\sin\theta}\frac{\partial}{\partial r}\{rh_l^{(1)}(k_sr)\}P_l^k(\cos\theta)\mathbf{e}_\phi\right]e^{ik\phi}
\end{aligned}\right\} \quad (A1)$$

where $h_l^{(1)}(\ )$ is the lth order spherical Hankel function of the first kind and $P_l^k(\ )$ is the associated Legendre function of the first kind. Spherical vector wave function $\mathbf{L}_{kl}^{(3)m}$, $\mathbf{M}_{kl}^{(3)m}$, $\mathbf{N}_{kl}^{(3)m}$ in Eqs. (7) are obtained by replacing k_p,k_s by k_p^m,k_s^m in Eqs. (A1). $\mathbf{L}_{kl}^{(1)m}$, $\mathbf{M}_{kl}^{(1)m}$, $\mathbf{N}_{kl}^{(1)m}$ are also obtained by replacing $h_l^{(1)}(\ )$ by the lth order spherical Bessel function of the first kind $j_l(\ )$ in Eqs. (A1). Spherical vector wave functions $\mathbf{L}_{kl}^{(1)0}$, $\mathbf{M}_{kl}^{(1)0}$, $\mathbf{N}_{kl}^{(1)0}$ in Eq. (8) are obtained by replacing $h_l^{(1)}(\ )$, k_p,k_s by $j_l(\ )$,k_p^0, k_s^0, respectively, in Eqs. (A1).

APPENDIX B

The matrices $\mathbf{L}_l^i$, $\mathbf{N}_l^i$ in the first equation of (20) are

$$\mathbf{L}_l^i = \begin{bmatrix} L_{11}^{li} & L_{12}^{li} \\ L_{21}^{li} & L_{22}^{li} \end{bmatrix}, \quad \mathbf{N}_l^i = \begin{bmatrix} N_{11}^{li} & N_{12}^{li} \\ N_{21}^{li} & N_{22}^{li} \end{bmatrix} \quad (A2)$$

$$\left.\begin{aligned}
L_{11}^{li} &= \left\{l^2 - l - \frac{(k_sa_n)^2}{2}\right\}j_l(k_pa_n) + 2k_pa_nj_{l+1}(k_pa_n)\\
L_{12}^{li} &= l(l+1)\{(l-1)j_l(k_sa_n) - k_sa_nj_{l+1}(k_sa_n)\}\\
L_{21}^{li} &= (l-1)j_l(k_pa_n) - k_pa_nj_{l+1}(k_pa_n)\\
L_{22}^{li} &= \left\{l^2 - 1 - \frac{(k_sa_n)^2}{2}\right\}j_l(k_sa_n) + k_sa_nj_{l+1}(k_sa_n)
\end{aligned}\right\} \quad (A3)$$

$$\left.\begin{aligned} N_{11}^{li} &= lj_l(k_p a_n) - k_p a_n j_{l+1}(k_p a_n) \\ N_{12}^{li} &= l(l+1) j_l(k_s a_n) \\ N_{21}^{li} &= j_l(k_p a_n) \\ N_{22}^{li} &= (l+1) j_l(k_s a_n) - k_s a_n j_{l+1}(k_s a_n) \end{aligned}\right\}. \quad \text{(A4)}$$

The matrices $\mathbf{K}_l$, $\mathbf{M}_l$ in the second equation of (20) are obtained by replacing the lth order spherical Bessel function of the first kind $j_l(\ )$ by the lth order spherical Hankel function of the first kind $h_l^{(1)}(\ )$ in Eqs. (A2)–(A4). The matrices $\mathbf{L}_l^m(a_m)$, $\mathbf{N}_l^m(a_m)$ in Eqs. (21) are obtained by replacing $k_p a_n, k_s a_n$ by $k_p^m a_m, k_s^m a_m$ in Eqs. (A2)–(A4). $\mathbf{K}_l^m(a_m)$, $\mathbf{M}_l^m(a_m)$ are also obtained by replacing $j_l(\ )$, $k_p a_n, k_s a_n$ by $h_l^{(1)}(\ ), k_p^m a_m, k_s^m a_m$, respectively, in Eqs. (A2)–(A4). The matrices $\mathbf{L}_l^0$, $\mathbf{N}_l^0$ in Eqs. (22) are obtained by replacing $k_p a_n$, $k_s a_n$ by $k_p^0 a_0, k_s^0 a_0$ in Eqs. (A2)–(A4).

APPENDIX C

The far-field scattering amplitude for the scattering P waves $g(\theta, \phi)$ and the far-field scattering amplitudes in the θ and ϕ directions for the scattering S waves $h_1(\theta, \phi)$, $h_2(\theta, \phi)$ are

$$g(\theta, \phi) = \sum_{l=0}^{\infty} A_{0l}(-i)^l P_l(\cos\theta) \quad \text{(A5)}$$

$$h_1(\theta, \phi) = \sum_{l=0}^{\infty} \sum_{k=-1}^{1} (-i)^l \left\{ C_{kl} \frac{\partial}{\partial\theta} P_l^k(\cos\theta) + \frac{B_{kl}}{k_s} \frac{k}{\sin\theta} P_l^k(\cos\theta) \right\} e^{ik\phi} \quad \text{(A6)}$$

$$h_2(\theta, \phi) = -\sum_{l=0}^{\infty} \sum_{k=-1}^{1} (-i)^{l+1} \left\{ C_{kl} \frac{k}{\sin\theta} P_l^k(\cos\theta) + \frac{B_{kl}}{k_s} \frac{\partial}{\partial\theta} P_l^k(\cos\theta) \right\} e^{ik\phi} \quad \text{(A7)}$$

Integral Equation Method via Domain Decomposition and Collocation for Scattering Problems

Xiaogang Zeng

Fang Zhao[1]

Department of Civil and Environmental Engineering, Florida International University, Miami, FL 33199

In this paper an exterior domain decomposition (DD) method based on the boundary element (BE) formulation for the solutions of two or three-dimensional time-harmonic scattering problems in acoustic media is described. It is known that the requirement of large memory and intensive computation has been one of the major obstacles for solving large scale high-frequency acoustic systems using the traditional nonlocal BE formulations due to the fully populated resultant matrix generated from the BE discretization. The essence of this study is to decouple, through DD of the problem-defined exterior region, the original problem into arbitrary subproblems with data sharing only at the interfaces. By decomposing the exterior infinite domain into appropriate number of infinite subdomains, this method not only ensures the validity of the formulation for all frequencies but also leads to a diagonalized, blockwise-banded system of discretized equations, for which the solution requires only O(N) *multiplications, where* N *is the number of unknowns on the scatterer surface. The size of an individual submatrix that is associated with a subdomain may be determined by the user, and may be selected such that the restriction due to the memory limitation of a given computer may be accommodated. In addition, the method may suit for parallel processing since the data associated with each subdomain (impedance matrices, load vectors, etc.) may be generated in parallel, and the communication needed will be only for the interface values. Most significantly, unlike the existing boundary integral-based formulations valid for all frequencies, our method avoids the use of both the hypersingular operators and the double integrals, therefore reducing the computational effort. Numerical experiments have been conducted for rigid cylindrical scatterers subjected to a plane incident wave. The results have demonstrated the accuracy of the method for wave numbers ranging from 0 to 30, both directly on the scatterer and in the far-field, and have confirmed that the procedure is valid for critical frequencies.*

1 Introduction

In this paper we are concerned with the problem of scattering by a rigid obstacle in an acoustic medium, and its solution via localized boundary integral equation methods, which is intended as a prototype for a class of more general scattering problems that occur in such diverse fields as elastodynamics and electromagnetism.

Boundary element methods have been widely used for studying problems of wave scattering by rigid or deformable bodies submerged in a compressible, inviscid fluid because of their ability to reduce by one the dimension of the problems. For exterior problems, they have the added attraction of automatically satisfying the appropriate radiation conditions. Some recent work on applications of BE methods to wave scattering problems may be found, among others, in Jean and Mathews (1990), Krishnasamy et al. (1990), Seybert et al. (1988), and Zeng et al. (1992a). Survey is also available in, e.g., Amini and Harris (1990), Givoli (1991), and Zeng (1992b). The price one pays for this reduction in problem dimensionality is that, contrary to partial differential equation formulations in the domain, which upon discretization lead to large but sparse algebraic systems, boundary formulations give rise to smaller but full systems of equations. The nonlocality of boundary methods makes their use difficult in practice for problems that involve radiating or scattering bodies if the wavelength of the excitation is small compared to the largest

[1]To whom all correspondence should be sent.

Contributed by the Applied Mechanics Division of THE AMERICAN SOCIETY OF MECHANICAL ENGINEERS for publication in the ASME JOURNAL OF APPLIED MECHANICS.

Discussion on this paper should be addressed to the Technical Editor, Professor Lewis T. Wheeler, Department of Mechanical Engineering, University of Houston, Houston, TX 77204-4792, and will be accepted until four months after final publication of the paper itself in the ASME JOURNAL OF APPLIED MECHANICS.

Manuscript received by the ASME Applied Mechanics Division, May 17, 1993; final revision, Sept. 27, 1993. Associate Technical Editor: R. L. Huston.

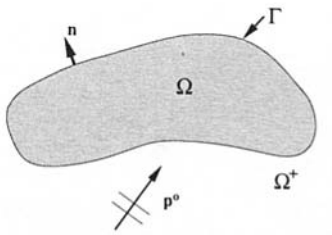

Fig. 1 Rigid scatterer immersed in a compressible, inviscid fluid

dimension of the body, even with the largest computers now available. This difficulty has been addressed in the domain finite element and finite differences communities by developing infinite elements (Zienkiewicz et al., 1985) and artificial absorbing boundaries (Givoli, 1991). There has also been some effort to overcome this difficulty associated with boundary elements through localization. In the early 1980s, Kagawa et al. (1983) developed an infinite boundary element technique for two-dimensional problems that produced sparse impedance matrices, but due perhaps to the somewhat ad-hoc procedure used in their derivation, such infinite elements have not been adopted in practice. More recently, using novel basis and testing functions, Canning (1990) developed a technique that localizes the important interactions within the impedance (or compliance) matrix to only a small number of entries. A systematic variational boundary integral equation methods based on an exterior domain decomposition has been developed by Zeng et al. (1992a) for directly generating sparse, symmetric, impedance matrices. This method involves the use of double-integrals as well as the normal derivative of the double-layer potential, i.e., a hypersingular operator, to derive a stable procedure that is valid for all frequencies.

In this paper, we describe a new BE method based on the domain decomposition of the exterior region in the spirit of (Zeng et al., 1992a) in order to obtain a new sparse formulation that avoids the double integrals and the hypersingular operators. In the rest of this paper, we describe the proposed methodology as it applies to rigid three-dimensional scatterers (the extension to deformable bodies is straightforward), but illustrate its applicability with numerical examples in two dimensions, for wave numbers in the range of 0 to 30.

2 Statement of Problem and Formulation

Consider the geometry shown in Fig. 1. The region Ω in $\mathbf{R}^3$ is occupied by a rigid scatterer, with boundary Γ, and exterior Ω^+, which represents a homogeneous, compressible, inviscid fluid with density ρ and speed of sound c. We assume that there is an incident steady-state harmonic fluid motion given by a pressure $P^0(\mathbf{x}, t) = \mathrm{Re}[p^0(\mathbf{x}) \exp(i\omega t)]$, where ω is the frequency of excitation, and that the scatterer is held fixed. We denote the total pressure in the fluid by $Q(\mathbf{x}, t) = \mathrm{Re}[q(\mathbf{x}) \exp(i\omega t)]$, and the scattered pressure by $P(\mathbf{x}, t) = \mathrm{Re}[p(\mathbf{x}) \exp(i\omega t)] = Q - P^0$. The scattering problem then consists in finding p such that

$$\nabla^2 p + k^2 p = 0, \quad \text{in } \Omega^+, \quad p_n = -p_n^0, \quad \text{on } \Gamma, \quad (1a, b)$$

$$p \text{ satisfies a radiation condition in } \Omega^+, \quad (1c)$$

where $k^2 \equiv \omega^2/c^2$, $\mathbf{n}$ is the outward unit vector normal to Γ and the subscript n denotes normal derivative. Equation $(1a)$ is the standard Helmholtz equation that governs the pressure in the fluid, and $(1b)$ is the Neumann condition that requires the normal velocity of the fluid of vanish at the interface Γ with the scatterer.

In order to solve subsequently this problem we decompose the exterior region Ω^+ into M subdomains Ω^m, with Γ^m denoting the boundary of Ω^m, and Γ_m^m the part of the interface Γ common to Γ^m, as shown in Fig. 2. By renaming

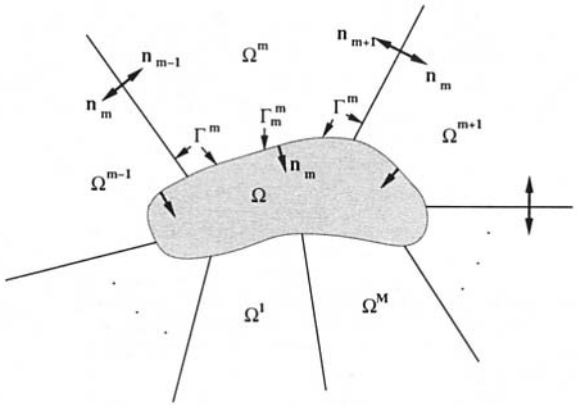

Fig. 2 Scatterer and fluid, showing partitioning into macro-elements

p within Ω^m as $p^{(m)}$, (1) may then be rewritten as follows:

$$\nabla^2 p^{(m)} + k^2 p^{(m)} = 0, \quad \text{in } \Omega^m, \quad m = 1, 2, \ldots, M, \quad (2a)$$

$$p^{(i)} = p^{(j)}, \quad p_{n_i}^{(i)} = -p_{n_j}^{(j)}, \quad \text{on } \Gamma^i \cap \Gamma^j,$$

$$i, j = 1, 2, \ldots, M, \quad (2b, c)$$

$$p_{n_m}^{(m)} = p_n^0, \quad \text{on } \Gamma_m^m, \quad m = 1, 2, \ldots, M, \quad (2d)$$

$$p^{(m)} \text{ satisfies a radiation condition, } \quad m = 1, 2, \ldots, M. \quad (2e)$$

To actually ensure that $(2a)$ and $(2e)$ are satisfied by $p^{(m)}$, we make use of Helmholtz representation formula:

$$p^{(m)} = \mathfrak{D}_m[p^{(m)}] - \mathfrak{S}_m[p_{n_m}^{(m)}], \quad \text{in } \Omega^m, \quad (3)$$

in which $\mathfrak{S}_m$ and $\mathfrak{D}_m$ are the single and double layers:

$$\mathfrak{S}_m[\chi](\mathbf{x}) \equiv \int_{\Gamma^m} \chi(\mathbf{y}) G(|\mathbf{x} - \mathbf{y}|) d\Gamma^m(\mathbf{y}), \quad (4a)$$

$$\mathfrak{D}_m[\chi](\mathbf{x}) \equiv \int_{\Gamma^m} \chi(\mathbf{y}) \frac{\partial}{\partial n_y} G(|\mathbf{x} - \mathbf{y}|) d\Gamma^m(\mathbf{y}), \quad (4b)$$

and $G(z)$ is the fundamental singularity, or Green's function, for $(1a, c)$,

$$G(z) \equiv -\frac{1}{4\pi z} \exp(ikz), \quad \text{in } \mathbf{R}^3,$$

$$G(z) \equiv \frac{i}{4} H_0^{(2)}(ikz), \quad \text{in } \mathbf{R}^2. \quad (5a, b)$$

Thus, $p^{(m)}$ in (3) automatically satisfies $(2a)$ and $(2e)$ for arbitrary $p^{(m)}$ and $p_{n_m}^{(m)}$. For smooth χ and Γ one has the jump relations

$$\mathbf{S}_m[\chi]^- = S_m[\chi], \quad \mathfrak{D}_m[\chi]^- = \frac{1}{2}\chi + D_m[\chi], \quad (6a, b)$$

where the minus sign denotes the limit on Γ^m from Ω^m. Boundary integral methods based on Helmholtz representation formula (3) are usually referred to as *direct* since the pressure $p^{(m)}$ at any point within the fluid is expressed directly in terms of the physical quantities $p^{(m)}$ and $p_{n_m}^{(m)}$ on the boundary. By using the symbols $\phi^{(m)}$ and $\psi^{(m)}$ to denote the values of $p^{(m)}$ and $p_{n_m}^{(m)}$ on Γ^m, (3) may be written as

$$p^{(m)} = \mathfrak{D}_m[\phi^{(m)}] - \mathfrak{S}_m[\psi^{(m)}], \quad \text{in } \Omega^m. \quad (7)$$

From (6) and (7) it follows that

$$\frac{1}{2}\phi^{(m)} - \mathfrak{D}_m[\phi^{(m)}] + \mathfrak{S}_m[\psi^{(m)}] = 0, \quad \text{on } \Gamma^m,$$

$$m = 1, 2, \ldots, M. \quad (8)$$

Equation (8) and the continuity conditions (2*b*, *c*) as well as the boundary condition (2*d*) are the basic relationship for the numerical implementation described in the next section. Using ϕ and ψ, conditions (2*b*, *c*) and (2*d*) may be written as

$$\phi^{(i)} = \phi^{(j)}, \quad \psi^{(i)} = -\psi^{(j)}, \quad \text{on } \Gamma^i \cap \Gamma^j, \quad i, j = 1, 2, \ldots, M, \quad (9a, b)$$

$$\psi^{(m)} = p_n^0, \quad \text{on } \Gamma_m^m, \quad m = 1, 2, \ldots, M. \quad (9c)$$

Remarks. (i) For a given boundary condition (9*c*), the boundary integral Eq. (8) is valid for all frequencies. This follows directly from the fact that (8) has no critical frequencies since Ω^m is unbounded. It is, thus, clear that decomposing Ω^+ into two or more unbounded subdomains, in addition to leading to a local formulation, makes the present method free from the usual defect associated with standard integral formulations.

(ii) The system of algebraic equations obtained upon discretization of the unknowns ϕ^m and ψ^m will be blockwise-banded since, like the finite element (FE) method, unknowns in one subdomain are coupled only with those of neighboring subdomains. The size of the submatrix (block) of each subdomain may be adjusted to meet the requirement of a particular computer architecture.

(iii) The present method promises condensation of $\psi^{(m)}$ in terms of $\phi^{(m)}$, either sequentially or in parallel. The resultant system will be smaller yet still blockwise-banded.

(iv) While the basic ideas behind the present exterior domain decomposition method come from (Zeng et al., 1992a), the numerical implementation is simpler due to the fact that there are no hypersingular operators and double integrals in this formulation.

3 Finite Element Discretization

We consider here the numerical solution of the problem described in (8) and (9) using the collocation method and the FE discretization as in (Zeng et al., 1992a). To solve for $\phi^{(m)}$ and $\psi^{(m)}$, we first divide the boundary Γ^m of each subdomain $\Omega^{(m)}$ into finite elements (cf. Fig. 3) and let the governing integral Eq. (8) be satisfied at the nodal points,

$$\frac{1}{2}\phi_k^{(m)} - \mathfrak{D}_m\left[\phi_k^{(m)}\right] + \mathfrak{S}_m\left[\psi_k^{(m)}\right] = 0, \quad k = 1, 2, \ldots, \quad K_m, \quad m = 1, 2, \ldots, M, \quad (10)$$

where K_m is the number of nodal points on Γ^m. Since $\phi^{(i)}$ and $\phi^{(j)}$ must be continuous at the interface $\Gamma^i \cap \Gamma^j$, we select a single mesh for this interface and approximate $\phi^{(i)}$ and $\phi^{(j)}$ on $\Gamma^i \cap \Gamma^j$ by identical interpolating functions defined by their nodal values. This ensures that ϕ will be continuous across the interfaces. The pressure derivatives transition conditions (cf. Eq. (9*b*))

$$\psi_{k_i}^{(i)} + \psi_{k_j}^{(j)} = 0, \quad \text{on } \Gamma^i \cap \Gamma^j, \quad i, j = 1, 2, \ldots M, \quad (11)$$

are also satisfied collocationally in our numerical scheme. For simplicity, $\psi^{(i)}$ and $\psi^{(j)}$ across the common boundary $\Gamma^i \cap \Gamma^j$ are interpolated using identical shape functions (or elements) in this study. Equations (10), (11), and the boundary condition

$$\psi_k^{(m)} = p_n^0, \quad \text{on } \Gamma_m^m, \quad m = 1, 2, \ldots, M \quad (12)$$

give sufficient number of equations to determine all the ϕ and ψ unknowns.

On Γ^m, $\phi^{(m)}$ and $\psi^{(m)}$ may be approximated, in general, by standard finite elements. The shape functions for $\phi^{(m)}$ and $\psi^{(m)}$ may be either constant, linear, or quadratic. In this study, we use a quadratic shape function that corresponds to three-node element as shown in Fig. 3. Special treatment, however, is required in order to represent these functions on $\Gamma^i \cap \Gamma^j$ due to the infinite extent of these interfaces. The procedure consists of introducing a strip of standard elements on each interface $\Gamma^i \cap \Gamma^j$ up to a certain distance away from Γ, and then using the mapped infinite elements developed originally for field equations by Zienkiewicz et al. (1985) to extend the solution to infinity. A detailed description of these infinite elements, which are based on assumed approximating functions that vary harmonically with kr and decay asymptotically as $1/kr$ and $1/\sqrt{kr}$ in three and two dimensions, is given therein, and an account of how they apply to the boundary integral approach may be found in (Zeng et al., 1992a).

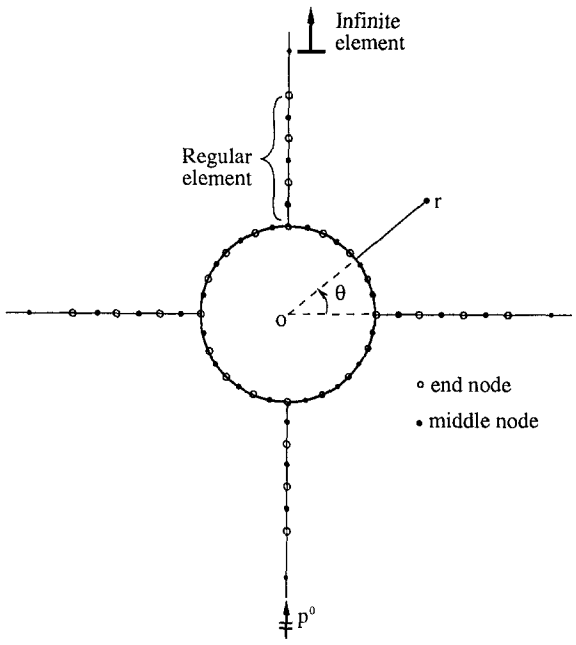

Fig. 3 Boundary element mesh for a circular cylindrical scatterer (four macro-elements each comprised of three regular elements and an infinite element on each ray and four regular elements on the arc)

To illustrate the condensation and the solution scheme of discretized system, it is convenient to consider two-dimensional scattering problems[2]. Denote the three boundary segments of a typical subdomain Ω^m, as shown in Fig. 2, as Γ_0^m, Γ_+^m, and Γ_-^m, where Γ_+^m and Γ_-^m represent, respectively, the two, i.e., the right and the left, ray boundary segments of the subdomain, while $\Gamma_0^m \equiv \Gamma_m^m$ is the boundary portion that has a finite length. Equation (10) may then be rewritten as follows:

$$\frac{1}{2}\phi_k^{(m)} - D_m\left[\phi_k^{(m)}\right] + S_m^{\pm}\left[\psi_k^{(m)}\right] = -S_m^0\left[\psi_k^{(m)}\right], \quad k = 1, 2, \ldots, K_m, \quad (13)$$

where $S_m[\psi_k^{(m)}] \equiv S_m^0[\psi_k^{(m)}] + S_m^+[\psi_k^{(m)}] + S_m^-[\psi_k^{(m)}] \equiv S_m^0[\psi_k^{(m)}] + S_m^{\pm}[\psi_k^{(m)}]$, and

$$S_m^0\left[\psi_k^{(m)}\right] \equiv \int_{\Gamma_0^m} G(|\mathbf{x}_k - \mathbf{y}|)\,\phi(\mathbf{y})\,d\Gamma_0^m(\mathbf{y}),$$

$$S_m^{\pm}\left[\psi_k^{(m)}\right] \equiv \int_{\Gamma_{\pm}^m} G(|\mathbf{x}_k - \mathbf{y}|)\,\psi(\mathbf{y})\,d\Gamma_{\pm}^m(\mathbf{y}). \quad (14a, b)$$

[2]The three-dimensional case is similar but the numbering scheme is more cumbersome.

In matrix form, Eqs. (13) may be expressed as

$$\begin{bmatrix} \mathbf{A}_{11}^{(m)} & \mathbf{A}_{12}^{(m)} & \mathbf{A}_{13}^{(m)} & \mathbf{A}_{14}^{(m)} & \mathbf{A}_{15}^{(m)} \\ \mathbf{A}_{21}^{(m)} & \mathbf{A}_{22}^{(m)} & \mathbf{A}_{23}^{(m)} & \mathbf{A}_{24}^{(m)} & \mathbf{A}_{25}^{(m)} \\ \mathbf{A}_{31}^{(m)} & \mathbf{A}_{32}^{(m)} & \mathbf{A}_{33}^{(m)} & \mathbf{A}_{34}^{(m)} & \mathbf{A}_{35}^{(m)} \end{bmatrix} \begin{Bmatrix} \boldsymbol{\phi}_0^{(m)} \\ \boldsymbol{\phi}_+^{(m)} \\ \boldsymbol{\phi}_-^{(m)} \\ \boldsymbol{\psi}_+^{(m)} \\ \boldsymbol{\psi}_-^{(m)} \end{Bmatrix} = \begin{Bmatrix} \mathbf{f}_0^{(m)} \\ \mathbf{f}_+^{(m)} \\ \mathbf{f}_-^{(m)} \end{Bmatrix}, \quad (15)$$

in which $\boldsymbol{\phi}_0^{(m)}$, $\boldsymbol{\phi}_+^{(m)}$, $\boldsymbol{\phi}_-^{(m)}$ are the nodal point value vectors of ϕ corresponding to the boundary segments Γ_0^m, Γ_+^m, and Γ_-^m, respectively; $\boldsymbol{\psi}_+^{(m)}$ and $\boldsymbol{\psi}_-^{(m)}$ are the nodal point value vectors of ψ corresponding to the segments Γ_+^m and Γ_-^m; whereas $\mathbf{f}_0^{(m)}$, $\mathbf{f}_+^{(m)}$, $\mathbf{f}_-^{(m)}$ are known vectors associated with the boundary segments Γ_0^m, Γ_+^m, and Γ_-^m, respectively. The condensation procedure may be described as follows. First, we rewrite Eq. (15) as

$$\begin{bmatrix} \mathbf{A}_{21}^{(m)} & \mathbf{A}_{22}^{(m)} & \mathbf{A}_{23}^{(m)} \\ \mathbf{A}_{31}^{(m)} & \mathbf{A}_{32}^{(m)} & \mathbf{A}_{33}^{(m)} \end{bmatrix} \begin{Bmatrix} \boldsymbol{\phi}_0^{(m)} \\ \boldsymbol{\phi}_+^{(m)} \\ \boldsymbol{\phi}_-^{(m)} \end{Bmatrix} + \begin{bmatrix} \mathbf{A}_{24}^{(m)} & \mathbf{A}_{25}^{(m)} \\ \mathbf{A}_{34}^{(m)} & \mathbf{A}_{35}^{(m)} \end{bmatrix} \begin{Bmatrix} \boldsymbol{\psi}_+^{(m)} \\ \boldsymbol{\psi}_-^{(m)} \end{Bmatrix} = \begin{Bmatrix} \mathbf{f}_+^{(m)} \\ \mathbf{f}_-^{(m)} \end{Bmatrix}, \quad (16a)$$

and

$$\begin{bmatrix} \mathbf{A}_{11}^{(m)} & \mathbf{A}_{12}^{(m)} & \mathbf{A}_{13}^{(m)} \end{bmatrix} \begin{Bmatrix} \boldsymbol{\phi}_0^{(m)} \\ \boldsymbol{\phi}_+^{(m)} \\ \boldsymbol{\phi}_-^{(m)} \end{Bmatrix} + \begin{bmatrix} \mathbf{A}_{14}^{(m)} & \mathbf{A}_{15}^{(m)} \end{bmatrix} \begin{Bmatrix} \boldsymbol{\psi}_+^{(m)} \\ \boldsymbol{\psi}_-^{(m)} \end{Bmatrix} = \{\mathbf{f}_0^{(m)}\}. \quad (16b)$$

Next from Eq. (16a), one can solve for $[\boldsymbol{\psi}_+^{(m)}, \boldsymbol{\psi}_-^{(m)}]^T$ in terms of $[\boldsymbol{\phi}_0^{(m)}, \boldsymbol{\phi}_+^{(m)}, \boldsymbol{\phi}_-^{(m)}]^T$ to obtain

$$\begin{Bmatrix} \boldsymbol{\psi}_+^{(m)} \\ \boldsymbol{\psi}_-^{(m)} \end{Bmatrix} \equiv \begin{Bmatrix} \mathbf{q}_+^{(m)} \\ \mathbf{q}_-^{(m)} \end{Bmatrix} - \begin{bmatrix} \mathbf{K}_+^{(m)} \\ \mathbf{K}_-^{(m)} \end{bmatrix} \begin{Bmatrix} \boldsymbol{\phi}_0^{(m)} \\ \boldsymbol{\phi}_+^{(m)} \\ \boldsymbol{\phi}_-^{(m)} \end{Bmatrix}. \quad (17)$$

Substituting the above expression into (16b) yields

$$\left[\mathbf{K}_0^{(m)}\right] \begin{Bmatrix} \boldsymbol{\phi}_0^{(m)} \\ \boldsymbol{\phi}_+^{(m)} \\ \boldsymbol{\phi}_-^{(m)} \end{Bmatrix} = \left\{\mathbf{q}_0^{(m)}\right\}. \quad (18)$$

The assemblage process of expressions (17) and (18) into a system of global "stiffness" (impedance) equations is similar to the *direct stiffness method* in regular FE methods. The construction of the element stiffness matrix and load vector in the regular FE procedure now becomes the construction of an *effective* "stiffness" matrix and the associated "load" vector for the *macro-element* Ω^m. It is apparent that expressions (18) give the equations that are associated with the nodal points on Γ_0^m. To derive the equations that are associated with points on $\Gamma_\pm^m$, we denote the two macro-elements adjacent to Ω^m as Ω^l and Ω^n, respectively. The transition condition of the pressure derivative (11) may then be expressed as

$$\left\{\boldsymbol{\psi}_+^{(m)}\right\} + \left\{\boldsymbol{\psi}_-^{(l)}\right\} = \{0\}, \quad \text{on } \Gamma_+^m,$$

$$\left\{\boldsymbol{\psi}_-^{(m)}\right\} + \left\{\boldsymbol{\psi}_+^{(n)}\right\} = \{0\}, \quad \text{on } \Gamma_-^m \quad (19)$$

Inserting Eq. (17) into the above equations yields

$$\left[\mathbf{K}_+^{(m)}\right] \begin{Bmatrix} \boldsymbol{\phi}_0^{(m)} \\ \boldsymbol{\phi}_+^{(m)} \\ \boldsymbol{\phi}_-^{(m)} \end{Bmatrix} + \left[\mathbf{K}^{(l)}\right] \begin{Bmatrix} \boldsymbol{\phi}^{(l)} \\ \boldsymbol{\phi}_+^{(l)} \\ \boldsymbol{\phi}_-^{(l)} \end{Bmatrix} = \left\{\mathbf{q}_+^{(m)}\right\} + \left\{\mathbf{q}_-^{(l)}\right\}, \quad \text{on } \Gamma_+^m, \quad (20a)$$

and

$$\left[\mathbf{K}_-^{(m)}\right] \begin{Bmatrix} \boldsymbol{\phi}_0^{(m)} \\ \boldsymbol{\phi}_+^{(m)} \\ \boldsymbol{\phi}_-^{(m)} \end{Bmatrix} + \left[\mathbf{K}_+^{(n)}\right] \begin{Bmatrix} \boldsymbol{\phi}_0^{(n)} \\ \boldsymbol{\phi}_+^{(n)} \\ \boldsymbol{\phi}_-^{(n)} \end{Bmatrix} = \left\{\mathbf{q}_-^{(m)}\right\} + \left\{\mathbf{q}_+^{(n)}\right\}, \quad \text{on } \Gamma_-^m. \quad (20b)$$

It is obvious that (20a, b) give the equations that are associated with the nodal points on boundaries Γ_+^m and Γ_-^m (cf. Eq. (10)), and the first terms at both the right and left-hand sides in Eqs. (20a, b) represent the contribution of the mth macro-element to the global system of equations. Thus, by combining (18) and (20a, b) and using the standard FE procedure, one arrives at the *effective* "stiffness" matrix equation for the macro-element Ω^m

$$\begin{bmatrix} \mathbf{K}_0^{(m)} \\ \mathbf{K}_+^{(m)} \\ \mathbf{K}_-^{(m)} \end{bmatrix} \begin{Bmatrix} \boldsymbol{\phi}_0^{(m)} \\ \boldsymbol{\phi}_+^{(m)} \\ \boldsymbol{\phi}_-^{(m)} \end{Bmatrix} = \begin{Bmatrix} \mathbf{q}_0^{(m)} \\ \mathbf{q}_+^{(m)} \\ \mathbf{q}_-^{(m)} \end{Bmatrix}, \quad \text{or } \mathbf{K}^{(m)}\boldsymbol{\phi}^{(m)} = \mathbf{q}^{(m)}, \quad (21)$$

where $\mathbf{K}^{(m)}$ and $\mathbf{q}^{(m)}$ represent the *effective* "stiffness" (impedance) matrix and "load" vector for the macro-element Ω^m. Applying the *direct stiffness method* in FE technique, the "stiffness" matrices $\mathbf{K}^{(m)}$ and "load" vectors $\mathbf{q}^{(m)}$, $m = 1, 2, \ldots, M$, are assembled into a system of global "stiffness" equations $\mathbf{K}\boldsymbol{\phi} = \mathbf{q}$, which will be used to determine $\boldsymbol{\phi}$.

It is worthwhile to point out that in obtaining $\mathbf{K}^{(m)}$ and $\mathbf{q}^{(m)}$, all the computation is done within subdomain Ω^m. Therefore, one may perform the computation either sequentially or in parallel. Also, as in the standard FE method, only one "stiffness" matrix needs to be constructed for all the macro-elements that have the same geometric configuration and material properties, while the rest may be obtained by duplication.

Remarks. The resultant system with M rays, N nodes directly on the scatterer surface, and L nodes on each ray has a total of $N + ML$ unknowns, and a bandwidth of $2N/M + 3L$. Thus the number of multiplications required to solve this system directly is in the order of $(N + ML)(2N/M + 3L)^2$. Results of numerical experiments have shown that only a few nodes on each ray have already produced good results[3]. Thus L can be a small number. If the number of rays is chosen in such a way that N/M remains constant or bounded for increasing N, the number of multiplications will be of order $O(N)$ for large-scale problems. The corresponding memory requirement is of the order $O(N)$ (double or single precision numbers) also. Comparing to the standard BE methods, which require $O(N^3)$ multiplications for direct solution schemes and $O(N^2)$ memory size, the present method seems to be more effective for solving large-scale problems.

4 Numerical Examples

In order to assess the accuracy of our new procedure and to verify its validity for critical frequencies, we first apply it to

[3]Examples in Section 4 use three transition elements along each ray. Additional results show that only one transition element already gives good results.

Table 1 Normalized scattered pressure $(r/a)^{1/2}|p(r, \theta)|/p^0$ at different locations (four angular partitions; three standard radial elements in each radial line)

Locations of Test Points						
$ka = 2.4048256$						
Directly on Scatterer $(r/a = 1)$						
No. of Elements	Back Scatterer (270°)		Forward Scatterer (90°)		Side Scatterer (0°, 180°)	
	Real	Imaginary	Real	Imaginary	Real	Imaginary
8	-0.8153	0.3505	0.5678	1.3651	0.2366	0.1166
16	-0.8077	0.3431	0.5728	1.3339	0.2379	0.1140
32	-0.8076	0.3426	0.5732	1.3337	0.2382	0.1136
Exact	-0.8074	0.3430	0.5728	1.3363	0.2380	0.1133
No. of Elements	Far Field $(r/a = 100)$					
	Back Scatter (270°)		Forward Scatter (90°)		Side Scatter (0°, 180°)	
8	-0.6517	-0.0600	-0.8225	0.4978	-0.0839	0.4132
16	-0.6551	-0.0644	-0.8305	0.4971	-0.0890	0.4110
32	-0.6551	-0.0645	-0.8312	0.4971	-0.0891	0.4111
Exact	-0.6551	-0.0645	-0.8310	0.4972	-0.0890	0.4110
$ka = 8.6537279$						
Directly on Scatterer $(r/a = 1)$						
No. of Elements	Back Scatterer (270°)		Forward Scatterer (90°)		Side Scatterer (0°, 180°)	
	Real	Imaginary	Real	Imaginary	Real	Imaginary
16	-0.7117	0.6476	0.5337	0.3545	0.3902	-0.0830
32	-0.7725	0.6019	0.5064	0.4264	0.3547	0.0793
64	-0.7733	0.6045	0.5081	0.4274	0.3588	0.0774
Exact	-0.7735	0.6031	0.5058	0.4304	0.3576	0.0779
No. of Elements	Far Field $(r/a = 100)$					
	Back Scatter (270°)		Forward Scatter (90°)		Side Scatter (0°, 180°)	
16	-0.7458	0.1714	1.8675	-0.9392	-0.0719	0.5559
32	-0.6688	0.1668	1.8882	-0.9981	-0.0867	0.5178
64	-0.6733	0.1694	1.8775	-0.9990	-0.0796	0.5189
Exact	-0.6710	0.1697	1.8825	-1.0000	-0.0802	0.5174

the same two-dimensional scattering problem for a fixed rigid circular cylinder of radius a to an incident plane wave of amplitude p^0 as in (Zeng et al., 1992a). We consider the case with 4 angular partitions, for varying numbers of elements directly on the scatterer. Three regular elements will be placed along each ray, in addition to the finite element, as shown in Fig. 3. Since the infinite element approximations are based on large-distance asymptotic expansions, the purpose of the regular finite elements along radial lines is to serve as a transition between the scatterer and the region where the asymptotic solution becomes applicable. The size of this transition region obviously depends on the wave number.

In all our calculations, three-noded quadratic isoparametric elements are used to represent the boundary Γ, the pressure $\phi^{(m)}$, and the normal derivative of the pressure $\psi^{(m)}$. With these shape functions, all the entries of the individual submatrices in (15) are evaluated by ordinary Gauss-Legendre numerical integration using only four Gaussian points per standard element, except for the diagonal terms of the submatrices containing the singular operator S_m, and D_m, defined by (4*a*) and (4*b*), which are integrated after subtracting off singularities. Detailed description of the discretization and integration schemes used in this study may be found in Zeng et al., (1992a) and Zeng, (1992b).

In order to verify the new localized integral equation method, the integration over the infinite elements is first performed approximately by neglecting contributions beyond a radius of $100/k$, and by subdividing the interval of integration into 16 subintervals, each of which is integrated by a 4-point Gauss-Legendre integration. The numerical results will show, however, that neglecting the tail end of the rays does not affect significantly the accuracy of the method.

Table 1 gives the forward-scattered, the back-scattered, and the side-scattered normalized pressures in the fluid, both directly on the scatterer $(r/a = 1)$ and in the far field $(r/a = 100)$, for two different normalized frequencies ka, calculated for different numbers of elements on the periphery of the scatterer. Note that the scattered pressure has been normalized by the amplitude of the incident wave and by the dimensionless radius at the observation point. The two particular wave numbers correspond to critical frequencies of the problems and are selected to illustrate how the new localized boundary integral method performs for critical wave numbers for which ordinary integral methods fail. The tabulated results clearly show convergence to the corresponding exact solutions. Naturally, the number of elements required to attain a prescribed accuracy increases with the wave number, due to the reduced wave length.

Figure 4 shows the amplitude of the scattered pressure at various locations, both on and outside the scatterer, for a wide range of frequencies. Exact solutions are represented by thick solid lines while dashed lines denote the approximate solutions from the DD-based BE formulation. The calculations are performed for wave numbers ka from 0.001 to 30 with a step-size of 0.1, using a varying number of elements on the boundary Γ as needed. Thus, while only 16 elements are sufficient at low frequencies, 128 elements are used for $ka = 30$. Up to this frequency the DD-based BE and the exact solutions are essentially indistinguishable. To show the poor performance of standard boundary integral formulations, results from directly solving the integral equation $1/2\,p^+ + D[p^+] = -S[p_n^0]$ using collocation method with the same number of nodes on Γ as that for the DD-based BE method are also shown in Fig. 4. The results shown in Fig. 4 indicate that the standard BE method fails not only at the critical frequencies, as expected, but also performs poorly within a sizable interval around each frequency. As the wave number increases and the critical frequencies become clustered together, the solution deteriorates completely.

To illustrate how the DD-based BE approximation for the total and scattered pressure compares with the exact solution

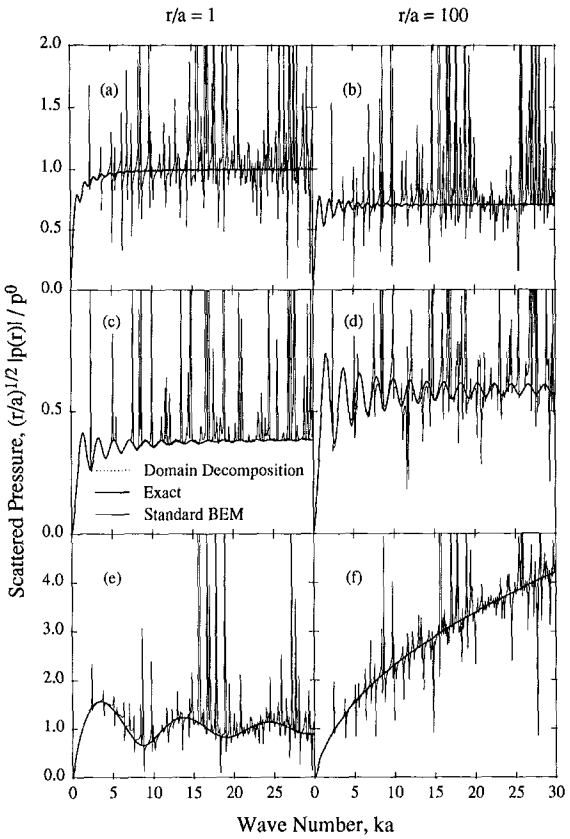

Fig. 4 Normalized amplitude of scattered pressure at various locations as a function of wave number ((*a*) $r/a = 1$, $\theta = 270$ deg; (*b*) $r/a = 100$, $\theta = 270$ deg, (*c*) $r/a = 1$, $\theta = 0$ deg, 180 deg, (*d*) $r/a = 100$, $\theta = 0$ deg, 180 deg; (*e*) $r/a = 1$, $\theta = 90$ deg; (*f*) $r/a = 100$, $\theta = 90$ deg)

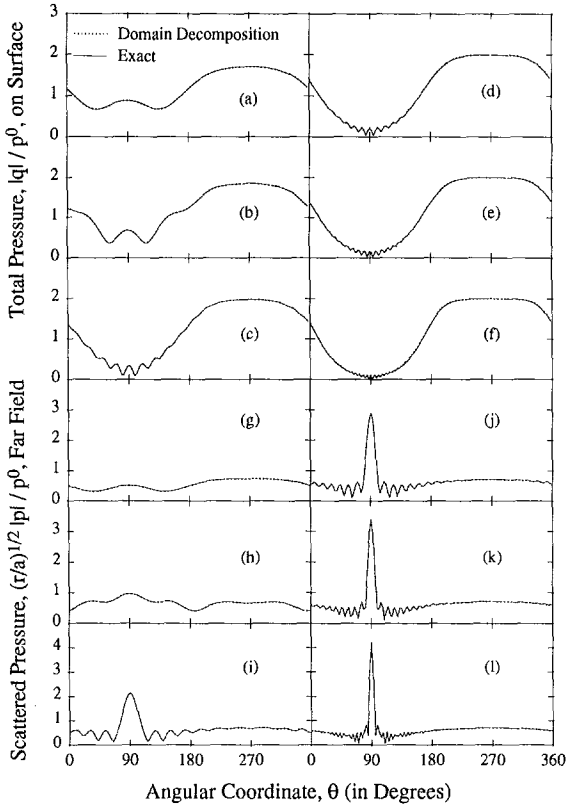

Fig. 5 Normalized amplitude of total pressure, (*a*)–(*f*), on scatterer surface, and scattered pressure, (*g*)–(*l*), in far-field ($r/a = 100$), for different wave numbers as a function of angular position (*a*, *g*) $ka = 1$; (*b*, *h*) $ka = 2.4048256$; (*c*, *i*) $ka = 8.6537278$; (*d*, *j*) $ka = 15$; (*e*, *k*) $ka = 20$; (*f*, *l*) $ka = 30$)

Table 2 Effect of number of macro-elements (angular partitions) on normalized scattered pressure $(r/a)^{1/2}|p(r, \theta)|/p^0$ ($ka = 8.6537279$, three standard radial elements in each radial line, 32 elements on $r = a$)

Angular Position	No. of Partitions	Surface ($r/a = 1$) Real	Surface ($r/a = 1$) Imaginary	Far Field ($r/a = 100$) Real	Far Field ($r/a = 100$) Imaginary
Forward	8	0.5075	0.4264	1.8877	-0.9989
Scatter	4	0.5081	0.4274	1.8877	-0.9990
($\theta = 90°$)	Exact	0.5058	0.4339	1.8825	-1.0000
Side	8	0.3581	0.0785	0.0804	0.5179
Scatter	4	0.3588	0.0774	0.0796	0.5189
($\theta = 0°, 180°$)	Exact	0.3675	0.0779	0.0802	0.5174
Back	8	-0.7735	0.6039	0.6716	0.1695
Scatter	4	-0.7733	0.6045	0.6733	0.1694
($\theta = 270°$)	Exact	-0.7735	0.6031	0.6710	0.1697

over the entire periphery of the scatterer and the far-field within the fluid, Figs. 5(*a*)–5(*f*) depict the normalized amplitude of the total pressure on the surface of the scatterer as a function of the angular coordinate θ, for several wave numbers, while Figs. 5(*g*)–5(*l*) show the corresponding scattered pressure at a distance $r/a = 100$. Again, the two solutions practically coincide, for all values of θ. These figures illustrate how the normalized amplitude of the total pressure directly on the scatterer tends to 2, as for a flat scatterer, within the bulk of the insonified region and becomes small, and almost smooth, except for a small high frequency perturbation in the shadow region, as the wave number increases. Apart from this oscillatory behavior in the shadow region, the total pressure on the scatterer practically becomes independent of the wave number as the wave number becomes large. In the far field the same general oscillatory and smooth behavior occurs, except that the largest scattering occurs, of course, in front of the scatterer.

Table 2 serves to examine how the change of the number of angular partitions affects the accuracy of the solution for a given wave number and for a fixed number of elements on the boundary of the scatterer. These results show that the solution is basically insensitive to the number of angular partitions. The main advantages of introducing a larger number of angular partitions (macro-elements) are (1) to obtain a sparse global matrix which might simplify significantly the computation; (2) to best match the multiprocessor machine configuration if the problem is solved on a multiprocessor computer.

Finally, to evaluate the presented method for more general scattering problems, we consider a scatterer that has a cross-section consisting of a square with side $2b$ and two half-circles of a radius b, $a = 2b$ (cf. Fig. 6(*c*)). Figure 6 shows the amplitude of the scattered pressure at various locations. All the results are generated by using 8 angular partitions with three regular elements placed along each ray. Since there is no analytical solution for this problem, for comparison, we also plot in Fig. 6 the results generated from the stable *nonlocal* boundary integral formulation given in (Zeng, 1992b). To illustrate the performance of the standard boundary integral formulation for this case, results from the standard BE method are also shown in this figure. Again, the calculation is performed for wave numbers ka from 0.001 to 30. It is clear from Fig. 6 that while the present DD-based BE and the stable nonlocal BE solutions are essentially indistinguishable, the standard BE solution fails at and near the critical frequencies.

5 Conclusions

The exterior domain decomposition method presented in this paper combines the BE method with the sparsity of algebraic systems ordinarily encountered only in domain dis-

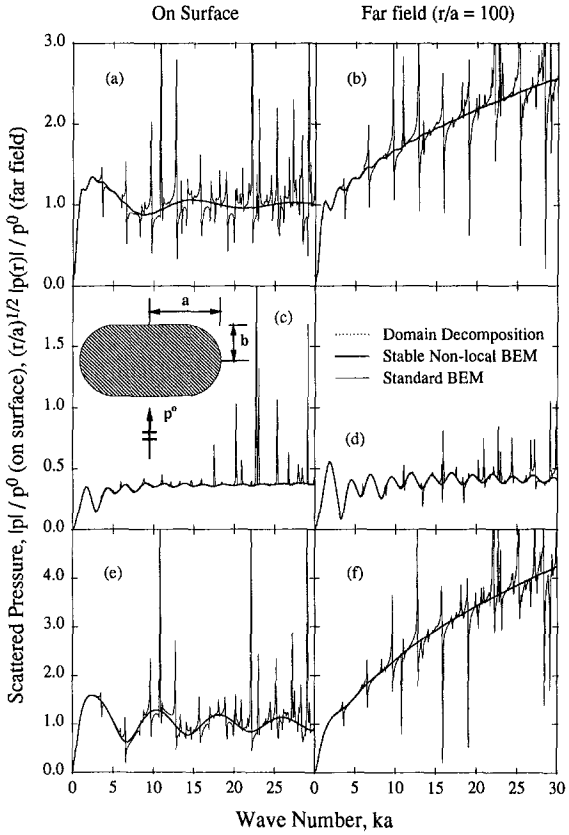

Fig. 6 Normalized amplitude of scattered pressure at various locations as a function of wave number ((*a*) $r/b = 1$, $\theta = 270$ deg; (*b*) $r/a = 100$, $\theta = 270$ deg; (*c*) $r/a = 1$, $\theta = 0$ deg, 180 deg; (*d*) $r/a = 100$, $\theta = 0$ deg. 180 deg; (*e*) $r/b = 1$, $\theta = 90$ deg; (*f*) $r/a = 100$, $\theta = 90$ deg)

cretization procedures. The main difference between our approach and the existing *stable* methodologies for acoustic scattering problems is that the new method uses exclusively single and double-layer potentials, avoiding completely both the hypersingular operator and the double integrals. Therefore, our method not only avoids the treatment of the hypersingular operators in the traditional methods based on collocation but also eliminates the requirement of additional integrations of the double integrals in various variational-based formulations.

From the initial examination of the results of numerical experiments it appears that the DD-based method provides a practical and accurate means for solving time-harmonic scattering problems at all frequencies. The procedure may be formally extended to more general situations, including radiation and scattering problems involving deformable inclusions and an elastic exterior. Its main potential advantage over standard boundary integral equation methods lies primarily in its power to generate blockwise-banded, algebraic systems of equations. Moreover, by its very design, it may also lend itself naturally to the implementation on parallel machines. By appropriately selecting the number and location of the subdomains, this method offers the possibility of exploiting optimally the parallel features of a particular parallel architecture.

Acknowledgments

We thank the reviewers for their constructive comments.

References

Amini, S., and Harris, P. J., 1990, "A Comparison Between Various Boundary Integral Formulations of the Exterior Acoustic Problem," *Computer Methods in Applied Mechanics and Engineering*, Vol. 84, pp. 59–75.

Canning, F. X., 1990, "The Impedance Matrix Localization (IML) Method for Moment-Method Calculations," *IEEE Antennas and Propagation Magazine*, Vol. 32, pp. 18–30.

Givoli, D., 1991, "Non-reflecting Boundary Conditions," *Journal of Computational Physics*, Vol. 94, pp. 1–29.

Jeans, R. A., and Mathews, I. C., 1990, "Solution of Fluid-structure Interaction Problems Using a Coupled Finite Element and Variational Boundary Element Technique," *Journal of Acoustic Society of America*, Vol. 88, pp. 2459–2466.

Kagawa, Y., Yamabuchi, T., and Kitagami, S., 1983, "Infinite Boundary Element and Its Application to Combined Finite-boundary Element Technique for Unbounded Field Problem," *Boundary Element Methods in Engineering*, C. A. Brebbia, ed., Springer-Verlag, Berlin, pp. 1017–1026.

Krishnasamy, G., Schmerr, L. W., Rudolphi, T. J., and Rizzo, F. J., 1990, "Hypersingular Boundary Integral Equations: Some Applications in Acoustic and Elastic Wave Scattering," ASME JOURNAL OF APPLIED MECHANICS, Vol. 57, pp. 404–414.

Seybert, A. F., Wu, T. W., and Wu, X. F., 1988, "Radiation and Scattering from Elastic Solid and Shell Using the BEM," *Journal of Acoustic Society of America*, Vol. 84, pp. 1906–1912.

Zeng, X., Kallivokas, L., and Bielak, J., 1992a, "Stable Localized Symmetric Integral Equation Method for Acoustic Scattering Problems," *Journal of Acoustic Society of America*, Vol. 91, pp. 2510–2518.

Zeng, X., 1992b, "Stable Symmetric FEM-BEM Coupling Method for Fluid-Structure Interface Problems with Applications," PhD. Thesis, Dept. of Civil Engineering, Carnegie Mellon University, Pittsburgh, PA.

Zienkiewicz, O. C., Bando, K., Bettes, P. Emson, C., and Chiam, C., 1985, "Mapped Infinite Elements for Exterior Wave Problems," *International Journal for Numerical Methods in Engineering*, Vol. 21, pp. 1229–1251.

Vibration Modes and Frequencies of Timoshenko Beams With Attached Rigid Bodies

M. W. D. White

G. R. Heppler
Mem. ASME

Department of Systems Design Engineering, University of Waterloo, Waterloo, Ontario N2L 2G1, Canada

The equations of motion and boundary conditions for a free-free Timoshenko beam with rigid bodies attached at the endpoints are derived. The natural boundary conditions, for an end that has an attached rigid body, that include the effects of the body mass, first moment of mass, and moment of inertia are included. The frequency equation for a free-free Timoshenko beam with rigid bodies attached at its ends which includes all the effects mentioned above is presented and given in terms of the fundamental *frequency equations for Timoshenko beams that have no attached rigid bodies. It is shown how* any *support / rigid-body condition may be easily obtained by inspection from the reported frequency equation. The mode shapes and the orthogonality condition, which include the contribution of the rigid-body masses, first moments, and moments of inertia, are also developed. Finally, the effect of the first moment of the attached rigid bodies is considered in an illustrative example.*

1 Introduction

Presently, vibrating beams are most frequently modeled using the Bernoulli-Euler model of a beam. There are, however, situations where the Bernoulli-Euler model is not the best choice, either because the beam being modeled is short and thick or because several modes need to be considered in the analysis. The Timoshenko beam model (Timoshenko, 1921) is a more complete model in that it accounts for the effects of transverse shear and rotatory inertia and it is a better choice when the either of the above situations prevail (Timoshenko, 1974). In robotics applications it is sometimes the case that the robot links should be considered flexible and because of its superior completeness the Timoshenko beam theory would be a good choice to model the robot links with. Further, because robots carry payloads which can be frequently modeled as rigid bodies it is of interest to determine the effect that the presence of an attached rigid body has on the natural frequencies and the modes of the beam.

Huang (1961, 1964) used the coupled differential equations presented by Timoshenko to determine the frequency equations and mode shapes for six common support conditions. Comparison is made between several important beam theories, including the classical (Bernoulli-Euler) beams, shear beams, Rayleigh beams (Strutt (Lord Rayleigh), 1877), and Timoshenko beams. More recently Zu and Han (1992) have presented a parallel development to Huang's (1961, 1964) but for a beam which is rotating about its longitudinal axis.

Grant (1978) reports the frequency equations for the same boundary conditions as reported by Huang (1961) but with the effect of a particle mass at an arbitrary point along the beam included. The mode shapes for one of the fundamental boundary condition cases (supported-supported) are presented and the orthogonality condition is also given.

Bruch and Mitchell (1987) investigate the specific case of a cantilevered Timoshenko beam with a particle end mass. The boundary conditions for the free end with a mass attached are stated, as well as the frequency equation for the beam in question. The mode shapes for the beam-mass system are also presented.

Liu (1989) suggests two ways in which the work of Bruch and Mitchell could be extended: (1) the addition of springs at the hub to model inertial properties of the robotic arm, and (2) recognition that the center of mass of the tip body may not be coincident with the end of the beam.

Storch and Gates (1985) also considered the case where the center of mass of the tip body has an arbitrary offset with respect to the beam attachment point. Using a Bernoulli-Euler formulation, they addressed the critical buckling frequencies, natural frequencies, and mode shapes of a cantilever beam with an end rigid body subject to constant axial acceleration. They did not, however, note the effect of the offset center of mass on the beam dynamics.

The purpose of this paper is to expand and generalize Huang's initial findings (1961, 1964). Using Hamilton's Principle, the governing equations for a Timoshenko beam with

Contributed by the Applied Mechanics Division of THE AMERICAN SOCIETY OF MECHANICAL ENGINEERS for publication in the ASME JOURNAL OF APPLIED MECHANICS.

Discussion on this paper should be addressed to the Technical Editor, Professor Lewis T. Wheeler, Department of Mechanical Engineering, University of Houston, Houston, TX 77204-4792, and will be accepted until four months after final publication of the paper itself in the ASME JOURNAL OF APPLIED MECHANICS.

Manuscript received by the ASME Applied Mechanics Division, Mar. 4, 1993; final revision, Dec. 27, 1993. Associate Technical Editor: D. J. Inman.

rigid bodies at either end are derived along with the necessary boundary conditions. The natural boundary conditions for an end that has an attached rigid body that include the effects of the body mass, first moment of mass, and moment of inertia are presented for the first time. Next, the frequency equation for the unrestrained Timoshenko beam with attached rigid bodies (including the zeroth, first, and second mass moment effects) is developed and is shown to degenerate to any other support case in the appropriate limits of the end masses and inertias. As an example of the relevance of the degeneracy property, the frequency equation for the cantilever beam with an end mass found in Bruch and Mitchell (1987) is found directly from the generalized Timoshenko frequency equation. This is simplified by expressing the frequency equation in terms of the *fundamental* frequency equations for Timoshenko beams that have no attached rigid bodies. The form in which the frequency equation has been reported shows how the mass, first moment, and moment of inertia may combine in establishing the dominance of one term over the other.

To compliment the frequency equation, the generalized mode shape for a free-free Timoshenko beam with attached rigid bodies is also presented. These mode shapes include the complete contributions of the rigid bodies.

To complete the analytical presentation the generalized orthogonality conditions for the Timoshenko beam are given. The orthogonality condition includes the contribution of the rigid body masses, first moments, and moments of inertia. In conclusion, a numerical example which illustrates some interesting and, we believe, not previously known phenomena related to the effect that the first moment has on the natural frequency behavior of the beam is presented.

2 Timoshenko Beam Equations

The derivation begins with the kinetic and potential energy expressions for a Timoshenko beam that has rigid bodies attached to its ends. The kinetic energy is given by

$$T = \frac{1}{2}\int_0^L \left(\rho A\dot{y}^2 + \rho I\dot{\psi}^2\right)dx + \frac{1}{2}\left(m_0\dot{y}_0^2 + m_p\dot{y}_L^2 + J_0\dot{\psi}_0^2 + J_p\dot{\psi}_L^2\right) + C_0\dot{y}_0\dot{\psi}_0 + C_p\dot{y}_L\dot{\psi}_L \quad (1)$$

and the potential energy is given by

$$V = \frac{1}{2}\int_0^L EI\left(\frac{\partial\psi}{\partial x}\right)^2 + \kappa^2 GA\left(\frac{\partial y}{\partial x} - \psi\right)^2 dx \quad (2)$$

Table 1 Force and natural boundary conditions for a Timoshenko beam with attached rigid bodies

Natural	Forced
$\left[\kappa^2 GA\left(\frac{\partial y}{\partial x} - \psi\right)\right]_{x=0} - m_0\ddot{y}_0 - C_0\ddot{\psi}_0 = 0$	$y\|_{x=0} = 0$
$\left[\kappa^2 GA\left(\frac{\partial y}{\partial x} - \psi\right)\right]_{x=L} + m_p\ddot{y}_L + C_p\ddot{\psi}_L = 0$	$y\|_{x=L} = 0$
$\left[EI\frac{\partial\psi}{\partial x}\right]_{x=0} - J_0\ddot{\psi}_0 - C_0\ddot{y}_0 = 0$	$\psi\|_{x=0} = 0$
$\left[EI\frac{\partial\psi}{\partial x}\right]_{x=L} + J_p\ddot{\psi}_L + C_p\ddot{y}_L = 0$	$\psi\|_{x=L} = 0$

where it has been assumed that the x-axis is coincident with the neutral axis of the beam. The notation $(\dot{})$ implies differentiation with respect to time and m_0 is the mass at $x = 0$ (hub mass), C_0 is the first moment of the mass at $x = 0$, J_0 is the moment of inertia at $x = 0$, m_p is the mass at $x = L$ (payload mass), C_p is the first moment of the mass at $x = L$, and J_p is the moment of inertia at $x = L$.

Application of Hamilton's Principle over both dependent variables $y(x, t)$ (displacement) and $\psi(x, t)$ (bending slope) yields the following two coupled equations of motion:

$$\rho A\ddot{y} - \kappa^2 GA\left(\frac{\partial^2 y}{\partial x^2} - \frac{\partial\psi}{\partial x}\right) = 0 \quad (3)$$

and

$$\rho I\ddot{\psi} - EI\frac{\partial^2\psi}{\partial x^2} - \kappa^2 GA\left(\frac{\partial y}{\partial x} - \psi\right) = 0 \quad (4)$$

as well as the forced and natural boundary conditions for the problem which include the effects of the attached masses.

At any one end, one of four possible boundary conditions must be specified. With reference to Table 1 the following cases may be specified. A "clamped" end would be specified by the enforcement of the two forced boundary conditions $y = 0$ and $\psi = 0$. An unrestrained end is specified by the enforcement of the two natural boundary conditions that pertain to the end of interest. It is important to notice that the general natural boundary condition expressions are different for opposite ends of the beam. When there is no body attached to an unrestrained end the unrestrained boundary condition has been referred to as a "free" end (Huang, 1961) where $(y' - \psi) = 0$ and $\psi' = 0$, regardless of which end is free. The remaining two possible boundary conditions are the

Nomenclature

A = beam cross-sectional area
C_0, f_0 = first moment of the mass at $x = 0$, $\xi = 0$
C_p, f_1 = first moment of the mass at $x = L$, $\xi = 1$
E = Young's modulus
G = shear modulus
I = second moment of the area
J_0, q_0 = moment of inertia at $x = 0$, $\xi = 0$
J_p, q_1 = moment of inertia at $x = L$, $\xi = 1$
L = beam length
m_0, p_0 = mass at $x = 0$, $\xi = 0$
m_p, p_1 = mass at $x = L$, $\xi = 1$
r_g = radius of gyration of the cross-section
r_{gp} = radius of gyration of the rigid body attached at $x = L$
x, ξ = axial coordinates
y, Y = transverse deflections
y_0, Y_0 = transverse deflections of $x = 0$, $\xi = 0$
y_L, Y_1 = transverse deflections of $x = L$, $\xi = 1$
κ^2 = shear correction factor
ρ = volume mass density
ψ, Ψ = bending slopes
ψ_0, Ψ_0 = bending slope at $x = 0$, $\xi = 0$
ψ_L, Ψ_0 = bending slope at $x = L$, $\xi = 1$
ω = natural frequency

combinations of the forced and natural boundary conditions. In the case where there is no body on the end, the combination $y = 0$ and $\psi' = 0$ results in a "supported" (pinned) end (Huang, 1961), and the combination $\psi = 0$ and $(y' - \psi) = 0$ is termed a rollered (White, 1992) or guided (Levinson and Cooke, 1982) end. The case of a rollered end where there is an end mass has not been treated previously.

Equations (3) and (4) may be uncoupled to produce two fourth order equations in y and ψ; specifically

$$EI\frac{\partial^4 y}{\partial x^4} + \rho I\frac{\rho}{\kappa^2 G}\frac{\partial^4 y}{\partial t^4} + \rho A\frac{\partial^2 y}{\partial t^2} - \left(\rho I + \frac{\rho EI}{\kappa^2 G}\right)\frac{\partial^4 y}{\partial x^2 \partial t^2} = 0 \quad (5)$$

and

$$EI\frac{\partial^4 \psi}{\partial x^4} + \rho I\frac{\rho}{\kappa^2 G}\frac{\partial^4 \psi}{\partial t^4} + \rho A\frac{\partial^2 \psi}{\partial t^2} - \left(\rho I + \frac{\rho EI}{\kappa^2 G}\right)\frac{\partial^4 \psi}{\partial x^2 \partial t^2} = 0. \quad (6)$$

Now, assuming separation of variables in the form

$$y(x, t) = Y(x)e^{jwt} \quad \text{and} \quad \psi(x, t) = \Psi(x)e^{jwt}$$

and by introducing the nondimensional length and coefficients

$$\xi = \frac{x}{L} \quad \text{and} \quad b^2 = \frac{\rho AL^4\omega^2}{EI}, \quad r^2 = \frac{I}{AL^2}, \quad s^2 = \frac{EI}{\kappa^2 AGL^2}$$

the coupled Eqs. (3), (4) and uncoupled Eqs. (5), (6) may be expressed as

$$s^2\Psi'' + (b^2s^2r^2 - 1)\Psi + Y'/L = 0 \quad (7)$$

$$Y'' + b^2s^2Y - L\Psi' = 0 \quad (8)$$

and

$$Y^{IV} + b^2(r^2 + s^2)Y'' + b^2(b^2r^2s^2 - 1)Y = 0 \quad (9)$$

$$\Psi^{IV} + b^2(r^2 + s^2)\Psi'' + b^2(b^2r^2s^2 - 1)\Psi = 0, \quad (10)$$

respectively. The nondimensional parameter b may be interpreted as the nondimensional frequency, the parameter r is related to rotatory inertia effects, and the parameter s is related to shear effects. As noted by Huang (1964), the equation of motion for a Bernoulli-Euler beam may be obtained from the Timoshenko equations by setting $r = s = 0$ (thus not including the effects of rotatory inertia or shear). Similarly, the equation of motion for a shear beam can be recovered by setting $r = 0$, and for a Rayleigh beam by setting $s = 0$.

Using the separation of variables and the same nondimensionalization, the natural boundary conditions for an unrestrained beam with rigid bodies attached to the ends may be found to be

$$\left[\frac{1}{L}Y' - \Psi + \frac{1}{L}p_0b^2s^2Y + f_0b^2s^2\Psi\right]_{\xi=0} = 0 \quad (11)$$

$$\left[\frac{1}{L}Y' - \Psi - \frac{1}{L}p_1b^2s^2Y - f_1b^2s^2\Psi\right]_{\xi=1} = 0 \quad (12)$$

$$\left[\Psi' + q_0b^2\Psi + \frac{1}{L}f_0b^2Y\right]_{\xi=0} = 0 \quad (13)$$

$$\left[\Psi' - q_1b^2\Psi - \frac{1}{L}f_1b^2Y\right]_{\xi=1} = 0 \quad (14)$$

where

$$p_0 = \frac{m_0}{\rho AL}, \quad p_1 = \frac{m_p}{\rho AL}, \quad f_0 = \frac{C_0}{\rho AL^2}, \quad f_1 = \frac{C_p}{\rho AL^2}, \quad q_0 = \frac{J_0}{\rho AL^3} \quad \text{and} \quad q_1 = \frac{J_p}{\rho AL^3}.$$

The p_i are the nondimensional end masses, the f_i are the nondimensional first moments, and the q_i are the nondimensional moments of inertia.

The solutions to Eqs. (9) and (10) yield the following expressions for Y and Ψ:

$$Y = C_1\cosh(b\alpha\xi) + C_2\sinh(b\alpha\xi) + C_3\cos(b\beta\xi) + C_4\sin(b\beta\xi) \quad (15)$$

$$\Psi = C_1'\sinh(b\alpha\xi) + C_2'\cosh(b\alpha\xi) + C_3'\sin(b\beta\xi) + C_4'\cos(b\beta\xi) \quad (16)$$

where

$$\begin{pmatrix}\alpha\\ \beta\end{pmatrix} = \frac{1}{\sqrt{2}}\left(\mp(r^2 + s^2) + \sqrt{(r^2 - s^2)^2 + \frac{4}{b^2}}\right)^{1/2}. \quad (17)$$

The C_i and C_i' coefficients in the general solutions for Y and Ψ are related through Eqs. (7) and (8) by

$$C_1' = \frac{b}{L}\frac{(\alpha^2 + s^2)}{\alpha}C_1 \quad \text{or} \quad C_1 = \frac{L}{b\alpha}\left[1 - b^2s^2(\alpha^2 + r^2)\right]C_1'$$

$$C_2' = \frac{b}{L}\frac{(\alpha^2 + s^2)}{\alpha}C_2 \quad \text{or} \quad C_2 = \frac{L}{b\alpha}\left[1 - b^2s^2(\alpha^2 + r^2)\right]C_2'$$

$$C_3' = \frac{-b}{L}\frac{(\beta^2 - s^2)}{\beta}C_3 \quad \text{or} \quad C_3 = \frac{-L}{b\beta}\left[1 + b^2s^2(\beta^2 - r^2)\right]C_3'$$

$$C_4' = \frac{b}{L}\frac{(\beta^2 - s^2)}{\beta}C_4 \quad \text{or} \quad C_4 = \frac{L}{b\beta}\left[1 + b^2s^2(\beta^2 - r^2)\right]C_4'. \quad (18)$$

The expression for α has caused confusion among researchers due to the fact that α becomes imaginary if

$$\sqrt{(r^2 - s^2)^2 + \frac{4}{b^2}} < (r^2 + s^2).$$

When α becomes imaginary, a substitution, in the form of $\alpha = j\alpha'$, is needed (Huang, 1964) so that the solutions for Y and Ψ become

$$Y = C_1\cos(b\alpha'\xi) + C2\sin(b\alpha'\xi) + C_3\cos(b\beta\xi) + C_4\sin(b\beta\xi) \quad (19)$$

$$\Psi = jC_1'\sin(b\alpha'\xi) + C_2'\cos(b\alpha'\xi) + C_3'\sin(b\beta\xi) + C_4'\cos(b\beta\xi) \quad (20)$$

where $j = \sqrt{-1}$.

Because (19) and (20) are different from (15) and (16) an alternate set of frequencies, or a "second spectrum" will result when they are used with the boundary conditions to produce a frequency equation. Discussion about the exis-

tence of the second spectrum of frequencies for the Timoshenko beam has been lengthy including: Abbas and Thomas (1977), Anderson (1953), Barr (1956, 1993), Kapur (1966), Levinson and Cooke (1982), Stephen (1982), and Traill-Nash and Collar (1953), and remains a topic on which there are many opinions. Experimental confirmation of the existence of the second spectrum has been claimed by Barr (1993).

3 Frequency Equations

The frequency equation for an unsupported Timoshenko beam with rigid bodies attached at either end is obtained by applying the natural boundary conditions (11)–(14). Using this procedure, the frequency equation for the free-free Timoshenko beam with attached rigid bodies is

$$\begin{aligned}
&\alpha\beta\sigma\tau\mathbf{F}_{ff} - b\alpha\beta^2\sigma\gamma\cosh(b\alpha)\cos(b\beta)(p_0+p_1)\mathbf{F}_{sf}\\
&+b\beta\sigma\gamma\cosh(b\alpha)\cos(b\beta)(q_0+q_1)\mathbf{F}_{rf}\\
&+\alpha\beta\big((p_0q_0-f_0^2)+(p_1q_1-f_1^2)\big)\mathbf{F}_{cf}\\
&+b^2\alpha^2\beta^2\gamma^2\sinh(b\alpha)p_0p_1\mathbf{F}_{ss} - b^2\gamma^2\sinh(b\alpha)q_0q_1\mathbf{F}_{rr}\\
&+b^2\alpha\beta\gamma^2\cosh(b\alpha)(p_0q_1+p_1q_0)\mathbf{F}_{sr}\\
&+b^3\alpha\beta^2\sigma\gamma\cosh(b\alpha)\cos(b\beta)\big(p_1(p_0q_0-f_0^2)\\
&+p_0(p_1q_1-f_1^2)\big)\mathbf{F}_{cs} - b^3\beta\sigma\gamma\cosh(b\alpha)\cos(b\beta)\\
&\times\big(q_1(p_0q_0-f_0^2)+q_0(p_1q_1-f_1^2)\big)\mathbf{F}_{cr}\\
&+b^2\alpha\beta(p_0q_0-f_0^2)(p_1q_1-f_1^2)\mathbf{F}_{cc}\\
&+2\big[\alpha\beta(\sigma-\tau)[\cosh(b\alpha)\cos(b\beta)-1]\\
&+(\alpha^2\sigma+\beta^2\tau)\sinh(b\alpha)\sin(b\beta)\big](f_0-f_1)\\
&+2b\alpha\beta\gamma[\beta\cosh(b\alpha)\sin(b\beta)-\alpha\sinh(b\alpha)\cos(b\beta)]\\
&\times(p_0f_1-p_1f_0)+2b\gamma[\beta\sinh(b\alpha)\cos(b\beta)\\
&-\alpha\cosh(b\alpha)\sin(b\beta)](q_0f_1-q_1f_0)\\
&\times\big[4(\alpha^2-\beta^2)\sinh(b\alpha)\sin(b\beta)\\
&-8\alpha\beta\cosh(b\tau)\cos(b\beta)+2b\alpha\beta[(\sigma-\tau)(2+b\gamma)]\big]f_0f_1\\
&+G_1\big(f_1(p_0q_0-f_0^2)-f_0(p_1q_1-f_1^2)\big)=0 \quad (21)
\end{aligned}$$

where $G_1 = 2b^2[\alpha\beta(\sigma-\tau)[1-\cosh(b\alpha)\cos(b\beta)] - (\alpha^2\tau + \beta^2\sigma)\sinh(b\alpha)\sin(b\beta)]$ and where

$$\gamma = (\alpha^2+\beta^2), \quad \tau = (\beta^2-s^2) \quad \text{and} \quad \sigma = (\alpha^2+s^2).$$

The factors $\mathbf{F}_{ij}$, $i, j \in \{f, c, r, s\}$ are the frequency equations that may be found for beams that have no attached bodies. The subscripts indicate the particular constraint conditions: an f subscript represents a free end, s represents a supported (pinned) end, r represents a rollered end, and c represents a clamped end (White, 1992). Equation (21) shows how the mass, the first moment of the mass, and the moment of inertia of an attached rigid body may combine in establishing the dominance of one term over another.

If the center of mass of an attached rigid body is coincident with its point of attachment on the neutral axis of the beam, the first moment effects are eliminated ($f_0 = f_1 = 0$). For this case, the simplified frequency equation for the free-free Timoshenko beam with attached rigid bodies is

$$\begin{aligned}
&\alpha\beta\sigma\tau\mathbf{F}_{ff} - b\alpha\beta^2\sigma\gamma\cosh(b\alpha)\cos(b\beta)(p_0+p_1)\mathbf{F}_{sf}\\
&+b\beta\sigma\gamma\cosh(b\alpha)\cos(b\beta)(q_0+q_1)\mathbf{F}_{rf}\\
&+\alpha\beta(p_0q_0+p_1q_1)\mathbf{F}_{cf} + b^2\alpha^2\beta^2\gamma^2\sinh(b\alpha)p_0p_1\mathbf{F}_{ss}\\
&-b^2\gamma^2\sinh(b\alpha)q_0q_1\mathbf{F}_{rr}\\
&+b^2\alpha\beta\gamma^2\cosh(b\alpha)(p_0q_1+p_1q_0)\mathbf{F}_{sr}\\
&+b^3\alpha\beta^2\sigma\gamma\cosh(b\alpha)\cos(b\beta)(p_0p_1q_0+p_0p_1q_1)\mathbf{F}_{cs}\\
&-b^3\beta\sigma\gamma\cosh(b\alpha)\cos(b\beta)(p_0q_0q_1+p_1q_0q_1)\mathbf{F}_{cr}\\
&+b^2\alpha\beta p_0p_1q_0q_1\mathbf{F}_{cc}=0 \quad (22)
\end{aligned}$$

3.1 Degeneracy. Despite the apparent complexity of the frequency equation for the general case, an interesting result arises: the specific basic support cases (combinations of free, supported, clamped, and rollered ends) are recovered in the appropriate limits of the end masses and inertias in the general case. Specifically, a free end with no attached rigid body is recovered as $p_i \to 0$, $f_i \to 0$, and $q_i \to 0$; a simply supported end is recovered as $p_i \to \infty$, $f_i \to 0$, and $q_i \to 0$; a rollered end is recovered as $p_i \to 0$, $f_i \to 0$, and $q_i \to \infty$; and a clamped end is recovered as $p_i \to \infty$, $f_i \to 0$, and $q_i \to \infty$.

This property makes it simple to recover the frequency equation for *any* other support case from the general frequency equation. As an illustration, consider the case of a cantilever beam carrying a payload, as presented by Bruch and Mitchell (1987). To recover the frequency equation for this specific support case from the generalized frequency equation, let $p_0 \to \infty$, $f_0 \to 0$, and $q_0 \to \infty$, while p_1 and q_1 are finite numbers defined by the dimensions of the beam and the attached payload. As these limits are applied, any term containing both p_0 and q_0 will dominate the frequency equation. Extracting these terms from the general frequency Eq. (22) gives the frequency equation of a cantilevered Timoshenko beam with a rigid body attached at the tip as

$$\begin{aligned}
&\alpha\mathbf{F}_{cf} + b^3\sigma\gamma\cosh(b\alpha)\cos(b\beta)(\alpha\beta p_1\mathbf{F}_{cs} - q_1\mathbf{F}_{cr})\\
&+b^2p_1q_1\mathbf{F}_{cc}=0 \quad (23)
\end{aligned}$$

which agrees with the results obtained by Bruch and Mitchell (1987). Including the first moment effects would yield Eq. (31).

3.2 Frequency Equations for the Basic Cases. To complete the equations presented above, the frequency equations for all the fundamental support cases not presented by Huang (1961) are given below. The frequency equation for the clamped-roller case (with no end masses) was presented by Levinson and Cooke (1982), while the frequency equations involving all the other rollered ends are previously unreported and are due to White (1992) and White and Heppler (1993).

(a) roller-roller ($\mathbf{F}_{rr} = 0$)

$$\sin b\beta = 0 \quad (24)$$

(b) supported-roller ($\mathbf{F}_{sr} = 0$)

$$\cos b\beta = 0 \quad (25)$$

(c) clamped-roller ($\mathbf{F}_{cr} = 0$)

$$\tanh(b\alpha) + \lambda\zeta\tan(b\beta) = 0 \quad (26)$$

(d) roller-free ($\mathbf{F}_{rf} = 0$)

$$\zeta\tanh(b\alpha) + \lambda\tan(b\beta) = 0 \quad (27)$$

where $\lambda = \alpha/\beta$ and $\zeta = (\beta^2 - s^2)/(\alpha^2 + s^2)$

4 Mode Shapes

The mode shapes for $f_i = 0$ are reported here because the case in which $f_i \neq 0$ is too lengthy. They may be found in

White and Heppler (1993). To form the mode shapes, any three boundary conditions may be used to eliminate three integration constants in terms of the remaining one. The mode shape plots will be identical, no matter what combinations of the boundary conditions are used, although the form of the equations may be quite different. The displacement mode shapes were derived by using the shear and moment conditions at the base, and the shear condition at the tip to affect the elimination. They may be expressed as

$$Y = \alpha\eta_1 \cosh(b\alpha\xi) + \alpha\eta_2 \sinh(b\alpha\xi) + \eta_3 \cos(b\beta\xi) + \beta\eta_4 \sin(b\beta\xi) \quad (28)$$

where

$$\eta_1 = \beta\tau[\cosh(b\alpha) - \cos(b\beta)] + b\gamma \sin(b\beta)q_0 + b\beta\tau[\alpha \sinh(b\alpha) + \beta \sin(b\beta)]p_1 + b^2\beta[\tau \cosh(b\alpha) + \sigma \cos(b\beta)]p_0q_0 + b^2\beta\gamma \cos(b\beta)q_0p_1 + b^3\beta[\alpha\tau \sinh(b\alpha) - \beta\sigma \sin(b\beta)]p_1q_0p_1$$

$$\eta_2 = -[\alpha\sigma \sin(b\beta) + \beta\tau \sinh(b\alpha)] - b\alpha\beta\gamma \cos(b\beta)p_0 + b\alpha\beta[\sigma \cos(b\beta) + \tau \cosh(b\alpha)]p_1 + b^2\tau[\alpha \sin(b\beta) - \beta \sinh(b\alpha)]p_0q_0 - b^2\alpha\beta^2\gamma \sin(b\beta)p_0p_1 + b^3\alpha\beta\tau[\cos(b\beta) - \cosh(b\alpha)]p_0q_0p_1$$

$$\eta_3 = \alpha\beta\sigma[\cosh(b\alpha) - \cos(b\beta)] - b\beta\gamma \sinh(b\alpha)q_0 + b\alpha\beta\sigma[\alpha \sinh(b\alpha) + \beta \sin(b\beta)]p_1 - b^2\alpha\beta[\tau \cosh(b\alpha) + \sigma \cos(b\beta)]p_0q_0 - b^2\alpha\beta\gamma \cosh(b\alpha)q_0p_1 + b^3\alpha\beta[\beta\sigma \sin(b\beta) - \alpha\tau \sinh(b\alpha)]p_0q_0p_1$$

and

$$\eta_4 = [\beta\tau \sinh(b\alpha) + \alpha\sigma \sin(b\beta)] + b\alpha\beta\gamma \cosh(b\alpha)p_0 + b\alpha\beta[\tau \cosh(b\alpha) + \sigma \cos(b\beta)]p_1 + b^2\sigma[\alpha \sin(b\beta) - \beta \sinh(b\alpha)]p_0q_0 + b^2\alpha^2\beta\gamma \sinh(b\alpha)p_0p_1 + b^3\alpha\beta\sigma[\cos(b\beta) - \cosh(b\alpha)]p_0q_0p_1.$$

In a similar fashion, the Ψ mode shape was formed using the shear and moment boundary conditions at the base, and the moment condition at the tip, which yielded

$$\Psi = b\tau\Phi_1 \cosh(b\alpha\xi) + b\tau\Phi_2 \sinh(b\alpha\xi) + b\tau\Phi_3 \cos(b\beta\xi) + b\tau\Phi_4 \sin(b\beta\xi) \quad (29)$$

where

$$\Phi_1 = \alpha\beta\sigma[\cos(b\beta) - \cosh(b\alpha)] - b\alpha\beta^2\gamma \sin(b\beta)p_0 + b\sigma[\alpha \sin(b\beta) - \beta \sinh(b\alpha)]q_1 + b^2\alpha\beta[\sigma \cosh(b\alpha) + \tau \cos(b\beta)]p_0q_0 + b^2\alpha\beta\gamma \cos(b\beta)p_0q_1 - b^3[\beta\sigma \sinh(b\alpha) + \alpha\tau \sin(b\beta)]p_0q_0q_1$$

$$\Phi_2 = \beta[\alpha\sigma \sinh(b\alpha) - \beta\tau \sin(b\beta)] + b\beta\gamma \cos(b\beta)q_0 + b\beta[\sigma \cosh(b\alpha) + \tau \cos(b\beta)]q_1 - b^2\beta\sigma[\alpha \sinh(b\alpha) + \beta \sin(b\beta)]p_0q_0 - b^2\gamma \sin(b\beta)q_0q_1 + b^3\beta\sigma[\cosh(b\alpha) - \cos(b\beta)]p_0q_0q_1$$

$$\Phi_3 = -\alpha\beta\tau[\cos(b\beta) - \cosh(b\alpha)] + b\alpha^2\beta\gamma \sinh(b\alpha)p_0 - b\tau[\beta \sinh(b\alpha) - \alpha \sin(b\beta)]q_1 - b^2\alpha\beta[\sigma \cosh(b\alpha) + \tau \cos(b\beta)]p_0q_0 - b^2\alpha\beta\gamma \cosh(b\alpha)p_0q_1 + b^3[\alpha\tau \sin(b\beta) + \beta\sigma \sinh(b\alpha)]p_0q_0q_1$$

and

$$\Phi_4 = \alpha[\alpha\sigma \sinh(b\alpha) - \beta\tau \sin(b\beta)] - b\alpha\gamma \cosh(b\alpha)q_0 - b\alpha[\sigma \cosh(b\alpha) + \tau \cos(b\beta)]q_1 - b^2\alpha\tau[\beta \sin(b\beta) + \alpha \sinh(b\alpha)]p_0q_0 + b^2\gamma \sinh(b\alpha)q_0q_1 + b^3\alpha\tau[\cosh(b\alpha) - \cos(b\beta)]p_0q_0q_1.$$

Since not every combination of the p_i and q_i are present in either mode shape, they do not exhibit the same degeneracy properties as the frequency equation for the case where the beam is unrestrained and has attached rigid bodies. However, the mode shapes that correspond to combinations of $p_i \to 0$ and $q_i \to 0$ limits may be recovered from the free-free mode shapes that include the contribution of the end masses, Eqs. (28) and (29) above. Any case which corresponds to $p_i \to \infty$ or $q_i \to \infty$ must be derived directly from the boundary conditions.

If the limits of $p_i \to 0$ and $q_i \to 0$ are taken in the mode shapes above, one form of the massless free-free mode shape is recovered. It is not the one presented in Huang (1964) because of a different choice of elimination boundary conditions, but Huang's form may be recovered through the massless free-free frequency equation.

4.1 Orthogonality Conditions. The orthogonality condition (White and Heppler, 1993) for the general free-free Timoshenko beam with rigid bodies attached to its ends is useful since it details the relationship between the different modes and provides a means by which they can be consistently assigned definite magnitudes, the so-called orthonormalization procedure. The orthogonality relationship may be derived by using the coupled differential Eqs. (7) and (8) as well as the boundary conditions (11)–(14) and may be found to be

$$\int_0^1 (Y_iY_j + r_g^2\Psi_i\Psi_j)d\xi + \sum_{k=0}^{1}\left[p_k(Y_iY_j)\,|_k + Lf_k(\Psi_iY_j = Y_i\Psi_j)\,|_k + L^2q_k(\Psi_i\Psi_j)\,|_k\right] = 0 \quad (30)$$

where r_g is the radius of gyration of the cross-section. The first term represents the contribution of the distributed beam mass, while the second term is the contribution of the masses of the attached rigid bodies. The first moments of the mass are given as coupling terms in the third term, and the moments of inertia of the attached rigid bodies contribute in the final term. The full development of the orthogonality condition may be found in White and Heppler (1993).

5 First Moment Effects

To this point the effects of the first moment, C_p, have been assumed to be small and therefore have been neglected. To investigate the validity of this assumption the mass, M_p, of an attached rigid body is held constant while the first moment of the mass, C_p, and the moment of inertia, J_p, are varied.

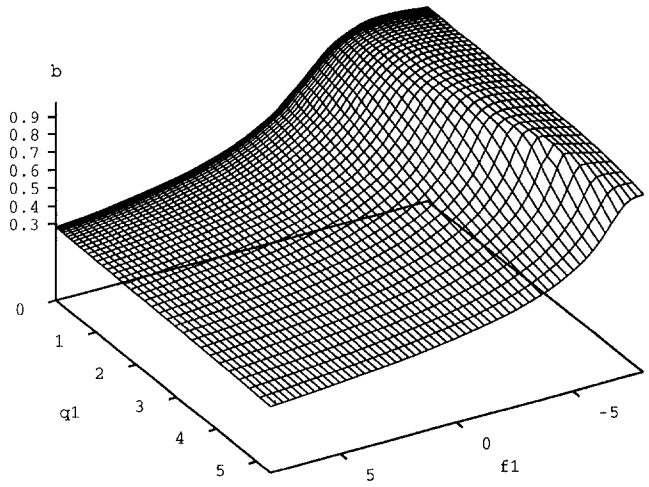

Fig. 1 First natural frequency

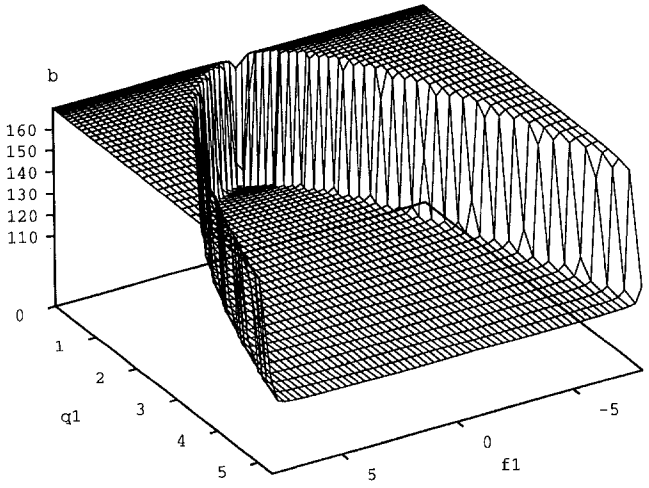

Fig. 2 Fifth natural frequency

5.1 Frequency Equation. To find the frequency equation for the cantilever beam including first moment effects, let $p_0 \to \infty$, $f_0 \to 0$ and $q_0 \to \infty$ in (21). Also, consider p_1, q_1, and f_1 as finite numbers defined by the dimensions of the beam and the attached payload. The frequency equation that results is

$$\alpha\beta\,\mathbf{F}_{cf} + \beta b^3\sigma\gamma \cosh(b\alpha)\cos(b\beta)(\alpha\beta p_1\mathbf{F}_{cs} - q_1\mathbf{F}_{cr}) + b^2\beta(p_1q_1 - f_1^2)\mathbf{F}_{cc} + 2b^2[\alpha\beta(\sigma - \tau) \times [1 - \cosh(b\alpha)\cos(b\beta)] - (\alpha^2\tau + \beta^2\sigma)\sinh(b\alpha)\sin(b\beta)]f_1 = 0 \qquad (31)$$

5.2 Results. The frequency Eq. (31) will now be used to determine the effect of including the first moment on the natural frequencies of the cantilever beam.

The theoretical limit for C_p ranges from $-M_p r_{gp}$ to $+M_p r_{gp}$, with J_p ranging from 0 to $M_p r_{gp}^2$, where r_{gp} is the radius of gyration of the rigid body attached at the payload end. By varying r_{gp}, the natural frequencies for the beam may be calculated for a variety of J_p and C_p values. Three-dimensional plots of nondimensional natural frequency versus q_1 and f_1 of the first and fifth natural frequencies for a cantilever beam with $r = 0.02005$, $s = 0.02665$, and $p_1 = 0.9570$ are shown in Figs. 1–2.

The first mode exhibits monotonically declining values with increasing moment of inertia values which is as expected. It also displays a monotonically declining behavior as the first moment varies from its extreme negative value to its extreme positive value. An examination of a set of plots of the frequency equation that are parametric in f_1 shows that this behavior is only possible for the first mode but it is still unclear which terms in the actual frequency equation are governing this response.

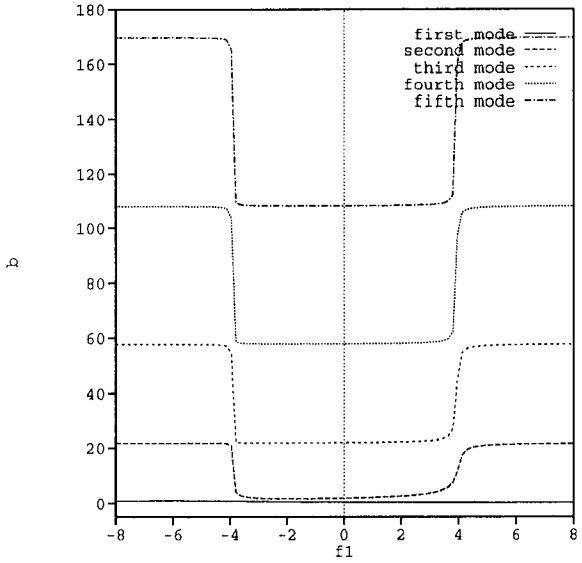

Fig. 3 The effect of varying first moment for constant second moment, $q_1 = 1.2694$

Although only the fifth mode is presented here, the second through fifth modes display similar behavior. The interesting point to note is the sharp increase in the natural frequency values near the outer limits of the theoretically possible range for C_p. This sharp increase arises due to the $p_1q_1 - f_1^2$ term in Eq. (31). This term passes through zero as C_p is increased past its outer bounds, due to the fact that $p_1q_1 = f_1^2$ when $f_1 = M_p r_{gp}$ or $-M_p r_{gp}$. Thus in this region, the positive contribution of the $(p_1q_1 - f_1^2)$ term is first greatly reduced, then eliminated, and then returned as a negative value as we cross the limiting values of C_p. In turn, the sharp increase in natural frequency results. Also note that in the region between $-M_p r_{gp}$ and $M_p r_{gp}$, the first moment has virtually no effect on the natural frequencies. Therefore, the assumption that first moment effects may be neglected appears to be reasonable.

The relationship between adjacent modes is also an interesting one. Figure 3 shows how the first five natural frequencies change for a fixed value of the moment of inertia, while varying the first moment.

In this figure the shallow monotonic decline of the first frequency is evident as is the sharp increase in the frequency values when f_1 takes on values that are outside the physically admissible range of values. It can also be observed that the "plateau" values for mode $n - 1$ approach, but never actually reach, the "valley" values for mode n and that the depth of the "valley" increases with increasing mode number.

6 Summary

Using Hamilton's Principle, the differential equations of motion and boundary conditions for a Timoshenko beam with rigid bodies attached at either end are found. Utilizing the solutions to the equations of motion in the boundary conditions gives the frequency equation for the beam. Here it is noted that this generalized frequency equation is merely a weighted combination of each of the ten fundamental sup-

port cases, each of which may be recovered from the generalized equation in the appropriate limits of the end masses and moments of inertia. The generalized mode shapes for both displacement and bending slope are then presented. The degeneration properties exhibited by the frequency equation are not present in the mode shapes. The mode shapes for different support cases may be found by taking limits in the boundary conditions of the problem. The general orthogonality condition for the Timoshenko beam with attached masses has been reported. To investigate the assumption that first moment effects are negligible, the natural frequencies of a cantilever beam are plotted for varied values of the first moment and for the example presented here, provided that it is positive, the first moment does appear to be negligible.

References

Abbas, B. A. H., and Thomas, J., 1977, "The Second Frequency Spectrum of Timoshenko Beams," *Journal of Sound and Vibration*, Vol. 51, No. 1, pp. 123–137.

Anderson, R. A., 1953, "Flexural Vibrations in Uniform Beams According to the Timoshenko Theory," ASME JOURNAL OF APPLIED MECHANICS, Vol. 75, pp. 504–510.

Barr, A. D. S., 1956, "Some Notes on the Resonance of Timoshenko Beams and the Effects of Lateral Inertia on Flexible Vibration," *Proceedings of the 9th International Congress of Applied Mechanics*, Vol. 7, pp. 448–458.

Barr, A. D. S., 1993, "Parametric Vibration in Beams," *Proceedings of the 14th Canadian Congress of Applied Mechanics*, Vol. 1, pp. 3–9.

Bruch, J. C., and Mitchell, T. P., 1987, "Vibrations of a Mass-loaded Clamped-Free Timoshenko Beam," *Journal of Sound and Vibration*, Vol. 114, No. 2, pp. 341–345.

Grant, D. A., 1978, "The Effect of Rotary Inertia and Shear Deformation on the Frequency and Normal Mode Equations of Uniform Beams Carrying a Concentrated Moving Mass," *Journal of Sound and Vibration*, Vol. 57, No. 34, pp. 357–365.

Huang, T. C., 1961, "The Effect of Rotary Inertia and of Shear Deformation on the Frequency and Normal Mode Equations of Uniform Beams With Simple End Conditions," ASME JOURNAL OF APPLIED MECHANICS, Vol. 28, pp. 579–584.

Huang, T. C., 1964, "Eigenvalues and Modifying Quotients of Vibration of Beams," Report No. 25, Engineering Experiment Station, University of Wisconsin, Madison, Wisconsin.

Kapur, K., 1966, "Vibrations of a Timoshenko Beam, Using Finite-Element Approach," *Journal of the Acoustical Society of America*, Vol. 40, No. 5, pp. 1058–1063.

Levinson, M., and Cooke, D. W., 1982, "On the Two Frequency Spectra of Timoshenko Beams," *Journal of Sound and Vibration*, Vol. 84, No. 3, pp. 319–326.

Liu, W. H., 1989, "Comments on "Vibrations of a Mass-loaded Clamped-Free Timoshenko Beam,'" *Journal of Sound and Vibration*, Vol. 129, No. 2, pp. 343–344.

Strutt, J. W., (Lord Rayleigh) 1877, *Theory of Sound*, Macmillan, London.

Stephen, N. G., 1982, "The Second Frequency Spectrum of Timoshenko Beams," *Journal of Sound and Vibration*, Vol. 80, No. 4, pp. 578–582.

Storch, J., and Gates, S., 1985, "Transverse Vibration and Buckling of a Cantilevered Beam with Tip Body Under Axial Acceleration," *Journal of Sound and Vibration*, Vol. 99, No. 1, pp. 43–52.

Timoshenko, S. P., 1921, "On the Correction for Shear or the Differential Equations for Transverse Vibration of Prismatic Bars," *Philosophy Magazine*, Ser. 6, Vol. 41, pp. 744–746.

Timoshenko, S., Young, D. H., and Weaver, W., 1974, *Vibration Problems in Engineering*, 4th ed., John Wiley and Sons, New York.

Traill-Nash, R. W., and Collar, A. R., 1953, "The Effects of Shear Flexibility and Rotatory Inertia on the Bending Vibrations of Beams," *Quarterly Journal of Mechanics and Applied Math*, Vol. 6, No. 2, pp. 186–222.

White, M. W. D., 1992, "Mathematical Model of a Timoshenko Beam," 4th Year Project Report, Department of Systems Design Engineering, University of Waterloo, Waterloo, Ontario, Canada.

White, M. W. D., and Heppler, G. R., 1993, "Vibration Modes and Frequencies of Timoshenko Beams with Attached Rigid Bodies," ConStruct Group Technical Report TR-93-001, Department of Systems Design Engineering, University of Waterloo, Waterloo, Ontario, Canada.

Zu, J. W. Z., and Han, R. P. S., 1992, "Natural Frequencies and Normal Modes of a Spinning Timoshenko Beam with General Boundary Conditions," ASME JOURNAL OF APPLIED MECHANICS, Vol. 59, pp. S197–S204.

Zheng-Dong Ma[2]
Professor,
Department of Applied Mechanics,
Jilin University of Technology,
Changchun, P. R. China,
Mem. ASME

Noboru Kikuchi
Professor,
Mem. ASME.

Hsien-Chie Cheng
Graduate Student.

Department of Mechanical Engineering
and Applied Mechanics,
The University of Michigan,
Ann Arbor, MI 48109-2215

Ichiro Hagiwara
Senior Researcher,
Vehicle Laboratory,
Central Engineering Laboratories,
Nissan Motor Company, Ltd.,
1, Natsushima-cho,
Yokosuka, 237, Japan

Topological Optimization Technique for Free Vibration Problems[1]

A topological optimization technique using the conception of OMD (Optimal Material Distribution) is presented for free vibration problems of a structure. A new objective function corresponding to multieigenvalue optimization is suggested for improving the solution of the eigenvalue optimization problem. An improved optimization algorithm is then applied to solve these problems, which is derived by the authors using a new convex generalized-linearization approach via a shift parameter which corresponds to the Lagrange multiplier and the use of the dual method. Finally, three example applications are given to substantiate the feasibility of the approaches presented in this paper.

Introduction

The newest development in structural optimal design is topology optimization. Even though the use of previous techniques which were developed for sizing optimization and shape optimization problems have made it possible to obtain the optimal size and shape of a structure, it is necessary to obtain an optimal topology for a truly optimal design.

Optimization of the topology of a continuum structure was rarely attempted before Bendsøe and Kikuchi (1988) presented their method that is based on a simple idea of transforming the problem to find the OMD (Optimal Material Distribution) within a specified design domain. It is assumed that the material is not homogeneous, but instead has a variable solid-cavity microstructure. By using the homogenization method and mathematical tools of optimization, the OMD with respect to given loads and boundary conditions can be obtained. This process results in a truly optimal structure, and, theoretically, the final structure is optimal in topology, shape, and size.

This idea has opened up a new dimension in structural optimization, and it has been successfully applied to the problems of structural static stiffness (e.g., Bendsøe and Kikuchi, 1988; Suzuki and Kikuchi, 1990, 1991; Olhoff et al., 1991). In the structural dynamic problem, a solution for the eigenvalue optimization has been obtained by Diaz and Kikuchi (1992) using an extension of the above method. Recently, Ma et al. (1992) have developed this method for solving frequency response optimization problems. However, a dynamic problem is quite different from the static one. It was shown (Ma et al., 1992) that even though the previous optimization algorithm, which is based on a traditional OC (Optimality Criteria) method, is well-convergent in static problems (Bendsøe and Kikuchi, 1988), but does not work well in the dynamic case, especially when the exciting frequency becomes high. Therefore, an improved optimization algorithm was developed (Ma et al., 1992) in order to overcome the difficulty mentioned above. The basic idea in that

[1]This paper was presented at the session entitled "Symposium on Recent Advances in Structural Mechanics," 1992 ASME Winter Annual Meeting, Nov. 8–13, Anaheim, CA.

[2]Currently Associate Research Scientist, Department of Mechanical Engineering and Applied Mechanics, The University of Michigan, Ann Arbor, MI 48109-2215.

Contributed by the Applied Mechanics Division of THE AMERICAN SOCIETY OF MECHANICAL ENGINEERS for publication in the ASME JOURNAL OF APPLIED MECHANICS.

Discussion on this paper should be addressed to the Technical Editor, Professor Lewis T. Wheeler, Department of Mechanical Engineering, University of Houston, Houston, TX 77204-4792, and will be accepted until four months after final publication of the paper itself in the ASME JOURNAL OF APPLIED MECHANICS.

Manuscript received by the ASME Applied Mechanics Division, Dec. 14, 1992; final revision, June 21, 1993. Associate Technical Editor: R. L. Huston.

development is to make a convex generalized linearization approach using a shift parameter which corresponds to the Lagrange multiplier, and employs the dual method to separate a multivariables minimization problem to several one-dimensional problems. Then an improved resizing rule is obtained, which has much better convergency and can be reduced to the previous one if choosing a zero value as the shift parameter. The concept of convex linearization and the use of duality is also the basis of the widely used optimization methods CONLIN (Fleury and Braibant, 1986; Fleury, 1989) and MMA (Svanberg, 1987), but the new algorithm is more efficient and suitable for the problem. It has been shown that the new algorithm has the simplicity of the OC method, and it has good convergency in the frequency response problem (Ma et al., 1992). Several examples of the frequency response problem have been given in a previous report. In this paper, we shall develop the new technique to improve the solution of the eigenvalue optimization problem.

As shown in this paper, in the eigenvalue optimization problem, if one follows a specified mode of the structure so as to optimize (usually maximize) its eigenvalue, then the number of this mode may be changed within the optimization process. For example, if k is the original number of order of the mode, then during the optimization process it may change to $k + p$ finally, where $p > 0$. In contrast, if we follow the number of modal order, e.g., to optimize the kth eigenvalue, then the mode being the object of optimization process may be changed to another one. In this case, the sensitivities of the objective function become discontinuous, and oscillation may be caused in the objective function within the optimization process (Fig. 10). In order to overcome this problem, a new objective function is suggested in this paper, which corresponds to a specified multieigenvalue optimization problem. It will be shown that the use of this objective function and the improved optimization algorithm mentioned above can greatly improve the solution, and can optimize not only a single eigenvalue but also multieigenvalues by choosing the weighting functions and shift parameter properly.

First, the structural optimization problem is transformed to an OMD problem using a specified two-dimensional microstructure. Then, a new objective function is proposed for improving the solution of the eigenvalue optimization problem. The sensitivity analysis of the objective function is also given. An improved optimization algorithm is then presented for solving the problems. Finally, three examples are given to substantiate the feasibility of the approach presented in this paper.

The OMD Problem

In general, a structural optimization problem can be conceived as an OMD (Optimal Material Distribution) problem within a prescribed admissible structural domain assuming the loading and boundary conditions to be given (Bendsøe and Kikuchi, 1988; Olhoff et al., 1991; Ma et al., 1992). As shown in Fig. 1, it is considered that the structural domain is filled by a nonhomogeneous material that has a variable microstructure. To simplify the problem, in the plane-stress problem, we assume that the microstructure is formed inside an empty rectangle in a unit cell as shown in Fig. 1, where, a, b, and θ are regarded as the design variables. The inside cavity of the microstructure is variable along with the design variables, a and b, while the microstructure becomes a complete void when $a = b = 0$, and a complete solid when $a = b = 1$. θ stands for the rotation of the unit cell.

In the optimization process, the microstructures are changed between empty and solid. Therefore, if the total amount of the material of the structure is assumed constant, then the pieces of the material are moved from one part of the structure to another while the optimization process progresses (Fig. 2). By moving the material for the aim of reducing the objective function, finally we can obtain an OMD that gives the optimal structure.

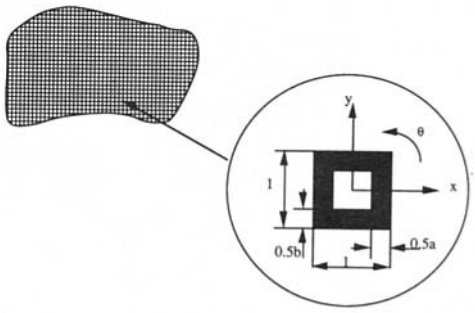

Fig. 1 Microstructure in a structural domain

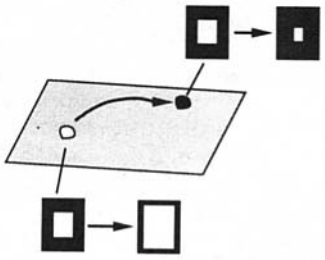

Fig. 2 Moving material from a portion of the structural to another portion

The linearly elastic coefficients E_{ijkl} and mass density ρ are utilized to characterize the problem. Here, in general, E_{ijkl} and ρ are functions of the spatial coordinate. It is assumed

$$E_{ijkl} = \begin{cases} E^0_{ijkl} & \text{in solid} \\ 0 & \text{in cavity} \end{cases}, \quad \rho = \begin{cases} \rho_0 & \text{in solid} \\ 0 & \text{in cavity} \end{cases} \tag{1}$$

where E^0_{ijkl} and ρ_0 are the elasticity tensor and mass density of the solid portion in the structural domain, respectively.

Using the homogenization method, the homogenized elastic coefficients E^h_{ijkl} and mass density ρ^h, which are corresponding to an unrotated cell, can be obtained as follows:

$$E^h_{ijkl} = \frac{1}{|Y|}\int_Y \left(E_{ijkl} - E_{ijpq}\frac{\partial \chi^{kl}_p}{\partial y_q} \right) d\mathbf{y}, \quad \rho^h = \frac{1}{|Y|}\int_Y \rho d\mathbf{y} \tag{2}$$

where Y is the domain of the cell, and χ^{kl}_p is the solution of the microstructural problem that characterizes the micromechanical behavior of the microstructure (Bendsøe and Kikuchi, 1988; Ma et al., 1992).

Finite element discretization can also be employed to solve the problem. For the free vibration problem, the fundamental finite element equation can be written as

$$(\mathbf{K} - \lambda_n \mathbf{M})\phi_n = 0 \tag{3}$$

where λ_n stands for the nth eigenvalue of the structure ($n = 1, 2, \ldots$), and ϕ_n the corresponding eigenvector. $\mathbf{M}$ and $\mathbf{K}$ stand for the mass matrix and stiffness matrix, respectively.

$$\mathbf{K} = \mathop{A}_{e=1}^{n_{el}} \mathbf{k}_e, \quad \mathbf{M} = \mathop{A}_{e=1}^{n_{el}} \mathbf{m}_e \tag{4}$$

where $\mathop{A}_{e=1}^{n_{el}}$ stands for the finite element assembly operator, and, $\mathbf{k}_e$ and $\mathbf{m}_e$ are the element stiffness and mass matrices obtained by

$$\mathbf{k}_e = \int_{\Omega_e} \mathbf{B}^T_e \mathbf{D}_e \mathbf{B}_e d\Omega, \quad \mathbf{m}_e = \int_{\Omega_e} \rho_e \mathbf{N}^T_e \mathbf{N}_e d\Omega \tag{5}$$

where $\mathbf{B}_e$ and $\mathbf{N}_e$ stand for the strain shape function and shape function, respectively. $\mathbf{D}_e = \mathbf{T}_e^T \mathbf{D}^h \mathbf{T}_e$ and $\rho_e = \rho^h$ are the rotated homogenized stiffness and mass density, where $\mathbf{T}_e = \mathbf{T}_e(\theta)$ is the transformation matrix for the eth element.

Assuming the design variables with respect to an arbitrary finite element Ω_e are a_e, b_e and θ_e, then the element stiffness matrix $\mathbf{k}_e$ and mass matrix $\mathbf{m}_e$ are functions of a_e, b_e and θ_e, i.e.,

$$\mathbf{k}_e = \mathbf{k}_e(a_e, b_e, \theta_e), \quad \mathbf{m}_e = \mathbf{m}_e(a_e, b_e) \tag{6}$$

Eigenvalue Optimization Problem

Objective Function. Maximizing a chosen eigenvalue of the system is usually used as the subject in an eigenvalue optimization problem (e.g., Olhoff, 1981). However, in the eigenvalue optimization problem, when one maximizes a lower eigenvalue, higher eigenvalues may fall down to the lower values. It means that if the optimization process is to follow a specified mode of the structure, then the order number of this mode may be changed during the optimization process. For example, at the beginning we may wish to optimize the kth eigenvalue, but finally the optimal solution obtained may correspond to the $k + p$th mode, where $p > 0$. Thus the problem is changed to an unexpected one. In contrast, if one follows the number of modal order, e.g., to optimize the kth eigenvalue, then the mode being optimized may change to another one. In this case, the sensitivities of the objective function become discontinuous, and may cause oscillation and divergence in the iterative process. In order to overcome this problem, a specified multieigenvalue optimization problem is suggested as

$$\text{Minimize } f = -\Lambda \tag{7}$$

where,

$$\Lambda = \lambda_0 + \sum_{i=1}^{m} w_i \Big/ \sum_{i=1}^{m} \frac{w_i}{\lambda_{n_i} - \lambda_0} \tag{8}$$

We label Λ as the mean eigenvalue, where λ_{n_i} ($n_i = n_1, n_2, \ldots, n_m$) are the chosen eigenvalues, and w_i ($i = 1, 2, \ldots, m$) the given weighting coefficients. λ_0 is a specified shift parameter. It will be shown that this objective function can greatly improve the solution of the optimization problem, and it can be used to optimize either a single eigenvalue or multieigenvalue by choosing the shift parameter and weighting coefficients properly.

In fact, if we assume $m = 1$, Eq. (8) is reduced to $\Lambda = \lambda_{n1}$, and the optimization problem becomes one of maximizing the n_1th eigenvalue λ_{n1}. In the general case, assuming $\sum_{i=1}^{m} w_i = 1$, Eq. (7) can be rewritten as

$$\text{Minimize } g \tag{9}$$

where,

$$g = \frac{1}{\Lambda - \lambda_0} = \sum_{i=1}^{m} \frac{w_i}{\lambda_{n_i} - \lambda_0} \tag{10}$$

and $f = -(1/g + \lambda_0)$. As shown in Eq. (10), the eigenvalue which is the closest to the shift parameter λ_0 has the largest contribution to the objective function g, if assuming all of the weighting coefficients w_i ($i = 1, 2, \ldots, m$) are the same. In the special case, $\lambda_0 = 0$, the lowest eigenvalue in λ_{n_i} ($n_i = n_1, n_2, \ldots, n_m$) has the largest contribution to the objective function. Therefore, the eigenvalue that is the closest to λ_0 will be the major object of the optimization problem. This implies this eigenvalue will experience the largest change. When two modes exchange their order within the optimization process, where both eigenvalues are in Eq. (10), the change in the objective function will be smoother than in the case when one of these eigenvalues is not in λ_{n_i} ($n_i = n_1, n_2, \ldots, n_m$). It is because the contribution of these modes must be smoothly changed once they have already been accounted for in the objective function. Moreover, by properly choosing different values as the weighting coefficients w_i ($i = 1, 2, \ldots, m$), one can increase or reduce the contributions of the other eigenvalues in λ_{n_i} ($n_i = n_1, n_2, \ldots, n_m$) to make a desired multieigenvalue optimization.

Note that the "singularities" of the optimal structure, which are discussed by (e.g., Olhoff, 1981), can also be avoided by using the new objective function presented here. This will be discussed in Example 2.

Sensitivity Analysis. In the optimization process, the finite element mesh is fixed, but the density of the material in an element is changed along with the design variables defined in Fig. 1. The sensitivity of the objective function with respect to an arbitrary design variable x can be obtained as

$$\frac{\partial \Lambda}{\partial x} = -\frac{(\Lambda - \lambda_0)^2}{\sum_{i=1}^{m} w_i} \sum_{i=1}^{m} \frac{w_i}{(\lambda_{n_i} - \lambda_0)^2} \frac{\partial \lambda_{n_i}}{\partial x} \tag{11}$$

where

$$\frac{\partial \lambda_{n_i}}{\partial x} = \phi_{n_i}^T \left(\frac{\partial \mathbf{K}}{\partial x} - \lambda_{n_i} \frac{\partial \mathbf{M}}{\partial x} \right) \phi_{n_i} = \phi_{n_i,e}^T \left(\frac{\partial \mathbf{k}_e}{\partial x} - \lambda_{n_i} \frac{\partial \mathbf{m}_e}{\partial x} \right) \phi_{n_i,e} \tag{12}$$

(for x is a design variable of the finite element e)

(refer, e.g., Ma and Hagiwara, 1991a) where $\phi_{n_i,e}$ stands for the component of n_ith eigenvector with respect to the eth finite element Ω_e of the structure, and $\partial \mathbf{k}_e/\partial x$ and $\partial \mathbf{m}_e/\partial x$ are calculated by

$$\frac{\partial \mathbf{k}_e}{\partial x} = \int_{\Omega_e} \mathbf{B}_e^T \frac{\partial \mathbf{D}_e}{\partial x} \mathbf{B}_e d\Omega, \quad \frac{\partial \mathbf{m}_e}{\partial x} = \int_{\Omega_e} \frac{\partial \rho_e}{\partial x} \mathbf{N}_e^T \mathbf{N}_e d\Omega. \tag{13}$$

It should be noted that Eq. (12) is calculated at element level only. For example, if we use four-node quadrilateral elements, just 72 multiplications are needed for each derivative calculation with respect to a design variable. Therefore, the sensitivity analysis using the method mentioned here is very simple and highly efficient, especially when compared to the use of a finite-difference method.

If the structure has repeated eigenvalues, the sensitivity calculated by Eq. (12) will be incorrect. In this case a sensitivity analysis method for systems with repeated eigenvalues can be employed to overcome this difficulty (e.g., Ma and Hagiwara, 1991b).

Constraint Function and its Sensitivity

Consider a constraint of total mass of the structure:

$$\int_{\Omega} \rho_e d\Omega \le V_0 \tag{14}$$

where V_0 is the given total mass of the structure. In the problem which uses the microstructure shown in Fig. 1, $\rho_e = \rho_0(a_e + b_e - a_e b_e)$, and the constraint function becomes

$$h(a_e, b_e) = \sum_{e=1}^{n_{el}} \rho_0 \Omega_e (a_e + b_e - a_e b_e) - V_0 \le 0. \tag{15}$$

Then the sensitivities of the constraint function with respect to design variables a_e and b_e can be obtained as

$$\frac{\partial h}{\partial a_e} = \rho_0 \Omega_e (1 - b_e) \text{ and } \frac{\partial h}{\partial b_e} = \rho_0 \Omega_e (1 - a_e). \quad (16)$$

Constraints of the minimum and maximum values of a_e and b_e are also considered for the problem

$$\underline{a}_e \le a_e \le \bar{a}_e, \quad \underline{b}_e \le b_e \le \bar{b}_e, \quad (e = 1, 2, \ldots, n_{el}) \quad (17)$$

where $\underline{a}_e(\underline{b}_e)$ and $\bar{a}_e(\bar{b}_e)$ stand for the minimum and maximum values of the design variables $a_e(b_e)$, respectively.

Optimization Algorithm

In the general case, the optimization problem can be written as

$$\underset{\mathbf{X}, \Theta}{\text{Minimize}} f \quad (18)$$

$$\text{Subject to} \quad h(\mathbf{X}) \le 0, \quad (19a)$$

$$\underline{x} \le x_i \le \bar{x}_i, \ (i = 1, 2, \ldots, N) \quad (19b)$$

where $\mathbf{X} = \text{col}\{x_i\}$ $(x_i \in A \cup B)$, $\Theta = \text{col}\{\theta_i\}$ are vectors of the design variables, A and B stand for the set of design variables a_i and b_i, respectively; $\underline{x}_i$ and $\bar{x}_i$ are the minimum and maximum values of the design variables, x_i, respectively; and $N = 2n_{el}$.

It is very important to find an efficient updating rule for the optimization problem, because we may deal with thousands of design variables in a calculation. A previous updating rule which bases on the OC method was employed by Bendsøe and Kikuchi (1989) for updating the design variable vector $\mathbf{X}$. Even though the optimization algorithm based on this updating rule is very efficient in computation and converges for the static problems, it does not work well in the dynamic case. Therefore, a new optimization algorithm was developed in order to overcome the difficulty mentioned above (Ma et al., 1992).

We can prove this idea mathematically by using a generalized reciprocal approximation, which linearizes the objective function with respect to the intermediate variables, and the dual method, which separates a multivariable optimization problem into several one-directional problems.

The Lagrangian function of the optimization problem is defined as

$$L = f + \lambda h + \sum_{i=1}^{N} \left[\alpha_{-i}(\underline{x}_i - x_i) + \alpha_{+i}(x_i - \bar{x}_i) \right] \quad (20)$$

where λ, α_{-i}, and α_{+i} are the Lagrange multipliers. If assuming Eq. (19a) to be active, then we have $\lambda > 0$.

The basic idea in this development is to use a shift parameter which corresponds to the Lagrange multiplier to obtain a convex approach for the problem. Making a new objective function

$$f^* = f - \mu h \quad (21)$$

where μ is a given shift parameter, Eq. (20) can be rewritten as

$$L = f^* + \lambda^* h + \sum_{i=1}^{N} \left[\alpha_{-i}(\underline{x}_i - x_i) + \alpha_{+i}(X_I - \bar{x}_I) \right] \quad (22)$$

where $\lambda^* = \lambda + \mu$. Now we have a new optimization problem, which is completely equivalent to the original one (Ma et al., 1992).

Using a generalized reciprocal approximation, we assume intermediate linearization variables as

$$y_i = \left(\frac{1}{x_i} \right)^{\xi_i}, \quad (i = 1, 2, \ldots, N) \quad (23)$$

where $\xi_i (i = 1, 2, \ldots, N)$ are parameters which can be determined by the known property of the objective function. For example, if f is an almost linear function of $1/x_i$, $\xi_i = 1$ is a proper choice. In this paper, we assume $\xi_1 = \xi_2 = \ldots = \xi_N = \xi$. Then f^* can be linearly approximated in the space of y_i at $y_i = y_i^k = (x_i^k)^{-\xi}$ $(i = 1, 2, \ldots, N)$ as

$$f^k = f_0^k + \sum_{i=1}^{N} a_i^k x_i^{-\xi} \quad (24)$$

where x_i^k $(i = 1, 2, \ldots, N)$ are the kth approximations of the design variables obtained in the preceding iteration step of the optimization process, and f_0^k is a constant,

$$a_i^k = \frac{\partial f^*}{\partial y_i}\Big|_{y_i = y_i^k} = -\frac{1}{\xi}\left(\frac{\partial f}{\partial x_i} - \mu \frac{\partial h}{\partial x_i} \right)_{x_i = x_i^k} \left(x_i^k \right)^{\xi + 1}, \quad (i + 1, 2, \ldots, N). \quad (25)$$

If we choose the shift parameter μ in the kth iteration step as

$$\mu^k \ge \left[\frac{\partial f}{\partial x_i} \Big/ \frac{\partial h}{\partial x_i} \right]\Big|_{x_i = x_i^k} \quad (\text{for } i = 1, 2, \ldots, N) \quad (26)$$

then we have $a_i^k \ge 0$ $(i = 1, 2, \ldots, N)$, and the approximation of objective function f^k is convex as $\xi > 0$ and $x_i^k \ge 0$, $(i = 1, 2, \ldots, N)$.

In this problem, the constraint function h is a linear function with respect to an individual design variable x_i, therefore it can be linearly approximated as

$$h^k = h_0^k + \sum_{i=1}^{N} b_i^k x_i \quad (27)$$

where $h_0^k < 0$ is a constant, and

$$b_i^k = \frac{\partial h}{\partial x_i}\Big|_{x_i = x_i^k}, \quad \left(b_i^k \ge 0; i = 1, 2, \ldots, N \right). \quad (28)$$

Assuming I_-^k and I_+^k are the sets of number of the design variables which result in the minimum and maximum values, respectively, and I^k is the set of numbers of the other design variables, i.e.,

$$I_-^k = \left\{ i | x_i = \underline{x}_i \right\}, \quad I_+^k = \left\{ i | x_i = \bar{x}_i \right\},$$

$$I^k = \left\{ i | \underline{x}_i < x_i < \bar{x}_i \right\}. \quad (29)$$

Then the Lagrangian function in the kth iteration, Eq. (22), can be approximated as

$$L^k(\mathbf{X}, \lambda, \boldsymbol{\alpha}) = l_0^k + \sum_{i \in I^k} l_i^k + \sum_{i \in I_-^k} l_{-i}^k + \sum_{i \in I_+^k} l_{+i}^k \quad (30)$$

where, $\boldsymbol{\alpha}$ stands for the vector of the Lagrange multipliers $\alpha_{-i} (i \in I_-^k)$ and $\alpha_{+i} (i \in I_+^k)$.

$$l_0^k = f_0^k + \lambda h_0^k + \sum_{i \in I_-^k} \alpha_{-i} \underline{x}_i - \sum_{i \in I_+^k} \alpha_{+i} \bar{x}_i \quad (31)$$

$$l_i^k = a_i^k x_i^{-\xi} + \lambda b_i^k x_i, \quad (\text{for } i \in I^k) \quad (32a)$$

$$l_{-i}^k = a_i^k x_i^{-\xi} + \lambda b_i^k x_i - \alpha_{-i} x_i, \quad \left(\text{for } i \in I_-^k\right) \quad (32b)$$

$$l_{+i}^k = a_i^k x_i^{-\xi} + \lambda b_i^k x_i + \alpha_{+i} x_i, \quad \left(\text{for } i \in I_+^k\right) \quad (32c)$$

and for simplicity, the index "*" on λ is omitted.

Since the approximated Lagrangian function $L^k(\mathbf{X}, \lambda, \boldsymbol{\alpha})$ is convex, we can use the dual method to solve the problem (e.g., Haftka and Gurdal, 1992). The dual problem is defined by

$$\max_{\lambda,\, \alpha} L_m^k(\lambda, \boldsymbol{\alpha}) \tag{33a}$$

$$\text{subject to } \lambda \geq 0,\ \boldsymbol{\alpha} \geq 0 \tag{33b}$$

where

$$L_m^k(\lambda, \boldsymbol{\alpha}) = \min_{\mathbf{x}} L^k(\mathbf{X}, \lambda, \boldsymbol{\alpha}). \tag{34}$$

Because the minimization problem Eq. (34) is separable, it can be replaced with an N one-dimensional minimization problems as follows:

$$(a)\ \text{For } i \in I^k: \quad \min_{x_i} l_i^k(x_i) = a_i^k x_i^{-\xi} + \lambda b_i^k x_i \tag{35}$$

$$(b)\ \text{For } i \in I_-^k: \quad \min_{x_i} l_{-i}^k(x_i) = a_i^k x_i^{-\xi} + \lambda b_i^k x_i - \alpha_{-i} x_i \tag{36}$$

$$(c)\ \text{For } i \in I_+^k: \quad \min_{x_i} l_{+i}^k(x_i) = a_i^k x_i^{-\xi} + \lambda b_i^k x_i + \alpha_{+i} x_i. \tag{37}$$

Solving Eq. (35), we can obtain its solution as

$$x_i^* = \lambda^{-\eta} e_i^k, \left(\text{for } \underline{x}_i < \lambda^{-\eta} e_i^k < \bar{x}_i\right) \tag{38}$$

where $\eta = 1/(\xi + 1)$, and

$$e_i^k = \left(\frac{\xi a_i^k}{b_i^k}\right)^{\eta} = \left[\mu^k - \left(\frac{\partial f/\partial x_i}{\partial h/\partial x_i}\right)\Big|_{x_i = x_i^k}\right]^{\eta} x_i^k. \tag{39}$$

Solving Eqs. (36) and (37), we can obtain

$$\alpha_{-i} = -\xi a_i^k \underline{x}_i^{-(\xi+1)} + \lambda b_i^k = b_i^k\left[\lambda - \left(e_i^k/\underline{x}_i\right)^{1/\eta}\right], \quad \left(\text{for } \lambda^{-\eta} e_i^k \leq \underline{x}_i\right) \tag{40}$$

and

$$\alpha_{+i} = b_i^k\left[\left(e_i^k/\bar{x}_i\right)^{1/\eta} - \lambda\right], \quad \left(\text{for } \lambda^{-\eta} e_i^k \geq \bar{x}_i\right). \tag{41}$$

Substituting Eqs. (38) (40), and (41) into Eqs. (31), (32), and (30) yields

$$L^k = \tilde{f}_0^k + \lambda \tilde{h}_0^k + \lambda^{1-\eta}(1-\eta)^{-1} \sum_{i \in I^i} b_i^k e_i^k \tag{42}$$

where $\tilde{f}_0^k$ and $\tilde{h}_0^k$ are constants.

To solve the maximization problem Eq. (33), we have

$$\frac{\partial L^k}{\partial \lambda} = \tilde{h}_0^k + \lambda^{-\eta} \sum_{i \in I^k} b_i^k e_i^k = 0. \tag{43}$$

Then the Lagrange multiplier can be obtained as

$$\lambda^* = \left(\frac{-1}{\tilde{h}_0^k} \sum_{i \in I^k} b_i^k e_i^k\right)^{1/\eta}. \tag{44}$$

It should be noted that because the sets I_-^k, I^k and I_+^k are dependent on the solution of Lagrange multiplier λ^*, an iterative calculation is required for obtaining λ^*.

In summary, the improved optimization algorithm can be described by the following.

(a) Give the initial value of the design variables, x_i^k ($i = 1, 2, \ldots, N$) and θ_i^k ($i = 1, 2, \ldots, n_{el}$) for $k = 0$.

(b) Solve the eigenvalue problem Eq. (3) with respect to $x_i = x_i^k$, $\theta_i = \theta_i^k$

(c) Calculate $\partial f/\partial x_i$ and $\partial h/\partial x_i$ with respect to $x_i = x_i^k$, $\theta_i = \theta_i^k$.

(d) Calculate μ^k using

$$\mu^k = \max_{1 \leq i \leq N}\left\{\left(\frac{\partial f/\partial x_i}{\partial h/\partial x_i}\right)\Big|_{x_i = x_i^k}\right\}. \tag{45}$$

(e) Calculate

$$e_i^k = \hat{D}_i^k x_i^k, \quad (i = 1, 2, \ldots, N) \tag{46}$$

where

$$\hat{D}_i^k = \left(\mu^k - \left(\frac{\partial f/\partial x_i}{\partial h/\partial x_i}\right)\Big|_{x_i = x_i^k}\right)^{\eta} \tag{47}$$

(f) Determine the Lagrange multiplier by an inner loop using

$$\tilde{\lambda}^k = \frac{-1}{\tilde{h}_0^k} \sum_{i \in I^k} b_i^k e_i^k \tag{48}$$

where $\tilde{\lambda}^k = (\lambda^k)^{\eta}$,

$$\tilde{h}_0^k = h_0^k + \sum_{i \in I_-^k} b_i^k \underline{x}_i + \sum_{i \in I_+^k} b_i^k \bar{x}_i, \tag{49}$$

$$I_-^k = \left\{i | e_i^k/\tilde{\lambda} \leq \underline{x}_i\right\},$$
$$I^k = \left\{i | \underline{x}_i < e_i^k/\tilde{\lambda} < \bar{x}_i\right\},$$
$$I_+^k = \left\{i | e_i^k/\tilde{\lambda} \geq \bar{x}_i\right\}. \tag{50}$$

(g) Modify the design variables as follows:

$$x_i^{k+1} = \begin{cases} \underline{x}_i & \text{if } i \in I_-^k \\ e_i^k/\tilde{\lambda}^k & \text{if } i \in I^k \\ \bar{x}_i & \text{if } i \in I_+^k \end{cases}, \quad (i = 1, 2, \ldots, N) \tag{51}$$

(h) Determine θ_i^{k+1} using $\partial f/\partial \theta_i = 0$.

(i) Let $k = k + 1$, and repeat (b) to (h) until some convergence criteria are fulfilled.

Obviously, this algorithm can also be extended to deal with the optimization problem with multiconstraints instead of Eq. (19a) in which just one constraint was considered. A discussion about this development will be left to a separate report.

Examples

Three examples will be shown in this section. One is to determine the optimal reinforcements for a given two-story planar frame. The others are to simulate the well-known optimum beam design problems, a simple-supported beam and a fixed-fixed supported beam.

Example 1: Reinforcement Optimization of a Two-Story Planar Frame. In the optimal reinforcement problem, a core structure is specified at the beginning, and it is assumed to be unchanged in the optimization process. As shown in Fig. 3, the design domain is specified as a rectangle, 5.0 in horizontal length and 8.0 in vertical height with two fixed supported boundaries at the bottom of the domain. The design domain is filled by a nonhomogeneous material with the microstructure shown in Fig. 1, where, in the solid portion, Young's modules is $E^0 = 100$, Poisson's ratio $\nu = 0.3$ and mass density $\rho_0 = 1.0 \times 10^{-6}$. A finite element model of the design domain is generated by using 2,560 (40×64) four-node plane quadrilateral finite elements with 2,665 nodes. Consequently, we have 5,330 D.O.Fs. for the structural domain 7,680 design variables for the optimization process.

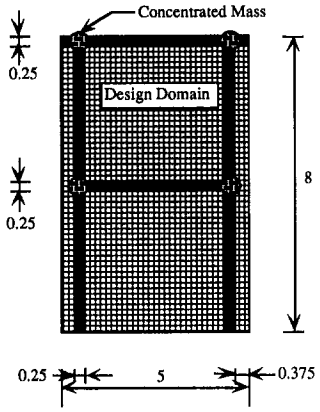

Fig. 3 Optimal reinforcement problem

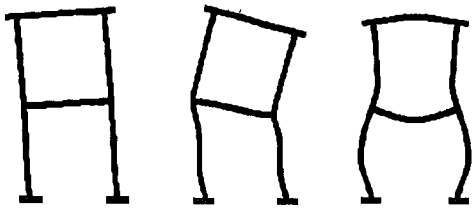

Fig. 4 Three eigenmodes of the core structure

Table 1 Weighting coefficients for the optimization problems

	w_1	w_2	w_3	w_4	w_5
Case 1	1.0	----	----	----	----
Case 2	----	1.0	1.0	----	----
Case 3	----	----	1.0	1.0	----
Case 4	0.01	0.01	0.001	1.0	----
Case 5	0.01	0.01	0.01	0.001	1.0

As shown in Fig. 3, a two-story planar frame with four concentrated masses is given as the core structure, where each concentrated mass is $5.0 \times \rho_0$. Figure 4 shows first, second, and fifth vibration modes of the core structure. These modes correspond to eigenfrequencies of 14.4 Hz, 42.1 Hz, and 136.7 Hz, respectively.

Within the optimization process, the material is added only to reinforce the core structure in the design domain. The constraint of total mass (except the concentrated masses) is specified as $V_0 = 17.0 \times \rho_0$ (the area of whole design domain is 40.0). Five cases, each case is corresponding to an eigenvalue optimization problem, are considered for optimizing the lowest five eigenfrequencies, respectively, using the multieigenvalue optimization technique proposed in this paper. Table 1 shows the weighting coefficients used in these problems, where the shift parameter $\lambda_0 = 0.0$.

As shown in Table 1, case 1 is a single eigenvalue optimization problem. The outer cases are multieigenvalue optimization problems where modes 2 and 3 are used for case 2; modes 3 and 4 for case 3; modes 1, 2, 3, and 4 for case 4; and modes 1, 2, 3, 4 and 5 for case 5.

Table 2 shows the optimal eigenfrequencies obtained in each case. As shown in Table 2, all diagonal terms in the table have the largest value in their columns, respectively. This implies that the ith eigenfrequency has the greatest change in the case i than the other cases where $i = 1, 2, \ldots, 5$. The values of these eigenfrequencies are 50.8 Hz, 140.2 Hz, 163.8 Hz, 269.3 Hz, and 270.7 Hz, respectively. Comparing these values with the initial ones, the improvements obtained in the lowest five eigenfrequencies are 252 percent, 233 percent, 79 percent, 169 percent, and 98 percent, respectively.

Table 2 Optimal eigenfrequencies of the problems

Hz	f_1	f_2	f_3	f_4	f_5
Case 1	50.8 (352%)	109.3 (259%)	116.3 (127%)	171.3 (154%)	183.3 (134%)
Case 2	37.3 (259%)	140.2 (333%)	150.1 (164%)	151.3 (136%)	173.9 (127%)
Case 3	21.5 (149%)	77.3 (183%)	163.8 (179%)	191.7 (172%)	198.7 (145%)
Case 4	35.9 (249%)	94.5 (224%)	100.2 (110%)	269.3 (242%)	270.5 (197%)
Case 5	42.8 (296%)	108.9 (259%)	111.2 (122%)	242.8 (218%)	270.7 (198%)
Initial	14.4	42.1	91.4	111.2	136.7

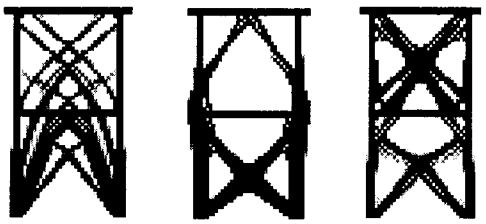

Fig. 5 Optimal structures

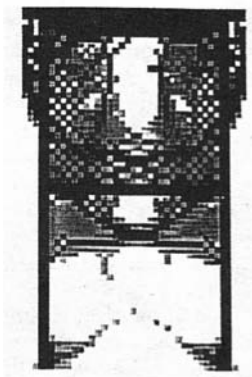

Fig. 6 Final structure of the single-eigenvalue optimization

Three optimal structures of the reinforcement optimization problems are given in Fig. 5. As shown in Fig. 5, the optimal reinforcements are very different if the weighting coefficients are different. By comparing the optimal structures in Fig. 5 with the mode shapes of the initial structure shown in Fig. 4, it is seen that reinforcement is added to resist the largest deformations in the mode shapes. Figure 6 shows a divergent example which used the single eigenvalue optimization technique. It is shown that if just a single mode (in this case, mode 5) is used, the optimization process may be divergent, and finally the optimal structure cannot be obtained. This problem has been overcome by using the multieigenvalue optimization technique proposed in this paper.

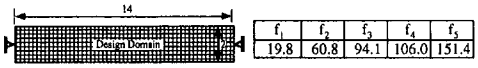

f_1	f_2	f_3	f_4	f_5
19.8	60.8	94.1	106.0	151.4

Fig. 7 Initial structure

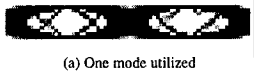

w_1	w_2	w_3	w_4	w_5
--	1.0	--	--	--
f_1	f_2	f_3	f_4	f_5
35.6	179.5	191.5	200.4	207.5

(a) One mode utilized

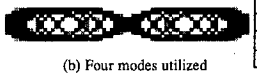

w_1	w_2	w_3	w_4	w_5
--	1.0	1.0	1.0	1.0
f_1	f_2	f_3	f_4	f_5
27.8	175.0	274.0	279.9	409.8

(b) Four modes utilized

Fig. 8 Optimization for the second eigenvalue

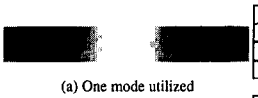

w_1	w_2	w_3	w_4	w_5
--	--	1.0	--	--
f_1	f_2	f_3	f_4	f_5
2.7	16.3	336.1	337.9	340.2

(a) One mode utilized

w_1	w_2	w_3	w_4	w_5
--	--	1.0	1.0	1.0
w_6	w_7			
1.0	1.0			
f_1	f_2	f_3	f_4	f_5
26.1	89.3	282.4	322.1	422.9

(b) Five modes utilized

Fig. 9 Optimization for the third eigenvalue

Example 2: Layout Optimization of a Simple Supported Beam. In the optimal layout problem, only a design domain and boundary conditions are given. As shown in Fig. 7, the design domain is specified as a rectangle, 14.0 in horizontal length and 2.0 in vertical height with two simple supports at the left and right ends. This problem is similar to the well-known shape optimization problem of a simple supported beam (e.g., Olhoff, 1981). The finite element mesh is generated using 700 (70 × 10) finite elements with 781 nodes, we the have 1,582 D.O.Fs. for the structural domain and 2,100 design variables for the optimization process in this problem. As shown in Fig. 7, the lowest five eigenfrequencies of the initial structure are 19.8 Hz, 60.8 Hz, 94.1 Hz, 106.0 Hz, and 151.4 Hz, respectively.

Several cases are considered. In all cases the constraints of total mass are given as $V_0 = 17.0 \times \rho_0$ (the area of whole design domain is 28.0), and the shift parameter λ_0 is assumed zero, Figs. 8 and 9 show the optimal layouts obtained using the technique presented in this paper. Figure 8 shows the results corresponding to the second eigenvalue optimization, where Fig 8(a) is obtained by using the second mode only, Fig. 8(b) modes 2, 3, 4, and 5. As shown in Fig. 8, both cases have similar layouts of the outside, but the topologies of the inside are different. This is because the second eigenvalue dominated the optimization process in both cases, and higher modes gave some contributions in the case 2. Even though the optimal value of the second eigenfrequency may be a little reduced when higher modes are used in the optimization process, the final structure is stronger against higher frequency (Fig. 8(b)), since the higher eigenfrequencies are greatly increased. Therefore, using the multieigenvalue optimization technique makes it possible to design a better structure.

Figure 9 shows the results corresponding to the third eigenvalue. Where Fig. 9(a) is obtained by using the third mode only. As shown in Fig. 9(a), if just a single mode is used, the final structure will be discontinuous. This phenomenon is well known as the "singularity" of the optimal structure (e.g., Olhoff, 1981), but it can be avoided by using the multieigenvalue optimization technique presented in this paper as shown in Fig. 9(b), in which the final structure is obtained by using the five modes (modes 3 to 7).

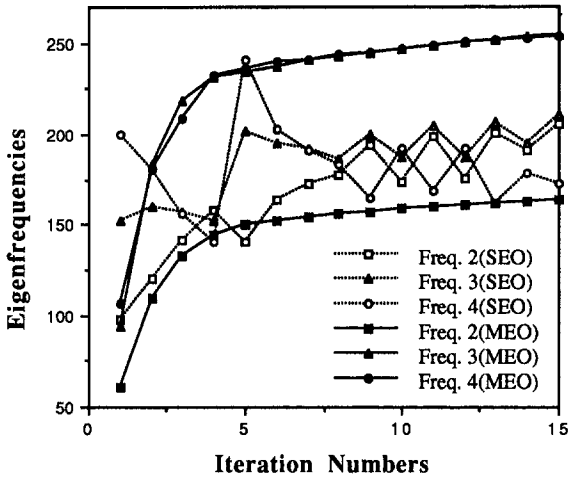

Fig. 10 Changes of eigenfrequencies in the optimization process

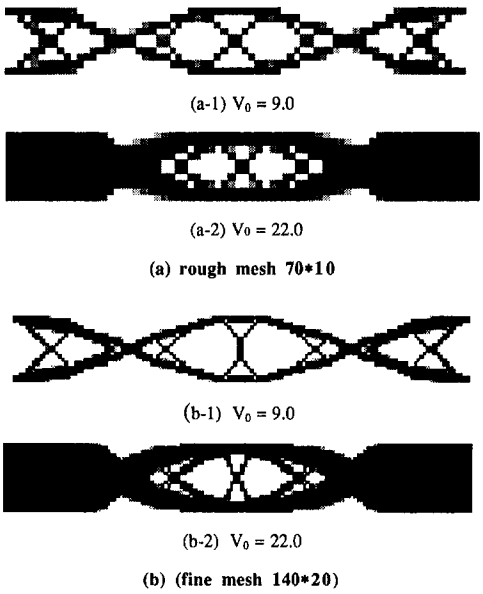

Fig. 11 The optimal structures with respect to various total mass constraints

In order to show the improvement in the convergency of the optimization process, Fig. 10 gives the histories of changes in three lower eigenfrequencies by tracing their modes within the first 15 iteration steps. Dash lines give the histories corresponding to Fig. 8(a), which uses the second mode only for optimizing the second eigenvalue. Thus it is a single eigenvalue optimization (SEO) problem. Solid lines gives the histories corresponding to Fig. 8(b), which uses modes 2–5 for the same purpose. Thus, it is a multieigenvalue optimization (MEO) problem. It is shown that by using the multieigenvalue optimization technique proposed in this paper makes it possible to greatly improve the convergency in the eigenvalue optimization process.

Example 3: Layout Optimization of a Fixed-Fixed Beam. This example is to demonstrate how the optimal structures are changed by different total mass constraints, and to investigate whether or not the results are dependent on the finite element mesh. The problem is to optimize the fundamental eigenfrequency. In this problem, the design domain is speci-

fied same as Fig. 7, but with two fixed supported boundaries at the left and right ends of the design domain and a concentrated mass ($5.0 \times \rho_0$) at the center of the design domain. The problem is similar to the shape optimization problem of a fixed-fixed supported beam with a central mass. Figure 11(a) shows the optimal structures obtained using a rough mesh (70×10), where the total mass constraints are given as $V_0 = 9.0 \times \rho_0$ (Fig. 11(a-1)) and $22.0 \times \rho_0$ (Fig. 11(a-2)), respectively (the area of whole design domain is 28.0). Figure 11(b) shows the results obtained using a fine mesh (140×20), where each finite element used in Fig. 11(a) has been divided into four elements. It is shown that when material is added to the design domain, the optimal structure approaches to a continuum instead of a skeleton, and the results are relatively insensitive to mesh size in this problem.

Conclusion

A new objective function corresponding to multiple eigenvalues has been proposed for improving the solution of the eigenvalue optimization problem. An improved optimization algorithm is then applied to solve the problems. It has been shown that the use of the multieigenvalue optimization technique and the improved updating algorithm can greatly improve the solution, and optimize not only a single eigenvalue but also multiple eigenvalues in a generalized weighted average meaning. The feasibility of the approaches presented in this paper has been substantiated through the examples.

References

Bendsøe, M. P., and Kikuchi, N., 1988, "Generating Optimal Topologies in Structural Design Using a Homogenization Method," *Comput. Methods Appl. Mech. Energ.*, Vol. 71, pp. 197–24.

Bendsøe, M. P., 1989, "Optimal Shape Design as a Material Distribution Problem," *Structural Optimization*, Vol. 1, pp. 193–202.

Diaz, A., and Kikuchi, N., 1992, "Solution to Shape and Topology Eigenvalue Optimization Problems Using a Homogenization Method," *International Journal for Numerical Methods in Engineering*, to appear.

Fleury, C., and Braibant, V., 1986, "Structural Optimization: A New Dual Method Using Mixed Variables," *International Journal for Numerical Methods in Engineering*, Vol. 23, pp. 409–428.

Fleury, C., 1989, "Efficient Approximation Concepts Using Second Order Information," *International Journal for Numerical Methods in Engineering*, Vol. 28, pp. 2041–2058.

Haftka, R. T., and Grandhi, R. V., 1986, "Structural Shape Optimization—A Survey," *Comput. Methods Appl. Mech. Energ.*, Vol. 57, pp. 91–106.

Haftka, R. T., and Gurdal, Z., 1992, "Elements of Structural Optimization," 3rd rev. and expanded ed., Kluwer Academic Publishers, The Netherlands, pp. 283–318.

Ma, Z.-D., and Hagiwara, I., 1991a, "Sensitivity Analysis Methods for Coupled Acoustic-Structural Systems, Part 1: Modal Sensitivities," *AIAA Journal*, Vol. 29, No. 11, pp. 1787–1795.

Ma, Z.-D., and Hagiwara, I., 1991b, "Development of New Mode-Superposition Technique for Truncating the Lower and/or Higher Frequency Modes, 3rd Report, An Application of Eigenmode Sensitivity Analysis Method for Systems with Repeated Eigenvalues," *Transactions of the JSME*, Vol. 57, No. 536C, pp. 1156–1163 (in Japanese); *JSME International Journal*, Series C, Vol. 37, No. 1, pp. 14–20.

Ma, Z.-D., Kikuchi, N., and Hagiwara, I., 1992, "Structural Topology/Shape Optimization for a Frequency Response Problem," *Computational Mechanics*, Vol. 13, No. 3, pp. 157–174.

Olhoff, N., 1981, "Optimization of Transversely Vibrating and Rotating Shafts," *Optimization of Distributed Parameter Structures*, E. J. Haug and J. Cea, eds., Sijthoff and Noordhoff, pp. 177–199.

Olhoff, N., and Taylor, J. E., 1983, "On Structural Optimization," ASME JOURNAL OF APPLIED MECHANICS, Vol. 50, pp. 1134–1151.

Olhoff, N., Bendsøe, M., and Rasmussen, J., 1991, "On CAD-Integrated Structural Topology and Design Optimization," *Comput. Methods Appl. Mech. Energ.*, Vol. 89, pp. 259–279.

Suzuki, K., and Kikuchi, N., 1990, "Generalized Layout Optimization of Shape and Topology in Three-Dimensional Shell Structures," Rept. No. 90-05, Dept. Mich. Engrg. and Appl. Mech., Comp. Mech. Lab., University of Michigan, USA.

Suzuki, K., and Kikuchi, N., 1991, "A Homogenization Method for Shape and Topology Optimization," *Comput. Methods Appl. Mech. Energ.*, Vol. 93, pp. 291–318.

Svanberg, K., 1987, "The Method of Moving Asymptotes—A New Method for Structural Optimization," *International Journal for Numerical Methods in Engineering*, Vol. 24, pp. 359–373.

Study of Transient Coupled Thermoelastic Problems With Relaxation Times

Han-Taw Chen

Hou-Jee Lin

Department of Mechanical Engineering,
National Cheng Kung University,
Tainan, Taiwan 701,
Republic of China

A new hybrid numerical method based on the Laplace transform and control volume methods is proposed to analyze transient coupled thermoelastic problems with relaxation times involving a nonlinear radiation boundary condition. The dynamic thermoelastic model of Green and Lindsay is selected for the present study. The following computational procedure is followed for the solution of the present problem. The nonlinear term in the boundary condition is linearized by using the Taylor's series approximation. Afterward, the time-dependent terms in the linearized equations are removed by the Laplace transform technique, and then the transformed field equations are discretized using the control volume method with suitable shape functions. The nodal dimensionless temperature and displacement in the transform domain are inverted to obtain the actual physical quantities, using the numerical inversion of the Laplace transform method. It is seen from various illustrative problems that the present method has good accuracy and efficiency in predicting the wave propagations of temperature, stress, and displacement. However, it should be noted that the distributions of temperature, stress, and displacement can experience steep jumps at their wavefronts. In the present study, the effects of the relaxation times on these thermoelastic waves are also investigated.

Introduction

The classical theory of thermoelasticity based on the parabolic-type heat conduction equation implies that thermal disturbances propagate with infinite speed through the elastic medium. This prediction may be suitable for most engineering applications; however, it is a physically unacceptable situation, especially at a very low temperature near absolute zero or for extremely short-time responses. Thus, various modified dynamic thermoelastic theories were proposed to analyze problems with "second sound" effects, such as Lord and Shulman (1967) and Green and Lindsay (1972). Lord and Shulman (1967) proposed a new theory based on a modified Fourier's law of heat conduction with one relaxation time. The resulting heat equation becomes hyperbolic, and implies a finite wave speed for the thermal signal. Green and Lindsay (1972) formulated a more rigorous theory of thermoelasticity based on an entropy production inequality. Two relaxation times were introduced in Green and Lindsay's theory for the thermoelastic process. A remarkable feature of this theory is that it does not violate the classical Fourier's law when the material has a center of symmetry at each point. Various problems characterizing these two theories have been investigated, and they reveal some interesting phenomena. These nonclassical theories are often regarded as the generalized dynamic theory of thermoelasticity. Brief reviews of this topic have been reported by Francis (1972), Ignaczak (1981), and Chandrasekharaiah (1986).

The generalized dynamic theory of thermoelasticity is a sophisticated coupled field theory because the coupled displacement and temperature fields must be solved simultaneously. In addition, this thermoelasticity theory again allows thermal disturbances to propagate with finite velocity. Thus, it is difficult to apply analytical methods to investigate such problems except for some special cases. Accordingly, various approximate and numerical methods were proposed to analyze such problems. Norwood and Warren (1969), Sherief (1986), Dhaliwal and Rokne (1988, 1989), and Anwar (1991) applied the integral transform method to investigate such problems with various boundary conditions. However, they obtained only short-time solutions. Öncü and Moodie (1991) used Padé-extended ray series expansion to analyze the generalized thermoelasticity in a semi-infinite medium. It is evident that the above methods can't always provide all the desired informations concerning problems with complicated geometry and variable material properties. This explains why there has been a growing interest in the numerical scheme

Contributed by the Applied Mechanics Division of THE AMERICAN SOCIETY OF MECHANICAL ENGINEERS for publication in the ASME JOURNAL OF APPLIED MECHANICS.

Discussion on this paper should be addressed to the Technical Editor, Professor Lewis T. Wheeler, Department of Mechanical Engineering, University of Houston, Houston, TX 77204-4792, and will be accepted until four months after final publication of the paper itself in the ASME JOURNAL OF APPLIED MECHANICS.

Manuscript received by the ASME Applied Mechanics Division, Jan. 13, 1993; final revision, Aug. 31, 1993. Associate Technical Editor: J. N. Reddy.

for such problems in recent years. Accordingly, various numerical methods have been developed for solving such problems. However, the major difficulty encountered in the numerical solution of such problems is numerical oscillations near the wavefronts of the temperature, displacement, and stress distributions. Prevost and Tao (1983) used the finite element method and the implict-explicit scheme to analyze a dynamic thermoelastic problem in a semi-infinite slab on the basis of Green and Lindsay's dynamic thermoelastic model. They modeled the half-space using two groups of elements in conjunction with the four-node (plane-strain) bilinear isoparametric element. One group consists of 75 equally spaced elements, while the other group consists of 20 equally spaced elements. It is seen that the uncoupled results obtained by Prevost and Tao (1983) did not agree well with the analytical solution. The same problem was solved by Chen and Weng (1988) using the hybrid application of the finite element method and the Laplace transform scheme. Unfortunately, a comparison between their results and those obtained by Prevost and Tao (1983) was not made. The finite element method combined with a time approximation was applied to solve one-dimensional linear thermoelasticity with finite wave speed by Gladysz (1986). Noda (1989) used the Laplace transform method in conjunction with a suggested admissible solution to solve the generalized thermoelastic problem for an infinite solid with a hole. However, these methods (Prevost and Tao, 1983; Gladysz, 1986; Chen and Weng, 1988; Noda, (1989) have not yet been applied to analyze nonlinear transient coupled thermoelastic problems with relaxation times involving a nonlinear radiation boundary condition. The major difficulty encountered in the numerical solution of the present problem is that numerical oscillations in the neighborhood of wavefronts can be found. A recent review on this topic has been given by Chen and Lin (1993).

The purpose of the present study is to provide a new approach for determining a more accurate solution of transient coupled thermoelastic problems with relaxation times involving a case with a nonlinear radiation boundary condition. The effects of surface radiation on the distributions of temperature, stress, and displacement in the medium will also be discussed. To the author's knowledge, there is no such study in the open literature. The mathematical formulation of the present method is as follows. The nonlinear term in the boundary condition is linearized by using the Taylor's series approximation. The Laplace transform method is used to remove the time-dependent terms, and then the transformed field equations are discretized by using the control volume method. The important task of the present method is that the shape functions must carefully be selected from the corresponding field equations in the transform domain. It is seen from various illustrative examples that the present results are more accurate than those of Prevost and Tao (1983) within the context of classical uncoupled thermoelasticity. Moreover, the number of nodes required in the present study is less than those required in Prevost and Tao's numerical scheme (1983). In the present problem, the magnitudes of steep jumps in the distributions of temperature, displacement, and stress depend on the nature of the thermoelastic coupling coefficient, thermal boundary conditions, and thermal relaxation times. Thus, the effects of these parameters on thermoelastic waves will also be investigated.

Mathematical Formulation

The fundamental equations of the linearized thermoelastic theory given by Green and Lindsay (1972) are applied to analyze the present problem. Cartesian tensors are used throughout. The conservation of mass, equation of motion, and energy balance equation are, respectively, given as conservation of mass

$$\rho_0/\rho = 1 + U_{k,k}, \tag{1}$$

equation of motion

$$\rho\ddot{U}_i = \sigma^*_{ij,j} + \rho b_i \tag{2}$$

$$\sigma^*_{ij} = \sigma^*_{ji}, \tag{3}$$

energy balance equation

$$\rho T_0 \dot{S} = -\dot{q}_{k,k} + \rho g \tag{4}$$

where ρ is the density; ρ_0 the reference density; σ^*_{ij} the stress tensor; U_i displacement vector; b_i body force vector; q_k the heat flux vector; T_0 the reference temperature of the natural (stress-free) state of the solid body; S the entropy density; g the heat source per unit volume.

The supersposed dots ($\dot{}$) are used to denote material time differentiation and a comma (,) to denote partial differentiation with respect to the spatial coordinates $xj(j = 1, 2, 3)$. To further derive the following constitutive equations, the absolute temperature T is defined as

$$T = T_0(1 + \omega) \tag{5}$$

where T is the absolute temperature; θ the dimensionless temperature.

The present study follows the constitutive equations given by Prevost and Tao (1983).

$$\sigma^*_{ij} = C_{ijkl}\epsilon_{kl} - \beta_{ij}T_0\left(\theta + t_1\dot{\theta}\right) \tag{6}$$

$$q_i + t_0\dot{q}_i = -K_{ij}T_0\theta_{,j} \tag{7}$$

$$S = S_0 + c\theta + ct_2\dot{\theta} + \beta_{ij}\epsilon_{kl}/\rho \tag{8}$$

where C_{ijkl} is the tensor of elastic moduli; ϵ_{ij} the strain tensor ($\epsilon_{kl} = (U_{k,l} + U_{l,k})/2$); β_{ij} tensor of thermal moduli; K_{ij} the tensor of thermal conductivity; c the specific heat; t_0 the relaxation time (proposed by Lord and Shulman, 1967); t_1 and t_2 the relaxation time (proposed by Green and Lindsay, 1972). When t_0, t_1, and t_2 vanish, Eqs. (6)–(8) reduce to the classical coupled theory. In Lord and Shulman's theory, $t_1 = t_2 = 0$ and Fourier's law of heat conduction is modified by introducing the relaxation time t_0. In Green and Lindsay's theory, $t_0 = 0$ and both the Duhamel–Neuman relations and entropy density function, respectively, shown in Eqs. (6) and (8) are modified by introducing two relaxation times t_1 and t_2.

Eliminating S, q_i, and σ^*_{ij} by using Eqs. (2)–(5) leads to the following linear coupled field equations in terms of displacement U_i and temperature θ:

$$\rho\ddot{U}_i + \beta_{ij}T_0\left(\theta + t_1\dot{\theta}\right)_{,j} - \left(C_{ijkl}U_{k,l}\right)_{,j} = \rho b_i \tag{9}$$

$$\rho c(t_0 + t_2)\ddot{\theta} + \rho c\dot{\theta} + \beta_{ij}\left(\dot{U}_{i,j} + t_0\ddot{U}_{i,j}\right) - \left(K_{ij}\theta_{,j}\right)_{,i} = \rho\left(g + t_0\dot{g}\right)/T_0. \tag{10}$$

For the case of isotropic materials, Eqs. (6) and (8) can be reduced to the following forms:

$$\sigma^*_{ij} = \lambda\delta_{ij}\epsilon_{kk} + 2\mu\epsilon_{ij} - \beta T_0\left(\theta + t_1\dot{\theta}\right)\delta_{ij} \tag{11}$$

$$\rho S = \rho c\left(\theta + t_2\dot{\theta}\right) + \beta\epsilon_{kk} \tag{12}$$

where λ and μ are Lame's constant; δ_{ij} the Kronecker delta.

Thus, for isotropic materials and in the absence of body force and heat sources, the field Eqs. (9) and (10) can be simplified as

$$\rho\ddot{U}_i - (\lambda + \mu)U_{j,ji} - \mu U_{i,jj} + T_0\left(\beta\theta + t_1\beta\dot{\theta}\right)_{,i} = 0 \tag{13}$$

$$\rho c(t_0 + t_2)\ddot{\theta} + \rho c\dot{\theta} - K\theta_{,ii} + \beta\left(\dot{U}_{i,i} + t_0\ddot{U}_{i,i}\right) = 0. \tag{14}$$

For the convenience of analysis, the governing Eqs. (13) and (14) will be transformed into dimensionless forms. To do this, the following dimensionless parameters are introduced:

$$L = \alpha/C_s \qquad C_s^2 = (\lambda + 2\mu)/\rho \qquad \eta = x/L \qquad \xi = \alpha t/L^2$$

$$\alpha = K/\rho c \qquad \tau_0 = \alpha t_0/L^2 \qquad \tau_1 = \alpha t_1/L^2 \qquad \tau_2 = \alpha t_2/L^2$$

$$\sigma_x = \sigma_x^*/\beta T_0 \qquad \beta = (3\lambda + 2\mu)\alpha_t$$

$$u = (\lambda + 2\mu)U/(\beta L T_0)\,\delta = \beta^2 T_0/\rho c(\lambda + 2\mu) \tag{15}$$

where δ is the linear thermoelastic coupling coefficient; C_s the speed of the elastic stress wave; α the thermal diffusivity; and α_t the coefficient of linear thermal expansion of the material.

With these dimensionless parameters, Eqs. (13)–(14) are then transformed into a set of the dimensionless forms

$$\frac{\partial^2 u}{\partial \xi^2} + \frac{\partial \theta}{\partial \eta} + \tau_1 \frac{\partial^2 \theta}{\partial \xi \partial \eta} - \frac{\partial^2 u}{\partial \eta^2} = 0 \tag{16}$$

$$(\tau_0 + \tau_2)\frac{\partial^2 \theta}{\partial \xi^2} + \frac{\partial \theta}{\partial \xi} + \delta\left(\frac{\partial^2 u}{\partial \xi \partial \eta} + \tau_0 \frac{\partial^3 u}{\partial \xi^2 \partial \eta}\right) - \frac{\partial^2 \theta}{\partial \eta^2} = 0. \tag{17}$$

It is evident that the problem is uncoupled when $\delta = 0$. Under this mathematical formulation, the speed of the temperature wave may be computed as (Prevost and Tao, 1983)

$$C_t = \sqrt{\frac{K}{\rho c(t_0 + t_2)}} \tag{18}$$

Thus C_t is infinite for the case of the classical thermoelastic model, i.e., $t_0 = t_2 = 0$. For the case of Green and Lindsay's thermoelastic model, C_t is finite. Based on thermodynamical arguments, Green (Prevost and Tao, 1983) showed that the first relaxation time t_1 is restricted by $t_1 \geq t_2 \geq 0$. Thus, the assumption of $t_1 = t_2$ is made in the present study. Using the definition of the dimensionless parameters for C_t, τ_0, τ_2, and L, as shown in Eq. (15), it follows that

$$\tau_0 + \tau_2 = C_s^2/C_t^2 \tag{19}$$

where τ_0 or τ_2 can be denoted as the square ratio of the elastic and thermal wave speeds. Thus, $\tau_0 + \tau_2 > 1$ implies that the elastic wave speed is faster than the thermal wave speed.

Numerical Analysis

The computational procedures of the present method are that the nonlinear term in the radiative boundary condition is linearized by using the Taylor's series approximation. Afterward, the time-dependent terms in the linearized differential equations are removed by the Laplace transform scheme, and then the field equations and boundary conditions in the transform domain are discretized using the control volume method with suitable shape functions. The dimensionless temperature, axial displacement, and axial stress in the transform domain are inverted to obtain physical results by using the inversion scheme of Hoing and Hirdes (1984). Assume that the initial conditions in the present study can be expressed as

$$\theta(0,\eta) = 0, \qquad \frac{\partial \theta}{\partial \xi}(0,\eta) = 0,$$

$$u(0,\eta) = 0, \qquad \frac{\partial u}{\partial \xi}(0,\eta) = 0. \tag{20}$$

The Laplace transforms of Eqs. (16)–(17) with respect to ξ are, respectively,

$$\frac{\partial^2 \tilde{u}}{\partial \eta^2} - B\frac{\partial \tilde{\theta}}{\partial \eta} - A\tilde{u} = 0 \tag{21}$$

$$\frac{\partial^2 \tilde{\theta}}{\partial \eta^2} - E\frac{\partial \tilde{u}}{\partial \eta} - C\tilde{\theta} = 0 \tag{22}$$

where s is the Laplace transform parameter. $A = s^2$, $B = s\tau_1 + 1$, $C = s^2(\tau_0 + \tau_2) + s$, and $E = \delta(s + \tau_0 s^2)$. $\tilde{\theta}$ and $\tilde{u}$ are, respectively, defined as

$$\tilde{\theta}(s,\eta) = \int_0^\infty e^{-s\xi}\theta(\xi,\eta)d\xi$$

$$\tilde{u}(s,\eta) = \int_0^\infty e^{-s\xi}u(\xi,\eta)d\xi. \tag{23}$$

The discretized forms of Eqs. (21)–(22) can be obtained by using the control volume method. The shape functions can arbitrarily be chosen for most problems. However, the selection of the shape functions is an important task for the present study because there exist steep jumps in the distributions of temperature, axial displacement, and axial stress. Otherwise, a poor selection of the shape functions will affect the accuracy of the numerical results. This fact has been demonstrated in the work of Chen and Lin (1993). The following procedure will express how to obtain the suitable shape functions of the present problem. Thus, the associated homogeneous second-order ordinary differential equations of Eqs. (21)–(22) are introduced.

$$\frac{\partial^2 \tilde{u}}{\partial \eta^2} - A\tilde{u} = 0 \tag{24}$$

$$\frac{\partial^2 \tilde{\theta}}{\partial \eta^2} - C\tilde{\theta} = 0 \qquad \eta_i \leq \eta \leq \eta_{i+1} \qquad i = 1, 2, \ldots, (n-1) \tag{25}$$

where $\eta_1 = 0$ and $\eta_n = 1$.

Under this circumstance, the following simple notations must be used:

$$\tilde{\theta}(s,\eta_i) = \tilde{\theta}_i, \quad \tilde{\theta}(s,\eta_{i+1}) = \tilde{\theta}_{i+1}, \quad \tilde{u}(s,\eta_i) = \tilde{u}_i, \quad \text{and} \quad \tilde{u}(s,\eta_{i+1}) = \tilde{u}_{i+1} \tag{26}$$

The analytical solutions of Eqs. (24)–(25) in the interval $[\eta_i, \eta_{i+1}]$ with the boundary conditions (26) are, respectively,

$$\tilde{u}(s,\eta) = \frac{1}{\sinh(\sqrt{A}\,l)}\left(\sinh\sqrt{A}\,(\eta_{i+1} - \eta)\,\tilde{u}_i + \sinh\sqrt{A}\,(\eta - \eta_i)\tilde{u}_{i+1}\right) = N_1(\eta_{i+1})\tilde{u}_i + N_2(\eta_i)\tilde{u}_{i+1} \tag{27}$$

$$\tilde{\theta}(s,\eta) = \frac{1}{\sinh(\sqrt{C}\,l)}\left(\sinh\sqrt{C}\,(\eta_{i+1} - \eta)\tilde{\theta}_i + \sinh\sqrt{C}\,(\eta - \eta_i)\tilde{\theta}_{i+1}\right) = M_1(\eta_{i+1})\tilde{\theta}_i + M_2(\eta_i)\tilde{\theta}_{i+1} \tag{28}$$

where $l = \eta_{i+1} - \eta_i$ denotes the distance between two nodes and is uniform in the present study; $N_i(z)$ and $M_i(z)$, $i = 1, 2$, are denoted as the hyperbolic shape functions and are, respectively, given as

$$N_1(z) = \frac{\sinh\sqrt{A}\,(z - \eta)}{\sinh(\sqrt{A}\,l)} \qquad N_2(z) = \frac{\sinh\sqrt{A}\,(\eta - z)}{\sinh(\sqrt{A}\,l)}$$

$$M_1(z) = \frac{\sinh\sqrt{C}\,(z - \eta)}{\sinh(\sqrt{C}\,l)} \qquad M_2(z) = \frac{\sinh\sqrt{C}\,(\eta - z)}{\sinh(\sqrt{C}\,l)}. \tag{29}$$

Similarly, the analytical solutions of Eqs. (24)–(25) in the interval $[\eta_{i-1}, \eta_i]$ can also be obtained as

$$\tilde{u}(s, \eta) = N_1(\eta_i)\tilde{u}_{i-1} + N_2(\eta_{i-1})\tilde{u}_i \quad (30)$$

$$\tilde{\theta}(s, \eta) = M_1(\eta_i)\tilde{\theta}_{i-1} + M_2(\eta_{i-1})\tilde{\theta}_i. \quad (31)$$

Integrations of Eqs. (21)–(22) within the ith control volume $[\eta_{i-1/2}, \eta_{i+1/2}]$ are, respectively,

$$\int_{\eta_{i-1/2}}^{\eta_{i+1/2}} \left[\frac{\partial^2 \tilde{u}}{\partial \eta^2} - B\frac{\partial \tilde{\theta}}{\partial \eta} - A\tilde{u} \right] d\eta = 0 \quad (32)$$

$$\int_{\eta_{i-1/2}}^{\eta_{i+1/2}} \left[\frac{\partial^2 \tilde{\theta}}{\partial \eta^2} - E\frac{\partial \tilde{u}}{\partial \eta} - C\tilde{\theta} \right] d\eta = 0 \quad (33)$$

where $\eta_{i+1/2} = (\eta_{i+1} + \eta_i)/2$ and $\eta_{i-1/2} = (\eta_{i-1} + \eta_i)/2$.

Performing the integration produces the following results.

$$\left.\frac{d\tilde{u}}{d\eta}\right|_{\eta_{i+1/2}} - \left.\frac{d\tilde{u}}{d\eta}\right|_{\eta_{i-1/2}} - A\int_{\eta_{i-1/2}}^{\eta_{i+1/2}} \tilde{u} d\eta - B\tilde{\theta}\Big|_{\eta_{i-1/2}}^{\eta_{i+1/2}} = 0 \quad (34)$$

and

$$\left.\frac{d\tilde{\theta}}{d\eta}\right|_{\eta_{i+1/2}} \left.\frac{d\tilde{\theta}}{d\eta}\right|_{\eta_{i-1/2}} - C\int_{\eta_{i-1/2}}^{\eta_{i+1/2}} \tilde{\theta} d\eta - E\tilde{u}\Big|_{\eta_{i-1/2}}^{\eta_{i+1/2}} = 0 \quad (35)$$

Inserting the approximations of $\tilde{\theta}$ and $\tilde{u}$, as shown in Eqs. (27), (28), (30), and (31), and evaluating the resulting integrals produces the following discretized forms:

$$\tilde{u}_{i-1} - 2\cosh\sqrt{A}\,l\tilde{u}_i + \tilde{u}_{i+1} - P\left(\tilde{\theta}_{i+1} - \tilde{\theta}_{i-1}\right) = 0 \quad (36)$$

$$\tilde{\theta}_{i-1} - 2\cosh\sqrt{C}\,l\tilde{\theta}_i + \tilde{\theta}_{i+1} - R\left(\tilde{u}_{i+1} - \tilde{u}_{i-1}\right) = 0 \quad (37)$$

where

$$P = \frac{B\sinh\left(\sqrt{A}\,l\right)}{2\sqrt{A}\,\cosh\left(\sqrt{C}\,l/2\right)}$$

and

$$R = \frac{E\sinh\left(\sqrt{C}\,l\right)}{2\sqrt{C}\,\cosh\left(\sqrt{A}\,l/2\right)}.$$

The arrangement of Eqs. (36)–(37) in conjunction with the prescribed boundary conditions yields the following vector-matrix equation.

$$[K]\{\phi\} = \{F\} \quad (38)$$

where $[K]$ denotes a $(2n \times 2n)$ band matrix with complex numbers; $\{\phi\}$ a $(2n \times 1)$ vector representing the unknown dimensionless nodal temperature and displacement in the transform domain : and $\{F\}$ a $(2n \times 1)$ vector representing the forcing terms. The direct Gauss elimination method is used to determine $\tilde{\theta}_i$ and $\tilde{u}_i$, and then the numerical inversion of the Laplace transform (Honig and Hirdes, 1984) is applied to invert them to the physical quantities θ_i and u_i.

Illustrative Examples

In the following, two different examples are presented for demonstrating the accuracy and efficiency of the present numerical scheme for the dynamic coupled thermoelasticity problems with relaxation times involving a nonlinear boundary condition. All the computations are performed on a PC with an 80486 microprocessor, and the program is written in FORTRAN.

Example 1: Half-Space Subject to Surface Heating. This problem considered is a one-dimensional generalized thermoelasticity problem in a semi-infinite solid which is subjected to surface heating on its traction-free boundary, $x = 0$. Suddenly, the wall at $x = 0$ is impulsively stepped to a fixed temperature $2T_0$. Thus the dimensionless boundary conditions for this problem can be expressed as

$$\theta(\xi,0) = 1 \qquad \sigma_x(\xi,0) = 0$$

$$\theta(\xi,\eta) = 0 \qquad \sigma_x(\xi,\eta) = 0 \text{ as } \eta \to \infty. \quad (39)$$

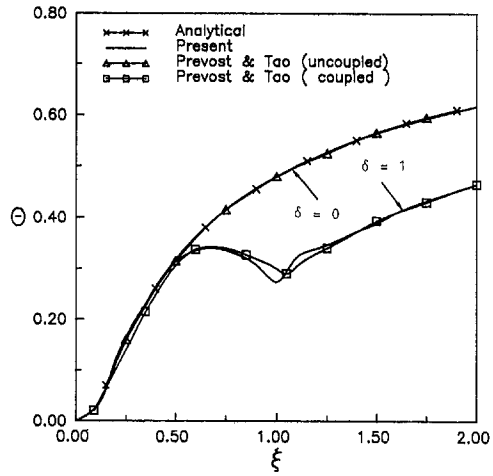

Fig. 1(a) Comparison of the dimensionless temperature at $\eta = 1$

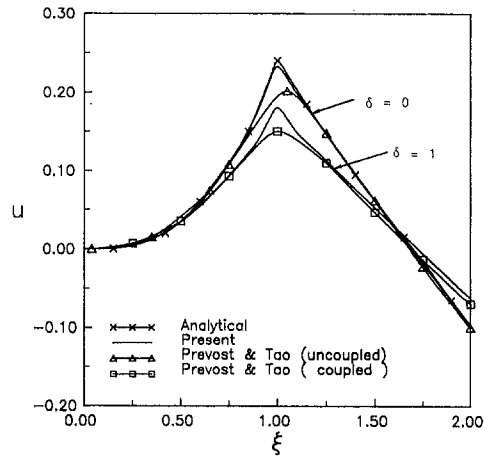

Fig. 1(b) Comparison of the dimensionless axial displacement at $\eta = 1$

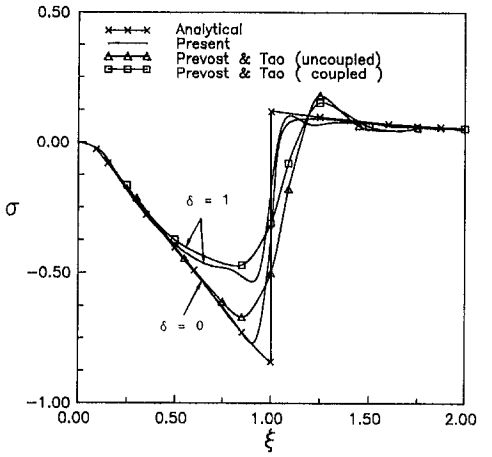

Fig. 1(c) Comparison of the dimensionless axial stress at $\eta = 1$

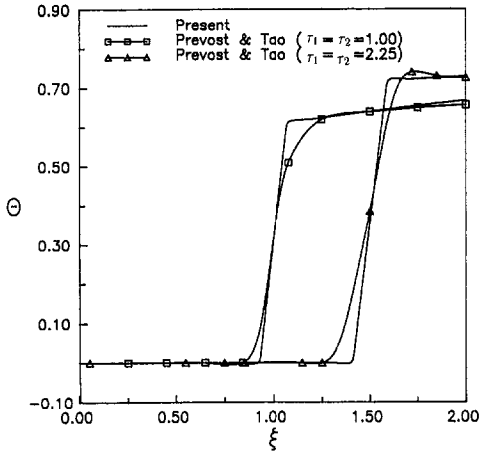

Fig. 2(*a*) Comparison of the dimensionless temperature at $\eta = 1$ with two relaxation times

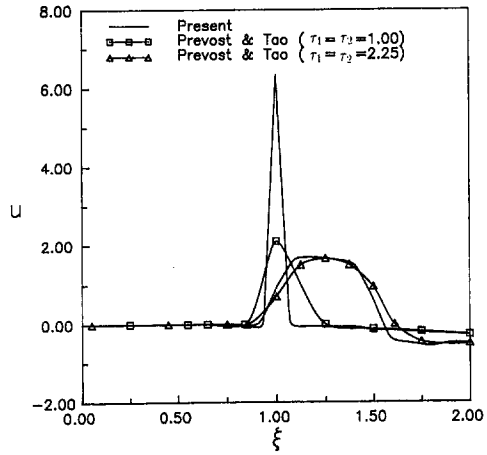

Fig. 2(*b*) Comparison of the dimensionless axial displacement at $\eta = 1$ with two relaxation times

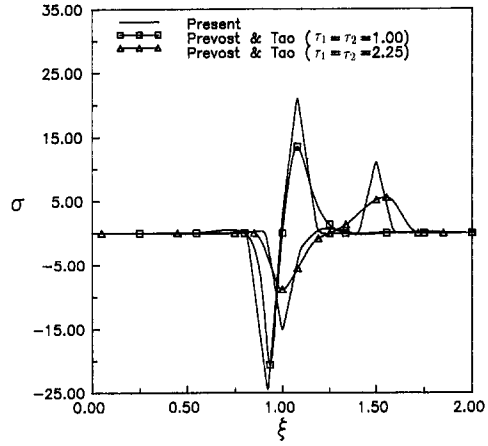

Fig. 2(*c*) Comparison of the dimensionless axial stress at $\eta = 1$ with two relaxation times

The same problem was investigated numerically by Prevost and Tao (1983), Chen and Weng (1988), and Dhaliwal and Rokne (1989). Sternberg and Chakravorty (1959) investigated this problem analytically within the context of the classical coupled thermoelasticity using the Laplace transform method. Figure 1 show a comparison of the dimensionless temperature, axial displacement, and axial stress at $\eta = 1$ among the analytical solutions (1959), results of Prevost and Tao (1983), and present results. It is seen that the present results have better agreement with the analytical solutions than those of Prevost and Tao (1983) for the uncoupled case ($\delta = 0$), especially near the wavefronts. Comparison between the present results and those of Prevost and Tao (1983) for the coupled case ($\delta = 1$) with the classical thermoelastic model is also shown in Fig. 1. It is seen from Prevost and Tao's numerical results that the axial displacement and axial stress are underpredicted and some stress oscillations occur in the vicinity of $\xi = 1$. To damp out the stress oscillations in their scheme, they introduced artificial numerical damping. Figure 1 shows the effects of the thermoelastic coupling coefficient on the response of the thermoelastic system. It is evident that its effect on the responses is significant near the wave fronts though realistic values of δ are small for most metal materials ($\delta = 10^{-2} \sim 10^{-1}$). On the other hand, in classical coupled thermoelastical problems the coupling effect is felt only in the vicinity of the wavefronts. Figure 2 show a comparison of the dimensionless temperature, axial stress between the present results and those of Prevost and Tao (1983) for the uncoupled problem with Green and Lindsay's thermoelastic model. The effects of various relaxation times are also shown in Fig. 2 where $\tau_1 = \tau_2 = 1$ and $\tau_1 = \tau_2 = 2.25$, i.e., $C_t = C_s$ and $C_t = 2C_s/3$, are selected. It is seen from Figs. 1–2 that the incorporation of the first and second relaxation times drastically affects the responses and the magnitudes of steep jumps. It can also be found that there occur two waves propagating with different but finite speeds. This result can be explained from the definition of τ_2 shown in Eq. (19). Equation (19) demonstrates that the elastic wave speed is faster than the thermal wave speed for $\tau_2 > 1$. Nevertheless, the propagation speed of the thermal wave is faster than that of the elastic wave for $\tau_2 < 1$. In accordance with the comparative results of Fig. 1 for the classical thermoelastic model, the present method should have better accuracy than Prevost and Tao's numerical scheme even for the problem with Green and Lindsay's thermoelastic model. In most problems of elastic wave propagation, the conditions prevailing at the wavefronts are of great importance. The steep jumps at the wavefronts not only control the behaviors behind the wavefronts, but are usually critical from a technical standpoint because they are most likely to result in spallation or fracture of the material. It is worth mentioning that the 51-node and 101-node modelings with uniform space size are required for obtaining the numerical results respectively shown in Fig. 1 and Figs. 2 – 3. Obviously, the number of nodes in the present study is less than those in Prevost and Tao's numerical scheme (1983). The numerical results of the dimensionless temperature, axial displacement, and axial stress for the coupled problem with $\delta = 0.02$ and $\tau_1 = \tau_2 = 1$ are shown in Fig. 3. It is seen that the magnitudes of steep jumps in the distributions of displacement and stress for the uncoupled case are larger than those for the coupled case ($\delta = 0.02$). As described in the problem with the classical thermoelastic model, the coupling coefficient for the problem with Green and Lindsay's thermoelastical model is still not a negligible effect even for most metal materials.

Example 2: Half-Space with Surface Radiation. Most previous works were restricted to linear generalized thermoelastic problems. Few investigators analyzed nonlinear problems associated with nonlinear thermal boundary conditions. Thus, Example 2 investigates the same problem as the first example except that the left boundary surface at $x = 0$ dissipates heat by radiation into the ambient at temperature T_∞. The main purpose of this study is to illustrate the efficiency of the present method for such a problem. Accordingly, the thermal boundary condition at $x = 0$ can be written as

$$q = \alpha_s \sigma \left(T_\infty^4 - T^4\right) \qquad \text{at } x = 0 \qquad (40)$$

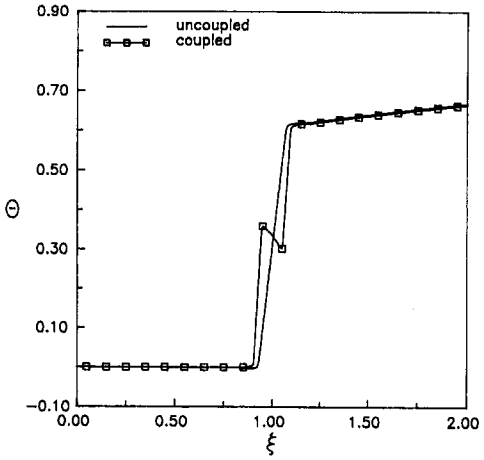

Fig. 3(a) Comparison of the dimensionless temperature at $\eta = 1$ with two relaxation times and $\delta = 0.02$

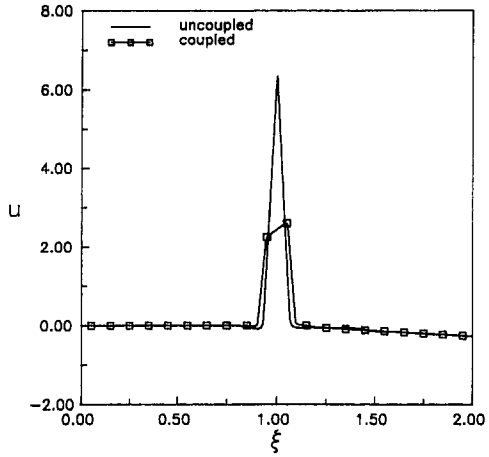

Fig. 3(b) Comparison of the dimensionless axial displacement at $\eta = 1$ with two relaxation times and $\delta = 0.02$

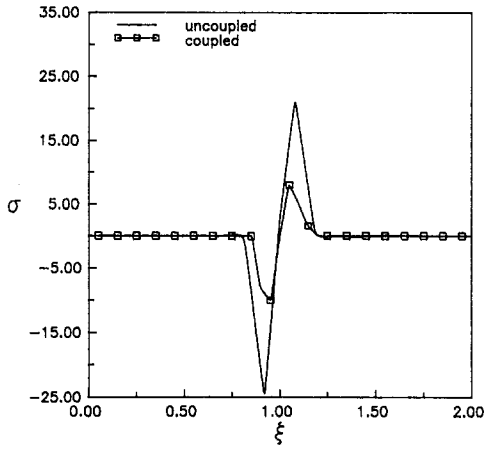

Fig. 3(c) Comparison of the dimensionless axial stress at $\eta = 1$ with two relaxation times and $\delta = 0.02$

where α_s is the surface absorptivity and σ is the Stefan – Boltzmann constant.

The following dimensionless parameters will be introduced in order to transform Eq. (40) into a dimensionless form

$$Rc = \frac{a_s \sigma L T_0^3}{K} \qquad Q = \frac{qL}{T_0 K}. \tag{41}$$

The physical significance of Rc is the ratio of conduction to radiation flux (Glass and Özisik, 1985). In Eq. (41), the value of Rc is a parameter that affects the linearity of the problem. Thus, a small value of Rc corresponds to a negligible amount of radiative transfer at $\eta = 0$, while a large value of Rc implies strong radiation. This implies that the problem for a large value of Rc is extremely nonlinear. $Rc = 0$ implies that there is no radiation, and the boundary condition (40) becomes linear.

For simplicity, we take $T_\infty = 0$. Thus, the dimensionless form of Eq. (40) in conjunction with Eqs. (5) and (41) is

$$Q = -\mathrm{Rc}(1 + \theta)^4 \qquad at\ \eta = 0. \tag{42}$$

Linearizing the nonlinear term $(1 + \theta)^4$ using the Taylor's series approximation leads to the following linearized form of the boundary condition (42) as

$$Q = -Rc(1 - 3\bar{\theta} + 4\theta)(1 + \bar{\theta})^3 \qquad at\ \eta = 0 \tag{43}$$

where $\bar{\theta}$ is the previously calculated surface temperature.

The Laplace transform of Eq. (43) is

$$\tilde{Q} = -Rc\left(\frac{1 - 3\bar{\theta}}{s} + 4\bar{\theta}\right)(1 + \theta)^3. \tag{44}$$

Again, the dimensionless form of Eq. (7) with the dimensionless parameters shown in Eqs. (15) and (41) is

$$Q + \tau_0 \frac{\partial Q}{\partial \xi} = -\frac{\partial \theta}{\partial \eta}. \tag{45}$$

Thus, the Laplace transform of Eq. (45) with respect to ξ is

$$(1 + \tau_0 s)\tilde{Q} = -\frac{\partial \tilde{\theta}}{\partial \eta} \tag{46}$$

Substituting Eqs. (28) and (44) into Eq. (46) produces the following discretized form at $\eta = 0$:

$$-\left[\cosh\left(\sqrt{C}\,l\right) + 4ZF\left(1 + \bar{\theta}_1\right)^3\right]\tilde{\theta}_1 + \tilde{\theta}_2 = \frac{ZF}{s}\left(1 - 3\bar{\theta}_1\right)\left(1 + \bar{\theta}_1\right)^3 \tag{47}$$

where $Z = \dfrac{Rc \sinh\left(\sqrt{C}\,l\right)}{\sqrt{C}}$ and $F = (1 + \tau_0 s)$.

It should be noted that Eq. (38) is still linear simultaneous equations for Example 2. An initial guess of the first nodal temperature at a specific dimensionless time ξ_s, $\bar{\theta}_1$, is given, and then $[K]$ and $\{F\}$ can be calculated. Thus, the nodal dimensionless temperature θ_i and displacement u_i can be obtained by using the application of the direct Gauss elimination method and the numerical inversion of the Laplace transform. The updated value of θ_1 is used to calculate $[K]$ and $\{F\}$ for iteration. This computational procedure is performed repeatedly until the relative error between the current nodal temperature and the value at the previous iteration is less than a value of tolerance of 10^{-4}. In the present computation, four iterations are sufficient for obtaining a convergent result. The detailed illustration can review the work of Chen and Lin (1991). Three different values of Rc considered in this study ranged from 1.0 to 10.0. The case of $Rc = 0$ corresponds to no surface radiation. Thus, this case is not shown in Figs. 4–5. Figures 4–5 show the distributions of the dimensionless temperature, axial displacement, and axial stress at $\delta = 0.0168$, $\xi = 1$, 2, and $Rc = 1$, 5, 10 for $\tau_1 = \tau_2 = 0.64$ and $\tau_1 = \tau_2 = 1.5625$. It is seen that the maximum peak value of the axial stress σ_x declines with decreasing Rc at $\xi = 1$, 2, . In other words, the stronger the surface radiation, the larger the peak value of σ_x. These two figures also show that the peak value of σ_x decreases with increasing value of ξ.

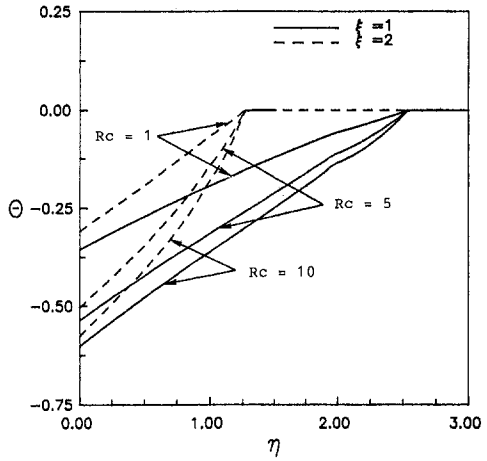

Fig. 4(*a*) Distribution of the dimensionless temperature at $\xi = 1, 2$ for $\tau_1 = \tau_2 = 0.64$, $\delta = 0.0168$, and various *Rc*

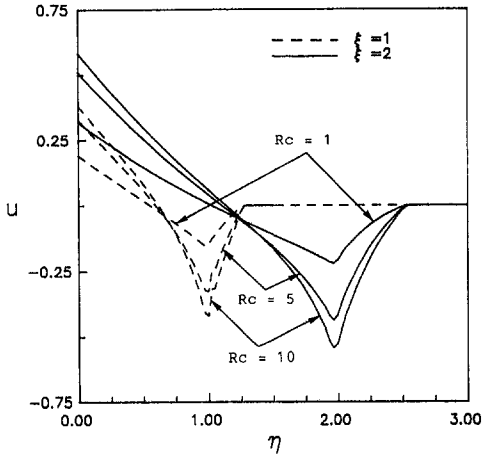

Fig. 4(*b*) Distribution of the dimensionless axial displacement at $\xi = 1, 2$ for $\tau_1 = \tau_2 = 0.64$, $\delta = 0.0168$, and various *Rc*

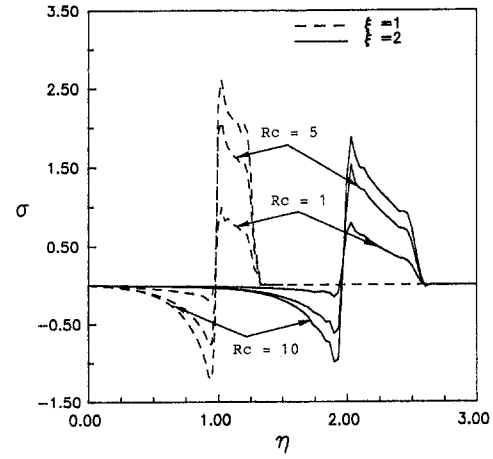

Fig. 4(*c*) Distribution of the dimensionless axial stress at $\xi = 1, 2$ for $\tau_1 = \tau_2 = 0.64$, $\delta = 0.0168$, and various *Rc*

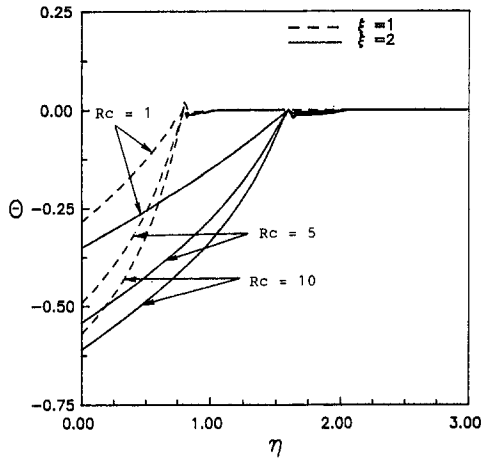

Fig. 5(*a*) Distribution of the dimensionless temperature at $\xi = 1, 2$ for $\tau_1 = \tau_2 = 1.5625$, $\delta = 0.0168$, and various *Rc*

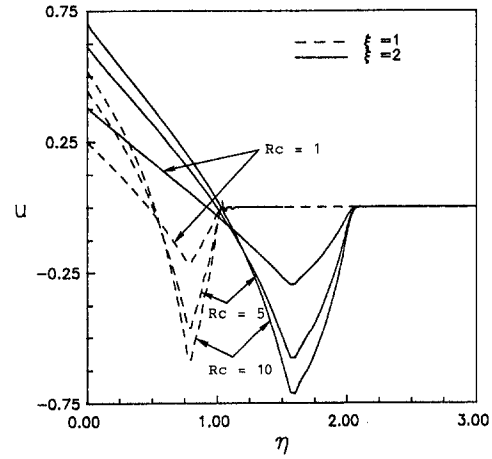

Fig. 5(*b*) Distribution of the dimensionless axial displacement at $\xi = 1, 2$ for $\tau_1 = \tau_2 = 1.5625$, $\delta = 0.0168$, and various *Rc*

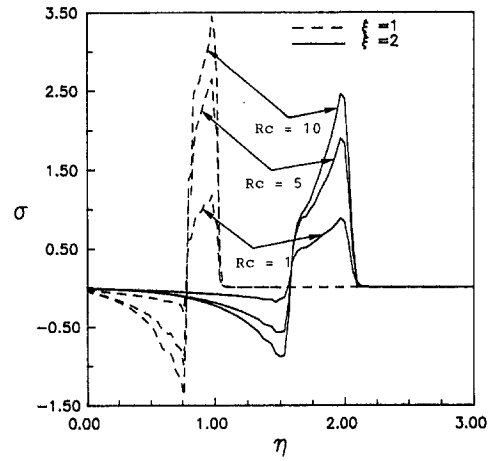

Fig. 5(*c*) Distribution of the dimensionless axial stress at $\xi = 1, 2$ for $\tau_1 = \tau_2 = 1.5625$, $\delta = 0.0168$, and various *Rc*

Figures 4–5 also show that there occur two waves propagating with different but finite speeds. The propagation speed of the elastic wave is faster than that of the thermal wave for $\tau_2 > 1$. An interesting phenomenon can be found. Namely, the larger the value of ξ, the wider the zone between two steep jumps in the axial stress distribution.

These findings shown in Figs. 4–5 were not reported in the past. Thus, a comparison of the numerical results using the 51 and 101 modeling nodes is made. No significant differences are observed in the comparisons for these two different models. This conclusion implies that the present method can successfully be applied to solve such a problem with surface radiation.

Conclusions

The hybrid application of the Laplace transform and control volume methods in conjunction with suitable shape functions is successfully applied to analyze the generalized thermoelastic problem involving a nonlinear case with surface radiation. The suitable shape functions are obtained from the associated homogenous equations in the transform domain. It is seen from results of two different illustrative problems that the present method gives both oscillation-free and highly accurate results for the present problems. The present study only gives an indication of basic procedures for such problems. In contrast with the time-step integration method, the present method doesn't need to consider the restrictions on the permissible time-step and stability which interfere with the efficiency of computation.

It is found from the present study that the magnitudes of steep jumps occurring in the wave propagations of temperature, axial displacement, and axial stress depend on the values of the coupling coefficients and relaxation times, etc. At the same time, it can also be seen that there occur two waves propagating with different but finite speeds for problems with Green and Lindsay's dynamic thermoelastic model.

References

Anwar, M. N. Y., 1991, "Problem in Generalized Thermoelasticity for a Half-Space Subject to Smooth Heating of Its Boundary," *Journal of Thermal Stresses*, Vol. 14, pp. 241–254.

Chandrasekharaiah, D. S., 1986, "Thermoelasticity with Second Sound: A Review," *Appl. Mech. Rev.*, Vol. 39, pp. 355–376.

Chen, H. T., and Lin, J. Y., 1991, "Hybrid Laplace Transform Technique for Nonlinear Transient Thermal Problems," *Int. J. Heat Mass Transfer*, Vol. 34, pp. 1301–1308.

Chen, H. T., and Lin, J. Y., 1993, "Numerical Analysis for Hyperbolic Heat Conduction," *Int. J. Heat Mass Transfer*, Vol. 36, pp. 2891–2898.

Chen, T. C., and Weng, C. I., 1988, "Generalized Coupled Transient Thermoelastic Plane Problems by Laplace Transform/Finite Element Method," ASME JOURNAL OF APPLIED MECHANICS, Vol. 55, pp. 377–382.

David, D., and Tao, D., 1989, "A Numerical Technique for Dynamic Coupled Thermoelasticity Problems with Relaxation Times," *Journal of Thermal Stresses*, Vol. 12, pp. 483–487.

Dhaliwal, R. S., and Rokne, J. G., 1988, "One-Dimensional Generalized Thermoelastic Problems for a Half-Space," *Journal of Thermal Stresses*, Vol. 11, pp. 257–271.

Dhaliwal, R. S., and Rokne, J. G., 1989, "One-Dimensional Thermal Shock Problem with Two Relaxation Times," *Journal of Thermal Stresses*, Vol. 12, pp. 259–279.

Falques, A., 1982, "Thermoelasticity and Heat Conduction with Memory Effects," *Journal of Thermal Stresses*, Vol. 5, pp. 145–160.

Francis, P. H., 1972, "Thermo-mechanical Effects in Elastic Wave Propagation: A Survey," *Journal of Sound Vibration*, Vol. 21, pp. 181–192.

Gladysz, J., 1986, "Approximate One-Dimensional Solution in Linear Thermoelasticity with Finite Wave Speed," *Journal of Thermal Stresses*, Vol. 9, pp. 45–57.

Glass, D. E., and Özisik, 1985, "Hyperbolic Heat Conduction with Surface Radiation," *Int. J. Heat Mass Transfer*, Vol. 28, pp. 1823–1830.

Green, A. E., and Lindsay, K. E., 1972, "Thermoelasticity," *Journal of Elasticity*, Vol. 2, pp. 1–7.

Honig, G., and Hirdes, U., 1984, "A Method for the Numerical Inversion of Laplace Transforms," *Journal of Computational Applied Mathematics*, Vol. 10, pp. 113–132.

Ignaczak, J., 1981, "Linear Dynamic Thermoelasticity: A Survey," *The Shork and Vibration Digest*, Vol. 13, pp. 3–8.

Lord, H. W., and Shulman, Y., 1967, "A Generalized Dynamic Theory of Thermoelasticity," *Journal of the Mechanics and Physics of Solids*, Vol. 15, pp. 299–309.

Noda, N., Furukawa, T., and Ashida, F., 1989, "Generalized Dynamic Theory of Thermoelasticity," *Journal of the Mechanics and Physics of Solids*, Vol. 15, pp. 299–309.

Noda, N., Furukawa, T., and Ashida, F., 1989, "Generalized Thermoelasticity in an Infinite Solid with a Hole," *Journal of Thermal Stresses*, Vol. 12, pp. 385–402.

Norwood, F. R., and Warren, W. E., 1969, "Wave Propagation in the Generalized Dynamical Theory of Thermoelasticity," *Quarterly Journal of Mechanics and Applied Mathematics*, Vol. 22, pp. 283–290.

Öncü, T. S., and Moodie, T. B., 1991, "Padé-Extended Ray Series Expansions in Generalized Thermoelasticity," *Journal of Thermal Stresses*, Vol. 14, pp. 85–99.

Prevost, J. H., and Tao, D., 1983, "Finite Element Analysis of Dynamic Coupled Thermoelasticity Problems with Relaxation Times," ASME JOURNAL OF APPLIED MECHANICS, Vol. 50, pp. 817–822.

Tao, D., and Prevost, J. H., 1984, "Relaxation Effects on Generalized Thermoelasticity Wave," *Journal of Thermal Stresses*, Vol. 7, pp. 79–89.

Sherief, H. H., 1986, "Fundamental Solution of the Generalized Thermoelastic Problems for Short Times," *Journal of Thermal Stresses*, Vol. 9, pp. 151–164.

Sternberg, E., and Chakravorty, J. G., 1959, "On Inertia Effects in a Transient Thermoelastic Problem," ASME JOURNAL OF APPLIED MECHANICS, Vol. 26, pp. 503–509.

On First-Order Decoupling of Equations of Motion for Constrained Dynamical Systems

T. A. Loduha
Research Assistant.

B. Ravani
Professor.
Mem. ASME.

Department of Mechanical and Aeronautical Engineering,
University of California,
Davis, CA 95616-5294

In this paper we present a method for obtaining first-order decoupled equations of motion for multirigid body systems. The inherent flexibility in choosing generalized velocity components as a function of generalized coordinates is used to influence the structure of the resulting dynamical equations. Initially, we describe how a congruency transformation can be formed that represents the transformation between generalized velocity components and generalized coordinate derivatives. It is shown that the proper choice for the congruency transformation will insure generation of first-order decoupled equations of motion for holonomic systems. In the case of nonholonomic systems, or holonomic systems with unreduced configuration coordinates, we incorporate an orthogonal complement in conjunction with the congruency transformation. A pair of examples illustrate the results. Finally, we discuss numerical implementation of congruency transformations to achieve first-order decoupled equations for simulation purposes.

Introduction

Constrained multirigid body systems refer to systems of interconnected bodies and particles which are subjected to various motion constraints. Such systems are abundantly relevant in engineering for modeling a wide variety of mechanical systems. Much attention has been focused on formulation procedures to yield the differential equations describing the motion of multibody systems (Crandall et al., 1968; Gibbs, 1879; Gibbs, 1961; Hartog, 1948; Huston, 1990; Kane and Levinson, 1985; Roberson and Schwertassek, 1988; Scott, 1988; Storch and Gates, 1989). In most cases the resulting equations are numerically integrated to obtain trajectories characterizing the system's motion. In addition, the equations of motion are often analyzed directly to determine the nature of the nonlinear behavior. This paper demonstrates a method, using Kane's[1] equations (Kane and Levinson, 1985), for generating equations of motion which are decoupled in the highest derivative terms. We will refer to such equations as being *first-order decoupled.* Nonlinear differential equations of this form are more easily integrated numerically, as well as better fit for analysis. The procedure of generalized velocity component selection based on a congruency transformation (Wade, 1951) is developed and used to achieve first-order decoupled form of the equations of motion.

Considerable attention has been placed on contending with holonomic and nonholonomic, linear and nonlinear motion constraints on multirigid body systems (Kamman and Huston, 1984; Kane, 1972; Nikravesh and Haug, 1983; Wang and Huston, 1988; Wehage and Haug, 1982; Wampler et al., 1985; Xu et al., 1990). A common way to deal with constraints is to impose them at an early stage of the analysis by reducing the set of dependent generalized coordinates to an independent one. If the constraints are nonholonomic the generalized coordinate derivatives are reduced accordingly. However, many consider it to be more effective to first perform the dynamical analysis for the unconstrained system, and then reduce the resulting equations to a consistent set with the constraint equations. For example, Kamman and Huston (1984), using Kane's formulation, show that the projection of existing equations of motion onto an *orthogonal complement* yields the desired reduced equations. An orthogonal complement, say **C**, of matrix **B** would satisfy the equation $\mathbf{BC} = \mathbf{0}$. Ben-Israel and Greville (1974) and Lawson and Hanson (1974) discuss the mathematical significance of the orthogonal complement. The use of the orthogonal complement to impose motion constraints is illustrated by Hemami and Weimer (1981), Huston (1990), Kamman and Huston (1984), Wang and Huston (1988), and Xu et al. (1990). Hemami and Weimer (1981) use the orthogonal complement similarly for contracting equations generated by the Lagrange formulation. Wampler et al. (1985) discuss a method for

[1] It has been pointed out (see Desloge, 1987 and Huston, 1987) that these equations are actually a particular form of the Gibbs-Appell equations (see Gibbs, 1879 and 1961).

Contributed by the Applied Mechanics Division of THE AMERICAN SOCIETY OF MECHANICAL ENGINEERS for publication in the ASME JOURNAL OF APPLIED MECHANICS.

Discussion on this paper should be addressed to the Technical Editor, Professor Lewis T. Wheeler, Department of Mechanical Engineering, University of Houston, Houston, TX 77204-4792, and will be accepted until four months after final publication of the paper itself in the ASME JOURNAL OF APPLIED MECHANICS.

Manuscript received by the ASME Applied Mechanics Division, Feb. 22, 1993; final revision, May 27, 1993. Associate Technical Editor: R. L. Huston.

reduction of existing equations of motion subject to additional constraints by recombining terms from the original equations. A numerical procedure for imposing constraints during integration based on generalized coordinate partitioning is presented by Nikravesh and Haug (1983) and Wehage and Haug (1982). One common element of each of these methods is the application of the constraints after conducting the dynamical analysis. Conversely, we illustrate a method that imposes constraints at an intermediate step of the kinematical analysis to enable decoupling for nonholonomic systems, or systems where the holonomic constraints are yet to be applied.

The following discussion addresses the use of generalized velocity component selection to achieve first-order decoupling of multirigid body systems. The idea of the congruency transformation is explained and utilized here. A simple example is conducted to clarify the procedure for finding the congruency transformation for holonomic systems. Next, a procedure is discussed for decoupling of systems with nonholonomic constraints, or holonomic systems with unreduced configuration coordinate descriptions. The result, using orthogonal complements, is a modified nonsquare transformation between generalized coordinate time derivatives and a reduced set of generalized velocity components. Decoupling using the orthogonal complement is demonstrated by relaxing a constraint from the first example. Lastly, we discuss the numerical application of congruency transformations.

Dynamics of Holonomic Multirigid Body-Systems

First-Order Decoupled Equations of Motion. In the process of formulating equations of motion, for example, using Kane's method, the analyst must choose a linear combination of first time derivatives of generalized coordinates to define generalized velocity components. These, in a general form, were initially introduced by Gibbs (1879, 1961), but were exploited in more detail by Kane (see, for example Kane (1972) and Kane and Levinson (1985)). Kane and his coworkers have referred to these quantities as "generalized speeds." Some of the problems for such a term have been pointed out by Papastavridis (1992), who considers either "nonholonomic components of the velocity vector" or "quasi-velocities" to be more appropriate terms. Singh and Likins (1985) mention the term "derivatives of quasicoordinates" as an alternative. Here, for lack of a better name, we shall simply call them *generalized velocity components*. The resulting equations of motion, using the generalized velocity components, in matrix notation, are of the form

$$\mathbf{M}\dot{\mathbf{u}} = \mathbf{g}(\mathbf{q}, \mathbf{u}) \tag{1}$$

where $\mathbf{u}$ and $\mathbf{q}$ are vectors of generalized velocity components and generalized coordinates, respectively. $\mathbf{M}$ is a matrix whose elements are functions of generalized coordinates and the inertia properties of the system, and $\mathbf{g}$ is a nonlinear vector function of generalized velocity components and generalized coordinates. The technique presented here will generate equations of this form where $\mathbf{M}$ can be made diagonal by judicious selection of generalized velocity components. Nonlinear differential equations of this form are dramatically easier to numerically integrate, as the need for computing $\mathbf{M}^{-1}$ at each iteration is eliminated. In addition, performing various analyses of nonlinear behavior—tests for stability, nature of critical points, chaos, etc.—is facilitated if the system equations are written in state plane form. A diagonal $\mathbf{M}$ matrix in Eq. (1) satisfies this requirement.

Kane's Equations. Consider a system of p rigid bodies whose configuration can be described completely by the set of n generalized coordinates $(q_1, q_2, \ldots, q_r, \ldots, q_n)$, or $\mathbf{q} = [q_1, q_2, \ldots, q_r, \ldots, q_n]^T$. Kane's equations (Kane and Levinson, 1985) are formed by letting the sum of generalized active forces and generalized inertia forces equal zero. These equations are actually a particular form of the Gibbs-Appell equations (see Desloge, 1987; Huston, 1987). Kane (1972) originally referred to them as Lagrange's form of D'Alembert's principle. In these equations the generalized active force vector can be expressed as

$$\mathbf{F} = \sum_{i=1}^{p} \left[\mathbf{V}_i^T \mathbf{f}_i + \Gamma_i^T \tau_i\right] \tag{2}$$

where $\mathbf{f}$ is the resultant active force acting at the mass center of the ith body, and τ_i is the resultant moment. $\mathbf{V}$ and Γ_i are the partial velocity and partial angular velocity matrices, which are written as

$$\underset{(3 \times n)}{\mathbf{V}_i} = \frac{\partial \mathbf{v}_i}{\partial \mathbf{u}^T} \tag{3}$$

and

$$\underset{(3 \times n)}{\Gamma_i} = \frac{\partial \omega_i}{\partial \mathbf{u}^T}. \tag{4}$$

These partial velocities are taken with respect to the generalized velocity component vector $\mathbf{u}$. The generalized velocity components are a linear combination of the first time derivatives of generalized coordinates. For ease of substitution this relation is expressed as

$$\dot{\mathbf{q}} = \mathbf{T}\mathbf{u}. \tag{5}$$

We shall refer to the matrix $\mathbf{T}$ as the *rate transformation* matrix. Since we are considering holonomic systems here, $\mathbf{T}$ is a square matrix of order n. The generalized inertia force vector is written as

$$\mathbf{F}^* = -\sum_{i=1}^{p} \left[m_i \mathbf{V}_i^T \mathbf{a}_i + \Gamma_i^T \dot{\mathbf{H}}_i\right] \tag{6}$$

where $\mathbf{a}_i$ is the mass center acceleration of the ith body and $\dot{\mathbf{H}}_i$ is the time rate of change of angular momentum of body i with respect to the Newtonian reference frame. Finally, n dynamical equations of motion are obtained by letting the vector sums from Eqs. (2) and (6) equal the zero vector:

$$\mathbf{F} + \mathbf{F}^* = \mathbf{0} \tag{7}$$

Equation (7) is the matrix form of the so-called Kane's equations. It should be pointed out that in this paper, as with other references on constrained multibody systems (see, for example, Huston, 1990), we shall use the term *configuration coordinates* in addition to *generalized coordinates*. In constrained multibody systems configuration coordinates refer to the variables that describe a system's configuration, but may be dependent upon one another. Generalized coordinates represents reduced, or independent configuration coordinates.

The Influence of Generalized Velocity Component Selection. Since our goal in this paper is to prescribe a choice of generalized velocity components that would yield decoupled equations of motion, it is first necessary to reveal the influence of such a selection on the resulting dynamical equations. In other words, we would like to expose the location of the matrix $\mathbf{T}$, from Eq. (5), within Kane's equations. The acceleration of the mass center of the ith body can be written as

$$\mathbf{a}_i = \mathbf{V}_i\dot{\mathbf{u}} + \dot{\mathbf{V}}_i\mathbf{u}. \tag{8}$$

We also know the angular acceleration of body i can be expressed as

$$\dot{\omega}_i = \Gamma_i\dot{\mathbf{u}} + \dot{\Gamma}_i\mathbf{u}. \tag{9}$$

From this we can write the derivative of angular momentum as

$$\dot{\mathbf{H}}_i = \mathbf{I}_i\Gamma_i\dot{\mathbf{u}} + \mathbf{I}_i\dot{\Gamma}_i\mathbf{u} + \mathbf{W}_i\mathbf{I}_i\omega_i \tag{10}$$

where $\mathbf{I}_i$ is the central inertia matrix and $\mathbf{W}_i$ is the angular velocity matrix associated with the ith body, and written in terms of body i's natural frame. Thus, the generalized inertia force becomes

$$\mathbf{F}^* = -\sum_{i=1}^{p}\Big[m_i\mathbf{V}_i^T\mathbf{V}_i\dot{\mathbf{u}} + m_i\mathbf{V}_i^T\dot{\mathbf{V}}_i\mathbf{u} + \Gamma_i^T\mathbf{I}_i\Gamma_i\dot{\mathbf{u}} + \Gamma_i^T\mathbf{I}_i\dot{\Gamma}_i\mathbf{u} + \Gamma_i^T\mathbf{W}_i\mathbf{I}_i\omega_i\Big]. \tag{11}$$

From the relation depicted in Eq. (5), it is easily shown that the partial velocity matrix of Eq. (3) can be expressed as

$$\frac{\partial\mathbf{v}_i}{\partial\mathbf{u}^T} = \frac{\partial\mathbf{v}_i}{\partial\dot{\mathbf{q}}^T}\mathbf{T} = \frac{\partial\mathbf{r}_i}{\partial\mathbf{q}^T}\mathbf{T} \tag{12}$$

where is $\mathbf{r}_i$ the Euclidean position of body i's mass center with respect to the inertial reference frame. We can write this as

$$\mathbf{V}_i = \mathbf{J}_i\mathbf{T} \tag{13}$$

where $\mathbf{J}_i$ is the partial derivative of $\mathbf{r}_i$ body's mass center position with respect to the vector of the generalized coordinates. Similarly, Eq. (4) is

$$\frac{\partial\omega_i}{\partial\mathbf{u}^T} = \frac{\partial\omega_i}{\partial\dot{\mathbf{q}}^T}\mathbf{T} \tag{14}$$

or

$$\Gamma_i = \Omega_i\mathbf{T} \tag{15}$$

where Ω_i is the partial derivative of body i's angular velocity with respect to the time derivative of the generalized coordinate vector. Substitution of Eqs. (13) and (15) into Eq. (6) gives the following expression for the equations of motion:

$$-\sum_{i=1}^{p}\Big[m_i\mathbf{T}^T\mathbf{J}_i^T\mathbf{J}_i\mathbf{T}\dot{\mathbf{u}} + m_i\mathbf{T}^T\mathbf{J}_i^T\frac{d}{dt}(\mathbf{J}_i\mathbf{T})\mathbf{u} + \mathbf{T}^T\Omega_i^T\mathbf{I}_i\Omega_i\mathbf{T}\dot{\mathbf{u}} + \mathbf{T}^T\Omega_i^T\mathbf{I}_i\frac{d}{dt}(\Omega_i\mathbf{T})\mathbf{u} + \mathbf{T}^T\Omega_i^T\mathbf{W}_i\mathbf{I}_i\omega_i - \mathbf{T}^T\mathbf{J}_i^T\mathbf{f}_i - \mathbf{T}^TJ_i^T\mathbf{f}_i - \mathbf{T}^T\Omega_i^Tm_i\Big] = \mathbf{0}. \tag{16}$$

By letting

$$\mathbf{A} = -\sum_{i=1}^{p}\Big[m_i\mathbf{J}_i^T\mathbf{J}_i + \Omega_i^T\mathbf{I}_i\Omega_i\Big], \tag{17}$$

a complete set of equations of motion can be expressed as

$$\mathbf{T}^T\mathbf{A}\mathbf{T}\dot{\mathbf{u}} - \sum_{i=1}^{p}\Big[m_i\mathbf{T}^T\mathbf{J}_i^T\frac{d}{dt}(\mathbf{J}_i\mathbf{T})\mathbf{u} + \mathbf{T}^T\Omega_i^T\mathbf{I}_i\frac{d}{dt}(\Omega_i\mathbf{T})\mathbf{u} + \mathbf{T}^T\Omega_i^T\mathbf{W}_i\mathbf{I}_i\omega_i - \mathbf{T}^T\mathbf{J}_i^T\mathbf{f}_i - \mathbf{T}^T\Omega_i^Tm_i\Big] = \mathbf{0} \tag{18a}$$

and

$$\dot{\mathbf{q}} = \mathbf{T}\mathbf{u}. \tag{18b}$$

It is now clear that $\mathbf{T}$ manifests itself in the transformation $\mathbf{T}^T\mathbf{A}\mathbf{T}$ in the first term of the left-hand side of Eq. (18*a*), as far as first-order generalized velocity components are concerned. We now wish to explain how the analyst can choose the rate transformation matrix $\mathbf{T}$ in Eq. (18*b*) to assure that the coefficient matrix for the first-order generalized speed vector in Eq. (18*a*) is diagonal.

Selecting T for Decoupling. Clearly, from the above results, first-order decoupled equations of motion will be generated if $\mathbf{T}^T\mathbf{A}\mathbf{T}$ is a diagonal matrix. Therefore, we first consider how this transformation can be influenced by $\mathbf{T}$ to satisfy this condition. Notice that if the eigenvectors of $\mathbf{A}$ are used as the columns of $\mathbf{T}$, a diagonal matrix results under the similarity transformation $\mathbf{T}^{-1}\mathbf{A}\mathbf{T}$. Moreover, $\mathbf{A}$ is symmetric, hence, its eigenvectors can be chosen to be orthogonal. With orthogonal eigenvectors we know that $\mathbf{T}^{-1} = \mathbf{T}^T$, and the similarity transformation effectively appears as the leading matrix for the first-order terms of Eq. (18*a*). Thus, a sufficient condition for obtaining first-order decoupled equations of motion is that the rate transformation matrix $\mathbf{T}$ be comprised of the eigenvectors of $\mathbf{A}$. However, it should be emphasized that this is *not* a necessary condition for decoupling. In fact it can be much less laborious to choose the elements of $\mathbf{T}$ to satisfy a congruency transformation than to symbolically determine the eigenvectors of $\mathbf{A}$. We will now show that decoupling can be achieved by satisfying an alternative sufficiency condition. That is, if $\mathbf{T}$ is chosen to fulfill a specific congruency transformation, Eq. (18*a*) will be decoupled in first-order terms. Consider the following definition (see, for example, Wade, 1951). If for two given matrices $\mathbf{A}$ and $\mathbf{N}$ there exists a nonsingular matrix $\mathbf{T}$ that satisfies the relation

$$\mathbf{T}^T\mathbf{A}\mathbf{T} = N \tag{19}$$

then $\mathbf{A}$ and $\mathbf{N}$ are said to be congruent. Furthermore, we shall utilize a theorem (see Wade, 1951) stating that a symmetric matrix can be reduced by a congruency transformation to a diagonal matrix of the same rank. The principal motivation behind employing congruency transformations to achieve decoupling is that the rate transformation matrix can be formed directly with various combinations of the elements of the $\mathbf{A}$ matrix. At this point we propose an algorithm for obtaining the matrix $\mathbf{T}$ that yields a diagonal matrix under the congruency transformation of Eq. (19). This, in turn, would be used in Eq. (18*b*) as a rate transformation matrix. Consider the symmetric $\mathbf{A}$ matrix written as

$$\mathbf{A} = \begin{bmatrix} a_{11} & a_{12} & \cdots & a_{1n} \\ a_{12} & a_{22} & \cdots & \cdots \\ \cdot & \cdot & \cdot & \cdot \\ a_{1n} & \cdots & \cdots & a_{nn} \end{bmatrix}. \tag{20}$$

The transformation matrix $\mathbf{T}$ will be composed of m factors, such that it can be written

$$\mathbf{T} = \mathbf{T}_1\mathbf{T}_2\mathbf{T}_3\ldots\mathbf{T}_m \tag{21}$$

where m is the number of degrees-of-freedom less one ($m = n - 1$). $\mathbf{T}_1$ would be constructed as follows:

$$\mathbf{T}_1 = \begin{bmatrix} 1 & -a_{12}/a_{11} & \cdots & -a_{1k}/a_{11} & \cdots & -a_{1n}/a_{11} \\ 0 & 1 & \cdots & \cdots & \cdots & 0 \\ \cdot & \cdot & 1 & \cdot & \cdot & \cdot \\ \cdot & \cdot & \cdot & \cdot & \cdot & \cdot \\ 0 & 0 & \cdots & \cdots & 0 & 1 \end{bmatrix}. \tag{22}$$

When the congruency transformation

$$\mathbf{T}_1^T\mathbf{A}\mathbf{T}_1 = A' \tag{23}$$

is performed, the resulting A' is a matrix with zero elements in row one and column one, except for the element a_{11} (see Eq. (24)). In other words, it will be block diagonal with the

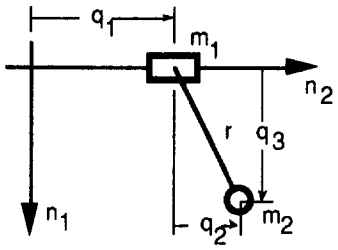

Fig. 1 A sliding pendulum

lower right m by m submatrix remaining undiagonalized, and is given here as

$$\mathbf{A}' = \mathbf{T}_1^T\mathbf{A}\mathbf{T}_1 = \begin{bmatrix} a_{11} & 0 & 0 & \dots & 0 \\ 0 & b_{11} & b_{12} & \dots & b_{1m} \\ 0 & b_{21} & b_{22} & \dots & b_{2m} \\ \cdot & \cdot & \cdot & \cdot & \cdot \\ 0 & b_{m1} & b_{m2} & \dots & b_{mm} \end{bmatrix}. \quad (24)$$

The same procedure is performed on this result, except $\mathbf{T}_2$ is constructed as

$$\mathbf{T}_2 = \begin{bmatrix} 1 & 0 & \dots & \dots & 0 \\ 0 & 1 & -b_{12}/b_{11} & \dots & -b_{1m}/b_{11} \\ 0 & 0 & 1 & \dots & 0 \\ \cdot & \cdot & \cdot & \cdot & \cdot \\ 0 & 0 & \dots & 0 & 1 \end{bmatrix}. \quad (25)$$

The congruency transformation is performed again:

$$\mathbf{T}_2^T\mathbf{T}_1^T\mathbf{A}\mathbf{T}_1\mathbf{T}_2 = \mathcal{A}'' \quad (26)$$

This is repeated until a total of m transformations have been completed, and the **A** matrix is converted to diagonal form. One additional requirement is that **T** be nonsingular. However, this is assumed since the final diagonal matrix is of the same rank as the original **A** matrix. Therefore, **T** must be of full rank. Before discussing the use of the orthogonal complement, an example is presented to illustrate decoupling with the congruency transformation.

Example of Decoupling With the Congruency Transformation. Consider the following system of two particles connected by a rigid, massless rod. Sliding mass m_1 is constrained to move along the horizontal axis $\mathbf{n}_2$, and the mass m_2 must stay on the constant radius arc with respect to m_1 in the $\mathbf{n}_1 - \mathbf{n}_2$ plane, as shown in Fig. 1.

Using the generalized coordinates q_1 and q_2, the matrix **A** is assembled using $\mathbf{J}_1$ and $\mathbf{J}_2$ for each of the masses. This gives

$$\mathbf{J}_1 = \begin{bmatrix} 0 & 0 \\ 1 & 0 \end{bmatrix} \quad (27)$$

and

$$\mathbf{J}_2 = \begin{bmatrix} 0 & -rsq_2 \\ 1 & rcq_2 \end{bmatrix} \quad (28)$$

which can be combined according to Eq. (17) to obtain

$$\mathbf{A} = \begin{bmatrix} -m_1 - m_2 & -m_2rcq_2 \\ -m_2rcq_2 & -m_2r^2 \end{bmatrix}. \quad (29)$$

Equation (19) is used to form the congruency transformation for **A** as

$$\mathbf{T} = \begin{bmatrix} 1 & -m_2rcq_2/(m_1 + m_2) \\ 0 & 1 \end{bmatrix}. \quad (30)$$

For this system the resultant applied force vectors for each mass are

$$\mathbf{f}_1 = \begin{bmatrix} m_1g \\ 0 \end{bmatrix} \quad (31)$$

and

$$\mathbf{f}_2 = \begin{bmatrix} m_2g \\ 0 \end{bmatrix}. \quad (32)$$

The above matrices can then be assembled using Eq. (18*a*) to yield the following dynamical equations:

$$\begin{bmatrix} -m_1 - m_2 & 0 \\ 0 & m_2r^2 - m_2^2r^2c^2q_2/(m_1 + m_2) \end{bmatrix}\dot{\mathbf{u}} = \begin{bmatrix} 0 \\ -m_2^2r^2cq_2sq_2u_2^2/(m_1 + m_2) \end{bmatrix} + \begin{bmatrix} 0 \\ -m_2grsq_2 \end{bmatrix}. \quad (33)$$

The complete set of equations of motion are Eq. (33) and the following equation using the rate transformation matrix given in Eq. (30):

$$\dot{\mathbf{q}} = \begin{bmatrix} 1 & -m_2rcq_2/(m_1 + m_2) \\ 0 & 1 \end{bmatrix}\mathbf{u}. \quad (34)$$

Equation (34) shows that the generalized velocity components obtained using the congruency transformation include mass terms. This is slightly different from the definition of the relationship between **u** and $\dot{\mathbf{q}}$, as defined by Kane (1985) to be a function of **q** and time, and not of the mass properties of the system. It also indicates another problem with the term "generalized speeds," or even "generalized velocity components," for the elements of the vector **u**, since they depend on mass properties in the more general context used in this paper. We shall, however, continue using "generalized velocity components" since the term "generalized" may be interpreted that **u** is not just like a common velocity vector.

Dynamics of Nonholonomic Multibody Systems

The equations of motion given in Eqs. (18*a*) and (18*b*) become invalid if the multibody system includes constraints which are nonholonomic. If this is the case, the constraints can be applied to the system with an orthogonal complement, and the transformation between generalized coordinate derivatives and generalized velocity components is no longer one-to-one. Additionally, situations might arise where a model is given with unreduced configuration coordinates along with holonomic constraint equations that are yet to be applied. Again, the orthogonal complement is used to impose such constraints. These ideas are discussed next, and illustrated with an example.

The Orthogonal Complement. Huston (1990) shows that if the motion constraint equations, either holonomic or nonholonomic, are written as

$$\mathbf{B}\dot{\mathbf{q}} = \mathbf{0} \quad (35)$$

and the unconstrained equations of motion are as depicted in Eq. (1), a valid set of reduced equations describing the dynamics of the constrained system is

$$\mathbf{C}^T\mathbf{M}\ddot{\mathbf{q}} = \mathbf{C}^T\mathbf{g}(\dot{\mathbf{q}}, \mathbf{q}) \quad (36)$$

where **C** is the orthogonal complement of **B**. Recall **C** is the orthogonal complement of **B** if $\mathbf{BC} = \mathbf{0}$ is satisfied. **C** can be thought of as a non-square transformation between the unreduced generalized coordinate derivative vector $\dot{\mathbf{q}}$, and a reduced generalized coordinate derivative vector, say $\dot{\mathbf{z}}$:

$$\dot{\mathbf{q}} = \mathbf{C}\dot{\mathbf{z}}. \quad (37)$$

Let us rewrite Eq. (36) in similar form to Eq. (16) by first writing

$$-\sum_{i=1}^{p}\Big[m_i\mathbf{C}^T\mathbf{J}_i^T\mathbf{J}_i\ddot{\mathbf{q}}+m_i\mathbf{C}^T\mathbf{J}_i^T\frac{d}{dt}(\mathbf{J}_i)\dot{\mathbf{q}}+\mathbf{C}^T\Omega_i^T\mathbf{I}_i\Omega_i\ddot{\mathbf{q}}+\mathbf{C}^T\Omega_i^T\mathbf{I}_i\frac{d}{dt}(\Omega_i)\dot{\mathbf{q}}+\mathbf{C}^T\Omega_i^T\mathbf{W}_i\mathbf{I}_i\omega_i-\mathbf{C}^T\mathbf{J}_i^T\mathbf{f}_i-\mathbf{C}^T\Omega_i^T\tau_i\Big]=\mathbf{0}. \quad (38)$$

We can substitute the expression for $\ddot{\mathbf{q}}$ given in Eq. (37) into Eq. (38) to establish equations of motion in terms of the new reduced generalized coordinate vector $\mathbf{z}$ and its derivatives:

$$-\sum_{i=1}^{p}\Big[m_i\mathbf{C}^T\mathbf{J}_i^T\mathbf{J}_i\mathbf{C}\ddot{\mathbf{z}}+m_i\mathbf{C}^T\mathbf{J}_i^T\frac{d}{dt}(\mathbf{J}_i\mathbf{C})\dot{\mathbf{z}}+\mathbf{C}^T\Omega_i^T\mathbf{I}_i\Omega_i\mathbf{C}\ddot{\mathbf{z}}+\mathbf{C}^T\Omega_i^T\mathbf{I}_i\frac{d}{dt}(\Omega_i C)\dot{\mathbf{z}}+\mathbf{C}^T\Omega_i^T\mathbf{W}_i\mathbf{I}_i\omega_i-\mathbf{C}^T\mathbf{J}_i^T\mathbf{f}_i-\mathbf{C}^T\Omega_i^T\tau_i\Big]=\mathbf{0}. \quad (39)$$

One can see that the role of the matrix $\mathbf{C}$ in Eq. (39) is equivalent to that of $\mathbf{T}$ in Eq. (16). Hence, we can view

$$\mathbf{J}_i\mathbf{C}=\frac{\partial\mathbf{v}_i}{\partial\dot{\mathbf{z}}^T} \quad (40)$$

and

$$\Omega_i\mathbf{C}=\frac{\partial\omega_i}{\partial\dot{\mathbf{z}}^T} \quad (41)$$

as special partial velocity matrices. Generalized velocity components can be introduced easily using the transformation

$$\dot{\mathbf{z}}=\mathbf{T}\mathbf{u}. \quad (42)$$

With this, the transformation between unreduced generalized coordinate derivatives and reduced generalized velocity components is written as

$$\dot{\mathbf{q}}=\mathbf{C}\mathbf{T}\mathbf{u}. \quad (43)$$

A new set of equations of motion in terms of reduced generalized velocity components can now be given as

$$-\sum_{i=1}^{p}\Big[m_i\mathbf{T}^T\mathbf{C}^T\mathbf{J}_i^T\mathbf{J}_i\mathbf{C}\mathbf{T}\dot{\mathbf{u}}+m_i\mathbf{T}^T\mathbf{C}^T\mathbf{J}_i^T\frac{d}{dt}(\mathbf{J}_i\mathbf{C}\mathbf{T})\mathbf{u}+\mathbf{T}^T\mathbf{C}^T\Omega_i^T\mathbf{I}_i\Omega_i\mathbf{C}\mathbf{T}\dot{\mathbf{u}}+\mathbf{T}^T\mathbf{C}^T\Omega_i^T\mathbf{I}_i\frac{d}{dt}(\Omega_i\mathbf{C}\mathbf{T})\mathbf{u}+\mathbf{T}^T\mathbf{C}^T\Omega_i^T\mathbf{W}_i\mathbf{I}_i\omega_i-\mathbf{T}^T\mathbf{C}^T\mathbf{J}_i^T\mathbf{f}_i+\mathbf{T}^T\mathbf{C}^T\Omega_i^T\tau_i\Big]=\mathbf{0} \quad (44)$$

which are accurate in describing the behavior of the *constrained* system. Note that the matrix product $\mathbf{CT}$ shown in Eq. (43) represents a modified, nonsquare, rate transformation matrix.

There are several procedures for determining the orthogonal complement matrix as demonstrated by Huston (1990) and Hemami and Weimer (1981). Here, we will consider the zero-eigenvalue approach discussed by Huston. If there are m motion constraints imposed on a system that has n degrees-of-freedom, the m by n matrix $\mathbf{B}$ from Eq. (35) will be of rank m. $\mathbf{B}$ premultiplied by its transpose will be a symmetric n by n matrix also of rank m. Hence, $\mathbf{B}^T\mathbf{B}$ will have

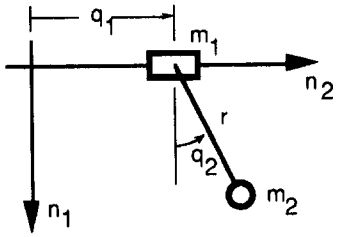

Fig. 2 A sliding pendulum with unreduced configuration coordinates

$(n-m)$ independent eigenvectors associated with the zero eigenvalues. If the columns of $\mathbf{C}$ are comprised of these eigenvectors we have

$$\mathbf{B}^T\mathbf{B}\mathbf{C}=\mathbf{0}. \quad (45)$$

Premultiplying by $\mathbf{C}^T$ gives

$$\mathbf{C}^T\mathbf{B}^T\mathbf{B}\mathbf{C}=\mathbf{0} \quad (46)$$

or

$$\mathbf{B}\mathbf{C}=\mathbf{0}. \quad (47)$$

Therefore, $\mathbf{C}$ is the orthogonal complement of $\mathbf{B}$. With $\mathbf{C}$ specified, we can now focus on the coefficient matrix for generalized velocity component derivatives from Eq. (44) by grouping all other terms into the function $\mathbf{h}$. This gives

$$\mathbf{T}^T\mathbf{C}^T\mathbf{A}\mathbf{C}\mathbf{T}\dot{\mathbf{u}}=\mathbf{h}(\mathbf{q},\mathbf{u}). \quad (48)$$

The matrix $\mathbf{A}$ is the same as defined in Eq. (17). To obtain first-order decoupled equations for the constrained system we simply choose $\mathbf{T}$ to be the proper congruency transformation, this time for $\mathbf{C}^T\mathbf{A}\mathbf{C}$, using the procedure outlined earlier.

Example: Unreduced Configuration Coordinates. We will now repeat the example carried out above, but now using the dependent configuration coordinates shown in Fig. 2.

The constraint imposed by the rigid rod is temporarily removed. The position Jacobians for the two masses now appear as

$$\mathbf{J}_1=\begin{bmatrix}0&0&0\\1&0&0\end{bmatrix} \quad (49)$$

and

$$\mathbf{J}_2=\begin{bmatrix}0&1&0\\1&0&1\end{bmatrix}. \quad (50)$$

The resulting $\mathbf{A}$ matrix is

$$\mathbf{A}=\begin{bmatrix}-m_1-m_2&0&-m_2\\0&-m_2&0\\-m_2&0&-m_2\end{bmatrix}. \quad (51)$$

Now we must find the orthogonal complement to reimpose the constraint. Therefore, the constraint representation should be put in the form of Eq. (35). For the simple pendulum this constraint is written as

$$\mathbf{B}\dot{\mathbf{q}}=[0\quad q_2\quad q_3]\dot{\mathbf{q}}=0. \quad (52)$$

To find an orthogonal complement the zero eigenvectors of $\mathbf{B}^T\mathbf{B}$ must be found. However, for this problem the vectors comprising $\mathbf{C}$ can be obtained even more simply, using the Gram-Schmidt process, for example. The orthogonal complement is found to be

$$\mathbf{C}=\begin{bmatrix}1&0\\0&-q_3\\0&q_2\end{bmatrix}. \quad (53)$$

We can form $\mathbf{C}^T\mathbf{AC}$ to allow determination of $\mathbf{T}$ as

$$\mathbf{T} = \begin{bmatrix} 1 & -m_2 q_2/(m_1 + m_2) \\ 0 & 1 \end{bmatrix}. \tag{54}$$

The necessary components are now available to produce the constrained dynamical equations of motion using Eq. (44). The applied force vectors remain the same as in the previous example. The dynamical equations in terms of the reduced generalized velocity component vector are

$$\begin{bmatrix} -m_1 - m_2 & 0 \\ 0 & -m_2^2 q_2^2/(m_1 + m_2) + m_2 r^2 \end{bmatrix} \dot{\mathbf{u}} = \begin{bmatrix} 0 \\ -m_2^2 q_3 q_2 u_2^2/(m_1 + m_2) \end{bmatrix} + \begin{bmatrix} 0 \\ m_2 g q_3 \end{bmatrix}. \tag{55}$$

The additional equations of motion stemming from the transformation between configuration coordinates and reduced generalized velocity components are

$$\dot{\mathbf{q}} = \begin{bmatrix} 1 & -m_2 q_2/(m_1 + m_2) \\ 0 & 1 \end{bmatrix} \mathbf{u}. \tag{56}$$

Numerical Implementation of Congruency Transformations

Very often one must analyze large-scale systems where it would be very tedious to symbolically obtain the proper congruency transformation. For this reason, we now discuss numerical implementation of the congruency transformation so that it may be used on more complicated systems. Recall the expression for the equations of motion shown in Eq. (16), except here we do not require the matrix $\mathbf{T}$ to be a diagonalizing congruency transformation. In this case $\mathbf{T}$ may be any matrix that yields a valid vector of generalized velocity components. The equations of motion for a holonomic system are

$$-\sum_{i=1}^{p} \Big[m_i \mathbf{T}^T \mathbf{J}_i^T \mathbf{J}_i \mathbf{T}\dot{\mathbf{u}} + m_i \mathbf{T}^T \mathbf{J}_i^T \frac{d}{dt}(\mathbf{J}_i \mathbf{T})\mathbf{u} + \mathbf{T}^T \Omega_i^T \mathbf{I}_i \Omega_i \mathbf{T}\dot{\mathbf{u}} + \mathbf{T}^T \Omega_i^T \mathbf{I}_i \frac{d}{dt}(\Omega_i \mathbf{T})\mathbf{u} + \mathbf{T}^T \Omega_i^T \mathbf{W}_i \mathbf{I}_i \omega_i - \mathbf{T}^T \mathbf{J}_i^T \mathbf{f}_i - \mathbf{T}^T \Omega_i^T \tau_i \Big] = \mathbf{0}. \tag{57}$$

Notice that the derivative of the rate transformation matrix $\mathbf{T}$ appears in two of the terms in Eq. (57). Even though it would be possible to select $\mathbf{T}$ to be a diagonalizing congruency transformation at each iteration of the numerical integration, we would be left with the cumbersome task of specifying its time derivative as well. Hence, the following development allows selection of a matrix Ψ which is independent of the original dynamical equations (Eq. (57)), and does not appear in derivative form. However, one must still choose a valid linear combination of generalized coordinate derivatives (prescribed by $\mathbf{T}$) to define generalized velocity components, as usually done with conventional application of Kane's equations. For example, it is common to choose a trivial set of generalized velocity components by selecting $\mathbf{T}$ as the identity matrix. Denote the matrix products premultiplying $\mathbf{u}$ from Eq. (57) as

$$\mathbf{A} = \mathbf{T}^T \left(-\sum_{i=1}^{p} \left[m_i \mathbf{J}_i^T \mathbf{J}_i + \Omega_i^T \mathbf{I}_i \Omega_i \right] \right) \mathbf{T} \tag{58}$$

and the remaining vector sum as $\mathbf{h}(\mathbf{q}, \mathbf{u})$ so the equations of motion can be written as

$$\mathbf{A}\dot{\mathbf{u}} = \mathbf{h}(\mathbf{q}, \mathbf{u}). \tag{59}$$

Let us introduce the vector $\mathbf{x}$ in the following expression:

$$\dot{\mathbf{u}} = \Psi \mathbf{x}. \tag{60}$$

Substituting this into Eq. (59) yields

$$\mathbf{A}\Psi\mathbf{x} = \mathbf{h}(\mathbf{q}, \mathbf{u}). \tag{61}$$

We can now premultiply both sides of Eq. (61) by Ψ^T giving us

$$\Psi^T \mathbf{A}\Psi\mathbf{x} = \Psi^T \mathbf{h}(\mathbf{q}, \mathbf{u}). \tag{62}$$

However, notice the left-hand side of Eq. (62) is a congruency transformation on the symmetric matrix $\mathbf{A}$. If Ψ is chosen as prescribed earlier, $\Psi^T\mathbf{A}\Psi$ will be diagonal. Let $\mathbf{L} = \Psi^T\mathbf{A}\Psi$ so Eq. (62) becomes

$$\mathbf{L}\mathbf{x} = \Psi^T \mathbf{h}(\mathbf{q}, \mathbf{u}). \tag{63}$$

Vector $\mathbf{x}$ can be written as

$$\mathbf{x} = \mathbf{L}^{-1}\Psi^T \mathbf{h}(\mathbf{q}, \mathbf{u}) \tag{64}$$

when the inverse of $\mathbf{L}$ is simply comprised of the reciprocals of its diagonal elements. Finally, the resulting first-order decoupled form in terms of $\dot{\mathbf{u}}$ is

$$\dot{\mathbf{u}} = \Psi\mathbf{L}^{-1}\Psi^T \mathbf{h}(\mathbf{q}, \mathbf{u}). \tag{65}$$

We see that Eq. (65) is well structured for direct numerical integration without inversion of the $\mathbf{A}$ matrix.

Conclusion

We have proposed and demonstrated a method for creating rigid-body equations of motion that are decoupled in first-order terms. This is achieved by properly choosing a congruency transformation that specifies generalized velocity components. For nonholonomic systems, or holonomic systems with unreduced configuration coordinates, the congruency transformation is used in conjunction with an orthogonal complement to the constraint array. In both cases, the resulting equations are in a form that make it convenient for nonlinear behavior analyses. Moreover, it becomes an easy matter to implement general integration routines for first-order differential equations to obtain generalized coordinate trajectories for simulation purposes.

Acknowledgment

The financial support of this work by US Army Research Office grant no. DAAL-03-90-G-0005 is gratefully acknowledged.

References

Ben-Israel, A., and Greville, T. N. E., 1974, *Generalized Inverses: Theory and Applications*, John Wiley and Sons, New York.

Crandall, S. H., Karnopp, D. C., Kurtz, E. F., Jr., and Pridmore-Brown, D. C., 1968, *Dynamics of Mechanical and Electromechanical Systems*, Robert E. Krieger, Malabar, FL.

Desloge, E. A., 1987, "Relationship Between Kane's Equations and the Gibbs-Appell Equations," Engineering Notes, *Journal of Guidance, Control and Dynamics*, Vol. 10, Jan.-Feb., pp. 120–122.

Gibbs, J. W., 1879, "On the Fundamental Formulae of Dynamics," *American Journal of Mathematics*, Vol. II, pp. 49–64.

Gibbs, J. W., 1961, *The Scientific Papers of J. Willard Gibbs*, Vol. II, Dover, New York.

Hartog, J. P. D., 1948, *Mechanics*, Dover Publications, New York.

Hemami, H., and Weimer, F. C., 1981, "Modeling of Nonholonomic Dynamic Systems With Applications," ASME JOURNAL OF APPLIED MECHANICS, Vol. 48, pp. 177–182.

Huston, R. L., 1990, *Multibody Dynamics*, Butterworth-Heinemann, Boston.

Huston, R. L., 1987, "On the Equivalence of Kane's Equations and

Gibbs' Equations for Multibody Dynamics Formulations," *Mechanics Research Communications*, Vol. 14, No. 2, pp. 123–131.

Kamman, J. W., and Huston, R. L., 1984, "Dynamics of Constrained Multibody Systems," ASME JOURNAL OF APPLIED MECHANICS, Vol. 51, pp. 899–903.

Kane, T. R., 1972, *Dynamics*, Stanford, CA.

Kane, T. R., and Levinson, D. A., 1985, *Dynamics: Theory and Applications*, McGraw-Hill, New York.

Lawson, C. L., and Hanson, R. J., 1974, *Solving Least Squares Problems*, Prentice-Hall, Englewood Cliffs, N.J.

Nikravesh, P. E., and Haug, E. J., 1983, "Generalized Coordinate Partitioning for Analysis of Mechanical Systems with Nonholonomic Constraints," ASME *Journal of Mechanisms, Transmissions, and Automation in Design*, Vol. 105, pp. 379–384.

Papastavridis, J. G., 1992, "Discussion on the Paper Entitled: Dynamics of Nonholonomic Mechanical Systems Using a Natural Orthogonal Complement," ASME JOURNAL OF APPLIED MECHANICS, Vol. 59, pp. 242–244.

Papastavridis, J. G., 1988, "On the Nonlinear Appell's Equations and the Determination of Generalized Reaction Forces," *Int. J. Engng. Sci.*, Vol. 26, No. 6, pp. 609–625.

Roberson, R. E., and Schwertassek, R., 1988, *Dynamics of Multibody Systems*, Springer-Verlag, Berlin.

Scott, D., 1988, "Can a Projection Method of Obtaining Equations of Motion Compete with Lagrange's Equations," *American Journal of Physics*, Vol. 56, May, pp. 451–456.

Singh, R. P., and Likins, P. W., 1985, "Generalized Coordinate Partitioning for Constrained Dynamical Systems," ASME JOURNAL OF APPLIED MECHANICS, Vol. 52, pp. 943–948.

Storch, J., and Gates, S., 1989, "Motivating Kane's Method for Obtaining Equations of Motion for Dynamic Systems," Engineering Notes, *Journal of Guidance, Control and Dynamics*, Vol. 12, July–Aug., pp. 593–595.

Wade, T. L., 1951, *The Algebra of Vectors and Matrices*, Addison-Wesley, Cambridge, MA.

Wang, J. T., and Huston, R. L., 1988, "Computational Methods in Constrained Multibody Dynamics: Matrix Formalisms," *Computers and Structures*, Vol. 29, No. 2, pp. 331–338.

Wehage, R. A., and Haug, E. J., 1982, "Generalized Coordinate Partitioning for Dimension Reduction in Analysis of Constrained Dynamic Systems," ASME *Journal of Mechanical Design*, Vol. 104, pp. 247–255.

Wampler, C., Buffinton, K., and Shu-hui, J., 1985, "Formulation of Equations of Motion for Systems Subject to Constraints," ASME JOURNAL OF APPLIED MECHANICS, Vol. 52, pp. 465–470.

Xu, M., Liu, C., and Huston, R. L., 1990, "Analysis of Nonlinearly Constrained Non-Holonomic Multibody Systems," *International Journal of Non-Linear Mechanics*, Vol. 25, No. 5, pp. 511–519.

S. Toll

J.-A. E. Manson[1]

Laboratoire de Technologie des Composites et Polymères, Ecole Polytechnique Fédérale de Lausanne, CH-1015 Lausanne, Switzerland

Elastic Compression of a Fiber Network

A constitutive equation for a planar fiber network under transverse compression is derived allowing for an in-plane fiber orientation distribution. The fibers are assumed to be well dispersed in space and to have a large aspect ratio and uniform diameter. A compression experiment, performed on a glass-fiber network obtained by ashing a commercial composite preform, is accurately described by the theory.

Introduction

In various manufacturing processes for composite materials solid fibers are suspended in a liquid matrix and the whole is formed by the application of pressure. If the fibers are sufficiently long, they form a load-supporting network which may substantially contribute to the stress state in the suspension. The magnitude of this stress contribution depends on the volume fraction, fiber orientation distribution, and the spatial arrangement of the fibers. In many processes, such as compression moulding, the fiber orientation distribution is planar or close to planar, and the network is compressed in the direction perpendicular to the plane of orientation. The compressive stress exerted by the network in that direction is the concern of the present work.

A fiber network has a volume in excess of that occupied by the fibers, that depends on the specific fiber arrangement. On loading the network, the fibers will deform to decrease that excess volume and thus increase the fiber volume fraction. A large number of empirical or semi-empirical models have been suggested to describe the load-volume fraction relation for different types of fiber assemblies. Aligned fiber beds appear to derive their excess volume from the inherent misalignment or waviness of the fibers. Gutowski et al. (1992) have proposed a model for the compressibility of aligned fiber beds based on the assumption that the fibers form arches of a constant height-to-length ratio. The resulting equation contains three adjustable parameters. Van Wyk (1946) suggested a model for the compression of wool with three-dimensional random orientation. His result is a simple power law:

$$P = k\phi^3, \tag{1}$$

where P is the compressive force per unit area, ϕ is the volume fraction, and k is an adjustable constant of proportionality. There is plenty of experimental support for this expression. Already Schofield (1938) proposed it as an empirical equation based on his experiments on compression of wool.

Both of the above models are based on the bending of fiber segments between fiber-fiber contact points. This concept will here be applied to a third case: a fiber network with an general planar, but nonaligned fiber orientation distribution. A constitutive theory is thus developed on purely mechanistic grounds using no adjustable parameters.

Problem Formulation

The fiber network under consideration is idealized as follows:

1 The structure of the fiber network is statistically homogeneous.

2 The fibers are approximately straight and all oriented in the same plane.

3 The fibers are well dispersed in space, in the sense that they do not form bundles of parallel fibers.

4 The fibers are sufficiently long that the constitutive behavior does not depend on the fiber length distribution. Under what conditions this requirement is fulfilled will be discussed later on.

5 The fiber diameter is uniform.

6 Since we only concerned with the fiber network itself, the space between the fibers is regarded as void, i.e., there is nothing there to store or dissipate energy.

7 The deformation is elastic; i.e., no sliding between fibers in contact is allowed as this would give rise to inelastic dissipation. This is a necessary condition for the existence of a positive definite strain energy function, on which the present derivation relies.

The network is subjected to a uniaxial compressive stress P directed perpendicular to the plane of orientation. We seek the constitutive relation

$$P = P[\phi, \psi(\theta)],$$

where ϕ is the fiber volume fraction, and $\psi(\theta)$ is the in-plane fiber orientation distribution function.

[1]To whom all correspondence should be addressed.

Contributed by the Applied Mechanics Division of THE AMERICAN SOCIETY OF MECHANICAL ENGINEERS for publication in the ASME JOURNAL OF APPLIED MECHANICS.

Discussion on this paper should be addressed to the Technical Editor, Professor Lewis T. Wheeler, Department of Mechanical Engineering, University of Houston, Houston, TX 77204-4792, and will be accepted until four months after final publication of the paper itself in the ASME JOURNAL OF APPLIED MECHANICS.

Manuscript received by the ASME Applied Mechanics Division, Dec. 2, 1992; final revision, Aug. 2, 1993. Associate Technical Editor: G. J. Dvorak.

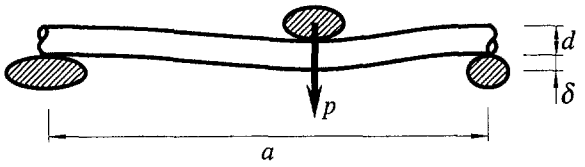

Fig. 1 Example of node geometry

Theory

Each fiber makes contact with a number of other fibers crossing above and below. When an external uniaxial pressure is applied the fibers act as beams supported at the contact points. A segment of a fiber deflects between two supporting fibers under the load of a third. Such a segment will be called a node, and one of several possible realizations is illustrated in Fig. 1.

A node will be characterized by the node spacing, a, the nodal force p, the node deflection δ, and the nodal compliance

$$s = \frac{d\delta}{dp}, \tag{2}$$

which depends on the node geometry and the end conditions. The end conditions are determined by the neighboring nodes. As the section in Fig. 1 deflects, it encounters another fiber with a probability which depends on the volume fraction and orientation distribution. In this way new nodes are continuously generated during compression, and the average node spacing $\bar{a}$ and nodal compliance $\bar{s}$ decrease accordingly. The response of the network is thus nonlinear.

It will be necessary to make some assumption of the statistical distribution of nodal forces or displacements. One cannot assume uniformity in either, since a newly formed node must have $p \approx 0$ whereas an old node carries a finite force. Instead we shall assume uniformity in the *incremental* node force dp; i.e., on incremental compression of the network, the increase in the uniaxial pressure is evenly distribution among the nodes existing at the time. This is equivalent to assuming that the force carried by a node is uniquely determined by the volume fraction at which it is formed (or force free). Since the node compliance is nonuniform, the incremental node deflection $d\delta$ will be nonuniform. However, this allows us to write the average incremental node deflection in terms of the average nodal compliance:

$$\overline{d\delta} = \bar{s}dp. \tag{3}$$

A strain energy function can now be defined

$$d\mathcal{W} = \eta\overline{pd\delta}, \tag{4}$$

where η is the node density, the number of nodes per unit volume. Substituting (2) for $d\delta$ and using the uniformity of dp,

$$d\mathcal{W} = \eta\overline{s}\overline{p}\,dp. \tag{5}$$

Substituting (3) for dp we obtain

$$d\mathcal{W} = \eta\frac{\overline{ps}}{\bar{s}}\overline{d\delta}. \tag{6}$$

Next we need to relate $\overline{d\delta}$ to the fiber volume fraction ϕ. Since the total fiber volume ϕV is constant,

$$d\phi = d\left(\frac{\phi V}{V}\right) = \phi V d\left(\frac{1}{V}\right) = -\phi\frac{dV}{V}, \tag{7}$$

where V is the total volume of the network. Now, recognizing that if $\bar{\delta} = d$ the network is collapsed, i.e., $V = 0$, and assuming that $\bar{\delta} \ll d$, we can write

$$\frac{dV}{V} = -\frac{\overline{d\delta}}{d} \tag{8}$$

and arrive at

$$\overline{d\delta} = \frac{d}{\phi}d\phi. \tag{9}$$

Now, by substitution of (9) into (6), we have

$$d\mathcal{W} = \eta\frac{\overline{ps}}{\bar{s}}\frac{d}{\phi}d\phi. \tag{10}$$

Differentiation of the strain energy function with respect to a change in the total volume gives the uniaxial pressure:

$$P = -\frac{d\mathcal{W}}{dV}V = \frac{d\mathcal{W}}{d\phi}\phi = d\cdot\eta\frac{\overline{ps}}{\bar{s}}. \tag{11}$$

To eliminate the unknown nonuniform p, (11) is again differentiated with respect to p and (3) substituted for dp:

$$dP = d\cdot\eta dp = d\cdot\eta\frac{\overline{d\delta}}{\bar{s}}. \tag{12}$$

Substituting Eq. (9) we have

$$dP = \frac{d^2\cdot\eta}{\bar{s}\phi}d\phi \tag{13}$$

and can integrate with respect to ϕ:

$$P = d^2\int_0^\phi\frac{\eta}{\bar{s}\phi}d\phi. \tag{14}$$

The volume occupied by an average fiber is

$$\frac{\pi}{4}d^2\bar{l},$$

where $\bar{l}$ is the average fiber length. The number of fibers per unit volume is thus

$$\frac{4\phi}{\pi d^2\bar{l}}.$$

Multiplying this by the number of nodes per fiber, $\bar{l}/\bar{a}$ where $\bar{a}$ is the average node spacing, gives the number of nodes per unit volume,

$$\eta = \frac{4\phi}{\pi d^2\bar{a}}, \tag{15}$$

and Eq. (14) becomes

$$P = \frac{4}{\pi}\int_0^\phi\frac{d\phi}{\bar{a}\bar{s}}. \tag{16}$$

An important feature of this result is that the node properties a and s enter only as averages. It now remains to find appropriate forms of these average functions $\bar{a}(\phi)$ and $\bar{s}(\phi)$, both of which will depend on the fiber orientation distribution.

The average number $\overline{N}_i$ of fiber centerlines intersecting a cylindrical test volume of length $\bar{l}$ and diameter D circumscribing an average fiber is exactly (Toll, 1993)

$$\overline{N}_i = n\bar{l}^2Df + \frac{1}{4}\pi n\bar{l}D^2(g+1), \tag{17}$$

where n is the number fraction of fibers and f and g are functions of the fiber orientation distribution. At large aspect ratios l/D the second term may be neglected:

$$\overline{N}_i = n\bar{l}^2Df. \tag{18}$$

The average number of fiber-fiber *contacts* $\overline{N}_c$ along an average fiber can be set equal to the average number of fiber

centerlines intersecting a test cylinder of diameter $D = 2d$; thus, in terms of volume fraction,

$$\bar{N}_c = 2n\bar{l}^2 df = \frac{8}{\pi}\frac{\bar{l}}{d} f\phi. \tag{19}$$

This result has also been obtained by Komori and Makishima (1977). The average node spacing is now obtained as

$$\bar{a} = 2\frac{\bar{l}}{\bar{N}_c} = \frac{\pi}{4}\frac{d}{f\phi}. \tag{20}$$

The orientation function f is defined as (Toll, 1993)

$$f = \oint\oint |\sin(\theta' - \theta)| \psi(\theta')\psi(\theta) d\theta' d\theta, \tag{21}$$

where $\psi(\theta)$ is the in-plane fiber orientation distribution function. The function f can assume values between 0, at unidirectional, and $2/\pi$, at planar random orientation.

The estimation of the average nodal compliance is more difficult because of the uncertainty in the node geometry and end conditions. A simple model can be based on the fiber segment depicted in Fig. 1: a cylindrical beam supported with a no-rotation condition at each end and loaded with p at the midsection. The compliance of such a beam, as known from elementary beam theory, gives the nodal compliance

$$\bar{s} = \frac{\overline{a^3}}{3\pi E d^4}, \tag{22}$$

where E is the Young's modulus of the fiber. It is not obvious whether this model is too stiff or too compliant: on the one hand, the end condition of no rotation is more restrictive than the true end condition—continuity of rotation; on the other hand, the central loading gives higher compliance than a more likely unsymmetrical one. Equation (22) involves the third moment of the node spacing a. This can be estimated by assuming the contact points along a given fiber to be spaced at random. We then have an exponential distribution of contact point spacings,

$$f_a(x) + \frac{1}{\bar{a}} e^{-x/\bar{a}}. \tag{23}$$

Taking the third moment of (23) we obtain

$$\overline{a^3} = 6\bar{a}^3. \tag{24}$$

Thus we have

$$\bar{s} = \frac{2\bar{a}^3}{\pi E d^4}. \tag{25}$$

Substituting Eqs. (20) and (25) into (16) and integrating gives the final result:

$$P = \frac{512}{5\pi^4} E f^4 \phi^5 \approx E f^4 \phi^5. \tag{26}$$

Finally we provide some additional results. Combining (15) and (20), the node density is obtained as

$$\eta = \frac{16}{\pi^2}\frac{f\phi^2}{d^3}. \tag{27}$$

Using $P = \bar{p}\eta d$ and (26), the average nodal force $\bar{p}$ can be written explicitly:

$$\bar{p} = \frac{32}{5\pi^2} E d^2 f^3 \phi^3. \tag{28}$$

$$\tag{29}$$

Experiment

A compression experiment was performed, using a commercial "Glass Mat reinforced Thermoplastic sheet" (GMT) with discontinuous fibers and polypropylene matrix (AZDEL, Inc.). This composite is produced by a slurry deposition process similar to that used for paper making, and contains well-dispersed fibers with almost perfectly planar orientation. The fiber diameter and length are about 12 μm and 12 mm, respectively. The fiber volume fraction of the composite as determined by ashing is about 0.087.

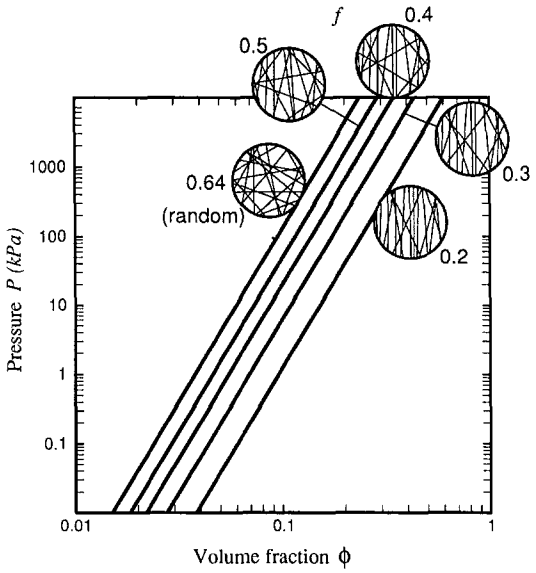

Fig. 2 Theoretical P-ϕ relation for various fiber orientation distributions

The in-plane fiber orientation distribution was determined by metallographic polishing followed by digital image analysis. This technique has been described by Toll and Andersson (1991). The orientation function f was then calculated according to Eq. (21):

$$f^{\mathrm{GMT}} = 0.46.$$

A fiber network was prepared by ashing the GMT material at 560°C for one hour. This network was compressed between two circular parallel plates by the application of weights, while recording the distance between the plates. The plate diameter was 50 mm, and the mass of glass fibers between the plates was 1.96 g.

Results and Discussion

Figure 2 shows the theoretical log-log plot of P versus ϕ according to Eq. (26) at various fiber orientation distributions. This curve is a straight line of slope 5, and the effect of changing the orientation distribution is to shift the curve along the ϕ-axis.

Figure 3 shows the experimental datapoints along with the theoretical P-ϕ relation for the ashed GMT material. For illustration purposes the number of nodes per fiber, $l/\bar{a}$, as a function of ϕ has been calculated according to Eq. (20) and indicated in the figure. The data suggest an upper and a lower limit to the applicability of the theory; at very low and very high volume fractions the theory is too stiff, whereas in an intermediate range the data agree very accurately with the theoretical curve.

A real fiber network possesses a finite unloaded volume fraction ϕ_0, due to the action of volume and surface related forces such as gravity and electrostatics. The volume fraction will tend to ϕ_0 as $P \to 0$ thus explaining the deviation of the first data point from the straight line.

For the tested fiber network ϕ_0 was about 0.02, corresponding to about 12 nodes per fiber, and the first datapoint at $\phi = 0.03$ corresponds to some 18 nodes per fiber. This

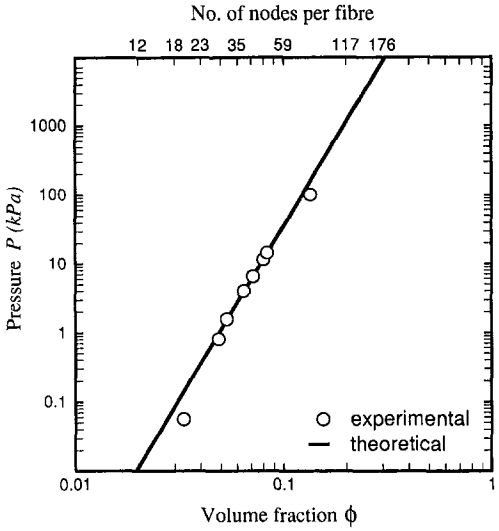

Fig. 3 Experimental P-ϕ datapoints along with the theoretical prediction for the fiber orientation distribution measured ($f = 0.46$). The average number of nodes per fiber, according to Eq. (20), is also indicated.

ought to be sufficiently many for the fiber ends not to significantly affect the response, and thus our neglect of fiber ends, or equivalently assumption of infinite fiber length, holds. If the fibers were shorter, the effect of the fiber ends would have caused ϕ_0 to be even higher. At high volume fractions (the last datapoint) clearly audible fiber breakage occurs. Since this is an inelastic effect not accounted for, the theory again overestimates P. However, the rather low level of this upper applicability limit is peculiar of this experiment: the ashing procedure most certainly damages the fiber surfaces and reduces the fiber strength. In an actual manufacturing process the fibers are well protected by a polymer matrix and fiber breakage should occur only at much higher pressure.

The exceptional experimental agreement is reassuring but unexpected. After all, we have made a series of assumptions whose validity cannot be expected to be complete. The simple beam that we have used to model the compliance of a fiber segment is totally symmetric and thus has certain weaknesses. It cannot account for the fact that the direction of contact force is not simply alternating, or that the beam segment is not loaded midway between the supports. In addition, we have made assumptions such as uniform incremental nodal forces, perfect dispersion, and no sliding between fibers. Nevertheless, we find a perfect agreement with the experimental data.

The same basic mechanism of beam bending between contact points was used in Van Wyk's model of a three-dimensional network. The resulting form is also very similar, except that in the three-dimensional case $P \propto \phi^3$ rather than $P \propto \phi^5$. There is, however, no analytical solution for the constitutive parameter k in Eq. (1).

When the fibers of a node form wide angles at the contact points it seems appropriate to derive the nodal compliance from a simple beam model. However, when contacting fibers are close to parallel, the contact *surface* may become substantial and a contact point no longer is an appropriate description. This means that Eq. (26) most likely does not apply at very high fiber alignments. This is, however, no limitation of the result (16), provided that appropriate functions $\bar{s}$ and $\bar{a}$ can be found.

Acknowledgment

The authors wish to thank Fonds National Suisse de la Recherche Scientifique for the financial support, and Azdel, Inc., USA, for supplying the GMT material. We also wish to thank Prof. Geoff Gibson, University of Newcastle, for helpful suggestions.

References

Gutowski, T. G., and Dillon, G., 1992, "The Elastic Deformation of Lubricated Carbon Fiber Bundles: Comparison of Theory and Experiments," *Journal of Composite Materials*, Vol. 26, pp. 2330–2347.

Komori, T., and Makishima, K., 1977, "Numbers of Fiber-to-Fiber Contacts in General Fiber Assemblies," *Textile Research Journal*, Vol. 47, pp. 13–17.

Toll, S., 1993, "Note: On the Tube Model for Fibre Suspensions," *Journal of Rheology*, Vol. 37, pp. 123–125.

Toll, S., and Andersson, P.-O., 1991, "Microstructural Characterisation of Injection Moulded Composites Using Image Analysis," *Composites*, Vol. 22, pp. 298–306.

van Wyk, C. M., 1946, "Note on the Compressibility of Wool," *Journal of the Textile Institute*, Vol. 37, pp. T285–T292.

Schofield, J., 1938, "Researches on Wool Felting, Part 1," *Journal of the Textile Institute*, Vol. 29, pp. T239–T252.

Journal of Applied Mechanics

Brief Notes

A Brief Note is a short paper that presents a specific solution of technical interest in mechanics but which does not necessarily contain new general methods or results. A Brief Note should not exceed 1500 words *or equivalent* (a typical one-column figure or table is equivalent to 250 words; a one line equation to 30 words). Brief Notes will be subject to the usual review procedures prior to publication. After approval such Notes will be published as soon as possible. The Notes should be submitted to the Technical Editor of the JOURNAL OF APPLIED MECHANICS. Discussions on the Brief Notes should be addressed to the Editorial Department, ASME, United Engineering Center, 345 East 47th Street, New York, N. Y. 10017, or to the Technical Editor of the JOURNAL OF APPLIED MECHANICS. Discussions on Brief Notes appearing in this issue will be accepted until two months after publication. Readers who need more time to prepare a Discussion should request an extension of the deadline from the Editorial Department.

A Note on the Stability and Instability of the System With Time Variable Parameters

L. Cveticanin[1]

1 Introduction

In the previous time a lot of stability and instability theories were developed for the systems with time variable parameters described as

$$\ddot{x} + C(t)\dot{x} + K(t)x = 0, \tag{1}$$

where $C(t)$ and $K(t)$ represent the arbitrary time-dependent damping and rigidity coefficients, x is a deflection function and $(\dot{}) \equiv d/dt$, $(\ddot{}) \equiv d^2/dt^2$, but all of them have some restrictions. Most of the theories are based on the Liapunov direct stability and instability theorems and the Liapunov function is assumed as an energy-type function

$$V = \frac{1}{2}f_1(t)\dot{x}^2 + \frac{1}{2}f_2(t)x^2, \tag{2}$$

where $f_1(t)$ and $f_2(t)$ are time variable functions. Merkin (1971) assumed the case when $f_1(t) = f_2(t) = 1$, and the stability conditions are defined only for the case when the functions $C(t)$ and $K(t)$ have constant values. In the paper of Shrivastava (1981) the theorem of stability is defined for the case when $C(t)$ and $K(t)$ are arbitrary functions. The disadvantage of the method is that it does not give the conditions of asymptotical stability or instability. An extension is done by Ahmadian (1986) for $C(t)$ and $K(t)$ monotony functions. The suggested theorems give the conditions of asymptotical stability and instability only for some special types of rigidity and damping functions.

In this paper a new type of Liapunov function is formed which allows to follow the classical Liapunov results on asymptotic stability and instability of nonautonomous systems and represents an extension of the previous results. A stability theorem for a special type of second-order different equation with complex deflection function is also defined.

2 Analysis

Let us assume a function V in a total square form:

$$V = \frac{1}{2}f_1(t)\dot{x}^2 + \frac{1}{2}f_2(t)x^2 + f_3(t)x\dot{x}. \tag{3}$$

The corresponding time derivative after substituting (1) is

$$\dot{V} = \frac{1}{2}\dot{f}_1(t)\dot{x}^2 + \frac{1}{2}\dot{f}_2(t)x^2 - K(t)x\dot{x}f_1(t) - C(t)\dot{x}^2f_1(t) - f_2(t)x\dot{x} + \dot{f}_3(t)x\dot{x} + f_3(t)\dot{x}^2 - f_3(t)K(t)\dot{x}x - f_3(t)C(t)\dot{x}^2. \tag{4}$$

Using the Eqs. (3) and (4), the conditions for asymptotic stability and instability of (1) will be defined.

Theorem of Asymptotic Stability.

Theorem 1: If there are bounded positive definite functions $f_1(t)$ and $f_2(t)$ which are nonsingular and continuously differentiable and a positive definite function $f_3(t)$ which is also continuously differentiable and satisfies the relation

$$f_3^2(t) < f_1(t)f_2(t), \tag{5a}$$

and if

$$C(t)f_1(t) - f_3(t) - \frac{1}{2}\dot{f}_1(t) > 0, \tag{5b}$$

$$f_3(t)K(t) - \frac{1}{2}\dot{f}_2 > 0, \tag{5c}$$

$$4\left[C(t)f_1(t) - f_3(t) - \frac{1}{2}\dot{f}_1(t)\right]\left[f_3(t)K(t) - \frac{1}{2}\dot{f}_2\right] - \left[f_2 + \dot{f}_3 - f_3C(t) - K(t)f_1(t)\right]^2 > 0, \tag{5d}$$

the unperturbed motion described with (1) is asymptotically stable.

Proof: If the functions $f_1(t)$ and $f_2(t)$ are positive definite and have a small upper limit, and if the condition (5*a*) is satisfied, the function V (3) represents a positive definite bounded function for all $t \geq t_o$ and $\max(|x|, |\dot{x}|, |y|, |\dot{y}|) \leq h$.

[1]Faculty of Technical Sciences, V. Vlahovica 3, 21000 Novi Sad, Yugoslavia.

Contributed by the Applied Mechanics Division of THE AMERICAN SOCIETY OF MECHANICAL ENGINEERS for publication in the ASME JOURNAL OF APPLIED MECHANICS. Manuscript received by the ASME Applied Mechanics Division, Sept. 13, 1993; final revision, Apr. 20, 1994. Associate Technical Editor: P. D. Spanos.

The time derivative $\dot{V}$ is a negative definite function for (5*b*)–(5*d*). The function V and its derivative $\dot{V}$ satisfy all the conditions of the Liapunov theorem of asymptotic stability (see Leipholz, 1970).

Propositions:

(1) The asymptotic stability is not possible for $C(t) \le 0$, because the condition (5*b*) is never satisfied.

(2) The motion is asymptotic stable for $K(t)$ positive (according to (5*c*)).

Example. Let us analyze the asymptotic stability for some monotony functions $C(t)$ and $K(t)$.

We assume the functions $f_1 = 1$, $f_2 = K(t) + C(t)/2$, $f_3 = 1/2$. The unperturbed motion described by (1) is asymptotically stable for

$$C(t) > 1/2, \quad K(t) - \dot{K}(t) - \dot{C}(t)/2 > 0. \tag{6}$$

(1) If $C(t)$ is a decreasing function or a constant which satisfies the condition (6) and $K(t)$ is also a decreasing function or a constant value, the motion is asymptotically stable, i.e., it tends to the position (0, 0).

(2) If $C(t)$ is increasing and satisfying (6) and $K(t)$ is increasing or decreasing, respectively, the stability conditions are

$$K_{\min} - \dot{K}_{\max} - \dot{C}_{\max}/2 > 0,$$

$$K_{\min} + \dot{K}_{\min} - \dot{C}_{\max}/2 > 0.$$

(3) For a constant damping parameter and $K(t)$ increasing or decreasing, respectively, the stability conditions are

$$K_{\min} - \dot{K}_{\max} > 0,$$

$$K_{\min} + \dot{K}_{\min} > 0.$$

Theorem of Instability.

Theorem 2: If there are bounded positive functions $f_1(t)$ and $f_2(t)$ which are nonsingular and continuously differentiable and a positive function $f_3(t)$ which is also continuously differentiable and satisfies the relation

$$f_3^2(t) \le f_1(t) f_2(t), \tag{7a}$$

and if

$$f_3(t) - C(t) f_1(t) + \frac{1}{2}\dot{f}_1(t) > 0, \tag{7b}$$

$$\frac{1}{2}\dot{f}_2 - f_3(t) K(t) > 0, \tag{7c}$$

$$4\left[f_3(t) - C(t) f_1(t) + \frac{1}{2}\dot{f}_1(t)\right]\left[\frac{1}{2}\dot{f}_2 - f_3(t) K(t)\right] - \left[f_2 + \dot{f}_3 - f_3 C(t) - K(t) f_1(t)\right]^2 > 0, \tag{7d}$$

the unperturbed motion described as (1) is instable.

Proof: If the functions $f_1(t)$ and $f_2(t)$ are positive and have an infinitely small upper bound for $t \ge t_o$ and $x_i \equiv \max(|x|, |\dot{x}|) \le h$ and the condition (7*a*) is satisfied, the function V (3) is positive, semi-definite, and bounded. For the conditions (7*b*)–(7*d*) the time derivative $\dot{V}$ (4) is a positive definite function. As V has the same sign as $\dot{V}$ for arbitrarily large t when x_i are arbitrarily small, the function V represents a Liapunov function which satisfies the conditions of the Liapunov theorem of instability (see Leipholz, 1970).

Note: If the functions $f_1(t)$ and $f_2(t)$ are not only bounded but also positive definite and the function $f_3(t)$ satisfies the relations (7*b*–7*d*), then the function V is positive definite with a small upper limit and for that function the instability is totality in the Liapunov sense (see Hahn, 1959, pp. 16).

Propositions:

(1) The instability may occur not only for negative values of $C(t)$ but also non-negative which satisfies the relation (7*b*).

(2) The instability conditions are satisfied for $K(t)$ negative definite.

Example. Let us assume the Liapunov function where $f_1 = 1$, $f_2 = K(t) + C(t)/2$, $f_3 = 1/2$. The instability conditions are satisfied for

$$C(t) < 1/2, \ \dot{K}(t) + \dot{C}(t)/2 - K(t) > 0. \tag{8}$$

The second relation is satisfied for $K(t) < 0$. The condition (8) is then

$$C(t) < 1/2, \ -|\dot{K}(t)| + \dot{C}(t)/2 + |K(t)| > 0. \tag{9}$$

(1) If the damping is a constant value which satisfies (8) (including $C = 0$) and $K(t)$ is a negative decreasing function the motion is always instable. The same conclusion corresponds for $C(t)$ a positive increasing function and a negative decreasing function.

(2) If $C(t)$ is positive increasing or negative decreasing and satisfying (8) and $K(t)$ is negative increasing, the instability conditions are

$$|K_{\min}| - |\dot{K}_{\max}| + \dot{C}_{\min}/2 > 0.$$

(3) For $C(t)$ is positive decreasing or negative increasing and satisfying (8) and $K(t)$ is negative increasing or decreasing, respectively, the instability conditions are

$$|K_{\min}| - |\dot{K}_{\max}| - \dot{C}_{\max}/2 > 0,$$

$$|K_{\min}| + |\dot{K}_{\min}| - \dot{C}_{\max}/2 > 0.$$

Comments. The only possibility to analyze the asymptotic stability and instability applying of the Liapunov function of the energy type is to extend it with a term $f_3(t)x\dot{x}$. For $f_3(t) = 0$ the condition (5*c*) or (7*c*) can never been satisfied because for a limited and definite function f_2 the time derivative is $\dot{f}_2(t) = 0$ for $t \to \infty$.

3 Stability Analysis of a System With Complex Deflection Function

Let us consider a linear second-order differential equation with complex deflection function z and time variable parameters

$$\ddot{z} + C(t)\dot{z} + K(t)z - iG(t)\dot{z} = 0 \tag{9}$$

where $C(t)$, $K(t)$, and $G(t)$ represent the arbitrary time-dependent damping, rigidity, and gyroscopic coefficients, respectively, $z = x + iy$ complex deflection function, $i = \sqrt{-1}$ is imaginary unit. Let us assume a function of the energy form

$$V = \frac{1}{2} f_1(t)\left(\dot{x}^2 + \dot{y}^2\right) + \frac{1}{2} f_2(t)\left(x^2 + y^2\right) \tag{10}$$

where $f_1(t)$ and $f_2(t)$ are arbitrary time variable functions. It is an extension of the function suggested by Ahmadian (1986) where $f_1(t) = 1$, $f_2(t) = K(t)$. The time derivative of the function (10) according to (9) is

$$\dot{V} = \frac{1}{2}\dot{f}_1(t)\left(\dot{x}^2 + \dot{y}^2\right) + \frac{1}{2}\dot{f}_2(t)\left(x^2 + y^2\right) - K(t)\left(x\dot{x} + y\dot{y}\right) f_1(t) - C(t)\left(\dot{x}^2 + \dot{y}\right) f_1(t) - f_2(t)\left(x\dot{x} + y\dot{y}\right). \tag{11}$$

Let us formulate the Theorem of stability.

Theorem 3: If there are positive-definite continuously differentiable functions $f_1(t)$ and $f_2(t)$ and if it is

$$C(t)f_1(t) - \frac{1}{2}\dot{f}_1(t) \geq 0, \tag{12a}$$

$$-\frac{1}{2}\dot{f}_2 \geq 0, \tag{12b}$$

$$4\left[C(t)f_1(t) - \frac{1}{2}\dot{f}_1(t)\right]\left[-\frac{1}{2}\dot{f}_2\right] - \left[f_2 - K(t)f_1(t)\right]^2 \geq 0, \tag{12c}$$

the unperturbed motion described as (9) is stable.

Proof: According to the fact that the functions $f_1(t)$ and $f_2(t)$ are positive-definite, the function V (10) is a positive definite function for $t \geq t_o$ and $\max(|x|, |\dot{x}|, |y|, |\dot{y}|) \leq h$. The time derivative of V is a function (11) which is negative semi-definite or is identically zero according to (12*a*)–(12*c*). The function V represents a Liapunov function (see La Salle, 1968) which satisfies the conditions of stability theorem (see Hahn, 1959).

To satisfy the conditions (12) the following requirements have to be fulfilled:

(1) The function $f_2(t)$ has to be a positive decreasing or a positive constant function.

(2) If the damping is neglected, the function $f_1(t)$ has to be a non-negative function.

(3) The stability condition (12*a*) may be satisfied, not only for positive damping but also for the case when the damping is zero and $K(t)$ is a positive definite function.

(4) For the case when $C(t)$ is a positive definite function, the motion is stable for $K(t)$ non-negative.

(5) The gyroscopic effect has no influence on the stability properties of the system. The same conclusion is given by Cveticanin (1992).

(6) The functions $C(t)$ and $K(t)$ may be also periodical.

Note: The conditions of simple stability (12) correspond also for the system (1).

Example. Let us consider the case when

$$C(t) = 1 + \frac{1}{t+1}, \quad K(t) = \delta + \epsilon\cos(\Omega t), \quad \text{where } (\delta - \epsilon) > 0,\ t \geq 0. \tag{13}$$

We introduce the functions

$$f_1(t) = \frac{1}{(t+1)K(t)} \quad \text{and} \quad f_2(t) = \frac{1}{t+1}. \tag{14}$$

As the stability conditions (12) are satisfied, it can be concluded that the unperturbed motion of the system is stable.

References

Ahmadian, M., 1986, "On the Stability of Multiple Parameter Time-Varying Dynamic Systems," *Int. J. Non-Linear Mechanics*, Vol. 21, No. 6, pp. 483–488.

Cveticanin, L., 1992, "Dynamic Behavior of a Rotor with Time-Dependent Parameters," *International Journal of the JSME*.

Hahn, W., 1959, *Theorie und Anwendung der Direkten Methode von Liapunov*, Springer-Verlag, Berlin, pp. 142.

La Salle, J. P., 1968, "Stability Theory for Ordinary Differential Equations," *J. of Differential Equations*, Vol. 4, No. 1, pp. 57–65.

Leipholz, H., 1970, *Stability Theory: An Introduction to the Stability of Dynamic Systems and Rigid Bodies*, Academic Press, New York, pp. 277.

Merkin, D. R., 1971, *Vedenie v teoriju ustojchivosti dvizhenija*, Nauka, Moscow, pp. 312.

Shrivastava, S. K., 1981, "Stability Theorems for Multidimensional Linear Systems with Variable Parameters," ASME JOURNAL OF APPLIED MECHANICS, Vol. 48, pp. 174–177.

Stresses in Open-Ended Cylindrical Shells

J. T.-S. Wang[2] and C.-C. Lin[2]

Timoshenko and Woinowsky-Krieger (1959) stated on p. 501 in their book that if the ends of a thin circular cylindrical shell are free and the loading is not symmetrical with respect to the axis of the cylinder, the deformation consists principally in bending. The present study presents some explorations from the standpoint of stress distribution to qualitatively verify the statement for an open-ended cylindrical shell under normal loading which does not vary along the axis of the shell.

The following equilibrium equations, without the effect of body forces, in cylindrical polar coordinates for stress distribution which is independent of the longitudinal axis, can be found in textbooks on mechanics of solids such as the book by Fung (1965):

$$\frac{\partial\sigma_r}{\partial r} + \frac{1}{r}\frac{\partial\tau_{\theta r}}{\partial\theta} + \frac{\sigma_r - \sigma_\theta}{r} = 0 \tag{1}$$

$$\frac{\partial\tau_{r\theta}}{\partial r} + \frac{2}{r}\tau_{r\theta} + \frac{1}{r}\frac{\partial\sigma_\theta}{\partial\theta} = 0 \tag{2}$$

for $a < r < b$ where a and b are radii of curvatures of the inner and outer surfaces of the shell, respectively; r and θ are radial and circumferential coordinates, respectively. If R is the radius of curvature of the middle surface and h is the thickness of the cylindrical shell, then $a = R\text{-}h/2$ and $b = R + h/2$.

Load Independent of θ

When the load is independent of θ, $\tau_{r\theta} = 0$ and the other two stress components are also independent of θ. The only equilibrium equation reduced from Eq. (1) becomes

$$\frac{d}{dr}(r\sigma_r) = \sigma_\theta. \tag{3}$$

The effective loading q per unit mid-surface area is related to the loadings q_0 and q_i on the outer and inner surfaces, respectively, as follows:

$$qR = q_0 b - q_i a. \tag{4}$$

The following four combinations of surface loadings are considered in the exploration:

Case 1. $q_0 b = -q_i a = qR/2$.

Since $r\sigma_r$ varies from $-qR/2$ to $qR/2$ as ζ varies from $-h/2$ to $h/2$ where ζ is the radial coordinate measured from the mid-surface of the cylindrical shell, we consider that $r\sigma_r$ varies as an odd function of ζ.

[2]Institute of Applied Mathematics, National Chung-Hsing University, Taichung, Taiwan 40227, R.O.C.

Contributed by the Applied Mechanics Division of THE AMERICAN SOCIETY OF MECHANICAL ENGINEERS for publication in the ASME JOURNAL OF APPLIED MECHANICS. Manuscript received by the ASME Applied Mechanics Division, Feb. 7, 1994; final revision, June 7, 1994. Associate Technical Editor: W. K. Liu.

Let us formulate the Theorem of stability.

Theorem 3: If there are positive-definite continuously differentiable functions $f_1(t)$ and $f_2(t)$ and if it is

$$C(t)f_1(t) - \frac{1}{2}\dot{f}_1(t) \geq 0, \tag{12a}$$

$$-\frac{1}{2}\dot{f}_2 \geq 0, \tag{12b}$$

$$4\left[C(t)f_1(t) - \frac{1}{2}\dot{f}_1(t)\right]\left[-\frac{1}{2}\dot{f}_2\right] - \left[f_2 - K(t)f_1(t)\right]^2 \geq 0, \tag{12c}$$

the unperturbed motion described as (9) is stable.

Proof: According to the fact that the functions $f_1(t)$ and $f_2(t)$ are positive-definite, the function V (10) is a positive definite function for $t \geq t_o$ and $\max(|x|, |\dot{x}|, |y|, |\dot{y}|) \leq h$. The time derivative of V is a function (11) which is negative semi-definite or is identically zero according to (12*a*)–(12*c*). The function V represents a Liapunov function (see La Salle, 1968) which satisfies the conditions of stability theorem (see Hahn, 1959).

To satisfy the conditions (12) the following requirements have to be fulfilled:

(1) The function $f_2(t)$ has to be a positive decreasing or a positive constant function.

(2) If the damping is neglected, the function $f_1(t)$ has to be a non-negative function.

(3) The stability condition (12*a*) may be satisfied, not only for positive damping but also for the case when the damping is zero and $K(t)$ is a positive definite function.

(4) For the case when $C(t)$ is a positive definite function, the motion is stable for $K(t)$ non-negative.

(5) The gyroscopic effect has no influence on the stability properties of the system. The same conclusion is given by Cveticanin (1992).

(6) The functions $C(t)$ and $K(t)$ may be also periodical.

Note: The conditions of simple stability (12) correspond also for the system (1).

Example. Let us consider the case when

$$C(t) = 1 + \frac{1}{t+1}, \quad K(t) = \delta + \epsilon\cos(\Omega t), \quad \text{where } (\delta - \epsilon) > 0,\ t \geq 0. \tag{13}$$

We introduce the functions

$$f_1(t) = \frac{1}{(t+1)K(t)} \quad \text{and} \quad f_2(t) = \frac{1}{t+1}. \tag{14}$$

As the stability conditions (12) are satisfied, it can be concluded that the unperturbed motion of the system is stable.

References

Ahmadian, M., 1986, "On the Stability of Multiple Parameter Time-Varying Dynamic Systems," *Int. J. Non-Linear Mechanics*, Vol. 21, No. 6, pp. 483–488.

Cveticanin, L., 1992, "Dynamic Behavior of a Rotor with Time-Dependent Parameters," *International Journal of the JSME*.

Hahn, W., 1959, *Theorie und Anwendung der Direkten Methode von Liapunov*, Springer-Verlag, Berlin, pp. 142.

La Salle, J. P., 1968, "Stability Theory for Ordinary Differential Equations," *J. of Differential Equations*, Vol. 4, No. 1, pp. 57–65.

Leipholz, H., 1970, *Stability Theory: An Introduction to the Stability of Dynamic Systems and Rigid Bodies*, Academic Press, New York, pp. 277.

Merkin, D. R., 1971, *Vedenie v teoriju ustojchivosti dvizhenija*, Nauka, Moscow, pp. 312.

Shrivastava, S. K., 1981, "Stability Theorems for Multidimensional Linear Systems with Variable Parameters," ASME JOURNAL OF APPLIED MECHANICS, Vol. 48, pp. 174–177.

Stresses in Open-Ended Cylindrical Shells

J. T.-S. Wang[2] and C.-C. Lin[2]

Timoshenko and Woinowsky-Krieger (1959) stated on p. 501 in their book that if the ends of a thin circular cylindrical shell are free and the loading is not symmetrical with respect to the axis of the cylinder, the deformation consists principally in bending. The present study presents some explorations from the standpoint of stress distribution to qualitatively verify the statement for an open-ended cylindrical shell under normal loading which does not vary along the axis of the shell.

The following equilibrium equations, without the effect of body forces, in cylindrical polar coordinates for stress distribution which is independent of the longitudinal axis, can be found in textbooks on mechanics of solids such as the book by Fung (1965):

$$\frac{\partial\sigma_r}{\partial r} + \frac{1}{r}\frac{\partial\tau_{\theta r}}{\partial\theta} + \frac{\sigma_r - \sigma_\theta}{r} = 0 \tag{1}$$

$$\frac{\partial\tau_{r\theta}}{\partial r} + \frac{2}{r}\tau_{r\theta} + \frac{1}{r}\frac{\partial\sigma_\theta}{\partial\theta} = 0 \tag{2}$$

for $a < r < b$ where a and b are radii of curvatures of the inner and outer surfaces of the shell, respectively; r and θ are radial and circumferential coordinates, respectively. If R is the radius of curvature of the middle surface and h is the thickness of the cylindrical shell, then $a = R\text{-}h/2$ and $b = R + h/2$.

Load Independent of θ

When the load is independent of θ, $\tau_{r\theta} = 0$ and the other two stress components are also independent of θ. The only equilibrium equation reduced from Eq. (1) becomes

$$\frac{d}{dr}(r\sigma_r) = \sigma_\theta. \tag{3}$$

The effective loading q per unit mid-surface area is related to the loadings q_0 and q_i on the outer and inner surfaces, respectively, as follows:

$$qR = q_0 b - q_i a. \tag{4}$$

The following four combinations of surface loadings are considered in the exploration:

Case 1. $q_0 b = -q_i a = qR/2$.

Since $r\sigma_r$ varies from $-qR/2$ to $qR/2$ as ζ varies from $-h/2$ to $h/2$ where ζ is the radial coordinate measured from the mid-surface of the cylindrical shell, we consider that $r\sigma_r$ varies as an odd function of ζ.

[2]Institute of Applied Mathematics, National Chung-Hsing University, Taichung, Taiwan 40227, R.O.C.

Contributed by the Applied Mechanics Division of THE AMERICAN SOCIETY OF MECHANICAL ENGINEERS for publication in the ASME JOURNAL OF APPLIED MECHANICS. Manuscript received by the ASME Applied Mechanics Division, Feb. 7, 1994; final revision, June 7, 1994. Associate Technical Editor: W. K. Liu.

Case 2. $q_0 b = qR$ and $q_i = 0$.

We consider a linear variation of ζ through the thickness of the thin shell for $r\sigma_r$, hence

$$r\sigma_r = qR\left(0.5 + \frac{\zeta}{h}\right). \tag{5}$$

Case 3. $q_0 = 0$ and $q_i a = -qR$.

We consider the same form of variation of $r\sigma_r$ as in Case 2, as a result

$$r\sigma_r = qR\left(-0.5 + \frac{\zeta}{h}\right). \tag{6}$$

Case 4. $q_0 b = q_i a = q^*$.

The effective load $q = 0$ for this case, and we consider that $r\sigma_r$ is constant through the thickness,

$$r\sigma_r = q^*. \tag{7}$$

By integrating Eq. (3) through the thickness of the shell, we have

$$[r\sigma_r]_a^b = \int_a^b \sigma_\theta dr = N_\theta \tag{8}$$

where N_θ is the stress resultant. By using the surface traction conditions at $r = a$ and b, we arrive at

$$N_\theta = qR \tag{9}$$

for Cases 1 through 3 listed before. For the fourth case,

$$N_\theta = 0. \tag{10}$$

Results given by Eqs. (9) and (10) are the well-known solutions based on the classical membrane theory of shells.

Multiplying Eq. (3) by r, and then integrating the resulting equation through the thickness, we have

$$\int_a^b r d(r\sigma_r) = \int_a^b r\sigma_\theta dr. \tag{11}$$

The right-hand side of Eq. (11) represents the moment of σ_θ through the thickness about the axis of the cylinder, i.e.,

$$\int_a^b r\sigma_\theta dr = N_\theta R + M_\theta \tag{12}$$

where M_θ is the stress couple at the section. By using Eqs. (9) and (10), we have for Cases 1 through 3,

$$\int_a^b r\sigma_\theta dr = qR^2 + M_\theta, \tag{13a}$$

and for Case 4,

$$\int_a^b r\sigma_\theta dr = 0 + M_\theta. \tag{13b}$$

The left-hand side of Eq. (11) when integrated by parts becomes

$$\int_a^b r d(r\sigma_r) = \left[r^2\sigma_r\right]_a^b - \int_a^b r\sigma_r dr \tag{14}$$

which is equal to qR^2 for Cases 1 through 3, and 0 for Case 4. When the results of Eq. (14) are equated to Eqs. (13a) and (13b), we conclude that $M_\theta = 0$ for all four cases. Hence, the state of stress in the shell is principally membrane when the normal load on the shell is symmetrical about the axis of the cylinder.

Loads Dependent on θ

When the normal load on a cylindrical shell is dependent on θ, $\tau_{r\theta}$ exists in the shell but takes on zero values at the inner and outer surfaces of the shell for the loading condition under consideration. We consider that the variation of the in-plane stress σ_θ can be represented in a separable form of r and θ as follows:

$$\sigma_\theta = g(\theta)\sigma(r). \tag{15}$$

Integrating Eq. (2) through the thickness of the shell, we have

$$\left[r^2\tau_{r\theta}\right]_a^b + \frac{dg}{d\theta}\int_a^b r\sigma dr = 0. \tag{16}$$

Since $\tau_{r\theta} = 0$ at a and b and we consider that $\frac{dg}{d\theta} \neq 0$, hence

$$\int_a^b r\sigma_\theta dr = 0. \tag{17}$$

As noted before, the left-hand side of Eq. (17) represents the moment of σ_θ through the shell thickness about the axis of the cylinder. Hence,

$$\int_a^b r\sigma_\theta dr = N_\theta R + M_\theta = 0. \tag{18}$$

Equation (18) gives

$$M_\theta = -N_\theta R. \tag{19}$$

The in-plane stress σ_θ for the extreme fibers at $\zeta = \pm h/2$ of each section based on the classical shell theory are

$$\sigma_\theta = \frac{N_\theta}{h} \pm \frac{6M_\theta}{h^2} = \frac{N_\theta}{h}\left(1 \mp 6\frac{R}{h}\right). \tag{20}$$

While the first term in the parentheses represents the membrane effect, the second term represents the bending effect. For $R = 10h$ as being suggested on page 25 in the book by Kraus (1967) as the thickness limitation for thin elastic shells, the bending effect is 60 times of the membrance effect. Hence, the state of stress is principally bending when loads that are not symmetrical about the axis of the cylinder but dependent on θ.

Acknowledgments

The research was supported by the grant NSC 82-0401-E005-077 from the National Science Council (NSC) of R.O.C. The first author is grateful to Professor Chien-Chang Lin, Dean of the College of Science at the National Chung-Hsing University for inviting him as the NSC Visiting Chair Professor from the Georgia Institute of Technology.

References

Fung, Y. C., 1965, *Foundation of Solid Mechanics*, Prentice-Hall, Englewood Cliffs, NJ.

Kraus, H., 1967, *Thin Elastic Shells*, John Wiley and Sons, New York.

Timoshenko, S., and Woinowsky-Krieger, S., *Theory of Plates and Shells*, 2nd ed., McGraw-Hill, New York.

Amplitude Bounds of Linear Free Vibrations

W. Schiehlen[3,5] and Bin Hu[4,5]

Linear free vibrations are completely characterized by their eigenfrequencies and eigenmodes. However, in engineering applications the amplitudes of a vibrating system have to be bounded, too. The information on the amplitudes of linear vibrations is available from the general solution for each set of initial conditions, which usually are unknown vector quantities. The initial energy is a scalar quantity which is used to identify the amplitude bounds of arbitrarily damped linear vibrating systems.

Introduction

For reasons of safety and reliability, the maximum peak values of the vibration responses excited by initial disturbances must be taken into account in the engineering. These maximum peak values are defined as maximum amplitudes of vibrations. Since it is not practical to solve the differential equations for every possible initial condition to find the exact maximum amplitudes, for economic reason, some amplitude bounds are very useful. For a classically damped system, Müller and Schiehlen (1985) have given amplitude bounds for normal coordinates. Thomson (1988) has presented an approach to calculate approximate amplitude bounds for original physical coordinates using the first three modes. However, this approach is not applicable to nonclassically damped systems. On the other hand, bounds of vibration responses have been extensively studied (see Nicholson (1987) and Yae and Inman (1987)). These response bounds vary with time. Using the bounds, one can indirectly get some amplitude bounds, too, but these amplitude bounds are usually not easy to compute. Therefore, simple amplitude bounds for free vibrations are presented here.

The equations of free vibrations of an n-degree-of-freedom linear system can be written as

$$\mathbf{M}\ddot{\mathbf{y}} + \mathbf{C}\dot{\mathbf{y}} + \mathbf{K}\mathbf{y} = \mathbf{0}, \quad \dot{\mathbf{y}}(t_0) = \dot{\mathbf{y}}_0, \quad \mathbf{y}(t_0) = \mathbf{y}_0, \tag{1}$$

where the inertia matrix $\mathbf{M}$, the velocity matrix $\mathbf{C}$, and the stiffness matrix $\mathbf{K}$ are of the order $n \times n$. The displacement $\mathbf{y}(t)$ is an n-dimensional vector. Further, $\mathbf{y}_0$ and $\dot{\mathbf{y}}_0$, respectively, are the initial displacements and the initial velocities at the initial time $t = t_0$. The velocity matrix $\mathbf{C}$ can be decomposed as $\mathbf{C} = \mathbf{D} + \mathbf{G}$, where $\mathbf{D}$ is symmetric, $\mathbf{D} = \mathbf{D}^T$, and $\mathbf{G}$ is antisymmetric, $\mathbf{G} = -\mathbf{G}^T$. The matrix $\mathbf{D}$ describes the dissipative forces and the matrix $\mathbf{G}$ represents the gyroscopic forces. For dissipative systems, the matrices $\mathbf{M}$ and $\mathbf{K}$ are symmetric and positive definite and the matrix $\mathbf{D}$ is positive semi-definite.

Simple Amplitude Bounds

The amplitude bounds proposed are defined as follows: For linear vibrations governed by Eqs. (1), where E_0 is the initial energy, $E_0 = \frac{1}{2}\dot{\mathbf{y}}_0^T\mathbf{M}\dot{\mathbf{y}}_0 + \frac{1}{2}\mathbf{y}_0^T\mathbf{K}\mathbf{y}_0$, and M_{ii}^{-1} and $K_{ii}^{-1}(i = 1, 2, \ldots, n)$ are the diagonal elements of the matrices $\mathbf{M}^{-1}$ and $\mathbf{K}^{-1}$, there exist simple amplitude bounds given as

$$\max_t |y_i(t)| \le \sqrt{2K_{ii}^{-1}E_0}, \quad \max_t |\dot{y}_i(t)| \le \sqrt{2M_{ii}^{-1}E_0}, \quad i = 1, 2, \ldots, n. \tag{2}$$

Considering Eqs. (1) and multiplying them by $\dot{\mathbf{y}}^T$, we have

$$\dot{\mathbf{y}}^T\mathbf{M}\ddot{\mathbf{y}} + \dot{\mathbf{y}}^T\mathbf{C}\dot{\mathbf{y}} + \dot{\mathbf{y}}^T\mathbf{K}\mathbf{y} = 0 \tag{3}$$

i.e.,

$$\frac{d}{dt}\left(\frac{1}{2}\dot{\mathbf{y}}^T\mathbf{M}\dot{\mathbf{y}}\right) + \dot{\mathbf{y}}^T\mathbf{D}\dot{\mathbf{y}} + \dot{\mathbf{y}}^T\mathbf{G}\dot{\mathbf{y}} + \frac{d}{dt}\left(\frac{1}{2}\mathbf{y}^T\mathbf{K}\mathbf{y}\right) = 0. \tag{4}$$

Because $\mathbf{G}$ is antisymmetric, $\dot{\mathbf{y}}^T\mathbf{G}\dot{\mathbf{y}} = 0$, hence

$$\frac{d}{dt}\left(\frac{1}{2}\dot{\mathbf{y}}^T\mathbf{M}\dot{\mathbf{y}} + \frac{1}{2}\mathbf{y}^T\mathbf{K}\mathbf{y}\right) = -\dot{\mathbf{y}}^T\mathbf{D}\dot{\mathbf{y}}. \tag{5}$$

We define the energy function as

$$E(\mathbf{y},\dot{\mathbf{y}}) = \frac{1}{2}\dot{\mathbf{y}}^T\mathbf{M}\dot{\mathbf{y}} + \frac{1}{2}\mathbf{y}^T\mathbf{K}\mathbf{y}. \tag{6}$$

From (5), it follows

$$\frac{d}{dt}E(\mathbf{y},\dot{\mathbf{y}}) = -\dot{\mathbf{y}}^T\mathbf{D}\dot{\mathbf{y}}. \tag{7}$$

Since $\mathbf{D}$ is positive semidefinite, we get

$$E(\mathbf{y},\dot{\mathbf{y}}) \le E(\mathbf{y}_0,\dot{\mathbf{y}}_0) = E_0. \tag{8}$$

Defining $\mathbf{x} = \begin{bmatrix}\mathbf{y}\\ \dot{\mathbf{y}}\end{bmatrix}$ as the state vector and introducing sets

$$A := \{\mathbf{x} | \mathbf{x} \text{ belongs to the orbits of Eqs. (1)}\}, \tag{9}$$

$$B := \{\mathbf{x} | E(\mathbf{x}) := E(\mathbf{y},\dot{\mathbf{y}}) \le E_0\}, \tag{10}$$

$$C_i := \{\mathbf{x} | x_i = 0\}, \ i = 1, 2, \ldots, n, \tag{11}$$

then we can see from (8) that $A \subset B$. Choosing $2n$ continuous mappings,

$$P_i: P_i(\mathbf{x}) = P_i\left([x_1, x_2, \ldots, x_{2n}]^T\right) = |x_i|, \ \mathbf{x} \in \mathbf{R}^{2n}, \tag{12}$$

then $P_i(\mathbf{x})$ is differentiable except $\mathbf{x} \in C_i$. Further, $P_i(\mathbf{x})$ has the minimum in $\mathbf{x} \in C_i$. Because the set B is a closed bounded set and $P_i(\mathbf{x})$ is continuous in B, $P_i(\mathbf{x})$ has the maximum $|x_i^*|$ in B. Since $\dfrac{\partial P_i(\mathbf{x})}{\partial \mathbf{x}} \neq \mathbf{0}$ for $\mathbf{x} \in B \cap C_i^c$, the maximal point $\mathbf{x}^*$ lies only on the boundary of B, i.e., the surface of the ellipse $B^* = \{\mathbf{x} | E(\mathbf{x}) = E_0\}$. Because of $A \subset B$, we have

$$\max_{\mathbf{X}\in A} P_i(\mathbf{x}) \le \max_{\mathbf{X}\in B} P_i(\mathbf{x}) = \max_{\mathbf{X}\in B^*} P_i(\mathbf{x}) \tag{13}$$

that is, the amplitude of x_i is smaller than $|x_i^*|$.

Now we search the maximum $|x_i^*|$ of $P_i(\mathbf{x})$ in B^*. If $\mathbf{x} = \begin{bmatrix}\mathbf{y}\\ \dot{\mathbf{y}}\end{bmatrix} \in B^*$, then

$$E(\mathbf{x}) = E(\mathbf{y},\dot{\mathbf{y}}) = \frac{1}{2}\dot{\mathbf{y}}^T\mathbf{M}\dot{\mathbf{y}} + \frac{1}{2}\mathbf{y}^T\mathbf{K}\mathbf{y} = E_0. \tag{14}$$

First the state variable $x_1 = y_1$ is considered, then from (14), it follows that y_1 is a function of the other state variables. If $P_1(\mathbf{x})$ has the maximum $|y_1^*|$ at the point $\mathbf{x} = \mathbf{x}^*$, it yields

$$\frac{\partial P_1(\mathbf{x})}{\partial y_j} = \frac{\partial |y_1|}{\partial y_j} = 0 \quad j = 2, 3, \ldots, n, \tag{15}$$

[3]Professor, Mem. ASME.
[4]Guest Scholar.
[5]Institute B of Mechanics, University of Stuttgart, Pfaffenenwaldring 9, 70550 Stuttgart, Germany.

Contributed by the Applied Mechanics Division of THE AMERICAN SOCIETY OF MECHANICAL ENGINEERS for publication in the ASME JOURNAL OF APPLIED MECHANICS. Manuscript received by the ASME Applied Mechanics Division, Jan. 27, 1994; final revision, Apr. 15, 1994. Associate Technical Editor: S. W. Shaw.

and

$$\frac{\partial P_1(\mathbf{x})}{\partial \dot{y}_j} = \frac{\partial |y_1|}{\partial \dot{y}_j} = 0 \quad j = 1, 2, \ldots, n. \tag{16}$$

Differentiating (14) under the condition (15) and (16), one obtains

$$\sum_{j=1}^{n} k_{ij} y_j^* = 0, \quad i = 2, 3, \ldots, n \tag{17}$$

$$\mathbf{M}\ddot{\mathbf{y}}^* = \mathbf{0}. \tag{18}$$

Assume

$$\mathbf{\Lambda}_{n-1} := [k_{12}, \ldots, k_{1n}]^T, \tag{19}$$

$$\mathbf{\Theta}_{n-1} := \begin{bmatrix} k_{22} & \ldots & k_{2n} \\ . & \ldots & . \\ . & \ldots & . \\ . & \ldots & . \\ k_{n2} & \ldots & k_{nn} \end{bmatrix}, \tag{20}$$

$$\mathbf{y}^*_{(n-1)} := [y_2^*, \ldots, y_n^*]^T \tag{21}$$

then

$$\mathbf{K} = \begin{bmatrix} k_{11} & \mathbf{\Lambda}_{n-1}^T \\ \mathbf{\Lambda}_{n-1} & \mathbf{\Theta}_{n-1} \end{bmatrix}, \tag{22}$$

(23)

and Eqs. (17) can be written as

$$\mathbf{\Lambda}_{n-1} y_1^* + \mathbf{\Theta}_{n-1} \mathbf{y}^*_{(n-1)} = 0. \tag{24}$$

Following from (18) and (24), it yields

$$E(\mathbf{y}^*, \dot{\mathbf{y}}^*) = \frac{1}{2}[y_1^*, \mathbf{y}^*_{(n-1)}] \begin{bmatrix} k_{11} & \mathbf{\Lambda}_{n-1}^T \\ \mathbf{\Lambda}_{n-1} & \mathbf{\Theta}_{n-1} \end{bmatrix} \begin{bmatrix} y_1^* \\ \mathbf{y}^*_{(n-1)} \end{bmatrix} \tag{25}$$

$$= \frac{1}{2}[y_1^*, \mathbf{y}^*_{(n-1)}] \begin{bmatrix} k_{11} y_1^* + \mathbf{\Lambda}_{n-1}^T \mathbf{y}^*_{(n-1)} \\ 0 \end{bmatrix} \tag{26}$$

$$= \frac{1}{2}\left(k_{11} y_1^{*2} + y_1^* \mathbf{\Lambda}_{n-1}^T \dot{\mathbf{y}}^*_{(n-1)}\right) \tag{27}$$

$$= \frac{1}{2}\left(k_{11} y_1^{*2} - y_1^* \mathbf{\Lambda}_{n-1}^T \mathbf{\Theta}_{n-1}^{-1} \mathbf{\Lambda}_{n-1} y_1^*\right) \tag{28}$$

$$= \frac{1}{2}\left(k_{11} - \mathbf{\Lambda}_{n-1}^T \mathbf{\Theta}_{n-1}^{-1} \mathbf{\Lambda}_{n-1}\right) y_1^{*2}. \tag{29}$$

Assuming further

$$\mathbf{K}^{-1} := \left(K_{ij}^{-1}\right)_{n \times n}, \tag{30}$$

$$\mathbf{a}_{n-1} := \left[K_{12}^{-1}, \ldots, K_{1n}^{-1}\right]^T, \tag{31}$$

$$\mathbf{B}_{n-1} := \begin{bmatrix} K_{22}^{-1} & \ldots & K_{2n}^{-1} \\ . & \ldots & . \\ . & \ldots & . \\ . & \ldots & . \\ K_{n2}^{-1} & \ldots & K_{nn}^{-1} \end{bmatrix}, \tag{32}$$

then

$$\mathbf{K}^{-1} = \begin{bmatrix} K_{11}^{-1} & \mathbf{a}_{n-1}^T \\ \mathbf{a}_{n-1} & \mathbf{B}_{n-1} \end{bmatrix}. \tag{33}$$

From $\mathbf{K}\mathbf{K}^{-1} = \mathbf{I}$, we get

$$\begin{bmatrix} k_{11} & \mathbf{\Lambda}_{n-1}^T \\ \mathbf{\Lambda}_{n-1} & \mathbf{\Theta}_{n-1} \end{bmatrix} \begin{bmatrix} K_{11}^{-1} & \mathbf{a}_{n-1}^T \\ \mathbf{a}_{n-1} & \mathbf{B}_{n-1} \end{bmatrix} = \mathbf{I}. \tag{34}$$

Therefore,

$$k_{11} K_{11}^{-1} + \mathbf{\Lambda}_{n-1}^T \mathbf{a}_{n-1} = 1, \tag{35}$$

$$\mathbf{\Lambda}_{n-1} K_{11}^{-1} + \mathbf{\Theta}_{n-1} \mathbf{a}_{n-1} = \mathbf{0}. \tag{36}$$

From (36) and (35) it follows that

$$\mathbf{\Lambda}_{n-1}^T \mathbf{\Theta}_{n-1}^{-1} \mathbf{\Lambda}_{n-1} = -\frac{\mathbf{\Lambda}_{n-1}^T \mathbf{a}_{n-1}}{K_{11}^{-1}} = -\frac{1 - k_{11} K_{11}^{-1}}{K_{11}^{-1}}$$

$$= -\frac{1}{K_{11}^{-1}} + k_{11}. \tag{37}$$

Substituting (37) into (29), one gets

$$E(\mathbf{y}^*, \dot{\mathbf{y}}^*) = \frac{\dot{y}_1^{*2}}{2K_{11}^{-1}} = E_0, \tag{38}$$

$$|y_1^*| = \sqrt{2K_{11}^{-1} E_0}. \tag{39}$$

If $E_0 > 0$, it follows from (27)

$$E(\mathbf{y}^*, \dot{\mathbf{y}}^*) = \frac{1}{2} y_1^* \sum_{j=1}^{n} k_{1j} y_j^* = E_0, \tag{40}$$

resulting in

$$c := \sum_{j=1}^{n} k_{1j} y_j^* \neq 0. \tag{41}$$

At the point $(y_1^*, y_2^*, \ldots, y_n^*, \dot{y}_1^*, \dot{y}_2^*, \ldots, \dot{y}_n^*)$, one has the following second partial derivatives:

$$\frac{\partial^2 y_1}{\partial y_i \partial y_j} = -\frac{k_{ij}}{c} \quad i, j \in \{2, 3, \ldots, n\}, \tag{42}$$

$$\frac{\partial^2 y_1}{\partial \dot{y}_i \partial y_j} = 0 \quad i \in \{1, 2, \ldots, n\} \quad j \in \{2, 3, \ldots, n\}, \tag{43}$$

$$\frac{\partial^2 y_1}{\partial \dot{y}_i \partial \dot{y}_j} = -\frac{m_{ij}}{c} \quad i, j \in \{1, 2, \ldots, n\}. \tag{44}$$

Since the matrix $\mathbf{M}$ and $\mathbf{\Theta}_{n-1}$ are positive definite, the Hessian matrix of y_1 with respect to $[y_2, \ldots, y_n, \dot{y}_1, \ldots, \dot{y}_n]^T$ is negative definite for $c > 0$. Hence, $y_1^* = \sqrt{2K_{11}^{-1} E_0}$ is the maximum. For $c < 0$, the Hessian matrix is positive definite, and $y_1^* = -\sqrt{2K_{11}^{-1} E_0}$ is the minimum. This means that

$$\max_{X \in B^*} P_1(\mathbf{x}) = P_1(\mathbf{x}^*) = |y_1^*| = |y_1|_{\max} = \sqrt{2K_{11}^{-1} E_0}. \tag{45}$$

Secondly, one searches the maximum of $|y_j|$, $j \in \{2, \ldots, n\}$. A transformation is chosen as

$$\mathbf{y}' = [y_j, y_2, \ldots, y_{j-1}, y_1, y_{j+1}, \ldots, y_n]^T = \mathbf{T}\mathbf{y}, \tag{46}$$

where

$$T_{1j} = 1, \quad T_{j1} = 1, \tag{47}$$

$$T_{ij} = 1 \quad \text{for } i \neq 1, i \neq j, \tag{48}$$

$$T_{ij} = 0 \quad \text{for the others.} \tag{49}$$

The transformation T is a permutation,

$$\mathbf{T} = \mathbf{T}^T, \quad \mathbf{T}^2 = \mathbf{I}.$$

From $\mathbf{y} = \mathbf{T}^{-1}\mathbf{y}' = \mathbf{T}\mathbf{y}'$ follows

$$E(\mathbf{y}, \dot{\mathbf{y}}) = \frac{1}{2}\dot{\mathbf{y}}^T \mathbf{M}\dot{\mathbf{y}} + \frac{1}{2}\mathbf{y}^T \mathbf{K}\mathbf{y} \tag{50}$$

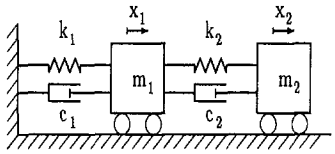

Fig. 1 A dissipative oscillator with two degrees-of-freedom

$$= \frac{1}{2}\dot{\mathbf{y}}'^T\mathbf{T}^T\mathbf{M}\mathbf{T}\dot{\mathbf{y}}' + \frac{1}{2}\mathbf{y}'^T\mathbf{T}^T\mathbf{K}\mathbf{T}\mathbf{y}' \quad (51)$$

$$= \frac{1}{2}\dot{\mathbf{y}}'^T\mathbf{T}^T\mathbf{M}\mathbf{T}\dot{\mathbf{y}}' + \frac{1}{2}\mathbf{y}'^T\mathbf{K}'\mathbf{y}', \quad (52)$$

where $\mathbf{K}' = \mathbf{T}^T\mathbf{K}\mathbf{T}$. Following from (45), one gets

$$|y_1'|_{\max} = \sqrt{2K_{11}'^{-1}E_0}. \quad (53)$$

That means

$$|y_j|_{\max} = \sqrt{2(T^TK^{-1}T)_{11}^{-1}E_0} = \sqrt{2K_{jj}^{-1}E_0}. \quad (54)$$

Similarly it is proved that

$$|\dot{y}_j|_{\max} = \sqrt{2M_{jj}^{-1}E_0}, \quad j \in \{1, \ldots, n\}. \quad (55)$$

Finally, we get the inequalities (2) from (13).

Example

We give here an example to show how to get the amplitude bounds by using the aforementioned theorem. For simplicity, a dissipative oscillator with two degrees-of-freedom is considered (see Fig. 1). Its differential equation reads as follows:

$$\begin{bmatrix} m_1 & 0 \\ 0 & m_2 \end{bmatrix}\begin{bmatrix} \ddot{x}_1 \\ \ddot{x}_2 \end{bmatrix} + \begin{bmatrix} (c_1 + c_2) & -c_2 \\ -c_2 & c_2 \end{bmatrix}\begin{bmatrix} \dot{x}_1 \\ \dot{x}_2 \end{bmatrix} + \begin{bmatrix} (k_1 + k_2) & -k_2 \\ -k_2 & k_2 \end{bmatrix}\begin{bmatrix} x_1 \\ x_2 \end{bmatrix} = \begin{bmatrix} 0 \\ 0 \end{bmatrix}. \quad (56)$$

The inertia matrix, damping matrix, and stiffness matrix are symmetric and positive definite. Then

$$\mathbf{M} = \begin{bmatrix} m_1 & 0 \\ 0 & m_2 \end{bmatrix} > 0, \quad \mathbf{C} = \begin{bmatrix} (c_1 + c_2) & -c_2 \\ -c_2 & c_2 \end{bmatrix} > 0,$$

$$\mathbf{K} = \begin{bmatrix} (k_1 + k_2) & -k_2 \\ -k_2 & k_2 \end{bmatrix} > 0, \quad (57)$$

$$E_0 = \frac{1}{2}\left[m_1\dot{x}_{1_0}^2 + m_2\dot{x}_{2_0}^2 + (k_1 + k_2)x_{1_0}^2 - 2k_2x_{1_0}x_{2_0} + k_2x_{2_0}^2\right], \quad (58)$$

$$M_{11}^{-1} = \frac{1}{m_1}, \quad M_{22}^{-1} = \frac{1}{m_2}, \quad K_{11}^{-1} = \frac{1}{k_1}, \quad K_{22}^{-1} = \frac{1}{k_1} + \frac{1}{k_2}. \quad (59)$$

Using the theorem, one gets the amplitude bounds as

$$\max_t|x_1(t)| \le \sqrt{\frac{2E_0}{m_1}}, \quad \max_t|x_2(t)| \le \sqrt{\frac{2E_0}{m_2}}, \quad (60)$$

$$\max_t|\dot{x}_1(t)| \le \sqrt{\frac{2E_0}{k_1}}, \quad \max_t|\dot{x}_2(t)| \le \sqrt{\frac{2E_0}{k_1} + \frac{2E_0}{k_2}}. \quad (61)$$

Conclusions

The presented amplitude bounds provide a simple relation to the initial energy and the inertia and stiffness properties. They can be easily computed and every state variable can be analyzed separately. Using these advantages, one can easily judge the level of vibrations and choose parameters in designs, for example, to reduce some vibrations.

The presented amplitude bounds do not depend on damping, which is convenient when applied, since we rarely know the exact damping of a system. On the other hand, because the influence of damping on the amplitude bounds is not considered, the estimations of the maximum amplitudes are too conservative for systems with large damping.

References

Müller, P. C., and Schiehlen, W. O., 1985, *Linear Vibrations*, Martinus Nijhoff Publishers, Dordrecht, The Netherlands, pp. 136.

Nicholson, D. W., 1987, "Response Bounds for Nonclassically Damped Mechanical Systems Under Transient Loads," ASME JOURNAL OF APPLIED MECHANICS, Vol. 54, pp. 430–433.

Thomson, W. T., 1988, *Theory of Vibration with Applications*, London Allen & Unwin, Sydney, Australia, pp. 178.

Yae, K. H., and Inman, D. J., 1987, "Response Bounds for Linear Underdamped Systems," ASME JOURNAL OF APPLIED MECHANICS, Vol. 54, pp. 419–423.

Interaction Diagram of a Circular Bar in Torsion and Extension

P. Fuschi[6] and C. Polizzotto[6]

For a circular bar of perfectly plastic material and subjected to a cyclically variable torque and a constant axial force, the interaction (or generalized Bree) diagram is derived by a direct method in which Melan's theorem is used to locate the nonratchetting load boundary.

Introduction

A circular bar of length L is subjected to a cyclically variable torque $M_T = T\mu(t)$, $T > 0$, $-1 \le \mu(t) \le 1$, and a constant axial force $N \ge 0$. The material is elastic-perfectly plastic, obeys the normality rule and the Mises yield function $f(\sigma,\tau) \equiv (\sigma^2 + 3\tau^2)^{1/2} \le \sigma_y$, where σ_y = yield stress and $\sigma = \sigma(x)$, $\tau = \tau(x)$ are normal and shear stresses at the circle of radius $x = r/R$, $0 \le x \le 1$. The beam theory is used (planar cross-sections before and after deformation). Let us set $N = \alpha P_y$ and $T = \beta T_e$, where $P_y = \pi R^2\sigma_y$ = axial plastic limit load, $T_e = \sigma_y I/\sqrt{3}R$ = elastic limit torque, $I = \pi R^4/2$ = second polar area moment, and α, β scalar parameters. In the positive quadrant of the (α, β)-plane, Fig. 1, an interaction diagram can be envisaged which consists of different domains, each of which corresponds to a different type of long-term steady-state response to the load, namely: B_S

[6]Dipartimento di Ingegneria Strutturale & Geotecnica, DISeG, Universita di Palermo, I-90128, Palermo,Italy.

Contributed by the Applied Mechanics Division of THE AMERICAN SOCIETY OF MECHANICAL ENGINEERS for publication in the ASME JOURNAL OF APPLIED MECHANICS. Manuscript received by the ASME Applied Mechanics Division, Nov. 29, 1993; final revision, June 8, 1994. Associate Technical Editor: J. W. Rudnicki.

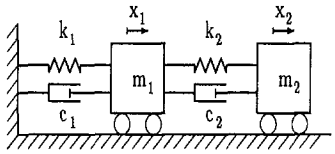

Fig. 1 A dissipative oscillator with two degrees-of-freedom

$$= \frac{1}{2}\dot{\mathbf{y}}'^T\mathbf{T}^T\mathbf{M}\mathbf{T}\dot{\mathbf{y}}' + \frac{1}{2}\mathbf{y}'^T\mathbf{T}^T\mathbf{K}\mathbf{T}\mathbf{y}' \quad (51)$$

$$= \frac{1}{2}\dot{\mathbf{y}}'^T\mathbf{T}^T\mathbf{M}\mathbf{T}\dot{\mathbf{y}}' + \frac{1}{2}\mathbf{y}'^T\mathbf{K}'\mathbf{y}', \quad (52)$$

where $\mathbf{K}' = \mathbf{T}^T\mathbf{K}\mathbf{T}$. Following from (45), one gets

$$|y_1'|_{\max} = \sqrt{2K_{11}'^{-1}E_0}. \quad (53)$$

That means

$$|y_j|_{\max} = \sqrt{2(T^TK^{-1}T)_{11}^{-1}E_0} = \sqrt{2K_{jj}^{-1}E_0}. \quad (54)$$

Similarly it is proved that

$$|\dot{y}_j|_{\max} = \sqrt{2M_{jj}^{-1}E_0}, \quad j \in \{1, \ldots, n\}. \quad (55)$$

Finally, we get the inequalities (2) from (13).

Example

We give here an example to show how to get the amplitude bounds by using the aforementioned theorem. For simplicity, a dissipative oscillator with two degrees-of-freedom is considered (see Fig. 1). Its differential equation reads as follows:

$$\begin{bmatrix} m_1 & 0 \\ 0 & m_2 \end{bmatrix}\begin{bmatrix} \ddot{x}_1 \\ \ddot{x}_2 \end{bmatrix} + \begin{bmatrix} (c_1 + c_2) & -c_2 \\ -c_2 & c_2 \end{bmatrix}\begin{bmatrix} \dot{x}_1 \\ \dot{x}_2 \end{bmatrix} + \begin{bmatrix} (k_1 + k_2) & -k_2 \\ -k_2 & k_2 \end{bmatrix}\begin{bmatrix} x_1 \\ x_2 \end{bmatrix} = \begin{bmatrix} 0 \\ 0 \end{bmatrix}. \quad (56)$$

The inertia matrix, damping matrix, and stiffness matrix are symmetric and positive definite. Then

$$\mathbf{M} = \begin{bmatrix} m_1 & 0 \\ 0 & m_2 \end{bmatrix} > 0, \quad \mathbf{C} = \begin{bmatrix} (c_1 + c_2) & -c_2 \\ -c_2 & c_2 \end{bmatrix} > 0,$$

$$\mathbf{K} = \begin{bmatrix} (k_1 + k_2) & -k_2 \\ -k_2 & k_2 \end{bmatrix} > 0, \quad (57)$$

$$E_0 = \frac{1}{2}\left[m_1\dot{x}_{1_0}^2 + m_2\dot{x}_{2_0}^2 + (k_1 + k_2)x_{1_0}^2 - 2k_2x_{1_0}x_{2_0} + k_2x_{2_0}^2\right], \quad (58)$$

$$M_{11}^{-1} = \frac{1}{m_1}, \quad M_{22}^{-1} = \frac{1}{m_2}, \quad K_{11}^{-1} = \frac{1}{k_1}, \quad K_{22}^{-1} = \frac{1}{k_1} + \frac{1}{k_2}. \quad (59)$$

Using the theorem, one gets the amplitude bounds as

$$\max_t|x_1(t)| \le \sqrt{\frac{2E_0}{m_1}}, \quad \max_t|x_2(t)| \le \sqrt{\frac{2E_0}{m_2}}, \quad (60)$$

$$\max_t|\dot{x}_1(t)| \le \sqrt{\frac{2E_0}{k_1}}, \quad \max_t|\dot{x}_2(t)| \le \sqrt{\frac{2E_0}{k_1} + \frac{2E_0}{k_2}}. \quad (61)$$

Conclusions

The presented amplitude bounds provide a simple relation to the initial energy and the inertia and stiffness properties. They can be easily computed and every state variable can be analyzed separately. Using these advantages, one can easily judge the level of vibrations and choose parameters in designs, for example, to reduce some vibrations.

The presented amplitude bounds do not depend on damping, which is convenient when applied, since we rarely know the exact damping of a system. On the other hand, because the influence of damping on the amplitude bounds is not considered, the estimations of the maximum amplitudes are too conservative for systems with large damping.

References

Müller, P. C., and Schiehlen, W. O., 1985, *Linear Vibrations*, Martinus Nijhoff Publishers, Dordrecht, The Netherlands, pp. 136.

Nicholson, D. W., 1987, "Response Bounds for Nonclassically Damped Mechanical Systems Under Transient Loads," ASME JOURNAL OF APPLIED MECHANICS, Vol. 54, pp. 430–433.

Thomson, W. T., 1988, *Theory of Vibration with Applications*, London Allen & Unwin, Sydney, Australia, pp. 178.

Yae, K. H., and Inman, D. J., 1987, "Response Bounds for Linear Underdamped Systems," ASME JOURNAL OF APPLIED MECHANICS, Vol. 54, pp. 419–423.

Interaction Diagram of a Circular Bar in Torsion and Extension

P. Fuschi[6] and C. Polizzotto[6]

For a circular bar of perfectly plastic material and subjected to a cyclically variable torque and a constant axial force, the interaction (or generalized Bree) diagram is derived by a direct method in which Melan's theorem is used to locate the nonratchetting load boundary.

Introduction

A circular bar of length L is subjected to a cyclically variable torque $M_T = T\mu(t)$, $T > 0$, $-1 \le \mu(t) \le 1$, and a constant axial force $N \ge 0$. The material is elastic-perfectly plastic, obeys the normality rule and the Mises yield function $f(\sigma,\tau) \equiv (\sigma^2 + 3\tau^2)^{1/2} \le \sigma_y$, where σ_y = yield stress and $\sigma = \sigma(x)$, $\tau = \tau(x)$ are normal and shear stresses at the circle of radius $x = r/R$, $0 \le x \le 1$. The beam theory is used (planar cross-sections before and after deformation). Let us set $N = \alpha P_y$ and $T = \beta T_e$, where $P_y = \pi R^2\sigma_y$ = axial plastic limit load, $T_e = \sigma_y I/\sqrt{3}R$ = elastic limit torque, $I = \pi R^4/2$ = second polar area moment, and α, β scalar parameters. In the positive quadrant of the (α, β)-plane, Fig. 1, an interaction diagram can be envisaged which consists of different domains, each of which corresponds to a different type of long-term steady-state response to the load, namely: B_S

[6]Dipartimento di Ingegneria Strutturale & Geotecnica, DISeG, Universita di Palermo, I-90128, Palermo,Italy.

Contributed by the Applied Mechanics Division of THE AMERICAN SOCIETY OF MECHANICAL ENGINEERS for publication in the ASME JOURNAL OF APPLIED MECHANICS. Manuscript received by the ASME Applied Mechanics Division, Nov. 29, 1993; final revision, June 8, 1994. Associate Technical Editor: J. W. Rudnicki.

(elastic response, i.e., elastic shakedown), B_F (alternating plasticity, i.e., plastic shakedown) and B_R (ratchetting, i.e., incremental collapse). B_E is a subdomain of B_S collecting the loads (α, β) under which the entire response is elastic. The load domain $B := B_S \cup B_F \cup B_R$ is bounded by the plastic collapse limit load curve, which is known to have (Lubliner, 1990) the parametric equations:

$$\alpha = 2\zeta\left[(1+\zeta^2)^{1/2} - \zeta\right],$$
$$\beta = (4/3)\left[2\zeta^3 - (2\zeta^2 - 1)(1+\zeta^2)^{1/2}\right], \qquad (1)$$

where the parameter $\zeta = \sqrt{3}\dot{u}/R\dot{\theta}$ is related to the collapse mechanisms $\dot{u}$, $\dot{\theta}$, with u = axial displacement, θ = torsional rotation.

Since the other details of the interaction diagram are not known in the literature, to the authors' knowledge, it is the purpose of the present Brief Note to report them. For later use the elastic stress response is reported here, i.e.,

$$\sigma^E = \alpha\sigma_y, \quad \tau^E = \left(\sigma_y/\sqrt{3}\right)\beta x\mu(t), \quad 0 \le x \le 1, t \ge 0. \qquad (2)$$

It is easy to recognize that the fully elastic domain B_E is the quadrant bounded by the circle $\alpha^2 + \beta^2 = 1$. This curve was derived by Kachanov (1969) as a lower bound to the elastic shakedown boundary.

Elastic Shakedown Domain (B_S)

The boundary of B_s can be determined by known methods of shakedown theory (König, 1987; Polizzotto, 1993a, b). The shear stress $\tau^E(x,t)$ oscillates, at every x, between $\tau^E_{(1)} = (\sigma_y/\sqrt{3})\beta x$ (at times $t_{(1)}$ at which $\mu = 1$) and $\tau^E_{(2)} = -(\sigma_y/\sqrt{3})\beta x$ (at times $t_{(2)}$ at which $\mu = -1$). For $\alpha = 0$, the elastic stress paths $S^E(x)$ belong to the τ-axis of the (σ,τ)-plane, Fig. 2(c), and find themselves in a "neutral" configuration with respect to the Mises ellipse (i.e., symmetrically located). As far as $\alpha = 0$ and $\beta \le 1$, elastic shakedown occurs. For $\alpha = 0$ and $\beta = \beta^* = 1$, the largest stress path, $S^E(1)$, touches the Mises ellipse (at points A, B in Fig. 2(c)) and the bar is exposed to an impending alternating plasticity collapse mode, whereas $\beta^* = 1$ is the peak value of the elastic shakedown limit load as a function of α, called "plastic shakedown load multiplier" in (Polizzotto, 1993b). On superposition, upon the bar loaded with $\beta = 1$, of an axial force $N = \alpha P_y \equiv 2\pi R^2 \int_0^1 \sigma(x)x\,dx$ with $\sigma(x)$ arbitrary but plastically admissible, the steady-state response of the bar does not change, such that an upper plateau embedded in the line $\beta = \beta^*$ must exist in the boundary of B_S (segment a–b in Fig. 1).

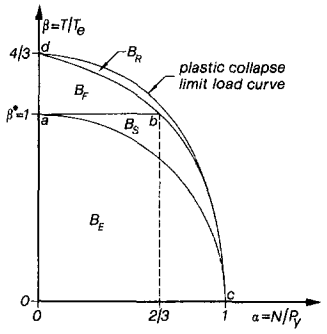

Fig. 1

The falling branch of the above boundary curve is found by Melan's theorem, i.e., by determining the maximum axial force $N = \alpha P_y$ which is possible to apply upon the bar, already loaded by the load $(\alpha = 0, \beta \le 1)$, without violating the yield conditions. To this purpose, let $\sigma^* = \sigma^E + \sigma^S$ and $\tau^* = \tau^E + \tau^S$, be normal and shear stresses at the shakedown limit, σ^S and τ^S being self-stresses. Since, obviously, the max α value is obtained when the yield condition is attained at all circles x in (0,1), by the condition $f(\sigma^*,\tau^*) = \sigma_y$ for all x in (0,1) and at times $t_{(1)}$ and $t_{(2)}$, we obtain

$$\sigma^S = \sigma_y\left[-\alpha + (1 - \beta^2 x^2)^{1/2}\right], \quad \tau^S \equiv 0, \qquad (3)$$

and the stress profiles at times $t_{(1)}$ and $t_{(2)}$ are the ellipse arches D_1C and D_2C of Fig. 2(c), respectively, (for $\beta = 1$, it is $D_1 \equiv A$, $D_2 \equiv B$). Then, the condition of self-equilibrium for σ^S gives

$$\alpha = (2/3\beta^2)\left[1 - (1 - \beta^2)^{3/2}\right] \qquad (4)$$

which is the equation of the falling branch of the elastic shakedown load boundary (curve b-c in Fig. 1). For $\beta < .65$, this curve practically coincides with curve (1). For $\beta = .85$, the stresses σ^*,τ^* at the elastic shakedown limit are depicted in Figs. 2(a,b) and compared with those at the plastic collapse (ultimate) limit. Any load (α,β) on curve (4) promotes a steady-state response with an impending ratchetting collapse mode, activated as soon as the axial force is increased. The ratchetting mechanism consists in translations $u/2$ of the free cross-section at every half-cycle, with axial plastic strains $\epsilon^p_{(1)} = \epsilon^p_{(2)} = \text{const} = u/2L$, and alternating shear plastic strains, i.e., $\gamma^p_{(1)} + \gamma^p_{(2)} = 0$ everywhere.

Plastic Shakedown Domain (B_F)

The boundary of B_F can be determined by a method as in (Polizzotto, 1993c, d; see also Ponter and Karadeniz, 1985), similar to that of the previous section. For $\alpha = 0$ and $1 < \beta < 4/3$, the elastic stress paths $S^E(x)$ exceed the yield ellipse in the outer ring $1/\beta < x \le 1$. The plastic overpotential turns

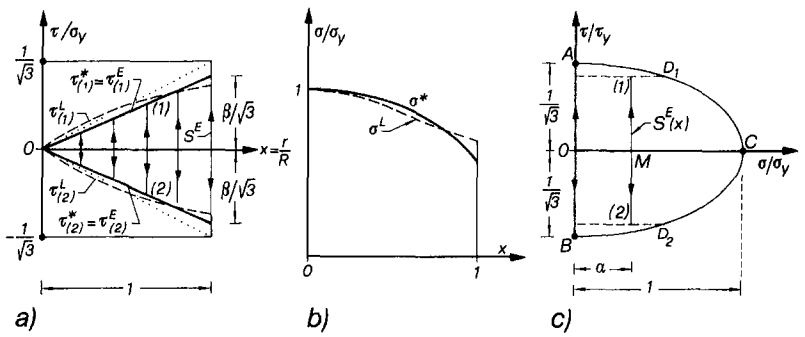

Fig. 2

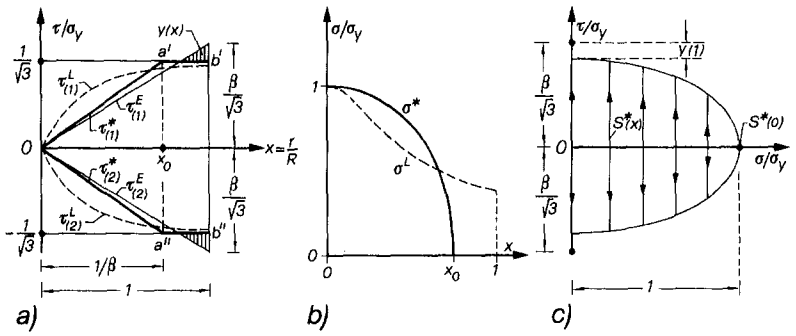

Fig. 3

out to be $y = 0$ for $0 \le x \le 1/\beta$ and $y = (\sigma_y/\sqrt{3})(\beta x - 1)$ for $1/\beta \le x \le 1$, Fig. 3(*a*). The stress paths $S^E(x)$ are all located over the τ-axis of the (σ,τ)-plane, Fig. 3(*c*), and are in neutral configurations (characterized by the circumstance that the plastic overpotential $y(x)$ is minimum with respect to any other configuration of $S^E(x)$). In these conditions, by a theorem given in (Polizzotto, 1993d), plastic shakedown occurs with only alternating plastic shear strains taking place in the ring $x_0 \le x \le 1$. x_0 is determined by the consideration that, in the actual steady cycles, the maximum and minimum shear stresses $\tau^*_{(k)} = \tau^E_{(k)} + \tau^S_{(k)}$, $(k = 1, 2)$ are at the yield limit in the ring $x_0 \le x \le 1$, but below it in the circle $0 \le x \le x_0$, such that the diagrams of $\tau^*_{(1)}$ and $\tau^*_{(2)}$ are as depicted in Fig. 3(*a*), lines Oa′b′ and Oa″b″. Thus, since $\tau^S_{(1)} = -\tau^S_{(2)} = -(\sigma_y/\sqrt{3})(\beta x - 1)$ for $x_0 \le x \le 1$ and $\tau^S_{(1)} = -\tau^S_{(2)} = -(\sigma_y/\sqrt{3})(\beta - 1/x_0)x$ for $0 \le x \le x_0$, the condition of self-equilibrium for $\tau^S_{(1)}$ gives

$$x_0 = (4 - 3\beta)^{1/3}, \tag{5}$$

valid for $1 \le \beta \le 4/3$, (the value $\beta = 4/3$ specifies the plastic collapse limit torque, $T_y = (4/3)T_e$).

The boundary of B_F is determined by applying Melan's theorem to the bar elastic core, that is, evaluating the maximum axial force $\alpha P_y = 2\pi R^2 \int_0^{x_0} \sigma^*(x) x dx$ to apply to the core, such as to lead it to the (partial) elastic shakedown limit. Since, by the yield condition,

$$\sigma^* = \sigma_y\left[1 - (x/x_0)^2\right]^{1/2} \quad \text{for } 0 \le x \le x_0 \tag{6}$$

(but $\sigma^* = 0$ for $x_0 \le x \le 1$), we obtain

$$\alpha = (2/3)(4 - 3\beta)^{2/3}, \tag{7}$$

which is the searched-for equation (line d-b in Fig. 1). In this state, the stress paths $S^*(x), x_0 \le x \le 1$, are located over the τ-axis of the (σ,τ)-plane, whereas those related to $0 \le x \le x_0$ are located at distances $\sigma^*(x)$ from the stress origin, Fig. 3(*c*) with the stress profiles coincident with the ellipse quadrant arches. The stresses σ^*, τ^* at the transition B_F/B_R are depicted in Figs. 3(*a,b*) and compared with those at the plastic collapse (ultimate) limit. If the axial force exceeds (7), a ratchetting collapse mode similar to that described previously for $\beta < 1$ is activated, with the stress paths $S^*(x)$, $0 \le x \le 1$, shifted somewhere away from the origin along the σ-axis in Fig. 3(*c*).

Conclusion

The interaction diagram of a circular bar in torsion and extension has been derived by a direct method grounded on Melan's theorem. This direct method being unable to provide, by itself, the steady-cycle plastic strains, a full analysis of the bar steady cycle has been addressed, obtaining results (not reported here for lack of space) which confirm those previously presented.

References

Kachanov, L. M., 1969, *Fundamentals of the Theory of Plasticity*, MIR Publishers, Moscov (English translation), p. 363.

König, J. A., 1987, *Shakedown of Elastic-Plastic Structures*, PWN-Polish Scientific Publishers, Warsaw and Elsevier, Amsterdam.

Lubliner, J., 1990, *Plasticity Theory*, Macmillan, New York, p. 345.

Polizzotto, C., 1993a, "On the Conditions to Prevent Plastic Shakedown of Structures: Part I:—Theory," ASME JOURNAL OF APPLIED MECHANICS, Vol. 60, pp. 15–19.

Polizzotto, C., 1993b, "On the Conditions to Prevent Plastic Shakedown of Structures: Part II—The Plastic Shakedown Limit Load," ASME JOURNAL OF APPLIED MECHANICS, Vol. 60, pp. 20–25.

Polizzotto, C., 1993c, "A Study on Plastic Shakedown of Structures: Part I—Basic Properties," ASME JOURNAL OF APPLIED MECHANICS, Vol. 60, pp. 318–323.

Polizzotto, C., 1993d, "A Study on on Plastic Shakedown of Structures: Part II—Theorems," ASME JOURNAL OF APPLIED MECHANICS, Vol. 60, pp. 324–330.

Ponter, A. R. S., and Karadeniz, S., 1985, "An Extended Shakedown Theory of Structures That Suffer Cyclic Thermal Loadings: Part 1—Theory," ASME JOURNAL OF APPLIED MECHANICS, Vol. 52, pp. 877–882.

Symmetries of the Amplitude Equations of an Inextensional Beam With Internal Resonance

Z. C. Feng[7] and L. G. Leal[8]

We study the symmetries admitted by the amplitude equations governing the nonlinear nonplanar parametric responses of an inextensional beam (Nayfeh and Pai, 1989). As a result of these symmetries, the differential equations can be integrated in two limiting cases.

[7]Department of Mechanical Engineering, Massachusetts Institute of Technology, Cambridge, MA 02139. Assoc. Mem. ASME.

[8]Department of Chemical and Nuclear Engineering, University of California at Santa Barbara, Santa Barbara, CA 93106.

Contributed by the Applied Mechanical Division of THE AMERICAN SOCIETY OF MECHANICAL ENGINEERS for publication in the ASME JOURNAL OF APPLIED MECHANICS. Manuscript received by the ASME Applied Mechanics Division, Oct. 7, 1993; final revision, Mar. 23, 1994. Associate Technical Editor: F. Y. M. Wan.

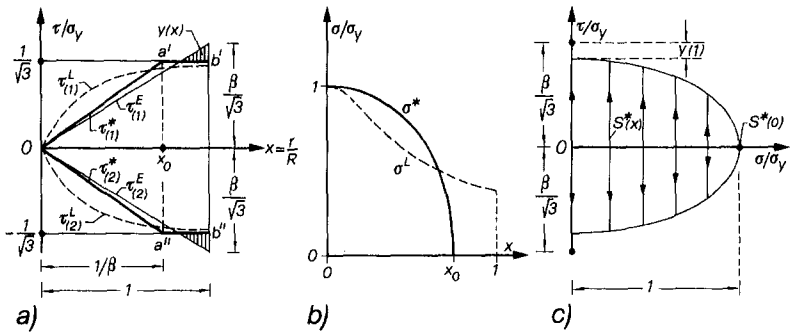

Fig. 3

out to be $y = 0$ for $0 \le x \le 1/\beta$ and $y = (\sigma_y/\sqrt{3})(\beta x - 1)$ for $1/\beta \le x \le 1$, Fig. 3(*a*). The stress paths $S^E(x)$ are all located over the τ-axis of the (σ,τ)-plane, Fig. 3(*c*), and are in neutral configurations (characterized by the circumstance that the plastic overpotential $y(x)$ is minimum with respect to any other configuration of $S^E(x)$). In these conditions, by a theorem given in (Polizzotto, 1993d), plastic shakedown occurs with only alternating plastic shear strains taking place in the ring $x_0 \le x \le 1$. x_0 is determined by the consideration that, in the actual steady cycles, the maximum and minimum shear stresses $\tau^*_{(k)} = \tau^E_{(k)} + \tau^S_{(k)}$, $(k = 1, 2)$ are at the yield limit in the ring $x_0 \le x \le 1$, but below it in the circle $0 \le x \le x_0$, such that the diagrams of $\tau^*_{(1)}$ and $\tau^*_{(2)}$ are as depicted in Fig. 3(*a*), lines Oa'b' and Oa''b''. Thus, since $\tau^S_{(1)} = -\tau^S_{(2)} = -(\sigma_y/\sqrt{3})(\beta x - 1)$ for $x_0 \le x \le 1$ and $\tau^S_{(1)} = -\tau^S_{(2)} = -(\sigma_y/\sqrt{3})(\beta - 1/x_0)x$ for $0 \le x \le x_0$, the condition of self-equilibrium for $\tau^S_{(1)}$ gives

$$x_0 = (4 - 3\beta)^{1/3}, \tag{5}$$

valid for $1 \le \beta \le 4/3$, (the value $\beta = 4/3$ specifies the plastic collapse limit torque, $T_y = (4/3)T_e$).

The boundary of B_F is determined by applying Melan's theorem to the bar elastic core, that is, evaluating the maximum axial force $\alpha P_y = 2\pi R^2 \int_0^{x_0} \sigma^*(x)x\,dx$ to apply to the core, such as to lead it to the (partial) elastic shakedown limit. Since, by the yield condition,

$$\sigma^* = \sigma_y\left[1 - (x/x_0)^2\right]^{1/2} \quad \text{for } 0 \le x \le x_0 \tag{6}$$

(but $\sigma^* = 0$ for $x_0 \le x \le 1$), we obtain

$$\alpha = (2/3)(4 - 3\beta)^{2/3}, \tag{7}$$

which is the searched-for equation (line d-b in Fig. 1). In this state, the stress paths $S^*(x), x_0 \le x \le 1$, are located over the τ-axis of the (σ,τ)-plane, whereas those related to $0 \le x \le x_0$ are located at distances $\sigma^*(x)$ from the stress origin, Fig. 3(*c*) with the stress profiles coincident with the ellipse quadrant arches. The stresses σ^*, τ^* at the transition B_F/B_R are depicted in Figs. 3(*a,b*) and compared with those at the plastic collapse (ultimate) limit. If the axial force exceeds (7), a ratchetting collapse mode similar to that described previously for $\beta < 1$ is activated, with the stress paths $S^*(x)$, $0 \le x \le 1$, shifted somewhere away from the origin along the σ-axis in Fig. 3(*c*).

Conclusion

The interaction diagram of a circular bar in torsion and extension has been derived by a direct method grounded on Melan's theorem. This direct method being unable to provide, by itself, the steady-cycle plastic strains, a full analysis of the bar steady cycle has been addressed, obtaining results (not reported here for lack of space) which confirm those previously presented.

References

Kachanov, L. M., 1969, *Fundamentals of the Theory of Plasticity*, MIR Publishers, Moscov (English translation), p. 363.

König, J. A., 1987, *Shakedown of Elastic-Plastic Structures*, PWN-Polish Scientific Publishers, Warsaw and Elsevier, Amsterdam.

Lubliner, J., 1990, *Plasticity Theory*, Macmillan, New York, p. 345.

Polizzotto, C., 1993a, "On the Conditions to Prevent Plastic Shakedown of Structures: Part I:—Theory," ASME JOURNAL OF APPLIED MECHANICS, Vol. 60, pp. 15–19.

Polizzotto, C., 1993b, "On the Conditions to Prevent Plastic Shakedown of Structures: Part II—The Plastic Shakedown Limit Load," ASME JOURNAL OF APPLIED MECHANICS, Vol. 60, pp. 20–25.

Polizzotto, C., 1993c, "A Study on Plastic Shakedown of Structures: Part I—Basic Properties," ASME JOURNAL OF APPLIED MECHANICS, Vol. 60, pp. 318–323.

Polizzotto, C., 1993d, "A Study on on Plastic Shakedown of Structures: Part II—Theorems," ASME JOURNAL OF APPLIED MECHANICS, Vol. 60, pp. 324–330.

Ponter, A. R. S., and Karadeniz, S., 1985, "An Extended Shakedown Theory of Structures That Suffer Cyclic Thermal Loadings: Part 1—Theory," ASME JOURNAL OF APPLIED MECHANICS, Vol. 52, pp. 877–882.

Symmetries of the Amplitude Equations of an Inextensional Beam With Internal Resonance

Z. C. Feng[7] and L. G. Leal[8]

We study the symmetries admitted by the amplitude equations governing the nonlinear nonplanar parametric responses of an inextensional beam (Nayfeh and Pai, 1989). As a result of these symmetries, the differential equations can be integrated in two limiting cases.

[7]Department of Mechanical Engineering, Massachusetts Institute of Technology, Cambridge, MA 02139. Assoc. Mem. ASME.

[8]Department of Chemical and Nuclear Engineering, University of California at Santa Barbara, Santa Barbara, CA 93106.

Contributed by the Applied Mechanical Division of THE AMERICAN SOCIETY OF MECHANICAL ENGINEERS for publication in the ASME JOURNAL OF APPLIED MECHANICS. Manuscript received by the ASME Applied Mechanics Division, Oct. 7, 1993; final revision, Mar. 23, 1994. Associate Technical Editor: F. Y. M. Wan.

1 Introduction

In a recent study of the vibration of an inextensional beam, Nayfeh and Pai (1989) (hereafter referred as N & P) have derived amplitude equations for two bending modes that are in one-to-one resonance. However, the coefficients of the nonlinear terms in these amplitude equations could only be evaluated numerically. In this paper, we will show that the coefficients of the nonlinear terms in the amplitude equations actually satisfy certain equalities that can be proven without the necessity of direct numerical evaluation. Given these equalities, the amplitude equations can be integrated in two limiting cases. We resort to the previous work of Feng and Sethna (1990) and Feng and Wiggins (1993), respectively, for the analysis of these two limiting cases.

2 Ampitude Equations

The planar and nonplanar responses of a fixed-free beam subjected to a principal parametric excitation have been studied by many authors. N & P contains references for these investigations. N & P considers uniform beams with rectangular cross-sections. Cubic nonlinearities due to both the curvature and inertia are included in their formulation. Employing the method of multiple time scales, N & P obtain ordinary differential equations for the complex amplitudes of the two resonant modes A_1 and A_2:

$$-i(2\omega_{1m}A_1' + \mu\omega_{1m}A_1) - \delta_2 z^4 A_1 - \left[\delta_0\alpha_1 + \frac{\delta_0^2}{\beta_\gamma}\alpha_2 + (1+\delta_0)\alpha_3\right]\left(2A_1A_2\bar{A}_2 + \bar{A}_1A_2^2\right) - 3(1+\delta_0)\alpha_4 A_1^2\bar{A}_1 + 2\alpha_5\omega_{1m}^2\bar{A}_1A_1^2 + 2\alpha_6\omega_{2n}^2\bar{A}_1A_2^2 - 2\alpha_7 g\omega_{2n}^2\bar{A}_1 e^{2i\omega_{2n}\sigma T_2} = 0 \quad (1a)$$

$$-i(2\omega_{1m}A_2' + \mu\omega_{2n}A_2) + \left[\delta_0\beta_1 - \frac{\delta_0^2}{\beta_\gamma}\beta_2 - \beta_3\right] \times \left(2A_2A_1\bar{A}_1 + \bar{A}_2A_1^2\right) - 3\beta_4 A_2^2\bar{A}_2 + 2\beta_5\omega_{2n}^2\bar{A}_2A_2^2 + 2\beta_6\omega_{1m}^2\bar{A}_2A_1^2 - 2\beta_7 g\omega_{2n}^2\bar{A}_2 e^{2i\omega_{2n}\sigma T_2} = 0 \quad (1b)$$

where

$$\alpha_1 = \int_0^1 \Phi_m\left[\Phi_n''\int_1^s \Phi_m''\Phi_n''dt - \Phi_n'''\int_0^s \Phi_m''\Phi_n'dt\right]'ds,$$

$$\alpha_2 = \int_0^1 \Phi_m\left[\Phi_n''\int_0^s\int_1^s \Phi_m''\Phi_n''dsds\right]''ds,$$

$$\alpha_3 = \int_0^1 \Phi_m[\Phi_m'(\Phi_n'\Phi_n'')']'ds,$$

$$\alpha_4 = \int_0^1 \Phi_m[\Phi_m'(\Phi_m'\Phi_m'')']'ds,$$

$$\alpha_5 = \int_0^1 \Phi_m\left[\Phi_m'\int_1^s\int_0^s \Phi_m'^2dsds\right]'ds,$$

$$\alpha_6 = \int_0^1 \Phi_m\left[\Phi_m'\int_1^s\int_0^s \Phi_n'^2dsds\right]'ds,$$

$$\alpha_7 = \int_0^1 [(s-1)\Phi_m\Phi_m'' + \Phi_m\Phi_m']ds, \quad (2)$$

as given in the Appendix of N & P. The values for β_i are obtained from α_i by interchanging m and n. For a precise definition of rest of the parameters, the reader is referred to N & P.

The equations given in (1) are nonautonomous. However, they can easily be converted to autonomous ones by letting $A_1 = e^{i\omega_{2n}\sigma T_2}Z_1$ and $A_2 = e^{i\omega_{2n}\sigma T_2}Z_2$ to get

$$2\omega_{2n}Z_1' = -\mu\omega_{2n}Z_1 + i\left[\left(\delta_2 z^4 - 2\omega_{2n}^2\sigma\right)Z_1 + 2\alpha_7 g\omega_{2n}^2\bar{Z}_1 - 4R_5Z_1^2\bar{Z}_1 + 4R_2Z_2^2\bar{Z}_1 + 4R_6Z_1Z_2\bar{Z}_2\right] \quad (3a)$$

$$2\omega_{2n}Z_2' = -\mu\omega_{2n}Z_2 + i\left[-2\omega_{2n}^2\sigma Z_2 + 2\beta_7 g\omega_{2n}^2\bar{Z}_2 - 4E_5Z_2^2\bar{Z}_2 - 4E_2Z_1^2\bar{Z}_2 - 4E_6Z_1Z_2\bar{Z}_1\right] \quad (3b)$$

where

$$R_2 = \frac{1}{4}\left[-2\alpha_6\omega_{2n}^2 + \delta_0\alpha_1 + \frac{\delta_0^2}{\beta_\gamma}\alpha_2 + (1+\delta_0)\alpha_3\right]$$

$$R_5 = \frac{1}{2}\alpha_5\omega_{1m}^2 - \frac{3}{4}(1+\delta_0)\alpha_4,$$

$$R_6 = \frac{1}{2}\left[\delta_0\alpha_1 + \frac{\delta_0^2}{\beta_\gamma}\alpha_2 + (1+\delta_0)\alpha_3\right]$$

$$E_2 = \frac{1}{4}\left[2\beta_6\omega_{1m}^2 + \delta_0\beta_1 - \frac{\delta_0^2}{\beta_\gamma}\beta_2 - \beta_3\right]$$

$$E_5 = \frac{1}{2}\beta_5\omega_{2n}^2 - \frac{3}{4}\beta_4,\ E_6 = \frac{1}{2}\left[\delta_0\beta_1 - \frac{\delta_0^2}{\beta_\gamma}\beta_2 - \beta_3\right] \quad (4)$$

as defined in the Appendix of N & P.

3 Symmetries of the Amplitude Equations

The symmetries of the amplitude equations are in fact equalities satisfied by the constants E_j and R_j ($j = 2, 5, 6$). We first establish the equalities satisfied by the constants α_1 α_2, etc., as summarized in the following propositions.

Proposition 1: For arbitrary m and n, (i) $\alpha_1 + \alpha_3 = -\beta_1$, (ii) $\alpha_2 = \beta_2$, (iii) $\alpha_3 = \beta_3$, (iv) $\alpha_6 = \beta_6$.

Proposition 2: For $m = n$, $\alpha_i = \beta_i$, $i = 1, 2, 3, 4, 5, 6$. Furthermore, $\alpha_3 = \alpha_4$, $\alpha_5 = \alpha_6$.

The proof of Proposition 1 is based on repeated use of integration by parts and the formula for interchanging order of integration, namely,

$$\int_0^\alpha dx\int_0^x f(y)dy = \int_0^\alpha (\alpha - y)f(y)dy. \quad (5)$$

In addition, we recall that the shape function Φ_i, its explicit form given in N & P, satisfies these boundary conditions

$$\Phi_i(s_0)\Phi_i''(s_0) = 0, \quad \Phi_i(s_0)\Phi_i'''(s_0) = 0 \quad \Phi_i'(s_0)\Phi_i''(s_0) = 0, \quad (6)$$

at both $s_0 = 0$ and $s_0 = 1$.

As an illustration, to show (i), we first rewrite the definition of α_1 so that there can be no confusion about the dummy integration variables. Integrating by parts and applying (6), we have

$$\alpha_1 = -\int_0^1 \Phi_m'(s)\Phi_n''(s)\int_1^s \Phi_m''(t)\Phi_n''(t)dtds + \int_0^1 \Phi_m'(s)\Phi_n'''(s)\int_0^s \Phi_m''(t)\Phi_n'(t)dtds.$$

Applying (5) to the first term and simplifying the second term through integration by parts, we obtain

$$\alpha_1 = -\int_0^1 \Phi_m''(s)\Phi_n''(s)\int_0^s [\Phi_m'(t)\Phi_n''(t) - \Phi_n'(t)\Phi_m''(t)]dtds - \int_0^1 \Phi_m'(s)\Phi_n'(s)\Phi_m''(s)\Phi_n''(s)ds.$$

Simplifying α_3 through integration by parts twice, we get

$$\alpha_3 = 2\int_0^1 \Phi_m'(s)\Phi_n'(s)\Phi_m''(s)\Phi_n''(s)ds.$$

Thus, (i) follows by recalling that β_1 is obtained by interchanging m and n the expression of α_1.

Theorem 1. For arbitrary m and n, $R_2 = -E_2$, $R_6 = -E_6$.

Theorem 2. For $m = n$, in addition to the results stated in Theorem 1, we have $R_5 = E_5$ and $E_2 - E_5 + E_6 = 0$.

Proof: These theorems are direct consequences of Proposition 1 and Proposition 2. Recall also that for $m = n$, $\delta_0 = 0$.

Because of Theorem 1, the amplitude Eqs. (3) can be expressed as

$$\dot{Z}_1 = -dZ_1 + i[-(s-b)Z_1 + F_1Z_1^* + \pi_{11}Z_1^2Z_1^* + \pi_2Z_1Z_2Z_2^* + \pi_3Z_1^*Z_2^2] \quad (7a)$$

$$\dot{Z}_2 = -dZ_2 + i[-(s+b)Z_2 + F_2Z_2^* + \pi_{12}Z_2^2Z_2^* + \pi_2Z_1Z_2Z_1^* + \pi_3Z_2^*Z_1^2] \quad (7b)$$

where

$$d = \mu\omega_{2n},\ s = 2\omega_{2n}^2\sigma - \frac{1}{2}\delta_2 z^4,\ b = \frac{1}{2}\delta_2 z^4,$$
$$F_1 = 2\alpha_7 g\omega_{2n}^2,\ F_2 = 2\alpha_7 g\omega_{2n}^2,\ \pi_{11} = -4R_5,$$
$$\pi_{12} = -4E_5,\ \pi_2 = 4R_6,\ \pi_3 = 4R_2,$$

and dots represent differentiation with respect to τ, where $\tau = \frac{T^2}{2\omega_{1m}}$. We have used superscript * to denote complex conjugate for consistency with the notation in Feng and Sethna (1990).

For the special case $m = n$, due to Theorem 2, we have

$$\pi_{11} = \pi_{12}, \qquad \pi_1 - \pi_2 - \pi_3 = 0. \quad (8)$$

4 Consequences of the Symmetries of the Amplitude Equations

The dynamical system (7) has very important properties that make it possible for us to determine the dynamics through an analytical approach. In Feng and Sethna (1990), it is shown that these systems can be derived from a Hamiltonian function in the case when $d = 0$. Furthermore, for the free oscillation case where $F_1 = F_2 = 0$, the dynamical system is completely integrable which is accomplished by a series of coordinate transformations. The variables are first transformed into action angle variables by letting

$$Z_1 = (2I_1)^{1/2}\sin\theta_1 + i(2I_1)^{1/2}\cos\theta_1,$$
$$Z_2 = (2I_2)^{1/2}\sin\theta_2 + i(2I_2)^{1/2}\cos\theta_2.$$

The action-angle variables are further transformed into a new set of variables according to

$$q_1 = \theta_1 - \theta_2,\quad q_2 = \theta_2,\quad p_1 = I_1,\quad p_2 = I_1 + I_2.$$

After that, another coordinate transformation is introduced to eliminate the parameter π_3:

$$p_1 = \frac{P_1}{|\pi_3|},\ p_2 = \frac{P_2}{|\pi_3|},\ q_1 = (1 + \operatorname{sgn}\pi_3)\frac{\pi}{4} + Q_1,$$
$$q_2 = (1 + \operatorname{sgn}\pi_3)\frac{\pi}{4} + Q_2.$$

The final equations obtained for the general case (7) become

$$\dot{P}_1 = 4P_1(P_2 - P_1)\sin 2Q_1, \quad (9a)$$

$$\dot{Q}_1 = -2(b + \gamma P_2) + 2(2P_1 - P_2)(\alpha - \cos 2Q_1), \quad (9b)$$

$$\dot{P}_2 = 0, \quad (9c)$$

$$\dot{Q}_2 = s + (b + \gamma P_2) - 2P_1(\alpha - \cos 2Q_1) - 2\gamma P_1 - (\gamma + 2\delta)P_2 \quad (9d)$$

where

$$\alpha = \frac{-\frac{\pi_{11} + \pi_{12}}{2} + \pi_2}{|\pi_3|},\quad \gamma = \frac{\pi_{11} - \pi_{12}}{2|\pi_3|},$$
$$\delta = \frac{3\pi_{12} - \pi_{11}}{2|\pi_3|}.$$

When $m = n$, Theorem 2 implies that some coefficients in Eq. (7) satisfy identities in (8). Equations (7) with these special properties have been studied in Feng and Wiggins (1993). For the special case of $b = d = 0$, the amplitude equations in the real form, obtained by $Z_1 = x_1 + iy_1$, $Z_2 = x_2 + iy_2$, are shown to have $O(2)$ symmetry. Introducing the coordinate transformation

$$x_1 = q_1\cos q_2,\quad x_2 = q_1\sin q_2,\quad y_1 = p_1\cos q_2 - p_2q_1^{-1}\sin q_2,$$
$$y_2 = p_1\sin q_2 + p_2q_1^{-1}\cos q_2,$$

and setting $F_1 = F_2 = 1$, and $\pi_{11} = \pi_1$ without loss of generality, we obtain

$$\dot{q}_1 = [s - \pi_1(q_1^2 + p_1^2 + p_2^2q_1^{-2}) + 1]p_1 \quad (10a)$$

$$\dot{p}_1 = [-s + \pi_1(q_1^2 + p_1^2 + p_2^2q_1^{-2})](q_1 - p_2^2q_1^{-3}) + (q_1 + p_2^2q_1^{-3}) \quad (10b)$$

$$\dot{q}_2 = p_2[(s+1)q_1^{-2} - \pi_1(q_1^2 + p_1^2 + p_2^2 + q_1^{-2})q_1^{-2} + 2\pi_3] \quad (10c)$$

$$\dot{p}_2 = 0. \quad (10d)$$

The dynamical systems (9) and (10) are shown to be integrable in Feng and Sethna (1990) and in Feng and Wiggins (1993). Furthermore, homoclinic and heteroclinic orbits are shown to occur for the both systems. It is also shown that parametric forcing or symmetry breaking terms can create homoclinic tangels which lead to chaotic vibration of the beam.

References

Feng, Z. C., and Sethna, P. R., 1990, "Global bifurcation and chaos in parametrically forced systems with one-one resonance," *Dynamics and Stability of Systems*, Vol. 5, pp. 201–225.

Feng, Z., and Wiggins, S., 1993, "On the existence of chaos in a class of two-degree-of-freedom, damped, strongly parametrically forced mechanical systems with broken O(2) symmetry," *ZAMP*, Vol. 44, pp. 201–248.

Nayfeh, A. H., and Pai, P. F., 1989, Non-linear non-planar parametric responses of an inextensional beam," *International Journal of Nonlinear Mechanics*, Vol. 24, pp. 139–158.

Tensile Crack-Tip Stress Fields in Elastic-Perfectly Plastic Crystals

Y. Huang[9]

1 Introduction

Rice (1987) analyzed the plane-strain asymptotic stress field and deformation field around a tensile crack tip for elastic-perfectly plastic single-crystal solids. It was found that the yield surface is a polygon for slip systems {1 1 1} ⟨1 1 0⟩ in fcc (face-centered cubic) or {1 1 0} ⟨1 1 1⟩ and {1 2 1} ⟨1 1 1⟩ in bcc (body-centered cubic) crystals. The stresses around the crack tip are constants within each angular sector surrounding the tip, though they vary among sectors and are discontinuous. The stresses in each sector correspond to a vertex on the polygon of yield locus, and adjacent sectors correspond to adjacent vertices. The yield surface in terms of in-plane stresses is shown in Fig. 1(*a*) for the crack orientation studied by Rice—crack plane (0 1 0), x_2-axis; crack-tip direction [1 0 $\bar{1}$]; and crack growth direction [1 0 1], x_1-axis.

Only the upper half-plane is studied due to symmetry. Rice (1987) showed that the boundary of each annular sector must be coincidental with the following six angles in the polar coordinate θ: 0 deg, 35.26 deg [$\tan^{-1}(1/\sqrt{2}) \equiv \alpha$], 54.74 deg ($\pi/2, -\alpha$), 90 deg, 125.26 deg ($\pi/2 + \alpha$), 144.74 deg ($\pi - \alpha$), and 180 deg. Moreover, the stress discontinuity across a sector boundary satisfies

$$\left[\left[\frac{1}{2}(\sigma_{11} + \sigma_{22})\right]\right] = -[[L]] \qquad (1)$$

where the left-hand side is the jump in mean in-plane stress and L is the arc length around the yield surface, increasing in the direction A → B → C → D (Fig. 1(*a*)). Based on these observations, Rice found an asymptotic near-tip four-sector stress field (shown in Fig. 1(*b*)) and the stresses for fcc crystals:

Sector D, 125.26 deg $\le \theta \le$ 180 deg:

$$\sigma_{22} = 0, \quad \sigma_{11} = \sqrt{6}\,\tau, \quad \sigma_{12} = 0 \qquad (2a)$$

Sector C, 90 deg $\le \theta \le$ 125.26 deg:

$$\sigma_{22} = \sqrt{6}\,\tau, \quad \sigma_{11} = \frac{3}{2}\sqrt{6}\,\tau, \quad \sigma_{12} = -\sqrt{3}\,\tau \qquad (2b)$$

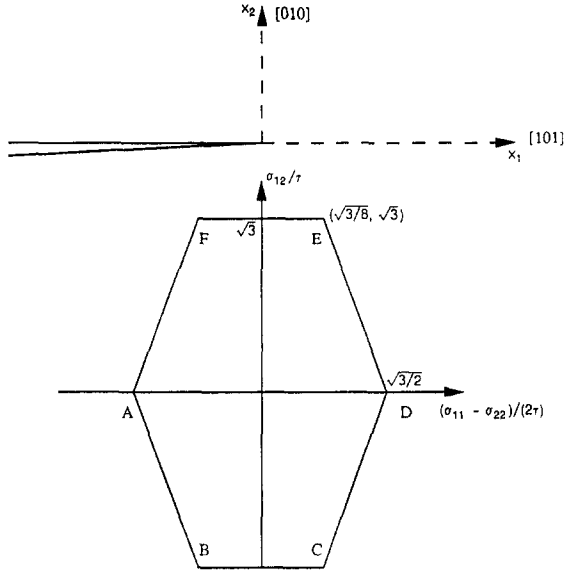

Fig. 1(*a*)

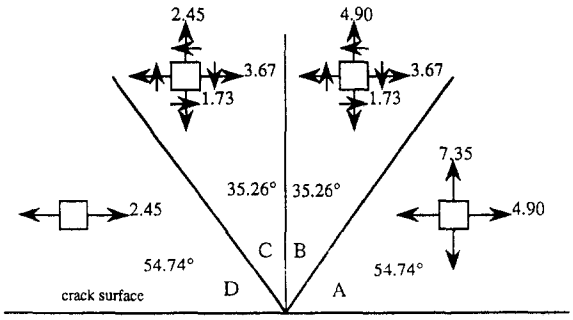

Fig. 1(*b*)

Fig. 1 Rice's (1987) solution for a crack in an fcc crystal: (*a*) crack orientation and yield surface; (*b*) four-sector stress field

Sector B, 54.74 deg $\le \theta \le$ 90 deg:

$$\sigma_{22} = 2\sqrt{6}\,\tau, \quad \sigma_{11} = \frac{3}{2}\sqrt{6}\,\tau, \quad \sigma_{12} = -\sqrt{3}\,\tau \qquad (2c)$$

Sector A, 0 deg $\le \theta \le$ 54.74 deg:

$$\sigma_{22} = 3\sqrt{6}\,\tau, \quad \sigma_{11} = 2\sqrt{6}\,\tau, \quad \sigma_{12} = 0 \qquad (2d)$$

where τ is the critical shear strength for the {1 1 1} ⟨1 1 0⟩ slip system in fcc crystals. It is observed that there is a tensile stress state on the crack surface, $\sigma_{11}|_{\theta=\pi} = 2.45\,\tau$ and that the maximum stress ahead of a crack, $\sigma_{22}|_{\theta=0}$ is 7.35 τ.

The shear stress must be zero on the crack surface ($\theta = \pi$) and ahead of the crack ($\theta = 0$), hence, the sectors including these two rays must correspond to vertex A or D (Fig. 1(*a*)). There are four possibilities: (i) sector A around $\theta = 0$ and sector D around $\theta = \pi$, (ii) sector D for both $\theta = 0$ and $\theta = \pi$, (iii) sector A for both $\theta = 0$ and $\theta = \pi$, and (iv) sector D for $\theta = 0$ and sector A for $\theta = \pi$. It can be shown that Rice's (1987) solution is the *only* possible stress field in (i) and that there is *no* solution for (iv) that can lead to a tensile stress ahead of the crack, i.e., $\sigma_{22}|_{\theta=0} > 0$. The aim of the present study is to find other asymptotic near-tip stress fields, such as (ii) and (iii), around a stationary, tensile crack tip in elastic-perfectly plastic crystals. Though some experimental and computational work has been done recently (e.g., Mohan et al., 1992a, b; Shield and Kim, 1991) suggesting that the nature of plastic hardening and finite deformation effects play an important role in the evolution of the crack-tip stress field, the analysis here is limited to elastic-perfectly plastic

[9]Department of Aerospace and Mechanical Engineering, The University of Arizona, Tucson, AZ 85721.

Contributed by the Applied Mechanics Division of THE AMERICAN SOCIETY OF MECHANICAL ENGINEERS for publication in the JOURNAL OF APPLIED MECHANICS. Manuscript received by the ASME Applied Mechanics Division, May 3, 1993; final revision, June 15, 1994. Associate Technical Editor: C. F. Shih.

References

Feng, Z. C., and Sethna, P. R., 1990, "Global bifurcation and chaos in parametrically forced systems with one-one resonance," *Dynamics and Stability of Systems*, Vol. 5, pp. 201–225.

Feng, Z., and Wiggins, S., 1993, "On the existence of chaos in a class of two-degree-of-freedom, damped, strongly parametrically forced mechanical systems with broken O(2) symmetry," *ZAMP*, Vol. 44, pp. 201–248.

Nayfeh, A. H., and Pai, P. F., 1989, Non-linear non-planar parametric responses of an inextensional beam," *International Journal of Nonlinear Mechanics*, Vol. 24, pp. 139–158.

Tensile Crack-Tip Stress Fields in Elastic-Perfectly Plastic Crystals

Y. Huang[9]

1 Introduction

Rice (1987) analyzed the plane-strain asymptotic stress field and deformation field around a tensile crack tip for elastic-perfectly plastic single-crystal solids. It was found that the yield surface is a polygon for slip systems {1 1 1} ⟨1 1 0⟩ in fcc (face-centered cubic) or {1 1 0} ⟨1 1 1⟩ and {1 2 1} ⟨1 1 1⟩ in bcc (body-centered cubic) crystals. The stresses around the crack tip are constants within each angular sector surrounding the tip, though they vary among sectors and are discontinuous. The stresses in each sector correspond to a vertex on the polygon of yield locus, and adjacent sectors correspond to adjacent vertices. The yield surface in terms of in-plane stresses is shown in Fig. 1(*a*) for the crack orientation studied by Rice—crack plane (0 1 0), x_2-axis; crack-tip direction [1 0 $\bar{1}$]; and crack growth direction [1 0 1], x_1-axis.

Only the upper half-plane is studied due to symmetry. Rice (1987) showed that the boundary of each annular sector must be coincidental with the following six angles in the polar coordinate θ: 0 deg, 35.26 deg [$\tan^{-1}(1/\sqrt{2}) \equiv \alpha$], 54.74 deg ($\pi/2, -\alpha$), 90 deg, 125.26 deg ($\pi/2 + \alpha$), 144.74 deg ($\pi - \alpha$), and 180 deg. Moreover, the stress discontinuity across a sector boundary satisfies

$$\left[\left[\frac{1}{2}(\sigma_{11} + \sigma_{22})\right]\right] = -[[L]] \qquad (1)$$

where the left-hand side is the jump in mean in-plane stress and L is the arc length around the yield surface, increasing in the direction A → B → C → D (Fig. 1(*a*)). Based on these observations, Rice found an asymptotic near-tip four-sector stress field (shown in Fig. 1(*b*)) and the stresses for fcc crystals:

Sector D, 125.26 deg $\le \theta \le$ 180 deg:

$$\sigma_{22} = 0, \quad \sigma_{11} = \sqrt{6}\,\tau, \quad \sigma_{12} = 0 \qquad (2a)$$

Sector C, 90 deg $\le \theta \le$ 125.26 deg:

$$\sigma_{22} = \sqrt{6}\,\tau, \quad \sigma_{11} = \frac{3}{2}\sqrt{6}\,\tau, \quad \sigma_{12} = -\sqrt{3}\,\tau \qquad (2b)$$

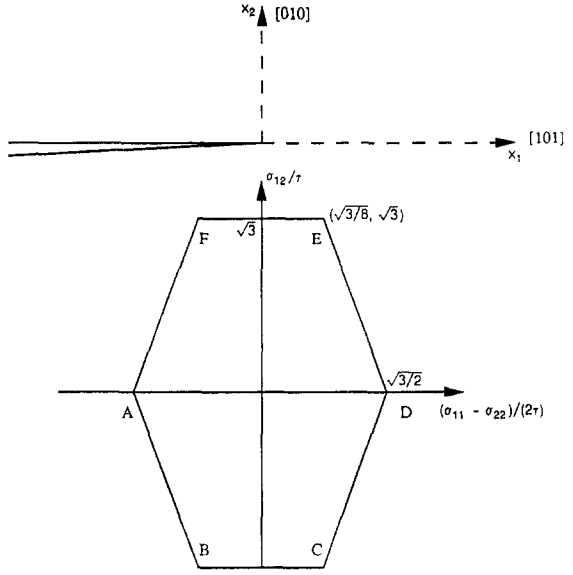

Fig. 1(*a*)

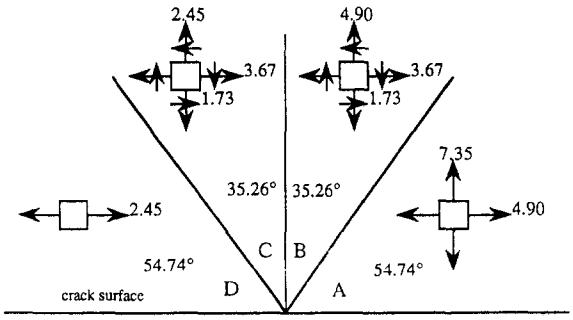

Fig. 1(*b*)

Fig. 1 Rice's (1987) solution for a crack in an fcc crystal: (*a*) crack orientation and yield surface; (*b*) four-sector stress field

Sector B, 54.74 deg $\le \theta \le$ 90 deg:

$$\sigma_{22} = 2\sqrt{6}\,\tau, \quad \sigma_{11} = \frac{3}{2}\sqrt{6}\,\tau, \quad \sigma_{12} = -\sqrt{3}\,\tau \qquad (2c)$$

Sector A, 0 deg $\le \theta \le$ 54.74 deg:

$$\sigma_{22} = 3\sqrt{6}\,\tau, \quad \sigma_{11} = 2\sqrt{6}\,\tau, \quad \sigma_{12} = 0 \qquad (2d)$$

where τ is the critical shear strength for the {1 1 1} ⟨1 1 0⟩ slip system in fcc crystals. It is observed that there is a tensile stress state on the crack surface, $\sigma_{11}|_{\theta=\pi} = 2.45\,\tau$ and that the maximum stress ahead of a crack, $\sigma_{22}|_{\theta=0}$ is 7.35 τ.

The shear stress must be zero on the crack surface ($\theta = \pi$) and ahead of the crack ($\theta = 0$), hence, the sectors including these two rays must correspond to vertex A or D (Fig. 1(*a*)). There are four possibilities: (i) sector A around $\theta = 0$ and sector D around $\theta = \pi$, (ii) sector D for both $\theta = 0$ and $\theta = \pi$, (iii) sector A for both $\theta = 0$ and $\theta = \pi$, and (iv) sector D for $\theta = 0$ and sector A for $\theta = \pi$. It can be shown that Rice's (1987) solution is the *only* possible stress field in (i) and that there is *no* solution for (iv) that can lead to a tensile stress ahead of the crack, i.e., $\sigma_{22}|_{\theta=0} > 0$. The aim of the present study is to find other asymptotic near-tip stress fields, such as (ii) and (iii), around a stationary, tensile crack tip in elastic-perfectly plastic crystals. Though some experimental and computational work has been done recently (e.g., Mohan et al., 1992a, b; Shield and Kim, 1991) suggesting that the nature of plastic hardening and finite deformation effects play an important role in the evolution of the crack-tip stress field, the analysis here is limited to elastic-perfectly plastic

[9]Department of Aerospace and Mechanical Engineering, The University of Arizona, Tucson, AZ 85721.

Contributed by the Applied Mechanics Division of THE AMERICAN SOCIETY OF MECHANICAL ENGINEERS for publication in the JOURNAL OF APPLIED MECHANICS. Manuscript received by the ASME Applied Mechanics Division, May 3, 1993; final revision, June 15, 1994. Associate Technical Editor: C. F. Shih.

fcc single-crystal solids with small deformation gradients. Moreover, only solutions that have a tensile stress ahead of the crack, i.e., $\sigma_{22}|_{\theta=0} > 0$, are presented.

2 Near-Tip Stress Fields

Booker and Davis (1972) and Rice (1973) developed the plane-strain slip-line theory for anisotropic plastic materials and concluded that $(\sigma_{11} + \sigma_{22})/2 + L$ is constant along a line of one family of characteristics and $(\sigma_{11} - \sigma_{22})/2 - L$ is constant along the line of the other family. Equation (1) can be regarded as a consequence of $(\sigma_{22} + \sigma_{22})/2 + L$ being a constant. However, one can also conclude that

$$\left[\left[\frac{1}{2}(\sigma_{11} + \sigma_{22})\right]\right] = [[L]] \tag{3}$$

may hold at the boundary of annular sectors from the fact that $(\sigma_{11} + \sigma_{22})/2 - L$ is a constant. (Equation (3) cannot be ruled out from Rice's (1987) derivation of Eq. (1).) In a study of an interface crack between an elastic-perfectly plastic solid and a rigid substrate, Guo and Keer (1990) found an asymptotic solution that exhibits a feature similar to Eqs. (1) and (3), i.e., the radial ray θ = constant corresponds to one family of characteristics for small θ and corresponds to the other family for large θ.

Type (ii) solutions, i.e., sector D for both crack surface and $\theta = 0$, are discussed first. Sector D around the crack surface is identical to Rice's (1987), i.e.,

Sector D, 125.26 deg $\leq \theta \leq$ 180 deg:

$$\sigma_{22} = 0, \quad \sigma_{11} = \sqrt{6}\,\tau, \quad \sigma_{12} = 0. \tag{4a}$$

The next sector must be sector C due to the continuity of tractions across the sector boundary. The jump in stresses satisfies Eq. (1), i.e.,

$$(\sigma_{11} + \sigma_{22})_C = (\sigma_{11} + \sigma_{22})_D + 2L$$

where $L = 3\sqrt{6}\,\tau/4$ is the distance between vertices D and C on the yield surface. This leads to

Sector C, 35.26 deg $\leq \theta \leq$ 125.26 deg:

$$\sigma_{22} = \sqrt{6}\,\tau, \quad \sigma_{11} = \frac{3}{2}\sqrt{6}\,\tau, \quad \sigma_{12} = -\sqrt{3}\,\tau. \tag{4b}$$

Equation (4b) is identical to (2b), but the annular sector's range in Eq. (4b), 35.26 deg − 125.26 deg, is larger than that for Eq. (2b), because the sector including $\theta = 0$ in (ii) corresponds to vertex D and the only possible angles over which a jump from C to D occurs are 35.26 deg and 125.26 deg. It is also interesting to point out that the sector boundary $\theta = 35.26$ deg is very close to the angle, 40 deg, where Mohan et al. (1992b) observed shear-strain concentrations. The next sector is D, and Eq. (3) holds across the discontinuity at $\theta = 35.26$ deg in order to ensure $\sigma_{22}|_{\theta=0} > 0$, i.e.,

$$(\sigma_{11} + \sigma_{22})_D = (\sigma_{11} + \sigma_{22})_C + \frac{3}{2}\sqrt{6}\,\tau,$$

which leads to

Sector D, 0 deg $\leq \theta \leq$ 35.26 deg:

$$\sigma_{22} = \frac{3}{2}\sqrt{6}\,\tau, \quad \sigma_{11} = \frac{5}{2}\sqrt{6}\,\tau, \quad \sigma_{12} = 0. \tag{4c}$$

This three-sector solution DCD is shown in Fig. 2(a). The stress ahead of the crack, $\sigma_{22}|_{\theta=0} = 3.67\,\tau$, in this three-sector solution is only half that for Rice's (1987) four-sector solution ABCD given in Eq. (2d), and the horizontal stress component, $\sigma_{11}|_{\theta=0} = 6.12\,\tau$ is slightly larger than that for the four-sector solution, $\sigma_{11}|_{\theta=0} = 4.90\,\tau$. It is evident from this analysis that the asymptotic stress field DCD in Eq. (4) is the only possible solution in (ii) that gives a tensile stress, $\sigma_{22}|_{\theta=0} > 0$, ahead of the crack and where all sectors correspond to vertices on the yield surface.

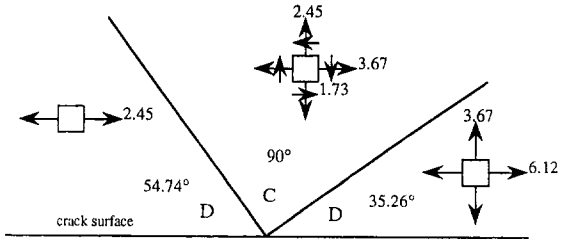

Fig. 2(a)

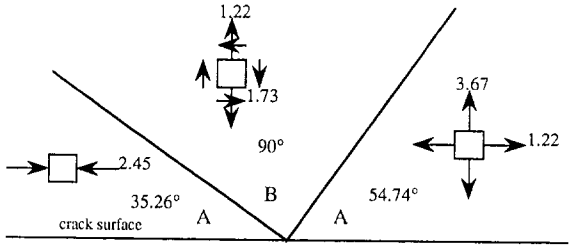

Fig. 2(b)

Fig. 2 Other asymptotic stress fields: (a) three-sector field with a tensile stress state on the crack surface; (b) three-sector field with a compressive stress state on the crack surface

Type (iii) solutions give sector A around the crack surface on which there is a compressive stress state, $\sigma_{11}|_{\theta=\pi} < 0$. This type of solution may occur when a large compressive T-stress is imposed. Thus, sector A that includes the crack surface is

Sector A, 144.74 deg $\leq \theta \leq$ 180 deg:

$$\sigma_{22} = 0, \quad \sigma_{11} = -\sqrt{6}\,\tau, \quad \sigma_{12} = 0 \tag{5a}$$

where the boundary $\theta = 144.74$ deg is the only possible angle for stress discontinuity in order to ensure the continuity of tractions, and the next sector must sector B, given by

Sector B, 54.74 deg $\leq \theta \leq$ 144.74 deg:

$$\sigma_{22} = \frac{\sqrt{6}}{2}\tau, \quad \sigma_{11} = 0, \quad \sigma_{12} = -\sqrt{3}\,\tau \tag{5b}$$

where Eq. (3) has been used. The B-sector boundaries, $\theta = 54.74$ deg and $\theta = 144.74$ deg, are the only two possible angles for a jump from B to A in order to ensure the sector including $\theta = 0$ is an A-sector. Equation (1) applies at $\theta = 54.74$ deg, so that there is a tensile stress, $\sigma_{22}|_{\theta=0} > 0$, ahead of the crack, and the sector is given by

Sector A, 0 deg $\leq \theta \leq$ 54.74 deg:

$$\sigma_{22} = \frac{3}{2}\sqrt{6}\,\tau, \quad \sigma_{11} = \frac{\sqrt{6}}{2}\tau, \quad \sigma_{12} = 0. \tag{5c}$$

The three-sector solution ABA in Eq. (5) is shown in Fig. 2(b). It is observed that the stress ahead of the crack, $\sigma_{22}|_{\theta=0} = 3.67\,\tau$, is the same as the three-sector solution DCD in Eq. (4), which is half that for the four-sector solution ABCD. However, the horizontal stress component for ABA, $\sigma_{11}|_{\theta=0}$, is much less than those for the ABCD and DCD fields. It is evident from this analysis that the three-sector solution ABA in Eq. (5) is the only possible solution that gives a compressive stress state on the crack surface and a tensile stress ahead of the crack, $\sigma_{22}|_{\theta=0} > 0$, and where all sectors correspond to vertices. Further numerical study is necessary in order to determine the condition governing these asymptotic fields.

References

Booker, J. R., and Davis, E. H., 1972, "A General Treatment of Plastic

Anisotropy Under Conditions of Plane Strain," *Journal of the Mechanics and Physics of Solids*, Vol. 20, pp. 239–253.

Guo, Q., and Keer, L. M., 1990, "A Crack at the Interface Between an Elastic-Perfectly Plastic Solid and a Rigid Substrate," *Journal of the Mechanics and Physics of Solids*, Vol. 38, pp. 843–857.

Mohan, R., Ortiz, M., and Shih, C. F., 1992a, "An Analysis of Cracks in Ductile Single Crystals—I. Anti-Plane Shear," *Journal of the Mechanics and Physics of Solids*, Vol. 40, pp. 291–313.

Mohan, R., Ortiz, M., and Shih, C. F., 1992b, "An Analysis of Cracks in Ductile Single Crystals—II. Mode I Loading," *Journal of the Mechanics and Physics of Solids*, Vol. 40, pp. 315–337.

Rice, J. R., 1973, "Plane Strain Slip Theory for Anisotropic Rigid-Plastic Materials," *Journal of the Mechanics and Physics of Solids*, Vol. 21, pp. 63–74.

Rice, J. R., 1987, "Tensile Crack Tip Fields in Elastic-Ideally Plastic Crystals," *Mechanics of Materials*, Vol. 6, pp. 317–335.

Shield, T. W., and Kim, K. S., 1991, "Diffraction Theory of Optical Interference Moire and a Device for Production of Variable Virtual Reference Gratings: A Moire Microscope," *Experimental Mechanics*, Vol. 31, pp. 126–134.

An Analysis for the Effects of Compressive Load Excursions on Fatigue Crack Growth in Metallic Materials

G. A. Kardomateas[10,11] and R. L. Carlson[10,12]

1 Introduction

The variable amplitude loading of service load spectra often includes compressive excursions. Since it seemed reasonable to assume that compressive loads do not induce opening of the crack and hence do not contribute to crack growth, it had been recommended that analyses of crack growth may exclude the compressive excursions, i.e., only cycles with tensile loading need to be included. However, a number of experimental investigations on the effects of compressive excursions indicated that neglecting them can be expected to lead to nonconservative crack growth predictions (Carlson and Kardomateas, 1994).

Based on elastic compression of the asperities, single asperity models had been presented by Beevers et al. (1984). These discrete asperity models provide a rational explanation of the observed behavior due to closure obstruction in load sequences that involve cycling in tension with a positive load ratio, and involve mostly elastic loading/unloading of the asperities. For compressive excursions of sizable magnitude, an inelastic model accounting for the plastic crushing of the asperities is required.

2 Formulation

For a properly loaded specimen, the distribution of the asperities is essentially uniform across the specimen thickness. This suggests the possibility of representing the asperities configuration through the thickness by an effective (through-thickness) line contact.

[10]School of Aerospace Engineering, Georgia Institute of Technology, Atlanta, GA 30332-0150.

[11]Associate Professor, Mem. ASME.

[12]Professor Emeritus.

Contributed by the Applied Mechanics Division of THE AMERICAN SOCIETY OF MECHANICAL ENGINEERS for publication in the ASME JOURNAL OF APPLIED MECHANICS. Manuscript received by the ASME Applied Mechanics Division, Apr. 21, 1993; final revision, Apr. 26, 1994. Associate Technical Editor: R. M. McMeeking.

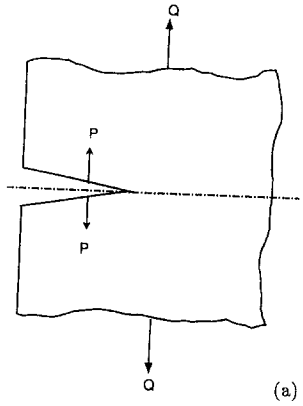

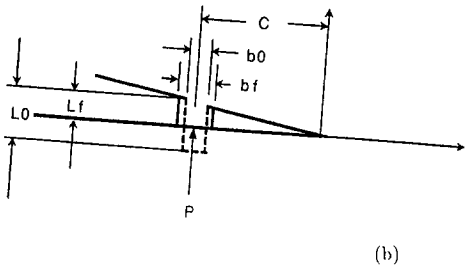

Fig. 1 (*a*) External (global) and crack tip (local) loading; (*b*) a single asperity on the upper crack face

Consider an asperity at a distance C from the crack tip in a specimen of thickness t (Fig. 1). The presence of both externally applied forces and crack face forces is illustrated in Fig. 1(*a*) whereas the details of the proposed model are indicated in Fig. 1(*b*). Only the upper crack face is shown with the asperity developing a force P. The stress intensity factor produced by concentrated, opposing line loads on the faces of a finite center crack of length $2a$, can be determined from Sih et al. (1962) for both the Mode I and Mode II cases. The opening mode stress intensity factor for plane strain in terms of the local crack face force from Sih et al. (1962) is

$$K_{I,\text{local}} = \left(\frac{1}{\pi C}\right)^{1/2}\left(2 - \frac{C}{a}\right)^{1/2}\frac{P}{t}. \tag{1}$$

This expression is also valid for a single-edge crack of length a (this can be easily shown by following the same procedure as in Sih et al., 1962).

The contribution of the external load will be represented by $K_{I,\text{global}}$. By superposition, the total stress intensity factor is

$$K_I = K_{I,\text{local}} + K_{I,\text{global}}. \tag{2}$$

The dimension L_0 represents the initial magnitude of the interference produced by the asperity. The effective initial width of the asperity is b_0 (Fig. 1(*b*)). The load P will now be determined from a displacement condition at the asperity site, which includes the plastic crushing of the asperity.

The vertical displacement at the upper crack face, i.e., at $\theta = \pi$ and an arbitrary r, is

$$U_2(r, \pi) = U_{2,\text{global}} + U_{2,\text{local}}. \tag{3}$$

By use of the stress intensity factors for the global and the local load, we can write the displacement at the asperity site, $r = C$, $\theta = \pi$:

Anisotropy Under Conditions of Plane Strain," *Journal of the Mechanics and Physics of Solids*, Vol. 20, pp. 239–253.

Guo, Q., and Keer, L. M., 1990, "A Crack at the Interface Between an Elastic-Perfectly Plastic Solid and a Rigid Substrate," *Journal of the Mechanics and Physics of Solids*, Vol. 38, pp. 843–857.

Mohan, R., Ortiz, M., and Shih, C. F., 1992a, "An Analysis of Cracks in Ductile Single Crystals—I. Anti-Plane Shear," *Journal of the Mechanics and Physics of Solids*, Vol. 40, pp. 291–313.

Mohan, R., Ortiz, M., and Shih, C. F., 1992b, "An Analysis of Cracks in Ductile Single Crystals—II. Mode I Loading," *Journal of the Mechanics and Physics of Solids*, Vol. 40, pp. 315–337.

Rice, J. R., 1973, "Plane Strain Slip Theory for Anisotropic Rigid-Plastic Materials," *Journal of the Mechanics and Physics of Solids*, Vol. 21, pp. 63–74.

Rice, J. R., 1987, "Tensile Crack Tip Fields in Elastic-Ideally Plastic Crystals," *Mechanics of Materials*, Vol. 6, pp. 317–335.

Shield, T. W., and Kim, K. S., 1991, "Diffraction Theory of Optical Interference Moire and a Device for Production of Variable Virtual Reference Gratings: A Moire Microscope," *Experimental Mechanics*, Vol. 31, pp. 126–134.

An Analysis for the Effects of Compressive Load Excursions on Fatigue Crack Growth in Metallic Materials

G. A. Kardomateas[10,11] and R. L. Carlson[10,12]

1 Introduction

The variable amplitude loading of service load spectra often includes compressive excursions. Since it seemed reasonable to assume that compressive loads do not induce opening of the crack and hence do not contribute to crack growth, it had been recommended that analyses of crack growth may exclude the compressive excursions, i.e., only cycles with tensile loading need to be included. However, a number of experimental investigations on the effects of compressive excursions indicated that neglecting them can be expected to lead to nonconservative crack growth predictions (Carlson and Kardomateas, 1994).

Based on elastic compression of the asperities, single asperity models had been presented by Beevers et al. (1984). These discrete asperity models provide a rational explanation of the observed behavior due to closure obstruction in load sequences that involve cycling in tension with a positive load ratio, and involve mostly elastic loading/unloading of the asperities. For compressive excursions of sizable magnitude, an inelastic model accounting for the plastic crushing of the asperities is required.

2 Formulation

For a properly loaded specimen, the distribution of the asperities is essentially uniform across the specimen thickness. This suggests the possibility of representing the asperities configuration through the thickness by an effective (through-thickness) line contact.

[10]School of Aerospace Engineering, Georgia Institute of Technology, Atlanta, GA 30332-0150.

[11]Associate Professor, Mem. ASME.

[12]Professor Emeritus.

Contributed by the Applied Mechanics Division of THE AMERICAN SOCIETY OF MECHANICAL ENGINEERS for publication in the ASME JOURNAL OF APPLIED MECHANICS. Manuscript received by the ASME Applied Mechanics Division, Apr. 21, 1993; final revision, Apr. 26, 1994. Associate Technical Editor: R. M. McMeeking.

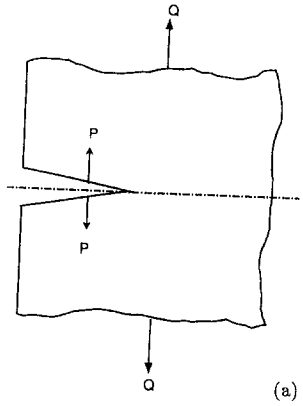

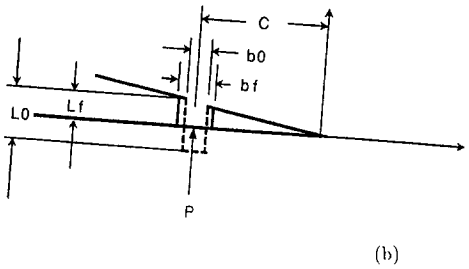

Fig. 1 (*a*) External (global) and crack tip (local) loading; (*b*) a single asperity on the upper crack face

Consider an asperity at a distance C from the crack tip in a specimen of thickness t (Fig. 1). The presence of both externally applied forces and crack face forces is illustrated in Fig. 1(*a*) whereas the details of the proposed model are indicated in Fig. 1(*b*). Only the upper crack face is shown with the asperity developing a force P. The stress intensity factor produced by concentrated, opposing line loads on the faces of a finite center crack of length $2a$, can be determined from Sih et al. (1962) for both the Mode I and Mode II cases. The opening mode stress intensity factor for plane strain in terms of the local crack face force from Sih et al. (1962) is

$$K_{I,\text{local}} = \left(\frac{1}{\pi C}\right)^{1/2}\left(2 - \frac{C}{a}\right)^{1/2}\frac{P}{t}. \tag{1}$$

This expression is also valid for a single-edge crack of length a (this can be easily shown by following the same procedure as in Sih et al., 1962).

The contribution of the external load will be represented by $K_{I,\text{global}}$. By superposition, the total stress intensity factor is

$$K_I = K_{I,\text{local}} + K_{I,\text{global}}. \tag{2}$$

The dimension L_0 represents the initial magnitude of the interference produced by the asperity. The effective initial width of the asperity is b_0 (Fig. 1(*b*)). The load P will now be determined from a displacement condition at the asperity site, which includes the plastic crushing of the asperity.

The vertical displacement at the upper crack face, i.e., at $\theta = \pi$ and an arbitrary r, is

$$U_2(r, \pi) = U_{2,\text{global}} + U_{2,\text{local}}. \tag{3}$$

By use of the stress intensity factors for the global and the local load, we can write the displacement at the asperity site, $r = C$, $\theta = \pi$:

$$U_2(C, \pi) = \frac{2}{G}\left(\frac{C}{2\pi}\right)^{1/2}(1-\nu)K_{I,\text{global}} + \frac{2(1-\nu)}{\pi G}\left(1-\frac{C}{2a}\right)^{1/2}\frac{P}{t}, \quad (4)$$

where G is the shear modulus and ν the Poisson's ratio. The condition for determining the force P is the displacement at the asperity site

$$U_2(C, \pi) = L_f, \quad (5)$$

where L_f is the interference height for a given external load during closure. This will be considered next.

The asperity is assumed under uniaxial compression $\sigma_{22} = \sigma$ (all other stress components are zero). Moreover, the total equivalent strain of the asperity is

$$\bar{\epsilon}^T = \bar{\epsilon}^e + \bar{\epsilon}^p, \quad (6)$$

where $\bar{\epsilon}^e$ is the elastic and $\bar{\epsilon}^p$ the plastic component (we consider positive the asperity stress σ and strain ϵ when they are compressive). Notice that in uniaxial compression, although there are other nonzero components of strain, namely, $\epsilon_{11} = \epsilon_{33} = -\epsilon_{22}/2$, it turns out that $\bar{\epsilon} = \epsilon_{22}$. Hence, since $\bar{\epsilon}^e = \sigma/\mathrm{E}$, $\bar{\epsilon}^T = \ln(L_0/L_f)$, the plastic component is

$$\bar{\epsilon}^p = ln\,\frac{L_0}{L_f} - \frac{\sigma}{E}, \quad (7)$$

where E is the modulus of elasticity. Assume now an equivalent true stress vs. integrated equivalent plastic strain law

$$\bar{\sigma} = \sigma_0(\epsilon_0 + \bar{\epsilon}^p)^n. \quad (8)$$

The two constants σ_0, and n are found from two points on the stress-strain curve beyond yield, usually the maximum load and the fracture point, whereas ϵ_0 is found from the yield point, i.e., $\epsilon_0 = (\sigma_Y/\sigma_0)^{1/n}$. The constant n is the strain-hardening exponent. Notice that $\bar{\sigma} = \sigma$.

Next, denote by $A_0 = tb_0$ the initial cross-sectional area of the asperity. For simplicity, we shall consider the material as being incompressible in both the elastic and the plastic ranges when cross-sectional area calculations are performed (this would be strictly accurate if the Poisson's ratio is 0.5; however, the error introduced for the usual value of 0.3 can be reasonably expected to be small, if the elastic strains are small compared to the plastic ones). Therefore, the incompressibility requirement gives a relationship for the current cross-section A_f and the stress $\sigma = P/A_f$:

$$A_f L_f = A_0 L_0, \quad \sigma = \frac{PL_f}{A_0 L_0}. \quad (9)$$

Using (7), (8), and (9) gives one equation in P, L_f:

$$\left[\frac{PL_f}{\sigma_0 A_0 L_0}\right]^{1/n} = \ln\frac{L_0}{L_f} - \frac{PL_f}{EA_0 L_0} + \epsilon_0. \quad (10a)$$

The other equation needed to solve for L_f and P is found from (4) and (5):

$$L_f = \frac{2}{G}\left(\frac{C}{2\pi}\right)^{1/2}(1-\nu)K_{I,\text{global}} + \frac{2(1-\nu)}{\pi G}\left(1-\frac{C}{2a}\right)^{1/2}\frac{P}{t}. \quad (10b)$$

Notice that the final, crushed asperity width can be found from the volume preservation condition (9) and the transverse strain equality $\epsilon_{11} = \epsilon_{33}$:

$$b_f = b_0\sqrt{L_0/L_f}. \quad (11)$$

The description of the asperity behavior for the two separate phases, i.e., the loading and unloading one, will follow next.

Loading Phase. During the application of the external cyclic load, Q, asperity loading may occur from the initial configuration or it may involve reloading after the asperity has been plastically crushed to a reduced height. Hence, during the decreasing external load cycle (loading the asperity) from a general position (Q_i, $P_i = 0$, L_i, A_i) to a position ($Q_f < Q_i$, P, $L_f \le L_i$, $A_f \ge A_i$), the following conditions may develop:

(a) No asperity contact takes place and $K_I = K_{I,\text{global}}$ if, from (10b):

$$\frac{2(1-\nu)}{G}\left(\frac{C}{2\pi}\right)^{1/2}K_{I,\text{global}} > L_i. \quad (12)$$

(b) If asperity contact takes place and during asperity loading (decreasing external load), the asperity compresses below yield, then (10a) is replaced with the equation found by setting $\bar{\epsilon}^p = 0$ in (7), or

$$\frac{P}{EA_i} = -\ln\frac{L_f}{L_i} \simeq 1 - \frac{L_f}{L_i}. \quad (13)$$

Then the asperity load and final asperity height are found by eliminating L_f from (10b) and (13).

(c) If the foregoing conditions are not met and the asperity loading is taking place in the plastic range, then the system of Eqs. (10) is numerically solved.

The current asperity height, L_i, and cross-sectional area, A_i, have been used in (13) instead of the initial values, L_0 and A_0, respectively, since on reloading after a compressive excursion, the asperity is loaded elastically from the current (crushed asperity) dimensions.

Unloading Phase. During the increasing external load cycle (unloading the asperity to zero asperity load), from a position (Q_f, P_u, L_f, A_f) to a position ($Q_i > Q_f$, $P = 0$, $L_i > L_f$, $A_i < A_f$), we recover not the initial asperity height L_0, but the final compressed one, L_f, plus the change in height that is given by the elastic solution that corresponds to the load P_u at which unloading takes place, $\sigma L_i/E$, i.e.,

$$L_i = L_f + \frac{P_u L_f}{EA_f}; \quad A_i = L_0 A_0/L_i. \quad (14)$$

Notice that L_i is now the "new" (after unloading) interference height.

3 Model Predictions

Consider a metal with the mechanical properties: $E = 200$ GN/m^2, $\nu = 0.3$, yield strength $\sigma_y = 400$ MN/m^2, strain-hardening exponent $n = 0.30$ and the constant of Eq. (8), $\sigma_0 = 700$ MN/m^2. The other constant in the relation (8) that describes the behavior beyond yield is found by fitting the yield point, i.e., $\epsilon_0 = (\sigma_y/\sigma_0)^{1/n}$. These material constants are typical of a hot rolled steel. A single-edge-cracked specimen of thickness $t = 13$ mm and width $w = 26$ mm with a crack of length $a = 11$ mm is assumed.

For this case of single-edge through crack of length a in a plate of width w under uniform remote normal load Q, the stress intensity factor is (e.g., Hellan, 1984):

$$K_I(Q) = \frac{Q}{wt}\sqrt{\pi a}\left(1.12 - 0.23\frac{a}{w} + 10.6\frac{a^2}{w^2} - 21.7\frac{a^3}{w^3} + 30.4\frac{a^4}{w^4}\right). \quad (15)$$

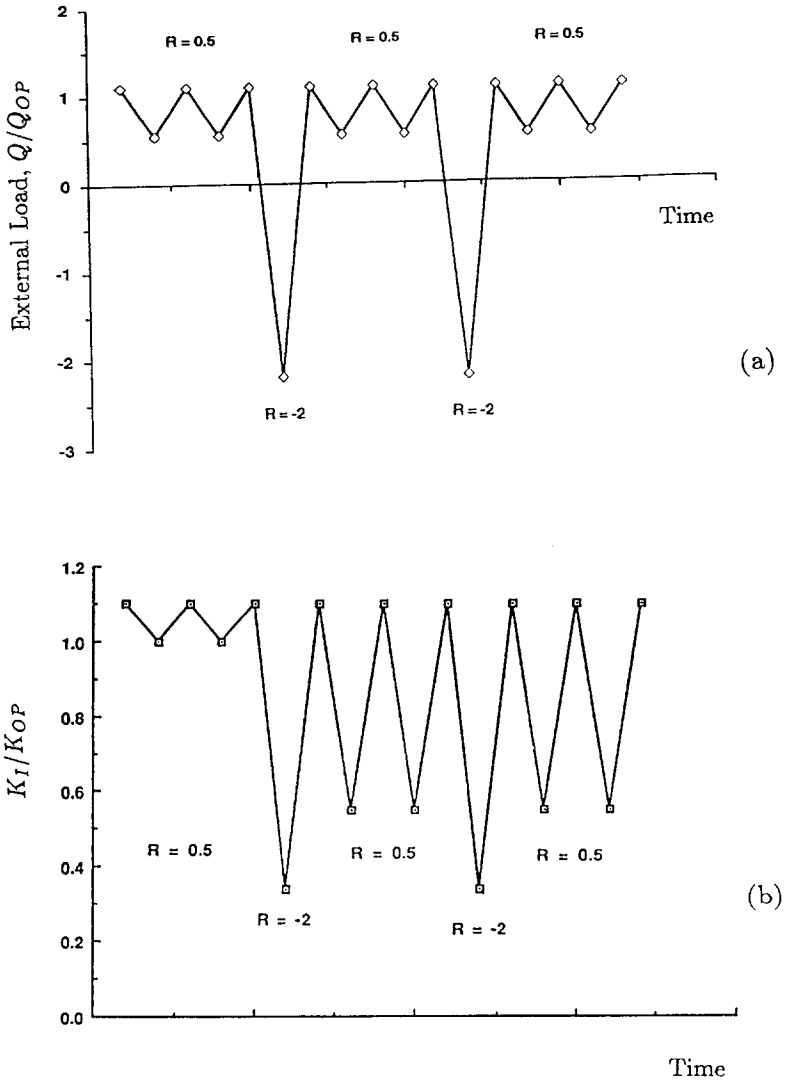

Fig. 2 (*a*) Applied load sequence; (*b*) the total stress intensity factor at different moments during the application of the load sequence

Consider a single asperity configuration with an initial interference height $L_0 = 25$ μm and initial width $b_0 = 50$ μm. The distance from the crack tip is $C = 15$ μm. These are typical dimensions of experimentally observed asperities as reported by Beevers et al. (1984). First, the opening load (load at which asperity contact is established), Q_{OP}, is found by setting $P = 0$ in (10*b*):

$$K_{OP} = \frac{L_0 G}{2(1-\nu)}\left(\frac{C}{2\pi}\right)^{-1/2} = K_I(Q_{OP}). \qquad (16)$$

A load sequence as shown in Fig. 2(*a*) is applied. First, the specimen is cycled between $1.1Q_{OP}$ and $0.55Q_{OP}$, so that the load ratio is positive, $R = 0.5$. Then a compressive excursion to $-2.2Q_O P$, i.e., a negative $R = -2$, is applied. Subsequently, the initial, positive $R = 0.5$ is resumed.

The quantity that controls the fatigue crack growth rate is the range in the total stress intensity factor ΔK. Figure 2(*b*) shows the total stress intensity factor at the different stages of the loading sequence. In all segments, at the maximum positive external load, $K = K_{I,\text{global}}$ and the range ΔK is affected by the minimum (positive or negative) external load, at which asperity contact may develop, and a nonzero $K_{\text{I,local}}$ may be generated. At the first $R = 0.5$ load segment, ΔK is relatively small (because of the rather large $K_{I,\text{local}}$ at the load minimum). During the compressive excursion, which crushes the asperity, ΔK is increased substantially. Notice that at the minimum, negative load point, K is positive, nonzero.

4 Conclusions

It has been shown that an inelastic, discrete asperities model can be used to demonstate the effect of compressive excursions during fatigue crack growth. By reducing the height of roughness asperities, the effective range of the stress intensity factor is increased. Subsequent increases in crack growth rate can then be expected to follow.

Acknowledgments

The studies which led to the preparation of this paper were initiated during the support of the Warner Robins Air Logistics Center, Robins AFB under Contact No. F09603-91-G-0096-0013. The authors are grateful for the encouragement provided by the Project Monitor, Mr. Gary Chamberlain.

References

Beevers, C. J., Carlson, R. L., Bell, K., and Starke, E. A., 1984, "A

Model for Fatigue Crack Closure," *Engineering Fracture Mechanics*, Vol. 19, pp. 93–100.

Carlson, R. L., and Kardomateas, G. A., 1994, "Effects of Compressive Load Excursions on Fatigue Crack Growth," *International Journal of Fatigue*, Vol. 16, pp. 141–146.

Hellan, K., 1984, *Introduction to Fracture Mechanics*, McGraw-Hill, New York.

Sih, G. C., Paris, P. C., and Erdogan, F., 1962, "Crack-Tip Stress Intensity Factors for Plane Extension and Plate Bending Problems," ASME JOURNAL OF APPLIED MECHANICS, Vol. 29, pp. 306–312.

An Alternative Derivation of Some New Perspectives on Constrained Motion

A. A. Barhorst[13]

An alternative derivation of some recently reported results is presented. Specifically, some results regarding the fundamental view of Lagrangian mechanics and nonholonomic constraints.

Introduction

In a recent paper (Udwadia and Kalaba, 1992), the general nonholonomic equations of motion for rigid bodies were developed via a constrained optimization procedure. The authors utilized the theory of generalized inverses for matrices. The resulting evolution equations were cast as an error equation similar to state feedback in the modern control theory. The authors mentioned that this interpretation of the nonholonomic dynamics is new and enlightening.

In this Note, the intent is to show that the error type interpretation is also available from a physical formulation of the nonholonomic equations of motion. The presentation herein is more restrictive than the work in (Udwadia and Kalaba, 1992), but it does appear to cover all the cases that arise in engineering systems.

Derivation

Without loss of generality and to facilitate brevity, suppose a system of P particles with N degrees-of-freedom is undergoing holonomic motion, uniquely described by N-independent generalized coordinates. D'Alembert's principle for this system of particles can be written as

$$\sum_p {}^N\delta^o\mathbf{r}^p \cdot \left(\mathbf{F}_p - m_p^o\mathbf{a}_N^p\right) = 0 \tag{1}$$

where ${}^N\delta^o\mathbf{r}^p$ is the absolute variation of the position of the pth particle as seen in the Newtonian frame N with origin o. The vector $\mathbf{F}_p$ is the resultant of forces on the p particle[14], ${}^o\mathbf{a}_N^p$ is its absolute acceleration, and m_p its mass. The vector variation can be written as (Kane and Levinson, 1983; Everett, 1988; Desloge, 1987)

$$\begin{aligned} {}^N\delta^o\mathbf{r}^p &= \frac{\partial^o\mathbf{v}_N^p}{\partial u_n}\delta u_n \\ &= \frac{\partial^o\mathbf{a}_N^p}{\partial \dot{u}_n}\delta u_n \end{aligned} \tag{2}$$

with summation on repeated indices implied. The quantities u_n $(n = 1, 2, \ldots, N)$ are quasi-coordinates or generalized speeds, the simplest choice being the time derivative of the holonomic generalized coordinates $\dot{q}_n$, an alternative choice being a convenient linear combination of the $\dot{q}_n$. With independent variations δu_n, the system's time evolution is modeled with

$$\sum_p \frac{\partial^o\mathbf{v}_N^p}{\partial u_n} \cdot \left(\mathbf{F}_p - m_p^o\mathbf{a}_N^p\right) = 0 \tag{3}$$

for each of the N generalized speeds u_n. Kinematic differential equations relating $\dot{q}_n$ to u_n must also be supplied. If one chooses the simple form $u_n = \dot{q}_n$ for the generalized speeds, then the equations of motion can be written as

$$\boldsymbol{M}(q, t)\ddot{q} = \boldsymbol{Q}(\dot{q}, q, t) \tag{4}$$

where the matrix $\boldsymbol{M}$ has dimension $N \times N$, and $\boldsymbol{Q}$, $\dot{q}$, and q are $N \times 1$ column vectors. The mass matrix $\boldsymbol{M}(q, t)$ and the column vector $\boldsymbol{Q}(\dot{q}, q, t)$ are chosen to be partitioned as follows:

$$\begin{bmatrix} M_{11} & M_{12} \\ M_{21} & M_{22} \end{bmatrix} \begin{Bmatrix} \ddot{q}_m \\ \ddot{q}_{n'} \end{Bmatrix} = \begin{Bmatrix} Q_m \\ Q_{n'} \end{Bmatrix} \tag{5}$$

where

$$\begin{aligned} M_{11} &= m_p \frac{\partial^o\mathbf{v}_N^p}{\partial \dot{q}_m} \cdot \frac{\partial^o\mathbf{v}_N^p}{\partial \dot{q}_m}, \quad M_{12} = \frac{\partial^o\mathbf{v}_N^p}{\partial \dot{q}_m} \cdot \frac{\partial^o\mathbf{v}_N^p}{\partial \dot{q}_{n'}} \\ M_{21} &= m_p \frac{\partial^o\mathbf{v}_N^p}{\partial \dot{q}_{n'}} \cdot \frac{\partial^o\mathbf{v}_N^p}{\partial \dot{q}_m}, \quad M_{22} = m_p \frac{\partial^o\mathbf{v}_N^p}{\partial \dot{q}_{n'}} \cdot \frac{\partial^o\mathbf{v}_N^p}{\partial \dot{q}_{n'}} \end{aligned} \tag{6}$$

and

$$\begin{aligned} Q_m &= \frac{\partial^o\mathbf{v}_N^p}{\partial \dot{q}_m} \cdot \left(\mathbf{F}_p - m_p\mathbf{G}_p\right) \\ Q_{n'} &= \frac{\partial^o\mathbf{v}_N^p}{\partial \dot{q}_{n'}} \cdot \left(\mathbf{F}_p - m_p\mathbf{G}_p\right) \end{aligned} \tag{7}$$

with summation on p implied. The vector $\mathbf{G}_p$ is the gyroscopic terms left after the linear terms in $\ddot{q}$ have been moved to the left-hand side of the equation.

Now consider the same system of particles under the influence of M nonholonomic constraints of the form (Neimark and Fufaev, 1972; Barhorst and Everett, 1993):

$$\delta u_m = A_{mn'}\delta u_{n'}, \quad n' \in \left\{I_i^{N-M}\right\}, \quad m \in \left\{I_d^M\right\} \tag{8}$$

where $\{I_i^{N-M}\}$ means the set of all $N - M$ indices associated to independent generalized speeds. $\{I_d^M\}$ is the set of M indices associated to dependent generalized speeds. Also, $\{I_d^M\} \in \{I_i^{N-M}\}$. The constraint tensor $A_{mn'}$ is a function of the generalized coordinates q and time. Considering Eq. (8), the vector variation in Eq. (1) can be written as

$${}^N\delta^o\mathbf{r}^p = \left(\frac{\partial^o\mathbf{v}_N^p}{\partial u_{n'}} + \frac{\partial^o\mathbf{v}_N^p}{\partial u_m}A_{mn'}\right)\delta u_{n'}, \quad n' \in \left\{I_i^{N-M}\right\}, \quad m \in \left\{I_d^M\right\} \tag{9}$$

with summation on repeated indices. Substitution of Eq. (9) into Eq. (1) allows general conclusions to be drawn.

[13]Assistant Professor, Mechanical Engineering, Texas Tech University, Lubbock, TX 79409-1021. Mem. ASME.

[14]The nonconstraint subset of forces make the ultimate contribution.

Contributed by the Applied Mechanics Division of THE AMERICAN SOCIETY OF MECHANICAL ENGINEERS for publication in the ASME JOURNAL OF APPLIED MECHANICS. Manuscript received by the ASME Applied Mechanics Division, Oct. 12, 1993; final revision, Mar. 21, 1994. Associate Technical Editor: E. J. Haug, Jr.

Model for Fatigue Crack Closure," *Engineering Fracture Mechanics*, Vol. 19, pp. 93–100.

Carlson, R. L., and Kardomateas, G. A., 1994, "Effects of Compressive Load Excursions on Fatigue Crack Growth," *International Journal of Fatigue*, Vol. 16, pp. 141–146.

Hellan, K., 1984, *Introduction to Fracture Mechanics*, McGraw-Hill, New York.

Sih, G. C., Paris, P. C., and Erdogan, F., 1962, "Crack-Tip Stress Intensity Factors for Plane Extension and Plate Bending Problems," ASME JOURNAL OF APPLIED MECHANICS, Vol. 29, pp. 306–312.

An Alternative Derivation of Some New Perspectives on Constrained Motion

A. A. Barhorst[13]

An alternative derivation of some recently reported results is presented. Specifically, some results regarding the fundamental view of Lagrangian mechanics and nonholonomic constraints.

Introduction

In a recent paper (Udwadia and Kalaba, 1992), the general nonholonomic equations of motion for rigid bodies were developed via a constrained optimization procedure. The authors utilized the theory of generalized inverses for matrices. The resulting evolution equations were cast as an error equation similar to state feedback in the modern control theory. The authors mentioned that this interpretation of the nonholonomic dynamics is new and enlightening.

In this Note, the intent is to show that the error type interpretation is also available from a physical formulation of the nonholonomic equations of motion. The presentation herein is more restrictive than the work in (Udwadia and Kalaba, 1992), but it does appear to cover all the cases that arise in engineering systems.

Derivation

Without loss of generality and to facilitate brevity, suppose a system of P particles with N degrees-of-freedom is undergoing holonomic motion, uniquely described by N-independent generalized coordinates. D'Alembert's principle for this system of particles can be written as

$$\sum_p {}^N\delta^o\mathbf{r}^p \cdot \left(\mathbf{F}_p - m_p^o\mathbf{a}_N^p\right) = 0 \tag{1}$$

where ${}^N\delta^o\mathbf{r}^p$ is the absolute variation of the position of the pth particle as seen in the Newtonian frame N with origin o. The vector $\mathbf{F}_p$ is the resultant of forces on the p particle[14], ${}^o\mathbf{a}_N^p$ is its absolute acceleration, and m_p its mass. The vector variation can be written as (Kane and Levinson, 1983; Everett, 1988; Desloge, 1987)

$$\begin{aligned} {}^N\delta^o\mathbf{r}^p &= \frac{\partial^o\mathbf{v}_N^p}{\partial u_n}\delta u_n \\ &= \frac{\partial^o\mathbf{a}_N^p}{\partial \dot{u}_n}\delta u_n \end{aligned} \tag{2}$$

with summation on repeated indices implied. The quantities u_n $(n = 1, 2, \ldots, N)$ are quasi-coordinates or generalized speeds, the simplest choice being the time derivative of the holonomic generalized coordinates $\dot{q}_n$, an alternative choice being a convenient linear combination of the $\dot{q}_n$. With independent variations δu_n, the system's time evolution is modeled with

$$\sum_p \frac{\partial^o\mathbf{v}_N^p}{\partial u_n} \cdot \left(\mathbf{F}_p - m_p^o\mathbf{a}_N^p\right) = 0 \tag{3}$$

for each of the N generalized speeds u_n. Kinematic differential equations relating $\dot{q}_n$ to u_n must also be supplied. If one chooses the simple form $u_n = \dot{q}_n$ for the generalized speeds, then the equations of motion can be written as

$$\boldsymbol{M}(q, t)\ddot{q} = \boldsymbol{Q}(\dot{q}, q, t) \tag{4}$$

where the matrix $\boldsymbol{M}$ has dimension $N \times N$, and $\boldsymbol{Q}$, $\dot{q}$, and q are $N \times 1$ column vectors. The mass matrix $\boldsymbol{M}(q, t)$ and the column vector $\boldsymbol{Q}(\dot{q}, q, t)$ are chosen to be partitioned as follows:

$$\begin{bmatrix} M_{11} & M_{12} \\ M_{21} & M_{22} \end{bmatrix} \begin{Bmatrix} \ddot{q}_m \\ \ddot{q}_{n'} \end{Bmatrix} = \begin{Bmatrix} Q_m \\ Q_{n'} \end{Bmatrix} \tag{5}$$

where

$$\begin{aligned} M_{11} &= m_p \frac{\partial^o\mathbf{v}_N^p}{\partial \dot{q}_m} \cdot \frac{\partial^o\mathbf{v}_N^p}{\partial \dot{q}_m}, \quad M_{12} = \frac{\partial^o\mathbf{v}_N^p}{\partial \dot{q}_m} \cdot \frac{\partial^o\mathbf{v}_N^p}{\partial \dot{q}_{n'}} \\ M_{21} &= m_p \frac{\partial^o\mathbf{v}_N^p}{\partial \dot{q}_{n'}} \cdot \frac{\partial^o\mathbf{v}_N^p}{\partial \dot{q}_m}, \quad M_{22} = m_p \frac{\partial^o\mathbf{v}_N^p}{\partial \dot{q}_{n'}} \cdot \frac{\partial^o\mathbf{v}_N^p}{\partial \dot{q}_{n'}} \end{aligned} \tag{6}$$

and

$$\begin{aligned} Q_m &= \frac{\partial^o\mathbf{v}_N^p}{\partial \dot{q}_m} \cdot \left(\mathbf{F}_p - m_p\mathbf{G}_p\right) \\ Q_{n'} &= \frac{\partial^o\mathbf{v}_N^p}{\partial \dot{q}_{n'}} \cdot \left(\mathbf{F}_p - m_p\mathbf{G}_p\right) \end{aligned} \tag{7}$$

with summation on p implied. The vector $\mathbf{G}_p$ is the gyroscopic terms left after the linear terms in $\ddot{q}$ have been moved to the left-hand side of the equation.

Now consider the same system of particles under the influence of M nonholonomic constraints of the form (Neimark and Fufaev, 1972; Barhorst and Everett, 1993):

$$\delta u_m = A_{mn'}\delta u_{n'}, \quad n' \in \left\{I_i^{N-M}\right\}, \quad m \in \left\{I_d^M\right\} \tag{8}$$

where $\{I_i^{N-M}\}$ means the set of all $N - M$ indices associated to independent generalized speeds. $\{I_d^M\}$ is the set of M indices associated to dependent generalized speeds. Also, $\{I_d^M\} \in \{I_i^{N-M}\}$. The constraint tensor $A_{mn'}$ is a function of the generalized coordinates q and time. Considering Eq. (8), the vector variation in Eq. (1) can be written as

$${}^N\delta^o\mathbf{r}^p = \left(\frac{\partial^o\mathbf{v}_N^p}{\partial u_{n'}} + \frac{\partial^o\mathbf{v}_N^p}{\partial u_m}A_{mn'}\right)\delta u_{n'}, \quad n' \in \left\{I_i^{N-M}\right\}, \quad m \in \left\{I_d^M\right\} \tag{9}$$

with summation on repeated indices. Substitution of Eq. (9) into Eq. (1) allows general conclusions to be drawn.

[13]Assistant Professor, Mechanical Engineering, Texas Tech University, Lubbock, TX 79409-1021. Mem. ASME.

[14]The nonconstraint subset of forces make the ultimate contribution.

Contributed by the Applied Mechanics Division of THE AMERICAN SOCIETY OF MECHANICAL ENGINEERS for publication in the ASME JOURNAL OF APPLIED MECHANICS. Manuscript received by the ASME Applied Mechanics Division, Oct. 12, 1993; final revision, Mar. 21, 1994. Associate Technical Editor: E. J. Haug, Jr.

The second term in the parentheses of Eq. (9), dot multiplied into the d'Alembert force deficit in Eq. (1), can be thought of as the amount of generalized force needed to bring the system into compatibility with the constraints at this instant (Neimark and Fufaev, 1972; Barhorst and Everett, 1993). This concept is key to understanding the control error type interpretation of the evolution of the dynamic system. However, there is really no need to keep the terms in the parentheses separated. These relationships are just the partial velocities (written explicitly in the felicitous coordinates) for the system in its constrained configuration. For practical engineering applications it is usually frugal (relative to net mathematical operations) and straightforward to use the natural coordinates implied by the geometry of the system under study (Kane and Levinson, 1985). However, for this presentation the distinction between the partial velocities will remain.

With independent $\delta u_{n'}$ (satisfying the nonholonomic constraints) the time evolution of the system is modeled with

$$\sum_p \left(\frac{\partial^o \mathbf{v}_N^p}{\partial u_{n'}} + \frac{\partial^o \mathbf{v}_N^p}{\partial u_m} A_{mn'} \right) \cdot \left(\mathbf{F}_p - m_p^o \mathbf{a}_N^p \right) = 0 \quad (10)$$

for each $n' \in \{I_i^{N-M}\}$. Since the dependent variables due to the constraints have been left in the formulation, the extra coordinates are determined from the nonvariational form of the nonholonomic constraint (Neimark and Fufaev, 1972; Kane and Levinson, 1985):

$$u_m = A_{mn'} u_{n'} + d_m(t) \quad (11)$$

or

$$\dot{u}_m = A_{mn'} \dot{u}_{n'} + b_m(t) \quad (12)$$

and any kinematic differential equations of the form

$$\dot{q}_n = L_{ni} u_i + z_n(t), \quad (i, n = 1, 2, \ldots, N) \quad (13)$$

with summation on i implied.

With the assumption that the simple choice of $u_n = \dot{q}_n$ is utilized, the equations of motion for the nonholonomic system, with the full complement of N generalized coordinates, can be written as

$$\boldsymbol{M}'(q, t)\ddot{q} = \boldsymbol{Q}'(\dot{q}, q, t) \quad (14)$$

or

$$\begin{bmatrix} I & -A_{mn'} \\ M_{21} + M'_{21} & M_{22} + M'_{22} \end{bmatrix} \begin{Bmatrix} \ddot{q}_m \\ \ddot{q}_{n'} \end{Bmatrix} = \begin{Bmatrix} b_m \\ Q_{n'} + Q' \end{Bmatrix} \quad (15)$$

where the partition $A_{mn'}$ is the matrix of coefficients from Eq. 12. The other undefined terms are

$$M'_{21} = m_p \frac{\partial^o \mathbf{v}_N^p}{\partial \dot{q}_m} \cdot \frac{\partial^o \mathbf{v}_N^p}{\partial \dot{q}_m} A_{mn'} = A^T_{mn'} M_{11} \quad (16)$$

$$M'_{22} = m_p \frac{\partial^o \mathbf{v}_N^p}{\partial \dot{q}_m} \cdot \frac{\partial^o \mathbf{v}_N^p}{\partial \dot{q}_{n'}} A_{mn'} = A^T_{mn'} M_{12} \quad (17)$$

and

$$Q' = \frac{\partial^o \mathbf{v}_N^p}{\partial \dot{q}_m} A_{mn'} \cdot \left(\mathbf{F}_p - m_p \mathbf{G}_p \right) = A^T_{mn'} Q_m \quad (18)$$

where the superscript T denotes transpose.

The proposed nonholonomic equations of motion are (Udwadia and Kalaba, 1992):

$$\boldsymbol{M}(q, t)\ddot{q} = \boldsymbol{Q}(\dot{q}, q, t) + \boldsymbol{Q}_c(\dot{q}, q, t) \quad (19)$$

where the terms are as in Eq. (4) with the exception of the generalized force $\boldsymbol{Q}_c(\dot{q}, q, t)$ that enforces the constraints. $\boldsymbol{Q}_c(\dot{q}, q, t)$ is readily determined from the analysis herein.

Substitution of $\ddot{q}$ from Eq. (14) into Eq. (19) gives

$$\boldsymbol{Q}_c = \boldsymbol{M}\boldsymbol{M}'^{-1}\{\boldsymbol{Q}' - \boldsymbol{M}'\boldsymbol{M}^{-1}\boldsymbol{Q}\}. \quad (20)$$

With straightforward matrix manipulations it is possible to partition the vector on the right-hand side above as

$$\{\boldsymbol{Q}' - \boldsymbol{M}'\boldsymbol{M}^{-1}\boldsymbol{Q}\} = \begin{Bmatrix} b - \boldsymbol{A}\boldsymbol{M}^{-1}\boldsymbol{Q} \\ Q' - [M'_{21} \quad M'_{22}]\boldsymbol{M}^{-1}\boldsymbol{Q} \end{Bmatrix}. \quad (21)$$

The bottom partition can be shown to be identically zero with the aid of Eqs. (16)–(18), therefore the generalized constraint forces can be written as

$$\boldsymbol{Q}_c = \boldsymbol{M}\boldsymbol{M}^{-1}\boldsymbol{I}\{b - \boldsymbol{A}\boldsymbol{M}^{-1}\boldsymbol{Q}\} \quad (22)$$

where $b = \{b_m\}$. The long matrix $\boldsymbol{A}$ is partitioned as

$$\boldsymbol{A} = [I \quad -A_{mn'}] \quad (23)$$

and the tall augmented identity matrix $\boldsymbol{I}$ is partitioned as

$$\boldsymbol{I} = \begin{bmatrix} I \\ 0 \end{bmatrix}. \quad (24)$$

Comparing these results with the results in (Udwadia and Kalaba, 1992), it is seen that

$$K = \boldsymbol{M}^{1/2}(\boldsymbol{A}\boldsymbol{M}^{-1/2})^{\dagger} = \boldsymbol{M}\boldsymbol{M}'^{-1}\boldsymbol{I} \quad (25)$$

where $(\cdot)^{\dagger}$ denotes the Moore-Penrose pseudo-inverse.

The evolution of the difference between the nonholonomic system and the holonomic system can be obtained by rearranging Eq. (19) while utilizing Eq. (22) and is

$$\ddot{q} - a = \boldsymbol{M}'^{-1}\boldsymbol{I}\{b - \boldsymbol{A}a\} \quad (26)$$

where $a = \boldsymbol{M}^{-1}\boldsymbol{Q}$. It can be seen that $\boldsymbol{M}$ is the standard positive definite mass/inertia matrix and is nonsingular. $\boldsymbol{M}'$ is also invertible which can be verified by utilizing the equations for matrix inversion by partitions.

Discussion

It can be seen that by taking the physical approach to the formulation of the nonholonomic equations of motion gives the same error-type interpretation of the evolution of the system's dynamics (Eq. (26)) as discussed in (Udwadia and Kalaba, 1992). However, the physical interpretation herein leads to a much simpler formula for the gain matrix K and reduces the number of operations needed to form the matrix. Of course, the results described herein are more restrictive than in (Udwadia and Kalaba, 1992) because (1) the system's configuration is assumed to be described by independent generalized coordinates written with consideration of the holonomic constraints, and (2) the constraint matrix $\boldsymbol{A}$ is required to be in the form shown in Eq. (12) or (23), which only allows nonholonomic constraints of the form described above. However, it is a widely used practice to incorporate holonomic and nonholonomic constraints consistent with Eq. (12), therefore the restrictions enumerated above are not that restrictive.

Another advantage of using the physical approach to model a nonholonomic system is that one can "see" the contribution of each coordinate by virtue of the dot products used to form the mass matrix and the generalized force vector. This allows an analyst to obtain a better "feel" for the system's dynamics, which may lead to an improved overall understanding of the system, which may lend an advantage to a design engineer.

If one's aim is to model the time evolution of a nonholonomic mechanical system, then, from an engineering viewpoint, it is recommended that one use the method of Gibbs-Appell (Desloge, 1987) or Kane (Kane and Levinson, 1985)

and natural or felicitous coordinates. This recommendation is based on the observation that the work required to generate and integrate the equations of motion take fewer operations (see Eq. (25)) and are closer to the physics of the problem than the scheme discussed in (Udwadia and Kalaba, 1992).

Acknowledgment

The author wishes to thank the College of Engineering at Texas Tech University for providing 1992–93 line item funding, which allowed the author to pursue other duties besides teaching.

References

Barhorst, A. A., and Everett, L. J., 1993, "Contact/Impact in Hybrid Parameter Multiple Body Systems," *Proceedings of the ASME 16th Annual Energy-Sources Technology Conference & Exhibition, Dynamics and Vibrations Symposium*, Houston, TX.

Desloge, E. A., 1987, "Relationship between Kane's Equations and the Gibbs-Appell Equations," *Journal of Guidance, Control, and Dynamics*, Vol. 10, No. 1, pp. 120–122.

Everett, L. J., 1988, "An Alternative Algebra for Deriving Equations of Motion of Compliant Manipulators," *Journal of Robotic Systems*, Vol. 5, No. 6, pp. 553–566.

Kane, T. R., and Levinson, D. A., 1983, "Multibody Dynamics," ASME JOURNAL OF APPLIED MECHANICS, Vol. 50, pp. 1071–1078.

Kane, T. R., and Levinson, D. A., 1985, *Dynamics Theory and Applications*, McGraw-Hill, New York.

Neimark, J. I., and Fufaev, N. A., 1972, *Dynamics of Non-Holonomic Systems*, American Mathematical Society, Providence, RI (Translated from the Russian by J. R. Barbour).

Udwadia, F. E., and Kalaba, R. E., 1992, "A New Perspective on Constrained Motion," *Proceedings of The Royal Society, London, Series A*, Vol. 439, No. 9, pp. 407–410.

Discussion of a Procedure for Obtaining Bounds on the Overall Response of Power-Law Two-Phase Solids

B. J. Lee[15] and M. E. Mear[16]

1 Introduction

Ponte Castaneda (1991) has introduced a clever technique for obtaining bounds on the overall response of nonlinear two-phase materials. The procedure exploits information for a comparison composite in which the actual nonlinear matrix material is replaced by a homogeneous, isotropic linearly elastic comparison matrix material. Here we consider a generalization of Ponte Castaneda's procedure in which a special class of *anisotropic* comparison solids is used to obtain a bound for isotropic nonlinear composites. The work is motivated by a desire to develop a procedure which provides bounds which are superior to those obtained using an isotropic comparison matrix, yet which retains the simplicity afforded by using a homogeneous comparison matrix material.

Although the comparison matrix is anisotropic, the bounds generated by the procedure are isotropic. This result is achieved by selecting the secant compliances for the comparison matrix such that they have the same "directional properties" as those for the matrix material evaluated at the macroscopic stress (also see Duva, 1984; He and Hutchinson, 1981; Tandon and Weng, 1988). Certain parameters are left free in the compliances so that the degree of anisotropy can be varied, and the isotropic comparison solid originally considered by Ponte Castaneda is obtained as a special case.

The procedure is formulated for plane-strain deformation of power-law solids containing inhomogeneities which are either rigid or vacuous. Calculations are carried out for dilute concentrations of circular inhomogeneities, and the utility of the procedure for obtaining bounds on the overall response of the nonlinear composites is evaluated.

Overall Response of Composite

Consider the deformation of a nonlinear matrix which contains circular cylindrical inhomogeneities that are aligned with respect to the x_3-direction of a reference cartesian coordinate system $\{x_1, x_2, x_3\}$. The matrix material is assumed to be isotropic, incompressible, and to be characterized by the potential of the stress

$$\phi(\boldsymbol{\sigma}) = \frac{\epsilon_o \sigma_o}{n+1}\left(\frac{\sigma_e}{\sigma_o}\right)^{n+1} \tag{1}$$

where $\{\sigma_o, \epsilon_o, n\}$ are material constants, $\sigma_e = (3\sigma'_{ij}\sigma'_{ij}/2)^{1/2}$ is the effective stress, and $\sigma'_{ij} = \sigma_{ij} - (\sigma_{kk}/3)\delta_{ij}$ is the stress deviator. The stress-strain relation is then given as

$$\epsilon_{ij} = \frac{\partial \phi}{\partial \sigma_{ij}} = \frac{3\epsilon_o}{2\sigma_o}\left(\frac{\sigma_e}{\sigma_o}\right)^{n-1}\sigma'_{ij} \tag{2}$$

and the secant compliances for the matrix, defined such that $\epsilon_{ij} = m_{ijkl}\sigma_{kl}$, are given by

$$m_{ijkl} = \frac{3\alpha\epsilon_o}{2n\sigma_o}\left(\frac{\sigma_e}{\sigma_o}\right)^{n-1}\left\{\frac{1}{2}\left(\delta_{ik}\sigma_{jl} + \delta_{il}\delta_{jk}\right) - \frac{1}{3}\delta_{ij}\delta_{kl} + \frac{3\beta}{\sigma_e^2}\sigma'_{ij}\sigma'_{kl}\right\} \tag{3}$$

where $\alpha = 1$ and $\beta = (n-1)/2$. In terms of these compliances, the potential for the matrix material can be expressed as $\phi(\boldsymbol{\sigma}) = m_{ijkl}\sigma_{ij}\sigma_{kl}/(n+1)$.

The second-phase inhomogeneities are taken to be either rigid or vacuous, and it is assumed that they are distributed in such a way that the solid is macroscopically homogeneous and isotropic in the plane of deformation. To determine the overall (plane-strain) response of such a composite, let tractions $t_i = \Sigma_{ij}n_j$ be prescribed on the exterior surface of a representative volume element, where n_j is the outwardly directed unit normal to the surface and Σ_{ij} is the macroscopic stress tensor (Hill, 1967). If the volume element has in-plane area A_r and is bounded by the curve C_r, then the macroscopic potential of the stress $\Phi(\boldsymbol{\Sigma})$, defined such that the (work conjugate) macroscopic strain is given by

$$E_{ij} = \frac{\partial \Phi}{\partial \Sigma_{ij}} \tag{4}$$

[15]Department of Civil Engineering, Feng Chia University, Taichung, Taiwan, R.O.C.

[16]Department of Aerospace Engineering and Engineering Mechanics, The University of Texas at Austin, Austin, TX 78712.

Contributed by the Applied Mechanics Division of THE AMERICAN SOCIETY OF MECHANICAL ENGINEERS for publication in the ASME JOURNAL OF APPLIED MECHANICS. Manuscript received by the ASME Applied Mechanics Division, Sept. 27, 1993; final revision, Mar. 25, 1994. Associate Technical Editor: J. W. Rudnicki.

and natural or felicitous coordinates. This recommendation is based on the observation that the work required to generate and integrate the equations of motion take fewer operations (see Eq. (25)) and are closer to the physics of the problem than the scheme discussed in (Udwadia and Kalaba, 1992).

Acknowledgment

The author wishes to thank the College of Engineering at Texas Tech University for providing 1992–93 line item funding, which allowed the author to pursue other duties besides teaching.

References

Barhorst, A. A., and Everett, L. J., 1993, "Contact/Impact in Hybrid Parameter Multiple Body Systems," *Proceedings of the ASME 16th Annual Energy-Sources Technology Conference & Exhibition, Dynamics and Vibrations Symposium*, Houston, TX.

Desloge, E. A., 1987, "Relationship between Kane's Equations and the Gibbs-Appell Equations," *Journal of Guidance, Control, and Dynamics*, Vol. 10, No. 1, pp. 120–122.

Everett, L. J., 1988, "An Alternative Algebra for Deriving Equations of Motion of Compliant Manipulators," *Journal of Robotic Systems*, Vol. 5, No. 6, pp. 553–566.

Kane, T. R., and Levinson, D. A., 1983, "Multibody Dynamics," ASME JOURNAL OF APPLIED MECHANICS, Vol. 50, pp. 1071–1078.

Kane, T. R., and Levinson, D. A., 1985, *Dynamics Theory and Applications*, McGraw-Hill, New York.

Neimark, J. I., and Fufaev, N. A., 1972, *Dynamics of Non-Holonomic Systems*, American Mathematical Society, Providence, RI (Translated from the Russian by J. R. Barbour).

Udwadia, F. E., and Kalaba, R. E., 1992, "A New Perspective on Constrained Motion," *Proceedings of The Royal Society, London, Series A*, Vol. 439, No. 9, pp. 407–410.

Discussion of a Procedure for Obtaining Bounds on the Overall Response of Power-Law Two-Phase Solids

B. J. Lee[15] and M. E. Mear[16]

1 Introduction

Ponte Castaneda (1991) has introduced a clever technique for obtaining bounds on the overall response of nonlinear two-phase materials. The procedure exploits information for a comparison composite in which the actual nonlinear matrix material is replaced by a homogeneous, isotropic linearly elastic comparison matrix material. Here we consider a generalization of Ponte Castaneda's procedure in which a special class of *anisotropic* comparison solids is used to obtain a bound for isotropic nonlinear composites. The work is motivated by a desire to develop a procedure which provides bounds which are superior to those obtained using an isotropic comparison matrix, yet which retains the simplicity afforded by using a homogeneous comparison matrix material.

Although the comparison matrix is anisotropic, the bounds generated by the procedure are isotropic. This result is achieved by selecting the secant compliances for the comparison matrix such that they have the same "directional properties" as those for the matrix material evaluated at the macroscopic stress (also see Duva, 1984; He and Hutchinson, 1981; Tandon and Weng, 1988). Certain parameters are left free in the compliances so that the degree of anisotropy can be varied, and the isotropic comparison solid originally considered by Ponte Castaneda is obtained as a special case.

The procedure is formulated for plane-strain deformation of power-law solids containing inhomogeneities which are either rigid or vacuous. Calculations are carried out for dilute concentrations of circular inhomogeneities, and the utility of the procedure for obtaining bounds on the overall response of the nonlinear composites is evaluated.

Overall Response of Composite

Consider the deformation of a nonlinear matrix which contains circular cylindrical inhomogeneities that are aligned with respect to the x_3-direction of a reference cartesian coordinate system $\{x_1, x_2, x_3\}$. The matrix material is assumed to be isotropic, incompressible, and to be characterized by the potential of the stress

$$\phi(\boldsymbol{\sigma}) = \frac{\epsilon_o \sigma_o}{n+1}\left(\frac{\sigma_e}{\sigma_o}\right)^{n+1} \tag{1}$$

where $\{\sigma_o, \epsilon_o, n\}$ are material constants, $\sigma_e = (3\sigma'_{ij}\sigma'_{ij}/2)^{1/2}$ is the effective stress, and $\sigma'_{ij} = \sigma_{ij} - (\sigma_{kk}/3)\delta_{ij}$ is the stress deviator. The stress-strain relation is then given as

$$\epsilon_{ij} = \frac{\partial \phi}{\partial \sigma_{ij}} = \frac{3\epsilon_o}{2\sigma_o}\left(\frac{\sigma_e}{\sigma_o}\right)^{n-1}\sigma'_{ij} \tag{2}$$

and the secant compliances for the matrix, defined such that $\epsilon_{ij} = m_{ijkl}\sigma_{kl}$, are given by

$$m_{ijkl} = \frac{3\alpha\epsilon_o}{2n\sigma_o}\left(\frac{\sigma_e}{\sigma_o}\right)^{n-1}\left\{\frac{1}{2}\left(\delta_{ik}\sigma_{jl} + \delta_{il}\delta_{jk}\right) - \frac{1}{3}\delta_{ij}\delta_{kl} + \frac{3\beta}{\sigma_e^2}\sigma'_{ij}\sigma'_{kl}\right\} \tag{3}$$

where $\alpha = 1$ and $\beta = (n-1)/2$. In terms of these compliances, the potential for the matrix material can be expressed as $\phi(\boldsymbol{\sigma}) = m_{ijkl}\sigma_{ij}\sigma_{kl}/(n+1)$.

The second-phase inhomogeneities are taken to be either rigid or vacuous, and it is assumed that they are distributed in such a way that the solid is macroscopically homogeneous and isotropic in the plane of deformation. To determine the overall (plane-strain) response of such a composite, let tractions $t_i = \Sigma_{ij}n_j$ be prescribed on the exterior surface of a representative volume element, where n_j is the outwardly directed unit normal to the surface and Σ_{ij} is the macroscopic stress tensor (Hill, 1967). If the volume element has in-plane area A_r and is bounded by the curve C_r, then the macroscopic potential of the stress $\Phi(\boldsymbol{\Sigma})$, defined such that the (work conjugate) macroscopic strain is given by

$$E_{ij} = \frac{\partial \Phi}{\partial \Sigma_{ij}} \tag{4}$$

[15]Department of Civil Engineering, Feng Chia University, Taichung, Taiwan, R.O.C.

[16]Department of Aerospace Engineering and Engineering Mechanics, The University of Texas at Austin, Austin, TX 78712.

Contributed by the Applied Mechanics Division of THE AMERICAN SOCIETY OF MECHANICAL ENGINEERS for publication in the ASME JOURNAL OF APPLIED MECHANICS. Manuscript received by the ASME Applied Mechanics Division, Sept. 27, 1993; final revision, Mar. 25, 1994. Associate Technical Editor: J. W. Rudnicki.

can be expressed as (Hill, 1967)

$$\Phi(\boldsymbol{\Sigma}) = \frac{1}{A_r} \sup_{\boldsymbol{\sigma}^a} \int_{A_m} \phi(\boldsymbol{\sigma}^a) dA \tag{5}$$

where σ_{ij}^a represents statically admissible stress fields and where A_m denotes the area of the matrix material.

For the class of two-phase materials considered here, the macroscopic potential can be expressed in the form (e.g., Lee and Mear, 1992a,b)

$$\Phi(\boldsymbol{\Sigma}) = (1 + p)\Phi^o \tag{6}$$

where

$$\Phi^o = \frac{\epsilon_o \sigma_o}{n+1} \left(\frac{\Sigma_e}{\sigma_o} \right)^{n-1} \tag{7}$$

is the macroscopic potential in the absence of the inhomogeneities,

$$\Sigma_e = \left[\frac{3}{4} (\Sigma_{11} - \Sigma_{22})^2 + \frac{3}{2} (\Sigma_{12}^2 + \Sigma_{21}^2) \right]^{1/2} \tag{8}$$

is the macroscopic effective stress, and the function p depends upon the hardening exponent and the volume fraction and distribution of inhomogeneities. When the inhomogeneities are vacuous, p also depends upon the stress triaxiality $X \equiv \Sigma_m/\Sigma_e$ where

$$\Sigma_m = (\Sigma_{11} + \Sigma_{22})/2 \tag{9}$$

is the macroscopic mean stress. We remark that when the volume fraction c is dilute, $p = c\hat{p}$ where $\hat{p}$ is independent of the volume fraction and distribution of inhomogeneities (assuming only that the distribution is such that the solid is macroscopically homogeneous and isotropic in the plane of deformation).

Procedure to Obtain Bounds

Following Ponte Castaneda (1991), we introduce a *comparison composite* which is comprised of a linearly elastic matrix with (as yet arbitrary) material constants but which has the same distribution of inhomogeneities as the nonlinear composite. Let ϕ_c denote the potential of the stress for the linear comparison matrix material, and introduce the function ψ according to

$$\phi(\boldsymbol{\sigma}) = \phi_c(\boldsymbol{\sigma}) - \psi(\boldsymbol{\sigma}). \tag{10}$$

Then with the constant ψ_- defined by

$$\psi_- \equiv \sup_{\boldsymbol{\sigma}} \{\phi_c(\boldsymbol{\sigma}) - \phi(\boldsymbol{\sigma})\} \tag{11}$$

it follows from (5) that

$$\Phi \geq \Phi_c - (1 - c)\psi_- \tag{12}$$

where Φ_c is the macroscopic potential for the linear comparison composite. For any given linear comparison matrix (not necessarily isotropic or homogeneous), (12) provides a lower bound on Φ.

Using this relation, a bound on the constitutive potential for a nonlinear composite can be obtained if the exact constitutive potential (or a lower bound on this quantity) for a linear elastic matrix containing an equivalent distribution of inhomogeneities is known. Of course, as the actual nonlinear composite is isotropic in the plane of deformation, it is desired that the bounding procedure yield an expression for the overall response which is itself isotropic. Ponte Castaneda (1991) has considered the case in which the comparison solid is isotropic, but here we examine a broader class of comparison solids which are anisotropic yet which render an isotropic bound. To obtain the best such bound an optimization on material constants of the linear comparison matrix is carried out, as discussed in the next section.

Anisotropic Comparison Solid

Let the comparison solid be comprised of a linearly elastic matrix material with compliances given by $m_{ijkl}^c = m_{ijkl}(\boldsymbol{\Sigma})$ where m_{ijkl} is given by (3) and where α and β are now treated as variables. Note that the compliances m_{ijkl}^c can be regarded as the compliances for a homogeneous linearly elastic transversely isotropic body, and that it is necessary to enforce the restrictions $\alpha > 0$ and $\beta > -1/2$ so that the compliances are positive definite.

It is now convenient to introduce a coordinate system $\{\bar{x}_1, \bar{x}_2, x_3\}$ obtained by a rotation of the $\{x_1, x_2, x_3\}$ system about the x_3-axis until the $\bar{x}_1$ and $\bar{x}_2$ axes are coincident with the in-plane eigenvectors for the macroscopic stress. The components of the macroscopic stress deviator relative to this coordinate system, $\bar{\Sigma}'_{ij}$, are given in terms of the principal stresses $\{\bar{\Sigma}_{11}, \bar{\Sigma}_{22}, \bar{\Sigma}_{33}\}$ as $\bar{\Sigma}'_{11} = -\bar{\Sigma}'_{22} = 1/2(\bar{\Sigma}_{11} - \bar{\Sigma}_{22})$ and $\bar{\Sigma}'_{33} = 0$, and the components of the compliances of the comparison matrix material relative to the $\{\bar{x}_1, \bar{x}_2, x_3\}$ system are given by

$$\bar{m}_{ijkl}^c = \frac{3\epsilon_o \alpha}{n\sigma_o} \left(\frac{\Sigma_e}{\sigma_o} \right)^{n-1} \left\{ \frac{1}{2} (\delta_{ik}\delta_{jl} + \delta_{il}\delta_{jk}) - \frac{1}{3} \delta_{ij}\delta_{kl} + \beta(\delta_{1i}\delta_{1j} - \delta_{2i}\delta_{2j})(\delta_{1k}\delta_{1l} - \delta_{2k}\delta_{2l}) \right\}. \tag{13}$$

The potential of the linear comparison matrix is then obtained as

$$\phi_c(\boldsymbol{\sigma}) = \frac{1}{2} \bar{m}_{ijkl}^c \bar{\sigma}_{ij} \bar{\sigma}_{kl} = \frac{\epsilon_o \alpha}{2n\sigma_o} \left(\frac{\Sigma_e}{\sigma_o} \right)^{n-1} \left[(1 + 2\beta)\bar{u}^2 + \bar{w}^2 \right] \tag{14}$$

where $\bar{\sigma}_{ij}$ are the components of the local stress relative to the $\{\bar{x}_1, \bar{x}_2, x_3\}$ system, $\bar{u}^2 = 3/4(\bar{\sigma}_{11} - \bar{\sigma}_{22})^2$ and $\bar{w}^2 = 3/2(\bar{\sigma}_{12}^2 + \bar{\sigma}_{21}^2)$.

From (11) it then follows that ψ_- is given by

$$\psi_- = \sup_{\bar{u},\bar{w}} \left\{ \frac{\epsilon_o \alpha}{2n\sigma_o} \left(\frac{\Sigma_e}{\sigma_o} \right)^{n-1} \left[(1 + 2\beta)\bar{u}^2 + \bar{w}^2 \right] - \frac{\epsilon_o}{(n+1)\sigma_o^n} (\bar{u}^2 + \bar{w}^2)^{\frac{n+1}{2}} \right\} \tag{15}$$

and when the indicated optimization is carried out, it emerges that there is a local maximum located along $\bar{u} = 0$ and another located along $\bar{w} = 0$. Which is the global maximum depends upon β, and when $\beta = 0$ the maxima coincide. The results of the calculation can be summarized as

$$\psi_- = \frac{1}{2} \epsilon_o \sigma_o \frac{n-1}{n+1} (\alpha\gamma_c)^{(n+1)/(n-1)} \left(\frac{\Sigma_e}{\sigma_o} \right)^{n+1} \tag{16}$$

where

$$\gamma_c = \begin{cases} 1 & -1/2 < \beta \leq 0 \\ 1 + 2\beta & \beta > 0 \end{cases}. \tag{17}$$

Consider now a linear comparison solid which contains the same distribution of rigid inclusions or voids as does the actual nonlinear composite, and let this comparison solid be subject to the same stress state $\boldsymbol{\Sigma}$ as is the actual solid (and upon which the compliances (13) are based). The potential for the comparison composite is then found as

$$\Phi_c(\boldsymbol{\Sigma}) = \frac{1}{2}\alpha(1+2\beta)\epsilon_o\sigma_o(1+p_c)\left(\frac{\Sigma_e}{\sigma_o}\right)^{n+1} \tag{18}$$

where p_c depends upon the volume fraction and the distribution of the inhomogeneities as well as upon β, but it does not depend upon α. This function is independent of α because all components of the compliance are proportional to α, hence so should be the macroscopic potential. For voids, p_c also depends upon the stress triaxiality X, and since the solid is linear this dependence must be of the form $p_c = f + gX^2$ where $\{f, g\}$ are functions of β, the void volume fraction and the details of the void distribution.

For any given $\{\alpha, \beta\}$, a bound for the potential of the nonlinear composite follows from (12) as

$$\Phi \geq \left\{\frac{n+1}{2}\alpha(1+2\beta)(1+p_c) - \frac{n-1}{2}(1-c)(\alpha\gamma_c)^{(n+1)/(n-1)}\right\}\Phi^o \equiv \Phi_b \tag{19}$$

and we now seek the best such bound over admissible values of α and β as

$$\Phi_{glb} = \sup_{\alpha,\beta}\Phi_b. \tag{20}$$

Noting that Φ_b is an analytic function of α, we form $\partial\Phi_b/\partial\alpha = 0$ to obtain the value of α giving an extremal of Φ_b for a given value of β. The result is

$$\alpha = \left[\frac{(1+2\beta)(1+p_c)}{(1-c)\gamma_c^{(n+1)/(n-1)}}\right]^{(n-1)/2} \tag{21}$$

from which we then obtain

$$\Phi_{glb} = \Phi^o(1-c)^{(1-n)/2}\sup_{\beta}\left[\frac{(1+2\beta)(1+p_c)}{\gamma_c}\right]^{(n+1)/2}. \tag{22}$$

Results for Dilute Concentration of Inhomogeneities

We now specialize the results given above to cases in which the concentration of rigid inclusions or voids can be considered dilute *for the linear comparison solid*. Then $p_c = c\hat{p}_c$ where $\hat{p}_c$ is independent of the volume concentration of inhomogeneities.

To determine $\hat{p}_c$ it suffices to solve a kernel problem for a single inhomogeneity embedded within an infinite region of the matrix material (e.g., Lee and Mear, 1992a,b), and the solution to this kernel problem can be obtained from the results of Yang and Chou (1976). To utilize their solution, we introduce moduli for the comparison matrix as

$$\hat{l}^c_{ijkl} = \frac{2n\sigma_o}{3\epsilon_o\alpha}\left(\frac{\Sigma_e}{\sigma_o}\right)^{1-n}\left\{\frac{1}{2}\left(\delta_{ij}\delta_{kl}+\delta_{il}\delta_{jk}\right)+\kappa\delta_{ij}\delta_{kl} - \frac{\beta}{1+2\beta}\left(\delta_{1i}\delta_{2j}-\delta_{2i}\delta_{2j}\right)\left(\delta_{1i}\delta_{2j}-\delta_{2i}\delta_{2j}\right)\right\} \tag{23}$$

where the parameter κ represents a ficticious compressibility which has been introduced to facilitate the solution of the kernel problem (note that $\hat{l}^c_{ijkl}$ is the inverse of $\overline{m}^c_{ijkl}$ only when $\kappa = 0$). For rigid inclusions it is not necessary to consider a compressible matrix, but for voids difficulties arise in the solution of the kernel problem if the compressibility is not present. The limit $\kappa \to \infty$ is taken at an appropriate stage of the analysis to obtain the results corresponding to an incompressible matrix (see Budiansky et al. (1982) where a similar calculation for an isotropic matrix is discussed). The calculation is straightforward (but somewhat lengthy), hence we omit the details and simply state the final results as

$$\hat{p}_c = \begin{cases} -\left(1+\sqrt{1+2\beta}\right) & \text{rigid inclusion} \\ 1+(3X^2+1)/\sqrt{1+2\beta} & \text{void} \end{cases}. \tag{24}$$

The optimal bound based on the anisotropic comparison solid is then obtained from (22) with $p_c = c\hat{p}_c$ where $\hat{p}_c$ is given by (24). It is readily verified that the optimal bound is achieved for $\beta = 0$ and that it is given by

$$\Phi_{glb} = \frac{(1+p_c)^{\frac{n+1}{2}}}{(1-c)^{\frac{n-1}{2}}}\Phi^o. \tag{25}$$

This result coincides with that obtained by directly using Ponte Castaneda (1991) original procedure based on an isotropic comparison solid.

Thus, despite the additional freedom (for use in the optimization process) afforded by the anisotropic comparison solid, Ponte Castaneda's original procedure provides the best bound. Of course, this result has been established only for the case of plane-strain deformation of power-law solids containing a dilute concentration of circular voids or rigid inclusions. Under what circumstances, if any, the generalized technique provides bounds which are superior to those obtained with the original procedure remains unknown, and for this reason additional investigation of the technique may be warranted.

References

Budiansky, B., Hutchinson, J. W., and Slutsky, S., 1982, "Void Growth and Collapse in Viscous Solids," *Mechanics of Solids*, H. G. Hopkins and M. J. Sewell, eds., Pergamon Press, New York, p. 13.

Duva, J. M., 1984, "A Self-Consistent Analysis of the Stiffening Effect of Rigid Inclusions on a Power-Law Material," *J. Eng. Mater. Technol.*, Vol. 106, p. 317.

He, M. Y., and Hutchinson, J. W., 1981, "The Penny Shaped Crack and the Plane Strain Crack in an Infinite Body of Power-Law Material," JOURNAL OF APPLIED MECHANICS, Vol. 48, p. 830.

Hill, R., 1967, "The Essential Structure of Constitutive Laws for Metal Composites and Polycrystals," *Journal of the Mechanics and Physics of Solids*, Vol. 15, p. 79.

Lee, B. J., and Mear, M. E., 1992a, "Effective Properties of Power-Law Solids Containing Elliptical Inhomogeneities Part I: Rigid Inclusions," *Mechanics of Materials*, Vol. 13, pp. 313–335.

Lee, B. J., and Mear, M. E., 1992b, "Effective Properties of Power-Law Solids Containing Elliptical Inhomogeneities Part II: Voids," *Mechanics of Materials*, Vol. 13, pp. 336–356. (Also see Errata, *Mechanics of Materials*, Vol. 15, pp. 159–160.)

Ponte Castaneda, P., 1991, "The Effective Mechanical Properties of Nonlinear Isotropic Composites," *Journal of the Mechanics and Physics of Solids*, Vol. 39, pp. 45–71.

Tandon, G. P., and Weng, G. J., 1988, "A Theory of Particle-Reinforced Plasticity," ASME JOURNAL OF APPLIED MECHANICS, Vol. 55, pp.126–135.

Yang, H. C., and Chou, Y. T., 1976, "Generalized Plane Problems of Elastic Inclusions in Anisotropic Solids," ASME JOURNAL OF APPLIED MECHANICS, Vol. 43, pp. 424–430.

Stress Concentration Equations for Straight-Shank and Countersunk Holes in Plates

K. N. Shivakumar[17] and J. C. Newman, Jr.[18]

Stress concentration equations for straight shank and countersunk holes in a large plate subjected to various loading conditions encountered in service were developed from three-dimensional finite element solutions. For straight shank holes, three types of loading: remote tension, remote bending, and pin loading were considered; and for the countersunk hole only remote tension and bending loads were considered. The equations are within one percent of the finite element results and are valid for isotropic materials with Poisson's ratio of 0.3.

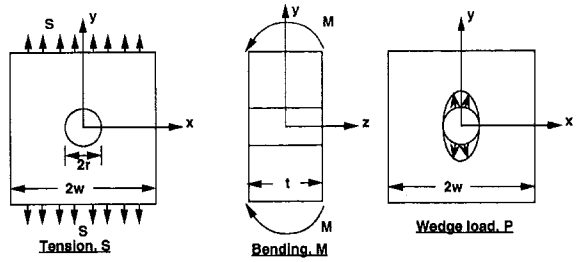

(a) Loading on straight shank rivet hole

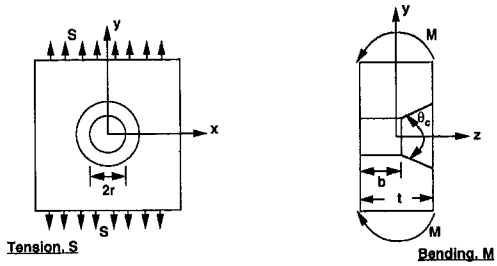

(b) Loading on countersunk rivet hole

Fig. 1 Loading types on straight shank and countersunk rivet holes in plates

Introduction

Riveted joints are commonly used in joining structural components. Joining introduces stress discontinuities in the form of holes, change in the load path due to lapping, and additional loads like rivet bearing and bending moments. Accurate estimations of these local stresses are needed to predict joint strength and fatigue life. Exhaustive studies on stress concentration factors for holes and notches in two-dimensional bodies have been reported in the literature (Peterson, 1974; Savin, 1961). Studies have also been made on three-dimensional stress concentrations at circular holes in plates subjected to remote tensile loads (Green, 1948; Folias and Wang, 1990). Only two papers in the literature reported results on stress concentration at countersunk holes. They were from the photoelastic experiments (Whaley, 1965; Cheng, 1978). Recently an exhaustive finite element analysis (Shivakumar and Newman, 1992) was conducted on stress concentration at straight shank and countersunk holes. Three types of loads, namely: remote tension, remote bending, and simulated pin loading were considered for the straight shank hole. Two types of loads, remote tension and remote bending, were considered for countersunk holes. Based on these results, three-dimensional, stress concentration factor equations were developed. This paper summarizes the developed three-dimensional stress concentration factor equations.

Rivet Hole Configurations

Plates with straight shank and countersunk rivit holes are shown in Fig. 1. In the plate with a countersunk hole, the thickness was divided into two sections: the cylindrical section referred to as the straight shank (depth, b) and the conical section referred to as the countersink (depth, $t - b$). The two sections meet to form an edge referred to as the countersunk edge. The stress concentrations will depend on the countersunk depth. The two extreme cases of countersunk holes are when $b = 0$ (knife edge) and $b = t$ (straight shank hole). The countersink angle is θ_c (see Fig. 1(b)). In the analysis, the plate width and height were selected large enough so that the stress concentration solutions would not be greatly affected by the remote boundaries. A wide range of hole-radius-to-thickness ratios (r/t) and b/t ratios were considered in generating the data base on stress concentration solutions (Shivakumar and Newman, 1992).

Loading Conditions

Figure 1(a) shows the three types of loads that were applied to the plate with the straight shank hole: remote tension stress (S), remote bending moment (M per unit width), and wedge load (P). The wedge load is imposed on the hole boundary as a normal pressure loading, defined as $(2P/\pi rt)\cos\phi$ and applied over the angle $\phi = \pm 90$ deg. The bending moment is applied as an equivalent remote stress varying linearly through the plate thickness. For countersunk holes, two loading types, remote tension and remote bending, were considered.

Definition of Stress Concentration Factor

Remote Tension Load. The tension stress concentration factor (K_t) is the ratio of hoop stress (σ_{yy}) at $\phi = 90$ deg along the hole bore and the remote applied stress (S),

$$K_t(z) = \frac{\sigma_{yy}(z)}{S}. \tag{1}$$

Remote Bending Load. The stress concentration factor for bending (K_b) is ratio of hoop stress at $\phi = 90$ deg along the hole bore and the remote outer-fiber bending stress ($6M/t^2$),

$$K_b(z) = \frac{\sigma_{yy}(z)}{6M/t^2}. \tag{2}$$

[17]Department of Mechanical Engineering, North Carolina A & T State University, Greensboro, NC 27405.
[18]NASA Langley Research Center, Hampton, VA 23631.

Contributed by the Applied Mechanics Division of THE AMERICAN SOCIETY OF MECHANICAL ENGINEERS for publication in the ASME JOURNAL OF APPLIED MECHANICS. Manuscript received by the ASME Applied Mechanics Division, Sept. 8, 1992; final revision, Apr. 14, 1994. Associate Technical Editor: A. K. Noor.

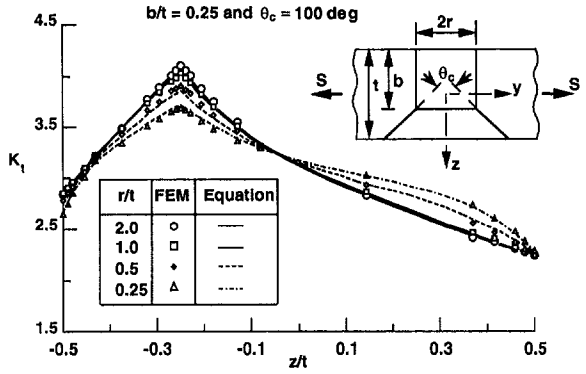

Fig. 2 Comparison of tension stress concentration factor equation with finite element results for countersunk rivet holes

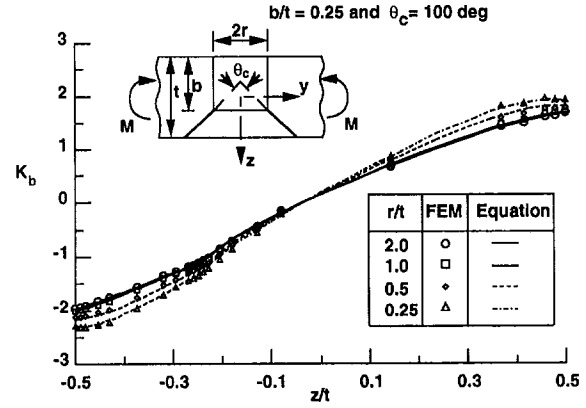

Fig. 3 Comparison of bending stress concentration factor equation with finite element results for countersunk rivet holes

Wedge Load. The stress concentration factor for wedge loading (K_w) is ratio of hoop stress at $\phi = 90$ deg along the hole bore and the bearing stress $P/(2rt)$,

$$K_w(z) = \frac{\sigma_{yy}(z)}{P/(2rt)}. \tag{3}$$

Pin Load. The stress concentration for pin loading (K_p) was obtained from a superposition of remote tension and wedge loading (Shivakumar and Newman, 1992). K_p is defined as the ratio of hoop stress at $\phi = 90$ deg along the hole bore and the bearing stress $P/(2rt)$,

$$K_p(z) = \frac{\sigma_{yy}(z)}{P/(2rt)}. \tag{4}$$

Stress Concentration Factor Equations

Stress concentration factor equations were developed by fitting to the finite element results given in Shivakumar and Newman (1992). Separate equations were developed for straight shank and countersunk holes subjected to different loading conditions.

Straight Shank Hole. The configuration for a plate with a straight shank hole is symmetric about the $z = 0$ plane, see Fig. 1(a). The tension and wedge load are symmetric about the $z = 0$ plane, whereas the bending load is antisymmetric about the $z = 0$ plane. Therefore, an even power polynomial in z and a general polynomial in r/t was used to fit stress concentration factor results for tension and wedge loads. An odd power polynomial in z and a general polynomial in r/t was used to fit the bending stress concentration factor results. The form of the stress concentration factor equations are

$$K_m = \sum_{i=0}^{4} \sum_{j=0}^{4} \alpha_{ij}(r/t)^i(z/t)^{2j} \tag{5}$$

where $m = t$ for remote tension and $m = w$ for wedge loading and

$$K_b = \sum_{i=0}^{4} \sum_{j=1}^{4} \alpha_{ij}(r/t)^i(z/t)^{2j-1} \tag{6}$$

for bending loads. The coefficients (α_{ij}) for all three cases are given in Shivakumar and Newman (1992). Equations (5) and (6) apply over the range $0.1 \le r/t \le 2.5$.

The stress concentration equation for simulated pin loading is written as (Shivakumar and Newman, 1992)

$$K_p = \frac{K_w + (r/w)K_t}{2}. \tag{7}$$

Equation (7) is restricted to $r/w = 0.1$ because K_t and K_w were generated for a plate with $r/w = 0.1$.

Countersunk Rivet Holes. The configurations of the countersunk hole dictate that two separate stress concentration factor equations be fit: one equation for the straight shank part $\{-0.5 \le z/t \le (b/t - 0.5)\}$ and the other equation for the countersunk portion $\{(b/t\ 0.5) \le z/t \le 0.5\}$. The stress concentration factor equations are given by

$$K_m = \sum_{i=0}^{3} \sum_{j=0}^{4} \alpha_{ij}(r/t)^i(z/t)^j \tag{8}$$

for $-0.5 \le z/t \le (b/t - 0.5)$ and

$$K_m = \sum_{i=0}^{3} \sum_{j=0}^{4} \beta_{ij}(r/t)^i\{(z - b + t/2)/(t - b)\}^j \tag{9}$$

for $(b/t - 0.5) \le z/t \le 0.5$. Equations (8) and (9) apply over the range $0.25 \le r/t \le 2.5$. Coefficients α_{ij} and β_{ij} for various b/t ratios are given in Shivakumar and Newman (1992). Figures 2 and 3 show a typical comparison between Eqs. (8) and (9) with the finite element results for tension and bending loads, respectively. The equations were within ± 1 percent of the finite element results.

References

Cheng, Y. F., 1978, "Stress-Concentration Factors for a Countersunk Hole in a Flat Bar in Tension and Transverse Bending," ASME JOURNAL OF APPLIED MECHANICS, Vol. 45, pp. 929–932.

Folias, E. S., and Wang, J. J., 1990, "On the Three-Dimensional Stress Field Around a Circular Hole in a Plate of Arbitrary Thickness," *Computational Mechanics*, Vol. 6, pp. 379–391.

Green, A. E., 1948, "Three-Dimensional Stress System in Isotropic Plates," *Transactions of the Royal Society, London*, Vol. A, pp. 240–285.

Peterson, E. E., 1974, *Stress Concentration Factors*, John Wiley and Sons, New York.

Savin, G. N., 1961, *Stress Concentration Around Holes*, Pergamon Press, New York.

Shivakumar, K. N., and Newman, J. C., Jr., 1992, "Stress Concentrations for Straight-Shank and Countersunk Holes in Plates Subjected to Tension, Bending and Pin Loads," NASA TP-3192, June.

Whaley, R. E., 1965, "Stress-Concentration Factors for Countersunk Holes," *Experimental Mechanics*, Vol. 5, pp. 257–261.

Exact Expressions for the Roots of the Secular Equation for Rayleigh Waves

M. Rahman[19,21] and J. R. Barber[20,21]

1 Introduction

The speed c_R at which Rayleigh waves can propagate over the surface of an isotropic linear elastic half-space is a root of the equation

$$R(V) \equiv \left(2 - M_2^2\right)^2 - 4\sqrt{\left(1 - M_1^2\right)\left(1 - M_2^2\right)} = 0, \quad (1)$$

where

$$M_1 = \frac{V}{c_1}; \quad M_2 = \frac{V}{c_2}, \quad (2)$$

$c_1 = \sqrt{(\lambda + 2\mu)/\rho}$, $c_2 = \sqrt{\mu/\rho}$ are the dilatational and shear wave speeds, respectively, λ, μ are Lamé's constants and ρ is the density.

Multiplying Eq. (1) by the expression $(2 - M_2^2)^2 + 4\sqrt{\left(1 - M_1^2\right)\left(1 - M_2^2\right)}$, of which the only real zero is $V = 0$, and cancelling the factor M_2^2 corresponding to this trivial root, we obtain the equation

$$m^3 - 8m^2 + (24 - 16\Lambda)m - 16(1 - \Lambda) = 0 \quad (3)$$

where $m = M_2^2$,

$$\Lambda = \frac{c_2^2}{c_1^2} = \frac{(1 - 2\nu)}{2(1 - \nu)} \quad (4)$$

and ν is Poisson's ratio. We note that for the range $-1 \le \nu \le 0.5$, $0 \le \Lambda \le 0.75$.

Equation (3) is a cubic equation in m and can therefore be solved explicitly by standard methods. In view of the simplicity of this procedure, it is remarkable that the resulting closed-form solutions are not given in any of the standard reference works on Elastodynamics, (e.g., Achenbach, 1984; Aki and Richards, 1980; Auld, 1973; Ben Menahem and Singh, 1981; Brekhovskikh and Godin, 1990; Bullen, 1962; Cagniard, 1964; Eringen and Suhubi, 1975; Ewing et al., 1957; Fedorov, 1968; Hanyga, 1985; Jeffreys, 1952; Kolsky, 1952; Love, 1944; Mal and Singh, 1991; Viktorov, 1967), except for the special cases $\nu = 0$, 0.25, nor as far as the present authors have been able to ascertain are they available elsewhere in the literature. The purpose of the present Note is therefore to develop the closed-form solutions of (3), and hence of the Rayleigh Eq. (1) for general values of ν.

Of course, numerical solutions for c_R are easily obtained to any desired accuracy and are widely available in the literature. However, apart from the aesthetic appeal of a closed-form solution, we note that the Rayleigh function $R(V)$ appears widely in the solution of classical elastodynamic problems. For example, it appears in the denominator of Lamb's solution (1904) for an impulsive normal force on the surface of a half-space and in Cole and Huth's solution (1958) for a line load moving steadily over the surface of the half-plane. Both these results can be used as Green's functions to generate convolution integrals for more general boundary value problems and the availability of an explicit factorization of the rationalized form (3) of $R(V)$ permits such integrals to be broken down into simpler terms by partial fractions.

2 Solution

Equation (3) can be reduced to the standard form

$$x^3 + px + q = 0 \quad (5)$$

by the substitution

$$x = m - \frac{8}{3} \quad (6)$$

where

$$p = \frac{8}{3}(1 - 6\Lambda); \quad q = \frac{16}{27}(17 - 45\Lambda). \quad (7)$$

2.1 Nature of the Roots. The sign of the discriminant

$$D = -\left(\frac{q^2}{4} + \frac{p^3}{27}\right) \quad (8)$$

of Eq. (5) determines the nature of the three roots. In particular,

(1) if $D > 0$, Eq. (5), and hence Eq. (3), has three distinct real roots.
(2) if $D = 0$, the equation has three real roots, at least two of which are equal.
(3) if $D < 0$, the equation has one real and two complex conjugate roots.

Substituting (7) into (8), it is easily verified that $D(\Lambda)$ is negative at $\Lambda = 0$ and changes sign once in the range $0 \le \Lambda \le 0.75$.

The exact value of Λ at which this sign change occurs is the root of the equation $D(\Lambda) = 0$, which can be written in the form

$$\Lambda^3 - \frac{107}{64}\Lambda^2 + \frac{31}{32}\Lambda - \frac{11}{64} = 0. \quad (9)$$

This is also a cubic equation and it can be converted into the form (5) by the substitution

$$\Lambda = x + \frac{107}{192} \quad (10)$$

in which case

$$p^* = \frac{455}{12288}; \quad q^* = \frac{77293}{3538944} \quad (11)$$

where the *s are used to distinguish these quantities from those defined in Eq. (7). Substituting these results into (8), we find that $D^* < 0$ and hence deduce that Eq. (9) has only one real root. The value of this root is obtained from Cardan's formula (Cowles and Thompson, 1947) as

$$x^* = \sqrt[3]{-\frac{q^*}{2} + \sqrt{-D^*}} + \sqrt[3]{-\frac{q^*}{2} - \sqrt{-D^*}}. \quad (12)$$

Substituting for p^*, q^*, D^* from Eqs. (11), (8) and using (10), we find that the corresponding critical value of Λ is

[19]Visiting Scholar.
[20]Professor.
[21]Department of Mechanical Engineering and Applied Mechanics, University of Michigan, Ann Arbor, MI 48109-2125.

Contributed by the Applied Mechanics Division of THE AMERICAN SOCIETY OF MECHANICAL ENGINEERS for publication in the ASME JOURNAL OF APPLIED MECHANICS. Manuscript received by the ASME Applied Mechanics Division, Oct. 11, 1993; final revision, Mar. 3, 1994. Associate Technical Editor: D. M. Barnett.

$$\Lambda^* = \frac{107}{192} + \sqrt[3]{-\frac{77293}{7077888} + \sqrt{\frac{6859}{56623104}}} + \sqrt[3]{-\frac{77293}{7077888} - \sqrt{\frac{6859}{56623104}}} = 0.3214984\ldots. \quad (13)$$

Solving Eq. (4) for ν, we find

$$\nu = \frac{(1 - 2\Lambda)}{2(1 - \Lambda)} \quad (14)$$

and the value corresponding to Λ^* is

$$\nu^* = 0.2630821\ldots. \quad (15)$$

Since Λ^* is the only real root of (9) we conclude that

(1) for $-1 < \nu < \nu^*$, Eq. (3) has three distinct real roots.
(2) for $\nu = \nu^*$, Eq. (3) has three real roots, two of which are equal.
(3) for $\nu^* < \nu^* < 0.5$, Eq. (3) has one real root (one of which is the Rayleigh root) and a pair of complex conjugate roots.

Hayes and Rivlin (1962) report that a similar conclusion was reached by Somigliana, who gave the critical value as $\nu^* = 0.2637$.

2.2 Expressions for the Roots. We now proceed to determine explicit expressions for the roots in these three ranges.

Case 1: $-1 < \nu < \nu^*$.

For this case, the three roots of Eq. (3) are all real and can be written in the form

$$m_1 = \frac{8}{3} + 2\sqrt{-\frac{p}{3}}\cos\left(\phi + \frac{2\pi}{3}\right) \quad (16)$$

$$m_2 = \frac{8}{3} + 2\sqrt{-\frac{p}{3}}\cos\left(\phi + \frac{4\pi}{3}\right) \quad (17)$$

$$m_3 = \frac{8}{3} + 2\sqrt{-\frac{p}{3}}\cos\phi \quad (18)$$

(see Cowles and Thompson, 1947), where

$$\phi = \frac{1}{3}\arccos\left(\frac{3q}{2p\sqrt{-p/3}}\right). \quad (19)$$

If we define the principal value of $\arccos(x)$ in Eq. (19) to lie in the range $0 \le x \le \pi$, it follows that $m_1 < m_2 < m_3$. The root corresponding to the Rayleigh wave speed is m_1—i.e.,

$$c_R = c_2\sqrt{m_1} \quad (20)$$

and the other two roots both correspond to speeds higher than the dilatational wave speed—i.e., $m_2, m_3 > M_1^2$ for all ν. Hayes and Rivlin (1962) show that the elastodynamic solutions corresponding to these roots involve physically unacceptable unbounded fields at infinity.

Case 2: $\nu = \nu^*$.

This can be regarded as a limit of the preceeding case, in which $\phi \to \frac{\pi}{3}$ and m_2, m_3 become equal. The results are

$$m_1 = \frac{8}{3} + 2\sigma \quad (21)$$

$$m_2 = m_3 = \frac{8}{3} - \sigma \quad (22)$$

where

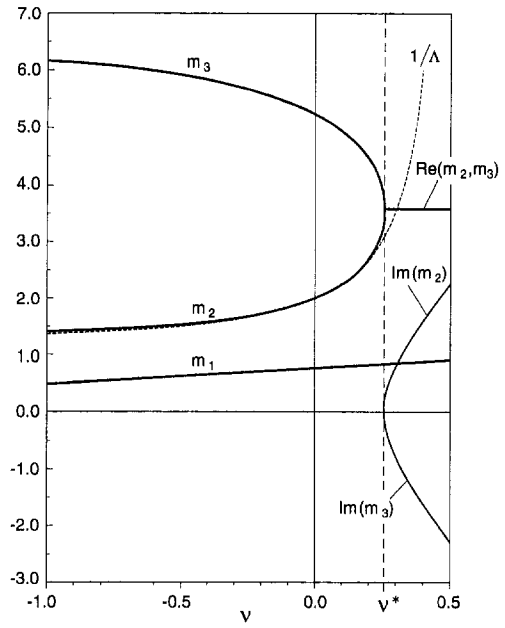

Fig. 1 The three roots, m_1, m_2, and m_3, as functions of ν

$$\sigma = \frac{2}{3}\sqrt[3]{\frac{11 - 56\nu^*}{2(1 - \nu^*)}} \quad (23)$$

Case 3: $\nu^* < \nu < 0.5$.

In this case only the Rayleigh root m_1 is real and the three roots of Eq. (3) are given by Cardan's formula as

$$m_1 = \frac{8}{3} + \gamma + \eta \quad (24)$$

$$m_2 = \frac{8}{3} - \frac{\gamma + \eta}{2} + i\frac{\sqrt{3}}{2}(\gamma - \eta) \quad (25)$$

$$m_3 = \frac{8}{3} - \frac{\gamma + \eta}{2} - i\frac{\sqrt{3}}{2}(\gamma - \eta) \quad (26)$$

where

$$\gamma = \frac{2}{3}\sqrt[3]{-(17 - 45\Lambda) + \sqrt{(17 - 45\Lambda)^2 + 8(1 - 6\Lambda)^3}} \quad (27)$$

$$\eta = \frac{2}{3}\sqrt[3]{-(17 - 45\Lambda) - \sqrt{(17 - 45\Lambda)^2 + 8(1 - 6\Lambda)^3}} \quad (28)$$

and Λ is defined by Eq. (4).

3 Conclusion

This completes the solution for the roots of Eq. (3). In each case a closed-form expression for the Rayleigh wave speed can be written in the form

$$c_R = c_2\sqrt{m_1}. \quad (29)$$

The three roots, m_1, m_2, m_3 are shown as functions of ν in Fig. 1. It is notable that the second root, m_2, is very close to the function $1/\Lambda$, when ν is small. In fact, it can be shown that

$$m_2 = \frac{1}{\Lambda} + 32\epsilon^4 + O(\epsilon^5) \tag{30}$$

for $\nu \ll 1$, where

$$\epsilon = \frac{1}{2} - \Lambda = \frac{\nu}{2(1-\nu)}. \tag{31}$$

We also note that the results permit the left-hand side of (3) to be factorized explicitly in the form $(m - m_1)(m - m_2)(m - m_3)$. It follows that the function $R(V)^{-1}$, which appears in Lamb's solution (1904) for an impulsive load and Cole and Huth's solution (1985) for a moving line load, can be written in the rationalized form

$$\frac{1}{R(V)} = \frac{\left(2 - M_2^2\right)^2 + 4\sqrt{\left(1 - M_1^2\right)\left(1 - M_2^2\right)}}{M_2^2\left(M_2^2 - m_1\right)\left(M_2^2 - m_2\right)\left(M_2^2 - m_3\right)} \tag{32}$$

which can be expanded as a set of partial fractions if desired.

Acknowledgments

J. R. Barber is pleased to acknowledge support from the National Science Foundation under Contract No. MSS-9200762.

References

Achenbach, J. D., 1984, *Wave Propagation in Elastic Solids*, Elsevier, New York.

Aki, K., and Richards, P. G., 1980, *Quantitative Seismology: Theory and Methods*, Vol. I, Freeman, San Francisco, CA.

Auld, B. A., 1973, *Acoustic Fields and Waves in Solids*, Vol. I and Vol. II, John Wiley and Sons, New York.

Ben Menahem, A., and Singh, S. J., 1981, *Seismic Waves and Sources*, Springer-Verlag, New York.

Brekhovskikh, L. M., and Godin, O. A., 1990, *Acoustics of Layered Media: Plane and Quasi-plane Waves*, Vol. I, Springer-Verlag, Berlin, Germany.

Bullen, K. E., 1963, *An Introduction to Theory of Seismology*, Cambridge University Press, Cambridge, U.K.

Cagniard, L., 1964, *Reflection and Refraction of Progressive Seismic Waves*, McGraw-Hill, New York.

Cole, J. D., and Huth, J. H., 1958, "Stresses Produced in a Half-Plane by Moving Loads," ASME JOURNAL OF APPLIED MECHANICS, Vol. 25, pp. 433–436.

Cowles, W. H., and Thompson, J. E., 1947, *Algebra*, D. Van Nostrand Company, New York.

Eringen, A. C., and Suhubi, E. S., 1975, *Elastodynamics: Linear Theory*, Vol. 2, Academic Press, New York.

Ewing, W. M., Jardetzky, W. S., and Press, F., 1957, *Elastic Waves in Layered Media*, McGraw-Hill, New York.

Fedorov, F. I., 1968, *Theory of Elastic Waves in Crystals*, Plenum Press, New York.

Hanyga, A., ed., 1985, *Seismic Wave Propagation in the Earth*, Elsevier-PWN, Amsterdam.

Hayes, M., and Rivlin, R. S., 1962, "A Note on the Secular Equation for Rayleigh Waves," *ZAMP*, Vol. 13, pp. 80–83.

Jeffreys, H., 1952, *The Earth*, Cambridge University Press, Cambridge, U.K.

Kolsky, H., 1963, *Stress Waves in Solids*, Dover, New York.

Lamb, H., 1904, "On the Propagation of Tremors over the Surface of an Elastic Solid," *Phil. Trans. Royal Soc., London*, Vol. A203, pp. 1–42.

Love, A. E. H., 1944, *A Treatise on the Mathematical Theory of Elasticity*, 4th ed., Dover, New York.

Mal, A. K., and Singh, S. J., 1991, *Deformation of Elastic Solids*, Prentice-Hall, Englewood Cliffs, NJ.

Viktorov, I. A., 1967, *Rayleigh and Lamb Waves*, Plenum Press, New York.

Critical Strain Ranking of 12 Materials in Deformations Involving Adiabatic Shear Bands

R. C. Batra[22,25], X. Zhang[23], and T. W. Wright[24,25]

Batra and Kim (1992) studied the initiation and growth of shear bands in 12 materials deformed in simple shear. Each material was modeled by the Johnson-Cook (1983) law, values of material parameters were taken from Johnson and Cook's (1983) paper, and the effects of inertia forces and thermal conductivity were included. However, materials generally are rarely tested in simple shear and the material data used was derived from tests conducted over a moderate range of strains, strain rates, and temperatures. In this Note, we report results of numerical simulation of torsion tests similar to those performed by Marchand and Duffy (1988) on HY-100 steel and rank 12 materials according to the values of the nominal strain at which the torque begins to drop precipitously. Values of material parameters taken from Rajendran's report (1992) and likely to be valid over a large range of strains, strain rates, and temperatures are used. However, the effect of thermal conductivity has been neglected because the computer code DYNA3D (Whirley and Hallquist, 1991) employed to study the problem assumes locally adiabatic deformations. Batra and Kim (1991) have shown that for simple shearing deformations of viscoplastic materials, realistic values of thermal conductivity have little effect on the values of the nominal strain at which deformations begin to localize and thus shear bands initiate.

In the simulations reported herein, the initial thickness, $\omega(z)$, of the tube with inner radius of 4.75 mm is assumed to vary according to the relation

$$\omega(z) = 0.19\left[1.9 + 0.1\sin\left(\frac{1}{2} + \frac{2z}{2.5}\right)\pi\right]\text{mm}, \quad 0 \le z \equiv 2.5\ \text{mm}. \tag{1}$$

Here z denotes the position of a point along the axis of the tube with $z = 0$ being the fixed end. The end $z = 2.5$ mm is twisted so as to produce a nominal strain rate of 5000 s^{-1}. It is assumed that the angular speed increases from zero to the steady value of 2530 rad/s in 20 μs. The thickness variation, depicted in Fig. 1, clearly shows that the minimum tube thickness occurs at its center, and equals 90 percent of that at its outer edges.

The tube is assumed to be initially at rest, stress-free, and at the room temperature, T_o, of 25°C. The inner and outer surfaces of the tube are taken to be traction-free and thermally insulated, and its deformations are assumed to be

[22]Department of Engineering Science and Mechanics, Virginia Polytechnic Institute and State University, Blacksburg, VA 24061-0219.

[23]144 Yorkshire Boulevard, No. 206, Dearborn Heights, MI 48127.

[24]U.S. Army Research Laboratory, Aberdeen Proving Ground, MD 21005-5066.

[25]Fellow ASME.

Contributed by the Applied Mechanics Division of THE AMERICAN SOCIETY OF MECHANICAL ENGINEERS for publication in the ASME JOURNAL OF APPLIED MECHANICS. Manuscript received by the ASME Applied Mechanics Division, Sept. 7, 1993; final revision, Feb. 18, 1994. Associate Technical Editor: W. N. Sharpe, Jr.

The three roots, m_1, m_2, m_3 are shown as functions of ν in Fig. 1. It is notable that the second root, m_2, is very close to the function $1/\Lambda$, when ν is small. In fact, it can be shown that

$$m_2 = \frac{1}{\Lambda} + 32\epsilon^4 + O(\epsilon^5) \tag{30}$$

for $\nu \ll 1$, where

$$\epsilon = \frac{1}{2} - \Lambda = \frac{\nu}{2(1-\nu)}. \tag{31}$$

We also note that the results permit the left-hand side of (3) to be factorized explicitly in the form $(m - m_1)(m - m_2)(m - m_3)$. It follows that the function $R(V)^{-1}$, which appears in Lamb's solution (1904) for an impulsive load and Cole and Huth's solution (1985) for a moving line load, can be written in the rationalized form

$$\frac{1}{R(V)} = \frac{\left(2 - M_2^2\right)^2 + 4\sqrt{\left(1 - M_1^2\right)\left(1 - M_2^2\right)}}{M_2^2\left(M_2^2 - m_1\right)\left(M_2^2 - m_2\right)\left(M_2^2 - m_3\right)} \tag{32}$$

which can be expanded as a set of partial fractions if desired.

Acknowledgments

J. R. Barber is pleased to acknowledge support from the National Science Foundation under Contract No. MSS-9200762.

References

Achenbach, J. D., 1984, *Wave Propagation in Elastic Solids*, Elsevier, New York.

Aki, K., and Richards, P. G., 1980, *Quantitative Seismology: Theory and Methods*, Vol. I, Freeman, San Francisco, CA.

Auld, B. A., 1973, *Acoustic Fields and Waves in Solids*, Vol. I and Vol. II, John Wiley and Sons, New York.

Ben Menahem, A., and Singh, S. J., 1981, *Seismic Waves and Sources*, Springer-Verlag, New York.

Brekhovskikh, L. M., and Godin, O. A., 1990, *Acoustics of Layered Media: Plane and Quasi-plane Waves*, Vol. I, Springer-Verlag, Berlin, Germany.

Bullen, K. E., 1963, *An Introduction to Theory of Seismology*, Cambridge University Press, Cambridge, U.K.

Cagniard, L., 1964, *Reflection and Refraction of Progressive Seismic Waves*, McGraw-Hill, New York.

Cole, J. D., and Huth, J. H., 1958, "Stresses Produced in a Half-Plane by Moving Loads," ASME JOURNAL OF APPLIED MECHANICS, Vol. 25, pp. 433–436.

Cowles, W. H., and Thompson, J. E., 1947, *Algebra*, D. Van Nostrand Company, New York.

Eringen, A. C., and Suhubi, E. S., 1975, *Elastodynamics: Linear Theory*, Vol. 2, Academic Press, New York.

Ewing, W. M., Jardetzky, W. S., and Press, F., 1957, *Elastic Waves in Layered Media*, McGraw-Hill, New York.

Fedorov, F. I., 1968, *Theory of Elastic Waves in Crystals*, Plenum Press, New York.

Hanyga, A., ed., 1985, *Seismic Wave Propagation in the Earth*, Elsevier-PWN, Amsterdam.

Hayes, M., and Rivlin, R. S., 1962, "A Note on the Secular Equation for Rayleigh Waves," *ZAMP*, Vol. 13, pp. 80–83.

Jeffreys, H., 1952, *The Earth*, Cambridge University Press, Cambridge, U.K.

Kolsky, H., 1963, *Stress Waves in Solids*, Dover, New York.

Lamb, H., 1904, "On the Propagation of Tremors over the Surface of an Elastic Solid," *Phil. Trans. Royal Soc., London*, Vol. A203, pp. 1–42.

Love, A. E. H., 1944, *A Treatise on the Mathematical Theory of Elasticity*, 4th ed., Dover, New York.

Mal, A. K., and Singh, S. J., 1991, *Deformation of Elastic Solids*, Prentice-Hall, Englewood Cliffs, NJ.

Viktorov, I. A., 1967, *Rayleigh and Lamb Waves*, Plenum Press, New York.

Critical Strain Ranking of 12 Materials in Deformations Involving Adiabatic Shear Bands

R. C. Batra[22,25], X. Zhang[23], and T. W. Wright[24,25]

Batra and Kim (1992) studied the initiation and growth of shear bands in 12 materials deformed in simple shear. Each material was modeled by the Johnson-Cook (1983) law, values of material parameters were taken from Johnson and Cook's (1983) paper, and the effects of inertia forces and thermal conductivity were included. However, materials generally are rarely tested in simple shear and the material data used was derived from tests conducted over a moderate range of strains, strain rates, and temperatures. In this Note, we report results of numerical simulation of torsion tests similar to those performed by Marchand and Duffy (1988) on HY-100 steel and rank 12 materials according to the values of the nominal strain at which the torque begins to drop precipitously. Values of material parameters taken from Rajendran's report (1992) and likely to be valid over a large range of strains, strain rates, and temperatures are used. However, the effect of thermal conductivity has been neglected because the computer code DYNA3D (Whirley and Hallquist, 1991) employed to study the problem assumes locally adiabatic deformations. Batra and Kim (1991) have shown that for simple shearing deformations of viscoplastic materials, realistic values of thermal conductivity have little effect on the values of the nominal strain at which deformations begin to localize and thus shear bands initiate.

In the simulations reported herein, the initial thickness, $\omega(z)$, of the tube with inner radius of 4.75 mm is assumed to vary according to the relation

$$\omega(z) = 0.19\left[1.9 + 0.1\sin\left(\frac{1}{2} + \frac{2z}{2.5}\right)\pi\right]\text{mm}, \quad 0 \le z \equiv 2.5\ \text{mm}. \tag{1}$$

Here z denotes the position of a point along the axis of the tube with $z = 0$ being the fixed end. The end $z = 2.5$ mm is twisted so as to produce a nominal strain rate of 5000 s^{-1}. It is assumed that the angular speed increases from zero to the steady value of 2530 rad/s in 20 μs. The thickness variation, depicted in Fig. 1, clearly shows that the minimum tube thickness occurs at its center, and equals 90 percent of that at its outer edges.

The tube is assumed to be initially at rest, stress-free, and at the room temperature, T_o, of 25°C. The inner and outer surfaces of the tube are taken to be traction-free and thermally insulated, and its deformations are assumed to be

[22]Department of Engineering Science and Mechanics, Virginia Polytechnic Institute and State University, Blacksburg, VA 24061-0219.

[23]144 Yorkshire Boulevard, No. 206, Dearborn Heights, MI 48127.

[24]U.S. Army Research Laboratory, Aberdeen Proving Ground, MD 21005-5066.

[25]Fellow ASME.

Contributed by the Applied Mechanics Division of THE AMERICAN SOCIETY OF MECHANICAL ENGINEERS for publication in the ASME JOURNAL OF APPLIED MECHANICS. Manuscript received by the ASME Applied Mechanics Division, Sept. 7, 1993; final revision, Feb. 18, 1994. Associate Technical Editor: W. N. Sharpe, Jr.

locally adiabatic. The thermomechanical response of each one of the 12 materials is modeled by the Johnson-Cook (1983) law:

$$\sigma_m = \left(A + B\gamma_p^n\right)\left(1 + C \ln \dot{\gamma}_p/\dot{\gamma}_o\right)\left(1 - T^{*m}\right);$$

$$T^* = \frac{(T - T_o)}{(T_m - T_o)}, \quad (2)$$

where σ_m is the equivalent or the effective stress, A equals the yield stress in a quasi-static simple tension or compression test, B and n characterize the strain hardening of the material, C characterizes its strain rate sensitivity, and the factor $(1 - T^{*m})$ determines the decrease in the flow stress because of the temperature rise. In Eq. (2) γ_p is the effective plastic strain, T_m the melting temperature of the material, and $\dot{\gamma}_o$ is the reference strain rate of 1/sec. Values of material parameters A, B, n, C, m, the mass density ρ, and the specific heat c are taken either from Rajendran (1992) or from a handbook, and are listed in Table 1. Values of the shear and bulk moduli are needed to account for the small elastic deformations of the tube material.

The transient thermomechanical problem is analyzed by using the large-scale explicit finite element code DYNA3D (Whirley and Hallquist, 1991) with a suitably graded finite element mesh consisting of 8-noded brick elements with 30 elements along the axial length of the tube, 4 elements across the thickness, and 40 elements along the circumference. In the axial direction, elements are finer near the center of the tube and increase in size gradually as one moves towards the ends of the tube. Preliminary computations indicated that the deformations of the tube were axisymmetric and stayed uniform through the thickness of the tube.

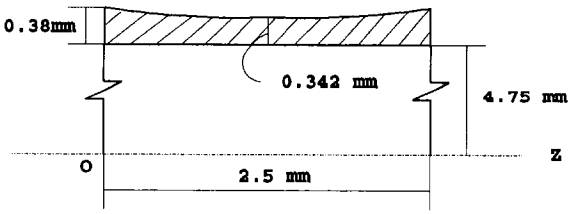

Fig. 1 The presumed variation in the thickness of the tube

Figures 2 and 3 depict the time history of the torque required to deform the tube and the evolution of the effective plastic strain at the tube center for the 12 materials studied. In each case, the torque initially increases because of the increase in the angular speed of the twisted end, and continues to increase because of the hardening of the mate-

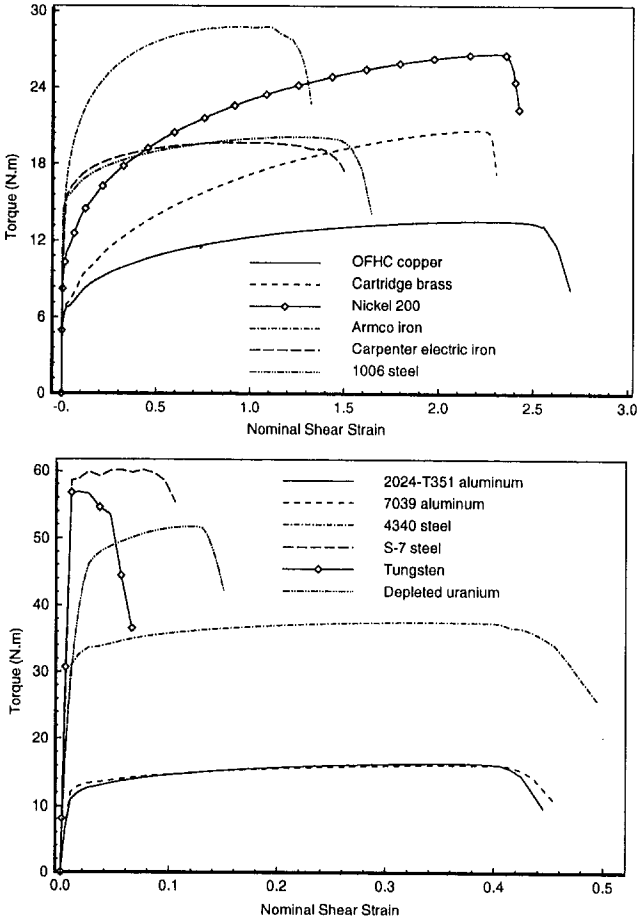

Fig. 2 The torque required to deform the tube versus the nominal shear strain

Table 1 Material constants for the Johnson-Cook model

Material	A MPa	B MPa	C	n	m	ρ kg/m³	θ_m °C	K GPa	μ GPa	c (J/kg°C)
OFHC Copper	89.63	291.64	0.025	0.31	1.09	8,960	1,083	138	42	383
Cartridge Brass	111.69	504.69	0.009	0.42	1.68	8,520	916	112	41	385
Nickel 200	163.40	648.10	0.006	0.33	1.44	8,900	1,453	198	80	446
Armco Iron	175.12	800.00	0.06	0.32	0.55	7,890	1,538	140	76	452
Carpenter Electric Iron	289.58	338.53	0.055	0.40	0.55	7,890	1,538	162	78	452
1006 Steel	350.25	275.00	0.022	0.36	1.00	7,890	1,538	169	80	452
2024-T351 Aluminum	264.75	426.09	0.015	0.34	1.00	2,770	502	76	28	875
7039 Aluminum	336.46	342.66	0.01	0.41	1.00	2,770	604	81	28	875
4340 Steel	792.19	509.51	0.014	0.26	1.03	7,840	1,520	157	76	477
S-7 Tool Steel	1538.89	476.42	0.012	0.18	1.00	7,750	1,490	246	117	477
Tungsten	1505.79	176.50	0.016	0.12	1.00	17,000	1,450	257	133	134
Depleted Uranium	1079.01	1119.69	0.007	0.25	1.00	18,600	1,200	92	58	117

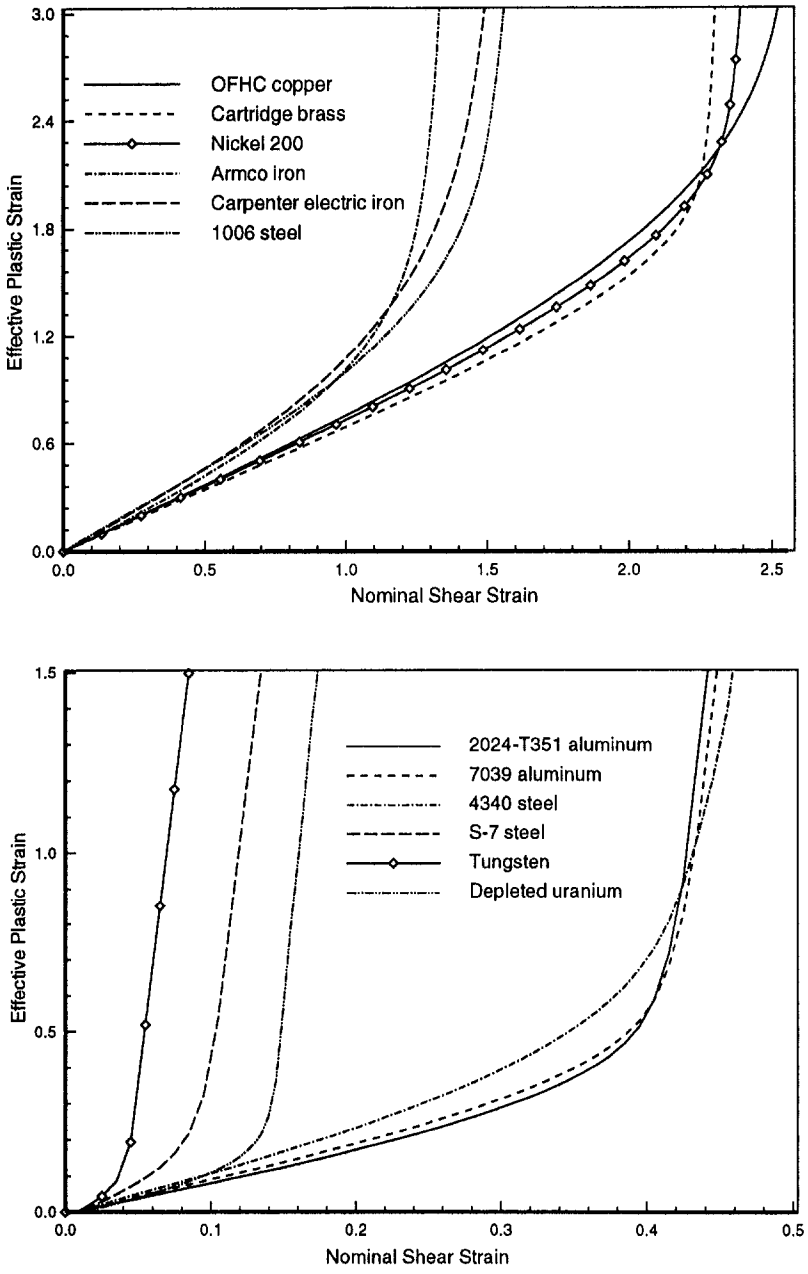

Fig. 3 The effective plastic strain at the band center versus the nominal shear strain

rial due to strain and strain rate effects. However, when thermal softening of the material at the tube center exceeds the hardening of material there, the torque required to deform the tube decreases. For each one of the 12 materials except one (Carpenter electric iron) studied herein, the torque drops precipitously prior to the slope of the torque versus nominal shear strain curve becoming zero. This is due to the rather high value of the assumed variation of the tube thickness. Computations done with five percent variation in the thickness for three materials, namely, OFHC copper, 4340 steel, and 2024-T351 aluminum, yielded similar results except that the slope of the curve representing the torque versus the nominal shear strain became zero prior to the rapid drop in the torque. For each material studied, the effective plastic strain at the tube center first gradually increases with an increase in the nominal strain, but when the torque begins to drop, the effective plastic strain at the tube center begins to increase sharply. We note that the deformations localized into essentially one element near the middle of the tube, and subsequently all of the deformations occurred only in this element. Computations were stopped shortly after this stage.

We presume that the shear band initiates when the torque drops quickly, which essentially coincides with the instant of rapid increase of the effective plastic strain at the tube center, and we rank materials according to the value of the nominal strain at which this occurs. Marchand and Duffy (1988), based on their experimental observations, pointed out that a shear band initiates when the shear stress begins to drop rapidly. In the twelve materials studied herein, shear bands initiate in the following order: Tungsten, S-7 tool steel, Depleted Uranium, 2024-T351 aluminum, 7039 aluminum, 4340 steel, Armco iron, Carpenter electric iron, 1006 steel, Cartridge brass, Nickel 200 and OFHC copper. Computations for the aforestated three materials with five percent thickness variation did not change their ranking as far as the nominal strain at the initiation of the shear band is concerned; this leads us to conclude that the amount of thickness variation does not affect the ranking. We note that the

nominal strain when the torque drops rapidly depends upon the assumed variation in the tube thickness, and also upon the finite element mesh used. Besides the size and shape of the geometric defect, other factors such as the mass density, specific heat, thermal conductivity, the nominal strain rate, strain and strain-rate hardening effects, and the rate of thermal softening affect the value of the nominal strain at the instant of the initiation of a shear band; e.g., see Wright (1992). Batra and Kim (1992) used a very fine finite element mesh within and around the shear band region to study the effect of geometric defect size on the localization of deformations in simple shearing deformations of different materials. They found that the defect size had no effect on the critical strain ranking of the 12 materials studied. The results presented herein are intended to help an experimentalist answer the following question: Among the 12 materials studied herein, having found the nominal strain at which a shear band initiates in torsional tests in a material, at what value of the nominal strain will a shear band initiate in an identical tube made of a different material? Also, these results should help ascertain the validity of any future analytical results obtained on the value of the nominal strain at which a shear band initiates in a material.

Ballistic experiments (Magness and Farrand, 1990) with tungsten and depleted uranium penetrators and steel targets suggest that shear bands initiate first in uranium, in contradiction to the ranking obtained herein. In penetration tests, the state of stress around a penetrator nose is triaxial rather than that of simple shearing. The problem of the initiation of shear bands under such general states of stress has not been studied so far.

Acknowledgments

This work was partially supported by the U.S. Army Research Office grant DAAL03-91-G-0084 and the NSF grant MSS9121279 to the University of Missouri-Rolla. X. Zhang and R. C. Batra thank Dr. Robert G. Whirley of the Lawrence Livermore Laboratory, California, for his help with the DYNA3D code.

References

Batra, R. C., and Kim, C. H., 1992, "Analysis of Shear Banding in Twelve Materials," *International Journal of Plasticity*, Vol. 8, pp. 425–452.

Batra, R. C., and Kim, C. H., 1991, "Effect of Thermal Conductivity on the Initiation, Growth and Band Width of Adiabatic Shear Bands," *International Journal of Engineering Science*, Vol. 29, pp. 949–960.

Johnson, G. R., and Cook, W. H., 1983, "A Constitutive Model and Data for Metals Subjected to Large Strains, High Strain Rates, and High Temperatures," *Proceedings of 7th International Symposium Ballistics*, The Hague, The Netherlands, pp. 541–548.

Magness, L. S., and Farrand, T., 1990, "Deformation Behavior and its Relationship to the Penetration Performance of High-Density KE Penetrator Materials," *Proceedings of 1990 Army Science Conference*, West Point, NY.

Marchand, A., and Duffy, J., 1988, "An Experimental Study of the Formation Process of Adiabatic Shear Bands in a Structural Steel," *Journal of the Mechanics and Physics of Solids*, Vol. 36, pp. 251–283.

Rajendran, A. M., 1992, "High Strain Rate Behavior of Metals, Ceramics and Concrete," Report #WL-TR-92-4006, Wright Patterson Air Force Base.

Whirley, R. G., and Hallquist, J. O., 1991, "DYNA3D User's Manual (A Nonlinear, 'Explicit,' Three-Dimensional Finite Element Code for Solid and Structural Mechanics)," UCRL-MA-107254, Univ. of California, Lawrence Livermore National Laboratory.

Wright, T. W., 1992, "Shear Band Susceptibility: Work Hardening Materials," *International Journal of Plasticity*, Vol. 8, pp. 583–602.

Existence of Stoneley Waves at an Unbonded Interface Between Two Micropolar Elastic Half-Spaces

M. Tajuddin[26]

Following Eringen's theory, the question whether a Stoneley mode can exist at an unbonded interface between two micropolar elastic half-spaces is examined analytically. Explicit conditions for its existence are derived when the two half-spaces are incompressible or Poisson solids whose material properties are close to each other.

1 Introduction

It is merely not possible to apply just the classical theory to engineering problems related to oriented media like polycrystalline materials or materials with a fibrous or coarse-grained structure. The micropolar theory of elasticity describing the behavior of oriented materials is proposed by Eringen (1966).

In the present analysis an attempt is made to study the micropolar effect on the Stoneley wave propagation at an unbonded interface between two half-spaces based on Eringen's theory together with the method of Murty (1975). By considering the plane harmonic waves, the analysis yields two frequency equations. It is seen from the first frequency equation that the wave is propagating with an extra velocity, known as micropolar wave, which has no counterpart in classical theory. This may be attributed to the micropolar nature of the medium. The second frequency equation is the counterpart of the Stoneley wave equation of classical theory discussed when the two half-spaces are incompressible or when the Poisson solids, those material properties are close to each other, by using a power series method. Explicit conditions for its existence are derived. The results of classical theory are shown as a special case (Murty, 1975).

2 Solution of the Problem

Consider two micropolar elastic half-spaces whose unbonded interface constitutes a plane surface $z = 0$. A set of rectangular coordinate axes is chosen with the origin at the interface, the x-axis in the direction of propagation and the z-axis into the interior of the lower half-space. In such a case the displacement and microrotation vectors are, respectively, $(u, 0, w)$ and $(0, \phi, 0)$, which are functions of x, z, and time t. The functions u, w, and ϕ satisfy the equations of motion if

[26]Department of Mathematics, Nizam College (O.U.), Hyderbad 500 001 (A.P.), India.

Contributed by the Applied Mechanics Division of THE AMERICAN SOCIETY OF MECHANICAL ENGINEERS for publication in the ASME JOURNAL OF APPLIED MECHANICS. Manuscript received by the ASME Applied Mechanics Division, May 25, 1993; final revision, Dec. 20, 1993. Associate Technical Editor: R. M. Bowen.

nominal strain when the torque drops rapidly depends upon the assumed variation in the tube thickness, and also upon the finite element mesh used. Besides the size and shape of the geometric defect, other factors such as the mass density, specific heat, thermal conductivity, the nominal strain rate, strain and strain-rate hardening effects, and the rate of thermal softening affect the value of the nominal strain at the instant of the initiation of a shear band; e.g., see Wright (1992). Batra and Kim (1992) used a very fine finite element mesh within and around the shear band region to study the effect of geometric defect size on the localization of deformations in simple shearing deformations of different materials. They found that the defect size had no effect on the critical strain ranking of the 12 materials studied. The results presented herein are intended to help an experimentalist answer the following question: Among the 12 materials studied herein, having found the nominal strain at which a shear band initiates in torsional tests in a material, at what value of the nominal strain will a shear band initiate in an identical tube made of a different material? Also, these results should help ascertain the validity of any future analytical results obtained on the value of the nominal strain at which a shear band initiates in a material.

Ballistic experiments (Magness and Farrand, 1990) with tungsten and depleted uranium penetrators and steel targets suggest that shear bands initiate first in uranium, in contradiction to the ranking obtained herein. In penetration tests, the state of stress around a penetrator nose is triaxial rather than that of simple shearing. The problem of the initiation of shear bands under such general states of stress has not been studied so far.

Acknowledgments

This work was partially supported by the U.S. Army Research Office grant DAAL03-91-G-0084 and the NSF grant MSS9121279 to the University of Missouri-Rolla. X. Zhang and R. C. Batra thank Dr. Robert G. Whirley of the Lawrence Livermore Laboratory, California, for his help with the DYNA3D code.

References

Batra, R. C., and Kim, C. H., 1992, "Analysis of Shear Banding in Twelve Materials," *International Journal of Plasticity*, Vol. 8, pp. 425–452.

Batra, R. C., and Kim, C. H., 1991, "Effect of Thermal Conductivity on the Initiation, Growth and Band Width of Adiabatic Shear Bands," *International Journal of Engineering Science*, Vol. 29, pp. 949–960.

Johnson, G. R., and Cook, W. H., 1983, "A Constitutive Model and Data for Metals Subjected to Large Strains, High Strain Rates, and High Temperatures," *Proceedings of 7th International Symposium Ballistics*, The Hague, The Netherlands, pp. 541–548.

Magness, L. S., and Farrand, T., 1990, "Deformation Behavior and its Relationship to the Penetration Performance of High-Density KE Penetrator Materials," *Proceedings of 1990 Army Science Conference*, West Point, NY.

Marchand, A., and Duffy, J., 1988, "An Experimental Study of the Formation Process of Adiabatic Shear Bands in a Structural Steel," *Journal of the Mechanics and Physics of Solids*, Vol. 36, pp. 251–283.

Rajendran, A. M., 1992, "High Strain Rate Behavior of Metals, Ceramics and Concrete," Report #WL-TR-92-4006, Wright Patterson Air Force Base.

Whirley, R. G., and Hallquist, J. O., 1991, "DYNA3D User's Manual (A Nonlinear, 'Explicit,' Three-Dimensional Finite Element Code for Solid and Structural Mechanics)," UCRL-MA-107254, Univ. of California, Lawrence Livermore National Laboratory.

Wright, T. W., 1992, "Shear Band Susceptibility: Work Hardening Materials," *International Journal of Plasticity*, Vol. 8, pp. 583–602.

Existence of Stoneley Waves at an Unbonded Interface Between Two Micropolar Elastic Half-Spaces

M. Tajuddin[26]

Following Eringen's theory, the question whether a Stoneley mode can exist at an unbonded interface between two micropolar elastic half-spaces is examined analytically. Explicit conditions for its existence are derived when the two half-spaces are incompressible or Poisson solids whose material properties are close to each other.

1 Introduction

It is merely not possible to apply just the classical theory to engineering problems related to oriented media like polycrystalline materials or materials with a fibrous or coarse-grained structure. The micropolar theory of elasticity describing the behavior of oriented materials is proposed by Eringen (1966).

In the present analysis an attempt is made to study the micropolar effect on the Stoneley wave propagation at an unbonded interface between two half-spaces based on Eringen's theory together with the method of Murty (1975). By considering the plane harmonic waves, the analysis yields two frequency equations. It is seen from the first frequency equation that the wave is propagating with an extra velocity, known as micropolar wave, which has no counterpart in classical theory. This may be attributed to the micropolar nature of the medium. The second frequency equation is the counterpart of the Stoneley wave equation of classical theory discussed when the two half-spaces are incompressible or when the Poisson solids, those material properties are close to each other, by using a power series method. Explicit conditions for its existence are derived. The results of classical theory are shown as a special case (Murty, 1975).

2 Solution of the Problem

Consider two micropolar elastic half-spaces whose unbonded interface constitutes a plane surface $z = 0$. A set of rectangular coordinate axes is chosen with the origin at the interface, the x-axis in the direction of propagation and the z-axis into the interior of the lower half-space. In such a case the displacement and microrotation vectors are, respectively, $(u, 0, w)$ and $(0, \phi, 0)$, which are functions of x, z, and time t. The functions u, w, and ϕ satisfy the equations of motion if

[26]Department of Mathematics, Nizam College (O.U.), Hyderbad 500 001 (A.P.), India.

Contributed by the Applied Mechanics Division of THE AMERICAN SOCIETY OF MECHANICAL ENGINEERS for publication in the ASME JOURNAL OF APPLIED MECHANICS. Manuscript received by the ASME Applied Mechanics Division, May 25, 1993; final revision, Dec. 20, 1993. Associate Technical Editor: R. M. Bowen.

$$u = \left[Ae^{pz} + Be^{-pz} + De^{qz} + Ee^{-qz} + Fe^{rz} + Ge^{-rz}\right]e^{is(x-ct)},$$
$$w = is\left[p^{-1}(Be^{-pz} - Ae^{pz}) + q^{-1}(Ee^{-qz} - De^{qz}) + \bar{\gamma}^{-1}(Ge^{-rz} - Fe^{rz})\right]e^{is(x-ct)}$$
$$\phi = \theta(Fe^{rz} + Ge^{-rz})e^{is(x-ct)}, \quad (1)$$

where s is the wave number, c is the wave speed, A, B, D, E, F, G are all constants, and p^2, q^2, r^2, θ, ϵ are related to the body waves of micropolar theory, viz.,

$$p^2 = \left[1 - c^2\rho(\lambda + 2\mu + k)^{-1}\right]s^2,$$
$$q^2 = \left[1 - c^2\rho(1 + \epsilon)^{-1}\mu^{-1}\right]s^2,$$
$$r^2 = 2\epsilon\mu\gamma^{-1} + \left(1 - c^2\rho j\gamma^{-1}\right)s^2, \quad \epsilon = k\mu^{-1},$$
$$\theta = r^{-1}\epsilon^{-1}\left[(1 + \epsilon)(2\epsilon\mu j^{-1}k^{-1} - s^2c^2\rho j\gamma^{-1}) + \rho\mu^{-1}c^2s^2\right]. \quad (2)$$

The remaining notations are standard as in Eringen (1966). Using (1) in the stress displacement relations, the relevant stresses can be computed. In the following, the subscripts 1 and 2 are used for dependent variables and material parameters in the upper and lower half-spaces, respectively. Further, the displacements, stresses, and microrotation functions must decrease with increasing distances from the plane $z = 0$, where $z > 0$ defines the lower half-space. The question whether a Stoneley mode can exist when two half-spaces are not in welded contact is examined theoretically on the basis of Murty (1975). The related boundary conditions at $z = 0$ are the normal components of the displacement vector and stress tensor, couple stress tensor, and the microrotation vectors are continuous while the shearing stress vanishes across the interface. Using (1) with the aforesaid conditions to write the related equations of both half-spaces into the boundary conditions, we obtain the frequency equation of the Stoneley wave propagation which gets factorized resulting in

$$\gamma_1\xi_1 + \gamma_2\xi_2 = 0, \quad (3)$$

and

$$\rho_2 d_2^4\left[1 - c^2\left(b_2^2 + \epsilon_2 d_2^2\right)^{-1}\right]^{-1/2}R_2(c) + \rho_1 d_1^4\left[1 - c^2\left(b_1^2 + \epsilon_1 d_1^2\right)^{-1}\right]^{-1/2}R_1(c) = 0. \quad (4)$$

In the above, b_1, d_1 and b_2, d_2 are the speeds of dilatational and shear waves, respectively, and ξ_1^2, ξ_2^2 are

$$\xi_1^2 = 2\epsilon_1 j_1^{-1}\theta_1^{-1} + \left(1 - c^2\rho_1 j_1\gamma_1^{-1}\right)s^2,$$
$$\xi_2^2 = 2\epsilon_2 j_2^{-1}\theta_2^{-1} + \left(1 - c^2\rho_2 j_2\gamma_2^{-1}\right)s^2, \quad (5)$$

where $R_2(c)$ is the frequency equation of Rayleigh waves in the micropolar elastic solid (medium 2), viz.,

$$R_2(c) = \left(2 + \epsilon_2 - c^2d_2^{-2}\right) - (2 + \epsilon_2)^2\left[1 - c^2\left(b_2^2 + \epsilon_2 d_2^2\right)^{-1}\right]^{1/2}\left[1 - c^2(1 + \epsilon_2)^{-1}d_2^{-2}\right]^{1/2}, \quad (6)$$

and $R_1(c)$ is similarly defined with suffix 2 replaced by suffix 1. Equation (6) equated to zero gives the frequency equation of the Rayleigh surface waves (Eringen, 1968). Equation (3) shows an extra velocity not observed in classical theory and purely depends on new micropolar elastic constants. Hence, the waves related to these modes are known as micropolar waves. Equation (4) is the counterpart of the Stoneley wave equation of classical theory, which can be obtained by ignoring the terms of ϵ from it (Murty, 1975). It determines the condition for the existence of a Stoneley mode for which there should exist a real value of wave speed c (c is less than the smaller of the two shear wave speeds d_1 and d_2). In general, the wave velocity of micropolar waves are different from that of the counterpart of the Stoneley wave equation of classical theory.

3 Results and Discussion

We see from (4) that when the two sides of an unbonded interface are of the same material, the speed of the Stoneley wave is the same as that of the Rayleigh wave on the free surface of one of the half-spaces (Eringen, 1968). In the limiting case of $d_2 \to 0$, Eq. (4) is reduced to the counterpart of frequency equation of Stoneley waves at a liquid-solid interface in connection with transmission of waves through oceans, which can be obtained by ignoring the micropolar terms from it (see Eq. 3.111, Ewing et al., 1957).

It is interesting to investigate the case of medium "2" differing from the medium "1" whose material properties are close to each other. Then an explicit expression for the Stoneley wave speed as a perturbation over the Rayleigh wave speed can be obtained. In particular, let

$$d_2 = d_1(1 + \delta_1), \quad b_2 = b_1(1 + \delta_2),$$
$$\rho_2 = \rho_1(1 + \delta_3), \quad \epsilon_2 = \epsilon_1(1 + \delta_4), \quad (7)$$

where $|\delta_i| \ll 1$ ($i = 1, 2, 3, 4$). Thus the frequency Eq. (4) can be solved by power series expansion in the parameters δ_i. To find the zeroth-order solution, consider the first-order terms by ignoring the squares and products of parameters. Assuming $d_1 < d_2$, we see that the zeroth-order solution c_o is

$$R_1(c_0) = 0. \quad (8)$$

When the medium "1" is incompressible, that is $b_1 \to \infty$ (Ewing et al., 1957), then the analogous Rayleigh wave speed c_o is obtained:

$$c_o = c_o' \simeq 0.955(1 + 0.736\epsilon_1)d_1, \quad (9)$$

and when the medium "1" is a Poisson solid (that is, $b_1 = \sqrt{3}d_1$),

$$c_o = c_o^P \simeq 0.919(1 + 0.932\epsilon_1)d_1. \quad (10)$$

The corresponding first-order change in the Rayleigh wave speed can also be obtained from (4) as follows:

$$R_1(c) + \left[R_1(c) + \Delta(c)\right] \times (1 + a_1\delta_1 + a_2\delta_2 + a_3\delta_3 + a_4\delta_4) = 0, \quad (11)$$

where $a_i (i = 1, 2, 3, 4)$ and $\Delta(c)$ are

$$a_1 = 4 - \epsilon_1 d_1^2\left(b_1^2 + \epsilon_1 d_1^2\right)^{-2}\left[1 - c^2\left(b_1^2 + \epsilon_1 d_1^2\right)^{-1}\right]^{-1},$$
$$a_2 = c^2 b_1^2\left(b_1^2 + \epsilon_1 d_1^2\right)^{-2}\left[1 - c^2\left(b_1^2 + \epsilon_1 d_1^2\right)^{-1}\right]^{-1}, \; a_3 = 1,$$
$$2a_4 = \epsilon_1 c^2 d_1^2\left(b_1^2 + \epsilon_1 d_1^2\right)^{-2}\left[1 - c^2\left(b_1^2 + \epsilon_1 d_1^2\right)^{-1}\right]^{-1},$$

$$\Delta(c) = 4c^2\delta_1 d_1^{-2}\left[2 - c^2 d_1^{-2} - M^{-1/2}N^{1/2}\right] - 4c^2 b_1^2\delta_2\left(b_1^2 + \epsilon_1 d_1^2\right)^{-2} M^{1/2}N^{-1/2} + \epsilon_1\delta_1\left[4c^2 d_1^{-2} - 4c^2 d_1^{-2}\left(b_1^2 + \epsilon_1 d_1^2\right)^{-2} M^{1/2}N^{-1/2}\right] - 4c^2\epsilon_1\delta_2 b_1^2\left(b_1^2 + \epsilon_1 d_1^2\right)^{-2} \times M^{1/2}N^{-1/2} + \epsilon_1\delta_4\left[2\left(2 - c^2 d_1^{-2}\right) - 2c^2 d_1^2\left(b_1^2 + \epsilon_1 d_1^2\right)^{-2} \times M^{1/2}N^{-1/2} - 2c^2 d_1^{-2}M^{-1/2}N^{1/2} - 4M^{1/2}N^{1/2}\right]. \quad (12)$$

In (12), M and N are defined as

$$M = 1 - c^2 d_1^{-2}(1 + \epsilon_1)^{-1}, \quad N = 1 - c^2\left(b_1^2 + \epsilon_1 d_1^2\right)^{-1}.$$

To find the solution of (11), we write

$$c = c_o + \delta c, \quad (13)$$

and thus $R_1(c)$ is given up to first order by

$$R_1(c) = R_1(c_o) + \left(\frac{\partial R_1}{\partial c}\right)_{c_o}\delta c. \quad (14)$$

Replacing suffix 2 by suffix 1 in (6), $R_1(c)$ is obtained.

To find $(\partial R_1/dc)_{c_o}$, differentiate $R_1(c)$ with respect to c, and then finally replace c by c_o. Using (8), (13), and (14) into (11), we find

$$\delta c = -|\Delta(c_o)|/2\left(\frac{\partial R_1}{\partial c}\right)c_o, \quad (15)$$

where $\Delta(c_o)$ can be obtained from the expression of $\Delta(c)$ replacing c by c_o. Finally, using (9), (10), and (12)–(15), we obtain

$$c = c_o^I(1 + 0.5\delta_1 + 0.68\epsilon_1\delta_4), \quad (16)$$

for incompressible solids, while

$$c = c_o^P(1 + 0.432\delta_1 + 0.067\delta_2 + 0.455\epsilon_1\delta_1 + 0.455\epsilon_1\delta_2 + 0.82\epsilon_1\delta_4), \quad (17)$$

for Poisson solids. The terms containing ϵ_1 in (16) and (17) are the first-order correction to the Stoneley wave speed. Since $\epsilon > 0$, we can conclude that the micropolar effects increase the analogous speeds when compared to classical theory. Equating micropolar terms to zero, the analogous results of the classical theory of Murty (1975) is obtained as a special case. Thus, a Stoneley mode exists at an ideal unbonded interface between two micropolar elastic half-spaces under suitable conditions.

Acknowledgments

The author is thankful to Prof. Ray M. Bowen, Associate Editor, and the referees for suggestions for improving the quality of the paper.

References

Eringen, A. C., 1966, "Linear Theory of Micropolar Elasticity," *Journal of Mathematics and Mechanics*, Vol. 15, No. 6, pp. 909–923.

Eringen, A. C., 1968, "The Theory of Micropolar Elasticity," *Fracture*, Vol. II, H. Leibowitz, ed., Academic Press, London, Ch. 7, pp. 622–729.

Ewing, E. M., Jardetzsky, W. S., and Press, F., 1957, *Elastic Waves in Layered Media*, McGraw-Hill, New York.

Murty, G. S., 1975, "Wave Propagation at an Unbonded Interface Between Two Elastic Half-Spaces," *Journal of the Acoustical Society of America*, Vol. 58, pp. 1094–1095.

Two-Dimensional Dynamic Thermal Stresses in a Semi-infinite Circular Cylinder

Koichi Kaizu[27], Tsuyoshi Aoto[28], and Shinji Tanimura[29]

1 Introduction

The finite difference method based on the integration along the bi-characteristics is the most suitable method to the analysis of the two-dimensional stress wave propagation (Clifton, 1967; Tanimura et al., 1986). The advantage of this method is attributed to the fact that the characteristic surface coincides with the wave surface. Using this method, the propagation, reflection, and interaction of the stress waves in a body can be investigated in detail.

The purpose of this work is to develop the finite difference method based on the integration along the bi-characteristics for the two-dimensional dynamic thermal stresses. In order to clarify the dynamic effect on the thermal stresses under an instantaneous heating, the numerical results are presented for the variations of the stress distribution with time in a semi-infinite circular cylinder.

2 Governing Equations

Consider a semi-infinite circular cylinder having the diameter of $2a$. A ramp-shaped rising heating is assumed to be applied to the free-end surface of this cylinder. The influence of the temperature on the strain field is not taken into account. Cylindrical coordinate (r, θ, z) are taken, where the z-axis coincides with the axis of the cylinder. From the symmetric property, the equations of motion are given as follows:

$$\rho\,\partial v_r/\partial t = \partial\sigma_r/\partial \mathrm{r} + \partial\tau_{rz}/\partial z + (\sigma_r - \sigma_\theta)/r$$

$$\rho\,\partial v_z/\partial t = \partial\tau_{rz}/\partial r + \partial\sigma_z/\partial z + \tau_{rz}/r \quad (1)$$

where v_r and v_z are the velocity components. σ_r, σ_θ, σ_z and τ_{rz} denote stress components, ρ the density, and t the time.

The constitutive equations for an isotropic material in this case are

$$\partial v_r/\partial r = \{\dot\sigma_r - \nu(\dot\sigma_\theta + \dot\sigma_z)\}/E + \alpha\dot T$$

$$v_r/r = \{\dot\sigma_\theta - \nu(\dot\sigma_z + \dot\sigma_r)\}/E + \alpha\dot T$$

$$\partial v_z/\partial z = \{\dot\sigma_z - \nu(\dot\sigma_r + \dot\sigma_\theta)\}/E + \alpha\dot T$$

$$\partial v_r/\partial z + \partial v_z/\partial r = \dot\tau_{rz}/\mu \quad (2)$$

where T is the temperature and the dot denotes the time derivative. E is Young's modulus, μ is the Lame's constant, ν is Poisson's ratio, and α is the coefficient of linear expansion. The physical constants do not depend on the temperature.

From Eqs. (1)–(2), the governing equations in the dimensionless form may be written in a matrix form:

[27]Lecturer, Department of Mechanical Systems Engineering, University of Osaka Prefecture, Sakai, Osaka 593, Japan.

[28]Graduate School, University of Osaka Prefecture, Sakai, Osaka 593, Japan.

[29]Professor, Department of Mechanical Systems Engineering, University of Osaka Prefecture, Sakai, Osaka 593, Japan.

Contributed by the Applied Mechanics Division of THE AMERICAN SOCIETY OF MECHANICAL ENGINEERS for publication in the ASME JOURNAL OF APPLIED MECHANICS. Manuscript received by the ASME Applied Mechanics Division, July 6, 1993; final revision, Nov. 5, 1993. Associate Technical Editor: W. K. Liu.

$$\Delta(c) = 4c^2\delta_1 d_1^{-2}\left[2 - c^2 d_1^{-2} - M^{-1/2}N^{1/2}\right] - 4c^2 b_1^2\delta_2\left(b_1^2 + \epsilon_1 d_1^2\right)^{-2} M^{1/2}N^{-1/2} + \epsilon_1\delta_1\left[4c^2 d_1^{-2} - 4c^2 d_1^{-2}\left(b_1^2 + \epsilon_1 d_1^2\right)^{-2} M^{1/2}N^{-1/2}\right] - 4c^2\epsilon_1\delta_2 b_1^2\left(b_1^2 + \epsilon_1 d_1^2\right)^{-2} \times M^{1/2}N^{-1/2} + \epsilon_1\delta_4\left[2\left(2 - c^2 d_1^{-2}\right) - 2c^2 d_1^2\left(b_1^2 + \epsilon_1 d_1^2\right)^{-2} \times M^{1/2}N^{-1/2} - 2c^2 d_1^{-2}M^{-1/2}N^{1/2} - 4M^{1/2}N^{1/2}\right]. \quad (12)$$

In (12), M and N are defined as

$$M = 1 - c^2 d_1^{-2}(1 + \epsilon_1)^{-1}, \quad N = 1 - c^2\left(b_1^2 + \epsilon_1 d_1^2\right)^{-1}.$$

To find the solution of (11), we write

$$c = c_o + \delta c, \quad (13)$$

and thus $R_1(c)$ is given up to first order by

$$R_1(c) = R_1(c_o) + \left(\frac{\partial R_1}{\partial c}\right)_{c_o}\delta c. \quad (14)$$

Replacing suffix 2 by suffix 1 in (6), $R_1(c)$ is obtained.

To find $(\partial R_1/dc)_{c_o}$, differentiate $R_1(c)$ with respect to c, and then finally replace c by c_o. Using (8), (13), and (14) into (11), we find

$$\delta c = -|\Delta(c_o)|/2\left(\frac{\partial R_1}{\partial c}\right)c_o, \quad (15)$$

where $\Delta(c_o)$ can be obtained from the expression of $\Delta(c)$ replacing c by c_o. Finally, using (9), (10), and (12)–(15), we obtain

$$c = c_o^I(1 + 0.5\delta_1 + 0.68\epsilon_1\delta_4), \quad (16)$$

for incompressible solids, while

$$c = c_o^P(1 + 0.432\delta_1 + 0.067\delta_2 + 0.455\epsilon_1\delta_1 + 0.455\epsilon_1\delta_2 + 0.82\epsilon_1\delta_4), \quad (17)$$

for Poisson solids. The terms containing ϵ_1 in (16) and (17) are the first-order correction to the Stoneley wave speed. Since $\epsilon > 0$, we can conclude that the micropolar effects increase the analogous speeds when compared to classical theory. Equating micropolar terms to zero, the analogous results of the classical theory of Murty (1975) is obtained as a special case. Thus, a Stoneley mode exists at an ideal unbonded interface between two micropolar elastic half-spaces under suitable conditions.

Acknowledgments

The author is thankful to Prof. Ray M. Bowen, Associate Editor, and the referees for suggestions for improving the quality of the paper.

References

Eringen, A. C., 1966, "Linear Theory of Micropolar Elasticity," *Journal of Mathematics and Mechanics*, Vol. 15, No. 6, pp. 909–923.

Eringen, A. C., 1968, "The Theory of Micropolar Elasticity," *Fracture*, Vol. II, H. Leibowitz, ed., Academic Press, London, Ch. 7, pp. 622–729.

Ewing, E. M., Jardetzsky, W. S., and Press, F., 1957, *Elastic Waves in Layered Media*, McGraw-Hill, New York.

Murty, G. S., 1975, "Wave Propagation at an Unbonded Interface Between Two Elastic Half-Spaces," *Journal of the Acoustical Society of America*, Vol. 58, pp. 1094–1095.

Two-Dimensional Dynamic Thermal Stresses in a Semi-infinite Circular Cylinder

Koichi Kaizu[27], Tsuyoshi Aoto[28], and Shinji Tanimura[29]

1 Introduction

The finite difference method based on the integration along the bi-characteristics is the most suitable method to the analysis of the two-dimensional stress wave propagation (Clifton, 1967; Tanimura et al., 1986). The advantage of this method is attributed to the fact that the characteristic surface coincides with the wave surface. Using this method, the propagation, reflection, and interaction of the stress waves in a body can be investigated in detail.

The purpose of this work is to develop the finite difference method based on the integration along the bi-characteristics for the two-dimensional dynamic thermal stresses. In order to clarify the dynamic effect on the thermal stresses under an instantaneous heating, the numerical results are presented for the variations of the stress distribution with time in a semi-infinite circular cylinder.

2 Governing Equations

Consider a semi-infinite circular cylinder having the diameter of $2a$. A ramp-shaped rising heating is assumed to be applied to the free-end surface of this cylinder. The influence of the temperature on the strain field is not taken into account. Cylindrical coordinate (r, θ, z) are taken, where the z-axis coincides with the axis of the cylinder. From the symmetric property, the equations of motion are given as follows:

$$\rho\,\partial v_r/\partial t = \partial\sigma_r/\partial \mathrm{r} + \partial\tau_{rz}/\partial z + (\sigma_r - \sigma_\theta)/r$$

$$\rho\,\partial v_z/\partial t = \partial\tau_{rz}/\partial r + \partial\sigma_z/\partial z + \tau_{rz}/r \quad (1)$$

where v_r and v_z are the velocity components. σ_r, σ_θ, σ_z and τ_{rz} denote stress components, ρ the density, and t the time.

The constitutive equations for an isotropic material in this case are

$$\partial v_r/\partial r = \{\dot\sigma_r - \nu(\dot\sigma_\theta + \dot\sigma_z)\}/E + \alpha\dot T$$

$$v_r/r = \{\dot\sigma_\theta - \nu(\dot\sigma_z + \dot\sigma_r)\}/E + \alpha\dot T$$

$$\partial v_z/\partial z = \{\dot\sigma_z - \nu(\dot\sigma_r + \dot\sigma_\theta)\}/E + \alpha\dot T$$

$$\partial v_r/\partial z + \partial v_z/\partial r = \dot\tau_{rz}/\mu \quad (2)$$

where T is the temperature and the dot denotes the time derivative. E is Young's modulus, μ is the Lame's constant, ν is Poisson's ratio, and α is the coefficient of linear expansion. The physical constants do not depend on the temperature.

From Eqs. (1)–(2), the governing equations in the dimensionless form may be written in a matrix form:

[27]Lecturer, Department of Mechanical Systems Engineering, University of Osaka Prefecture, Sakai, Osaka 593, Japan.

[28]Graduate School, University of Osaka Prefecture, Sakai, Osaka 593, Japan.

[29]Professor, Department of Mechanical Systems Engineering, University of Osaka Prefecture, Sakai, Osaka 593, Japan.

Contributed by the Applied Mechanics Division of THE AMERICAN SOCIETY OF MECHANICAL ENGINEERS for publication in the ASME JOURNAL OF APPLIED MECHANICS. Manuscript received by the ASME Applied Mechanics Division, July 6, 1993; final revision, Nov. 5, 1993. Associate Technical Editor: W. K. Liu.

$$L[W]=A^t W_t+A^r W_r+A^z W_z-B=0 \tag{3}$$

where the vectors W and B and matrices A^t, A^r, and A^z are

$$A^t=\begin{bmatrix}1&0&0&0&0&0\\0&1&0&0&0&0\\0&0&M&0&Q&0\\0&0&0&H&0&0\\0&0&Q&0&N&0\\0&0&0&0&0&H\end{bmatrix},\quad A^r=\begin{bmatrix}0&0&-1&-1&0&0\\0&0&0&0&0&-1\\-1&0&0&0&0&0\\-1&0&0&0&0&0\\0&0&0&0&0&0\\0&-1&0&0&0&0\end{bmatrix}$$

$$A^z=\begin{bmatrix}0&0&0&0&0&-1\\0&0&0&0&-1&0\\0&0&0&0&0&0\\0&0&0&0&0&0\\0&-1&0&0&0&0\\-1&0&0&0&0&0\end{bmatrix},\quad W=\begin{bmatrix}u\\v\\p\\q\\s\\n\end{bmatrix},\quad B=\begin{bmatrix}2q/r\\n/r\\u/r-\alpha\dot{T}\\-u/r\\-\alpha\dot{T}\\0\end{bmatrix}$$

and

$$t=c_1\hat{t}/b,\quad r=\hat{r}/b,\quad z=\hat{z}/b,\quad u=\hat{v}_r/c_1,\quad v=\hat{v}_z/c_1,$$

$$p=(\hat{\sigma}_r+\hat{\sigma}_\theta)/2\rho c_1^2,\quad q=(\hat{\sigma}_r-\hat{\sigma}_\theta)/2\,\rho c_1^2,\quad s=\hat{\sigma}_z/\rho\,c_1^2,\quad n=\hat{\tau}_{rz}/\rho\,c_1^2,$$

$$\Gamma=c_1/c_2,\quad E=\hat{E}/\rho\,c_1^2,\quad T=\hat{T}/T_0,\quad \alpha=\hat{\alpha}T_0$$

$$H=2(1+\nu)/E,\quad M=2(1-\nu)/E,\quad N=1/E,\quad Q=-2\nu/E$$

where a hat $\hat{}$ denotes the corresponding dimensional quantity and b and T_0 are the representative length and representative temperature, respectively, c_1 is the velocity of dilatational waves and c_2 the velocity of shear waves.

The system of Eq. (3) is a system of semilinear hyperbolic partial differential equations with constant coefficients. Integration of the system is carried out by integrating the difference equation along bi-characteristics, which was developed by Clifton (1967). The outline of the derivation will be described as follows.

The differential equations along bi-characteristics are as follows:

$$\cos\lambda du+\sin\lambda dv+\cos^2\lambda(dp+dq)+\sin^2\lambda ds+\sin 2\lambda dn=-S_1(\lambda)dt \tag{4}$$

for $c=1$, and

$$2\Gamma\sin\lambda du-2\Gamma\cos\lambda dv+\Gamma^2\sin 2\lambda(dp+dq)-\Gamma^2\sin 2\lambda ds-2\Gamma^2\cos 2\lambda ds=-S_2(\lambda)dt$$

for $c=1/\Gamma$, where

$$S_1(\lambda)=\{(\Gamma^2-2)/\Gamma^2\}(-\sin^2\lambda u_r+\sin 2\lambda u_z/2+\sin 2\lambda v_r/2-\cos^2\lambda v_z)-\sin^2\lambda\cos\lambda p_r+\sin\lambda\cos^2\lambda p_z-\sin^2\lambda\cos\lambda q_r+\sin\lambda\cos^2\lambda q_z+\sin^2\lambda\cos\lambda s_r-\sin\lambda\cos^2\lambda s_z+\sin\lambda\cos 2\lambda n_r-\cos\lambda\cos 2\lambda n_z-\{(\Gamma^2-2)/\Gamma^2\}(u/r)-2\cos\lambda(q/r)-\sin\lambda(n/r)+\{(3\Gamma^2-4)/\Gamma^2\}\alpha T_t$$

$$S_2(\lambda)=-\sin 2\lambda\,u_r+2\cos^2\lambda u_z-2\sin^2\lambda v_r+\sin 2\lambda v_z-2\Gamma\sin^3\lambda p_r+\Gamma\sin 2\lambda\sin\lambda p_z-2\Gamma\sin^3\lambda q_r+\Gamma\sin 2\lambda\sin\lambda q_z-\Gamma\sin 2\lambda\cos\lambda s_r+2\Gamma\cos^3\lambda s_z+4\Gamma\sin^2\lambda\cos\lambda n_r-4\Gamma\sin\lambda\cos^2\lambda n_z-4\Gamma\sin\lambda(q/r)+2\Gamma\cos\lambda(n/r) \tag{5}$$

and c denotes the dimensionless wave velocity and λ ($0\leqq\lambda\leqq 2\pi$) is a parameter (Clifton, 1967).

By integrating Eq. (4) along the bi-characteristics for which $\lambda=\lambda_i$, from the point (r_0, z_0, t_0) to the point (r_0, z_0, t_0-k) where this characteristic intersects the plane $t=t_0-k$ and by using the increment of variable as

$$\delta W=W(r_0, z_0, t_0)-W(r_0, z_0, t_0-k), \tag{6}$$

we have

$$\cos\lambda_i\delta u+\sin\lambda_i\delta v+\cos^2\lambda_i(\delta p+\delta q)+\cos^2\lambda_i\delta s+\sin 2\lambda_i\delta n=(-k/2)\{S_1(\lambda_i)^0+S_1(\lambda_i)_i\}-W_1(\lambda_i) \tag{7}$$

for $c=1$ and

$$2\Gamma\sin\lambda_i\delta u-2\Gamma\cos\lambda_i\delta v+\Gamma^2\sin 2\lambda_i(\delta p+\delta q)-\Gamma^2\sin 2\lambda_i\delta s-2\Gamma^2\cos\lambda_i\delta n=(-k/2)\{S_2(\lambda_i)^0+S_2(\lambda_i)_i,\}-W_2(\lambda_i)$$

for $c=1/\Gamma$, where

$$W_1(\lambda_i)=\cos\lambda_i(u_0-u_i)+\sin\lambda_i(v_0-v_i)+\cos^2\lambda_i(p_0-p_i)+\cos^2\lambda_i(q_0-q_i)+\sin^2\lambda_i(s_0-s_i)+\sin 2\lambda_i(n_0-n_i)$$

$$W_2(\lambda_i)=2\Gamma\sin\lambda_i(u_0-u_{i,})-2\Gamma\cos\lambda_i(v_0-v_{i,})+\Gamma^2\sin 2\lambda_i(p_0-p_{i,}+q_0-q_{i,})-\Gamma^2\sin 2\lambda_i(s_0-s_{i,})-2\Gamma^2\cos\lambda_i(n_0-n_{i,})$$

and k is the dimensionless time interval. The superscript 0 denotes evaluation of the function at the point (r_0, z_0, t_0) and the subscript 0 denotes evaluation of the function at the point (r_0, z_0, t_0-k). The subscript i denotes evaluation of the function at the point where the bi-characteristic λ_i on the characteristic cone intersects the plane $t=t_0-k$.

Six additional differential equations, obtained by integrating Eq. (3) along the time axis, are as follows:

$$\delta u=(k/2)\{p_r^0+q_r^0+n_z^0+2(q_0+\delta q)/r_0+p_{r0}+q_{r0}+n_{z0}+2q_0/r_0\}$$

$$\delta v=(k/2)(n_r^0+s_z^0+(n_0+\delta n)/r_0+n_{r0}+s_{z0}+n_0/r_0)$$

$$\Gamma^2\delta p+(3\Gamma^2-4)\alpha\delta T=(k/2)\{(\Gamma^2-1)u_r^0+(\Gamma^2-2)v_z^0+(\Gamma^2-1)(u_0+\delta u)/r_0+(\Gamma^2-1)u_{r0}+(\Gamma^2-2)v_{z0}+(\Gamma^2-1)u_0/r_0\}$$

$$\Gamma^2\delta q=(k/2)\{u_r^0-(u_0+\delta u)/r_0+u_{r0}-u_0/r_0\}$$

$$\Gamma^2\delta s+(3\Gamma^2-4)\alpha\delta T=(k/2)\{(\Gamma^2-2)u_r^0+\Gamma^2 v_z^0+(\Gamma^2-2)(u_0+\delta u)/r_0+(\Gamma^2-2)u_{r0}+\Gamma^2 v_{z0}+(\Gamma^2-2)u_0/r_0\}$$

$$\Gamma^2\delta n=(k/2)\{v_z^0+u_r^0+v_{z0}+u_{r0}\}. \tag{8}$$

All the terms on the right-hand side of Eqs. (7) and (8) can be evaluated from data on the plane $t=t_0-k$ except those terms having the superscript 0. All the terms involving partial

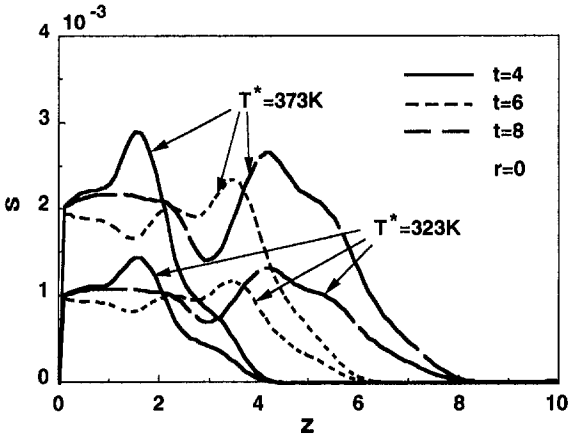

Fig. 1 Distribution of the stress s along the axis of the circular cylinder

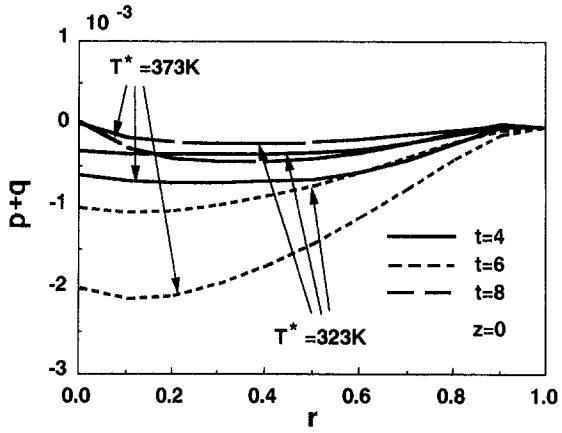

Fig. 2 Distribution of the stress $p+q$ at the $z=0$

derivatives at the point (r_0, z_0, t_0) can be eliminated by forming linear combinations of Eq. (8) and the equations obtained by writing Eq. (7) for $\lambda_i = (i-1)\pi/2$, with $i = 1, 2, 3, 4$. Consequently, six equations which determine the unknown increments δu, δv, δp, δq, δs, and δn are expressed as

$$\delta u = (k/r_0)\delta q + a_1, \quad \delta v = (k/2r_0)\delta n + a_2$$

$$\delta p = \{k(\Gamma^2-2)/2\Gamma^2 r_0\}\delta u - \delta q - \{(3\Gamma^2-4)/\Gamma^2\}\alpha\delta T + a_3$$

$$\delta q = a_4 - (k/2\Gamma^2 r_0)\delta u, \quad \delta s = \{(\Gamma^2-2)/(\Gamma^2-1)\}\delta p - (\alpha/N)\delta T + a_s, \quad \delta n = a_6$$

$$a_1 = (k^2/2)[\{(\Gamma^2-2)/\Gamma^2\}(u_{r0}/r_0 - u_0/r_0^2) + u_{rr0} + u_{zz0}/\Gamma^2 + \{(\Gamma^2-1)/\Gamma^2\}v_{rz0}] + k(p_{r0} + q_{r0} + 2q_0/r_0 + n_{z0}) + \{(3\Gamma^2-4)/\Gamma^2\}\alpha T_{r0}$$

$$a_2 = (k^2/2\Gamma^2)[\{(\Gamma^2-2)/r_0\}u_{z0} + (\Gamma^2-1)u_{rz0} + v_{rr0} + \Gamma^2 v_{zz0}] + k(s_{z0} + n_0/r_0 + n_{r0}) + \{(3\Gamma^2-4)/\Gamma^2\}\alpha T_{z0}$$

$$a_3 = (k^2/2)[p_{rr0} + q_{rr0} + 2q_{r0}/r_0 - 2q_0/r_0^2 + \{2(\Gamma^2-1)/\Gamma^2\}n_{rz0} + \{(\Gamma^2-2)/\Gamma^2\}(s_{zz0} + n_{z0}/r_0)] + k[u_{r0} + \{(\Gamma^2-2)/\Gamma^2(u_0/r_0 + v_{z0})] + \{(3\Gamma^2-4)/\Gamma^2\}k^2\alpha[T_{rr0} + \{(\Gamma^2-2)/\Gamma^2\}T_{zz0}]$$

$$a_4 = (k^2/2)(p_{rr0} + q_{rr0} + 2q_{r0}/r_0 - q_0/r_0^2 + n_{rz0}) + k\{u_{r0} - u_0/r_0\} + \{(3\Gamma^2-4)/2\Gamma^2\}k^2\alpha T_{rr0}$$

$$a_5 = (k^2/2N)(n_{rz0} + n_{z0}/r_0 + s_{zz0}) + (k/N)v_{z0} + \{k^2(3\Gamma^2-4)/2N\Gamma^2\}\alpha T_{zz0}$$

$$a_6 = [(k^2/2)(p_{rz0} + q_{rz0} + 2q_{z0}/r_0 + s_{rz0} + n_{rr0} + n_{zz0} + n_{r0}/r_0 - n_0/r_0^2) + k(u_{z0} - v_{r0})]/\Gamma^2. \quad (9)$$

The boundary conditions are as follows:

$$\begin{aligned} &\text{heated end } (z=0) \quad : s=0,\ n=0 \\ &\text{side surface } (r=a) \quad : p+q=0,\ n=0. \end{aligned} \quad (10)$$

For points on the boundary or the corner, we can make use of boundary conditions instead of lost relations along bi-characteristics which are out of the region.

3 Heat Conduction

From the symmetric property, the heat conduction equation in cylindrical coordinate (r, θ, z) takes the following form:

$$\kappa\{\partial^2 T/\partial r^2 + (1/r)\partial T/\partial r + \partial^2 T/\partial z^2\} = \partial T/\partial t \quad (11)$$

where κ is the heat conductivity.

The heat function $F(r, z, t)$ is assumed as follows:

$$F(r, 0, t) = \begin{cases} 0 & \text{for } t<0, \\ T_m t/t_r & \text{for } t<t_r, \\ T_m & \text{for } t_r<t \end{cases} \quad (12)$$

where $T_m = T^*/T_0$ and t_r is the nondimensional rising time. The boundary conditions are assumed as follows:

$$T(r, 0, t) = F(r, 0, t), \quad T(a, z, t) = 273 \text{ [K]}. \quad (13)$$

In order to solve this equation, we replace the partial derivatives of the components of vector W in the direction r and z by the corresponding finite equations.

4 Numerical Results

The numerical calculation is carried out on an example as follows: $a=0.01$ [m], $b=0.01$ [m], parameters in the heat function $t_r=1$, $T_0=273$ [K], and $T^*=323$ [K] and 373 [K]. Meanwhile, since the material is steel, the material constants are chosen as follows: $E=206$ [GPa], $\nu=0.3$, $\rho=7860$ [kg/m^3], $\alpha=11\times10^{-6}$ [1/K] and $\kappa=2.27\times10^{-5}$ [m^2/s].

In this study, we take $k=0.025$ and $h=0.1$, which is in agreement with the study concerning the stability of difference equations (Clifton, 1967).

Figure 1 shows the distribution of the stress s along the axis of the cylinder. It is found that stress waves propagate in the cylinder in a complex manner with time and that values of stresses are dependent on the temperature.

Figure 2 shows the distribution of the stress $p+q$ at the $z=0$ (the heated surface). The stress distribution is changed with time because the stress waves go and return in the r-direction.

In summary, the dynamic response of the semi-infinite cylinder under instantaneous heating can be investigated in detail by this method. This method can get a wide application and the same idea might be applied to the other problems for the dynamic thermal stresses.

Acknowledgment

A part of this work is supported by the Grant-in-Aid for Scientific Researches of the Ministry of Education, Science and Culture of Japan.

References

Clifton, R. J., 1967, "A Difference Method for Plane Problems in Dynamic Elasticity," *Quarterly of Applied Mathematics*, Vol. 25, pp. 97-116.

Tanimura, S., Igaki, H., and Liu, K., 1986, "Dynamic Behavior of a Circular Cylinder under Impulsive Loads (Stress Concentration Associated with Stress Waves)," *Transactions of the Japan Society of Mechanical Engineering*, Vol. 52, No. 484, pp. 2680-2684 (in Japanese).

A Theoretical Investigation of the Effect of Structural Stiffness in Underwater Shock Wave Loading Using the Plane Wave Approximation

R. L. Dawson[30] and G. M. Sullivan[30]

The equations of motion for an explosively loaded infinite plate with stiffness are derived. The structural response of this plate is compared to that of an explosively loaded infinite plate without stiffness. The effect of stiffness on water cavitation and plate displacement is determined.

Introduction

Consider a water-bounded, air-backed, rigid plate with infinite edges struck at normal incidence by an explosive shock wave. (An infinite plate will exclude any edge effects from the water boundary.) The exponential shock wave pressure is $P_m e^{-t/\theta}$, ρ_a is the mass per unit area associated with the plate, ρ_0 is the density of water, and c is the speed of sound in water. Assuming any fluid inertial effects are negligible, the resulting force per unit area applied at the plate is given by

$$F(t) = \rho_a \frac{d^2y}{dt^2} = 2P_m e^{-t/\theta} - \rho_0 c \frac{dy}{dt}. \tag{1}$$

Equation (1) was originally derived by Taylor in 1941. The fluid and the plate interact and the shock wave loading will be modified by the plate displacing through the water. If the plate moves faster than the fluid particles then the density of the water near the plate will diminish considerably causing a region of water vapor. This condition is known as cavitation and will cause the loading from the shock wave to be abated. Cavitation will occur at the vapor pressure of the water, which will be assumed to be at zero pressure. Thus, cavitation at the plate will occur when

$$\rho_0 c \frac{dy}{dt} \geq 2P_m e^{-t/\theta}. \tag{2}$$

The nonlinear, one-dimensional, load function known as the plane wave approximation (PWA) can be stated by combining Eqs. (1) and (2). The PWA applies Eq. (1) until the water cavitates, at which time the force is zeroed. The solution is exact for the assumptions stated until the time of cavitation.

Response Formulation

Taylor solved the equations of motion for an unstiffened infinite plate. Now consider a water-bounded infinite plate on a uniform elastic foundation with a stiffness per area of K. Fluid inertia will again be neglected. Three solutions exist depending upon the values of the variables chosen (Kennard, 1941). The solutions can be simplified by noting that nondimensional frequency is $\omega\theta$ where $\omega^2 = K/\rho_a$ (the systems in vacuum natural frequency), t/θ is nondimensional time, and a is nondimensional mass which is equal to $\rho_a/\rho_0 c\theta$. Using the classical definition from a single-degree-of-freedom system, the system is overdamped when $1/a > 2\omega\theta$. The resulting solution is (noting that $Y = dy/dt = 0$ at $t = 0$)

$$y = \frac{2P_m\theta}{\rho_0 c\{1 - a[1 + (\omega\theta)^2]\}} \left\{ \left(\frac{\lambda_2 + 1}{\lambda_2 - \lambda_1} \right) e^{\lambda_1 t/\theta} - \left(\frac{\lambda_1 + 1}{\lambda_2 - \lambda_1} \right) e^{\lambda_2 t/\theta} - e^{-t/\theta} \right\} \tag{3}$$

where

$$\lambda_{1,2} = \frac{1}{2}\left\{ -\frac{1}{a} \pm \sqrt{\frac{1}{a^2} - 4(\omega\theta)^2} \right\}. \tag{4}$$

When $1/a = 2\omega\theta$ the system is critically damped

$$y = \frac{2P_m\theta}{\rho_0 c\{1 - a[1 + (\omega\theta)^2]\}} \times \left\{ e^{-t/2a\theta} - \left(\frac{2a - 1}{2a} \right) \frac{t}{\theta} e^{-t/2a\theta} - e^{-t/\theta} \right\}. \tag{5}$$

When $2\omega\theta > 1/a$ the system is underdamped

$$y = \frac{2P_m\theta}{\rho_0 c\{1 - a[1 + (\omega\theta)^2]\}} \times \left\{ e^{-t/2a\theta} \left[\cos\left(\beta \frac{t}{\theta} \right) - \left(\frac{2a - 1}{2a\beta} \right) \sin\left(\beta \frac{t}{\theta} \right) \right] - e^{-t/\theta} \right\} \tag{6}$$

$$\beta = \frac{1}{2}\sqrt{4(\omega\theta)^2 - \frac{1}{a^2}}. \tag{7}$$

Water Pressure Formulation

The total shock wave pressure is simply the sum of the incident and reflected pressure at the plate. When the total pressure is set to zero, the time of cavitation as a function of location from the plate can be determined, as noted by Temperly in 1944. In a similar fashion, the time and location of cavitation for a plate with spring forces can be determined by setting the total water pressure to zero. Unfortunately, these equations cannot be solved directly, and a numerical procedure must be employed to determine the time and location of cavitation. Letting x be the distance into the water from the plate, then $x/\theta c$ is this distance nondimensionalized. If the plate is overdamped or $1/a > 2\omega\theta$, then the resulting equation for time and location of cavitation is

[30] Carderock Division, Naval Surface Warfare Center, Underwater Explosions Research Department, Portsmouth, VA 23709-5000.

Contributed by the Applied Mechanics Division of THE AMERICAN SOCIETY OF MECHANICAL ENGINEERS for publication in the ASME JOURNAL OF APPLIED MECHANICS. Manuscript received by the ASME Applied Mechanics Division, Apr. 13, 1993; final revision, Oct. 4, 1994. Associate Technical Editor: T. R. Akylas.

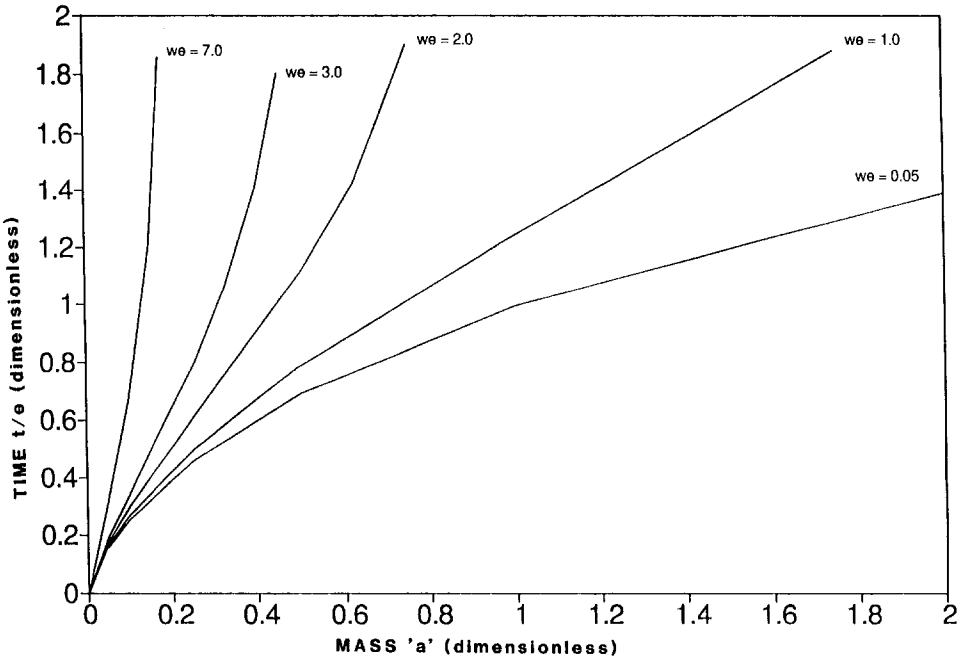

Fig. 1 Initial time of cavitation

$$\sinh\left(\frac{x}{\theta c}\right)+a[1+(\omega\theta)^2]\cosh\left(\frac{x}{\theta c}\right)$$
$$=-\left(\frac{\lambda_2+1}{\lambda_2-\lambda_1}\right)\lambda_1 e^{\lambda_1\left(\frac{t}{\theta}-\frac{x}{\theta c}\right)+\frac{t}{\theta}}+\left(\frac{\lambda_1+1}{\lambda_2-\lambda_1}\right)\lambda_2 e^{\lambda_2\left(\frac{t}{\theta}-\frac{x}{\theta c}\right)+\frac{t}{\theta}}. \quad (8)$$

When $1/a=2\omega\theta$ the system is critically damped:

$$\sinh\left(\frac{x}{\theta c}\right)+a[1+(\omega\theta)^2]\cosh\left(\frac{x}{\theta c}\right)$$
$$=e^{-\frac{1}{2a}\left(\frac{t}{\theta}-\frac{x}{\theta c}\right)+\frac{t}{\theta}}\left[1-\frac{(2a-1)}{(2a)^2}\left(\frac{t}{\theta}-\frac{x}{\theta c}\right)\right]. \quad (9)$$

When $2\omega\theta>1/a$ the system is underdamped:

$$\sinh\left(\frac{x}{\theta c}\right)+a[1+(\omega\theta)^2]\cosh\left(\frac{x}{\theta c}\right)$$
$$=e^{-\frac{1}{2a}\left(\frac{t}{\theta}-\frac{x}{\theta c}\right)+\frac{t}{\theta}}\left[\cos\left\{\beta\left(\frac{t}{\theta}-\frac{x}{\theta c}\right)\right\}-c_1\sin\left\{\beta\left(\frac{t}{\theta}-\frac{x}{\theta c}\right)\right\}\right] \quad (10)$$

with

$$c_1=\frac{1}{2a}\left[\frac{2a-1}{2a\beta}-2a\beta\right]. \quad (11)$$

Discussion of Results

Temperly indicated that when stiffness is not included the initial point of cavitation is always at the plate, $x/\theta c=0$. Equations (8) through (10) indicate that the inclusion of stiffness to an explosively loaded plate can cause a layer of water to exist between the plate and the initial cavitation point. The fact that it was possible for cavitation to occur at some distance from the plate was recognized by Kennard in 1943; however, Kennard did not tie this phenomenon to plate stiffness. When cavitation starts at a distance away from the plate, cavitation then moves both toward and away from the plate simultaneously, but cavitation may not reach the plate in all cases.

Initial cavitation times are found by iterating Eqs. (8) through (10) (Fig. 1). The case of $\omega\theta=0.05$ nearly corresponds to that of Taylor's no stiffness solution. It can be seen that regardless of the mass chosen, the cavitation time of a plate with stiffness will always be greater than the nonstiffened cavitation time.

Figure 1 also reveals the existence of cavitation. The figure indicates cavitation will always occur for a plate with no stiffness, but may not happen for a similar plate with stiffness. For example, if $a=1$ then Fig. 1 indicates that with no stiffness cavitation will occur at $t/\theta=1$. But if $\omega\theta=2$, then cavitation will not occur within the practical boundaries of time which were selected. Thus, this graph has important value for two reasons. First of all, if the stiffness of a plate is ignored then this can lead to erroneous conclusions as to the presence of cavitation. Secondly, it has been previously demonstrated (by Dawson in 1991) that the accuracy of the PWA is closely tied to the existence of cavitation. Figure 1 can be used as a tool for the analyst to determine not only if cavitation can be a potential problem, but to aid in selecting the loading schemes to be used in the analysis.

Figure 2 shows the percentage difference in displacement between a plate with and without stiffness as a function of dimensionless time. Once the water was cavitated, then the load is terminated, as indicated by the PWA. Any further displacement of the unstiffened plate will be based upon its own momentum. The dashed lines in Fig. 2 indicate the occurrence of cavitation for the unstiffened plate. When the dashed lines are terminated prior to the end of the graph, this shows that the stiffened plate has cavitated. From Fig. 2 it can be seen that Taylor's plate theory will always cavitate before that of a plate with stiffness.

A positive value of displacement difference indicates that the displacement for the unstiffened plate is greater than that of the stiffened plate. From Fig. 2 the displacement from the unstiffened plate will always be equal to or greater than the displacement of a stiffened plate. In other words, the unstif-

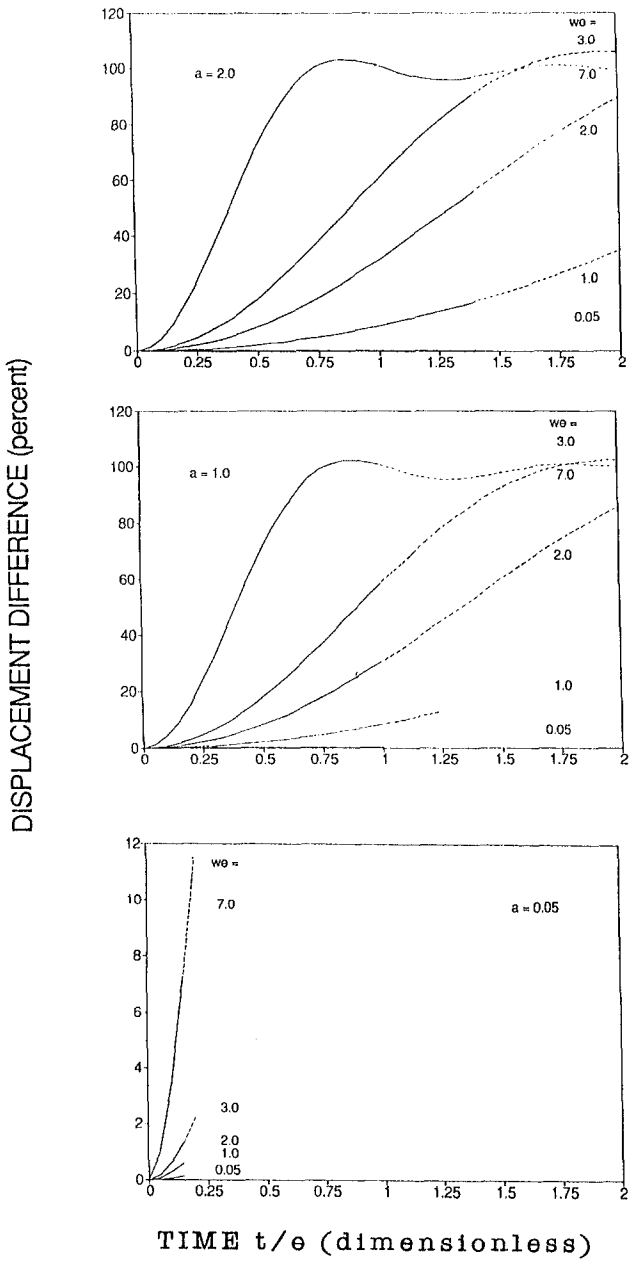

Fig. 2 Displacement difference (percent)

fened plate will always serve as an upper bound for displacement calculation.

References

Dawson, R. L., 1991, "The Use of the Plane Wave Fluid-Structure Interaction Loading Approximation in NASTRAN," NASTRAN User's Coloquium, Apr., David Taylor Research Center, Williamsburg, VA.

Kennard, E. H., 1941, "Report on Underwater Explosions," David Taylor Model Basin Underwater Explosion (UNDEX) Research, Oct; Office of Naval Research (ONR, 1950).

Kennard, E. H., 1943, "Explosive Load on Underwater Structures as Modified by Bulk Cavitation," David Taylor Model Basin, May, UNDEX Research (ONR, 1950).

Taylor, G. I., 1941, "The Pressure and Impulse of Submarine Explosion Waves on Plates," Cambridge University, July, UNDEX Research (ONR, 1950).

Temperly, H. N. V., 1944, "Theoretical Investigation of Cavitation Phenomena Occurring When an Underwater Pressure Pulse is Incident on a Yielding Surface: I," Admiralty UNDEX Works, Aug., UNDEX Research (ONR, 1950).

The Influence of Transient Flexural Waves on Dynamic Strains in Cylinders

T. E. Simkins[31]

The displacement response of a semi-infinite, thin-walled cylinder to a pressure moving at a constant velocity has been solved by Sing-chih Tang in closed form except for an integral term which Tang was forced to evaluate numerically. In this paper, an asymptotic evaluation of this integral is given which adds considerably to the physical interpretation of the solution. In brief, the asymptotic evaluation represents the long-term propagation of transients in the cylinder and their interaction with the steady-state solution.

Nomenclature

X = $\sqrt{12}x/h$
W = w/h
T = $\sqrt{12}v_d t/h$
P = $p/12\kappa G$
E = Young's modulus
w = midwall radial displacement
κ = shear correction factor
R = tube radius at midwall
V_c = critical value of $V_p = \sqrt{2\delta q}$
v_d^2 = $E/(1-\nu^2)\rho$
q^2 = $E/12\kappa G\ (h/R)^2$
δ^2 = $(1-\nu^2)\kappa G/E$
G = $E/2(1+\nu)$
x = distance from tube entrance
t = time
ν = Poisson's ratio
v_p = pressure velocity
K_c = $\sqrt{\delta q}$
V_p = v_p/v_d
Ω^2 = $K^4+\delta^2 q^2$
λ_1^2 = $\delta q/2$
K = $kh/\sqrt{12}$
h = tube wall thickness
p = pressure
ρ = density
k = wave number

1 Introduction and Background

The problem of a cylinder of infinite length subjected to a uniform pressure load moving at constant velocity has been studied by Jones and Bhuta (1964), Reismann (1965), and Tang (1965). These studies have resulted in steady-state solutions to

[31]Research Mechanical Engineer, Benet Laboratories, SMCAR-CCB-RA, B115, Watervliet Arsenal, Watervliet, NY 12189. Current address: 7 Lance Avenue, Troy, NY 12180.

Contributed by the Applied Mechanics Division of THE AMERICAN SOCIETY OF MECHANICAL ENGINEERS for publication in the JOURNAL OF APPLIED MECHANICS. Manuscript received by the ASME Applied Mechanics Division, Mar. 11, 1993; final revision, Nov. 16, 1993. Associate Technical Editor: J. N. Reddy.

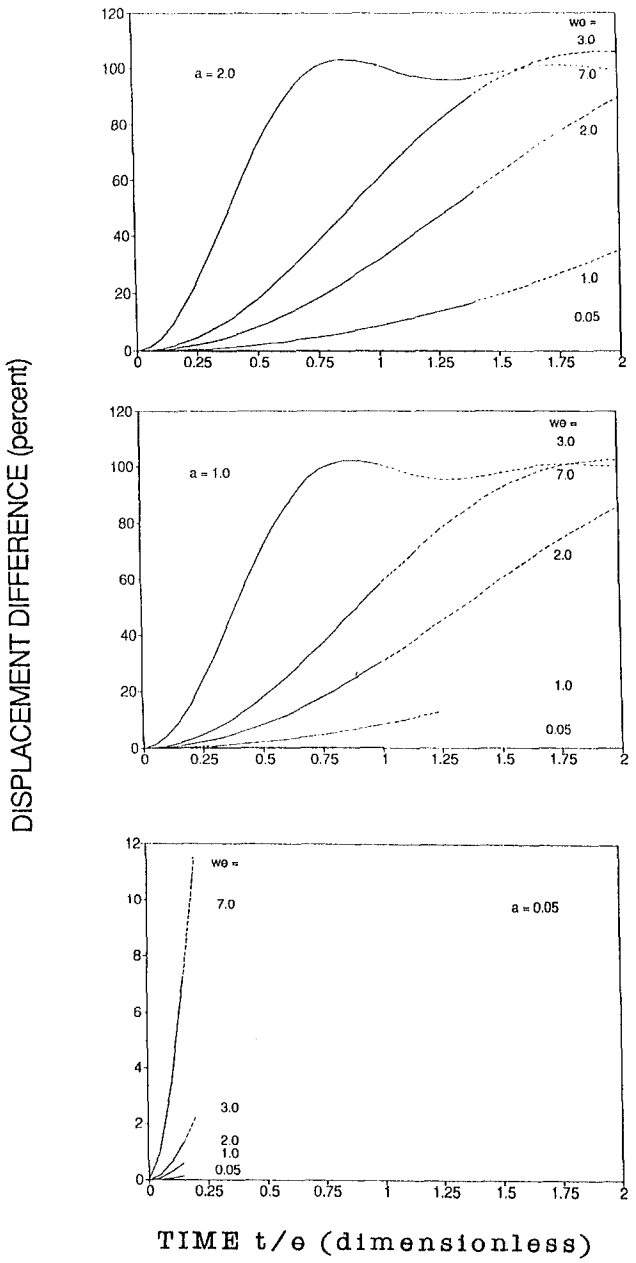

Fig. 2 Displacement difference (percent)

fened plate will always serve as an upper bound for displacement calculation.

References

Dawson, R. L., 1991, "The Use of the Plane Wave Fluid-Structure Interaction Loading Approximation in NASTRAN," NASTRAN User's Coloquium, Apr., David Taylor Research Center, Williamsburg, VA.

Kennard, E. H., 1941, "Report on Underwater Explosions," David Taylor Model Basin Underwater Explosion (UNDEX) Research, Oct; Office of Naval Research (ONR, 1950).

Kennard, E. H., 1943, "Explosive Load on Underwater Structures as Modified by Bulk Cavitation," David Taylor Model Basin, May, UNDEX Research (ONR, 1950).

Taylor, G. I., 1941, "The Pressure and Impulse of Submarine Explosion Waves on Plates," Cambridge University, July, UNDEX Research (ONR, 1950).

Temperly, H. N. V., 1944, "Theoretical Investigation of Cavitation Phenomena Occurring When an Underwater Pressure Pulse is Incident on a Yielding Surface: I," Admiralty UNDEX Works, Aug., UNDEX Research (ONR, 1950).

The Influence of Transient Flexural Waves on Dynamic Strains in Cylinders

T. E. Simkins[31]

The displacement response of a semi-infinite, thin-walled cylinder to a pressure moving at a constant velocity has been solved by Sing-chih Tang in closed form except for an integral term which Tang was forced to evaluate numerically. In this paper, an asymptotic evaluation of this integral is given which adds considerably to the physical interpretation of the solution. In brief, the asymptotic evaluation represents the long-term propagation of transients in the cylinder and their interaction with the steady-state solution.

Nomenclature

X = $\sqrt{12}x/h$
W = w/h
T = $\sqrt{12}v_d t/h$
P = $p/12\kappa G$
E = Young's modulus
w = midwall radial displacement
κ = shear correction factor
R = tube radius at midwall
V_c = critical value of $V_p = \sqrt{2\delta q}$
v_d^2 = $E/(1-\nu^2)\rho$
q^2 = $E/12\kappa G\ (h/R)^2$
δ^2 = $(1-\nu^2)\kappa G/E$
G = $E/2(1+\nu)$
x = distance from tube entrance
t = time
ν = Poisson's ratio
v_p = pressure velocity
K_c = $\sqrt{\delta q}$
V_p = v_p/v_d
Ω^2 = $K^4+\delta^2 q^2$
λ_1^2 = $\delta q/2$
K = $kh/\sqrt{12}$
h = tube wall thickness
p = pressure
ρ = density
k = wave number

1 Introduction and Background

The problem of a cylinder of infinite length subjected to a uniform pressure load moving at constant velocity has been studied by Jones and Bhuta (1964), Reismann (1965), and Tang (1965). These studies have resulted in steady-state solutions to

[31]Research Mechanical Engineer, Benet Laboratories, SMCAR-CCB-RA, B115, Watervliet Arsenal, Watervliet, NY 12189. Current address: 7 Lance Avenue, Troy, NY 12180.

Contributed by the Applied Mechanics Division of THE AMERICAN SOCIETY OF MECHANICAL ENGINEERS for publication in the JOURNAL OF APPLIED MECHANICS. Manuscript received by the ASME Applied Mechanics Division, Mar. 11, 1993; final revision, Nov. 16, 1993. Associate Technical Editor: J. N. Reddy.

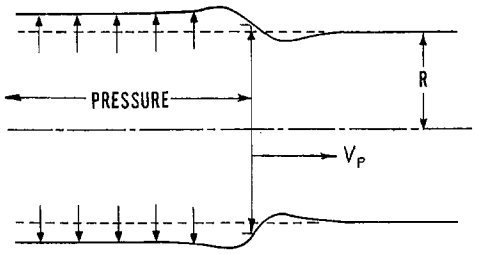

Fig. 1 Moving pressure in a cylinder of infinite length

the problem, employing somewhat different paradigms. In his publication, Tang also gave the solution to the initial value problem of a uniform pressure entering and traveling along a semi-infinite cylinder at a constant velocity. Dörr (1940) also studied this problem. Of the two, Tang's work will be referred to in the sequel. Tang's solution to this problem, however, includes an integral that he was only able to evaluate numerically making a qualitative interpretation of the result incomplete. The work herein makes use of the method of stationary phase to obtain an asymptotic evaluation of this integral from which significant additional information is obtained.

A synopsis of progress to date requires a brief review of the steady-state solution and its physical interpretation. The physics involved can be represented by the simplest possible model of the problem. To this end, a thin-walled cylinder, extending to infinity in both directions, is first assumed. The cylinder is subjected to a uniform and axisymmetric steplike pressure moving at a constant velocity, V_p, in the axial direction as shown in Fig. 1. Using Tang's notation, the equation of motion under these conditions is

$$\frac{\partial^4 W}{\partial X^4}+\delta^2 q^2 W+\frac{\partial^2 W}{\partial T^2}=\delta^2 P(1-H(X-V_pT))$$

$$-\infty<X<\infty \text{ and } T\geq 0. \quad (1)$$

P is constant and represents the magnitude of the moving pressure. H is the Heaviside step function:

$$H(X-V_pT)=0 \quad X\leq V_pT$$

$$=1 \quad X>V_pT.$$

The steady-state solution to this system has been given in the previously cited references. Letting V_c denote the lowest *critical velocity* of the moving pressure, Tang's results for this problem appear as follows.

For $V_p<V_c$:

$$W(X, T)=W_1(X-V_pT) \quad (2)$$

where

$$W_1(\eta)=\frac{P}{2q^2}\left\{2-e^{m\eta}\left[\cos n\eta+\frac{n^2-m^2}{2mn}\sin n\eta\right]\right\};\ \eta\leq 0$$

$$W_1(\eta)=\frac{P}{2q^2}\left\{e^{-m\eta}\left[\cos n\eta-\frac{n^2-m^2}{2mn}\sin n\eta\right]\right\};\ \eta\geq 0$$

where $K=\pm n\pm im$ is a (complex) root of the equation:

$$K^4-V_p^2K^2+\delta^2q^2=0. \quad (3)$$

For $V_p>V_c$:

$$W(X, T)=W_0(X-V_pT) \quad (4)$$

where

$$W_0(\eta)=\frac{P}{q^2}-\frac{P\delta^2}{n_2^2(n_1^2-n_2^2)}\cos n_2\eta;\ \eta\leq 0$$

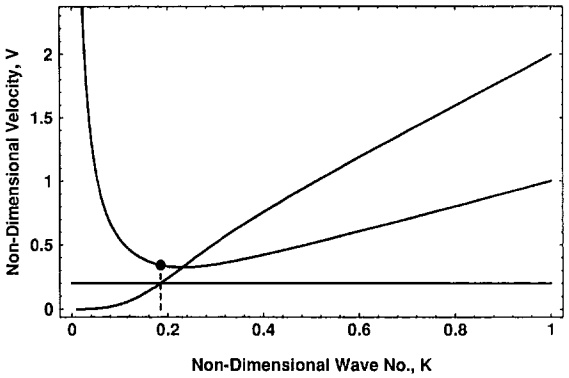

Fig. 2 Dispersion characteristics for a thin-walled cylinder

$$W_0(\eta)=-\frac{P\delta^2}{n_1^2(n_1^2-n_2^2)}\cos n_1\eta;\ \eta\geq 0$$

and where $K=\pm n_1,\ \pm n_2$ is a real root of Eq. (3).

Equation (3) is identical to the dispersion equation for freely propagating flexural waves if $V_{ph}(K)$ is substituted for V_p, where V_{ph} represents the *phase velocity* of a flexural wave having real wave number K. The *group velocity* of such a wave is then simply

$$V_g(K)=KV'_{ph}(K)+V_{ph}(K);\ Im(K)=0. \quad (4)$$

As pointed out by Reismann (1965), a condition for resonance is established when $V_g(K)=V_{ph}(K)=V_p$. From Eq. (4) this condition amounts to the vanishing of $V'_{ph}(K)$. Setting V'_{ph} equal to zero gives a value $K_c=\sqrt{\delta q}$ such that $V_{ph}(K_c)=V_c=\sqrt{2\delta q}$, a critical velocity of the pressure load which will cause W_1 to become unbounded. While there are other critical pressure velocities, only the lowest, V_c, is available from this elementary model. The curves representing $V_g(K)$ and $V_{ph}(K)$ are shown in Fig. 2.

Figures 3(*a*) and 3(*b*) show the radial displacement, W_1, in the neighborhood of the moving pressure front when $V_p=.85V_c$ and $V_p=.985V_c$, respectively. The plots have been normalized with respect to P/q^2, the deformation caused by a static application of P throughout the entire cylinder. When normalized in this way, the ordinate can be called the *dynamic amplification*. The abcissa represents the nondimensional distance measured from the pressure front. The figures exemplify the displacement amplification that occurs as V_p approaches V_c. Figure 4 summarizes this amplification as a function of the pressure velocity, V_p, and somewhat resembles that derived from the harmonic excitation of a single-degree-of-freedom system in which the abcissa is the forcing frequency. Thus one is tempted to draw at least a loose analogy between the two problems.

2 Semi-Infinite Cylinder: The Initial Value Problem

Once again the governing differential equation is taken to be (1). In treating this problem, Tang chose zero values for the initial velocity and displacement. Fixed radial displacements were chosen as the end condition at $X=0$ and the displacement was required to be bounded as $X\to\infty$. Tang found that when $V_p<V_c$, the radial displacement of the tube wall in response to a moving pressure entering the tube at $X=0$ at constant velocity, V_p, to be

$$W(X, T)=W_1(X-V_pT)+W_2(X+V_pT)$$

$$+W_3(\lambda_1X)+I(X, T) \quad (5)$$

where $W_1(\eta)$ is as defined in the previous section and

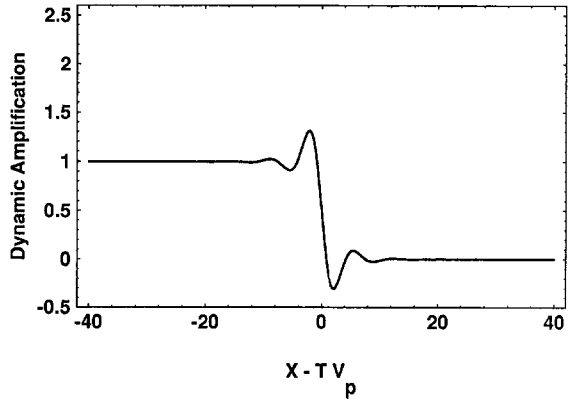

Fig. 3(*a*) $V_p = .85V_{cr}$

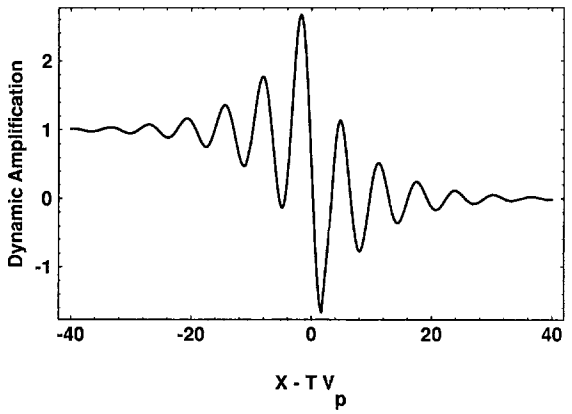

Fig. 3(*b*) $V_p = .985V_{cr}$

Fig. 3 Radial deformation in the neighborhood of the pressure front (*a*) $V_p = .85V_c$; (*b*) $V_p = .985V_c$

$$W_2(\eta) = \frac{P}{2q^2} e^{-mn} \left(\cos n\eta - \frac{n^2 - m^2}{2mn} \sin n\eta \right)$$

$$W_3(\eta) = -\frac{P}{q^2} e^{-\eta} \cos \eta$$

$$I(X, T) = \frac{-2\delta^2 P}{\pi} \int_0^\infty \left(\frac{1}{\Omega^2} - \frac{1}{\Omega^2 - V^2K^2} \right) \frac{\cos \Omega T \sin KX}{K} dK$$

and

$$\Omega^2 - K^4 + \delta^2 q^2.$$

Physically it can be expected that the pressure, which enters the tube at velocity V_p, will excite a strong transient as it suddenly expands the tube at the entrance, $X = 0$. However, even without damping, dispersion can be expected to attenuate the effect of this transient deformation as it travels sufficiently far into the tube at which time the deformation near the pressure front should appear very much like the steady-state solution $W_1(X - V_pT)$, given in the previous section. This expectation is supported by the explicit appearance of W_1 in the displacement expression (5). Except for $W_1(X - V_pT)$ and $I(X, T)$, the remaining terms in Eq. (5) are needed to satisfy the diaphragm boundary condition and have negligible effects at sufficiently large X. This restriction on X depends on the difference between V_p and V_c; i.e., X must increase as $V_p \to V_c$ if the same level of approximation is to be maintained. The deformation near the pressure front, $X = V_pT$, is of particular interest.

As noted by Tang, all of the terms in Eq. (5) except $I(X, T)$ can be interpreted as steady-state solutions to particular loadings of the infinite cylinder. It follows that any transient effects are contained in $I(X, T)$. This term is analogous to that which appears in the solution to the harmonically forced oscillator and, in keeping with this analogy, can be thought of as a *transition* or *start-up* transient. Thus (at sufficiently large X) the two main terms in the solution in regions of the tube not too close to the entrance, especially in the neighborhood of the pressure front, are the steady-state solution corresponding to a moving pressure in an infinite tube and the transition term, $I(X, T)$.

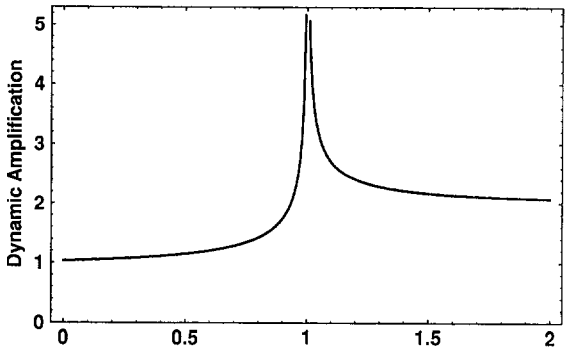

Fig. 4 Effect of pressure velocity on maximum radial displacement

Pursuing the analogy of the harmonically forced oscillator, where the "start-up" transient results in the formations of *beats* (a harmonic modulation of the steady-state response) which become more and more apparent as the natural and forcing frequencies approach each other, it might be expected that a similar effect occurs for the case at hand.

3 Asymptotic Expansion of $I(X, T)$

Substituting

$$\cos \Omega T \sin KX = \frac{1}{2} Im\{e^{(iKX + \Omega T)} + e^{i(KX - \Omega T)}\}$$

gives

$$I(X, T) = \frac{-2\delta^2 P}{\pi} \int_0^\infty F(K) \cos \Omega T \sin KX \, dK$$

$$= -\frac{\delta^2 P}{\pi} Im \left\{ \int_0^\infty F(K) e^{ih_1(K)T} dK + \int_0^\infty F(K) e^{ih_2(K)T} dK \right\} \quad (6)$$

where

$$F(K) = \frac{1}{K} \left\{ \frac{1}{\Omega^2} - \frac{1}{\Omega^2 - V^2K^2} \right\}$$

and

$$h_1(K) = \frac{KX}{T} + \Omega(K); \; h_2(K) = \frac{KX}{T} - \Omega(K).$$

Using the method of stationary phase as described by Whittam (1974) (see also Davies, 1948), the first term of an asymptotic expansion of (6) can be obtained for large T. The contribution from the first integral of (6) is negligible since $h_1(K)$ has no stationary point in the region $K > 0$. The major contribution

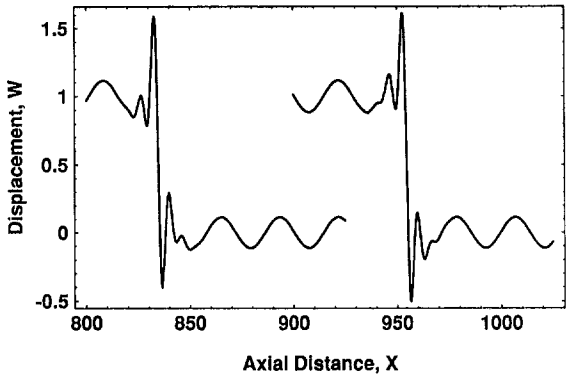

Fig. 5(*a*) Radial displacement at two stations along the cylinder at successive times

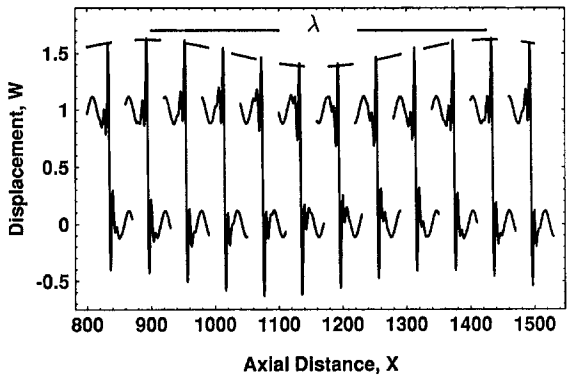

Fig. 5(*b*) Radial displacement at several stations along the cylinder at successive times. The beat wavelength is clearly visible.

from the second integral is from the neighborhood of $K=K_0$ where K_0 is the value of K such that $h_2(K)$ is stationary, i.e.,

$$h_2'(K_0)=\frac{X}{T}-\Omega'(K_0)=0$$

or

$$\Omega'(K_0)=\frac{X}{T}. \tag{7}$$

It is noted that $\Omega'(K_0)$ is simply the group velocity associated with the wave number K_0.

The stationary phase result for the second integral of (6) can then be written

$$-\frac{\delta^2 P}{\pi}\,Im\int_0^\infty F(K)e^{i(KX/T-\Omega(K))T}dK=$$

$$-\frac{\delta^2 P}{\pi}\,Im\left\{F(K_0)\sqrt{\frac{2\pi}{T|\Omega''(K_0)|}}e^{-i\Omega(K_0)T+iK_0X-i\pi/4\ \mathrm{sgn}\ \Omega''(K_0)}\right\}$$

$$=F(K_0)\delta^2 P\sqrt{\frac{2}{\pi T|\Omega''(K_0)|}}\sin[\Omega(K_0)T - K_0X+\frac{\pi}{4}\ \mathrm{sgn}\ \Omega''(K_0)].$$

From the expression for Ω^2,

$$\Omega''(K_0)=\frac{2K_0^2}{\Omega(K_0)^3}\,[\Omega^2(K_0)+2q^2\delta^2]>0.$$

Thus, the asymptotic evaluation for $I(X, T)$ is

$$F(K_0)\delta^2 P\sqrt{\frac{2}{\pi T\Omega''(K_0)}}\sin\left[\Omega(K_0)T-K_0X+\frac{\pi}{4}\right]. \tag{8}$$

4 Interpretation of Results

The stationary phase result states that the dominant part of the transient disturbance initiated at $(X=T=0)$ that arrives at a particular location X at time T will have traveled with a group velocity X/T and will consist of the dominant wave number K_0 determined from Eq. (7). If the motion at a fixed value of X is observed, where X is large enough for Eq. (8) to be satisfied and W_2+W_3 to be ignored, the displacement will consist of the steady-state terms, $W_1(X-V_pT)$ having frequency nV_p and $I(X, T)$ oscillating with frequency $\Omega(K_0)$. Referring again to Fig. 2, K_0 is the wave number of a freely propagating wave (excited at $X=0$ by the sudden entrance of the pressure front) having V_p as its group velocity. The figure also shows that the phase velocity of this free wave, $V(K_0)$ is greater than V_p. The beat frequency observed at fixed X is simply $(nV_p=\Omega(K_0))$:

Moving along with the pressure front, $X=V_pT$, Eq. (8) can be written

$$I(X, T)\sim F(K_0)\delta^2 P\sqrt{\frac{1}{\pi T\Omega''(K_0)}}\{\cos\beta T+\sin\beta T\} \tag{9}$$

where

$$\beta=\Omega(K_0)-K_0V_p.$$

Thus, for large T such that (8) is valid and $W2+W_3$ can be ignored, the radial displacement response (5) at the pressure front will essentially consist of a harmonic modulation of the steady-state response function $W_1(X-V_pT)$ decreasing in amplitude as $\sqrt{1/T}$ It is noted that β vanishes as $V_p\to V_c$.

Figures 5(*a*) and 5(*b*) show this displacement in the neighborhood of the pressure front progressively along the tube at successive times for the case $V_p/V_c=.918$. From Fig. 5(*b*) a *beat wavelength* can be observed—the distance, λ, along the cylinder corresponding to one period of the modulation. Substituting $T=X/V_p$ in Eq. (9),

$$\lambda=\frac{2\pi}{[\Omega(K_0)/V_p-K_0]}. \tag{10}$$

λ has engineering significance in that it represents the distance between strain maxima along the tube. The net effect of the transient is thus to periodically raise the strain levels in the tube, by an amount given by Eq. (9), to values greater than those predicted by the steady-state theory alone.

References

Dörr, J., 1943, "Der unenlichen federnd gebetteten Balken unter dem Einfluss einer gleichförmig between Last," *Ingenieur-Archiv*, Vol. 14, pp. 167-192.

Davies, R. M., 1948, "On a Critical Study of the Hopkinson Pressure Bar," *Phil. Trans.*, Ser. A., Vol. 240, p. 375.

Jones, J. P., and Bhuta, P. G., 1964, "Response of Cylindrical Shells to Moving Load," ASME JOURNAL OF APPLIED MECHANICS, Vol. 31, pp. 105-111.

Reismann, H., 1965, "Response of a Pre-stressed Cylindrical Shell to Moving Pressure Load," *Solid Mechanics*, Vol. 2, Part 2, S. Ostrach and R. H. Scanlon, eds., Pergamon Press, Oxford, pp. 349-363.

Tang, S., 1965, "Dynamic Response of a Tube Under Moving Pressure," ASCE *Journal of the Engineering Mechanics Division*, Vol. 91, No. EM 5, pp. 97-121.

Whittam, G. B., 1974, *Linear and Nonlinear Waves*, John Wiley and Sons, pp. 371-374.

A Note Related to Energy Release Rate Computations for Kinking Interface Cracks

P. H. Geubelle[32] and W. G. Knauss[33]

With the growing importance of composite materials and structures, including packaged electronic (chip) devices, the need to better understand and control failure behavior at and near interfaces has taken on also increased engineering significance. In comparison with fracture of homogeneous solids, the (linearly) elastic analysis of "brittle" interfacial fracture problems suffers from complications associated with the appearance of a contact zone very close to the tip of the interface crack and with the "oscillatory" character of the near-tip stress distribution. In contrast to homogeneous solids, this stress and deformation field behavior complicates the fracture analysis of the kinking behavior of an interface crack since it makes the usually so useful quantity of the energy release rate nonunique when the crack kinks away from the interface.

The question arises then as to whether the dependence of the energy release rate G on the length Δl of the (virtual) crack extension is related to the presence of a contact or interpenetration zone adjacent to the tip of the interface crack. The objective of the present note is to somewhat quantify the influence of the small contact zone on the Δl-dependence of the energy release rate. This analysis can, for example, be used in finite element investigations of the interface crack kinking behavior (Geubelle and Knauss, 1991) to determine whether the discretization of the crack-tip region eliminates sufficient detail so as to introduce a sizable error in the numerical computation of the energy release rate.

At least a partial answer to this question may be provided if one could determine the contribution to the energy release rate that derives from the immediate vicinity of the crack tip relative to that for a larger distance along the crack extension. Thus, if the total advance of the crack is Δl, one would be interested in determining what contribution to G derives from an arbitrary fraction δ of that length, but located immediately adjacent to the crack tip (Fig. 1). We provide an answer to this question in closed form *when the crack propagates along the interface*. While we recognize that propagation of a crack along an interface yields unique energy release rates, while the kink problem does not, we believe that the present contribution establishes a size scale relation that allows an estimate of the influence of the contact zone on the computed value of G.

The size r_c of the oscillation zone can be expressed as (Rice, 1988)

$$\frac{r_c}{l}=\exp\left[\frac{1}{\epsilon}\left(\tan^{-1}(2\epsilon)-\gamma-\text{sign}(\epsilon)\pi\right)\right] \tag{1}$$

where l is a characteristic length scale (such as, for example, the initial length of the crack) which appears in the definition of the stress intensity factors K_a (see relation (2) in (Geubelle and Knauss, 1991)), ϵ is the commonly used oscillatory index and $\gamma=\tan^{-1}(K_2/K_1)$. Assuming that the contact zone represents a fraction $\delta=r_c/\Delta l$ of the crack extension length Δl, it is of interest to know how much of the computed energy release rate corresponds to this fraction of the extension length. In other words, one tries to compute the ratio

$$h(\delta;\epsilon)=G_\delta/G, \tag{2}$$

where G is the total energy release rate corresponding to the extension Δl, and G_δ is the fraction of G corresponding to a fraction $\delta_*\Delta l$ of the crack extension.

A relatively simple analytical expression for $h(\delta;\epsilon)$ can be derived when the crack extension is along the interface ($\omega=0$ deg). In this case, one writes[34]

$$G=\lim_{\Delta l\to 0}\frac{1}{2\Delta l}\int_0^{\Delta l}[\sigma_{\alpha 2}(x_1)\Delta u_\alpha(\Delta l-x_1)]dx_1,$$

$$G_\delta=\lim_{\Delta l\to 0}\frac{1}{2\Delta l}\int_0^{\delta*\Delta l}[\sigma_{\alpha 2}(x_1)\Delta u_\alpha(\Delta l-x_1)]dx_1,\quad(0\le\delta\le 1) \tag{3}$$

where Δu_α are the displacement jumps across the crack and $\sigma_{\alpha\beta}$ are the stresses ahead of the crack tip. The analytical expression of G has been derived by Malyshev and Salganik (1965) as

$$G=\frac{\pi c_{12}(1+4\epsilon^2)}{2\cosh(\pi\epsilon)}, \tag{4}$$

where

$$c_{12}=\frac{(c_1+c_2)(K_1^2+K_2^2)}{8\pi(1+4\epsilon^2)\cosh(\pi\epsilon)}, \tag{5}$$

with the material constants c_α defined in Section 4 of Geubelle and Knauss (1991). Combining the expressions of the stresses along the interface and the displacement jumps behind the crack tip with (3*b*), one obtains

$$G_\delta=\lim_{\Delta l\to 0}\frac{c_{12}}{\Delta l}\left[\int_0^{\Delta l}\sqrt{\frac{\Delta l-x_1}{x_1}}\cos\left(\epsilon\ln\frac{\Delta l-x_1}{x_1}\right)dx_1\right.$$
$$\left.+2\epsilon\int_0^{\Delta l}\sqrt{\frac{\Delta l-x_1}{x_1}}\sin\left(\epsilon\ln\frac{\Delta l-x_1}{x_1}\right)dx_1\right]. \tag{6}$$

The transformation

$$y=\frac{\Delta l-x_1}{x_1} \tag{7}$$

leads to

$$h(\delta;\epsilon)=\frac{2\cosh(\pi\epsilon)}{\pi(1+4\epsilon^2)}\{\Re[I]+2\epsilon\Im[I]\}, \tag{8}$$

where

$$I=\int_{1-\delta/\delta}^{\infty}\frac{y^{1/2+i\epsilon}}{(y+1)^2}dy, \tag{9}$$

and $\Re[I]$ and $\Im[I]$ denote the real and imaginary parts of I, respectively. After integration by parts, (9) can be rewritten as

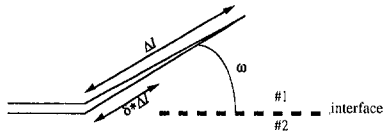

Fig. 1 Geometry of the interface crack kinking problem

[32]Graduate Student, Department of Aeronautics and Applied Mechanics, California Institute of Technology, Pasadena, CA 99125. Mem. ASME.

[33]Professor of Aeronautics and Applied Mechanics, Graduate Aeronautical Laboratories, California Institute of Technology, Mail Stop 105-50, Pasadena, CA 91125. Mem. ASME.

Contributed by the Applied Mechanics Division of The American Society of Mechanical Engineers for publication in the Journal of Applied Mechanics. Manuscript received by the ASME Applied Mechanics Division, Mar. 23, 1992; final revision, Oct. 26, 1993. Associate Technical Editor: M. E. Fourney.

[34]Greek indices take the values 1 and 2. Summation on repeated indices is implied.

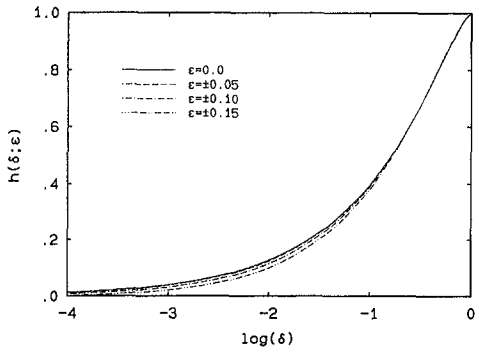

Fig. 2 $h(\delta;\epsilon)$ **versus crack extension fraction** δ **for various values of** ϵ

$$I=\delta^{1/2-i\epsilon}(1-\delta)^{1/2+i\epsilon}+\left(\frac{1}{2}+i\epsilon\right)B\left(\frac{1}{2}+i\epsilon,\frac{1}{2}-i\epsilon\right)\times\left\{1-I_{1-\delta}\left(\frac{1}{2}+i\epsilon,\frac{1}{2}-i\epsilon\right)\right\},\quad(10)$$

where $B(a,b)$ is the Beta function and $I_x(a,b)$ is the incomplete normalized Beta function (Abramowitz and Stegun, 1972) defined as

$$I_x(a,b)=\frac{B_x(a,b)}{B(a,b)},\quad(11)$$

where

$$B_x(a,b)=\int_0^x t^{a-1}(1-t)^{b-1}dt.\quad(12)$$

Using the properties

$$I_x(a,b)=1-I_{1-x}(b,a),\quad(13)$$

$$B\left(\frac{1}{2}+i\epsilon,\frac{1}{2}-i\epsilon\right)=\frac{\pi}{\cosh(\pi\epsilon)},\quad(14)$$

the final expression of the integral I is obtained as

$$I=\delta^{1/2-i\epsilon}(1-\delta)^{1/2+i\epsilon}+\left(\frac{1}{2}+i\epsilon\right)\frac{\pi}{\cosh(\pi\epsilon)}I_\delta\left(\frac{1}{2}-i\epsilon,\frac{1}{2}+i\epsilon\right).\quad(15)$$

The value of $h(\delta;\epsilon)$ is then computed by combining (8) and the following series representation of I

$$I=\frac{\delta^{1/2-i\epsilon}(1-\delta)^{1/2+i\epsilon}}{\frac{1}{2}-i\epsilon}\left[1+\frac{1+2i\epsilon}{3-2i\epsilon}\sum_{n=1}^{\infty}\rho_n\right],\quad(16)$$

where the coefficients ρ_n of the infinite sum are determined recursively by

$$\begin{cases}\rho_1=\delta,\\ \rho_n=\dfrac{n\delta}{\left(\frac{1}{2}+n-i\epsilon\right)}\rho_{n-1}.\end{cases}\quad(17)$$

The δ-variation of $h(\delta;\epsilon)$ is illustrated in Fig. 2 for various values of ϵ, showing very little effect of the oscillation parameter. Furthermore, the result indicates that the contribution to the value of the total energy release rate over the contact zone is limited to less than ten percent for values of $r_c/\Delta l$ of up to 0.01.

References

Abramowitz, M., and Stegun, I. A., 1972, *Handbook of Mathematical Functions*, Dover, New York.

Geubelle, P. H., and Knauss, W. G., 1991, "Propagation at the near Bimaterial Interfaces: Linear Analysis," *Galcit SM Report 91-17*, Caltech, submitted to ASME JOURNAL OF APPLIED MECHANICS.

Malyshev, B. M., and Salganik, R. L., 1965, "The Strength of Adhesive Joints Using the Theory of Crack," *Int. J. Fract. Mech.*, Vol. 1, pp. 114-128.

Rice, J. R., 1988, "Elastic Fracture Mechanics Concepts for Interfacial Cracks," ASME JOURNAL OF APPLIED MECHANICS, Vol. 55, pp. 98-103.

Journal of Applied Mechanics

Book Reviews

Introduction to Optimization of Structures, by N. V. Banichuk (English translation by V. Komkov of the 1986 Russian edition). Springer-Verlag, New York, 1990. 300 pp. Price: $89.00.

REVIEWED BY C. W. BERT[1]

This book presents an introduction and review of the state of the art of structural optimization from a Russian point of view. It has two parts: the first part, consisting of five chapters, presents the theory and techniques of structural optimization. The second part, consisting of three chapters, is devoted to applying the individual criteria of strength, rigidity, and stability.

Chapter 1 presents an overview of static, dynamic, and multicriteria optimal structural design. Chapter 2 introduces the concepts of auxiliary design parameters and dual optimization problems, while Chapter 3 discusses optimality conditions. Chapter 4 covers both analytical and numerical techniques for optimization of distributed-parameter structural systems. The specific techniques discussed include analytical, perturbation, finite difference, finite element, and boundary integral methods. Chapter 5 treats techniques for optimizing discrete structural systems.

Chapter 6 deals with designing for minimum weight on the basis of constraints on strength. Structures considered include beam webs, many-member trusses, shells of revolution, and plates with stress concentration. Chapter 7 is concerned with designing for rigidity criteria in straight and curved beams, torsion bars, shells, and plates subjected to either plane stress or plate bending. Chapter 8 involves optimization for either conservative or nonconservative elastic stability with emphasis on problems involving one physical dimension.

The book, unfortunately, does not give much detail on numerical/computational considerations nor does it consider structures composed of composite materials. However, it contains an extensive number of references (totaling 444) at the end of each chapter plus an additional bibliography listing 72 publications. The book is well written and it is recommended to those involved in structural optimization.

Tyre Models for Vehicle Dynamics Analysis, edited by H. B. Pacejka, Swets & Zeitlinger, Amsterdam, 1993. 192 pp. Price: $145.00.

REVIEWED BY C. W. BERT[1]

This volume constitutes the Proceedings of the First International Colloquium on Tyre Models for Vehicle Dynamics Analysis, held in Delft, The Netherlands, Oct. 21–22, 1991. It is also a supplement to Vol. 21 of the journal, *Vehicle System Dynamics*.

The volume contains 14 papers and two abstracts. The conference was truly international with papers from Austria, Czechoslovakia, Germany, Italy, Luxembourg, The Netherlands, Sweden, United Kingdom, and the U.S. The topics of the papers ranged from analytical, empirical, and numerical modeling to system identification and experimentation. This book should be of interest to engineers and researchers concerned with the title subject, as well as automotive dynamics specialists.

Concepts in Submarine Design, by Roy Burcher and Louis Rydill. Cambridge University Press, New York, 1994. 300 pages. Price: $74.95.

REVIEWED BY C. W. BERT[1]

This interesting book is the first one on this subject to appear in the past ten years. Its authors have been involved in design of naval submarines for about 30 years. Although emphasis is on naval submarines, much of the information should be applicable to other kinds of manned underwater vehicles.

The objective of the book is to introduce the process of designing a submarine by providing the fundamental principles. More emphasis is placed on creativity and concept synthesis than on methods of analysis.

The first chapter provides a brief introduction to the general principles of submarine design, followed by a short chapter on the history with emphasis on design milestones since 1899. Succeeding chapters cover hydrostatics, the weight/space relationship, structures, propulsion, geometric form and internal arrangements, dynamics and control, major systems, and construction and costs. The final chapter ties all of the previous aspects together in connection with the process of generating a conceptual design to meet the operational requirements. A list of references and bibliography are provided at the back of the book.

This book should be of great assistance to the novice embarking on a career in submarine design or operation. It may also be of interest to naval architects and marine engineers experienced with surface ships but not familiar with the special requirements for underwater vehicles.

[1]Benjamin H. Perkinson Chair and Director, School of Aerospace and Mechanical Engineering, The University of Oklahoma, Norman, OK 73019-0601. Fellow ASME.